Lecture Notes in Earth System Sciences

Daniel E. Harlov
Håkon Austrheim

Metasomatism and the Chemical Transformation of Rock

The Role of Fluids in Terrestrial and Extraterrestrial Processes

Springer

Lecture Notes in Earth System Sciences

For further volumes:
http://www.springer.com/series/10529

Daniel E. Harlov • Håkon Austrheim

Metasomatism and the Chemical Transformation of Rock

The Role of Fluids in Terrestrial and Extraterrestrial Processes

Springer

Daniel E. Harlov
Section 3.3
Chemistry and Deutsches
GeoForschungsZentrum - GFZ
Telegrafenberg
Potsdam
Germany

Håkon Austrheim
Physics of Geological Processes
University of Oslo
Oslo
Norway

ISSN 2193-8571 ISSN 2193-858X (electronic)
ISBN 978-3-642-28393-2 ISBN 978-3-642-28394-9 (eBook)
DOI 10.1007/978-3-642-28394-9
Springer Heidelberg New York Dordrecht London

Library of Congress Control Number: 2012940213

Printed on acid-free paper

Springer is part of Springer Science+Business Media (www.springer.com)

Contents

Chapter 1
Metasomatism and the Chemical Transformation of Rock: Rock-Mineral-Fluid Interaction in Terrestrial and Extraterrestrial Environments

Daniel E. Harlov and Håkon Austrheim

1.1 Metasomatism

The term metasomatism comes from the Greek μετά (meta = change) and σῶμα (soma = body). The term was originally coined by C.F. Naumann in Lehrbuch der Mineralogie, published by Engelman in Leipzig in 1826. The current definition of metasomatism, according to the IUGS Subcommission on the Systematics of Metamorphic Rocks (SSMR), is "a metamorphic process by which the chemical composition of a rock or rock portion is altered in a pervasive manner and which involves the introduction and/or removal of chemical components as a result of the interaction of the rock with aqueous fluids (solutions). During metasomatism the rock remains in a solid state." Metamorphism comes from the Greek μετά (meta = change) and μορφε (morphe = form) and is defined by the IUGS SSMR as "a process involving changes in the mineral content/composition and/or microstructure of a rock, dominantly in the solid state. This process is mainly due to an adjustment of the rock to physical conditions that differ from those under which the rock originally formed and that also differ from the physical conditions normally occurring at the surface of the Earth and in the zone of diagenesis. The process may coexist with partial melting and may also involve changes in the bulk chemical composition of the rock." From these two definitions it is obvious that metasomatism and metamorphism of silicate rocks are commonly interrelated with each other. However, they can also be mutually exclusive. For example, metamorphism can be isochemical such that the chemical and isotopic characteristics of the protolith sedimentary or igneous

D.E. Harlov (✉)
Section 3.3 Chemistry and Deutsches, GeoForschungsZentrum-GFZ, Telegrafenberg, Potsdam D-14473, Germany
e-mail: dharlov@gfz-potsdam.de

H. Austrheim
Physics of Geological Processes (PGP), University of Oslo, Blindern, 1048, Oslo N-0316, Norway
e-mail: h.o.austrheim@geo.uio.no

D.E. Harlov and H. Austrheim, *Metasomatism and the Chemical Transformation of Rock*, Lecture Notes in Earth System Sciences,
DOI 10.1007/978-3-642-28394-9_1,

lithologies are retained. Also, the chemical changes seen during the high-grade transition of metamorphic rocks from amphibolite- to granulite-facies, can be due to the removal of fluid-rich partial melts. In contrast, sediment diagensis, fluid-aided deposition of ore veins or ore deposits, sea floor alteration, and alteration of surrounding rock by hot springs or meteoric fluids are fluid-dominated metasomatic process, which are generally not considered to be metamorphic.

Fluid-aided mass transfer and subsequent mineral re-equilibration are the two defining features of metasomatism in silicate rocks and must be present in order for metamorphism to occur. Taking into account geological time scales, the amount of fluid required need not be great (considerably less than 0.01% of the total volume of the rock) nor even in continuous flow but the fluid must be able to actively flow along grain boundaries and be chemically reactive with respect to the minerals it encounters such that efficient mass transfer is promoted. If the fluids are quite chemically reactive the possibility exists of fluid flow through the minerals themselves in the form of migrating fluid inclusions or porosity (see Chap. 14). Natural observation, coupled with experimental replication and thermodynamic verification, allows for insights into the chemistry and physical nature of the metasomatising fluid as a function of P-T conditions and the general host rock chemistry to be obtained. In general, the limited or total re-equilibration of silicate, oxide, sulfide, and phosphate minerals due to the passage of fluids takes place as the result of a coupled dissolution-reprecipitation process (see Chap. 5). Evidence for the passage of fluids through rock can take the form of altered mineral trace-element chemistry, partial to total re-equilibration of mineral phases, reaction textures along mineral grain boundaries, and/or trails of fluid inclusions through minerals. Lack of fluids generally means lack of re-equilibration between minerals and consequently a lack of information regarding the true P-T-X history of the rock.

Coupled with igneous and tectonic processes, metasomatism has played a major role in the formation of the Earth's continental and oceanic crust and the lithospheric mantle as well as in their ongoing evolution and consequent mutual relationships with respect to each other. Metasomatic processes can include ore mineralization (see Chap. 7), alteration of oceanic lithosphere (see Chap. 8), and mass transport in and alteration of subducted oceanic and continental crust and the overlying mantle wedge (see Chaps. 9 and 10). The latter has subsequent implications for mass transport, fluid flow, and volatile storage in the lithospheric mantle overall (see Chap. 12), as well as both regional and localized crustal metasomatism (see Chap. 4). Metasomatic alteration of accessory minerals, such as zircon, monazite, xenotime, or apatite or major minerals, such as micas, feldspars, and amphiboles, can allow for the dating of metasomatic events and gives additional information regarding the chemistry of the fluids responsible (see Chap. 6). Indications of massive fluid flow and subsequent total alteration of the original rock include skarns, greisens, and the serpentinization of oceanic crust (see Chaps. 7 and 8). Evidence for widespread and pervasive metasomatism in the lithospheric mantle is naturally coupled with similar evidence in high-pressure rocks such as granulite-, eclogite-, and blueschist-facies rocks (see Chaps. 10 and 11). Under such P-T conditions, the boundary between what is considered a fluid and what is considered a melt becomes

significantly blurred. Here, critical and supercritical one phase and multiphase CO_2-H_2O-NaCl-KCl-$CaCl_2$ fluids can play an important role with respect in enabling mineral reactions such as the solid-state conversion of biotite and amphiboles to orthopyroxene and clinopyroxene during granulite-facies metamorphism (see Chap. 11). Evidence for similar fluids in the lithospheric mantle include veins of obvious metasomatic origin that contain abundant megacrysts of apatite enriched in CO_2 and Cl. In the case of ultramafic massifs, which expose large volumes of upper mantle material, the effects of fluid infiltration can be traced coherently over scales of meters to kilometers (see Chap. 12). Present day movement of fluids in both the lithospheric mantle and deep to middle crust can be observed by geophysical techniques such as electrical resistivity and seismic measurements (see Chap. 13). Such observations, along with modeling (see Chap. 14), help to further clarify the picture of actual metasomatic processes inferred from basic petrographic, mineralogical, and geochemical data.

Metasomatism and probable metamorphism is not limited to terrestrial environments but can occur in extraterrestrial environments where H_2O exists in liquid form. The best studied of these extraterrestrial environments are the asteroids, for which numerous examples from meteorites exist (see Chap. 15). This does not exclude other terrestrial worlds such as Mars, Europa ganymede, Callisto, Enceladus, or Titan on or in which H_2O can exist as a liquid. Presumably metasomatism could and probably does occur on these worlds. In the case of Mars both the Spirit and Opportunity Rovers have spent the last 8 years providing ample evidence for Mars' H_2O-rich past (see http://marsrovers.jpl.nasa.gov/home/).

The goal of this volume is to bring together a diverse group of experts on the role of fluids in shaping terrestrial and extraterrestrial environments; each of whom is responsible for a specific chapter covering some aspect of metasomatism. Each chapter is designed to provide an up-to-date review of the effects of metasomatism on both terrestrial and extraterrestrial environments. In that respect this volume should be regarded as a starting off point for the student or professional interested in obtaining a firm foundation regarding the various areas of metasomatism covered by the chapters in this book. Subsequently it should serve as a basis for rich research opportunities in the years to come. In the following sections each of the chapters is summarized per the unique viewpoint of the individual authors.

1.2 The Chemical Composition of Metasomatic Fluids in the Crust: Chapter 2

Any crustal fluid can give rise to metasomatism when it migrates from one rock type to another, and metasomatism is normally associated with past fluid flow paths, such as fractures, faults, shear zones, or lithologies that were more permeable than those around them. This chapter specifically concerns infiltration metasomatism, driven by advection of fluids. Fluid compositions can be buffered by local host

rocks, or be mass-limited, where large amounts of brine overwhelm the buffer capacity of the host, or be kinetically-limited, where their composition reflects different reaction rates of different host minerals. Representative analyses of a wide range of crustal fluids from the literature are presented and discussed. Except in near-surface settings, metasomatism is generally associated with brines, and highly concentrated brines are particularly effective metasomatic agents.

Leaving aside mid-ocean ridge geothermal systems, examples of metasomatic fluids are sedimentary basin brines and magmatic fluids, but mantle and metamorphic fluids can also give rise to metasomatism. Basinal brines may be buffered or may show extreme compositions. Low-Br, NaCl brines, derived by dissolution of halite, are anomalously depleted in many metals while Br-rich brines evolve from the bittern brines remaining after halite precipitation, and are anomalously rich in K; after participating in dolomitisation, they are rich in Ca as well. Both types are implicated in ore formation and metasomatism (e.g., albitisation) in both sedimentary basins and their underlying crystalline basement.

Many acid magmas give off significant amounts of acidic fluids, often rather saline, as they crystallize. These may also contain distinctive volatile components derived from the melt (e.g. B, F) that play a role in metasomatic effects, such as greisenisation. Their high contents of transition metals mean that they are also potential ore-formers. Some deep-derived magmas act as vectors to bring mantle fluids into the crust. These fluids appear to be brines that are also highly charged with CO_2. One effect of degassing at crustal levels is that these fluids become undersaturated in silica and may leach silica during fenitisation.

Fluids released by metamorphic reactions are not in general a major cause of metasomatism, because they are usually released very slowly by endothermic reactions taking place in an over-pressured, and therefore, low-permeability environment. However, important exceptions do occur, such as the formation of metamorphic skarns due to the transient generation of a secondary porosity as infiltrating, silica-saturated, aqueous fluids trigger decarbonation reactions in carbonate rocks. Rapid exhumation of mid-crustal rocks at the end of orogeny can also drive rapid dehydration leading to gold-bearing quartz veins and associated metasomatism.

Comparison of a wide range of crustal fluids shows that they share many systematic characteristics. These can reflect the temperature at which they have interacted with the host rocks, their salinity, or their origin. They provide a basis for interpreting some of the common chemical changes seen in metasomatic rocks.

1.3 Thermodynamic Modeling and Thermobarometry of Metasomatised Rocks: Chapter 3

Determining the P-T conditions at which metasomatic reactions occur provides insight into the physical conditions at which fluid-rock interaction occurs in the crust. However, application of thermodynamic modeling to metasomatised rocks is

not without pitfalls. As with "normal" metamorphic rocks, the main difficulty is to select mineral compositions that were in equilibrium during their crystallization. This essential task is particularly difficult in metasomatised rocks because it is often difficult to distinguish textures produced by changes in P-T conditions from those caused by fluid-rock interactions and associated changes in bulk composition. Furthermore, the selection of minerals in equilibrium in metasomatised rocks is made difficult by the great variability in the scale of mass transfer, and therefore equilibrium, which varies from micrometer to hand sample or larger scales, depending on the amount of fluid involved and the fluid transport mechanisms (e.g. pervasive or focused). Another major limitation is that the composition of the fluid coming in or out of the rock is unknown. Since the fluid is a major phase component of the system, neglecting its impact on the phase relations might be problematic for thermobarometry. Despite these pitfalls, examples can be found in nature where thermobarometry apparently has been successfully applied. Pseudo-section thermobarometry is particularly suitable for metasomatised rocks because the effects of mass transfer can be explored through P-T-X phase diagrams. The application of thermodynamic modeling to metasomatised rocks requires (1) detailed mineralogical and textural investigation in order to select appropriate mineral compositions; (2) geochemical analyses which define the relative and absolute mass changes involved during the metasomatic event(s); and (3) forward modeling of the effects of mass transfer on phase relations.

1.4 Structural Controls of Metasomatism on a Regional Scale: Chapter 4

Examples of structurally controlled regional metasomatism span most metamorphic temperatures, pressures, and tectonic settings. Permeability is crucial, and may be intrinsic or the result of deformation processes such as micro-fracturing (e.g. grain boundary sliding), fracturing, faulting, foliation and shear zone development, and hydro-fracturing. Chromatographic theory has been used to explain metasomatic zonation, and applies not only where mineral reaction and isotopic fronts formed normal to the fluid flow in a porous medium, but also where flow was parallel to fractures or lithological contacts. Metasomatic fronts may be sharp, or broadened by diffusion and dispersion effects during fluid advection. Although debate continues, many workers have provided mineralogical and isotopic evidence for the existence of high, time-integrated fluid fluxes and fluid flow directions in many thermal aureoles and regional metamorphic belts. Studies of quartz veins and vein selvages in metamorphic rocks have provided examples both of local derivation of veins and derivation of silica, and metasomatic changes in the selvages during advection of external fluids. There also is debate as to whether metamorphic fluids in the middle crust are solely derived from devolatilisation reactions at depth or if processes such as dilatancy pumping or syn-metamorphic intrusion can lead to lateral or downward fluid advection.

Regional metasomatism occurs in many Proterozoic metamorphic belts, but the Mount Isa Inlier is probably the best natural laboratory regarding structural controls. It exhibits enormous strain heterogeneity at all scales that led to fluid channeling, diverse reactive rocks, episodic metamorphic and intrusive events spanning at least 250 Ma, as well as abundant sources of reactive saline and hypersaline fluids. Examples of widespread metasomatism in the Mount Isa Inlier include Na-Ca alteration associated with extensive breccia development in calcsilicate rocks and albitisation of pelitic schists and metapsammitic rocks.

1.5 Mechanisms of Metasomatism and Metamorphism on the Local Mineral Scale: The Role of Dissolution-Reprecipitation During Mineral Re-equilibration: Chapter 5

Metamorphism and metasomatism both involve the re-equilibration of mineral assemblages due to changes in pressure, temperature, and/or chemical environment. Both processes involve material transport but on different length scales, and therefore every metamorphic reaction is metasomatic on a local scale. Fluids provide a transport mechanism that is orders of magnitude faster than solid-state diffusion and induce re-equilibration through dissolution of parent phases and reprecipitation of products. This chapter deals with some of the questions related to such processes, including the mechanisms of fluid transport through low-permeability rocks, how coupling between dissolution and precipitation preserves the volume of a rock during metamorphism and metasomatism, and how textural criteria are used to define mechanisms of reactions. These issues are illustrated by examples taken from experiments as well as reactions in nature including a review of some aspects of the transformation of aragonite to calcite; the albite to jadeite + quartz reaction; albitisation; the origin of compositional zoning and inclusions in apatite; garnet replacement textures during eclogitisation; and the reaction mechanisms that produce corona textures. The chapter ends with a summary of the mechanism of pseudomorphic replacement by interface-coupled dissolution-precipitation.

1.6 Geochronology of Metasomatic Events: Chapter 6

In order to date any geological event, suitable mineral geochronometers that record that and only that event must be identified and analyzed. In the case of metasomatism, recrystallisation is a key process that controls both the petrology and the isotopic record of minerals. It can occur both in the form of complete neocrystallisation (e.g. in a vein) and as pseudomorphism, whereby coupled dissolution-reprecipitation on the submicroscopic scale plays a central role.

Recrystallisation may be complete or not, raising the possibility that relicts of a pre-metasomatic assemblage could be preserved. Because recrystallisation is energetically less costly at almost any temperature compared to diffusion, and because radiogenic isotopes (except ^{4}He) never diffuse faster than the major elements forming the mineral structure, there is a strong causal link between petrographic relicts and isotopic inheritance. This has been demonstrated for zircon, monazite, titanite, amphibole, K-feldspar, biotite, and muscovite. Metasomatic assemblages commonly contain such mixtures between relicts and newly formed phases, whose geochronology is slightly more complex than that of simple ideal systems, but can be managed by techniques that have become routine in the last decade. Because of its crucial role in controlling isotopic systematics, the petrogenesis of a mineral needs to be understood in detail, using microchemical analyses and micro-imaging techniques, before mineral ages can be correctly interpreted. As the occurrence of recrystallization is limited by the availability of water, minerals act as "geohygrometers" that allow constraints to be placed on the nature and age of fluid circulation episodes, especially metasomatic events.

1.7 Effects of Metasomatism on Mineral Systems and Their Host Rocks: Alkali Metasomatism, Skarns, Greisens, Tourmalinites, Rodingites, Black-Wall Alteration, and Listvenites: Chapter 7

Metasomatism is one of the key processes in the genesis and development of a wide range of mineral systems. Metasomatism is generally associated with the activity of volatiles exsolved from magmas, which act both within the causative intrusions and in the surrounding country rocks. In this chapter, key aspects of alkali metasomatism, metasomatism related to the formation of skarn systems; greisens; boron metasomatism (tourmalinites), and metasomatism associated with ultramafic rocks, are discussed. Sodic and potassic alteration in many magmatic-hydrothermal systems, such as the early stages of porphyry-type mineralization, is perhaps the more common type of metasomatic alteration. However, the best expression of alkali metasomatism is that associated with alkaline complexes and carbonatites. These provide one of the most interesting and complex cases of metasomatism, known as fenitisation. Fenites can host economic resources of REE minerals. Metasomatic processes in skarn mineral systems are also quite complex and range from low- to high-temperature mineral associations. Skarn mineral systems are generally polymetallic and include base metals and/or magnetite-apatite. Furthermore, high-temperature-low-pressure metamorphism can produce regional-scale metasomatic alteration of country rocks. Greisens are also linked to alkali metasomatic processes, usually in highly fractionated granitic cupolas. Greisen is represented by two key minerals, quartz and white mica, although these may be accompanied by other phases such as tourmaline, fluorite, and topaz. Greisens are typically associated with sn and/or w mineralization. Boron metasomatism leads to pervasive or selective tourmalinisation, usually connected with sn-w deposits

and breccia pipes. Stratiform tourmalinites occur in sedimentary sequences hosting massive sulphide deposits. Metasomatic processes affecting ultramafic rocks, can produce rodingites and listvenites, which in some cases may host gold mineralisation.

1.8 Metasomatism Within the Oceanic Crust: Chapter 8

From ridge to trench, the oceanic crust undergoes extensive chemical exchange with seawater. This is critical in setting the chemical and isotopic composition of the oceans and their rocky foundation. Although the overall exchange fluxes are great, the first-order metasomatic changes of crustal rocks are generally minor (usually $< 10\%$ relative change in major element concentrations). Drastic fluid-induced metasomatic mass transfers are limited to areas of very high fluid flux such as hydrothermal upflow zones. Epidotisation, chloritisation, and serizitisation are common in these upflow zones. They often feature replacive sulfide mineralization, which form significant metal accumulations below hydrothermal vent areas. Diffusional metasomatism is subordinate in layered (gabbroic-doleritic-basaltic) crust, because the differences in chemical potential between the different lithologies are minor. In heterogeneous crust (mixed mafic-ultramafic lithologies), however, diffusional mass transfers between basaltic lithologies and peridotite is very common. These processes include rodingitisation of gabbroic dikes in the lithospheric mantle and steatitisation of serpentinites in contact with gabbroic intrusions. Drivers of these metasomatic changes are strong across contact differences in the activities of major solutes in the intergranular fluids. Most of these processes take place under greenschist-facies conditions, where differences in the activities of silica and protons in the fluids are most pronounced. Simple geochemical reaction path models provide a powerful tool for investigating these processes. Because the oceanic crust is hydrologically active throughout much of its lifetime, the diffusional metasomatic zones are commonly also affected by fluid flow, so that a clear distinction between fluid-induced and lithology-driven metasomatism is not always possible. Heterogeneous crust is common along slow and ultraslow spreading ridges, where much of the extension is accommodated by faulting (normal faults and detachment faults). Mafic-ultramafic contacts hydrate to greater extents and at higher temperatures, than uniform mafic or ultramafic masses of rock. Hence, these lithologic contacts become mechanically weak at great lithospheric depth and are prone to capture much of the strain during exhumation and uplift of oceanic core complexes. Metasomatism therefore plays a critical role in determining the rheological properties of the oceanic lithosphere along slow oceanic spreading centers, which, in terms of length, comprise half of the global mid-ocean ridge system.

1.9 Metasomatism in Subduction Zones of Subducted Oceanic Slabs, Mantle Wedges, and the Slab-Mantle Interface: Chapter 9

Physical juxtaposition of chemically disparate rocks, and the mobility of "fluids" at scales up to tens of km, lead to myriad metasomatic effects in subduction zones, with larger-scale manifestations including the metasomatism related to mass flux leading to arc magmatism and convergent margin volatiles cycling. Subduction-zone metasomatism is initiated at very shallow levels, as oceanic slabs enter the trenches, bend and are potentially infiltrated by seawater, and sedimentary sections begin their journey into forearcs resulting in extensive physical compaction, fluid expulsion, and diagenetic alteration. Studies of forearc fluid geochemistry (e.g., in accretionary complexes, the Marianas margin, and serpentinite seamounts) track this shallow-level metasomatic alteration, whereas high- and ultrahigh-pressure metamorphic suites provide records of fluid generation and flow, and related metasomatism to depths approaching those beneath volcanic fronts (and, in a smaller number of cases, depths beyond those beneath arcs). Uncertainty remains regarding the geochemical influence of strongly mechanically mixed zones along the slab-mantle interface (i.e., in the "subduction channel"), represented by mélange zones in many metamorphic suites. Experimental studies predict dramatic changes in the physicochemical properties and metasomatic capabilities of subduction zone "fluids" as a function of depth. However, studies of metamorphic suites have yet to document the results of these changes. Further work thus is required on UHP suites representing subduction-zone depths of 100 km or greater. Work on higher-P suites is also necessary in order to test the generally accepted hypothesis that subduction zone metamorphism serves as a geochemical "filter" altering the compositions of deeply subducting rocks that then contribute to arc magmatism and the geochemical heterogeneity of the deeper mantle sampled by ocean-island basalts

1.10 Metasomatism During High-Pressure Metamorphism: Eclogites and Blueschist-Facies Rocks: Chapter 10

High-pressure (HP) and ultrahigh-pressure (UHP) metamorphic rocks, which represent parts of ancient subducted slabs, are the obvious target for obtaining constraints on the P-T conditions, and the composition and type of slab-derived fluids responsible for metasomatism in subduction-zone environments. Solute-poor, aqueous fluids, derived by prograde HP metamorphic devolatilisation reactions in subducted slabs, are generally thought to be responsible for trace-element transfer between the slab and mantle wedge. Both the slab and mantle wedge are then metasomatised, leading to the modification of bulk rock composition. At deeper levels in subduction zones at UHP conditions, dense solute-rich

transitional fluids (intermediate between hydrous silicate melts and aqueous fluids) or hydrous silicate melts are thought to become more important in the mobilization and transport of elements. Petrological and fluid inclusion data suggest that solute-poor aqueous fluids (solute $<$ ~30 wt% of fluid) mainly dominate the fluid budget during HP metamorphism of oceanic and continental crust in subduction zones (70–40 km depth). This is supported by experimental data favoring an aqueous fluid under HP conditions in cold subduction zones. These fluids are regarded by some researchers as being relatively inefficient in mobilizing and transporting elements as, for instance, has been suggested by experimentally derived fluid-mineral partitioning data. This is consistent with some geochemical studies of HP veins, which suggest a locally highly restricted fluid flow and thus only localized (small-scale) element transport. Similar conclusions of only short-distance fluid transport have also been supported by some stable isotope studies in HP terrains and by many fluid inclusion studies. However, significant trace element changes have been reported in metasomatic depletion haloes surrounding eclogite-facies dehydration veins, which constitute major conduits of channelized high fluid flow during prograde HP-metamorphism or for zones of high fluid-rock ratios and fluid flow. Consequently, understanding of the metasomatic processes leading to the mobilization and redistribution of major and trace elements within subduction zone rocks is crucial for (quantitatively) evaluating the bulk compositional changes that occurred under HP and UHP conditions.

1.11 Prograde, Peak, and Retrograde Metamorphic Fluids and Associated Metasomatism in Upper Amphibolite- to Granulite-Facies Transition Zones: Chapter 11

Granulites constitute a major part of the (lower) continental crust, occurring on a regional scale in many metamorphic belts. Their origin is generally discussed in terms of vapor-absent melting and fluid-assisted dehydration. The latter model is supported by the occurrence of two immiscible free fluids at both peak and retrograde conditions, *viz*. CO_2 and highly saline brines. Evidence includes fluid remnants preserved as inclusions in minerals, but also large-scale metasomatic effects. Metasomatic effects induced by fluid percolation at different scales and stages include: (1) Control of state variables (H_2O activity or O_2 fugacity), regional oxidation and so-called "granulite-facies islands"; (2) Small-scale metasomatism at mineral intergrain boundaries (e.g. K-feldspar micro-veins and/or myrmekites); (3) Large-scale metasomatism at the amphibolite to granulite-facies transition zone, as evidenced by (1) incipient charnockites, (2) metasomatic redistribution of elements traditionally considered as immobile (e.g. Zr, Th, REE), (3) peak metamorphic to retrograde bulk chemical processes (scapolitisation, albitisation), and (4) long-distance action of granulite fluids. The importance and widespread occurrence of these effects imply that large quantities of fluids are stored in the lower crust at peak

metamorphic conditions, and then expelled towards shallower crustal levels during retrogradation. The origin of these fluids is complex; some fluids are crustal, either far remnants of sedimentary waters (brines) or linked to metamorphic/melt reactions. However, especially for high-temperature granulites, the greatest proportion, mainly CO_2, is derived from the upper mantle, which also contains the same fluids found in the lower crust.

1.12 Mantle Metasomatism: Chapter 12

Direct evidence for metasomatic processes in the subcontinental lithospheric mantle (SCLM) is provided by mantle rocks in two very different geological situations. The first comprises xenoliths and xenocrysts entrained in a spectrum of magmatic rocks. Kimberlitic and related magmas typically sample ancient cratonic lithospheric keels, which are thick (150–250 km), relatively depleted, and complexly metasomatised. Alkali basalts and related magmas mainly sample thinner, more fertile Phanerozoic (off-craton) tectonic domains, or regions where older SCLM has been thinned. The other type of occurrence ("ultramafic massifs", ophiolites, and some ocean-floor peridotites) comprises fragments of the upper mantle that have been tectonically exposed or emplaced into the crust. The ultramafic massifs have the advantage of exposing large volumes of upper mantle material so that rock-type relationships can be defined; intrusive magmatic relationships (e.g. veins, dikes) and the effects of fluid infiltration can be traced coherently over scales of meters to kilometers. However, the deformation associated with tectonic emplacement can obscure essential information. Xenoliths (and xenocrysts) are smaller samples, and relationships between rock types are seldom visible. However, they can also provide fragments of relatively unaltered lithospheric mantle, as they generally reach the surface within 50 h after their entrainment in the host magma. Some idea of their original spatial context can be derived from geothermobarometry, the calculation from mineral compositions of the pressure and temperature at the level where the xenoliths were sampled. Indirect evidence of mantle metasomatism can be provided by the trace element and isotopic characteristics of small-volume magmas (e.g. alkali basalts) that have interacted with low-temperature, low-degree melts in their passage through the lithosphere. The geophysical signatures of metasomatised mantle domains can be recognized in some regions by seismic and gravity responses (reflecting mineralogy and composition, hence density), by high heat flow (reflecting high contents of K-U-Th), and by magnetotelluric signals that may indicate dispersed grain-boundary fluids.

Important rock types in the lithospheric mantle are defined as follows: (1) Peridotite mantle wall rocks (over 95% by volume) are ultramafic (olivine-dominated) in composition and may contain orthopyroxene (harzburgites), clinopyroxene (wehrlites), or orthopyroxene + clinopyroxene (lherzolites) as well as an aluminous phase (garnet, spinel or plagioclase depending on the pressure-temperature environment; garnet and chromite may coexist). (2) Eclogites are

clinopyroxene + garnet rocks, mafic in bulk composition and equilibrated under high-pressure and low-geothermal gradient conditions in the lithospheric mantle; they may represent subducted crustal material or igneous intrusions. (3) Pyroxenites are mafic in composition and represent frozen basaltic magmas, cumulates, and fractionates; most commonly intruded into young (Phanerozoic) mantle domains, or more rarely into high levels in cratonic regions. By analogy they may be the lower-pressure/higher temperature equivalents of some types of eclogites from cratonic mantle.

Mantle metasomatism involves an enormous variety of fluid types. These include silicate melts ranging from mafic to ultramafic; carbonatite melts; sulphide melts; C-O-H fluids ranging from water to CH_4 and CO_2; dense brines and hydrosilicic fluids; and hydrocarbon-bearing fluids. Many of these appear to be miscible with one another under some environmental conditions, and immiscible under others. There is evidence of the coexistence and interaction of different fluid types within single volumes of the mantle on short time scales. The complexity of mantle metasomatic processes is far from understood at present, and offers abundant opportunities for innovative research.

1.13 Mapping the Distribution of Fluids in the Crust and Lithospheric Mantle Utilizing Geophysical Methods: Chapter 13

Metasomatism of the crust and upper mantle can cause profound changes in the composition of rocks. The presence of even small amounts of aqueous or magmatic fluids often controls the rate of metamorphic reactions. Most knowledge of metamorphic and metasomatic processes is based on geochemical studies of these rocks when they have been exhumed and exposed at the surface. This means that the fluids are being studied in ancient orogens, often when the fluids are no longer present, except in isolated fluid inclusions. Being able to observe the fluids that cause these processes in real time is essential to understanding how they occur. Geophysics allows us to map in situ fluid distributions in real time, because the presence of fluids causes significant changes to the physical properties of the rock such as electrical resistivity and seismic velocity. Subsurface variations in these properties can be measured with surface-based geophysical techniques. Electromagnetic methods, such as magnetotellurics (MT), can image electrical resistivity, and seismic methods can image seismic velocities and related quantities such as Poissons' ratio.

In this chapter the physical basis for using geophysical observations to map metasomatism in real time is described. This includes (1) an understanding of how the presence of fluids changes the properties of the rock; (2) how to measure these properties from the surface with geophysical imaging; and (3) a number of case studies that describe what geophysics can say about the fluid distribution in locations

where metasomatism is actively occurring. Metasomatism changes the mineralogy of crustal and upper mantle rocks in a permanent way, and can result in changes in both electrical resistivity and seismic velocity. This can provide evidence of past metasomatism. Examples of this type of observation are also discussed.

1.14 A Hydromechanical Model for Lower Crustal Fluid Flow: Chapter 14

Metamorphic devolatilisation generates fluids at or near lithostatic pressure. These fluids are ultimately expelled by compaction. It is doubtful that fluid generation and compaction operate on the same time scale at low metamorphic grade, even in rocks that are deforming by ductile mechanisms in response to tectonic stress. However, thermally activated viscous compaction may dominate fluid flow patterns at moderate to high metamorphic grades. Compaction-driven fluid flow organizes into self-propagating domains of fluid-filled porosity that correspond to steady-state wave solutions of the equations governing compaction. The effective rheology for compaction processes in heterogeneous rocks is dictated by the weakest lithology. Geological compaction literature invariably assumes linear viscous behavior, but lower crustal rocks may well be characterized by non-linear (power-law) viscous rheology. The steady-state solutions and scales derived here are general with respect to the dependence of the viscous rheology on effective pressure. These solutions are exploited to predict the geometry and properties of the waves as a function of rock rheology and the rate of metamorphic fluid production. In the viscous limit, wavelength is controlled by a hydrodynamic length scale δ, which varies inversely with temperature, and/or the rheological length scale for thermal activation of viscous deformation l_A, which is on the order of a kilometer. At high temperature, such that $\delta < l_A$, waves are spherical. With falling temperature, as $\delta \rightarrow l_A$, waves flatten to sill-like structures. If the fluid overpressures associated with viscous wave propagation reach the conditions for plastic failure, then compaction induces channelized fluid flow. The channeling is caused by vertically elongated porosity waves that nucleate with characteristic spacing δ. Because δ increases with falling temperature, this mechanism is amplified towards the surface. The passage of porosity waves is associated with pressure anomalies that generate an oscillatory lateral component to the fluid flux that is comparable to the vertical component. As the vertical component may be orders of magnitude greater than time-averaged metamorphic fluxes, porosity waves are a potentially important agent for metasomatism. The time and spatial scales of these mechanisms depend on the initial state that is perturbed by the metamorphic process. Average fluxes place an upper limit on the spatial scale and a lower limit on the time scale, but the scales are otherwise unbounded. Thus, inversion of natural fluid flow patterns offers the greatest hope for constraining the compaction scales. Porosity waves are a self-localizing

mechanism for deformation and fluid flow. In nature these mechanisms are superimposed on patterns induced by far-field stress and pre-existing heterogeneities.

1.15 Metasomatism in the Early Solar System: The Record from Chondritic Meteorites: Chapter 15

Mineralogic, petrologic, and isotopic studies of chondritic meteorites have revealed clear evidence of metasomatic processes during the earliest stages of the Solar System's evolution. The exact nature of these processes, as well as the conditions and environments where metasomatism occurred, are still the subject of vigorous debate. The interaction of aqueous fluids with early Solar System solids affected different chondrite groups to different degrees; even within a single chondrite group the effects of metasomatism can be highly variable.

Among the carbonaceous chondrite groups, the CV (Vigarano-type) and CO (Ornans-type) chondrites show the best-documented evidence of metasomatic effects. In the oxidized subgroup of the CV chondrites, Ca-Al-rich Inclusions (CAIs), Amoeboid Olivine Aggregates (AOAs), chondrules and matrix have all been extensively affected by Fe-alkali-halogen metasomatism. This has resulted in the formation of a wide range of secondary, dominantly anhydrous minerals, including grossular, andradite, wollastonite, monticellite, anorthite, forsterite, ferroan olivine, corundum, Na-melilite, nepheline, sodalite, wadalite, Al-diopside, kushiroite, ferroan diopside–hedenbergite pyroxenes, ilmenite, phosphates, magnetite, awaruite, tetrataenite, and Fe, Ni sulfides. Hydrous phases are much rarer, but include, margarite, vesuvianite, and kaolinite. The mineral assemblages that form are highly dependent on the primary mineralogy of the host object. For example, distinct mineral assemblages are produced by alteration of CAIs, chondrules, and matrix. Nebular and asteroidal scenarios that might be responsible for these metasomatic effects observed in the CV chondrites have been extensively discussed in the literature. Oxygen-isotope studies of the secondary minerals in CV chondrites, such as fayalite, magnetite, and Ca, Fe-rich silicates, indicate formation at relatively low temperatures ($<$550 K) from aqueous solutions, consistent with an asteroidal environment. On the other hand, primary minerals in CAIs show oxygen-isotope heterogeneity, with melilite and anorthite exhibiting enrichment in heavy isotopes compared with spinel, hibonite, Al, Ti-diopside, and forsterite. The origin of this selective isotopic exchange is still the subject of debate. It may have occurred by gas-solid or gas-melt exchange in the solar nebula or by isotopic exchange with an ^{16}O-depleted fluid in an asteroidal environment. The CO chondrites show significant evidence of metasomatic events, but the degree and extent of metasomatism is much less than that for the CV chondrites. Calcium-rich phases, such as melilite, plagioclase, and the glassy mesostasis in CAIs, AOAs, and chondrules have been affected the most and have been replaced by fine-grained alteration products. Although the secondary minerals in CO chondrites have not

been characterized in as much detail as the CV chondrites, nepheline, sodalite, ilmenite, ferroan olivine, and ferroan diopside–hedenbergite pyroxenes have all been positively identified. Collectively the data indicate that Fe-alkali metasomatism has also affected the CO chondrites, but the involvement of halogens is much less extensive. Although the alteration of CAIs, AOAs, and chondrules is extremely heterogeneous in CO chondrites, there is a general correlation between the degrees of metasomatism and metamorphism, indicating that the metasomatism occurred dominantly within an asteroidal environment. However, some rare CAIs in type 3.0 CO chondrites and chondrules in higher petrologic CO3 subtypes exhibit metasomatic effects that may be best explained by alteration prior to asteroidal accretion.

In comparison, the ordinary chondrites (H, L, and LL) show minimal evidence of metasomatic effects. Only a few unequilibrated ordinary chondrites show evidence of highly localized and minimal development of nepheline, sodalite, and scapolite. This only occurs in chondrules that contain Al-rich phases such as plagioclase. The most extensively metasomatised ordinary chondrite is Tieschitz (H3.6), which has a highly unusual component of matrix consisting of veins of nepheline and albite interstitial to the chondrules. Chondrule glass in this meteorite has been leached extensively of alkalis and Al, indicating extensive interaction with an aqueous fluid.

Finally, new evidence is coming to light which suggests that some more highly metamorphosed ordinary chondrites may have undergone metasomatism, as indicated by partial albitisation of plagioclase, replacement of low-Ca pyroxene by ferroan olivine, and remobilization of phosphate minerals. These limited data suggest that mineral-fluid interactions in the ordinary chondrites occurred late in the metamorphic history of these meteorites. Metasomatic effects may be much more extensively developed in the ordinary chondrites, but are cryptic in nature and have yet to be recognized. Research on the role of fluids in the geologic evolution of the parent bodies of ordinary chondrites is therefore still in its infancy.

1.16 Concluding Remarks

A perusal through Sects. 1.2 through 1.15 above gives some idea as to the scope and general depth of this Lectures in Geology series volume on Metasomatism. These sections, and the chapters that they represent, indicate the importance of metasomatic processes in helping to understand the evolution and stabilization of crust (and associated mantle) on terrestrial bodies where H_2O can occur as a liquid in the rock. Metasomatically induced chemical changes in the crust go hand-in-hand with tectonic changes and both act as a strong influence on long-term crustal structure, evolution, and stability. Introduction of H_2O into the Earth's mantle via subduction induces not only chemical changes but also directly influences the rate of slab movement and other tectonic processes. It is also responsible for igneous processes such as plutonic igneous magmatism as well as arc volcanism along continental margins associated with these subduction zones.

As the reader will discover when perusing the chapters making up this volume, our general understanding of how metasomatic processes influence terrestrial processes is only in its infancy. Considerably more work needs to be done before our knowledge of their relationship to each other grows beyond the bare bones, only partial understanding expressed here to a more complete and detailed picture. In this regard, the real purpose of this volume on Metasomatism is to serve as a foundation and inspiration for the interested student or researcher to further extend our insights and understanding regarding the role of metasomatic processes not just on the Earth but on any terrestrial world on which liquid H_2O is found.

Chapter 2
The Chemical Composition of Metasomatic Fluids in the Crust

Bruce W.D. Yardley

Abstract Any crustal fluid can give rise to metasomatism when it migrates from one rock type to another, and metasomatism is normally associated with specific fluid flow paths, such as fractures, faults, shear zones or lithologies which were more permeable than those around them. Examples of representative analyses of a wide range of crustal fluids from the literature are therefore presented and discussed. Except in shallow crustal settings, metasomatism is generally associated with brines, and highly concentrated brines are particularly effective metasomatic agents. Leaving aside mid-ocean-ridge geothermal systems, the most abundant sources of metasomatic fluids are sedimentary basin brines and magmatic fluids, but mantle and metamorphic fluids can also give rise to metasomatism. Basinal brines are initially of two types: low-Br, NaCl brines derived by dissolution of halite, and Br, Ca-rich brines evolved from the bitern brines remaining after halite precipitation. Both types are implicated in ore-formation and metasomatism (e.g. albitisation) in both sedimentary basins and their underlying crystalline basement. Many magmas give off significant amounts of acid fluids, often rather saline, as they crystallise, and these may also contain distinctive volatile components derived from the melt (e.g. B, F) that influence the metasomatic effects, such as greisenisation, that result. The high transition metal contents of magmatic brines mean that they are also potential ore-formers. Some deep-derived magmas act as vectors to bring mantle fluids into the crust. These appear to be brines that are also highly charged with CO_2, and one effect of degassing at crustal levels is that these fluids become silica undersaturated, for example they may leach silica during fenitisation. Skarns are a particularly important class of metasomatic rock, and owe their origin in part to the transient generation of secondary porosity as infiltrating silica-saturated aqueous fluids trigger decarbonation reactions in carbonate rocks. They may be formed from metamorphic fluids as well as magmatic

B.W.D. Yardley (✉)
School of Earth and Environment, University of Leeds, Leeds LS2 9JT, UK
e-mail: b.w.d.yardley@leeds.ac.uk

D.E. Harlov and H. Austrheim, *Metasomatism and the Chemical Transformation of Rock*, Lecture Notes in Earth System Sciences,
DOI 10.1007/978-3-642-28394-9_2,

ones, but in general metamorphic fluids are not a major cause of metasomatism, except where focussed in subduction, because they are usually released very slowly by endothermic reactions taking place in an over-pressured, and therefore low permeability, environment.

2.1 Introduction

Metasomatism, the process by which rocks change their composition while remaining effectively solid, is self-evidently important in the evolution of a wide range of rock types, but remains quite poorly understood. This is largely because it is complex, involving the interplay of chemical reactions with physical processes of fluid flow under P-T conditions where basic information about fluid properties in particular is often lacking. However another major difficulty for understanding metasomatism is that the fluid phase is seldom preserved for analysis. Despite the problems, metasomatism has steadily progressed from an untestable link in the logic of petrological speculations into a subject for rigorous investigation and appraisal. Initially this refinement was mainly from a geochemical standpoint, notably the Russian work of the mid twentieth century (Korzhinskii 1958, 1970), but the development of coupled hydraulic, thermal, chemical and mechanical simulation models for predicting the behaviour of waste repositories (Bethke 2007) holds out the prospect of a much more profound advance in our understanding of metasomatism in the foreseeable future (Ingebritsen and Appold in press).

In this chapter, I shall deal exclusively with metasomatism in the sense of changes to the bulk composition (excluding volatiles) of rock bodies on a scale much larger than the grain size, rather than metasomatism in the sense of local chemical changes affecting single grains and compensated for by complementary changes to other minerals nearby. For the most part, these changes arise through the introduction of fluid from an external source, which adds and removes material in solution, and this is a process defined as infiltration metasomatism by Korzhinskii (1958, 1970). To take account of the effects of fluid infiltration in thermodynamic analysis, Korzhinskii proposed a modification to the phase rule, distinguishing between mobile and immobile components. Mobile components are those that are introduced (or removed) in the fluid, so that their chemical potentials are dictated by the incoming fluid and its source, rather than by the rock undergoing metasomatism. Immobile components are dominated by material that is part of the rock throughout. The number of degrees of freedom in a metasomatic system is linked to the number of immobile components, not to the mobile ones. This is an extremely valuable concept, both for recognising metasomatic rocks and for inferring likely fluid composition. It makes the important prediction that metasomatic assemblages will contain relatively few phases, compared to isochemically metamorphosed rocks, and the chemical variability of any phases that are solid solutions will be less. Unequivocally metasomatic rocks such as veins and their immediate margins generally accord well with this prediction. As we learn more about the chemical composition of crustal fluids, it becomes easier to understand which components

are readily mobile and which are less likely to be so. Of course, the distinction is in reality an arbitrary one within a continuum.

Metasomatism may also arise at the interface between two contrasting lithologies as a result of diffusion of components between them, and is termed diffusion metasomatism. The development of metasomatic blackwalls around lenses of ultramafic rocks is a particularly important example (e.g. Bucher et al. 2005). Often products of diffusion metasomatism resemble those of infiltration metasomatism, but occur on a smaller scale because of the less effective transport mechanism. For example, the zones of relatively coarse silicate minerals developed by diffusion at an interface between marble and schist during amphibolites facies metamorphism (Vidale 1969) have many similarities with the coarse grained calc silicate skarns formed by the infiltration of silica-rich fluids into marble.

There are two main communities who have advanced our understanding of metasomatism, but their work has not always been well integrated. Metasomatism is often studied as a branch of petrology, generally in the context of metamorphic rocks. However many of the most detailed accounts and the most extensive examples of metasomatism, lie in the realm of ore deposit geology. These fields are sufficiently separate that the terminology is not always the same; in particular, the petrologist's "potassium metasomatism" of granitic rock is referred to in the literature of ore deposits as "potassic alteration". Since this chapter spans a wide spectrum of settings in which metasomatism occurs, I shall simply use the term metasomatism throughout. It is also worth noting that there are also other communities that embrace the study of metasomatic rocks and processes and have made important contributions. Studies of sediment diagenesis and of sea floor hydrothermal activity have arguably provided some of the most valuable insights of recent decades.

2.1.1 Metasomatic Fluids

Metasomatism arises when a fluid migrates to a region where it is out of equilibrium with its new host, and so it can be argued that all crustal fluids will act as metasomatic fluids in the right circumstances. It is convenient to think of three types of control on fluid chemistry in the crust. The composition of most crustal fluids is effectively buffered for a wide range of components by interactions with minerals in the host rock (Hanor 1994; Yardley 2005); *buffered fluids* are saturated solutions of common host rocks. There are some fluids, however, for example concentrated brines derived by halite dissolution, which contain such large dissolved loads that they overwhelm the buffer capacity of the host rocks (which thereby undergo metasomatism), while still retaining many of their original characteristics. They are still saturated solutions of their hosts, but since many components are not present in the remaining minerals, most components are unconstrained. These fluids have been termed *mass limited* by Houston et al. (2011). Finally, some fluids are *kinetically limited*. Crystalline rocks that have undergone retrograde hydration show very different degrees of reaction for

different mineral species, so that the fluid that gave rise to the retrogression will have a composition that mainly reflects dissolution of the more reactive minerals: olivine or orthopyroxene in mafic rocks, biotite and perhaps Al-silicates in pelitic schists, and so forth.

Looked at from a lithocentric viewpoint, metasomatic fluids are often characterised as sodic, potassic etc., according to the effects that they give rise to in the rocks that they infiltrate. However the chemical changes induced in rocks do not reflect the overall composition of the fluid. Instead they reflect the changes induced in the rock as the fluid evolves towards equilibrium with its new host. Most crustal fluids are dominated by NaCl, but hydrothermal halite deposits are remarkably rare; it is the more minor chemical components that produce distinctive rocks. For example, the scales precipitated from Na-Ca-Cl geothermal brines at the Salton Sea (Table 2.1) are dominated by silica, and many trace metals show extreme enrichment in the scale, including Al and chalcophile metals such as Cu (Skinner et al. 1967). In contrast, the major fluid components remain in solution to a large degree.

2.1.2 Controls on Metasomatism

Metasomatic fluids have three possible origins in a physical sense: they may be pre-existing pore fluids that escape or are expelled from host rocks, metamorphic fluids generated by the progress of devolatilisation reactions, or magmatic fluids released from a melt as it crystallises. The extent to which metasomatism occurs in a particular fluid flow pathway depends on both the concentration of dissolved solids in the fluid and the amount of fluid that passes through to form the metasomatised rock. In shallow settings where large fluid fluxes are possible, such as subaerial geothermal fields, significant chemical changes can be induced by the passage of very dilute waters. In many cases of metasomatism in the deeper crust however, the fluids are likely to have been brines with very high dissolved loads, so that chemical change can be achieved with relatively small fluxes. Many metasomatic rocks have quite different compositions from their precursors, even though other rocks retaining original sedimentary or igneous compositions occur close to hand, demonstrating the focussed nature of metasomatic flows. This is particularly obvious in the case of skarns replacing limestones or marbles, where the development of characteristic calc silicate skarn assemblages is commonly accompanied by complete breakdown of original carbonates within the skarn (Fig. 2.1), but interbedded silicate rocks remain fine grained and unmodified (Oliver 1992).

Table 2.1 Representative examples of crustal fluid compositions likely to be indicative of metasomatic fluids in the main crustal settings. Units are mg/kg except for Oilfield Formation Waters, in mg/l

Field/location	Sample	Temp (°C)	Na	K	Li	Mg	Ca	Sr	Ba	Fe	Mn	Zn	Pb	Cu	B	F	Cl	Br	SO_4	HCO_3
Seawater		15	10,670.0	399.0	0.2	1,250.0	411.0	8.1							4.5	13.0	19,350.0	67.3	2,700.0	142.0
Black smoker fluids (Michard et'al. 1984)																				
13°N			1,0345	938	5.7	0	641	7.9		100.5	33.5						19,500			
East Pacific rise			12,874	1,157	4.8	0	2,204	15		58.6	44						26,235			
Geothermal brines																				
Salton Sea (Williams and McKibben 1989)																				
SSSDP well 12,,-,,1985		305	53,000	16,700	194	33	27,400	411	203	1,560	1,450	518	100	5.9	257		151,000	99	65	
SSSDP well 3-,,1986		330	54,800	17,700	209	49	28,500	421	353	1,710	1,500	507	102	6.8	271		157,500	111	53	
Commercial well 10		295	41,400	11,800	152	33	20,900	345	156	969	855	323	67	2	197		116,000	78	53	
Commercial well 81		230	15,000	2,480	55	54	2,520	112	45	86	60	11	2.6		92		31,000	24	53	
Oil field formation waters																				
North Sea (Warren and Smalley 1994)																				
Miller		120	2,7650	1,280		105	645	72	780	47							44,260		5	2,470
Ravenspurn		104	69,200	1,500	27	3,700	25,500	1,100	15	160					22		142,200		260	
Scott		125	40,380	1,840		835	5,790	750	200	2.9					1		78,280		46	575
Central Mississippi (Carpenter et'al. 1974)																				
Bay springs field	#3	143	63,000	6,150	52	2,770	44,600	1,770	89	320	60	18	3				200,400	2,340	128	
Dollar field	#19	98	47,300	595	9	1,150	13,200	422	20	278	6	575	10				103,200	950		
South Magee field	#37	124	58,200	916		2,220	29,900	1,750	56	123	61	180	32				150,300	1,090	82	
Raleigh field	#66	135	76,200	979		2,400	36,500	2,260	109	294	102	342	96				193,400	1,510	3	
Offshore Louisiana (Land et'al. 1988)																				
	D/95	98	99,600	377	6.5	963	6,200	167	6	35.1	6.6	4.97			43		170,000	196	116	
	F/60	68	25,900	173	3.4	530	1,970	70	53	7	1.2	0.06			40		44,000	61	9.6	195
	G/4	132	26,880	107	5.7	103	805	87	12	4.4	0.83	0.04			77		43,530	38	38.7	551

(continued)

Table 2.1 (continued)

Field/location	Sample	Temp (°C)	Na	K	Li	Mg	Ca	Sr	Ba	Fe	Mn	Zn	Pb	Cu	B	F	Cl	Br	SO_4	HCO_3
Michigan Basin (Wilson and Long 1993b)																				
		52.7	23,000	9,500		6,080	60,000										153,000	1,270		
		54.6	9,820	22,600	61	12,800	124,000	6,030									263,000	3,020		
		29.7	39,400	3,320		8,350	49,900										168,000	2,230		
Alberta Basin (Connolly et'al. 1990)																				
Viking 2		47	22,000	102	5	416	1,070	182	365	7.13	0.62	0.04			7		36,100	172		
Rock creek 1		75	8,470	119	4	46	123	26	14	0.15	0.09	0.06			15		12,700	28	11	
M Jurassic 2		61	23,600	555	16	179	793	54	2	0.25	1.02	0.03			8		36,800	113	295	
Leduc 4		42	34,900	1,080	23	1,987	5,220	198	1	0.27	0.08				48		66,100	274	1,240	
Leduc 5		63	50,000	3,640	50	5,035	30,000	1,190	7	17.48	0.49	0.83			142		144,000	1,260	294	
Low grade metamorphic fluids																				
Pyrenees (McCaig et'al. 2000)																				
Gistain	P94-5Q	300	41,871	2,851	207	4,086	45,037	2,856		3,716	466	279		22	50		136,284	691.7	2,533	
Plan de Larri	P94-9	300	24,908	2,257		24,043	194,085	778	199	1,678	182			52	190		54,459	125.5		
Pic Long	55141-1	300	62,213	14,564	1,879	1,207	47,637	3,421	1,157	2,868	1,773	392		348	156		187,405	2,793	2,184	
La Glere	N90-4	300	53,366	7,829		155	31,790	1,894	384	486	656	790	187		59		155,332	3,063	464	
Pic de Port Vieux	54319-m	345	55,187	1,600	530	1,065	30,320	2,809	1,076	2,539	1,115	1,010		171	171		131,421	877	265	
Columbian emerald deposits (Banks et'al. 2000b)																				
Coscuez (in Quartz)	GG-5	320	54,590	11,622	2,031	639	44,027	1,605	1,064	23,791	3,308	573	131	115			211,091	100.6	1,189	
Chivor (in Emerald)	GG-11	320	116,142	5,888	430	1,568	19,151	407	198	5,086	569	174	54	104			230,202	27.4	352	
Orogenic „Au-Quartz„ fluids																				
Brusson, N. Italy (Yardley et'al. 1993)																				
	LD659	280	17,314	863	27	135	793	53	24	18	2.2	1.7	2.6	3.8	432	401	21,389	104	996	
	LD671	280	17,163	2,526	81	85	955		68	66	4	33.5		7.5	393	208	20,820	87	154	
	LD886	280	16,752	985	239	129	665	54	43	120	5	34.3		25.1	560	242	1,9112	70	102	
Basinal fluids from basement																				
Modum complex, Norway (Munz et'al. 1995)																				

	DOV-1	220	17,118	1,032	13	27	5,457	83	31	53	26	3		1	24		35,661	221	86
	IA-432	220	20,516	2,263	71	78	4,239	107	75	164	75	18		24	71		30,885	197	62
	IA-511G	220	45,707	7,110	144	128	24,581	1,307	2,163	2,370	248	80		37	144		74,456	297	887
Magmatic fluids																			
Mole granite (Heinrich et'al. 1992; Audetat et'al. 2000)																			
H et'al. 1992		550	78,000	37,000			3,200	30		60,000	18,000	5,200	3,300	900			266,000	420	
Leno1	1	450	130,000	93,000	520			46	200	170,000	44,000	14,000	10,000		650		430,000		
Wolf 12	A	400	72,300	45,600	433			170	170	67,700	19,400	5,200	3,400	160			208,500		
Cornwall (Bottrell and Yardley 1988; Smith et'al. 1996)																			
	54150	400	16,310	4,186	58	598	4,411		29	9,130	934	192		837	623	1,540	28,119	80	2,051
	2320	600	39,520	13,960	215	121	9,619	175	137	11,950	3,240	1,569			3,974	817	106,360	150	6,075
Golden dagger	SW-89-159	500	66,687	14,932	266	154	29,249	534	146	6,809	3,868	774	234	34	1,194	866	171,637	307	534
East Vitifer	SW-89-156	500	68,519	15,910	226	137	27,148	493	185	7,057	3,433	637	151	55	959	508	172,790	308	349
Kakkonda „high-T„ geothermal brine (Japan) (Kasai et'al. 1996)																			
	WD-1a	500	75,000	35,000			15,000			32,000	8,000						220,000		
Mantle fluids (Salts in solute only) (Tomlinson et'al. 2006)[a]																			
	PAN2		37,331	239,933		44,334	65,473		138,682	122,359							274,470		
	PAN3		39,729	269,643		23,159	40,770		179,353	62,440							339,500		
	PAN6		64,149	206,850		31,550	61,800		159,996	149,463							265,890		

[a]Analyses from Tomlinson et'al. (2006) have been renormalised to reflect likely fluid speciation: Si and Al as oxides and other cations and Cl have been normalised to 100% to represent the likely solute composition. The figures may be „over-estimates„ as it is likely that Mn is also a major component but was not reported

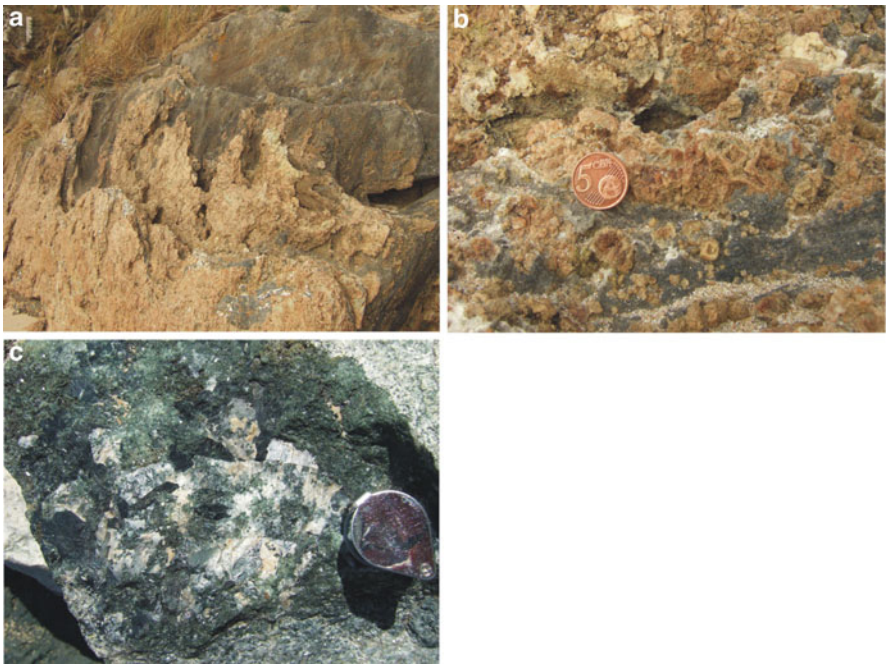

Fig. 2.1 Examples of skarns: (**a**) outcrop of grossular-rich skarn replacing pure calcite marble near the southern contact of the Omey granite, Connemara, Ireland. Detail is shown in (**b**); relict calcite marble is grey with streaks of white wollastonite. Garnet shows some colour variation according to andradite content but the *dark brown* mineral is idocrase. Minor diopside is also present. The formation of this skarn requires introduction of Al-silicate material in fluid from the adjacent granite, but it is unmineralised. In (**c**) coarse actinolite and calcite are part of a mineralised skarn associated with Zn mineralisation, Franklin Mine, New Jersey, USA

2.2 Settings of Metasomatism in the Crust

While it is impossible to document all the known types of metasomatism in this review (see Zharikov et al. 2007 for a summary of the classical divisions), I will try to summarise what is known about the main fluid types found in the crust and how they may relate to some of the major settings of metasomatism.

The most widespread, and arguably the most important, example of metasomatism through geological time has almost certainly been the sea floor alteration of basaltic rocks by convecting seawater, which affects the composition of the oceans as well as that of sea floor basalt (Humphris and Thompson 1978; see also Chap. 8). Here, large fluid fluxes impose significant metasomatic changes on basalt despite the relatively low dissolved load of the fluid (Table 2.1). Other near-surface settings can also permit extensive metasomatism, both because of the relatively large fluid fluxes that are possible in the near surface, and because of the potential for significant disequilibrium between fluids and the rocks into which they flow.

Sedimentary formation waters are commonly more saline than seawater and sediments may show evidence for extensive changes during diagenesis, including dolomitisation or silicification of limestones (Knauth 1979; Warren 2000) and albitisation of detrital plagioclase or K-feldspar in siliciclastic beds (Milliken 1989; Saigal et al. 1988). While some of these changes arise at least in part due to local redistribution of material (Bjorlykke 1998), others, including mineral dissolution as well as transformation, are almost certainly metasomatic (Wilkinson et al. 2001; Day-Stirrat et al. 2010). In addition, sedimentary brines are able to penetrate into underlying crystalline basement rocks along fractures and have been implicated in metasomatic changes including albitisation in basement rocks (Munz et al. 1995; Gleeson et al. 2003). In so doing, they move both metaphorically and literally across the boundary between sedimentary processes of diagenesis and metamorphic processes affecting crystalline rocks. Thus sedimentary basins and their underlying basement rocks are a major setting in which metasomatism can occur.

The crystallisation of igneous rocks can give rise to an entirely separate suite of metasomatic fluids, such as those responsible for the development of fenite or greisen. Fenite is a metasomatic rock rich in K-feldspar and albite, often with sodic pyroxene or amphibole and sometimes with nepheline; they are associated with alkaline igneous intrusions and carbonatites. In contrast, greisen is a metasomatised granite in which feldspars have been largely broken down to muscovite, and minerals such as tourmaline, topaz and ores of tin and tungsten may be present (see below). Not all intrusions are accompanied by significant metasomatism however, reflecting both differences in the amount of fluid released and in its composition. At very high pressures, or in the presence of suitable fluxing elements, the distinction between silicate melt and water becomes blurred, and metasomatism may be caused by the movement of fluids that are more melt-like than simply aqueous (Chap. 12). The importance of melts has been particularly recognised in the context of mantle metasomatism (Menzies and Murthy 1980). Magmas are an important vector for transferring mantle fluids into the crust, but some workers have identified metasomatic features in lower crustal rocks that they have attributed to the passage of mantle fluids directly (Newton and Manning 2002; Chap. 11).

The most problematic source of metasomatic fluids is metamorphism. The term metamorphic fluid is commonly used in stable isotope geochemistry to signify a fluid that has equilibrated with rocks at mid-crustal temperatures, but will be used here in the stricter petrological sense, to denote a fluid released from mineral lattices by metamorphic reactions, generally mixed with pre-existing pore fluid. There can be no doubt that some metasomatic features in metamorphic rocks arise through the passage of fluids released during progressive heating. These include: (a) metasomatic alteration associated with syn-metamorphic structures, such as the alteration of metabasites in anticline hinges from Knapdale, SW Scotland, described by Skelton et al. (1995) or the structurally controlled development of metasomatic actinolite beds near Mt. Isa (Huang and Rubenach 1995; Chap. 4); (b) the development of calc silicate skarn assemblages from marbles interbedded with schists, either in contact metamorphism (Kerrick 1977) or during regional heating (Yardley et al. 1991); (c) metasomatic modification of the wall rocks

around metamorphic veins, on a larger scale than can be ascribed to purely diffusional segregation (Ague 1994; Yardley 2009); and (d) replacement of amphibole-bearing assemblages by anhydrous charnockite or granulite in the lower crust, attributed to passage of fluids with low water activities (Newton 1989; Chap. 11), and conversely amphibolitisation of lower crustal granulites through brine influx (Markl and Bucher 1998). Additionally, orogenic gold deposits have been widely attributed to focussed flow of dilute metamorphic fluids (Goldfarb et al. 1988; Groves et al. 2003; Craw et al. 2010), while some examples of metasomatism of retrograde shear zones in basement slices are likely due to the passage of fluids released by the prograde metamorphism of interleaved sediments (Selverstone et al. 1991; McCaig 1997). However there are many examples of metasomatic alteration associated with deep faults or shear zones for which it is not possible to unequivocally identify the source of the fluid, and there is often little evidence to suggest a deep, metamorphic origin although that is what is commonly assumed.

The possibility of wider, pervasive metasomatic effects during prograde crustal metamorphism remains controversial (compare Oliver 1992; Ague 1994; Ferry 1994; Ague 2003; Bucholz and Ague 2010; Yardley 2009). Documentation is difficult where rocks do not exhibit obvious metasomatic effects such as a reduced number of phases. For example in many metamorphic belts, including the classic Barrovian terrane of Scotland, isograds are parallel to lithological units so that rocks at different grades may have had different compositions originally.

The reasons for doubting whether infiltration metasomatism is widespread during regional metamorphism arise from concerns about the availability of fluid and reflect widespread evidence for fluid overpressuring during metamorphism. Fluid pressures during prograde metamorphism are inferred to approach lithostatic pressure from phase relationships and vein textures. This is only possible if rocks are very impermeable, and so it is unlikely that rocks undergoing prograde dehydration will normally experience sufficient fluid flow to undergo significant metasomatism. Metamorphic fluids are produced very slowly because metamorphic devolatilisation reactions are strongly endothermic, while heat flow through the crust is very low (typically in the range 30–100 Wm^{-2}), giving rise to slow flow rates despite strong overpressuring (Yardley 1986; Connolly 2010). The threshold permeability above which advective transport of dissolved material may become more extensive than diffusional transport is of the order of 10^{-20} m^2 (Ingebritsen and Appold in press), and is therefore just below the maximum permeabilites likely to be attained in a rapidly heated sequence rich in hydrous minerals (10^{-18}–10^{-19} m^2, Yardley 2009). Fluids generated by regional metamorphism are also constrained by being unable to recirculate, since they are moving away from regions of overpressuring. As a result, it is likely that, except where strongly focussed, metamorphic fluids continuously re-equilibrate with the rocks through which they seep, without producing any clear chemical signature. Although not yet well understood, it is possible that metamorphism at very high pressures in subducted slabs may be more readily accompanied by metasomatism, because of the much greater solubility of rock components at pressures $\gg$ 1 GPa (Chap. 9).

The literature contains a number of examples of studies where metamorphic fluid compositions have been shown to be locally very variable on a small scale (e.g. Valley et al. 1983; Selverstone et al. 1992), arguing against wholesale fluid infiltration, while elsewhere there are examples of both focussed infiltration and local variations in fluids (Oliver and Wall 1987; Oliver 1992), demonstrating that metasomatism during metamorphism is selective to specific units and metamorphic conditions. Nevertheless a number of authors have proposed large and pervasive fluid fluxes through large rock volumes (e.g. Ferry 1994; Ague 1994), giving rise to subtle metasomatic effects. The fluxes claimed in some studies (summarised in Winter 2010, his Fig. 30.5) are as high as 10^5 m^3m^{-2}, but the source of the enormous quantities of reactive fluid that these imply has never been explained.

Many examples of metasomatism found in high grade metamorphic terranes are features that formed late in the cooling and uplift history rather than under peak metamorphic conditions (e.g. Kent et al. 2000). These include features such as albitisation and other low-grade changes which may be linked to deep penetration of basinal fluids, as discussed above, or to the emplacement of igneous intrusions and their release of fluids.

2.3 The General Characteristics of Crustal Fluids

The main sources of specific information about the chemistry of fluids at depths of more than a few kilometres are fluid inclusions in minerals and experimental measurements of fluid phase relations and mineral solubilities. However there is no abrupt break in fluid chemistry between those fluids that are sampled by deep drilling in oilfields and geothermal areas, and those that occur at depths beyond the reach of present drilling technologies (Yardley 2005), and so these relatively shallow fluids are also an important resource for understanding metasomatism. In addition to the growing data base on deep fluid types observed in fluid inclusions, the past 20 years have seen rapid developments in fluid inclusion elemental and isotopic analysis and these have transformed our understanding of deep fluids (Bottrell et al. 1988; Gunther et al. 1998; Audetat et al. 2000; Banks et al. 2000a). In particular, we now know a lot more about the levels of chloride in crustal fluids which is important because they cannot normally be predicted from experiments or from mineral chemistry. Fluid inclusion analysis provides information about a wide range of metals and non-metals in solution, but cannot yield information about some other key questions such as silica concentrations.

For the purposes of this paper, I shall first consider crustal fluids as composed predominantly of three components: water, carbon dioxide and chloride salts, commonly modelled simply as NaCl. At lower crust and upper mantle pressures (>1 GPa) dissolved rock-forming components (Al, Si) also become important, where a fluid phase is still present. The most basic relationships that guide our understanding of metasomatic fluids are the phase relationships in the H_2O–CO_2–NaCl system, and a representative sequence of phase diagrams for

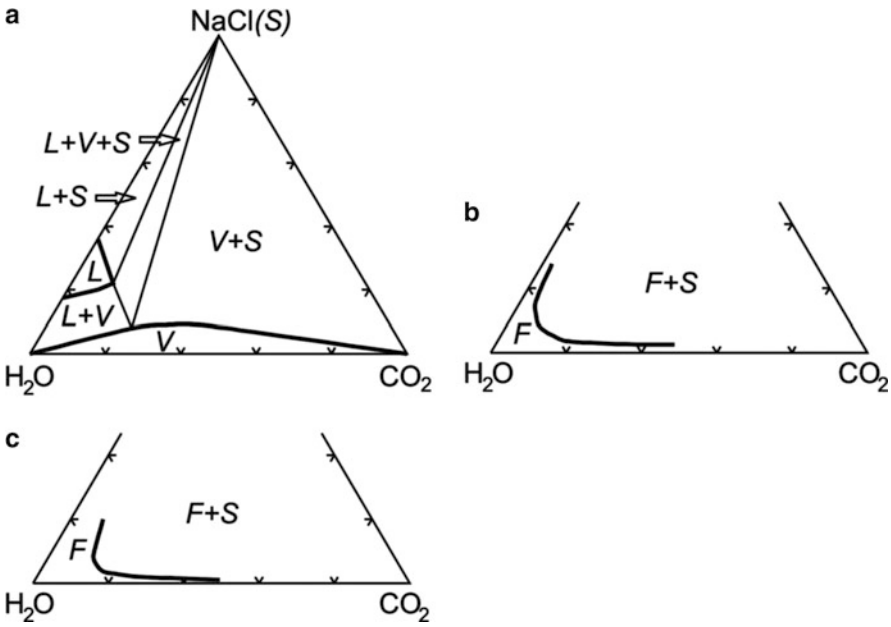

Fig. 2.2 Phase relationships in the system NaCl–H_2O–CO_2 after Liebscher (2007). Diagram modified from Yardley (2009). (**a**) 500°C at 50 MPa, (**b**) 800°C, 200 MPa, (**c**) 500°C, 500 MPa. *F* fluid, *L* liquid, *S* solid, *V* vapour, molar proportions are shown

these (after Liebscher 2007) is shown in Fig. 2.2. Extensive information about phase relations in saline mixed volatile fluids is now available through the development of synthetic fluid inclusions techniques (Sterner and Bodnar 1984; Tkachenko and Shmulovich 1992; Shmulovich and Plyasnova 1993; Schmidt and Bodnar 2000), and the equation of state of Duan et al. (1995) covers a wide range of crustal P-T conditions.

While there is extensive mutual solubility between H_2O and NaCl, and between H_2O and CO_2, fluids rich in all three components are only possible at extreme P-T conditions and are likely to unmix on cooling or depressurisation. At high temperatures, water reacts with silicate rocks to produce hydrous melts, and so aqueous fluids might not be expected at temperatures greater than about 700–750°C depending on pressure. However at lower-crustal pressures the effect of high salt concentrations is to suppress the activity of water allowing brines to persist to high temperatures (Aranovich and Newton 1996; Shmulovich and Graham 1996). This is very significant: water is necessary for fluids to carry a high dissolved load necessary for metasomatism, and highly saline brines are able to combine a high dissolved load with reduced water activity, enabling metasomatism under extreme conditions where water might otherwise be expected to have entirely dissolved into melt.

New experimental and theoretical results on quartz solubility (Newton and Manning 2000; Shmulovich et al. 2001, 2006; Evans 2007) have provided detailed

information over a range of relevant fluid compositions and confirm that at high pressures the silica contents of fluids may be very high. Even at sedimentary basin temperatures, formation waters evolve from seawater by diagenetic interaction, approaching chemical equilibrium with silicate host minerals (Hanor 1994; Houston et al. 2007). Because of such interactions, mineral solubilities may be significantly influenced by the presence of additional components that are ubiquitous in natural settings where the fluid is a saturated solution of its host rock. Notably, Newton and Manning (2008) have demonstrated that Al solubility is significantly enhanced in the presence of Si and Na so that the natural mobility of Al is much higher than would have been inferred from experiments on corundum solubility in pure water. This is of course in accord with the common occurrence of Al-rich minerals in hydrothermal veins.

Under most crustal pressures, aqueous fluid chemistry can nevertheless be thought of as dominated by dissolved salts. Chlorine is normally the dominant anion and Na, although at lower concentrations than Cl, the dominant cation. Extensive exchange of Na with other cations is possible, especially at high temperatures, and Ca, K, and Fe are all important in some crustal brines. Table 2.1 is a compilation of a range of crustal fluids from various depths, selected to illustrate some of the main chemical characteristics. Metal distributions in buffered crustal fluids are often different from those in coexisting rocks and are unaffected by changes in the relative proportions of minerals. For example, Mg concentrations are usually low in chloride fluids, due to preferential take up into minerals, resulting in higher Fe:Mg ratios in the fluid than in coexisting minerals (Eugster and Gunter 1981). Mg-rich fluids can occur in association with ultramafic rocks, or in bittern brines produced by seawater evaporation, but are not common. In contrast, Mn is partitioned into the fluid relative to minerals, especially under mildly oxidising conditions, so that fluids tend to have relatively high Mn:Fe ratios compared to rocks (Bottrell and Yardley 1991). At high pressures and temperatures, brines may also dissolve significant quantities of calcite or anhydrite (Newton and Manning 2002, 2005), although the solubilities of these minerals in pure water remain very low. Yardley (2005) demonstrated that concentrations of a range of transition metals, including Fe, Mn, Pb, and Zn, increase with both temperature and fluid salinity for buffered fluids equilibrated with typical crustal rocks. These relationships for Fe are illustrated in Fig. 2.3.

It is systematically the case that for buffered fluids, the proportion of Ca to Na is higher in more saline fluids, even if the plagioclase compositions, temperature, and pressure are the same. This is because any exchange reaction involving plagioclase, or an equivalent reaction involving albite and a Ca-bearing phase at lower temperatures, will have 1 Ca^{++} balanced by $2Na^{+}$ in order to retain charge balance. For example:

$$2NaAlSi_3O_8 + Ca^{++} = CaAl_2Si_2O_8 + 2Na^{+} + 4SiO_2$$

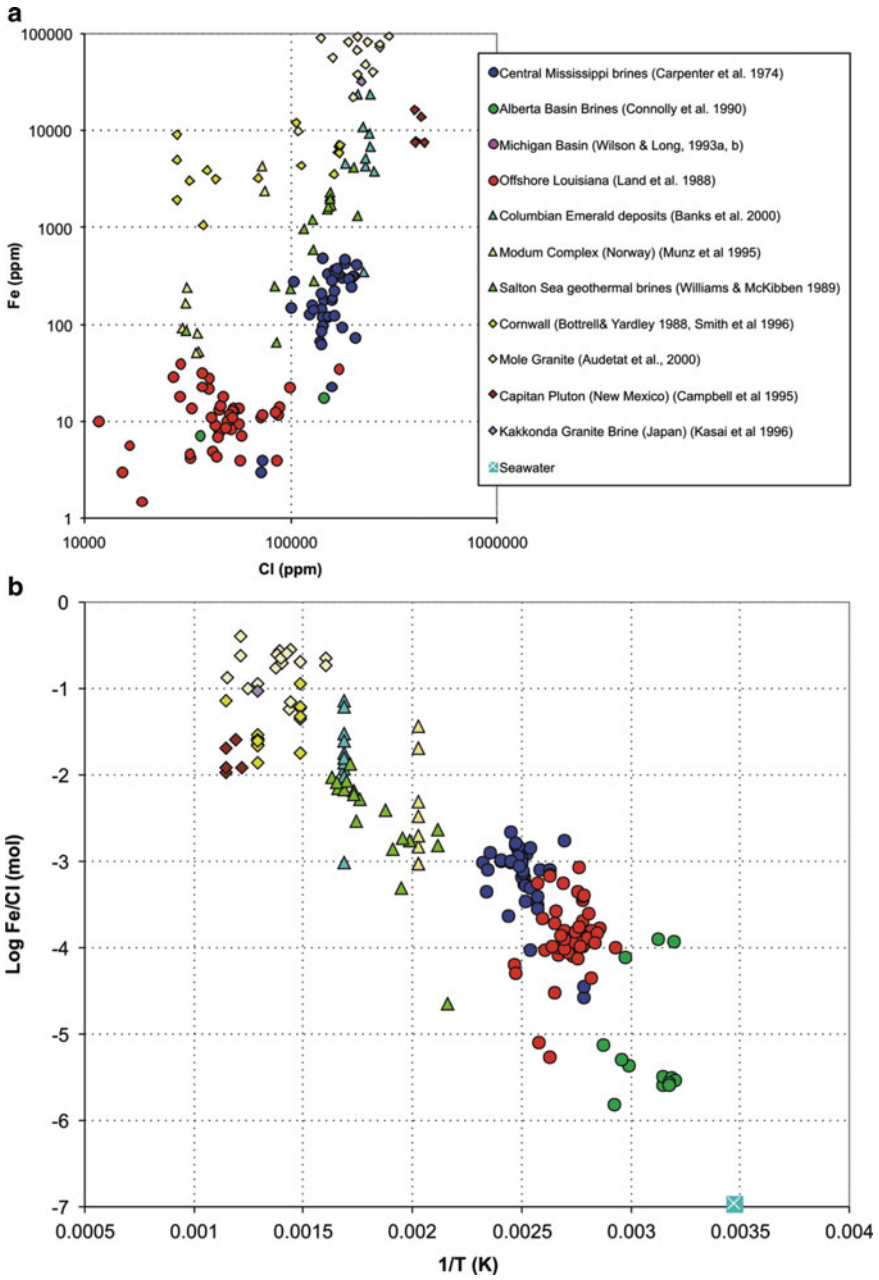

Fig. 2.3 Effects of chlorinity and temperature on the Fe content of crustal fluids (developed from Yardley 2005): (**a**) Relationship between concentrations of Cl and Fe. Superficially there is a steep slope to the data but a very poor fit, however note that the high temperature fluids (*diamond* symbols) lie at the top of the data cloud and define a much flatter positive correlation, while formation waters

The equilibrium constant for this reaction contains the term $(aNa^{+})^2/(aCa^{++})$ and so this is the term that must remain constant for fluids of all salinities in equilibrium with the same plagioclase at the same conditions. In more saline fluids, the concentrations of both these two major cations are of course higher, and so to retain a constant value for the equilibrium constant in which the Na activity is squared, the proportion of Ca to Na must increase with the total concentration of these cations.

While metasomatism is doubtless often the result of crustal fluids migrating from an environment, in which they have evolved to coexist in equilibrium with their host rocks, to a new environment in which they are out of equilibrium, this is not always the only mechanism. Some types of metasomatism are probably linked to phase separation, especially in the top 10 km of the crust. The strong partitioning of components between coexisting liquid and vapour or supercritical fluid and melt phases has long been recognised as an important driver for ore genesis (Cline and Bodnar 1991; Audetat et al. 2008) and can also result in metasomatism in general. When fluids unmix, rates of interaction between the immiscible fluids produced are likely to be much faster than rates of interaction with the host rock. While they coexist, the chemical potentials of all components in both immiscible phases must be equal, but these may correspond to very different concentrations. Thus a low salinity vapour phase is likely to be enriched in gases, including acid species, H_2 and other volatile elements, and some of these may influence transport of specific metals (for example S). The vapour phase will also migrate away from the denser coexisting liquid and so both will be able to evolve further without being constrained by coexistence with the initial immiscible partner. Brine from which a vapour has been removed will exhibit complementary chemical changes and is also a potent agent for metasomatism.

2.3.1 Crustal Brines

Brines play an important role in many kinds of metasomatism, and most originate by exsolution from crystallising magmas or from surface processes involving the evaporation of seawater. Very small quantities also arise as a consequence of hydration reactions consuming water from initially lower salinity fluids. Shallow brine generation arises through evaporation and the precipitation or dissolution of halite, and the behaviour of halite provides a robust marker for the origin of salinity in brines (Rittenhouse 1967). Bromine does not normally fractionate from Cl, but it is not incorporated to any significant degree in halite, so that the bittern brines

Fig. 2.3 (continued) (*circular* symbols) have the lowest Fe-contents but also yield a gentle positive slope, as does data from intermediate temperatures (*triangular* symbols). (**b**) Plot of Fe/Cl against 1/T (K). Much of the spread due to variations in chlorinity has been eliminated; note that the data fit a single linear trend from surface conditions to magmatic temperatures, spanning seven orders of magnitude in Fe/Cl. Much of the remaining scatter will reflect the effects of variation in pH and redox

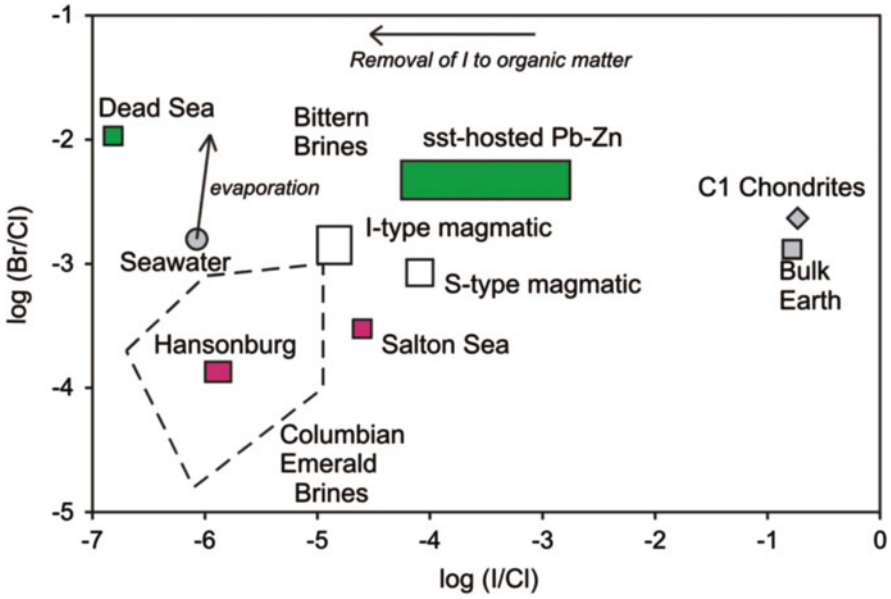

Fig. 2.4 Plot of halogen relations in crustal fluids, adapted from Yardley (2009). Redissolved evaporite brines highlighted in pink include the Hansonburg Pb-Zn ores (Bohlke and Irwin 1992), while bittern brines (*green*) include sandstone hosted Pb-Zn ore fluids from Kendrick et al. (2005)

remaining after halite has precipitated have distinctive high Br/Cl ratios. In contrast, brines derived by dissolution of halite are very depleted in Br. Fluid inclusion studies of low temperature ore fields demonstrate that bittern brines are much more common in the subsurface than the presence of evaporites in the geological column would lead one to expect (Yardley 2009), although brines derived from halite dissolution may also be important (e.g. Bohlke and Irwin 1992; Kesler et al. 1996; Banks et al. 2000b). The Br/Cl ratios of the different types of sedimentary brines bracket the Bulk Earth value (Fig. 2.4), and so a single analysis cannot always distinguish magmatic from sedimentary brines. Nevertheless, magmatic brines almost invariably have Br/Cl ratios close to Bulk Earth, and they can also be distinguished by their δ^{37}Cl values (Banks et al. 2000a).

2.4 Fluids from Major Crustal Settings for Metasomatism

2.4.1 Basinal Brines and Their Deep Derivatives

Deep sedimentary basins of the continents and continental margins often contain brines as the dominant pore fluid (or formation water), and while their cation chemistry may have been extensively modified by reaction with the host minerals,

they retain halide ions reflecting their origin as discussed above. Such brines play a major role in diagenesis, including the metasomatic processes of albitisation and dolomitisation (Davison and Criss 1996; Land 1995; Houston et al. 2011) but are also implicated in the genesis of ore deposits both within the basin itself and in adjacent basement rocks (Kesler et al. 1995, 1996; Gleeson et al. 2001, 2003; Banks et al. 2002; Boiron et al. 2005, 2010; Lüders et al. 2005; Wilkinson et al. 2005; Wilkinson 2010).

Brines derived by halite dissolution are dominated by NaCl with low concentrations of Ca, Mg, K, and Br, while those which originate as residual bittern brines are relatively Na-deficient with significant concentrations of Ca, Mg, K and Br. Formation waters show a strong tendency to equilibrate with their host rocks, even at oilfield temperatures (Hanor 1994) and while most are buffered fluids, as defined above, some are mass limited fluids retaining distinctive features such as high Na or K according to their origin, making them particularly potent agents of metasomatism.

Bittern brines derived by halite precipitation have low levels of Na relative to K, and high levels of Ca and Mg. These fluids not only have the potential to dolomitise limestones, they may also cause K metasomatism in quartzofeldspathic rocks as they equilibrate. In contrast brines formed by dissolution of halite are potential agents of albitisation. This is significant because in the context of metasomatism associated with magmatic fluids, K-metasomatism is indicative of hot fluids moving down temperature while Na-metasomatism results from up-temperature flow (see below). Sedimentary brines need not necessarily conform to these rules.

Figure 2.5 is a plot of K/Na (mol units) against 1/T for a range of crustal fluids (see legend) with a calculated curve for the microcline – albite equilibrium. The overall trend in the natural data tracks the equilibrium curve but lies above it. Deviations may arise through both varied natural feldspar compositions and non-ideal behaviour in the fluid, or could be due to poor estimates of the equilibration temperature for fluid inclusions. Even allowing for this however, there are many data points that plot off the trend, especially at low (basinal) temperatures. The Michigan Basin brines data base (Wilson and Long 1993a, b) is clearly not controlled by feldspar equilibrium, being far too rich in K relative to Na; these are examples of ancient bitterns, low in Na and with low Cl/Br (Table 2.1) and would cause K-metasomatism in any feldspathic rock that they infiltrated. In contrast, Offshore Louisiana brines from the study of Land et al. (1988) have interacted with halite beds (high Cl/Br), and have anomalously low levels of K, being very rich in Na. In both cases, these compositions appear to be mass-limited rather than buffered and both sets of brines have considerable potential to metasomatise feldspathic rocks. In contrast, many brines from the Central Mississippi (Carpenter et al. 1974) and North Sea (Warren and Smalley 1994) data sets do lie along the albite – K-feldspar equilibrium trend, suggesting that these are buffered brines. At higher temperatures there is much less variability in K/Na ratios reflecting increased buffering. The Columbian Emerald fluids (Banks et al. 2000b) have extremely high Cl/Br, typical of dissolved evaporate fluids, but although they lie below the equilibrium trend as might be expected, they have

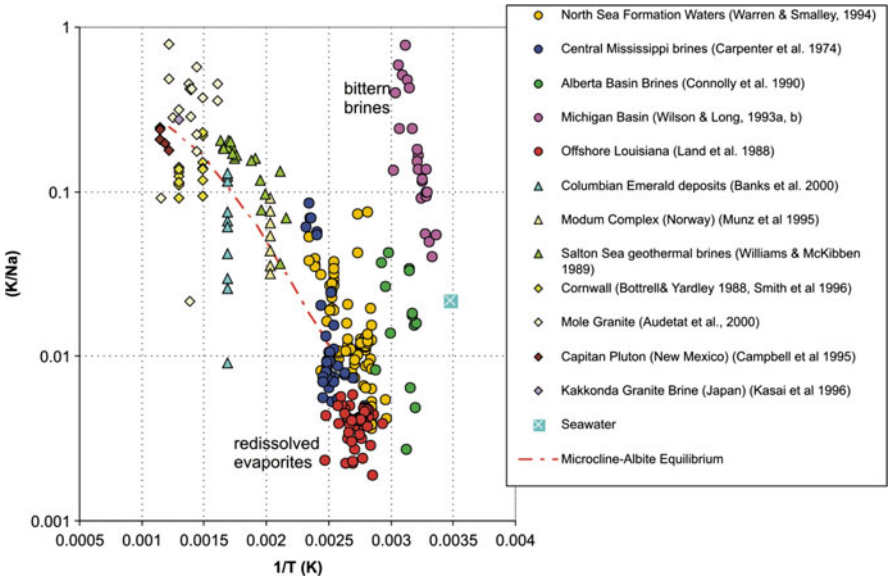

Fig. 2.5 Plot of K/Na ratios (by weight) of crustal fluids against 1/T (K), together with a line representing microcline-albite equilibrium in an ideal fluid. Seawater, and bittern brines (Michigan Basin data), are enriched in K relative to Na compared to feldspar-equilibrated fluids, while brines derived by halite dissolution (Offshore Louisiana) are depleted. Both these are examples of mass-limited brines, but many of the other basin fluids plotted are apparently buffered. At higher temperatures, more fluids lie near the feldspar equilibration trend, but the Columbian Emerald fluids, also redissolved evaporite brines, remain relatively depleted in K

higher K/Na ratios than comparable fluids from Offshore Louisiana, indicating enhanced wall rock interactions at the higher temperatures.

Further evidence of the persistence of primary characteristics in strong brines is given by the behaviour of Ca. Figure 2.6 is a plot of representative brine analyses from the compilations of Houston et al. (2011) and Yardley (2005), demonstrating the link between the relative proportions of Na and Ca (the major cations in almost all formation waters and many other crustal fluids) and temperature. As with Fig. 2.5, the two suites of mass limited brines demonstrate an enormous spread in X_{Ca}. The X_{Ca} parameter is not buffered by mineral equilibria, because it depends also on salinity (Houston et al. 2011). But as in Fig. 2.5, it appears that the higher temperature fluids are likely to be buffered. The relationship between X_{Ca} and Cl/Br provides a clear indication of the link between brine composition and the source of salinity for formation waters (Fig. 2.7a). Buffered brines identified on Fig. 2.5, notably the Central Mississippi data set, show some enrichment in Ca, as would be predicted (Houston et al. 2011), but mass-limited brines are either very low in X_{Ca} with high Cl/Br (i.e. formed by dissolution of evaporates), or very low in Cl/Br but with high X_{Ca} (i.e. bitterns). Thus the Michigan Basin and Offshore Louisiana brines plot at the two extremes of the formation water trend. When higher temperature brines are added to the plot (Fig. 2.7b), they show significant deviations from

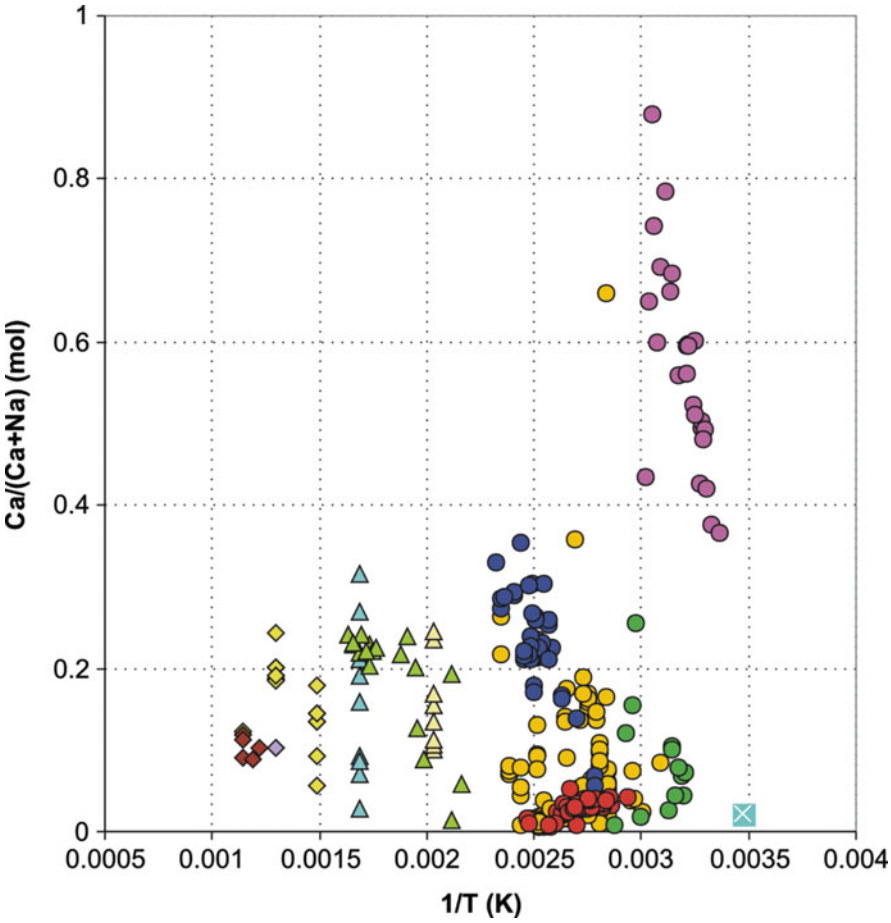

Fig. 2.6 Plot of X_{Ca} against 1/T (same key as Fig. 2.5). Note the large spread in X_{Ca} at low temperatures, where Ca-rich fluids are bittern brines that have dolomitized limestones. The narrower spread at high-T reflects increasing equilibration with plagioclase, but note that X_{Ca} depends on salinity and is not buffered by the coexisting mineral assemblage alone

the formation water trend, with both the high salinity Columbian Emerald brines and the Capitan Pluton brines, both derived from halite beds, showing significant levels of Ca (and other metals, Table 2.1). This is indicative of more extensive interactions with host rocks than occurs under basin conditions. This conforms with the enhanced K-levels noted above, and also the high Fe-levels (Fig. 2.3).

In recent times, the role of basinal brines in giving rise to mineralisation and metasomatism in underlying basement has been recognised in a number of areas. Dolomite veins in Caledonian metamorphic rocks of SW Scotland have been linked to penetration of post-orogenic basinal brines by Parnell et al. (2000), while Holness (2003) has found widespread evidence of fluid penetration into crystalline

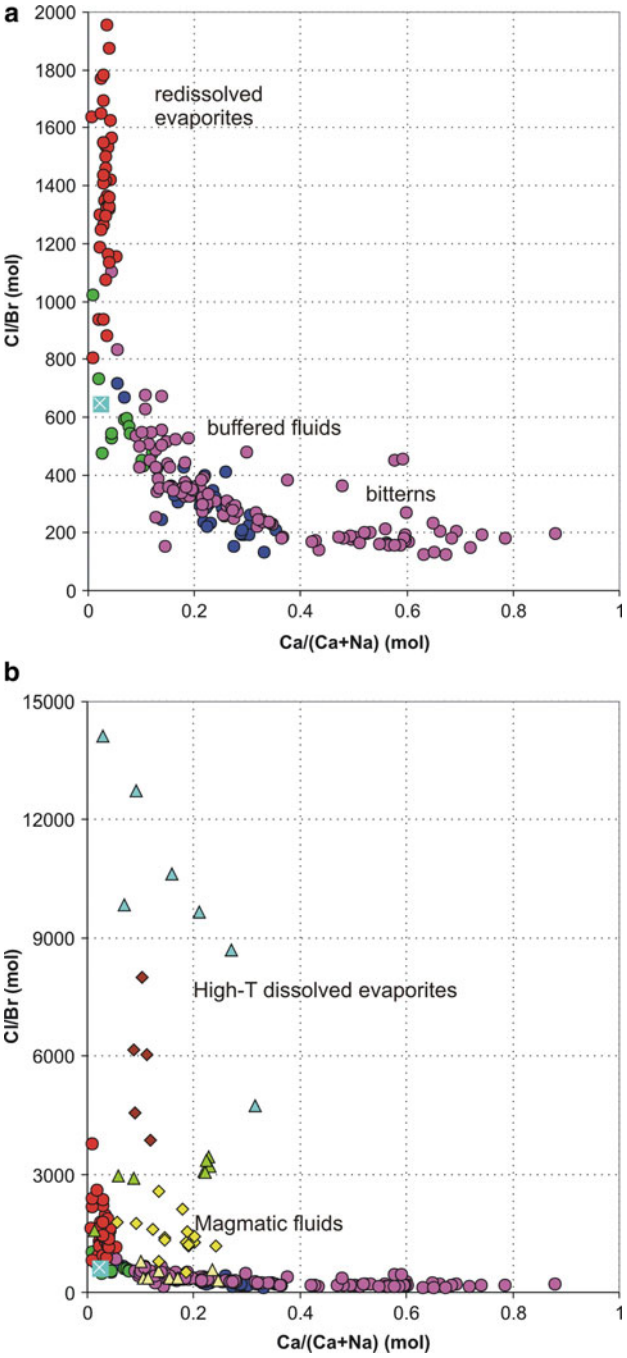

Fig. 2.7 Fluid analyses (same key as Fig. 2.5) plotted as Ca/(Ca + Na) against Cl/Br to demonstrate the links between brine chemistry and brine origin (based on Houston et al. 2011). (**a**) Sedimentary

rocks during exhumation. In the Cloncurry district of Queensland, widespread growth of actinolite and albite (i.e. sodic-calcic metasomatism) has affected basement crystalline rocks as they cooled through greenschist facies conditions under an extensional regime (De Jong and Williams 1995). Subsequent isotope studies implicate a major contribution from the infiltration of basinal fluids (Kendrick et al. 2008). Infiltration of both formation brines and associated hydrocarbons into Precambrian basement rocks has been recognised on the western flanks of the Oslo Graben by Munz et al. (1995, 2002) and Gleeson et al. (2003), and is associated with quartz veins and albitisation. Boiron et al. (2010) have documented a range of examples of ore deposits linked to brines moving between basin and basement, and cite Precambrian unconformity-type U deposits as an important example. Basement rocks beneath sedimentary basins fracture and extend during basinal development, and since the cooled basement rocks are essentially fluid absent at this stage (Yardley 2009), fluid from the overlying basement is readily drawn down. This will be particularly effective if the basal formations in the basin are overpressured.

2.4.2 Metasomatic Fluids Derived from Igneous Intrusions

Another very important source of metasomatic fluids is the crystallisation of magma bodies. A very wide range of fluid compositions can result, depending on both the initial magma chemistry and the conditions (especially depth) of crystallisation, and these have been studied primarily for their ore-forming potential (Ryabchikov 1981; Cline and Bodnar 1991; Audetat et al. 2008). Aqueous fluids may exsolve at an early stage and interact with silicate melts, or may appear only at the final stages. As well as being enriched in incompatible elements, they may also produce distinctive chemical effects through being out of equilibrium with the country rocks with respect to pH or redox state.

Although there is a wide range of metasomatic rocks associated with intrusions, three of the most common are fenites, greisens and skarns (Chap. 7). What we know about the fluids that give rise to such rocks comes from a combination of fluid inclusion studies (see review by Kamenetsky and Kamenetsky 2010), inferences from the chemical changes induced in the rocks, and experimental and theroretical studies of the relevant fluid systems.

Fig. 2.7 (continued) basin fluids showing that very calcic brines are also Br-enriched, mass limited bitterns, while the very sodic mass-limited brines are redissolved evaporite brines. Buffered brines, such as the Central Mississippi brines, show moderate Ca enrichment and lie along the same trend as bitterns. (**b**) Data from metamorphic and magmatic fluids compared with the basinal brines (note different y-axis scale). Note the much smaller range of Cl/Br for magmatic fluids (the Capitan Pluton fluids are derived from assimilated evaporites, Campbell et al 1995) and the much greater uptake of Ca by the metamorphic emerald-forming brines despite their origin by halite dissolution

Fluids may exsolve from magmas as brines, CO_2 fluids or aqueous vapours (Shmulovich et al. 1995; Hack et al. 2007). Alternatively, an initial fluid containing water, NaCl-KCl, and CO_2 components may undergo further unmixing after it has separated from the melt (Audetat et al. 2008). Overall, fluid composition is broadly dependent on magma composition, with basic rocks tending to contain CO_2-rich fluid inclusions (Kamenetsky and Kamenetsky 2010), however some granite-related pegmatite fluids evolve to low salinity, CO_2-rich waters (London 1986). As discussed above, magmatic fluids are likely to have buffered compositions with respect to major rock-forming components such as Fe, K, and Ca. The way in which the fluid composition evolves as fluid separates from the melt is further dependent on the pressure at which unmixing takes place (Cline and Bodnar 1991; Audetat et al. 2008). Some magmatic fluids involved in metasomatism almost certainly preserve a mantle signature (Bell and Simonetti 1996), but other types of metasomatism may be associated with fluids for which crustal interactions, or phase separation within the crust, play a significant role in determining their compositions.

2.4.3 Mantle Fluids and Fenites

The magmatic fluids that have the clearest evidence of a mantle signature are those reported exsolving from melt inclusions from fresh kimberlite material (Kamenetsky et al. 2004; Tomlinson et al. 2009) and those that give rise to mantle isotopic signatures found in fenites (Bell and Simonetti 1996). Fenites are metasomatic rocks of syenitic affinities, rich in alkali feldspars with sodic pyroxene and sometimes also amphiboles, nepheline, or apatite. They occur in association with alkali magmas, but also with carbonatites (Hamilton et al. 1979; Le Bas 2008). Fenitising fluids introduce alkalis, but do not result in an increase in silica content (Le Bas 2008). This implies that the incoming fluid has a relatively high ratio of Na and K to exchangeable H (i.e. H^+ or associated acid species such as HCl°) (Rubie and Gunter 1983), but unusually low silica. For magma to exsolve such a fluid is in marked contrast to the fluids inferred to exsolve from granites in the crust, which are typically both acid (and hence leach alkalis) and silica-rich (below).

Studies of inclusions in diamonds (Izraeli et al. 2001; Tomlinson et al. 2006, 2009) and of fresh kimberlite material itself (Kamenetsky et al. 2004) suggests that kimberlite melts contained a mix of CO_2, H_2O and chloride salts that can exsolve as a fluid phase. Tomlinson et al. (2006, 2009) have reported major and trace element compositions of fluid inclusions in diamonds from the Panda kimberlite, Canada. Because of the very small size of the individual inclusions, it is not possible to obtain sufficient information to reconstruct the total fluid composition, but the normalised major solute composition is shown in Table 2.1. Notable features are that $K > Na$ in molar terms. Iron is usually the next most abundant metal cation, in agreement with the trend noted by Yardley (2005), and Ba is among the most abundant cations. Frezzotti et al. (2010) also reported such fluids in inclusions from metasomatised peridotite xenoliths from Ethiopia, and quoted an overall molar composition of

$XCO_2 = 0.64$, $XH_2O = 0.33$ with the balance made up of chloride salts. Klein-BenDavid et al. (2010) have been able to use isotopic signatures of fluid inclusions in diamonds to demonstrate a mixed origin, with the deep mantle fluid modified by a more radiogenic fluid component released from ancient lithospheric mantle.

While considerable uncertainties remain as to the exact composition of the fluids that exsolve from mantle-derived magmas, they are clearly likely to contain significant quantities of chloride salts and carbon dioxide; indeed it is the effect of the salts in particular in lowering the activity of water (Aranovich and Newton 1996; Shmulovich and Graham 1996) that allow fluids with a significant water content to exist at magmatic temperatures.

Williams-Jones and Palmer (2002) carried out a fluid inclusion study of carbonatites and associated fenites that bears on the fate of such fluid components if they exsolve in the upper crust. They concluded that a CO_2-rich saline aqueous fluid exsolved from the carbonatite melt at high temperature (>700°C) and then unmixed further, exsolving a carbonic fluid. Such a sequence of exsolution accords well with some of the distinctive features of fenitisation. When a carbonic fluid ("vapour") and brine coexist at high temperatures, their very different structures mean that, although activities of all components are equal, concentrations are not. In particular, associated HCl^o is enriched in the vapour phase (Shmulovich et al. 1995). If the two phases separate at high temperature and then cool, the vapour phase will be highly acid, while the brine will be relatively alkali-rich (Shmulovich et al. 1995, their Figs. 8, 9). Thus the combination of exsolution and the physical separation of the phases as they flow may give rise to high pH saline aqueous fluids likely to cause alkali metasomatism. Exsolution may also account for the lack of silicification associated with fenitisation. Carbon dioxide lowers the solubility of quartz in water (Shmulovich et al. 2001; Newton and Manning 2000), and so the effect of exsolution of CO_2 from the aqueous phase is to leave it undersaturated with silica. For reference, the solubility of quartz in H_2O–CO_2 fluid at 800°C and 0.5 GPa with $XCO_2 = 0.7$ is slightly lower than that of quartz in pure water at 500°C and 0.5 GPa (Shmulovich et al. 2006) so the effect is a significant one.

2.4.4 Greisen Fluids

Greisen (Fig. 2.8) is a hydrothermally altered and metasomatised granite commonly associated with Sn-W mineralisation, and more generally with the waning stages of crystallisation of S-type granites. The formation of greisen involves the breakdown of feldspar to produce muscovite, and often the precipitation of quartz, together with minerals such as cassiterite, tourmaline, beryl and topaz, in veins or vugs. Experimental studies, subsequently refined by thermodynamic modelling (Hemley 1959; Gunter and Eugster 1980; Sverjensky et al. 1991) have demonstrated that chloride fluids equilibrated with granite mineralogy at elevated temperatures will have relatively high proportions of K and H species relative to Na species compared to fluids equilibrated with the same assemblage at lower

Fig. 2.8 Example of a greisen vein cutting granite (subsequently kaolinised), Cligga Head, Cornwall, UK. A central tourmaline vein is flanked by greisen in which feldspars are largely replaced by muscovite and quartz

temperatures. Hence the effect of movement of fluid from hot granite to cold granite is to leach alkalis from the rock to neutralise acidity (hence converting feldspar to mica), and to convert albite to K-feldspar, thereby exchanging K in the initial fluid for Na. This sequence accords well with observed gangue mineral zonation around many granite-hosted ore deposits (e.g. Halter et al. 1998). Additional effects undoubtedly occur due to the presence of significant levels of F and/or B in many greisen fluids, but these are much less well understood. Greisen fluids are probably closely linked to fluids that form pegmatites, where the impact of F and B in highly evolved fluids is known to be significant (Thomas et al. 2000)

Fluid inclusion studies of greisens from a wide range of areas all point to the involvement of moderately saline water (Jackson et al. 1989; Markl and Schumacher 1996; Smith et al. 1996; Conliffe and Feely 2006; Audetat et al. 2008), and suggest temperatures of formation in the range 200–450°C. The lowest temperature greisens are not always associated with classical granite mineralisation, and it has been suggested by Boiron et al. (1996) that they may form from fluids utilising heat and fracture networks in granite, but not necessarily derived from the granite magma itself. Examples of greisen fluids are included in Table 2.1.

2.4.5 Skarn Formation

Skarns are coarse grained rocks, usually dominated by Ca-rich minerals such as garnet, amphibole or pyroxene, and inferred to result from medium to high-T interactions between carbonate and silicate rocks mediated by movement of fluid (Fig. 2.1). The replacement of carbonate rocks by silicate minerals leads to exoskarns while less commonly the replacement of silicate rocks by similar calc-

silicates forms endoskarns. The formation of silicate skarns after marbles or limestones is an important feature of contact metamorphism, where there is generally a clear link to magmatic fluids, but some types also develop in regional metamorphism where there is little evidence of magmatic fluid involvement (Einaudi et al. 1981). Not surprisingly, the main focus in the literature is on skarns that are ore bodies (Meinert et al. 2005), but skarns occur wherever high temperature fluids from silicate lithologies encounter carbonate rocks.

Skarns typically form at temperatures of 450–600°C, and under these conditions quartz is only stable in dolomitic marbles in the absence of water. If water is able to infiltrate, silicate minerals result. A special feature of skarns is that reaction is very extensive; indeed the original carbonate rock may be completely consumed, and where it does remain it is as reasonably intact bed remnants surrounded by skarn in which no original carbonate remains (Fig. 2.1b). Marbles are normally rather impermeable, commonly retaining sedimentary isotope signatures rather than those of high metamorphic grades, but carbonate-breakdown reactions may lead to a transient increase in porosity and permeability, providing a positive feedback mechanism for further reaction (Balashov and Yardley 1998). Once reaction has begun, porosity opens up and more reactive fluid is forced in. Contact skarns are commonly mineralised and often rich in Fe. This accords with the elevated levels of many transition metals found in magmatic fluids, especially when salinity is high and does not require a special skarn fluid (e.g. the Mole Granite fluids reported by Heinrich et al. 1992, and Audetat et al. 2000, examples of which are included in Table 2.1). Available fluid inclusion data for contact skarns appear typical of magmatic fluids (Baker et al. 2004).

In regional metamorphism, skarn formation is also a process that takes place under conditions far from equilibrium, but here it may simply be the onset of thermally-driven decarbonation reactions within the marble that triggers skarn formation. For example Yardley et al. (1991) and Yardley (2009) have documented the development of a coarse and nearly monomineralic diopside bed from an original dolomitic marble layer during regional sillimanite zone metamorphism, and suggest that the breakdown of dolomite + quartz to diopside increased porosity and permeability of the layer and so triggered the influx of quartz-saturated water from the surrounding schists that reacted with the remaining dolomite. In such instances, the fluid would have been a quartz-saturated metamorphic fluid from nearby schists, and it is unlikely that a high salinity would be required since the main effects are the growth of silicates and Al-silicates in former marble, which do not require the influx of Cl-complexed metals.

Endoskarns typically involve breakdown of plagioclase feldspar and growth of epidote or Ca-garnets, and this is a reaction sequence that will develop as a response to the infiltration of fluids with a relatively high $(a\mathrm{Ca}^{++})/(a\mathrm{H}^{+})^{2}$ (e.g. Bowers et al. 1984). It seems probable that these fluids are the products of reaction between more normal aqueous fluids and marbles, taking place nearby to produce exoskarns.

2.5 Metasomatic Fluids During Deep Crustal Metamorphism

2.5.1 Metamorphic Fluids

Away from carbonate lithologies, most metamorphic fluids appear to be aqueous chloride solutions with a low to moderate CO_2 component (Crawford 1981; Stout et al. 1986). Despite the release of water by metamorphic dehydration reactions, metamorphic inclusion fluids are commonly more saline than seawater and as a result it is likely that immiscibility between aqueous and carbonic fluids is widespread at low to medium metamorphic grades (Crawford and Hollister 1986; Heinrich 2007). Yardley and Graham (2002) reported that there was a marked correlation between the salinity of metamorphic fluids in metasediments and the depositional environment in which the sediments formed. Shelf sequences commonly yield very saline metamorphic fluids that may reflect the original presence of evaporates or bittern brines.

Despite many reports of the salinity and sometimes CO_2 content of metamorphic fluids from microthermometry, there are relatively few quantitative analyses of metamorphic fluids because of the practical difficulties involved in analysis. Analyses are usually made of fluid inclusions in quartz, because other host minerals contribute an unacceptably high background for many elements of interest, but quartz readily recrystallises during a prolonged metamorphic history, and so unmodified primary fluid inclusions are rarely preserved at higher grades.

Because of "salting-out" effects on CO_2 solubility, CO_2-rich fluids are generally of relatively low salinity (comparable to seawater), and the analysis of orogenic gold deposit fluids in Table 2.1 is probably representative. CO_2 leads to a marked reduction in the solubility of silica because of its high solvation number (Shmulovich et al. 2006; Newton and Manning 2000). In contrast, saline low grade metamorphic fluids are represented in Table 2.1 by analyses of inclusions from veins in thrusts and shear zones of the Pyrenees (McCaig et al. 2000) and quartz-emerald veins from Columbia (Banks et al. 2000a).

2.5.2 Links Between Metamorphic and Sedimentary Brines

Sedimentary formation waters evolve continuously into metamorphic fluids with burial and heating, and some chemical signatures, such as salinity, appear to be retained in the metamorphic environment. However it is also likely that brines can continue to develop during metamorphism through further dissolution of halite at elevated temperatures, or through consumption of water to form hydrous minerals. Saline fluids involved in metasomatism during a regional metamorphic cycle may have been originally saline formation waters or may have acquired their salinity by remobilisation of evaporite deposits during metamorphism. In the case of the Columbian Emerald fluids discussed earlier, fluid inclusions have halite daughter

crystals at room temperature, and this, together with their high Cl/Br ratios, demonstrates an origin by halite dissolution at elevated subsurface temperatures.

There are several well-documented examples in which metamorphosed evaporite-bearing sequences develop metasomatic features indicative of the action of brines. In the Mary Kathleen district of Queensland, Cl-bearing scapolite occurs in metasediments that formerly contained evaporite minerals, and scapolitisation of metabasalts adjacent to the metasediments is widespread. It is inferred to reflect metasomatism by brines derived from the evaporite-bearing sediments (Ramsay and Davidson 1970; Oliver 1992). Similar effects are known from the Betic Cordillera of Spain (Gómez-Pugnaire et al. 1994). In the Mary Kathleen examples, metasomatism appears to have accompanied the peak of metamorphism, but in south Norway, another region in which basement rocks are extensively albitised, scapolite and albite may be related to the introduction of saline fluids generated by mobilisation of evaporites during later orogenesis (Engvik et al. 2011).

While some of the distinctive features of sedimentary brines are retained into metamorphism, progressive equilibration with wall rocks at progressively lower porosities will serve to gradually eliminate them, as demonstrated with Fig. 2.5, above. Inclusions of the Columbian Emerald fluids have halite daughter crystals, which dissolve at temperatures well above room temperature, indicative of further halite dissolution into the brine during diagenesis and low grade metamorphism.

At amphibolite facies temperatures and above, intermediate plagioclase is stable, and the Ca-Na relationships are then controlled by feldspar-fluid equilibria and by salinity. It is likely that high grade metamorphic fluids will show less variability in Ca-Na relationships than sedimentary formation waters, but data will be hard to acquire. Shmulovich and Graham (2008) have recently extended the classic work of Orville (1972) on Ca-Na partitioning between plagioclase and fluid to higher pressures and higher chloride fluids. In low salinity fluids, Na is strongly partitioned into the fluid phase, but this effect is much less marked in concentrated brines where the Ca/Na ratio in equilibrium with a particular plagioclase composition will always be higher than for a dilute fluid.

2.6 Conclusions

Metasomatism can be driven by almost any crustal fluid. However, those with a high dissolved load are more likely to be able to achieve significant chemical change to the rocks through which they pass, except in settings, such as in the upper crust, where very large fluid fluxes are possible.

Metasomatic changes in silica content are likely to reflect primarily changes in temperature, pressure (silica solubility increases with T and P) or gas content. The relatively high solvation number of aqueous silica means that the lowering of the H_2O activity by dissolution of CO_2 or other gas species will strongly reduce silica solubility. It is likely that similar factors also dominate alumina solubility, but far less data is available at present.

For most metals, concentrations in the fluid phase depend on Cl-concentration, which is not easily changed by fluid-rock interaction. Systematic changes in pH and the concentrations of K, Fe and other transition metals with temperature for fluids equilibrated with silicate rocks mean that movement of fluid along a temperature gradient will lead to metasomatism. Many of the most potent metasomatic fluids are hypersaline brines derived from sedimentary evaporate systems, and these may retain some original characteristics, such as very high Na for brines derived by halite dissolution, or high K, Ca and Mg for bittern brines, even after long crustal residence times. Such fluids not only produce albitisation and/or dolomitisation in sedimentary basins, they also produce similar metasomatic changes in crystalline basement rocks of the upper crust. Saline fluids derived from igneous bodies can also produce metasomatism, and distinctive chemical signatures rich in volatile elements can arise if the magma is highly evolved when the fluid separates.

Metamorphic fluid compositions evolve continuously from those of formation waters through diagenesis. However the low porosity and high fluid pressure of recrystallised rocks undergoing metamorphism, coupled with the slow rate at which fluids are released by strongly endothermic metamorphic reactions, means that only in special circumstances can metasosomatism be caused by metamorphic fluids in the strict sense. These include development of skarns as quartz – bearing dolomitic marbles are heated above the stability of dolomite + quartz creating widespread secondary porosity, and rapid release of fluids in response to rapid uplift of greenschists and slates, which can lead to gold-quartz veins and orogenic gold deposits. There is little data as yet on the composition of fluids associated with deep serpentinites in subduction zone systems, but it is reasonable to suppose that, like shallow fluids related to serpentinites, they may have unusual compositions prone to react with a range of crustal rock types, mirroring the changes seen in metasomatic blackwalls formed predominantly by diffusion metasomatism around ultrabasic bodies.

There has been extensive speculation in the past on the possible role of mantle fluids in metasomatism, and data is now emerging from a number of sources to indicate that mantle fluids are both highly saline and rich in CO_2. Major metasomatic changes in the strict sense of the term are due to the brine component of the mantle fluids, but passage of exsolved CO_2 through high grade rocks can probably also trigger dehydration while the aqueous fluid from which CO_2 has exsolved is likely to be strongly silica undersaturated.

While there are many aspects of metamorphic fluids that are not well understood, particularly in the context of subduction zone settings, our understanding has now advanced to the point where some aspects of metasomatism can be confidently related to specific fluid types and movement styles. We can predict the behaviour of a wide range of elements as a buffered fluid moves between lithologies or into zones of different temperature or pressure, and we can also recognise the effects of concentrated fluids related to evaporite formation. None of the general rules I have outlined is completely universal; all must be evaluated in context. For example cooling fluids that exsolve CO_2 may dissolve silica rather than precipitating it, while hypersaline "mass-limited" brines can produce metasomatic albite or K-feldspar irrespective of the direction of temperature change. Despite these

caveats, we are now in a position to interpret metasomatism in the context of the overall geological evolution of the rocks in which it occurs, and use it to refine geological models, not just to paper over cracks in our understanding.

Acknowledgements Many of the ideas expressed here were first developed on visits to Nick Oliver and Pat Williams at James Cook University, and especially on field trips with them. I would also like to acknowledge conversations with Andrew Putnis. The manuscript was prepared while I held a Humboldt Award at the Deutsche GeoForschungZentrum, Potsdam. I am particularly grateful to Wilhelm Heinrich and Chris Heinrich for pointing out some deficiencies and omissions in the original version and helping me realise how badly it was written.

References

Ague JJ (1994) Mass transfer during Barrovian metamorphism of pelites, south-central Connecticut. I: evidence for changes in composition and volume. Am J Sci 294:989–1057

Ague JJ (2003) Fluid infiltration and transport of major, minor and trace elements during regional metamorphism of carbonate rocks, Wepawaug Schist, Connecticut, USA. Am J Sci 303:753–816

Aranovich LY, Newton RC (1996) H_2O activity in concentrated NaCl solutions at high pressures and temperatures measured by the periclase-brucite equilibrium. Contrib Mineral Petrol 125:200–212

Audetat A, Günther D, Heinrich CA (2000) Magmatic-hydrothermal evolution in a fractionating granite: a microchemical study of the Sn-W-F mineralized Mole granite (Australia). Geochim Cosmochim Acta 64:3373–3393

Audetat A, Pettke T, Heinrich CA, Bodnar RJ (2008) The composition of magmatic-hydrothermal fluids in barren and mineralized intrusions. Econ Geol 3:877–908

Bach W, Jöns N, Klein F (this volume) Metasomatism within the oceanic crust. Chapter 8

Baker T, Achterberg EV, Ryan CG, Lang JR (2004) Composition and evolution of ore fluids in a magmatic-hydrothermal skarn deposit. Geology 32:117–120

Balashov VN, Yardley BWD (1998) Modeling metamorphic fluid flow with reaction-compaction-permeability feedbacks. Am J Sci 298:441–470

Banks DA, Green R, Cliff RA, Yardley BWD (2000a) Chlorine isotopes in fluid inclusions: determination of the origins of salinity in magmatic fluids. Geochim Cosmochim Acta 64:1785–1789

Banks DA, Guilliani G, Yardley BWD (2000b) Emerald mineralisation in Columbia: fluid chemistry and the role of brine mixing. Miner Deposita 35:699–713

Banks DA, Boyce AJ, Samson IM (2002) Constraints on the fluids forming Irish Zn-Pb-Ba deposits: evidence from the composition of fluid inclusions. Econ Geol 97:471–480

Bebout G (this volume) Metasomatism in subduction zones of subducted oceanic slabs, mantle wedges, and the slab-mantle interface. Chapter 9

Bell K, Simonetti A (1996) Carbonatite magmatism and plume activity: implications from the Nd, Pb and Sr isotope systematics of Oldoinyo Lengai. J Petrol 37:1321–1339

Bethke CM (2007) Geochemical and biogeochemical reaction modeling, 2nd edn. Cambridge University Press, Cambridge, 564 pp

Bjorlykke K (1998) Clay mineral diagenesis in sedimentary basins – a key to the prediction of rock properties. Examples from the North Sea basin. Clay Miner 33:15–34

Bohlke JK, Irwin JJ (1992) Brine history indicated by argon, krypton, chlorine, bromine and iodine analyses of fluid inclusions from the Mississippi valley type lead fluorite barite deposits at Hansonburg, New Mexico. Earth Planet Sci Lett 110:51–66

Boiron MC, Cathelineau M, Banks DA, Yardley BWD, Noronha F, Miller MF (1996) P-T-X conditions of late Hercynian fluid penetration and the origin of granite-hosted gold quartz veins in northwestern Iberia: a multidisciplinary study of fluid inclusions and their chemistry. Geochim Cosmochim Acta 60:43–57

Boiron MC, Cathelineau M, Banks DA, Buschaert S, Fourcade S, Coulibaly Y, Michelot JL, Boyce A (2005) Fluid transfers at a basement/cover interface Part II. Large-scale introduction of chlorine into the basement by Mesozoic basinal brines. Chem Geol 192:121–140

Boiron MC, Cathelineau M, Richard A (2010) Fluid flows and metal deposition near basement/cover unconformity: lessons and analogies from Pb-Zn-F-Ba systems for the understanding of Proterozoic U deposits. Geofluids 10:270–292

Bottrell SH, Yardley BWD (1988) The composition of a primary granite-derived ore fluid from S.W. England, determined by fluid inclusion analysis. Geochim Cosmochim Acta 52:585–588

Bottrell SH, Yardley BWD (1991) The distribution of Fe and Mn between chlorite and fluid – evidence from fluid inclusions. Geochim Cosmochim Acta 55:241–244

Bottrell SH, Yardley BWD, Buckley F (1988) A modified crush-leach method for the analysis of fluid inclusion electrolytes. Bull Mineral 111:279–290

Bowers TS, Jackson KJ, Helgeson HC (1984) Equilibrium activity diagrams for coexisting minerals and aqueous solutions at pressures and temperatures to 5 kb and 600°C. Springer, Berlin

Bucher K, De Capitani C, Grapes R (2005) The development of a margarite-corundum blackwall by metasomatic alteration of a slice of mica schist in ultramafic rock, Kvesjöen, Norwegian Caledonides. Can Mineral 43:129–156

Bucholz CE, Ague JJ (2010) Fluid flow and Al transport during quartz-kyanite vein formation, Unst, Shetland Islands, Scotland. J Metamorph Geol 28:19–39

Campbell AR, Banks DA, Phillips RS, Yardley BWD (1995) Geochemistry of Th-U-REE mineralizing magmatic fluids, Capitan Mountains, New Mexico. Econ Geol 90:1271–1287

Carpenter AB, Trout ML, Pickett EE (1974) Preliminary report on the origin and chemical evolution of lead-and-zinc-rich oilfield brines in Central Mississippi. Econ Geol 69:1191–1206

Cline JS, Bodnar RJ (1991) Can economic porphyry copper mineralization be generated by a typical calc-alkaline melt? J Geophys Res 96:8113–8126

Conliffe J, Feely M (2006) Microthermometric characteristics of fluids associated with granite and greisen quartz and vein quartz and beryl from the Rosses Granite complex, Donegal, NW Ireland. J Geochem Explor 89:73–77

Connolly JAD (2010) The mechanics of metamorphic fluid expulsion. Elements 6:165–172

Connolly CA, Walter LM, Baadsgaard H, Longstaffe FJ (1990) Origin and evolution of formation waters, Alberta basin, western Canada sedimentary basin. I. Chemistry. Appl Geochem 5:375–395

Craw D, Upton P, Yu B-S, Horton T, Chen Y-G (2010) Young orogenic gold mineralisation in active collisional mountains, Taiwan. Miner Deposita 45:631–646

Crawford ML (1981) Fluid inclusions in metamorphic rocks-low and medium grade. In: Hollister LS, Crawford ML (eds) Short course in fluid inclusions, vol. 6. Mineralogical Association of Canada short course notes Quebec, pp 157–181

Crawford ML, Hollister LS (1986) Metamorphic fluids: the evidence from fluid inclusions. In: Walther JV, Wood BJ (eds) Fluid-rock interactions during metamorphism. Springer, New York, pp 1–35

Davisson ML, Criss RE (1996) Na-Ca-Cl relations in basinal fluids. Geochim Cosmochim Acta 60:2743–2752

Day-Stirrat RJ, Milliken KL, Dutton SP, Loucks RG, Hillier S, Aplin AC, Schleicher AM (2010) Open-system chemical behaviour in deep Wilcox Group mudstoes, Texas gulf coast, USA. Mar Pet Geol 27:1804–1818

De Jong G, Williams PJ (1995) Giant metasomatic system formed during exhumation of mid-crustal Proterozoic rocks in the vicinity of the Cloncurry Fault, northwest Queensland. Aust J Earth Sci 42:281–290

Duan Z, Moller N, Weare JH (1995) Equation of state for the NaCl – H2O – CO system: prediction of phase equilibria and volumetric properties. Geochim Cosmochim Acta 59:2869–2882
Einaudi MT, Meinert LD, Newberry RJ (1981) Skarn deposits. Econ Geol 100:317–391
Engvik AK, Mezger K, Wortelkamp S, Bast R, Corfu F, Kornellussen A, Ihlen P, Bingen B, Austrheim H (2011) Metasomatism of gabbro – mineral replacement and element mobilization during the Sveconorwegian metamorphic event. J Metamorph Geol 29:399–423
Eugster HP, Gunter WD (1981) The compositions of supercritical metamorphic solutions. Bull Mineral 104:817–826
Evans K (2007) Quartz solubility in salt-bearing solutions at pressures to 1 GPa and temperatures to 900°C. Geofluids 7:451–467
Ferry JM (1994) Overview of the petrologic record of fluid-flow during regional metamorphism in northern New England. Am J Sci 294:905–988
Frezzotti ML, Ferrando S, Peccerillo A, Petrelli M, Tecce F, Perucchi A (2010) Chlorine-rich metasomatic H_2O-CO_2 fluids in amphibole-bearing peridotites from Injibara (Lake Tana region, Ethiopian plateau): nature and evolution of volatiles in the mantle of a region of continental flood basalts. Geochim Cosmochim Acta 74:3023–3039
Gleeson SA, Wilkinson JJ, Stuart FM, Banks DA (2001) The origin and evolution of base metal mineralising brines and hydrothermal fluids, south Cornwall, UK. Geochim Cosmochim Acta 65:2067–2079
Gleeson SA, Yardley BWD, Munz IA, Boyce AJ (2003) Infiltration of basinal fluids into high-grade basement, south Norway: sources and behaviour of waters and brines. Geofluids 3:33–48
Goldfarb RJ, Leach DL, Pickthorn WJ, Patterson CJ (1988) Geology 16:440–443
Gómez-Pugnaire MT, Franz G, Sánchez-Vizcaino VL (1994) Retrograde formation of NaCl-Scapolite in high pressure metaevaporites from the Cordilleras Béticas, Spain. Contrib Mineral Petrol 116:448–461
Groves DI, Goldfarb RJ, Robert F, Hart CJR (2003) Gold deposits in metamorphic belts: overview of current understanding, outstanding problems, future research and exploration significance. Econ Geol 98:1–29
Gunter WD, Eugster HP (1980) Mica-feldspar equilibria in supercritical alkali chloride solutions. Contrib Mineral Petrol 75:235–250
Günther D, Audetat A, Frischknecht R, Heinrich CA (1998) Quantitative analysis of major, minor and trace elements in fluid inclusions using laser-ablation-inductively coupled plasma-mass spectrometry (LA-ICP-MS). J Anal Atom Spect 13:263–270
Hack AC, Thompson AB, Aerts M (2007) Phase relations involving hydrous silicate melts, aqueous fluids, and minerals. Rev Mineral Geochem 65:129–185
Halter WE, Williams-Jones AE, Kontak DJ (1998) Modeling fluid-rock interaction during greisenization at the East Kemptville tin deposit: implications for mineralization. Chem Geol 150:1–17
Hamilton DL, Freestone IC, Dawson JB, Donaldson CH (1979) Origin of carbonatites by liquid immiscibility. Nature 279:52–54
Hanor JS (1994) Origin of saline fluids in sedimentary basins. In: Parnell J (ed) Geofluids, origin, migration and evolution of fluids in sedimentary basins, vol 78, Geological Society Special Publications. Geological Society, London, pp 151–174
Heinrich W (2007) Fluid immiscibility in metamorphic rocks. Rev Mineral Geochem 65:389–430
Heinrich CA, Ryan CG, Mernagh TP, Eadington PJ (1992) Segregation of ore metals between magmatic brine and vapour – a fluid inclusion study using PIXE micoanalysis. Econ Geol 87:1566–1583
Hemley JJ (1959) Some mineralogical equilibria in the system K_2O-Al_2O_3-SiO_2-H_2O. Am J Sci 257:241–270
Holness MB (2003) Growth and albitization of K-feldspar in crystalline rocks in the shallow crust: a tracer for fluid circulation during exhumation? Geofluids 3:89–102
Houston SJ, Yardley BWD, Smalley PC, Collins IR (2007) Rapid fluid-rock interactions in oilfield reservoirs. Geology 35:1143–1146

Houston SJ, Smalley PC, Laycock A, Yardley BWD (2011) The relative importance of buffering and brine inputs in controlling the abundance of Na and Ca in sedimentary formation waters. Mar Pet Geol 28:1242–1251

Huang W, Rubenach M (1995) Structural controls on syntectonic metasomatic tremolite and tremolite-plagioclase pods in the Molanite Valley, Mt. Isa, Australia. J Struct Geol 17:83–94

Humphris SE, Thompson RN (1978) Hydrothermal alteration of oceanic basalts by seawater. Geochim Cosmochim Acta 42:107–125

Ingebritsen SE, Appold MS (in press) The physical hydrogeology of ore deposits. Econ Geol

Izraeli ES, Harris JW, Navon O (2001) Brine inclusions in diamonds: a new upper mantle fluid. Earth Planet Sci Lett 187:323–332

Jackson NJ, Willis Richards J, Manning DAC, Sams MS (1989) Evolution of the Cornubian ore field, southwest England. 2. Mineral-deposits and ore-forming processes. Econ Geol 84:1101–1133

Kamenetsky VS, Kamenetsky MB (2010) Magmatic fluids immiscible with silicate melts: examples from inclusions in phenocrysts and glasses, and implications for magma evolution and metal transport. Geofluids 10:293–311

Kamenetsky MB, Sobolev AV, Kamenetsky VS, Maas R, Danyushevsky LV, Thomas R, Pokhilenko NP, Sobolev NV (2004) Kimberlite melts rich in alkali chlorides and carbonates: a potent metasomatic agent in the mantle. Geology 32:845–848

Kasai K, Sakagawa Y, Miyazaki S, Sasaki M, Uchida T (1996) Supersaline brine obtained from Quaternary Kakkonda granite by the Nedo's deep geothermal well WD-1A in the Kakkonda geothermal field, Japan. Geotherm Res Counc Trans 20:623–629

Kendrick MA, Burgess R, Harrison D, Bjorlykke A (2005) Noble gas and halogen evidence for the origin of Scandinavian sandstone-hosted Pb-Zn deposits. Geochim Cosmochim Acta 69:109–129

Kendrick M, Baker T, Fu B, Phillips D, Williams PJ (2008) Noble gas and halogen constraints on regionally extensive mid-crustal Na-Ca metasomatism, the Proterozoic eastern Mount Isa block, Australia. Precambrian Res 163:131–150

Kent AJR, Ashley PM, Fanning CM (2000) Metasomatic alteration associated with regional metamorphism: an example from the Willyama Supergroup, South Australia. Lithos 54:33–62

Kerrick DM (1977) Genesis of zoned skarns in Sierra-Nevada, California. J Petrol 18:144–181

Kesler SE, Appold MS, Walter LM, Martini AM, Huston TJ, Kyle JR (1995) Na-Cl-Br systematics in Mississippi Valley-type brines. Geology 23:641–644

Kesler SE, Martini AM, Appold MS, Walter LM, Huston TJ, Furman F (1996) Na-Cl-Br systematics of fluid inclusions from Mississippi Valley-type deposits, Appalachian basin: constraints on solute origina and migration paths. Geochim Cosmochim Acta 60:225–233

Klein-BenDavid O, Pearson DG, Nowell GM, Ottley C, McNeill JCR, Cartigny P (2010) Mixed fluid sources involved in diamond growth constrained by Sr-Nd-Pb-C-N isotopes and trace elements. Earth Planet Sci Lett 289:123–133

Knauth LP (1979) A model for the origin of chert in limestone. Geology 7:274–277

Korzhinskii DS (1958) Physicochemical basis of the analysis of the paragenesis of minerals. Consultants Bureau, New York

Korzhinskii DS (1970) Theory of metasomatic zoning. Oxford University Press, Oxford

Land LS (1995) Na-Ca-Cl saline formation waters, Frio Formation (oligocene), south Texa, USA – products of diagenesis. Geochim Cosmochim Acta 59:2163–2174

Land LS, Macpherson GL, Mack LE (1988) The geochemistry of saline formation waters, Miocene, offshore Louisiana. Gulf Coast Assoc Geol Socs Trans 38:503–511

Le Bas MJ (2008) Fenites associated with carbonatites. Can Mineral 46:915–932

Liebscher A (2007) Experimental studies in model fluid systems. Rev Mineral 65:15–47

London D (1986) Mamatic-hydrothermal transition in the Tanco rare-earth pegmatite: evidence from fluid inclsuions and phase-equilibrium experiments. Am Mineral 71:376–395

Lüders V, Reutel C, Hoth P, Banks DA, Mingram B, Pettke T (2005) Fluid and gas migration in the North German Basin: fluid inclusion and stable isotope constraints. Int J Earth Sci 94:990–1009

Markl G, Bucher K (1998) Composition of fluids in the lower crust inferred from metamorphic salt in lower crustal rocks. Nature 391:781–783

Markl G, Schumacher JC (1996) Spatial variations in temperature and composition of greisen-forming fluids; an example from the Variscan Triberg granite complex, Germany. Econ Geol 91:576–589

McCaig AM (1997) The geochemistry of volatile fluid flow in shear zones. In: Holness MB (ed) Deformation-enhanced fluid transport in the Earth's crust and mantle. Mineralogical Society, London

McCaig AM, Tritlla J, Banks DA (2000) Fluid mixing and recycling during Pyrenean thrusting: evidence from fluid inclusion halogen ratios. Geochim Cosmochim Acta 64:3395–3412

Meinert LD, Dipple GM, Nicolescu S (2005) World skarn deposits. Econ Geol 100:299–336

Menzies M, Murthy VR (1980) Mantle metasomatism as a precursor to the genesis of alkaline magmas – isotopic evidence. Am J Sci 280:622–638

Michard G, Albarede F, Michard A, Minster J-F, Charlou J-L, Tan N (1984) Chemistry of solutions from the 13°N East Pacific rise hydrothermal site. Earth Planet Sci Lett 67:297–307

Milliken KL (1989) Petrography and composition of authigenic feldspars, Oligocene Frio formation, south Texas. J Sediment Petrol 59:361–374

Munz IA, Yardley BWD, Banks DA, Wayne D (1995) Deep penetration of sedimentary fluids into basement rocks from southern Norway: evidence from hydrocarbon and brine inclusions in quartz veins. Geochim Cosmochim Acta 59:239–254

Munz IA, Yardley BWD, Gleeson SA (2002) Petroleum infiltration of high-grade basement, South Norway: pressure–temperature–time (P–T–t–X) constraints. Geofluids 2:41–53

Newton RC (1989) Metamorphic fluids in the deep crust. Annul Rev Earth Planet Sic 17:385–412

Newton RC, Manning CE (2000) Quartz solubility in H_2O and H_2O–CO_2 solutions at deep crust – upper mantle pressures and temperatures: 2–15 kbar and 500–900°C. Geochim Cosmochim Acta 64:2993–3005

Newton RC, Manning CE (2002) Experimental determination of calcite solubility in H_2O–NaCl solutions at deep crust/upper mantle pressures and temperatures: implications for metasomatic processes in shear zones. Am Mineral 87:1401–1409

Newton RC, Manning CE (2005) Solubility of anhydrite, CaSO4, in NaCl–H_2O solutions at high pressures and temperatures: applications to fluid-rock interaction. J Petrol 46:701–716

Newton RC, Manning CE (2008) Solubility of corundum in the system Al_2O_3-SiO_2-H_2O-NaCl at 800°C and 10 kbar. Chem Geol 249:250–261

O'Reilly S, Griffin W (this volume) Mantle metasomatism. Chapter 12

Oliver NHS (1992) Internal control of fluid compositions in amphibolite-facies scapolitic calc-silicates, Mary Kathleen, Australia. Contrib Mineral Petrol 111:94–112

Oliver NHS, Wall VJ (1987) Metamorphic plumbing system in Proterozoic calc-silicates, Queensland, Australia. Geology 15:793–796

Orville PM (1972) Plagioclase ion exchange equilibria with aqueous chloride solutions: results at 700°C and 2000 bars in the presence of quartz. Am J Sci 272:234–272

Parnell J, Baron M, Davidson M, Elmore D, Engel M (2000) Dolomitic breccia veins as evidence for extension and fluid flow in the Dalradian of Argyll. Geol Mag 137:447–462

Pirajno F (this volume) Metasomatism and mineral systems. Chapter 7

Ramsay CR, Davidson LR (1970) The origin of scapolite in the regionally metamorphosed rocks of Mary Kathleen, Queensland, Australia. Contrib Mineral Petrol 25:41–51

Rittenhouse G (1967) Bromine in oilfield waters and its use in determining the possibilities of origins of these waters. AAPG Bull 51:2430–2440

Rubenach M (this volume) Mechanics of metasomatism on a regional scale. Chapter 4

Rubie DC, Gunter WD (1983) The role of speciation in alkaline igneous fluids during fenite metasomatism. Contrib Mineral Petrol 82:165–175

Ryabchikov ID (1981) Mobilization of ore metals by supercritical fluids from crystallizing magmas. Phys Chem Earth 13–14:529–536

Saigal GC, Morad S, Bjorlykke K, Egeberg PK, Aagaard P (1988) Diagenetic albitisation of detrital K-feldspar in Jurassic, lower Cretaceous, and tertiary clastic reservoirs from offshore Norway. 1. Textures and origin. J Sediment Petrol 58:1003–1013

Schmidt C, Bodnar RJ (2000) Synthetic fluid inclusions: XVI. PTVX properties in the system H_2O-NaCl-CO_2 at elevated temperatures, pressures and salinities. Geochim Cosmochim Acta 64:3853–3869

Selverstone J, Franz C, Thomas S, Getty SR (1992) Fluid variability in 2 GPa eclogites as an indicator of fluid behaviour during subduction. Contrib Mineral Petrol 112:341–357

Selverstone J, Morteani G, Staude J-M (1991) Fluid channelling during ductile shearing: transformation of granodiorite into aluminous schist in the Tauern window, eastern Alps. J Metamorph Geol 9:419–431

Shmulovich KI, Graham CM (1996) Melting of albite and dehydration of brucite in H_2O-NaCl fluids to 9 kbars and 700–900 degrees C: implications for partial melting and water activities during high pressure metamorphism. Contrib Mineral Petrol 124:370–382

Shmulovich KI, Graham CM (2008) Plagioclase – aqueous solution equilibrium: concentration dependence. Petrology 16:177–192

Shmulovich KI, Plyasunova NV (1993) High-temperature high-pressure phase equilibria in the ternary system H_2O-CO_2-salt ($CaCl_2$, NaCl). Geokhimiya 5:666–684

Shmulovich KI, Tkachenko SI, Plyasunova NV (1995) Phase equilibria in fluid systems at high pressures and temperatures. In: Shmulovich KI, Yardley BWD, Gonchar GG (eds) Fluids in the crust. Chapman & Hall, London, pp 193–214

Shmulovich KI, Graham CM, Yardley BWD (2001) Quartz, albite and diopside solubilities in H2O-NaCl and H2O-CO2 fluids at 0.5–0.9 GPa. Contrib Mineral Petrol 141:95–108

Shmulovich KI, Graham CM, Yardley BWD (2006) Solubility of quartz in crustal fluids: experiments and general equations for salt solutions and H_2O–CO_2 mixtures at 400–800°C and 0.1–0.9 GPa. Geofluids 6:154–167

Skelton ADL, Graham CM, Bickle MJ (1995) Lithological and structural controls on regional 3-D fluid-flow patterns during greenschist facies metamorphism of the Dalradian of the SW Scottish Highlands. J Petrol 36:563–586

Skinner BJ, White DE, Rose HJ, Mays RE (1967) Sulfides associated with the Salton Sea geothermal brine. Econ Geol 62:316–330

Smith MP, Banks DA, Yardley BWD (1996) Fluid inclusion and stable isotope constraints on the genesis of the Cligga Head Sn-W deposit, SW England. Eur J Mineral 8:961–974

Sterner SM, Bodnar RJ (1984) Synthetic fluid inclusions in natural quartz. 1. Compositional types synthesized and applications to experimental geochemistry. Geochim Cosmochim Acta 48:2659–2668

Stout MZ, Crawford ML, Ghent ED (1986) Pressure-temperature and evolution of fluid compositions of Al_2SiO_5-bearing rocks, Mica Creek, BC, in light of fluid inclusion data and mineral equilibria. Contrib Mineral Petrol 92:236–247

Sverjensky DA, Hemley JJ, D'Angelo WM (1991) Thermodynamic assessment of hydrothermal alkali feldspar-mica-aluminosilicate equilibria. Geochim Cosmochim Acta 55:989–1004

Thomas R, Webster JD, Heinrich W (2000) Melt inclusions in pegmatite quartz: complete miscibility between silicate melts and hydrous fluids at low pressure. Contrib Mineral Petrol 139:394–401

Tkachenko SI, Shmulovich KI (1992) Liquid vapor equilibrium in the systems water salt (NaCl, KCl, $CaCl_2$, $MgCl_2$) at 400–600 degrees-C. Dokl Akad Nauk 326:1055–1059

Tomlinson EL, Jones AP, Harris JW (2006) Co-existing fluid and silicate inclusions in mantle diamonds. Earth Planet Sci Lett 250:581–595

Tomlinson EL, Müller W, EIMF (2009) A snapshot of mantle metasomatism: trace element analysis of coexisting fluid (LA-ICP-MS) and silicate (SIMS) inclusions in fibrous diamonds. Earth Planet Sci Lett 279:362–372

Touret J, Nijland T (this volume) Fluids and metasomatism in continental granulite lower crust, notably in upper amphibolite- to granulite-facies transition zones. Chapter 11

Valley JW, McLelland J, Essene EJ, Lamb W (1983) Metamorphic fluids in the deep crust: evidence from the Adirondacks. Nature 301:226–228
Vidale R (1969) Metasomatism in a chemical gradient and the formation of calc-silicate bands. Am J Sci 267:857–874
Warren J (2000) Dolomite: occurrence, evolution and economically important associations. Earth Sci Rev 52:1–81
Warren EA, Smalley PC (1994) North sea formation waters atlas, vol 15, Geological Society Memoir. The Geological Society, London
Wilkinson JJ (2010) A review of fluid inclusion constraints on mineralization in the Irish ore field and implications for the genesis of sediment-hosted Zn-Pb deposits. Econ Geol 105:417–442
Wilkinson M, Milliken KL, Haszeldine RS (2001) Systematic destruction of K-feldspar in deeply buried rift and passive margin sandstones. J Geol Soc 158:675–683
Wilkinson JJ, Everett CE, Boyce AJ, Gleeson SA, Rye DM (2005) Intracratonic crustal seawater circulation and the genesis of subseafloor zinc-lead mineralization in the Irish orefield. Geology 33:805–808
Williams AE, McKibben MA (1989) A brine interface in the Salton Sea Geothermal System, California: fluid geochemical and isotopic characteristics. Geochim Cosmochim Acta 53:1905–1920
Williams-Jones AE, Palmer DAS (2002) The evolution of aqueous-carbonic fluids in the Amba Dongar carbonatite, India: implications for fenitisation. Chem Geol 185:283–301
Wilson TP, Long DT (1993a) Geochemistry and isotope chemistry of Michigan Basin brines: Devonian formations. Appl Geochem 8:81–100
Wilson TP, Long DT (1993b) Geochemistry and isotope chemistry of Ca-Na-Cl brines in Silurian strata, Michigan Basin, USA. Appl Geochem 8:507–524
Winter JD (2010) Principles of igneous and metamorphic petrology, 2nd edn. Prentice-Hall, New York
Yardley BWD (1986) Fluid migration and veining in the Connemara Schists, Ireland. In: Walther JV, Wood BJ (eds) Advances in physical geochemistry, vol 5. Springer, New York, pp 109–131
Yardley BWD (2005) Metal concentrations in crustal fluids and their relationship to ore formation. Econ Geol 100:613–632
Yardley BWD (2009) The role of water in crustal evolution. J Geol Soc 166:585–600
Yardley BWD, Graham JT (2002) Origins of salinity in metamorphic fluids. Geofluids 2:249–256
Yardley BWD, Bottrell SH, Cliff RA (1991) Evidence for a regional-scale fluid loss event during mid-crustal metamorphism. Nature 490:151–154
Yardley BWD, Banks DA, Bottrell SH, Diamond LW (1993) Post-metamorphic gold-quartz veins from N.W. Italy: the composition and origin of the ore fluid. Mineral Mag 57:407–422
Zharikov VA, Pertsev NN, Rusinov VL, Callegari E, Fettes DJ (2007) Metasomatism and metasomatic rocks. Recommendations by the IUGS subcommission on the systematics of metamorphic rocks, 9. http://www.bgs.ac.uk/scmr/docs/papers/paper_9.pdf

Chapter 3
Thermodynamic Modeling and Thermobarometry of Metasomatized Rocks

Philippe Goncalves, Didier Marquer, Emilien Oliot, and Cyril Durand

Abstract Determining the P-T conditions at which metasomatism occurs provides insight into the physical conditions at which fluid-rock interaction occurs in the crust. However, application of thermodynamic modeling to metasomatized rocks is not without pitfalls. As with "normal" metamorphic rocks, the main difficulty is to select mineral compositions that were in equilibrium during their crystallization. This essential task is particularly difficult in metasomatized rocks because it is often difficult to distinguish textures produced by changes in P-T conditions from those caused by fluid-rock interactions and associated changes in bulk composition. Furthermore, the selection of minerals in equilibrium in metasomatized rocks is made difficult by the great variability of scale of mass transfer (see Chaps. 4 and 5), and therefore equilibrium, which varies from micrometer- to hand-sample or larger scale, depending on the amount of fluid involved and the fluid transport mechanisms (e.g. pervasive or focused). Finally, another major limitation that is discussed in detail in Chap. 5, is that fluid composition coming in or out of the rock is unknown. Since fluid is a major phase component of the system, neglecting its impact on the phase relations might be problematic for thermobarometry. Despite these pitfalls, we describe in this contribution examples where thermobarometry has been apparently successfully applied. We emphasize that pseudosection thermobarometry is particularly suitable

P. Goncalves (✉) • D. Marquer
UMR6249 Chrono-Environnement, CNRS – Université de Franche-Comté, 16 route de Gray, Besançon Cedex 25030, France
e-mail: philippe.goncalves@univ-fcomte.fr

E. Oliot
UMR6249 Chrono-Environnement, CNRS – Université de Franche-Comté, 16 route de Gray, Besançon Cedex 25030, France

UMR-CNRS 7516 Institut de Physique du Globe de Strasbourg, 1 rue Blessig, Strasbourg Cedex 67084, France

C. Durand
UMR 8217 Géosystèmes, CNRS – Université Lille 1, Villeneuve d'Asq cedex 59655, France

D.E. Harlov and H. Austrheim, *Metasomatism and the Chemical Transformation of Rock*, Lecture Notes in Earth System Sciences,
DOI 10.1007/978-3-642-28394-9_3,

for metasomatized rocks because the effects of mass transfer can be explored through P-T-X phase diagrams. Application of thermodynamic modeling to metasomatized rocks requires (1) detailed mineralogical and textural investigation to select appropriate mineral compositions, (2) essential geochemical analyses to define the relative and absolute mass changes involved during the metasomatic event(s), and (3) forward modeling of the effects of mass transfer on phase relations.

3.1 Introduction

Metasomatism can be described as an alteration process that simultaneously involves reactions and changes in whole-rock composition in the presence of a fluid phase at fixed or variable pressure and temperature. Metasomatic changes are driven by a local disequilibrium (chemical potential gradient) induced by the interaction of the parent rock with a chemically-reactive fluid. Evidence for metasomatism during tectono-metamorphic processes and orogenesis is abundant on all scales. On a large scale, the most unambiguous indicators of transport of large quantities of dissolved material in a fluid, i.e. metasomatism, are probably the alteration of crystalline rocks (e.g., albitization of plutonic rocks, rodingitization of gabbros, and skarns developed in carbonate rocks) and the formation of veins and associated ore deposits (e.g., Ferry and Dipple 1991; Ague 1994, 1995, 2003; Ferry 1994; Penniston-Dorland and Ferry 2008). On a smaller scale (thin-section to micrometer scale), evidence is subtle but probably more widespread. Following the pioneering work of Carmichael (1969), Putnis and Austrheim (2010) have reconsidered most metamorphic reactions (defined as a mineral re-equilibration in response to changes in pressure and/or temperature) as metasomatic reactions because material transport in a fluid is required to convert minerals from one phase to another, even in "apparently" fluid-absent reactions, such as the granulite-eclogite facies transition (Austrheim 1987). Indeed, mass transport in a fluid is orders of magnitude faster than solid-state diffusion at temperatures below melting, and solid-state diffusion operates on a length-scale shorter than the reaction microstructure and requires a much larger activation energy (Putnis and Austrheim 2010).

All metasomatic systems are considered as chemically open, where the type and amount of mass transfer during metasomatism is controlled by pressure (P), temperature (T), compositions of the fluid and rock (X) and the fluid/rock ratio (f/R) (e.g., Beinlich et al. 2010). Although understanding and quantifying metasomatism and its consequences on mineral reactions require consideration of all these parameters, the accurate estimation of P-T conditions appears critical. Indeed, thermobarometry of metasomatized rocks means that the P-T conditions of fluid flow in the crust, and alteration or formation of ore deposits can be estimated.

Application of thermobarometry requires selection of appropriate equilibrium mineral compositions. This task is difficult in metasomatic rocks because they tend to preserve complex chemical zoning and textures. The identification of the mechanism responsible for the chemical zoning is critical for properly selecting mineral

compositions for thermobarometry (Steffen and Selverstone 2006). Chemical zoning can be due to changing P-T conditions (e.g., Spear and Selverstone 1983; Florence and Spear 1991) and fluid compositions, or variations in effective bulk composition due to fractionation during mineral growth or metasomatism (Wintsch and Knipe 1983; Yardley and Schumacher 1991; Stüwe 1997). In a metasomatized rock, the mineralogical reactions driven by the compositional and physical changes can be superimposed upon one another. Furthermore, during the fluid-rock interactions, mineral re-equilibration occurs locally by the mechanism of coupled dissolution and reprecipitation (Putnis and Austrheim 2010) that can lead to complex zoning at the micron scale (McWilliams et al. 2007).

Most conventional thermometers and barometers have been calibrated for average bulk compositions (pelite, basalt), which do not consequently span the unusual rock compositions of metasomatized rocks. Furthermore, mineral composition, and consequently, net-transfer reaction barometers, are sensitive to the buffering assemblage, and therefore to the bulk rock composition (Caddick and Thompson 2008). Can we then apply conventional thermobarometry to rocks with unusual bulk composition and with inappropriate buffering assemblages? Pseudosections offer an interesting and powerful alternative to conventional thermobarometry because calculated phase diagrams permit the user to take into account the effects of bulk composition and its effects on phase relations. Although, we focus on thermobarometry based on mineral equilibria in this contribution, it is noteworthy that there are alternative and complementary techniques, like stable isotopes and fluid inclusion thermobarometry, which are useful in metasomatic rocks.

The objective of this Chapter is to determine whether or not metasomatic rocks can be read like "normal metamorphic rocks" and to give some recommendations on the application of thermodynamic modeling to metasomatized rocks. We start by describing a few textural and mineralogical evidences for metasomatic reactions. Then, the different thermobarometric techniques available are described. The goal here is to discuss the prerequisites and assumptions for a reliable application of thermobarometry. We use four examples: strongly metasomatized rocks (scapolitized gabbros and albitites), a crenulation cleavage developed in metapelitic schists (Williams et al. 2001), a shear zone in a granodioritic rock (Fourcade et al. 1989; Goncalves et al. 2012), and a mafic polymetamorphic rock (Mahan et al. 2008), where metasomatism has been described and thermobarometry successfully applied. The first examples (scapolitized gabbros and albitites) are used mainly to highlight the difficulty of applying mineral equilibria thermobarometry on "unusual" mineral assemblages and the benefits of using alternative techniques, like stable isotopes and fluid inclusions. The second example from Williams et al. (2001) is used primarily to highlight the difficulties of choosing the right mineral compositions in metasomatized rocks. The last two examples are advantageous because of the local preservation unaltered parent rock, thus allowing us to model and discuss the effects of mass transfer on phase relations using P-T and P-X pseudosections.

3.2 Textural and Mineralogical Evidences for Metasomatic Reactions

On the macroscopic scale, evidences of metasomatic reactions (mineral and compositional changes) are readily observable in many rock types, if an unaltered rock (i.e., the reference frame) is preserved in the vicinity of the metasomatized sample and if the transition between the unaltered and altered rock (i.e., the reaction front) is sharp. Figure 3.1 shows two examples of field pictures of metasomatism: (a) scapolitization of a metagabbro from SE-Norway (Engvik et al. 2011) and (b) an endo- and exoskarn from the French Pyrenees (Durand et al. 2006, 2009).

On the micron scale, metasomatic textures are more difficult to recognize. Thermodynamic modeling of metasomatism requires to clearly distinguish the textural and mineralogical changes driven by metasomatism, from those induced by variations in pressure and temperature. This task is particularly difficult because, in most cases, there is no first-order difference between metasomatic and metamorphic textures, such as chemical zoning or coronitic textures (Putnis and Austrheim 2010). A review of the macro- and micro-textural evidences for mineral reactions driven by fluid-induced compositional changes can be found in Putnis and Austrheim (2010), and we present below some additional textures that can be interpreted unequivocally (in our opinion) as metasomatic reactions.

For example, Fig. 3.2 shows a metasomatic reaction consisting of the partial replacement of a kyanite - quartz assemblage by symplectites of sapphirine–plagioclase and spinel–plagioclase with a moat of plagioclase in a felsic granulite from the East Athabasca mylonite triangle in the western Canadian Shield (Baldwin et al. 2007). There is little doubt that to proceed, this reaction requires mass transfer of chemical elements (like Ca, Fe and Mg) on a length-scale greater than the reaction microstructure. Material transport via a fluid phase appears to be the only possible mechanism. To constrain the P-T conditions of formation of this reaction texture, Baldwin et al. (2007) used petrogenetic grids that considered variations in the chemical potential for the mobile components (CaO, FeO, MgO).

Figure 3.3b is a Ca X-ray map of a poly-metamorphic garnet observed in garnet–chloritoid-bearing mica schists from the Gran Paradiso nappe in the Western Alps (Le Bayon et al. 2006). The entire garnet consists of an early, pre-Alpine (Variscan) garnet porphyroblast that grew under low-pressure conditions (~620°C, 6 kbar) overgrown by an Alpine garnet that grew during decompression from peak conditions of 490°C, 18–20 kbar. Alpine garnet occurred as (1) a zoned overgrowth, with a Ca-rich inner part that is characterized by irregular boundaries, and a Ca-poor outer part, and (2) Ca-rich sealed fractures (Fig. 3.3a, b). These features are consistent with fluid-assisted growth of the Alpine garnet. We also speculate that this garnet may be considered as metasomatic, and that the Alpine garnet formed through a coupled dissolution-reprecipitation process during infiltration of an externally-derived Ca-rich fluid. Similar garnet textures has been observed in the Bergen Arc (western Norway), where metastable Precambrian granulite facies garnet were locally reequilibrated under eclogite facies conditions during the

Fig. 3.1 Field picture of (**a**) preserved lenses of metagabbro transformed to scapolitized metagabbro, South Norway (Engvik et al. 2011) (see more details in Sect. 3.4.1) and (**b**) the development of endoskarn and exoskarn at the contact between limestone and granodiorite (Querigut massif, Pyrenees). The endoskarn consists of a Kfs-Qtz-Cpx-Amp-Pl assemblage developed at the expense of the magmatic assemblage Pl-Amp-Bt-Qtz-Kfs due to enrichment in K_2O. The exoskarn shows a continuous and complex mineralogical evolution from a Cal-Cpx-Amp-Qtz-An assemblage to a Grt-Wo/Czo-Cpx-Qtz assemblage formed by calcite loss (CaO and CO_2 loss) and decarbonation reactions (Durand et al. 2006, 2009)

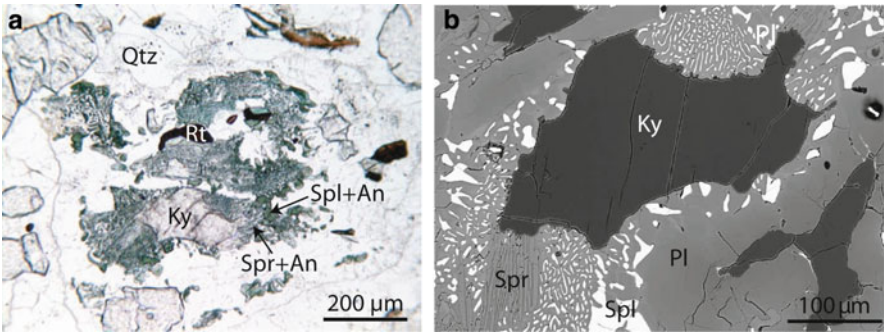

Fig. 3.2 Photomicrograph and backscattered electron image of a kyanite relict surrounded by symplectites of sapphirine–plagioclase and spinel–plagioclase in contact with quartz (Baldwin et al. 2007). This coronitic reaction is interpreted as a metasomatic reaction that involves mass transfer of chemical elements, like Ca, Fe and Mg, on a length scale greater than the reaction microstructure

Caledonian orogeny (Pollok et al. 2008). The eclogitization through dissolution/precipitation was driven by localized fluid infiltration, along grain-scale fractures, subgrain boundaries, porosity formed during the dissolution-precipitation process itself (Pollok et al. 2008)

In most cases, ascribing a particular texture to a metasomatic vs. a metamorphic reaction is ambiguous. The best way to circumvent this difficulty is to find metasomatic systems where a reference frame, corresponding to the unaltered system without metasomatic assemblages, can be easily identified. A rock affected by heterogeneous deformation could be an appropriate system because fluid flow,

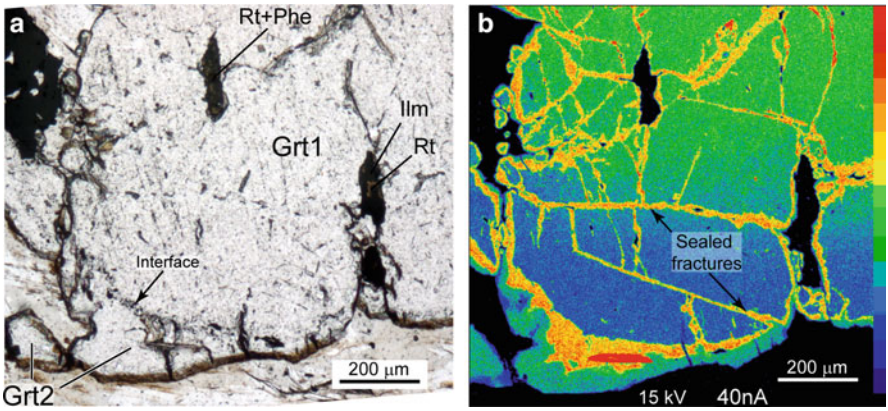

Fig. 3.3 Photomicrograph and its corresponding Ca X-ray map of a multistage garnet (Le Bayon et al. 2006). Garnet consists of an early garnet porphyroclast (Grt1) overgrown by a Ca-rich garnet (Grt2). Garnet 2 growth was fluid-assisted as shown by the occurrence of Ca-rich sealed fractures. Grt2 grew through a dissolution-precipitation process during the infiltration of an externally-derived Ca-rich fluid

and therefore, metasomatism is focused mainly into the high strain zones, while the undeformed rocks likely preserve the pre-metasomatism assemblages. These undeformed rocks can be regarded as the unaltered reference frame (or the parent rock), which is essential to deduce the effects of syn-kinematic mass transfer on phase relations.

3.3 Thermobarometry Methods

Estimation of pressure and temperature conditions of formation of metamorphic mineral assemblages (thermobarometry) is critical to constrain P-T paths and to understand in detail the thermo-mechanical behavior of the lithosphere during orogenesis. The way rocks respond to changes in P-T conditions is strongly influenced by the presence or not of fluids (see Chap. 5). Indeed, many authors have shown that the preservation of peak metamorphic assemblages and its partial or complete replacement during the retrograde path is directly related to when fluids are or not available in the system (e.g., Guiraud et al. 2001; Mahan et al. 2006). Consequently, if thermobarometry is applied successfully to metasomatic rocks, it is then possible to determine the P-T conditions of fluid circulation.

Thermobarometry in metasomatized rocks can be achieved by mineral equilibria methods, like in "normal" metamorphic rocks but its application is not always straightforward and not without pitfalls in the unusual metasomatic assemblages. To overcome this difficulty, mineral equilibria thermobarometry can be combined with stable isotopes and fluid inclusion techniques, which are of particular interest in rocks involving intense fluid-rock interactions.

3.3.1 Thermobarometry Based on Mineral Equilibria

3.3.1.1 Inverse Versus Forward Modeling

Thermobarometry can be achieved either by conventional inverse modeling thermobarometry or forward modeling using the calculation of P-T pseudosections (phase diagram sections computed for a specific bulk composition that provides mineral modes and compositions as a function of environmental variables). The basics and conditions of application of inverse modeling, also called conventional thermobarometry, can be found in most text books and will not be discussed here (e.g., Spear 1993; Philpotts and Ague 2009). During the last decade, particular attention has been paid to the pseudosection modeling approach (forward modeling). Connolly and Petrini (2002) and Powell and Holland (2008) emphasize the thermodynamic and technical reasons for this interest: (1) The thermodynamic mineral end-member data base has been improved and expanded upon (Berman and Aranovich 1996; Holland and Powell 1998 and updated version in 2011). (2) New thermodynamic models for mineral solid solutions and silicate liquids are being continuously developed and improved (Kelsey et al. 2004; Vidal et al. 2005; Diener et al. 2007; Dubacq et al. 2010). Furthermore, some activity-composition models for major silicates can handle a large set of phase components that include Ti, Mn, and Fe^{3+} (white mica, biotite, amphibole, garnet, sapphirine, clinopyroxene, etc.) (e.g. Diener et al. 2007; Green et al. 2007; White et al. 2007; Tajčmanová et al. 2009; Taylor-Jones and Powell 2010). These two major advances allow for modeling phase relations in geologically realistic systems like TiMnCaNaKFMASHO. (3) In parallel to these thermodynamic advances, the construction of pseudosections became less laborious due to the development and improvement of fully or semi-automated computational techniques. Four software packages are available to calculate pseudosections and phase diagrams: THERMOCALC (Holland and Powell 1998; Powell et al. 1998), Perple_X (Connolly 1990, 2005; Connolly and Petrini 2002), Theriak/Domino (de Capitani and Brown 1987; de Capitani and Petrakakis 2010) and Program Gibbs (Spear 1988). (4) Compared to conventional inverse thermobarometry, the pseudosection approach has the advantage of internal thermodynamic consistency. (5) Thermometers and barometers used in inverse modeling are commonly calibrated for restricted ranges in composition despite being sensitive to mineral assemblage and bulk-rock composition (Caddick and Thompson 2008). (6) Finally, pseudosections, which are by definition a forward model of phase relations, provide additional information not available through conventional thermobarometry, including the P-T extent of the stability field of the stable assemblage, and the evolution of phase relations (mode and composition of each phases) as a function of pressure and temperature or other variables like chemical potential (Baldwin et al. 2007; White et al. 2008). These features have been extensively used to better constrain P-T paths by using chemical zoning in garnet combined with P-T pseudosections contoured for garnet composition (e.g., Štípská and Powell 2005).

3.3.1.2 Prerequisites for Pseudosection Thermobarometry on Metasomatized Rocks

The first prerequisite for the application of pseudosections to thermobarometry is that the assumption of thermodynamic equilibrium is verified. As Powell and Holland (2008) stated "much of the metamorphic community has implicitly adopted a macroscopic equilibrium model of metamorphism", although rocks commonly preserve textural evidence for disequilibrium on a microscopic scale, e.g., reaction textures, mineral zoning and occurrences of inclusions armored in porphyroblasts. The preservation of these disequilibrium features in the context of a macroscopic equilibrium model is mainly due to kinetic effects (e.g. the sluggishness of volume component diffusion in the solid-state and reaction overstepping due to delayed nucleation). However, modeling of phase relations in this case is still possible via equilibrium thermodynamics by applying the assumption of "local equilibrium" (Carmichael 1969; Korzhinskii 1970; Thompson 1959). This principle states that a system in disequilibrium due to gradients in intensive parameters (P, T or chemical potential of a component) can be subdivided into smaller sub-systems that can be treated separately as in equilibrium.

The second prerequisite for the application of pseudosection thermobarometry is that the equilibration volume and effective bulk composition can be precisely and accurately estimated. This is the major caveat on forward modeling of phase equilibria because there are no methods to adequately define the equilibrium volume (Stüwe 1997). Metasomatism modifies the composition of equilibration on a scale that is almost impossible to quantify if the spatial relationships with the unaltered parent rock are unknown. Finally, in metasomatic systems, the shape of the equilibrium volume will be largely controlled by the geometry of fluid pathways on all scales (grain boundaries, inter-connected porosity network, anastomosing shear bands and shear zones, etc.).

In highly metasomatized rocks, like high strain zones or vein selvages, the equilibrium prerequisite is commonly fulfilled because the elevated fluid/rock ratio favors element mobility and subsequent equilibration. Furthermore, in these systems, the equilibrium volume for major components is assumed in most cases to be larger than the hand sample size, thus allowing for the use of bulk rock composition as the effective bulk composition for the modeling.

3.3.2 Stable Isotope Thermometry

In this section, we discuss the main conditions for an accurate application of stable isotope thermometry. A detailed review can be found in Valley (2001). Thermometry was one of the first applications of oxygen isotope studies due to the strong dependency of the $^{18}O/^{16}O$ ratio with regard to temperature (Urey 1947; McCrea 1950; Urey et al. 1951; O'Neil and Clayton 1964; Shieh and Taylor 1969; Bottinga and Javoy 1975; Javoy 1977; Clayton 1981). Other stable isotope

ratios are also temperature dependent, like $^{13}C/^{14}C$ and $^{34}S/^{32}S$ (Valley and O'Neil 1981; Graham and Valley 1992). Stable isotope thermometry is based on the inverse relation between temperature and the equilibrium constant (K_{eq}) of an isotopic exchange reaction between the isotopic end-member compositions of two minerals 1, 1*, 2 and 2* in Reaction 3.1 (the asterix corresponds to the mineral with the heavy isotope).

$$a.1 + b.2^{*} = a.1^{*} + b.2 \tag{3.1}$$

where a and b represent stoichiometric coefficients. The equilibrium constant is also called the isotopic fractionation factor (α) if the reaction is written such that one mole of the light isotope and heavy isotope are exchanged between minerals 1 and 2 (Chacko et al. 2001). The thermometer is based on the general Eq. 3.2

$$10^{3}.\ln \alpha_{(1-2)} = \frac{A_{(1-2)}.10^{6}}{T^{2}} + B_{(1-2)} \tag{3.2}$$

where A and B are constant values determined either by experimental, theoretical and empirical methods (see Bottinga and Javoy 1973; Friedman and O'Neil 1977; Kyser 1987; Zheng 1999). The analysis of two coexisting phases should uniquely determine the temperature of equilibrium. Although, the theory of stable isotope thermometry is simple, several first order conditions must be met for its accurate application (Valley 2001).

The first condition that applies to all thermobarometric approaches is equilibrium. If the goal is to determine the temperature of formation (or resetting) of a mineral assemblage, then isotopic equilibrium must be reached at the time of mineral pair formation (or resetting) and these isotopic compositions must be preserved during later evolution, at least on the scale of the measurements. Many authors have shown that isotopic equilibrium, which is expected at peak metamorphic conditions during regional metamorphism, is commonly not attained (Shelton and Rye 1982; Blattner and Lassey 1989) and/or is partially reset during retrogression by isotopic exchange via diffusion (Dodson 1973; Javoy 1977; Huebner et al. 1986; Giletti 1986). In these conditions, temperatures obtained via stable isotope thermometry are apparent temperatures that might not have a geological meaning. Several approaches have been developed to correct the effects of volume and grain-boundary diffusion (Giletti 1986; Gregory and Criss 1986; Eiler et al. 1993, 1995; Eiler and Valley 1994). A full review of these approaches is beyond the scope of this paper and can be found in Valley (2001). Valley (2001) shows that reliable stable isotope thermometry requires very detailed diffusion modeling. Equilibrium conditions for mineral formation in high grade rocks and magmatic rocks can also be altered by dissolution/precipitation mechanism, providing a unique opportunity to study more complex aspects than the thermal history, like the fluid/rock interaction history (fluid source, temperature of fluid infiltration) which is of particular interest for metasomatism.

The second condition for successful stable isotope thermometry is to get a mineral pair with fractionation factors sensitive to temperature. Then, these fractionation factors must be well constrained in order to obtain an accurately calibrated thermometer. A critical evaluation of various calibrations is provided by Chacko et al. (2001). Among other conclusions, Chacko et al. (2001) point out that there is a plethora of calibrations of fractionation factors for minerals and fluids of geological interest, (not all of which are in agreement), making use of stable isotope thermometry some how not trivial. Constant values A and B of Eq. 3.2 are well determined experimentally for mineral (pure end-members)/water or carbonate pairs (Kyser 1987) and are then combined to recalculate the isotopic fractionation factor between the two minerals. However, compositional effects due to cation substitution can have a significant effect on isotopic fractionation (Kohn and Valley 1998) and therefore should be systematically included in thermometers involving complex solid solutions (e.g. garnet, amphibole, epidote, O'Neil and Taylor 1967). Although the compositional effect on fractionation factors can be predicted theoretically by combining data for end-members (Kohn and Valley 1998), more experimental data are required to evaluate the effects of complex substitutions (Chacko et al. 2001). If mineral pair thermometers are directly applied, without compositional effect corrections, only pure end-members should be analyzed for stable isotopes. Another condition, relevant to calibration issues, applies to empirically calibrated thermometers (e.g. Bottinga and Javoy 1975). In addition to the equilibrium conditions, the application of empirical thermometers should be applied to natural rocks that have been equilibrated at or near the same conditions as the thermometer being calibrated. This last condition, combined with the restricted amount of data on complex solid solutions or the use of only pure end-members, reduces significantly the number of samples suitable for thermometry.

Finally, the third condition is related to the analysis of the isotopic ratio. The main source of errors is directly related to the agreement between the size of the sample analyzed and the equilibrium volume preserved. If a rock has been affected by an isotopically complex history due to polymetamorphism and/or metasomatism, it might preserve multiple generations of the mineral and/or mineral chemical zoning produced by diffusion and dissolution-precipitation events. The scale of equilibrium would then be on the micron to millimeter size. In such cases, bulk rock analysis or bulk-mineral analysis, separated by hand picking, would be inappropriate. Modern in-situ and high resolution techniques, like laser and ion probes (Eldrige et al. 1987; Crowe et al. 1990; Sharp 1990; Valley and Graham 1991; Crowe and Vaughan 1996; McKibben and Riciputi 1998) allows for the study of intra-mineral zonation. When combined with high resolution imaging techniques, like X-ray compositional mapping and/or cathodoluminescence, it would help identifying the origin of isotope fractionation variation, isotopic alteration processes (diffusion, dissolution-precipitation), and the interpretation of thermometric results (Valley 2001).

To conclude, Valley (2001) states that "the best stable isotope thermometers, (...), involve relatively common minerals, and occur in rocks where equilibration can be evaluated. The ideal case is a rock where all minerals crystallized at a

specific temperature (diagenetic, metamorphic or igneous), and then cooled rapidly in a closed system". Most metasomatic rocks do not meet any of these requirements and therefore stable isotope thermometry should be performed with care in metasomatic rocks. A detailed petrologic study and in-situ isotope analysis are critical to identify the scale of equilibrium and select the appropriate mineral compositions in equilibrium. Then interpretation must be preceded by an accurate modeling of the stable isotope intra- and inter-mineral diffusion, after mineral crystallization.

3.3.3 Thermometry Based on Fluid Inclusions

Fluid inclusions are microscopic bubbles of fluid that are trapped during the growth of the host mineral (primary fluid inclusion) or during the development of healed fractures within the host crystal after its development (secondary fluid inclusion) (Roedder 1984). The study of fluid inclusions can give direct information about the composition of the metamorphic fluid during its entrapment and can be used to estimate the P-T conditions of the entrapment. Combination of these two aspects of fluid inclusions can then allow for reconstruction of P-T-X_{fluid} evolution (Roedder 1984; Lamb et al. 1987, 1991; Touret 1987; Fu et al. 2003; Ohyama et al. 2008).

The estimation of P-T conditions during the entrapment of a fluid inclusion is based on the calculation of its density by microthermometry and composition by nondestructive chemical analyses like micro-Raman analyses. After a careful characterization of the different generations of fluid inclusions, ten or more of microthermometric analyses must be performed on each population in order to evaluate their homogeneity and thus define a statistical "real" density (Roedder 1984; Touret 2001). Isochores (lines of equal density in a P-T diagram) can be calculated based on a PVTX equation of state for fluids (Dubessy et al. 1999). Fluid inclusion thermobarometry is based on the combination of isochores that represent the possible P-T conditions of fluid entrapment in a P-T diagram, with independent P-T estimates obtained by either mineral equilibria thermobarometry and/or stable isotope thermometry.

Accurate application of fluid inclusion thermobarometry is possible only if there is no variation in the volume, no leakage of the fluid inclusion, and no reactions within the fluid system since the fluid entrapment. These basic assumptions are not always verified. For example, experimental studies have shown that volume changes in fluid inclusions may occur (Whitney et al. 2000; Burnley and Davis 2004) and/or the composition of fluid inclusions may change after entrapment (Sterner and Bodnar 1989; Hall et al. 1991; Hall and Sterner 1993).

Although fluids in fluid inclusions are in equilibrium with the mineral host, the calculated isochores are only dependent on the composition and density of the fluid. Therefore, if the conditions cited above are met, fluid inclusion thermobarometry can be applied in rocks where mineral equilibria thermobarometry is not possible because of the lack of appropriate mineral assemblages and/or if the mineral equilibrium has not been preserved. This constitutes a major advantage in metasomatic rocks characterized by "unusual" mineral assemblages.

3.4 Applications

3.4.1 Thermobarometry of Unambiguously Metasomatized Rocks (Scapolitization and Albitization)

Extracting P-T conditions from strongly metasomatized rocks only by mineral equilibria thermobarometry is a difficult task because intense fluid-rock interactions result in unusual bulk rock compositions and assemblages that are not particularly suitable to apply mineral equilibria thermobarometry.

For instance, gabbros from the Proterozoic Bamble and Kongsberg sector, South Norway, were pervasively transformed over large areas into scapolite-metagabbro (Austrheim et al. 2008; Engvik et al. 2011). The intensively metasomatized part of the rock consists of scapolite (with a meionite content lower than 40%), amphibole, phlogopite with accessory rutile, apatite, titanite, tourmaline, sapphirine, corundum and zircon. Application of conventional thermobarometry is almost impossible on such exotic assemblage because there are no thermometers and barometers empirically or experimentally calibrated for these assemblages. Pseudosection modeling and thermobarometry are also very limited by the fact that there are no robust activity-composition models for some first-order metasomatic phases like scapolite (Tenczer et al. 2011). Furthermore, a-X models for common silicate phases (amphiboles, sapphirine) that are known to be robust in common bulk rock composition might not be appropriate for the unusual metasomatic compositions (Diener et al. 2007; Taylor-Jones and Powell 2010). The progression of a sharp metasomatic/reaction front produces monomineralic layers or high variance assemblages (Korzhinskii 1970) that are stable over a wide range of P-T conditions and therefore are not favorable at all to determine precise P-T conditions. Finally, modelling accurately phase relations in this metasomatic system would require taking into account Ti, P, B and O as thermodynamic components. Although much effort is being devoted to the elucidation of P-bearing phase relationships in natural and experimental systems (e.g. Harlov et al. 2002, 2005, 2007a, b, 2008, 2011; Harlov and Forster 2003; Harlov and Hetherington 2010), the lack of internally consistent thermodynamic data for end-members and the absence of a-X models prevent the integration of these phases into the thermodynamic modeling software packages utilized for calculating phase diagrams. The role of fluid chemistry is also major and will be discuss later. Based on the stability of scapolite with a low meionite content as determined by Aitken (1983), the stability of enstatite in fluid-rich and saline conditions (Harley 1989; Ballèvre et al. 1997; Pawley 1998) and the stability of sapphirine (Seifert 1974), Engvik and Austrheim (2010) conclude that the scapolitization could have developed at ~600–700°C during regional amphibolite-facies metamorphism. These (P-)T constraints for the metasomatism are probably the best results that we can expect using the available thermobarometric methods based on mineral equilibria.

The lack of direct mineral equilibria P-T estimations of metasomatism can be circumvented when field relations and petrology show unequivocal relationships

between metasomatism, deformation and metamorphism. P-T conditions from two distinct albitization events (1,600–1,580 Ma and 1,550–1,500 Ma) recognized in the eastern part of the Mount Isa Block (Australia) were tightly constrained using indirect estimations determined on host rocks or veins associated with albitites (Oliver et al. 2004). The 1,600–1,580 Ma metasomatic event conditions were constrained on "normal" pelitic assemblages overprinting albite at 500–550°C, < 4 kbar (Rubenach and Lewthwaite 2002). The 1,550–1,500 Ma event was constrained at 450–600°C, 2–4.5 kbar by a multi-method approach, consisting of mineral equilibria thermobarometry, and fluid inclusion microthermobarometry, on assemblages concurrently developed in host-rocks and veins (see reference in Oliver et al. 2004). These results are consistent with temperatures of ~510–540°C calculated from albite and quartz $\delta^{18}O$ equilibria performed on pegmatite and aplite that are spatially and temporally associated with albitite (Mark and Foster 2000).

3.4.2 Thermobarometry of Crenulation Cleavage Development: An Example of Discrete and Small Scale Metasomatism

The goal of this section is to emphasize the importance of detailed microtextural studies in order to interpret results from thermobarometry. Although this point is common to all thermobarometric studies, the selection of appropriate minerals in equilibrium is particularly difficult in metasomatized (and deformed) rocks because dissolution-precipitation and mass transfer on very variable scales (from micron to meter), result in complex textures and chemical zoning. Under these conditions, the common assumption that two minerals in contact are in chemical equilibrium is not systematically verified (Vidal et al. 2006). To illustrate this effect from deformation and metasomatism, we use an example from Williams et al. (2001) that have applied conventional thermobarometry on rocks that show complex textures and chemical zoning due to deformation and mass transfer during crenulation cleavage formation.

Crenulation cleavage, which results from the superimposition of at least two distinct deformation events, can provide first order tectonic information only if the P-T conditions of formation of the deformation fabrics are accurately constrained. As noted by Williams et al. (2001), to do so "it is critical to select the assemblages and compositions that were in equilibrium during the deformation event of interest". Minerals from crenulation cleavages developed in pelitic schists are characterized by complex zoning that can be attributed to either metamorphic reactions, metasomatic reactions, preservation of metastable pre-crenulation cleavage minerals or a very limited length-scale of equilibrium (Williams et al. 2001; McWilliams et al. 2007). Although the lowest strain zones (Quartz + Feldspar (QF) domains) in a crenulation cleavage do not correspond strictly to an unaltered reference frame, they can be used as the least-altered reference to be compared

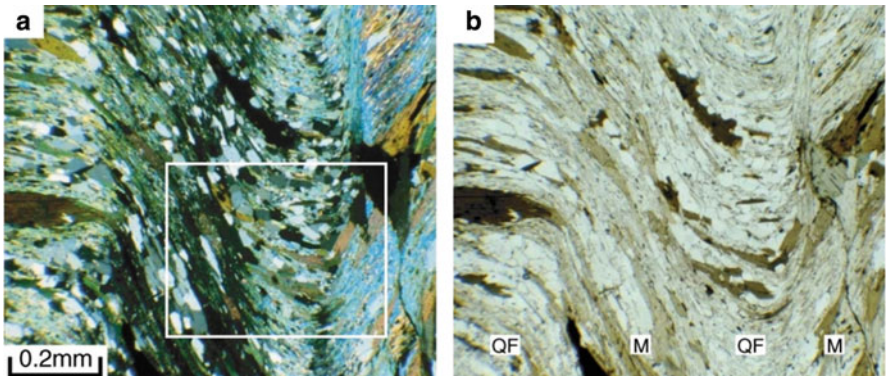

Fig. 3.4 Photomicrograph ((**a**): crossed polars; (**b**): uncrossed polars) of a typical crenulation cleavage showing the QF and M domains (Williams et al. 2001)

with the highest strain zones (Mica (M) domains) in order to unravel the origin of the mineralogical zoning and highlight microstructures that are developed, in part, due to local mass transfer and fluid circulation.

A rock with a well-developed crenulation cleavage is a typical metasomatic system where syn-kinematic phase relations are controlled by pressure, temperature, and variations in bulk composition, fluid composition, and the kinetics of the dissolution/precipitation mechanism. In this metasomatic system, the issue of the length-scale of material transport, and therefore equilibrium volume, is critical (McWilliams et al. 2007) and has received much debate over the past 20 years, much like an earlier controversy surrounding the development of slaty cleavage (e.g., Goldstein et al. 1998; Wintsch et al. 1991). Some authors suggest that crenulation cleavage formation is associated with large volume loss and changes in bulk composition due to dissolution and removal of material over distances greater than the centimeter or "hand sample" size (e.g., Bell et al. 1986; Caron et al. 1987). Alternatively, a "closed system" model, without bulk composition and volume change, has been proposed (Mancktelow 1994; McWilliams et al. 2007). In this case, mass transfer occurs on a length-scale not greater than the millimeter to centimeter between the M and QF domains (Mancktelow 1994; Williams et al. 2001) or below hundreds of micrometers (McWilliams et al. 2007).

The example detailed below from the Moretown Formation in western Massachusetts (USA) shows that selecting the appropriate phases and compositions for thermobarometry is difficult because of (1) the preservation of pre-cleavage mineral relics and (2) mass transfer during cleavage formation that resulted in the chemical and mineralogical differentiation into mica-rich microfold limbs (M domains) with quartz-feldspar rich hinges (QF domains) characterized by complex chemical zoning on the grain scale.

Williams et al. (2001) used high-resolution compositional X-ray maps to investigate mass transfer during cleavage development in interbedded schists and greywackes from the Moretown formation of western Massachusetts. The

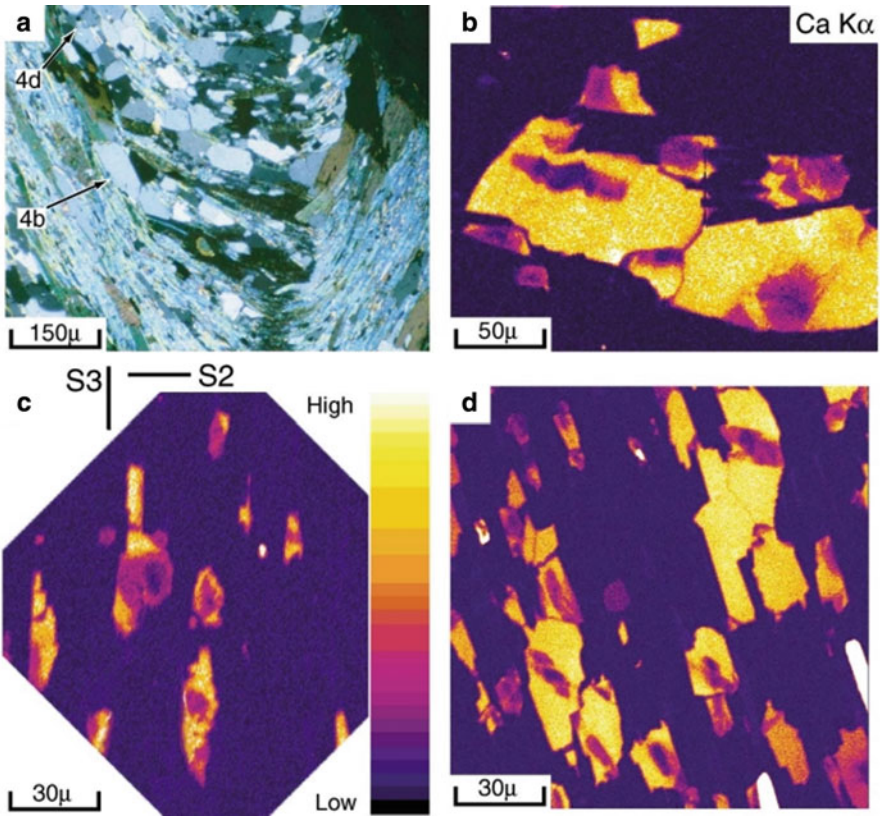

Fig. 3.5 (**a**) Close up view of Fig 3.3a. *Arrows* indicate the location of the Ca X-ray map on (**b**) and (**d**). (**b**) High-resolution Ca X-ray map of a plagioclase grain from the QF domain showing the two generations of plagioclase (*purple* = An03; *Yellow* = An14–16). (**c**) Ca X-ray map of plagioclase from the M domains. Ca-poor cores are highly resorbed and the Ca-rich overgrowth are aligned with S3. (**d**) Ca X-ray map of plagioclase from the transition zone between QF and M domains. Ca-poor cores have a preferred orientation close to the S2 cleavage while Ca-rich overgrowths have a preferred orientation parallel to S3 (cf. Williams et al. 2001)

Moretown formation is characterized by upright folds (F3) that display a crenulation cleavage oriented parallel to the axial surfaces of the F3 folds. These F3 structures affect a pre-existing cleavage (S2). The mica-rich crenulation limbs (M domains) consist of muscovite, biotite, and ilmenite while the mica-poor crenulation hinges (QF domains) contain quartz, plagioclase, garnet, biotite, muscovite, and ilmenite aligned within the S2 surface (Fig. 3.4). Garnet shows rim overgrowths that are interpreted to be contemporaneous with the S3 cleavage.

In this lithology, thermobarometry, and more particularly barometry, is very sensitive to plagioclase and garnet composition. Figure 3.5a shows a typical fold hinge developed during the formation of this crenulation cleavage with the location of the QF and M domains. High-resolution Ca maps show a sharp core-rim zoning that is interpreted as two distinct generations of plagioclase (Fig. 3.5b–d). In the fold

hinge, Ca-poor cores (An03) have a distinct preferred orientation parallel to the S2 cleavage. Ca-rich (An14–16) overgrowths are more equant and are parallel to the S2 cleavage. In contrast to the crenulation limbs, Ca-poor cores are highly resorbed with smaller aspect ratios that roughly define the earlier orientation of the S2 cleavage (Fig. 3.5c). Ca-rich overgrowths are elongated and aligned parallel to the S3 crenulation cleavage. Williams et al. (2001) concluded that Ca-rich overgrowths were produced by a dissolution-precipitation process during the S3 crenulation cleavage formation. Ca-poor cores represent pre-crenulation cleavage relics, which were stable during S2 cleavage formation. Garnet developed narrow overgrowths that contain sigmoidal S2 inclusion trails consistent with syn-D3 growth.

White micas present in both limbs and hinges are also sensitive to deformation and metasomatism during crenulation cleavage formation. Figure 3.6 is a Na compositional X-ray map that shows that white micas are significantly zoned, with two compositions: a high-Na muscovite and a low-Na phengite (Fig. 3.6). Low-Na phengite, which is more abundant in the crenulation limbs (M domains), surrounds the muscovite and is strongly aligned within the S3 foliation (Williams et al. 2001). All these textural features suggest that the phengite grew during S3 foliation cleavage development, and we speculate that the phengite precipitated from a fluid phase in equilibrium with other phases.

P-T conditions during the crenulation cleavage formation (D3) have been estimated using the thermodynamic database and multi-equilibrium method of Berman (1991). Ca-rich plagioclase rims (from either the fold limbs or fold hinges) combined with garnet overgrowths, Na-poor phengite, matrix biotite, ilmenite and quartz yield conditions of 600–650°C and 1.1 GPa (Fig. 3.7). Although, Williams et al. (2001) suggest that D3 Ca-rich plagioclase can be produced only by the metamorphic breakdown of D2 albite and epidote, we suggest that Ca-metasomatism at variable length-scales (smaller and greater than the crenulation cleavage-scale) cannot be completely ruled out. In fact, high resolution maps and mass balance calculations of Williams et al. 2001 suggest that deformation-induced solution transfer of silica is required to deplete quartz from the crenulation limb domains. If mass transfer of Si and Ca (?) occurred between the D2 and D3 event, an inappropriate plagioclase composition, and more particularly the use of the S2 Ca-poor plagioclase core, would yield meaningless pressures over-estimated by 0.4–0.5 GPa that cannot be directly interpreted as the conditions of the D2 event. This example illustrates the need to consider and quantify local chemical mass transfer prior to carrying out thermodynamic calculations.

3.4.3 Thermobarometry of Metasomatic Shear Zones

Ductile shear zones are commonly considered as open-systems where metasomatism can be significant due to the intense fluid-rock interactions involved during deformation. Many authors have shown that shear zone formation is coeval and promoted by dramatic mineral transformations due to syn-kinematic metamorphic

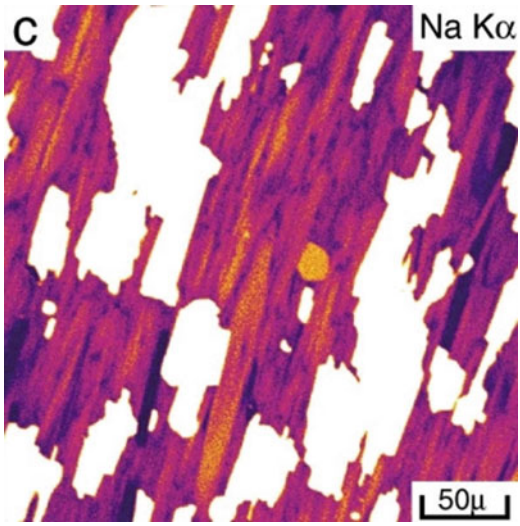

Fig. 3.6 Na X-ray map of white mica from the M domain showing the two generations of white mica. Low-Na phengite, which are more abundant in the crenulation limbs (M domains), are strongly aligned within the S3 foliation and overgrow the high Na muscovite (Williams et al. 2001)

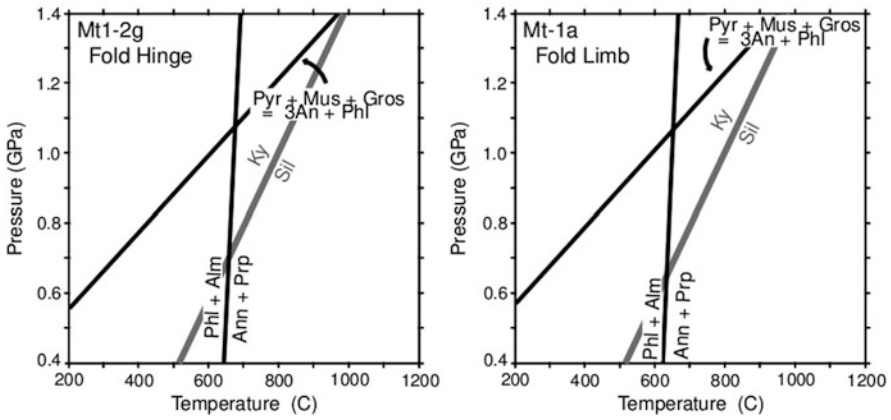

Fig. 3.7 Equilibria corresponding to the Garnet-biotite thermometer and garnet-muscovite-biotite-quartz barometer using Ca-rich plagioclase, Na-poor *white* mica, garnet rim, matrix biotite and quartz from the hinge and limb. Calculations were preformed with the software of Berman (1991). P-T conditions are consistent with the development of the S3 crenulation at 1.1 GPa (From Williams et al. (2001))

reactions governed by changes in P-T conditions, fluid-rock interactions and mass-transfer (Marquer and Burkhard 1992; Wintsch et al. 1995, 2005; Yonkee et al. 2003; Barnes et al. 2004; Mahan et al. 2006; Sassier et al. 2006; Oliot et al. 2010; Rolland et al. 2003). Therefore, estimating the P-T conditions during the

deformation in a shear zone requires taking into account the variability of fluid and rock compositions in time and space (Yonkee et al. 2003). Aside from these difficulties, shear zones have the advantage of preserving along their strain gradients various degrees of fluid-rock interaction and, more importantly, the lowest strain rock (ideally the undeformed protolith) can be used as a reference frame. Therefore, assuming that there are negligible pre-deformation chemical heterogeneities, it is straightforward to quantify the amount of mass transfer across the strain gradient and highlight the mineralogical changes due to mass transfer and/or variations in the P-T conditions during deformation. There is abundant literature dealing with metasomatism in shear zones, where mineralogical and chemical changes are well characterized and quantified using major and minor element mass balance calculations combined with stable and radiogenic isotope data (Fourcade et al. 1989; Dipple and Ferry 1992; Demeny et al. 1997; McCaig 1984; Keller et al. 2004; Rossi et al. 2005; Sassier et al. 2006; Glodny and Grauert 2009; Oliot et al. 2010; Rolland et al. 2003). In this contribution, we describe results obtained from a shear zone in the Grimsel granodiorite (Aar massif, Switzerland).

The Grimsel granodiorite is a Variscan intrusive that was affected by Alpine heterogeneous deformation, which is characterized by a network of anastomosing shear zones wrapping around lens-shaped domains of weakly deformed rocks on different scales (Choukroune and Gapais 1983; Marquer et al. 1985; Gapais et al. 1987). One of these shear zones is characterized by intense mass transfer and mineralogical changes along a 80 m-wide strain gradient, from the undeformed granodioritic protolith to an ultramylonitic zone. The main features observed in this shear zone are summarized below (Marquer et al. 1985; Fourcade et al. 1989):

1. With increasing strain, we observe a loss of CaO and Na_2O coupled with a gain in MgO, K_2O, and H_2O (Fig. 3.8). In the highest strain zone (chlorite-bearing ultramylonite), the system becomes CaO-free with a relative gain in MgO of up to 250% (not shown in Fig. 3.8) (Goncalves et al. 2012).
2. The undeformed and unaltered parent rock consists of K-feldspar, quartz, biotite. Primary (magmatic) plagioclase has been completely transformed into albite and epidote (Fig. 3.9a). With deformation, large amounts of phengite are crystallized at the expense of metastable magmatic phases like K-feldspar in the orthogneiss via metamorphic/metasomatic reactions, such as $Kfs + Ep + Bt + H_2O + MgO = Ms + Qtz + Ab + CaO$ and $Kfs + Ab + Bt + H_2O + MgO = Ms + Qtz + Ep + Na_2O$. In the mylonite and ultramylonite, porphyroclasts have been completely broken down and/or recrystallized into new metamorphic phases (Fig. 3.9b). The ultramylonite and millimeter-scale shear bands in the mylonite and orthogneiss are characterized by the complete breakdown of metamorphic epidote and the occurrence of chlorite in equilibrium with a CaO-free assemblage consisting of biotite, albite and white mica (Fig. 3.9c). These changes in mineralogy are interpreted to be the result of the bulk reaction $Ep + Bt + Ab + H_2O + MgO + K_2O = Chl + Ms + Qtz + CaO + Na_2O$.

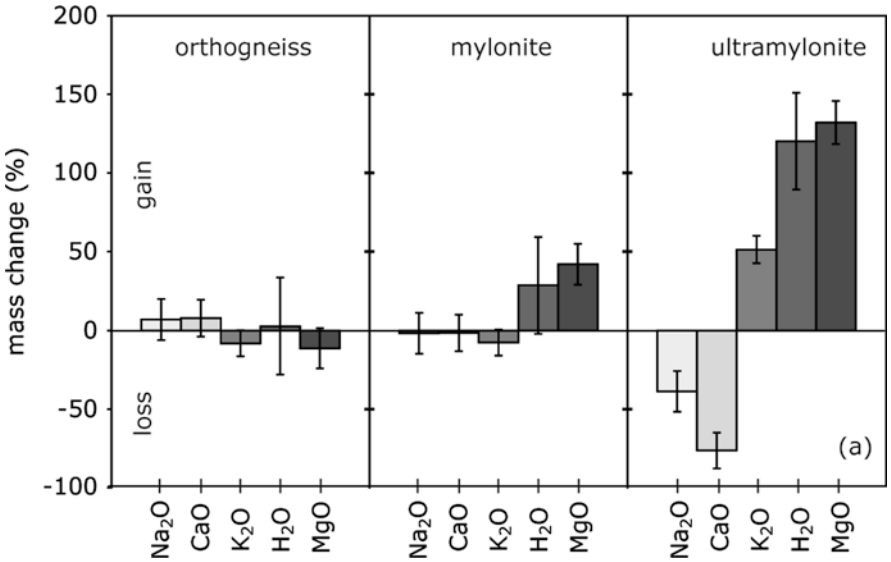

Fig. 3.8 Relative mass transfer along the strain gradient from the undeformed Aar granodiorite (reference composition) to the ultramylonite estimated using the Baumgartner and Olsen (1995) approach. Mass transfer has not been calculated on the chlorite-bearing ultramylonite assemblage but a rough estimation on photomicrographs and backscattered images suggests that on chlorite-bearing shear bands and ultramylonite the system becomes CaO-free with a relative gain in MgO up to 250%

3. In terms of mineral compositional variation along the strain gradient, white mica appears to be one of the most sensitive phases to syn-kinematic changes in bulk composition. Phengite, produced by the breakdown of K-feldspar, has a limited range in Si-content from 3.25 to 3.30 p.f.u. In contrast, in the chlorite-bearing ultramylonite, the amount of Tschermak substitution measured in phengite decreases continuously from 3.25 to a minimum value of 3.15 Si p.f.u. (Challandes et al. 2008; Goncalves et al. 2012).
4. P-T conditions from early Miocene deformation, estimated independently of this work, have been estimated at 450°C and 6 kbar (Challandes et al. 2008).

The observation of chlorite crystallization coupled with a decrease in the Si-content of white-mica in the highest strain zones could be misinterpreted as a retrograde feature during shear zone development. We demonstrate below that these mineralogical changes can rather be interpreted as the result of isobaric and isothermal metasomatism during deformation.

In quartzo-feldspathic rocks under HP-LT conditions, one approach to estimating pressure conditions is the barometer calibrated by Massonne and Schreyer (1987), which is based on the amount of Tschermak substitution in phengite. Geodynamic interpretations frequently rely on this geobarometer, which has been extensively used over the past three decades (cited more than 590 times, ISI Web of Knowledge, August 25th 2010).

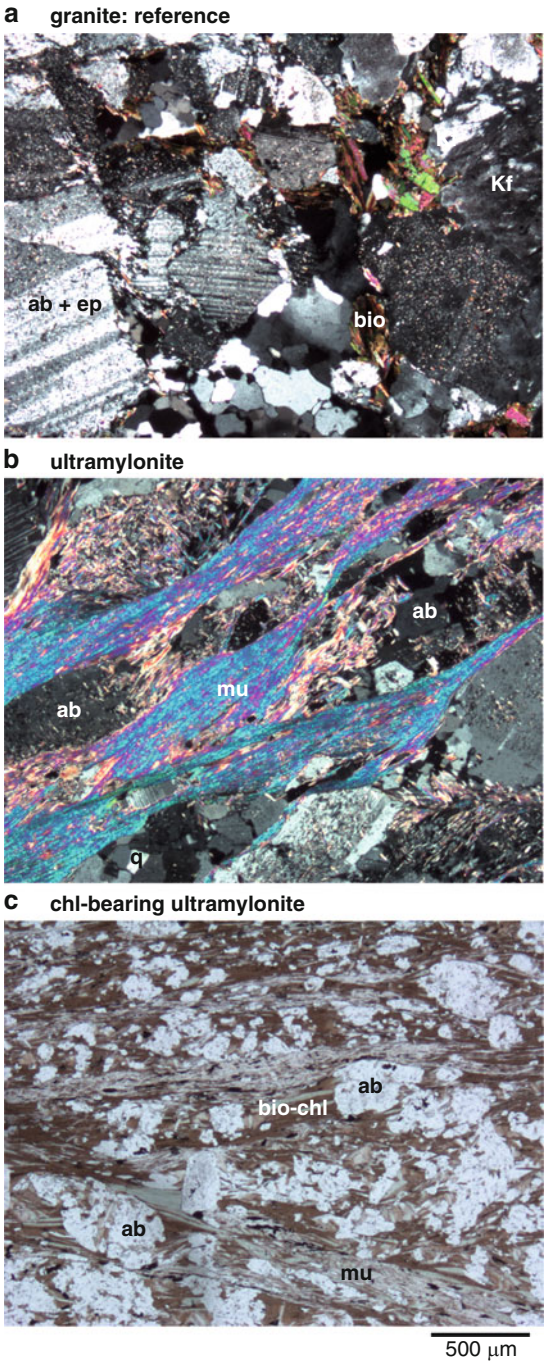

Fig. 3.9 Representative textures and assemblages observed along the strain gradient. The scale bar at the *bottom* of the figure applies to all three photomicrographs. (**a**) Undeformed granite showing magmatic K-feldspar, biotite and recrystallized quartz. Magmatic plagioclases are replaced by a metamorphic albite porphyroblast and epidote. (**b**) Ultramylonite showing the development of large amounts of white mica in equilibrium with albite. Magmatic K-feldspar and metamorphic epidote are no more present. (**c**) Ultramylonite showing the local development of chlorite-bearing assemblages in equilibrium with albite, biotite and muscovite

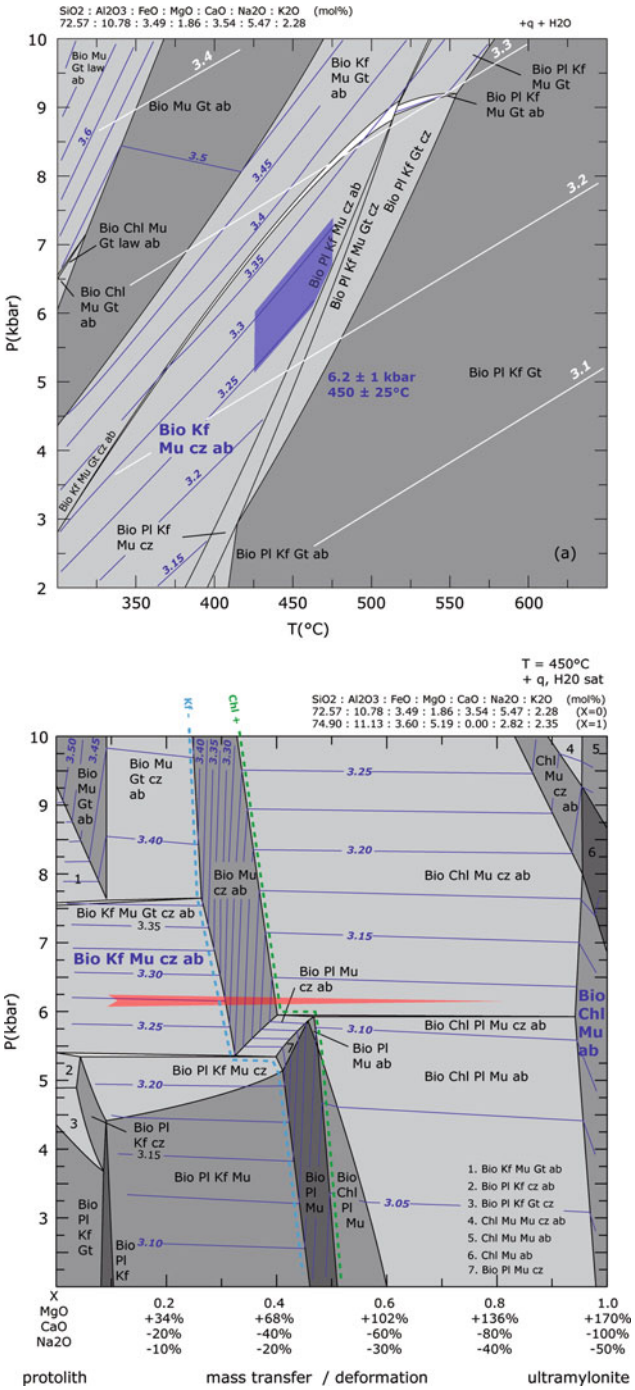

Fig. 3.10 (**a**) PT pseudosections calculated with the protolith composition in the NaCaFMASH system under water saturated conditions. Silicon content per formula unit in white micas is contoured. The white isopleths are from Massone and Schreyer (1987) and the blue isopleths are calculated. The

Application of the "Si in phengite" barometer requires the coexistence of phengite with K-feldspar, phlogopite, quartz and H_2O in excess (Massonne and Schreyer 1987). If phengite is not in equilibrium with the limiting assemblage cited above (in most cases, K-feldspar is missing) only a minimum pressure estimate can be derived from this barometer (Massonne and Schreyer 1987). To highlight the dependency of the Tschermak substitution in white mica on this mineral assemblage, a P-T pseudosection, calculated using the composition of the undeformed Grimsel granodiorite, has been contoured with isopleths for Si p.f.u. in phengite (Fig. 3.10a). Although the absolute position of the isopleth in the K-feldspar – phengite – biotite – quartz stability field is different from that presented in Massonne and Schreyer (Fig. 6, 1987), their observation that the Si content in phengite is dependent on the buffering assemblage is confirmed. For instance, Fig. 3.10a shows that at high pressure where K-feldspar is not stable, the calculated isopleths are shifted to higher pressure resulting in a significant discrepancy with the Si isopleths of Massonne and Schreyer (1987) for phengite in the limiting assemblage with K-feldspar, phlogopite and quartz.

Mass transfer and induced changes in the mineral assemblage also have a strong influence on the phengite composition. The P-X pseudosection in Fig. 3.10b shows the effect of mass transfer on phase relations. It has been calculated at 450°C under water saturated conditions with X corresponding to the change in bulk composition from unaltered granodiorite (X = 0) to chlorite-bearing ultramylonite (X = 1). The ultramylonite composition (X = 1) corresponds to the unaltered composition affected by a gain of 170% in MgO, a loss of 100% in CaO and 50% in Na_2O (K_2O gains have not been taken into account in this model). All the other components are kept constant. It appears that syn-kinematic metasomatism under constant pressure and temperature has a strong effect on the mineralogical assemblage. At the pressure of interest (6 kbar), mass transfer induces the crystallization of white mica at the expense of K-feldspar, followed by the breakdown of biotite and epidote to produce more white mica and ultimately chlorite (Figs. 3.10b and 3.11). The P-X pseudosection contoured for the Si content of white mica (Fig. 3.10b) shows that the process of rock equilibration during mass transfer induces a decrease in the Si-content of phengite from 3.25 to 3.27 (when in equilibrium with K-feldspar + epidote + albite) down to 3.12 p.f.u. when white mica is in equilibrium with the chlorite-bearing assemblage of the ultramylonite at the same P-T conditions (Fig. 3.10b). The strong dependency of the Tschermak substitution in white mica on mass transfer occurs only when white mica is in equilibrium with biotite, epidote, albite and quartz (in the absence of K-feldspar and chlorite).

Fig. 3.10 (continued) blue area corresponds to the preferred P-T conditions of metamorphism. (**b**) P-X compositions calculated at T = 450°C under water saturated conditions. The x-axis corresponds to the bulk composition, which varies from the protolith composition (x = 0) to an ultramylonite composition after being affected by a relative gain of 170% MgO coupled with a relative loss of 100% CaO and 50% loss Na_2O. The P-X pseudosection is contoured for the Si content in the phengite. The *red arrow* shows the effects of an isobaric isothermal metasomatism on the phase relations

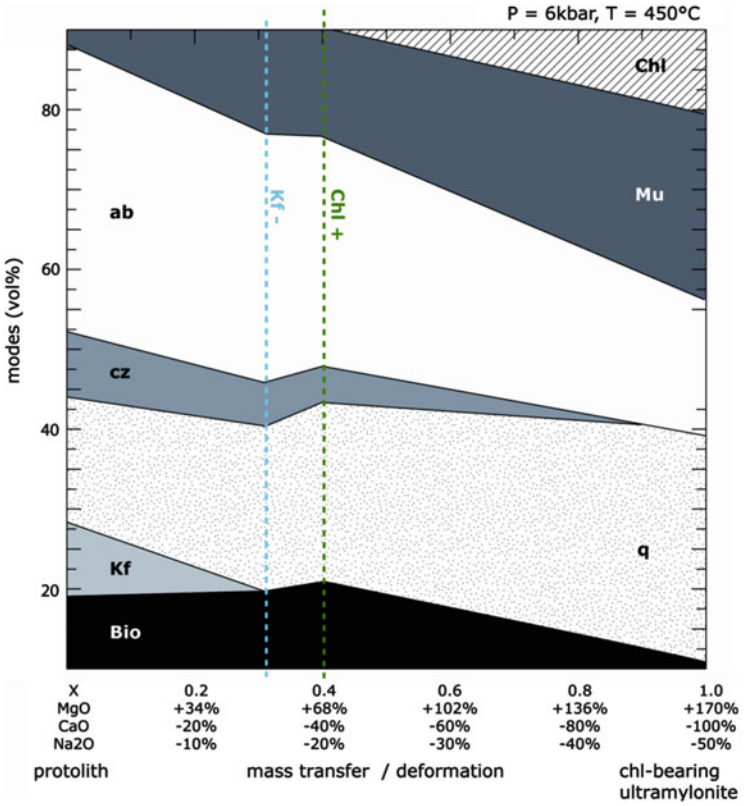

Fig. 3.11 Predicted mineralogical evolution estimated at 6 k bar and 450°C as a function of mass transfer. See caption of Fig. 3.10 for an explanation of the x-axis

To conclude, the unique observation of slightly substituted phengite in the ultramylonite may be incorrectly interpreted in terms of a decompression of about 3 kbar during the deformation event under closed system conditions. The combined effect of strain variability with mass transfer on the white mica composition has been also documented by Arancibia and Morata (2005) in a low-grade mylonite generated in an ignimbrite protolith. They show that the Si-content in phengite increases from 3.04 to 3.30 with increasing strain due to syn-deformational K-metasomatism. In this case, inappropriate application of a barometer based on the white mica composition would give meaningless high pressure conditions. The role of micro- to macro-scale syn-kinematic mass transfer and fluid conditions on the white mica composition have been underestimated in past studies and some P-T-t paths may need to be re-evaluated. As mentioned by Massone and Schreyer (1987), Wei et al. (2004) and Wei and Powell (2006), application of the phengite barometer must be done with care and knowledge of its limitations, particularly in open metasomatic systems.

3.4.4 Thermobarometry on High Grade Polymetamorphic Rocks

Polymetamorphic rocks are likely to have been affected by metasomatism during their P-T-t path evolution. Therefore estimating P-T conditions through pseudosections require definition of the effective bulk composition for each metamorphic assemblage. Mafic rocks from the Athabasca granulite terrane, western Canadian Shield, preserve two distinct high-pressure events (M1 and M2) (Mahan et al. 2008). The rock studied by Mahan et al. (2008) is a deformed mafic granulite that consists of centimeter-scale M1 lenses of coarse anhedral, intergrown, inclusion-free garnet (Grt1) and clinopyroxene (Cpx1) with minor ilmenite (Ilm1) and quartz (Qtz1), surrounded by an anastomosing mylonitic matrix foliation defined by brown amphibole (Amph2) and plagioclase (Pl2) with disaggregated layers of Grt1 + Cpx1 phases (Fig. 3.12a, b) that suggest local fluid circulation. The matrix also contains a second-generation of isolated garnet (Grt2) with abundant inclusions of anhedral quartz, clinopyroxene, brown amphibole, plagioclase, and ilmenite (Fig. 3.12b). Finally, a "M3 granulitization" (dehydration of the M2 amphibolite-facies assemblage), consisting of a fine-grained assemblage of orthopyroxene (Opx3), clinopyroxene (Cpx3), ilmenite (Ilm3), and plagioclase (Pl3), is observed around the margins of matrix Amph2 (Fig. 3.12c).

In polymetamorphic rocks, the equilibration volume and effective bulk composition may differ significantly for each preserved assemblage (Stüwe 1997). Therefore, one of the main challenges in applying pseudosection modeling to these samples is estimation of the effective bulk composition relevant for each assemblage. Furthermore, the occurrence of deformation and associated fluid percolation during the M2 event might induce metasomatism and consequently lead to a change in bulk composition between the M1 and M2–M3 events. In this case study, Mahan et al. (2008) chose two distinct bulk compositions for mineral equilibria modeling. To quantify the P-T conditions of the M1 assemblage, a bulk composition was estimated from the coarse-grained Grt-Cpx-Ilm lenses via a combination of image analysis (backscatter electron images and compositional X-ray maps) and mineral compositions. M2 and M3 assemblages are modeled using the same whole-rock bulk composition measured by XRF on the hand-sample. The use of a whole-rock bulk composition for the M2 amphibolite facies assemblage is justified by the pervasive development of this hydrated assemblage throughout the rock volume and its synkinematic nature. In contrast, the M3 assemblage is restricted to narrow reaction bands (100–200 μm-wide) around the margins of Amph2. However, the fluids and dissolved components liberated during the transformation of the M2 amphibolite into the M3 granulite may have been transported over distances greater that the hand-sample scale, thus leading to an equilibrium volume much greater than the observed size of the M3 reaction band. Mass balance calculations indicate that the M2 event is characterized by significant gain in Na_2O, TiO_2 coupled with a decrease in FeO (Mahan et al. 2008).

P-T pseudosections calculated for the two bulk compositions are presented in Fig. 3.13. The M1 assemblage is stable in a large high-variance stability field at

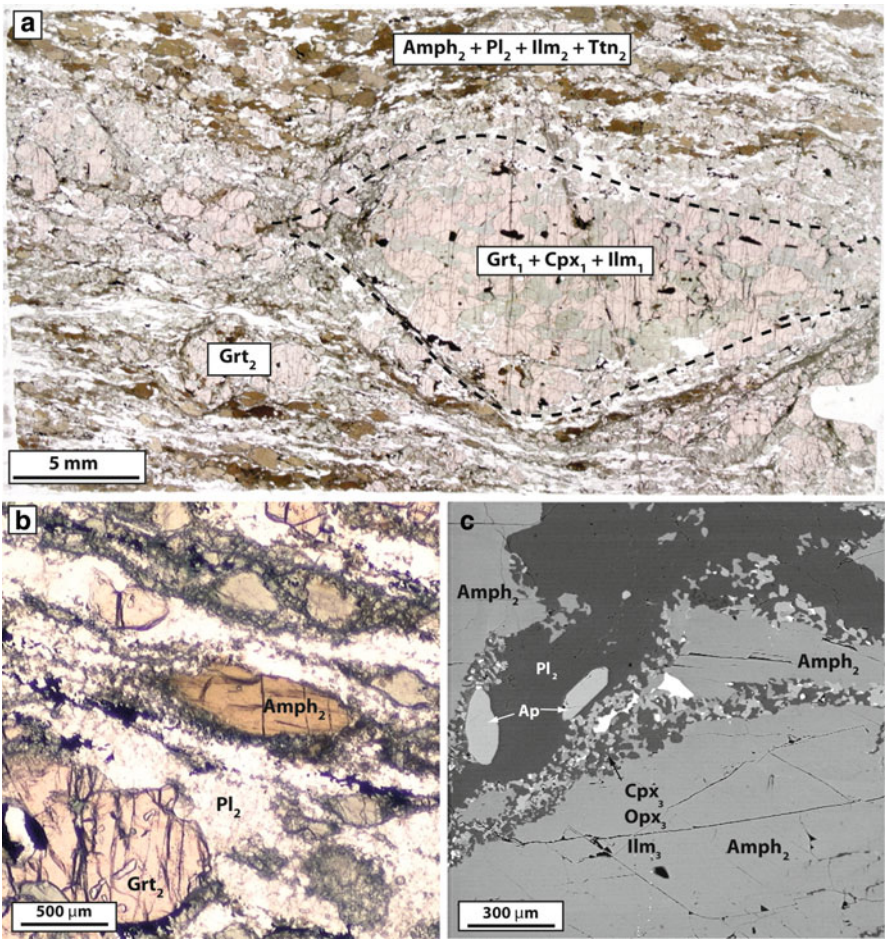

Fig. 3.12 (**a**) Photomicrograph of lenses of the M1 Grt + Cpx + Ilm + Qtz assemblage wrapped by a *brown* amphibole-bearing S2 matrix fabric. (**b**) Close-up view of the S2 matrix fabric showing the Amph2 + Pl2 assemblage with the second generation of garnet (Grt2). (**c**) Backscattered electron image of the reaction zone around Amph2 that produced the M3 assemblage (Opx3, Cpx3, Ilm3 and Pl3) (Mahan et al. 2008)

temperatures >800°C and pressures ranging from 1.15 to 1.40 GPa, in good agreement with results obtained via multi-equilibrium thermobarometry (see the ellipse in Fig. 3.13a). P-T conditions for the M2 and M3 assemblages are shown in Fig. 3.13b. The M2 assemblage is stable in a narrow field between 0.8 and 0.95 GPa at <740°C, while M3 peak conditions occurred at ~ 1.0 GPa and 800–900°C. This three-stage evolution has been successfully modeled using P-T pseudosections because (1) the early M1 effective bulk composition has been estimated on key low-strain localities where the M1 assemblage is preserved and (2) mass transfer that occurred during the D2 deformation event has been taken into

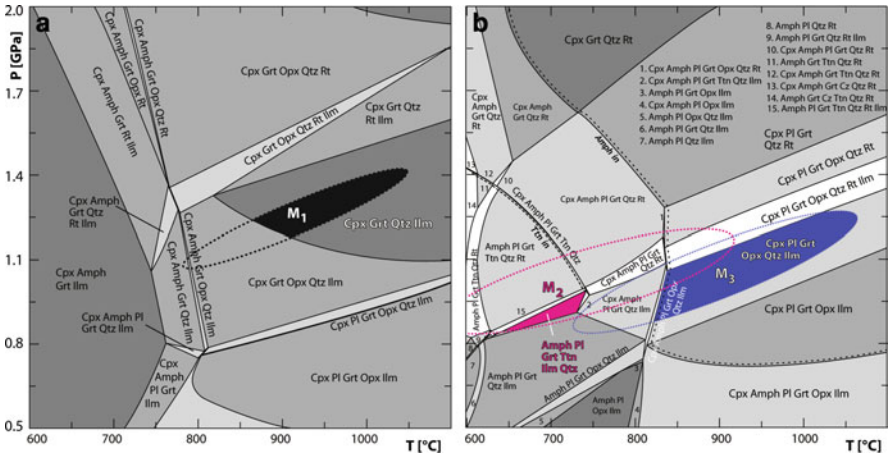

Fig. 3.13 (**a**) P–T pseudosection calculated for the M1 bulk composition in the NCFMASHT system under fluid-saturated conditions. Error ellipse is the 1σ ellipse obtained with the average P-T mode of THERMOCALC, with the *black-shaded* portion within the stability field for the observed M1 assemblage. (**c**) P–T pseudosection using the whole-rock XRF composition suitable for the M2 and M3 assemblage. Error ellipses are 1σ ellipses from Ave-PT for M2 and M3 with the *pink-shaded* and *blue-shaded* portion within the stability field for the M2 and M3 assemblages, respectively. Ttn-in and Amph-in boundaries are highlighted (Mahan et al. 2008)

account to model the D2 and D3 events. In other words, this work is made possible mainly because the rock selected is affected by heterogeneous strain that facilitates the recognition of the reference frame and the most altered assemblages.

3.5 Discussion

3.5.1 Recommendations for Thermobarometry on Metasomatic Rocks

The examples described for the different lithologies and scales above show that an isobaric and isothermal metasomatism can have a significant influence on phase relations and can produce mineral assemblages indistinguishable from those produced by changes in P-T conditions in a closed system. Probably the best example cited in this contribution is the crystallization of a chlorite-bearing assemblage in the highest-strain zone of a granodioritic shear zone in the Aar massif (Switzerland). The mineralogical changes are driven by fluid-infiltration and mass transfer (MgO gain coupled with CaO and Na_2O loss) at constant pressure and temperature. This demonstrates that variations in bulk-rock composition must be taken into account in phase relation modeling and thermobarometry.

In comparison to reactions driven by changes in physical conditions, reactions due to fluid-rock interactions (dissolution-precipitation) are transient and spatially heterogeneous either when fluid flow is pervasive or channelized by structural heterogeneities, like fractures, shear bands, or lithological contact (Jamtveit and Yardley 1997; Ague 2003). In these rocks, such features produce localized and complex reaction textures (Fig. 3.2) and zoned minerals (Figs. 3.3, 3.5 and 3.6), because equilibrium is achieved on the micron scale at the interface between the fluid and the precipitating products (Putnis and Austrheim 2010). The preservation of these textural and mineralogical heterogeneities makes the selection of appropriate mineral compositions in equilibrium difficult. This difficulty can be minimized by combining detailed microstructural observations with high-resolution X-ray mapping, which permit explicit assessment of major element zoning allowing for the location of the best areas to collect quantitative data for thermobarometry (e.g. Williams et al. 2001; Dumond et al. 2007; Mahan et al. 2006, 2008). However, the rocks that have experienced the most vigorous fluid flow and metasomatism (for example, the highest strain zone in a shear zone or vein selvage) are expected to be in equilibrium on the hand-sample scale and should not preserve the disequilibrium features described above. Therefore, to identify with confidence the mineral reactions related only to metasomatism, we encourage application of the systematic approach used by Beinlich et al. (2010) or Oliot et al. (2010) that consists of studying a suite of samples along a metasomatic gradient from the unaltered or weakly altered rock (Fig. 3.14a, b), where disequilibrium features are likely to be retained, to the most altered rocks that undergo the most extensive fluid-rock interactions.

Conventional thermobarometry on metasomatic rocks (that have not been recognized as such) may yield meaningless results and interpretations. Using the Aar shear zone example (Fig. 3.10), we have highlighted the importance of the buffering assemblage and syn-kinematic chemical mass transfer on mineral compositions. However, we note that in the case of the Si-in-phengite barometer, calibrated by Massone and Schreyer (1987), and probably most thermobarometers, mineral compositions are insensitive to bulk rock composition variations when the buffered assemblage is present. To take into account the effects of metasomatism, pseudosection modeling correlated with careful mass balance calculations offers a good alternative to conventional thermobarometry. Pseudosections (P-X, T-X, or X-X), contoured with isolines for mineral composition and modes, can be used primarily to explore the effects of metasomatism and buffering assemblages on mineral compositions at fixed P-T conditions. This phase relation modeling must obviously be preceded by a detailed geochemical analysis and mass balance calculations in order to determine the least altered "reference frame" host rock, identification of the immobile elements, and the relative and absolute mass and volume changes during metasomatism. Once again, we suggest performing this task on the largest possible suite of samples collected systematically along a metasomatic (+/− strain) gradient. Several procedures for mass balance calculations are available in the literature (e.g. Gresens 1967; Grant 1986; Potdevin and Marquer 1987; Baumgartner and Olsen 1995; Ague 2003).

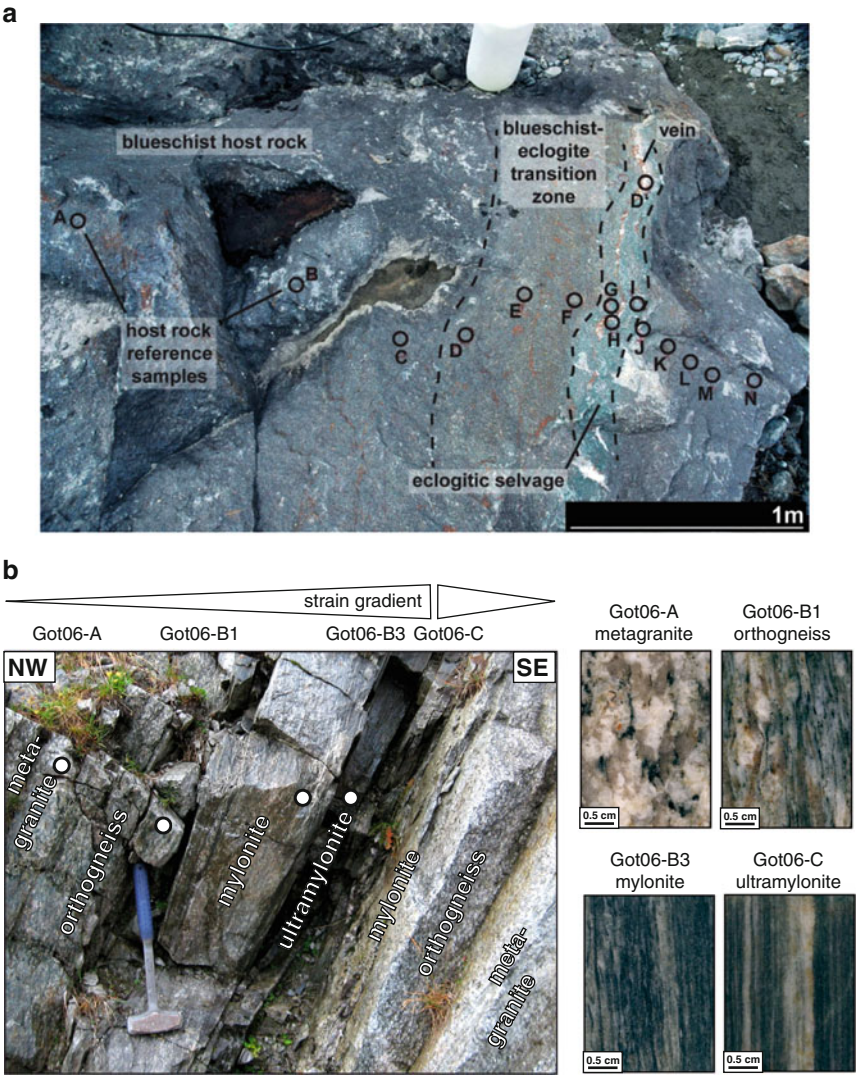

Fig. 3.14 (**a**) Outcrop photograph showing the sample profile from the host rock to the metasomatic vein selvage. *Black circles* indicate locations where samples were drilled out. The eclogitization of the vein selvage was caused by fluid infiltration under peak metamorphic conditions that have been estimated on the blueschist host reference sample and the eclogitic selvage at 21 ± 1.5 kbar and 510 ± 30°C (Beinlich et al. 2010). (**b**) Outcrop photograph showing a metric-sized ductile shear zone that has been used to study the effects of synkinematic mass transfer on phase relations (Oliot et al. 2010)

In situations where mineralogical and geochemical investigations and quantifications have been well established, the construction of P-T pseudosections, contoured for mineral compositions on a suite of metasomatic rocks, provides a

unique opportunity to precisely constrain the P-T conditions of fluid infiltration. For instance, Beinlich et al. (2010) have demonstrated that the eclogitization of blueschists around a vein was driven only by changes in bulk composition (mainly a gain of 115% of CaO) caused by the infiltration of a Ca-rich fluid. P-T pseudosections calculated for the unaltered blueschist composition (reference frame) and the altered eclogite composition indicate the same P-T conditions of 21 ± 1.5 kbar and 510 ± 30°C, suggesting that this blueschist-eclogite transition happened at identical P-T conditions. Oliot et al. (2010) applied the same approach to a meter-scale lower amphibolite-grade shear zone that is characterized by a gain of CaO, FeO and H_2O with increasing strain. P-T conditions for the metasomatism and deformation were estimated using P-T pseudosections calculated four distinct bulk compositions, i.e. the unaltered granitic parent rock, the orthogneiss, the mylonite, and the ultramylonite (Fig. 3.15a–d). Each pseudosection is contoured for the Si p.f.u. content in phengite and the anorthite content in plagioclase (see Oliot et al. 2010, for further explanations). Results show that P-T conditions are similar for the four different compositions (Fig. 3.15a–d) and the superposition of the P–T calibrations (Fig. 3.15e) allows for the refinement of the P-T conditions of metasomatism and therefore syn-kinematic fluid flow at 490 ± 15°C and 7.3 ± 0.5 kbar.

To conclude, pseudosection calculations can be used to retrieve the physical conditions of metamorphism and metasomatism in addition to predicting the mineral assemblages and compositions that should have developed during P-T-X evolution (forward modeling). In both cases, a detailed assessment of the mechanisms of equilibration at the field- and microscopic-scale is necessary.

3.5.2 Future Research on the Thermodynamics of Metasomatism

The on-going research and development of the thermodynamic database for mineral end-members (e.g. Holland and Powell 1998 and updated version in 2011), activity-composition models for major silicates in large component systems (TiMnCaNaKFMASHO) (e.g. Diener et al. 2007; Tajčmanová et al. 2009; Dubacq et al. 2010; Taylor-Jones and Powell 2010), and programs for calculating and displaying P-T-X phase diagrams (Perple_X, Thermocalc, Theriak-Domino) collectively support exciting future advances in research on metasomatic systems. However, more efforts should be put on the development of a-X models for typical metasomatic phases like scapolite, epidote or wollastonite group minerals as well as the so-called "accessory phases", like phosphates and Boron silicates which are common minerals in metasomatic rocks.

Fluid infiltration plays a fundamental role during mineral transformation and growth, not only as a catalyst that favor element transport and reactions but also as a phase, which participates to the mineral equilibria (Putnis and Austrheim 2010, see Chap. 5). Indeed, if re-equilibration of a mineral assemblage in metamorphic/metasomatic rocks occurs via the mechanism of (1) dissolution of minerals, (2) transport of dissolved components in a fluid either by diffusion in a static fluid or by

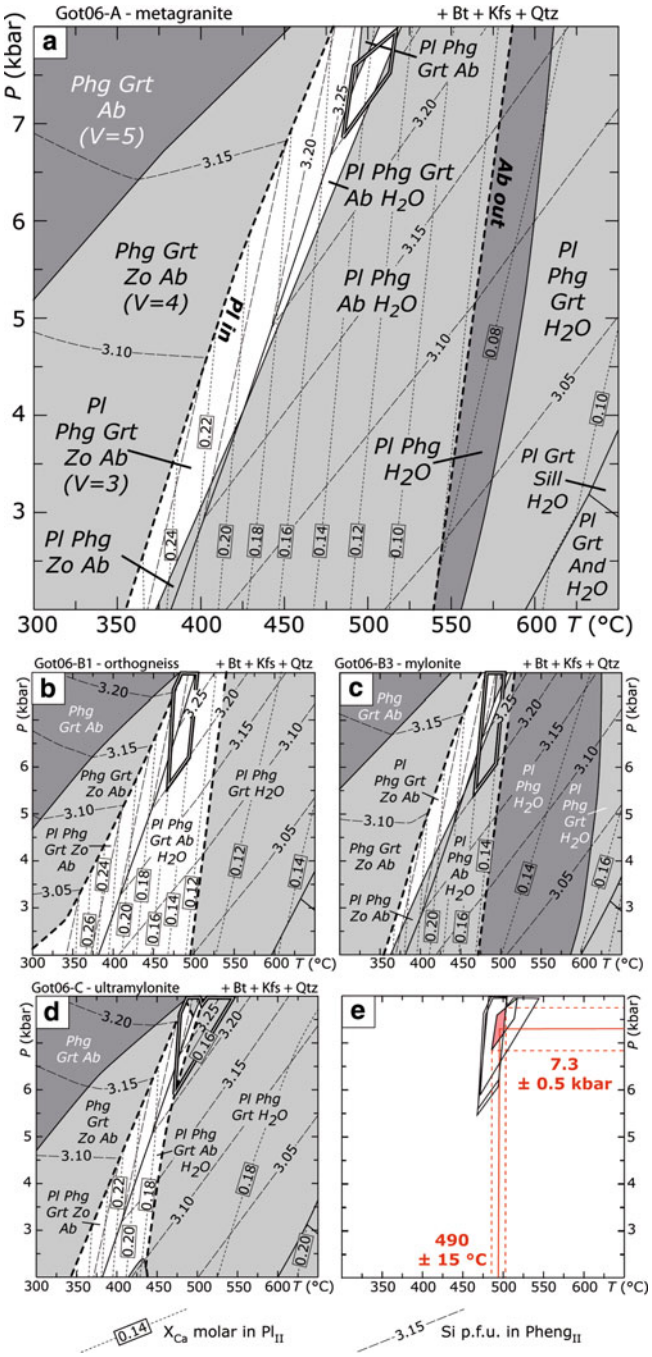

Fig. 3.15 P–T pseudosections calculated in the MnCNKFMASH system for (**a**) the metagranite bulk rock composition, (**b**) the orthogneiss composition, (**c**) the mylonite composition and (**d**) the

advection, and (3) precipitation of new minerals, then particular attention should be paid to the fluid chemistry with dissolved ions in equilibrium with the precipitating phase(s) (Dolejs and Wagner 2008; Putnis and Austrheim 2010, see Chap. 5). Fluid chemistry (amounts of dissolved ions) depends on pressure, temperature, the fluid species involved (in the C-O-H-S system: H_2O, H_2, O_2, CO_2, CO, CH_4, S_2, SO_2, H_2S and COS), the ligand concentration (e.g. chloride) in the fluid that is used to form complexes with the cations released during incongruent dissolution of minerals, the mineral assemblage in equilibrium with the fluid, and lastly the minerals (Jamtveit and Yardley 1997). All of these variables make the description of fluid chemistry and mineral solubility very difficult and are therefore ignored in most thermobarometric estimations of metasomatism. Although experimental work and thermodynamic models regarding mineral solubility are ongoing (e.g. Dolejš and Wagner 2008; Fockenberg et al. 2008; Dolejš and Manning 2010), the experimental databases and thermodynamic parameters of mineral solubility in aqueous fluids at high temperature remains limited and restricted to end-member minerals in simple chemical systems (see review in Ague 2003). Modeling metasomatism in realistic geological chemical systems requires improved knowledge of mineral solubilities at elevated temperatures and pressures.

3.6 Conclusions

Geothermobarometry and pseudosection thermodynamic modeling provide useful results for understanding tectonometamorphic processes, including fluid-rock interactions, however its application is not without pitfalls. In open systems like metasomatized rocks, where the mineral re-equilibration occurs mainly via a dissolution-precipitation mechanism, the stable mineralogical assemblage depends not only on variations in pressure and temperature, but also on changes in bulk-rock composition and fluid chemistry.

Pitfalls known for isochemical metamorphic rocks apply also to metasomatized rocks. For instance, application of thermobarometry in metasomatized rocks requires that the selected minerals represent an equilibrated mineral assemblage during the fluid-rock interaction. There is no way to prove that this equilibrium assumption is valid, but if geothermobarometry is applied on rocks with well characterized and understood mineral textures and phase relations, the "equilibrium pitfall" can be significantly minimized.

Fig. 3.15 (continued) ultramylonite composition. Sample locations are shown as *white dots* in Fig. 3.14. Silicon p.f.u. isopleths of *white* mica and $X_{CaO} = CaO/(CaO + Na_2O)$ isopleths of plagioclase are plotted to constrain the metamorphic conditions of the deformation (*black boxes*). (**e**) Preferred P–T conditions (7.3 ± 0.5 kbar and 490 ± 15°C) of the Alpine deformation in the central Gotthard Massif calculated from the superposition of the four previous P–T estimations (Oliot et al. 2010)

Application of thermodynamic modeling to metasomatized rocks also requires definition of a reference frame (i.e., the unaltered or least-altered rock) in order to (1) distinguish mineral reactions and assemblages due to changes in P-T conditions under closed system conditions from those driven by metasomatism and (2) define, through mass balance calculations, the relative and absolute mass and volume changes during metasomatism. Practically and contrary to normal metamorphic rocks where a single sample can be used, a multi-sample suite with various degrees of metasomatism must be studied. Phase relation modeling and geothermobarometry can be undertaken as in P-T-X pseudosections that are contoured with isolines for mineral composition and modes. Pseudosections are a good alternative to conventional thermobarometry because, in addition to the quantification of pressure and temperature, pseudosections can be used to explore the effects of metasomatism and fluid transfer (X) on phase relations.

There are currently two major pitfalls that tend to prevent the direct application of mineral equilibria thermobarometry to metasomatized rocks. (1) There are no appropriate activity-compositions for common phases observed in metasomatized rocks (e.g. scapolite) such that the a-X models for major silicates developed for "normal" bulk rock compositions might not be suitable for the "unusual" metasomatic bulk compositions. (2) The major pitfall is related to fluid chemistry (see Chap. 5). Fluids involved in the process of equilibration during metasomatism contain dissolved components that play a role with respect to phase relations and mass transfer. Therefore fluids should be included in thermodynamic modeling as a complex composition and not only as a C-O-H phase. Unfortunately, it is very difficult to get information on the composition of a fluid moving in and out of the rock as well as its composition when in equilibrium with the local mineral assemblage in natural rocks.

Despite these two major limitations, the examples used in this contribution show that thermobarometry can be successfully applied to metasomatized rocks. Therefore, we would like to conclude, that metasomatized rocks can generally be read like "normal" metamorphic rocks, although they are usually more complex due to variations in bulk composition and fluid-rock interactions. Pseudosection thermobarometry seems particularly suitable for metasomatized rocks because the effects of mass transfer on phase relations can be easily predicted. Pseudosections are a powerful tool only if they are coupled with a detailed mineralogical/textural investigation and geochemical analysis essential to defining the composition of the protolith (reference frame) and mass changes that occurred during metasomatism.

Acknowledgments This work was funded by the French ministry of research with additional funding provided by the Université de Franche-Comté (BQR2006). Discussions with N. Manchtelow, K. Schulmann, O. Vidal and M. Williams helped shape the ideas that were largely influenced by the work of A. Putnis. This paper was significantly improved by the review comments of Jane Selverstone and Gregory Dumond. Daniel Harlov and Håkon Austrheim are gratefully acknowledge for the invitation to this volume and for their constructive comments and editorial handling

References

Ague JJ (1994) Mass-transfer during Barrovian metamorphism of pelites, south-central Connecticut.1. Evidence for changes in composition and volume. Am J Sci 294:989–1057

Ague JJ (1995) Deep-crustal growth of quartz, kyanite and garnet into large-aperture, fluid-filled fractures, north-eastern Connecticut, USA. J Metamorph Geol 13:299–314

Ague JJ (2003) Fluid infiltration and transport of major, minor, and trace elements during regional metamorphism of carbonate rocks, Wepawaug Schist, Connecticut, USA. Am J Sci 303: 753–816

Aitken B (1983) T-XCO2 stability relations and phase-equilibria of a calcic carbonate scapolite. Geochim Cosmochim Acta 47:351–362

Arancibia G, Morata D (2005) Compositional variations of syntectonic white-mica in low-grade ignimbritic mylonite. J Metamorph Geol 27:745–767

Austrheim H (1987) Eclogitization of lower crustal granulites by fluid migration through shear zones. Earth Planet Sci Lett 81:221–232

Austrheim H, Putnis CV, Engvik AK et al (2008) Zircon coronas around Fe-Ti oxides: a physical reference frame for metamorphic and metasomatic reactions. Contrib Mineral Petrol 156:517–527

Baldwin JA, Powell R, Williams ML et al (2007) Formation of eclogite, and reaction during exhumation to mid-crustal levels, snowbird tectonic zone, western Canadian shield. J Metamorph Geol 25:953–974

Ballèvre M, Hensen B, Reynard B (1997) Orthopyroxene-andalusite symplectites replacing cordierite in granulites from the Strangways Range (Arunta block, central Australia): a new twist to the pressure-temperature history. Geology 25:215–218

Barnes JD, Selverstone J, Sharp ZD (2004) Interactions between serpentinite devolatilization, metasomatism and strike-slip strain localization during deep-crustal shearing in the Eastern Alps. J Metamorph Geol 22:283–300

Baumgartner LP, Olsen SN (1995) A least-squares approach to mass-transport calculations using the isocon method. Econ Geol Bull Soc 90:1261–1270

Beinlich A, Klemd R, John T et al (2010) Trace-element mobilization during Ca-metasomatism along a major fluid conduit: eclogitization of blueschist as a consequence of fluid-rock interaction. Geochim Cosmochim Acta 74:1892–1922

Bell TH, Rubenach MJ, Fleming PD (1986) Porphyroblast nucleation, growth and dissolution in regional metamorphic rocks as a function of deformation partitioning during foliation development. J Metamorph Geol 4:37–67

Berman RG (1991) Thermobarometry using multi-equilibrium calculations – a new technique, with petrological applications. Can Mineral 29:833–855

Berman RG, Aranovich LY (1996) Optimized standard state and solution properties of minerals.1. Model calibration for olivine, orthopyroxene, cordierite, garnet, ilmenite in the system FEO-MGO-CaO-Al2O3-TiO3-SiO2. Contrib Mineral Petrol 126:1–24

Blattner P, Lassey KR (1989) Stable-isotope exchange fronts, Damköhler numbers, and fluid to rock ratios. Chem Geol 78:381–392

Bottinga Y, Javoy M (1973) Comments on oxygen isotope geothermometry. Earth Planet Sci Lett 20:250–265

Bottinga Y, Javoy M (1975) Oxygen isotope partitioning among the minerals in igneous and metamorphic rocks. Rev Geophys 13:401–418

Burnley PC, Davis MK (2004) Volume changes in fluid inclusions produced by heating and pressurization: an assessment by finite element modeling. Can Mineral 42:1369–1382

Caddick MJ, Thompson AB (2008) Quantifying the tectono-metamorphic evolution of pelitic rocks from a wide range of tectonic settings: mineral compositions in equilibrium. Contrib Mineral Petrol 156:177–195

Carmichael DM (1969) On the mechanism of prograde metamorphic reactions in quartz-bearing pelitic rocks. Contrib Mineral Petrol 20:244–267

Caron JM, Potdevin JL, Sicard E (1987) Solution deposition processes and mass-transfer in the deformation of a minor fold. Tectonophysics 135:77–86
Chacko T, Cole DR, Horita J (2001) Equilibrium oxygen, hydrogen and carbon isotope fractionation factors applicable to geologic systems. Rev Mineral Geochem 43:1–81
Challandes N, Marquer D, Villa IM (2008) P-T-t modelling, fluid circulation, and Ar-39-Ar-40 and Rb-Sr mica ages in the Aar Massif shear zones (Swiss Alps). Swiss J Geosci 101:269–288
Choukroune P, Gapais D (1983) Strain pattern in the Aar granite (central Alps) – orthogenesis developed by bulk inhomogeneous flattening. J Struct Geol 5:411–418
Clayton RN (1981) Isotopic thermometry. In: Newton R, Navrotsky A, Wood BJ (eds) The thermodynamics of minerals and melts. Springer, Berlin
Connolly JAD (1990) Multivariable phase-diagrams – an algorithm based on generalized thermodynamics. Am J Sci 290:666–718
Connolly JAD (2005) Computation of phase equilibria by linear programming: a tool for geodynamic modeling and its application to subduction zone decarbonation. Earth Planet Sci Lett 236:524–541
Connolly JAD, Petrini K (2002) An automated strategy for calculation of phase diagram sections and retrieval of rock properties as a function of physical conditions. J Metamorph Geol 20:697–708
Crowe DE, Vaughan RG (1996) Characterization and use of isotopically homogeneous standards for in situ laser microprobe analysis of 34S/32S ratios. Am Mineral 81:187–193
Crowe DE, Valley JW, Baker KL (1990) Micro-analysis of sulfur-isotope ratios and zonation by laser microprobe. Geochim Cosmochim Acta 54:2075–2092
De Capitani C, Brown TH (1987) The computation of chemical-equilibrium in complex-systems containing nonideal solutions. Geochim Cosmochim Acta 51:2639–2652
De Capitani C, Petrakakis K (2010) The computation of equilibrium assemblage diagrams with Theriak/Domino software. Am Mineral 95:1006–1016
Demeny A, Sharp ZD, Pfeiffer HR (1997) Mg-metasomatism and formation conditions of Mg-chlorite-muscovite-quartzphyllites (leucophyllites) of the Eastern Alps (W Hungary) and their relations to Alpine whiteschists. Contrib Mineral Petrol 128:247–260
Diener JFA, Powell R, White RW et al (2007) A new thermodynamic model for clino- and orthoamphiboles in the system Na2O-CaO-FeO-MgO-Al2O3-SiO2-H2O-O. J Metamorph Geol 25:631–656
Dipple GM, Ferry JM (1992) Metasomatism and fluid-flow in ductile fault zones. Contrib Mineral Petrol 112:149–164
Dodson MH (1973) Closure temperature in cooling geochronological and petrological systems. Contrib Mineral Petrol 40:259–274
Dolejš D, Manning CE (2010) Thermodynamic model for mineral solubility in aqueous fluids: theory, calibration and application to model fluid-flow systems. Geofluids 10:20–40
Dolejš D, Wagner T (2008) Thermodynamic modeling of non-ideal mineral-fluid equilibria in the system Si-Al-Fe-Mg-Ca-Na-K-H-O-Cl at elevated temperatures and pressures: implications for hydrothermal mass transfer in granitic rocks. Geochim Cosmochim Acta 72:526–553
Dubacq B, Vidal O, De Andrade V (2010) Dehydration of dioctahedral aluminous phyllosilicates: thermodynamic modelling and implications for thermobarometric estimates. Contrib Mineral Petrol 159:159–174
Dubessy J, Moissette A, Bakker RJ et al (1999) High-temperature Raman spectroscopic study of H2O-CO2-CH4 mixtures in synthetic fluid inclusions: first insights on molecular interactions and analytical implications. Eur J Mineral 11:23–32
Dumond G, Mahan KH, Williams ML et al (2007) Crustal segmentation, composite looping pressure-temperature paths, and magma-enhanced metamorphic field gradients: upper granite gorge, Grand Canyon, USA. Geol Soc Am Bull 119:202–220
Durand C, Boulvais P, Marquer D et al (2006) Stable isotope transfer in open and closed system across chemically contrasted boundaries: metacarbonate – granitoid contacts in the Quérigut magmatic complex (Eastern Pyrenees, France). J Geol Soc Lond 163:827–836

Durand C, Marquer D, Baumgartner L et al (2009) Large calcite and bulk-rock volume loss in metacarbonate xenoliths from the Quérigut massif (French Pyrenees). Contrib Mineral Petrol 157:749–763

Eiler JM, Valley JW (1994) Preservation of premetamorphic oxygen isotope ratios in granitic orthogneiss from the adirondack mountains, New York, USA. Geochim Cosmochim Acta 58:5525–5535

Eiler JM, Valley JW, Baumgartner LP (1993) A new look at stable isotope thermometry. Geochim Cosmochim Acta 57:2571–2583

Eiler JM, Valley JW, Graham CM, Baumgartner LP (1995) Ion microprobe evidence for the mechanism of stable isotope retrogression in high-grade metamorphic rocks. Contrib Mineral Petrol 118:365–378

Eldrige CS, Compston W, Williams IS et al (1987) In situ microanalysis for 34S/32S ratios using the ion microprobe SHRIMP. Int J Mass Spectrom 76:65–83

Engvik AK, Austrheim H (2010) Formation of sapphirine and corundum in scapolitised and Mg-metasomatised gabbro. Terra Nova 22:166–171

Engvik AK, Mezger K, Wortelkamp S et al (2011) Metasomatism of gabbro – mineral replacement and element mobilization during the Sveconorwegian metamorphic event. J Metamorph Geol 29:399–423

Ferry JM (1994) Overview of the petrologic record of fluid-flow during regional metamorphism in Northern New-England. Am J Sci 294:905–988

Ferry JM, Dipple GM (1991) Fluid-flow, mineral reactions, and metasomatism. Geology 19: 211–214

Florence FP, Spear FS (1991) Effects of diffusional modification of garnet growth zoning on p-t path calculations. Contrib Mineral Petrol 107:487–500

Fockenberg T, Burchard M, Maresch WV (2008) The solubility of natural grossular-rich garnet in pure water at high pressures and temperatures. Eur J Mineral 20:845–855

Fourcade S, Marquer D, Javoy M (1989) O-18/O-16 variations and fluid circulation in a deep shear zone – the case of the alpine ultramylonites from the Aar massif central Alps, Switzerland. Chem Geol 77:119–131

Friedman I, O'Neil JR (1977) Compilation of stable isotope fractionation factors of geochemical interest. In: Fleischer M (ed) Data of geochemistry, vol 440-KK, 6th edn, U.S. Geological survey professional paper. U.S. Govt. Print. Off, Washington

Fu B, Touret J, Zheng Y et al (2003) Fluid inclusions in granulites, granulitized eclogites and garnet clinopyroxenites from the Dabie-Sulu terranes, eastern China. Lithos 70:293–319

Gapais D, Bale P, Choukroune P et al (1987) Bulk kinematics from shear zone patterns – some field examples. J Struct Geol 9:635–646

Giletti BJ (1986) Diffusion effects on oxygen isotope temperatures of slowly cooled igneous and metamorphic rocks. Earth Planet Sci Lett 77:218–228

Glodny J, Grauert B (2009) Evolution of a hydrothermal fluid-rock interaction system as recorded by Sr isotopes: a case study from the Schwarzwald, SW Germany. Miner Petrol 95:163–178

Goldstein A, Knight J, Kimball K (1998) Deformed graptolites, finite strain and volume loss during cleavage formation in rocks of the taconic slate belt, New York and Vermont, U.S.A. J Struct Geol 20:1769–1782

Goncalves P, Oliot E, Marquer D, Connolly JAD (2012) Role of chemical processes on shear zone formation: an example from the Grimsel metagranodiorite (Aar massif, Central Alps). J Metamorph Geol in press

Graham C, Valley JW (1992) Sulphur isotope analysis of pyrites. Chem Geol Isot Geosci 101:169–172

Grant JA (1986) The isocon diagram-a simple solution to gresens equation for metasomatic alteration. Econ Geol 81:1976–1982

Green E, Holland T, Powell R (2007) An order-disorder model for omphacitic pyroxenes in the system jadeite-diopside-hedenbergite-acmite, with applications to eclogitic rocks. Am Mineral 92:1181–1189

Gregory RT, Criss RE (1986) Isotopic exchange in open and closed systems. Rev Mineral Geochem 16:91–127

Gresens RL (1967) Composition-volume relationships of metasomatism. Chem Geol 2:47–65
Guiraud M, Powell R, Rebay G (2001) H2O in metamorphism and unexpected behaviour in the preservation of metamorphic mineral assemblages. J Metamorph Geol 19:445–454
Hall DL, Sterner S (1993) Preferential water-loss from synthetic fluid inclusions. Contrib Mineral Petrol 114:489–500
Hall DL, Bodnar RJ, Craig JR (1991) Evidence for postentrapment diffusion of hydrogen into peak metamorphic fluid inclusions from the massive sulfide deposits at ducktown, Tennessee. Am Mineral 76:1344–1355
Harley S (1989) The origins of granulites – a metamorphic perspective. Geol Mag 126:215–247
Harlov DE, Forster HJ (2003) Fluid-induced nucleation of (Y + REE)-phosphate minerals within apatite: nature and experiment. Part II. Fluorapatite. Am Mineral 88:1209–1229
Harlov DE, Hetherington CJ (2010) Partial high-grade alteration of monazite using alkali-bearing fluids: experiment and nature. Am Mineral 95:1105–1108
Harlov DE, Forster HJ, Nijland TG (2002) Fluid-induced nucleation of (Y + REE)-phosphate minerals within apatite: nature and experiment. Part I. Chlorapatite. Am Mineral 87:245–261
Harlov DE, Wirth R, Forster HJ (2005) An experimental study of dissolution-reprecipitation in fluorapatite: fluid infiltration and the formation of monazite. Contrib Mineral Petrol 150: 268–286
Harlov DE, Marschall HR, Hanel M (2007a) Fluorapatite-monazite relationships in granulite-facies metapelites, Schwarzwald, southwest Germany. Mineral Mag 71:223–234
Harlov DE, Wirth R, Hetherington CJ (2007b) The relative stability of monazite and huttonite at 300–900 degrees C and 200–1000 MPa: metasomatism and the propagation of metastable mineral phases. Am Mineral 92:1652–1664
Harlov DE, Procházka V, Förster H et al (2008) Origin of monazite-xenotime-zircon-fluorapatite assemblages in the peraluminous Melechov granite massif, Czech Republic. Miner Petrol 94:9–26
Harlov DE, Wirth R, Hetherington CJ (2011) Fluid-mediated partial alteration in monazite: the role of coupled dissolution-reprecipitation in element redistribution and mass transfer. Contrib Mineral Petrol 162:329–348
Holland TJB, Powell R (1998) An internally consistent thermodynamic data set for phases of petrological interest. J Metamorph Geol 16:309–343
Huebner M, Kyser TK, Nisbet EG (1986) Stable-isotope geochemistry of high-grade metapelites from the central zone of the Limpopo Belt. Am Mineral 71:1343–1353
Jamtveit B, Yardley B (1997) Fluid flow and transport in rocks. Chapman and Hall, London
Javoy M (1977) Stable isotopes and geothermometry. J Geol Soc Lond 133:609–636
Keller LM, Abart R, Stünitz H et al (2004) Deformation, mass transfer and mineral reactions in an eclogite facies shear zone in a polymetamorphic metapelite (Monte Rosa nappe, western Alps). J Metamorph Geol 22:97–118
Kelsey DE, White RW, Holland TJB et al (2004) Calculated phase equilibria in K2O-FeO-MgO-Al2O3-SiO2-H2O for sapphirine-quartz-bearing mineral assemblages. J Metamorph Geol 22:559–578
Kohn MJ, Valley JW (1998) Oxygen isotope geochemistry of the amphiboles: isotope effects of cation substitutions in minerals. Geochim Cosmochim Acta 62:1947–1958
Korzhinskii DS (1970) Theory of metasomatic zoning. Oxford University Press, Oxford
Kyser TK (1987) Equilibrium fractionation factors for stable isotopes. In: Kyser TK (ed) Stable isotope geochemistry of low temperature fluids. Mineralogical Association of Canada, Toronto
Lamb W, Valley J, Brown P (1987) Post-metamorphic CO2-rich fluid inclusions in granulites. Contrib Mineral Petrol 96:485–495
Lamb W, Brown P, Valley J (1991) Fluid inclusions in Adirondack granulites – implications for the retrograde P-T path. Contrib Mineral Petrol 107:472–483
Le Bayon B, Pitra P, Ballevre M et al (2006) Reconstructing P-T paths during continental collision using multi-stage garnet (Gran Paradiso nappe, Western Alps). J Metamorph Geol 24:477–496

Mahan KH, Goncalves P, Williams ML et al (2006) Dating metamorphic reactions and fluid flow: application to exhumation of high-P granulites in a crustal-scale shear zone, western Canadian Shield. J Metamorph Geol 24:193–217

Mahan K, Goncalves P, Flowers R et al (2008) The role of heterogeneous strain in the development and preservation of a polymetamorphic record in high-P granulites, western Canadian shield. J Metamorph Geol 26:669–694

Mancktelow NS (1994) On volume change and mass-transport during the development of crenulation cleavage. J Struct Geol 16:1217–1231

Mark G, Foster DRW (2000) Magmatic-hydrothermal albite-actinolite-apatite-rich rocks from the Cloncurry district, NW Queensland, Australia. Lithos 51:223–245

Marquer D, Burkhard M (1992) Fluid circulation, progressive deformation and mass-transfer processes in the upper crust – the example of basement cover relationships in the external crystalline massifs, Switzerland. J Struct Geol 14:1047–1057

Marquer D, Gapais D, Capdevila R (1985) Chemical-changes and mylonitization of a granodiorite within low-grade metamorphism (Aar massif, central Alps). Bull Minéral 108:209–221

Massonne HJ, Schreyer W (1987) Hengite geobarometry based on the limiting assemblage with k-feldspar, phlogopite, and quartz. Contrib Mineral Petrol 96:212–224

McCaig AM (1984) Fluid-rock interaction in some shear zones from the pyrenees. J Metamorph Geol 2:129–141

McCrea JM (1950) On the isotopic chemistry of carbonates and a paleotemperature scale. J Chem Phys 18:849–857

McKibben MA, Riciputi LR (1998) Sulfur isotopes by ion microprobe. Rev Econ Geol 7:121–139

McWilliams CK, Wintsch RP, Kunk MJ (2007) Scales of equilibrium and disequilibrium during cleavage formation in chlorite and biotite-grade phyllites, SE Vermont. J Metamorph Geol 25:895–913

O'Neil J, Clayton R (1964) Oxygen isotope thermometry. In: Craig H, Miller S, Wasserburg G (eds) Isotopic and cosmic chemistry. North Holland, Amsterdam

Ohyama H, Tsunogae T, Santosh M (2008) CO2-rich fluid inclusions in staurolite and associated minerals in a high-pressure ultrahigh-temperature granulite from the Gondwana suture in southern India. Lithos 101:177–190

Oliot E, Goncalves P, Marquer D (2010) Role of plagioclase and reaction softening in a metagranite shear zone at mid-crustal conditions (Gotthard Massif, Swiss Central Alps). J Metamorph Geol 28:849–871

Oliver N, Cleverley J, Mark G et al (2004) Modeling the role of sodic alteration in the genesis of iron oxide-copper-gold deposits, Eastern Mount Isa block, Australia. Econ Geol 99:1145–1176

O'Neil JR, Taylor HP (1967) The oxygen isotope and cation exchange chemistry of feldspars. Am Mineral 52:1414–1437

Pawley A (1998) The reaction talc plus forsterite = enstatite + H2O: new experimental results and petrological implication. Am Mineral 83:51–57

Penniston-Dorland SC, Ferry JM (2008) Element mobility and scale of mass transport in the formation of quartz veins during regional metamorphism of the Waits river formation, east-central Vermont. Am Mineral 93:7–21

Philpotts AR, Ague JJ (2009) Principles of igneous and metamorphic petrology, 2nd edn. Cambridge University Press, Cambridge

Pollok K, Lloyd GE, Austrheim H, Putnis A (2008) Complex replacement patterns in garnets from Bergen Arcs eclogites: a combined EBSD and analytical TEM study. Chem Erde Geochem 68:177–191

Potdevin JL, Marquer D (1987) Quantitative methods for the estimation of mass transfers by fluids in deformed metamorphic rocks. Geodin Acta 1:193–206

Powell R, Holland TJB (2008) On thermobarometry. J Metamorph Geol 26:155–179

Powell R, Holland T, Worley B (1998) Calculating phase diagrams involving solid solutions via non-linear equations, with examples using THERMOCALC. J Metamorph Geol 16:577–588

Putnis A, Austrheim H (2010) Fluid-induced processes: metasomatism and metamorphism. Geofluids 10:254–269

Roedder E (1984) Fluid inclusions. Rev Mineral 12:3–10

Rolland Y, Cox S, Boullier A et al (2003) Rare earth and trace element mobility in mid-crustal shear zones: insights from the Mont Blanc Massif (Western Alps). Earth Planet Sci Lett 214:203–219

Rossi M, Rolland Y, Vidal O et al (2005) Geochemical variations and element transfer during shear zone development and related episyenites at middle crust depths: insights from the Mont-Blanc granite (French-Italian Alps). In: Bruhn D, Burlini L (eds) High strain zones: structure and physical properties, Geological Society of London, Special Publications. Geological Society, London

Rubenach M, Lewthwaite K (2002) Metasomatic albitites and related biotite-rich schists from a low-pressure polymetamorphic terrane, Snake Creek Anticline, Mount Isa Inlier, north-eastern Australia: microstructures and P-T-d paths. J Metamorph Geol 20:191–202

Sassier C, Boulvais P, Gapais D et al (2006) From granitoid to kyanite-bearing micaschist during fluid-assisted shearing (Ile d'Yeu, France). Int J Earth Sci 95:2–18

Seifert F (1974) Stability of sapphirine – study of aluminous part of system Mgo-Al2O3-SiO2-H2O. J Geol 82:173–204

Sharp ZD (1990) A laser-based microanalytical method for the in situ determination of oxygen isotope ratios of silicates and oxides. Geochim Cosmochim Acta 54:1353–1357

Shelton KL, Rye DM (1982) Sulfur isotopic compositions of ores from Mines Gaspe, Quebec: an example of sulfate-sulfide isotopic disequilibria in ore-forming fluids with applications to other porphyry-type deposits. Econ Geol 77:1688–1709

Shieh YN, Taylor HP (1969) Oxygen and carbon isotope studies of contact metamorphism of carbonate rocks. J Petrol 10:307–331

Spear FS (1988) The Gibbs method and Duhem theorem – the quantitative relationships among P, T, chemical-potential, phase-composition and reaction progress in igneous and metamorphic systems. Contrib Mineral Petrol 99:249–256

Spear FS (1993) Metamorphic phase equilibria and pressure-temperature-time paths. Mineralogical Society of America, Washington, DC

Spear FS, Selverstone J (1983) Quantitative p-t paths from zoned minerals – theory and tectonic applications. Contrib Mineral Petrol 83:348–357

Steffen KJ, Selverstone J (2006) Retrieval of P-T information from shear zones: thermobarometric consequences of changes in plagioclase deformation mechanisms. Contrib Mineral Petrol 151:600–614

Sterner SM, Bodnar RJ (1989) Synthetic fluid inclusions.7. Re-equilibration of fluid inclusions in quartz during laboratory-simulated metamorphic burial and uplift. J Metamorph Geol 7: 243–260

Štípská P, Powell R (2005) Constraining the P-T path of a MORB-type eclogite using pseudosections, garnet zoning and garnet-clinopyroxene thermometry: an example from the Bohemian Massif. J Metamorph Geol 23:725–743

Stüwe K (1997) Effective bulk composition changes due to cooling: a model predicting complexities in retrograde reaction textures. Contrib Mineral Petrol 129:43–52

Tajčmanová L, Connolly JAD, Cesare B (2009) A thermodynamic model for titanium and ferric iron solution in biotite. J Metamorph Geol 27:153–165

Taylor-Jones K, Powell R (2010) The stability of sapphirine plus quartz: calculated phase equilibria in FeO-MgO-Al2O3-SiO2-TiO2-O. J Metamorph Geol 28:615–633

Tenczer V, Hauzenberger CA, Fritz H et al (2011) The P-T-X((fluid)) evolution of meta-anorthosites in the eastern granulites, Tanzania. J Metamorph Geol 29:537–560

Thompson JB (1959) Local equilibrium in metasomatic processes. In: Abelson PH (ed) Researches in geochemistry. Wiley, New York

Touret JLR (1987) Fluid inclusions and pressure-temperature estimates in deep-seatzed rocks. In: Helgeson HC (ed) Chemical transport in metasomatic processes, NATO ASI Series. D. Reidel, Dordrecht

Touret JLR (2001) Fluids in metamorphic rocks. Lithos 55:1–25

Urey HC (1947) The thermodynamic properties of isotopic substances. J Chem Soc :562–581

Urey HC, Lowenstam HA, Epstein S et al (1951) Measurement of paleotemperatures and temperatures of the Upper Cretaceous of England, Denmark and the Southeastern United State. Geol Soc Am Bull 62:399–416

Valley JW (2001) Stable isotope thermometry at high temperatures. Rev Mineral Geochem 43:365–413

Valley JW, Graham CM (1991) Ion microprobe analysis of oxygen isotope ratios in granulite facies magnetites: diffusive exchange as a guide to cooling history. Contrib Mineral Petrol 109:38–52

Valley JW, O'Neil JR (1981) Exchange between calcite and graphite: a possible thermometer in Grenville marbles. Geochim Cosmochim Acta 45:411–419

Vidal O, Parra T, Vieillard P (2005) Thermodynamic properties of the Tschermak solid solution in Fe-chlorite: application to natural examples and possible role of oxidation. Am Mineral 90: 347–358

Vidal O, De Andrade V, Lewin E et al (2006) P-T-deformation-Fe3+/Fe2+ mapping at the thin section scale and comparison with XANES mapping: application to a garnet-bearing metapelite from the Sambagawa metamorphic belt (Japan). J Metamorph Geol 24:669–683

Wei CJ, Powell R (2006) Calculated phase relations in the system NCKFMASH (Na2O-CaO-K2O-FeO-MgO-Al2O3-SiO2-H2O) for high-pressure metapelites. J Petrol 47:385–408

Wei CJ, Powell R, Clarke GL (2004) Calculated phase equilibria for low- and medium-pressure metapelites in the KFMASH and KMnFMASH systems. J Metamorph Geol 22:495–508

White RW, Powell R, Holland TJB (2007) Progress relating to calculation of partial melting equilibria for metapelites. J Metamorph Geol 25:511–527

White RW, Powell R, Baldwin JA (2008) Calculated phase equilibria involving chemical potentials to investigate the textural evolution of metamorphic rocks. J Metamorph Geol 26:181–198

Whitney DL, Cooke ML, Du Frane SA (2000) Modeling of radial microcracks at corners of inclusions in garnet using fracture mechanics. J Geophys Res Solid Earth 105:2843–2853

Williams ML, Scheltema KE, Jercinovic MJ (2001) High-resolution compositional mapping of matrix phases: implications for mass transfer during crenulation cleavage development in the Moretown Formation, western Massachusetts. J Struct Geol 23:923–939

Wintsch RP, Knipe RJ (1983) Growth of a zoned plagioclase porphyroblast in a mylonite. Geology 11:360–363

Wintsch RP, Kvale CM, Kisch HJ (1991) Open-system, constant-volume development of slaty cleavage, and strain-induced replacement reactions in the Martinsburg Formation, Lehigh Gap, Pennsylvania. Geol Soc Am Bull 103:916–927

Wintsch RP, Christoffersen R, Kronenberg AK (1995) Fluid-rock reaction weakening of fault zones. J Geophys Res Solid Earth 100:13021–13032

Wintsch RP, Aleinikoff JN, Yi K (2005) Foliation development and reaction softening by dissolution and precipitation in the transformation of granodiorite to orthogneiss, Glastonbury complex, Connecticut, USA. Can Mineral 43:327–347

Yardley BWD, Schumacher JC (1991) Geothermometry and geobarometry – introduction. Mineral Mag 55:1–2

Yonkee WA, Parry WT, Bruhn RL (2003) Relations between progressive deformation and fluid-rock interaction during shear-zone growth in a basement-cored thrust sheet, Sevier orogenic belt, Utah. Am J Sci 303:1–59

Zheng YF (1999) Oxygen isotope fractionation in carbonate and sulfate minerals. Geochem J 33:109–126

Chapter 4
Structural Controls of Metasomatism on a Regional Scale

Mike Rubenach

Abstract Examples of structurally controlled regional metasomatism span most metamorphic temperatures, pressures, and tectonic settings. Permeability is crucial, and may be intrinsic or the result of deformation processes such as micro-fracturing (e.g. grain boundary sliding), fracturing, faulting, foliation and shear zone development, and hydro-fracturing. Chromatographic theory has been developed to explain metasomatic zonation, and applies not only where mineral reaction and isotopic fronts formed normal to the fluid flow in a porous medium, but also where flow was parallel to fractures or lithological contacts. Metasomatic fronts may be sharp or broadened by diffusion and dispersion effects during fluid advection. In the upper crust, fluid advection involved in regional metasomatism, such as silicification, albitization, potassic alteration and dolomitization, is controlled mainly by intrinsic permeability, faults, fractures and microfractures in sedimentary basins, volcanic sequences and some granites. For skarn formation, fluid advection is controlled by interface-coupled dissolution-precipitation ("reaction-controlled permeability") in addition to fractures and microfractures. Cross-layer diffusion in addition to layer-parallel advection is probably important in the formation of skarns along lithological contacts. Although subject to some debate, many workers have provided mineralogical and isotopic evidence for the existence of high time-integrated fluid fluxes and fluid flow directions in many thermal aureoles and regional metamorphic belts. Studies of quartz veins and vein selvages in metamorphic rocks have provided examples both of local derivation of veins and derivation of silica and metasomatic changes in the selvages during advection of external fluids. Also subject to debate is whether metamorphic fluids in the middle crust are solely derived from devolatilization reactions at depth or whether such processes as dilatancy pumping or syn-metamorphic intrusion can lead to lateral or downward fluid advection. Regional metasomatism occurs in many Proterozoic metamorphic

M. Rubenach (✉)
School of Earth Sciences, James Cook University, Townsville 4811, Queensland, Australia
e-mail: Michael.Rubenach@jcu.edu.au

D.E. Harlov and H. Austrheim, *Metasomatism and the Chemical Transformation of Rock*, Lecture Notes in Earth System Sciences,
DOI 10.1007/978-3-642-28394-9_4,

belts, but the Mount Isa Inlier is probably the best natural laboratory regarding structural controls. It exhibits enormous strain heterogeneity at all scales that led to fluid channeling, diverse reactive rocks, episodic metamorphic and intrusive events spanning at least 250 Ma, and abundant sources of reactive saline and hypersaline fluids. Examples of widespread metasomatism in the Mount Isa Inlier include Na-Ca alteration associated with extensive breccia development in calcsilicate rocks, albitization of schists and metapsammitic rocks, and the formation in high-strain zones of tremolite pods, quartz-chlorite rocks, and unusual cordierite-rich rocks.

4.1 Introduction

This chapter is mainly concerned with the structural controls on regional metasomatism, i.e. metasomatism not restricted to a single occurrence but commonly repeated in numerous localities over scales of tens of meters to tens of kilometers. Most of the examples discussed in this chapter are from settings in the upper crust and from greenschist- to amphibolite-facies rocks in the middle crust. Metasomatism during diagenesis in sediments, low-grade metamorphism of volcanic rocks, and metasomatism in thermal aureoles are briefly considered. Metasomatism in blueschist-, eclogite-, and granulite-facies, along with hydrothermal processes in the oceanic crust, and metasomatism associated with ore deposits are discussed elsewhere (see Chaps. 7–11). The development of metasomatic zones, both mineralogical and isotopic, in various fluid advection- and diffusion-related scenarios are also considered. Metasomatism is conventionally considered to involve bulk changes in non-volatile elements, but this chapter also includes changes in volatile contents and changes in isotope values where relevant to metasomatic processes and structural controls of fluid flow.

Historical summaries of aspects of fluid flow and metasomatism in sedimentary, volcanic and metamorphic rocks include those of Korzhinskii (1970), Fyfe et al. (1978), Cathles (1990), Parnell (1994), Rumble (1994), Ferry (1994a), Oliver (1996), Jamtveit and Yardley (1997), and Vernon and Clarke (2008, their Chap. 6), while important recent contributions include Yardley (2009), Putnis and Austrheim (2010), and Ague (2011). Reviews of structural controls on fluid flow and metasomatism include those of Oliver (1996), Ferry and Gerdes (1998) and Ague (2003, 2004).

4.2 Key Concepts Regarding Regional Metasomatism

4.2.1 Metasomatic Zones

For metasomatism to be achieved mass transport of components needs to take place. This may occur via advection ("infiltration" in the older literature) whereby

components are transported during fluid flow, or diffusion through a stagnant fluid, or a combination of both processes (Korzhinskii 1970). Transport of components occurs via advection or diffusion down their chemical potential gradients (Vidale 1969). Advection may result in a series of zones (mineralogical and isotopic) on a scale of centimeters to hundreds of meters in width. Sharp fronts are predicted from advection theory, but diffusion, dispersion, and kinetic effects commonly lead to a broadening of advective fronts (Bear 1972; Fletcher and Hoffman 1974; Bickle 1992; Ague 2003). Dispersion of transported components during fluid flow results from different fluid velocities in the main fluid channels compared with flow in adjacent rocks, together with the complex pathways of actual flow. Advective transport ("chromatographic model") predicts mineral reaction and isotopic fronts normal to the direction of fluid flow in a porous medium (Fletcher and Hoffman 1974). The fronts propagate through the rock column at different velocities as a function of concentrations in the fluid, exchange kinetics, and component distribution coefficients between the fluid and the rock column (Korzhinskii 1970; Fletcher and Hoffman 1974). In order to explain the commonly observed small number of phases in many metasomatic zones, Korzhinskii proposed a modification of the Gibbs Phase Rule from F = C-P + 2 to F = C-P + 2-m, where F is the variance, C the number of independent chemical components, P the number of coexisting phases, and m the number of components with externally controlled chemical potentials ("perfectly mobile components") (Korzhinskii 1950, 1959; Vidale and Hewitt 1973). Under equilibrium conditions metasomatism typically results in zones with high variance, but lower variance (i.e. more phases in individual samples) could occur if there is significant deviation from equilibrium as a result of kinetic affects. For example refractory minerals, such as garnet, may persist after they should have reacted out. In fact rocks typically travel along a P-T-t (pressure-temperature-time) path that may include several heating and cooling stages, and although the peak temperature assemblage is likely to be the best preserved, metastable persistence of phases along the prograde path and partial overprint on the cooling path are common occurrences.

There are circumstances where lithologies, such as marble, are impervious but a series of zones nevertheless form. In such cases fluid flow was essentially parallel rather than normal to contacts (Gerdes and Valley 1994; Cartwright 1997; Yardley and Lloyd 1995; Cartwright and Buick 1995). Fluid flow and the formation of metasomatic zones parallel to lithological contacts and fractures may also occur for silicate-bearing metacarbonates during regional metamorphism (e.g. Ague 2003) and during skarn formation (e.g. Gerdes and Valley 1994; Meinert et al. 2005). Multiple metasomatic pulses with fluids of variable temperatures and/or compositions, a common situation during the formation of skarns (Chap. 7, Meinert et al. 2005) can also provide practical problems in applying phase rule principles unless the sequence of metasomatic assemblages is well established. Similarly, early-formed metasomatic rocks may be overprinted by later regional metamorphic assemblages (see Sect. 4.4.2.1).

4.2.2 Porosity, Permeability and Mass Transport

Given typical temperatures and geological time frames, solid-state diffusion (diffusion through crystal lattices) is insufficient to account for regional metasomatism (e.g. Fyfe and Kerrich 1985; Putnis and Austrheim 2010). Thus reasonably high values of porosity and permeability are essential requirements for fluid mass transport by either diffusion through the fluid or fluid advection. Porosity is the percentage of pore spaces, whereas permeability measures the ease of fluid passage through the rock, so that the size, shape and connectivity of pores is critical, as is connectivity of micro-fractures and fractures (e.g. Cox et al. 1991). Permeability may be transient and while little or no evidence of former permeability (e.g. micro-fractures) may be preserved in some rocks, larger structures such as faults, fractures, veins and their selvages provide easily recognized evidence of former permeable zones. Permeability may be intrinsic (e.g. pore spaces in many pyroclastic rocks, carbonates and sandstones). Laboratory measurements indicate 13 orders of magnitude of intrinsic permeability, with sandstone, limestone, and some basalts at the higher end of the scale at 10^{-9}–10^{-16} m^2, whereas unfractured igneous and metamorphic rocks, shale and fault gouge are at the lower end at 10^{-16}–10^{-22} m^2 (Brace 1980). However, geochemical studies of fluid-rock interaction, although subject to debate, infer quite high fluid-rock ratios during metamorphism in some areas (e.g. Ferry 1986, 1992, 1994b; Ferry and Gottschalk 2009). High apparent metamorphic permeability have been estimated from diffusion, dispersion, and advection equations (Norton 1988; Bickle and McKenzie 1987; Bickle and Baker 1990; Baumgartner and Ferry 1991; Ferry and Dipple 1991). During active ductile deformation, porosity can be created by micro-dilatency (grain boundary sliding) and by hydro-fracturing (Etheridge et al. 1983; Lyubetskaya and Ague 2010). Hydro-fracturing occurs where the fluid pressure exceeds the minimum confining pressure (σ_3) plus the local tensile strength (Beach 1977; Cox and Etheridge 1989; Ferry 1994a). Another important process is reaction-enhanced permeability, whereby volume loss occurs during devolatilization (especially CO_2 release from impure marble) and/or via the formation of higher density solid phases during prograde metamorphism, although to what extent the newly-formed pore spaces thus formed collapse at higher confining pressures and/or during deformation is uncertain. Putnis and Austrheim (2010) also point out that mineral replacement mechanisms and porosity development may be quite complex, and the overall process could be more accurately termed “interface-coupled dissolution-precipitation” (see Chap. 5). Although porosity produced by reactions is important in shallow aureoles where the pore spaces produced are less likely to collapse due to lower confining pressures or directed stresses, it is clearly an important factor in the development of high fluid fluxes parallel to lithological contacts (e.g. Cartwright and Buick 1995). In many impure marbles and calc-silicate rocks the process can be self-perpetuating since the permeability-forming reactions proceeding at the lower XCO_2 values produce metamorphic aquifers, channeling water-rich fluids derived from magmas or devolatilization of other lithologies in the sequence. In

metamorphic terranes fluid flow may also be channeled through fractures, micro-fractures, shear zones, and mylonite zones that are either pre-existing (and open) or which formed synchronous with metasomatism. While many shear zones and other high-strain zones show little evidence of metasomatism, others show major chemical and/or isotopic changes indicative of substantial fluid flow (Beach 1976, 1980; Dipple and Ferry 1990; McCaig 1997; Streit and Cox 1998).

Although diffusion of ions through a stagnant fluid residing in pore spaces or micro-fractures can result in localized examples (e.g. selvages adjacent to some quartz veins, Yardley 2009), regional metasomatism is mainly the result of advection of an external fluid through pore spaces, fractures, micro-fractures and shear zones. Such structures are commonly caused by tectonic processes but in some cases may be the result of brecciation or hydro-fracturing due to high fluid pressures produced by devolatilization during prograde regional metamorphism, or magmatic fluids originating from cooling intrusions (e.g. Hanson 1992; Lyubetskaya and Ague 2010).

4.2.3 Reaction Progress and Time Integrated Fluid Fluxes

Reaction progress is calculated from the modal proportions of minerals involved in reactions that have not gone to completion, and allows computation of the amount of fluid that has interacted with the rock (produced, consumed or both) (Brimhall 1979; Ferry 1983). Fluid-rock ratios were determined in earlier studies from mineral reaction progress data or using stable isotope data, but this concept was replaced by more realistic time-integrated fluid fluxes that measure the fluid flux over the entire period of the reaction (e.g. Ferry 1996). Modeling of the geochemical data allowed computation of the direction of fluid flow (e.g. Ferry and Dipple 1991; Baumgartner and Ferry 1991; Ferry and Dipple 1992; Nabelek 1991; Cartwright and Weaver 1993; Dipple and Ferry 1992; Ferry et al. 2002). For example fluid flow may be determined as up- or down-temperature, and in a vertical or horizontal direction, but caution is needed as the results may be ambiguous (e.g. Nabelek and Labotka 1993; Cartwright 1994; Cartwright and Oliver 1994).

4.2.4 Single Pass Fluid Flow, Convection and Dilatancy Pumping

Metasomatism may result from the infiltration of fluids derived during devolatization reactions deeper in the crustal section during regional metamorphism (Wood and Walther 1986). In some areas fluids could also originate from a subducted slab (e.g. Oliver 1996). Advective circulation, e.g. of meteoric fluids, can occur in the upper crust where the fluid pressure is under hydrostatic conditions. High thermal gradients, resulting, for example, from igneous intrusions, would provide a driving mechanism for such fluid advection. Hydraulic heads resulting

from topography has also been proposed to drive fluids through zones of relatively high permeability in the upper crust (e.g. Garven 1995; Upton and Craw 2009).

Convective circulation has also been proposed for the middle crust (Etheridge et al. 1983, 1984), however many authors argue that this is very unlikely as the fluid density difference essential for convection would not be achieved under lithostatic conditions and therefore single-pass infiltration of fluids was far more likely (Yardley 2009; Wood and Walther 1986). However, as is discussed in more depth later in this chapter, there are examples of extensively developed structurally-controlled regional metasomatism that required high fluid-rock ratios unlikely to have been achieved during single pass advection. For example, a dilatancy pumping mechanism (Sibson 1989) through shear zones with dilatant zones is proposed for the Mary Kathleen region in northwestern Queensland (Oliver et al. 1990). Modeling by Lyubetskaya and Ague (2010) indicates that emplacement of hot magmas into relatively low-temperature middle crustal rocks can lead to strong dehydration and hydro-fracturing extending for up to tens of kilometers from the magma, and which can result in up-temperature fluid flow. They propose that this model applies to Buchan and Barrovian metamorphism in the Scottish Highlands. Another model is the development of porosity waves, where compaction-driven fluid flow results in fractures and waves of fluid-filled porosity (Chap. 14, Connolly 2010). Connolly proposes that the tube-like structures in oxygen isotope and reaction progress data for metasomatized metabasic sills from Scotland (Skelton et al. 2000) may provide evidence for such porosity waves.

4.2.5 Contacts, Veins and Metasomatic Zones: Summary

Figure 4.1 is a summary of many of the scenarios regarding metasomatism, fluid-rock patterns, and mineralogical and isotopic fronts in relationship to contacts, veins, and selvages. It is based on the above discussion and on Oliver and Bons (2001), who derived a vein type classification based on the vein-wall rock geometry and fluid flow patterns. In Fig. 4.1a, magmatic fluids infiltrate a porous impure marble from a granite, forming skarns with several zones and an oxygen isotope front in the marble located a considerable distance downstream from the last mineralogic front (oxygen is the most abundant element in fluids). A good example is the Alta Stock Aureole, Utah (Cook and Bowman 2000). However in many skarns, marble in the aureole is relatively impermeable and fluid flow is parallel to the contact, as depicted in Fig. 4.1b. Reaction at the contact, probably initiated by bi-metasomatic diffusion, created porosity via volume reduction thereby allowing infiltration of fluids parallel to the contact. The reactions proceeded by lateral replacement of marble such that the oxygen and carbon isotope fronts are coincident with the skarn-marble contact. Examples include the Valentine wollastonite skarn in the Adirondacks (Gerdes and Valley 1994) and the Redcap Creek high temperature skarns from Chillagoe, northeastern Australia (Figs. 4.2–4.3, Sect. 4.3.3, Cartwright 1997). Note that in this example the fluids do not necessarily

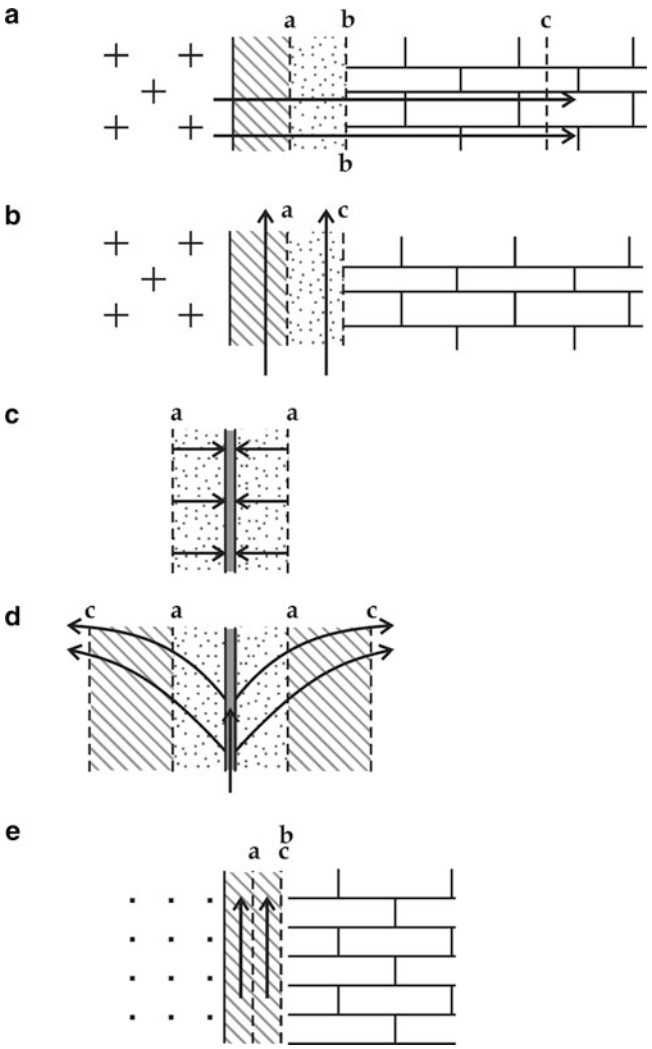

Fig. 4.1 This shows a series of possible relationships between contacts, mineralogical fronts (**a**, **b**), an oxygen isotope front (**c**) and fluid flow and/or diffusion (*arrows*). Lithologies are granite (*crosses*), marble (*brick symbol*), quartz veins (*dark stipple*), metasomatic zones (*light stipple* and *hatching*), and sandstone (*coarse dots*). The scenarios a–e are described in the text

initiate from the intrusive at the contact, but could come from a subsequent igneous body. Other likely examples are the Ubehebe Peak aureole in California (Roselle et al. 1999) and the Beinn an Dubhaich aureole, Skye, Scotland (Ferry and Rumble 1997).

Figures 4.1c and d depict quartz veins. Figure 4.1c is essentially a closed system in which silica has diffused from the selvage to form the vein in the fracture through a stagnant pore fluid, probably driven by a pressure drop in the fracture. Little to no

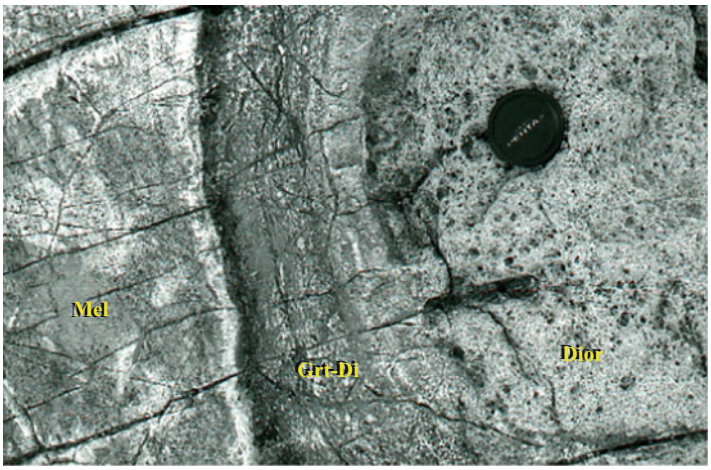

Fig. 4.2 The photo shows diorite (Dior) replaced on its margins by garnet-diopside endoskarn (Grt-Di), in contact with a melilite exoskarn (Mel) consisting mainly of melilite and calcite. The mineralogical fronts are very sharp. The photo is from a high temperature skarn at Redcap Creek, north of Chillagoe, Queensland, Australia

silica or other components were added to the vein or selvage from an external fluid. Examples include veins in Connemara studied by Yardley and Bottrell (1992). By contrast, the system in Fig. 4.1d was open and much of the quartz in the vein, together with components added to the selvage, were derived from infiltration of an external fluid. Examples include some Connemara veins (Yardley 1986, 2009 his Fig. 4.10), and the kyanite-bearing quartz veins from the Wepawaug Schist, Connecticut (Ague 2011).

Figure 4.1e depicts fluid flow along a contact between a low permeability metasedimentary or igneous rock on the left and a reactive marble on the right. The situation is similar to 4.1b except that the fluid is of metamorphic origin, for example devolatilization fluids from deeper in the sequence.

Not represented in Fig. 4.1 are combinations between the given examples or other possible scenarios, such as pervasive flow though porous sedimentary or pyroclastic sequences, pervasive flow through micro-fracture-rich shear zones, or fluid flow focused through hydro-fractures in metamorphic rocks associated with igneous intrusions (e.g. Lyubetskaya and Ague 2010).

4.3 Controls on Metasomatism in the Upper Crust

In this section the lower boundary of the upper crust is arbitrarily defined as being around 0.2 GPa, typically above the brittle-ductile transition. At such shallow depths some rocks have inherent permeability sufficient to allow fluid infiltration and metasomatism. In the upper crust fractures and micro-fractures are fairly common and can be locally abundant. Ductile shear zones are generally rare, but

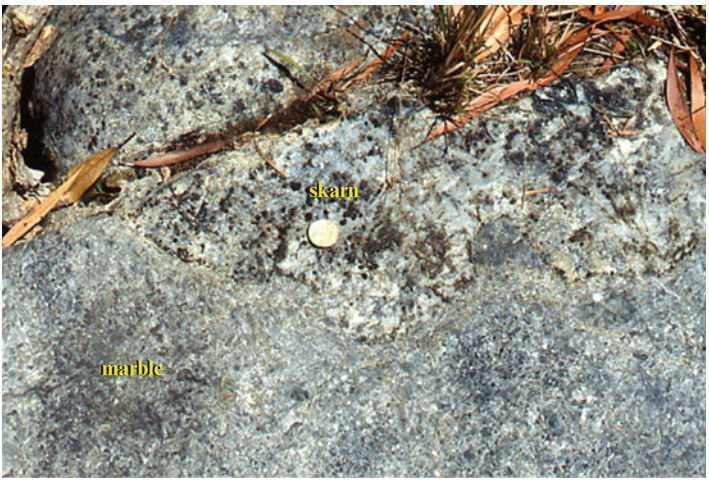

Fig. 4.3 Sharp contact between a stage 2 wollastonite-garnet-vesuvianite exoskarn and a coarse pure marble. The skarn has replaced stage 1 massive tilleyite, relicts of which are present up to the marble contact. Oxygen and carbon isotope data (Cartwright 1997) show very steep gradients from "magmatic" to "sedimentary " values at such exoskarn/marble contacts, indicating that fluid flow was parallel rather than normal to contacts, and that diffusion/dispersion into the marble was very limited

may form where temperatures are elevated, for example in some thermal aureoles. Scenarios considered are metasomatism accompanying diagenesis in sedimentary basins, metasomatism associated with low-grade metamorphism of volcanic rocks, structural controls and zonation in skarn formation, and albitization of granites and volcanic rocks.

4.3.1 Metasomatism During Diagenesis of Sediments

Metasomatism during diagenesis includes silicification, carbonate dissolution, potassic alteration, albitization, calcite formation, and dolomitization (e.g. Pettijohn and Baston 1959; Boles 1982; Fedo et al. 1997; Davidson 1999; Scholle and Ulmer-Scholle 2003; Beinlich et al. 2010). Sources of fluids include pore fluids (during compaction), meteoric fluids, seawater, evaporitic brines, and migrating basinal fluids (e.g. Bjorlykke 1994, 1997). The fluid flow is controlled by internal porosity, fractures, and faults. Permeability may be enhanced by dissolution in aquifers or otherwise decrease during precipitation in pore spaces. On a continental scale, the various hydrogeologic and tectonic scenarios for groundwater flow are reviewed in Garven (1995). These include gravity- or topography-driven flow, thermally driven convection in sag or rift basins, overpressuring during compaction, tectonically driven flow in fold/thrust belts, and seismic pumping along faults (Garven 1995). Numerical modeling studies of large scale fluid flow and implications regarding

diagenesis, metasomatism and ore deposition in sedimentary basins include those of Garven (1985, 1995), Person and Garven (1994), and McClellan and Oliver (2008).

In a detailed study of the Paleoproterozoic Huronian Supergroup in Canada, Fedo et al. (1997) described regional-scale potassium metasomatism of shales through illitization of kaolin and albitization of siltstones and sandstones. They suggested that the regional metasomatism resulted from deep basinal brines that were heated by plutonism driven during collision tectonics or gravity induced groundwater circulation.

In a study of metasomatism in volcaniclastic beds within the shale-dominated Proterozoic McArthur River Group in northern Australia, Davidson (1999) recognized a westward zonation from microcline to albite away from the syn-sedimentary Emu fault zone that forms a half-graben margin to the basin. He suggested that the regional alteration was proportional to the hydraulic head generated by transpression along the fault. He argued that over a long period saline meteoric fluids were focused from the horst into the adjacent basin, preferentially reacting with the volcaniclastic rocks. By contrast, metasomatism associated with the deposition of the stratiform Zn-Pb HYC deposit near the base of the sedimentary sequence was related to "episodic fault release of (separate) high-temperature deep-basin brines" (Davidson 1999).

Polito et al. (2006) undertook a study of sandstone diagenesis in the Proterozoic Mount Isa basin that hosts the giant Zn-Pb and Cu deposits by incorporating fluid inclusion and isotopic studies along with detailed sedimentary studies. They found that deposition of diagenetic cement converted marine-dominated clastic units into aquitards at a depth of less than 5 km, whereas in the lower mainly fluvial units, at 5–10 km of burial, dissolution of silica and formation of diagenetic illite and chlorite resulted in diagenetic aquifers. They suggest that the diagenetic aquifers were the source of metals, and that late diagenetic quartz veins reflect the same fluids that migrated along faults from the diagenetic aquifers to form the ore deposits.

4.3.2 Metasomatism Associated with Low-Grade Metamorphism

Studies of metasomatism of low-grade metamorphic rocks (mainly zeolite, prehnite-pumpellyite faces, overlapping with lower greenschist-facies) have primarily concerned meta-igneous rocks. Metasomatism of basaltic rocks comprising oceanic crust, resulting from seawater circulation through faults, fractures and intrinsic permeability (e.g. pillow lavas and volcanic breccias) at or near spreading centers, is discussed in Chap. 8. However, this section is mainly concerned with the Taupo Volcanic Zone from the North Island of New Zealand, probably the most extensively studied example of a continental volcanic arc as a result of it being active and the extensive drilling of the geothermal fields. Although metasomatism in the zone has received only a little attention (e.g. Steiner 1977; Lonker et al. 1990), many aspects of the structurally controlled fluid flow in the Taupo Volcanic Zone are probably relevant to continental arc systems elsewhere. For example, Permo-Carboniferous calcalkaline volcanic rocks throughout north Queensland,

Australia show ubiquitous low-grade metamorphism and variable metasomatism, with assemblages including chlorite, epidote, calcite, ankerite, sericite, and albite. However there has been no detailed studies of the structural controls on the regional metasomatism.

More than 20 active geothermal fields occur over a strike length of 100 km of the Taupo volcanic rift system (Bibby et al. 1995; Rowland and Sibson 2004). The rift has been infilled with Quaternary rhyolitic pyroclastic rocks (air-fall pyroclastics and ignimbrites), flows of rhyolitic, dacitic, andesitic, and basaltic compositions, and clastic and volcaniclastic sedimentary rocks. The basement is comprised of Mesozoic metasedimentary rocks, and intrusive rocks include dykes and sills. Convective circulation is largely controlled by a combination of intrinsic permeability (e.g. in air-fall pyroclastics) and the densely distributed faults and fractures that comprise the rift architecture. The rift faults are orientated NE-SW, but the rift basins have been segmented by NW-SE accommodation zones, faults, and fractures, which are also very important (Rowland and Sibson 2004). The accommodation zones may be controlled by basement faults (Rowland and Sibson 2004). Convective circulation occurs to a depth of 7–8 km, extending into the basement rocks where suitably-oriented fractures and faults have been reactivated (Rowland and Sibson 2004). Dykes, which are aquitards because of their low permeabilities, are also a control on the fluid flow patterns, while caldera fractures and faults provide additional permeable zones. The fluids are mainly meteoric, with some magmatic contribution, and as a generalization the NE-SW rift structures act as the drawdown regions with enhanced axial flow whereas much of the upflow is in the accommodation zones (Rowland and Sibson 2004). The authors note that the precipitation of minerals in faults and fractures requires continuous reactivation of the structures.

Studies of metasomatism of silicic volcanics in continental detachment terranes include those of Chapin and Lindley (1986) and Ennis et al. (2000). Widespread potassic alteration of silicic ignimbrites occur near Socorro, New Mexico, and are interpreted in terms of downward percolation of alkaline brines during basin and range extension.

4.3.3 Structural Controls of Metasomatism in Thermal Aureoles: Skarns

Skarns are by far the most abundant metasomatic lithologies produced during thermal metamorphism. Their genesis from a mineralization perspective is dealt with by Einaudi et al. (1981), Lentz (1998), Meinert et al. (2005) and in Chap. 7, so this section briefly reviews structural controls and some physico-chemical processes involved in their formation. Skarns consist predominantly of calcsilicate minerals, such as grandite garnet, pyroxene, and wollastonite, that may replace not only marble and calc-silicate hornfelses, but also siliciclastic sedimentary rocks, volcanic and intrusive rocks. Most occur in the thermal aureoles. Skarns that have replaced plutonic rocks are called endoskarns and skarns in the surrounding aureole

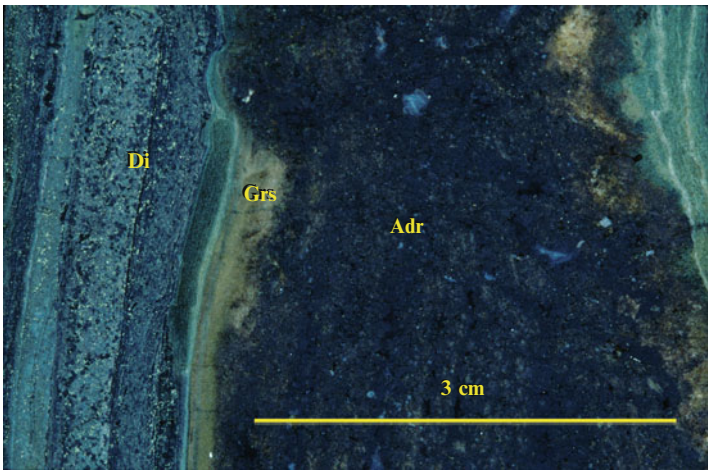

Fig. 4.4 Skarn sample, King Island scheelite deposit, Tasmania, Australia (see Kwak 1978). Layered reaction skarns (diopside Di and grossularite-rich garnet Grt) formed at the contacts between hornfelsed siltstone and marble layers. A central marble layer, and parts of the reaction skarns, have been replaced by a younger scheelite-bearing andradite garnet (Adr) during advection of magmatic fluids

are referred to as exoskarns (Figs. 4.2–4.4). Skarns typically exhibit a temporal evolution with early-formed higher temperature phases overprinting isochemical thermal metamorphic marble and hornfels, in turn variably replaced by later lower temperature assemblages. Stable isotope studies indicate that the earlier fluids are generally magmatic, and that meteoric and/or basinal fluids may also be involved in the middle and late stages of skarn formation (Chap. 7, Meinert et al. 2005). Along with the temporal evolution skarns commonly show a spatial zonation. For mineralized skarns, Meinert et al. (2005) describe a number of scenarios of marble replacement outwards from a pluton contact, including a zone showing an increase in pyroxene relative to garnet followed by a wollastonite-rich zone. Where magmatic fluid flow was normal to the pluton-marble contact the $\partial^{18}O$ front occurs outboard of the mineralogical front that defines the skarn-marble contact.

In addition to the more massive "infiltration" skarns formed by larger-scale advection through carbonates, smaller-scale "reaction skarns" that occur at contacts between carbonate and silicate lithologies (e.g. sandstones, shales, and basalts) are a fairly common occurrence (Meinert et al. 2005). Reaction skarns generally precede and may be partly replaced by the more common garnet-pyroxene advection-related skarns that commonly host mineralization. A typical example is from the King Island scheelite-bearing skarn (Kwak 1978) is shown in Fig. 4.4. It consists of layers of pyroxene that have replaced hornfelsed sedimentary rock, followed by brown garnet, with or without vesuvianite and wollastonite layers that have replaced marble. Such layering is commonly explained by bi-metasomatic diffusion driven by chemical potential gradients. Phase relationships in assemblages that include minerals such as grossularite-rich garnet, vesuvianite,

and wollastonite indicate formation at very low X_{CO2} conditions. This implies, that in addition to cross-layer diffusion, advection of water-rich fluids removed CO_2 produced in the reaction fluids parallel to the layering. It is quite likely that permeability created by reactions during the initial bi-metasomatic diffusion allowed subsequent layer-parallel fluid flow. Although examples of layers with high variance assemblages and sharp contacts do occur, gradational and irregular contacts and low variance assemblages are also common, probably the result of dispersion in addition to diffusion.

For fluid flow related to skarn formation the two major structural controls are fractures and reaction enhanced permeability (e.g. Meinert et al. 2005). Brittle structures include faults, joints and micro-fractures. Fractures within associated plutonic rocks include dilational cooling joints along with tectonic joints imposed during cooling. Such fractures in igneous rock allow for circulation of Ca-bearing fluids that have already interacted with carbonates, forming veins containing minerals such as garnet, wollastonite, pyroxene and calcite. Such veins are quite common in the granodiorite bodies related to the abundant skarns in the Chillagoe area of north Queensland, Australia (see appendix in Meinert et al. 2005). Also common in some locations near Chillagoe are decimeter-wide zones of replacement of biotite and hornblende by diopside and titanite along networks of microfractures in granodiorite. Besides tectonic process, other mechanisms producing fractures include hydro-fracturing and porosity waves (Connolly 2010, Chap. 14), both induced by high fluid pressures. Examples of fluid flow and skarn formation controlled by networks of fractures and microfractures in marble include the Stephen Cross Quarry, Quebec, Canada (Cartwright and Weaver 1993), and the formation of unusual very finely-layered laminar skarns at Moina in Tasmania and the Pinnacles area, Mount Garnet, Queensland, Australia (Kwak and Askins 1981a,b).

Although fluid flow through marble can be controlled by fractures and microfractures or by reaction enhanced permeability, in the case of impure marbles, many pure carbonate marbles are impervious. This can be explained by wetting angles and lack of connectivity along grain boundaries (Holness and Graham 1991). Nevertheless, pure calcite marbles in some examples have allowed for the transient passage of fluid along grain boundaries and twin lamellae, as shown by Graham et al. (1998) from a cathode luminescence/ion microprobe study. Similar studies should be undertaken in other areas of marbles adjacent to skarn contacts (in conjunction with whole rock isotope analyses) to ascertain whether leakage of some magmatic fluids has occurred along calcite grain boundaries. The very steep $\partial^{18}O$ gradients at wollastonite-marble contacts from the Valentine wollastonite deposit in New York State indicate that the marbles were relatively impermeable and fluid flow was parallel rather than normal to contacts (Gerdes and Valley 1994). A similar scenario occurs at the Redcap Creek high temperature skarn near Chillagoe, north Queensland (Figs. 4.2–4.3), for which some isotope data is presented in Cartwright (1997). These data show very steep isotope gradients within a few centimeters of skarn-marble contacts. It is suggested that reaction-enhanced permeability, produced by diffusion across diorite- and gabbro-marble contacts, allowed for contact-parallel advection of magmatic fluids, which formed inner

melilite and distal tilleyite exoskarns that extend tens of meters from the igneous contacts. Permeability in the higher temperature exoskarns allowed advection by younger cooler fluids resulting in wollastonite and vesuvianite skarns, but there is no evidence in the isotope data that these later fluids penetrated the adjacent marbles.

A number of detailed isotope studies, commonly coupled with phase relationships and reaction progress investigations, have examined the fluid flow directions in carbonate-bearing aureoles, some of which contain skarns. The flow direction has been the subject of debate (e.g. Nabelek et al. 1984; Labotka et al. 1988; Jamtveit et al. 1992a,b; Roselle et al. 1999; Cook and Bowman 2000). Ferry et al. (2002) conducted a study of the Monzoni and Predazzo aureoles, northern Italy, and reviewed studies of 13 other aureoles. They conclude that in the case of the Italian and 10 other aureoles, the fluid flow was predominantly vertical moving upwards with or without a horizontal component away from the pluton. Of the remaining three, one is uncertain and fluid flow in the two others was horizontal away from the pluton. Besides flow along faults, fractures, and dyke contacts, the fluid flow was mainly controlled by bedding. In the cases of horizontal fluid flow the bedding is horizontal. Calculated time-integrated fluid fluxes are in the range of 10^2–10^4 mol fluid/cm^2, in agreement with the hydrodynamic modeling by Hanson (1992) and Cook et al. (1997). A very large skarn system in the aureole of the Proterozoic Burstall Granite at Mary Kathleen, western Queensland, Australia (1,740–1,730 Ma), extends for at least 3 km from the granite contact (Cartwright and Oliver 1994). Magmatic fluids from the granite produced massive andradite-rich skarns and banded andradite clinopyroxene skarns, with sharp discontinuities in the major element chemistry and ∂^{18}O values at the skarn-marble contacts. Fluid flow in the marbles was up-temperature, if entirely related to the aureole event, but may have been up- or down temperature if it continued into the regional rocks during peak metamorphism at ~1,580 Ma. The banded skarns were largely bedding controlled. Interestingly the Mary Kathleen U-REE deposit did not form during the formation of the aureole-related skarns but consists of younger dilational regional metamorphic skarn veins that developed during movement on a ductile shear zone at or after the regional metamorphic peak (Oliver et al. 1999).

4.3.4 Regional Albitization in the Upper Crust

Albitization and Na-Ca alteration in upper crustal sedimentary, volcanic and granitic rocks has been recorded from many continental locations (e.g. Battles and Barton 1995; Lee and Lee 1998; Holness 2003; Engvik et al. 2008). In the case of sedimentary and some volcanic situations the rocks have intrinsic permeability as a result of sufficiently high porosity and connectivity. Otherwise, in intrusive and many volcanic rocks, the fluid flow is controlled by microfractures, fractures and faults. Albitization is also known in many oceanic crust locations, where seawater has circulated through volcanic sequences (Mottl 1983, Chap. 8). In some areas there is a link between Na and Na-Ca metasomatism and the formation

of IOCG deposits (iron oxide-Cu-Au ± U, REE; Hitzman et al. 1992; Barton and Johnson 1996).

Sodic and sodic-calcic alteration is extensively developed in Permian to Jurassic arc-related igneous rocks (volcanic and plutonic) in the western USA (Battles and Barton 1995). Potassic, hydrolytic, argillic, sericitic, and chloritic alteration is also present in places. The alteration is mainly fracture controlled, and in part is also related to veins and breccias (Battles and Barton 1995). The alteration haloes around veins commonly coalesce producing large areas of pervasively altered rocks (Battles and Barton 1995). Magmatism overlapped with the alteration, and although the fluids were moderately to highly saline marine, most likely from meteoric waters, there is also probably a magmatic component in some areas (Battles and Barton 1995).

Another scenario for albitization on a local or regional scale concerns Na(Ca, Mg) alteration of mainly pelitic rocks within 1–2 m of dolerite contacts. Such metasomatism ("adinoles"), which also involves removal of K and Si, is described from a shallow level dolerite dyke swarm in the Tallacht area near Dublin, Ireland by Angus and Kanaris-Sotiriou (1995), who also reference other areas in Europe. The alteration occurred during the cooling of the dykes. They propose that a larger mafic intrusion at depth initiated a circulating hydrothermal system, with the dykes acting as impermeable bodies that focused fluids along the contacts. No syn-intrusion ductile deformation was identified, and explanation for the higher permeability of the contact pelites (relative to unaltered contact psammites) was not provided. However the examples described by Angus and Kanaris-Sotiriou (1995) have analogies to regional albitites from the Snake Creek Anticline described in Sect. 4.4.2.1.

4.4 Controls on Regional Metasomatism in the Middle Crust

This section reviews the observations, interpretations and controversies concerning structural controls, vein selvages, time integrated fluid fluxes and fluid sources for metasomatic rocks in Barrovian and Buchan rocks. It also examines in more detail some of the Proterozoic metamorphic belts of Australia, in particular the Mount Isa Inlier where Nick Oliver, and to a less extent the author, have published a series of papers on the extraordinarily diverse and extensive regional metasomatic rocks.

4.4.1 Controls on Mid-Crustal Metasomatism: Barrovian Metasomatic Rocks

Barrovian metamorphic rocks (i.e. kyanite to sillimanite sequences with pressures in the range 0.4–1.0 GPa) are dominant in Phanerozoic metamorphic belts (Ague in

press), although in many Precambrian belts lower pressure metamorphic rocks (Buchan zones) are more abundant. Regional metasomatic rocks are described from the Barrovian of the Caledonides of Scotland, the Appalachians of the northeastern United States, and the South Island of New Zealand. Major issues include the magnitude of fluid fluxes in metasomatic rocks, whether selvage/vein systems are open or closed, whether external fluids were sourced entirely from devolatilization deeper in the crustal sequences, and if dilatancy pumping is an important mechanism moving for fluids deeper and/or laterally.

4.4.1.1 Time Integrated Fluid Fluxes

The concept of reaction progress (based on mineral modes and phase equilibria) was first introduced by Brimhall (1979) and applied to regional metamorphic rocks by Ferry (1983a, 1983b). Ferry also developed the concept of "fluid rock ratios", later modified to the more appropriate "time-integrated fluid fluxes". Ferry and his colleagues have championed application of these concepts in a number of publications, in particular concerning impure calc-silicate rocks from the Waterville and Waits River formations in New England, north-eastern USA (e.g. Ferry 1984, 1987, 1994b; Ferry and Dipple 1991). Although there may be only limited metasomatism (volatiles, Na, Ca) in these formations, these studies indicate very large time-integrated fluid fluxes. The existence of these is important in understanding fluid flow in the crust and the origin of regional metasomatism.

Problems in the methods concerning cross layer diffusion or flow are discussed in Penniston-Dorland and Ferry (2006), but they nevertheless conclude that enormous quantities of fluid were channeled through specific layers, although the fluid sources remain uncertain. Yardley (2009) questions the assumptions in these methods and remains unconvinced concerning the values of fluid fluxes during metamorphism of these areas. For example he proposes that increasing salinity leads to a decrease in time-integrated fluid fluxes. However, phase considerations and oxygen isotope modeling of rocks from four thermal aureoles led Ferry and Gottschalk (2009) to conclude that increasing salinity requires even higher time-integrated fluxes. Yardley (2009) also suggests that large time-integrated fluid fluxes disappear if the reactions are kinetically controlled or if there is significant cross-layer transport by diffusion. However this is refuted in studies of classic areas of infiltration-driven regional metamorphism (Ferry et al. 2005; Penniston-Dorland and Ferry 2006; Wing and Ferry 2002, 2007; Ferry 2007). The most advanced calculation of time-integrated fluid flux involves linear inverse theory, which allowed for the determination of the 3-dimensional fluid flow pattern from fluid advection and oxygen isotope data for the Wait River Formation (Wing and Ferry 2002, 2007). They found that the mean flux vectors lie along the average lithological layering, which is controlled by the regional syn-metamorphic folds.

The flux was directed upward at 32° to the horizontal. They calculated that the regionally-averaged time-integrated fluid flux was 2.2×10^4 mol fluid/cm^2 rock.

Studies of many other areas, both regional and thermal metamorphism, also suggest the existence of large time-integrated fluid fluxes. Modeling of O_2 and Sr_2 isotope data in the regionally metamorphosed Trois Seigners Massif in the Pyrenees indicates time-integrated fluid fluxes of over 10^4 m^3m^{-2} Bickle (1992), Lyubetskaya and Ague (2010) argue that localized large time-integrated fluid fluxes of ~10^3 $m_{fluid}{}^3m_{rock}{}^{-2}$ are possible during metamorphism of pelites in collisional orogens. Ferry et al. (2002), in a study of two classic aureoles in northern Italy and a review of 13 others, present evidence for time-integrated fluid fluxes in the range 10^2–10^4 mol/cm^2.

4.4.1.2 Changes in Bulk Compositions During Development of Foliation and Prograde Metamorphism

Regarding loss of components in foliation development, Gray (1997) argues that volume losses in slates from the eastern USA and the Lachlan Fold Belt in southeastern Australia vary from 0 to more than 50%. Nevertheless it is quite a controversial topic whether significant volume loss occurs during cleavage development in metamorphic rocks (Vernon 1998). It is argued that grains of minerals, such as quartz, feldspars, and carbonates in contact with phyllosilicates, are more prone to a large increase in dislocation density and therefore to dissolution and removal by solution during the formation of slaty cleavages and crenulation cleavages (e.g. Bell 1981, 1986).

Studies by Breeding and Ague (2002) of the Haast Schists of New Zealand and by Ague (1994a,b) of the Wepawaug Schist of Connecticut indicate overall gains in silica when the quartz veins along with the silica-depleted selvages were taken into account. Qui et al. (2011) found depletions in Li concentrations in the greenschist-facies Otago Schist (Haast Schist) composites (quartz veins included) compared with sub-greenschist-facies composites, although the ∂^7Li values showed no change. They suggest that Li depletion resulted from both dehydration reactions and dilution by the addition of quartz veins. Cox (1993) argues that losses from pelitic rocks from the higher grade Haast Schist, compared with their lower grade Torlesse equivalents, may be balanced by abundant quartz veins in the Haast Schist. Because of possible variations in the chemistry of metasedimentary rocks in lower and higher metamorphic grade in any particular area, Yardley (2009) is not convinced by the arguments for chemical changes with increasing metamorphic grade.

4.4.1.3 Interpretation of Quartz Veins and Selvages in Barrovian Metamorphic Belts

Detailed studies have been done of vein-selvage relationships in pelitic Barrovian metamorphic rocks from Connecticut, Scotland, and New Zealand. In the

Wepawaug Schist, Connecticut, quartz veins comprise several percent of the chlorite zone and increase up to 20–30% in the staurolite-kyanite zone (Ague 1994a,b, 2003). The quartz veins contain kyanite in the staurolite-kyanite zone. The selvages (centimeters to tens of centimeters wide) are rich in garnet, kyanite, and biotite, and are relatively depleted in quartz, plagioclase, and muscovite (Ague 1994a, b, in press). Mass balance calculations showed 40–80% of the vein silica was derived from the selvages, that silica was also added from external sources, and that Al, Fe, Mn, Zn, Li, REE, and Y were concentrated in the selvages while K, Ba, Pb, Sn, and later, Na and Sr were lost. Ague (2011) concludes that through-going external fluids infiltrated the fractures (veins) and that chemical changes in the selvages were partly derived from the infiltrating external fluid and partly by diffusion. Ague (2011) emphasizes the channelized nature of the fluid flow, with metasomatism concentrated in narrow selvages. Thus careful and detailed sampling is necessary to demonstrate mass transport of components. The controversies in the literature concerning the extent of metasomatism in selvages may reflect differences in sampling strategies.

In a study of the formation of quartz veins and selvages from the Waits River Formation, Vermont, Penniston-Dorland and Ferry (2008) found that over 90% of the silica was externally derived, and that addition of Si and Ca to the veins was not matched by removal from the selvages. Selvages showed losses of Si, K, Ba, Rb, Mg, and Cs relative to unaltered rocks.

Veins in Dalradian metamorphic rocks, from a section of the Stonehaven coast in Scotland, were studied by Masters and Ague (2005) in a traverse that included greenschist-facies near the Highland Boundary Fault up through to staurolite grade 2 km north. Veins, which are comparatively more abundant in the metapelites than in the metapsammites, vary from 5% to more than 15% of the outcrop, and were emplaced during deformation and metamorphism. Masters and Ague (2005) propose that the greater abundance of veins in metapelitic rocks may be the result of hydro-fracturing resulting from higher fluid pressures generated by devolatilization during metamorphism. The veins are accompanied by centimeter- to decimeter-wide selvages containing porphyroblasts of biotite, garnet, chloritoid, and staurolite (depending on the local metamorphic grade) and plagioclase that has replace muscovite. Masters and Ague (2005) postulate large fluid fluxes of at least ~10^4 m_{fluid}^3/m_{rock}^2 that passed through the fracture-vein systems. They examined two models, one requiring up-temperature fluid flow down the Highland Boundary Fault, whereas the second, more favored model, postulates fluids derived from the ophiolitic rocks of the Highland Border Group passing upwards into the overlying Dalradian metamorphic rocks. Hydro-fracturing and up-temperature fluid are also an outcome of thermal modeling of the metamorphic peak in the Scottish Highlands. Here large mafic and felsic sills were emplaced during crustal thickening, supplying a significant portion of the thermal budget. Fluid flow was directed towards the intrusions (Lyubetskaya and Ague 2010).

During greenschist-facies metamorphism in the southwestern Scottish Highlands, the rocks were infiltrated by an H_2O-CO_2 fluid that formed asymmetric zonation in metabasic sills. The margins were altered to carbonate-bearing assemblages while the interiors remain carbonate-free (Skelton et al. 1995). On a larger scale the fluid

flow was preferentially through phyllites rather than interlayered metapsammites, probably controlled by microfractures and fractures associated with strong ductile deformation, and was preferentially focused into the axial planes of major antiforms. The layer-parallel fluid flow was far greater than layer-perpendicular flow and/or cross layer diffusion. The time-integrated fluid flux was calculated using the reaction front advective theory of Bickle and McKenzie (1987) and Bickle and Baker (1990). The fluid flow patterns were mapped out in the area, and while the average time-integrated flux was calculated at 100 m^3/m^2, locally high fluxes of up to 4×10^2 m^3/m^2 were also determined (Skelton et al. 1995). The authors conclude that the amounts of fluid are compatible with being derived by devolatilization reactions in the underlying metamorphic rocks.

The Southern Alps of New Zealand, with on-going tectonism at the Pacific-Australian plate boundary, have provided an ideal natural laboratory for fluid flow studies. Numerous warm springs along the Alpine Fault are exit zones of crustal fluids. An electrical resistivity model, derived from a magnetotelluric transect, has enabled three-dimensional mechanical modeling of the relationships between rheology, permeability creation, and fluid flow in the Southern Alps (Upton and Craw 2009). Because of the high stain rates and uplift/erosion rates, metamorphic rocks formed earlier in the active convergent margin are well exposed, particularly adjacent to the Alpine Fault. Rocks east of the Alpine Fault comprise a Mesozoic accretionary prism. While the less-deformed low metamorphic rocks contain very few quartz veins, quartz veins in greenschist-facies rocks commonly comprise 10–30% of the rock (Breeding and Ague 2002). Using Zr as an immobile reference frame, these authors did a mass-balance analysis and concluded that the veined higher-grade rocks had undergone addition of external silica and Na and loss of K. They deduced from an average silica addition that the time-integrated fluid flux was as high as 10^4–10^5 m^3/m^2. They suggest that the fluids were sourced from altered oceanic crustal rocks located in the underlying subducted slab. However, the conclusions regarding the origin of the veins, and the fluid fluxes responsible for them, remain controversial (Yardley 2009).

4.4.2 Controls on Low-Pressure Metasomatic Rocks

This section is concerned mainly with the abundant regional metasomatism in Proterozoic low-pressure metamorphic belts in eastern and central Australia, especially in the Mount Isa Inlier, north Queensland (Fig. 4.5), but includes examples from Connemara, South Australia and Norway.

Metasomatism in the Mount Isa Inlier differs considerably from the Barrovian examples described above in the abundance of belts of strike lengths on the scale of tens of kilometers, the variety of metasomatic types, and very limited relationships to quartz veins and their selvages. Sedimentary and volcanic rocks were deposited in the Mount Isa Inlier mainly in the Paleoproterozoic, and the major regional divisions (Western and Eastern successions and Kalkadoon Block) are shown in the

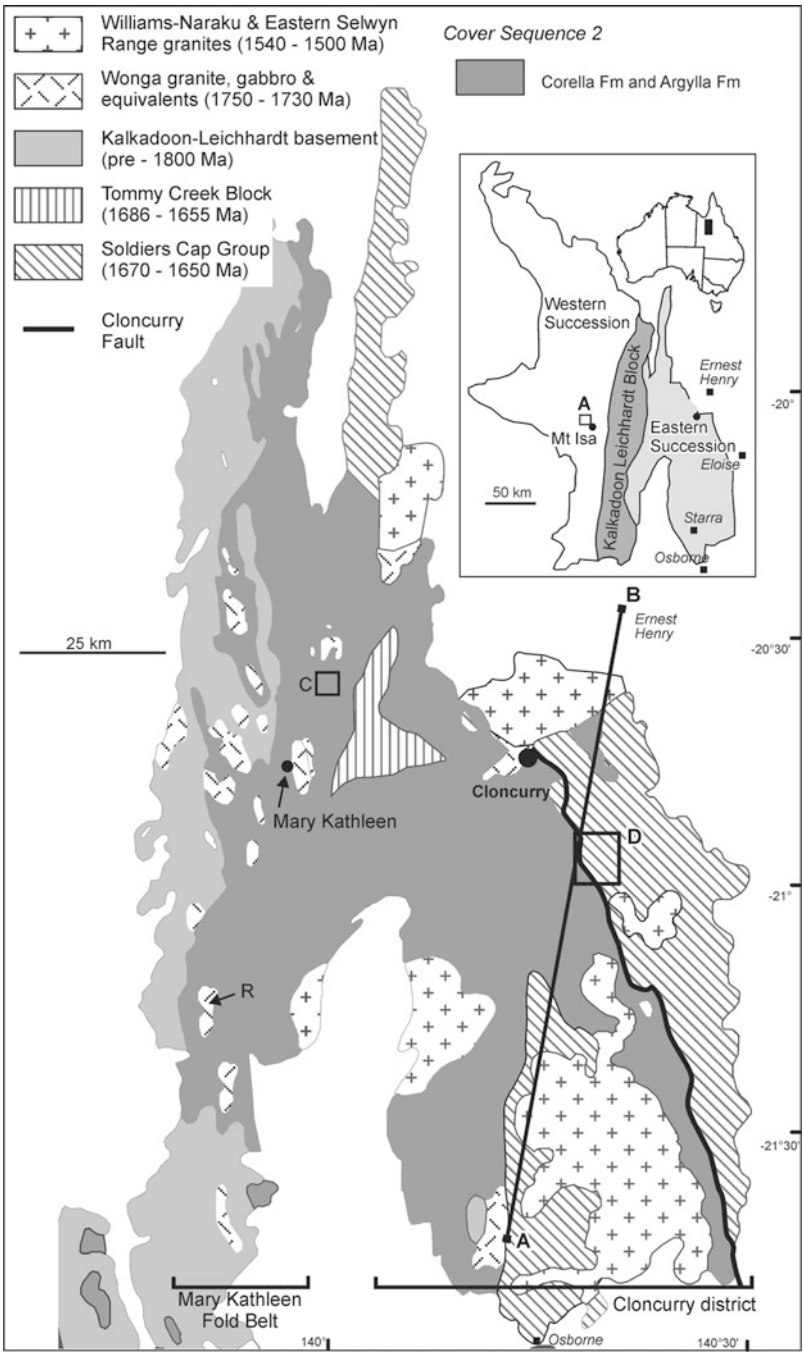

Fig. 4.5 Simplified map of the Eastern Succession, Mount Isa Inlier, modified after Oliver et al. (2004). The inset shows the main tectonic divisions of the Mount Isa Inlier, and A in the inset shows the location of Fig. 4.14. A line AB shows the location of the section in Fig. 4.10. The boxes C and D show the location of Figs. 4.6 and 4.7, respectively. R is the location of the Revenue Granite

Table 4.1 Simplified geological history of the Mount Isa Inlier, Queensland, Australia. IOCG refers to iron-oxide Cu-Au mineralization

Event	Western fold belt	Metasomatism western	Eastern fold belt	Metasomatism eastern
Intrusion/deformation/ metamorphism	D_3	Cu mineralization	Williams/Naraku Batholiths 1,500–1,550 Ma D_3, D_4	Breccias extensive Na-Ca alteration IOCG mineralization
Deformation/ metamorphism	Regional D_2 metamorphic peak ~1,580 Ma	Tremolite pods Cordierite metasomatism	Regional D_2 metamorphic peak 1,580–1,595 Ma	
Deposition	Mount Isa group 1,655–1,670 Ma	Zn-Pb-(Cu) mineralization		
Deformation/ metamorphism	Sybella event 1,672 Ma		D_1 1,650 Ma	Extensive Albitization IOCG mineralization
Intrusion	Sybella Batholith 1,655–1,673 Ma		Dolerite sills diorite granite ~1,640–1,690 Ma	
Deposition			Soldiers cap group ~1690–1650 Ma	
Deformation/ metamorphism/ plutonism			Wonga event 1,730–1,740 Ma	Extensive Na-Ca
Deposition	Haslingden group ~1,780–1,790 Ma	Chlorite-quartz schists, epidozites	Corella Fm ~1,750 Ma	

inset in Fig. 4.5. Multiple deformation, metamorphic, metasomatic and intrusive events took place in the Isan Orogeny over the period from 1,500 to 1,650 Ma, while significant more localized events include the Wongan Event ~1,740 Ma and the Sybella Event ~1,670 Ma. The geological history of the Mount Isa Inlier, where relevant to metasomatic rocks, is summarized in Table 4.1.

4.4.2.1 Structural Controls on Metasomatism in the Eastern Succession, Mount Isa Inlier

The main subdivisions (Mary Kathleen Belt and Cloncurry district), together with important units such as the Corella Formation and Soldiers Cap Group of the Eastern Succession are shown in Fig. 4.5. The Corella Formation (also referred to as Doherty Formation in the Cloncurry District) is dominated by scapolite-bearing calc-silicate rocks and marble (former evaporate-bearing dolomitic shales, siltstone and limestone), whereas the ~1,650–1,690 Ma Soldiers Cap Group consists mainly of metamorphosed siliciclastic turbidites, with basalts at the top of the exposed sequence. Metasomatism is widespread throughout the Eastern Succession (e.g.. Oliver 1995; Rubenach et al. 2008). The most important groups are as follows:

1. Considerable metasomatism occurs throughout the Corella Formation in the Mary Kathleen Fold Belt, and is most intense along a central 100×12 km high-strain zone known as the Wonga Belt. The metasomatism has overprinted meta-igneous as well as metasedimentary rock, and occurred during deformation in three major phases (Oliver 1995). Phase 1, ~1,740 Ma, was broadly synchronous with granite and dolerite intrusions, which resulted in scapolite-albite shear zones in the granite, pervasive scapolitization of some metadolerites and metagranites, local K-Na metasomatism, large-scale garnet-pyroxene banded and massive exoskarns in marble, wollastonite-vesuvianite skarn in marble, and endoskarn in granite, at 500–700°C and 0.1–0.2 MPa (Cartwright and Oliver 1994; Oliver 1995). Phase 2 probably commenced in the Isan Orogeny where the metamorphic peak is synchronous with the regional D_2 event at ~1,580 Ma. This produced numerous calcite pods with associated wall rock albitization, some with copper deposits, and allanite-uraninite mineralization in garnet-pyroxene veins that include those of the former Mary Kathleen Mine (Oliver et al. 1999). Titanite associated with a calcite pod at the Knobby Quarry (Fig. 4.6) gave a U-Pb age of 1,555 Ma (Oliver et al. 2004), Phase 3 metasomatism includes epidote-actinolite-albite-calcite breccias and alteration zones, probably synchronous with late folding at 1,550–1,500 Ma. In comparison with breccias in the Cloncurry District these breccias do not accompany synchronous igneous intrusions and are much more limited in scale, although one at Mount Philip is 10 km in length.
2. Early albitization in the Soldiers Cap Group, Cloncurry District. The albitites are particularly abundant in the Snake Creek Anticline (Figs. 4.5, 4.7) and in the Osborne Mine (Fig. 4.5) but occur in numerous smaller areas between the larger occurrences. Monazite dates from the albitites, determined largely by electron microprobe analysis, yielded ages mainly in the range 1,640–1,680 Ma (Rubenach et al. 2008). The albitites have replaced metapsammitic and metapelitic rocks in and adjacent to small shear zones and on the contacts of some dolerite sills, one of which was dated at 1,686 Ma (Rubenach et al. 2008).
3. Metasomatized breccias are abundant throughout the Corella Formation in the Cloncurry District, comprising more than 50% of outcrop occurring over an area of more than 3000 km^2 (Oliver et al. 2006). They are related spatially and temporally to the 1,500–1,530 Ma Williams and Naraku batholiths and smaller gabbro bodies, and are particularly abundant along the Cloncurry Fault Zone (de Jong and Williams 1995; Oliver et al. 2006; Marshall and Oliver 2008; Oliver et al. 2008; Austin and Blenkinsop 2010; Rubenach et al. 2008). In some areas along the Cloncurry Fault Zone they comprise over 70% of the outcrop (Fig. 4.7). Over 90% of the clasts are metasomatized. The most common alteration assemblages include albite (generally hematite-stained), amphiboles, clinopyroxene, calcite, biotite, microcline, and magnetite. Although tectonic and fault breccias occur locally, the majority of the breccias are hydrothermal in origin. Many of the iron-oxide copper-gold deposits (IOCG's) in the district, including the large Ernest Henry deposit, formed in breccia pipes (Williams 1998; Mark et al. 2006).

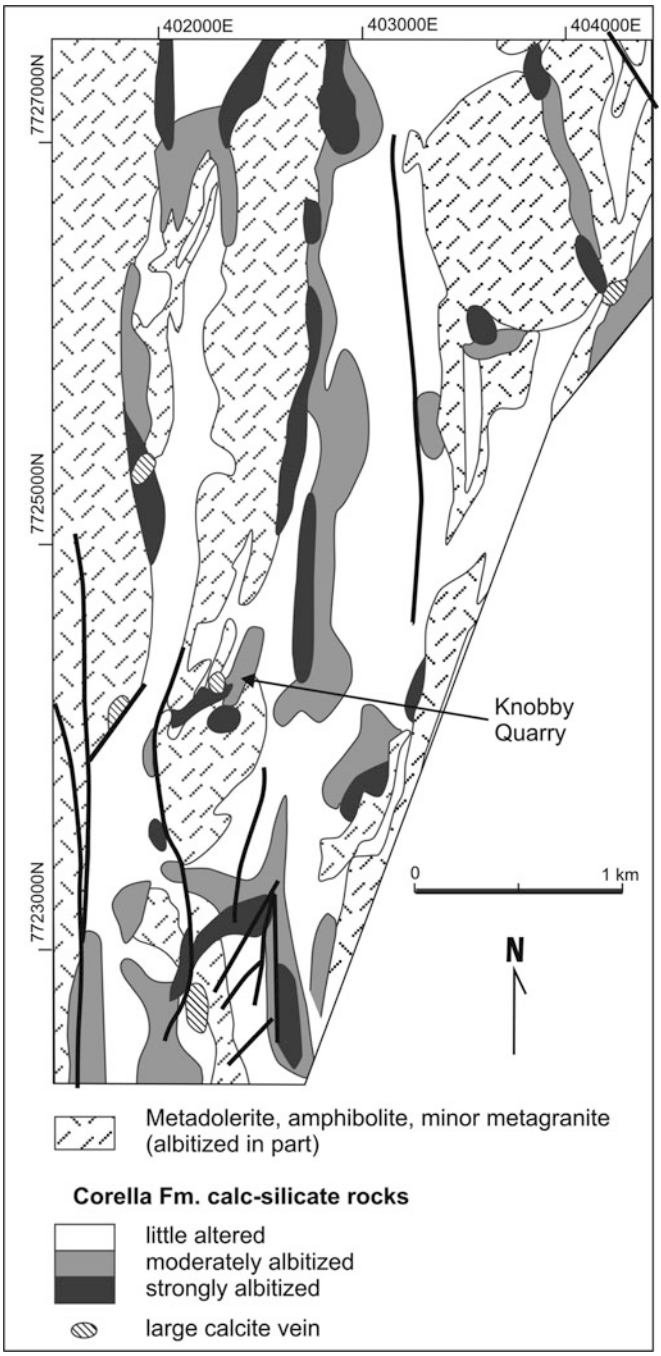

Fig. 4.6 Map of the Knobby quarry area, Mary Kathleen fold belt, modified after Oliver et al. (2004). The map depicts the degree of albitization in the area, and shows locations of large veins and pipes consisting mainly of coarse-grained hydrothermal calcite

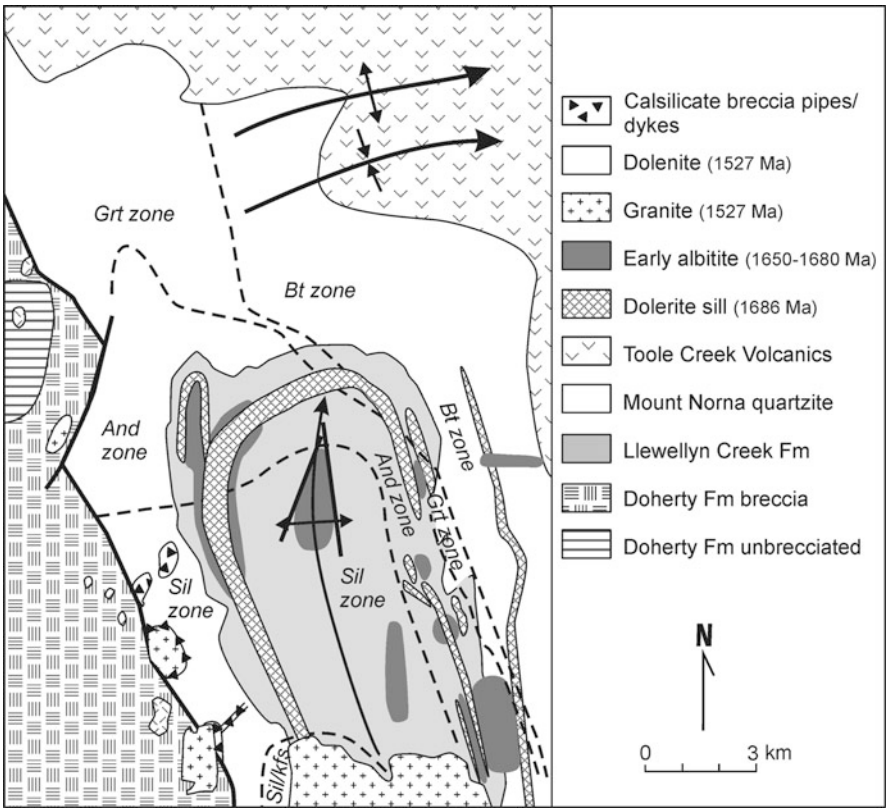

Fig. 4.7 Map of the Snake Creek Anticline, modified after Rubenach et al. (2008). The Llewellyn Creek Formation, the Mount Norna Quartzite, and the Toole Creek Volcanics are units of the Soldiers Cap Group. It shows areas of more intense albitization in the Soldiers Cap Group (two locations). The Doherty Formation is also referred to in the literature as the Corella Formation. The metamorphic zones are biotite Bt, garnet Grt, andalusite And (with or without staurolite), sillimanite (Sil), and sillimanite/K-feldspar Sil/Kfs. The *thick line* represents the Cloncurry Fault Zone, which marks the boundary between the Doherty Formation and the Mount Norna Quartzite

Mary Kathleen Fold Belt: Structural Controls, Modeling and Fluid Sources

The extensive metasomatic rocks in the Mary Kathleen Fold Belt have been subjected to detailed studies by N. Oliver and colleagues. The Knobby Quarry area (Fig. 4.4) is representative of the metasomatism in the belt, and shows the development of albitites and calcite pods in relation to contacts between the Corella Formation calc-silicate rocks and metadolerite bodies, the latter being variably boudinaged. Further south the Revenue Granite area (Fig. 4.5) provides another example. The granite was altered to diopside, chlorine-rich scapolite, and albite along shear zones formed soon after emplacement during the Wongan event (Aslund et al. 1995).

Although structural controls such as shear zones, fractures, and strain shadows are obvious in the Mary Kathleen Fold Belt the precise timing (i.e. Wongan at ~1,740 Ma, Isan Orogeny peak at 1,580 Ma, or late Isan D_3 or D_4 at ~1,550–1,520 Ma) is not clear in cases where cross-cutting foliations are absent, and where later deformation events reactivated or reused earlier foliations rather than produce new overprinting foliations (e.g. Bell 1986). Oliver et al. (1990) studied the relationships between the metasomatism and inferred stress and strain patterns and developed models for the fluid flow pathways. The metagabbro bodies were relatively brittle, so they readily fractured providing fluid access and allowing scapolite alteration and scapolite-diopside-calcite veins to form. Sub-horizontal veins developed normal to the inferred minimum principal stress, suggesting tensile failure at high fluid pressure relative to local stresses (Oliver et al. 1990). Scapolite replacement of the metadolerite is typically 30–70%, but locally up to 90%. The ductility contrast between these bodies and the surrounding metasedimentary rocks resulted in strong ductile deformation, fracturing and brecciation of the latter allowing focusing of fluids into the more deformed zones. Albitization of the metasedimentary rocks developed up to 100 m from the metadolerite contacts. Figure 4.8a, modified from Oliver et al. (1990), depicts typical deformation patterns (shear zones, calcite pods, boudinage, and breccias) and fluid/rock ratios at the termination of a metadolerite lens, while Fig. 4.8b is a model of the stress variations. The authors conclude that enormous quantities of fluid were involved, and although a belt of 50 × 6 km was studied in detail the metasomatism extends for at least 100 km in total. While in part magmatic, the fluids were probably largely derived from the Corella Formation or a similar metamorphosed evaporite-bearing dolomitic sequence no longer exposed. Oliver et al. (1990) estimate that the source volume for single-pass infiltration of fluids derived from metamorphic devolatilization would be greater than 5×10^5 km^3, which is very unlikely. Derivation from a subducted slab was also not an option as the Mount Isa Inlier was a considerable distance from a plate boundary. As repeated circulation in convection cells (Etheridge et al. 1983) is very unlikely at crustal depths corresponding to ~0.4 MPa, dilatancy pumping is the preferred mechanism (Sibson 1987; Oliver et al. 1990). Episodic dilatancy resulting from the strong deformation and ductility heterogeneity in the area would allow fluids to flow into dilatant fractures, followed by pumping (down, up or laterally) into new fractures during subsequent fault movements. The model is illustrated in Fig. 4.9.

Some of the complexity of metasomatism in the Mary Kathleen Fold Belt is illustrated in Fig. 4.10. This shows relatively unaltered metasedimentary rocks with an overprinted irregular zone of albitization cored by actinolite and cut by a series of thin albite veins. Ignoring the thin albite veins, the geometry could be consistent with metasomatic zones formed by channeling of external fluids along a central fracture in a single event. However, as discussed in Oliver and Bons (2001), albitization involved removal of Fe and Mg from the Corella Formation into the central actinolite veins. This suggests that several stages were involved. Albite metasomatism occurred at an earlier stage and the central actinolite body formed later, possibly from Fe and Mg removed during albite formation associated with a nearby fracture (Oliver and Bons 2001).

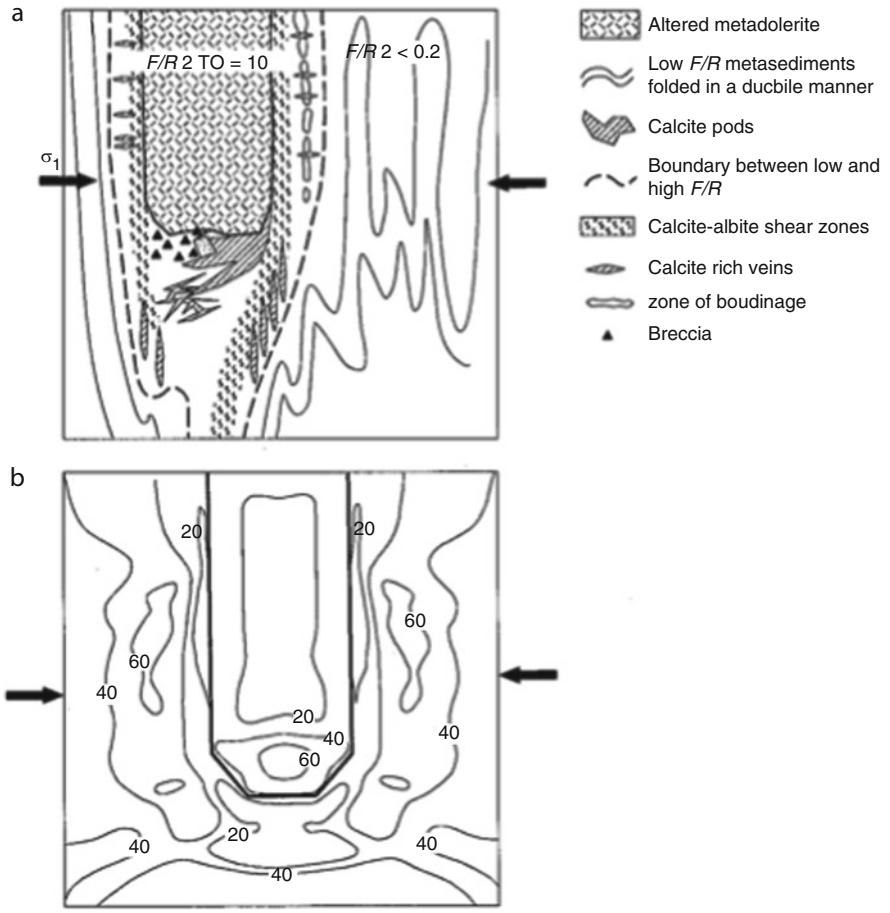

Fig. 4.8 Schematic map and model illustrating relationships between deformation, metasomatism, fluid flow, and stress distribution around a metadolerite pod within highly deformed calc-silicate rocks in the Mary Kathleen Fold Belt, modified after Oliver et al. (1990). The direction of the principle stress, σ_1, is shown as *arrows*. (**a**) This shows shear zones, inferred high fluid rock ratios (F/R) in the metadolerite and contact zones compared with the distal country rocks, and the location of hydrothermal calcite pods and breccias in the strain shadow. (**b**) A model of the stress distribution during a high strain event. The contours represent effective mean stress

The Cloncurry District: Early Albitites and Giant Hydrothermal Breccia Systems

The complexity of determining the timing of metasomatism within the tectonothermal evolution of the Eastern Succession is highlighted by studies in the Snake Creek Anticline. Early albitization is spatially related to metadolerite contacts and to small localized shear zones (Figs. 4.7, 4.11). In many locations metapsammites have been preferentially replaced, with interbedded pelitic schists commonly replaced by albite-bearing biotite-rich schists (Fig. 4.12). In each lithology

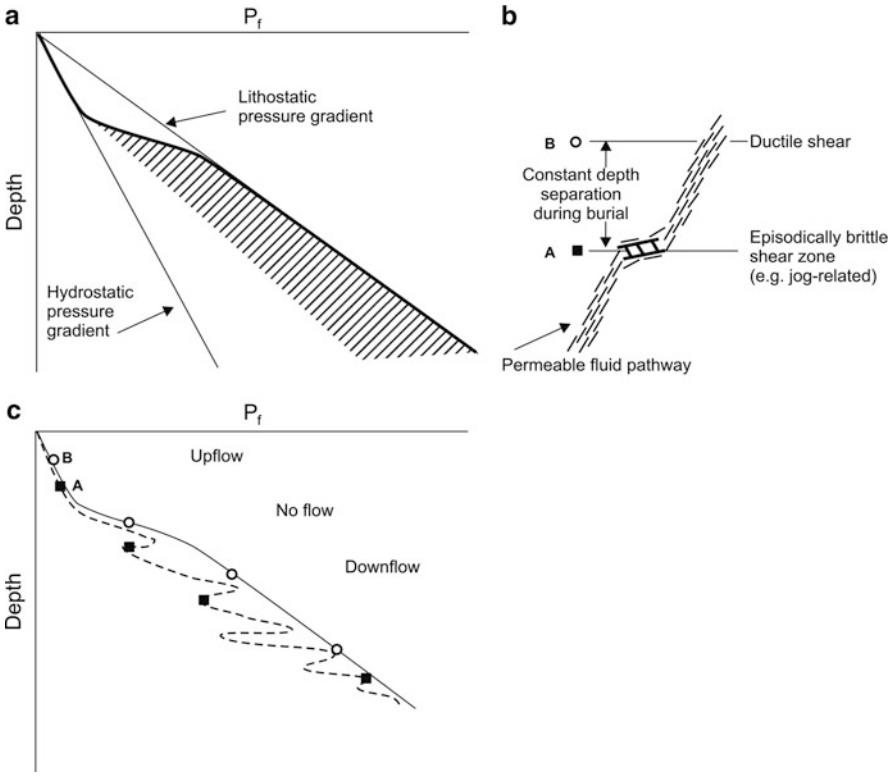

Fig. 4.9 A series of sketches, modified after Oliver et al. (1990), illustrating their model for dilatancy control of fluid flow during deformation in the Mary Kathleen Fold Belt. (**a**) This depicts the upper crust where fluid in pores and fractures is under hydrostatic pressure (open to the surface), and the middle crust where fluids are under lithostatic pressure. The hatched area illustrates a region where fluid pressure may be temporarily lowered during dilatancy development accompanying strong deformation. (**b**) This sketch illustrates episodic dilatancy development on an active shear zone, and two locations, A and B, on the shear zone. (**c**) This illustrates how fluids may be pumped up or down a shear zone depending on dilatant pressure changes and whether the fluid pressure at A is higher or lower than that at B

muscovite was destroyed and K removed, while Fe and Mg commonly removed from the metapsammitic rocks and added to the pelitic schists (Rubenach 2005). The degree of replacement is variable, from less than 10% to over 90% albite in the metapsammitic rocks, roughly 10–50% albite in biotite-rich schists, and over 95% albite in some highly strained metasomatized pelitic rocks. Zones 1–20 m wide of intense albitization occur along parts of the sill contacts, with wider zones of patchy metasomatism and variable degrees of replacement occurring between the sills (Fig. 4.7). Two areas of concentrated albitization occur in the core of the anticline, one being bounded by faults that are probably not structural controls. On an outcrop scale some of the albitization is related to the shear zones (Fig. 4.11), but otherwise appears to occur in random patches where metapsammitic rocks have

Fig. 4.10 Photo of a complex vein system from the Cameron River, Mary Kathleen Fold Belt. The centre of the vein, occupied by actinolite, is surrounded by a zone of lighter coloured albitization. Thin albite veins are almost *white*. The country rocks, calc-silicate rocks of the Corella Formation, are medium *grey*

been albitized and interbedded muscovite-rich schists may or may not have been replaced by biotite-rich schists. Sporadic albitization of metapsammitic rocks occur in many other areas in the anticline core, but are almost absent from the northeast and southwest parts (Fig. 4.7).

In contrast, unmetasomatized schists and metapsammitic rocks in the Snake Creek Anticline contain muscovite and no albite. Porphyroblasts grew at a number of stages along a complex P-T-t path that included a clockwise loop at 0.5–0.6 GPa followed by the peak temperature event at ~0.4 GPa late in the regional D_2 event at ~1,585 Ma (Rubenach et al. 2008). Close to the metadolerite sills, the albitites and biotite-rich schists typically contain garnet and staurolite, with or without andalusite and local gedrite (Fig. 4.12). In the core of the anticline they contain cordierite (mainly pseudomorphs), andalusite and sillimanite, with rarer staurolite and kyanite. Cordierite was largely restricted to D_1 at 1,650 Ma, whereas andalusite, staurolite and garnet grew in multiple events (Rubenach et al. 2008). Kyanite grew late in the D_1 or early in the D_2 events and sillimanite grew largely in D_2.

Because of the spatial association of albitization with shear zones that appeared to be local D_2-related high-strain zones, albitization was initially assigned to syn-D_2 (Rubenach and Barker 1998; Rubenach and Lewthwaite 2002). Subsequently outcrops were found with D_1-related fresh cordierite containing abundant albite inclusions. Electron microprobe dating of monazite in albitites provided ages mainly in the range 1,640–1,680 Ma, with a smaller peak at ~1,585 Ma corresponding to peak metamorphic temperatures. Thus albitization overlaps with the intrusion of the sills (one dated at 1,686 Ma) and with D_1 at 1,650 Ma. The albitization-related shear zones (Fig. 4.11) were therefore probably early structures

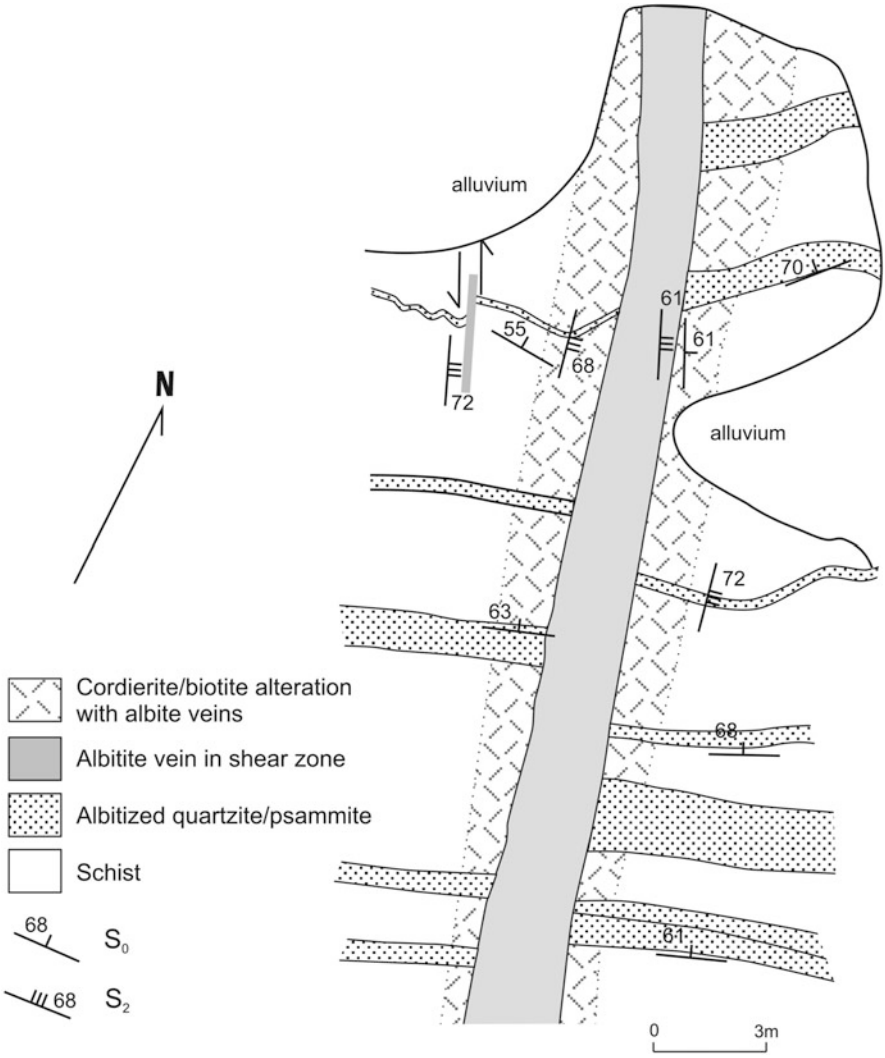

Fig. 4.11 Map of an albite-rich shear zone in the core of a mesoscopic fold, Snake Creek Anticline, after Rubenach and Lewthwaite (2002). The unmetasomatized schists consist of muscovite, quartz, biotite, andalusite, and garnet. The schists are interlayered with metapsammitic rocks, consisting of muscovite and quartz where not albitized, but unaltered metapsammitic rocks are located many tens of metres on either side of the map. Most of the shear zone consists of over 95% albite, with minor biotite, rutile, and quartz, which have replaced metasedimentary rocks. Cordierite, replaced by biotite, occurs at the edge of the albite-rich shear zone. In a zone roughly 2 m wide adjacent to the shear zone, the schist has been replaced by a biotite-rich albite-quartz-cordierite-andalusite assemblage, and contains thin albite veins that are fracture-filled. The shear zone foliation is parallel to the S_2 axial plane foliation in the schists but this is almost certainly the result of reactivation of a much earlier shear zone. Fluids infiltrated the original fracture/shear zone replacing the immediate country rocks by an inner albite zone and an outer biotite-rich schist zone (in the pelitic rocks only). They penetrated the more permeable metapsammitic rocks replacing muscovite (and some quartz) by albite for many tens of metres from the central shear zone

Fig. 4.12 Photo of metasomatized metapsammitic rocks and schists (metaturbidites) Sandy Creek gorge, southeast corner of the Snake Creek Anticline (Fig. 4.7). The photo is representative of a 200 m-wide section of metasomatic rocks located between two metadolerite sills. The metapsammitic rocks have been selectively albitized, and now consist of albite with or without quartz, garnet, staurolite, and gedrite. The interbedded pelitic schists are now almost free of muscovite, and consist of biotite, quartz, garnet, staurolite, and andalusite. Nearby some pelitic rocks consist of albite, garnet, staurolite, and gedrite, with or without andalusite, and with no muscovite or quartz. Fluids causing the metasomatism were channeled along metadolerite contacts early in the deformation history, and the porphyroblasts grew later during the D_1, D_2, and D_4 events (Rubenach et al. 2008)

subsequently reactivated during D_2 and other events, resulting, in the absence of other data, in an incorrect timing for albitization based on field criteria.

The localization of part of the albitization along metadolerite contacts has some analogies with the examples described from near Dublin and other locations by Angus and Kanaris-Sotiriou (1995). A similar model is proposed, namely fluids circulated by a large-scale magmatic system of which the sills are a part. The sills acted as aquitards, which resulted in focusing the fluids along contacts. However at Snake Creek fluids were also focused along fractures and/or shear zones away from the contacts. Albitization probably overlapped with the development of a shallowly-dipping foliation (D_{1a}) and associated cordierite metamorphism. The depth at which albitization was initiated is uncertain, but the pressure was less than 0.4 MPa when andalusite grew in D_{1b} (Rubenach et al. 2008). The controls on permeability within individual beds is also uncertain. Intrinsic porosity, especially in the psammitic layers, is a possibility, but more likely microfractures formed during ductile deformation, both in the mica-bearing metapsammites and pelitic rocks. Higher strains, and therefore micro-fracture densities, localized along shear zones and the ductility contrast zones along metadolerite contacts. The source of the fluids remains uncertain. The main possibilities are the adjacent or underlying

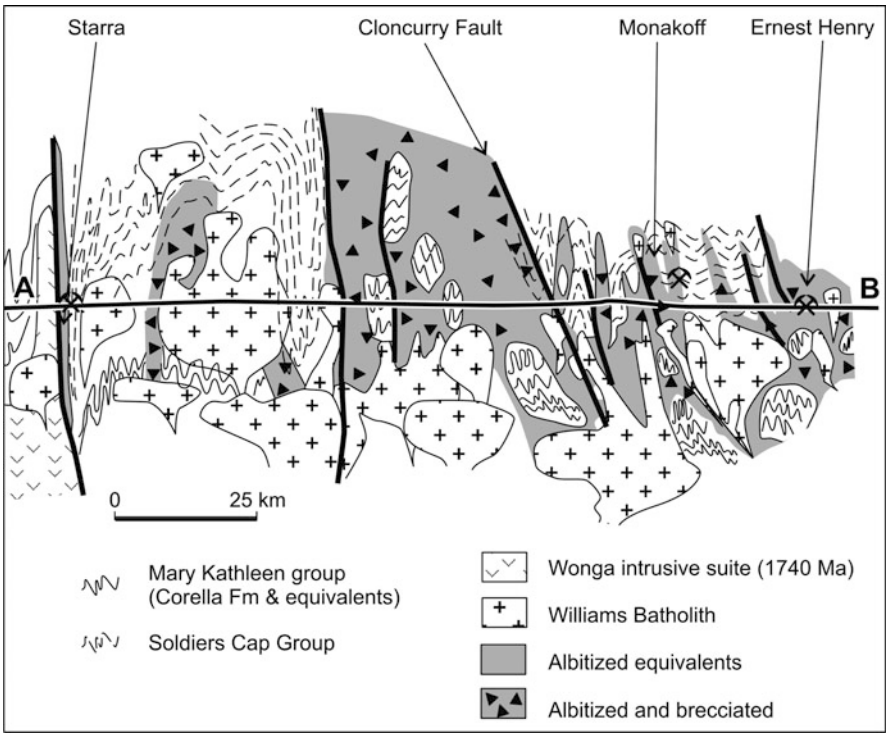

Fig. 4.13 Diagrammatic section through the Cloncurry District, based on A–B of Fig. 4.5, modified from Oliver et al. (2004). This schematically illustrates widespread albitization and brecciation in relation to granite intrusions in the Eastern Fold Belt, Mount Isa Inlier. The IOCG deposits at Starra and Ernest Henry, and the polymetallic Monakoff deposit also formed during this 1,500–1,530 Ma period of igneous intrusion, hydrothermal breccia development, and Na-Ca metasomatism

Corella/Doherty Formation that was rich in evaporites (or scapolite where metamorphosed), and/or magmatic fluids. Quartz veins that can be linked to albitization are quite rare, but limited fluid inclusion studies, including analyses of halogens and noble gases, suggest a deep magmatic or metamorphic fluid source (Kendrick et al. 2008).

The Cloncurry District: Giant Hydrothermal Breccia Systems

The scale of brecciation and metasomatism in the Corella/Doherty Formation in the Cloncurry is referred to above. The association with granites and gabbros of the 1,500–1,530 Ma Williams and Naraku batholiths has been long recognized (e.g. de Jong and Williams 1995), and small bodies of granite and gabbro occur in the Snake Creek Anticline area (Figs. 4.7, 4.11). Rare clasts of granite, and even rarer gabbro,

Fig. 4.14 Typical hydrothermal milled breccia in the Doherty Formation, Snake Creek Anticline. Alteration consists mainly of hematite-stained albite, with amphiboles and calcite

Fig. 4.15 This shows a typical hydrothermal breccia (*lower*) in contact with the bedded Doherty Formation calc-silicate rocks. The latter originally consisted of calcite, quartz, microcline, biotite, and scapolite, but for meters to tens of meters from the breccia contacts they have been altered to the same assemblage as the breccias, namely albite, amphiboles, and calcite

occur in the breccias, and a few breccia dykes cutting granite have been observed. Some granite bodies extending across the Cloncurry Fault into the Soldiers Cap Group are partly surrounded by carapaces of breccias consisting of clasts of calc-silicate rocks but not of country rock schists. Breccia dykes and pipes with clasts of calc-silicate rocks and rarer gabbro and granite, including some believed to have been partly molten, occur within the Soldiers Cap Group, in places kilometers from the nearest exposure of Corella/Doherty Formation (Oliver et al. 2006; Bertelli and Baker 2010). Calc-silicate clasts up to 14 m in length occur in the Suicide Ridge breccia dyke about 1 km from the nearest calcsilicate outcrop, testimony to the energy involved in forming some of the breccias.

Zircons from the largest body of granite in the Snake Creek Anticline were dated using the SHRIMP at 1,527 Ma (Rubenach et al. 2008). There is considerable evidence that the intrusions were synchronous not only with the brecciation but also with the D_4 crenulation cleavage event and late andalusite and staurolite growth in the Soldiers Cap Group. Aureole assemblages indicate a depth of around 10 km for the intrusions and brecciation (Oliver et al. 2006). The two feldspars in the smaller granite bodies from the area have been pervasively albitized, but fractures or microfractures that may have provided fluid access are not evident. The most common breccia type is poorly sorted and matrix supported, with subangular to subrounded clasts (Fig. 4.11). Most clasts were calc-silicate rocks, originally consisting of some combination of calcite, microcline, scapolite, biotite, quartz and clinopyroxene, but the metasomatized equivalents are dominated by hematite-stained albite, with or without amphiboles, pyroxene, biotite, and magnetite. The matrix typically consists of the same minerals, but commonly includes calcite. Less common are small areas with subangular to angular clasts showing little alteration in clast-supported breccias. Clasts of over 10 m in size occur in some locations, and 100 m-scale bodies of calc-silicate rocks within the breccias are either giant clasts or, more likely, are in situ Corella/Doherty Formation. Such large clasts and blocks have intact bedding, but have been altered to the same assemblages as in the surrounding breccias (Fig. 4.12).

A model proposed for the breccias involves the abrupt explosive release of overpressured magmatic-hydrothermal fluids (including abundant CO_2 in the magmas) (Oliver et al. 2006). The authors suggest that the wall-rocks from the intrusions were strongly fractured but that they sat under low permeability barriers. Pressure variations of up to 150 MPa are inferred from studies of CO_2 fluid inclusions (Oliver et al. 2006; Bertelli and Baker 2010) (Fig. 4.16). Although magmatic fluids were a critical part of the fluid budget, fluid inclusion studies also support the view that a significant portion of the fluids causing the subsequent Na-Ca metasomatism of the breccias were derived from sedimentary formation waters that dissolved halite (or scapolite) (Kendrick et al. 2008). Given the scale of brecciation in the Cloncurry District this implies that once the breccias had formed, enormous quantities of upper to middle crustal fluids were able to penetrate down to at least 10 km in the crust.

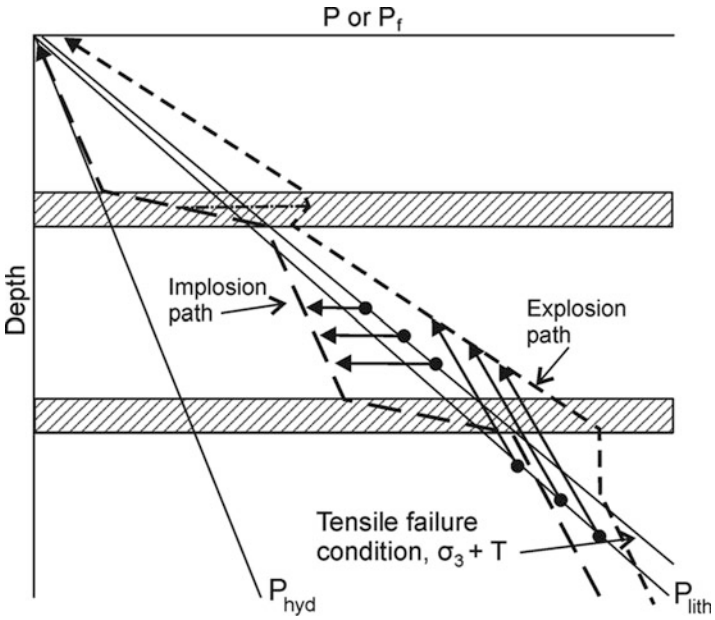

Fig. 4.16 Schematic diagram illustrating the inferred processes producing fluidized breccias in the Eastern Fold Belt, Mount Isa Inlier, modified from Oliver et al. (2006). It shows hydrostatic (P_{hyd}) and lithostatic (P_{lith}) pressures with depth. The horizontal bars represent permeability barriers. The tensile failure conditions are also shown. *Arrows* with *dots* represent two possible paths for brecciation, explosion, or implosion The preferred model for most of the hydrothermal breccias is the explosion path, whereby a combination of a greatly over pressurized fluid supply and a very rapid pressure build-up under the barrier leads to explosive brecciation and entrainment of clasts in a rapid up-flow of fluid. The implosion path results in spalling of clasts in a fault zone as a result of a sudden pressure decrease

4.4.2.2 Structural Controls on Metasomatism in the Mount Isa Area

A variety of regional metasomatic lithologies occur in metasedimentary rocks and metabasalts of the Proterozoic Haslingden Group west of the Mount Isa Fault in the Mount Isa area (Fig. 4.17). These include chlorite-quartz and epidozite alteration of metabasalts, metasomatic tremolite and plagioclase-tremolite pods, and unusual cordierite-rich rocks associated with boudinage of metadolerite dykes.

Chlorite-quartz alteration and less common smaller pods of epidozites (epidote + quartz + titanite) are exposed along a 30 km belt west of Mount Isa, of which the area in Fig. 4.17 is a part. The alteration occurs as elongate highly strained schist lenses ranging from a few meters to many hundreds of meters in length and up to 30 m in width. The largest occur along major faults (Fig. 4.17) whereas the smaller lenses are highly strained but are not obviously related to faults or fractures. The foliation in the schists is essentially the regional D_2 that formed in the Isan Orogeny ~1,580 Ma but it is a crenulation cleavage with evidence of at least one earlier foliation. Locally the schist assemblages include talc, anthophyllite or cummingtonite,

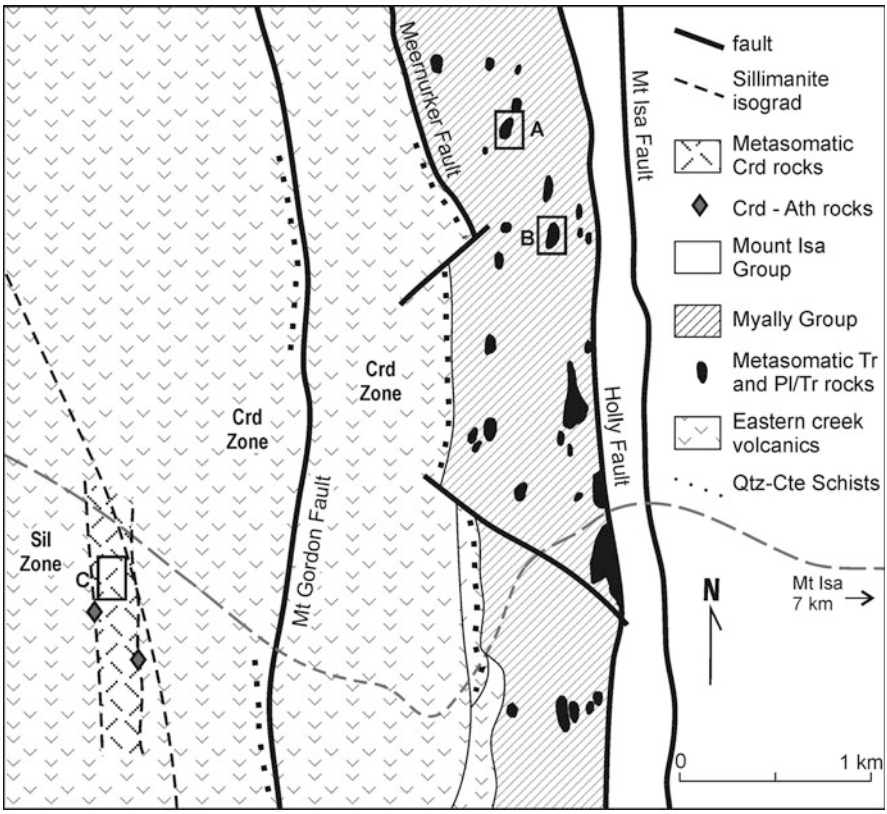

Fig. 4.17 Map of the area west of Mount Isa, modified from Rubenach (1992) and Huang and Rubenach (1995). Metasomatic rocks include: (1) pods of metasomatic tremolite (Tr) and plagioclase-tremolite (Pl-Tr) in the Myally group; (2) quartz-chlorite schists formed from metabasalts along parts of the Mount Gordon and Meernurker Faults; and (3) a zone containing cordierite-anthophyllite rocks (Crd-Ath) and metasomatic cordierite-rich pelitic rocks, the latter having replaced schists in contact with abundant metadolerite boudins. Boxes A, B, and C show the locations of Figs. 4.18, 4.19, and 4.20 respectively

with the amphiboles having overgrown the foliation late in D_2 during the peak metamorphic temperature event. In the sillimanite zone the chlorite-quartz schists were metamorphosed to cordierite-anthophyllite bodies (Rubenach 1992). It is clear that major faults adjacent to the larger lenses have had a long history of movement events, the last of which postdated the metamorphic peak. So although the metasomatism occurred early in the structural history its precise timing is uncertain. Possibilities include during rifting in the basin development or it was synchronous with early ductile deformation. The alteration is very similar to that described from mid-ocean ridges where circulation of seawater occurred during rifting and volcanism (e.g. Mottl 1983). Sedimentation in the Mount Isa Inlier formed in a series of intracontinental rifts rather than deep ocean basins, but it is suggested that the

chlorite-quartz and epidozite alteration of basalts in the Mount Isa area was analogous to alteration at mid-ocean ridges, namely circulation of fairly hot convective seawater along active faults and fractures.

The structural controls on the development of a series of tremolite and plagioclase-tremolite pods in the Molanite Valley west of Mount Isa are described in Huang and Rubenach (1995). The host unit is the Loch Ness Formation (identified as the Bortala Formation in earlier studies), which consists of greenschist-facies schists, quartzites, and calcareous or dolomitic metapsammitic rocks with scattered marble lenses. Tremolite pods, generally comprised of 95–100% randomly-oriented tremolite prisms, occur in the high-strain eastern half of the fault-bounded unit, while pods of plagioclase-rich rocks, containing sheaves of tremolite aligned in the S_2 foliation, occur in an anticline hinge in the western half (Fig. 4.18). Some of the tremolite pods are partly enveloped by talc-chlorite schists derived from dolomite-rich, calc-silicate rock or impure marble (Fig. 4.18). On the basis of small bodies of relict precursors and preserved sedimentary structures, massive tremolite has not only replaced marble but also quartzite and metapsammite. Structural and microstructural observations suggest this took place early in the development of D_2 (Huang and Rubenach 1995). The fluid source is unknown.

Many of the plagioclase-tremolite pods are centred around lenticular quartz veins (Fig. 4.19). The host lithologies are schists and metapsammitic rocks comprised of quartz, muscovite, biotite, chlorite and accessory hematite. The contacts with the pods are remarkably sharp. The alignment of tremolite sheaves in S_2 and the slight deflection of S_2 across the contacts suggest the pods formed late in D_2. It is proposed that dilatant fractures, now occupied by the quartz, opened during the ductile deformation, allowing infiltration of fluids. Oxygen isotope studies have revealed that quartz from the veins, the pods, and the host rocks is the same at 9–10‰. This indicates a classic infiltration scenario such as depicted in Fig. 4.1d, where the fluids penetrated both the pod and the host rocks, with the isotopic front some distance from the mineralogical front.

Unusual cordierite-bearing metasomatic rocks occur in the lower part of the sillimanite zone along a 20 km belt in the Haslingden Group rocks. They formed around boudinaged pods of metadolerite dykes and in layers connecting pods as shown in Fig. 4.20. The host rocks are mainly muscovite-rich schists containing cordierite porphyroblasts, quartz, and biotite, with or without andalusite and sillimanite (Rubenach 1992). The metasomatic rocks consist of cordierite and quartz, with or without andalusite, sillimanite, minor biotite, and rare plagioclase. The metadolerite pods appear to show no alteration, except plagioclase is bytownite or anorthite up to one meter from the contact, while andesine is the usual composition in the metadolerite. Cordierite consists of two microstructural types in the metasomatic rocks. Earlier cores show inclusion trails that are truncated or curved into the enclosing S_2 foliation, identical to trails in cordierite in the host schists. More abundant is cordierite enclosing the cores and which contains inclusion trails aligned in S_2, which has clearly replaced the host muscovite. Mineral elongation in the schists plunges steeply south, as do intense lineations in some of the metasomatic rocks. The metasomatism involved addition of Mg and Fe and

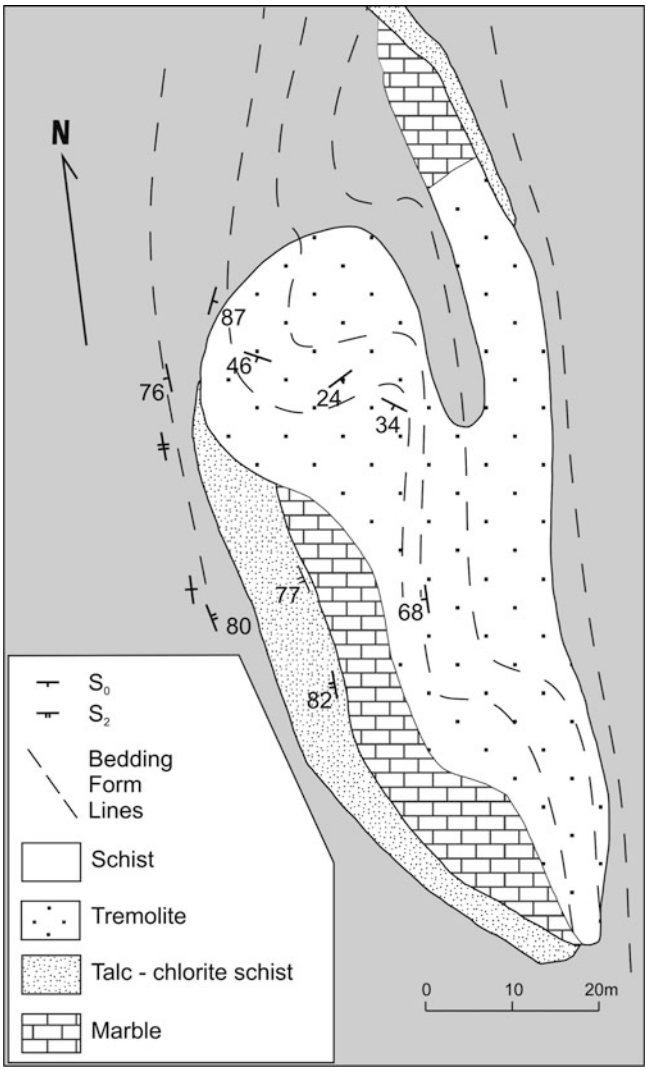

Fig. 4.18 Metasomatic tremolite pod with preserved fold hinges, commonly absent from the highly-strained enclosing schists. The tremolite has replaced marble, quartzite and psammite. Marble is preserved in strain shadows. Highly foliated talc-rich schist has replaced impure marble on the western side of the tremolite pod. The metasomatism is interpreted as forming syn-D_2

removal of K from the original schist (and some Na from the margins of the metadolerite). It is suggested that the fluids infiltrated microfractures that developed around the pods during the high-strain boudinage event. Microfractures are no longer visible but could have been removed during recrystallization. Pods of cordierite-anthophyllite, derived from the metamorphism of chlorite-quartz schists, occur in association with the metasomatic cordierite rocks (Fig. 4.4).

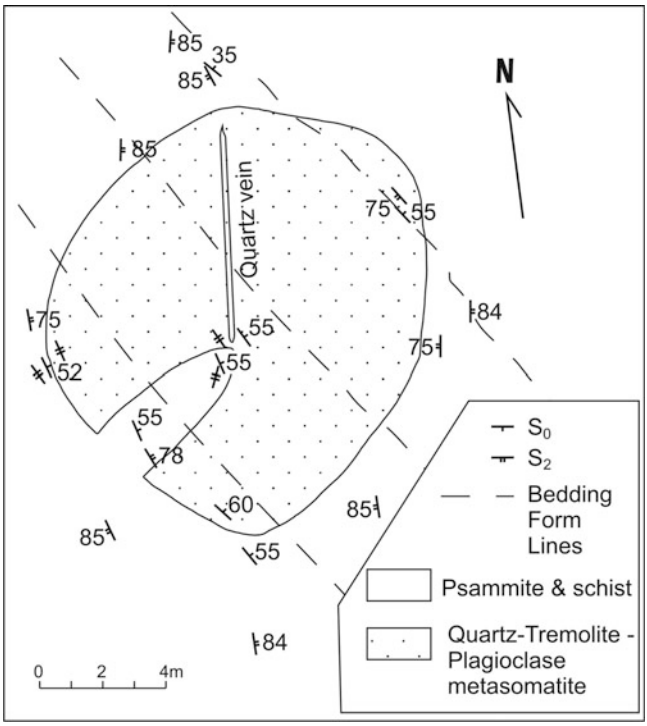

Fig. 4.19 Map of a metasomatic plagioclase-tremolite-quartz pod, centred on a quartz vein, which has replaced the quartz-muscovite-chlorite-biotite schist and metapsammitic rock. Bedding is undeflected while the S_2 foliation partly wraps around and refracts through the pod, suggesting syn-D_2 metasomatism

Devolatization of these schists is a likely source of fluids of fluids since they would have been saturated in Mg and under-saturated in K and Na (Fig. 4.20).

4.4.2.3 Sodic and Sodic-calcic Alteration in the Curnamona Province

Syn-metamorphic metasomatism has been described from an area of many hundreds of square kilometers in the Proterozoic Curnamona Province in South Australia. These show many similarities to those in the Eastern Succession of the Mount Isa Inlier in terms of lithologies, crustal depth, age, and inferred fluid sources. The metasomatism is mainly sodic-calcic, and includes albite-rich alteration zones in metasedimentary rocks, garnet-epidote-rich alteration zones, clinopyroxene- and actinolite-matrix breccias, and replacement ironstones (Chap. 7, Kent et al. 2000; Clark et al. 2006). The main structural controls are mid-crust shear zones. Isotopic studies indicate that the fluids are consistent with devolatilization of metasedimentary rocks of the host Willyama Supergroup deeper in the crust.

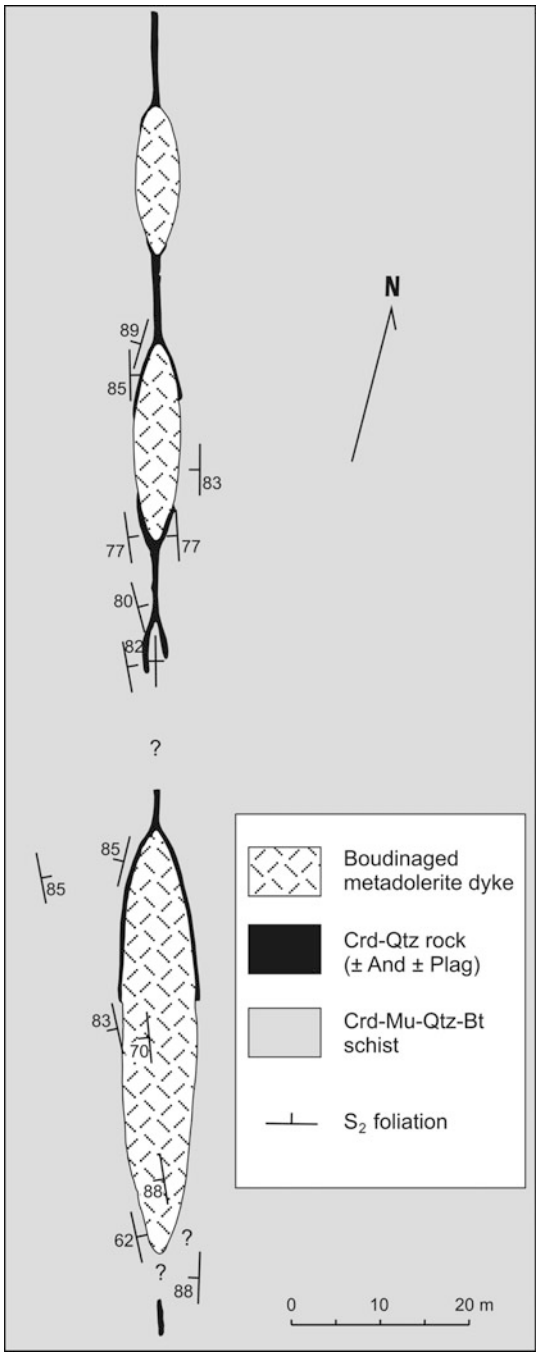

Fig. 4.20 Map of three bodies of a boudinaged metadolerite body, showing metasomatic cordierite rocks that formed around parts of their margins and within schists in the interboudin regions. The country rocks are mainly cordierite-bearing, muscovite-biotite schists, while the cordierite metasomatic rocks consist mainly of cordierite and quartz, with or without andalusite, biotite, sillimanite, and (one sample) plagioclase. It is proposed that fluids derived from the devolatilization of nearby chlorite-quartz rocks (to form cordierite-anthophyllite rocks) infiltrated and replaced highly strained schists around the boudins, adding Mg and Fe, and removing K

4.4.2.4 Albitization of Granite, Bamble Sector, Norway

Another example of regional albitization is in the Bamble Sector of southeast Norway. Here replacement of precursor plagioclase in granite by hematite-stained albite was controlled by fractures (Engvik et al. 2008). The albitized and scapolitized areas of the Bamble sector, alike the Mount Isa area, is spatially related to orthoamphibole cordierite rocks (Engvik et al. 2011).

4.4.2.5 Veins and Metasomatism in Connemara, Ireland

In his studies of veins in Dalradian metamorphic rocks from Connemara, Ireland, Yardley concludes that the fluids were mainly derived from dewatering of nearby higher grade rocks (Yardley 1986, 2009; Yardley and Bottrell 1992). In most cases there are no metasomatic selvages, with the rare exception of the veins at Knockaunbaun with decimeter-scale selvages containing staurolite, tourmaline, garnet, muscovite and plagioclase. The veins mainly formed after the Barrovian metamorphism during D_3 low-pressure metamorphism, probably due to hydrofracturing caused by dewatering and increase in fluid pressure.

4.5 Conclusions and Future Research

Some aspects of regional metasomatism are well established and non-controversial. Examples include the theoretical basis of metasomatic zoning, the occurrence of intrinsic permeabilities in porous sedimentary and pyroclastic rocks, and convective circulation of fluids under hydrostatic conditions in the upper crust. Similarly channelized fluid flow and metasomatism controlled by fractures, faults and shear zones are fairly well documented. Although the development of porosity via microfractures during ductile deformation is sound from theoretical and experimental perspectives, recrystallization during ongoing deformation/metamorphism has commonly removed most traces of these. In the absence of evidence for reaction-enhanced permeability or interface-coupled dissolution-precipitation (Chap. 5), microfractures are invoked for many metasomatized rocks (e.g. the albitized metapsammitic rocks in the Snake Creek Anticline). Another problem concerns determining the precise timing of metasomatism in a multiply deformed polymetamorphic terrain. The early albitites in the Snake Creek provide a good example of the problems involved, as overprinting deformation, metamorphic, and fluid infiltration events can obscure characteristics of the structural controls, mineralogy, fluid composition, and age of the original metasomatism. Reactivation of foliations in subsequent events is also fairly common (Bell 1986) and can provide problems in timing of metasomatism relative to foliation development.

Many aspects of regional metasomatism, particularly involving rocks in the middle or lower crust, are subject to debate. Examples include the following:

1. Is most regional metasomatism the result of single-pass upward flow of devolatilization fluids from deeper in the crust or is dilatancy pumping a viable mechanism in some areas?
2. Are the enormous values for time-integrated fluid fluxes real or an artifact of models used in their estimation? The scale of Na-Ca metasomatism in the Eastern Fold Belt, Mount Isa Inlier, certainly suggests advection of very large quantities of fluids over a number of metasomatic events.
3. Are significant volume losses inferred for cleavage or foliation development in some areas real? This requires considerable more research that includes well-controlled sampling.
4. The sources of fluids in some areas are clear, but in other localities stable isotope studies can yield ambiguous results. More isotopic research and fluid inclusion studies that include halogen and noble gas analyses are required.
5. Selvages around quartz veins remain subject to debate. Was the mass transport local, were large fluxes of external fluids also involved, and did large chemical changes actually occur? The study by Ague (2011) has involved more detailed controlled sampling, and clearly more studies like this are necessary. The conclusion of Ague (2011) that fluid flow and metasomatism may be quite heterogeneously developed along a single vein or across a series of veins may help in resolving some of the problems, especially as many workers typically sample one or two traverses across a vein. More studies are necessary to follow up this idea.

Acknowledgments The author has spent over 38 years at James Cook University researching metamorphic and metasomatic rocks of north Queensland, and colleagues T. Bell, T. Blenkinsop, D. Foster, W. Laing, N. Oliver, and P. Williams are particularly thanked for numerous discussions, especially on field trips. J. Ague, J. Ferry and B. Yardley provided very helpful reviews and suggestions. The editors, D. Harlov and H. Austrheim are thanked for their help and patience.

References

Ague JJ (1994a) Mass transfer during Barrovian metamorphism of pelites. south-central Connecticut. I: evidence for changes in composition and volume. Am J Sci 297:679–706

Ague JJ (1994b) Mass transfer during Barrovian metamorphism of pelites. south-central Connecticut. II: channelized fluid flow and the growth of staurolite and kyanite. Am J Sci 297:1061–1134

Ague JJ (2003) Fluid infiltration and transport of major, minor, and trace elements during regional metamorphism of carbonate rocks, Wepawaug Schist, Connecticut, USA. Am J Sci 303:753–816

Ague JJ (2004) Fluid flow in the deep crust. In: Holland HD, Tuekian KK, Rudnick RL (eds) Treatise on geochemistry, vol 3, The Crust. Elsevier, Amsterdam, pp 195–228

Ague JJ (2011) Extreme channelization of fluid and the problem of element mobility during Barrovian metamorphism. Amer Mineral 96:333–352

Angus NS, Kanaris-Sotiriou R (1995) Adinoles revisited: hydrothermal Na (Ca)-metasomatism of pelitic screens adjacent to tholeiitic dykes in the Dublin terrane. Ireland Mineral Mag 59:367382

Aslund T, Oliver NHS, Cartwright I (1995) Metasomatism of the revenue granite and aureole rocks, Mt Isa Inlier, Queensland: syndeformational fluid flow and fluid-rock interaction. Aust J Earth Sci 42:291–299

Austin JR, Blenkinsop TG (2010) Cloncurry fault zone: strain partitioning and reactivation in a crustal-scale deformation zone, Mt Isa Inlier. Aust J Earth Sci 57:1–21

Barton MD, Johnson DA (1996) Evaporitic-source model for igneous-related Fe oxide-(REE-Cu-Au-U) mineralization. Geology 24:259–262

Battles DA, Barton MD (1995) Arc-related sodic hydrothermal alteration in the western United States. Geology 24:913–916

Baumgartner LP, Ferry JM (1991) A model for coupled fluid-flow and mixed-volatile mineral reactions with applications to regional metamorphism. Contrib Miner Petrol 106:273–286

Beach A (1976) The interrelation of fluid transport, deformation, geochemistry, and heat flow in early proterozoic shear zones in the Lewisian complex. Phil Trans Roy Soc Lond A280:596–604

Beach A (1977) Vein arrays, hydraulic fractures and pressure-solution structures in a deformed flysch sequence. S.W. England. Tectonophysics 40:201–226

Beach A (1980) Retrograde metamorphic process in shear zones with special reference to the Lewisian complex. J Struct Geol 2:257–263

Bear J (1972) Dynamics of fluids in porous media. Dover, New York

Beinlich A, Austrheim H, Glodny J, Erambert M, Anderson TB (2010) CO_2 sequestration and extreme Mg depletion in serpentinized peridotite clasts from the Devonian Soland basin, SW-Norway. Geochim Cosmo Acta 74:6935–6994

Bell TH (1981) Foliation development – the contribution, geochemistry and significance of progressive bulk inhomogeneous shortening. Tectonophysics 75:273–296

Bell TH (1986) Foliation development and refraction in metamorphic rocks: reactivation of earlier foliations and decrenulation due to shifting patterns of deformation partitioning. J Metam Geol 4:421–444

Bertelli M, Baker T (2010) A fluid inclusion study of the suicide ridge breccia pipe, Cloncurry District, Australia: implications for breccia genesis and IOCG mineralization. Precamb Res 179:69–87

Bibby HM, Caldwell TG, Davey FJ, Webb TH (1995) Geophysical evidence on the structure of the Taupo volcanic zone and its hydrothermal circulation. J Volcan Geotherm Res 68:29–58

Bickle MJ (1992) Transport mechanisms by fluid-flow in metamorphic rocks: oxygen and strontium decoupling in the Trois Seigneurs massif – a consequence of kinetic dispersion? Am J Sci 292:289–316

Bickle MJ, Baker J (1990) Advective-diffusive transport of isotopic fronts: an example from Naxos, Greece. Earth Planet Sci Lett 97:78–93

Bickle MJ, McKenzie D (1987) The transport of heat and matter by fluids during metamorphism. Contrib Miner Petrol 95:384–392

Bjorlykke K (1997) Lithological control on fluid flow in sedimentary basins. In: Jamveit B, Yardley BWD (eds) Fluid flow and transport in rocks, mechanisms and effects. Chapman & Hall, London, pp 15–34

Bjorlykke K (1994) Fluid flow processes and diagenesis in sedimentary basins. In: Parnell J (ed) Geofluids: origin, migration and evolution of fluids in sedimentary Basins, vol 78, Geological Society Special Publication. Geological Society, London, pp 127–140

Boles JR (1982) Active albitization of plagioclase, Gulf Coast tertiary. Am J Sci 282:165–180

Brace WF (1980) Permeability of crystalline and argillaceous rocks. Int J Rock Mech Miner Sci 17:241–251

Breeding CM, Ague JJ (2002) Slab-derived fluids and quartz-vein formation in an accretionary prism, Otago Schist, New Zealand. Geology 30:499–502

Brimhall GH (1979) Lithologic determination of mass transfer mechanisms of multiple-stage porphyry copper mineralization at Butte, Montana: vein formation by hypergene leaching and enrichment of the potassium silicate protolith. Econ Geol 74:556–589

Cartwright I (1994) The two dimensional pattern of metamorphic fluid flow at Mary Kathleen, Australia: fluid focusing, transverse dispersion, and implications for modeling fluid flow. Am Miner 79:526–535

Cartwright I (1997) Permeability generation and resetting of traces during metamorphic fluid flow: implications for advection-dispersion models. Contrib Miner Petrol 129:198–208

Cartwright I, Buick IS (1995) Formation of wollastonite-bearing marbles during late regional metamorphic channeled fluid flow in the upper calcsilicate unit of the Reynolds range group, central Australia. J Metam Geol 13:397–417

Cartwright I, Oliver NHS (1994) Fluid flow during contact metamorphism at Mary Kathleen, Queensland, Australia. J Petrol 35:1493–1519

Cartwright I, Weaver TR (1993) Fluid-rock interaction between syenites and marbles at Stephen cross quarry, Quebec, Canada: petrological and stable isotope data. Contrib Miner Petrol 113:533–544

Cathles LM (1990) Scales and effects of fluid flow in the upper crust. Science 248:323–328

Chapin CE, Lindley JI (1986) Potassium metasomatism of igneous and sedimentary rocks in detachment terranes and other sedimentary basins: economic implications. Arizona Geol Soc Dig 16:118–126

Clark C, Hand M, Faure K, Schmid Mumm A (2006) Up-temperature flow of surface derived fluids in the mid crust: the role of pre-orogenic burial of hydrated fault rocks. J Metam Geol 24:367–387

Connolly JAD (2010) The mechanics of metamorphic fluid expulsion. Elements 6:165–172

Cook SJ, Bowman JR (2000) Mineralogical evidence for fluid-rock interaction accompanying prograde contact metamorphism of siliceous dolomites: Alta Stock, Utah, USA. J Petrol 41:739–757

Cook SJ, Bowman JR, Foster CB (1997) Contact metamorphism surrounding the Alta Stock: finite element model simulation of heat- and $^{18}O^{16}O$ mass-transport during prograde metamorphism. Amer J Sci 297:1–55

Cox SC (1993) Veins, fluids, fractals, scale and schist- an investigation of fluid-rock interaction during deformation of the Torlesse Terrane, New Zealand. Ph.D. thesis, University of Otago, Dunedin

Cox SF, Etheridge MA (1989) Coupled grain-scale dilatancy and mass transfer during deformation at high fluid pressure: examples from Mount Lyell, Tasmania. J Struct Geol 11:147–162

Cox SF, Wall VJ, Etheridge MA, Potter TF (1991) Deformation and metamorphic processes in the formation of mesothermal vein-hosted gold deposits – examples from the Lachlan Fold Belt in central Victoria, Australia. Ore Geol Rev 6:391–423

Davidson GJ (1999) Feldspar metasomatism along a Proterozoic rift-basin margin- "Smoke" around a base-metal "fire" (HYC deposit, Australia) or a product of background diagenesis? Geol Soc Am Bull 111:663–673

de Jong G, Williams PJ (1995) Giant metasomatic system formed during exhumation of mid-crustal Proterozoic rocks in the vicinity of the Cloncurry Fault, northwest Queensland. Aust J Earth Sci 42:281–290

Dipple GM, Ferry JM (1990) Identification of the scales of differential element mobility in a ductile fault zone. J Metam Geol 8:645–651

Dipple GM, Ferry JM (1992) Fluid flow and stable isotope alteration in rocks at elevated temperatures with applications to metamorphism. Geochim Cosmo Acta 56:3539–3550

Einaudi M, Meinert LD, Newberry RJ (1981) Skarn deposits. In: Economic geology 75th anniversary, El Paso, pp 317–391 (referred to also top of page 11, so should remain)

Engvik AK, Putnis A, Fitzgerald JD, Austrheim H (2008) Albitization of granitic rocks: the mechanism of replacement of oligoclase by albite. Can Miner 46:1401–1415

Engvik AK, Mezger K, Wortelkamp S, Bast R, Corfu F, Korneliussen A, Ihlen P, Bingen B, Austrheim H (2011) Metasomatism of gabbro – mineral replacement and element mobilization during the Sveconorwegian metamorphic event. J Metam Geol 29:399–423

Ennis DJ, Dunbar NW, Campbell AR, Chapin CE (2000) The effects of K-metasomatism on the mineralogy and geochemistry of silicic ignimbrites near Socorro, New Mexico. Chem Geol 167:285–312

Etheridge MA, Wall VJ, Vernon RH (1983) The role of the fluid phase during regional metamorphism and deformation. J Metam Geol 1:205–226

Etheridge MA, Wall VJ, Cox SF, Vernon RH (1984) High fluid pressures during regional metamorphism and deformation. J Geophys Res 89:4344–4358

Fedo CM, Young GM, Nesbitt HW, Hanchar JM (1997) Potassic and sodic metasomatism in the southern province of the Canadian shield: evidence from the paleoproterozoic serpent formation, Huronian Supergroup, Canada. Precamb Res 84:17–36

Ferry JM (1983) On the control of temperature, fluid composition, and reaction progress during metamorphism. Am J Sci 283A:201–232

Ferry JM (1986) Reaction progress: a monitor of fluid-rock interaction during metamorphic and hydrothermal events. In: Walther JV, Woods BJ (eds) Fluid-Rock interactions during metamorphism. Springer, New York, pp 60–88

Ferry JM (1984) A biotite isograd in south-central Maine, U.S.A.: mineral reactions, fluid transfer, and heat transfer. J Petrol 25:871–893

Ferry JM (1987) Metamorphic hydrology at 13 km depth and 400–500°C. Am Miner 72:39–58

Ferry JM (1992) Regional metamorphism of the waits river formation, eastern Vermont. Delineation of a new type of giant metamorphic hydrothermal system. J Petrol 33:45–94

Ferry JM (1994a) A historical review of metamorphic fluid flow. J Geophys Res 99:15487–15498

Ferry JM (1994b) Overview of the petrologic record of fluid flow during regional metamorphism in northern New England. Am J Sci 294:905–988

Ferry JM (1996) Prograde-retrograde fluid flow during contact metamorphism of siliceous carbonate rocks from the Ballachulish aureole, Scotland. Contrib Miner petrol 24:235–254

Ferry JM (2007) The role of volatile transport by diffusion and dispersion in driving biotite-forming reactions during regional metamorphism of the Gile Formation, Vermont. Am Miner 92:1288–1302

Ferry JM, Dipple GM (1991) Fluid flow, mineral reactions and metasomatism. Geology 19:211–214

Ferry JM, Dipple GM (1992) Models for coupled fluid flow, mineral reaction, and isotopic alteration during contact metamorphism: the Notch Peak aureole, Utah. Am Miner 77:577–591

Ferry JM, Gerdes M (1998) Chemically reactive fluid flow during metamorphism. Ann Rev Earth Planet Sci 26:255–287

Ferry JM, Gottschalk M (2009) The effect of fluid salinity on infiltration-driven contact metamorphism of carbonate rocks. Contrib Miner Petrol 158:619–636

Ferry JM, Rumble D III (1997) Formation and destruction of periclase by fluid flow in two contact aureoles. Contrib Miner Petrol 130:313–334

Ferry JM, Rumble DIII, Wing BA, Penniston-Dorland SC (2005) A new interpretation of centimeter-scale variations in the progress of infiltration-driven metamorphic reactions: case study of carbonated metaperidotite, Val d'Efra, Central Alps Switzerland. J Petrol 46:1725–1746

Ferry JM, Wing BA, Penniston-Dorland SC, Rumble D III (2002) The direction of fluid flow during the contact metamorphism of siliceous carbonate rocks: new data for the Monzoni and Predazzo aureoles, northern Italy, and a global review. Contrib Miner Petrol 142:679–699

Fletcher RC, Hoffman AW (1974) Simple models of diffusion and combined diffusion-infiltration metasomatism. In: Hoffman AW, Giletti B, Yoder HS Jr, Yund RA (eds) Geochemical transport and kinetics. Carnegie Institute of Washington, Washington, pp 242–262

Fyfe WS, Kerrich R (1985) Fluids and thrusting. Chem Geol 49:353–362

Fyfe WS, Price NJ, Thompson AB (1978) Fluids in the Earth's crust. Elsevier, Amsterdam

Garven G (1985) The role of regional fluid flow in the genesis of the pine point deposit, Western Canada sedimentary basin. Econ Geol 80:307–324
Garven G (1995) Continental-scale groundwater flow and geologic processes. Ann Rev Earth Planet Sci 23:89–117
Gerdes ML, Valley JW (1994) Fluid flow and mass transport at the Valentine wollastonite mine, Adirondack Mountains, New York. J Metam Geol 12:589–608
Graham CM, Valley JW, Eiler JM, Wada H (1998) Timescales and mechanisms of fluid infiltration in a marble: an ion microprobe study. Contrib Miner Petrol 132:371–389
Gray DR (1997) Volume loss and slaty cleavage development. In: Sengupta S (ed) Evolution of geological structures in micro- to macro-scales. Chapman Hall, London, pp 273–291
Hanson RB (1992) Effects of fluid production on fluid flow during regional and contact metamorphism. J Metam Geol 10:87–97
Hitzman NW, Oreskes N, Carlson WD (1992) Geological characteristics and tectonic setting of proterozoic iron oxide (Cu-Au-U-REE) deposits. Precamb Res 58:241–287
Holness MB (2003) Growth and albitization of K-feldspar in crystalline rocks in the shallow crust: a tracer for fluid circulation during exhumation. Geofluids 3:89–102
Holness MB, Graham CM (1991) Equilibrium dihedral angles in the system H_2O-CO_2-NaCl-calcite, and implications for fluid flow during metamorphism. Contrib Miner Petrol 119:301–313
Huang W, Rubenach MJ (1995) Structural controls on syn-tectonic metasomatic tremolite and tremolite-plagioclase pods in the Molanite Valley, Mt. Isa, Australia. J Struct Geol 17:83–94
Jamtveit B, Bucher-Nurminen K, Stijfhoon DE (1992a) Contact metamorphism of layered shale-carbonate sequences in the Oslo rift: I. Buffering, infiltration and the mechanism of mass transport. J Petrol 33:377–422
Jamtveit B, Grorud HF, Bucher-Nurminen K (1992b) Contact metamorphism of layered shale-carbonate sequences in the Oslo rift: II. Migration of isotopic and reaction fronts around cooling plutons. Earth Planet Sci Let 114:131–148
Jamtveit B, Yardley BWD (1997) Fluid flow and transport in rocks, mechanisms and effects. Chapman & Hall, London
Kendrick MA, Baker T, Fu B, Phillips D, Williams PJ (2008) Noble gas and halogen constraints on regionally extensive mid-crustal Na-Ca metasomatism, the Proterozoic Eastern Mount Isa Block, Australia. Precamb Res 163:131–150
Kent AJR, Ashley PM, Fanning CM (2000) Metasomatic alteration associated with regional metamorphism: an example from the Willyama Supergroup, South Australia. Lithos 54:33–62
Korzhinskii DS (1950) Phase rule and geochemical mobility of elements. In: Eighteenth international geological congress, Part 2 Sect. A, London, pp 50–57
Korzhinskii DS (1959) Physicochemical basis of the analysis of the paragenesis of minerals. Consultants Bureau, New York
Korzhinskii DS (1970) The theory of metasomatic zoning. Clarendon, Oxford
Kwak TAP (1978) Mass balance relationships and skarn forming processes at the King Island scheelite deposit, Tasmania, Australia. Am J Sci 278:943–968
Kwak TAP, Askins PW (1981a) The nomenclature of carbonate replacement deposits, with emphasis on Sn-F (Be-Zn) 'wrigglite' skarns. Geol Soc Aust J 28:123–136
Kwak TAP, Askins PW (1981b) The geology and genesis of laminar F-Sn-W (-Be-Zn) skarns at Moina, Tasmania, Australia. Econ Geol 76:439–467
Labotka TC, Nabelek PI, Papike JJ (1988) Fluid infiltration through the big horse limestone member in the Notch Peak contact-metamorphic aureole, Utah. Amer Miner 73:1302–1324
Lee JI, Lee YI (1998) Feldspar albitization in Cretaceous non-marine mudrocks, Gyeongsang Basin, Korea. Sedimentology 45:1959–1981
Lentz DR (1998) Mineralized intrusion-related skarn systems, vol 26, Min Soc Canada Short Course Series. Mineralogical Association of Canada, Ottawa, p 66
Lonker SW, Fitzgerald JD, Hedenquist JW, Walshe JL (1990) Mineral-fluid interactions in the Broadlands-Ohaaki geothermal system, New Zealand. Am J Sci 290:995–1068

Lyubetskaya T, Ague JJ (2010) Modeling metamorphism in collisional orogens intruded by magmas: II. Fluid flow and implications for Barrovian and Buchan metamorphism, Scotland. Am J Sci 310:459–491

Mark G, Oliver NHS, Williams PJ (2006) Mineralogical and chemical evolution of the Ernest Henry Fe oxide-Cu-Au ore system, Cloncurry district, northwest Queensland. Miner Deposita 40:769–801

Marshall LJ, Oliver NHS (2008) Constraints on the hydrothermal pathways within Mary Kathleen Group stratigraphy of the Cloncurry iron-oxide-copper-gold District, Australia. Precamb Res 163:151–158

Masters RL, Ague JJ (2005) Regional-scale fluid flow and element mobility in Barrow's metamorphic zones, Stonehaven, Scotland. Contrib Miner Petrol 97:1–18

McCaig AM (1997) The geochemistry of volatile fluid flow in shear zones. In: Holness MB (ed) Deformation-enhanced fluid transport in the earth's crust and mantle. Chapman and Hall, London, pp 227–266

McLellan JG, Oliver NHS (2008) Application of numerical modeling to extension, heat and fluid flow in the genesis of giant banded iron formation-hosted hematite ore deposits. Soc Econ Geol Rev 15:185–196

Meinert LD, Dipple GM, Nicolescu S (2005) World skarn deposits. In: Hedenquist JW, Thompson JFH, Goldfarb RJ, Richards JPC (eds) Economic geology 100th anniversary volume. Soc Econ Geol, Littleton, pp 299–336

Mottl MJ (1983) Metabasalts, axial hot springs, and the structure of hydrothermal systems at mid-ocean ridges. Bull Geol Soc Am 94:161–180

Nabelek PI (1991) Stable isotope monitors. In: Kerrick DM (ed) Contact metamorphism, vol 26, Reviews in Mineralogy. Mineralogical Society of America, Washington, DC, pp 395–435

Nabelek PI, Labotka TC (1993) Implications of geochemical fronts in the Notch Peak contact aureole, Utah, USA. Earth Planet Sci Lett 119:539–559

Nabelek PI, Labotka TC, O'Neil JR, Papike JJ (1984) Contrasting fluid/rock interaction between the Notch Peak granitic intrusion and argillites and limestones in western Utah: evidence from stable isotopes and phase assemblages. Contrib Miner Petrol 86:25–34

Norton DL (1988) Metasomatism and permeability. Am J Sci 288:604–618

Oliver NHS (1995) Hydrothermal history of the Mary Kathleen Fold Belt, Mt Isa Block, Queensland. Aust J Earth Sci 42:267–280

Oliver NHS (1996) Review and classification of structural controls on fluid flow during regional metamorphism. J Metam Geol 14:477–492

Oliver NHS, Bons PD (2001) Mechanisms of fluid flow and fluid-rock interaction in fossil metamorphic hydrothermal systems inferred from vein-wall rock patterns, geometry and microstructure. Geofluids 1:137–162

Oliver NHS, Butera K, Rubenach MJ, Marshall LJ, Cleverley JS, Mark G, Fu B, Tullemans F, Esser D (2008) The protracted hydrothermal evolution of the Mount Isa eastern succession: a review and tectonic implications. Precamb Res 163:108–130

Oliver NHS, Cleverley JS, Mark G, Pollard PJ, Fu B, Marshall LJ, Rubenach MJ, Williams PJ, Baker T (2004) Modeling the roll of sodic alteration in the genesis of iron oxide-copper-gold deposits, eastern Mount Isa Block, Australia. Econ Geol 99:1145–1176

Oliver NHS, Pearson PJ, Holcombe RJ, Ord A (1999) Mary Kathleen metamorphic-hydrothermal uranium-rare earth deposit: ore genesis and a numerical model of coupled deformation and fluid flow. Aust J Earth Sci 46:467–484

Oliver NHS, Rubenach MJ, Fu B, Baker T, Blenkinsop TG, Cleverley JS, Marshall LJ, Ridd PJ (2006) Granite-related overpressure and volatile release in the mid crust: fluidized breccias from the Cloncurry district, Australia. Geofluids 6:346–358

Oliver NHS, Valenta RK, Wall VJ (1990) The effect of heterogeneous stress and strain on metamorphic fluid flow, Mary Kathleen, Australia, and a model for large-scale fluid circulation. J Metam Geol 8:311–331

Parnell J (1994) Geofluids: origin, migration and evolution of fluids in sedimentary Basins, vol 78, Geological Society Special Publication. Geological Society, London
Penniston-Dorland SC, Ferry JM (2006) Development of spatial variations in reaction progress during regional metamorphism of micaceous carbonate rocks, northern New England. Am J Sci 306:475–524
Penniston-Dorland SC, Ferry JM (2008) Element mobility and scale of mass transport in the formation of quartz veins during regional metamorphism of the waits river formation, east-central Vermont. Am Miner 93:7–21
Person M, Garven G (1994) A sensitivity study of the driving forces on fluid flow during continental-rift basin evolution. Geol Soc Am Bull 106:461–475
Pettijohn FJ, Baston H (1959) Chemical composition of argillites of the Cobalt Series (Precambrian) and the problem of soda-rich sediments. Geol Soc Am Bull 70:593–599
Polito PA, Kyser TK, Southgate PN, Jackson MJ (2006) Sandstone diagenesis in the Mount Isa Basin: an isotopic and fluid inclusion perspective in relationship to district-wide Zn, Pb and Cu mineralization. Econ Geol 101:1159–1185
Putnis A, Austrheim H (2010) Fluid-induced processes: metasomatism and metamorphism. Geofluids 10:254–269
Qiu L, Rudnick RL, Ague JJ, McDonough WF (2011) A lithium isotope study of sub-greenschist-facies metamorphism in an accretionary prism, New Zealand. Earth Planet Sci Let 301:213–221
Roselle GT, Baumgartner LP, Valley JW (1999) Stable isotope evidence of heterogeneous fluid infiltration at the Ubhebe Peak contact aureole, Death Valley national park, California. Am J Sci 299:93–138
Rowland JV, Sibson RH (2004) Structural controls on hydrothermal flow in a segmented rift system, Taupo Volcanic Zone, New Zealand. Geofluids 4:259–283
Rubenach MJ (1992) Proterozoic low pressure/high temperature metamorphism and an anticlockwise P-T-t path for the Hazeldene area, Mount Isa Inlier, Queensland. Aust J Metam Geol 10:333–346
Rubenach MJ (2005) Relative timing of albitization and chlorine enrichment in biotite in Proterozoic schists, Snake Creek Anticline, Mount Isa Inlier, northeastern Australia. Canad Miner 43:349–72
Rubenach MJ, Barker AJ (1998) Metamorphic and metasomatic evolution of the Snake Creek Anticline, eastern succession, Mount Isa Inlier. Aust J Earth Sci 45:363–372
Rubenach MJ, Foster DRW, Evins PM, Blake KL, Fanning CM (2008) Age constraints on the tectonothermal evolution of the Selwyn Zone, Eastern Fold Belt, Mount Isa Inlier. Precamb Res 163:81–107
Rubenach MJ, Lewthwaite KA (2002) Metasomatic albitites and related biotite-rich schists from a low-pressure metamorphic terrane, Snake Creek Anticline, Mount Isa Inlier, north-eastern Australia: microstructures and P-T-d paths. J Metam Geol 20:191–202
Rumble DIII (1994) Water circulation in metamorphism. J Geophys Res 99:15499–15502
Scholle PA, Ulmer-Scholle DS (2003) A color guide to the petrography of carbonate rocks: grains, textures, porosity, diagenesis, vol 77, American Association of Petroleum Geologists Memoir. American Association of Petroleum Geologists, Tulsa
Sibson RH (1987) Earthquake rupturing as a mineralizing agent in hydrothermal systems. Geology 15:701–704
Sibson RH (1989) Earthquake faulting as a structural process. J Struct Geol 11:1–14
Skelton ADL, Graham CM, Bickle MJ (1995) Lithological and structural controls on regional 3-D fluid flow patterns during greenschist-facies metamorphism of the Dalradian of the SW Scottish Highlands. J Petrol 36:563–586
Skelton ADL, Valley JW, Graham CM (2000) The correlation of reaction and isotopic fronts and the mechanism of metamorphic fluid flow. Contrib Miner Petrol 138:364–375
Steiner A (1977) The Waiakei geothermal area, North Island, New Zealand. New Zeal Geol Surv Bull 90:136

Streit JE, Cox SF (1998) Fluid infiltration and volume change during mid-crustal mylonitization of Proterozoic granite, King Island, Tasmania. J Metam Geol 16:197–212
Upton P, Craw D (2009) Mechanisms of strain-rate-and reaction-dependent permeability in the mid-crust of the Southern Alps: insight from three-dimensional mechanical models. Geofluids 9:287–302
Vernon RH (1998) Chemical and volume changes during deformation and prograde metamorphism of sediments. In: Treloar PJ, O'Brien P (eds) What drives metamorphism and metamorphic reactions? vol 138, Geological society London special publication. Geological Society, London, pp 215–246
Vernon RH, Clarke GL (2008) Principles of metamorphic geology. Cambridge University Press, New York
Vidale R (1969) Metasomatism in a chemical gradient and the formation of calc-silicate bands. Am J Sci 267:857–874
Vidale R, Hewitt DA (1973) "Mobile" components in the formation of calc-silicate bands. Am Miner 58:91–97
Williams PJ (1998) Metalliferous economic geology of the Mount Isa eastern succession, Queensland. Aust J Earth Sci 45:329–342
Wing BA, Ferry JM (2002) Three-dimensional geometry of metamorphic fluid flow during Barrovian regional metamorphism from an inversion of combined petrologic and stable isotope data. Geology 30:639–642
Wing BA, Ferry JM (2007) Magnitude and geometry of reactive fluid flow from direct inversion of spatial patterns of geochemical alteration. Am J Sci 307:793–832
Wood BW, Walther JV (1986) Fluid flow during metamorphism and its implications for fluid-rock ratios. In: Walther JV, Wood BJ (eds) Fluid-Rock interactions during metamorphism. Springer, New York, pp 89–108
Yardley BWD (1986) Fluid migration and veining in the Connemara Schists, Ireland. In: Walther JV, Wood BJ (eds) Fluid-rock interaction during metamorphism. Springer, New York, pp 109–131
Yardley BWD (2009) The role of water in the evolution of the continental crust. J Geol Soc Lond 166:585–600
Yardley BWD, Bottrell SH (1992) Silica mobility and fluid movement during metamorphism of the Connemara schists, Ireland. J Metam Geol 10:453–464
Yardley BWD, Lloyd GE (1995) Why metasomatic fronts are metasomatic sides. Geology 23:53–56

Chapter 5
Mechanisms of Metasomatism and Metamorphism on the Local Mineral Scale: The Role of Dissolution-Reprecipitation During Mineral Re-equilibration

Andrew Putnis and Håkon Austrheim

Abstract Metamorphism and metasomatism both involve the re-equilibration of mineral assemblages due to changes in pressure, temperature and/or chemical environment. Both processes involve material transport but on different length scales, and therefore every metamorphic reaction is metasomatic on a local scale. Fluids provide a transport mechanism which is orders of magnitude faster than solid state diffusion and induce re-equilibration through dissolution of parent phases and reprecipitation of products. This chapter deals with some of the questions related to such processes, including the mechanisms of fluid transport through low permeability rocks, how coupling between dissolution and precipitation retains the volume of a rock during metamorphism and metasomatism, and how textural criteria are used to define mechanisms of reactions. These issues are illustrated by examples taken from experiments as well as reactions in nature including a review of some aspects of the transformation of aragonite to calcite, the albite to jadeite + quartz reaction, albitization, the origin of compositional zoning and inclusions in apatite, garnet replacement textures during eclogitization and the reaction mechanisms that produce corona textures. The chapter ends with a summary of the mechanism of pseudomorphic replacement by interface-coupled dissolution-precipitation.

A. Putnis (✉)
Institut für Mineralogie, University of Münster, Corrensstrasse 24, Münster 48149, Germany
e-mail: putnis@uni-muenster.de

H. Austrheim
Physics of Geological Processes, University of Oslo, P.O. Box 1048, Blindern N-0316 Oslo, Norway

D.E. Harlov and H. Austrheim, *Metasomatism and the Chemical Transformation of Rock*, Lecture Notes in Earth System Sciences,
DOI 10.1007/978-3-642-28394-9_5,

5.1 Introduction

The underlying factors driving metasomatism and metamorphism have been known for many years. It is instructive to look back on the state of knowledge summarised in the highly influential books of Turner and Verhoogen (1951, 1960) where the chemical principles governing metamorphism were clearly outlined, albeit in a descriptive way. No clear distinction between metamorphism and metasomatism was made, although "metasomatic metamorphism" was defined as metamorphism involving a substantial change in chemical composition. The role of fluids and deformation as catalytic influences was implied throughout, and in the discussion of the rates of metamorphic reactions it was suggested that metamorphism occurs only when a rock is simultaneously subjected to one or both of these catalytic influences at temperature and pressure conditions within the "metamorphic range".

Since that time very significant advances have been made in our understanding of the global tectonics that creates different regions of pressure and temperature within the crust. Understanding the effect of pressure, differential stress and temperature on mechanisms of mineral and rock deformation has benefited enormously from advances in materials science, and deformation-mechanism maps (Frost and Ashby 1982) have had an important influence on the way different regimes of rock deformation have been understood. The application of transmission electron microscopy (TEM) to visualise defects associated with deformation was also based on the influence of materials science on mineralogy, an influence accelerated by the fact that the first TEM studies of lunar rocks returned by the Apollo Program were made by materials scientists, not mineralogists. The interpretation of mineral microstructures at the TEM scale (Wenk 1976) was also based squarely on a "materials science approach", a term also used in the application of materials science principles to mineralogy teaching (Putnis 1992).

The same approach has been used to understand the way in which minerals respond to changes in temperature and pressure. This response, sometimes called "mineral behaviour" (Putnis and McConnell 1980), documents the various types of phase transformations that take place to reduce the free energy and involves a rich variety of chemical and structural reorganisation mechanisms. The need to quantify the thermodynamics of these phase transformations has also underpinned the development of metamorphic petrology, from the situation described by Turner and Verhoogen (1960) to the present day. With the acquisition of thermodynamic data for a wide range of minerals (and increasingly mineral solid solutions) it has become possible to use computer programs such as THERMOCALC (Holland and Powell 1998) to define the stability fields of different mineral assemblages in pressure-temperature (P-T) space, and to construct P-T pseudosections to show the mineral phase relationships for a specific bulk composition. The popularity of this thermodynamic approach to metamorphic petrology is obvious when the goal is to define the equilibrium pressure and temperature attained for a specific mineral assemblage in a rock.

From a sequence of stable mineral assemblages, usually inferred from an interpretation of textures in a metamorphic rock, P-T paths can be constructed on the pseudosections and interpreted in terms of the metamorphic history of the rock. Common methods of inferring P-T paths rely on evidence for incomplete reactions as a rock moves from one P-T regime to another. The partial preservation of a previous assemblage, either as mineral inclusions, partial replacement textures or reaction coronas, is used to infer that the two assemblages define equilibrium on either side of a univariant reaction curve. The textural interpretation of metamorphic rocks introduces the question of the reaction mechanism, an issue not addressed in a thermodynamic description of the relationship between two different mineral assemblages related by a reaction in P-T space. However, the interpretation of metamorphic textures in terms of metamorphic events is problematic, as pointed out by Vernon et al. (2008) and Putnis and Austrheim (2010) and will be discussed later in this chapter.

The success of the thermodynamic approach in interpreting metamorphic assemblages in isochemical rock systems has driven a wedge between metamorphism and metasomatism as rock-forming processes. While metamorphism seems to be based on a solid foundation of thermodynamics of reactions, allowing quantification of the crustal conditions where it has taken place, metasomatism has been considered as a somewhat elusive and descriptive process often relegated to describing unusual mineral assemblages which cannot be readily explained by the metamorphism of 'normal' rocks, and only relevant in a restricted range of localised hydrothermal environments such as skarns. However, we should point out that in practical and applied aspects of petrology such as in ore-prospecting, the concept of large-scale metasomatism is widely accepted as a mechanism for the mass transfer required to produce an ore-body.

Nevertheless, the obvious problems associated with not knowing the composition of fluids moving in or out of a particular rock body during metasomatism, not often knowing the composition of the parent rock which may be totally replaced, nor how a fluid can pervasively infiltrate a low permeability rock, made the study of metasomatism unattractive compared with the certainties inspired by a solid grasp of the thermodynamics of metamorphic reactions.

The ultimate demise of metasomatism as a large-scale rock forming process can be traced back to the 'granite controversy' in the mid twentieth century when the petrological community became divided into the metasomatists who argued that granites had a metasomatic origin (granitization) (Read 1957) and magmatists who favoured an igneous origin. The magmatists won the argument with the experimental work of Tuttle and Bowen (1958) and for many years metasomatism was neglected as a large-scale rock-forming process.

The description of metamorphic reaction mechanisms moved towards a 'solid state' interpretation, with mass transport by volume or grain-boundary diffusion, together with deformation by solid state creep. While the role of fluids in increasing reaction rates was well known, their compositional role in metamorphic reactions was an inconvenient complication in a thermodynamic description.

The importance of studying the textures of metamorphic rocks at all scales from the field to the nano-scale cannot be overestimated. Classic examples such as the demonstration that the eclogitisation of granulitic rocks in the Bergen Arcs, western Norway is more dependent on fluid access and deformation than *P–T* conditions alone (Austrheim 1987; Jamtveit et al. 1990; Austrheim et al. 1997), and the determination of fluid fluxes necessary to maintain metamorphic reactions (Ague 1994, 2003) has been the basis for a gradual reappraisal of the role of fluids in metamorphism and the mechanistic relationships between metamorphism and metasomatism. The role of the fluid phase in metamorphism, underrated for many years, has recently experienced a comeback (Philpotts and Ague 2009; Jamtveit and Austrheim 2010 and references therein) and the fact that aqueous fluids must be involved in the large scale re-equilibration in metamorphic reactions has been demonstrated by petrological, mineralogical, microstructural and isotopic data.

When we consider re-equilibration reactions in the presence of a fluid phase on a local mineral scale, the distinction between a metamorphic and a metasomatic mechanism disappears. No reaction can take place without transport of chemical components, and the distinction between metamorphism and metasomatism depends on an arbitrary selection of a length scale over which mobility takes place. As Carmichael (1969) has pointed out, on a small spatial scale every metamorphic reaction is chemically "open" with transport of reactants over some distance, while on a larger scale it may be closed i.e. isochemical.

The predominant mechanism of reequilibration of solids in the presence of an aqueous fluid involves processes of dissolution, transport and precipitation. A typical metamorphic or metasomatic reaction involves a complex chemical process where the coupling of each of these individual steps may result in the disappearance of one phase and the appearance of another. Textural studies of even an apparently simple reaction such as the kyanite to sillimanite inversion during prograde Barrovian type metamorphism probably involves a complex sequence of locally metasomatic reactions involving the dissolution of kyanite and quartz and precipitation of muscovite while in adjacent parts of the rock muscovite may break down to form sillimanite and quartz. Carmichael (1969) is a particularly instructive paper to read in this context.

An important general outcome is that a chemically balanced metamorphic reaction which may reflect the parent and product phases which can be identified in a rock, does not describe a reaction mechanism. A chemically balanced equation such as:

$$\begin{aligned} KAl_3Si_3O_{10}(OH)_2 + \ SiO_2 = \ KAlSi_3O_8 + \ Al_2SiO_5 + H_2O \\ \text{muscovite} + \text{quartz} = \text{K} - \text{feldspar} + \ \text{andalusite} \end{aligned} \tag{5.1}$$

does not literally mean that muscovite directly reacts with quartz, but that muscovite, quartz and possibly other minerals in the rock go into solution, which moves

a certain distance through the rock ultimately precipitating K-feldspar and andalusite elsewhere.

An important aspect of any metamorphic or metasomatic reaction is also to consider the volume changes involved in a reaction. A century ago Lindgren (1912, 1918) recognised the problem that in a rigid rock the dissolution of parent phases and the simultaneous precipitation of product phases must take place without a change in the volume of the rock. Thus metamorphic and metasomatic reactions should be balanced on volume. The same issues are still discussed in the current literature, and a very topical example is the reaction describing the serpentinisation of olivine by aqueous solution, which been written in many different ways. For example:

$$2Mg_2SiO_4 + 3H_2O \Rightarrow Mg_3[Si_2O_5](OH)_4 + Mg(OH)_2 \tag{5.2}$$

$$2Mg_2SiO_4 + 2H^+ + 2H_2O \Rightarrow Mg_3[Si_2O_5](OH)_4 + Mg^{2+} \tag{5.3}$$

$$3Mg_2SiO_4 + H_4SiO_{4(aq)} + 2H_2O \Rightarrow 2Mg_3[Si_2O_5](OH)_4 \tag{5.4}$$

$$5Mg_2SiO_4 + 2H_2O + 8H^+ \Rightarrow 2Mg_3[Si_2O_5](OH)_4 + 4Mg^{2+} + H_4SiO_{4(aq)} \tag{5.5}$$

Given the approximate molar volumes of olivine (~46.5 cm^3), serpentine – antigorite (~110 cm^3) and brucite (~24.5 cm^3) and only taking into account the volumes of the solid phases, it is clear that reactions 5.2 through 5.4 all involve large increases in volume of the rock, whereas reaction 5.5 is approximately isovolumetric, but requires both Mg and Si to be removed in solution. In an open system it is always possible to write an equation to preserve solid volume using fractional molar quantities of solid phases and allowing the other components to be added or subtracted by the fluid phase. Determining the most appropriate form of the reaction is however still problematic. Some of the reactions require unacceptably large volume increases, which are not consistent with textural observations in the field or on a thin section scale, while volume balancing reactions involve a large amount of water to remove relatively low solubility silica.

This chapter will be concerned with a number of the issues raised above, addressed using examples from nature as well as from experiments.

1. If fluids are required for metamorphic and metasomatic reactions to occur, what is the mechanism for fluid infiltration through a rock?
2. How are dissolution – transport – precipitation processes coupled to retain the volume of a rock during metamorphism and metasomatism?
3. How reliable are the textural criteria for defining a metamorphic reaction and deriving a P-T path?

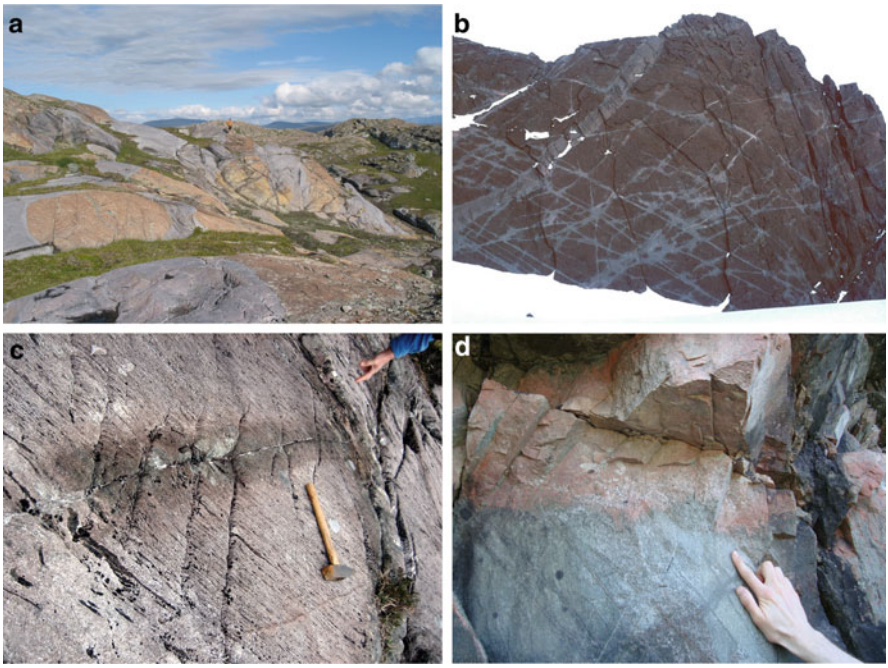

Fig. 5.1 (**a**) Interfaces between talc-rich and serpentinite rich rocks at Linnajavre, northern Norway. (**b**) Rock wall at Rakekniven, Dronning Maud Land, Antactica with reaction interfaces between amphibolitized rocks and granulites. The wall is 300 m high. (**c**) A *dark* band of eclogite along a fracture in granulites, Bergen Arcs, western Norway. (**d**) Reaction interface between *pink* albitite and *darker* parent rock, Bamble Sector, southern Norway

5.2 Reaction Interfaces

To determine the mechanism of metamorphic and metasomatic reactions we need to find examples of interfaces and reaction textures that contain both the parent and the product phases of a reaction. Reaction interfaces can be observed at all scales. Figure 5.1a shows reaction interfaces between talc rich and serpentine-rich rocks which can be seen on bare rock exposures in Northern Norway. Figure 5.1b shows a cliff face in Antarctica where it is clear that reactions from the darker granulites to the greener amphibolites are associated with fractures. Figure 5.1c shows a dark band of eclogite following a fracture within the lighter anorthositic granulite in the Bergen Arcs, western Norway. Finally, Fig. 5.1d shows a reaction interface between pink albitic feldspar and the grey parent rock being replaced in the Bamble Sector, southern Norway.

The common feature in all of these images is that some kind of a reaction took place at an interface which was arrested in its progress through the parent rock. The reasons for these metamorphic – metasomatic reactions stopping at the interface are more likely to be related to limitations in the fluid availability or the fluid transport

than with any variations in temperature or pressure. When we see such reaction interfaces on a small scale, it may seem that it is merely a localised phenomenon. However, large volumes of rock may be affected in this way, but without seeing an interface with the parent rock, their origin may be misinterpreted. Although there are textural similarities in the examples above, the minerals and the physical and chemical conditions for the reactions are very different in each case. In the examples below we will consider the reactions taking place at the interfaces shown in Fig. 5.1c, d in more detail.

5.3 Fluid-Mineral Interaction at the Mineral Interface

5.3.1 Example 1: Aragonite: Calcite

When a fluid interacts with a mineral with which it is out of equilibrium, the most obvious process is that it will begin to dissolve. Whatever the solubility of the mineral, it will continue to dissolve until it reaches equilibrium with the fluid. In low permeability rocks, the amount of fluid will always be limited and confined to grain boundaries, fractures and pores. The rate of dissolution also varies from one mineral to another and depends highly on fluid composition. If we consider a trivial case such as the interaction of calcite ($CaCO_3$) with pure water, the calcite will dissolve until the ion activity product ($IAP = a_{Ca^{2+}}.a_{CO_3^{2-}}$) is equal to the solubility product of calcite. On the other hand, if the reacting phase is aragonite, an aqueous solution in equilibrium with aragonite at low T and P is supersaturated with respect to calcite, because aragonite is less stable and hence more soluble than calcite under these conditions. The question then is whether calcite would precipitate from this solution, and hence whether this dissolution-precipitation mechanism is an efficient way of converting aragonite to calcite.

This simple example, which can be increased in complexity by choosing minerals with more complex chemistry reacting with multicomponent aqueous solutions, forms the basis for the principles of fluid-mediated equilibration of minerals (Putnis and Putnis 2007). Whenever a mineral is in contact with an aqueous solution, the dissolution of even a few monolayers of the parent surface, mixed at the interface with the original aqueous solution, may result in an interfacial fluid composition, which is supersaturated with respect to a more stable solid phase (or phases). If this product phase shares some crystal structural features, such as similar interatomic distances on the surface, with the parent phase, it may nucleate on the surface of the parent, initiating a process which could eventually produce a pseudomorphic replacement of one mineral by another chemically or structurally different mineral. This would imply a coupling of the dissolution and precipitation and some mechanism whereby the fluid phase could remain in contact with the parent solid throughout the replacement.

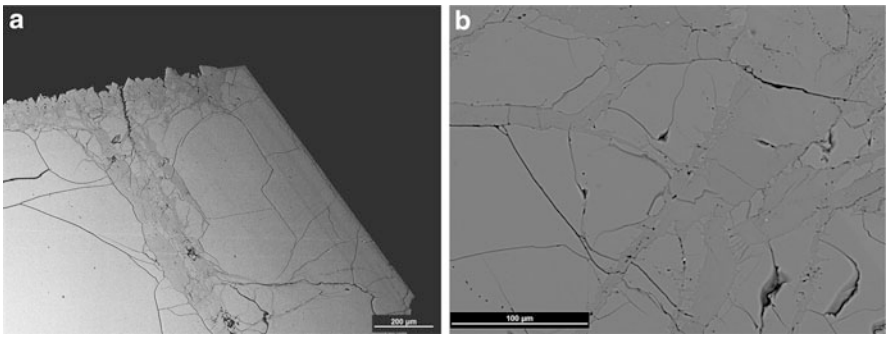

Fig. 5.2 BSE image of an aragonite crystal partially replaced by calcite in a hydrothermal experiment at 160°C. (**a**) The calcite is the slightly *darker* phase forming along the central fracture as well as overgrowths on the surface of the aragonite. (**b**) Calcite replacing aragonite along a network of fractures. The *dark spots* within the calcite are pores

A perfect pseudomorphic replacement can be considered as one end of a spectrum of dissolution-transport-precipitation processes, in which the coupling between dissolution and precipitation takes place at the actual reaction interface. The simplest case to consider would be if there was no compositional change in the solid, for example, in the replacement of aragonite by calcite. In nature, aragonite that formed as a stable phase in high pressure rocks transforms to calcite during uplift, although whether the mechanism involves a fluid phase is not known (Wang and Liou 1991). Polymorphic transformations from one crystal structure to another can also take place in a dry system, although the kinetics of solid state mechanisms are orders of magnitude slower that those involving a fluid phase (Cardew and Davey 1985). The preservation of aragonite in high pressure rocks is cited as evidence that under such circumstances no fluid was present (Carlson and Rosenfeld 1981).

In low temperature replacements such as in cave and marine aragonite deposits there is morphological evidence that aragonite has been replaced by calcite (Mazzullo 1980; Martín-García et al. 2009), but for the present purposes the experimental work by Perdikouri et al., (2008, 2011) illustrates the main issues. Figure 5.2 shows a back-scattered scanning electron microscope image of a cross-section through a partially replaced aragonite crystal where the external morphology is preserved. The image shows relict 'islands' of aragonite within the calcite product. The most obvious features in this image are the fractures through the calcite product and the fine pores at the aragonite-calcite interface, seen more clearly in Fig. 5.2b.

Even in this simple example there are some quite complex issues that need to be addressed. Aragonite is more soluble than calcite at 25°C. For illustration purposes we take the solubility of aragonite as 14.2 ppm and calcite as 12.5 ppm in pure water. If aragonite is in contact with a given volume of pure water, it will begin to dissolve and a boundary layer of interfacial solution will quickly reach saturation with respect to aragonite i.e. 14.2 ppm. Assuming that this supersaturation with

respect to calcite is sufficient to nucleate calcite at this interface, then a small amount of calcite will precipitate to reduce the concentration of this interfacial solution to 12.5 ppm. In this initial stage of dissolution of aragonite and precipitation of calcite much more aragonite dissolves than calcite precipitates. The concentration in the interfacial solution then depends on the rate of diffusion of Ca^{2+} and CO_3^{2-} from the interfacial solution into the bulk solution i.e. the maintenance of a compositional gradient in the fluid, and the rate at which aragonite continues to dissolve and calcite precipitates. As long as the interfacial fluid remains undersaturated with respect to both aragonite and calcite, the replacement can continue with generation of porosity due to a greater mass of aragonite dissolved than calcite precipitated, i.e. a *volume deficit* reaction. During the replacement the bulk fluid concentration gradually increases in Ca^{2+} and CO_3^{2-} until it may reach saturation with respect to calcite (12.5 ppm). At this point the fluid is still undersaturated with respect to any aragonite left, but the mass of aragonite dissolved to raise the fluid composition to 14.2 ppm will be the same as the mass of calcite, which will precipitate to bring the fluid composition back to 12.5 ppm, and no further porosity can be produced. In this case any remaining aragonite would be armoured by a non-porous calcite layer and the replacement would stop.

So far we have only considered the situation from the point of view of the relative solubilities of the parent and product phases. Furthermore we have assumed that the system maintains local equilibrium. However, we must also take into account the fact that aragonite is considerably denser (2.93 g/cm^3) than calcite (2.71 g/cm^3). Thus the molar volume of aragonite is 34.14 cm^3/mole, and calcite is 36.90 cm^3/mole, a difference of +8%. This increase in molar volume associated with the replacement of aragonite by calcite will act to reduce the porosity formed as a result of the solubility differences discussed above. In the early stages of replacement the solubility difference dominates the porosity formation, but as the solution concentration approaches equilibrium with respect to calcite the difference in mass between the amount of aragonite dissolved relative to the calcite precipitated becomes smaller and the molar volume increase will begin to dominate. A detailed analysis of reaction paths during coupled dissolution and precipitation in a model salt system can be found in Pollok et al. (2011).

A further factor which needs to be considered is the mechanical effect of a molar volume increase during replacement. It has been shown in experiments and modeling that the stress generated by a significant volume change during a replacement reaction can exceed the fracture strength of rocks and minerals (Malthe-Sørenssen et al. 2006; Jamtveit et al. 2009). Fracturing becomes an important mechanism for increasing the permeability, allowing fluid to continue to access the unreplaced aragonite, even when porosity generation ceases. In a situation where aragonite, formed at high pressure in nature, is replaced by calcite during uplift, the relaxation due to pressure decrease may be able to sustain fracturing and volume expansion and allow continued replacement even when the fluid is saturated with respect to calcite and fracturing is the only mechanism for allowing continued fluid infiltration.

The balance between porosity generation and fracturing depends on the fluid: solid ratio. The point at which no further porosity can be generated due to the

combined factors of solubility decrease and volume increase depends on the volume of fluid. If the fluid is present in a confined fluid film on grain boundaries, saturation with respect to calcite may be reached quite early during a partial replacement and fracturing may then be the only mechanism for fluid transport. Another aspect related to fluid: mineral ratio is the amount of fluid required to pseudomorphically replace aragonite by calcite. If we consider a situation where a fluid, already saturated with respect to calcite, interacts with aragonite, then to maintain an isovolumetric replacement the excess volume has to be dissolved into the fluid phase. As an example, for an isovolumetric replacement, 1 g of aragonite would be replaced by 0.925 g of calcite, with 75 mg of $CaCO_3$ taken up by the fluid. Using the solubility of calcite as 12.5 ppm, 6 l of water would be required to take up this amount of $CaCO_3$. In this example we have considered the fluid as pure water, although it must be noted that the solubility of calcite is very dependent on the composition and pH of the relevant fluid.

Another factor to consider is the likely stress generated by a volume expansion reaction if the parent and product are confined in a rigid rock. Merino and co-workers (Merino et al. 1993; Nahon and Merino 1997; Merino and Banerjee 2008) have advanced a model where pseudomorphism is dependent on the confining stress such that the pressure exerted on the parent phase by the growing product causes its dissolution through a pressure-solution mechanism, and hence is the origin of the coupling between the rates of dissolution and precipitation. Although this may be an additional factor to consider, we know from laboratory studies that pseudomorphic replacement can take place in a free solution, without any stress generated at the reaction interface. The degree of spatial coupling between dissolution and precipitation has been shown to be dependent on the composition of the fluid (Xia et al. 2009a; King et al. 2010). This issue has been discussed in some detail in Putnis (2009).

Similar problems are encountered when we consider the volume changes associated with other replacement processes. Isovolumetric replacement in reactions which involve removal of low solubility components such as silica in reaction 5.5 above, requires the continuous flux of aqueous solution, with ultimately very high fluid:rock ratios.

5.3.2 *Example 2: Albite ⇔ Jadeite + Quartz*

The reaction of albite to jadeite + quartz is very important in petrology as it defines the onset of high pressure metamorphism and forms the basis for geobarometers and the stability of plagioclase and Na-bearing pyroxene + quartz assemblages at depth. The chemically balanced reaction is usually written:

$$NaAlSi_3O_8 \Leftrightarrow NaAlSi_2O_6 + SiO_2 \tag{5.6}$$

and the phase diagram is shown in Fig. 5.3.

Textural studies of jadeite-bearing assemblages from the Kaczawa Mountains (Sudetes, SW Poland) show that albite can be pseudomorphically replaced by

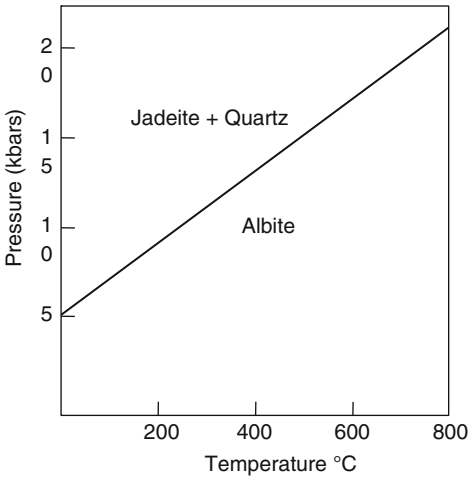

Fig. 5.3 Phase diagram showing the approximate stability fields of albite, and jadeite + quartz

jadeite without the simultaneous formation of quartz. Figure 5.4 (Kryza et al. 2011) shows albite being partially replaced by jadeite along the margins, with the jadeite growing into the albite without any apparent change in the occupied volume. Given that the molar volumes of albite and jadeite are 100.1 cm^3 and 60.4 cm^3 respectively, a mole for mole replacement would involve a ~40% volume decrease. It is clear that Eq. 5.6 does not represent a reaction mechanism, even if the net result in a rock is the disappearance of albite and the growth of jadeite. If we take the textural observations at face value and assume that the replacement is isovolumetric, then we should write that approximately 0.6 moles of albite are replaced by one mole of jadeite. For mass balance this would require *input* of Na, Al and Si, presumably from a fluid containing these components. Such fluid compositions are consistent with fluids expected in subduction zones (Manning 2004).

During uplift, when jadeite is no longer stable relative to albite, reactions with fluids tend to dissolve jadeite and precipitate albite. However, this can also take place isovolumetrically, as shown in Fig. 5.5 (Shigeno et al. 2005). The jadeite relics are optically continuous indicating that they are all part of the same parent jadeite crystal and that no rotation of the jadeite has taken place during the replacement. If we write the replacement by reaction with silica in solution according to:

$$NaAlSi_2O_6 + SiO_{2(aq)} \Leftrightarrow NaAlSi_3O_8 \tag{5.7}$$

it is not consistent with an isovolumetric replacement. To conserve the volume, 1.65 moles of jadeite should react to form 1 mole of albite. For mass balance excess Na, Al and Si would need to be *removed* by the fluid phase.

We have not attempted to speculate on the volumes of fluid that may be required to transport major components during albite – jadeite reactions, but we re-emphasise the fact that such element mobility is a requirement to account for the observed textures. Furthermore, there must be a mechanism for the fluid to

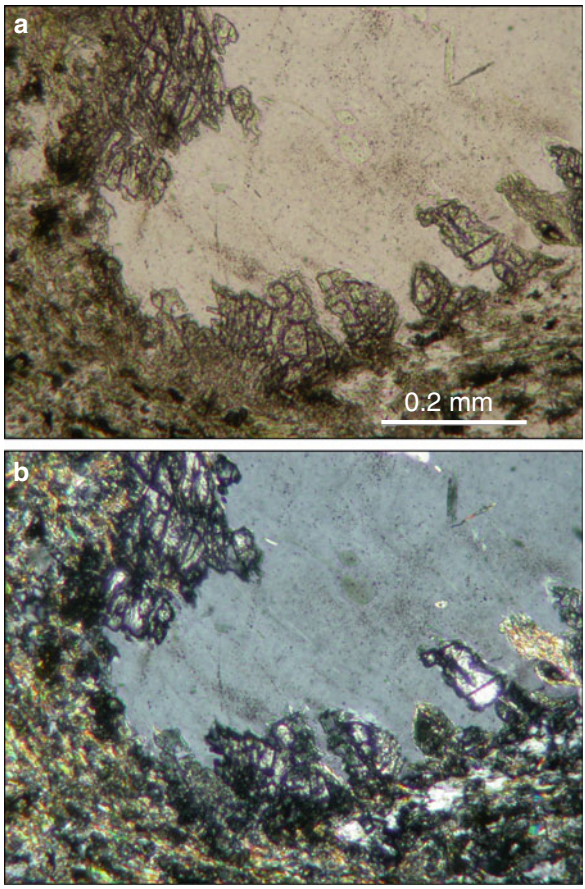

Fig. 5.4 A pair of polarised-light micrographs showing albite (*central* area) partially replaced by jadeite along the rims. (**a**) plane polarised light. (**b**) crossed polars. Image courtesy of Ryszard Kryza. See also Kryza et al. (2011)

completely infiltrate the rock so that every part of the parent phase or assemblage is at some stage in contact with the fluid from which the product precipitates.

5.3.3 Example 3: Albitization

The albitization of plagioclase and ultimately of whole rocks is a common example of the result of the interaction of saline fluids with minerals and is one of the most common fluid-mineral reactions taking place in the earth's shallow crust. Albitization occurs at temperatures as low as those during diagenesis in sedimentary basins to temperatures associated with hydrothermal reactions (Perez and Boles 2005). The pseudomorphic replacement of plagioclase by albite is a common observation in natural samples, and on the basis of the kinetics, the oxygen isotope redistribution, and textural details such as sharp reaction interfaces and the

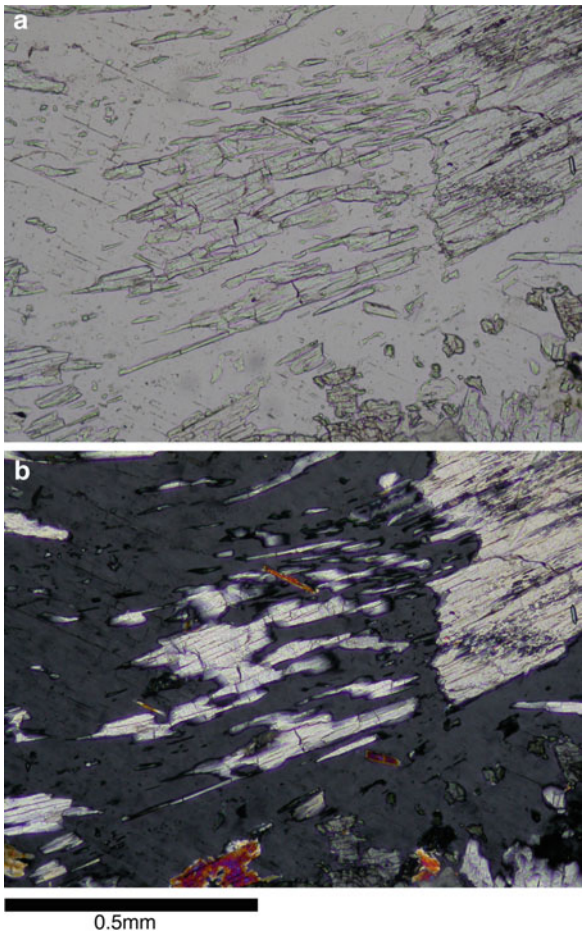

Fig. 5.5 A pair of polarised-light micrographs showing jadeite (*central* area, *higher* relief) partially replaced by albite. The jadeite relics were all part of a former larger single crystal. (**a**) plane polarised light. (**b**) crossed polars. The albite is in extinction, and the jadeite relics are crystallographically continuous. Image courtesy of Mika Shigeno. See also Shigeno et al. (2005)

pervasive porosity in the albite, has been described by an interface-coupled dissolution-precipitation reaction mechanism (O'Neil and Taylor 1967; Putnis 2002; Engvik et al. 2008; Putnis 2009). Hydrothermal experiments on albitization of oligoclase and labradorite plagioclase (Labotka et al. 2004; Hövelmann et al. 2010) and of K-feldspar (Norberg et al. 2011) have also experimentally demonstrated that albitization can take place within weeks at 500–600°C suggesting that in nature, the observation of incomplete reaction is likely to be due to lack of fluid, in other words the reaction front coincides with a fluid front in the rock.

Figure 5.6a shows a thin reaction zone of *pink* feldspar along a fracture through a granitoid rock in the Bamble sector, southern Norway. This is similar to the broader albitisation front shown in Fig. 5.1d, that also shows on a small scale, the processes that take place also on a large scale in this area, forming kilometre wide

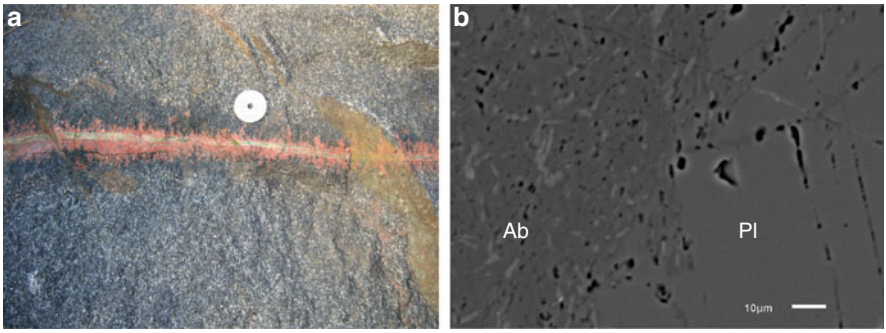

Fig. 5.6 (**a**) A thin albitisation reaction zone along a fracture through an amphibolite in the Bamble sector, southern Norway. The *pink* feldspar is albite. (**b**) BSE image of the albitisation reaction within a single crystal of feldspar. The smooth-textured feldspar on the *right* of the image is the parent oligoclase (Pl, approximately $Ab_{80}An_{20}$). On the *left* is the albite (Ab), containing fine lighter sericite and a high density of pores (*dark spots*)

outcrops of "albitites", rocks whose origin has been debated for some time (Elliott 1966; Bodart 1968; Engvik et al. 2008).

A more detailed study of samples from the reaction interface (Fig. 5.6b) shows that in single feldspar crystals the interface between almost pure albite and the parent oligoclase (~$An_{20}Ab_{80}$) is sharp on a sub-micron scale (see also Engvik et al. 2008) and significantly, the albite is highly porous and contains sericite (fine mica) which is also associated with the replacement. Electron diffraction also confirms that the crystallographic orientation of the feldspar is preserved. These features are typical of interface-coupled dissolution-precipitation reactions in which the parent phase (in this case oligoclase) begins to dissolve congruently in the fluid phase, resulting in the supersaturation of the interface fluid with respect to other phases (in this case albite + sericite). As the parent feldpar contains virtually no potassium, we assume that the potassium in the sericite has been introduced, together with the Na, by the fluid. The nucleation of albite is enhanced by the epitaxial relations between the dissolving parent and the precipitating product, resulting in a continuity in crystal structure across the reaction interface.

As albite is Na and silica-rich compared with oligoclase, the replacement must involve either addition of Na and Si or the removal of Al and Ca. As the replacement is isovolumetric the latter must be the case, so that a typical reaction for the albitisation of a calcic plagioclase by albite would have the form:

$$\begin{aligned} &NaAlSi_3O_8.CaAl_2Si_2O_8 + H_4SiO_{4(soln.)} + Na^+ \\ &\Rightarrow 2NaAlSi_3O_8 + Al^{3+} + Ca^{2+} + 4OH^-, \end{aligned}$$

neglecting the small molar volume difference between the feldspars and the porosity generation due to the differences in solubility between the parent and product in the fluid phase. The small molar volume change between the solid parent and

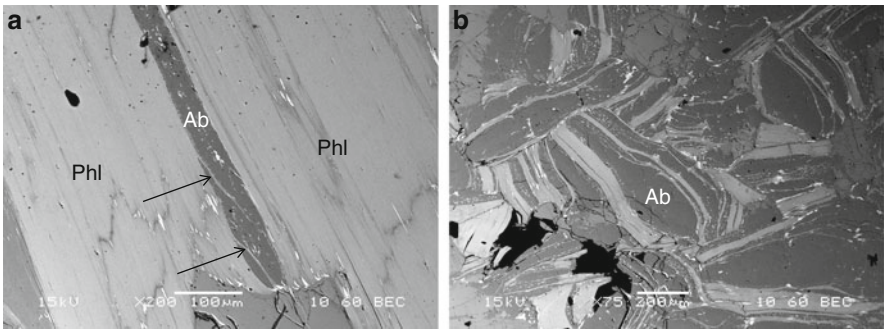

Fig. 5.7 BSE images of albite invading a phlogopite-rich rock in the Bamble sector, southern Norway. The albite (*dark*) parts separate the phlogopite layers (*arrowed* in (**a**)). (**b**) More extensive albitisation showing the various degrees of separation of the layers in the formerly single crystal of phlogopite

product phases is presumably why the albitisation of plagioclase is not associated with any fractures. A cross section through an experimentally albitised labradorite shows a sharp reaction interface between the parent and product phase and no obvious fracture generation.

In an interface-coupled dissolution-precipitation process the rate controlling step is the dissolution rate (Xia et al. 2009a; Moody et al. 1985). It is assumed that albite precipitation follows immediately after the dissolution step. However, in many albitised terrains, where eventually the whole rock may be converted to albite, albite nucleation and growth takes place throughout the rock and is not confined to replacing plagioclase. Figure 5.7 shows albite growing between the layers of phlogopite mica and separating the layers as it grows. In places the albite does appear to replace some of the phlogopite although in most of the image the albite has invaded the phlogopite interlayers. The separation of phlogopite sheets by the growing albite provides a convenient marker for the volume occupied by the albite, a volume that in a solid rock must be compensated by dissolution elsewhere. The growth of albite may then be controlled by the supply of reactants and hence the transport pathways thorough the rock.

This is an example of a dissolution-precipitation reaction which is not coupled at a reaction interface, but must involve a longer transport term for the albite components in solution. As the mineral assemblage is albitised, the dissolution – transport – precipitation steps must still be coupled to maintain the overall integrity of the rock. A similar situation is envisaged during metamorphism where on a local scale, the dissolution of some components of the rock is balanced by the growth of new phases (Carmichael 1969).

5.3.4 *Example 4: The Origin of Compositional Zoning and Inclusions in Apatite*

Natural apatites show a variety of compositional variations and inclusions within single crystals whose interpretation provides further evidence of the mechanisms and consequences of fluid mineral interactions. Apatite has the general formula $Ca_5(PO_4)_3(OH,F,Cl)$, where the OH, F, and Cl ions can mutually replace each other to form the almost pure end-members. Significantly, apatite has the ability to incorporate a wide range of trace elements including light and heavy rare earth elements (REEs) into its structure, including components of monazite [(Ce,LREE, Th)(PO_4)] and xenotime [(Y,HREE,Th)(PO_4)]. Natural apatites often show compositional zoning with variations in (OH) and Cl content, as well as inclusions of monazite and xenotime. Harlov and co-workers (Harlov and Förster 2003; Harlov et al. 2002, 2005) have made a detailed study of natural apatites and were able to reproduce the same features in hydrothermal replacement experiments, providing evidence about the composition of natural aqueous solutions as well as the mechanism of the reactions.

Figure 5.8 shows three examples of the textures in natural apatites. Figure 5.8a shows a chlorapatite in which the darker central zone is Cl-depleted, and OH-enriched and contains numerous bright inclusions of monazite and xenotime, compared with the paler Cl-rich apatite. Figure 5.8b shows a fluorapatite with numerous oriented inclusions of monazite and xenotime, whose lamellar nature and orientations are suggestive of an exsolution process. In both cases there is abundant evidence that the rocks containing the apatites have been metasomatised (Harlov et al. 2002; Harlov and Förster 2003). Figure 5.8c shows similar observations on natural OH-rich apatite replacing Cl-rich apatite described by Engvik et al. (2009).

Hydrothermal experiments by Harlov and co-workers showed that the replacement of one apatite by another is rapid (months to weeks) at temperatures between 300°C and 500°C, reproducing the textural and compositional features found in nature. Figures 5.9a, b show partially reacted chlorapatite and fluorapatite in which the monazite inclusions were formed only in the reacted areas where the apatite is depleted in REEs and Y. The extent of replacement depended on temperature, but the textures and product compositions depended on initial fluid composition. Oriented sections show that the monazite inclusions are lamellar and oriented parallel to the c-axis of the apatite (Fig. 5.9b). TEM observations confirmed that the product apatite contains both micro and nanopores, and is crystallographically continuous with the parent apatite.

The conclusions drawn from these studies were that the formation of the depleted (or ‘leached’) areas of the apatite was not consistent either texturally or on the time-scale of the experiments with a volume diffusion mechanism of element exchange but was consistent with a coupled dissolution-precipitation mechanism. The interpretation of the pores and inclusions in metasomatised apatites is that under the conditions of the fluid-mineral interaction, the REE-bearing apatites are metastable, and have a higher solubility than the eventual product phases.

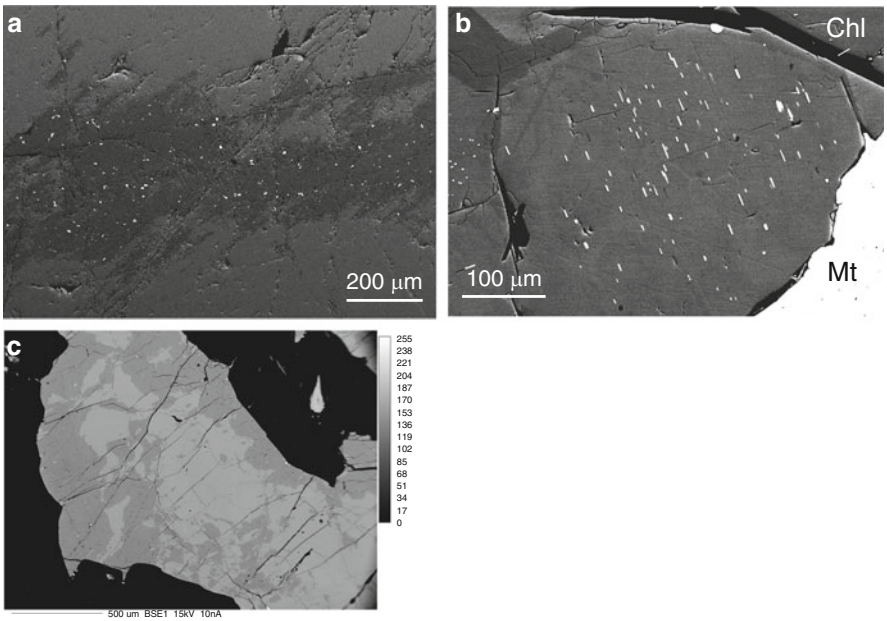

Fig. 5.8 BSE images of partially metasomatised natural apatites. (**a**) Metasomatised area (*dark*) in non-metasomatised chlorapatite (*light*) from Ødegårdens Verk, Norway, showing abundant inclusions of monazite and xenotime (*bright spots*). The inclusions only occur in the metasomatised area. (Harlov et al. 2002). (**b**) Fluid-induced monazite and xenotime inclusions in fluorapatite from Kiruna, northern Sweden. (Harlov and Förster 2003). (**c**) OH-rich apatite (*darker*) replacing Cl-rich apatite (*light*) in the Bamble Sector, southern Norway. (Engvik et al. 2009)

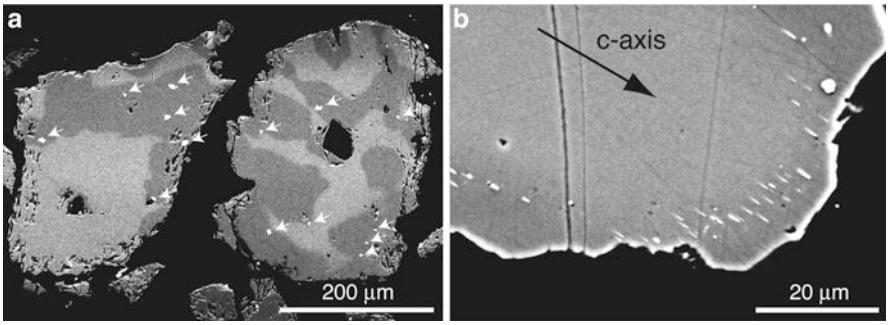

Fig. 5.9 BSE images of experimentally metasomatised apatites. (**a**) Partially metasomatised chlorapatite (*dark regions*) containing monazite and xenotime inclusions (*arrowed*). The unreacted regions are light. (Harlov et al. 2002). (**b**) Partially metasomatised fluorapatite. The darker reacted areas are along the rim of the crystal and contain bright lamellae of monazite oriented parallel to the apatite c-axis. (Harlov et al. 2005)

Therefore, even if the absolute solubility of the apatite may be very low, a very small amount of dissolution of the apatite solid solution results in an interfacial fluid, which is supersaturated with respect to a different apatite composition, depleted in REE and altered in OH, Cl, or F content. The loss of some of the apatite to the fluid, due to the solubility difference between parent and product, gives rise to the porosity. The crystallographic continuity between parent and product enhances epitxial nucleation from the interfacial solution, and the trace elements and REEs in the solution nucleate separately to form the inclusions.

This is an example of a phase separation driven by fluid infiltration, dissolution and precipitation rather than by a classical solid-state exsolution mechanism, which would involve diffusion of these components through the parent apatite. Similar explanations have been given for the formation of thorite ($ThSiO_4$) inclusions in altered zircons (Geisler et al. 2007) as well as thorite, uraninite, and Na-britholite inclusions in metasomatised monazite and xenotime (Seydoux-Guillaume et al. 2007; Hetherington and Harlov 2008; Harlov et al. 2011). A further observation is that such fluid-induced inclusions may also be oriented, giving the appearance of solid state exsolution. One significant difference between solid state exsolution and a fluid-induced phase separation is that in the former, the bulk composition of the original solid solution and the total exsolved phases is unchanged, whereas in a fluid-induced phase separation components may be exchanged between the solid and the fluid, changing the bulk composition of both.

5.3.5 *Example 5: Garnet Replacement Textures During Eclogitisation of Granulite*

Figure 5.1c shows a field photograph of localised eclogite formation in the Bergen Arcs, western Norway where the paler granulite is being converted to darker eclogite along a zone parallel to a fracture. This well-studied area has been described by many authors including Austrheim and Griffin (1985), Austrheim (1987), Erambert and Austrheim (1993) and Bjørnerud et al. (2002). In terms of P-T conditions eclogite formation implies a significant increase in pressure relative to the conditions under which the granulite formed and eclogites are characteristic of rocks involved in subduction processes. This is also consistent with the known tectonics associated with the Caladonian orogeny in Norway (Austrheim 1987; Boundy et al. 1992; Bingen et al. 2001).

If we now look at a single crystal of garnet from near the reaction interface (Erambert and Austrheim 1993; Schneider et al. 2007; Pollok et al. 2008), we see a complex pattern of chemical zonation (Fig. 5.10). The dark core of the garnet represents the Mg-richer original granulitic composition while the pale parts of this garnet single crystal represent the typical Fe-richer eclogitic composition of garnet. The basic process involved interchange of Mg and Fe. If we assume that the eclogitisation is fluid induced (Austrheim 1987) then this zonation pattern in the

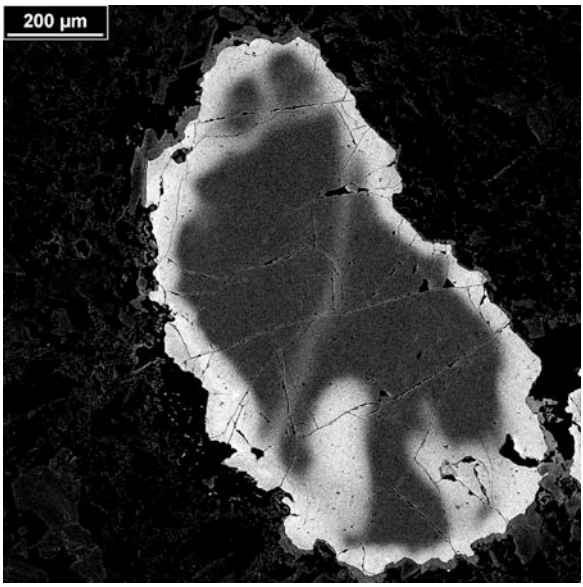

Fig. 5.10 A partially replaced garnet crystal from the Bergen Arcs, Norway where granulite has been eclogitised by a fluid. The darker core has the original composition of a granulitic garnet, while the pale rim has the lower Mg/Fe ratio of an eclogitic garnet. (Pollok et al. 2008)

partially eclogitised garnet must also be fluid induced. The pattern of replacement, especially the thin pale band through the centre of the crystal is consistent with a healed fracture along which fluid once passed. The zonation pattern in the garnet is not consistent with a solid state diffusional interchange which would be too slow at the relevant temperature and time-scale to produce the thick reaction rims, nor the complex zonation seen here (Jamtveit et al. 1990).

There are a number of other features in this garnet that are consistent with an interface-coupled dissolution-precipitation mechanism. The pale rim is crystallographically continuous with the core, but has texturally re-equilibrated with no subgrain boundary texture characteristic of the granulitic core (Pollok et al. 2008). However, the interface between the core and the rim is not as sharp as one would expect from an interface-coupled dissolution-precipitation mechanism, with a continuous increase in Fe and decrease in Mg over a 30 µm profile from the granulitic into the eclogitic part. There could be a number of explanations for such a profile. If the reaction interface represents the end-point of the reaction because of the lack of fluid or fluid transport, then the profile may indicate a slowly increasing Mg content towards the original garnet core due to the fact that the solution from which the garnet precipitated would have had reduced Fe-content due to the limited mass transfer of Fe to the reaction interface. An alternative explanation may be that the profile is caused by solid state diffusion after the fluid event that caused the eclogitisation and resulted in a "smearing out" of an initially sharp reaction front, as the eclogitic part and the granulitic part of the garnet are clearly not in equilibrium. A further factor which should be considered, especially when interpreting analytical data across interfaces, is that the apparent sharpness of the compositional profile will depend on the orientation of the interface relative to the analysed surface.

5.3.6 *Example 6: "Corona" Structures*

When two minerals, which may have been in equilibrium at some point, are taken to pressure and temperature conditions under which they are no longer form a stable pair, reaction between the two minerals may take place. The reactions produce a band of new product minerals at the interface, commonly referred to as corona structures. The classical description of the formation of such reactions uses the thermodynamic argument that chemical potential gradients will exist across an interface between a pair of incompatible minerals, and diffusional fluxes will operate to form a set of mineral layers such that local equilibrium exists across each interface. The theoretical treatment of such a situation was developed by Fisher (1973) and applied to a model interfacial reaction system of calcite + anorthite reacting to form gehlenite + wollastonite by Joesten (1977). The thermodynamic approach to such a problem is not concerned with the mechanism of mass transport and assumes that an interfacial fluid through which components may diffuse may be present. By assuming different magnitudes of fluxes, corona structures can be generated, and the specific sequence of mineral phases in an interfacial layer predicted.

The significance of corona structures in the context of this chapter is that they have been proposed to be among the most reliable indicators of a metamorphic event, representing an arrested reaction, which captures a time frame where the minerals in the corona are in equilibrium with the two reacting minerals on either side (Vernon et al. 2008). Such information would then allow the reaction to be identified on a P-T pseudosection and form part of the interpretation for a P-T path for the host rock.

However, there is evidence that real systems as opposed to thermodynamic models are not as simple, nor should we expect them to be, considering that any fluid in the earth will not be pure water. In the first example of a corona, Fig. 5.11a shows a corona from a classic locality in the granulites of the Bergen Arcs (Griffin 1972) where the corona formed by reaction between olivine (dark at the core) and plagioclase (pale) to form layers of orthopyroxene adjacent to the olivine, then clinopyroxene and finally garnet adjacent to the plagioclase. Figure 5.11b shows an evolved stage of the reaction where the olivine core is consumed leaving a core of pyroxene surrounded by garnet. The element fluxes involve transport of Mg and Fe out from the core and Si and Ca in from the plagioclase. The progressive layering reflects the steps in chemical potential along the gradients from olivine to plagioclase. Although it is highly likely that fluids are implicated in the reactions, there are not enough data on the precise compositions and amounts of the reaction products to be able to unequivocally state that the reactions are isochemical. Nevertheless, the situation does seem to approximate well to the theoretical expectations described in Joesten (1977).

An indication that the mechanism of mass transport can be complex is shown in Fig. 5.12 which shows a corona structure from the Kråkeneset gabbro located in the Western Gneiss Region of Norway (Lund and Austrheim 2004). This corona also

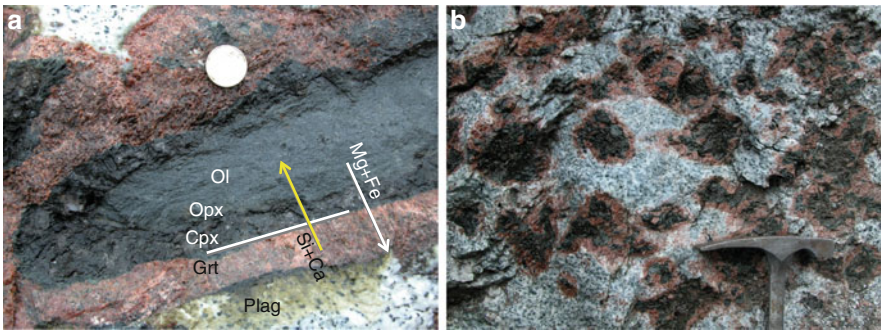

Fig. 5.11 (**a**) Corona structures in the anorthositic granulites on Holsnøy, Bergen Arcs, Norway with details of the reaction zones formed between the olivine core and plagioclase. (**b**) More evolved coronas where the olivine has been consumed leaving a core of pyroxene surrounded by garnet

formed between olivine and plagioclase but the mineral layers are not arranged in a way we would expect from simple counter-diffusion of components across the corona as there is a double layer of orthopyroxene. Furthermore, the reaction rims are discontinuous and cracks in the olivine contain the reaction products. The presence of a fluid phase is also verified by the presence of amphibole, but it should be emphasised that the formation of a hydrous mineral is not a prerequisite as an indicator for fluid-mineral reaction, as we see from the next example of a corona.

Figure 5.13 shows a reaction between kyanite and garnet during the decompression of an eclogite, where the reaction products are plagioclase + sapphirine (Straume and Austrheim 1999). In detail, the reaction layer adjacent to the kyanite is a symplectitic intergrowth of sapphirine and plagioclase, while adjacent to the garnet the product is plagioclase. However, notice that the reaction products do not form on all garnet-kyanite grain boundaries, only on those along which fractures have propagated, and therefore along which fluid has been able to pass. The reaction is also not isochemical, as the presence of ~10% albite component in the plagioclase clearly shows that the reaction is not only between garnet and kyanite but must involve an external sodium source.

Equilibration by solid-state diffusion of components between the two phases played no significant role in the development of the rim. The dissolution of both garnet and kyanite by the fluid created a compositional gradient in the interfacial fluid, with the fluid at the garnet interface more Ca rich than the fluid at the kyanite interface. The zonation of the reaction rim, with a layer of plagioclase nucleating on the garnet indicates a chemical potential gradient in the fluid phase. The residual fluid containing the other components of the dissolution (Ca, Mg, Fe, Al, Si), together with Na from the infiltrating fluid, co-crystallise to form the sapphirine + plagioclase symplectite. The "reaction rim" continues through a kyanite-kyanite contact (arrowed in Fig. 5.13) where the interface is filled with the symplectite, demonstrating the mobility of these elements in the fluid phase through the fracture. Note again that the presence of a fluid phase in a reaction does not necessarily imply

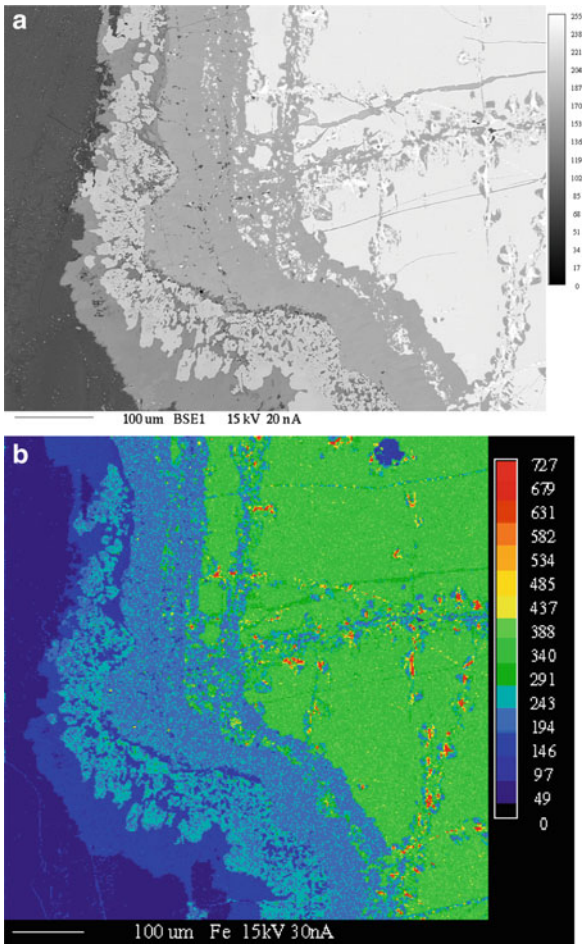

Fig. 5.12 (**a**) BSE image of complex reaction rims formed between plagioclase and olivine. (**b**) Fe element map of the same area. Note the two rims of orthopyroxene and that reaction products also form within fractures in the orthopyroxene and Fe-oxide. (Image: M.Erambert)

the formation of hydrous minerals even when the fluid components may play a significant role in the thermodynamics.

These examples show that coronas are often complex and their interpretation in terms of "metamorphic events" is quite problematic. The equilibrium (if any) established in a corona is between the fluid at the interface (formed from both the infiltrating solution and the dissolving parent) and the product phases in the reaction rim. If the infiltrating solution is out of equilibrium with the parent kyanite + garnet assemblage, then the corona, does not represent a reliable indicator of a metamorphic reaction, as the reaction is not isochemical. Although we may infer that the infiltrating fluid contains Na, we can make no assumptions about the composition of the outgoing fluid. The determination of P, T conditions for the reaction becomes problematic, as the fluid is an integral component in the reaction and its thermodynamics must be taken into account.

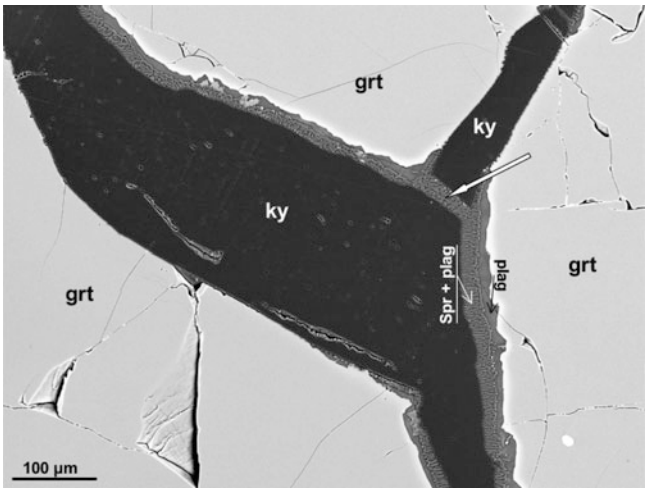

Fig. 5.13 BSE image of a grain boundary between garnet (*light*) and kyanite (*dark grey*). A fracture follows part of the grain boundary from *lower right* to *upper left*. The reaction products (plagioclase adjacent to the garnet and sapphirine-plagioclase symplectite adjacent to the kyanite) only form where the fracture is present and not on all garnet-kyanite boundaries. The kyanite-kyanite grain boundary (*large arrow*) is filled with the sapphirine + plagioclase symplectite. (Straume and Austrheim 1999)

5.4 Fluid Transport Through Rocks

In all the examples we have discussed the implication is that there is a mechanism by which fluids can pervasively move through low permeability rocks during fluid-mineral interaction. A number of fluid-transport pathways have been proposed: either pre-existing pathways in the intrinsic rock porosity (e.g. grain boundaries), permeability created by deformation (e.g. grain-scale dilatancy), or transport by the fluid event itself (hydraulic fracturing from fluid overpressure during devolatisation). The concept of "reaction-enhanced permeability" has been discussed for some time and is considered to be dependent on a volume decrease between parent and product solid phases in a metamorphic reaction (MacDonald and Fyfe 1985; Rumble and Spear 1983; Cartwright 1997; Ferry 2000). However, as we have seen in our examples the change in molar volume is not the only issue, which has to be considered. An increase in molar volume associated with a reaction may cause fracturing, as in the case of aragonite to calcite However, development of new flowpaths does not in itself explain how re-equilibration of an entire crystal could take place. Volume diffusion through the volume between closely spaced micro-fractures has usually been invoked as an explanation (Cox and Etheridge 1989).

Recent advances in understanding the mechanism of pseudomorphic mineral replacement processes (Putnis 2002; Putnis and Mezger 2004; Putnis et al. 2005; Putnis and Putnis 2007; Xia et al. 2009a; Putnis 2009) have shown that reactive

fluids can pass through individual crystal grains by a mechanism termed interface-coupled dissolution-precipitation. In the context of fluid flow, porosity generation is a key feature of this mechanism. Figure 5.5b, the replacement of a more calcic plagioclase (oligoclase) by albite, shows that interconnected porosity and hence permeability must have been generated by the replacement process. This allows continuous contact between the fluid and the reaction interface as it moves through the crystal, allowing advective transport of fluid through the pores and providing diffusional pathways for element transport. For example, albitization of plagioclase involves addition of Na and Si and removal of Al and Ca, as well as trace elements all of which are transported through the fluid phase in the pores (Hövelmann et al. 2010). The porosity is not only a consequence of a reduction in solid molar volume, which in the case of albite replacing oligoclase is too small to account for the observed porosity, but depends on the relative solubilities of parent and product phases in the reactive fluid. In other words, more parent material may be dissolved than product reprecipitated thus generating porosity. Indeed, it has been shown that even in a pseudomorphic reaction in which there is a molar volume increase, porosity may still be generated by the reaction (Putnis et al. 2007; Xia et al. 2009b).

The generation of porosity during mineral replacement reactions has been reported in a large number of studies on both natural and experimental samples (Putnis 2009, and references therein). The general principle that some material may be lost to the fluid phase due to solubility differences is not restricted to pseudomorphic replacement, and may equally apply to a metamorphic reaction where dissolution and precipitation are not as spatially coupled as in a pseudomorphic reaction.

Porosity generated by interface coupled dissolution–precipitation – allowing pervasive fluid transport through mineral grains, dissolving the parent at the reaction front and precipitating the product in its wake – eliminates the need to invoke solid-state diffusion at any stage during re-equilibration. Establishing interconnected porosity allows diffusion to and from the reaction interface through the fluid phase.

It is worth noting however, that there have been studies of fluid-induced replacement reactions where no interconnected porosity has been observed in the product phase (e.g. Norberg et al. 2011) even when the evidence for rapid mass transport is compelling. There are a number of possible factors, which could explain the lack of observed porosity:

1. The evolution of the fluid composition is such that while there is porosity generated in the early part of a reaction the reaction path results in reduced porosity with time (Pollok et al. 2011). This could also explain the experimental observation that replacement is not complete.
2. Porosity is a non-equlibrium and transient microstructure and would be expected to anneal out with time (Putnis 2009)
3. The porosity may be restricted to the parent-product interface

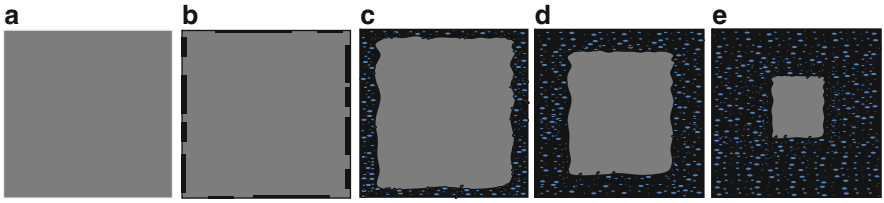

Fig. 5.14 Schematic diagram of a pseudomorphic replacement reaction. When a solid (**a**) comes into contact with a fluid with which it is out of equilibrium, dissolution of even a few monolayers of this parent may result in an interfacial fluid which is supersaturated with respect to a product phase, which may nucleate on the surface (**b**). (**c**–**e**) Continued dissolution and precipitation at the parent-product interface depends on the generation of interconnected porosity in the product phase allowing mass transport through the fluid phase and the migration of the reaction interface from the surface through the parent

4. The porosity may be on too fine a scale to be observed (see e.g. the TEM images of 'porosity' in Niedermeier et al. 2009) or may be obliterated by specimen preparation (e.g. polishing surfaces imaged by SEM).

5.5 Summary

The mechanism of pseudomorphism by interface-coupled dissolution-precipitation

The mechanism of mineral replacement by interface-coupled dissolution-precipitation is illustrated schematically in Fig. 5.14. The re-equilibration of a mineral in the presence of a fluid with which it is out of equilibrium first involves some dissolution of the parent phase. Even the dissolution of a few monolayers of the parent will result in a fluid which is supersaturated with respect to a more stable phase. The precipitation of this phase on the surface of the parent phase is dependent on the kinetics of nucleation: existence of epitaxial (crystallographic) relations between parent and product will favour nucleation, as will a high value of supersaturation at the fluid-mineral interface (i.e. a low solubility of the product phase). When the crystallographic relationships between parent and product are high (e.g. replacing a solid solution composition by another with the same structure, as in replacing one feldspar by another), a parent single crystal may be replaced by a single crystal of the product phase (Hövelmann et al. 2010; Niedermeier et al. 2009) although sub-grain formation in an albite reaction product has also been observed (Norberg et al. 2011). If the crystal structures of the parent and product phases are different, a polycrystalline product is likely to result. The product may also be multi-phase if the original interaction between the parent phase and the fluid results in an interfacial fluid layer which is supersaturated with respect to more than one phase.

Whatever the nature of the product, continuation of the transformation reaction depends on keeping open fluid transport pathways to the reaction interface. In other

words porosity must be generated in the product phase. The generation of porosity depends on both the relative molar volumes of the two phases and, more importantly, on their relative solubilities in the fluid. If the original mineral dimensions are preserved by the initial dissolution and nucleation, and the product has a smaller molar volume than the parent, then porosity will result. Secondly, the solubility of the more stable phase is necessarily lower than the less stable parent phase and therefore more solid will be dissolved than reprecipitated, again resulting in porosity. In *volume deficit* reactions the combination of these two factors results in a net volume reduction. On the other hand, if the combination of these factors leads to a *volume excess*, the reaction may not be able to proceed by this mechanism (Pollok et al. 2011).

A further factor which allows fluid transport to a reaction site is fracturing. From the limited number of experimental studies made on fracturing during fluid-mineral reactions (e.g. Jamtveit et al. 2009 and references therein) a significant volume change between parent and product phases seems to be a prerequisite. The examples used indicate that transport along fractures is important. Figures 5.12 and 5.13 show that transport along fractures is also involved in the formation of corona structures. This focused form of transport may also take place through dissolution and reprecipitation where stresses induce a pertubation of the reaction front (Jamtveit et al. 2000).

Dissolution and precipitation may be very closely coupled, resulting in an exact pseudomorph preserving nanoscale features of the parent, or they can become spatially separated, depending on whether the overall reaction is dissolution controlled, or precipitation controlled, respectively (Xia et al. 2009a).

Acknowledgements This chapter has benefitted from discussions with Muriel Erambert, Bjørn Jamtveit, Timm John and Christine Putnis. We thank Ted Labotka and Nikolaus Norberg for suggestions on an earlier version of the manuscript. The work has been supported by funding from the EU Initial Training Network: Mechanisms of Mineral Replacement – Delta-Min: www.delta-min.com (PITN-GA-2008-215360), a Humboldt Foundation Research Award to H.A. and grants from the Norwegian Research Council to the Norwegian Center of Excellence - Physics of Geological Processes (PGP).

References

Ague JJ (1994) Mass transfer during Barrovian metamorphism of pelites, south-central Connecticut. II: Channelized fluid flow and the growth of staurolite and kyanite. Am J Sci 294:1061–1134

Ague JJ (2003) Fluid flow in the deep crust. In: Treatise on geochemistry, vol 3.06. Elsevier, Amsterdam, pp 195–228

Austrheim H (1987) Eclogitization of lower crustal granulites by fluid migration through shear zones. Earth Planet Sci Lett 81:221–232

Austrheim H, Griffin WL (1985) Shear deformation and eclogite formation within granulite-facies anorthosites of the Bergen arcs, Western Norway. Chem Geol 50:267–281

Austrheim H, Erambert M, Engvik AK (1997) Processing of crust in the root zone of the Caledonian continental collision zone: the role of eclogitzation. In: Touret JLR, Austrheim H (eds) Collision orogens: zones of active transfer between crust and mantle, vol 273, Tectonophysics., pp 129–156

Bingen B, Davis WJ, Austrheim H (2001) Zircon U-Pb geochronology in the Bergen arc eclogites and the proterozoic protolith, and implications for the pre-scandian evolution of the Caledonides in western Norway. Geol Soc Am Bull 113:640–649

Bjørnerud MG, Austrheim H, Lund MG (2002) Processes leading to eclogitization (densification) of subducted and tectonically buried crust. J Geophys Res Solid Earth 107:2252–2269

Bodart DE (1968) On the paragenesis of albitites. Nor Geol Tids 48:269–280

Boundy TM, Fountain DM, Austrheim H (1992) Structural development and petrofabrics of eclogite facies shear zones, Bergen Arcs, western Norway: implications for deep crustal deformational processes. J Metam Geol 10:127–146

Cardew PT, Davey RJ (1985) The kinetics of solvent-mediated phase transformations. Proc R Soc A 398:415–428

Carlson WD, Rosenfeld JL (1981) Optical determination of topotactic aragonite-calcite growth kinetics: metamorphic implications. J Geol 89:615–638

Carmichael DM (1969) On the mechanism of prograde metamorphic reactions in quartz-bearing pelitic rocks. Contrib Miner Petrol 20:244–267

Cartwright I (1997) Permeability generation and resetting of tracers during metamorphic fluid flow: implications for advection-dispersion models. Contrib Miner Petrol 129:198–208

Cox SF, Etheridge MA (1989) Coupled grain-scale dilatancy and mass transfer during deformation at high fluid pressures: examples from Mt Lyell, Tasmania. Journ Struct Geol 11:147–162

Elliott RB (1966) The association of amphibolite and albitite, Kragero, south Norway. Geol Mag 103:1–7

Engvik AK, Putnis A, Fitz Gerald JD, Austrheim H (2008) Albitisation of granitic rocks: the mechanism of replacement of oligoclase by albite. Can Miner 46:1401–1415

Engvik AK, Golla-Schindler U, Berndt-Gerdes J, Austrheim H, Putnis A (2009) Intragranular replacement of chlorapatite by hydroxy-fluor-apatite during metasomatism. Lithos 112: 236–246

Erambert M, Austrheim H (1993) The effect of fluid and deformation on zoning and inclusion patterns in poly-metamorphic garnets. Contrib Miner Petrol 115:204–214

Ferry JM (2000) Patterns of mineral occurrence in metamorphic rocks. Am Miner 85:1573–1588

Fisher GW (1973) Nonequilibrium thermodynamics as a model for diffusion-controlled metamorphic processes. Am J Sci 273:897–924

Frost HJ, Ashby MF (1982) Deformation – mechanism maps – the plasticity and creep of metals and ceramics. Pergamon, New York

Geisler T, Schaltegger U, Tomaschek T (2007) Re-equilibration of zircon in aqueous fluids and melts. Elements 3:43–50

Griffin WL (1972) Formation of eclogites and coronas in anorthosites, Bergen Arcs, Norway. Geol Soc Am Mem 135:37–63

Harlov DE, Förster H-J, Nijland TG (2002) Fluid-induced nucleation of (Y + REE)-phosphate minerals within apatite: nature and experiment. Part I Chlorapatite Am Miner 87:245–261

Harlov DE, Förster H-J (2003) Fluid-induced nucleation of (Y + REE)- phosphate minerals within apatite: nature and experiment. Part II Fluorapatite Am Miner 88:1209–1229

Harlov DE, Wirth R, Förster H-J (2005) An experimental study of dissolution-reprecipitation in fluorapatite: fluid infiltration and the formation of monazite. Contrib Miner Petrol 150:268–286

Harlov DE, Wirth R, Hetherington CJ (2011) Fluid-mediated partial alteration in monazite: the role of coupled dissolution-reprecipitation in element redistribution and mass transfer. Contrib Miner Petrol 162:329–348

Hetherington CJ, Harlov DE (2008) Metasomatic thorite and uraninite inclusions in xenotime and monazite from granitic pegmatites, Hidra anorthosite massif, southwestern Norway: mechanics and fluid chemistry. Am Miner 93:806–820

Holland TJB, Powell R (1998) An internally consistent thermodynamic data set for phases of petrological interest. J Met Geol 16:309–343
Hövelmann J, Putnis A, Geisler T, Schmidt BC, Golla-Schindler U (2010) The replacement of plagioclase feldspars by albite: observations from hydrothermal experiments. Contrib Miner Petrol 159:43–59
Jamtveit B, Bucher-Nurminen K, Austrheim H (1990) Fluid controlled eclogitization of granulites in deep crustal shear zones, Bergen arcs, western Norway. Contrib Miner Petrol 104:184–193
Jamtveit B, Austrheim H, Malthe-Sørenssen A (2000) Accelerated hydration of the Earth's crust induced by stress perturbation. Nature 408:75–78
Jamtveit B, Putnis CV, Malthe-Sørenssen A (2009) Reaction induced fracturing during replacement processes. Contrib Miner Petrol 157:127–133
Jamtveit B, Austrheim H (2010) Metamorphism: the role of fluids. Elements 6:153–158
Joesten R (1977) Evolution of mineral assemblage zoning in diffusion metasomatism. Geochim Cosmochim Acta 41:649–670
King HE, Plümper O, Putnis A (2010) The effect of secondary phase formation on the carbonation of olivine. Envir Sci Tech 44:6503–6509
Kryza R, Willner W, Massonne H-J, Muszyński A, Schertl H-P (2011) Blueschist-facies metamorphism in the Kaczawa Mountains (Sudetes, SW Poland) of the Central-European Variscides: P-T constraints by a jadeite-bearing metatrachyte. Min Mag 75:241–262
Labotka TC, Cole DR, Fayek M, Riciputi LR, Staderman FJ (2004) Coupled cation and oxygen exchange between alkali feldspar and aqueous chloride solution. Am Miner 89:1822–1825
Lindgren W (1912) The nature of replacement Econ. Geology 7:521–535
Lindgren W (1918) Volume changes in metamorphism. Journ Geol 26:542–554
Lund MG, Austrheim H (2004) High-pressure metamorphism and deep crustal seismicity: evidence from contemporanous formation of pseudotachylytes and eclogite facies coronas. Tectonophysics 372:59–83
MacDonald AH, Fyfe WS (1985) Rate of serpentinisation in seafloor environments. Tectonophysics 116:123–135
Malthe-Sørenssen A, Jamtveit B, Meakin P (2006) Fracture patterns generated by diffusion controlled volume changing reactions. Phys Rev Lett 96:245501
Manning CE (2004) The chemistry of subduction-zone fluids. Earth Planet Sci Lett 223:1–16
Martín-García R, Alonso-Zarza AM, Martín-Pérez A (2009) Loss of primary texture and geochemical signatures in speleothems due to diagenesis: evidences from Castañar Cave, Spain. Sediment Geol 221:141–149
Mazzullo SJ (1980) Calcite pseudospar replacive of marine acicular aragonite, and implications for aragonite cement diagenesis. J Sediment Petrol 50:409–422
Merino E, Nahon D, Wang Y (1993) Kinetics and mass transfer in pseudomorphic replacement; application to replacement of parent minerals and kaolinite by Al, Fe and Mn oxides during weathering. Am J Sci 293:135–155
Merino E, Banerjee A (2008) Terra rossa genesis, implications for karst, and eolian dust: a geodynamic thread. Journ Geol 116:62–75
Moody JB, Jenkins JE, Meyer D (1985) An experimental investigation of the albitization of plagioclase. Can Miner 23:583–596
Nahon D, Merino E (1997) Pseudomorphic replacement in tropical weathering: evidence, geochemical consequences, and kinetic-rheological origin. Am J Sci 297:393–417
Niedermeier DRD, Putnis A, Geisler T, Golla-Schindler U, Putnis CV (2009) The mechanism of cation and oxygen exchange in alkali feldspars under hydrothermal conditions. Contrib Miner Petrol 157:65–76
Norberg N, Neusser G, Wirth R, Harlov D (2011) Microstructural evolution during experimental albitization of K-rich alkali feldspar. Contrib Miner Petrol 162:531–546
O'Neil JR, Taylor HP (1967) The oxygen isotope and cation exchange chemistry of feldspars. Am Miner 52:1414–1437

Perdikouri C, Kasioptas A, Putnis CV, Putnis A (2008) The effect of fluid composition on the mechanism of the aragonite to calcite transition. Miner Mag 72:111–114
Perdikouri C, Kasioptas A, Schmidt BC, Geisler T, Putnis A (2011) Experimental study of the aragonite to calcite transition in aqueous solution. Geochim Cosmochim Acta 75:6211–6224
Perez R, Boles AR (2005) An empirically derived kinetic model for albitization of detrital plagioclase. Am J Sci 305:312–343
Philpotts A, Ague JJ (2009) Principles of igneous and metamorphic petrology. Cambridge University Press, Cambridge
Pollok K, Lloyd GE, Austrheim H, Putnis A (2008) Complex replacement patterns in garnets from Bergen Arcs eclogites: A combined EBSD and analytical TEM study. Chemie der Erde 68:177–191
Pollok K, Putnis CV, Putnis A (2011) Mineral replacement reactions in solid solution-aqueous solution systems: volume changes, reactions paths and end-points using the example of model salt systems. Am J Sci 311:211–236
Putnis A (1992) Introduction to mineral sciences. Cambridge University Press, Cambridge
Putnis A (2002) Mineral replacement reactions: from macroscopic observations to microscopic mechanisms. Miner Mag 66:689–708
Putnis A (2009) Mineral replacement reactions. In: Oelkers EH, Schott J (eds) Thermodynamics and kinetics of water-rock interaction, vol 70, Reviews in mineralogy & geochemistry. Mineralogical Society of America, Chantilly, pp 87–124
Putnis A, McConnell JDC (1980) Principles of mineral behaviour. Blackwell, Oxford
Putnis A, Putnis CV (2007) The mechanism of reequilibration of solids in the presence of a fluid phase. J Solid State Chem 180:1783–1786
Putnis A, Austrheim H (2010) Fluid induced processes: metasomatism and metamorphism. Geofluids 10:254–269
Putnis CV, Mezger K (2004) A mechanism of mineral replacement: isotope tracing in the model system KCl-KBr-H_2O. Geochim Cosmochim Acta 68:2839–2848
Putnis CV, Tsukamoto K, Nishimura Y (2005) Direct observations of pseudomorphism: compositional and textural evolution at a fluid-solid interface. Am Mineral 90:1909–1912
Putnis CV, Geisler T, Schmid-Beurmann P, Stephan T, Giampaolo C (2007) An experimental study of the replacement of leucite by analcime. Am Mineral 92:19–26
Read HH (1957) The granite controversy. Murby, London
Rumble D, Spear FS (1983) Oxygen-isotope equilibration and permeability enhancement during regional metamorphism. J Geol Soc London 140:619–628
Schneider J, Bosch D, Monie P, Bruguier O (2007) Micro-scale element migration during eclogitisation in the Bergen arcs (Norway): a case study on the role of fluids and deformation. Lithos 96:325–352
Seydoux-Guillaume A-M, Wirth R, Ingrin J (2007) Contrasting response of $ThSiO_4$ and monazite to natural irradiation. Eur J Miner 19:7–14
Shigeno M, Mori Y, Nishiyama T (2005) Reaction microtextures in jadeitites from Nishisonogi metamorphic rocks, Kyushu, Japan. Journ Miner Petrol Sci 100:237–246
Straume AK, Austrheim H (1999) The importance of fracturing during retro-metamorphism of eclogites. J Metam Geol 17:637–652
Turner FJ, Verhoogen J (1951) Igneous and metamorphic petrology. McGraw Hill, New York
Turner FJ, Verhoogen J (1960) Igneous and metamorphic petrology, 2nd edn. McGraw Hill, New York
Tuttle OF, Bowen NL (1958) Origin of granite in the light of experimental studies in the system NaAlSi3O8- KAlSi3O8-SiO2-H2O, vol 74, Geol Soc Am Mem. Geological Society of America, Washington
Vernon RH, White RW, Clarke GL (2008) False metamorphic events inferred from misinterpretation of microstructural evidence and P-T data. J Metam Geol 26:437–449

Wang X, Liou JG (1991) Regional ultrahigh-pressure coesite-bearing eclogitic terrane in central China: evidence from country rocks, gneiss, marble and metapelite. Geology 19:933–936
Wenk H-R (1976) Electron microscopy in mineralogy. Springer, Berlin
Xia F, Brugger J, Chen G, Ngothai Y, O'Neill B, Putnis A, Pring A (2009a) Mechanism and kinetics of pseudomorphic mineral replacement reactions: a case study of the replacement of pentlandite by violarite. Geochim Cosmochim Acta 73:1945–1969
Xia F, Brugger J, Ngothai Y, O'Neill B, Chen G, Pring A (2009b) Three dimensional ordered arrays of nanozeolites with uniform size and orientation by a pseudomorphic coupled dissolution-reprecipitation replacement route. Cryst Growth Des 9:4902–4906

Chapter 6
Geochronology of Metasomatic Events

Igor M. Villa and Michael L. Williams

Abstract In order to date any geological event, suitable mineral geochronometers that record that and only that event must be identified and analyzed. In the case of metasomatism, recrystallisation is a key process that controls both the petrology and the isotopic record of minerals. It can occur both in the form of complete neocrystallisation (e.g. in a vein) and in the form of pseudomorphism, whereby dissolution/reprecipitation at the submicroscopic scale plays a central role. Recrystallisation may be complete or not, raising the possibility that relicts of a pre-metasomatic assemblage may be preserved. Because recrystallisation is energetically less costly at almost any temperature than diffusion, and because radiogenic isotopes (except ^{4}He) never diffuse faster than major elements forming the mineral structure, there is a strong causal link between petrographic relicts and isotopic inheritance (as demonstrated for zircon, monazite, titanite, amphibole, K-feldspar, biotite, and muscovite). Metasomatic assemblages commonly contain such mixtures between relicts and newly formed phases, whose geochronology is slightly more complex than that of simple, ideal systems, but can be managed by techniques that have become routine in the last decade and which are described in this chapter. Because of its crucial role in controlling the isotope systematics, the petrogenesis of a mineral needs to be understood in extreme detail, especially using microchemical analyses and micro-imaging techniques, before mineral ages can be correctly interpreted. As the occurrence of recrystallization is limited by the availability of water, minerals act as "geohygrometers" that allow constraints to

I.M. Villa (✉)
Institut für Geologie, Universität Bern, Baltzerstrasse 3, 3012 Bern, Switzerland

Dipartimento di Scienze Geologiche e Geotecnologie, Università di Milano Bicocca, 20126 Milano, Italy
e-mail: igor@geo.unibe.ch

M.L. Williams
Department of Geosciences, University of Massachusetts, Amherst, MA 01003, USA
e-mail: mlw@geo.umass.edu

D.E. Harlov and H. Austrheim, *Metasomatism and the Chemical Transformation of Rock*, Lecture Notes in Earth System Sciences,
DOI 10.1007/978-3-642-28394-9_6,

be placed on the nature and age of fluid circulation episodes, especially metasomatic events.

6.1 Introduction

The importance of fluid–rock interactions has long been recognized in most geologic environments. Metasomatism can dramatically change the composition and geochemical character of rocks. It can lead to ore formation and fertility for subsequent partial melting or metamorphism. Metasomatism can also cause changes in rheology and deformation mechanisms, and it will also be very important in future attempts to sequester carbon or other materials through fluid–rock interaction. Increasing numbers of workers acknowledge, and take into account, the importance of fluid infiltration events in controlling the isotope record of rocks. Evidence for metasomatic processes can be overwhelming or it can be extremely subtle, affecting only a subset of minerals in a rock. Even relatively minor metasomatic events can complicate interpretations of bulk geochemistry or provenance, but if they are recognized, their characterization and that of the associated fluids can greatly enhance our understanding of geologic histories, processes, and environments.

It is important to develop ways of dating past metasomatic events. The general principles of isotope geochronology can be found in classic textbooks (e.g. Faure 1986). While dating special cases of metasomatic ore-forming events has a long history (e.g., Corfu and Muir 1989), in recent time there has been a growing recognition that metasomatic events are part of a continuum of fluid-controlled geochemical processes. In this chapter, we will emphasize certain general theoretical and experimental aspects, which are germane to the problem of dating metasomatic parageneses, all the while emphasizing the interpretive aspect. In order to date a geological event, suitable mineral geochronometers that record that specific event must be identified and analysed. In the case of metasomatism, several processes can affect the isotopic record of minerals and so allow or obstruct dating. Because the goal is to find isotopic systems that are newly set during metasomatism (or completely reset), it is essential to understand the ways in which geochronometers can be set or reset. In addition to magmatic crystallization, which does not pertain to metasomatic/metamorphic rocks, various mechanisms can achieve partial or complete resetting. This chapter will review and assess the relative importance of these processes. We will illustrate especially two chronometer systems, U-Pb monazite geochronology and ^{39}Ar-^{40}Ar geochronology (a modification of the K-Ar dating method, whereby a sample is irradiated with fast neutrons in order to produce ^{39}Ar from ^{39}K), because both have particular power for dating metasomatic events. They allow the creation of age maps, age spectra, or concordia/discordia diagrams. This age information is “redundant”, in that it provides more than one age for every mineral, thus offering a highly desirable internal consistency and/or compatibility check.

What makes metasomatic events datable? A typical aspect of metasomatism, the circulation of hot aqueous fluids in rocks, could in principle be viewed as a mechanism for resetting the isotopic record by thermal diffusion. However, as will be discussed in detail below, this mechanism is actually subordinate. The principal control on isotopic closure, recrystallization, is closely linked to the circulation of hot aqueous fluids, which in turn is usually associated with the formation of characteristic mineral parageneses. Recrystallisation is a tell-tale sign of metasomatism: both in the form of complete neocrystallisation (e.g. in a vein) and in the form of complete or partial replacement (pseudomorphism), whereby dissolution/reprecipitation at the submicroscopic scale, mediated by an aqueous fluid, plays a central role (e.g., Putnis 2002, 2009; see also Chap. 5). Recrystallisation may be complete or not, raising the possibility that relicts and the inheritance of a pre-metosomatic assemblage are preserved at the macroscopic or submicroscopic scale.

Fluid circulation can be observed at different scales. At the meter scale, it results in macroscopic veins filled by characteristic parageneses that record pressures and temperatures, which can be lower than those of the wall rocks. At the mm scale, it results in partial or total replacement reactions that affect some minerals, but can leave others less affected to the degree that they can be identified as relicts. As very recent petrologic work has shown, relicts and replacement textures can be observed even at scales smaller than the μm (see e.g. Fig. 6.3). If metasomatism involves veins and new distinct mineral assemblages (neocrystallization), the task of dating fluid circulation is straightforward, as it is only required to physically isolate the vein assemblages for compositional characterization and dating. However, if metasomatism involves the transformation (partial or complete) of an existing assemblage to a new assemblage, the task may be much more difficult. It is necessary to find datable minerals (chronometer phases) or subdomains within minerals that grew or recrystallized during metasomatism such that the particular clock can be interpreted as being set or reset to the time of metasomatism. These must be separated or distinguished from chronometers that preserve a complete or partial record of premetasomatic events. Both types can occur together in the same field area and possibly in the same rock sample (e.g., Corfu and Muir 1989; Engvik et al. 2011).

6.2 Theoretical Background

6.2.1 Radioactive Decay

Isotopic geochronology is based on measuring the ratios of radioactive parent isotopes to radiogenic daughter isotopes. The ratio recorded by a mineral allows the calculation of an age, t:

$$t = (1/\lambda)^{*}\ln((F-F_0)/P) \tag{6.1}$$

where λ is the decay constant, F and P the number of daughter and parent atoms measured at present, and F_0 the number of daughter atoms that were present at the time the mineral clock recorded zero time. Solving for t requires the accurate knowledge of F_0. In some instances, it is legitimate to neglect the uncertainty deriving from assuming a slightly incorrect F_0. This is done in the U-He and K-Ar dating methods, which assume that rare gases are never incorporated in a newly formed mineral, and to some degree in U-Pb dating of zircon, monazite, and other U-rich minerals, under the assumption that divalent Pb cannot substitute well for Zr as does tetravalent U. However, in most instances it is incorrect to assume a value for F_0 a priori, and it becomes necessary to accurately determine or estimate it. This is particularly true for the Rb-Sr, Sm-Nd, and Lu-Hf systems, but also for the U-Pb system, in the case of minerals that do not have such a wide Pb-vs-U compatibility contrast, or in the case of metasomatism because the radiogenic daughter (Pb) may not be completely released during an alteration event.

6.2.2 Isochrons

In order to reconstruct the isotopic composition in a mineral at a time inaccessible to us now, it is necessary to resort to an indirect argument. Consider a well-stirred magma, which has stayed totally molten for a sufficiently long time to have achieved complete isotopic equilibrium. When the magma solidifies, all minerals have the same amount of F_0 relative to some other isotope of the same element (the so-called "common isotope", denoted as C): the F_0/C ratio is the same for all. When a mineral crystallizes it incorporates all of its constituent elements according to their availability and their partition coefficients.

While F_0/C is constant at equilibrium, the partition coefficients for the two-element pair ensure that in every mineral the P/C ratio is different. Thus, at the time of magma solidification, the crystallizing minerals define a horizontal alignment in an isochron diagram such as that shown in Fig. 6.1. As time passes, parent nuclides decay (i.e. the P/C ratio decreases) while at the same time daughter nuclides are formed (i.e. the F/C ratio increases). Data-points representing the minerals move upward and to the left in Fig. 6.1a. Because the number of daughter nuclides is proportional to the number of parent nuclides:

$$F(t) = P(t) \cdot (e^{\lambda t} - 1), \tag{6.2}$$

the increase of the F/C ratio is proportional to that of the P/C ratio, whereby the F/P ratio is constant for all points that are isochronous (have the same age). These points having the same age define a straight line called an isochron line (see, e.g., Faure 1986), given by

$$y = y_0 + bx \tag{6.3}$$

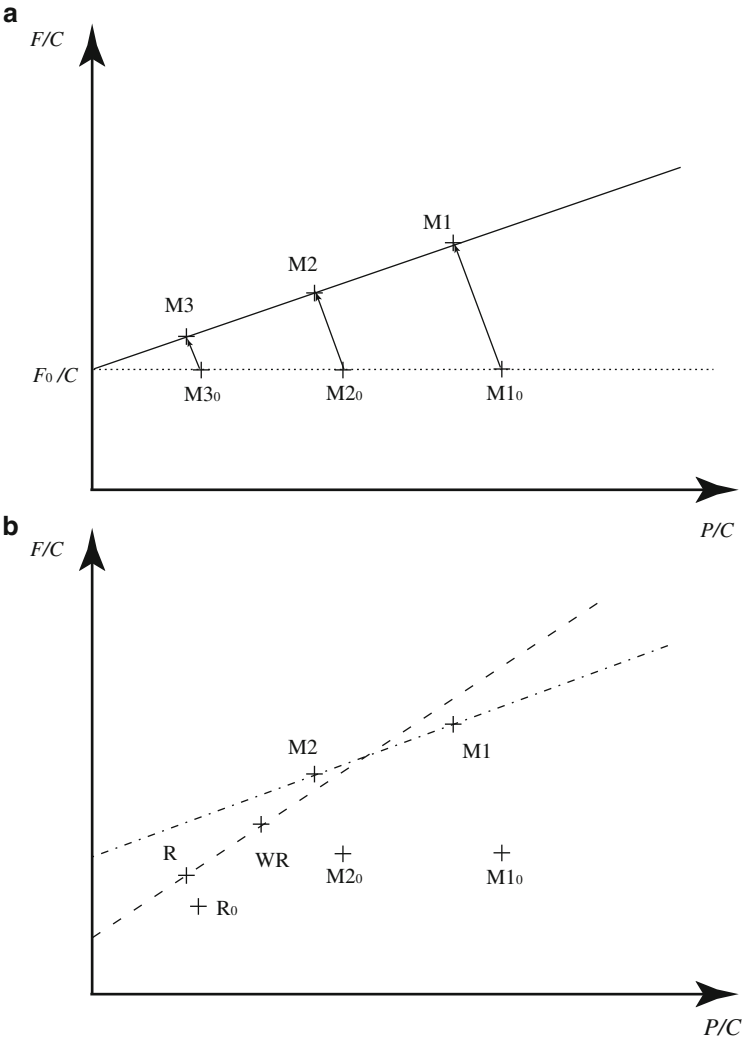

Fig. 6.1 Isochron diagram. (**a**) Any diagram in which cogenetic and contemporaneous samples define a straight line, termed isochron (from Greek "contemporaneous"), can be used to calculate an age. In the present example, with the abscissa proportional to the concentration of the parent nuclide, and the ordinate to that of the daughter nuclide, the age can be calculated from the slope, as follows. When an equilibrium assemblage is formed, each mineral ($M1_0$, $M2_0$, $M3_0$) initially lies on the horizontal dotted line at $y = F_0/C$. With increasing age, parent nuclides decay while at the same time daughter nuclides are created. The isotopic evolution of each mineral can therefore be represented by a trajectory towards the upper left (shown by *arrows*). The concentration of radiogenic daughters, F^*, is only a function of time and the concentration of parents, $F^* = P$ (exp $(\lambda t) - 1$). Therefore, in a set of isochronous minerals the ratio F^*/P is constant and the present-day points (M1, M2, M3) define a line whose slope is $b = F^*/P = \exp(\lambda t) - 1$ and whose intercept is F_0/C. (**b**) An isochron diagram in which not all minerals were in isotopic equilibrium at the same time. Minerals M1 and M2 were formed during metasomatic recrystallization, mineral R is a

where $x = P/C$, $y = F/C$, $y_0 = F_0/C$, and $b = e^{\lambda t}$-1. The isochron age is calculated from the slope, b.

Also note that the word "isochron" (Greek for contemporaneous) denotes any locus of isochronous points in any suitable diagram, independently of the axes chosen for a particular visualization; other choices of axes than those discussed here have been presented, e.g., by Podosek and Huneke (1973) and Provost (1990).

6.2.3 Ages

The interpretation of t as the age of a geological event has evolved over the last century, ever since the first age determination by Rutherford (1906). The value of t calculated from Eq.6.1 is not always the time when the mineral was first formed. The reasons why, and the extent to which they differ, are seldom straightforward.

One difficulty is that the assumption of initial equilibrium is difficult to test. It does not always hold, even in melts. In anatectic magmatic rocks, (partial) remelting of the crustal protolith was documented to be insufficient to reset all minerals to equilibrium (e.g. Ferrara et al. 1989; Christensen et al. 1995). Therefore, the only reliable isochrons are the overdetermined ones, i.e. those formed by three or more independent points. By allowing a statistical examination of deviations, it is possible to test the isochrons for internal consistency. This is commonly done using a statistical parameter called the mean square of weighted deviates, MSWD (McIntyre et al. 1966), which has a value = 1 if the scatter of points from the regression line is accounted for by the individual analytical uncertainties. While acceptance or rejection of an isochron age as legitimate is up to individual researchers, it should be kept in mind that MSWD values greater than 1 imply that data points lie off the regression line by more than their analytical uncertainty (Fig. 6.1b). If this occurs, presumably some of the data record a geological process that differs significantly in age from that defined by the other data points, and it is incumbent upon geochronologists to try and understand the cause of such scatter. Commonly, this cause can be found by a petrological investigation.

An important aspect that needs to be discussed is the way in which laboratory analyses shape the questions that can be asked by geochronologists at the present time. A century ago, Rutherford (1906) performed a "bulk analysis". Average F and

Fig. 6.1 (continued) restite. At the time when M1 and M2 formed, R_0 did not have the same isotopic composition F_0/C as $M1_0$ and $M2_0$. The whole rock, WR, only consists of M1, M2, and R. The correct age is given by the line through M1 and M2 (*dot-dashed line*). The *dashed line* that includes WR gives an incorrect age, because WR contains mineral R, which does not fullfill the requirement of initial equilibrium. The MSWD of an illegitimate isochron through M1, M2 and WR is therefore excessively high

P were determined on the bulk of a gram-sized aliquot, irrespective of second-order complications such as chemical or isotopic zoning, so that *t* in Eq. 6.1 reflects the average property of the analyzed material. In the last decades, petrography underwent a massive change of paradigms with the coming of age of electron microscopy as discussed by Allen (1992) and Veblen (1992), and by the possibility to perform electron probe microchemical analyses precisely on the mineral varieties thus identified. These two review papers document two crucial innovations. Firstly, "minerals" as they were considered a century ago are no longer so well defined at the 1–10 nm scale; mixtures and intergrowths are the rule, especially in metamorphic minerals. Secondly, sub-μm inclusions are very commonly present. While inclusions per se are no indictment of isotopic dating techniques, it is necessary to keep in mind that most radioactive parent nuclides are trace elements. As accessory minerals such as zircon and monazite are especially enriched in rare earth elements (REE), U, and Th, it is intuitive that one sub-μm inclusion of such an accessory phase can dominate the radioactive budget of a "mineral". This effect was documented by, e.g., Zhou and Hensen (1995) for Sm-Nd in garnet, and DeWolf et al. (1996) for U-Pb in garnet. In turn, it is commonly difficult to ascertain on textural grounds whether such micro/nanoinclusions are part of an equilibrium paragenesis or are relicts of some earlier metamorphic event. The relicts documented by Seydoux-Guillaume et al. (2003) by electron microscopy were much smaller than 1 μm, which indicates that the problem may exist at a scale, which has so far escaped the attention of isotope analysts. Even major minerals, when viewed using back-scattered electron imaging (BSE) or analysed by electron microprobe, frequently show the coexistence of several generations. In order to improve the interpretation of the isotope record of zoned minerals, isotope analysts have attempted to reduce sample sizes so as to progress beyond bulk analyses to the sub-grain level. Mapping the distributions of ages, isotope ratios, or chemical components within minerals has allowed great progress in our understanding of what Eq. 6.1 actually means, and of what geological events are amenable to dating. The interplay between petrology and geochronology is an extremely tight one (Vance et al. 2003) and it has been suggested (Villa 2002) that geochronology cannot yield reliable results without a complementary petrological groundwork.

In summary, dating requires a petrological study to ascertain which set of minerals is cogenetic and can be regressed together in an isochron (see, e.g., the discussion by Glodny et al. 2008). It is critical that the phases used to define the isochron be of identical age. That is why the technique must be used with caution in metamorphic and metasomatic rocks that involve progressive growth and breakdown of minerals along a P-T path. In particular, the requirement to find cogenetic phases in order to constrain F_0 has so far severely hampered the efforts (see, e.g., Thöni and Jagoutz 1992) to obtain Rb-Sr or Sm-Nd age differences between heterogeneous growth zones of minerals, with sparse exceptions (e.g., Vance and O'Nions 1990; Stosch and Lugmair 1990; Müller et al. 2000). However, for some (but not all) applications of the K-Ar and U-Pb systems F_0 can be assumed to be close enough to zero. This opens up the possibility of obtaining ages of specific

mineral zones such as metasomatic assemblages without the need to identify cogenetic phases in order to obtain an isochron.

6.2.4 Spatial Resolution and Stepwise Release

Chemical zonation profiles with a shape that is significantly different from a simple bell-function are a characteristic feature of petrological disequilibria in minerals and, therefore, almost always of isotopic disequilibrium as well. The presence of mineral assemblages pertaining to more than one event (e.g., a metamorphic peak and a retrogression; a magmatic event and a metasomatic overprint; the erosion of crystalline rocks and authigenic overgrowth in the sedimentary basin; etc.) is a problem whenever the chemical heterogeneity corresponds to a diachronism of the carrier phases that form the mixture. The geochronology of such mixtures of diachronously grown phases is slightly more complex than that of simple, "ideal" systems, but can be managed by techniques that have become routine in the last decades, namely the two complementary "SR techniques": spatially resolved analyses, and stepwise release analyses. SR techniques have been instrumental in shaping a better understanding of geochronology because they allow the distributions of elemental or isotopic compositions to be obtained on the subgrain scale. This, in turn, allows the recognition and the isotopic characterization of diachronous components of mixtures. SR techniques may be particularly important for dating metasomatism, as metasomatic events are often partial, affecting rims, fractures, pore spaces etc, and leaving relict domains. With appropriate techniques, this allows the possibility of extracting geochronologic information about the alteration event and also about previous events in the geologic history, but as noted above, these interpretations must be built from detailed petrologic analysis.

Spatially resolved analyses can exploit any means to extract compositional or isotopic data from a selected portion of a mineral. Physical drilling and fragmentation are sometimes used (e.g., in the Rb-Sr "microchrons" by Müller et al. 2000), but the most frequent approaches involve sampling (vaporization, sputtering, etc.) of ca. 5–50 μm diameter spots of minerals by means of a primary beam, which also ionizes the radiogenic isotopes of interest (the secondary ion beam) or by compositional analysis by exciting characteristic X-rays of parent and daughter elements within specific compositional domains. The most widespread applications of *in situ* geochronology by microbeam pertain to the ^{39}Ar-^{40}Ar method (Megrue 1973; Hames and Cheney 1997; Di Vincenzo et al. 2001) and the U-Pb method (Compston et al. 1984; Gebauer et al. 1988; Williams et al. 2007).

The primary beam should impinge upon the sample in immediate proximal connection to a mass spectrometer and can be a laser beam (Megrue 1973; Christensen et al. 1995), an energetic ion beam (Compston et al. 1984), or an electron microprobe beam (Williams and Jercinovic 2002). By the combination of microchemical analyses with U-Pb dating, Williams and Jercinovic (2002) and Williams et al. (2007) were able to demonstrate the decisive importance of imaging

in order to accurately understand the isotopic record. The factor limiting the achievable resolution is not the size of the primary beam, but the need to produce a sufficiently intense secondary ion beam or characteristic X-rays such that counting uncertainties are acceptably small. The use of "age mapping" (Goncalves et al. 2005) covers a large number of geological problems. Of particular interest for the dating of metasomatic minerals is the possibility to determine the in-situ distribution of ages within single crystals, and between different crystals of the same mineral.

The immediate and obvious link between microchemical/microtextural analysis and geochronology provided by the spatially resolved analyses is also implicitly at the base of the stepwise release of isotopes from a mineral, which follows a different principle. Historically, the first successful attempts to obtain a (redundant) series of ages from a single sample were obtained by ^{39}Ar-^{40}Ar stepwise heating technique (Merrihue and Turner 1966), in which the sample Ar is extracted in a series of partial extractions at increasing oven temperatures. In Pb-Pb stepwise leaching (a much later development: e.g., Frei et al. 1997; Bouvier and Wadhwa 2010), samples are sequentially leached with different acids. Both stepwise release approaches exploit the fact that different minerals, i.e. different components of a polymineralic mixture, have crystal structures with different average bond lengths and strengths. The effects of increasing oven temperature and acid molarity/composition results in selective breakdown of some crystal structures, whose isotope signatures are thus made accessible to analysis, while other crystal structures are broken down and analyzed only at a later stage.

The ^{39}Ar-^{40}Ar stepheating technique was initially credited with the potential of allowing the calculation of an "internal" isochron from the Ar released in different heating steps of a single mineral, if the sample has never been perturbed since its formation (Merrihue and Turner 1966, their Fig. 2). In perturbed whole rocks, such as those analysed by Merrihue and Turner (1966, their Fig. 5) and Turner et al. (1971, their Fig. 1), isochron diagrams fail to give an alignment. This is intuitive, as in a polymineralic system the metamorphosed phases are no longer cogenetic, and violate the prerequisites for isochron formation. Isochrons can equally be obtained by regressing together laser spot analyses, provided they all were obtained on a monogenetic mineral generation. A very popular visualization of ^{39}Ar-^{40}Ar stepheating data is the age spectrum diagram (Fig. 6.2a, b), in which the age of individual heating steps is plotted against the cumulative release of an Ar isotope, most frequently ^{39}Ar. Interpretive difficulties can occur if step ages are not constant but internally discordant.

A decisive side-effect of the U-Th-Pb and ^{39}Ar-^{40}Ar methods, as well as electron microprobe "chemical" geochronology, is that the chemical signature is also revealed at the same time in the same analysis as the age determination proper. Electron microprobe "chemical" geochronology offers the most complete microchemical characterization of intra-crystalline zonations. An ^{39}Ar-^{40}Ar analysis yields the concentrations of three elements (K, Ca, Cl) and their ratios to radiogenic ^{40}Ar (Ar*) and to common isotope ^{36}Ar (Merrihue 1965). From five concentrations it is always possible to construct four isotope ratios having a common denominator. To first order, Ar isotopic ratios (such as, e.g.,

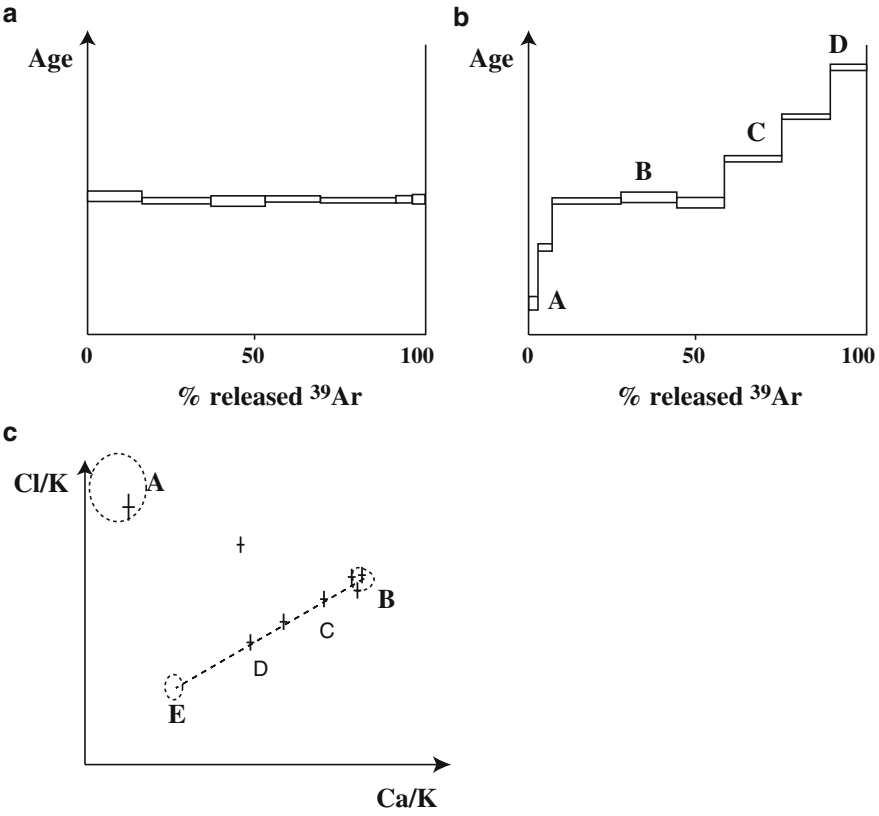

Fig. 6.2 ^{39}Ar-^{39}Ar data presentation. (**a**) Age spectrum diagram. The age calculated for each step is plotted as a function of the cumulative release of ^{39}Ar. The height of the boxes is the uncertainty on the step age. The portion of the age spectrum with ordinate values such that the weighted average of the relevant step ages has an MSWD < 1 is called a "plateau". The example represents a volcanic mineral whose eruption age is given by the plateau. Note, however, that "plateaus" do not a priori guarantee that their age is geologically meaningful, especially in the case of micas (Foland 1983; Hodges et al. 1994; Sletten and Onstott 1999). (**b**) Discordant age spectrum. In this example (a heterogeneous, partly metasomatized-metamorphosed amphibole) only a small part of the relevant information on the sample is provided by the age spectrum per se, and additional clues on the mineralogical identity of the Ar reservoirs must be derived by other means, such as comparing microchemical analyses with Ar isotope correlation diagrams (see c). Four portions of the spectrum can be described. In the first heating step(s), denoted by A, the apparent age is low; ages become constant at higher degassing temperatures (B), then rise in the last heating steps (C, D). (**c**) Ar isotope correlation diagram. The abscissa and the ordinate are constructed from the ^{37}Ar, ^{38}Ar and ^{39}Ar measured in each heating step. Three regions can be identified on the basis of electron probe microanalyses (fields enclosed by *dashed lines*): A, low-Ca, high-Cl secondary phases (clays, phyllosilicates); B, chemical composition of amphibole generation Am_2; E, chemical composition of amphibole generation Am_1. The stepheating results are plotted as crosses and can be directly compared to the sample mineralogy. It is clear that the first heating step with its high Cl/K ratio and low age must be viewed as degassing of secondary alteration phases. The three heating steps with constant Ca/K, Cl/K and Ar/K ratios are identified as Ar released only by amphibole generation Am_2; the closer the chemical match with the EMP analysis, the more correct

$^{37}Ar/^{38}Ar$) mirror the chemical signature (in this example, the Ca/Cl ratio); second-order perturbations, such as those due to differential recoil of ^{39}Ar, ^{38}Ar, and ^{37}Ar (Onstott et al. 1995) are negligible in samples whose relevant grain sizes are $\gg 1$ μm. The four ratios constructed from the five Ar isotopes define the coordinate axes of a four-dimensional space. As an example, if the common denominator is K-derived ^{39}Ar, the four-dimensional space is formed by the ratios Ca/K, Cl/K, Ar*/K, and Ar_{tr}/K (tr denoting the trapped non-radiogenic ^{36}Ar and ^{40}Ar). Every three-isotope correlation diagram is a two-dimensional projection of a four-dimensional distribution of data points.

Why should one be concerned about the Ca/Cl ratio in a mineral, if the age is calculated from the Ar/K ratio? The answer lies in the need to unravel polyphase mixtures by comparing element signatures with independent electron microprobe microchemical data (Villa et al. 2000). The possibility to simultaneously date a mineral and detect its chemical signature is an essential tool to detect and diagnose chemical heterogeneities in the analyzed minerals and to assess the viability of dating a metasomatic event in altered minerals. It may also provide a direct means of characterizing or constraining the composition of altering fluids.

Figure 6.2c is the chemical diagnostic diagram that is needed to understand the Ar isotope information hidden in the partly metamorphosed-metasomatized amphibole of Fig. 6.2b, and which is inaccessible if one limits the interpretation to just the age spectrum. The diagram shows the three reservoirs present in the amphibole separate: minor Cl-rich alteration phases, and two amphibole generations, Am_1 and Am_2. These three reservoirs define a triangle ABE, within which all step analyses plot. Insight on phase mixtures gained from metamorphic minerals (amphiboles, feldspars, micas) equally well applies to all other polymineralic systems (basalts, shales, pseudotachylites, etc.). The desirability of obtaining $^{38}Ar/^{39}Ar$ (Cl/K) and $^{37}Ar/^{39}Ar$ (Ca/K) ratios to constrain the interpretation of ^{39}Ar-^{40}Ar data results in a minimum sample size approaching or even exceeding the mg, as in most samples Cl/K ratios are $<<0.01$, and in mica Ca/K is also very low (with the exception of paragonite). The need to resolve Ca and Cl from background thus limits the spatial resolution of the ^{39}Ar-^{40}Ar laser microprobe, as excessively small samples end up

Fig. 6.2 (continued) the age estimate of the actual Am_2 crystallization. The steps with increasing ages (C, D) do not match the chemical composition of any particular mineral, and are no true end-members. Instead, because of the regular trends of the Ca/K, Cl/K and Ar/K ratios, they must be viewed as binary mixtures between end-member reservoirs B and E. On the other hand, the chemical signature of amphibole generation Am_1 as determined by electron microprobe is never found in the heating steps. This means that Am_1 never is the only reservoir releasing Ar, and that its Ar is always accompanied by some Ar released by Am_2. The age of generation Am_2 is given by the "plateau" steps B; that of Am_1 is found by extrapolating the age trend defined by steps B, C, and D to the known chemical composition E. The interpretation of the partial information provided by the age spectrum alone is incomplete, and only establishing a context with the chemical information makes the interpretation robust

losing the chemical information and forgoing the opportunity to identify the presence of μm-scale intergrowths and inclusions.

6.3 Isotopic Closure: Inheritance and Loss of Radiogenic Isotopes

6.3.1 Inheritance

It is commonly found that different chronometers in a rock give different apparent ages. Most of the time, but not always, zircon dated by U-Pb gives the oldest apparent age in a rock, i.e., the other geochronometers give younger apparent ages and thus have retained less radiogenic daughter isotopes than the zircon. This difference in retentivity does not mean that zircon apparent ages are a priori more accurate than those of other minerals.

It is frequently observed that granitoids intruding sediments of known age contain zircon with apparent ages that are older than the intruded country rocks. As an example, cores of zircon grains from the Adamello pluton, which intruded Mesozoic sediments, yield Proterozoic ages (Mayer et al. 2003). This does not mean that the pluton is older than the sediments it intrudes; the solution of this paradox lies in isotopic inheritance. Zircon grains normally do not release the accumulated Pb even when immersed in a 900°C hot magma (Mezger and Krogstad 1997). Thus, anatectic granitoids, such as the Eo/Oligocene Adamello pluton, commonly contain inherited zircon cores that retain the old age of the partially melted pre-existing crust. Zircon grains only date their own crystallization (Mezger and Krogstad 1997). Because zircon grains not only crystallize from a magma, but also accrete metamorphic rims from hydrothermal solutions, it is possible to disambiguate a U-Pb analysis by supplementing it with a petrographic characterization of the analyzed grain, e.g. by cathodoluminescence (CL). CL images were already in use by Krogh (Krogh and Medenbach, unpublished data, 1976; Medenbach 1976). Their connection with SIMS dating in more recent years (e.g. Gebauer et al. 1988) has spawned an interest in linking the isotope systematics to petrology, microchemistry, and microtextures (see, e.g., Williams and Jercinovic 2002; Vance et al. 2003; Corfu et al. 2003).

Isotopic inheritance is not limited to zircon. Almost every attempt to document isotopic inheritance associated with relict mineral cores that record geological events that are older than the rims has been successful. These include amphibole (Villa et al. 2000), biotite (Phillips and Onstott 1988), K-feldspar (Villa et al. 2006), monazite (Crowley and Ghent 1999), muscovite (Hammerschmidt and Frank 1991; Hames and Cheney 1997), and titanite (Corfu 1996), in addition to zircon. Of special interest is the ^{87}Sr and ^{40}Ar inheritance in minerals, such as feldspars and micas, which in the past were considered to be not very retentive (e.g., Faure 1986). Direct observations of ^{87}Sr variation amongst individual feldspar grains (Christensen et al. 1995) and of ^{40}Ar variations within a cm-sized muscovite

porphyroclast (Hames and Cheney 1997) prompted the respective authors to interpret their data in terms of isotope inheritance, permitted by extremely slow diffusion. Similarly, recent studies of diffusion (and closure) for U and Pb in zircon or monazite have determined very high closure temperatures and extremely sluggish diffusion even at relatively high temperatures. This behavior had been predicted empirically (Dahl 1997), and subsequently documented experimentally (see, e.g., Gardés et al. 2006; Cherniak 2010).

It has been argued (Villa 1998) that petrographic relics, as a rule, entail isotopic inheritance. The reason is that most radiogenic daughters have either a higher charge or a higher radius (or both), and therefore an inherently lower mobility, than the structure-forming ions, the only exceptions being certainly ^{4}He and possibly (but improbably) OH^{-}(Villa 2006). Thus, all other radiogenic daughters should have lower diffusivities than the structure-forming ions and only become mobile when the whole structure is modified, such as during recrystallization. Conclusive results on the atomic-scale mechanisms controlling the transport of isotopes are comparatively recent. Labotka et al. (2004) demonstrated that in albite the mobility of the second-fastest diffusing species, OH^{-}, is actually limited by dissolution/reprecipitation in an aqueous medium. Further confirmation that mobility of trace Ar atoms is lower than that of structure-forming cations was provided for K-feldspar by Nyfeler et al. (1998), and for amphibole by Villa et al. (2000) and Di Vincenzo and Palmeri (2001). An apparent exception, biotite, will be discussed below. If diffusion of radiogenic daughters is so slow, why do some geochronometers give apparent ages that are significantly younger than the independently known age of the geological event being dated? The mechanism whereby isotopes are "lost" (or, more correctly, exchanged with the intercrystalline medium) needs to be understood in order to reconcile the a priori atomistic argument with the geological observations and in order to date a metasomatic event.

6.3.2 Loss/Exchange of Radiogenic Isotopes

In the previous section, we have encountered two mechanisms by which mineral chronometers are rejuvenated. The most obvious mechanism in zircon is recrystallization, which is also observed in several other minerals (Fig. 6.3). In fact, this mechanism normally controls isotope exchange in all minerals (Cole et al. 1983) and, more in general, the formation of all metamorphic parageneses (Lasaga 1986; Putnis 2009). The reason is that the rate constants for fluid-mediated isotope transport are orders of magnitude larger, and activation energies much smaller, than those for diffusion (Cole et al. 1983). However, recrystallization is not the only cause of isotope loss/exchange, and we still need to take into account others, at least theoretically. Temperature can also play a role in reducing the retentivity of a geochronometer by increasing diffusivity. The problem is, the number of terrestrial rocks that have escaped any interaction with aqueous fluids (i.e. in which

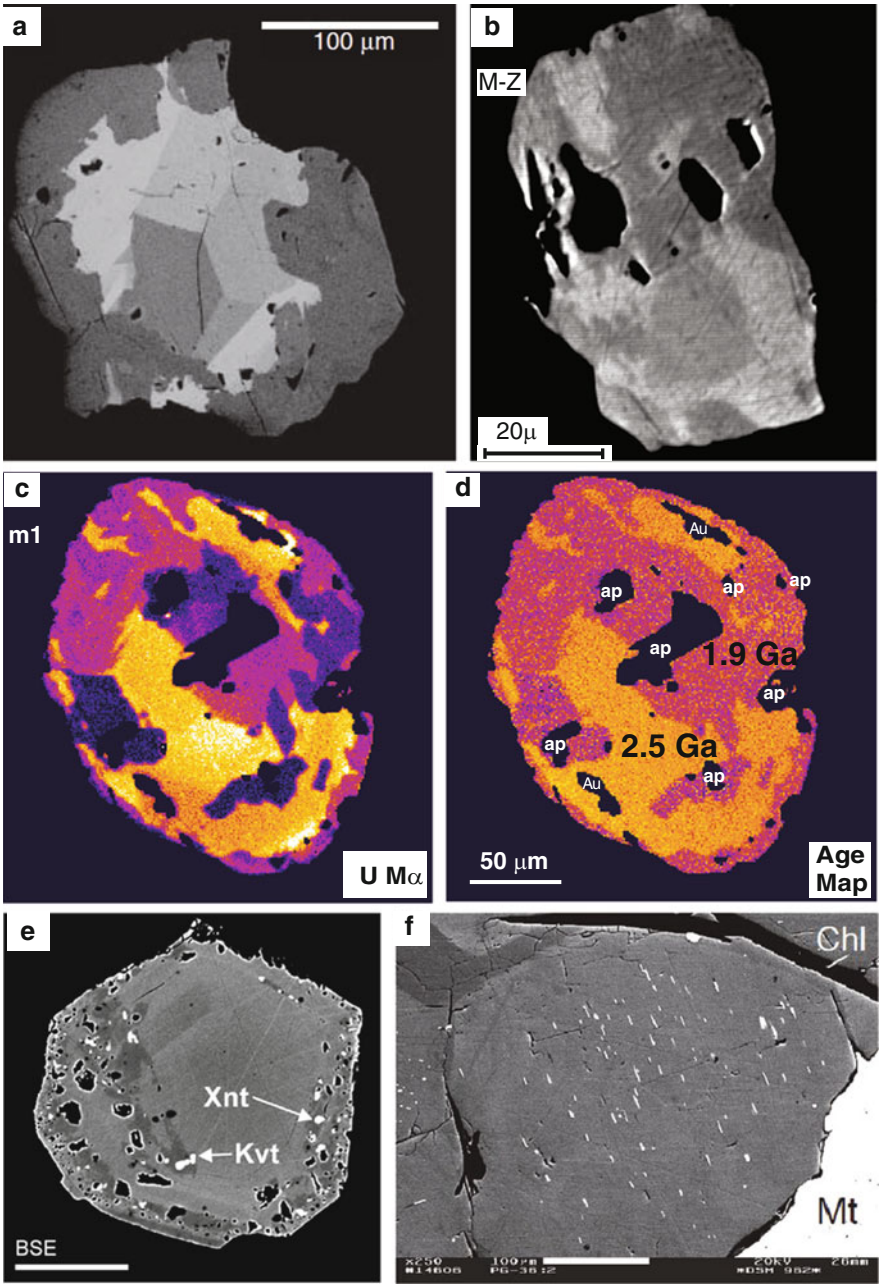

Fig. 6.3 (continued)

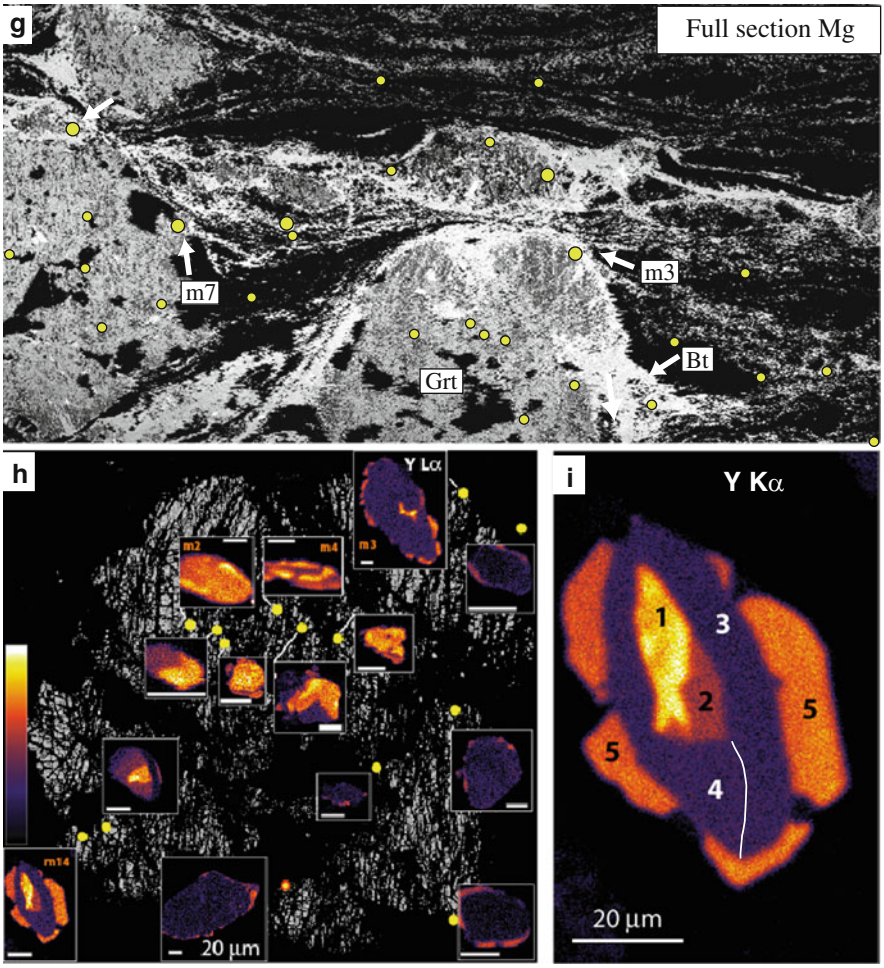

Fig. 6.3 (continued)

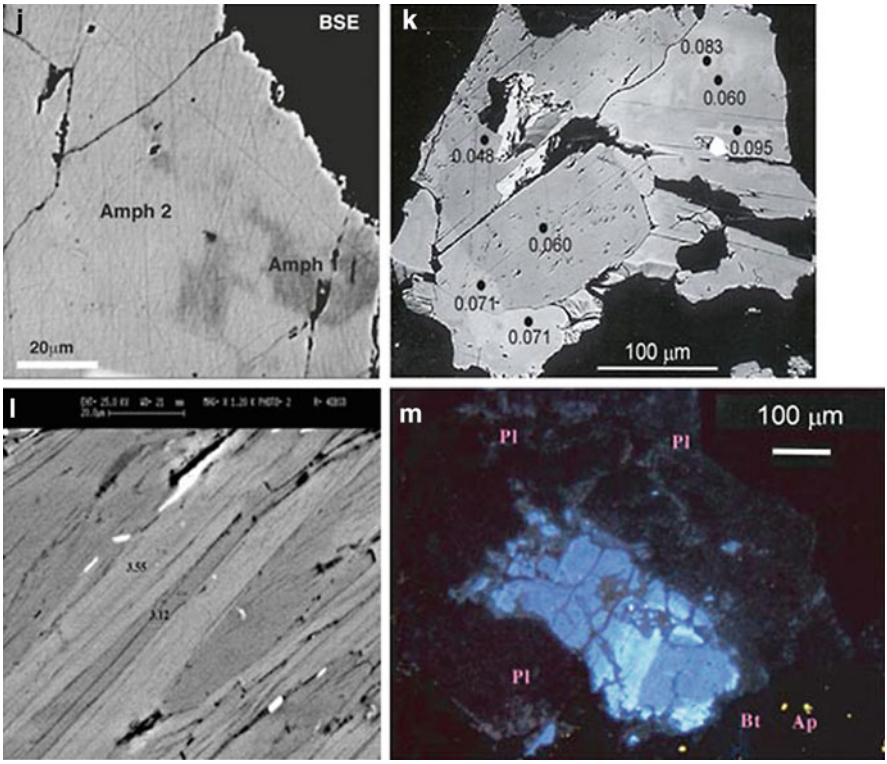

Fig. 6.3 Complex microstructures and microchemistry of minerals used for dating. (**a**) BSE image of monazite altered by coupled dissolution-reprecipitation process, from Cocherie et al. (2005), see also Harlov et al. (2011). (**b**) BSE image of monazite from Williams et al. (2011). (**c**) U compositional map of altered natural monazite from Athabasca granulite terrain, Canada (Williams et al. 2011). (**d**) "age" map of the same monazite. (**e**) Porosity and new mineral inclusions in altered zircon (from Geisler et al. 2007) (**f**). Altered apatite with oriented inclusions of monazite (from Harlov and Förster 2003). (**g**) Full-thin-section Mg Kα compositional map of a thin section from the East Athabasca Lake granulite terrain from a region interpreted to have been infiltrated by fluids during thrusting (Mahan et al. 2006). Yellow points show the location of monazite crystals. (**h**) Mn Kα compositional map of central garnet crystal with YLα maps of monazite crystals superimposed. Note that monazite from garnet core, near-rim, and rim are different reflecting three major generations of monazite. High-Y rims constrain the age of garnet break-down and fluid infiltration. (**i**) Y Lα compositional map of one monazite grain from garnet rim region. Note high-Y overgrowth interpreted to reflect fluid infiltration. (**j**) Back-scattered electron (BSE) image of amphibole sample LF-6 (Fig. 5c of Villa et al. 2000), in which relict patches of high-pressure amphibole generation Am1 ($Na_{M4} > 0.55$) are about 20 μm in diameter. They are encased in ca. 100 μm-sized replacive overgrowths of lower pressure amphibole generation Am2 ($Na_{M4} < 0.45$). The $^{39}Ar-^{40}Ar$ stepheating data (their Fig. 7b) assign an age > 75 Ma for Am1, corresponding to steps with Ca/K = 20–25, and an age of 60–65 Ma for Am2, in steps with Ca/K = 10–15. (**k**) BSE image of biotite CA 4200 (analyzed by ^{39}Ar-^{40}Ar stepheating by Villa et al. 2001). Relict patches of Fe-rich magmatic biotite Bt1 are irregularly substituted by hydrothermal Bt2. Numbers on selected spots represent the Cl concentration in atoms per formula unit. Light and dark grey tones correspond to average atomic number. The step

diffusion was not overrun by dissolution/reprecipitation) is exceedingly small. Only in these rare cases is diffusion the sole promoter of isotope resetting.

The straightforward criterion to assess the extent of thermally activated ("Fick's Law") diffusion is the presence of a bell-shaped gradient in isotope concentrations and ratios. Diffusion always follows Fick's Law; where diffusion is the factor limiting isotopic closure, a bell-shaped isotope gradient is necessarily observed. If no bell-shaped gradient is directly observed, other processes must have overrun Fick's Law diffusion. On the other hand, the tell-tale sign of fluid ingress and fluid-assisted dissolution/reprecipitation are patchy textures. Observation of a patchy texture in a mineral is certain evidence that the spatial distribution of its major structure-forming cations was controlled by open-system recrystallization (e.g., Schneider et al. 2007, Figs. 3–4). The key question that links isotope mobility with major element mobility is: has there ever been the observation of a patchily zoned crystal (i.e. one whose major element distribution was controlled by aqueous fluids) that displayed a bell-shaped spatial distribution of at least one isotopic system (except that of He)? A positive answer would imply that the mobility of that particular isotope can be larger than that of the major structure-forming cations; that Fick's Law diffusion of a trace isotope in an inert matrix is a common phenomenon; and that there is no automatic correspondence between petrographic relicts and isotope inheritance.

In-situ dating over three decades has never described bell-shaped isotope gradients in patchily zoned minerals. On the contrary, age mapping usually coincides with microchemical mapping (Williams et al. 2007). This is best explained by a common cause for recrystallization and isotope transport. The cause, fluid-mediated dissolution/reprecipitation (see Chap. 5), depends mainly on the fluid chemistry and only very loosely on temperature, i.e. provides a "geohygrometric" but not a geothermometric datum.

Fig. 6.3 (continued) ages obtained by stepwise heating anticorrelate with the Cl/K ratios. This allows dating of the Cl-rich biotite generation to $\leq$ 0.6 Ma and of the Cl-poor one to ca. 2.5 Ma. Note that the size of this grain is much smaller than that required for detection of ^{38}Ar by laser microprobe. (**l**) BSE image of polygenic white mica (Villa 2006). The field of view is 100 x 70 μm, Sample FL 24 shows layer-by-layer replacive retrogression of high-pressure phengite (Si content $>$ 3.5 atoms per formula unit (apfu), light grey) by greenschist-facies muscovite (Si $<$ 3.2 apfu, dark grey) occurring on the 5 μm scale. ^{39}Ar-^{40}Ar stepheating data for this mixed-generation sample yield an age mid-way between the 49 Ma age of preserved high-pressure phengite and the 40 Ma age of pure greenschist muscovite retrogression. (**m**) Cathodoluminescence image of microcline from the Aare granite. The bright and dull blue hues correspond both to stoichiometric K-feldspar. They define a vein-and-patch texture that results from fluid ingress and subsequent replacement reactions. Stepwise heating reveals a staircase-shaped age spectrum. To the extent that the step ages correlate with the Ca/K and Cl/K ratios, the age spectrum of the microcline does not reveal a core-to-rim zonation of the Ar concentration (whose existence would be surprising indeed, given the strongly patchy texture, far removed from a diffusive bell-shaped chemical profile). Instead, it reveals a mixture between a Ca-poor "Kfs-1" older than 35 Ma and a Ca-rich "Kfs-2" that records the same fluid circulation event at 9 Ma that was dated by Rb-Sr and ^{39}Ar-^{40}Ar on micas by Challandes et al (2008)

A useful concept in geochronology is that of petrological (dis)equilibrium. Equilibrium occurs when a mineral chronometer is free of both inheritance and retrogression. In such a case, the chemical and isotopic composition acquired upon crystallization is only affected by diffusion. A visual test thereof is the absence of sharp, patchy, irregular gradients. In a purely diffusive system, the spatial distributions of elements and isotopes must show a bell-shaped diffusion profile (e.g., Lasaga 1983). Whenever spatial distributions depart from a smooth bell-shaped profile, petrologists recognize the occurrence of multiple, discrete mineral generations that have not equilibrated completely. The concepts of "isotopic inheritance" and of "petrological disequilibrium" are inextricably intertwined, as will be discussed in the following sections.

In cases where the analyzed rock was affected by fluid activity and partial retrogression reactions, a disequilibrium paragenesis is observed. In cases where the petrological equilibrium is perturbed, the isotopic record is also perturbed, and the reacted minerals record the secondary event (to the extent that they are completely recrystallized) or a mixed age (to the extent that partial relics are preserved). It is only in equilibrated rocks that thermal diffusion of radiogenic daughter isotopes (^{40}Ar, ^{87}Sr, $^{206\text{-}7\text{-}8}$Pb, etc) can be quantified. A frequent misunderstanding overemphasizes the role of diffusional re-equilibration and ignores the faster processes that normally overrun it (dissolution-reprecipitation, fluid-induced and strain-induced recrystallization, retrogression reactions, etc.) and incorrectly interprets apparent ages as an invertible function of temperature. The mechanism for resetting the isotope record in nature depends more on the availability of recrystallization-enhancing aqueous fluids than on reaching a preset temperature.

These observations thus require a major shift of perspective on the significance of mineral ages. Just as the "diffusionist" view that zircon discordance is due to thermal disturbances (e.g., Steiger and Wasserburg 1969) has been put to rest by the petrological understanding that it is dominated by recrystallization (e.g., Mezger and Krogstad 1997), blanket interpretations of intra-mineral age variations in terms of a purely thermal history neglecting the petrogenetic context are no longer tenable. Recrystallisation is energetically less costly at almost any temperature than diffusive reequilibration (Cole et al. 1983; Villa 2010, p. 4–6, and references therein). Indeed, disequilibrium recrystallization promoted by aqueous fluids and/or deformation has been observed in metamorphic terrains and near granites, contact aureoles, and faults (e.g., Mahan et al. 2006). The emerging picture, capable of reconciling petrological, microtextural and geochronological observations, is that isotopic ages reflect mainly initial crystallization or recrystallization during high fluid activity.

Only dry rocks can preserve the record of pure diffusion (e.g., Kamber et al. 1995), as they were not modified by fluids. The absence of late-stage interaction with aqueous fluids is the main reason why preservation of metastable parageneses outside their stability field is possible at all, such as for granulites and eclogites. Most eclogitic rocks were retrogressed when they were exhumed into the upper crust and were exposed to sufficiently abundant aqueous fluids transported in cracks, normally in the greenschist facies (Proyer 2003). The same mineral, white mica, can

thus record both a greenschist retrogression age in some rocks and a very different post-eclogitization cooling age in other rocks of the same unit (see, e.g., De Sigoyer et al. 2000).

The sporadic documentation of *bona fide* diffusion in dry parageneses does not mean that diffusion can be generally assumed to have been the dominant process in all rocks. Similarly, the reproducibility of the mineral age sequence in many metamorphic terrains does not mean that this sequence proceeds from diffusion alone. On the contrary, Dahl (1997) pointed out that isotope retentivity is controlled by "ionic porosity", a proxy for the average length/strength of atomic bonds in crystal structures. Whichever mechanism has caused the breaking of bonds also enhanced isotope exchange (Villa 2006). Such mechanisms include temperature, deformation, and interaction with aqueous fluids. Minerals, "despite this diversity. . .repeat the same progression of (apparent) ages" (Dahl 1997, p. 278). Thus, the same sequence of atomic bond length/strengths will control not only isotopic retentivity but also weatherability, ability to survive metamorphism as a relict, etc.

Recent efforts to harmonize isotope geochemistry with petrology and microchemistry have a general implication for datability of metasomatic (and metamorphic) rocks. Regardless of the temperature at which metasomatism occurred, the most important observation that is required for a geochronological study is whether the rock consists only of newly (re)crystallized minerals or if instead it contains relicts. In the former case, dating of the metasomatic event, or the end of diffusive reequilibration after it, is simple. In the latter case, disequilibrium prevailed, and it becomes necessary to find ways to disentangle the isotope record. Because only the newly formed phases (rims, reaction patches, etc.) record the age of metasomatism, geochronologists have the choice between precise "bulk" dating of whole grains (U-Pb TIMS, ^{39}Ar-^{40}Ar stepheating) aided by scrupulous petrological groundwork, and spatially resolved analyses of sub-grain domains (EMPA, LA-ICP-MS, SIMS, ^{39}Ar-^{40}Ar laser microprobe). It must be emphasized that these techniques are complementary and are neither rivals nor mutually exclusive.

Because of the variety of possible micro- and nanometer-scale processes, the isotopic record is usually not influenced by a single macroscopic parameter, and the petrological context of each and every sample must be established first. Thus, a microtextural-microchemical and petrological investigation is a prerequisite for a meaningful sample choice. In order to date any geological event, and metasomatic events in particular, suitable mineral geochronometers that record that and only that event must be identified and analyzed. The ultimate goal is to completely determine the metasomatic reaction(s) in order to identify one, and hopefully several, chronometer phases that can constrain the age of metasomatism with high confidence.

The issue of F_0 (Eq. 6.1) is particularly critical for dating metasomatic reactions such as those described above in the case that metasomatic reactions affected some, but not the totality, of the minerals. If Pb is retained or incorporated into monazite during an alteration reaction, then the age of the metasomatic event or of the original parent monazite is severely compromised. Further, depending on whether Th or U are increased or decreased in the product phase, systematic errors can be

positive or negative, i.e. apparent ages can be older or younger than that of the metasomatic event. It may not be necessary for the inherited daughter isotope to be crystallographically incorporated into the recrystallized domains. Seydoux-Guillaume et al. (2003) documented Pb-rich domains and volume defects within altered monazite that were interpreted as inherited Pb from an earlier monazite phase. The nanometer-scale inclusions would be analyzed by any current analytical technique as part of the host crystal and incorporated into Eq. 6.1. However, Williams et al. (2011) analyzed experimentally altered monazite and determined that essentially all preexisting Pb was removed from the altered domains in these crystals. The age of these domains was essentially reset to zero and at some time in the future, a date from these domains would yield the time of metasomatism. At present, no definitive textural or compositional characteristics allows determining or interpreting F_0 in altered monazite. Thus, dates from more than one chronometer, for example, neocrystallized monazite inclusions and altered monazite domains in host phases, or different grains from different microstructural contexts in the same rock, can increase confidence in geochronological interpretations. Determining metasomatic reactions and thus, relationships between chronometer phases is particularly critical.

6.4 Dating Metasomatism

6.4.1 Characterization of Geochronometers in Metasomatic Assemblages

During metasomatism, minerals in a rock can be removed (by dissolution), precipitated, or recrystallized by interaction with an infiltrating fluid. That is, the process involves modifications to an existing rock that contains isotopic clocks that record some previous crystallization or recrystallization event. The challenge in constraining the age of the metasomatism is identifying isotopic chronometers (clocks) that have been started or entirely reset at the time of infiltration.

While metasomatic veins can involve exotic fluids and mobilization of elements normally considered immobile (such as Zr in peralkaline fluids in Zabargad Island (Oberli et al. 1987) or U in oxidizing fluids), normally the radioactive parents most easily mobilized are ^{87}Rb and ^{40}K, both being very water-soluble. The distinction between metasomatic and metamorphic events can be very blurred if we consider the point of view of a radiogenic isotope being retained or exchanged. That isotope will leave the crystal in which it resides whenever that crystal is destroyed. Following Putnis (2002, 2009), all recrystallization processes can be viewed as fluid-mediated nano-scale dissolution/reprecipitation processes. If the availability of water-rich fluids and the prevailing pressure-temperature-activity-composition (P-T-a-X) conditions promote recrystallization, then the daughter isotope, being more incompatible than the parent, will generally be excluded

from the reprecipitated, newly formed crystal. The nanometer-scale dissolution/reprecipitation process is given different names according to the large-scale context: aqueous alteration (e.g. muscovite to kaolinite), retrogression (e.g. phengite to muscovite), metasomatism (e.g. fine-grained sericite to coarse muscovite, or muscovite to sericite), metamorphism (e.g. kyanite to muscovite), recrystallization (zircon, monazite, xenotime to a new zircon, monazite, xenotime). In all cases, the result is predicted to involve resetting the isotopic clock to near zero.

It is clear that interaction with aqueous fluids is recorded, first and foremost, by petrological markers. If an interaction with a water-rich fluid is proposed to explain the isotope data, the principal evidence must be the petrological documentation of a metasomatic/fluid paragenesis and metasomatically induced chemical reactions. It will be beneficial to keep in mind that the main limitation on the recrystallization rate is the availability of appropriately reactive fluids, not temperature. As an example, adularia can grow (and replace feldspar) at any temperature between ca. 100°C and 400°C (Smith 1974, p.2) and even at lower temperature in ocean-floor sediments (Kastner and Siever 1979; Girard and Onstott 1991; Spötl et al. 1996). This provides the important conclusion that the presence of recystallization can be used as a "paleohygrometer" but not as a paleothermometer, as isotopic closure is only a vague function of temperature. The very use of the oxygen isotopic composition as a precise and accurate thermometer is questioned by the contrast between diffusion and recrystallization documented by Labotka et al. (2004).

Textural and compositional characterization of chronometer phases and of associated assemblages in general is a critical and absolutely essential first step for dating metasomatism as it is for dating any geologic or tectonic event. There is a thin line dividing characterization as a self-referential purpose from petrologic characterization as a means to illuminate additional facets of the geologic problem under investigation. Isotope records taken alone, without proper petrologic context, can be misinterpreted even if their analytical quality is excellent. Analytical precision is not *per se* a guarantee of accuracy; the latter always requires an external validation. Compositional imaging (mapping) can be a useful petrologic tool, able to reveal textural and structural domains within chronometer phases and can be invaluable for interpreting new geochronologic data. Imaging by cathodoluminescence (CL) and backscattered electrons (BSE) have been widely used for characterizing zircon, monazite, xenotime, titanite, apatite texture and microstructure (Fig. 6.3a, b). However, linkages between image intensities and specific compositional variables are not typically known or calibrated. Also, images may be particularly sensitive to certain components and insensitive to others giving false impressions of homogeneity of chronometer phases. Wavelength dispersive (WDS) electron microprobe mapping of chronometer phases is increasingly used to characterize zoning and domainal structure. These maps have the distinct advantage of highlighting specific compositional components and thus can link chronometers to specific chemical reactions. However detectability limits restrict the use of these maps to relatively abundant trace components and images can be complicated by background and interference phenomena (Jercinovic et al. 2008). Under optimal conditions, composition maps can be combined to generate age maps that can be

particularly useful for relating chronometer structure to rock texture and structure (Fig. 6.3c, d) (Goncalves et al. 2005; Williams et al. 1999).

Recent experiments carried out on homogeneous starting monazite crystals show some of the textures and compositions characteristic of partial alteration (Harlov and Hetherington 2010; Harlov et al. 2011). In general, altered domains tend to have relatively sharp but curving boundaries, although some boundaries are straight and aligned with rational crystal faces. Altered domains can be aligned along microcracks or inclusions although many have no recognizable structural control (Fig. 6.3e, f). Based on the most distinctive textures, it is likely that a number of natural monazite grains also reflect fluid related alteration, either by hydrothermal fluids, metamorphic fluids, or melts (for example, Hawkins and Bowring 1997; 1999; Baldwin et al. 2006; Petrik and Konecny 2009; Williams et al. 2011). With increased recognition of dissolution-reprecipitation processes will come a broader understanding of the bulk compositions, fluid compositions, geologic environments, and P-T-a-X conditions that typically lead to alteration, recrystallization, and resetting of ages. The composition of altering fluids, including melts, is apparently critical for the alteration process. For example, monazite is particularly reactive in alkali-bearing fluids at amphibolite facies conditions (Harlov et al. 2011; Hetherington et al. 2010). Some other fluid compositions, under similar conditions, yield little or essentially no alteration. This emphasizes the fact that selecting appropriate bulk compositions and appropriate chronometer phases is a necessary requirement for dating metasomatic events. However, both laboratory experiments and field research on natural samples are at a very early stage in understanding the thresholds limiting fluid-rock reactions.

One technique that can be very useful for investigating metasomatic events involves full-thin-section compositional mapping (see Williams et al. 2006). Full-thin-section, or large-area, compositional maps are generated using the electron microprobe (Williams and Jercinovic 2002) or high-resolution SEM (Kelly et al. 2010), typically with relatively large pixel spacing and a defocused beam. Specific elements are chosen in order to highlight minerals of interest and also the background rock texture (i.e. Ce or La for monazite, Y for xenotime, Zr for zircon; Mg, Ca, or Al for background texture). These maps can provide the location of all accessory phase chronometers (to a size of several micrometers or less) within the context of the rock (Fig. 6.3g). The distribution of chronometers can reveal metamorphic or hydrothermal reactions, i.e. xenotime at the margins of anhedral garnet, or along selvages of veins. Maps of individual minerals (i.e. monazite, xenotime) can be superimposed on the full-section images in order to relate internal compositional geometry to the larger textural or structural setting (Fig. 6.3h, i). Similar full-section or large-area maps should be useful for other petrologic or chronometer systems (i.e. ^{39}Ar-^{40}Ar or Rb-Sr) by providing for alteration assemblages or particular zoning patterns. Examples are shown in Fig. 6.3j–m.

Many geochronological studies pass directly from textural analysis of chronometer phases to geochronology. However, compositional analysis of whole minerals or of subdomains is invaluable for linking chronometers to host rock processes and assemblages. In some cases, such as microprobe monazite analysis, compositional

characterization is a necessary part of the geochronologic analysis but in other cases, such as U-Pb TIMS analysis of zircon, it may involve an additional analytical process, i.e. separate ion microprobe or LA-ICP-MS analysis (e.g., Barth and Wooden 2010). For characterizing metasomatism, compositional analysis can have two major advantages: (1) it may help to fingerprint the specific domain or generation that grew during metasomatism and thus can constrain the age of metasomatism and (2) the composition of the chronometer may help to constrain the composition of the metasomatizing fluids. In the case of altered zircon, it has been argued that addition of major elements (Ca, Fe, Al) is a characteristic sign of altered, formerly metamict domains (Geisler et al. 2007). Zircon produced during fluid-related recrystallization of non-metamict domains tends to lack these added elements. This may provide a way to discriminate between these two types of altered/recrystallized zircon, a distinction that may be very important for geochronology. The first type tends to be discordant while the second can be concordant and may directly date the time of metasomatism (Geisler et al. 2007).

Micas have long been known to record, first and foremost, reactions on the retrograde path (e.g., Arnold and Jäger 1965). Even if diffusion should, in principle, also play a detectable role in resetting ages, to date there has been no report of a bell-shaped age profile that could be assigned to diffusion without superimposed faster processes. On the contrary, age profiles obtained by laser microprobe demonstrate that accretion and patchy resetting are predominant (Onstott et al. 1990; Hodges et al. 1994; Hames and Cheney 1997). This does not mean that diffusion is nonexistent in micas. It only means that in grains that are sufficiently large (several mm) to allow age-mapping it has not been observed so far. In fact, in small grains from some amphibolite-facies rocks from the Central Alps, Allaz et al. (2011) argued that Ar was being lost due to volume diffusion, corresponding to a "closure temperature" of ca. 500°C. However, they did not obtain K-Ar age profiles across individual grains that could demonstrate the bell-shaped age decrease that would provide the conclusive proof. Instead, they observed a dependence of ages on retrograde reactions, with a larger proportion of the variation in biotite ages accounted for by chloritization and other retrograde reactions than that accounted for by cooling alone. This reinforces the notion that interactions with fluids, even when they are subordinate, achieve a greater mobilization of radiogenic Ar than thermally activated diffusion. The latter has a similar order of magnitude as the mobility of the lattice-forming cations, as indicated by the fact that the true "closure temperature" of the K-Ar system in biotite is substantially above the lower limit of the biotite "isograd".

Of special interest, when micas are analyzed, is the control on petrological equilibrium provided by stoichiometry. Many analyses of the 1960s and 1970s report K concentrations that are lower than those of pure mica. While sometimes this is just an effect of impure mineral separates, this is a cause of concern about the reliability of some of the literature data. Because retrogression (chloritization, sagenitization, sericitization, and other reactions) frequently leads to alkali loss from ideal micas, and because it has been clearly demonstrated that retrogression reactions result in lowered ages (Arnold and Jäger 1965; Di Vincenzo et al. 2003,

2004; Schobert 2005; Malusà et al. 2011), the K concentration in micas should be monitored carefully. The default assumption should be that every mica that went through greenschist facies conditions on its retrograde path from higher P-T conditions was affected by fluid ingress, and that only a few exceptions exist, limited to anhydrous rocks that preserve the high-grade petrological equilibrium. Retrogression can occur on a scale smaller than that of optical microscopy (e.g., Figs. 2 and 3 of Di Vincenzo et al. 2004), so the burden of proving that a mica with a substoichiometric K concentration is unaffected by retrogression reactions may require a considerable EMPA or TEM imaging effort.

Once chronometer phases have been identified and characterized, the critical step in chronologic analysis is to select the analytical method with the spatial and temporal resolution to constrain the age of the event of interest. As noted above, if metasomatic re-equilibration is complete, that is if phases are entirely recrystallized, then whole mineral techniques such as stepwise heating, ID-TIMS, or isochron analysis yield straightforward, accurate results. However, if metasomatism involved partial recrystallization of minerals or assemblages, then altered domains must be defined and characterized with petrologic analysis. As mentioned above, two complementary approaches can unravel the isotope record of a mineral mixture: a "bulk" analysis using the appropriate discrimination diagrams (concordia for U-Pb, chemical correlation diagrams for ^{39}Ar-^{40}Ar stepheating), or a spatially resolved analysis. If alteration patches are very large (> 100 μm), ^{39}Ar-^{40}Ar laser analyses are feasible (Villa et al. 1996, Fig. 5; Müller et al. 2002, Fig. 12). For intermediate patch sizes (10-20 μm or more), LA-ICP-MS or SIMS analyses can constrain the U-Pb or Th-Pb age of metasomatized domains. If recrystallized minerals or domains are even smaller, and at the same time sufficiently old to have accumulated measurable Pb, the electron microprobe may the instrument of choice for constraining the age of the metasomatized minerals or domains (Williams et al. 2011).

6.4.2 Examples and Opportunities for Dating Metasomatism

Micas, monazite, zircon, titanite, xenotime, and allanite are all potentially useful chronometers of metasomatic events as all have been shown to be produced or recrystallized during fluid-related events. Even amorphous silica (opal) may hold some promise (Neymark et al. 2000). Monazite may be particularly useful because of its wide compositional range; complete analyses can exceed 20 or more elements (Jercinovic et al. 2008). Thus, new growth domains or recrystallized domains tend to be recognizable based on compositional changes and could be linked to certain fluid compositions. Distinct compositional domains with sharp boundaries are common in monazite, and in many cases, the geometry of the domains can be related to microstructure or microtexture in the host rock (Fig. 6.3). Compositional domains in monazite are typically interpreted in terms of successive growth events, but altered or recrystallized domains are increasingly recognized or interpreted (Harlov et al.

2011). As noted above, diffusion is extremely slow in monazite and thus domains can preserve their composition through later thermal events. Finally, significant experimental work has shown that monazite, as well as xenotime and allanite, can be susceptible to fluid-aided, coupled dissolution-reprecipitation (Putnis 2002, 2009; Putnis and Austrheim 2010; Harlov et al. 2011; see also Chap. 5). It fact, this may be the major means of resetting or disturbing monazite ages. Dissolution-reprecipitation reactions may complicate interpretations of monazite ages, but alternatively, they may provide a means of dating metasomatism if altered domains can be recognized as such, based on texture or composition and, as discussed above, if removal of daughter isotopes (i.e. Pb) is complete at the time of alteration.

Three situations may be particularly useful for dating metasomatism using monazite. First, some entirely new monazite generations (i.e. new crystals or rims on existing crystals) may grow as a result of metasomatic reactions. For example, if metasomatic fluids lead to garnet resorption, new Y-rich monazite may develop as a sink for Y released from garnet (Mahan et al. 2006). Second, fine monazite inclusions have been recognized as products of dissolution-reprecipitation reactions. For example, alteration of fluor- and chlorapatite with growth of monazite and xenotime inclusions has been observed in experiments and in natural samples (Harlov et al. 2002; Harlov and Förster 2003; Harlov et al. 2005; Hansen and Harlov 2007). These small inclusions, having grown at the time of alteration, offer a direct means of dating the metasomatic alteration of the apatite. However, because of their small size, the electron microprobe may be the only means of analyzing or isolating the new crystals and thus, only crystals of sufficient age can be dated with precision. Similarly, uraninite and thorite inclusions, produced during alteration of monazite and xenotime, could provide a direct dating target (Hetherington and Harlov 2008). The third situation involves dating altered domains within monazite or xenotime crystals themselves. This requires that any preexisting Pb be removed during the alteration process (see Williams et al. 2011 and Harlov et al. 2011). As noted above, even if Pb is not compatible with the new monazite or xenotime lattice, it may be concentrated in volume defects and could be analyzed inadvertently (Seydoux-Guillaume et al. 2003).

Two alteration settings have been discussed with respect to zircon (Krogh and Davis 1974, 1975; Geisler et al. 2007), and both offer the possibility of constraining the age of the alteration/metasomatism event. The first involves fluid-mediated alteration and recovery of radiation-damaged, metamict or amorphous zircon. The altered domains can have a distinctive texture involving inward curving reaction domains with locally cracked rim domains indicative of volume change during radiation damage and recovery processes (see figures in Geisler et al. 2003). The altered domains are commonly characterized by dramatically increased levels of solvent cations such as Ca, Fe, and Al (Geisler et al. 2003; Rayner et al. 2005). The altered domains can yield discordant dates that can indicate the age of the metasomatic event by the lower concordia intercept with the discordia line. The second type of zircon alteration involves direct replacement of zircon by a new zircon composition as a result of coupled dissolution-reprecipitation (e.g., Tomaschek et al. 2003; Tomaschek 2004; Harlov and Dunkley 2010). Altered domains are typically

characterized by increased porosity, crystallographically aligned mineral inclusions, and reduced abundance of trace components. The altered zircon, if domains are large enough for ion microprobe analysis and if the Pb is completely removed, can provide a direct constraint on the age of metasomatism. Analyses of mineral inclusions (most commonly, xenotime) can be used to verify the age of metasomatism.

Xenotime may also offer opportunities for dating metasomatic events. In addition to the precipitation of xenotime inclusions during dissolution-reprecipitation reactions, xenotime has been observed as overgrowths on zircon, probably because zircon is isostructural with xenotime. Some overgrowths on detrital zircon have been interpreted to have formed during diagenesis of sedimentary rocks, but hydrothermal xenotime has also been documented (see Rasmussen 1996, 2005; Rasmussen et al. 2004; Hetherington et al. 2008).

One additional opportunity for dating metasomatic events could involve dating primary zircon (or monazite or xenotime) within hydrothermal quartz or carbonate veins in altered rocks (Davis et al. 1994; Pettke et al. 2005; Schaltegger 2007). Petrological analysis must be used to relate the veins to particular metasomatic events/reactions in the host rocks. It is possible that dissolution-precipitation reactions in the host rocks occurred during vein formation and thus, compositional analysis of vein-hosted zircon may provide links between vein forming events and host-rock alteration.

The ^{39}Ar-^{40}Ar data by Maineri et al. (2003) attempt to clarify the timing of alkali-metasomatic processes at a raw ceramic material mine formed by sericite replacing magmatic muscovite. Because of the young ages involved (between 9 and 6 Ma), absolute age uncertainties allow a remarkably good time-resolution. Fluid inclusion analyses round off a genetic model whereby the circulation of comparatively low-T, low salinity meteoric fluids metasomatized an aplite 2.2 ± 0.1 Ma after the latter's emplacement, and 0.8 ± 0.1 Ma before another granitoid intrusion in a nearby area. The constraints provided by the ^{38}Ar/^{39}Ar ratios, i.e. the Cl/K ratios, of the analyzed white micas demonstrate that neither a pure magmatic nor a pure metasomatic mica were sampled. However, end-members were dated using the extrapolation to EMPA values described in Fig. 6.2.

The Rb-Sr data by Glodny et al. (2008) demonstrate that isotopic closure of the Rb-Sr system essentially records fluid interaction even in high-grade metamorphic rocks. One key aspect of their work was identifying those minerals of a rock that were in mutual equilibrium, both petrological and isotopic (the parallelism between the two has already been emphasized earlier). The characterization of metasomatic assemblages is covered to a much more extensive degree in other chapters of this book, as well as in petrology textbooks. The main point that a geochronologist should always bear in mind is that geochronology is a petrologic issue, not a separate discipline that "dates" entities (minerals or mineral mixtures) without establishing their identity and their context.

6.5 Concluding Remarks

During metasomatism, minerals in a rock can be removed (by dissolution), precipitated, or recrystallized by interaction with an infiltrating fluid. That is, the process involves modifications to an existing rock that contains isotopic clocks that record some previous crystallization or recrystallization event. The challenge in constraining the age of the metasomatism is identifying isotopic chronometers (clocks) that were started or entirely reset at the time of infiltration. The mechanism for resetting the isotope record in nature depends more on the availability of recrystallization-enhancing aqueous fluids than on reaching a preset temperature. Mineral geochronometers should be viewed as "geohygrometers" that essentially date, and characterize isotopically, fluid circulation episodes. Metasomatic events that achieve a complete recrystallization of the mineral assemblage provide accurate ages, and provide overdetermined internal isochrons that have a low MSWD.

Incomplete metasomatic recrystallization results in disequilibrium parageneses. Because petrographic relics, as a rule, entail isotopic inheritance, dating rocks in petrological disequilibrium requires the use of spatially resolved analyses or of stepwise release of isotopes from discrete phases. Intracrystalline variations of isotope ratios, i.e. ages, can be assembled in "age maps", which can be related to compositional maps that constrain the petrogenesis of a mineral. It is important to realize that overgrowths and recrystallization are really two parts of the same fluid-driven process that also provides the fastest mechanism for isotope exchange and age resetting.

Acknowledgements Reviews by Fernando Corfu, Pete Dahl, Gianfranco Di Vincenzo, and Klaus Mezger improved earlier versions of the manuscript.

References

Allaz J, Berger A, Engi M, Villa IM (2011) The effects of retrograde reactions and of diffusion on ^{39}Ar-^{40}Ar ages of micas. J Petrol 52:691–716

Allen FM (1992) Mineral definition by HRTEM: problems and opportunities. Rev Mineral 27:289–333

Arnold A, Jäger E (1965) Rb-Sr-Altersbestimmungen an Glimmern im Grenzbereich zwischen voralpinen Alterswerten und alpiner Verjüngung der Biotite. Eclogae Geol Helv 58:367–390

Baldwin JA, Bowring SA, Williams ML, Mahan KH (2006) Geochronological constraints on the evolution of high-pressure felsic granulites from an integrated electron microprobe and ID-TIMS geochemical study. Lithos 88:173–200

Barth AP, Wooden JL (2010) Coupled elemental and isotopic analyses of polygenetic zircons from granitic rocks by ion microprobe, with implications for melt evolution and the sources of granitic magmas. Chem Geol 277:149–159

Bouvier A, Wadhwa M (2010) The age of the Solar System redefined by the oldest Pb–Pb age of a meteoritic inclusion. Nature Geosci 3: 637–641

Challandes N, Marquer D, Villa IM (2008) P-T-t modelling, fluid circulation, and 39Ar-40Ar and Rb-Sr mica ages in the Aar Massif shear zones (Swiss Alps). Swiss J Geosci 101: 269–288

Cherniak DJ (2010) Diffusion in accessory minerals: zircon, titanite, apatite, monazite and xenotime. Rev Mineral Geochem 72:827–869

Christensen JN, Halliday AN, Lee DC, Hall CM (1995) In situ Sr isotopic analysis by laser ablation. Earth Planet Sci Lett 136:79–85

Cocherie A, Be Mezeme E, Legendre O, Fanning CM, Faure M, Rossi P (2005) Electron microprobe dating as a tool for determining the closure of Th-U-Pb systems in migmatitic monazites. Am Mineral 90:607–618

Cole DR, Ohmoto H, Lasaga AC (1983) Isotopic exchange in mineral-fluid systems. I. Theoretical evaluation of oxygen isotopic exchange accompanying surface reactions and diffusion. Geochim Cosmochim Acta 47:1681–1693

Compston W, Williams IS, Meyer CE (1984) U-Pb geochronology of zircons from lunar breccia 73217 using a sensitive high mass-resolution ion microprobe. Proc Lunar Planet Sci Conf 14:525–534

Corfu F (1996) Multistage zircon and titanite growth and inheritance in an Archean gneiss complex, Winnipeg River Subprovince, Ontario. Earth Planet Sci Lett 141:175–186

Corfu F, Muir TL (1989) The Hemlo Heron Bay greenstone belt and Hemlo Au Mo deposit, Superior Province: II. Timing of metamorphism, alteration and Au mineralization from titanite, rutile, and monazite U Pb geochronology. Chem Geol 79:201–223

Corfu F, Hanchar JM, Hoskin PWO, Kinny P (2003) Atlas of zircon textures. Rev Mineral Geochem 53:468–500

Crowley JL, Ghent ED (1999) Electron microprobe study of the U-Th-Pb systematics of metamorphosed monazite: the role of Pb diffusion versus overgrowth and recrystallization. Chem Geol 157:285–302

Dahl PS (1997) A crystal-chemical basis for Pb retention and fission-track annealing systematics in U-bearing minerals, with implications for geochronology. Earth Planet Sci Lett 150: 277–290

Davis DW, Schandl ES, Wasteneys HA (1994) U-Pb dating of minerals in alteration halos of Superior Province massive sulfide deposits - syngenesis versus metamorphism. Contrib Mineral Petrol 115:427–437

De Sigoyer J, Chavagnac V, Blichert-Toft J, Villa IM, Guillot S, Luais B, Cosca M, Mascle G (2000) Dating the Indian continental subduction and collisional thickening in the northwest Himalaya: multichronology of the Tso Morari eclogites. Geology 28:487–490

DeWolf CP, Zeissler CJ, Halliday AN, Mezger K, Essene EJ (1996) The role of inclusions in U-Pb and Sm-Nd garnet geochronology: stepwise dissolution experiments and trace uranium mapping by fission track analysis. Geochim Cosmochim Acta 60:121–134

Di Vincenzo G, Palmeri R (2001) An ^{40}Ar-^{39}Ar investigation of high-pressure metamorphism and the retrogressive history of mafic eclogites from the Lanterman Range (Antarctica): evidence against a simple temperature control on argon transport in amphibole. Contrib Mineral Petrol 141:15–35

Di Vincenzo G, Ghiribelli B, Giorgetti G, Palmeri R (2001) Evidence of a close link between petrology and isotope records: constraints from SEM, EMP, TEM and in situ ^{40}Ar-^{39}Ar laser analyses on multiple generations of white micas (Lanterman Range, Antarctica). Earth Planet Sci Lett 192:389–405

Di Vincenzo G, Viti C, Rocchi R (2003) The effect of chlorite interlayering on ^{40}Ar-^{39}Ar biotite dating: an ^{40}Ar-^{39}Ar laserprobe and TEM investigation of variably chloritised biotites. Contrib Mineral Petrol 145:643–648

Di Vincenzo G, Carosi R, Palmeri R (2004) The relationship between tectono-metamorphic evolution and argon isotope records in white mica: constraints from in situ ^{40}Ar-^{39}Ar laser analysis of the Variscan basement of Sardinia. J Petrol 45:1013–1043

Engvik AK, Mezger K, Wortelkamp S, Bast R, Corfu F, Korneliussen A, Ihlen P, Bingen B, Austrheim H (2011) Metasomatism of gabbro - mineral replacement and element mobilization during the Sveconorwegian metamorphic event. J Metamorph Geol 29: 399–423

Faure G (1986) Principles of isotope geology, 2nd edn. Wiley, Chichester

Ferrara G, Petrini R, Serri G, Tonarini S (1989) Petrology and isotope geochemistry of San Vincenzo rhyolites (Tuscany, Italy). Bull Volcanol 51:379–388

Foland KA (1983) $^{40}Ar/^{39}Ar$ incremental heating plateaus for biotites with excess Ar. Chem Geol 41:3–21

Frei R, Villa IM, Kramers JD, Nägler TF, Przybylowicz WJ, Prozesky VM, Hofmann B, Kamber BS (1997) Single mineral dating by the Pb-Pb step-leaching method: assessing the mechanisms. Geochim Cosmochim Acta 61:393–414

Gardés E, Jaoul O, Montel J-M, Seydoux-Guillaume A-M, Wirth R (2006) Geochim Cosmochim Acta 70:2325–2336

Gebauer D, Av Q, Compston W, Williams IS, Grünenfelder M (1988) Archean zircons in a retrograded Caledonian eclogite of the Gotthard massif (Central Alps, Switzerland). Schweiz Mineral Petrog Mitt 68:485–490

Geisler T, Pidgeon RT, Kurtz R, van Bronswijk W, Schleicher H (2003) Experimental hydrothermal alteration of partially metamict zircon. Am Mineral 88:1496–1513

Geisler T, Schaltegger U, Tomaschek F (2007) Re-equilibration of zircon in aqueous fluids and melts. Elements 3:43–50

Girard J-P, Onstott TC (1991) Application of $^{40}Ar/^{39}Ar$ laser-probe and step-heating techniques to the dating of diagenetic K-feldspar overgrowths. Geochim Cosmochim Acta 55:3777–3793

Glodny J, Kuhn A, Austrheim H (2008) Diffusion versus recrystallization processes in Rb-Sr geochronology: isotopic relics in eclogite facies rocks, western Gneiss region, Norway. Geochim Cosmochim Acta 72:506–525

Goncalves P, Williams ML, Jercinovic MJ (2005) Electron microprobe age mapping. Am Mineral 90:578–585

Hames WE, Cheney JT (1997) On the loss of $^{40}Ar^*$ from muscovite during polymetamorphism. Geochim Cosmochim Acta 61:3863–3872

Hammerschmidt K, Frank E (1991) Relics of high pressure metamorphism in the Lepontine Alps (Switzerland) - 40Ar-39Ar and microprobe analyses on white micas. Schweiz Mineral Petrogr Mitt 71:261–274

Hansen EC, Harlov DE (2007) Whole-rock, phosphate, and silicate compositional trends across an amphibolite- to granulite-facies transition, Tamil Nadu, India. J Petrol 48:1641–1680

Harlov DE, Dunkley DJ (2010) Experimental high-grade alteration of zircon using akali- and Ca-bearing solutions: resetting the zircon geochronometer during metasomatism V41D-2301 presented at 2010 Fall Meeting, AGU, San Francisco, 13–17 Dec 2010

Harlov DE, Förster H-J (2003) Fluid-induced nucleation of REE-phosphate minerals in apatite: nature and experiment. Part II. Fluorapatite. Am Mineral 88:1209–1229

Harlov DE, Hetherington CJ (2010) Partial high-grade alteration of monazite using alkali-bearing fluids: experiment and nature. Am Mineral 95:1105–1108

Harlov DE, Förster H-J, Nijland TG (2002) Fluid-induced nucleation of (Y + REE)-phosphate minerals within apatite: nature and experiment. Part I. Chlorapatite. Am Mineral 87:245–261

Harlov DE, Wirth R, Förster H-J (2005) An experimental study of dissolution-reprecipitation in fluorapatite: fluid infiltration and the formation of monazite. Contrib Mineral Petrol 150: 268–286

Harlov DE, Wirth R, Hetherington CJ (2011) Fluid-mediated partial alteration in monazite: the role of coupled dissolution–reprecipitation in element redistribution and mass transfer. Contrib Mineral Petrol 162:329–348

Hawkins DP, Bowring SA (1997) U-Pb systematics of monazite and xenotime: case studies from the Paleoproterozoic of the Grand Canyon, Arizona. Contrib Mineral Petrol 127:87–103

Hawkins DP, Bowring SA (1999) U-Pb monazite, xenotime and titanite geochronological constraints on the prograde to post-peak metamorphic thermal history of Paleoproterozoic migmatites from the Grand Canyon, Arizona. Contrib Mineral Petrol 134:150–169

Hetherington CJ, Harlov DE (2008) Metasomatic thorite and uraninite inclusions in xenotime and monazite from granitic pegmatites, Hidra anorthosite massif, southwestern Norway: mechanics and fluid chemistry. Am Mineral 93:806–820

Hetherington CJ, Jercinovic MJ, Williams ML, Mahan KH (2008) Understanding geologic processes with xenotime: composition, chronology, and a protocol for electron probe microanalysis. Chem Geol 254:133–147

Hetherington CJ, Harlov DE, Budzyń B (2010) Experimental metasomatism of monazite and xenotime: mineral stability, REE mobility and fluid composition. Mineral Petrol 99: 165–184
Hodges KV, Hames WE, Bowring SA (1994) $^{40}Ar/^{39}Ar$ age gradients in micas from a high-temperature-low-pressure metamorphic terrain; evidence for very slow cooling and implications for the interpretation of age spectra. Geology 22:55–58
Jercinovic MJ, Williams ML, Lane ED (2008) In-situ trace element analysis of monazite and other fine-grained accessory minerals by EPMA. Chem Geol 254:197–215
Kamber BS, Blenkinsop TG, Villa IM, Dahl PS (1995) Proterozoic transpressive deformation in the Northern Marginal Zone, Limpopo Belt, Zimbabwe. J Geol 103:493–508
Kastner M, Siever R (1979) Low temperature feldspars in sedimentary rocks. Am J Sci 279: 435–479
Kelly N, Appleby S, Mahan K (2010) Mineralogical and textural characterization of metamorphic rocks using an automated mineralogy approach. In: Programs with abstracts, annual meeting of the geological society of America, Denver
Krogh TE, Davis GL (1974) Alteration in zircons with discordant U-Pb ages. Carnegie Inst WashYearb 73:560–567
Krogh TE, Davis GL (1975) Alteration in zircons and differential dissolution of altered and metamict zircon. Carnegie Inst WashYearb 74:619–623
Labotka TC, Cole DR, Fayek M, Riciputi LR, Stadermann FJ (2004) Coupled cation and oxygen-isotope exchange between alkali feldspar and aqueous chloride solution. Am Mineral 89: 1822–1825
Lasaga AC (1983) Geospeedometry: an extension of geothermometry. In: Saxena SK (ed) Kinetics and equilibrium in mineral reactions. Springer, New York
Lasaga AC (1986) Metamorphic reaction rate laws and development of isograds. Mineral Mag 50:359–373
Mahan KH, Goncalves P, Williams ML, Jercinovic MJ (2006) Dating metamorphic reactions and fluid flow: application to exhumation of high-P granulites in a crustal-scale shear zone, western Canadian Shield. J Metamorph Geol 24:193–217
Maineri C, Benvenuti M, Costagliola P, Dini A, Lattanzi PF, Ruggieri G, Villa IM (2003) Sericitic alteration at the La Crocetta deposit (Elba Island, Italy): interplay between magmatism, tectonics and hydrothermal activity. Miner Deposita 38:67–86
Malusà MG, Villa IM, Vezzoli G, Garzanti E (2011) Detrital geochronology of unroofing magmatic complexes and the slow erosion of Oligocene volcanoes in the Alps. Earth Planet Sci Lett 301:324–336
Mayer A, Cortiana G, Dal Piaz GV, Deloule E, De Pieri R, Jobstraibizer PG (2003) U-Pb single zircon ages of the Adamello batholith (Southern Alps). Mem Sci Geol 55:151–167
McIntyre GA, Brooks C, Compston W, Turek A (1966) The statistical assessment of Rb-Sr isochrons. J Geophys Res 71:5459–5468
Medenbach O (1976) Geochemie der Elemente in Zirkon und ihre räumliche Verteilung – eine Untersuchung mit der Elektronenstrahlmikrosonde. Unpublished Ph.D. thesis, Ruprecht-Karls-Universität Heidelberg
Megrue GH (1973) Spatial distribution of $^{40}Ar/^{39}Ar$ ages in lunar breccia 14301. J Geophys Res 78:3216–3221
Merrihue CM (1965) Trace-element determinations and potassium-argon dating by mass spectroscopy of neutron-irradiated samples. Trans Am Geophys Union 46:125
Merrihue CM, Turner G (1966) Potassium-argon dating by activation with fast neutrons. J Geophys Res 71:2852–2857
Mezger K, Krogstad EJ (1997) Interpretation of discordant zircon ages: an evaluation. J Metamorph Geol 15:127–140
Müller W, Aerden D, Halliday AN (2000) Isotopic dating of strain fringe increments: duration and rates of deformation in shear zones. Science 288:2195–2918
Müller W, Kelley SP, Villa IM (2002) Dating fault-generated pseudotachylytes: Comparison of 40Ar/39Ar stepwise-heating, laser-ablation and Rb/Sr microsampling analyses. Contrib Mineral Petrol 144:57–77
Neymark LA, Amelin YV, Paces JB (2000) $^{206}Pb–^{230}Th–^{234}U–^{238}U$ and $^{207}Pb–^{235}U$ geochronology of Quaternary opal, Yucca Mountain, Nevada. Geochim Cosmochim Acta 64:2913–2928

Nyfeler D, Armbruster T, Villa IM (1998) Si, Al, Fe order-disorder in Fe-bearing K-feldspar from Madagascar and its implication to Ar diffusion. Schweiz Mineral Petrog Mitt 78:11–21
Oberli F, Ntaflos Th, Meier M, Kurat G (1987) Emplacement age of the peridotites from Zabargad Island (Red Sea): a zircon U-Pb isotope study. Terra Cognita 7:334
Onstott TC, Phillips D, Pringle-Goodell L (1990) Laser microprobe measurement of chlorine and argon zonation in biotite. Chem Geol 90:145–168
Onstott TC, Miller ML, Ewing RC, Arnold GW, Walsh DS (1995) Recoil refinements: implications for the $^{40}Ar/^{39}Ar$ dating technique. Geochim Cosmochim Acta 59:1821–1834
Petrik I, Konecny P (2009) Metasomatic replacement of inherited metamorphic monazite in a biotite-garnet granite from the Nizke Tatry Mountains, Western Carpathians, Slovakia: chemical dating and evidence for disquilibrium melting. Am Mineral 94:957–974
Pettke Th, Audetat A, Schaltegger U, Heinrich CA (2005) Magmatic-to-hydrothermal crystallization in the W-Sn mineralized Mole Granite (NSW, Australia) - Part II: evolving zircon and thorite trace element chemistry. Chem Geol 22:191–213
Phillips D, Onstott TC (1988) Argon isotopic zoning in mantle phlogopite. Geology 16:542–546
Podosek FA, Huneke JC (1973) Argon in Apollo 15 green glass spherules (15426): ^{40}Ar-^{39}Ar age and trapped argon. Earth Planet Sci Lett 19:413–421
Provost A (1990) An improved diagram for isochron data. Chem Geol 80:85–99
Proyer A (2003) The preservation of high-pressure rocks during exhumation: metagranites and metapelites. Lithos 70:183–194
Putnis A (2002) Mineral replacement reactions: from macroscopic observations to microscopic mechanisms. Mineral Mag 66:689–708
Putnis A (2009) Mineral replacement reactions. Rev Mineral Geochem 70:87–124
Putnis A, Austrheim H (2010) Fluid-induced processes: metasomatism and metamorphism. Geofluids 10:254–269
Rasmussen B (1996) Early-diagenetic REE-phosphate minerals (florencite, gorceixite, crandallite, and xenotime) in marine sandstones: a major sink for oceanic phosphorus. Am J Sci 296: 601–632
Rasmussen B (2005) Radiometric dating of sedimentary rocks: the application of diagenetic xenotime geochronology. Earth Sci Rev 68:197–243
Rasmussen B, Fletcher IR, Bengtson S, McNaughton NJ (2004) SHRIMP U-Pbdating of diagenetic xenotime in the Stirling Range formation, Western Australia: 1.8 billion year minimum age for the Stirling biota. Precamb Res 133:329–337
Rayner N, Stern RA, Carr D (2005) Grain-scale variations in trace element composition of fluid-altered zircon, Acasta Gneiss complex, northwestern Canada. Contrib Mineral Petrol 148: 721–734
Rutherford E (1906) The mass and velocity of the α particles expelled from radium and actinium. Phil Mag Ser 6 12(70):348
Schaltegger U (2007) Hydrothermal zircon. Elements 3:51
Schneider J, Bosch D, Monié P, Bruguier O (2007) Micro-scale element migration during eclogitisation in the Bergen arcs (Norway): a case study on the role of fluids and deformation. Lithos 96:325–352
Schobert K (2005) Metasomatische Gesteine im Tal des Rio Pisco (Peru). Unpublished M.Sc. thesis, Universität Bern
Seydoux-Guillaume A-M, Goncalves P, Wirth R, Deutsch A (2003) Transmission electron microscope study of polyphase and discordant monazites; site-specific specimen preparation using the focused ion beam technique. Geology 31:973–976
Sletten VW, Onstott TC (1999) The effect of the instability of muscovite during in vacuo heating on $^{40}Ar/^{39}Ar$ step-heating spectra. Geochim Cosmochim Acta 62:123–141
Smith JV (1974) Feldspar minerals. Springer, Heidelberg
Spötl C, Kralik M, Kunk MJ (1996) Authigenic feldspar as an indicator of paleo-rock water interactions in Permian carbonates of the northern Calcareous Alps, Austria. J Sediment Res 66:139–146
Steiger RH, Wasserburg GJ (1969) Comparative U-Th-Pb systematics in 2.7×10^9 yr plutons of different geologic histories. Geochim Cosmochim Acta 33:1213–1232

Stosch HG, Lugmair GW (1990) Geochemistry and evolution of MORB-type eclogites from the Munchberg Massif, southern Germany. Earth Planet Sci Lett 99:230–249
Thöni M, Jagoutz E (1992) Some new aspects of dating eclogites in orogenic belts: Sm-Nd, Rb-Sr, and Pb-Pb isotopic results from the Austroalpine Saualpe and Koralpe type-locality (Carinthia/Styria, southeastern Austria). Geochim Cosmochim Acta 56:347–368
Tomaschek F (2004) Zircon reequilibration by dissolution-represipitation: reaction textures from flux-grown solid solutions. Beihefte zum Eur J Mineral 12:214
Tomaschek F, Kennedy AK, Villa IM, Lagos M, Ballhaus C (2003) Zircons from Syros, Cyclades, Greece - recrystallization and mobilization of zircon during high-pressure metamorphism. J Petrol 44:1977–2002
Turner G, Huneke JC, Podosek FA, Wasserburg GJ (1971) ^{40}Ar-^{39}Ar ages and cosmic ray exposure age of Apollo 14 samples. Earth Planet Sci Lett 12:19–35
Vance D, O'Nions RK (1990) Isotopic chronometry of zoned garnets: growth kinetics and metamorphic histories. Earth Planet Sci Lett 97:227–240
Vance D, Müller W, Villa IM (2003) Geochronology: linking the isotopic record with petrology and textures - an introduction. Geol Soc London Spec Pub 220:1–24
Veblen DR (1992) Electron microscopy applied to nonstoichiometry, polysomatism, and replacement reactions in minerals. Rev Mineral 27:181–229
Villa IM (1998) Isotopic closure. Terra Nova 10:42–47
Villa IM (2002) Mete isotopes without petrography?/'Tis but a jest, as sound chronology/Must needs base on complementarity. Keynote address, Internat Mineral Association congress, Edinburgh
Villa IM (2006) From the nm to the Mm: isotopes, atomic-scale processes, and continent-scale tectonic models. Lithos 87:155–173
Villa IM (2010) Disequilibrium textures vs equilibrium modelling: geochronology at the crossroads. Geol Soc London Spec Publ 332:1–15
Villa IM, Grobéty B, Kelley SP, Trigila R, Wieler R (1996) Assessing Ar transport paths and mechanisms for McClure Mountains Hornblende. Contrib Mineral Petrol 126:67–80
Villa IM, Hermann J, Müntener O, Trommsdorff V (2000) ^{39}Ar-^{40}Ar dating of multiply zoned amphibole generations (Malenco, Italian Alps). Contrib Mineral Petrol 140:363–381
Villa IM, Ruggieri G, Puxeddu M (2001) Geochronology of magmatic and hydrothermal micas from the Larderello geothermal field. In: Cidu R (ed) Water-rock interaction. Balkema, Lisse
Villa IM, Ruggieri G, Puxeddu M, Bertini G (2006) Geochronology and isotope transport systematics in a subsurface granite from the Larderello-Travale geothermal system (Italy). J Volcanol Geoth Res 152:20–50
Williams ML, Jercinovic MJ, Hetherington CJ (2007) Microprobe monazite geochronology: understanding geologic processes by integrating composition and chronology. Annu Rev Earth Planet Sci 35:137–175
Williams ML, Jercinovic MJ (2002) Microprobe monazite geochronology: putting absolute time into microstructural analysis. J Struct Geol 24:1013–1028
Williams ML, Jercinovic MJ, Terry MP (1999) Age mapping and dating of monazite on the electron microprobe: deconvoluting multistage tectonic histories. Geology 27:1023–1026
Williams ML., Jercinovic MJ, Goncalves P, Mahan KH (2006) Format and philosophy for collecting, compiling, and reporting microprobe monazite ages. Chem Geol 225:1–15
Williams ML, Jercinovic MJ, Harlov DE, Budzyń B, Hetherington CJ (2011) Resetting monazite ages during fluid-related alteration. Chem Geol 283:218–225
Zhou B, Hensen BJ (1995) Inherited Sm/Nd isotope components preserved in monazite inclusions within garnets in leucogneiss from East Antarctica and implications for closure temperature studies. Chem Geol 121:317–326

Chapter 7
Effects of Metasomatism on Mineral Systems and Their Host Rocks: Alkali Metasomatism, Skarns, Greisens, Tourmalinites, Rodingites, Black-Wall Alteration and Listvenites

Franco Pirajno

7.1 Introduction

Heat-liberating events, such as igneous intrusions emplaced into cool crustal rocks, will result not only in loss of heat to the surrounding environment, but also in the transport of volatile components, which are responsible for metasomatic processes. Some of the most impressive results of these processes are, for example, fenites (K- and Na-metasomatism), skarns (Ca-metasomatism) and tourmalinisation (B-metasomatism).

Lindgren (1933) described metasomatism as those "*processes by which new minerals may take the place of old ones*". In this definition any form of replacement, as for example silicification, irrespective of temperature and other environmental conditions, can be considered as a metasomatic process. Ramberg (1952) defined metasomatism as "*that process capable of changing the bulk composition of a solid rock*". According to Best (1982, p. 348), "*metasomatism involves major gains or losses of matter, usually made possible by flow of large quantities of fluids through an open rock body along significant temperature and composition gradients*". This is a "*constant volume replacement*", tending to preserve the fabric and textures of the rocks affected. Experimental and petrographic evidence suggest that large activity gradients are essential to implement metasomatism by either fluid flow or by diffusion (Bach and Klein 2009 and references cited therein). A definition of metasomatism, recommended by the International Union of Geological Sciences (IUGS), is: *a metamorphic process by which the chemical composition of a rock or rock portion is altered in a pervasive manner and which involves the introduction and/or removal of chemical components as a result of the interaction of the rock*

F. Pirajno (✉)
Geological Survey of Western Australia, 100 Plain Street, East Perth, WA 6004, Australia

Centre for Exploration Targeting, University of Western Australia, 35 Stirling Highway, Crawley, WA 6009, Australia
e-mail: franco.pirajno@dmp.wa.gov.au; franco.pirajno@uwa.edu.au

D.E. Harlov and H. Austrheim, *Metasomatism and the Chemical Transformation of Rock*, Lecture Notes in Earth System Sciences,
DOI 10.1007/978-3-642-28394-9_7,

with aqueous fluids (solutions). During metasomatism the rock remains in a solid state (Zharikov et al. 2007).

Zharikov et al. (2007), considered metasomatic processes to include:

(a) Ion-by-ion replacement in minerals
(b) Unlike magma-rock interaction and/or melt crystallisation, metasomatic processes are manifested by replacement of rocks in the solid state
(c) Substantial changes in chemical compositions by either addition or subtraction of major components, other than H_2O and CO_2
(d) Formation of regular zonations or zonal patterns, representing chemical equilibrium between two rocks or between a rock and the infiltrating fluid

Furthermore, Zharikov et al. (2007) subdivided metasomatic processes into the types summarised below:

Diffusional metasomatism relates to the diffusion of a solute through a stagnant fluid system. This diffusion occurs because of chemical gradients between the rock and pore fluid and does not require the movement of a fluid through the rock. **Infiltration metasomatism refers** to the transfer of material in the fluids, which infiltrates through the host rocks. The driving force is pressure and a large influx of externally buffered fluid. **Autometasomatism** takes place at the top of igneous intrusions during the post-magmatic stage. Albitisation is a classic example of autometasomatism. **Boundary metasomatism** is that which occurs in response to fluid activity gradients at the contact between two different lithologies. The generation of rodingites and blackwall alteration are related to boundary metasomatism. **Contact metasomatism** occurs at and along the contact between an igneous intrusion and the wallrocks. It can be further subdivided into endocontact and exocontact, meaning replacement of the causative igneous intrusion and replacement of the wallrock, respectively. Skarns provide the best example for both endo- and exocontact metasomatism.

In this chapter, I review some of the salient aspects of metasomatism and its effects that relate to or cause mineralisation. I mainly draw from my books (Pirajno 1992; 2009 and references cited therein), but also include new data and concepts. More specifically, I discuss and illustrate the main features and examples of:

1. Alkali metasomatism, which includes sea water interaction with mafic rocks (spilites), sodic and potassic metasomatism associated with intrusion-related mineral systems (porphyry Cu-Mo), and fenitisation (carbonatites with REE-Ta-Nb-U, REE-Ta-Li ongonite)
2. Contact metasomatism and skarn mineral systems (Au, Cu, Fe, Fe-P, Sn, W-Mo, Zn-Pb)
3. Greisen (autometasomatism) and associated Mo-W, U-Mo-F
4. Boron metasomatism (tourmalinites) and associated metallogeny
5. Metasomatism in ultramafic systems and Au mineralisation (rodingites and listvenites)

A summary of the more common metasomatic processes and associated key reactions are given in Table 7.1.

Table 7.1 Key examples of metasomatic processes

Type and general direction of increasing temperature ↓		Minerals; reactions	Enrichment+	Depletion−
Carbonate		Calcite: $CaCO_3$ Ankerite: $Ca(Fe, Mg, Mn)(CO_3)_2$ Dolomite: $CaMg(CO_3)_2$ Magnesite: $MgCO_3$ Siderite: $FeCO_3$	CO_2, Fe	SiO_2, Al, Na, K
Fluorite and topaz alteration		CaF_2 $Al_2(SiO_4)(F,OH)_2$	F	SiO_2
Steatitisation		Talc: $Mg_3(OH_2)(Si_2O_5)_2$	SiO_2, H_2O	
Rodingite		Diopside, grossular garnet, vesuvianite	CaO_2	SiO_2, Na_2O
Silicification		Secondary quartz, chalcedony, chert, opal	SiO_2	Mg, Ca, Fe, Mn, CO_2
Tourmaline		$XY_3Al_6(BO_3)_3(Si_8O_{18})(OH)_4$ X = Na, Ca; Y = Al, Fe, Li, Mg	Al, Mg, Ca, Fe, Na, Li, B, H_2O	SiO_2, CO_2
Listvenite		Serpentine → talc → Fe, Mg carbonates, quartz, albite, Cr-muscovite, ± sulphides	Ca, K, Na, CO_2, S, As	SiO_2, Mg, Fe, Cr, H_2O
Skarn		1 PROGRADE STAGE: e.g. Ca-skarn garnet, pyroxene, (±scheelite, sulphides)	SiO_2, Mg, Fe, S, As, B, f, Cl, W, Mo, P, Be, Sn	Ca, CO_2
		2 RETROGRADE STAGE: amphiboles, scapolite, epidote, vesuvianite, sulphides, carbonate	S, H_2O, Cu, Fe	Cl
Potassic alteration	Biotite	$K(Mg,Fe)_3[(OH)_2(Al,Fe)Si_3O_{10}]$	SiO_2, Al, Mg, Fe, K, H_2O	
	Feldspar	Microcline, Adularia: $K(AlSi_3O_8)$	Al, K	
Albitisation of K-feldspar (ion-exchange)		$K(Al_2Si_3O_8) + Na^+ \rightarrow Na(AlSi_3O_8) + K^+$	Na	K
Greisen		Fluorite, topaz, quartz, sericite, muscovite (phengite), tourmaline, albite	SiO_2, S, Cl, Be, B, Li, F, W, Sn	

7.2 Alkali Metasomatism

Alkali metasomatism involves the transfer of the alkali ions, Na and K, from a fluid phase, generated during the cooling of an igneous body, to the adjacent rocks. Albitite, microclinite, fenites, and the core zones of potassic alteration of porphyry systems are the most common products of alkali metasomatism (Plate 7.1a, b; Plate 7.2a, b). In igneous rocks there are at least three types of textures that can be attributed to alkali metasomatism. These include replacement coronas, granophyric textures, and perthitic textures. Replacement coronas refer to replacement along the grain margin of ferromagnesian silicates by Na-amphiboles, such as arfevedsonite or riebeckite. Examples of alkali metasomatism are provided by granophyric intergrowths (quartz + K-feldspar), which are usually distinguished by the turbidity of the K-feldspar component. Perthitic textures in feldspar may, in some cases, also be indicative of alkali metasomatism, rather than unmixing during cooling of a two-phase assemblage. Replacement of Na for K in feldspars, probably by ion exchange, is shown by the presence of albite inclusions in the K-feldspar host (see also Putnis and Austrheim, Chap. 5). These inclusions can occur either as irregular shapes, or as veinlets, and do not follow crystallographic directions, as would be the case for melt-fluid unmixing. Order–disorder relationships in alkali feldspar refer to the distribution of Al and Si in the unit cell and its departure from the monoclinic towards triclinic symmetry (obliquity) (see Sánchez-Muñoz et al. 2009 and references therein). This obliquity decreases with decreasing temperature and the K content increases. Thus the K content increases with ordered structures (e.g. towards a sanidine composition), whereas in passing from the ordered towards the disordered structure, Na migrates into the lattice to form distinct domains, giving rise to the perthitic texture. The structure can change back again towards a K-rich domain to form microcline with further decreasing of the temperature. Thus, the sequence from high to low temperature feldspar and possibly due to solid-state recrystallisation (Sánchez-Muñoz et al. 2009), is as follows:

$$\text{sanidine} \rightarrow \text{orthoclase} \rightarrow \text{perthite (orthoclase} + \text{albite)} \rightarrow \text{microcline}$$

In the presence of volatiles the composition of a granitic melt tends to be more alkaline than that formed under volatile-poor conditions. Experimental work reported by Pichavant and Manning (1984) shows that at 1 kbar and near-liquidus temperatures, the addition of B and/or HCl results in a decrease in the Si/alkali and Al/alkali ratios. Therefore both B and HCl cause a transfer of alkalis from the melt to the vapour/fluid phase, although the Na/K ratio may vary. This indicates that Na is leached from melts co-existing with B-bearing vapours, producing, in turn, an Al- or K-rich silicate melt. In the Q-Ab-Or-H_2O system, changes in the melt composition by the addition of B (or F) in a source region undergoing melting are reflected by the shift of the melt composition towards the Q-Or side of the ternary system. There is also experimental evidence that the solubility of H_2O in magmas may be enhanced in B-rich melts (Pichavant 1981), whereas F-rich systems do not appear to have the

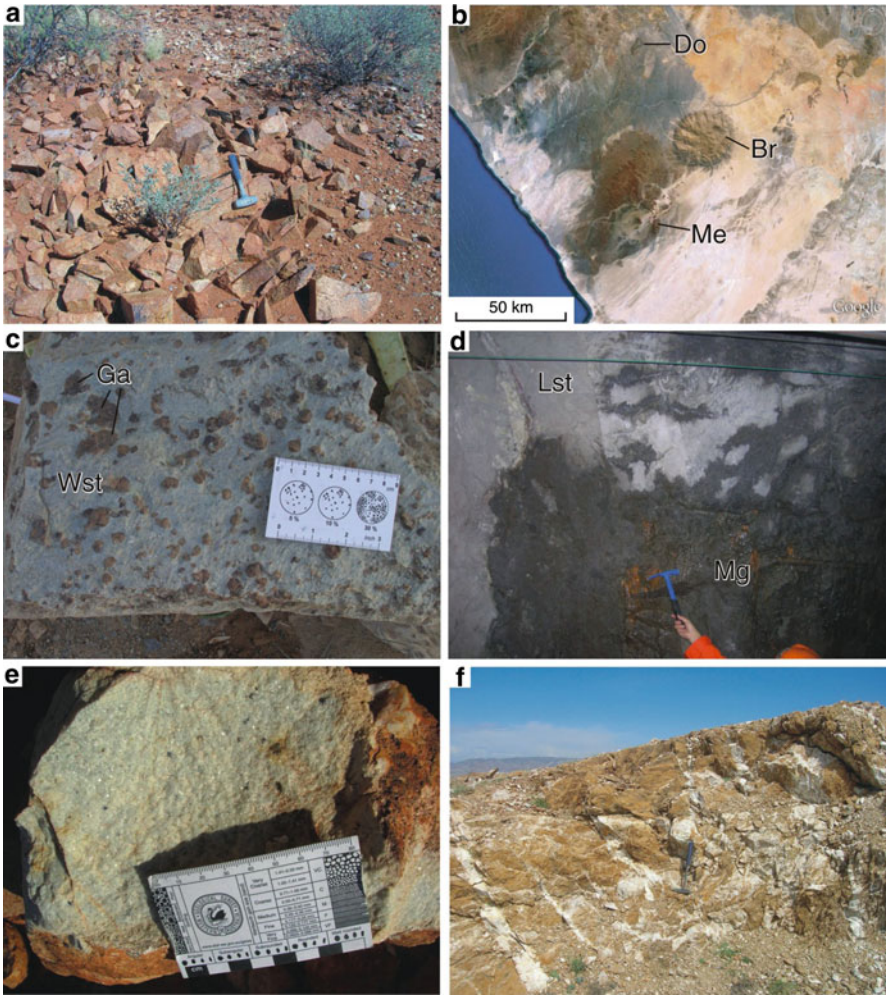

Plate 7.1 (**a**) Outcrop of pervasively fenitised rock (mostly microcline) associated with the Gifford Creek carbonatite complex in Western Australia. This rock resembles a syenite. Details in text. (**b**) Google Earth™ map showing a cluster of anorogenic ring complexes. Br is Brandberg. Me is Messum. Do is Doros (see Pirajno 2009 for more details). (**c**) Outcrop of wollastonite-garnet skarn from eastern Tianshan (Xinjiang Province, NW China). (**d**) Magnetite skarn replacing limestone, Longgiao Fe Mine, in Yangtze River Valley, China. (**e**) Hand specimen of greisen, Minnie Spring Mo occurrence, Gascoyne Complex, Western Australia. (**f**) Outcrop of listvenite cut by late quartz veins, Altay Orogen, NW China, near the Kalatongke Ni mine. The *brown colour* of this listvenite is largely due to oxidation of the Fe-carbonate

same effect. The experiments carried out by Pichavant and Manning (1984) indicate that progressive addition of F (between 1% and 4%) and B (between 1% and 4.5%) causes the ternary composition to shift towards the Ab corner. In other words, in the case of magmatic systems, which during fractionation and crystallisation are

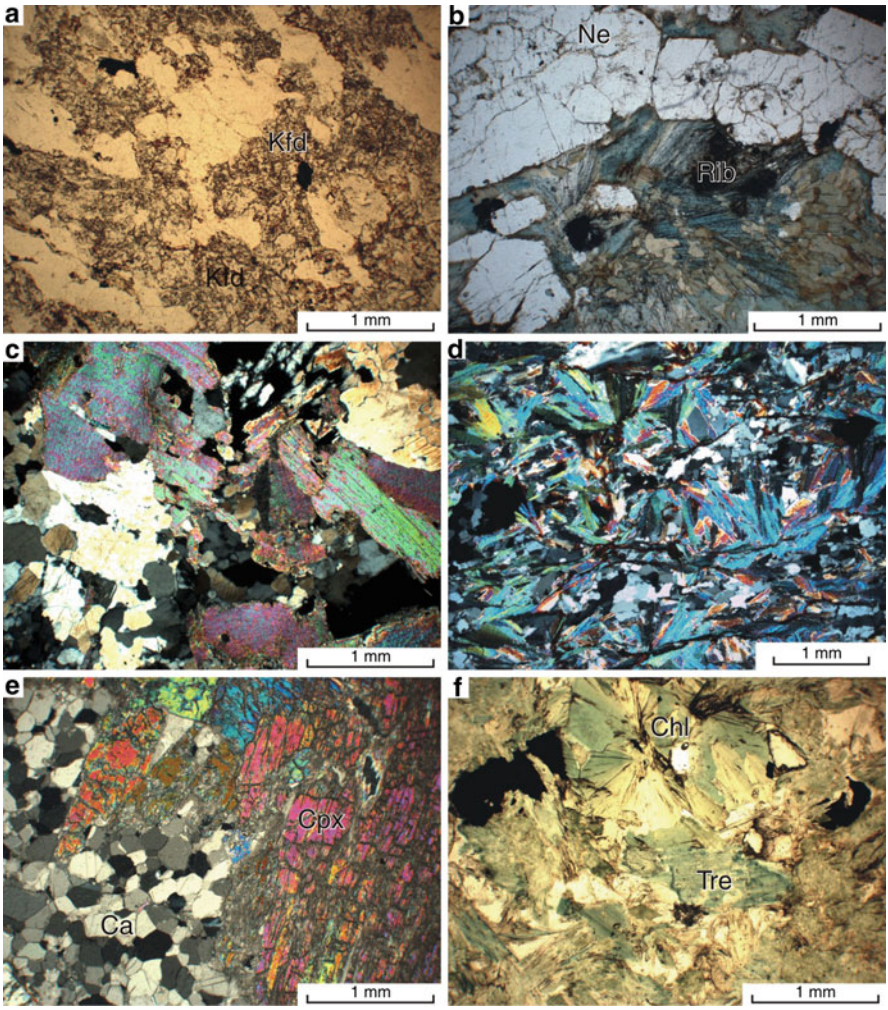

Plate 7.2 (**a**) Example of K metasomatism, shown by cloudy K-feldspar (Kfd) replacing a granitic rock along grain boundaries, Minnie Spring Mo occurrence, Gascoyne Province, Western Australia. (**b**) Fenite composed of nepheline (Ne) and riebeckite (Rib), Gifford Creek carbonatite complex, Gascoyne, Western Australia. (**c**) Coarse-grained greisen (quartz-muscovite) from the McConnochie Creek Mo occurrence, South Island, New Zealand. (**d**) A muscovite-rich greisen, Minnie Spring Mo-W-Cu occurrence, Gascoyne Province, Western Australia. (**e**) Clinopyroxene (Cpx)-calcite (Ca) prograde skarn, Navachab gold mine, Namibia. (**f**) Retrograde skarn with tremolite (Tre), chlorite (Chl), and sulphide (*black*), Dongguashan Cu mine, Yangtze River Valley, China

progressively enriched in B, F and Li, there is a concomitant enrichment in the Ab component, while the liquidus temperature is also depressed. Thus, with progressive crystallisation of the volatile-rich melt, Na and Si enter easily into a residual fluid phase. The opposite trend may be observed if the volatiles are removed from the

crystallising melt. In this case Ab, or peraluminous minerals, crystallise and the residual melt becomes progressively enriched in Q and Or. This is the K-rich assemblage that is, in fact, seen to appear under subsolidus conditions (potassic metasomatism). The removal of the volatiles from the melt can take place either by a second boiling (retrograde), or through the opening of the system by fracturing and adiabatic decompression, leading to boiling and volatile partitioning into the vapour phase (first boiling).[1] The nature of potassic metasomatism is therefore dependent on the rate of melt-fluid separation. In a closed-system potassic metasomatism is slow, and coarse-grained crystals are likely to form (microcline megacrysts). In a system that has become open by rapid decompression, on the other hand, a "pressure-quenched" intergrowth of quartz + K-feldspar would result, producing the type of granophyric texture that is so often observed in granitic systems associated with hydrothermal activity. The effect of F extraction from the melt would be similar to that of B extraction, producing a Na(K)-, Si-, B(F)-rich aqueous fluid.

In summary, increasing volatile content during crystallisation enriches the melt in the Ab content, while the fluid phase is enriched in K (decreasing Na/K in the fluid phase), resulting in transfer of K from fluid to the wall rocks. Conversely when volatiles are lost from the system, the residual melt becomes enriched in Or, while Na is transferred to the fluid phase. K-feldspar crystallises from the melt and Na in the fluid is transferred to the wall rocks. The evolution of an alkali-rich residual fluid phase from a nearly consolidated igneous body results in a series of post-magmatic and subsolidus growth of minerals, the mineralogical and geochemical evidence of which is compelling (Bowden 1985). Such changes are largely dependent on the intensity of the rock-fluid interaction. The subsolidus processes include cationic exchange reactions in feldspars, Na for K or K for Na (albitisation and microclinisation respectively) and changes in the structural state of feldspars. Other changes involving increasing amounts of H_2O (H^+ metasomatism) and/or "dry" volatiles include changing compositions of pyroxenes and amphiboles, growths of tri-octahedral micas, aegirine and riebeckite, as well as a series of F- or B-rich mineral assemblages. It must be pointed out that many of the replacement features of subsolidus changes can also be explained by magmatic crystallisation, or unmixing of solid solutions. However, subsolidus reactions are especially developed in the apical zones of plutons, and along fractures or in pods and lenses.

[1] The concept of boiling in magmas is very important for hydrothermal mineral systems: first boiling is that which occurs in a magma during decompression, causing exsolution of volatiles; second boiling takes place as a result of increasing concentration of volatiles during crystallisation, with continuous increase of H_2O and other volatile constituents in the residual melt fractions, such that at some stage, the pressure of H_2O equals the confining pressure and retrograde (second) boiling occurs, effectively creating a hydrothermal solution.

7.2.1 Sodic and Potassic Metasomatism

This aspect of metasomatism is characterised by Na-bearing minerals which are clearly in replacement relationships with primary magmatic minerals. The replacement of alkali feldspar by albite (albitisation or Na-feldspathisation) is the more common form of sodic metasomatism. This replacement may proceed from pre-existing perthites, or by direct replacement of K-feldspar with newly formed albites (Pollard 1983). Albitisation of K-feldspar can be written as follows :

$$\underset{\text{(microcline)}}{KAlSi_30_8} + \ Na^+ = \underset{\text{(albite)}}{NaAlSi_30_8} + K^+$$

The development of albite-rich rocks (albitites) is usually associated with "rare element" mineralisation (Nb, Ta, Sn, W, Li, Be). Sodium-enrichment is accompanied by elevated concentrations of Fe, U, Th, Zr, Nb, Sn, Zn, and HREE. Also, Na-metasomatised rocks tend to be enriched in Rb, Th, Nb, La, Ce, Hf, Zr, and Y with respect to K-metasomatised rocks (Kinnaird 1985). Several types of albitites have been recognised according to their mineralogy and rock type affected. In general, albitite is a leucocratic rock made up of albite and quartz, which contains some residual primary feldspars. Albitisation can affect a large mass of rock, and in some cases, on mobilisation, the albitised material can be injected as apophysis into the country rocks. In peraluminous granites, sodic metasomatism is manifested by textural and colour changes, due to coarsening domains in perthite and development of the so-called chessboard texture. Sodic metasomatism in peralkaline granites also brings about textural and colour changes, but these are due to growths of aegirine and arfvedsonite, and replacement of K in perthite by Na (Fig. 7.1), which leads to the development of albitites. Geochemically an enrichment in the same elements, as for the peraluminous granites, is noted. Albitisation is followed by incipient H^+ metasomatism, usually characterised by the growth of sericite and varying amounts of fluorite and topaz. Experimental work on silicate systems with volatile components such as Li, F, H_2O, and fluid inclusion studies of quartz from sodic granites, can be used to estimate the temperature-pressure conditions of sodic metasomatism. Results indicate a range of temperatures of between 400°C and 600°C approximately, at pressures of 1 kbar or less (Pollard 1983).

Sodic metasomatism is not only confined to mineral systems directly linked with the fractionation of granitic melts. Albitites and alkali amphiboles (e.g. riebeckite), are also found associated with U, Fe, and Pb-Zn-Ag deposits in high-grade metamorphic terranes. Uranium deposits, such as Valhalla in the Mt Isa district in Australia, several deposits in Ukraine (e.g. Krivoy-Rog district), and Lago Real in Brazil are hosted by granites, migmatites, gneisses, and ferruginous quartzite, metasomatically altered to albitites and alkali amphiboles (Cuney and Kyser 2009). The origin of the Na-rich fluids, commonly accompanied by Ca- bearing minerals (calcite, dolomite), is contentious. Na-Ca-rich fluids may have originated from the metamorphic devolitilisation of evaporite successions (basinal fluids), perhaps

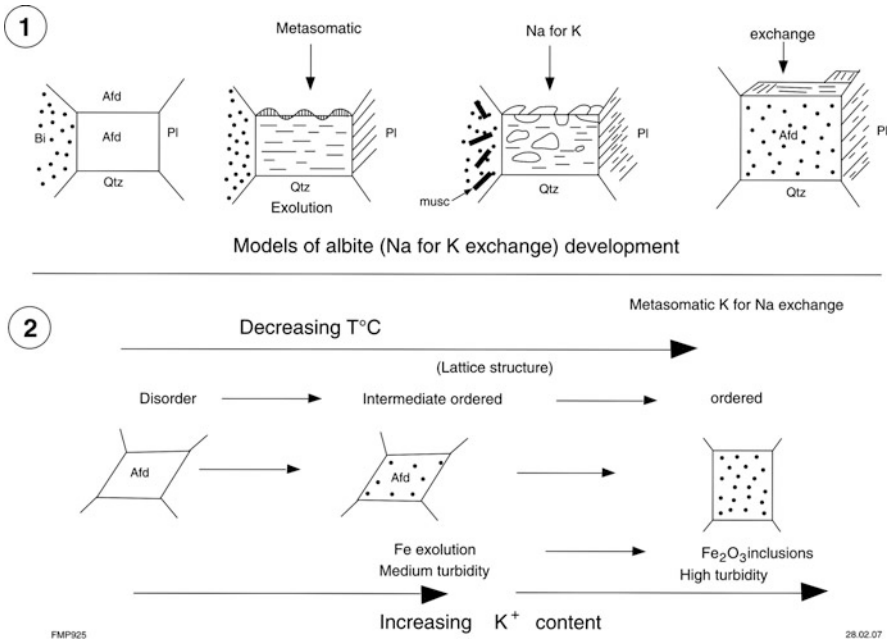

Fig. 7.1 Alkali metasomatism of alkali feldspar crystals. (1) Metasomatic exchange of Na for K with development of albite domains. (2) Metasomatic exchange K for Na with development of microcline. Turbidity results from the presence of minute exsolved hematite inclusions. Abbreviations Bi biotite, Qtz quartz, Afd alkali feldspar, Pl plagioclase, musc muscovite. After Pirajno (2009 and references therein)

mixed in places with fluids released from magmas (Polito et al. 2009 and references therein).

Potassic metasomatism (or K-feldspathisation or microclinisation) involves K for Na exchange mineral reactions, and is typically represented by the replacement of albitic plagioclase by microcline or orthoclase (Fig. 7.1). Other products of K for Na exchange reactions include the growth of new micas such as annite (Fe^{2+}-rich biotite) and amphibole compositions characteristic of Fe^{2+}-rich members (ferroedenite and ferroactinolite) (Bowden 1985). K-feldspathisation can assume regional proportions and leads to the development of microclinites, a feature commonly observed in haloes of fenitisation associated with carbonatites (see below). Field and petrographic evidence from Nigeria (Bowden et al. 1984) also shows, however, that K-feldspathisation post-dating Na-metasomatism, is generally confined to fractures in the roof zones of granitic plutons, and is related to early stages of vapour separation. Microclines typically develop in pockets or pods in the roof zones of plutons. Extreme K-feldspathisation may result in a vuggy-textured microclinite as a result of desilication (Kinnaird 1985). K-metasomatism is characterised by the presence of an intermediate to ordered microcline. Also, during the K for Na exchange, Fe is released from the lattice and oxidised to form minute hematite inclusions which give the microclines a distinct reddish colouration in hand specimens (Kinnaird 1985), whereas in thin-section this phenomenon is

manifested by the turbidity of the feldspar crystals. More recently, however, it has been suggested that the turbidity of feldspar is not due to solid state exsolution, but to sub-solidus fluid-rock interaction in which hematite precipitates in the pores of alkali feldspars (Putnis et al. 2007).

Fluid inclusion work on the Nigerian ring complexes, supported by textural evidence, suggests that CO_2 effervescence takes place in the system which enhances the K/H ratio of the remaining fluid, resulting in the development of K-feldspar at the expense of albite (Kinnaird 1985). In an ongoing process of alteration, potassic metasomatism is followed by incipient hydrolytic alteration characterised by the growth of siderophyllite or zinnwaldite aggregates, chlorites, and, in some cases, kaolinite. Temperature-pressure conditions for K metasomatism are not well known, but a minimum temperature of 630°C in the Q-Ab-Or system at 1 kbar, with 4% F, is considered possible (Manning 1982; Pollard 1983). Studies of fluid inclusions in K-feldspars indicate a range of temperatures from 320°C to 700°C, at 1.2 to 2 kbar.

7.2.1.1 Sea Water Metasomatism

Sea water metasomatism acts on basaltic rocks in oceanic crust, such as spreading centres or in rift settings, where the composition of basaltic lavas changes by acquiring Ca, Mg, and abundant Na, thereby becoming albite-normative (see reactions below). The changes in submarine mafic rocks are dominated in cation exchange of Na for Ca resulting in albite-rich rocks, epidosite and quartz-epidote-chlorite assemblages. Altered mafic rocks derived from these metasomatic processes (also called hydrothermal metamorphism) were known as "spilites" a term which is still in use, and refers to rocks showing a basaltic texture in which a greenschist facies mineralogy is developed by the above-mentioned processes (Coleman 1977). Spilitic lavas mostly consist of sodic plagioclase (replacing calcic plagioclase), altered products (actinolite, chlorite-epidote) from ferro-magnesian silicates (pyroxene, olivine), and titanite. The classic spilites of the old literature were often cited together with rocks of sodic rhyolitic composition, known as keratophyres. These terms are somewhat obsolete, but are still used predominantly in the non-English literature. Details of metasomatic processes on oceanic crust rocks are presented in Chap. 8.

Experimental studies on basalt-sea-water interaction, conducted using a range of temperatures and water to rock ratios, corroborate that substantial mass transfer occurs. This is characterised by cation fixation and hydrolysis reactions which increase in intensity with increasing temperature and water/rock ratios (Rosenbauer and Bischoff 1983; Seyfried and Janecky 1985). Transfer of Mg, SO_4^{2-}, Na, and Cl occurs from sea water to oceanic crust, whereas leaching and mass transfer of Li, K, Rb, Ca, Ba, Cu, Fe, Mn, Zn, and Si takes place from the oceanic crust to the fluids (Rona 1984). One of the most important aspects of basalt-sea-water interaction is the removal of Mg^{2+} from sea water, after which this cation becomes included in mineral phases such as smectite, chlorite and tremolite-actinolite. The transfer of Mg^{2+} takes place as $Mg(OH)_2$, and after its reaction with the rock-forming silicates,

H^+ is liberated and enters the fluid, increasing its acidity (pH decreases). This, in turn, produces further changes, during which the H^+ exchanges for cations, such as Ca and K, releasing them into the hydrothermal fluid. In addition to Mg^{2+}, Na^+ is also removed from sea water, generally at temperatures less than 300°C and water/rock ratios of between 5 and 10 (Mottl 1983). The transfer of Na^+ from the fluid is largely responsible for the formation of albite. Removal of Mg^{2+} and Na^+ is counterbalanced by the leaching of Ca^{2+} from the basalt. At temperatures greater than 150°C, K^+ and SiO_2 are leached from the mafic rocks. Experimental evidence indicates that SiO_2 exceeds quartz saturation at temperatures from 150°C to 500°C, causing precipitation of quartz. Some typical metasomatic reactions that take place during the hydrothermal metamorphism of basaltic rocks, produce talc, epidote minerals, and albite, as shown below (Seyfried et al. 1988):

Mg metasomatism:

$$3Mg^{2+} + 4SiO_2 + 4H_2O \rightarrow \underset{\text{talc(steatitisation)}}{Mg_3Si_4O10(OH)_2} + 6H^+$$

Ca metasomatism:

$$\underset{\text{anorthite}}{3CaAl_2Si_2O_8} + Ca^{2+} + 2H_2O \rightarrow \underset{\text{clinozoisite}}{Ca_2Al_3Si_3O_{12}(OH)} + 2H^+$$

Na metasomatism:

$$2Na^+ + 4SiO_2 + \underset{\text{anorthite}}{CaAl_2Si_2O_8} \rightarrow \underset{\text{albite}}{2NaAlSi_3O_8} + Ca^{2+}$$

An example of ancient spilites can be found in mafic oceanic rocks of the Palaeoproterozoic Bryah Basin (Pirajno et al. 2000; Pirajno 2004). These rocks are generally undeformed, massive, with Na_2O contents of up to 6 wt.%, abundant albite (13–23%), and clinopyroxene normative, with Mg# ranging from 47 to 68 (average 57.16; Pirajno et al. 2000). Outcrops of these ancient spilitic rocks are mostly aphyric and composed of acicular crystals of actinolite (forming sheaves with a plumose texture), epidote, prehnite, quartz, titanite, and carbonate, in a fine-grained groundmass of albite, microlites, chlorite, and epidote. Typically, the preserved texture is that of a brecciated or jigsaw-fit texture, outlined by epidote, carbonate, prehnite, and quartz along cooling joints (see also Rubenach, Chap. 4). In places these cooling joints can form structures that may be mistaken for pillow lavas. This texture is interpreted as hyaloclastite, a term that denotes fragmentation, due to quenching, of lavas flowing into shallow sea water (McPhie et al. 1993). Indeed, it is likely that the hyaloclastite texture is especially favourable to the interaction with sea water and subsequent Na metasomatism.

The phyric varieties of these spilitic rocks are characterized by a microlite-rich feldspar matrix, clinopyroxene granules, interstitial glass and chlorite, titanite,

and/or rutile. The albite phenocrysts are selectively altered to sericite, whereas the augite phenocrysts are fresh and exhibit distinct zoning. Vesicles are infilled (from rim to core) by albite, epidote, chlorite, and calcite. Minor sulphide specks, mainly chalcopyrite, may be present in the vesicular basalt. Pyroclastic rocks, characterized by eutaxitic textures, consist of glass shards and crystal and lithic fragments set in a devitrified and variably altered glassy matrix. Alteration phases are mainly chlorite, calcite, quartz, and albite. Hydraulic fracturing and veins of calcite, prehnite, quartz, and chlorite are abundant. At deeper levels (300–500 m), as shown from drill cores, albitic alteration imparts a pink to reddish colouration to veinlets and patches (Pirajno et al. 2000).

Celadonite and nontronite may also be part of a spilitic assemblage, as observed in the Keene Basalt, a submarine succession in the Neoproterozoic Northwest Officer basin, Western Australia (Grey et al. 2005). The succession consists of basaltic lava flows erupted in a rift setting and are characterised by extensive alteration of the cooling lavas due to interaction with sea water (Pirajno et al. 2006). In addition to the above, smectite clays, kaolinite-illite, and clinochlore are also present, though in lesser quantities. Celadonite is a dioctahedral mica (together with muscovite and phengite), with an ideal composition of $K(Mg,Fe)^{2+}(Fe,Al)^{3+}(OH)^2[Si_4O_{10}]$, a structure similar to glauconite, and of low-temperature paragenesis (Fleet 2003). Petrographic evidence indicates that the Keene Basalt celadonite and nontronite formed by alteration of ferromagnesian minerals, probably pyroxene and/or olivine.

Sea water metasomatism of basaltic rocks in the Iberian Pyrite Belt was documented using petrographic and whole-rock stable isotope systematics (Munhá and Kerrich 1980). These authors report that the $\delta^{18}O$ values from the spilites in the Iberian belt range from +10.87 to +15.71‰. These positive shifts in the $\delta^{18}O$ values, from an average value of $\delta^{18}O$ of about +6.5‰ in unaltered basaltic rocks, is attributed to subseafloor metasomatism of basaltic lavas (Putnis and Austrheim, Chap. 5). From various lines of evidence, Munhá and Kerrich (1980) suggested that the temperatures responsible for sea water metamorphism of basaltic rocks, that result in spilitisation, range from 350°C to 50°C. Higher temperature sea water metasomatic processes involving ultramafic rocks result in the formation of rodingite (see Sect. 7.6.1).

7.2.1.2 Alkali Metasomatism in Porphyry Systems

Porphyry ore systems constitute one of the world's major resources of Cu, Au and Mo. Many porphyry systems have giant size and most are generated above subduction zones at convergent plate margins and are associated with time-equivalent calc-alkaline magmas (Sillitoe 2010). Another class of porphyry systems is unrelated to convergent margins, but are located in intracontinental settings and associated with high-K calc-alkaline, alkaline and felsic magmas. In both tectonic settings, porphyry ore systems are typically formed by high-temperature magmatic-hydrothermal fluids and are called porphyry because of the pronounced porphyritic texture of the mineralised intrusive stocks. Hydrothermal alteration, metasomatism,

and mineralisation form more or less concentric shells centred on the intrusions associated with porphyry mineral systems. The effects of hydrothermal alteration and mineralisation extend into a large volume of wall rocks around and above the intrusives. Seedorff et al. (2005) considered that the processes leading to alteration in porphyry systems are: volatile addition (propylytic alteration), hydrolysis (sericitic, advanced argillic, and intermediate argillic), alkali exchange (potassic, sodic-calcic metasomatism), and the addition of silica. The principal variables in alteration processes are temperatures, pressure, fluid composition, and the composition of possible external fluids (meteoric, seawater, evaporites). Phase diagrams of the system K_2O-Al_2O_3-SiO_2-H_2O-KCl-HCl have been constructed by Hemley and Jones (1964) and Meyer and Hemley (1967) to define the boundaries of alteration types and mineral phases, progressively from 700°C through to 150°C (see also Seedorff et al. 2005). An idealised evolution diagram from metasomatism to hydrothermal alteration sequence, applicable to most porphyry systems, is presented in Fig. 7.2.

Potassic metasomatism is especially common and important in porphyry and epithermal mineralising systems, where it occurs in the high temperature core zones. The minerals, characteristic of this alteration, are K-feldspar and biotite in porphyries, and adularia in epithermal systems. Potassic alteration is usually accompanied by sulphide formation (chalcopyrite, pyrite, molybdenite). Anhydrite is a common associated mineral in porphyry environments. Biotite is often green in colour and Fe-rich. Potassium silicate alteration of plagioclase and mafic silicate minerals occurs at temperatures in the region of 600–450°C. Common assemblages are K-feldspar-biotite-quartz, K-feldspar-chlorite, and K-feldspar-biotite-magnetite, accompanied by varying quantities of other minerals such as albite, sericite, anhydrite, fluorapatite, and also occasionally rutile, derived from the breakdown of biotite. Here too, the K-feldspars of the potassic zones are characteristically reddish in colour due to minute hematite inclusions (see above).

7.2.2 Alkaline Anorogenic Ring Complexes, Carbonatites and Related Metasomatic Processes

Anorogenic magmatism is generally alkaline in composition. It is associated in space and time with extensional tectonics and more specifically with rifting events. The main products of rift magmatism are fissure-fed tholeiitic basalts (continental flood basalt, CFB), layered mafic-ultramafic intrusions (and their respective feeders represented by dyke swarms), A-type granitic rocks, and alkaline complexes. The latter includes volcano-plutonic ring complexes, carbonatite, kimberlite, lamproite, and central-vent alkaline volcanoes. Anorogenic alkaline complexes are generally H_2O-poor, and characterised by high concentrations of non-hydrous volatiles (CO_2, B, F), REE, and LILE incompatible elements, (P, Zr, Ba, Nb, U, Th, Sn, Ta, and W). These elements may form their own minerals, or they may enter the lattice of

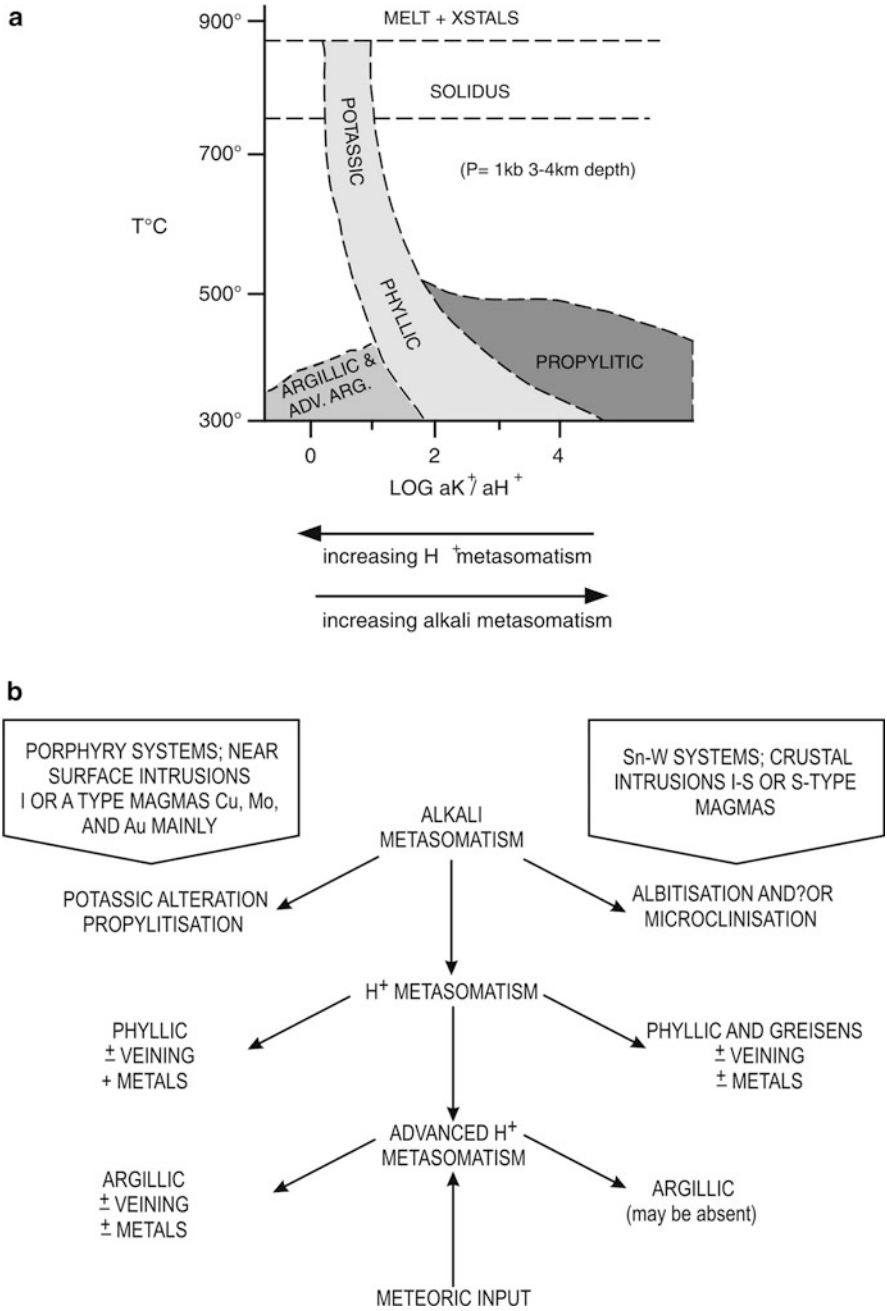

Fig. 7.2 Scheme of idealised hydrothermal alteration and metasomatism. (**a**) Illustrates types of alteration as a function of temperature and $K^+$and H^+ activities (after Burnham and Ohmoto 1980). Note that the argillic field includes minerals such as kaolinite (argillic) and pyrophyllite

rock-forming minerals (e.g. micas), that have crystallised in the subsolidus P-T range. The processes that lead to the enrichment of these elements are linked with the activity of residual alkali-rich fluids. Consequently, the concentration of alkalis, either in rock-forming minerals or in their own mineral species, is largely dependent on the original magma composition and the nature of the source regions where partial melting occurred.

Important rock associations of alkaline magmatism are kimberlites, mafic ultrapotassic rocks, syenite-pyroxenite-ijolite-carbonatite assemblages, alkali basalts, and peralkaline granite-syenite-gabbro assemblages. These rocks occur as dykes, pipes, hypabyssal and subvolcanic intrusions, and central volcano-plutonic structures, many of which form ring complexes, or are exposed as small hypabyssal plugs, isolated or in clusters, or as small dyke swarms. Most economic mineral deposits (excluding diamonds in kimberlites and ultrapotassic mafic rocks) are associated with central vent-type complexes of which two main groups are recognised (Bowden 1985): (1) alkali-granite-syenite (saturated-oversaturated) and (2) ijolite-carbonatite (undersaturated). They are schematically illustrated in Fig. 7.3 The idealised cross-sections shown in Fig. 7.3 also illustrate the importance of the level of erosion in terms of the preservation potential of the contained mineral deposits. Alkaline magmatism usually occurs during the early phases of rifting events, in which direct links are assumed with melt generation by mantle upwellings beneath thinned lithosphere and interaction with the subcontinental mantle lithosphere (SCML). Details of alkaline magmatism, associated with extensional tectonics, are available in Fitton and Upton (1987) and Storey et al. (1992). Comprehensive listings and descriptions of alkaline rocks and carbonatite occurrences of the world can found in Woolley (1987, 2001) and Woolley and Kjarsgaard (2008).

Alkaline magmatism is rather peculiar for the following interrelated reasons. First, alkaline magmas are strongly enriched in incompatible elements, such as Ti, P, Y, Nb, Ba, K, Na, Rb, Sr, Th, U, F, and REE. Second, because of the high abundances of incompatible elements, alkaline rocks can be an important resource of Cu, REE, phosphate, Au, and diamonds. Third, the products of alkaline magmatism are petrogenetically complex, a factor that has led to a plethora of confusing names. These features make alkaline rocks disproportionately important in relation to their volume, which is very minor compared to other forms of magmatism (e.g. subduction-related magmatism), excepting for the unique Mid-Proterozoic magmatism that produced A-type rapakivi granite-anorthosite complexes and related mineralisation (e.g. Vigneresse 2005). These are widespread bimodal intraplate magmatic systems, which, in addition to alkalis, are enriched in

Fig. 7.2 (continued) (advanced argillic), developed at temperatures lower than 350°C, more commonly between 200°C and 300°C. (**b**) Alkali metasomatism liberates H^+ This results in decreasing alkali/H^+ ratios and subsequent destabilisation of feldspars and micas, with growth of new mineral phases (greisen and phyllic stages). Advanced H^+ metasomatism is due to meteoric water input into the system, with oxidation and further H^+. Acid leaching and argillic alteration result from this stage

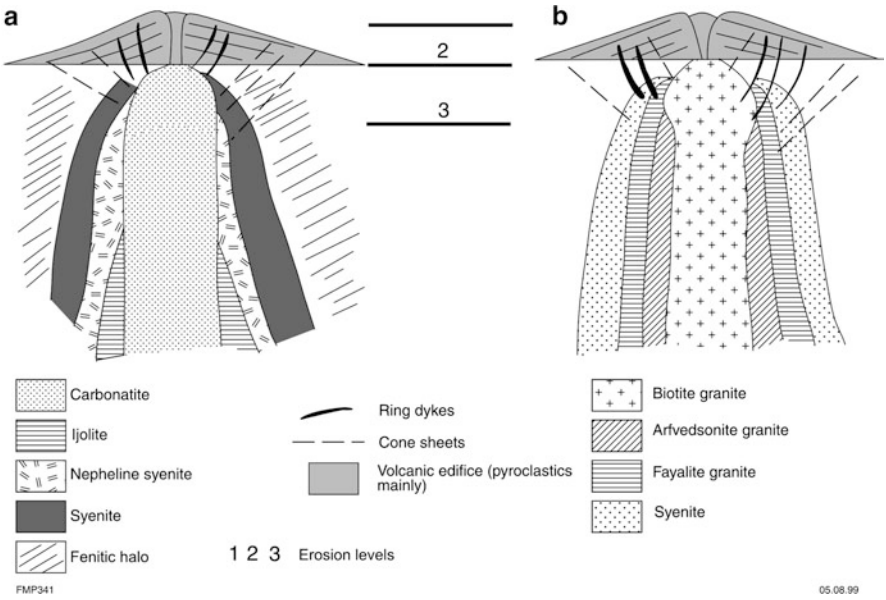

Fig. 7.3 Schematic cross-sections of (**a**) carbonatite, ijolite, syenite and nepheline syenite and (**b**) alkaline granites and syenite; (After Bowden 1985). These anorogenic magmatic systems are typically associated with haloes of intense alkali metasomatism

Fe, Ti, Y, Nb, F, Cu, W, Mo, Sn, In, and Be, and thought to be related to upwelling mantle plumes (Sharkov 2010; Bédard 2010).

There is evidence that the source of continental rift alkaline magmas is metasomatised lithospheric mantle. Bailey (1983, 1987) pointed out that large quantities of CO_2, F, and Cl are emitted from modern rifts such as the East African Rift System, suggesting that rifts are the sites of upwelling asthenospheric melts rich in Cl, F, C, P, etc. These melts penetrate the lithosphere, metasomatising it and causing further partial melting and developing thermal anomalies. This phenomenon of mantle degassing and metasomatism, as envisaged by Bailey (1983, 1984, 1987), may also explain the origin of kimberlites and lamproites, which may be carriers of diamonds. It is probably for this reason that numerous breccia pipes, the expression of explosive volatile exsolution, are associated with alkaline magmatism. In some cases breccia pipes are nested, that is they are formed during a number of events.

7.2.2.1 Fenites

One of the most interesting cases of anorogenic alkali metasomatism is that which takes place around alkaline complexes and carbonatites in stable continental areas. This phenomenon is known as fenitisation, and the rocks affected are called fenites. Fenitisation is a type of alkali metasomatism and is a consequence of Na and/or

K-rich fluids related to the cooling of carbonatites or ijolite intrusions. Le Bas (1987) stated that "*products of fenitization are mineralogically syenitic, with the result that they are sometimes misidentified as igneous syenites*". The name fenite is derived from the Fen carbonatite in Norway where this type of alteration was first documented by Brögger (1921). Names that are complicated and difficult to remember have been adopted by different authors to describe fenitic rocks. Verwoerd (1966) proposed that the naming of fenitic rocks should be prefixed by the principal mineral components followed by fenite (e.g. orthoclase-aegirine-augite fenite). Kresten (1988) considered three styles of fenites: (1) aureole fenites; (2) vein fenites; and (3) contact fenites. Aureole fenites are characterised by incipient growths of K-feldspar and sericite. Alkali amphiboles occur in higher temperature aureole fenites. Vein fenites comprise riebeckite and K-feldspars. Contact fenites are characterised by almost complete replacement of original minerals by K-feldspar, alkali amphibole, sodic pyroxene, and carbonate.

Fenites are formed through progressive metasomatism of the country rocks surrounding alkaline complexes and carbonatite intrusions. This usually involves the elimination of free quartz (desilication) and the development of alkali mineral phases. Carmichael et al. (1974) attributed these metasomatic effects to residual alkali-rich fluids deriving from the fractionation of alkaline magmas. The fluids are in strong disequilibrium with the country rocks, producing haloes of alteration products which may, in some cases, as mentioned above, actually resemble primary igneous rocks. The process is thought to be a solid-state transformation due to the expulsion, from the igneous complex, of hot, highly reactive volatiles and their subsequent infiltration into the country rocks. The spatial relationships of alkaline and carbonatite magmas and their fenitised envelopes are illustrated in Fig. 7.3

The composition of fenites is dependent on both the nature of the country rocks affected and the igneous complexes from which the fenitising fluids evolve. Fenitic envelopes occur mainly around carbonatites, but other alkaline complexes are also surrounded by alteration haloes with a fenitic character. Since most anorogenic alkali complexes and allied rocks occur in stable continental areas, fenite envelopes are, for the greater part, found within granitoids and/or basement gneisses. However, fenitisation has also been noted in mafic igneous rocks and sedimentary rocks, as observed in the Okorusu nepheline-syenite carbonatite complex, which developed its fenitic envelope in sedimentary wall rocks and which converted these rocks into a "massive alkali pyroxenite" that retains the sedimentary structures (Verwoerd 1966). Two styles of fenitisation are recognised, one associated with carbonatites and the other with ijolites. Carbonatites form intense K-feldspar fenitisation, whereas ijolite magmatism is associated with Na-K fenitisation and the production of aegirine-bearing rocks (Le Bas 1977).

The precise temperature, pressure, and composition of the fenitising fluids are not well understood, but from the available data (Woolley et al. 1972; Ferguson et al. 1975; Verwoerd 1966; Le Bas 1977), it can be surmised that the composition of the fenitising fluids ranges from Na + K + CO_2-rich (carbonatitic magmas) to saline brines enriched in Na and/or CO_2. Temperatures of the fluids, based on mineral equilibria, range from 450°C up to 700°C (alkaline magmas) with pressure from a few hundred bars up to 5 kbar.

7.2.2.2 Mineral Systems Associated with Carbonatites and Haloes of Fenitic Alteration

Mariano (1989) provided an overview of the mineral potential of carbonatites. Details on rare earth elements (REE) mineral deposits, commonly hosted by carbonatites and alkaline complexes, can be found in Jones et al. (1996).

Mariano (1989) listed 34 deposits associated with carbonatite igneous systems. These deposits contain economic ores of REE, Nb, phosphates, Cu, Ti, vermiculite and fluorite. Of these, Bayan Obo (China), Mountain Pass (USA), and Palabora (South Africa) are the largest (see Pirajno 2009 for overviews and references). Carbonatite-related Fe-P, Nb-Ta, and Nb-REE deposits (e.g. Tomotr, Karasug, Beloziminskoe) are numerous in the Siberian Craton and surrounding orogenic belts (Seltmann et al. 2010). Carbonatites are the main host of REE mineralisation, both magmatic and hydrothermal. The Mountain Pass carbonatite typically contains bastnaesite-parisite as the primary magmatic minerals, albeit in a late-stage carbonatite. Hydrothermal REE minerals are more common, forming polycrystalline aggregates, veinlets and interstitial fillings. They are usually associated with barite, fluorite and monazite in varying amounts, which may or may not be economic. Bastnaesite [(REE)(CO_3)F] is one of the more important REE mineral species, together with ancylite [$SrCe(CO_3)_2{\cdot}(OH){\cdot}H_2O$], parasite [$(REE)_2Ca(CO_3)_3F_2$], synchysite [$(REE)Ca(CO_3)_2F$], and britholite [$(REE,Ca)_5(SiO_4,PO_4)_3(OH,F)$]. Most hydrothermal carbonatite-hosted REE deposits are small and uneconomic, although it is possible that a Bayan Obo style mineral system could be found in rift-related tectonic settings (Pirajno 2009). Weathering of carbonatite complexes results in dissolution of carbonate minerals, leaving residual and/or supergene monazite, apatite, and REE minerals, such as bastnaesite, parasite, and florencite [$(REE)Al_3(PO_4)_2$-$(OH)_6$]. At Mt Weld, in Western Australia, a 2,064 Ma carbonatite ring complex contains residual apatite at the base of the regolith, magnetite, vermiculite, and Y and lanthanide compounds, derived from the primary pyrochlore, ilmenite, rutile, monazite, and synchysite in the carbonatite rocks (http://www.portergeo.com.au/database/mineinfo.asp?mineid=mn770; Duncan and Willett 1990). Apatite is one of the principal accessory minerals in carbonatite and alkaline complexes and, in some cases, can exceed >50% by volume (Mariano 1989).

Carbonatites are also a major resource of Nb, which is mostly contained in minerals such as pyrochlore and ferrocolumbite, in addition to minerals in which Nb proxies for other elements (e.g. perovskite and titanite). Pyrochlore also precipitates from hydrothermal fluids and may be associated with bastnaesite and fluorite. Other ore minerals of economic importance include titanite, which can be quite abundant in carbonatite and alkaline complexes, whereas rutile and brookite can be found as disseminations in fenitic aureoles, associated with carbonate, fluorite, and low-temperature feldspar (Mariano 1989). Titanium can reach economic abundances in the mineral anatase, which is a weathering product of Ti-bearing minerals. Fluorite too forms a common accessory in many carbonatite and alkaline complexes. At Bayan Obo, fluorite associated with bastnasite, is a major

ore mineral. It must be borne in mind that F in hydrothermal fluids can move for long distances such that fluorite can be precipitated in host rocks that have no relationship with carbonatites or a carbonatite source. Other elements that can be important as economically viable ores are Ba and V. Barite can crystallise from carbonate melts or from low-temperature hydrothermal fluids, as is in the case at the Mountain Pass carbonatite (Castor 2008). Vanadium can be hosted in minerals such as aegirine and magnetite in carbonatites and alkaline ultramafic rocks. Copper is the major ore element of the Palabora carbonatite complex, where it may have resulted from the circulation of hydrothermal fluids (see Pirajno 2009 for an overview and references therein). Thorium and U are enriched in carbonatites and alkaline rocks, with Th usually being more abundant than U. Thorium- and U-bearing minerals of carbonatites include perovskite, pyrochlore, thorite, and REE mineral species.

An example of large-scale (regional) fenitisation and associated REE-U mineralisation can be found in Western Australia in an area intruded by the carbonatite dykes and sills of the Gifford Creek Carbonatite Complex (Pirajno et al. 2010). The carbonatitic suite consists of ferrocarbonatite-magnetite dykes, veins, and sills. The Complex, with poorly constrained ages ranging from ~1.68 to 1.00 Ga, was emplaced in the ~2.0 Ga Gascoyne Province and was investigated in detail by Pearson et al. (1995) and Pearson and Taylor (1996). The Gascoyne Province, located between the northwestern Archaean Yilgarn Craton and the Mesoproterozoic Ashburton Formation to the north, consists of a suite of Neoarchaean to Palaeoproterozoic granite gneisses that are interpreted as basement to various Proterozoic granitic rocks (2.0–1.9 Ga Dalgaringa Supersuite, 1.68–1.97 Ga Durlacher Supersuite, 1.83–1.62 Ga Moorarie Supersuite) and metasedimentary sequences. Details of the geology of the Province can be found in Sheppard et al. (2007). The Gifford Creek Carbonatite Complex is a suite of high-level ferrocarbonatite sills, dykes, and veins, associated with quartz and massive Fe oxide veins (Pirajno et al. 2010). This is a field of REE and U mineralisation (Flint and Abeysinghe 2000), hosted in sinuous veins and dykes of ferroan carbonatite and Fe oxides that intrude porphyritic granites of the Durlacher Supersuite. The ferroan carbonatite (ankerite, siderite), Fe oxide dykes and veins form a regional-scale stockwork-like system, associated with zones of alteration that have a distinct fenitic character. The fenitic haloes are characterised by the presence of feldspars and/or sodic amphiboles and magnetite, locally with monomineralic feldspar (orthoclasite) zones. Fenitisation of the country rock granitoids can form zones (aureoles) up to 2–4 km across, in which the granitic rocks exhibit sericitisation of primary feldspars and growth of new K-feldspar. Around the carbonatites, the granitic rocks show progressive replacement of the constituent minerals by K-feldspar, sericite and alkali amphibole. Pearson and Taylor (1996) noted "stock-like" zones of syenite in places, which they attributed to intense and pervasive fenitisation. Following the classification of Kresten (1988), these authors also recognised vein fenites, consisting of riebeckite, cutting across the above-described larger zones (aureole fenites). Pearson et al. (1995) suggested that the Gifford Creek Carbonatite Complex and the

associated extensive fenitisation of the intruded country rocks may represent the upper levels of unexposed major alkaline ring complexes. SEM and XRD analyses of carbonatites and fenitised rocks indicate that they contain monazite and pyrochlore along with less common ferrocolumbite, bastnasite, barite, and veins of aegirine-phlogopite-apatite-magnetite-pyrochlore (Pirajno et al. 2010).

7.3 Skarns

Skarns are calc-silicate rocks formed by the replacement of carbonate lithologies either during high-T, low-P regional metamorphism or by contact metasomatic processes related to igneous intrusions (Plate 7.1c, d; Plate 7.2e, f). Many skarns are associated with porphyry systems, where the porphyry stock intruded carbonate lithologies. Skarns are very important because they host a great variety of ores and constitute a distinct class of mineral deposits. Here, I briefly discuss the process of replacement of carbonate rocks by silicate minerals, generally through the addition of silica, as in the following reaction:

$$\underset{\text{calcite}}{CaCO_3} + SiO_2 \rightarrow \underset{\text{wollastonite}}{CaSiO_3} + CO_2$$

The addition of large quantities of silica results in a wide variety of calc-silicate minerals that include Ca, Fe, Mg, Mn silicates, such as epidote, clinozoisite, wollastonite, diopside, vesuvianite, tremolite-actinolite, andradite, grossularite, spessartite, rhodonite, phlogopite, and biotite. Skarns are developed at the contact between plutons and the invaded country rocks, the latter generally being carbonates and, less commonly, Ca-rich silicate rocks. Skarn genesis essentially involves isochemical contact metamorphism and metasomatism (prograde skarns), entirely due to the transfer of heat, fluids, and metals from a cooling plutonic body to the surrounding wall rocks. Skarn alteration systems are typically zoned in response to temperature variations and fluid evolution outward from the intrusive stock or pluton. This zonation begins with the endoskarn within the intrusion and continues outwards to the proximal and distal exoskarns that develop in the surrounding country rocks. Generally the carbonate rocks at and around the contacts of the intrusion are metamorphosed to marble (marmorised) or calc-silicates, in the case of impure carbonates. At the contact, proximal or prograde skarns are characterised by various combinations and volumetric abundances of garnet (grossularite-andradite), pyroxene, vesuvianite, wollastonite, and rhodonite. Retrograde stages of alteration occur towards the final stages of cooling, resulting in more intense hydrothermal activity, local mixing with meteoric waters, precipitation of sulphides and oxides, especially nearer the pluton's contacts, and overprinting of prograde assemblages. Mineral assemblages of retrograde skarns typically include hydrous phases, such as amphibole, biotite, epidote, and chlorite although, as cautioned by Meinert et al. (2005),

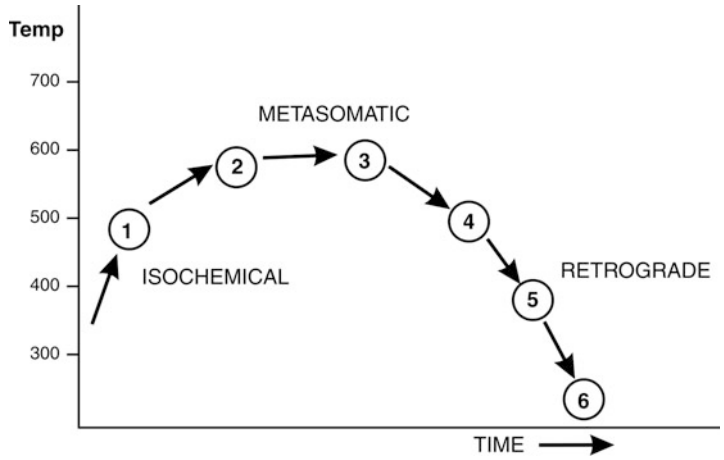

Fig. 7.4 Stages of skarn development as a function of time and temperature: (1) calcite and diopside; (2) calcite, diopside, wollastonite, vesuvianite (idocrase), and grossular; (3) andradite, diopside-hedenbergite, epidote, and powellite; (4) quartz, chalcopyrite, scheelite; (5) amphibole, calcite, epidote, and quartz; (6) zeolites (After Brown et al. (1985))

the presence of hydrous mineral phases does not necessarily imply retrograde processes. As mentioned above, retrograde minerals reflect decreasing temperature and salinity of the fluids, leading to a trend from amphibole-epidote → biotite → muscovite-chlorite → sulphides → carbonates (+fluorite or scheelite or powellite).

Skarns develop at temperatures ranging from between 700°C and 200°C and at pressures of between 0.3 and 3 kbar. The metasomatic fluids have salinities which range from 10 to about 45 wt.% NaCl equivalent. In summary, the formation of skarns can be related to three main stages (Fig. 7.4): (1) isochemical prograde thermal metamorphism; (2) metasomatism; and (3) retrograde hydrothermal alteration.

Metamorphic and metasomatic reactions characteristic of skarns involve the systems $CaO\text{-}MgO\text{-}SiO_2\text{-}H_2O$ and $CaO\text{-}Al_2O_3\text{-}Si_2O\text{-}CO_2\text{-}H_2O$ (Einaudi et al. 1981). Some typical reactions, as reconstructed from petrographic observations, are:

$$\text{tremolite} + 3\ \text{calcite} + 2\ \text{quartz} = 5\ \text{diopside} + CO_2 + H_2O;$$

$$9\ \text{hedenbergite} + 2H_2O = 3\ \text{andradite} + 9\ \text{quartz} + \text{magnetite};$$

$$3\ \text{hedenbergite} + H_2S = \text{andradite} + 3\ \text{quartz} + FeS_2;$$

$$2\ \text{andradite} + 4H_2S = 6\ \text{wollastonite} + 4FeS_2 + 3H_2O.$$

Garnets and pyroxenes are important components of skarns. Their internal zoning and various generations are a function of the changing physico-chemical conditions of the fluids. For this reason microprobe analyses of garnets and pyroxenes are important in establishing the nature and type of skarns. Ternary plots of the compositional distribution of garnets and pyroxenes (spessartine-grandite-andradite and johannsenite-diopside-hedenbergite respectively) can be used to characterise the class of skarns. For example, porphyry-related Cu skarns are characterised by the presence of andradite and diopside, whereas the grossularite-hedenbergite association is more typical of W-bearing skarns (Einaudi and Burt 1982).

Smirnov (1976) explained the mechanism of skarn genesis by the diffusion-infiltration model. This was refined by Einaudi et al. (1981) under the name of bimetasomatic diffusion. Einaudi and Burt (1982) considered infiltration to be the main mechanism of skarn genesis. The diffusion-infiltration theory holds that skarns result from a system with imbalanced chemistry (temperature gradients, composition of fluids, and composition of fertile host rocks, such as carbonates), developed in hot aqueous solutions, which impregnate both the intrusive igneous rocks and the carbonate lithologies on either side of the contact (Newberry 1991). This leads to the formation of endo- and exoskarns. Elements are dissolved from both sides and the solution tends to homogenise by diffusion from areas of high concentration to areas of low concentration. Exchange reactions take place along these diffusion fronts between the solutions and the enclosing lithologies. Due to the different mobilities of the elements concerned, their concentrations in the solution would fall toward the diffusion front at different rates giving rise to well-developed zoning and distinct mineral paragenesis. Smirnov (1976) considered four groups of compounds and elements in order of decreasing mobility. They are (1) H_2O and CO_2; (2) S, Cl, K, and Na; (3) O, Si, Ca, Mg, and Fe; and (4) P, W, and Al. Furthermore, three temperature stages are distinguished (Smirnov 1976). These include (1) a high temperature stage with pyroxene + garnet and pyroxene + epidote; (2) an intermediate temperature stage with two substages, one characterised by epidote + actinolite, and the other with epidote + chlorite; and (3) a low temperature stage subdivided into six substages with prehnite, pumpellyite, calcite + albite, calcite + quartz + sericite + chlorite, calcite + quartz + sericite + dolomite, and zeolite. These stages approximately correspond to those shown in Fig. 7.4.

A sequence of events in the genesis of skarns in a porphyry-related system is given below and depicted in Fig. 7.5. First, the intrusion of a pluton results in contact metamorphism of the carbonate wall rocks. This stage involves decarbonation and dehydration reactions to form diopside and wollastonite skarns. The timing of this stage would correspond with the crystallisation of the pluton's margins following the intrusion of the melt phase into the sedimentary lithologies. The temperature range is from 900°C to 500°C. Fluids, which are released from the partially solidified intrusion, infiltrate into and along fractures in the pluton and country rocks. This is the stage of potassic alteration and disseminated chalcopyrite mineralisation in the plutonic rocks. This stage also corresponds to the movement of fluids outward into structural breaks in the country rocks (fractures, contacts,

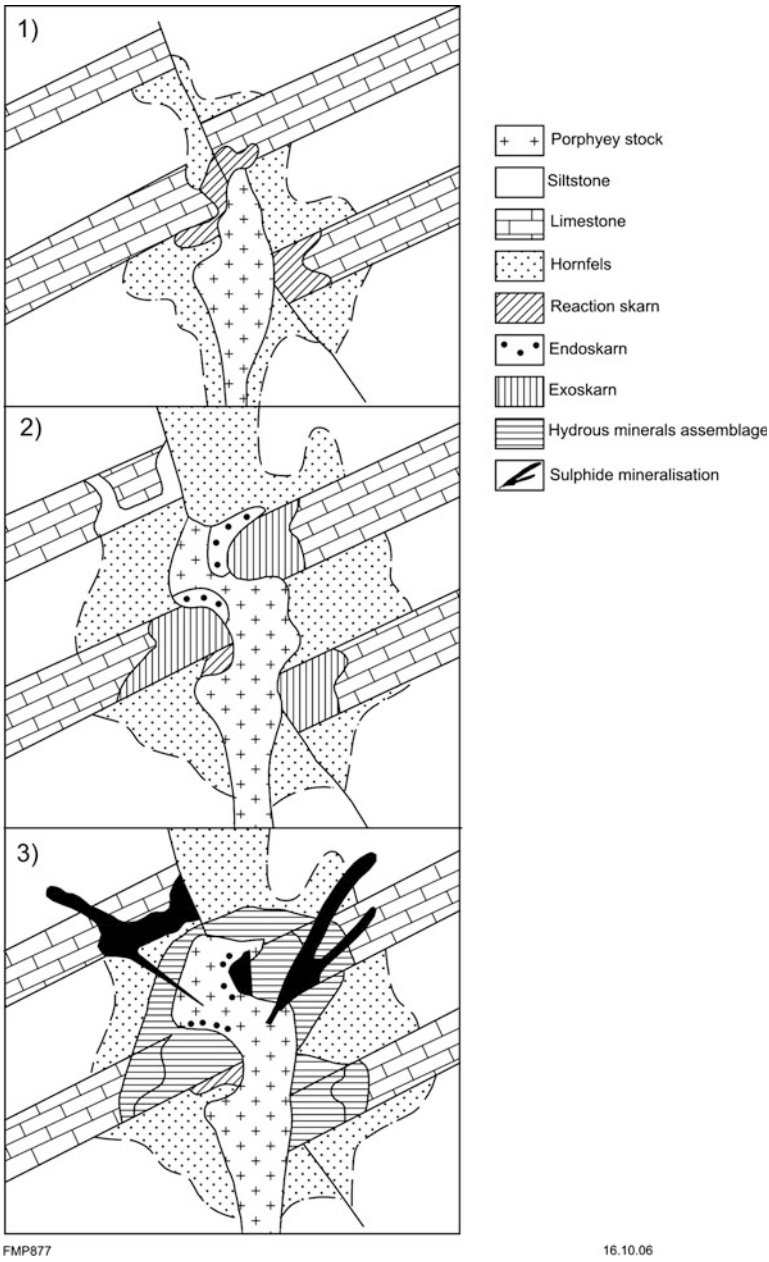

Fig. 7.5 Stages of skarn formation. These include: (1) isochemical stage with hornfels developing in non-carbonate units and commencement of reaction skarns in carbonate rocks; (2) metasomatic stage in which there is extensive development of exo- and endoskarns; and (3) a retrograde stage, which tends to destroy the earlier skarns and is dominated by hydrous minerals and sulphides (Modified after Einaudi et al. (1981))

permeable horizons) to form early skarn facies consisting of andradite, magnetite and sulphides. The temperature range is from approximately 600–400°C.

The next phase is one of ore deposition in the ongoing skarn development. An andradite-bearing skarn is replaced by magnetite, quartz, pyrite, and calcite, whereas a diopside-bearing skarn is replaced by actinolite, calcite, quartz, and some chalcopyrite. This corresponds to the waning stages of potassic alteration and the beginning of the quartz-sericite-pyrite alteration in the pluton with concomitant Cu ± Mo mineralisation. The range of temperatures is from 500°C to 300°C. The final stage (retrograde alteration) involves the destruction of the skarn assemblages, (due to the infiltration of lower-temperature meteoric water) and is characterised by the deposition of clay minerals (kaolinite, montmorillonite, nontronite), chlorite, calcite, quartz, hematite, pyrite, and/or locally silica-pyrite. Mineralisation generally consists of pyrite, sphalerite, galena, and tennantite. This stage of skarn destruction or retrograde alteration coincides with late phases of quartz-sericite-pyrite and argillic alteration of the porphyry intrusion and is therefore dominated by the incursion of meteoric waters in the system. Ore deposition is classified in broad terms by Einaudi (1982) into two types based on a morphological and textural basis. The first type coincides with the early phases of skarn genesis (generation of potassic-bearing fluids by the porphyry stock), whereas the second type is more or less associated with silicification as well as sericitic and argillic alteration of the porphyry pluton. These two styles may occur in the same deposit. Lateral and vertical zoning of both disseminated and lode mineralisation styles may be present and occur as a function of distance from the porphyry pluton (Fig. 7.5). The nature of the zoning also depends on the nature of the replaced lithologies (e.g. limestone, calcareous siltstone). In the disseminated mineralisation styles, a zone of bornite + chalcopyrite + magnetite closest to the intrusion is followed by an intermediate zone of pyrite + chalcopyrite, a peripheral pyrite ± chalcopyrite ± tennantite ± sphalerite ± galena, hematite, and/or magnetite. A distal zone occurs within the carbonate rocks and consists of pyrite + chalcopyrite + magnetite ± sphalerite ± tennatite ± pyrrhotite. In the lode style of mineralisation the following zonation from the intrusive contact outward may be present. These include a zone of pyrite + digenite + enargite ± Sn-Bi-W minerals; an intermediate zone of pyrite + bornite + chalcopyrite + tennantite ± sphalerite; a peripheral zone of pyrite + chalcopyrite + tennantite + sphalerite + galena ± hematite; a distal zone within the carbonate rocks of pyrite + bornite + chalcopyrite + tennantite + sphalerite + galena ± magnetite or hematite.

The above review is clearly generalised and focuses on the common features of porphyry-related skarn deposits. The reader should be aware that individual deposits will display many variations from the common theme. A special issue of Economic Geology (Meinert et al. 2000) is devoted to skarn deposits. Skarn ore systems can also be distinguished on the basis of their metal endowment. The most common and economically viable are Cu (±Fe ± Au ± Mo), Sn-W, and W skarns;

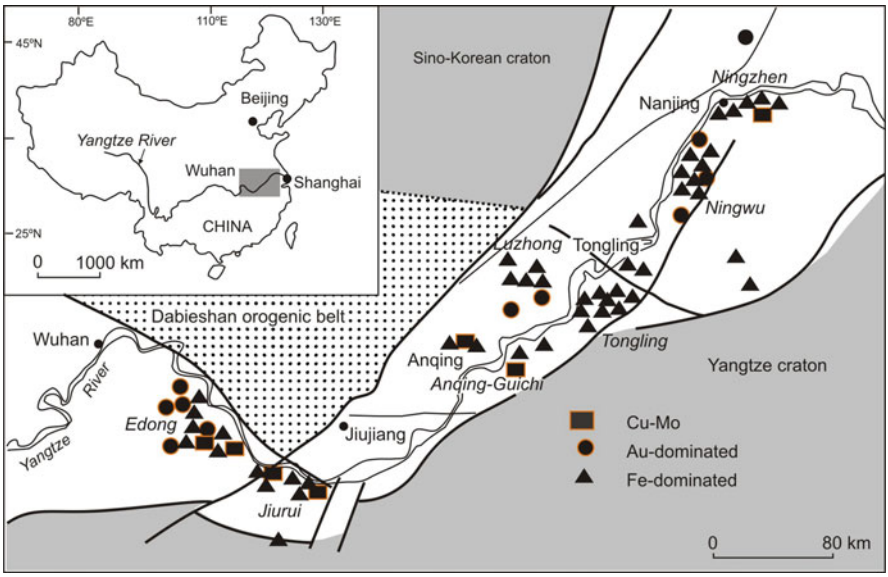

Fig. 7.6 The Yangtze River Valley metallogenic belt, at the boundary between the North China Craton and the Yangtze Craton and distribution of polymetallic skarn mineral systems (cf. Pan and Dong (1999) and Mao et al. (2006, 2011))

Au skarns; Fe-P (magnetite-apatite) and Fe skarns; Zn skarns; and Mo and Cu-Mo skarns. Key examples are discussed in some detail in Pirajno (2009), amongst which is the large metallogenic belt of the Yangtze River Valley in China on the northern margin of the Yangtze Craton. This metallogenic belt comprises numerous stratabound pyrite- and magnetite-rich and polymetallic skarns. The Yangtze River Valley metallogenic belt has been described in detail by Pan and Dong (1999) and Mao et al. (2006). The polymetallic skarn deposits in this belt can be considered as Fe-dominated and Au-dominated Cu-Mo skarns (Fig. 7.6).

7.3.1 Skarn-Like Alteration Associated with Regional Metasomatism

Regional high-temperature low-pressure metamorphism can result in mass-transfer processes capable of producing large scale metasomatic alteration of sedimentary and igneous rocks (e.g. Oliver et al. 1998). Large-scale metasomatic alteration, that is commonly associated with regional metamorphism and the passage of hot, saline, oxidised fluids, can produce skarn-like alteration zones dominantly

containing calc-silicate assemblages. Good examples of this type of metasomatism can be found in Australia. A special issue of Economic Geology (Williams 1998) is devoted to the McArthur River-Mt Isa-Cloncurry Mineral Province, where regional-scale K-metasomatism in the district and its relationship to mineralization is discussed in several papers. Another well documented example from Australia is the regional scale metasomatic alteration in rocks from the Olary Domain in the Proterozoic Curnamona Province (Kent et al. 2000). The following is summarised from these authors.

The Olary Domain is part of a Palaeoproterozoic inlier of the Willyama Supergroup (Curnamona Province) in South Australia. The Domain consists of quartzo-feldspathic rocks, calc-silicates, marble, graphitic pelite, albitite, tourmalinite (see below), banded iron-formation units and pelitic rocks. These lithostratigraphic units have ages ranging from ~1,710 to 1,650 Ma and are interpreted to have been deposited in a continental lacustrine and sabkha facies in a failed rift setting. The Olary sequence was intruded by several suites of granitoids and subjected to five deformation and metamorphic events. Further thermal and structural perturbations occurred during later orogenies (~1,200 Ma Musgravian; ~ 500 Ma Delamarian). All these events were accompanied by fluid flow, resulting in a protracted history of metasomatism and hydrothermal alteration of the Olary lithologies.

Styles of metasomatic alteration vary according to the rock type affected. Pelitic and granitic rocks exhibit extensive albitisation. Quartzo-feldspathic rocks show albitisation accompanied by minor amounts of magnetite, hematite, pyrite, chalcopyrite, and, locally, biotite + magnetite. Calc-silicate units grade into clinopyroxene- and actinolite-matrix breccias, massive garnet-epidote zones, and laminated Mn-rich (piemontite). Iron formations show Fe oxide enrichments (magnetite) and local growths of pyrite and chalcopyrite. The clinopyroxene- and actinolite-matrix breccias and garnet-epidote represent the most common metasomatic alteration styles. Garnet-epidote alteration zones range from small isolated veinlets to massive, stratabound replacements, up to 300 m across. This type of metasomatism tends to follow pre-existing fractures related to one or more of the deformation events that affected the Olary Domain. Kent and co-authors established that during the garnet-epidote metasomatism there was substantial enrichment in Fe^{3+}, Mn, Ca, Cl, Pb, Cu, Zn, U, and P, whereas Fe^{2+}, Mg, Na, K, and Rb were depleted (Kent et al. 2000). Fluid inclusion studies revealed homogenisation temperatures of primary and secondary inclusions (uncorrected for pressure) ranging from 191°C to 319°C with corresponding salinities (NaCl equivalent) of 19–33 wt.%. However, peak metamorphic pressures and temperatures in the Olary Domain have been estimated at 4–6 kbar and 550–650°C, respectively. These would correspond to a temperature correction of about 400–650°C for the fluid trapping temperatures suggesting that metasomatism took place after peak metamorphic conditions.

Kent et al. (2000) concluded that the source of the saline and oxidising metasomatic fluids derived from metamorphic devolitilasation of the metamorphic Olary lithologies. These authors pointed out that some of these rocks were originally oxidised (red beds, evaporites), resulting in iron formations, albitites,

and calc-silicates. During peak metamorphism, breakdown of volatile-bearing phases occurred and resulted in the release of large volumes of fluids. Devolitilisation reactions may have been enhanced by the intrusion of granitoid suites. The oxidised and saline fluids were capable of transporting Fe, Cu, Au, Mo, Pb, Zn, REE, U, and Mn metals. Some of the mineralisation associated with Olary-style metasomatism, such as Fe oxide-Cu-Au-U and Cu-Mo-Au associations, may well have resulted from the devolitilisation of red beds and evaporitic rocks (Barton and Johnson 1996).

7.3.2 *Skarn-Type Assemblages of Archaean Hypothermal Au Lodes*

Archaean lode Au mineralisation is hosted in ductile shear zones, brittle-ductile zones, brittle fault zones, brittle quartz vein arrays, and replacement style quartz reefs in banded iron-formations and other Fe-rich rocks. In addition to Au, other elements that are present, either as ore minerals or in various mineral phases in alteration envelopes are Ag, As, W, Bi, Te, Pb, Sb, and B. In the Yilgarn Craton (Western Australia), lode Au deposits form a broadly synchronous (2,635 $\pm$ 10 Ma) group, over a range of epithermal to hypothermal styles and metamorphic environments from greenschist- to granulite-facies (Groves 1993). The mineralising fluids are typically deeply sourced, of low-salinity and contain H_2O, CO_2, and CH_4, with temperatures ranging widely from 180°C to more than 700°C, and pressures of 1–5 kb (Groves et al. 1995). Mixing with cooler meteoric waters is suggested in some cases, especially for those deposits that are hosted in brittle structures and low-grade metamorphic rocks. The timing of the Archaean Au mineralisation is syn- to post-peak metamorphism. Data integrated from regional, structural, mineralogical, isotopic, fluid inclusion, geochemical, alteration, and tectonic setting studies have led to the crustal continuum model advocated by Groves (1993), a version of which is illustrated in Fig. 7.7. The crustal-continuum conceptual model predicts that lode Au mineralisation is by no means confined to greenschist facies rocks, but can also be found in higher grade terranes. Indeed, Mueller and Groves (1991) and Mueller et al. (1991) studied high-temperature (hypothermal) Au lodes of the Yilgarn Craton, which are located in amphibolites-facies greenstone rocks that show skarn-type mineral assemblages.

Gold lode deposits hosted in high-grade metamorphic greenstone rocks, such as Big Bell in the Murchison Province of the Yilgarn Craton, are characterized by microcline-muscovite-andalusite alteration (Mueller 1988; Mueller and Groves 1991). This alteration can be further subdivided into an inner zone (microcline-muscovite-andalusite), an intermediate zone (biotite-cordierite-plagioclase), and an outer zone of garnet-amphibole-biotite and biotite-epidote-calcite assemblages. In the Southern Cross and Western Gneiss Terrane of the Yilgarn Craton, the lode deposits are associated with an inner zone of garnet-pyroxene-biotite and an outer zone with amphibole-biotite alteration. In the Southern Cross greenstone belt of the

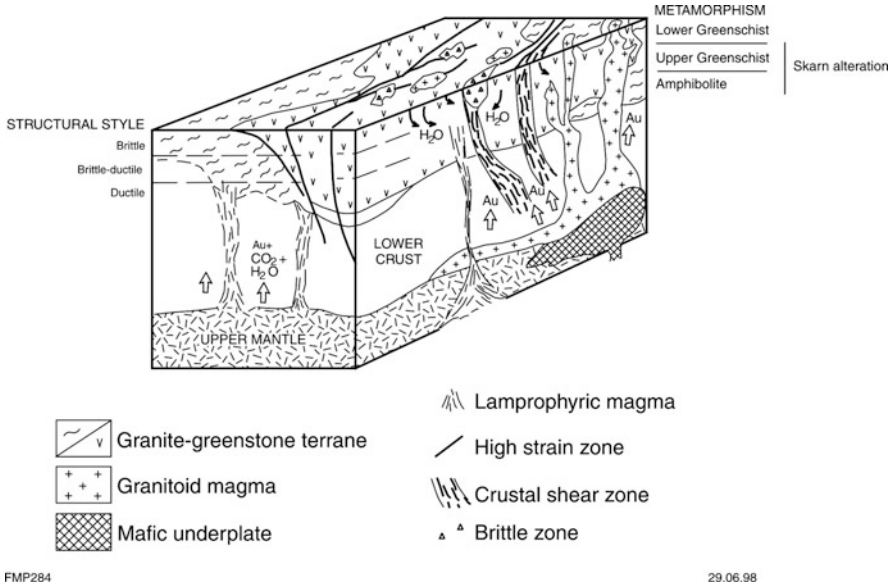

Fig. 7.7 Schematic block diagram showing the crustal continuum model, in which mantle degassing (CO_2 + H_2O + Au), metamorphic devolatilisation reactions, granitic, mafic, and lamprophyric melts combine to activate complex and large scale hydrothermal systems, resulting in large scale skarn-style alteration at deeper and higher temperature levels. Fluids are channelled along major crustal shear zones. Cool meteoric waters may locally mix with hotter CO_2-bearing deeply-sourced fluids. The mafic underplating, lamprophyric melts, and granitoids may be linked with mantle plume activity (This diagram is from Pirajno (2000) and based on Groves (1993) and Groves et al. (1995))

Yilgarn Craton, lodes hosted in amphibolite-facies rocks show an inner zone of amphibole-biotite-calcite alteration and an outer zone of chlorite-calcite-biotite alteration. Mueller and Groves (1991) suggested that these lode deposits formed in the lower parts of the greenstone belts, at depths of 10–15 km and a lithostatic pressure of 3–5 kbars over a series of peak alteration temperatures ranging from 500°C (amphibole-biotite-calcite) to 650°C (garnet-pyroxene-biotite), and up to 700°C (microcline-muscovite-andalusite). These authors concluded that these high temperature lode Au deposits qualify as the Au skarn type as described in Einaudi and Burt (1982). Furthermore, Sr isotope systematics of Au lodes in high-grade rocks show $^{87}Sr/^{86}Sr$ values from 0.7020 to 0.7035 in garnet-pyroxene-biotite skarns and from 0.7020 to 0.7043 in amphibole-biotite-calcite skarns (Mueller et al. 1991). According to Mueller et al. (1991), the Sr isotopic data indicate that the origin of the metasomatising fluids for these deep-seated Au skarns were derived from, or interacted with, anatectic granitic magmas and that metamorphic (devolitilisation) fluids did not participate in the formation of the deep-seated Au skarn systems.

7.4 Greisens

Greisen, an old Cornish miners' term, refers to a coarse-grained assemblage of quartz-muscovite with varying amounts of topaz, tourmaline, fluorite, oxides (cassiterite, hematite), wolframite, scheelite, sulphides of Fe, Cu, Mo, and Bi, as well as Cu-Bi-Pb sulphosalts (Plate 7.1e; Plate 7.2c, d). Although greisen alteration is common in continental porphyry systems, its most favourable environment is a granite stock or sheet emplaced within argillaceous-arenaceous rock sequences, associated with Sn-W mineralisation. The physico-chemical processes of greisenisation are not entirely understood. In general, greisen alteration is usually preceded by Na metasomatism (albitite), during which H^+ ions are produced, which then initiate the process of greisenisation. This involves the destabilisation and destruction of feldspars and biotites to form the assemblage quartz + muscovite. The process may be more complicated in mineralised systems, in which there is the introduction of B, F, and Li. This will result in a new series of reactions that may take place to form topaz, tourmaline, and oxide minerals. Silicification may accompany greisen alteration during and after, as evidenced by the common flooding of quartz in the greisen altered rocks. Muscovite preferentially replaces biotite, and during this process cations locked in the biotite lattice are released into the system. These cations are possibly responsible for the paragenetically later metallic mineralisation. Quartz + muscovite greisens may be followed by progressive stages of F- and/or B-metasomatism. In the latter case the development of tourmaline may be so extensive that quartz-tourmaline assemblages may dominate altogether. Subsequent to greisen alteration, sericitic and argillic rocks may develop due to increased H^+ activity.

7.4.1 Greisenisation Processes

Greisenisation processes include an early alkaline stage, a greisenisation stage, and a vein-depositing stage. In general, greisen systems evolve by decreasing alkali/H^+ ratios, resulting in the destabilisation of K-feldspar, plagioclase, and micas. This leads to the greisen stage *sensu stricto* with the replacement of these minerals by quartz and white mica (muscovite and/or phengite). In some cases muscovite may be very coarse and form thick monomineralic selvages along fractures. Other common mica compositions generated by the greisenising fluids include lithian siderophyllite, protolithionite, zinnwaldite, and lepidolite (Kinnaird 1985). Silicification usually takes place during and after greisenisation, and is evidenced by intense quartz flooding and replacements. Muscovite characteristically replaces feldspars and biotite. The reaction feldspar to muscovite (assuming Al to be immobile) may be written as follows:

$$\underset{\text{microcline}}{3(KAlSi_3O_8)} + 2H^+ = \underset{\text{muscovite}}{KAl_3(Si_3O_{10})(OH)_2} + 2K^+ + 6SiO_2$$

At this point it is pertinent to focus attention on the possible role played by these reactions in releasing metals into the system. Shcherba (1970), for example, noting that plagioclase and mica are the principal "carriers of rare metals", considered the leaching of the metallic elements from their original sites in the lattices of these rock-forming minerals to have occurred during greisenisation processes by virtue of the presence of F and Cl species in the fluids. Taylor (1979) commented on the Sn content of mineral phases of stanniferous granites (titanite 230–260 ppm, ilmenite 15–80 ppm, biotite 50–500 ppm). According to Eugster (1984), ilmenites may contain up to 1,000 ppm Sn, 100 ppm Mo, 60 ppm W, and 1,000 ppm Nb, whereas biotite may contain up to 1,000 ppm Sn, 10 ppm W, 60 ppm Mo, and 100 ppm Nb. Eugster (1984) and Barsukov (1957) asserted that the conversion of biotite to muscovite is of fundamental importance for the genesis of Sn-W deposits, emphasising the role played by both biotite and muscovite as "*excellent hosts*" for elements such as Sn, W, and Mo. The release of these elements from the mica lattice to form ore minerals is documented by the presence of sulphide and oxide minerals in the cleavage and/or microfractures of the micas in the greisenised granites (Pirajno 1982).

The structural relationships between the greisenised cupolas and the enclosing country rocks, and their degree of fracturing, determines the type of endo-exogreisen system. Types of greisen alteration within the cupola (endogreisen) and in the country rocks (exogreisen), above and around the greisenised granite rocks, are shown in Fig. 7.8. A greisenised cupola, lodged in a sedimentary sequence containing pelitic and psammatic rocks, will form a narrow aureole of contact metamorphism, usually identifiable by the presence of porphyroblastic biotite and, closer to the contact, cordierite. Spotted schists are a common feature in sedimentary sequences intruded by granitic rocks. Greisenisation overprints the thermal mineral assemblages and is, in most cases, characterised by the nucleation of muscovite, albite, and local tourmaline.

In mafic rocks greisenisation is characterised by the presence of chlorite-talc, phlogopite-actinolite, quartz-plagioclase, and quartz-muscovite. Although typical skarns are usually associated with porphyry systems, some skarns are spatially and genetically associated with greisen-related systems in which all gradations may be observed (Rose and Burt 1979). Greisen alteration of carbonate rocks usually takes place after their skarnification. The greisen solutions are neutralised on contact with the carbonate lithologies, as the anionic species (e.g. F, OH) become fixed by Ca and Al to form fluorite and topaz. The sequence of late post-magmatic processes leading to greisenisation is shown in Fig. 7.9. In this scheme, worked out by Pollard (1983), K-feldspathisation takes place as a result of separation of fluids from a residual granitic melt. This phase leads to a concentration of Na in the melt, resulting in the crystallisation of a Na-rich rock, usually with a high F content. The enrichment of the residual melt in Na and F results in post–magmatic albitisation, which is most common in the uppermost zones of the cupolas and along fractures. According to Pollard (1983), this may be due to the enhanced F content, and perhaps the influence of CO_2, which lower the solidus, and in so doing allows for an extended period of crystallisation that, in turn, promotes the expulsion

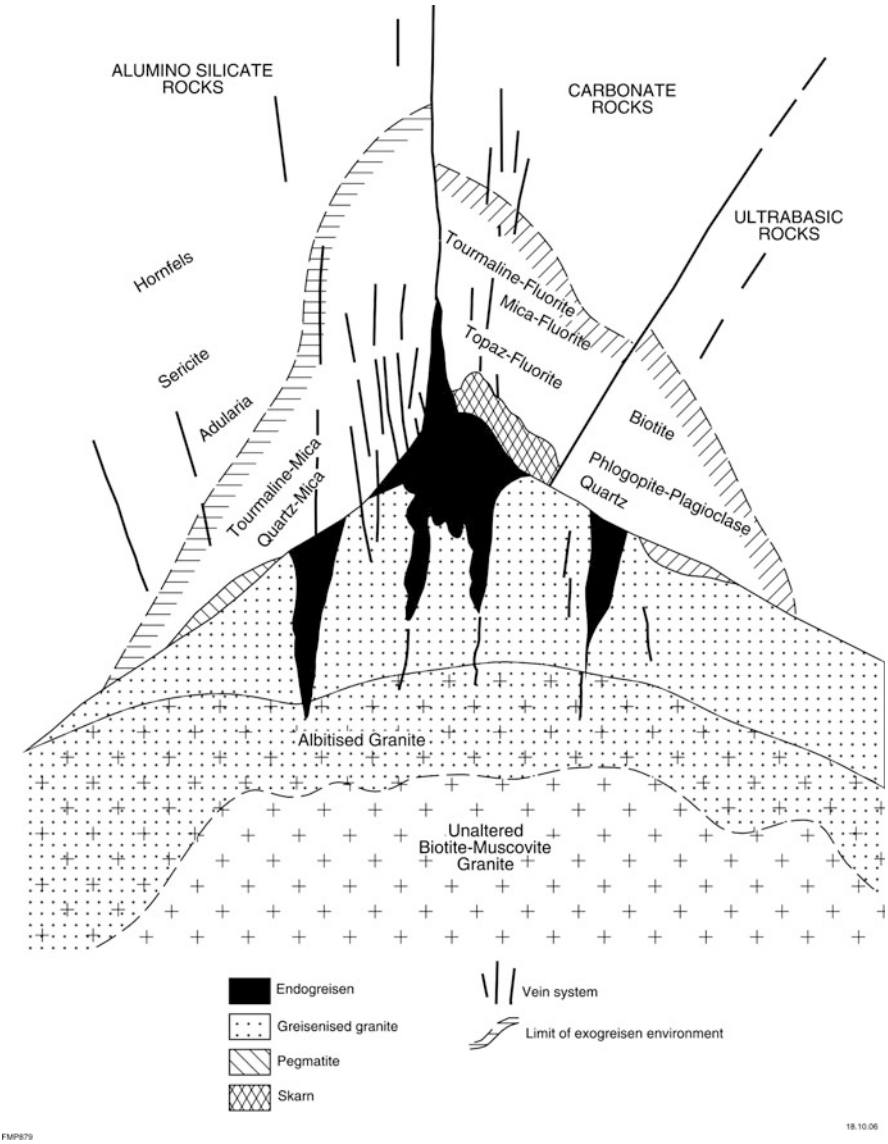

Fig. 7.8 The endo- and exogreisen systems in aluminosilicate, carbonate, and ultramafic rocks (Shcherba 1970)

of an aqueous phase to develop and collect in the apical parts of the granitic cupola. Greisenisation follows this stage of Na metasomatism (Fig. 7.9) during which the circulating hydrothermal fluids are characterised by enhanced activities of H^+ and of HF, and in which there is a wholesale destruction of the granitic mineral components to form greisen assemblages. Greisen alteration is the equivalent of

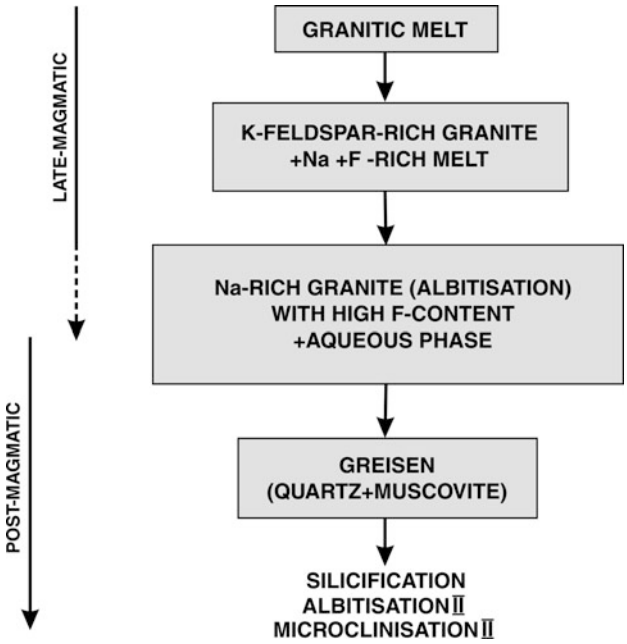

Fig. 7.9 Schematic illustration of late- to post-magmatic trends that are characteristic of greisenisation processes; the later post-magmatic minerals commonly overprint earlier phases (cf. Pollard (1983))

quartz-sericite-pyrite alteration of the porphyry systems such that in many porphyry deposits an early greisen alteration may be present (e.g. at Climax in Colorado), merging into a later quartz-sericite-pyrite so that a clear boundary between the two is not always discernable. Following greisen alteration, a second phase of Na- and K-metasomatism may occur, as indicated by the replacement of greisen minerals (e.g. topaz, muscovite) by albite and new growths of K-feldspars with the notable absence of perthitic feldspars (Pollard 1983). Post-greisenisation alteration results in quartz-sericitic and argillic alteration with illite ± kaolinite, chlorite, and carbonate minerals.

Fluid inclusion studies of greisen deposits generally confirm the magmatic origin of the fluids, even though there are cases, which have been interpreted as having resulted from the mixing of magmatic with meteoric waters. A classic review of salinities and the homogenisation temperature of fluid inclusions, from greisen-related mineral deposits, can be found in Roedder (1984). According to the type of greisen-related deposit (e.g. endogreisen to exogreisen and quartz veins) the nature of the greisenising fluids varies from high (~600–400°C and >40 wt.% NaCl equivalent) to low (~200°C and 10–15 wt.% NaCl equivalent) temperatures and salinities, respectively. Dissolved species include mainly NaCl, KCl, and CO_2, but phases such as anhydrite and borax have also been identified.

Burt (1981) studied greisen mineral equilibria in the system K_2O-Al_2O_3-SiO_2-H_2O-F_2O, in terms of the activities of HF (acidity) and KF (salinity). The exsolution

of a supercritical fluid phase, its ascent and evolution, marks the inception of-magmatic-hydrothermal activity in a granitic system. An increase in HF activity (μHF) brings about a tendency towards peraluminosity in the magma, and H^+ metasomatism (e.g. greisenisation) in the hydrothermal fluids. The opposite is obtained by increasing the salinity (expressed by μKF), during which there is increased peralkalinity in the magma, and alkali metasomatism (e.g. feldspathisation) in the fluids. The separation of a liquid phase from a vapour phase (boiling) results in the concentration of the heavier saline species (KCl, NaCl etc.) in the former, and the lighter species (HCl, HF etc.) in the latter. Consequently, according to Burt (1981), the concentration of acid volatiles in the vapour phase is greatly increased and this, apart from the process of albitisation and the release of H^+ ions referred to above, is considered to be one of the main causes of the greisenisation phenomena. These fluids can, at various stages, be modified by diluting meteoric waters, as testified by the common occurrence of clay minerals, such as in the Cornwall greisen-related mineral deposits (Laznicka 2006). Burt (1981) also draws attention to the importance of adding new elements to the system, for example Ca and W. In this case the activity of HF determines the stability of scheelite (lower μHF) or wolframite (higher μHF) in the system. At low HF activity the formation of scheelite could be as follows:

$$H_2WO_4 + Ca^{2+} = CaWO_4 + 2H^+$$

with increasing HF activity scheelite may convert to wolframite according to the following reaction:

$$CaWO_4 + FeO + 2HF = FeWO_4 + CaF_2 + H_2O.$$

scheelite wolframite fluorite

In vein-type greisens hydrothermal processes are at lower temperatures and there appears to be no evidence of boiling. Thus, in the case of greisenisation without boiling, F-bearing micas and topaz would form at high HF activity. Under conditions of very high F-activity topaz greisens form as a result of the instability of muscovite in the presence of HF as indicated by the reaction shown below for the topaz-rich greisens from the Mount Bischoff Sn deposit (Tasmania; Wright and Kwak 1989):

$$K_2Al_4(Si_6Al_2O_{20})(OH)_4 + 6HF = 3Al_2(SiO_4)(OH,F)_2 + 3SiO_2 + 2K^+ + 4H^+$$

muscovite topaz

Increases in the H_2O activity during cooling of the hydrothermal fluids results in the breakdown of topaz and feldspars to release large quantities of HF, along with the formation of muscovite and quartz. The release of F, together with

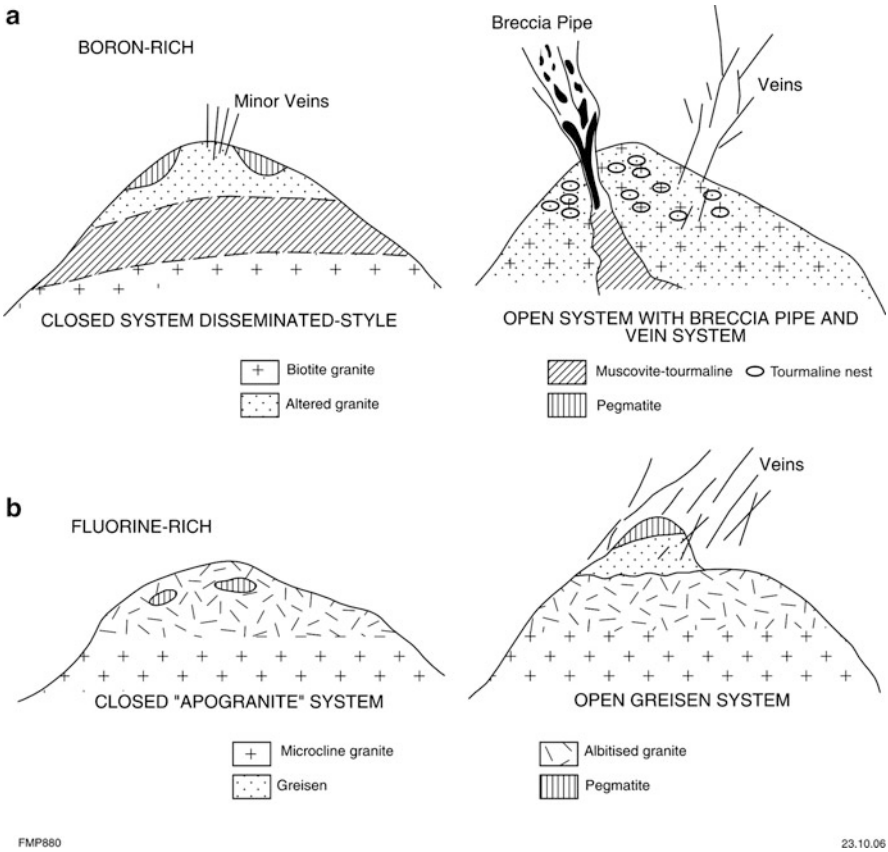

Fig. 7.10 (**a**) Boron-rich and (**b**) Fluorine-rich greisen systems. Details in text (After Pollard et al. (1987))

muscovitisation and chloritisation of biotite at depth, results in the leaching of metals, their complexing with F, and their subsequent transport upwards in the evolving system. The general features of the F-rich and B-rich greisen systems are shown in Fig. 7.10 (Pollard et al. 1987). As previously outlined, F-rich greisen systems are characterised by the presence of fluorite and/or topaz as well as Li-rich micas (e.g. lepidolite or protolithionite). Boron-rich greisen systems, on the other hand, are manifested by abundant tourmaline, which tends to form clots or nests in the cupola and are generally not mineralised. In open systems (Fig. 7.10), this mineral occurs in, and is associated with, breccia pipes, stockworks, and veins. These are generally the result of developing high B-rich volatile pressures during the crystallisation of B-rich magmas.

Greisen systems are typically associated with Sn and W mineralisation, usually accompanied by other ore elements such as Cu, Zn, Bi, Mo, U, and F. Common ore minerals are cassiterite, stannite, wolframite, scheelite, arsenopyrite, pyrite,

chalcopyrite, molybdenite, sphalerite, bismuth and bismuthinite. Other important minerals are topaz, fluorite, and apatite. Most greisen-affiliated Sn and W deposits are spatially and genetically related to S-type granitic rocks, or the ilmenite-type of granitic rock described by Ishihara (1977, 1981) and form dome-like (cupolas) or ridge-like intrusions. Details concerning Sn and W deposits with a greisen affiliation can be found in Taylor (1979) and in a collection of papers edited by Hutchison (1988). The general features of greisen-related Sn mineralisation have been discussed by Pollard et al. (1988), Taylor and Pollard (1988) and Hosking (1988). This mineralisation occurs as lenses, generally subparallel to the arcuate contacts of the granitic intrusion with the enclosing country rocks. In open systems, fracture-controlled, sheeted veins and stockworks, emanate from the greisenised granite into the country rocks (Fig. 7.11). Greisen mineral systems may have distinct metal zonations. These are usually manifested by a lower zone of Sn + Mo, extending upward and laterally through W + Bi to Cu, Zn, and Pb. In some cases, Au may also be present, as for example at Kirwans Hill in New Zealand (Pirajno and Bentley 1985) and the Au-Mo association in the Timbarra Tablelands pluton in New South Wales, Australia (Mustard 2004). However, these zonations are somewhat idealised and therefore each case has to be assessed separately. Time-paragenetic sequences of greisen-related ore assemblages, on the other hand, appear to follow some general rules that may be applicable to most greisen deposits. Deposition of the ore minerals usually starts with an oxide phase (cassiterite, wolframite), followed by sulphides (pyrite, chalcopyrite, pyrrhotite, arsenopyrite, molybdenite, and bismuthinite), and a late, lower temperature, carbonate-oxide stage characterised by calcite, siderite and iron oxides. At Panasqueira (Portugal), for example, the paragenetic sequence consists of an early oxide-silicate stage, a sulphide stage, and a late carbonate stage (Kelly and Rye 1979).

Examples of endogreisen and exogreisen mineral systems can be found at Zaaiplats and Rooiberg, both in South Africa and related to the 2,050–2,025 Ma Lebowa Granite Suite, which is part of the felsic phase of the Bushveld Igneous Complex. The Lebowa suite includes the Nebo granite, Bobbejankop granite, Klipkloof granite, and Lease granite. The Nebo granite is the most abundant, all the others being considered as late-stage fractionated variants (Walraven 1985). The Nebo granite, which is coarse-grained, is made up of K-feldspar, quartz, plagioclase, and hornblende in its lower portions and biotite in its uppermost portions. The Bobbejankop granite is a variety of the Nebo granite and distinguishable by its reddish colour, miarolitic texture, and the presence of tourmaline clusters. The endogranitic Sn deposits of the Bushveld Igneous Complex occur mostly within the Bobbejankop granite and its roof facies. At Rooiberg, Sn mineralisation is hosted in sedimentary rocks and is associated with exogreisen alteration. This mineralisation is characterised by pockets and veins containing cassiterite disseminations in a sericitic core enveloped by variable zones of tourmaline + carbonate, sericite + ankerite and hematite + K-feldspar. In Australia, the previously mentioned Mount Bischoff Sn deposit in NW Tasmania is related to both endo- and exogreisens.

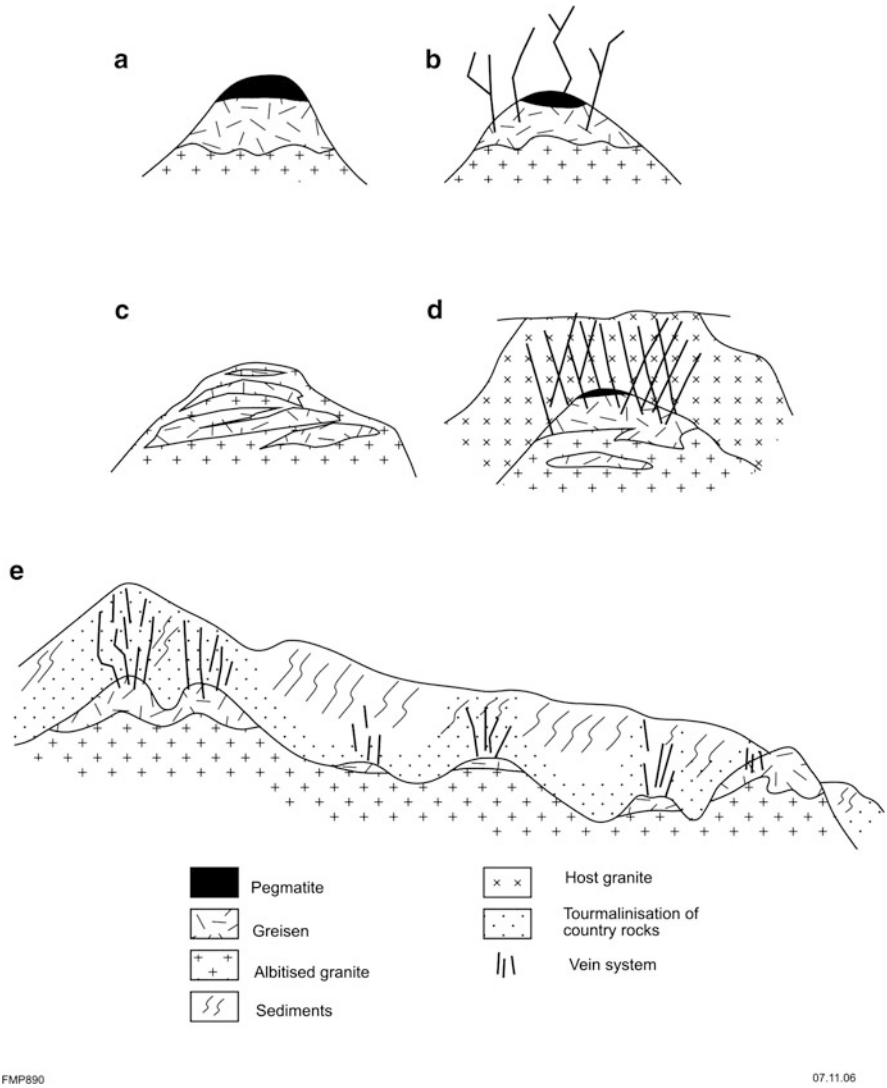

Fig. 7.11 Types of greisen systems, associated with high-level granitic cupolas. (**a**) and (**b**) are after Pollard et al. (1988). (**c**) and (**d**) are after Taylor and Pollard (1988). (**e**) is after Pirajno and Bentley (1985)

7.5 Tourmalinites

The three end-members of the Mg-Li-Fe tourmaline solid solution series are schorl (Fe-rich), elbaite (Al, Li-rich), and dravite (Mg-rich). The composition of tourmalines may be indicative of the environment in which they originated. For example, the Fe/Mg ratio tends to decrease with increasing distance from a granitic source (Pirajno and Smithies 1992). In general, Fe-rich tourmalines are associated

with Sn-W deposits of greisen affinity, whereas Mg-rich tourmalines are found with massive sulphide deposits and stratabound W deposits. Tourmalinite is the name given to rocks containing in excess of 15% tourmaline, and can be associated with exhalative ore deposits in rift settings (Plimer 1987). A detailed account of tourmaline, its association with and relationship to hydrothermal mineral systems, can be found in Slack (1996).

Pervasive to selectively pervasive tourmalinisation usually occurs associated with Sn-W deposits and breccia pipes. In many cases the country rocks surrounding greisenised granite cupolas have disseminated tourmaline, which tends to be particularly abundant in fracture zones. Quartz-tourmaline-dominated assemblages form pervasive replacements as well as cross-cutting veins and veinlets. The replacements can be on a very fine scale, so that the smallest features and textures are perfectly preserved. This type of tourmaline alteration is linked to the emplacement and crystallisation of B-rich granitic magmas, with the possibility that the B-enrichment may have been inherited from a source region containing evaporites or tourmaline-rich protoliths. Tourmaline breccia pipes may also be associated with the crystallisation of geochemically specialised granitic magmas, and they result from high volatile pressure exceeding the lithostatic load. Tourmaline breccia pipes occur associated with porphyry copper deposits, vein type Sn deposits, and as small polymetallic pipes containing W, Cu, Bi, As, and Au. Tourmaline-rich breccia pipes are elliptical to circular and range in diameter from a few metres to more than a kilometre (Kirwin 1985). Fluid inclusion data indicate that they form at depths ranging from between 1 and 3 km and at temperatures in excess of 300°C from highly saline fluids (Kirwin 1985). At the Krantzgerg W deposit in Namibia, tourmalinisation of the country rocks and hydraulic fractures infilled by tourmaline and tourmaline breccia pipes are common (Pirajno and Schlögl 1987). These features are related to the emplacement of the B-rich Erongo granite, a peraluminous anorogenic granite. At Rooiberg (see Sect. 7.4.1), the highly mineralised Sn-bearing orbicular pockets, which occur in sedimentary slabs, contain abundant tourmaline and carbonate minerals, replacing the quartz and plagioclase of the host sedimentary rock (Rozendaal et al. 1995). The above-mentioned Mount Bischoff Sn deposit has tourmaline-rich endo- and exogreisens (Wright and Kwak 1989). Some lode Au deposits in amphibolite facies rocks (see Sect. 7.3.2) have tourmaline in the lodes and/or wallrocks. The Zandrivier Au deposit is an auriferous tourmalinite in the Pietersburg greenstone belt in South Africa, in which the tourmalinite contains abundant Au-bearing arsenopyrite (Kalbskopf and Barton 2003). The Zandrivier auriferous tourmalinite is thought to have formed from ore fluids of magmatic derivation (Kalbskopf and Barton 2003).

Stratiform tourmalinites are widespread in Proterozoic and Palaeozoic sedimentary sequences associated with sediment-hosted massive sulphide deposits, as for example, at Sullivan in British Columbia, where a fine-grained quartz-tourmaline rock underlies the ore deposit. Tourmalinites are also present in the Broken Hill areas (Australia), and in Namaqualand (South Africa) (Slack 1996; Slack et al. 1984; Plimer 1987). These tourmaline-rich rocks are thought to be the result of submarine exhalations of basinal brines in rift environments, and are therefore neither epigenetic nor of the replacement type.

7.6 Metasomatism in Mafic and Ultramafic Rocks

Fluids derived from the serpentinisation of Fe-Mg silicate minerals, such as olivine and pyroxene, cause a series of reactions resulting in the extensive metasomatism of mafic-ultramafic rocks and their contact with the enclosing rocks. Rocks containing varying proportions of olivine + orthopyroxene + clinopyroxene can be represented by the chemical system SiO_2-MgO-CaO, which can also contain significant amounts of H_2O and, in some cases, CO_2. Phase equilibria in the chemical systems SiO_2-MgO-CaO and SiO_2-MgO-CaO$H_2O \pm CO_2$, have been experimentally well studied and the thermodynamic data reasonably well-constrained (Spear 1993). A reaction representing the conversion of olivine to serpentine is:

$$2Mg_2SiO_4 + H_2O + 2H^+ \rightarrow Mg_3Si_2(OH)_4 + Mg^{2+}$$

Serpentinisation is usually quite pervasive and may affect entire rock masses. Temperatures of serpentinisation processes range from as low as $<100°C$ (lizardite) to as high as 500°C (antigorite) (Spear 1993). Serpentinisation commonly occurs at spreading centres and along transform faults, due to penetration and reaction with sea water (see Chap. 8). The serpentinites from ophiolitic rocks contain the assemblage of lizardite + chrysotile + brucite ± magnetite. The latter is a common byproduct of serpentinisation and is due to expulsion and oxidation of Fe from the silicate lattice. Serpentinite is extremely ductile and is easily transported during tectonic movements. Tectonic transport of serpentinised oceanic crust to continental margins results in the emplacement of ophiolites (Coleman 1977). Serpentinisation of ultramafic rocks is also common in Archaean greenstone belts, in which serpentine minerals replace olivine in dunite and komatiites (Chen et al. 2005; Barnes 2006).

As introduced at the start of this section oceanic crust metamorphism and associated serpentinisation lead to a series of metasomatic reactions, one of which is albitisation and the formation of peculiar rocks known as rodingites, discussed below. In some cases Au, Ag, and Co mineralisation, associated with rodingite and carbonated serpentinites, have been reported (Leblanc and Lbouabi 1988).

7.6.1 Rodingites

Rodingites occur as dykes commonly found in the Dun Mountain ophiolite belt in New Zealand (the name derives from the Roding River near the town of Nelson, New Zealand). Rodingites consist of calc-silicate assemblages, dominantly Ca-rich garnet, with lesser diopside, wollastonite, tremolite-actinolite, vesuvianite, epidote, clintonite, titanite, phlogopite, microcline, and Mg-chlorite (Palandri and Read 2004). Together with albitites, rodingites may occur along contacts between serpentinites and country rocks, including gabbro, granite, graywacke, quartzite,

and argillite (Li et al. 2007). In submarine settings rodingite metasomatic alteration begins with epidote-clinozoisite, prehnite, tremolite, hydrogrossular, diopside, various chlorites and Fe hydroxides. Details of the experimental formation of serpentinite and rodingite at temperatures ranging from 25°C to 300°C and pressures of 0–100 bar can be found in Palandri and Reed (2004). These authors simulated reactions of mafic rocks (basalt or gabbro) with hyperalkaline Ca- and Al-rich fluids at 300°C to produce assemblages typical of rodingite (grossular, clinozoisite, vesuvianite, chlorite and diopside). Bach and Klein (2009) have modelled the thermodynamics involved in the interaction of a gabbro with fluids generated during serpentinisation, between 200°C and 300°C, leading to the formation of rodingites. The following can be summarised from both these experiments and the thermodynamic modelling (see Chap. 8).

Rodingites are enriched in CaO and depleted in silica and Na_2O, indicating that they form by strong Ca-metasomatism. Utilizing the example of a gabbro dyke intruded into a peridotite body, Bach and Klein (2009) emphasised the critical role of silica activities along the contacts with the ultramafic rock, where diffusion-related chemical gradients promote mass transfer of SiO_2 and MgO. The chemical potential of the aqueous silica appears to be greatest at temperatures less than 350°C, which would be ideal for rodingitisation to occur. But in their work, Bach and Klein (2009) suggested that the Ca-metasomatism necessary to form rodingites is related to strong diffusional mass transfer and concentration gradients, in both Ca and Si species, at temperatures of around 200–300°C (see also Chap. 8). Mafic-ultramafic contact zones are therefore preferentially affected, with precipitation of diopside and garnet, commonly resulting in monomineralic veins (e.g. diopsidite), which is dependent on the mineral phase with the highest degree of supersaturation. The bottom line here is that the assumption that anhydrous minerals form in high temperature regimes is not necessarily correct, according to the evidence provided by rodingitisation reactions. Thus, in the model of Bach and Klein (2009), diopside-rich rocks can form at low temperatures (200–300°C) from fluids buffered by these reactions activated during the serpentinisation of ultramafic rocks. These findings could have important repercussions for mineral systems thought to form during high temperature/low pressure metamorphism, such as Fe-rich skarn systems (Pirajno et al. 2011).

Li et al. (2007) added new data to our knowledge of rodingite formation. These authors investigated a range of rodingite compositions in an eclogite enclosed in serpentinised ultramafic rocks from an ophiolite belt in the western Tianshan orogen (Changawuzi ophiolite; NW China). The mineral assemblage of the precursor eclogite consisted of omphacite + garnet + clinozoisite + albite + rutile + Na-amphibole-titanite and had its origins during the HP or UHP metamorphism of a subducted slab. Coarse-grained rodingites, containing anhedral relics of the eclogitic precursor (mostly omphacite and garnet), consist of prehnite, diopside, and hydrogrossular garnet, whereas fine-grained rodingites have pervasively replaced the precursor eclogite and consist of clinochlore, prehnite, hydrogrossular garnet, epidote, diopside, and vesuvianite. Li et al. (2007) found that the completely rodingitised rocks were formed during three stages of increasing metasomatic

alteration. In order increasing alteration these include (1) prehnite-rodingite, (2) hydrogrossular-diopside-rodingite, and (3) vesuvianite-rodingite. These stages reflect a continuous evolution associated with decreasing silica and increasing CaO, culminating with the formation of vesuvianite during maximum Ca^{2+} influx. In this study, Li et al. (2007) were able to show that whereas rodingites are typically formed by seafloor metasomatism associated with serpentinisation, as discussed above, the rodingite rocks in the Changawuzi ophiolite were formed, following an additional serpentinisation event during the exhumation of the subducted slab. The metasomatic process leading to the rodingites began at temperatures of 430–410°C at depths of about 30 km and terminated at temperatures of 250–200°C at depths of 7–6 km.

7.6.2 Blackwall Alteration

Blackwall alteration generally takes place in contact zones between rocks of diverse composition and consist of "*black masses of biotite*", but chlorite, amphiboles and other minerals may also be present (Frost 1975). Blackwall is now recognised to occur by a combination of infiltration and diffusion metasomatism involving fluid flow and mass transfer.

Bucher and Frey (2002) explained the effects of disequilibrium and metamorphic reactions between contrasting rock types, such as granite and harzburgite. These reactions result in the formation of generally monomineralic zones or "shells" that surround a harzburgite lens in a granitoid. Depending on the P-T conditions, and in the case referred to above, biotite and/or amphibole shells would surround the harzburgite lens. This is what Bucher and Frey (2002) called "blackwall" alteration. Bucher et al. (2005) have documented the blackwall alteration in detail from an occurrence in the Norwegian Caledonides. In this instance a thin, biotite-rich blackwall separates mica schist from peridotite. Here, the blackwall rocks consist mainly of biotite (about 40 vol.%), associated with varying amounts of corundum, staurolite, tourmaline, white micas, apatite, epidote-allanite, monazite, zircon, rutile and ilmenite. The corundum amounts to about 25 vol.% and occurs as randomly oriented crystals that grew simultaneously with biotite. A finer-grained sample of blackwall rocks consists of biotite (30 vol.%), muscovite (20 vol.%), kyanite, paragonite, and staurolite. Corundum is also present as are large blades of margarite and blue tourmaline with margarite inclusions.

Bucher et al. (2005) modelled the P-T conditions for the formation of blackwall alteration using stability diagrams for the stable phases found in a mica schist and average lherzolite at 570°C and 5–6.5 kbar. According to these authors the driving force of the metasomatic process that form a corundum-rich blackwall is the reaction that changes forsterite into talc, in which silica is consumed and talc is formed. Thus, the loss of silica (desilication) from the mica schist is what effectively forms the blackwall assemblage of corundum-staurolite-biotite-margarite-paragonite. White micas, margarite, muscovite, and paragonite, with kyanite as an

intermediate product, characterise the late stages of blackwall-forming metasomatism. Bucher et al. (2005) concluded that blackwall alteration occurs by fluid advection along contacts or other structural boundaries.

7.6.3 *Listvenites*

Listvenite or listwänite is a term first coined by Rose (1837) to define a fuchsite (Cr-muscovite)-quartz-carbonate (ferroan-dolomite, ankerite, magnesite) rock, derived from metasomatic alteration of ultramafic rocks (Fryer et al. 1979; Kerrich and Fyfe 1981) (Plate 7.1f). Unlike, rodingite and blackwall rocks, listvenites can be economically important because they are commonly associated with lode Au, Ag mineralisation and less commonly with Au-Sb, Co, Sb, Cu and Ni (Šoŝtaríc et al. 2011; Zoheir and Lehmann 2011). Halls and Zhao (1995) clarified the terminology and classification of listvenite as well as the chemical and metasomatic processes leading to its formation. In the following I go over the main points of Halls and Zhao (1995) work and then briefly describe an example of a listvenite-hosted Au lode deposit (Zoheir and Lehmann 2011).

Since its first introduction the term listvenite has included a variety of carbonitised mafic and ultramafic rocks, where listvenite is taken as a carbonate rock with varying amounts of serpentine, talc, chlorite, phlogopite, quartz and, importantly, a chromian-muscovite (fuchsite; mariposite). However, Halls and Zhao (1995) pointed out that the term listvenite should be restricted to a rock derived from the metasomatic alteration of ultramafic rocks essentially consisting of carbonate (magnesite or ankerite), quartz and fuchsite. This is the definition that is recommended and adopted here.

The chemical processes leading to listvenisation involve replacement of primary and/or secondary ferromagnesian minerals in ultramafic rocks by Mg-Fe carbonates, with subsequent release of silica, in a reaction of the type shown below:

$$\underset{\text{Serpentine}}{(Mg,Fe)_3Si_2O_5(OH)_4} + 3CO_2 \rightarrow \underset{\text{brunnerite}}{3(Mg,Fe)CO_3} + 2SiO_2 + 2H_2O$$

Fuchsite or mariposite (Cr-muscovites) are essential components of the process, as a result of K metasomatism, in which Cr is leached out of chromite and/or Cr-bearing silicates in the ultramafic rock. Halls and Zhao (1995) emphasize that there is a clear mineralogical and chemical distinction between talc-carbonate alteration of ultramafics and the K-rich listvenites, which may contain up to 4 wt.% K_2O (Kerrich et al. 1987). Therefore, an influx of K is required for the formation of listvenite, which is the main factor in the formation of the chromian muscovite, an essential component of listvenite, and typically exhibiting a green colour. The T-P conditions for listvenite are in the range of 290–340°C and 1–3 kbar.

Listvenites have been recognised world-wide and particularly in lode Au deposits hosted in Archaean greenstone belts of Canada (e.g. Timmins, Kirkland

Lake, Val d'Or mineral districts and the Abitibi greenstone belt, Dubé and Gosselin 2007) and the world-class 120 Ma Mother Lode ore system in California (Walker et al. 2007). In some instances, Au mineralisation is associated with listvenite and albitite. Such is the case reported by Béziat et al. (1998) for the Laraboué gold prospect in the Boromo greenstone belt in Burkina Faso (West Africa), where auriferous listvenitic rocks are mainly composed of ferroan magnesite, dolomite, fuchsite, and relic chromite, accompanied by cobaltite and gersdorfite [(Co,Ni) AsS].

Zoheir and Lehmann (2011) studied the listvenite-associated lode Au mineralisation of the Barramiya deposit in Egypt. Gold mineralisation in the Barramiya deposit is hosted in quartz and quartz-carbonate veins, extending along strike from a few metres to 1 km, from 0.1 to 1 m thick and dip extensions of up to 400 m. These veins form a sheeted system of 15–20 m thick. The Au content of the veins ranges from trace to 18 g/t. Apart from quartz, the carbonate minerals that constitute the vein material comprise ankerite as the main phase, with ferroan-magnesite-siderite, dolomite and calcite filling open spaces. These carbonate minerals are also present in the wallrocks, replacing chlorite, actinolite, and serpentine. Ore minerals in the quartz veins and wallrocks are arsenopyrite, pyrite and lesser chalcopyrite, sphalerite, galena, tetrahedrite, pyrrhotite, gersfordite, and Au. Much of the Au is lattice-bound in the arsenopyrite (100 to > 1,000 ppm). Gangue minerals include sericite, mariposite, goethite, and rutile. Microthermometric analyses of fluid inclusions, carried out by Zoheir and Lehmann (2011) in quartz and quartz-carbonate minerals, showed a range of homogenisation temperatures (Th) ranging from 362°C to 337°C, with a cluster of values around 350°C. Raman spectroscopy revealed a carbonic phase in the inclusions consisting of a mixture of CH_4 and CO_2 in variable proportions.

The precise link between listvenite and mineralisation remains uncertain. Two possible scenarios can be considered. The first is a model proposed by Zoheir and Lehmann (2011), which suggests that CO_2- and CH_4-rich fluids resulting from the alteration of carbonaceous wallrocks, cause extensive carbonation and a drop in the fO_2 in the fluids. These then destabilise the Au-S complexes, resulting in the precipitation of Au in the lattice of sulphides (e.g. arsenopyrite, pyrite, and pyrrhotite). In this model Au is remobilised during deformation and redeposited as free-Au in the quartz veins. In the second model, Phillips and Powell (2010) propose a series of metamorphic devolitisation/dehydration reactions involving carbonate and mica alteration. During such reactions the deposition of sulphides and Au are most effective in host rocks with a suitable composition, usually mafic-ultramafic (ophiolitic) packages.

7.7 Concluding Remarks

Metasomatism that accompanies the formation of mineral systems is a complex and poorly known process. This chapter has endeavoured to highlight those features that are commonly seen or detected distally, within, and around orebodies. At the same time igneous systems are presented that are deemed responsible for local

and/or regional scale metasomatic processes. In some cases, the link between igneous systems, metasomatism, and, by association, mineralisation are practically direct. This is the case for alkaline and carbonatite complexes, fenitisation, and associated mineralisation, typically consisting of REE, U, Ta, Nb etc. In other cases, the link between igneous system(s), metasomatism, and mineralisation is less obvious but nevertheless, at least spatially, indisputable. This is the case of skarns in which, not uncommonly, low-T fluids (usually meteoric) overprint, partially or totally obliterating, the original higher T metasomatic alteration. With regard to greisens, the distinction between endo- and exo-greisens, is important. For the former, is a case of an igneous system "stewing in its own juice", in which case a cause and effect of metasomatism and mineralisation of the igneous rock is clear. However, as with the skarns, later and locally pervasive overprints can cause difficulties in establishing the original sources, especially for exoskarns that are distant from the igneous rocks.

Boron metasomatism is typically represented by varying degrees of tourmalinisation of wall rocks surrounding Sn-W mineralised granitic cupolas and breccia pipes associated with volatile-rich intrusions. Tourmalinites, on the other hand, are commonly stratiform and associated with sediment-hosted massive sulphide deposits, a feature that has prompted suggestions that they may be the product of submarine exhalations. This concept, however, has to be taken with caution because, as observed for igneous intrusion-related tourmalinisation, pervasive replacement of pre-existing rocks can easily be mistaken for chemical sediments.

Metasomatism of ultramafic rocks is typically represented by rodingites, blackwall rocks, and listvenites. Blackwall alteration provides an interesting case of localised metasomatism linked to disequilibrium reactions between contrasting rock types, such as felsic and ultramafic. Of these, listvenites are particularly important because they are commonly associated with Au lodes, as is the case for world-class mineral deposits (e.g. Mother Lode). Listvenites are easily recognised due to the presence of the green-coloured fuchsite (Cr-muscovite).

Metasomatism, in all its manifestations in the lithospheric mantle, in fractionating magmas at convergent and divergent margins and intracontinental rift systems, quite apart from its economic implications, is a highly stimulating discipline of the Earth Sciences, which will continue to challenge geoscientists well into the future.

Acknowledgments I thank Dan Harlov for inviting me to provide a chapter on metasomatic processes associated with mineral systems and for his useful suggestions. Rob Kerrich, Wolfgang Bach, Daniel Harlov and Håkon Austrheim are thanked for their constructive comments, which considerably improved this contribution. I publish this chapter with the permission of the Executive Director of the Geological Survey of Western Australia.

References

Bach W, Klein F (2009) The petrology of seafloor rodingites: insights from geochemical reaction path modelling. Lithos 112:103–117

Bailey DK (1983) The chemical and thermal evolution of rifts. Tectonophysics 94:585–598

Bailey DK (1984) Kimberlite: "the mantle sample" formed by ultrametasomatism. In: Kornprobst J (ed) Kimberlite and relate rocks. Elsevier, Amsterdam, pp 232–333
Bailey DK (1987) Mantle metasomatism – perspective and prospect. Geol Soc Lond 30:1–14, Sp Publ
Barnes SJ (2006) Komatiites: petrology, volcanology, metamorphism and geochemistry. Soc Econ Geol 13:13–49, Sp Publ
Barsukov VL (1957) The geochemistry of tin. Geokimiya 1:41–53
Barton MD, Johnson DA (1996) Evaporitic source model for igneous-related Fe oxide-(REE-Cu-Au-U) mineralization. Geology 24:259–262
Bédard JH (2010) Parental magmas of Grenville Province massif-type anorthosite and conjectures about why massif anorthosites are restricted to the Proterozoic. T Roy Soc Edin (Earth Env Sci) 100:77–103
Best MG (1982) Igneous and metamorphic petrology. Freeman, San Francisco, p 630
Béziat D, Bourges F, Debat P, Lompo M, Tollon F, Zonou S (1998) Albitite et "listvénite" sites de concentration aurifère inédits dans les ceintures de roches vertes birimiennes fortment hydrothermalisées du Burkina Faso. Bull Soc Géol Fr 169(4):563–571
Bowden P (1985) The geochemistry and mineralization of alkaline ring complexes in Africa (a review). J Afr Earth Sci 3:17–40
Bowden P, Kinnaird JA, Abaa SI, Ike EC, Turaki UM (1984) Geology and mineralization of the Nigerian anorogenic ring complexes. Geol Jahrb B 56:1–65
Brogger WC (1921) Die Eruptivgesteine des Kristianiagebiets IV. Das Fengebiet in Telemarken, Norwegen. Norsk Vidensk Akademie Oslo Skr Nat Kl 9, 408
Brown PE, Bowman JR, Kelly WC (1985) Petrologic and stable isotope constraints on the source and evolution of skarn-forming fluids at Pine Creek, California. Econ Geol 80:72–95
Bucher K, Frey M (2002) Petrogenesis of metamorphic rocks. Springer, Berlin, p 341
Bucher K, De Capitani C, Grapes R (2005) The development of a margarite-corundum blackwall by metasomatic alteration of a slice of mica schist in ultramafic rock, Kvesjoen, Norwegian Caledonides. Can Mineral 43:129–156
Burnham CW, Ohmoto H (1980) Late stage processes of felsic magmatism. Mining Geol 8:1–11, Sp Iss
Burt DM (1981) Acidity-salinity diagrams – application to greisen and porphyry deposits. Econ Geol 76:832–843
Carmichael IS, Turner FJ, Verhoogen J (1974) Igneous petrology. McGraw-Hill, New York
Castor SB (2008) The mountain pass rare-earth carbonatite and associated ultrapotassic rocks, California. Can Mineral 46:779–806
Chen SF, Morris PA, Pirajno F (2005) Occurrence of komatiites in the Sandstone greenstone belt, north-central Yilgarn Craton. Aust J Earth Sci 52:959–963
Coleman RG (1977) Ophiolites. Springer, Berlin/Heidelberg/New York
Cuney M, Kyser K (2009) Recent and not-so-recent developments in uranium deposits and implications for exploration, vol 39. Mineralogical Association of Canada, Quebec, Short Course
Dubé B, Gosselin P (2007) Greenstone-hosted quartz-carbonate vein deposits. In: Goodfellow WD (ed) Mineral Deposits of Canada: a synthesis of major deposit-types, district metallogeny, the evolution of geological provinces and exploration methods, vol 5. Geological Association of Canada, Ottawa, pp 49–73, Sp Publ
Duncan RK, Willett GC (1990) Mount weld carbonatite. In: Hughes FE (ed) Geology of the mineral deposits of Australia and Papua new guinea, vol 14. The Australasian Institute of Mining and Metallurgy, Parkville, pp 591–597, Monogr
Einaudi MT (1982) Description of skarns associated with porphyry copper plutons. In: Titley SR (ed) Advances in geology of the porphyry copper deposits, southwestern North America. University of Arizona Press, Tucson, pp 139–184
Einaudi MT, Burt DM (eds) (1982) A special issue devoted to skarn deposits – introduction, terminology, classification and composition of skarn deposits. Econ Geol 77(4):745–754

Einaudi MT, Meinert LD, Newberry RJ (1981) Skarn deposits. Econ Geol 75:317–391
Eugster HP (1984) Granites and hydrothermal ore deposits: a geochemical framework. Mineral Mag 49:7–23
Ferguson J, McIver JR, Danchin RV (1975) Fenitization associated with the alkaline carbonatite complex of Epemba, South West Africa. Trans Geol Soc S Afr 78:111–122
Fitton JG, Upton BGJ (eds) (1987) Alkaline igneous rocks, vol 30. Geological Society by Blackwell Scientific, Oxford, Sp Publ
Fleet ME (2003) Rock forming minerals, sheet silicates: micas, vol 3A, 2nd edn. Geological Society, London, p 758
Flint D, Abeysinghe PB (2000) Geology and mineral resources of the Gascoyne Region. Geological Survey of Western Australia, East Perth, p 29, Rec 2000/7
Frost BR (1975) Contact metamorphism of serpentinite, chloritic blackwall and rodingite at Paddy-Go-Easy Pass, Central Cascades, Washington. J Petrol 16:272–313
Fryer BJ, Kerrich R, Hutchinson RW, Peirce MG, Rogers DS (1979) Achaean precious-metal hydrothermal systems, Dome Mine, Abitibi Greenstone Belt. I. Patterns of alteration and metal distribution. Can J Earth Sci 16:421–439
Grey K, Hocking RM, Stevens MK, Bagas L, Carlsen GM, Irimies F, Pirajno F, Haines PW, Apak SN (2005) Lithostratigraphic nomenclature of the officer basin and correlative parts of the Paterson Orogen, Western Australia. Geol Surv West Aus Rpt 93:89
Groves DI (1993) The crustal continuum model for late-Archaean lode-gold deposits of the Yilgarn Block, Western Australia. Miner Deposita 28:366–374
Groves DI, Ridley JR, Bloem EMJ, Gebre-Mariam M, Hageman SG, Hronsky JMA, Knight JT, McNaughton NJ, Ojala J, Vielreicher RM, McCuaig TC, Holyland PW (1995) Lode-gold deposits of the Yilgarn block: products of late Archaean crustal scale overpressured hydrothermal systems. Geol Soc Lond 95:155–172, Sp Publ
Halls C, Zhao R (1995) Listvenite and related rocks: perspectives on terminology and mineralogy with reference to an occurrence at Cregganbaun, Co. Mayo, Republic of Ireland. Mineral Dep 30:303–313
Hemley J, Jones WR (1964) Chemical aspects of hydrothermal alteration with emphasis on hydrogen metasomatism. Econ Geol 59:538–569
Hosking KFG (1988) The world's major types of tin deposits. In: Hutchison CS (ed) Geology of tin deposits in Asia and the Pacific. Springer, Berlin/Heidelberg/New York, pp 3–49
Hutchison CS (ed) (1988) Geology of tin deposits in Asia and the Pacific. United Nations economic and social commission for Asia and the Pacific. Springer, Berlin/Heidelberg, p 718
Ishihara S (1977) The magnetite-series and ilmenite-series granitic rocks. Mining Geol 27: 293–305
Ishihara S (1981) The granitoid series and mineralization. Econ Geol 75:458–484
Jones AP, Wall F, Williams CT (eds) (1996) Rare earth minerals – chemistry, origin and ore deposits, vol 7, Mineralogical Society Series. Chapman and Hall, London, p 372
Kalbskopf SP, Barton JM (2003) The Zandrivier deposit, Pietersburg greenstone belt, South Africa: an auriferous tourmalinite. S Afr J Geol 106:361–374
Kelly WC, Rye RO (1979) Geologic, fluid inclusion, and stable isotope studies of the tin-tungsten deposits of Panasqueira, Portugal. Econ Geol 74:1721–1822
Kent AJR, Ashley PM, Fanning CM (2000) Metasomatic alteration associated with regional metamorphism: an example from the Willyama Supergroup, South Australia. Lithos 54:33–62
Kerrich R, Fyfe WS (1981) The gold – carbonate association: source of CO_2, and CO_2 fixation reactions in Archaean lode deposits. Chem Geol 42(8):265–294
Kerrich R, Fyfe WS, Barnett RL, Blair BB, Willmore LM (1987) Corundum, Cr-muscovite rocks at O'Briens, Zimbabwe: the conjunction of hydrothermal desilification and LIL-element enrichment – geochemical and isotopic evidence. Contrib Mineral Petrol 95:481–498
Kinnaird JA (1985) Hydrothermal alteration and mineralisation of the alkaline anorogenic ring complexes of Nigeria. J Afr Earth Sci 3:229–252
Kirwin DJ (1985) Tourmaline breccia pipes. Unpublished M.sc. thesis, James Cook University, North Queensland, 139pp

Kresten P (1988) The chemistry of fenitisation: examples from Fen, Norway. Chem Geol 68: 329–349
Laznicka P (2006) Giant metallic deposits – future resources of industrial minerals. Springer, Berlin
Le Bas MJ (1977) Carbonatite nepheline volcanism. Wiley, New York
Le Bas MJ (1987) Nephelinites and carbonatites. Geol Soc Lond 30:53–83, Sp Publ
Leblanc M, Lbouabi M (1988) Native silver mineralisation along a rodingite tectonic contact between serpentinite and quartz-diorite (Bon Azzer, Morocco). Econ Geol 83:1379–1391
Li XP, Zhang L, Wei C, Al Y, Chen J (2007) Petrology of rodingite derived from eclogite in western Tianshan, China. J Metamorph Geol 25:363–382
Lindgren W (1933) Mineral deposits. McGraw-Hill, New York, p 930
Manning DC (1982) An experimental study of the effects of fluorine on the crystallization of granite melts. In: Evans AM (ed) Metallization associated with acid magmatism. Wiley, Chichester, pp 191–203
Mao JW, Wang YT, Lehmann B, Yu JJ, Du A, Mei YX, Li YF, Zang WS, Stein HJ (2006) Molybdenite Re-Os and albite 40Ar/39Ar dating of Cu-Au-Mo and magnetite porphyry systems in the Yangzte River valley and metallogenic implications. Ore Geol Rev 29:307–324
Mao JW, Xie GQ, Chao,D, Pirajno F, Ishiyama D, Chen YC (2011) A tectono-genetic model for porphyry Cu-Au-Mo-Fe and magnetite-apatite deposits along the Middle-Lower Yangtze River Valley, eastern China. Ore Geol Rev 43(1):294–314
Mariano AN (1989) Economic geology of rare earth elements. In: Lipin BR, McKay GA (eds) Geochemistry and mineralogy of rare earth elements, vol 21, Reviews in mineralogy. Mineralogical Society of America, Washington, DC, pp 309–337
McPhie J, Doyle M, Allen R (1993) Volcanic textures. Tasmanian Govt Print Office, Hobart, 198p
Meinert LD, Lentz DR, Newberry RJ (eds) (2000) A special issue devoted to skarn deposits. Econ Geol 95(6):1183–1365
Meinert LD, Dipple GM, Nicolescu S (2005) World skarn deposits. Econ Geol 100:299–336
Meyer C, Hemley JJ (1967) Wall rock alteration. In: Barnes HL (ed) Geochemistry of hydrothermal ore deposits, 1st edn. Holt Rinehart and Winston, New York, pp 166–235
Mottl MJ (1983) Metabasalts, axial hot springs, and the structure of hydrothermal systems at mid-ocean ridges. Geol Soc Am Bull 94:161–180
Mueller AG (1988) Achaean gold-silver deposits with prominent calc-silicate alteration in the Southern Cross greenstone belt, Western Australia: analogues of Phanerozoic skarn deposits. Geol Dept & Univ Ext, Univ West Aust, Publ 12: 141–163
Mueller AG, Groves DI (1991) The classification of Western Australian greenstone-hosted gold deposits according to wallrock-alteration mineral assemblages. Ore Geol Rev 6:291–331
Mueller AG, De Laeter JR, Groves DI (1991) Strontium isotope systematics of hydrothermal minerals from epigenetic Archean gold deposits in the Yilgarn Block, Western Australia. Econ Geol 86:780–809
Munhá J, Kerrich R (1980) Sea water interaction in spilites from the Iberian pyrite belt. Contrib Mineral Petrol 73:191–200
Mustard R (2004) Textural, mineralogical and geochemical variation in the zoned Timbarra Tablelands pluton, New South Wales. Aust J Earth Sci 51:385–405
Newberry RJ (1991) Scheelite-bearing skarns in the Sierra Nevada region, California. Contrasts in zoning and mineral compositions and tests of the infiltration metasomatism theory. In: Barto-Kyriakidis RJ (ed) Skarns – their genesis and metallogeny. Theophrastus, Athens, pp 343–384
Oliver NHS, Rubenach MJ, Valenta RK (1998) Precambrian metamorphism, fluid flow and metallogeny of Australia. AGSO J Geol Geophys 17(4):31–53
Palandri JL, Read MH (2004) Geochemical models of metasomatism in ultrmafic systems: serpentinisation, rodingitisation and sea floor carbonate chimney precipitation. Geoch Cosmoch Acta 68:1115–1133

Pan Y, Dong P (1999) The lower Chanjiang (Yangzi/Yangzte River) metallogenic belt, East China: intrusion- and wall rock-hosted Cu-Fe-Au, Mo, Zn, Pb and Ag deposits. Ore Geol Rev 15:177–242

Pearson JM, Taylor WR (1996) Mineralogy and geochemistry of fenitized alkaline ultrabasic sills of the Gifford Creek complex, Gascoyne province, Western Australia. Can Mineral 34:201–219

Pearson JM, Taylor WR, Barley ME (1995) Geology of the alkaline Gifford Creek complex, Gascoyne complex, Western Australia. Aust J Earth Sci 43:299–309

Phillips GN, Powell R (2010) Formation of gold deposits: a metamorphic devolitilization model. J metamoroh Geol 28:689–718

Pichavant M (1981) An experimental study of the effect of boron on a water saturated haplogranite at 1 kbar vapour pressure. Contrib Mineral Petrol 76:430–439

Pichavant M, Manning D (1984) Petrogenesis of tourmaline granites and topaz granites; the contribution of experimental data. Phys Earth Planet Inter 35:31–50

Pirajno F (1982) Geology, geochemistry, mineralisation and metal zoning of the McConnochie greisenised granite, Reefton district, New Zealand. NZ J Geol Geophys 25:405–425

Pirajno F (1992) Hydrothermal mineral deposits. Springer, Berlin

Pirajno F (2000) Ore deposits and mantle plumes. Kluwer, Dodrecht

Pirajno F (2004) Oceanic plateau accretion onto the northwestern margin of the Yilgarn Craton, Western Australia: implications for a mantle plume event at ca, 2.0 Ga. J Geodyn 37:205–231

Pirajno F (2009) Hydrothermal processes and mineral systems. Springer, Berlin

Pirajno F, Bentley PN (1985) Greisen-related scheelite, gold and sulphide mineralisation at Kirwans Hill and Bateman Creek, Reefton District, Westland, New Zealand. N Z J Geol Geophys 28:97–109

Pirajno F, Schlögl HU (1987) The alteration-mineralisation of the Krantzberg tungsten deposit, South West Africa/Namibia. S Afr J Geol 90:499–508

Pirajno F, Smithies RH (1992) The FeO/Feo + MgO ratio of tourmaline: a useful indicator of spatial variations in granite-related hydrothermal mineral deposits. J Geochem Explor 42: 371–382

Pirajno F, Occhipinti SA, Swager CP (2000) Geology and mineralization of the Palaeoproterozoic Bryah and Padbury Basins Western Australia. Geological Survey of Western Australia, East Perth, p 52, Rep 59

Pirajno F, Haines PW, Hocking RM (2006) Keene Basalt, Northwest Officer Basin, Western Australia: tectono-stratigraphic setting and implications for possible submarine mineralisation. Aust J Earth Sci 53:1013–1022

Pirajno F, Sheppard S, González-Alvaréz I, Johnson SP, Thorne A (2010) The Gifford Creek carbonatite complex. Symp Proc IAGOD 2010, Giant ore deposits down under, Adelaide, 115–116

Pirajno F, Seltmann R, Yang YQ (2011) A Review of mineral systems and associated tectonic settings of Northern Xinjiang, NW China. Geosci Frontier 2(2):157–185

Plimer IR (1987) The association of tourmalinite with stratiform scheelite deposits. Miner Deposita 22:82–291

Polito PA, Kyser K, Stanley C (2009) The Proterozoic, albitite-hosted, Valhalla uranium deposit, Queensland, Australia: a description of the alteration assemblage associated with uranium mineralisation in diamond drill hole v39. Miner Deposita 44:11–40

Pollard PJ (1983) Magmatic and postmagmatic processes in the formation of rocks associated with rare element deposits. Trans Inst Min Metall 92:B1–B9

Pollard PJ, Pichavant M, Charoy B (1987) Contrasting evolution of fluorine- and boron-rich tin systems. Miner Deposita 22:315–321

Pollard PJ, Taylor RG, Cuff C (1988) Genetic modelling of greisen-style tin systems. In: Hutchison CS (ed) Geology of tin deposits in Asia and the Pacific. Springer, Berlin, pp 59–72

Putnis A, Hinrichs R, Putnis CV, Golla-Schindler U, Collins LG (2007) Hematite in porous red-clouded feldspars: evidence of large-scale crustal fluid-rock interaction. Lithos 95:10–18

Ramberg H (1952) The origin of metamorphic and metasomatic rocks. University of Chicago Press, Chicago, p 317

Roedder E (1984) Fluid inclusions. Mineralogical Society of America, Washington, DC, p 644, Rev Mineral 12
Rona PA (1984) Hydrothermal mineralization at seafloor spreading centers. Earth Sci Rev 20:1–104
Rose G (1837) Mineralogisch-geognostische Reise nach dem Ural,dem Altai und dem Kaspischen Meere. Vol 1: Reise nach dem nördlichen Ural und dem Altai. Berlin, CW Eichhoff (Verlag derSanderschen Buchhandlung), 641p.
Rose AW, Burt DM (1979) Hydrothermal alteration. In: Barnes HL (ed) Geochemistry of hydrothermal ore deposits, 2nd edn. Wiley, New York, pp 173–235
Rosenbauer RJ, Bischoff JL (1983) Uptake and transport of heavy metals by seawater: a summary of the experimental results. In: Rona PA, Bostrom K, Laubier L, Smith KL (eds) Hydrothermal processes at seafloor spreading centers. Plenum, New York, pp 177–198
Rozendaal A, Misiewicz JE, Scheepers R (1995) The tin zone: sediment-hosted hydrothermal tin mineralization at Rooiberg, South Africa. Miner Deposita 30:178–187
Sánchez-Muñoz L, Crespop E, García-Guinea J, de Moura OJM, Zagorsky VY (2009) What is a twin structure? An answer from microcline minefrals from pegmatites. Estudos Geol 19(2): 240–245
Seedorff E, Dilles JH, Proffett JM, Einaudi MT, Zurcher L, Stavast WJA, Johnson DA, Barton MD (2005) Porphyry deposits: characteristics and origin of hypogene features. Econ Geol 100: 251–298
Seltmann R, Soloviev S, Shatov V, Pirajno F, Naumov E, Cherkasov S (2010) Metallogeny of Siberia: tectonic, geologic and metallogenic settings of selected significant deposits. Aust J Earth Sci 57:655–706
Seyfried WE, Janecky DR (1985) Heavy metal and sulfur transport during subcritical and supercritical hydrothermal alteration of basalt: Influence of fluid pressure and basalt composition and crystallinity. Geochim Cosmochim Acta 49:2545–2560
Seyfried WE, Berndt ME, Seewald JS (1988) Hydrothermal alteration processes at mid-ocean ridges: constraints from diabase alteration experiments, hot spring fluids and composition of the oceanic crust. Can Mineral 26:787–804
Sharkov EV (2010) Middle-proterozoic anorthosite-rapakivi granite complexes: an example of within-plate magmatism in abnormally thick crust: evidence from the East European Craton. Precambrian Res 183:689–700
Shcherba GN (1970) Greisens. Int Geol Rev 12:114–255
Sheppard S, Rasmussen B, Muhling JR, Farrell TR, Fletcher IR (2007) Grenvillian-aged orogenesis in the Palaeoproterozoic Gascoyne complex, Western Australia: 1030–950 Ma reworking of the Proterozoic Capricorn orogen. J Metamorph Geol 25:477–494
Sillitoe RH (2010) Porphyry copper systems. Econ Geol 105:3–41
Slack JF (1996) Tourmaline associations with hydrothermal ore deposits. Rev Mineral 33:559–641
Slack JF, Herriman N, Barnes RG, Plimer IR (1984) Stratiform tourmalinites in metamorphic terranes and their geologic significance. Geology 12:713–716
Smirnov VI (1976) Geology of mineral deposits. MIR, Moscow
Šoštaríc SB, Palinkaŝ LA, Topa D, Spangeberg JE, Prochaska W (2011) Silver-base metal epithermal and listwaenite types of deposit Crnac, Rogozna Mts., Kosovo. Part I: ore mineral geochemistry and sulphur isotope study. Ore Geol Rev 40:65–80
Spear FS (1993) Metamorphic phase equlibria and pressure-temperature-time paths. Mineralogical Society of America, Washington, DC, p 799, Monogr
Storey BC, Alabaster T, Pankhurst RJ (eds) (1992) Magmatism and the causes of continental breakup, vol 68, Geological Society of London. The Geological Society, London, Sp Publ
Taylor RG (1979) Geology of tin deposits. Elsevier, Amsterdam
Taylor R, Pollard PJ (1988) Pervasive hydrothermal alteration in tin-bearing granites and implications for the evolution of ore-bearing magmatic fluids. Can Inst Min Metall 39: 86–95, Sp Vol
Verwoerd WJ (1966) Fenitization of basic igneous rocks. In: Tuttle DF, Gittens J (eds) Carbonatites. Wiley, New York, pp 295–308

Vigneresse JL (2005) The specific case of the Mid-Proterozoic rapakivi granites and associated suite within the context of the Columbia supercontinent. Precambrian Res 137:1–34

Walker RJ, Böhlke JK, McDonough WF, Li J (2007) Effects of Mother Lode-type gold mineralization on $^{187}Os/^{188}Os$ and platinum group element concentrations in peridotite: Alleghany District, California. Econ Geol 102:1079–1089

Walraven F (1985) Genetic aspects of the granophyric rocks of the Bushveld complex. Econ Geol 80:1166–1180

Williams PJ (ed) (1998) A special issue on the McArthur River-Mount Isa-Cloncurry minerals province. Econ Geol 98(8):139–178

Woolley AR (1987) The alkaline rocks and carbonatites of the world. Part 1: North and South America. British Museum Natural History, University Texas Press, London

Woolley AR (2001) Alkaline rocks and carbonatites of the world. Part 3: Africa. Geological Society, London

Woolley AR, Kjarsgaard BA (2008) Carbonatite occurrences of the world: map and database. Geological Survey of Canada, Open File 5796

Woolley AF, Symes RF, Elliot CJ (1972) Metasomatised (fenitized) quartzites from the Barralam complex, Scotland. Mineral Mag 38:819–836

Wright JH, Kwak TAP (1989) Tin-bearing greisens of Mount Bischoff, northwestern Tasmania, Australia. Econ Geol 84:551–574

Zharikov V, Pertsev N, Rusinov V, Callegari E, Fettes D (2007) Metasomatism and metasomatic rocks. In: Fettes D, Desmons J (eds) Metamorphic rocks – a classification and glossary of terms. Cambridge University Press, Cambridge, pp 58–68

Zoheir B, Lehmann B (2011) Listvenite-lode association at the Barramiya gold mine, Eastern Desert, Egypt. Ore Geol Rev 39:101–115

Chapter 8
Metasomatism Within the Ocean Crust

Wolfgang Bach, Niels Jöns, and Frieder Klein

Abstract From ridge to trench, the ocean crust undergoes extensive chemical exchange with seawater, which is critical in setting the chemical and isotopic composition of the oceans and their rocky foundation. Although the overall exchange fluxes are great, the first-order metasomatic changes of crustal rocks are generally minor (usually $<10\%$ relative change in major element concentrations). Drastic fluid-induced metasomatic mass transfers are limited to areas of very high fluid flux such as hydrothermal upflow zones. Epidotization, chloritization, and serizitization are common in these upflow zones, and they often feature replacive sulfide mineralization, forming significant metal accumulations below hydrothermal vent areas. Diffusional metasomatism is subordinate in layered (gabbroic-doleritic-basaltic) crust, because the chemical potential differences between the different lithologies are minor. In heterogeneous crust (mixed mafic-ultramafic lithologies), however, diffusional mass transfers between basaltic lithologies and peridotite are very common. These processes include rodingitization of gabbroic dikes in the lithospheric mantle and steatitization of serpentinites in contact to gabbroic intrusions. Drivers of these metasomatic changes are strong across-contact differences in the activities of major solutes in the intergranular fluids. Most of these processes take place under greenschist-facies conditions, where the differences in silica and proton activities in the fluids are most pronounced. Simple geochemical reaction path models provide a powerful tool for investigating these processes. Because the oceanic crust is hydrologically active throughout much of its lifetime, the diffusional metasomatic zones are commonly also affected by fluid flow, so that a clear distinction between fluid-induced and lithology-driven

W. Bach (✉) • N. Jöns
Department of Geosciences, University of Bremen, Klagenfurter Str, Bremen 28359, Germany
e-mail: wbach@uni-bremen.de

F. Klein
Department of Marine Chemistry and Geochemistry, Woods Hole Oceanographic Institution, Woods Hole, MA 02543, USA

D.E. Harlov and H. Austrheim, *Metasomatism and the Chemical Transformation of Rock*, Lecture Notes in Earth System Sciences,
DOI 10.1007/978-3-642-28394-9_8,

metasomatism is not always possible. Heterogeneous crust is common along slow and ultraslow spreading ridges, were much of the extension is accommodated by faulting (normal faults and detachment faults). Mafic-ultramafic contacts hydrate to greater extents and at higher temperatures than uniform mafic or ultramafic masses of rock. Hence, these lithologic contacts turn mechanically weak at great lithopheric depth and are prone to capture much of the strain during exhumation and uplift of oceanic core complexes. Metasomatism therefore plays a critical role in setting rheological properties of oceanic lithosphere along slow oceanic spreading centers, which – by length – comprise half of the global mid-ocean ridge system.

8.1 Introduction

Mass transfer between the lithosphere and the oceans is a first-order mechanism of chemical exchange between these two reservoirs. Metasomatic alteration of oceanic crust related to seawater circulation is most effective under conditions of high heat flow, i.e. in areas of seafloor spreading. The formation and hydrothermal alteration of oceanic crust along the 65,000 km long system of mid-ocean ridges and backarc spreading centers (Bird 2003) is critical in driving the chemical and isotopic differentiation of the Earth's crust. About 3 km^2 of new oceanic crust is accreted along oceanic spreading centers annually (Parsons 1981) so that the seafloor has been resurfaced and subducted many times in Earth's history. Presently, the oldest oceanic crust is 180 Ma old and the average age of oceanic crust is 61 Ma (Pollack et al. 1993). In addition to oceanic spreading centers, 22,000 km of intra-oceanic island arcs (Bird 2003) are loci of intense ocean-crust exchange (de Ronde et al. 2001; Baker et al. 2008). Intraplate volcanoes make up another significant portion of global magmatism and many active seamounts host hydrothermal systems (Malahoff et al. 1982; Cheminee et al. 1991; Bogdanov et al. 1997).

Long before the discovery of submarine hydrothermal vents, metamorphosed basalt, gabbro, and peridotite were recovered from fracture zones in the ocean basins (Matthews 1962; Quon and Ehlers 1963; Melson et al. 1966). It was soon clear to many researchers that these greenstones and serpentinites are products of hydrothermal alteration of oceanic crustal rocks by seawater, the circulation of which is facilitated by the permeable nature of the crust and the extremely high geothermal gradient in young oceanic lithosphere (Melson et al. 1968; Cann 1969; Miyashiro et al. 1971). Early on, geochemical reactions between crust and ocean associated with hydrothermal alteration were recognized as an important process in controlling crust-ocean chemical and isotopic exchange budgets (Hart 1970; Thompson and Melson 1970; Aumento 1971; Muehlenbachs and Clayton 1972; Humphris and Thompson 1978). In analogy with oceanic crustal sections in ophiolites (Gass and Smewing 1973; Stern et al. 1976; Gregory and Taylor 1981), in situ oceanic crust is believed to display a crude metamorphic layering ranging from granulite-facies conditions in the lowermost crust to amphibolite facies in upper gabbros and lower sheeted dikes to greenschist facies in the upper

sheeted dikes to zeolite facies in the extrusive series (Alt et al. 1986; Bideau et al. 1991; Kelley et al. 1993; Alt 1995; Gillis 1995; Manning et al. 1996; Dick et al. 2000). However, multiple retrogression events are commonly preserved in metamorphosed oceanic crustal rocks as well as in ophiolites, indicating that early high-temperature metamorphism, which likely took place close to the mid-ocean ridge spreading axes, was followed by subsequent episodes of fluid-rock interaction under lower metamorphic grades (Alt et al. 1986; Bideau et al. 1991; Bach et al. 2001). At any stage, alteration is usually not pervasive, but instead bound to fracture networks and zones of crystal-plastic deformation (Mével and Cannat 1991; Manning and MacLeod 1996). Oxidative seawater alteration (also referred to as 'seafloor weathering' and 'brownstone facies alteration'; Cann 1969; Thompson 1991) affects all oceanic rocks exposed at the seafloor and extends tens to hundreds of meters into the subseafloor. Minerals formed due to interaction with seawater during brownstone alteration include smectites, zeolites, carbonate (e.g., calcite, aragonite) and silica (e.g., opal, chalcedony). While their formation is associated with, in part, severe mass transfers (Ludden and Thompson 1978; Staudigel et al. 1981; Snow and Dick 1995), a detailed discussion of ocean floor weathering is outside the scope of this work.

The focus of this chapter is on metasomatic mass transfers developed in different sections of oceanic lithosphere, explicitly in places where strong contrasts in rock composition and/or focused fluid flow occur. In the broadest terms, metasomatism within the oceanic crust is either infiltrational or diffusional. Infiltrational metasomatism takes place in all types of oceanic crust and in all lithologies but only results in pronounced metasomatism where high fluid fluxes play a role. It occurs at spatial scales of centimeters (e.g., vein halos) to kilometers (hydrothermal upflow zones). Diffusional metasomatism is developed where lithologies, juxtaposed against each other, impose strongly contrasting chemical potentials of major constituents in the intragranular fluids within the two lithologies. As the drive for mass transfer is activity gradients maintained by the different lithologies, diffusional metasomatism does not require large fluid fluxes. These differences in lithologies can affect infiltrational metasomatism as well, for example where different lithologies are encountered along the path of large volume fluid flow.

To identify and discern the areas in the oceans that are affected by these different metasomatic processes, it is necessary to begin by reviewing what is currently known about lithospheric architecture and hydrothermal circulation. According to the widely accepted Penrose model (Anonymous 1972), all oceanic crust is uniform in architecture and thickness, featuring a "layer-cake" structure of basalt, diabase (sheeted dike complex), and gabbro. This principal crustal architecture is indeed applicable for nearly all oceanic crust formed at mid-ocean ridges spreading at full rates $>$55 mm/year crust. It is not a generally valid model, as it does not account for the crustal structure of many ridge segments formed at much slower spreading rates, which comprise $>$1/3rd of the global mid-ocean ridge system (Baker et al. 1996) and are characterized by a more heterogeneous crustal structure.

Spreading rate imparts a strong control on the relative proportions of magmatically versus tectonically accommodated extension. At fast spreading ridges, practically all extension is accommodated by magmatism. Seafloor topographies are smooth and extensional faults are rare and small-offset. At slow-spreading ridges, in

contrast, a significant (and variable) fraction of the extension created by plate divergence is accommodated by tectonic faulting (Sinton and Detrick 1992; Tucholke and Lin 1994). Long-lived and large-offset extensional faults develop as a consequence of slow spreading. At fast spreading ridges, hydrothermal circulation of seawater is controlled by magmatic diking, whereas it is tied to extensional faulting at slow spreading ridges (Wilcock and Delaney 1996). These differences are expressed in the style of seawater-rock interaction, and have been observed in deep drill holes within the oceanic crust and in ophiolites. Fast spread crust shows static alteration controlled by fractures and microcracks, while in slow spread crust, much of the intense alteration is related to brittle deformation in normal faults (Alt 1995).

Likewise, large areas along slow-spreading ridges, such as the Mid-Atlantic Ridge, feature mantle peridotite and not basalt at the seafloor (Cannat et al. 1995). There, mantle rocks are exhumed along large, shallow-dipping detachment faults forming corrugated surfaces on dome-like oceanic core complexes, which are now being recognized in more and more areas in the world's oceans (Tucholke et al. 1998; Smith et al. 2006; Ildefonse et al. 2007; Blackman et al. 2009; MacLeod et al. 2009). Where these core complexes form, they make up about ¼ of the area of the seafloor in the entire ridge segment (Cannat et al. 1995). The modern view of oceanic crust at slow spreading ridges pictures a succession of both homogeneous layer-cake crust and heterogeneous crust with attenuated or missing magmatic crust and gabbroic intrusions in partially serpentinized lithospheric mantle (Cannat et al. 1995; Mével 2003; Dick et al. 2008).

Recent investigations have shown that ultraslow spreading ridges (<20 mm full spreading rate year^{-1}) have unique morphologies consisting of linked amagmatic and magmatic accretionary segments. They lack transform faults, and have discontinuous volcanic centers separated by long stretches of avolcanic segments, in which the principal unit of accretion appears to be intrusion of mantle blocks to the seafloor (Dick et al. 2003; Michael et al. 2003).

8.2 Infiltrational Metasomatism

Infiltrational (in contrast to diffusional) metasomatism, due to interaction of circulating hydrothermal fluids with rocks from the oceanic lithosphere, is the most effective (and large-scale) process for setting the chemical compositions of both the oceans and the oceanic lithosphere. As gradients in temperature and differences in fluid-to-rock ratios are the main controlling factors, we first need to evaluate how hydrothermal fluids circulate through the crust and how they cool the crust. Fluid pathways and temperatures affect the chemical composition of the fluids and their potential for element transport. These fluids can then either cause subtle changes in the major element composition of the rocks in recharge and reaction zones ("ubiquitous alteration" in Fig. 8.1), or they are responsible for dramatic mass transfers in localized upflow zones that lead to transformation of basaltic rocks into epidosites or chlorite-quartz schists. The controlling factors and examples for infiltrational metasomatism in the oceanic lithosphere are detailed in the following sections.

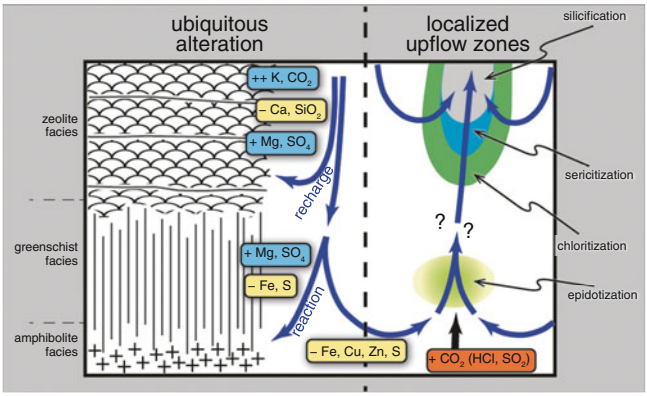

Fig. 8.1 Sketch of hydrothermal circulation, associated mass transfers, and metasomatic zones. The *left* part of the panel depicts basic structure, metamorphic facies, and some of the metasomatic mass transfers in "normal" layer-cake oceanic crust. Distinct metasomatic changes are associated with hydrothermal upflow zones as illustrated to the *right of the dashed vertical line*

8.2.1 Hydrothermal Circulation

Hydrothermal cooling of the oceanic lithosphere by circulation of seawater is responsible for about a quarter of the global heat loss (Stein and Stein 1994). Of the total hydrothermal heat loss of 7 to 11 $\times$ 10^{12} W, between 1 and 4 $\times$ 10^{12} W are tied to active circulation within a few km of the spreading axes (Sleep 1991; Stein and Stein 1994). The remaining heat loss is related to circulation of seawater within the uppermost permeable crust at temperatures that are a few degrees centigrade above ambient (Elderfield and Schultz 1996). This off-axis circulation of seawater extends thousands of km away from the spreading axes into crust of an average age of 65 Million years (Stein et al. 1995). Hence, about half of the seafloor is hydrothermally active and prone to metasomatic mass transfers. The temperature regime of metasomatism is amphibolite to zeolite facies in axial hydrothermal systems and zeolite to brownstone facies in off-axial systems (Thompson 1991; Alt 1995, Fig. 8.1).

On-axis circulation – In axial systems, seawater circulation is driven by heat released from crystallizing magma emplaced in the lower crust. Circulating seawater penetrates the crust in recharge zones, equilibrates with mafic rock under upper greenschist-facies conditions (400–450°C) in the reaction zone, and discharges to the seafloor in hydrothermal upflow zones (e.g., Alt 1995; Fig. 8.1). Seawater-derived crustal fluids quickly change their composition, as they react with increasing volumes of rock under elevated temperatures. Some of the most prominent changes are a loss of Mg and sulfate, while Ca and silica concentrations increase. Due to the low permeability of mid and lower crustal rocks (doleritic sheeted dikes and gabbros), the fraction of seawater penetrating deep into the crust and getting heated to temperatures $>$ 400°C is small. A simple heat budget calculation shows that the overall water-to-rock mass ratios in the hydrothermal reaction zone must be about 1. On the order of 1–4 TW of heat is removed by black smoker type vent fluids along

mid-ocean ridge axes. Given an enthalpy increase by about 1,900 J/g when seawater is heated from 2°C to 400°C at deep-sea pressures (300 bar; Bischoff and Rosenbauer 1985), 1–4 TW (10^{12} J/s) corresponds to a water flux of 0.53 to 2.12 × 10^9 g/s (or 1.7 to 6.6 × 10^{13} kg/year). In magmatic driven hydrothermal systems, this water flux can be related to a magma flux rate of 18 km^3/year (Cogne and Humler 2004). With a mean density of 2,800 kg/m^3, approximately 5 × 10^{13} kg magma crystallizes and cools per year, releasing heat that can drive circulation of seawater. Cooling from 1,200°C to 400°C provides about 800 J/g (given a heat capacity of basalt of 1 J/g K) which results in a heat flux of ca. 4 × 10^{16} kJ/year. A similar amount of latent heat is released during crystallization. Because both mass flux and specific enthalpy change are similar in the hydrothermal and magmatic processes, the overall fluid-to-rock ratio must be close to unity. Experimental (Mottl 1983), theoretical (Bowers and Taylor 1985), and observational (Humphris and Thompson 1978) evidence indicates that metasomatic changes during greenschist facies alteration at these low fluid-to-rock ratios are negligible.

Off-axis hydrothermal circulation – Similar estimates from heat and geochemical mass balance budgets indicate that the flux of seawater through oceanic crust is very large, such that it takes only on the order of 100 ka for the entire volume of the ocean to be cycled through the oceanic crust (see Elderfield and Schultz 1996 for details). Nonetheless, the overall metasomatic changes are subtle and can be described as propylitic alteration (hydration) with minor ion exchange (chiefly Mg-Ca). The changes are small because high fluid flux is limited to the uppermost crust, where temperatures are low and reaction rates slow. In the high-temperature reaction zone, where reaction rates are fast, water-rock ratios are small and the seawater-derived fluids are effectively rock-buffered.

8.2.2 Chemical Exchange Between Seawater and Crust

Both axial and off-axial hydrothermal systems are places of chemical mass transfer between the oceans and the crust that are fundamental in setting the composition of the oceans and controlling input fluxes into subduction zones (Alt 1995; Staudigel et al. 1996; Jarrard 2003). The rates and direction of chemical exchange are strongly dependent on temperature. Some elements (alkalis, B, C) are removed from circulating seawater at temperatures < 150°C, while, at higher temperatures, they are leached from the interacting rocks and become enriched in the circulating fluids (Seyfried and Bischoff 1979, 1981; Seyfried et al. 1984). Off-axis and on-axis hydrothermal systems may hence act as sinks and sources of these elements. The sink term associated with off-axis systems is commonly greater than the source term of axial systems (Hart and Staudigel 1982; Alt 1995; Staudigel et al. 1996). For Mg, P, and U, both on axis and off-axis circulation act as sinks (Mottl and Wheat 1994; Wheat et al. 1996; Mottl et al. 1998).

Compared to other fluids (meteoric, metamorphic, etc.), seawater is rich in Mg (53 mmoles/kg, mM). With its high pH (=8) and intermediate silica concentrations

(0.13 mM), seawater is supersaturated with respect to hydrous Mg-silicates even before it interacts with the oceanic crust. The abundance of low-temperature clay veins indicates that Mg-silicate precipitation is common in the subseafloor (Alt 1995). Although dissolution of mafic minerals and glass will add Mg to the intergranular fluid, the net effect of seawater circulation is the near quantitative loss of Mg from the fluid along its flow path, resulting from a decrease in the solubility of hydrous Mg-silicates as temperatures increase. At low temperatures, the loss of Mg from the circulating seawater is accommodated quantitatively by a corresponding gain in Ca released from the breakdown of glass and plagioclase. Because of the approximate 1:1 relation between Mg loss and Ca gain, the pH of the fluid is not affected. The reaction can be regarded as a simple cation-exchange reaction. Fluids sampled from a basaltic aquifer in the sediment-covered eastern flank of the Juan de Fuca Ridge show that Mg went from 53 to 2 mM, while Ca increased from 10 to 62 mM (Elderfield et al. 1999). The temperatures required to drive this exchange reaction almost to completion are not very high (62°C in the case of the eastern Juan de Fuca ridge flank). These fluids still have seawater-like pH values around 8 (Elderfield et al. 1999; Wheat and Mottl 2000). The reaction $Mg^{2+} + 2\ H_2O \rightarrow Mg(OH)_2 + 2\ H^+$, which is often held responsible for the Mg-deficient and acidic nature of seawater-derived hydrothermal solutions (e.g., Pirajno 2009), cannot account for the change in fluid composition observed in the aquifer of the Juan de Fuca Ridge flank. Evaluating the equilibrium state of this reaction will quickly show why that is the case. The reaction will only proceed to the right until brucite is saturated, which occurs at a pH of around 11 at 25°C. The Juan de Fuca example also shows that chloritization and albitization are not necessarily needed to achieve mass transfers in Ca and Mg. At temperatures in excess of 150°C, secondary Ca phases (anhydrite, laumontite, prehnite) form and buffer the Ca content of the fluid to lower concentrations. At this point, the fluid pH drops somewhat, and it undergoes a further decrease when epidote and actinolite become stable and take up more Ca at T >250°C. The drop in pH is hence related to uptake of Ca and release of protons (Seyfried et al. 1988). From that point on the fluid is buffered by albite-chlorite-actinolite-quartz to temperatures of 400–450°C, so that the chemical changes rocks undergo when interacting with these fluids are quite small. As will be shown in the next section, the overall water fluxes are also quite small. Most hydrothermally altered rocks show just an insignificant shift in chemical composition resulting from hydrothermal interactions.

8.2.3 Ocean Floor Metasomatism in Recharge and Reaction Zones

The extent of compositional metasomatic changes in oceanic crustal rock varies from minimal to extreme. All rocks altered at temperatures below around 750°C have experienced at least some addition of water. At higher temperatures, seawater-

derived aqueous fluids may still have percolated through rock, but they either trigger partial melting or hydrous alteration is cryptic (Lecuyer and Grurau 1996; McCollom and Shock 1998). If the water flux through a system is large, elements that are enriched in the fluid become more insoluble in the course of fluid-rock reaction, while fluid soluble elements become removed from the rock. This process operates as long as the fluid is in disequilibrium with the rock.

In recharge and reaction zones, the changes in rock composition are usually subtle for most major elements. The alteration is dominated by uptake of H_2O throughout the crust affected by seawater circulation. Carbon dioxide is also added to the oceanic crust, but carbonates are limited to the uppermost few hundred meters (e.g., Staudigel et al. 1996). Large changes in trace element compositions include the addition of B, U, and alkalis in the uppermost crust at low temperatures and high water-to-rock ratios, and the leaching of alkalis, base metals and S in the lower sheeted dike complex. These changes are explored in Alt (1995) and Staudigel et al. (1996) and are not discussed here in further detail.

Although seawater-crust interaction is critical in setting the composition of the oceans, the overall chemical changes of the oceanic crust, in terms of major elements, are small. Most significantly, the oceanic crust is a large sink for Mg, balancing the continental runoff (1.3×10^{11} kg Mg/year; Mackenzie 1992). Assuming that 50–100% of oceanic crust (or 2.5 to 5×10^{13} kg/year) is affected by hydrothermal alteration and that the average basaltic rock, subjected to alteration, has 9 wt.% MgO, the MgO concentration of average basaltic rock in the course of alteration needs to go up by 0.5–1 wt.% MgO. Magnesium-enrichment of the oceanic crust is not achieved primarily by forming chlorite during axial high-temperature circulation of seawater-derived fluids. This, again, can be concluded from heat budgets. Seawater has 1.29 g/kg Mg dissolved, which is near-quantitatively lost during interaction with basaltic rock. To account for a crustal sink of 1.3×10^{11} kg Mg/year, 10^{14} kg of seawater must be completely depleted in Mg. However, there is not enough heat available in axial hydrothermal systems (see above) to heat such a large quantity of seawater to greenschist-facies temperatures so that chlorite can form. The majority of this Mg must be lost in ridge flank hydrothermal systems under zeolite facies conditions. But Mg is lost during low-temperature alteration of glass and mafic minerals (e.g. Thompson 1991). The Mg uptake of the crust must therefore be accomplished by filling fractures and void space with Mg-rich smectite (Alt et al. 1996b). Because vein formation is not considered a metasomatic process (Zharikov et al. 2007), much of the Mg enrichment of the oceanic crust is not strictly metasomatic in origin.

Loss of Ca from the oceanic crust (1.9×10^{11} kg/year; Wheat and Mottl 2000) corresponds to 0.5–1 wt.% of CaO extracted from the mantle to form oceanic crust. Again, this is less than 10% of the relative Ca loss, given that the average basalt contains about 12 wt.% CaO. Calcium loss and Mg gain cancel each other out. Consequently, hydrothermal alteration, in addition to hydration, can be considered as a cation exchange process.

There is a comprehensive body of literature available discussing the geochemistry of hydrothermal systems and their relevance in crust-ocean exchange budgets

(Alt 1995; Kadko et al. 1995; Elderfield and Schultz 1996; Staudigel et al. 1996; Wheat and Mottl 2000; Bach et al. 2003).

8.2.4 *Metasomatism in Localized Upflow Zones*

Most petrologists would hardly consider relative elemental changes by 10% or so a significant metasomatic process. So the dominant fraction of oceanic crust is not metasomatized to great extents. Significant metasomatic mass transfers of major elements within the basaltic oceanic crust are developed only where high fluid fluxes and high temperatures prevail. These conditions are typical of hydrothermal upflow zones, where different metasomatic reactions can be observed, such as epidotization, chloritization, sericitization, and silicification (Fig. 8.1).

Epidotization – Epidosites are strongly Ca-metasomatized rocks and consist predominantly of epidote with subordinate quartz ± chlorite. Epidotization overprints earlier greenschist facies alteration and is developed parallel to dike margins. Zones of epidosites are up to 1 km wide in the Troodos Ophiolite and in it, epidosites and diabase are interbanded on a decimeter to meter-scale (Richardson et al. 1987). While oriented parallel to the dike margins, the epidosites have predominantly replaced the diabase in the centers of the dikes. Epidosite bands are irregular in shape and may break up in pipes. The temperatures involved have been estimated from fluid inclusion and stable isotope studies to be around 400°C (Harper et al. 1988; Richards et al. 1989; Richardson et al. 1987). Very high fluid-to-rock ratios, on the order of 1,000, have been invoked to account for the dramatic mass transfers involved in epidotization (Seyfried et al. 1988). Strontium isotope compositions of epidosites from ophiolites also indicate high fluid fluxes, but those are generally high in ophiolite sections, and the epidosites are not necessarily more radiogenic in Sr isotope composition (i.e. reveal greater fluid flux) than the hosting diabases (Bickle and Teagle 1992).

Epidosite genesis is still a bit of a mystery. This rock type is common in ophiolites, but the only place from the oceans where it has been found is from a tectonically exposed section of mid and lower arc crust in the Marianas (Banerjee et al. 2000). The formation of epidosite has been associated with the focusing of hydrothermal fluids in the transition between the reaction zone and the upflow zone (Richardson et al. 1987; Gillis 2002). The fluids should therefore have been saturated with greenschist-facies minerals observed in the reaction zone (sodic plagioclase, chlorite, actinolite, epidote). The fact that epidote (and quartz) replace this low variance greenschist facies assemblage indicates that there must be factors other than high fluid flux involved. Up-temperature fluid flow in response to dike emplacement and cooling has been invoked to explain epidosite formation (Rose and Bird 1994). This mechanism can explain why epidosite formation is most developed in the centers of thick dikes. Seyfried et al. (1988) point out that acidic fluids are required to remove Mg (in chlorite-free epidosites, Mg is almost quantitatively removed). Acidic fluids would also help mobilize rare earth elements that

are highly depleted in epidosites compared to the precursor diabase (Valsami and Cann 1992). Magmatic degassing of CO_2, HCl, and SO_2 could act as an external source of acidity required to drive epidosite formation. At the temperatures of epidotization (around 400°C), the acidity of CO_2 is strongly reduced (Bischoff and Rosenbauer 1996) so that influx of CO_2 as the only magmatic volatile will not drive epidotization. Hard mineral acids (HCl, H_2SO_4) are significantly more dissociated than CO_2 at 400°C, and even small quantities of these components in a rock-buffered fluid may destroy the mafic minerals (actinolite and chlorite) as well as albite in a diabase, leaving behind epidote and quartz. Dissolution of the albite, chlorite, and actinolite would create permeability, which – in turn – would promote fluid influx and trigger a positive feed back mechanism. This would explain the screen- and pipe-like occurrence of epidosite in the field. Degassing of HCl and SO_2 is common in arc and backarc magma-hydrothermal systems, while gases coming off tholeiitic magma at mid-ocean ridges are dominated by CO_2 (Graham and Sarda 1991). Epidosites are common in suprasubduction zone crust (fore arc, ophiolites with boninitic affinities), while they have not been documented to date from oceanic crust. Their formation may hence be tied to mineral acid influx, which is common in subduction-related magma-hydrothermal systems. Epidosites are reported to occur predominantly in the sheeted dike complex, although albite-bearing epidosites can extend into the lowermost part of the overlying volcanic series (Harper et al. 1988). The shallower parts of hydrothermal upflow zones, however, show different types of metasomatism dominated by chlorite, mica, quartz, and sulfide.

Chloritization, sericitization, and silicification – Chlorite-quartz rocks have been described from the transition zone between sheeted dikes and lava flows in drill hole 504B in the eastern equatorial Pacific (Alt et al. 1986, 1996a). These rocks are variably sulfidized by pyrite with small amounts of chalcopyrite, galena and sphalerite (Honnorez 2003). They are believed to have formed at the dike-lava transition, because of the pronounced increase in permeability across this boundary. In the zeolite-facies basalts, temperatures of fluid-rock interaction were $<$150–200°C, with alteration temperatures decreasing and the extent of oxidation and enrichment in alkalis increasing up sequence. The sudden drop in permeability coincides with a pronounced increase in alteration temperatures transitioning into the sheeted dike complex. This boundary may have acted as a hydrologic interface, where hot upwelling hydrothermal fluids were cooled rapidly, leading to the precipitation of quartz and sulfides. Abundant chlorite could form, because the system was connected to the ocean through a permeable lava sequence and seawater could recharge efficiently, leading to Mg-metasomatism. This zone is enriched in Mg, Mn, Cu, Zn, Pb, U, S, as well as CO_2 and depleted in Ca (Alt et al. 1986; Bach et al. 2003). A comprehensive review of the geochemistry and mineralogy of the crustal section sampled in ODP hole 504B is provided by Alt et al. (1996a) and Honnorez (2003).

The formation of chlorite-quartz rock has long been associated with the high fluid fluxes required to remove Ca and the alkalis from the rock (Cann 1969). Mottl (1983) provided firm evidence for high-variance quartz-chlorite-oxide assemblages

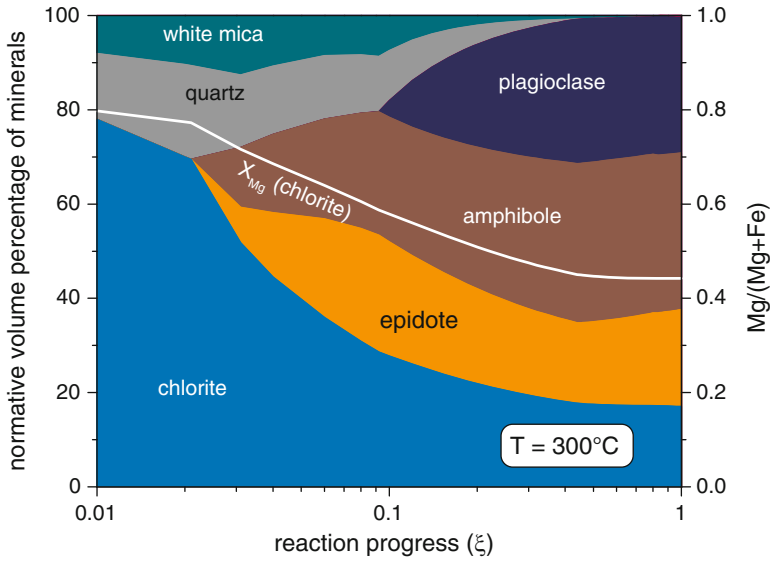

Fig. 8.2 Thermodynamic prediction of secondary mineral modes in basalt reacting with variable amount of seawater at 300°C. The prediction closely matches the modes observed in basalt-seawater hydrothermal experiments (cf. Mottl 1983). In this and the following presentations of reaction path models, increasing values of ξ represent increasing rock buffering in situ and thus less metasomatism (see appendix for calculation details)

replacing basalt at temperatures of 300°C and fluid-to-rock ratios > 50. The experimental results of Mottl (1983) are very similar to results obtained from reaction path modeling calculations presented in Fig. 8.2, where basalt of average Atlantic N-MORB composition (Klein 2004) was reacted with seawater at 300°C and 1 kbar. In the reaction path, seawater is added to the rock as an externally buffered fluid. The progress of the reaction is expressed by the reaction progress number (ξ). At high fluid-to-rock ratios (fluid-dominated system, low ξ), quartz and Mg-rich chlorite dominate. The variance of the assemblage then drops as more components become immobile with lower fluid-to-rock ratios (increased ξ). The assemblage predicted to form at low fluid-to-rock ratios (around 1, $\xi = 1$) is consistent with experimental results (Mottl 1983) and with field evidence from greenschist facies sheeted dike rocks (Humphris and Thompson 1978; Alt et al. 1996a). These results lend petrological support to the notion of low fluid-to-rock ratios derived from heat budget and stable isotope constraints. These data also indicate that epidosites cannot be derived from interaction with seawater, because chlorite (a phase consumed during epidotization) is expected to form when the interacting fluid is seawater-like in composition. The fact that chlorite becomes a dominant phase in the shallow upflow zone is therefore related to Mg influx from seawater. Seawater is entrained into the hydrothermal upflow zone, in which rapid upflow underpressures the fluids in the surrounding basaltic aquifers. It is expected, then, that chlorite is most enriched along an up-temperature flow path of seawater into a hydrothermal

upflow zone. Chlorite enrichment in the peripheral parts of hydrothermal upflow zones is indeed observed – in active hydrothermal systems as well as in ophiolites. The best-known modern example is the TAG hydrothermal system at the mid-Atlantic Ridge 26°N, which has been drilled by the Ocean Drilling Program (Humphris et al. 1995). Ophiolite examples include those from the Troodos (Richards et al. 1989; Wells et al. 1998) and Josephine (Zierenberg et al. 1988) ophiolites. All fossil and modern upflow zones have a roughly pipe-like structure with different metasomatic zones. Although variable in detail (e.g., Richards et al. 1989), all these metasomatic pipes feature an outer zone of chloritization. In the inner part of the metasomatic pipes, silicification and sulfidization prevail and in some examples sericitization (illite or paragonite) are developed between the chloritized and silicified zones. The metasomatic mass transfers within these pipes are significant (Table 8.1) and can be understood in terms of the thermodynamic driving force for mineral replacement reaction along specific reaction paths. One path is that of entrained seawater, which becomes heated in the peripheral parts of the upflow zone, causing chloritization. Because the entrained fluid is seawater-like (Teagle et al. 1998b; Tivey et al. 1998), the replacive chlorite is magnesian (Alt and Teagle 1998; Teagle et al. 1998a), and the rock is Mg-metasomatized (Humphris et al. 1998). Chloritized rocks from the deeper central parts of the upflow zones (>100–200 m below the seafloor) feature Fe-rich chlorite and lack Mg metasomatism. This pattern of chlorite distribution and composition is predicted in a reaction path model, in which basalt is titrated into seawater at 400°C (Fig. 8.3). Throughout the upflow zone, metasomatism is fluid-induced, but the fluids are mixtures of upwelling Fe- and H_2S-rich hydrothermal solutions and seawater. Hydrogen-sulfide contents of the mixed fluids play a role in setting chlorite compositions, because chlorite will compete for Fe with sulfide minerals that may be stable (Saccocia and Gillis 1995). In the core of the upflow zone, hydrothermal fluids rise to the seafloor without mixing with seawater at all. This is where sericitization and silicification will dominate. The drivers of these replacement reactions are physicochemical changes in fluids, which become cooler and more acidic on their way up. The rocks are completely stripped of Mg and Ca, but retain (or regain) a good fraction of the alkalis that are completely leached from rocks in the reaction zone. Sulfidization is common throughout the upflow zone, starting in the zone of Fe-rich chlorite enrichment and continuing up into the silicified shallowest part of the upflow zone. The dominant sulfide phase is pyrite with lesser chalcopyrite (Knott et al. 1998). The precipitation of sulfides and quartz (and other silica polymorphs) can be understood in terms of adiabatic cooling of the uprising fluid and the variable extents of conductive cooling. Precipitation of pyrite and dissociation of mineral acids in the course of cooling will make the fluid mildly acidic, which aids in leaching Mg from rocks in the core of the upflow zones. The same process will lead to a redistribution of metals in sulfides, leading to supergeneous enrichment of metals (e.g., Zn, Au) that can be solubilized in response to acidification due to pyrite precipitation (e.g., Tivey et al. 1995).

Table 8.1 Compositions of selected samples of metasomatized rocks from in situ oceanic crust (TAG) and ophiolites. All values given in weight percent; *n.d.* not determined

Rock	SiO_2	TiO_2	Al_2O_3	Fe_2O_3	MnO	MgO	CaO	Na_2O	K_2O	P_2O_5	S	H_2O	Source
Chloritized rock from outer zone	30.99	2.00	17.41	12.84	0.07	23.46	0.05	0.38	0.06	0.03	<0.11	2.03	Humphris et al. (1995)
Chloritized rock from upflow zone	35.88	1.13	13.82	23.13	0.06	9.82	0.05	0.11	0.01	<0.01	7.44	7.73	Humphris et al. (1995)
Palagonitized rock from upflow zone	41.88	0.64	5.99	26.50	<0.01	0.10	0.06	0.91	0.14	<0.01	23.78	0.89	Humphris et al. (1995)
Silicified rock from upflow zone	51.38	0.12	1.32	22.50	<0.01	0.16	0.09	0.23	0.04	<0.01	20.98	1.73	Humphris et al. (1995)
Epidosite, troodos ophiolite	59.10	1.11	13.80	10.45	0.10	2.03	11.08	0.06	0.01	0.07	n.d.	1.60	Richardson et al. (1987)
Diabase, troodos ophiolite	57.40	1.39	13.33	12.50	0.11	5.26	4.68	3.60	0.25	0.08	n.d.	3.00	Richardson et al. (1987)
Epidosite, josephine ophiolite	53.40	0.58	17.30	7.29	0.13	0.60	17.37	0.13	0.04	0.08	n.d.	2.59	Harper et al. (1988)
Diabase, josephine ophiolite	52.60	0.74	15.90	8.65	0.15	4.90	8.11	4.02	0.07	0.10	n.d.	5.53	Harper et al. (1988)

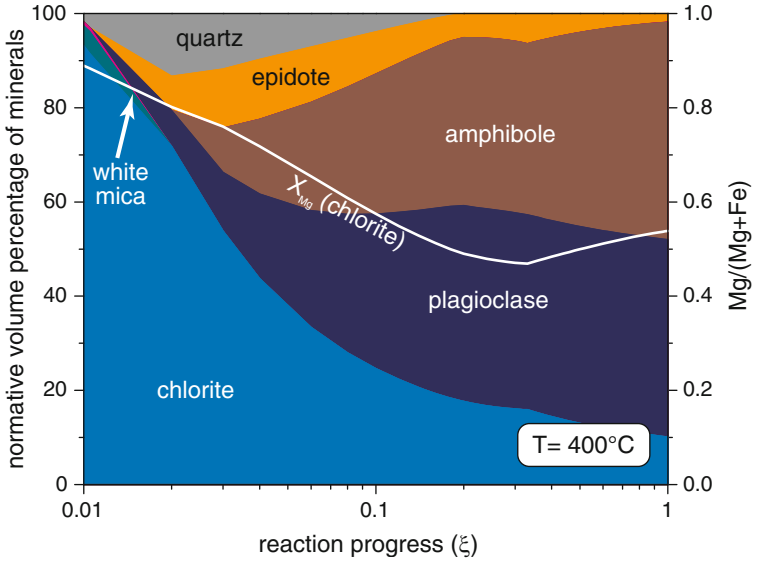

Fig. 8.3 Thermodynamic prediction of secondary mineral modes at 400°C in a system, in which hot seawater is advected into basalt. The fluid-dominated part (low ξ) is composed largely of magnesian chlorite, such as observed in peripheral parts of hydrothermal upflow zones

8.2.5 CO_2-Metasomatism of Seafloor Serpentinite

Carbon-dioxide metasomatism of seafloor serpentinite has received relatively little attention. However, in samples from IODP Leg 304 olivine is directly replaced by carbonate and Fe-rich talc or saponite (Andreani et al. 2009). Similar replacement reactions have been reported from ODP Leg 209 where olivine is replaced in favor of calcite and clay minerals (Kelemen et al. 2004). However, on land many outcrops of partly to fully serpentinized peridotites show evidence for variable extents of CO_2-metasomatism, i.e. some are altered to soapstone, a talc-carbonate rock (e.g., Hess 1933), others to listvenite, a rock composed of quartz, carbonate, and minor mica (e.g., Halls and Zhao 1995). In many cases, ultramafic bodies in contact with quartzo-feldspathic country rocks reveal a concentric metasomatic zoning with a peridotite core, which is surrounded by a serpentinite zone, a talc-carbonate zone, a steatite, and a 'blackwall' chlorite-schist (Chidester and Cady 1972; Koons 1981).

Although large scale CO_2-metasomatic alteration of abyssal mantle rocks has not been reported, we take the descriptions of Andreani et al. (2009) and Kelemen et al. (2004) as a tentative indication that direct mineral carbonation of serpentinized peridotite might actually take place on the seafloor. In this section we briefly discuss mineral carbonation of seafloor serpentinite and present a simple isothermal, isobaric reaction path model emulating infiltrational CO_2-

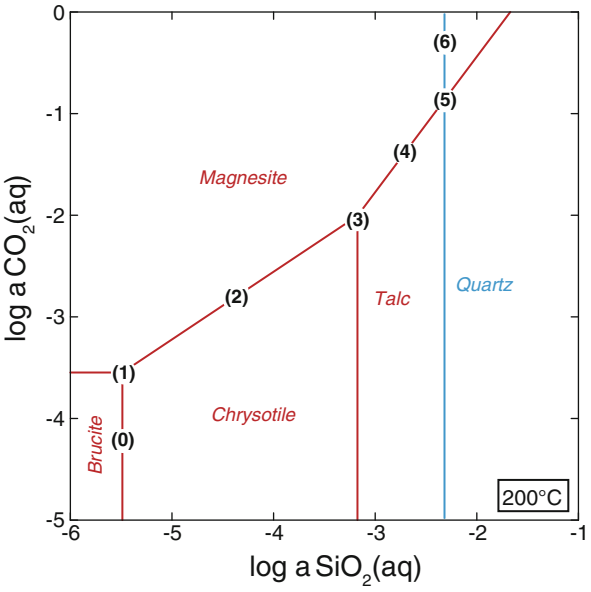

Fig. 8.4 Phase diagram of the system MgO-SiO_2-H_2O-CO_2 with predicted mineral assemblages labeled 0 through 6 (Modified from Klein and Garrido 2011). See text for explanation

metasomatism of serpentinized harzburgite using hydrothermally-altered CO_2-enriched seawater similar to those presented by Klein and Garrido (2011).

A serpentinized peridotite undergoing infiltration of CO_2-rich fluid will inevitably experience a significant change in mineralogy (Klein and Garrido 2011). Based on phase relations in the system MgO–SiO_2–H_2O–CO_2 (MSHC) (Fig. 8.4), at 200°C and 100 MPa the ideal alteration sequence consists of 7 distinct phase equilibria, which can be pictured as 6 spatially distinct metasomatic zones that form with progressive CO_2-metasomatism proximal to the serpentinite protolith: (0) serpentine – brucite (protolith), (1) serpentine – brucite – magnesite, (2) serpentine – magnesite, (3) serpentine – talc – magnesite, (4) talc – magnesite, (5) talc – quartz – magnesite, and finally (6) quartz – magnesite. In incompletely serpentinized peridotites, relict olivine and orthopyroxene will be replaced by serpentine + magnesite or talc + magnesite. Consistent with the MSHC carbonation sequence, Hansen et al. (2005) describe a serpentine–olivine–brucite (protolith) zone, a serpentine – magnesite zone, a talc – magnesite zone, and a quartz – magnesite zone in carbonate altered serpentinites from Atlin, British Columbia (cf. Dabitzias 1980; Koons 1981; Frost 1985; Böhlke 1989). The extent of mineral carbonation is a function of the protolith composition, the CO_2 activity (aCO_2,aq) of the infiltrating fluid, fluid flux, and temperature. In our model we use a 0.1 m CO_2,aq fluid as this represents the highest concentration of CO_2,aq measured to date in mid-ocean ridge hydrothermal systems (Lilley et al. 2003; Seewald et al. 2003). Figure 8.5 illustrates the predicted amounts of mineral phases in relation to the mass of the infiltrating fluid at a constant temperature of 200°C and a pressure of 1 kbar. Note that there is a linear function between the aCO_2,aq of the infiltrating fluid and reaction progress, e.g., doubling the aCO_2,aq would reduce the mass of fluid needed

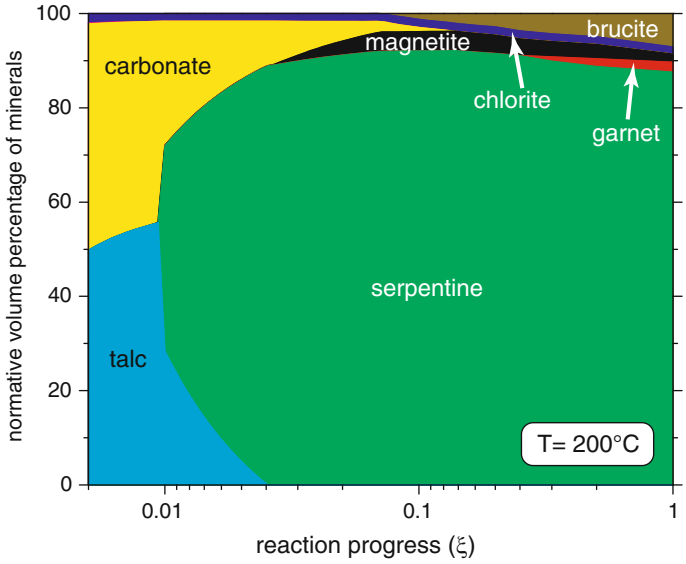

Fig. 8.5 Reaction path model of carbonation. Interacting fluid is seawater with 100 mmoles/kg dissolved inorganic carbon (cf. Klein and Garrido 2011). Rock is harzburgite (Ol:Opx:Cpx = 80:15:5 in vol.%; see Klein et al. (2009) for details)

to drive mineral carbonation to 50%. In addition to the six principal mineral assemblages mentioned before, minor phases like chlorite, garnet, magnetite, and hematite are predicted to be present in the system. Moreover, serpentine, talc, carbonate, and chlorite are predicted to host significant amounts of Fe, represented in our model by greenalite, minnesotaite, siderite, and daphnite, respectively. When we compare the phase relations in Fig. 8.4 with our modeling results in Fig. 8.5, it becomes apparent that only the first four metasomatic zones are predicted to form. In theory, zones 5 and 6, both of which comprise quartz, can form only if the fluid would be richer in CO_2,aq (at least 0.182 m CO_2,aq at 200°C and 1 kbar) or if the temperature would be lower. In general, all phase equilibria and geochemical potential gradients for mineral carbonation in the system $MgO–SiO_2–H_2O–CO_2$ are strongly dependent on temperature.

Mineral carbonation of serpentinite is a good example where both the infiltrational and the diffusional aspects of metasomatism are involved. At low temperatures, the activity gradients between zones 0 and 6 of CO_2,aq and SiO_2,aq are steep (Klein and Garrido 2011) and if zone 6 is representative of infiltrating CO_2-rich crustal fluids there will be an ample thermodynamic driving force for mineral carbonation. But it can be anticipated that mineral carbonation will be kinetically sluggish at low temperatures even if magnesite, talc, and quartz are highly supersaturated (cf. Gerdemann et al. 2003). With increasing temperature the CO_2 activities necessary to drive magnesite formation at the expense of serpentinite increase, i.e. the thermodynamic drive for carbonation reactions becomes smaller if the CO_2 is externally buffered to a constant value. Thus, neither low- nor high-temperature hydrothermal systems can be significantly affected by mineral

carbonation. This process seems to be restricted to areas where serpentinite is exposed to CO_2-rich fluids (e.g., due to magmatic degassing or metamorphic decarbonation of sediments) in a temperature range of approximately 150–300°C.

Carbonation of basaltic basement is almost exclusively by vein and void fill, and so is not considered a metasomatic process. However, old volcanic oceanic crust (>110 Ma) has appreciable amounts of carbonate, on the order of 5–6 wt.% $CaCO_3$, and the fluxes related to carbonate formation roughly offset the volcanic degassing fluxes of CO_2 (Staudigel et al. 1996; Alt and Teagle 1999). The formation of the basaltic, oceanic crust can therefore be considered roughly CO_2 neutral.

8.3 Diffusional Metasomatism

In contrast to infiltrational metasomatism, diffusional metasomatism is driven by chemical potential gradients present at lithological boundaries. Although an intergranular fluid is required, fluid flow sensu stricto is not necessary for chemical changes, but might be superimposed (see discussion). In the following sections, steatitization and rodingitization are presented as two prominent examples of metasomatism driven by chemical gradients at the interfaces of contrasting lithologies.

8.3.1 Silica-Metasomatism of Seafloor Serpentinite

A talc rock, often referred to as steatite, can form at the expense of serpentinized peridotite where excess silica is available. Among other peculiar geochemical characteristics, serpentinite features the lowest silica activities in terrestrial silicate systems, in particular under sub-greenschist facies conditions. At the seafloor the occurrence of talc in serpentinized peridotite or complete replacement of serpentinite by steatite is usually strongest in proximity to intrusions of gabbro (Bach et al. 2004) or plagiogranite (Jöns et al. 2009, 2010; Morishita et al. 2009), that provide silica during hydrothermal alteration. Talc-rich fault rocks are particularly common on detachment surfaces where they localize shear stress during the tectonic uplift of Oceanic Core Complexes at slow- and ultraslow-spreading ridges (Escartín et al. 2003; Boschi et al. 2006b; MacLeod et al. 2009). Similar rocks have been documented in (or near) oceanic fracture zones and within non-transform offset zones where ultramafic rocks are exposed on the seafloor (Kimball et al. 1985; Bach et al. 2004; D'Orazio et al. 2004; Dias and Barriga 2006). In contrast to talc-schist in detachment faults, talc mimicking serpentinite mesh textures indicates that Si-metasomatism can proceed under static conditions (Bach et al. 2004).

In the reaction path model calculated for a temperature of 400°C and 1 kbar pressure (Fig. 8.6) we use heated seawater that has been equilibrated with gabbro and equilibrate this fluid with partly serpentinized harzburgite to emulate Si-

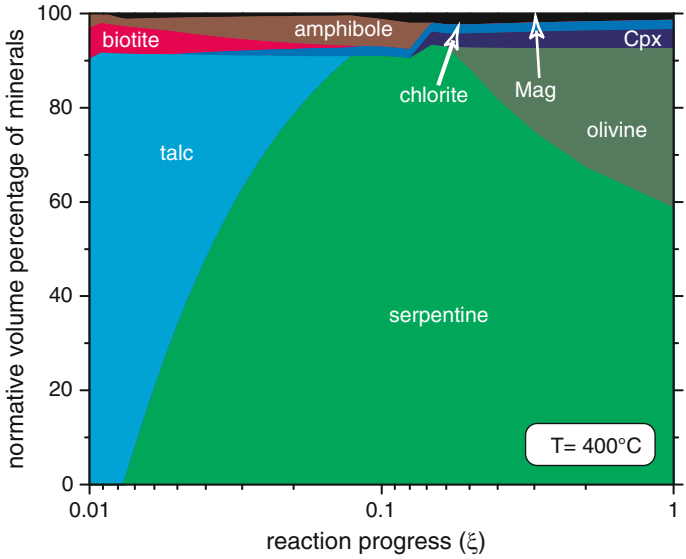

Fig. 8.6 Reaction path model of steatitization. Fluid is seawater reacted with basalt (Klein 2004) for a water-to-rock ratio of 1. Rock is harzburgite (Ol:Opx:Cpx = 80:15:5 in vol.%)

metasomatism. The partly serpentinized harzburgite is chiefly composed of olivine, minor amounts serpentine, clinopyroxene, chlorite, and magnetite. Upon infiltration with the silica-rich fluid, that is with increasing water-to-rock ratio (w/r), serpentine and magnetite form at the expense of olivine. When olivine is exhausted, the rock is predicted to be mainly composed of serpentine and minor amounts of magnetite, clinopyroxene, and chlorite. With increasing w/r, biotite precipitates, indicating the increasing control of the gabbro on phase equilibria, clinopyroxene is replaced by tremolite (a solid solution consisting of tremolite and ferro-actinolite), and chlorite dissolves. With further increase of w/r, talc replaces serpentine and magnetite dissolves. At the end of the model run the rock consists of more than 90 volume% talc as well as minor amounts of tremolite and biotite. Apart from the influence on the chemical composition of the oceanic crust, the occurrence of such talc-rich rock is of major importance for the localization of fault zones within the oceanic crust, which in turn might promote infiltrational metasomatism (see Sect. 8.4 "Metasomatism and deformation").

8.3.2 Rodingitization of Gabbro During Serpentinization of Abyssal Peridotite

Rodingite, a Ca-rich and silica-poor rock, is always associated with serpentinites. Therefore, rodingite is believed to form when mafic to felsic rocks interact with fluids that have previously been affected by reactions with ultramafic rocks (Thayer

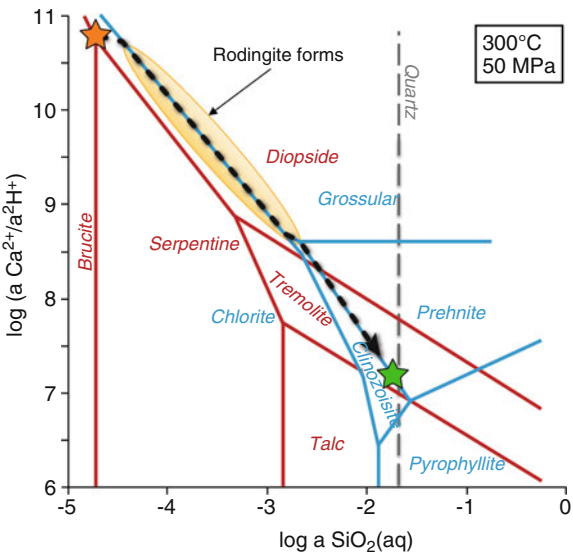

Fig. 8.7 Phase diagram of the systems MgO-SiO_2-H_2O and CaO-Al_2O_3-SiO_2-H_2O. Stable phase assemblages in hydrated ultramafic and mafic rocks are represented by *dots*. As serpentinization fluids encounter more and more basalt, they will evolve along the path indicated and will make rodingite (diopside-grossular-chlorite) (Redrawn from Bach and Klein 2009)

1966; Coleman 1967; Frost 1975; Evans 1977; Bach and Klein 2009). Serpentinization reactions generate alkaline, Ca-rich, and Si-poor fluids (Barnes and O'Neil 1969; Seyfried and Dibble 1980; Janecky and Seyfried 1986; Seyfried et al. 2007; Klein et al. 2009). Fluids influenced by serpentinization reactions are known from mid-ocean ridge settings (Kelley et al. 2001, 2005; Charlou et al. 2002; Schmidt et al. 2007), ophiolites (Feth et al. 1961; Barnes et al. 1967; Neal and Stanger 1983; Abrajano et al. 1988), and forearc regions of subduction zones (Mottl et al. 2003, 2004). Rodingites have been found in a range of tectonic settings, including seafloor spreading centers (Aumento and Loubat 1971; Honnorez and Kirst 1975; Bideau et al. 1991; Hekinian et al. 1993), rifted continental margins (Beard et al. 2002), and ophiolites (Barriga and Fyfe 1983; Hatzipanagiotou and Tsikouras 2001; Austrheim and Prestvik 2008; Iyer et al. 2008). Rodingitization is a metasomatic process, and the dominant mass transfers involved are removal of silica and addition of Ca (Coleman 1967).

Based on phase equilibria in the CMASH system, Bach and Klein (2009) conclude that at a pressure of 500 bar, rodingitization can proceed below ca. 300°C, where the composition of serpentinization fluids is buffered by the brucite–serpentine–diopside equilibrium (Fig. 8.7). At temperatures higher than 400°C, brucite is absent and the fluids are buffered by the talc–tremolite–serpentine equilibrium. Such fluids, e.g., the serpentinite-hosted black smoker fluids from the Logatchev and Rainbow hydrothermal fields on the Mid-Atlantic ridge, cannot form rodingite when interacting with gabbro. Instead these fluids promote the formation of monomineralic chlorite (blackwalls) at mafic/ultramafic boundaries. Furthermore, Bach and Klein (2009) conclude that rodingitization is most likely a result of diffusional metasomatism, driven by steep gradients in protons and silica activity set by the serpentine–brucite–diopside equilibrium on the ultramafic side

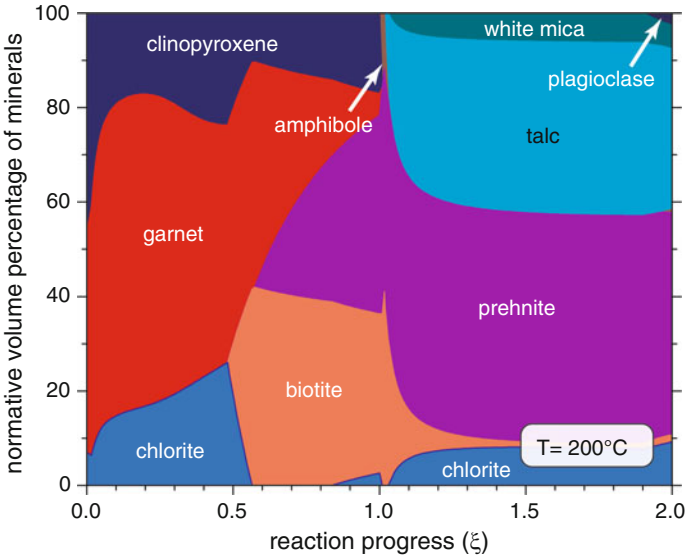

Fig. 8.8 Reaction path model of rodingitization. Fluid is seawater reacted with harzburgite (Ol:Opx:Cpx = 80:15:5 in vol%) at a water-to-rock ratio of 1. Rock is basalt (Klein 2004)

and the tremolite–albite–clinozoisite–quartz equilibrium on the mafic side of the lithological contact (Fig. 8.7). In contrast, the activity gradient in Ca^{2+} is virtually zero. Diffusive mass transfer of Ca into the rodingite is likely related to diffusion of hydroxo species (Bach and Klein 2009). Following this logic, rodingitization is not caused by the Ca-rich nature of the serpentinization fluids, but by the stability of Ca-silicates (such as diopside and hydrogrossular) at the low silica activities imposed by nearby serpentinite. This notion is in agreement with results of Frost and Beard (2007) and Frost et al. (2008), who also argued that Si loss, driven by a low $aSiO_2$ during serpentinization, and not Ca addition, is the principal metasomatic mechanism of rodingitization.

In the reaction path model, presented in Fig. 8.8, we use heated seawater that has been equilibrated with harzburgite at 200°C and 1 kbar pressure as the starting fluid for rodingitization. Gabbro is titrated into the serpentinization fluid and equilibrated with it at each incremental step of the reaction progress. The model results can be regarded as representing local fluid–rock equilibria with increasing distance from the gabbro/peridotite contact into the gabbro body. At the contact, the fluid is entirely controlled by reactions with harzburgite. Away from the contact, i.e. as w/r decreases, reactions with the gabbro will dominate the fluid compositions. From the peridotite/gabbro contact into the gabbro the predicted mineral zones are as follows: garnet → garnet + chlorite → clinopyroxene + chlorite + garnet → clinopyroxene + chlorite + garnet + biotite → prehnite + clinopyroxene + chlorite + garnet + biotite. Tremolite, replacing chlorite and talc, as well as the appearance of sodic plagioclase, is also predicted by the reactive path made.

For rodingitization at 300°C and 500 bar, Bach and Klein (2009) predict slightly different mineral transitions. These include clinopyroxene + garnet → garnet + clinopyroxene + chlorite → garnet + clinopyroxene + chlorite + epidote-ss (clinzoisite-epidote solid solution) → clinopyroxene + epidote-ss + chlorite → clinopyroxene + epidote-ss + tremolite → clinopyroxene + epidote-ss + tremolite + prehnite → prehnite + epidote-ss + tremolite → prehnite + epidote-ss + tremolite + plagioclase. Note that at 300°C the epidote-ss is predicted to be dominant while at 200°C it is predicted to be absent. Field observations of alteration sequences in rodingitized diorite from the JM Asbestos Mine in Québec reveal alteration patterns closely resembling the 300°C model, which is consistent with results from fluid inclusion analysis (Normand and Williams-Jones 2007). Remarkably, biotite is predicted to only occur between the zone of rodingitization and the prehnite-rich zone in the model calculated for 200°C and 1 kbar. Consistent with this result, Austrheim and Prestvik (2008) found phlogopite between the rodingite zone and clinozoisite zone in the Leka ophiolite, Norway.

8.4 Metasomatism and Deformation

Apart from the chemical compositions of fluids and rocks, which are the major driving forces for metasomatic element transport, the physical properties of the rocks also impose a strong influence, either promoting or inhibiting metasomatism. Feedback mechanisms of metasomatism and deformation are based on the fact that metasomatism leads to changing phase relations. In many cases this change is accompanied by a volume increase that is necessarily expected to lead to some internal deformation. This can clearly be seen when comparing the densities of the precursor rocks and the metasomatic products: e.g., a peridotite has a density of ca. 3.1–3.4 g/cm^3. If this rock is completely steatitized, the density decreases to ca. 2.8–2.9 g/cm^3, which in turn would mean that the volume increases, causing deformation. But of course elemental gains and losses have to be taken into account. Gresens (1967) pointed out that the composition-volume-relationship of metasomatic reactions is worth considering. In this work it is emphasized that only with a profound knowledge of the chemical composition, in combination with knowledge of how the rock volume has changed, can solid statements about elemental gains and losses be made. There is not always clear petrographic evidence for volumetric changes during metasomatism. In some cases, pseudomorphic replacement textures can indicate that no volume change has taken place during metasomatism. Austrheim et al. (2008) report zircon occurrences in metasomatically overprinted gabbros. As zircon was inert during metasomatism, Austrheim et al. (2008) were able to use its presence, within the reaction textures, as a physical reference frame that allowed deducing the direction of movement of the reaction fronts and to finally state that related metasomatic mineral reactions were not affecting the rock volume. However, the presence of such inert minerals is surely an exceptional case and the described method cannot be applied to all

metasomatic rocks. In most rocks, metasomatic reactions tend to be complete and precursor assemblages are completely consumed, inhibiting detailed determination of volume changes and related internal deformation.

On a larger scale, the presence of metasomatic rocks can influence the deformational behavior of substantial areas of the oceanic crust. Metasomatic mineral assemblages formed in rocks from the oceanic lithosphere commonly contain mechanically weak sheet silicates, e.g., plagioclase in gabbroic rocks might be replaced by chlorite or the olivine and orthopyroxene from an abyssal peridotite might become steatized (i.e. replaced by talc). Concerning their rheological behavior, such hydrated rocks are weaker (e.g., Escartín et al. 2001, 2008) and thus shearing will more easily affect these lithologies. In turn, formation of shear zones will promote further ingress of reactive fluids, supporting further metasomatism by increasing the local fluid-to-rock mass ratio. This feedback mechanism directly influences all types of infiltration metasomatism, which is strongly dependent on the fluid-to-rock ratio. However, this process brings fluids to previously dry portions of the oceanic crust and might indirectly support even diffusional metasomatism.

Understandably, the interplay between deformation and metasomatism is restricted to those parts of the oceanic lithosphere that undergo deformation. Ideal locations are transform faults, which occur along almost all mid-ocean ridges. In fast-spreading crust, however, transform faults are comparatively short-lived phenomena and the influence of tectonic processes is, compared to the intense magmatism, not of major importance. The same holds true also for ultraslow-spreading ridges that lack transform faults. Oceanic crust at slow-spreading ridges, such as at the Mid-Atlantic ridge, accommodates a large part of its extension by tectonic processes, and magmatism is spatially and temporally strongly variable. Here, transform faults are long-lived and therefore they are important structures for bringing significant amounts of water to lower crustal levels. Another structural characteristic specific to slow-spreading ridges is the occurrence of large low-angle detachment faults and the formation of oceanic core complexes. The latter are morphologically inside corner highs, and expose structurally deep footwall rocks at the ocean floor. In certain cases such detachment faults are proposed to be pathways for fluids venting at seafloor hydrothermal fields (e.g., McCaig et al. 2007). Finally, bending-related faulting of the oceanic lithosphere takes place near subduction zones, leading to trench-parallel faults that might reach deep enough to promote serpentinization in the lithospheric mantle (Ranero et al. 2003).

The main evidence for the assumption of increased fluid flow on shear zones is the occurrence of distinct mineral assemblages on fault surfaces, so-called “fault schists” (for a review of fault schist occurrences see Boschi et al. 2006a). They reveal a schistose texture and a “soapy” feel. Typical minerals are chlorite, talc and tremolitic to actinolitic amphibole. The major variables in controlling the formation of fault schist mineral assemblages are temperature, pressure, and the chemical composition of the fluid phase. Thus, these fault-related rocks are potentially important recorders of P-T, fluid and deformation conditions in oceanic shear zones. However, due to the simple mineralogy, determination of the formation

conditions necessary for fault schists is generally not straightforward. Oxygen isotope analyses provide evidence that fluids causing metasomatism on oceanic faults are dominated by seawater (Alt et al. 2007; McCaig et al. 2007; Jöns et al. 2009), whereas the influence of magmatically derived fluids is generally subordinate, especially in slow-spreading MOR settings.

Oceanic detachment faults, which are expressions of extensional tectonics that lead to exposure of oceanic core complexes, initiate as steep normal faults at depth, but through footwall rotation they shallow into low-angle normal faults. As they form in slow-spreading crust, they are generally long-lived features, which makes them preferred locations for intense fluid flow and fault schist formation. Temperature estimates based on recrystallization of mafic minerals (e.g., olivine), indicate that shear zones reach down to depths of granulite-facies conditions. In a few cases, temperatures are estimated using Ti-in-zircon thermometry, resulting in average values of ca. 820°C (Jöns et al. 2009). The fact that zircon is a common accessory mineral, within some ultramafic-hosted fault schists, points to the involvement of a magmatic melt, either of gabbroic or even of plagiogranitic composition. Magmatism in the root zone of the detachment fault system provides (a) heat for driving hydrothermal circulation, and (b) a chemical potential gradient promoting metasomatic mass transfer. Lithological differences, e.g., between abyssal peridotites and gabbroic intrusions, present the basis for another feedback mechanism. Comparing the alteration behavior under fluid saturated conditions, mafic and more evolved lithologies become hydrated at considerably higher temperatures than ultramafic rocks. This is based on the fact that at low pressures olivine contained in peridotites is stable down to temperatures of ca. 400°C. Below this temperature it breaks down to form serpentine + magnetite ± brucite, which would weaken the rock. Heterogeneous, slow-spreading lithosphere often features gabbroic intrusions and/or plagiogranitic melt impregnations hosted in mantle peridotite. These rocks are hydrated at much higher temperatures of ca. 600°C. Their hydration is predominantly determined by the stability of plagioclase under hydrous conditions. Chlorite and/or talc are among the products of plagioclase breakdown. The presence of such hydrous phyllosilicates under temperatures of ca. 600°C is of major importance for the formation of amphibolite-facies shear zones, the exhumation of lower-crustal rocks, and further fluid ingress. Understanding mineral phase relations in fault schists is of major importance for unraveling the metasomatic and uplift history of rocks from oceanic detachment fault systems, but further work is needed to obtain a more comprehensive picture.

8.5 Concluding Remarks

By default, layer-cake basaltic crust does not show diffusional metasomatism, because the rocks are all basaltic in composition. So the large gradients in chemical potential required to drive reactions and mass transfer are not available. In basaltic crust, metasomatism *sensu stricto* is restricted to hydrothermal upflow zones, where

upwelling hydrothermal solutions undergo changes in pressure and temperature and cause replacement reactions in the fractured rock through which they come up. These reactions comprise replacement of feldpar by mica (sericitization), pyritization, and silicification. Metasomatic zones are not generally well-developed, although a zone of sericitization may lead into a zone in which pyritization and silicification prevail. Chloritization is common in the peripheral and deep parts of upflow zones. It is caused by interaction of basaltic rock with seawater-like solutions that have not been equilibrated with rock. These fluids are abundant where seawater is entrained into upwelling hydrothermal fluids. Mixing of seawater and hydrothermal fluids causes the formation of chlorite and pyrite as well as quartz. The presence of magnesian chlorite indicates the seawater-dominated nature of the interacting fluids.

In heterogeneous crust accreted at slow spreading ridges, lithological contrasts are much greater than in the layer-cake mafic crust. Contrasts in chemical potential between mafic and ultramafic lithologies, in particular, are drivers of intense metasomatic reactions and mass transfers. Rodingitization of gabbro dikes in the lithospheric mantle is a good example of diffusional metasomatism. Although rodingites are associated with the Ca-rich nature of serpentinization fluids, thermodynamic calculation indicate that it is the pronounced difference in proton and silica activity that drives rodingitization. The differences in Ca-concentration between intergranular fluids in gabbro and peridotite are too small to explain rodingitization. Mass transfer of Ca is driven by large gradients in Ca-hydroxo-species and the stability of Ca-rich phases (diopside, hydrogrossular) at low silica-activities imposed by serpentinization of the hosting peridotite. Likewise, talc-alteration of serpentinite can be diffusional, if the serpentinites are juxtaposed against a large mass of gabbro. The type of metasomatic reaction observed (rodingitization of gabbro or steatitization of serpentinite) depends on the predominance of one lithology over the other and the flow path of the fluid. If a small ultramafic body of rock is surrounded by metapelitic schist (Read 1934; Fig. 8.9a), and there is no fluid flow during retrograde metamorphism, a concentric metasomatic zoning will develop, which is controlled by the quasi-infinite size of the intergranular fluid in the country rock driving replacement reactions within the serpentinite. Only in the center of objects greater than several meters may serpentinite be preserved. If there is fluid flow, however, the zoning will not be concentric. This can be seen in a classic example from Hess (1933), where a serpentinite body, embedded in a quartz-mica schist, has developed a talc zone on one end and a chlorite zone on the other. This type of zoning is to be expected if fluids were flowing through the system in the general direction indicated by the arrows in Fig. 8.9b. The quartz-saturated fluids coming from the schist will cause steatitization of serpentinite upon entering the ultramafic body. If the fluid flux is small, the zone of talc alteration is narrow, because silica will be reacted away quickly and the fluid loses its ability to make talc along its flow path within the ultramafic pod. It will become buffered by reactions with the ultramafic rock and corrosive with regards to the felsic country rock, once it leaves the ultramafic body. In the example given in this chapter the fluid caused chloritization of the country rock. Fluid flow controls the shape of the

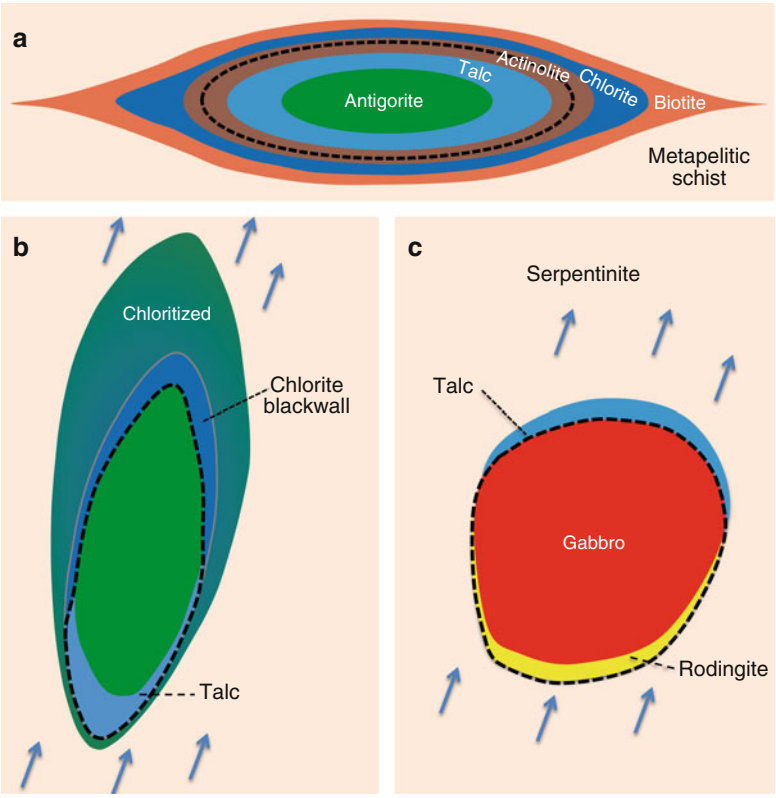

Fig. 8.9 (**a**) Symmetrical metasomatic zoning around an ultramafic pod in a metapelic schist (from Read (1934) in Winter (2001)). (**b**) Asymmetrical metasomatic zoning around an ultramafic pod in a quartz-mica schist (Hess 1933). (**c**) Hypothesized, asymmetrical zoning around a gabbro intrusion in the lithospheric mantle at a slow-spreading, magma-starved ridge segment. *Dashed line* marks pre-metasomatic contact between the rock body and the rock enclosing it

metasomatic zones if the fluid travels at a pace that exceeds the pace of element diffusion. This is not infiltration metasomatism but rather a special case of diffusional metasomatism where directed fluid flow affected the spatial distribution of the metasomatic zones.

Fluid flow is common within the oceanic crust, because of the large amounts of advective heat transport in huge fractions of the seafloor. We can expect to find exactly the same type of asymmetric metasomatic zoning around gabbro bodies in the lithospheric mantle. Indeed, we find both rodingitized outer zones of gabbro bodies as well as steatite halos in meta-ultramafic rocks at the contact with gabbroic rocks (Fig. 8.9c). These associations are common, because of large differences in the silica activity in intergranular fluid in mafic rocks on the one hand and, on the other hand, ultramafic rocks are sustained over a wide range of temperatures (Fig. 8.10). Intergranular fluids in serpentinite will cause rodingitization just as intergranular fluids, controlled by reactions with gabbro, will cause steatization of

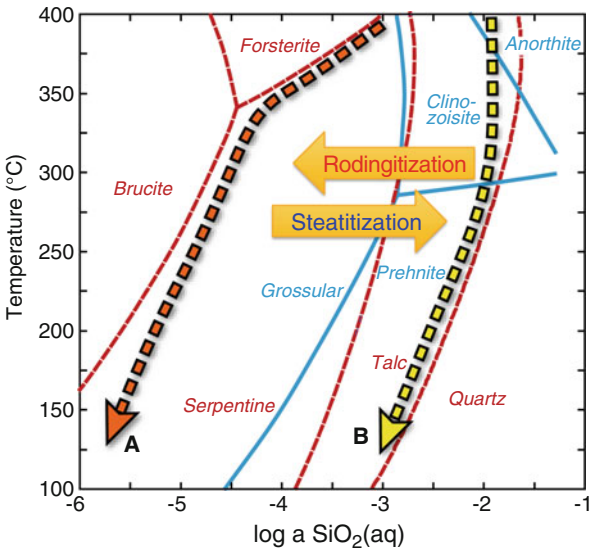

Fig. 8.10 Phase diagram of the systems $MgO–SiO_2–H_2O$ and $CaO–Al_2O_3–SiO_2–H_2O$, indicating that, throughout a large temperature range, serpentinizing fluids (path A) will make rodingite when encountering gabbro, while fluids controlled by hydrothermal alteration of gabbro will steatize serpentinite (Redrawn from Bach and Klein 2009)

the adjacent serpentinite. If fluid flow is massive, like in hydrothermal upflow zones, steatite pipes will develop such as seen in the basement underlying peridotite-hosted hydrothermal systems (Dias and Barriga 2006). Thus silica-metasomatism can be infiltrational where the Si is derived from fluid rock-reactions outside the peridotite and transported along faults, or diffusional where metasomatic mass transport of silica is promoted along a geochemical potential gradient between contrasting lithologies. This can explain the textural variety of steatitization observed (Bach et al. 2004; Boschi et al. 2006a, b).

The reactive nature of mafic-ultramafic boundaries is likely to play a crucial role in the exhumation of lithospheric mantle. The presence of mafic components in mantle rocks will favor the formation of chlorite and talc at high temperatures. These phases are rare in meta-ultramafic rocks in which the main phase (olivine) is stable above 350°C (at $P \leq 1$ kbar). Detachment fault rocks are commonly hybrid mantle – magmatic rocks (Escartín et al. 2003; Boschi et al. 2006a; Jöns et al. 2009). These rocks are susceptible to alteration to talc, tremolite, and chlorite at temperatures around 500–600°C, when the un-impregnated peridotite bordering the impregnated zones remains largely unaltered. The mechanical weakening of the altered domains will catch most of the strain and deformation-enhanced fluid ingress will lead to further hydrothermal alteration. These positive feedbacks between alteration, mechanic weakening, and fluid influx would make lithologies that are prone to hydration at elevated temperatures predestined to become areas of strain localization during exhumation. This model can also account for the fact that some oceanic core complexes appear to have large gabbroic intrusions in their centers, as deformation is predicted to be localized at contacts between gabbro and peridotite. Infiltrational metasomatism in a detachment fault seems to be dominant in some areas (McCaig et al. 2007) but not in others (Jöns et al. 2009). It is likely

that hybrid mantle-magmatic lithologies drive strain localization under amphibolite-facies conditions. The extent of subsequent infiltrational metasomatism is highly variable and depends on whether or not the detachment fault acted as a hydrothermal upflow zone.

Acknowledgments We acknowledge support from the Deutsche Forschungsgemeinschaft grant BA1605/1 and BA1605/2 as well as the Marum Research Cluster of Excellence. F. Klein acknowledges the financial support by an Ocean Ridge Initiative Research Award and the Deep Ocean Exploration Institute at the Woods Hole Oceanographic Institution. We are particularly grateful to Michael Hentscher for assembling the thermodynamic database. The paper benefited from insightful reviews of J. S. Beard and F. Pirajno. We thank Dan Harlov and Håkon Austrheim for helpful editorial advise.

Appendix

Thermodynamic calculations were used to predict phase relations in ocean floor metasomatism. In fluid-rock interactions, factors controlling the stable mineral assemblages, besides temperature and pressure, are the primary rock composition, the composition of the fluid entering the system, and the mass flux of that fluid through the system. The dependencies of the metasomatic assemblages on fluid flux and rock composition can be examined using simple isothermal and isobaric geochemical titration models, in which rock is added to a constant amount of H_2O. In oceanic crust metasomatism, the composition of the fluid entering the system (oceanic crust) is seawater. The composition of seawater is from Klein et al. (2009) as is the composition of mantle peridotite. Average mid-ocean ridge basalt from the mid-Atlantic Ridge (Klein 2004) was used as a starting composition for the basalt. In the models of diffusional metasomatism, the fluid into which the rock is titrated is seawater that has reacted with one rock type, before it is allowed to react with the other one. For instance, in the steatitization model, seawater was first equilibrated with basalt and the resulting fluid was reacted with serpentinite.

Geochemical reaction path modeling was conducted using EQ3/6 (Wolery and Jarek 2003). The database was compiled for a pressure of 100 MPa using SUPCRT92 (Johnson et al. 1991). Specifics about the database and calculations (solid solutions, activity models, etc.) are provided in Bach and Klein (2009), McCollom and Bach (2009), and Klein et al. (2009).

In all diagrams displaying results of the reaction path model calculations, we plot predicted modes versus a reaction progress number (ξ). ξ is scaled to the amount of rock titrated into the system. This must not be confused with physical water-to-rock ratios and we thus purposely do not report the mass of rock added in the models. The rock mass was chosen merely as an internal parameter to have the model predict the full range of a metasomatic sequence. In all models, $\xi = 1$ corresponds to approximately equal masses of rock and water. In other words, at $\xi = 1$, the intergranular fluid is entirely controlled by the rock added. As ξ approaches zero, the rock is more and more controlled by the composition of the

externally buffered fluid (seawater, intergranular fluids in basalt or in peridotite, etc.). In the models of diffusional metasomatism, one can look at ξ as a measure of distance to the interface between lithologies. Small ξ means close to the contact. With increasing ξ we move away from the contact and into the lithology that is being metasomatized under the influence of an externally buffered fluid.

References

Abrajano TA, Sturchio NC, Bohlke JK, Lyon GL, Poreda RJ, Stevens CM (1988) Methane-hydrogen gas seeps, Zambales Ophiolite, Philippines: deep or shallow origin? Chem Geol 71 (1–3):211–222

Alt JC (1995) Subseafloor processes in mid-ocean ridge hydrothermal systems. In: Humphris SE, Zierenberg RA, Mullineaux LS, Thomson RE (eds) Seafloor hydrothermal systems, Geophysical monograph. American Geophysical Union, Washington, DC, pp 85–114

Alt JC, Teagle DAH (1998) Probing the TAG hydrothermal mound and stockwork: oxygen-isotopic profiles from deep ocean drilling. In: Humphris SE, Herzig PM, Miller DJ, Zierenberg RA (eds) Proceedings of the ocean drilling program, scientific results, vol 158. Ocean drilling program, College Station, pp 285–295

Alt JC, Teagle DAH (1999) The uptake of carbon during alteration of ocean crust. Geochim Cosmochim Acta 63:1527–1535

Alt JC, Honnorez J, Laverne C, Emmermann R (1986) Hydrothermal alteration of a 1 km section through the upper oceanic crust. DSDP Hole 504B: mineralogy, chemistry and evolution of seawater-basalt interactions. J Geophys Res 91:309–335

Alt JC, Laverne C, Vanko D, Tartarotti P, Teagle DAH, Bach W, Zuleger E, Erzinger J, Honnorez J (1996a) Hydrothermal alteration of a section of upper oceanic crust in the eastern equatorial Pacific: a synthesis of results from DSDP/ODP Legs 69, 70, 83, 111, 137, 140, and 148 at Site 504B. In: Alt JC, Kinoshita H, Stokking LB, Michael PJ (eds) Proceedings of the ocean drilling program, scientific results, vol 148. Ocean drilling program, College Station, pp 417–434

Alt JC, Teagle DAH, Laverne C, Vanko D, Bach W, Honnorez J, Becker K (1996b) Ridge flank alteration of upper oceanic crust in the eastern Pacific: a synthesis of results for volcanic rocks of Holes 504B and 896A. In: Alt JC, Kinoshita H, Stokking LB, Michael PJ (eds) Proceedings of the ocean drilling program, scientific results, vol 148. Ocean drilling program, College Station, pp 435–450

Alt JC, Shanks WC, Bach W, Paulick H, Garrido CJ, Beaudoin G (2007) Hydrothermal alteration and microbial sulfate reduction in peridotite and gabbro exposed by detachment faulting at the Mid-Atlantic Ridge, 15°20′N (ODP Leg 209): a sulfur and oxygen isotope study. Geochem Geophys Geosyst 8(8):Q08002. doi:08010.01029/02007GC001617

Andreani M, Luquot L, Gouze P, Godard M, Hoise E, Gibert B (2009) Experimental study of carbon sequestration reactions controlled by the percolation of CO_2-rich brine through peridotites. Environ Sci Technol 43(4):1226–1231

Anonymous (1972) Penrose field conference on ophiolites. Geotimes 17:24–25

Aumento F (1971) Uranium content of mid-ocean ridge basalts. Earth Planet Sci Lett 11:90–94

Aumento F, Loubat H (1971) The Mid-Atlantic Ridge near 45 °N. XVI. Serpentinized ultramafic intrusions. Can J Earth Sci 8(6):631–663

Austrheim H, Prestvik T (2008) Rodingitization and hydration of the oceanic lithosphere as developed in the Leka ophiolite, north-central Norway. Lithos 104(1–4):177–198

Austrheim H, Putnis CV, Engvik AK, Putnis A (2008) Zircon coronas around Fe-Ti oxides: a physical reference frame for metamorphic and metasomatic reactions. Contrib Mineral Petrol 156:517–527

Bach W, Klein F (2009) The petrology of seafloor rodingites: insights from geochemical reaction path modeling. Lithos 112(1–2):103–117

Bach W, Alt JC, Niu Y, Humphris SE, Erzinger J, Dick HJB (2001) The geochemical consequences of late-stage low-grade alteration of lower ocean crust at the SW Indian Ridge: results from ODP Hole 735B (Leg 176). Geochim Cosmochim Acta 65:3267–3287

Bach W, Peucker-Ehrenbrink B, Hart SR, Blusztajn JS (2003) Geochemistry of hydrothermally altered oceanic crust: DSDP/ODP Hole 504B – Implications for seawater-crust exchange budgets and Sr- and Pb-isotopic evolution of the mantle. Geochem Geophys Geosyst 4(3). doi:10.1029/2002GC000419

Bach W, Garrido CJ, Harvey J, Paulick H, Rosner M (2004) Seawater-peridotite interactions – first insights from ODP Leg 209, MAR 15ºN. Geochem Geophys Geosyst 5(9):Q09F26. doi:10.1029/2004GC000744

Baker ET, Chen YJ, Phipps Morgan JP (1996) The relationship between near-axis hydrothermal cooling and the spreading rate of mid-ocean ridges. Earth Planet Sci Lett 142:137–145

Baker ET, Embley RW, Walker SL, Resing JA, Lupton JE, Nakamura K, de Ronde CEJ, Massoth GJ (2008) Hydrothermal activity and volcano distribution along the Mariana arc. J Geophys Res 113:B08S09. doi:10.1029/2007JB005423

Banerjee NR, Gillis KM, Muehlenbachs K (2000) Discovery of epidosites in a modern oceanic setting, the Tonga forearc. Geology 28(2):151–154

Barnes I, O'Neil JR (1969) The relationship between fluids in some fresh alpine-type ultramafics and possible modern serpentinization, Western United States. Geol Soc Am Bull 80: 1948–1960

Barnes I, Lamarche VC, Himmelberg G (1967) Geochemical evidence of present-day serpentinization. Science 156:830–832

Barriga FJAS, Fyfe WS (1983) Development of rodingite in basaltic rocks in serpentinites, East Liguria, Italy. Contrib Mineral Petrol 84:146–151

Beard JS, Fullagar PD, Sinha AK (2002) Gabbroic pegmatite intrusions, Iberia Abyssal Plain, ODP Leg 173, Site 1070: magmatism during a transition from non-volcanic rifting to sea-floor spreading. J Petrol 43(5):885–905

Bickle MJ, Teagle DAH (1992) Strontium alteration in the Troodos ophiolite: implications for fluid fluxes and geochemical transport in mid-ocean ridge hydrothermal systems. Earth Planet Sci Lett 113:219–237

Bideau D, Hebert R, Hekinian R, Cannat M (1991) Metamorphism of deep-seated rocks from the Garrett Ultrafast transform (East Pacific rise near 13°25′S). J Geophys Res 96:10079–10099. doi:10.1029/91JB00243

Bird P (2003) An updated digital model of plate boundaries. Geochem Geophys Geosyst 4(3):1027. doi:1010.1029/2001GC000252

Bischoff JL, Rosenbauer RJ (1985) An empirical equation of state for hydrothermal seawater (3.2 percent NaCl). Am J Sci 285:725–763

Bischoff JL, Rosenbauer RJ (1996) The alteration of rhyolite in CO_2 charged water at 200°C and 350°C: the unreactivity of CO_2 at higher temperature. Geochim Cosmochim Acta 60(20):3859–3867

Blackman DK, Canales P, Harding A (2009) Geophysical signatures of oceanic core complexes. Geophys J Int 178:593–613

Bogdanov YA, Bortnikov NS, Vikentyev IV, Gurvich EG, Sagalevich AM (1997) A new type of modern mineral-forming system: black smokers of the hydrothermal field at 14°45′N latitude, Mid-Atlantic Ridge. Geol Ore Deposit 39(1):58–78

Böhlke JK (1989) Comparison of metasomatic reactions between a common CO_2-rich vein fluid and diverse wall rocks; intensive variables, mass transfers, and Au mineralization at Alleghany, California. Econ Geol 84(2):291–327

Boschi C, Früh-Green GL, Escartin J (2006a) Occurrence and significance of serpentinite-hosted talc- and amphibole-rich fault rocks in modern oceanic settings and ophiolite complexes; an overview. Ofioliti 31(2):129–140

Boschi C, Früh-Green GL, Delacour A, Karson JA, Kelley DS (2006b) Mass transfer and fluid flow during detachment faulting and development of an oceanic core complex Atlantis Massif (MAR 30°N). Geochem Geophys Geosyst 7:Q01004. doi:10.1029/2005GC001074

Bowers TS, Taylor HP Jr (1985) An integrated chemical and stable-isotope model of the origin of midocean ridge hot spring systems. J Geophys Res 90, 12583–12606. doi:10.1029/JB090iB14p12583

Cann JR (1969) Spilites from the Carlsberg Ridge, Indian Ocean. J Petrol 10:1–19

Cannat M, Mével C, Maia M, Deplus C, Durand C, Gente P, Agrinier P, Belarouchi A, Dubuisson G, Humler E, Reynolds J (1995) Thin crust, ultramafic exposures, and rugged faulting patterns at the Mid-Atlantic Ridge (22°–24°N). Geology 23:49–52

Charlou J-L, Donval J-P, Fouquet Y, Jean-Baptiste P, Holm N (2002) Geochemistry of high H_2 and CH_4 vent fluids issuing from ultramafic rocks at the Rainbow hydrothermal field (36º14′N, MAR). Chem Geol 191:345–359

Cheminee J-L, Stoffers P, McMurtry G, Richnow H, Puteanus D, Sedwick P (1991) Gas-rich submarine exhalations during the 1989 eruption of Macdonald Seamount. Earth Planet Sci Lett 107:318–327

Chidester AH, Cady WM (1972) Origin and emplacement of Alpine-type ultramafic rocks. Nature 240:27–31

Cogne J-P, Humler E (2004) Temporal variations of oceanic spreading and crustal production rates during the last 180 My. Earth Planet Sci Lett 227:427–439

Coleman RG (1967) Low-temperature reaction zones and alpine rocks of California, Oregon, and Washington, vol 1247, US Geoligal Survey Bulletin. U.S. Govt. Print. Off, Washington, DC

Dabitzias SG (1980) Petrology and genesis of the Vavdos cryptocrystalline magnesite deposits, Chalkidiki Peninsula, northern Greece. Econ Geol 75(8):1138–1151

de Ronde CEJ, Baker ET, Massoth GJ, Lupton JE, Wright IC, Feely RA, Greene RR (2001) Intra-oceanic subduction-related hydrothermal venting, Kermadec volcanic arc, New Zealand. Earth Planet Sci Lett 193:359–369

Dias AS, Barriga F (2006) Mineralogy and geochemistry of hydrothermal sediments from the serpentinite-hosted Saldanha hydrothermal field (36°34′N; 33°26′W) at MAR. Mar Geol 225 (1–4):157–175

Dick HJB, Natland JH, Alt JC, Bach W, Bideau D, Gee JS, Haggas S, Hertogen JGH, Hirth G, Holm PM, Ildefonse B, Iturrino GJ, John BE, Kelley DS, Kikawa E, Kingdon A, LeRoux PJ, Maeda J, Meyer PS, Miller DJ, Naslund HR, Niu Y, Robinson PT, Snow J, Stephen RA, Trimby PW, Worm H-U, Yoshinobu A (2000) A long in situ section of the lower ocean crust: results of ODP Leg 176 Drilling at the Southwest Indian Ridge. Earth Planet Sci Lett 179: 31–51

Dick HJB, Lin J, Schouten H (2003) An ultraslow-spreading class of ocean ridge. Nature 426:405–412

Dick HJB, Tivey MA, Tucholke BE (2008) Plutonic foundation of a slow-spreading ridge segment: oceanic core complex at Kane Megamullion, 23°30′N, 45°20′W. Geochem Geophys Geosyst 9(5):Q05014. doi:05010.01029/02007GC001645

D'Orazio M, Boschi C, Brunelli D (2004) Talc-rich hydrothermal rocks from the St. Paul and Conrad fracture zones in the Atlantic Ocean. Eur J Mineral 16:73–83

Elderfield H, Schultz A (1996) Mid-ocean ridge hydrothermal fluxes and the chemical composition of the ocean. Annu Rev Earth Planet Sci Lett 24:191–224

Elderfield H, Wheat CG, Mottl MJ, Monnin C, Spiro B (1999) Fluid and geochemical transport through oceanic crust: a transect across the eastern flank of the Juan de Fuca Ridge. Earth Planet Sci Lett 172:151–165

Escartín J, Hirth G, Evans B (2001) Strength of slightly serpentinized peridotites: implications for the tectonics of ocean lithosphere. Geology 29:1023–1026

Escartín J, Mevel C, MacLeod CJ, McCaig AM (2003) Constraints on deformation conditions and the origin of oceanic detachments: the Mid-Atlantic Ridge core complex at 15º45′N. Geochem Geophys Geosyst 4(8). doi:10.1029/2002GC000472

Escartín J, Andreani M, Hirth G, Evans B (2008) Relationship between the microstructural evolution and the rheology of talc at elevated pressures and temperatures. Earth Planet Sci Lett 268:463–475
Evans BW (1977) Metamorphisms of alpine peridotite and serpentinite. Annu Rev Earth Planet Sci 5:398–447
Feth JH, Rogers SM, Robertson E (1961) Aqua de Ney, California, a spring of unique chemical character. Geochim Cosmochim Acta 22:75–86
Frost BR (1975) Contact metamorphism of serpentinite, chloritic blackwall and rodingite at Paddy-Go-Easy Pass, central cascades, Washington. J Petrol 16:272–313
Frost BR (1985) On the stability of sulfides, oxides and native metals in serpentinite. J Petrol 26:31–63
Frost BR, Beard JS (2007) On silica activity and serpentinization. J Petrol 48:1351–1368
Frost BR, Beard JS, McCaig A, Condliffe E (2008) The formation of micro-rodingites from IODP Hole U1309D: key to understanding the process of serpentinization. J Petrol 49:1579–1588
Gass IG, Smewing JD (1973) Intrusion, extrusion and metamorphism at constructive margins: evidence from the Troodos Massif, Cyprus. Nature 242:26–29
Gerdemann SJ, Dahlin DC, O'Connor WK, Penner LR (2003) Carbon dioxide sequestration by aqueous mineral carbonation of magnesium silicate minerals. In: Second annual conference on carbon sequestration, Alexandria, May 5–8, 2003. Report no. DOE/ARC-2003-018, OSTI ID: 898299 8 pp
Gillis KM (1995) Controls on hydrothermal alteration in a section of fast-spreading oceanic crust. Earth Planet Sci Lett 134:473–489
Gillis KM (2002) The rootzone of an ancient hydrothermal system exposed in the Troodos ophiolite, Cyprus. J Geol 110:57–74
Graham D, Sarda P (1991) Mid-ocean ridge popping rocks – implications for degassing at ridge crests – comment. Earth Planet Sci Lett 105(4):568–573
Gregory RT, Taylor HP (1981) An oxygen isotope profile in a section of Cretaceous oceanic crust, Samail ophiolite, Oman: evidence for $\delta^{18}O$ buffering of the oceans by deep (>5 km) seawater-hydrothermal circulation at mid-ocean ridges. J Geophys Res 86:2737–2755
Gresens RL (1967) Composition-volume relationships of metasomatism. Chem Geol 2:47–65
Halls C, Zhao R (1995) Listvenite and related rocks: perspectives on terminology and mineralogy with reference to an occurrence at Cregganbaun, Co. Mayo, Republic of Ireland. Miner Deposita 30(3):303–313
Hansen LD, Dipple GM, Gordon TM, Kellett DA (2005) Carbonated serpentinite (listwanite) at Atlin, British Columbia: a geological analogue to carbon dioxide sequestration. Can Mineral 43:225–239
Harper GD, Bowman JR, Kuhns R (1988) A field, chemical, and stable isotope study of subseafloor metamorphism of the Josephine ophiolite, California-Oregon. J Geophys Res 93: 4625–4656
Hart RA (1970) Chemical exchange between seawater and deep ocean basalts. Earth Planet Sci Lett 9:269–279
Hart SR, Staudigel H (1982) The control of alkalies and uranium in seawater by ocean crust alteration. Earth Planet Sci Lett 58:202–212
Hatzipanagiotou K, Tsikouras B (2001) Rodingite formation from diorite in the Samothraki ophiolite, NE Aegean, Greece. Geol J 36(2):93–109
Hekinian R, Bideau D, Francheteau J, Cheminee JL, Armijo R, Lonsdale P, Blum N (1993) Petrology of the East Pacific Rise crust and upper mantle exposed in Hess Deep (eastern equatorial Pacific). J Geophys Res 98:8069–8094
Hess HH (1933) The problem of serpentinization and the origin of certain chrysotile asbestos, talc, and soapstone deposits. Econ Geol 28(7):634–657
Honnorez J (2003) Hydrothermal alteration vs. ocean-floor metamorphism. A comparison between two case histories: the TAG hydrothermal mound (Mid-Atlantic Ridge) vs. DSDP/ODP Hole 504B (Equatorial East Pacific). Comptes Rendus Geosci 335:781–824
Honnorez J, Kirst P (1975) Petrology of rodingites from the equatorial Mid-Atlantic fracture zones and their geotectonic significance. Contrib Mineral Petrol 49:233–257

Humphris SE, Thompson G (1978) Hydrothermal alteration of oceanic basalts by seawater. Geochim Cosmochim Acta 42:107–125

Humphris SE, Herzig PM, Miller DJ, Alt JC (1995) The internal structure of an active sea-floor massive sulphide deposit. Nature 377:713–716

Humphris SE, Alt JC, Teagle DAH, Honnorez J (1998) Geochemical changes during hydrothermal alteration of basement in the stockwork beneath the active TAG hydrothermal mound. In: Humphris SE, Herzig PM, Miller DJ, Zierenberg RA (eds) Proceedings of the ocean drilling program, scientific results, vol 158. Ocean Drilling Program, College Station, pp 255–276

Ildefonse B, Blackman DK, John BE, Ohara Y, Miller DJ, MacLeod CJ (2007) Oceanic core complexes and crustal accretion at slow-spreading ridges. Geology 35(7):623–626

Iyer K, Austrheim H, John T, Jamtveit B (2008) Serpentinization of the oceanic lithosphere and some geochemical consequences: constraints from the Leka Ophiolite complex, Norway. Chem Geol 249(1–2):66–90

Janecky DR, Seyfried WE Jr (1986) Hydrothermal serpentinization of peridotite within the oceanic crust: experimental investigations of mineralogy and major element chemistry. Geochim Cosmochim Acta 50:1357–1378

Jarrard RD (2003) Subduction fluxes of water, carbon dioxide, chlorine, and potassium. Geochem Geophys Geosyst 4(5):8905. doi:8910.1029/2002GC000392

Johnson JW, Oelkers EH, Helgeson HC (1991) SUPCRT92: a software package for calculating the standard molal thermodynamic properties of minerals, gases, aqueous species, and reactions from 1 – 5000 bars and 0–1000°C. Comput Geosci 18:899–947

Jöns N, Bach W, Schroeder T (2009) Formation and alteration of plagiogranites in an ultramafic-hosted detachment fault at the Mid-Atlantic Ridge (ODP Leg 209). Contrib Mineral Petrol 157 (5):625–639

Jöns N, Bach W, Klein F (2010) Magmatic influence on reaction paths and element transport during serpentinization. Chem Geol 274(3–4):196–211

Kadko D, Barross J, Alt JC (1995) The magnitude and global implications of hydrothermal flux. In: Humphris SE, Zierenberg RA, Mullineaux LS, Thomson RE (eds) Seafloor hydrothermal systems, Geophysical monograph. American Geophysical Union, Washington, DC, pp 446–466

Kelemen PB, Kikawa E, Miller DJ, Abe N, Bach W, Carlson RL, Casey JF, Chambers LM, Cheadle M, Cipriani A, Dick HJB, Faul U, Garces M, Garrido C, Gee JS, Godard MM, Graham DW, Griffin DW, Harvey J, Ildefonse B, Iturrino GJ, Josef J, Meurer WP, Paulick H, Rosner M, Schroeder T, Seyler M, Takazawa E (2004) Site 1275. In: Proceedings of the ocean drilling program; initial reports; drilling mantle peridotite along the Mid-Atlantic Ridge from 14 degrees to 16 degrees N; covering Leg 209 of the cruises of the drilling vessel JOIDES Resolution; Rio de Janeiro, Brazil, to St George, Bermuda; sites 1268–1275, 6 May-6 July 2003, vol Texas A&M University Ocean Drilling Program College Station, pp 167

Kelley DS, Gillis KM, Thompson G (1993) Fluid evolution in submarine magma-hydrothermal systems at the Mid-Atlantic Ridge. J Geophys Res 98:19579–19596

Kelley DS, Karson JA, Blackman DK, Früh-Green GL, Butterfield DA, Lilley MD, Olson EJ, Schrenk MO, Roe KK, Lebon GT, Rivizzigno P, Party A-S (2001) An off-axis hydrothermal vent field near the Mid-Atlantic Ridge at 30°N. Nature 412:127–128

Kelley DS, Karson JA, Fruh-Green GL, Yoerger DR, Shank TM, Butterfield DA, Hayes JM, Schrenk MO, Olson EJ, Proskurowski G, Jakuba M, Bradley A, Larson B, Ludwig K, Glickson D, Buckman K, Bradley AS, Brazelton WJ, Roe K, Elend ML, Delacour A, Bernasconi SM, Lilley MD, Baross JA, Summons RE, Sylva SP (2005) A serpentinite-hosted ecosystem: the lost city hydrothermal field. Science 307:1428–1434

Kimball KL, Spear FS, Dick HJB (1985) High temperature alteration of Abyssal ultramafics from the Islas Orcadas fracture zone, South Atlantic. Contrib Mineral Petrol 91:307–320

Klein EM (2004) Geochemistry of the igneous oceanic crust. In: Holland HD, Turekian KK (eds) Treatise on geochemistry, vol 3. Elsevier, Amsterdam, pp 433–463

Klein F, Garrido CJ (2011) Thermodynamic constraints on mineral carbonation of serpentinized peridotite. Lithos 126:147–160
Klein F, Bach W, Jöns N, McCollom T, Moskowitz B, Berquó T (2009) Iron partitioning and hydrogen generation during serpentinization of abyssal peridotites from 15°N on the Mid-Atlantic Ridge. Geochim Cosmochim Acta 73(22):6868–6893
Knott R, Fouquet Y, Honnorez J, Petersen S, Bohn M (1998) Petrology of hydrothermal mineralization: a vertical section through the TAG mound. In: Herzig PM, Humphris SE, Miller DJ, Zierenberg RA (eds) Proceedings of the ocean drilling program, scientific results, vol 158. Ocean drilling program, College Station, pp 5–26
Koons PO (1981) A study of natural and experimental metasomatic assemblages in an ultramafic-quartzofeldspathic metasomatic system from the Haast Schist, South Island, New Zealand. Contrib Mineral Petrol 78:189–195
Lecuyer C, Grurau G (1996) Oxygen and strontium isotope compositions of Hess Deep gabbros (Holes 894 F and 894 G): high-temperature interaction of seawater with ocean crust layer 3. In: Mevel C, Gillis KM, Allan JF, Meyer PS (eds) Proceedings of the ocean drilling program, scientific results, vol 147, Ocean drilling program, College Station, pp 227–234
Lilley MD, Butterfield DA, Lupton JE, Olson EJ (2003) Magmatic events can produce rapid changes in hydrothermal vent chemistry. Nature 422:878–881
Ludden JN, Thompson G (1978) Behaviour of rare earth elements during submarine weathering of tholeiitic basalt. Nature 274:147–149
Mackenzie FT (1992) Chemical mass balance between rivers and oceans. In: Nierenberg WA (ed) Encyclopedia of earth system science, vol 1. Academic, New York, pp 431–445
MacLeod CJ, Searle RC, Murton BJ, Casey JF, Mallows C, Unsworth SC, Achenbach KL, Harris M (2009) Life cycle of oceanic core complexes. Earth Planet Sci Lett 287(3–4):333–344
Malahoff A, McMurtry GM, Wiltshire JC, Yeh H-W (1982) Geology and chemistry of hydrothermal deposits from active submarine volcano Loihi, Hawaii. Nature 298:234–239
Manning CE, MacLeod CJ (1996) Fracture-controlled metamorphism of Hess Deep gabbros, Site 894: contraints on the roots of mid-ocean ridge hydrothermal systems at fast-spreading centers. In: Mevel C, Gillis KM, Allan JF, Meyer PS (eds) Proceedings of the ocean drilling program, scientific results, vol 147, Ocean drilling program, College Station, pp 189–212
Manning CE, Weston PE, Mahon KI (1996) Rapid high-temperature metamorphism of East Pacific Rise gabbros from Hess Deep. Earth Planet Sci Lett 144:123–132
Matthews DH (1962) Altered lavas from the floor of the Eastern North Atlantic. Nature 194:368–369
McCaig AM, Cliff RA, Escartín J, Fallick AE, MacLeod CJ (2007) Oceanic detachment faults focus very large volumes of black smoker fluids. Geology 35:935–938
McCollom TM, Bach W (2009) Thermodynamic constraints on hydrogen generation during serpentinization. Geochim Cosmochim Acta 73:856–879
McCollom TM, Shock EL (1998) Fluid-rock interactions in the lower oceanic crust: thermodynamic models of hydrothermal alteration. J Geophys Res 103:547–575
Melson WG, Bowen VT, Van Andel T-H, Siever R (1966) Greenstones from the central valley of the Mid-Atlantic Ridge. Nature 209:604–605
Melson WG, Thompson G, Van Andel T-H (1968) Volcanism and metamorphism in the Mid-Atlantic ridge, 22°N latitude. J Geophys Res 73:5925–5941
Mével C (2003) Serpentinization of abyssal peridotite at mid-ocean ridges. Comptes Rendus Geosci 335:825–852
Mével C, Cannat M (1991) Lithospheric stretching and hydrothermal processes in oceanic gabbros from slow spreading ridges. In: Peters T, Nicolas A, Coleman RG (eds) Ophiolite genesis and the evolution of the oceanic lithosphere. Kluwer, Dordrecht, pp 293–312
Michael PJ, Langmuir CH, Dick HJB, Snow JE, Goldstein SL, Graham DW, Lehnert K, Kurras G, Jokat W, Muehe R, Edmonds HN (2003) Magmatic and amagmatic seafloor generation at the ultraslow-spreading Gakkel ridge, Arctic Ocean. Nature 423:956–961
Miyashiro A, Shido F, Ewing M (1971) Metamorphism in the Mid-Atlantic Ridge near 24° and 30°N. Philos Trans R Soc Lond A 268:589–603

Morishita T, Hara K, Nakamura K, Sawaguchi T, Tamura A, Arai S, Okino K, Takai K, Kumagai H (2009) Igneous, alteration and exhumation processes recorded in Abyssal peridotites and related fault rocks from an oceanic core complex along the central Indian ridge. J Petrol 50(7):1299–1325

Mottl MJ (1983) Metabasalts, axial hot springs, and the structure of hydrothermal systems at mid-ocean ridges. Geol Soc Am Bull 94:161–180

Mottl MJ, Wheat CG (1994) Hydrothermal circulation through mid-ocean ridge flanks: fluxes of heat and magnesium. Geochim Cosmochim Acta 58:2225–2237

Mottl MJ, Wheat G, Baker E, Becker N, Davis E, Feely R, Grehan A, Kadko D, Lilley M, Massoth G, Moyer C, Sansone F (1998) Warm springs discovered on 3.5 Ma oceanic crust, eastern flank of the Juan de Fuca Ridge. Geology 26:51–54

Mottl MJ, Komor SC, Fryer P, Moyer CL (2003) Deep-slab fluids fuel extremophilic Archaea on a Mariana forearc serpentinite mud volcano: ocean drilling program leg 195. Geochem Geophys Geosyst 4(11). doi:10.1029/2003GC000588

Mottl MJ, Wheat CG, Fryer P, Gharib J, Martin JB (2004) Chemistry of springs across the Mariana forearc shows progressive devolatilization of the subducting plate. Geochim Cosmochim Acta 68(23):4915–4933

Muehlenbachs K, Clayton RN (1972) Oxygen isotope geochemistry of submarine greenstones. Can J Earth Sci 9:471–478

Neal C, Stanger G (1983) Hydrogen generation from mantle source rocks in Oman. Earth Planet Sci Lett 66:315–320

Niu Y (2004) Bulk-rock major and trace element compositions of abyssal peridotites: implications for mantle melting, melt extraction and post-melting processes beneath mid-ocean ridges. J Petrol 45(12):2423–2458

Normand C, Williams-Jones AE (2007) Physicochemical conditions and timing of rodingite formation: evidence from rodingite-hosted fluid inclusions in the JM Asbestos mine, Asbestos, Quebec. GeochemTrans 25(8). doi:10.1186/1467-4866-1188-1111

Parsons B (1981) The rates of plate creation and consumption. Geophys J Roy Astr Soc 67: 437–448

Pirajno F (2009) Hydrothermal processes and mineral systems. Springer, Dordrecht/London, p 1250

Pollack HN, Hurter SJ, Johnson JR (1993) Heat flow from the Earth's interior: analysis of the global data set. Rev Geophys 31:267–280

Quon SH, Ehlers EG (1963) Rocks of Northern part of Mid-Atlantic ridge. Geol Soc Am Bull 74:1–8

Ranero CR, Morgan JP, McIntosh K, Reichert C (2003) Bending-related faulting and mantle serpentinization at the Middle America trench. Nature 425:367–373

Read HH (1934) On zoned associations of antigorite, talc, actinolite, chlorite, and biotite in Unst, Shetland Islands. Mineral Mag 23:519–540

Richards HG, Cann JR, Jensenius J (1989) Mineralogical zonation and metasomatism of the alteration pipes of Cyprus sulfide deposits. Econ Geol 84:91–115

Richardson CJ, Cann JR, Richards HG, Cowan JG (1987) Metal-depleted root zones of the Troodos ore-forming hydrothermal systems, Cyprus. Earth Planet Sci Lett 84:243–253

Rose NM, Bird DK (1994) Hydrothermally altered dolerite dykes in East Greenland: implications for Ca-metasomatism of basaltic protoliths. Contrib Mineral Petrol 116:420–432

Saccocia PJ, Gillis KM (1995) Hydrothermal upflow zones in the oceanic crust. Earth Planet Sci Lett 136:1–16

Schmidt K, Koschinsky A, Garbe-Schönberg D, de Carvalho LM, Seifert R (2007) Geochemistry of hydrothermal fluids from the ultramafic-hosted Logatchev hydrothermal field, 15°N on the Mid-Atlantic Ridge: temporal and spatial investigation. Chem Geol 242:1–21

Seewald JS, Cruse A, Saccocia PJ (2003) Aqueous volatiles in hydrothermal fluids from the Main Endeavour Field, northern Juan de Fuca ridge: temporal variability following earthquake activity. Earth Planet Sci Lett 216:575–590

Seyfried WE Jr, Bischoff JL (1979) Low temperature basalt interaction with seawater: an experimental study at 70°C and 150°C. Geochim Cosmochim Acta 43:1937–1947

Seyfried WE Jr, Bischoff JL (1981) Experimental seawater-basalt interaction at 300°C, 500 bars, chemical exchange, secondary mineral formation and implications for the transport of heavy metals. Geochim Cosmochim Acta 45:135–147
Seyfried WE, Dibble WEJ (1980) Sea water – peridotite interaction at 300°C and 500 bars: implications for the origin of oceanic serpentinites. Geochim Cosmochim Acta 44:309–321
Seyfried WE Jr, Janecky DR, Mottl MJ (1984) Alteration of the oceanic crust: implications for geochemical cycles of lithium and boron. Geochim Cosmochim Acta 48:557–569
Seyfried WE Jr, Berndt ME, Seewald JS (1988) Hydrothermal alteration processes at mid ocean ridges: constraints from diabase alteration experiments, hot-spring fluids and composition of the oceanic crust. In: Barrett TJ, Jambor JL (eds) Seafloor hydrothermal mineralization, vol 26. Mineralogical Association of Canada, Toronto/Canada, pp 787–804
Seyfried WE Jr, Foustoukos DI, Fu Q (2007) Redox evolution and mass transfer during serpentinization; an experimental and theoretical study at 200°C, 500 bar with implications for ultramafic-hosted hydrothermal systems at mid-ocean ridges. Geochim Cosmochim Acta 71(15):3872–3886
Sinton JM, Detrick RS (1992) Mid-ocean ridge magma chambers. J Geophys Res 97:197–216
Sleep NH (1991) Hydrothermal circulation, anhydrite precipitation, and thermal structure at ridge axes. J Geophys Res 96:2375–2387
Smith DK, Cann JR, Escartín J (2006) Widespread active detachment faulting and core complex formation near 13°N on the Mid-Atlantic Ridge. Nature 442:440–443
Snow JE, Dick HJB (1995) Pervasive magnesium loss by marine weathering of peridotite. Geochim Cosmochim Acta 59:4219–4235
Staudigel H, Hart SR, Richardson SH (1981) Alteration of the oceanic crust: processes and timing. Earth Planet Sci Lett 52:311–327
Staudigel H, Plank T, While B, Schmincke H-U (1996) Geochemical fluxes during seafloor alteration of the basaltic upper oceanic crust: DSDP Sites 417 and 418. In: Bebout GE, Scholl DW, Kirby SH, Platt JP (eds) Subduction top to bottom, vol 96, Geophysical monograph. American Geophysical Union, Washington, DC, pp 19–38
Stein CA, Stein S (1994) Constraints on hydrothermal heat flux through the oceanic lithosphere from global heat flow. J Geophys Res 99(B2):3081–3095
Stein CA, Stein S, Pelayo A (1995) Heat flow and hydrothermal circulation. In: Humphris SE, Zierenberg RA, Mullineaux LS, Thomson RE (eds) Seafloor hydrothermal processes, Geophysical monograph. American Geophysical Union, Washington, DC, pp 425–445
Stern C, De Wit MJ, Lawrence JR (1976) Igneous and metamorphic processes associated with the formation of Chilean ophiolites and their implications for ocean floor metamorphism, seismic layering, and magnetism. J Geophys Res 81:4370–4380
Teagle DAH, Alt JC, Chiba H, Humphris SE, Halliday AN (1998a) Strontium and oxygen isotopic constraints on fluid mixing, alteration and mineralization in the TAG hydrothermal deposit. Chem Geol 149:1–24
Teagle DAH, Alt JC, Halliday AN (1998b) Tracing the chemical evolution of fluids during hydrothermal recharge: constraints from anhydrite recovered in ODP Hole 504B. Earth Planet Sci Lett 155:167–182
Thayer TP (1966) Serpentinization considered as a constant-volume metasomatic process. Am Mineral 51:685–710
Thompson G (1991) Metamorphic and hydrothermal processes: basalt-seawater interactions. In: Floyd PA (ed) Oceanic basalts. Blackie, Glasgow/London, pp 148–173
Thompson G, Melson WG (1970) Boron contents of serpentinites and metabasalts in the oceanic crust: implications for the boron cycle in the oceans. Earth Planet Sci Lett 8:61–65
Tivey MK, Humphris SE, Thompson G, Hannington MD, Rona PA (1995) Deducing patterns of fluid flow and mixing within the active TAG mound using mineralogical and geochemical data. J Geophys Res 100:12527–12555. doi:10.1029/95JB00610
Tivey MK, Mills RA, Teagle DAH (1998) Temperature and salinity of fluid inclusions in anhydrite as indicators of seawater entrainment and heating in the TAG active mound. In: Herzig PM, Humphris SE, Miller DJ, Zierenberg RA (eds) Proceedings of the ocean drilling program, scientific results, vol 158. Ocean drilling program, College Station, pp 179–190

Tucholke BE, Lin J (1994) A geological model for the structure of ridge segments in slow spreading ocean crust. J Geophys Res 99(B6):11937–11958

Tucholke BE, Lin J, Kleinrock MC (1998) Megamullions and mullion structure defining oceanic metamorphic core complexes on the Mid-Atlantic Ridge. J Geophys Res 103:9857–9866

Valsami E, Cann JR (1992) Mobility of rare earth elements in zones of intense hydrothermal alteration in the Pindos ophiolite, Greece. In: Parson LM, Burton BJ, Browning P (eds) Ophiolites and their modern oceanic analogues, vol 60. Geological Society, London, pp 219–232

Wells DM, Mills RA, Roberts S (1998) Rare earth element mobility in a mineralized alteration pipe within the Troodos ophiolite, Cyprus. In: Mills RA, Harrison K (eds) Modern ocean floor processes and the geological record, vol 148. Geological Society, London, pp 153–176

Wheat CG, Mottl MJ (2000) Composition of pore and spring waters from baby bare: global implications of geochemical fluxes from a ridge flank hydrothermal system. Geochim Cosmochim Acta 64:629–642

Wheat CG, Feely RA, Mottl MJ (1996) Phosphate removal by oceanic hydrothermal processes: an update of the phosphorus budget in the oceans. Geochim Cosmochim Acta 60:3593–3608

Wilcock WSD, Delaney JR (1996) Mid-ocean ridge sulfide deposits: evidence for heat extraction from magma chambers or cracking fronts? Earth Planet Sci Lett 145:49–65

Winter JD (2001) An introduction to igneous and metamorphic petrology. Prentice Hall, New Jersey

Wolery TJ, Jarek RL (2003) Software user's manual EQ3/6 (version 8.0). Sandia National Laboratories, Albuquerque/New Mexico

Zharikov VA, Pertsev NN, Rusinov VL, Callegari E, Fettes DJ (2007) Metasomatism and metasomatic rocks. In: Recommendations by the IUGS Subcommission on the systematics of metamorphic rocks. Online document: http://www.bgs.ac.uk/scmr/docs/papers/paper_9.pdf. Accessed 6 Oct 2010

Zierenberg RA, Shanks WC III, Seyfried WE Jr, Koski RA, Strickler MD (1988) Mineralization, alteration, and hydrothermal metamorphism of the ophiolite-hosted Turner-Albright sulfide deposit, southwestern Oregon. J Geophys Res 93:4657–4674

Chapter 9
Metasomatism in Subduction Zones of Subducted Oceanic Slabs, Mantle Wedges, and the Slab-Mantle Interface

Gray E. Bebout

Abstract Physical juxtaposition of chemically disparate rocks, and the mobility of "fluids" at up to tens of kilometer scales, lead to myriad metasomatic effects in subduction zones, with larger scale manifestations including the metasomatism related to mass flux leading to arc magmatism and convergent margin volatiles cycling. Subduction-zone metasomatism is initiated at very shallow levels, as oceanic slabs entering trenches bend and are potentially infiltrated by seawater and as sedimentary sections begin their journey into forearcs resulting in extensive physical compaction, fluid expulsion, and diagenetic alteration. Studies of forearc fluid geochemistry (e.g., in accretionary complexes and, for the Marianas margin, in serpentinite seamounts) track this shallow-level metasomatic alteration, whereas high- and ultrahigh-pressure metamorphic suites provide records of fluid generation and flow, and related metasomatism to depths approaching those beneath volcanic fronts (and, in a smaller number of cases, depths beyond those beneath arcs). Uncertainty remains regarding the geochemical influence of strongly mechanically mixed zones along the slab-mantle interface (i.e., in the "subduction channel"), represented by mélange zones in many metamorphic suites. Experimental studies predict dramatic change in the physicochemical properties, and metasomatic capabilities, of subduction-zone "fluids," as a function of depth. However, the studies of metamorphic suites have yet to document results of this change and, toward this goal, further work is warranted on UHP suites representing subduction-zone depths of 100 km or greater. Work on higher-P suites is also necessary in order to test the generally accepted hypothesis that subduction-zone metamorphism serves as a geochemical "filter" altering the

G.E. Bebout (✉)
Department of Earth and Environmental Sciences, Lehigh University, 1 West Packer Avenue, Bethlehem, PA 18015-3001, USA
e-mail: geb0@lehigh.edu

D.E. Harlov and H. Austrheim, *Metasomatism and the Chemical Transformation of Rock*, Lecture Notes in Earth System Sciences,
DOI 10.1007/978-3-642-28394-9_9,

compositions of deeply subducting rocks that then contribute to arc magmatism and the geochemical heterogeneity of the deeper mantle sampled by ocean-island basalts.

9.1 Introduction

In subduction zones (see Stern 2002), chemically disparate lithologies (sediments, mafic and ultramafic rocks, and possibly mechanical mixtures thereof) are tectonically juxtaposed at sub-micron to kilometer scales, commonly in the presence of a mobile "fluid" phase (hydrous fluid, silicate melt, or possibly supercritical liquids; see discussions by Manning 2004; Hermann et al. 2006), offering up huge potential for mass transfer and related metasomatic alteration (see Fig. 9.1). The subduction zone inventory of H_2O figures prominently in virtually every aspect of subduction mass transfer, providing the primary solvent for mass transfer at all scales. Its gradual release from subducting slabs and sediments is initiated by mechanical expulsion at very shallow levels of the forearcs (releasing nearly one-half of the initially subducted H_2O; see Fig. 9.2, from van Keken et al. 2011; also see Hacker 2008) and, at greater depths, via a series of dehydration reactions (Fig. 9.1; see Schmidt and Poli 2003). Some of the resulting H_2O-rich fluid is thought to contribute to massive hydration and metasomatism in the hanging-walls of subduction zones. No more spectacular example of a product of metasomatism (and of subduction) exists than volcanic arc magmatism, for which the mostly widely accepted model of formation involves metasomatism of variably depleted mantle wedge ultramafic rocks, over tens to hundreds of kilometers scales, by H_2O-rich "fluids" emanating from subducting slabs. The voluminous work that has been conducted on Earth's modern volcanic arcs has provided us with a proposed inventory of slab/sediment-derived components delivered by these fluids into volcanic arc source regions (e.g., Pearce and Peate 1995; Elliott 2003). Recently, there has been growing interest in assessing trench-to-subarc chemical cycling in subduction zones through the integrated petrologic and geochemical study of high-pressure (HP) and ultrahigh-pressure (UHP) metamorphic suites, which represent the direct rock record of processes in subducting slabs and at the slab-mantle interface (see review by Bebout 2007a; Chap. 10). This chapter describes this "connection" between our knowledge of volcanic arc geochemical evolution and the seafloor lithologies thought to be subducting and contributing to volcanic arcs, i.e. metasomatic "processing" of the subducting rocks. Chemical processing during metamorphism could generate some of the hallmark chemical characteristics of volcanic arcs believed to be contributed from subducting slabs. Many have suggested that the chemical/isotopic heterogeneity inferred for the deep mantle, based on analyses of ocean-island basalts and other mantle products, reflects the subduction and metasomatic redistribution in fluids/melts of materials from oceanic slabs and sediments (see Hofmann 2003). Other important products of subduction zone mass transfer and metasomatism include the H_2O-rich

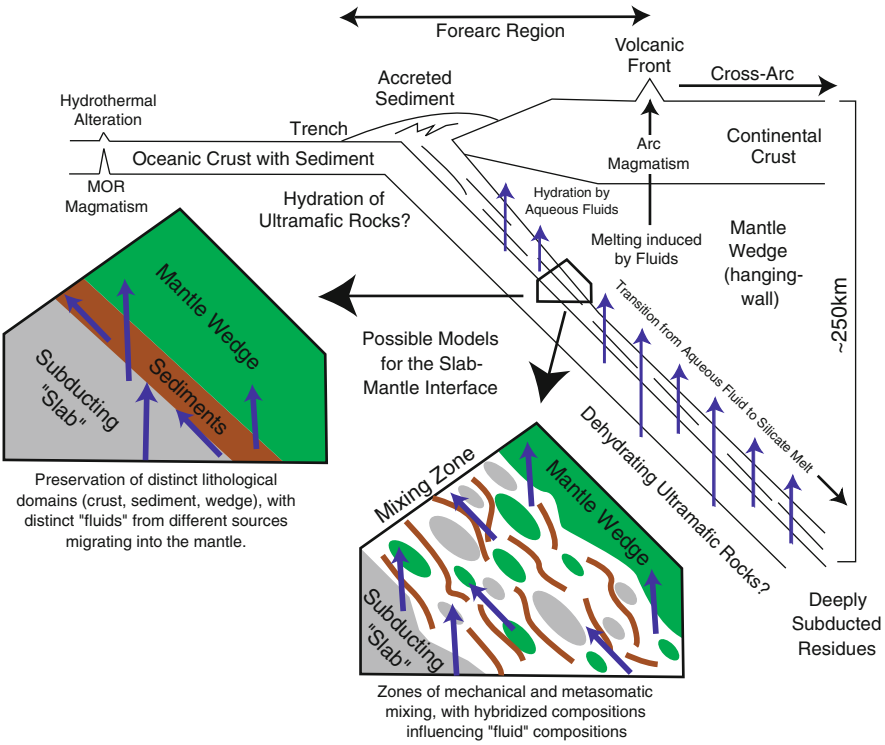

Fig. 9.1 Sketch of a ocean-continent subduction zone (from Bebout 2007a), illustrating key structural elements, some selected flux pathways, areas of remaining uncertainty in considerations of subduction-zone recycling, and two models for the nature of the slab-mantle interface (Stern 2002; see text for discussion). Oceanic crust (and its associated mantle part of the oceanic lithosphere), variably altered geochemically at mid-ocean ridges (MOR), and sediment deposited onto this crust, are deeply subducted, contributing fluids and elements to the mantle wedge (*hanging-wall*). It is possible that fluids are also contributed from the ultramafic part of the subducting oceanic lithosphere previously hydrated during slab bending in trench regions. On this figure (insets and main figure), the *blue arrows* indicate additions of slab-derived "fluids" to the mantle wedge. At shallower levels (forearc regions, in particular), these fluids are thought to be aqueous fluids, whereas the fluids added to the mantle wedge at greater depths (beneath volcanic arcs and into the deeper mantle) likely transition into being silicate melts

fluids venting onto the seafloor in modern forearcs (Kastner et al. 1991; Hulme et al. 2010) and the venting of important greenhouse gases (notably CO_2) into the atmosphere via arc volcanism.

In this chapter, a synthesis is provided concerning the field-based, theoretical and experimental perspectives of subduction-zone metasomatism, focusing on some of the large-scale manifestations of mass transfer in convergent margins

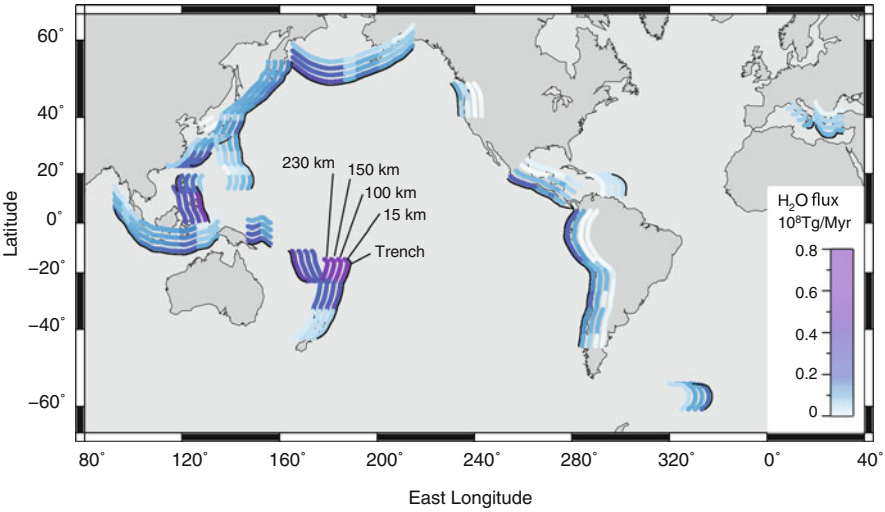

Fig. 9.2 Predicted H_2O flux at selected depths in the world's subduction zones (in Tg, 10^{12} grams, from van Keken et al. 2011), demonstrating the disparate delivery of H_2O to great depths in individual subduction zones as a function of their thermal structure (see calculated P-T paths for rocks subducting into these margins in Fig. 9.3). For each subduction zone segment, the black line indicates the trench position. The *parallel lines* in the direction of subduction successively show H_2O input to the forearc (at 15 km depth), H_2O flux at the approximate location of the volcanic front (at 100 km depth), H_2O flux at 150 km depth, and H_2O input to >230 km depth (entering the deeper mantle beyond subarcs)

(e.g., volcanic arc magmatism, forearc mantle wedge hydration and metasomatism, inputs and outputs of volatiles, and metasomatism in the deeper mantle leading to its geochemical heterogeneity). Chapter 10 provides a complementary discussion of the records of metasomatism in subduction-related metamorphic rocks. In some cases (e.g., field-based studies of metamorphic suites), studies of subduction zone metasomatism involve observations made on chemically changed rocks, whereas in other cases (inverse studies) observations are made on magmas (or hydrous fluids) derived from metasomatized sources. Integrating these records, which reflect processes occurring over a wide range of temperatures, pressures, and spatial scales, it is possible to make some generalizations regarding the significance of metasomatism for the global cycling of some chemical components. Also in this chapter, a brief discussion of C cycling is provided for the Central America convergent margin, detailing recent comparisons of C inputs (in sediments and oceanic crust) and outputs (volcanic gases) and incorporating insights regarding deep subduction-zone decarbonation, and related metasomatism, gained through recent study of HP and UHP metamorphic suites.

9.2 Inputs into Subduction Zones: Metasomatic Starting Materials

The interface between the subducting slab and the overlying mantle wedge is composed of heterogeneously deformed oceanic crust and sedimentary cover juxtaposed with variably hydrated and metasomatized hanging-wall ultramafic rocks (see Fig. 9.1; also see the discussion in Chap. 10). On average, the subducting oceanic lithosphere is composed of a 5–7 km thick section of oceanic crust, dominantly basaltic and gabbroic in composition, with an ultramafic lithospheric mantle section and a sedimentary veneer of varying thickness. Geochemical data for oceanic crust drilled on the seafloor, or accessed from on-land ophiolitic sequences, demonstrate a huge diversity of chemical compositions related to the nature and duration of seafloor fluid-rock interactions (see Alt and Teagle 2003; Kelley et al. 2003; Staudigel et al. 1996; Staudigel 2003; see Chap. 8). Mid- to lower-parts of the oceanic crust are believed to have a smaller impact on the slab chemical flux (ascending from the slab to the overlying mantle wedge), as they contain fewer volatile-bearing phases and thus experience only small amounts of dehydration yielding fluids with dissolved components (see Bebout 2007b). There has been considerable recent discussion of the possibility that the uppermost ultramafic part of the subducting lithosphere is extensively hydrated and metasomatized as a result of plate-bending near the trenches (Ranero et al. 2005), and that the slab-mantle interface could be infiltrated by large amounts of fluid emanating from these sub-crustal ultramafic rocks (see the blue arrows on Fig. 9.1). In slow to ultraslow spreading centers, such as on the modern-day Atlantic seafloor (similarly represented in Jurassic ophiolite fragments from the Alps), ultramafic rocks are present on the seafloor, at the top of the slab, and are thus more easily hydrated.

Sedimentary sequences, just beyond the trenches, range in thickness from $<$100 m to $>$4 km (but are mostly $<$1 km). Our knowledge of the lithology and compositions of subducting sediments has been summarized by Rea and Ruff (1996), Plank and Langmuir (1998), and Jarrard (2003). Approximately 76 wt% of the GLOSS (Globally Subducting Sediment) composite of Plank and Langmuir (1998) is composed of "terrigenous" sediment with its largest accumulation near the continental margins. The remainder of this composite consists of calcium carbonate (7 wt%), opal (10 wt%), and mineral-bound H_2O (7 wt%). However, this global composite must be used with caution. Its averaged composition does not reflect that of sediment being subducted into any individual margin. In some forearcs, sediment accretion processes and underplating result in the offscraping of the upper part of the sediment section, thus preventing its deep subduction (see Fig. 9.1). At other margins, perhaps most, materials from the forearc hanging-wall, largely sedimentary, are incorporated into the subducting package of rocks, resulting in their "erosion" and possible deep entrainment into the mantle (Scholl and von

Huene 2009; Clift et al. 2009). Fluid-related processes, including metasomatic redistribution, attending the subduction erosion process have not yet been evaluated. Exceptions are studies of the impact of subduction erosion on the dynamics and geochemistry of the Andean volcanic arc (see Kay et al. 2005; earlier discussion by Stern 1991).

Recent geophysical studies, of the slab-mantle interface, have identified zones of low seismic velocity at or near the top of the subducting oceanic lithosphere (e.g., Fukao et al. 1983; Hori et al. 1985; Matsuzawa et al. 1986; Helffrich et al. 1989; Helffrich 1996; Helffrich and Abers 1997). These low velocity domains have generally been interpreted as containing extensively hydrated assemblages in the subducting oceanic lithosphere (see discussion by Hacker et al. 2003b). However, Abers (2000, 2005) has speculated that they might also represent hydrated hanging-wall materials. The generation of zones rich in layered hydrous minerals, perhaps in part a mechanical mixing zone (see sketches of the makeup of the slab-mantle interface in Fig. 9.1), could also promote aseismic behavior at great depths in subduction zones (Peacock and Hyndman 1999).

9.3 Thermal Structure of Subduction Zones and Relevance for Metasomatism

A brief discussion of the thermal evolution of subduction zones is appropriate here, as much of the metasomatism discussed in this chapter occurs at the relatively high-P/T conditions in subduction zones. The tightly-packed isotherms calculated for at/or near the slab-mantle interface can lead to the flow of slab-derived fluids across steep temperature gradients. This condition increases the effect of varying fluid flow P-T trajectories on fluid-rock metasomatism, as the transport of fluids over tens of kilometers can be accompanied by large differences in the solubilities of various solutes (see Bebout and Barton 1993; Manning 2004). Increasingly, high-resolution thermal models, employing variable upper mantle viscosity and associated subduction-induced "corner flow", indicate that the slab-mantle interface and shallowest parts of the subducting oceanic crust could be warmer than predicted in earlier models, perhaps at or near temperatures required for partial melting of both sedimentary and mafic rocks (see van Keken et al. 2002; Rupke et al. 2004; Peacock 2003; Kelemen et al. 2003; Peacock et al. 2005; Syracuse et al. 2010). This warmer thermal structure, related to mantle convection, has profound implications for the nature of slab-derived "fluids" and element mobilities (see discussions below). Figure 9.3 (from Syracuse et al. 2010) shows calculated P-T paths for 56 present day subduction segments on the Earth, testing four separate assumptions regarding the causes of the partial coupling between the slab and the overriding plate directly downdip of the thrust zone, invoked to replicate the cold nose (cold forearc corner) observed in measurements of heat flow and seismic attenuation (see Kincaid and

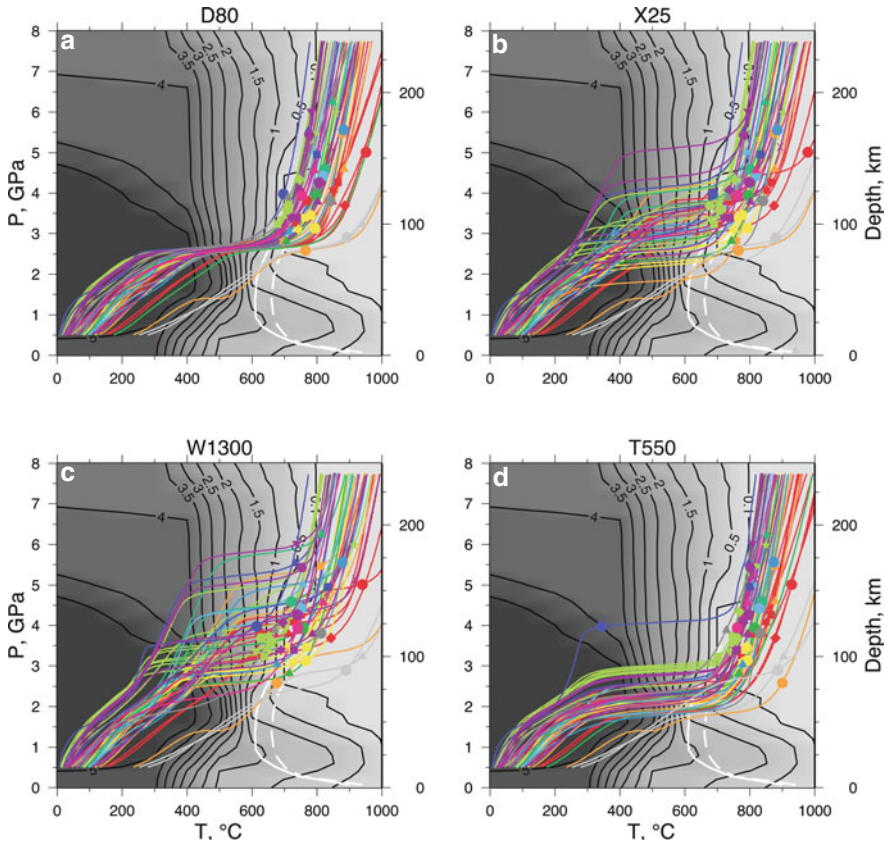

Fig. 9.3 Pressure–temperature paths of the slab surface for 56 modern volcanic arc segments, from Syracuse et al. (2010), with P–T beneath the volcanic arc highlighted (*colored circles*). These authors tested four separate assumptions about the causes of the partial coupling between the slab and the overriding plate directly downdip of the thrust zone: (1) the downdip end of the partial coupling is at a constant depth (**a**; D80), (2) it is at constant distance trenchward from the volcanic arc (**b**; X25), (3) it is defined by a critical surface slab temperature (**c**; W1300), or (4) it is adjusted such that the hottest part of the mantle wedge beneath the volcanic arc is at a constant temperature for all subduction zones (**d**; T550). Phase diagram for hydrated MORB (Hacker 2008) is shown beneath, with the shaded region indicating maximum wt% water bound in minerals. The water-saturated solidus for MORB to ~3 GPa is shown as the solid *white line* and the water-saturated solidus for oceanic sediments is shown as the *dashed white line* (Vielzeuf and Schmidt 2001; Schmidt et al. 2004). Note that recent estimates from slab fluid samples and water-to-solute ratios (e.g., H_2O/Ce) for modern subduction zones indicate subarc slab surface temperatures above the solidi of saturated sediment and basalt (750–950°C; Plank et al. 2009; Syracuse et al. 2010)

Sacks 1997; Wada and Wang 2009). These calculations demonstrate the large variability in the thermal structure of these subduction zone segments. Dumitru (1991) matched estimated geothermal gradients for the Franciscan paleoaccretionary margin to thermal models of forearc regions (for depths

<30 km), concluding that the most important variables in these models are the subduction rate, the age of the subducting slab and frictional heating (cf. Peacock 1992).

9.4 Driving Forces for Subduction Zone Metasomatism

In subduction zones, it is easy to imagine volumetrically significant metasomatism resulting both the juxtaposition and interactions among disparate lithologies (with fluids facilitating larger-scale interaction), and from fluid-rock interaction involving fluids moving along varying P-T trajectories/pathways (see discussion by Bebout and Barton 1993). Both factors obviously become important for scenarios involving larger-scale transport of fluid in the extremely lithologically diverse subduction setting, in particular if mélange zones are a common product of deformation and hydration along the slab-mantle interface (see Fig. 9.1 and a more detailed sketch of the slab-mantle interface, and its disparate lithologies, in Fig. 9.4a, from Breeding et al. 2004).

9.4.1 Metasomatism Driven by Activity Gradients Among Disparate Lithologies

For infiltration metasomatism, the chemical potential for reaction comes from either lithological contrasts or changes in *P-T* conditions along the fluid flow paths. Infiltration of fluids across contacts between contrasting lithologies leads to substantial mass transfer in many geological environments (e.g., contact metamorphism; see Barton et al. 1991). In subduction zones, such mass transfer, and related metasomatic alteration, are likely to be particularly important at boundaries between sedimentary, mafic, and ultramafic lithologies, among which there would be substantial chemical potential differences (see the example of a sketch of very complex slab-mantle interface by Breeding et al. 2004; see Fig. 9.4a). Fluids flowing between such units (see the "blow-up" sketches of the slab-mantle interface in Fig. 9.1) at constant P and T would react with the rocks, causing metasomatic changes in proportion to changes in solubility (see discussion by Bebout and Barton 1993).

9.4.2 Significance of Varying Fluid P-T Flow Trajectories

For the case of mass transfer along a flow path, with varying P and/or T, metasomatism would occur in response to changes in the fluid mineral equilibrium along the flow path. The simplest illustration of this relationship involves transport of

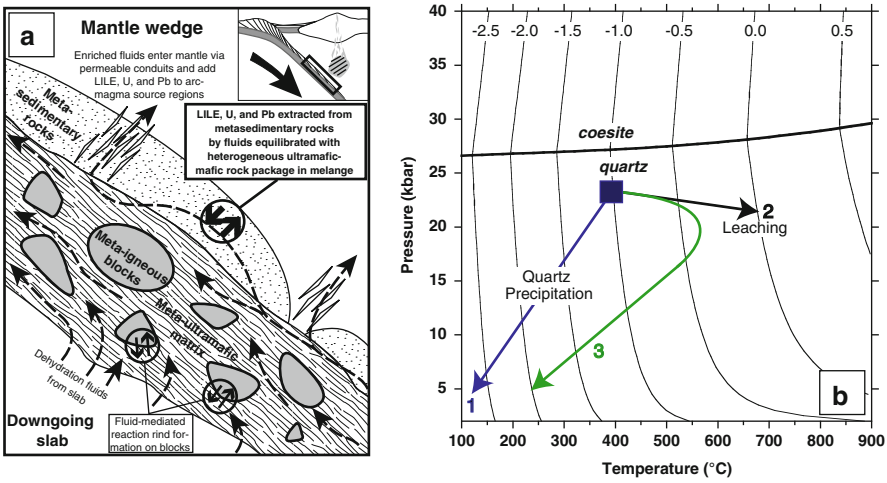

Fig. 9.4 Demonstration of plausible fluid P-T flow paths near the slab-mantle interface of subduction zones. (**a**) One view of the slab-mantle interface region, from Breeding et al. (2004) (also see sketches by Bebout and Barton 1989, 2002; Hermann et al. 2006; Bebout 2007a; see Fig. 9.1). (**b**) Quartz solubility as a function of P and T, plotted as contours of dissolved silica (isopleths of log molality of aqueous SiO_2 in equilibrium with quartz, from Manning 1994), and generalized "fluid" P-T flow trajectories that can be envisioned in a slab-mantle interface environment (see text for discussion; also see Bebout and Barton 1993). A critical end point on the hydrous melting curve of quartz lies at 1,080°C and 9.5–10 kbar (Newton and Manning 2008)

silica. Figure 9.4b (from Manning 1994) shows the solubility of quartz as a function of pressure and temperature. In quartz-saturated rocks, equilibrium 9.1:

$$SiO_{2,quartz} = SiO_{2,aqueous} \tag{9.1}$$

governs the amount of silica that is dissolved or precipitated per mass of fluid along a fluid P-T path. The same principle applies in quartz-undersaturated rocks. For example, in a hydrous peridotite, the equilibrium defined by reaction 9.2 (mineral phases are forsterite and serpentinite group minerals):

$$3Mg_2SiO_4 + 5SiO_{2,aq}(\sim \text{qtz saturation}) + 2H_2O = 2Mg_3[Si_4O_{10}](OH)_2 \tag{9.2}$$

could buffer aqueous silica at about one third the value of quartz saturation (see Fig. 9.8 in Bebout and Barton 1993; Newton and Manning 2008). In this case, higher water-to-rock ratios are required to move the same amount of silica as in the quartz-saturated example. However, in both cases, the silica concentrations, equilibrated with a uniform lithology (i.e., without the fluids encountering disparate lithologies along their paths), vary regularly with changes in pressure and temperature. The colored

arrows in Fig. 9.4b illustrate that changes relating to varying fluid P-T paths could be important over temperature and pressure intervals of ~100°C or a few kbar, well within the P-T intervals anticipated for fluid flow in subduction zones. In Fig. 9.4b, H_2O-rich fluid, evolved within the eclogite facies (at about 400°C and 25 kbar), flows either (1) down-temperature and toward the seafloor (i.e., along structures parallel to the slab-mantle interface; blue arrow), (2) upward (down-P) but up-temperature, as would occur within the slab as fluids approached the warmer slab-mantle interface (black arrow), or (3) initially up-T, then down-T and toward the seafloor (green arrow). Scenario (3) might be applicable for a case where within-slab fluids flow first upward toward the slab-mantle interface, then are channeled upward (toward the seafloor) along structures along the slab-mantle interface. This latter scenario is believed to be appropriate for the infiltration of the amphibolite-facies mélange unit, in the Catalina Schist, by H_2O-rich fluids derived in lower-T parts of the subduction zone (see sketches of fluid flow scenario in Bebout and Barton 1989; Bebout 1991a, b). As is illustrated in Fig. 9.4b, the nature of metasomatic changes is quite sensitive to the large-scale fluid flow path (cf. Barton et al. 1991 for discussion of significance in lower-P environments), with fluids either adding or removing silica from the rocks along their paths depending on the P-T fluid flow trajectory. Again, however, this discussion applies more directly for the unlikely case where an H_2O-rich fluid experiences varying large-scale P-T flow trajectories but at all times, along its path, is equilibrated with quartz. The slab-mantle interface is thought to be an environment in which fluids would interact with a wide range of mafic, sedimentary, and ultramafic lithologies, in addition to hybridized intermediate compositions.

As Bebout and Barton (1993) suggested, another possible scenario is for the pore fluid, entrained in pore spaces in subducting rocks, to metasomatically exchange with adjacent solids with changing P and T (depending on relative slab subduction and fluid Darcy velocities; see Fig. 9.11 in Bebout and Barton 1993). In the case of very slow fluid Darcy velocity, fluid "flow" paths mimic those of the subducting rocks at or near the slab-mantle interface (see Fig. 9.3). When released from the rocks, this fluid could then (like devolatilization-generated fluids) mobilize mass and experience varying P-T flow trajectories analogous to what is demonstrated in Fig. 9.4b, resulting in varying styles of metasomatism.

9.4.3 Expected Physicochemical Characteristics of "Fluids" Generated in Trench-to-Subarc Slab Environments

The chief agents for metasomatic redistribution in subduction zones are thought to be "fluids" of various types. A fluid, from a geological/geochemical perspective, is commonly regarded as being a substance that continually deforms (flows) under an applied shear stress, including liquids, gases, super-critical fluids (a substance at a temperature and pressure above its critical point), melts, and to some extent, plastic

solids (see the discussion by Manning 2004). There has been recent debate regarding the ways in which the physiochemical properties of subduction zone "fluids" evolve as a function of depth. There is a general consensus that, at the P-T conditions of most forearcs, fluids are relatively dilute hydrous solutions whereas, at greater depths beneath volcanic arcs and beyond, the fluids transition into being silicate melts and, perhaps in some cases, supercritical liquids. Recent experimentally determined datasets for element partitioning among aqueous fluids (of varying chlorinity), hydrous melts, and "supercritical liquids" demonstrate the capability of these "fluids" to convey these trace elements from subducting slab-crust lithologies into the mantle wedge (e.g., Ayers and Watson 1991; Brenan et al. 1995a, b, 1998; Keppler 1996; Kessel et al. 2005a, b; Hermann et al. 2006). These experimental studies have produced compelling arguments that these "fluids" are capable of producing many of the distinctive signatures of volcanic arc magmatism (e.g., the low Ce/Pb and low-HFSE concentrations of volcanic arc lavas; see Brenan et al. 1994, 1995a; Ayers and Watson 1991). Manning (2004) and Hermann et al. (2006) provided relatively recent appraisals of the physicochemical properties of subduction-zone "fluids" and their potential for metasomatism as a function of depth (see also Scambelluri and Philippot 2001; Zheng et al. 2011). They demonstrated the conditions under which a "transitional" fluid (supercritical liquid) could be stabilized for some rock bulk compositions, at the P-T conditions experienced by subducting slabs. Manning (2004) argued that these fully miscible fluids occur only under some restricted conditions, noting that the pressures and temperatures at which this transitional fluid is stabilized are highly dependent upon bulk rock compositions (for some systems, the critical curves lie at very high pressures) and that any fluid of this type generated in one lithology would, if mobilized, soon encounter a disparate lithology, potentially resulting in precipitation of much of the solute load.

Discussion of the physicochemical aspects of slab fluids (see Manning 2004; Hermann et al. 2006; Zheng et al. 2011) ties in with the recent development of thermal models of subduction indicating that the slab-mantle interface may be at or near the "wet" solidus for partial melting of both sediments and the uppermost AOC (see Syracuse et al. 2010; Fig. 9.3; Sect. 9.3 above). The peak P-T conditions calculated for a number of UHP suites fall near or above the wet solidi for partial melting of sediment and basalt, and geochemical work on UHP rocks can potentially yield insight regarding the nature of "fluids" produced at these conditions (see Hacker et al. 2005; discussion below). As noted above, Hermann et al. (2006) provides a discussion of the current debate regarding whether the slab fluid is an alkali-chloride aqueous fluid (Keppler 1996), a silicate melt, or a transitional supercritical liquid (Kessel et al. 2005a, b). More dilute aqueous solutions (e.g., present at the blueschist to eclogite transition at 60 or so km depths; see Manning 1998) are regarded as being relatively ineffective in removing trace elements, based on experimentally derived partitioning data (see Hermann et al. 2006). The silicate melts and supercritical liquids appear more viable as agents for transfer of slab components into volcanic arc source regions and appear to be able to explain the specific enrichments invoked in studies of volcanic arc magmatism (see

discussion of sediment melting by George et al. 2005). Based on O-isotope compositions of basalts and basaltic andesites, Eiler et al. (2005) argued for varying contributions of solute-rich aqueous fluid (lower-$\delta^{18}O$, from dehydration of hydrothermally altered rocks within the slab), and partial melts of sediments (higher-$\delta^{18}O$) along the Central American volcanic arc (cf. Carr et al. 2003).

9.5 Styles of Metasomatism Preserved in HP/UHP Rocks

Mass transfer in subduction zones, leading to metasomatism, occurs across a wide range of scales (sub-μm to hundreds of kilometers), largely depending upon whether it is a product of diffusion or the advection of fluids. Scales of diffusion, even involving a static intergranular fluid phase, are thought to be limited to up to the meter scale, whereas the mass transfer invoked in studies of volcanic arc magmatism, which involves advection of material in hydrous fluids and silicate melts, is obviously on the scale of kilometers to even hundreds of kilometers. In this section, some examples are provided of the types of observations made in studies of HP/UHP metamorphic rocks relevant to consideration of subduction zone metasomatism. The scales for which each example demonstrates metasomatic alteration are also briefly discussed. Bebout (2007a, b) and Klemd (Chap. 10) provide more detailed syntheses of the record of metasomatism in HP and UHP metamorphic suites. For the discussion below, Fig. 9.5 provides estimated peak metamorphic P-T conditions and, in some cases, estimated exhumation P-T paths, for the HP and UHP metamorphic suites from which relevant information has been extracted. In Sect. 9.6, examples are presented of observations regarding mass transfer relevant to consideration of the global-scale cycling of some elements and volatile components.

9.5.1 Elemental or Isotopic Exchange with Fluids

Figure 9.6 provides an example of Na-K and other element exchange between infiltrating fluids and gabbroic cobbles in a lawsonite-blueschist-facies metaconglomerate in the Catalina Schist (see similar examples on mineral replacement in Putnis and John 2010). In this case, cobbles are of inferred gabbroic compositions (based on textures, relict mineralogy, and concentrations of trace elements thought to be relatively immobile in metamorphic fluids; see Tenore-Nortrup and Bebout 1993). Hornblende, with igneous compositions, shows replacement by sodic amphibole and igneous plagioclase is entirely replaced by phengite with minor lawsonite (see textures in the photomicrograph in Fig. 9.6a). Both observations are consistent with significant metasomatism (or at least final reequilibration) of the cobbles under lawsonite-blueschist facies conditions. This phengite replacement resulted in significant additions of LILE such as Rb, Ba, and Cs, in addition to K (see

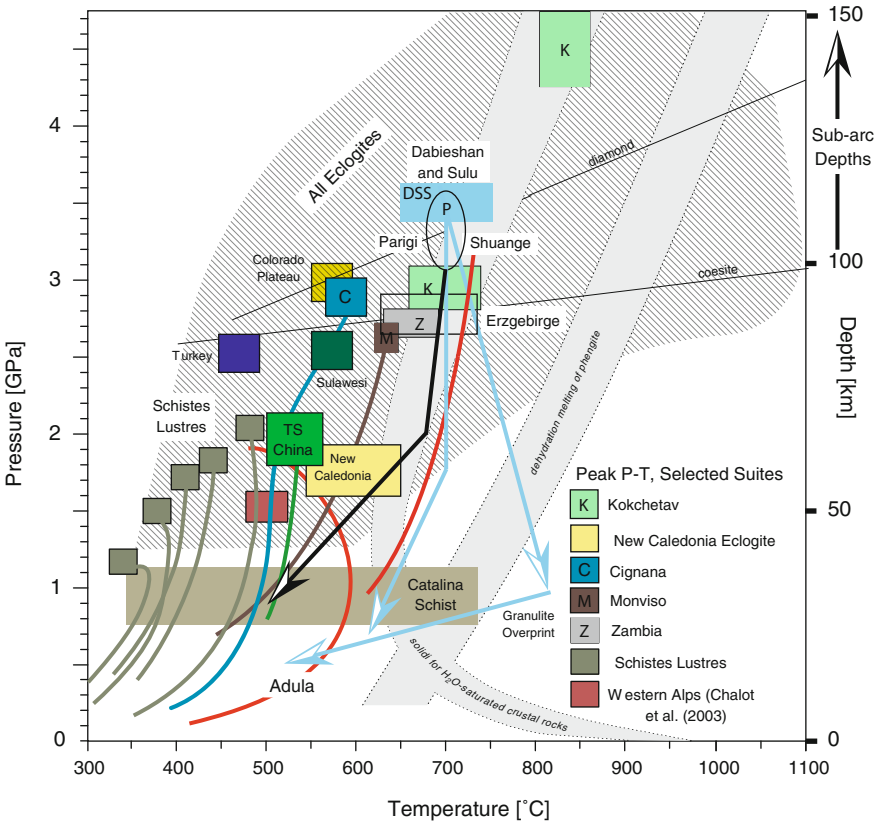

Fig. 9.5 The peak P-T conditions for metamorphic suites discussed in this chapter, some representative exhumation P-T paths, the positions of the wet and dehydration solidi for partial melting of mafic and sedimentary lithologies, and peak metamorphic conditions of some other selected UHP suites (figure from Bebout 2007b, modified after Hacker 2006; also note the patterned field for "All Eclogites", and the graphite-diamond and quartz-coesite equilibria). Colored rectangles are peak P-T conditions of the suites discussed in this chapter (mostly from Hacker 2006; references for peak P-T estimates provided therein). For the Schistes Lustres, the multiple fields are for individual units showing a wide range in grade (from Agard et al. 2002), and an estimated exhumation path is shown for each. Schematic exhumation paths for the Dabie-Sulu UHP rocks (light blue, straight-line segments), demonstrating dramatic granulite-facies overprinting in some of these rocks, are from Zheng et al. (2003; also see P-T path for the Shuange UHP locality in Dabie). Figure 9.15a provides greater detail regarding the peak P-T and varying prograde P-T paths of the units of the Catalina Schist. The P-T for the Western Alps is for the internal units (see Chalot-Prat et al. 2003), and peak metamorphic P-T estimates for Tianshan HP rocks are from Gao and Klemd (2001). The black, unfilled oval region is for the Parigi UHP locality of the Dora Maira Massif (see discussion in Hermann et al. 2006), and the black, unfilled rectangular region is for the Erzgebirge UHP rocks studied by Massone and Kopp (2005). The Adula rocks (exhumation path only) were investigated by Zack et al. (2001, 2002, 2003)

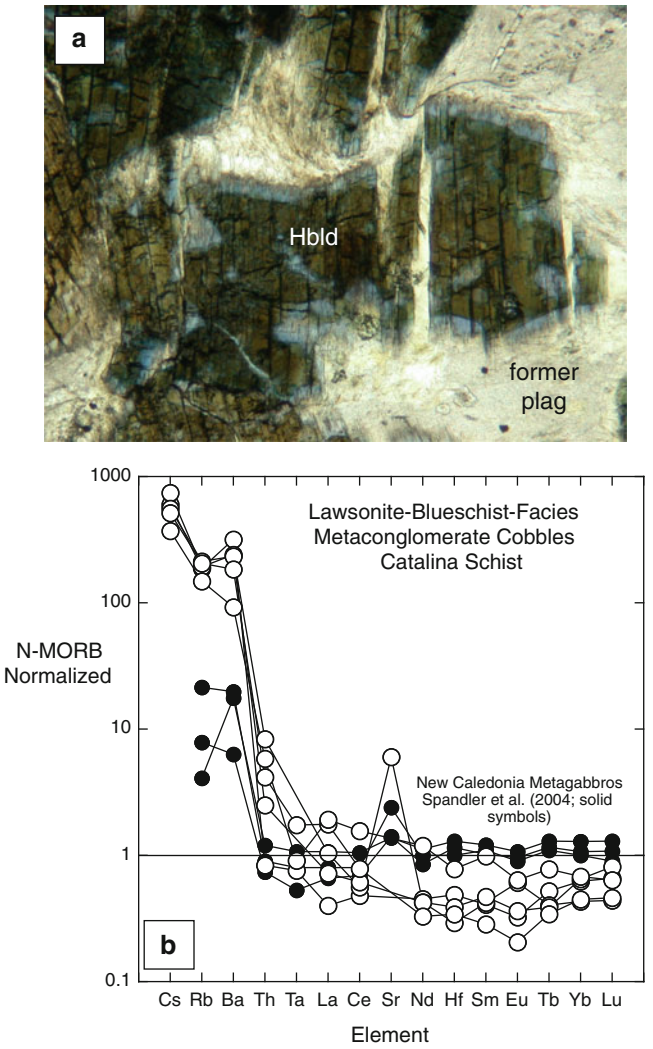

Fig. 9.6 Textures and geochemistry of metasomatized metaconglomerate cobbles metamorphosed and metasomatized at lawsonite-blueschist conditions in the Catalina Schist, California (from Tenore-Nortrup and Bebout 1993). In these cobbles, hornblendes with igneous compositions are variably replaced by sodic amphibole and plagioclase has been entirely replaced by phengite with minor lawsonite (**a**). Width across the image (long dimension) is 1.5 mm. Particularly this replacement of plagioclase by phengite is accompanied by dramatic enrichments in other LILE such as Cs, Rb, and Ba (**b**; normalized by N-MORB of Hofmann 1988). The same cobbles show whole-rock depletions in Na correlated with the K enrichments related to this phengitization. Also shown in (**b**) are the normalized concentrations in metagabbros from New Caledonia studied by Spandler et al. (2004)

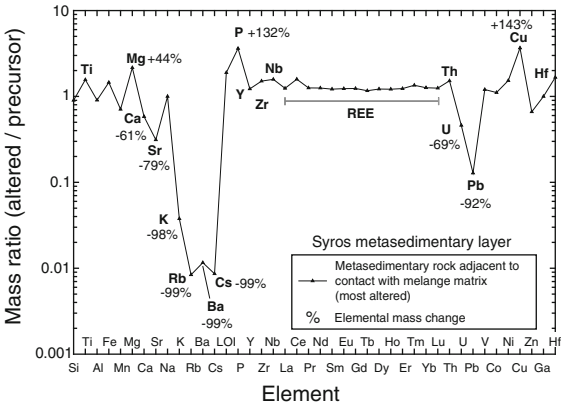

Fig. 9.7 Plot of trace element concentrations in metasedimentary rock having undergone metasomatic exchange with ultramafic mélange matrix, relative to the concentrations in the same layer but away from the interface with this mélange matrix (from Breeding et al. 2004)

Fig. 9.6b). The cobbles are also strongly enriched in N (which substitutes for K^+ as NH_4^+) with $\delta^{15}N$ inherited from metasedimentary rocks in the same tectonometamorphic units (see Bebout 1997). Moore et al. (1981) similarly suggested that the Na/K whole-rock ratios from similar conglomerate cobbles in the Franciscan Complex (California), resulted from the exchange of alkalis during fluid-rock interactions (see Fig. 9.7 in Bebout and Barton 1993). As in any study of chemical change in metamorphic rocks, it is necessary to consider the possibility of superimposed metasomatism representing the rock's full prograde (and retrograde) history, beginning with the near-surface weathering and/or diagenetic alteration of the protolith. Extensive alkali exchange has been documented in diagenetically altered sandstones (e.g., Boles and Ramseyer 1988; Morad 1988). Recent work by Beinlich et al. (2010a) documents extensive Mg removal during weathering resulting in the production of quartz-bearing rocks from peridotite conglomerate clasts. Association of metasomatism with metamorphism, at any grade, can depend on the ability to associate the chemical change with textures and mineral parageneses that can be linked to this metamorphism(e.g., the grain-scale metasomatism represented by partial replacement of igneous hornblende by sodic amphibole in Fig. 9.6a). In some cases, it is possible to use isotope compositions of metasomatic parageneses to link alteration to fluid flow at various stages of prograde and retrograde metamorphism, as in the Catalina Schist, for which Bebout and Barton (1989) were able to relate metasomatic change in ultramafic rocks in melange with regional-scale infiltration by H_2O-rich fluids generated in other parts of the subduction zone. Work by Shen et al. (2009) demonstrating that surface weathering produces distinctive Mg isotope compositions points to the intriguing possibility that low-temperature weathering signatures could be identified in deeply subducted rocks. Penniston-Dorland et al. (2011) suggested that Li concentrations and isotopic compositions of Catalina Schist metasedimentary rocks correlate with a chemical alteration index presented by Nesbitt and Young (1982) and used to determine extents of weathering in sediment sources.

9.5.2 Element Loss Due to Leaching into Infiltrating Fluids

Breeding et al. (2004) demonstrated dramatic loss of trace elements housed in phengite largely due to the destabilization of phengite in response to metasomatic interaction with nearby ultramafic rocks (see Fig. 9.7). Removal of components can involve infiltrating fluids (as in the case illustrated in Fig. 9.7) or can be related to the partitioning of elements into internally derived fluids released by devolatilization reactions (see discussions below of metasedimentary devolatilization).

9.5.3 Volume Strain Leading to Passive Enrichment in Residues

Removal of more fluid-mobile components from various rock compositions, in actively deforming rocks experiencing infiltration by reactive fluids, can result in strong enrichments in the less mobile components in the residues (see Bebout and Barton 2002). Figure 9.8 demonstrates this relationship for samples from the amphibolite-facies mélange matrix in the Catalina Schist. Here the most dramatic passive enrichments are represented by the extremely high-Cr, high-Al_2O_3 (nearly monomineralic) chlorite schists in Fig. 9.8a (see similar examples for the New Caledonia suite presented by Spandler et al. 2008).

9.5.4 Rinds on Metasomatized Tectonic Blocks in Mélange Zones, Representing Combinations of Mechanical and Metasomatic Processes

A number of recent studies have attempted to evaluate element mobility in subduction settings through the geochemical study of metasomatic rinds developed at the rims of mafic, sedimentary, or ultramafic blocks "floating" in a tectonic mélange (tectonic setting illustrated in Fig. 9.4a; see Bebout and Barton 2002; Spandler et al. 2008; Miller et al. 2009; Fig. 9.8). Bebout and Barton (2002) suggested that this rind material is then removed from the blocks during the deformation, resulting in the production of mélange domains with compositions resembling the rinds still existing on blocks in the same mélange unit (see lenticularly shaped lithological mélange domains in Fig. 9.8c; see the figure caption for further description of this outcrop).

9.5.5 Veins, Leucosomes, and Pegmatites

The abundant veins present in many exposures of HP and UHP metamorphic rocks are a direct product of mass transfer in fluid, at least at local (cm) scales. In some

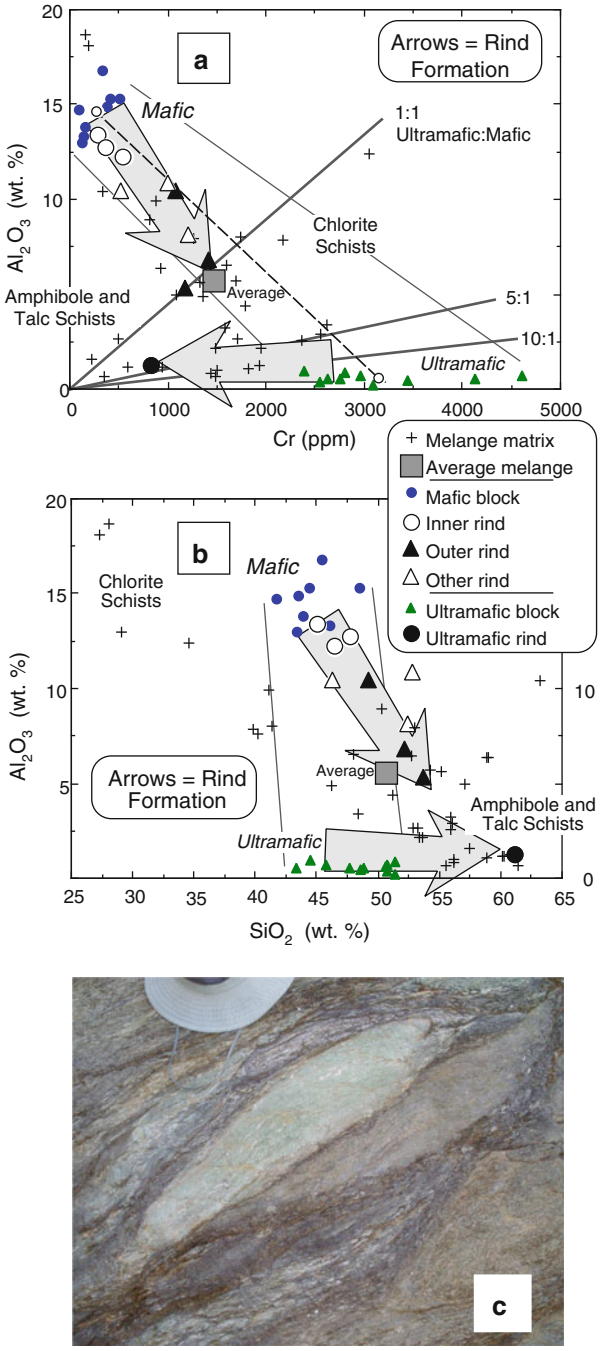

Fig. 9.8 Demonstration of the mechanical and metasomatic mixing producing the mélange matrix in the amphibolite unit of the Catalina Schist (from Bebout and Barton 2002). Chemical discrimination diagrams, demonstrating the conceptual model for mixing in the mélange unit.

cases, such veins are believed to reflect segregation of mass into fractures from directly neighboring host-rocks, whereas in other cases, isotopic or other evidence indicates that the veins reflect larger-scale transport of the vein material (see the full discussion of this distinction in Bebout 2007b; also see Chap. 10). Figure 9.9a, b provide examples of lawsonite-blueschist metasedimentary exposures in the Catalina Schist in which abundant veins reflect mobility of not only SiO_2, but also CaO, Al_2O_2, and Na_2O (the latter three oxides in calcite, albite, and Na-amphibole veins). Vein textures (see sketch in Fig. 9.9b) allow placement of the vein generations into a relative time sequence – assessment of the scales of element mobility, which must be made for each individual vein generation. Extensively quartz-veined exposures in the Otago Schist, illustrated in Fig. 9.9c, are believed to have had a greater than 10% addition of SiO_2 due to infiltrating fluids (see Breeding and Ague 2002). Quartz-bearing vein assemblages, commonly monomineralic quartz veins, are a nearly ubiquitous feature of forearc metasedimentary suites (ancient accretionary systems) and likely reflect the massive transfer of dissolved SiO_2 toward the seafloor in H_2O-rich fluids liberated by a combination of pore water expulsion and metamorphic dehydration (see Sadofsky and Bebout 2004).

More unusual occurrences of pegmatites and leucosomes, which develop during subduction-zone metamorphism (see Fig. 9.10; also see Garcia-Casco et al. 2008), represent the generation of silicate melts and the mobilization of these melts on varying scales. Figure 9.10 demonstrates that, in the Catalina Schist amphibolite-facies unit, pegmatites/leucosomes show a continuum of trace element compositions believed to reflect parentage of the melts in mafic or sedimentary sources or, perhaps, a mixing of melts produced in these contrasting lithologies. These pegmatites and leucosomes reflect water-saturated partial melting in a thermally-immature subduction zone setting in which temperatures near 650°C were achieved at depths of only 35–40 km (see the tectonometamorphic model in Grove et al. 2008). This occurred under, perhaps, analogous conditions similar to those in newly

Fig. 9.8 (continued) (**a**) Cr vs. Al_2O_3, (**b**) SiO_2 vs. Al_2O_3. On (**a**), the *darker-shaded lines* emanating from the origin represent the Cr–Al compositions resulting from varying ultramafic: mafic proportions (labelled for each). The envelopes of simple mixing of ultramafic and mafic compositions are schematically indicated on (**a**) and (**b**) by the regions between the two *subparallel, hand-drawn, solid lines*. The two *small, unfilled circles* on (**a**) are the mean mafic and ultramafic end-member compositions, with the *dashed line* connecting the two circles representing linear mixtures of the two end members. In general, much of the matrix in this mélange unit is enriched in SiO_2 relative to concentrations that could have resulted from simple mechanical mixing of the mafic and ultramafic endmembers. *Large, shaded arrows* on (**a**) and (**b**) indicate the compositional trends from mafic and ultramafic end members toward the compositions of the rinds developed on each block type. (**c**) Field photograph (hat for scale) of amphibolite-facies mélange matrix in the Catalina Schist, showing the development of (in 2-D) lenticular domains with compositions closely resembling either the rinds on metamafic blocks (the *darker-colored, more brownish domains*) or the rinds developed on metaultramafic blocks (the *lighter-colored, greenish domains*). Width across the image (long dimension) is 1 m

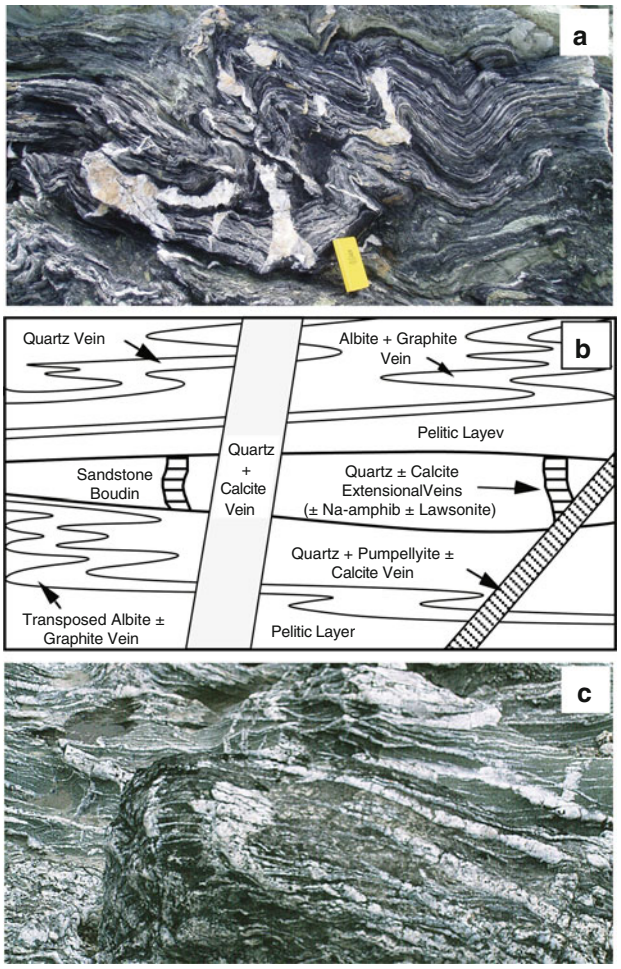

Fig. 9.9 Extensively veined metasedimentary rocks in the Catalina Schist lawsonite-blueschist unit (**a**, **b**; from Bebout and Barton 1993) and in an exposure from the Otago Schist (**c**; photograph courtesy of J. Ague, personal communication, August, 2010). The sketch in (**b**) illustrates veining textures in exposures such as that shown in (**a**). Exposures, such as that shown in (**c**), were inferred by Breeding and Ague (2002) to have had up to 10% additions of SiO_2 from infiltrating metamorphic fluids. Width across the image (long dimension) is 1.25 m

initiated modern subduction zones, forearcs at margins experiencing ridge-trench encounters, or in Archean subduction zones. Nevertheless, these features are not unlike the "IRS fluids" of Gill (1981), enriched in Incompatible elements such as the LILE (see Fig. 9.10), with Radiogenic Sr isotope compositions (for these pegmatites, $^{87}Sr/^{86}Sr$ of 0.7055 to 0.706, corrected to the 115 Ma age of the peak metamorphism; see Barton et al. 1988; Bebout 1989), and **S**iliceous (65–70 wt% SiO_2; see discussions in Sorensen and Barton 1987; Bebout and Barton 1993; Pearce and Peate 1995).

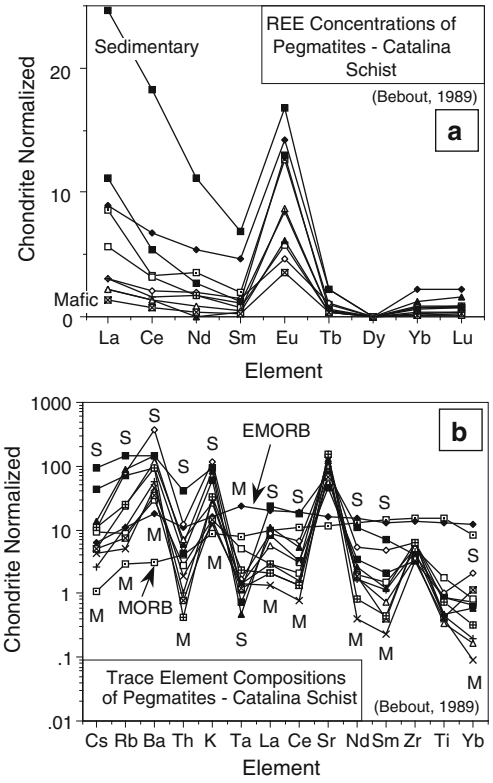

Fig. 9.10 Trace element compositions of pegmatites and leucosomes in the Catalina Schist, California (data from Bebout 1989), normalized to chondritic compositions of McDonough and Sun (1995). These pegmatites/leucosomes show a continuum of trace element compositions believed to reflect parentage of the melts in mafic or sedimentary sources or, perhaps, mixing of melts produced in these contrasting lithologies. Where present within metasedimentary exposures, the pegmatites or leucosomes are relatively enriched in LREE and LILE, whereas such features in metamafic exposures are the most depleted in LREE and LILE. Pegmatites within ultramafic mélange exposures, without an obvious spatial relationship with either sedimentary or mafic sources, have compositions on both (**a**) and (**b**) intermediate to those of the pegmatites and leucosomes within the metasedimentary or metamafic exposures. In (**b**), labels of "S" and "M" indicate the sedimentary or mafic compositional endmembers, respectively – for example, for Cs concentrations, the highest concentration corresponds to a pegmatite in a metasedimentary exposure ("S"), whereas the lowest concentration corresponds to a leucosome in a metamafic exposure ("M"). This relationship is reversed for Ta concentrations, for which the sediment-sourced pegmatites and leucosomes have the lowest concentrations

9.5.6 Geochemical Gradients Developed in Envelopes Near Veins or at Contacts Between Contrasting Lithologies

Partly because of the interest in defining magnitudes and scales of intercrystalline diffusion during HP/UHP metamorphism, recent studies of subduction-zone

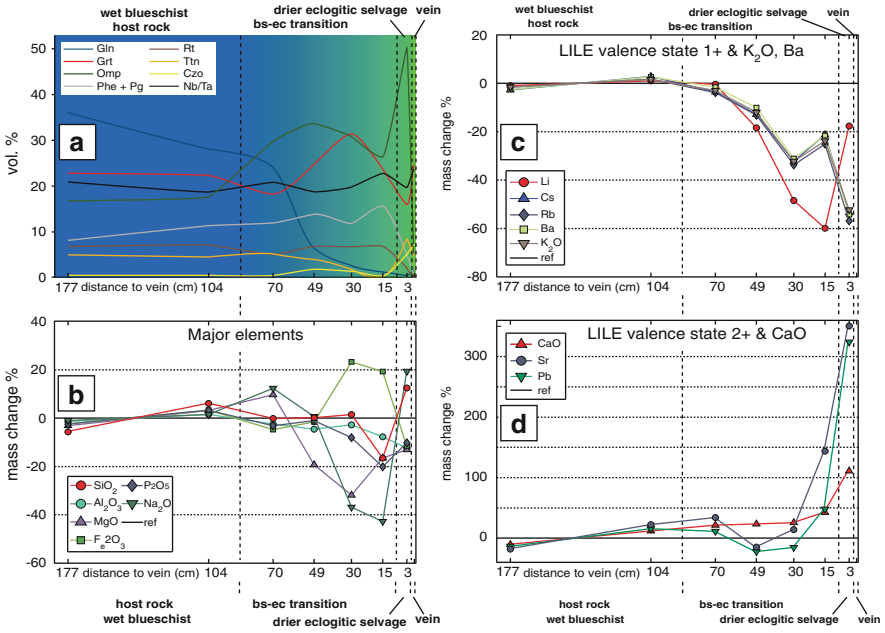

Fig. 9.11 Concentration ratio diagrams for major and trace elements, in combination with modal abundances of their major host minerals, plotted against distance of samples from a vein with a well-developed metasomatic envelope in the Tianshan, China (from Beinlich et al. 2010b). Concentration ratios are derived from mass-balance calculations and are relative to the least-altered blueschist host rock as well as to Sc as an immobile reference element. A positive deviation from the reference line indicates mass-gain. A negative deviation indicates mass-loss of a certain element and is given in % relative to the reference concentration (*black line*). Note that the scale of the y-axis varies between individual diagrams. (**a**) Whole-rock Nb/Ta ratios and modal abundances (in vol%) of the major host minerals for the trace elements of interest (mineral modes based on point-counting). (**b**) Mass change (%) of major elements, except CaO, MnO, K_2O, and TiO_2. (**c**) Relative concentrations of LIL elements with a valence state of 1+ together with Ba (2+) and Li indicating significant release into the fluid phase. (**d**) Strong enrichment of LIL (2+) elements and CaO within the eclogitic selvage, which were introduced by the fluid phase

metasomatism have increasingly been focused on the assessment of chemical gradients near veins and at lithological contacts. For example, for Li and its stable isotopes, there has been great interest in identifying any isotope fractionation related to intercrystalline diffusion (e.g., Penniston-Dorland et al. 2010). Figure 9.11 demonstrates the approach taken by Beinlich et al. (2010b), in which the authors demonstrated mineralogical and related geochemical change along a traverse of a blueschist-eclogite transition developed near veins in the Tianshan HP suite (China). This traverse again demonstrates the effect of not only metasomatic trace element additions, but also the stabilization or destabilization of mineral phases that can serve as hosts for certain trace elements (e.g., phengite for LILE, B, and Li; see Bebout et al. 1999, 2007).

9.5.7 *Isotopic Evidence for Scales and Sources of Mass Transfer*

In some cases, only isotopic data can aid in the evaluation of the scales of fluid and mass transfer and the sources of these materials. The plots of O isotope data in Fig. 9.12 show evidence of large-scale fluid flow in the Catalina Schist subduction complex (Fig. 9.12a) and demonstrate that the transport of these fluids was enhanced along fractures (now veins) and mélange zones (see Fig. 9.12b; from Bebout and Barton 1989; Bebout 1991a, b). Other isotopic studies of fluid mobility in ancient accretionary complexes include Vrolijk (1987) (also see work on the modern Barbados accretionary prism; Vrolijk et al. 1990), Sadofsky and Bebout (2004), and Sakakibara et al. (2007). Nelson (1995) documented kilometer-scale mobilization of fluids carrying sedimentary Nd- and Sr-isotope signatures, through analyses of metasomatic rinds on mafic tectonic blocks in the Franciscan Complex mélange.

9.5.8 *Direct Analyses of "Fluids" in Fluid and Melt Inclusions*

In some cases, the presence of abundant fluid inclusions that are demonstrably related to peak metamorphism allows for direct assessment of fluid composition by microanalysis of the inclusions. Figure 9.13 presents trace element compositions of fluids trapped as inclusions in subduction-related serpentinites (from Scambelluri et al. 2004a, b). In this case, the fluid inclusions are thought to represent fluids released by prograde serpentine dehydration reactions and this process is regarded as an analog for the deserpentinization occurring in convecting mantle wedges. Frezzotti et al. (2011) identified micro-diamond associated with C-O-H fluid inclusions, quartz, and magnesite, in garnetites at the UHP Lago di Cignana locality. Diamond-bearing fluid inclusions in these rocks contain bicarbonate, carbonate and sulphate ions, silica monomers, and crystals of carbonate and silicate, leading these authors to propose that the related carbon mobility resulted from the dissolution of carbonate and not decarbonation reactions.

Other, earlier studies of HP- or UHP-generated fluid inclusions in subduction-zone metamorphosed mafic rocks discovered either relatively saline fluid compositions (Monviso Complex, Italy; Philippot and Selverstone 1991) or more dilute, H_2O-rich compositions (Dominican Republic and California; Giaramita and Sorensen 1994). The latter authors suggested that these differences reflect differences in the fluid-flow regimes in the two settings. The Monviso example represents a within-slab tract of gabbroic rocks, metamorphosed in a more continental-type subduction setting (the more saline inclusions were also noted by Scambelluri et al. 1998, 2002; Nadeau et al. 1993; Scambelluri and Philippot 2001; Fu et al. 2002; Franz et al. 2001). The other settings reflect higher degrees of fluid flux in deforming mélange zones metamorphosed in a more oceanic setting (lower-salinity inclusions also noted by Sadofsky and Bebout 2004; also see Gao and

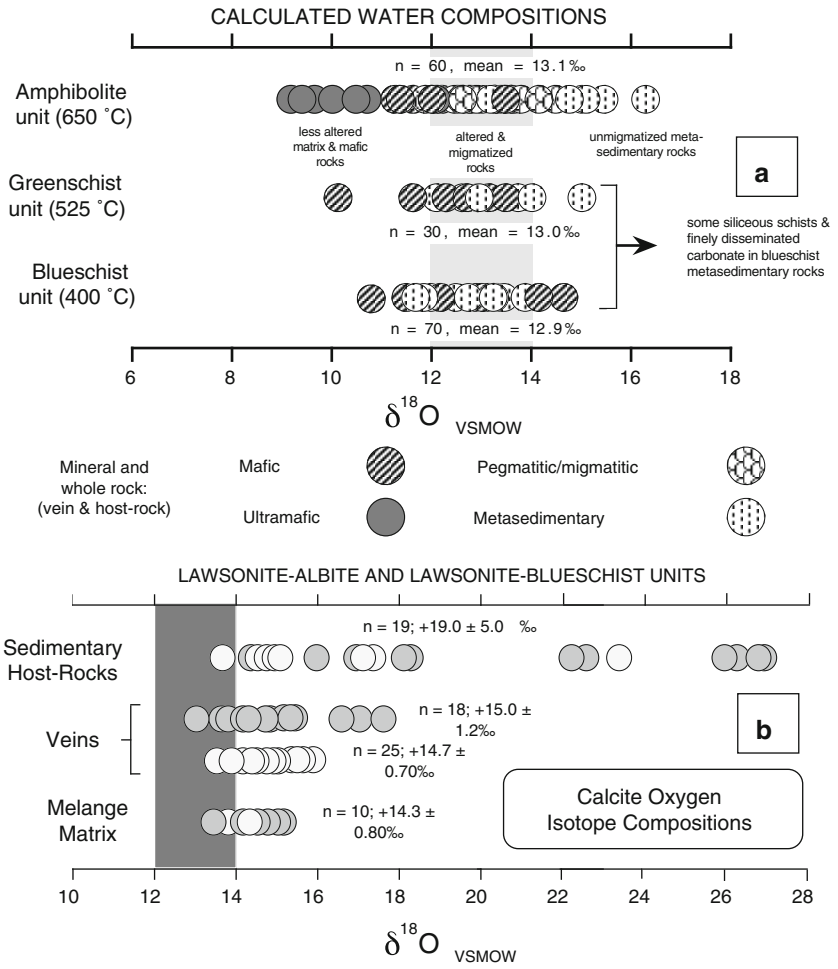

Fig. 9.12 Oxygen isotope systematics, in the Catalina Schist, indicating large-scale flow of H_2O-rich metamorphic fluid (**a**) and enhanced fluid flow in fractures and mélange zones (**b**). (**a**) Calculated H_2O $\delta^{18}O$, using $\delta^{18}O$ data for various metasomatic features and host-rocks and petrologically and/or isotopically inferred peak metamorphic temperatures (figure from Bebout and Barton 1989, 1993; sources of fractionation factors provided therein). In all units, $\delta^{18}O$ values are the most consistent with exchange involving H_2O-rich fluids with $\delta^{18}O_{VSMOW}$ of +13 + 1‰ (*shaded region*) in mélange zones (both mélange matrix altered mafic and ultramafic blocks in melange) and in/near prograde veins (see data for blueschist unit in Bebout 1991b). In the blueschist and greenschist units, some siliceous schists (metacherts) have $\delta^{18}O$ of >20‰ (see Bebout 199la). For the amphibolite unit, data are subdivided as representing "less altered matrix and mafic rocks", "altered and migmatized rocks", or "unmigmatized metasedimentary rocks". (**b**) $\delta^{18}O$ of calcite from metasedimentary rocks, veins, and mélange matrix in lawsonite-albite (*darker-shaded circles*) and lawsonite-blueschist (*lighter-shaded circles*) units (from Bebout 1991b). Shaded area shows calculated $\delta^{18}O$ range. $\Delta^{18}O_{calcite\text{-}water}$ is 2.5–4.3‰ for the peak metamorphic temperature range of 350–450°C inferred petrologically and isotopically. High values for finely disseminated calcite in metasedimentary rocks may reflect earlier diagenetic history. The more uniform $\delta^{18}O$ of the veins and mélange zones, relative to the coherent

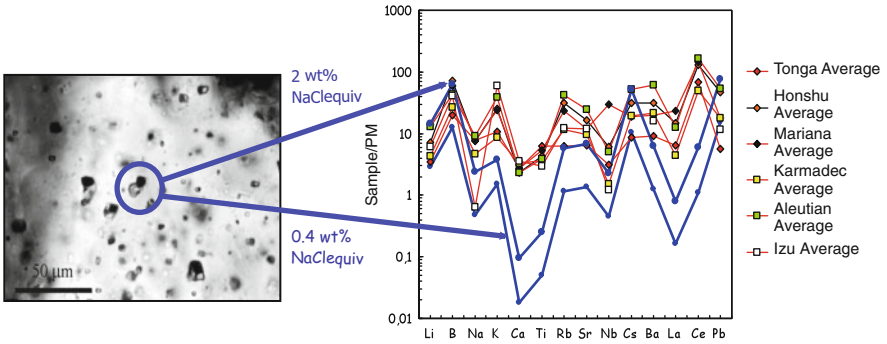

Fig. 9.13 Measured trace element concentrations of fluid inclusions believed to represent deserpentinization reactions in the orogenic peridotite suite at Almirez, compared with the volcanic arc lavas from several settings (from Scambelluri et al. 2004a, b). The lower part of the field between the *two blue-lined patterns* is the average of fluid inclusions recalculated using the value of 0.4 wt% NaCl equivalent for internal standardization, and the higher part is the average of inclusions recalculated using 2 wt% NaCl equivalent. Normalization is to the primitive mantle (data from McDonough and Sun 1995). The patterns for the fluid inclusions in some ways resemble those for volcanic arc lavas from the various settings indicated in the legend on the right side of the diagram (see discussion in Scambelluri et al. 2004a, b)

Klemd 2001, for discussion of low-salinity fluid inclusions in the Tianshan Complex (China)).

9.5.9 *General Comments Regarding the Scales of Metasomatism Represented in the Rock Record*

For most observations regarding metasomatism in subduction-related rocks (metamorphosed slab or mantle wedge), evaluation of the scales of the related mass transfer is limited by the scale of the observations. Many geochemical studies are conducted on hand-specimen-sized volumes of rock, limiting assessment of open-system behavior to that scale. However, more recent studies examining geochemical gradients across lithological traverses (Miller et al. 2009), or vein envelopes (Beinlich et al. 2010b), can evaluate mass transfer, at least at that scale (also see Widmer and Thompson 2001; Sorensen et al. 2010). In other cases, vast expanses (tens of meters to kilometers scale) of the same rock type, enriched in a component with an obvious external source, seemingly require metasomatic additions at that scale (Scambelluri et al. 2010). Isotope studies, such as an O

Fig. 9.12 (continued) metasedimentary rocks, was interpreted to reflect enhanced flow of fluid in fractures and along other zones of more intense deformation. Statistical data for these data are the mean and 1σ

isotope study of the Catalina Schist (Bebout and Barton 1989; Bebout 1991a, b), offer one means of identifying larger-scale fluid flow. In that case, the fluids that infiltrated a higher-grade (amphibolite) unit had $\delta^{18}O$ values consistent with previous equilibration with similar rocks but at lower temperatures (400–600°C; Bebout 1991a, b), leading to the conclusion that the fluids traveled up-temperature into this higher-grade unit. However, in some cases it is difficult to identify isotopic effects of large-scale flow of fluid through relatively uniform reservoirs (e.g., large expanses of sandstone-shale sequences in accretionary complexes) and without large temperature differences along flow paths, given the inherent isotopic heterogeneities in these rocks. In this case, the fluids can be relatively non-reactive, having previously, isotopically equilibrated with similar rocks at similar temperatures (see discussion in Sadofsky and Bebout 2004).

In some cases, "fluids" (aqueous fluid or silicate melts) can be directly sampled and analyzed, allowing for the evaluation of the metasomatism of their sources and allowing for the consideration of larger-scale mass transfer discussed in later sections of this chapter. Section 9.6 provides examples of "inverse" situations in which the metasomatism of a fluid source, and the relatively large-scale transport of the fluids, is implicit in the interpretation of the compositions of these fluids. Examples of this approach include (1) "inverse studies" of volcanic arc magmas and other mantle-derived melts in which inferences are made regarding the nature of the additions from slabs to mantle wedges or into the deeper mantle; (2) direct analyses of "fluids", venting onto the seafloor along faults in sedimentary prisms or from serpentinite seamounts (e.g., at the Marianas margin), which allow for the evaluation of mass transfer at depths in forearcs; and (3) the study of arc volcanic gases and the recycling behavior of major volatiles (CO_2, N_2, SO_2; Hilton et al. 2002), which represents a grand-scale example of an inverse study assessing subduction zone metasomatism, in which knowledge of the devolatilization history and isotope evolution of deeply subducting rocks can provide insight regarding the gross balance or imbalance of subduction zone inputs (from the seafloor) and outputs (in volcanic gases).

9.6 Large-Scale (Tens to Hundreds of Kilometers Scales) Pathways of Subduction Zone Metasomatism

One challenge, when evaluating various records of metasomatic processes, is to identify the products of mass transfer that are of sufficient magnitude and scale to affect large-scale ocean-to-mantle cycling (e.g., production of volcanic arc magmas; cycling of volatiles through convergent margins). Here, it is important to rely on geophysical observations that can help place constraints on the volumes of material involved and thus whether one is evaluating a process that can potentially influence the chemical cycling of an element of interest. Examples of these geophysical contributions are recent characterizations of the nature of the mantle

wedge and slab-mantle interface in modern subduction zones, and the proposed massive hydration of sub-crustal ultramafic rocks in oceanic lithosphere experiencing slab-bending in outer rise environments (see Ranero et al. 2005). The advection of massive volumes of hydrated ultramafic rock, in subducting slabs, could have a huge impact on subduction input flux of not only H_2O but also many other trace elements enriched during this hydration (e.g., B, Cl, Li, As; e.g., see Deschamps et al. 2010).

9.6.1 Outer Rise Metasomatism of Sub-Crustal Mantle Rocks in Slabs Entering Modern Subduction Zones

The observations made at the Central America margin, of traces of normal faults in the outer rise believed to penetrate to the upper mantle section of the bending lithospheric plate (see Ranero et al. 2005), revealed a new but somewhat difficult-to-quantify means of introducing volatiles into slabs soon to be subducted. Although the specifics regarding metasomatism of sub-crustal mantle rocks in slabs entering trenches (in outer rise environments), in response to infiltration by seawater, are largely unknown, many have inferred significant enrichment of elements by this hydration. Metasomatism at these levels could have a large impact on deeper subduction zone geochemical evolution, as dehydration could result in the mobilization of components enriched prior to subduction (see Ranero et al. 2005; Deschamps et al. 2010). The more recent considerations of subduction zone H_2O budgets include estimates of the magnitude of H_2O flux in this reservoir (e.g., Hacker 2008; van Keken et al. 2011).

9.6.2 Shallow (<30 km) Forearc Metasomatism Involving Seawater Expulsion from Subducting Sediments (and Oceanic Crust)

9.6.2.1 Magnitudes and Possible Significance of Forearc Pore Fluid Expulsion

Massive volumes of seawater are thought to be subducted into shallow parts of subduction zones, then mostly expelled during mechanical compaction and lithification of seafloor sediments (see von Huene and Scholl 1991; Moore and Vrolijk 1992; Jarrard 2003). These low-T fluids experience varying degrees of chemical exchange with the subducting sediments and oceanic crust, potentially imparting chemical change in the fluids, sediments, and crustal rocks. The abundant chemical and isotopic analyses of fluids venting from forearcs, into the ocean, and metamorphic suites representing subduction to 5–40 km depths, afford an analysis of the

magnitude and potential significance of this chemical exchange and flux on chemical cycling.

Rea and Ruff (1996) estimated that the global sedimentary subduction flux of solids is 1.43×10^{15} g/year and of pore fluids is 9.1×10^{14} g/year (9.1×10^{11} kg/year). This fluid flux is virtually identical to that of von Huene and Scholl (1991). Jarrard (2003) provided a similar flux estimate of 1.1×10^{15} g/year. The total mass of the hydrosphere is about 1.4×10^{21} kg (~1.36×10^{24} g). Thus, without mechanical fluid expulsion, the Earth's oceans would be subducted in ~1 billion (10^9) years (see Fyfe and Kerrich 1985). As a consequence, future research should evaluate whether, for some chemical components, the cycling of seawater through active sediment-dominated forearcs could contribute significantly to ocean water chemical evolution. As an example of potentially significant pore-water-sediment exchange, K-feldspar in clastic sedimentary sections, that were subducted to depths of up to 30 km (some at lawsonite-blueschist facies conditions), commonly show extensive to complete albitization, indicating extensive Na^+-K^+ exchange between fluids and the feldspars (see Moore et al. 1981; Fig. 9.7 in Bebout and Barton 1993). Sediment-rich forearcs could also be important sites for the return of C to the oceans and atmosphere, explaining some of the imbalance of arc volcanic return and subduction inputs (see Sect. 9.6.6). The significance of forearc fluid flux for ocean chemical evolution is made difficult by the great uncertainty in the fluxes of fluid, including the possibility that additional "external" pore water enters the system as meteoric water and is then expelled along faults to the seafloor (see discussion by Kastner et al. 1991).

9.6.2.2 Fate of Sediments During Early Subduction

During the earliest stages of subduction, sediments experience large amounts of compaction and deformation, resulting in the mechanical expulsion of pore waters (see Moore and Vrolijk 1992; Jarrard 2003; Hacker 2008). Reactions among clay minerals (smectite-illite; Brown et al. 2001; Moore et al. 2001; cf. Vrolijk 1990), particularly those producing low-grade metamorphic micas, result in the release of significant amounts of mineral-bound H_2O and produce relatively low-chloride fluids in accretionary wedges. At shallow levels of accretionary prisms, this metamorphic fluid is likely to be dwarfed by large amounts of expelled pore waters (see Moore and Vrolijk 1992). However, the loss of structurally bound H_2O during clay mineral transitions to low-grade micas has important implications for the more deeply subducted H_2O budget dominated by the hydroxyl contents of minerals such as the micas (see Rupke et al. 2002, 2004). Clay minerals, particularly illite, also host many of the trace elements of most interest to those studying volcanic arc lava "slab additions" (B, Li, N, Rb, Cs, and Ba; see discussion by Bebout et al. 1999). Other significant dehydration reactions, in shallow parts of accretionary prisms, include the transformation of opal-A (which contains ~11 wt% H_2O) to opal-CT (opal which shows the beginning of formation of domains of short-range ordering) to quartz (Moore and Vrolijk 1992).

9.6.2.3 Compositions of Fluids Venting from Shallow Parts of Forearcs Onto the Modern Seafloor

There is a wealth of geochemical data for pore fluids in accretionary prism sediments and more deformed zones, including décollement. These data provide a record of element mobilization, in some cases related to reactions of the types discussed above that produce low-salinity waters, which locally dilute the more saline pore waters (Elderfield et al. 1990; Kastner et al. 1991; Moore and Vrolijk 1992; also see discussions of forearc mud volcanoes in You et al. 2004; Godon et al. 2004). In addition to the dehydration or breakdown of clay minerals and opal-A (amorphous opal), influences on pore water chlorinity include the dissociation of methane gas hydrates (clathrates; see Kvenvolden 1993), clay membrane ion filtration, biogenic or thermogenic combustion of organic matter, dissolution of minerals, mixing of fluids from different sources, and decarbonation reactions and related reduction in CO_2 content. Fluids sampled in the décollement on ODP drilling legs commonly have decreased chlorinity, variable $^{87}Sr/^{86}Sr$, $\delta^{18}O$, and Sr concentrations, an increased CH_4, silica content and Mg^{+2}/Ca^{+2}, and a decreased Ca^{+2} content relative to fluids away from such structures (Kastner et al. 1991; cf. Elderfield et al. 1990; Zheng and Kastner 1997). Solomon et al. (2006) document liberation of Ba from barite at shallow levels beneath the décollement in the Costa Rica forearc, and discuss the possible implications of this Ba release for deeper subduction Ba cycling. Manning (2004) provided a summary of the compositions of the forearc fluids, comparing these compositions with those of fluids present at greater depths in subduction zones, and discussed the general evolution of salinity and total dissolved solute content with increasing depth.

9.6.2.4 Veins as Records of Large-Scale Forearc Fluid Mobility

Vein networks in exposures of paleoaccretionary rocks, formed at <30 km depths, record large-scale fluid-mediated mass (and heat) transfer, and more specifically, document the mobility of CH_4-bearing, low-chlorinity, H_2O-rich fluids (see Moore and Vrolijk 1992; Fisher 1996; Sadofsky and Bebout 2004). The specifics of vein formation, and the origin of the vein minerals (generally quartz- and/or calcite-rich), for example, introduced via advection of mineral components, or diffusion into fractures from nearby host rocks, are debated for individual cases (see Fisher 1996). Nevertheless, extensive vein networks (e.g., those in Fig. 9.9) are generally considered to reflect the upward migration of fluids generated by a combination of compaction and dehydration of more deeply buried sediments (see Bebout 1991a, b; Sadofsky and Bebout 2004; Sakakibara et al. 2007). This is supported by the relatively lower salinities, and elevated CH_4 concentrations in fluid inclusions within vein minerals, which is similar to the "freshening" observed in faults and décollement at shallower levels (Brown et al. 2001; Moore et al. 2001). Based partly on the Sr isotope compositions of the veins, Sample and Reid (1998) argued that some fluids originate in the subducting slab (cf. Breeding and Ague 2002).

9.6.2.5 Fluids Emanating from Marianas Forearc Serpentinite Seamounts

Serpentinite seamounts in the Marianas margin formed by release of fluids from subducting sediments and altered oceanic crust in shallow parts of the forearc and their reaction with the forearc ultramafic mantle wedge. In addition, mafic blueschist-facies clasts in these settings provide a confirmation of the P-T estimates from thermal models along the modern Marianas slab interface (see Maekawa et al. 1993; Peacock 1996), and a glimpse at the subducting oceanic crust from these depths in the forearc that complements the field record of mafic rocks in paleo-accretionary complexes such as the Franciscan Complex. Studies examining the major and trace element and isotopic compositions of these serpentinite muds (and the ultramafic clasts contained therein) from these seamounts have attempted to estimate the compositions of the fluids that generated the serpentinite at depth and have invoked additions of trace elements such as B, Li, As, and Cs to these fluids from subducting oceanic crust and sediment (see Ryan et al. 1996; Benton et al. 2001, 2004; Savov et al. 2005). One series of seamounts in the Marianas forearc allows an estimate of progressive fluid and element loss as a function of distance from the trench (depth to the slab; Mottl et al. 2004; also see Hulme et al. 2010) and provides a link with studies of devolatilization and fluid flow in paleoaccretionary complexes derived from these same depths. Mottl et al. (2004) interpreted trends in pore water Na/Cl, B, Cs, and especially K and Rb, across this suite of seamounts (Fig. 9.14) as reflecting their derivation from the top of the subducting plate, driven by increasing temperature, and suggested that the trends reflect dominantly upward flow, with minimal lateral mixing. The range of depth inferred for the top of the slab beneath these seamounts (16–29 km) falls within the depth ranges found in the Franciscan Complex, Western Baja Terrane, and Catalina Schist, for which the chemical effects of metasedimentary devolatilization have been investigated (Bebout et al. 1999; Sadofsky and Bebout 2003). The mobility of the elements deduced from these studies is compatible with the results of sediment-fluid experiments of You et al. (1996), indicating enhanced mobility of B, NH_4^+, As, Be, Cs, Li, Pb, and Rb in forearc fluids. Interestingly, Bebout et al. (1999) and Sadofsky and Bebout (2003) demonstrated that, in cool subduction zones, represented by most of the forearc metasedimentary suites, these fluid-mobile elements (B, Cs, As, and Sb) are largely retained in metasedimentary rocks subducted to depths of up to 45 km at concentration levels similar to those in seafloor sediments. Thus, it appears that the mobility of these elements at shallower levels represents a relatively small proportion of the inventory found in sediment in some forearcs.

9.6.3 Chemical Processing of Subducting Rocks Across Forearcs and to Beneath Volcanic Arcs

Study of sedimentary, mafic, and ultramafic rocks, peak-metamorphosed at pressures representing deep-forearc to subarc depths (30 to >100 km), can yield

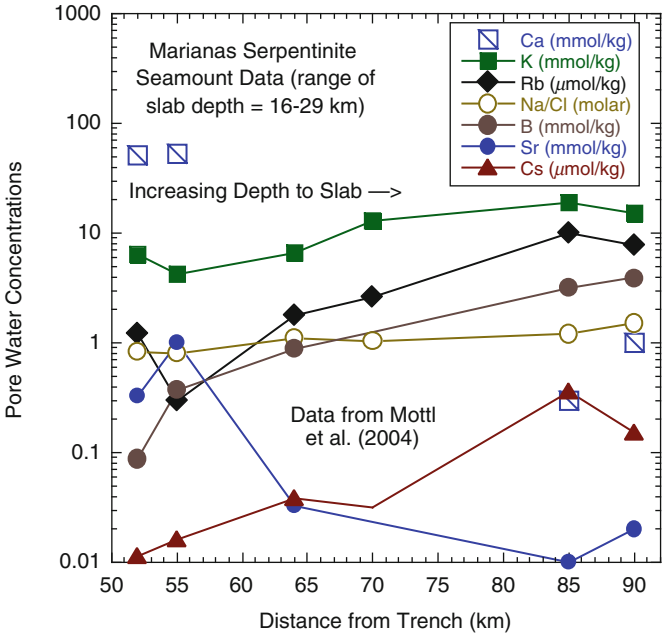

Fig. 9.14 Variations in pore water chemistry in the Marianas forearc serpentinites, as a function of distance from the trench, thought to represent progressive element loss from the subducting slab at 16–29 km depths (re-plotted data from Mottl et al. 2004; figure from Bebout 2007b). A number of compatibilities exist between these data and data for paleoaccretionary rocks in the Catalina Schist and Franciscan Complex (both in California), Western Baja Terrane (Baja, Mexico), and Sambagawa (Japan), including evidence for Sr loss at shallow levels, and increasing metamorphic losses of B, Rb, and Cs with increasing depth in the forearc. Vein geochemistry and, for B and Sr, whole-rock trends demonstrate the mobility of these elements in the forearc metasedimentary suites representing 5–30 km (see Bebout et al. 1999; Sadofsky and Bebout 2003)

field and geochemical evidence regarding the "chemical processing" of these rocks during prograde subduction-zone metamorphism along the slab-mantle interface (see Bebout 2007a). For some components (e.g., volatiles and elements particularly mobile in hydrous fluids or in melts), these observations bear directly on considerations of global-scale recycling budgets.

9.6.3.1 Records of Deep Forearc to Subarc Metasedimentary Devolatilization and Related Large-Scale Fluid Mobility

Recently conducted work on trace element compositions and devolatilization in several subduction-related metamorphosed sedimentary suites yields insight regarding the efficiency of deep subduction of trace elements in sediments. The Catalina Schist contains metasedimentary units that were subducted along prograde P–T paths ranging from very cool paths, similar to those predicted by thermal

models of modern subduction, to paths that are anomalously warm for most modern subduction zones, and for the amphibolite facies unit, sufficiently warm to result in partial melting (see Fig. 9.15; see Bebout et al. 1999, 2007). Some trace elements thought to be relatively mobile in fluids (Cs, B, As, Sb, and N) show dramatic depletion in rocks that experienced the higher-temperature paths (epidote–blueschist, epidote–amphibolite and amphibolite), but rocks experiencing the cooler paths largely retain these elements (lawsonite–albite and lawsonite–blueschist rocks). This observation is consistent with the retention of these elements to depths of up to ~45 km in most modern subduction zones (also see Sadofsky and Bebout 2003). Figure 9.15b, c demonstrate relationships among Rb, Cs, B, and Li concentrations in white micas (phengite), the dominant mineral reservoir for these elements, and compare these data with the whole-rock data for Rb and Cs concentrations in the Schistes Lustres and Lago di Cignana metasedimentary rocks (see the shaded horizontal field in Fig. 9.15c). Busigny et al. (2003) suggested that N, H, and Cs were retained in metasedimentary rocks from the Schistes Lustres and at Lago di Cignana. These metasedimentary rocks were subducted along relatively cool P–T paths to depths of ~60–90 km (see peak P–T conditions and exhumation paths for the Schistes Lustres in Fig. 9.5), approaching the depths of subducting slabs beneath volcanic fronts (cf. Bebout et al. 2011; see Fig. 9.15c). Together, the observations from the Catalina Schist and Alpine suites indicate that, in cool margins, these elements are largely available for addition to the mantle wedge beneath volcanic arcs. Depletion of elements such as Ba, Th, La, and Sm (used as tracers of sediment inputs in volcanic arc lavas, and, in studies of deeper mantle, geochemical heterogeneity; see Plank 2005) is not evident in these suites (and other HP metapelitic rocks; see Arculus et al. 1999; Spandler et al. 2003), and melting at greater depths is perhaps required for more significant removal and fractionation of these elements.

9.6.3.2 Deconvoluting Metasomatic Effects of Seafloor and Subduction-Zone Metasomatism on the Compositions of HP and UHP Mafic Rocks

Figure 9.16 (from Bebout 2007a) illustrates the difficulties in distinguishing between the effects of seafloor hydrothermal alteration and subduction-zone fluid-rock interactions on the compositions of deeply subducted mafic rocks. The plots in Fig. 9.16 show that the geochemical compositions of metabasaltic rocks subducted to depths of up to ~100 km, commonly overlap strongly with the compositions of their protoliths, i.e. the variably hydrothermally altered basalts on the seafloor. Any change in the compositions of these rocks due to subduction zone metasomatism is obscured by the heterogeneity related to magmatic and seafloor alteration processes. In these plots, the data from Sorensen et al. (1997), Saha et al. (2005), and Spandler et al. (2004) are for samples of mafic tectonic blocks in melange zones, some with metasomatic rinds developed at their margins. These rinds, believed to have developed during fluid-rock interactions in the mélange at HP or UHP metamorphic conditions, provide the clearest fingerprint of the geochemical

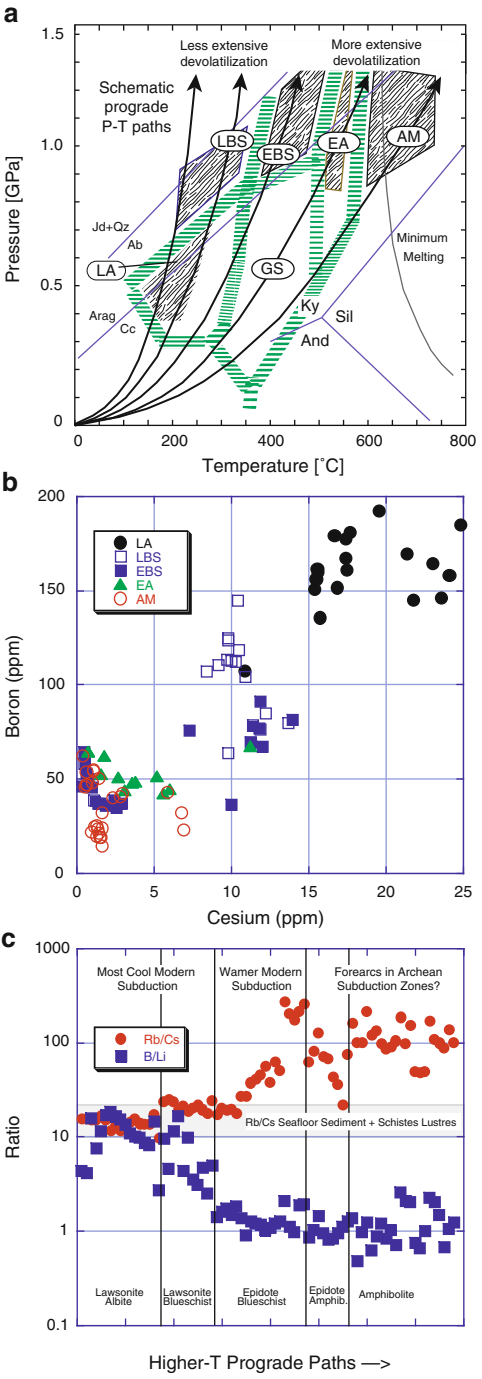

Fig. 9.15 Demonstration of varying change in LILE, B, and Li for metasedimentary rocks as a function of the prograde P-T path along which the rocks were metamorphosed (figure from Bebout 2007a). (**a**) Simplified P-T diagram demonstrating the range of prograde paths experienced by the units in the Catalina Schist. Rocks experiencing the high-temperature paths show more extensive loss of volatiles than the rocks experiencing the low-temperature paths (from Grove and Bebout 1995; Grove et al. 2008). (**b**) Boron and Cs concentrations in white micas in the metasedimentary rocks of the Catalina Schist, showing decrease in the rocks which experienced the higher-T prograde paths (see **a**). (**c**) Change in B/Li and Rb/Cs resulting from the loss of B and Cs, at higher grades, relative to Li and Rb, both of which show little change with increasing grade. Also shown (in *gray-shaded horizontal field*) is the range of Rb/Cs for seafloor sediment (data from Ben Othman et al. 1989; Plank and Langmuir 1998) and the Schistes Lustres and Lago di Cignana rocks (data for the HP/UHP metasedimentary rocks from Busigny et al. 2003)

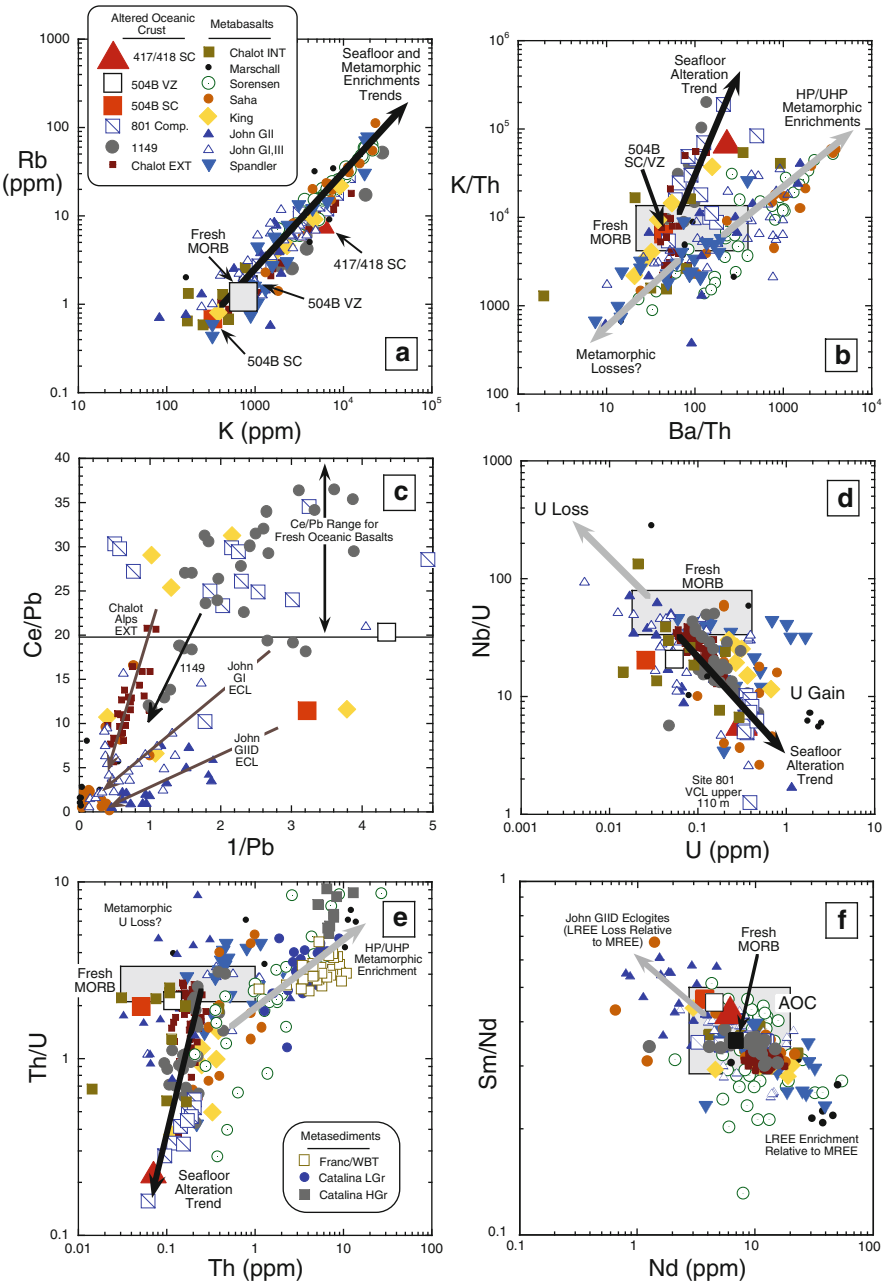

Fig. 9.16 Whole-rock element concentrations in metabasaltic rocks from HP and UHP metamorphic suites (figure from Bebout 2007a). These plots allow comparisons of the compositions of HP and UHP metabasalts with compositions of "fresh" (unaltered) seafloor basalts and AOC. (**a**, **b**) Relationships among concentrations of K, Rb, Ba, and Th for HP and UHP metabasalts and their presumed seafloor protoliths. In these figures, data for AOC from DSDP/ODP Sites 417/418

alteration attributable to subduction zone metamorphism. The data from Marschall (2005), King et al. (2004), and John et al. (2004) are for samples collected from larger expanses of more coherent metabasalt, away from any melange zones, and perhaps more representative of the coherent oceanic slab as it subducts. In each of the plots in Fig. 9.16, data for the metabasaltic rocks from these two settings are compared with data for fresh (unaltered) MORB and for various seafloor altered basalts (AOC; sources of data in figure caption), with the arrows on each plot

Fig. 9.16 (continued) (composite composition from Staudigel 2003), 504B (supercomposite and volcanic zone composite from Bach et al. 2003), and 801 C (various sub-composites) and 1149 (data for individual samples; data for both from Kelley et al. 2003), are used to define chemical trajectories associated with seafloor hydrothermal metasomatic alteration that can be considered when evaluating any metasomatism due to subduction-zone metamorphism (see *arrows* labeled, "Seafloor Alteration Trend"; shown as a field in **f**). Data for metasomatized tectonic blocks in mélange, and the metasomatic rinds developed on these blocks, from John and Schenk (2003), Saha et al. (2005), Sorensen et al. (1997), and Spandler et al. (2004) best define alteration trajectories that can be related directly to HP and UHP metasomatism. Data from King et al. (2004), John et al. (2004), and Marschall (2005) are for samples from more intact exposures of HP or UHP metamorphosed AOC. Most of the samples, for which data are presented here, have major and fluid-immobile trace element compositions similar to those in MORB, that is, deemed representative of magmatic products at mid-ocean ridges (including their Nd isotope compositions indicating their production in the depleted mantle; see Table 1 in Bebout 2007a). Several authors have, in more detail, related the compositions to expected spreading center differentiation trends (Spandler et al. 2004; John et al. 2004). Only the studies by Becker et al. (2002) and Arculus et al. (1999) invoke significant whole-rock loss of LILE during metamorphism of AOC, and those studies were limited by less thorough consideration of the full range of possible AOC protolith compositions (see text for discussion). The composition of "Fresh MORB" (N-MORB) in (**a**) is from Sun and McDonough (1989). The elevated Ba enrichments in many HP and UHP metamafic lithologies could reflect transfer of sedimentary Ba into subducting oceanic crustal lithologies in which high Ba/Th, Ba/La, and Ba/Nb signatures could then be entrained to greater depths. (**c**) Ce-Pb relationships for HP and UHP metabasalts and their presumed seafloor protoliths (after John et al. 2004; Miller et al. 1994). *Arrows* toward the origin indicate possible trends of Pb addition (and resulting decrease in Ce/Pb) during seafloor alteration ("1149"), very low-grade metamorphism related to ophiolite emplacement ("Chalot Alps EXT"), or possibly HP and UHP metamorphism ("John GI ECL" and "John GIID"; discussion by John et al. 2004). Data for HP metamorphic rocks from Marschall (2005) and Saha et al. (2005) seemingly also indicate Pb additions, perhaps during HP/UHP metamorphism. (**d**) Nb-U data for HP and UHP metabasalts in comparison with data for AOC and unaltered "fresh" MORB, demonstrating the overlap of the metabasaltic compositions with compositions attributable to seafloor alteration. (**e**) Th-U relationships for HP and UHP metabasaltic rocks in comparison with fresh MORB, AOC, and metasedimentary rocks from the Catalina Schist and from the Franciscan Complex and Western Baja Terrane. Note that the high-grade (amphibolite-facies) metasedimentary rocks in the Catalina Schist (*dark gray* filled squares labeled, "Catalina HGr") have elevated Th/U, relative to their low-grade equivalents, possibly reflecting removal of low-Th/U "fluids" (hydrous fluids or silicate melts). The *gray arrow* indicates a possible trend of Th enrichment, resulting in increased Th/U in some metabasaltic samples (e.g., data from Saha et al. 2005 and Sorensen et al. 1997). (**f**) Sm-Nd data for HP and UHP metabasalts, rinds, and AOC, as an example of a parent/daughter element pair possibly disrupted by subduction-zone metamorphism. It is evident that Sm/Nd can be shifted to higher or lower values, and the shifts to higher values are consistent with recent experimental work indicating that Nd is more strongly partitioned into hydrous fluids than Sm (see Kessel et al. 2005a)

distinguishing the chemical trends associated with HP and UHP metamorphism from the alteration associated with seafloor alteration.

LILE Enrichments

Potassium and Rb show large co-enrichments, both on the seafloor and during subduction-zone metamorphism, as demonstrated by the nearly complete overlap of K-Rb trends in data for altered oceanic crust (AOC; DSDP/ODP Sites 417/418, 504B, 801C, and 1149) and for both the metabasaltic rocks from more coherent exposures and the metasomatic rinds on tectonic blocks (Fig. 9.16a). Few of these metabasaltic samples have K-Rb concentrations lower than those of unaltered MORB and the AOC. However, significant HP and UHP metamorphic K-Rb losses could be obscured by uncertainty in the extent of seafloor alteration. In contrast with this rather frustrating relationship, Ba exhibits differing enrichment patterns, relative to those of K (and Rb), for seafloor and subduction-zone metasomatic alteration, seemingly providing one means of distinguishing between the two metasomatic histories (see the two trends in Fig. 9.16b; cf. King et al. 2007; Sorensen et al. 2005).

Variations Among the Concentrations of Ce, Nb, U, Th, and Pb

Figure 9.16c–e demonstrate some relationships for Ce-Nb-U-Th-Pb concentrations, similar to those for the LILE, and also demonstrate some possible evidence for the mobility of Pb and Th in HP and UHP fluids or melts. John et al. (2004) suggested that the deviations in their Ce-Pb data (Fig. 9.16c) from compositions of oceanic basalts (MORB and OIB) represent Pb additions during two stages of subduction-related alteration, one at peak metamorphic conditions and one during exhumation (see the arrows representing alteration trends for "John GI ECL" and "John GIID ECL" on Fig. 9.16c). However, Fig. 9.16c demonstrates similar trends for the extremely low-grade metabasalts from the External Units in the Alps ("Chalot Alps EXT"; metamorphosed at very low grade but not subducted; Chalot-Prat 2005) and for some AOC (e.g., some of the data from Site 1149). Seafloor alteration of basalt has long been known to produce enrichments in U, relative to REE, HFSE, Pb, and Th (Nb-U data for AOC in Fig. 9.16d; Staudigel 2003). Deviations in the Nb/U of HP and UHP metabasalts from of that of MORB, due to subduction-zone metamorphism, are difficult to demonstrate, as nearly all of the data for the metabasalts lie within the fields for AOC, and like the plots of the LILE, very few metabasaltic samples show obvious evidence for subduction-zone depletion in U relative to fresh MORB (i.e., few data fall in the upper left part of the plot in Fig. 9.16d). A small number of metabasaltic rocks, particularly the Group IID eclogites of John et al. (2004), show hints of U loss relative to Th, leading to higher Th/U relative to both MORB and AOC. These rocks are believed to have been metasomatized along zones of enhanced fluid infiltration during HP metamorphism

(see Fig. 9.16e). In Fig. 9.16e, Th-U data for metasomatic rinds on mafic tectonic blocks (particularly "Sorensen" and "Saha"), again, the clearest fingerprint of subduction-zone chemical alteration, seemingly reflect Th additions by HP and UHP metamorphic fluids, as they fall to the right of the seafloor alteration trend (see the gray arrow indicating the trajectory of metamorphic enrichment).

Possible REE Mobilization

Figure 9.16f demonstrates some possible loss of LREE (here represented by Nd) during HP metamorphism, relative to MREE (here represented by Sm), as indicated by a shift to higher Sm/Nd at lower Nd concentrations for the Group IID eclogites of John et al. (2004), thought to have experienced enhanced fluid-rock interactions. However, the Sm-Nd data for most HP and UHP metabasalts either overlap the range of data for N-MORB, and various AOC, or show some shift to higher Nd concentrations and lower Sm/Nd consistent with some LREE enrichment during metamorphism.

9.6.3.3 Coeval Mechanical and Metasomatic Processes Along the Slab-Mantle Interface

A growing number of studies have explored the possibility that coeval mechanical and metasomatic processes, along the slab-mantle interface, could produce highly metasomatized lithologies capable of exerting influence over the compositions of fluids transported in such zones (see King et al. 2006, 2007). Bebout and Barton (2002) demonstrated that, for Catalina Schist mélange matrix rocks (from a kilometer-scale mélange zone; see Fig. 9.17 and also Fig. 9.8), some whole-rock concentrations cannot be explained by simple mechanical mixing and must have involved additions (SiO_2) or subtractions (LILE) during infiltration of the mélange zone by hydrous fluids for which calculated fluid $\delta^{18}O$ values indicate an external, sedimentary source and thus kilometer-scale fluid flow (see Fig. 9.12). Other work on similar settings, involving fluid-rock interactions in mélange zones, and metasomatic exchange among disparate lithologies, has been undertaken by Breeding et al. (2004), Spandler et al. (2008), Miller et al. (2009), Marocchi et al. (2010), and Bulle et al. (2010). In each case, schistose rocks, rich in hydrous silicates such as chlorite and talc, are attributed to the strong deformation and metasomatism in the mélange zones.

9.6.3.4 Records of Mantle Wedge Metasomatism in Orogenic Peridotites

There has been considerable recent interest in the study of subduction-related peridotites (and xenoliths) as a means of investigating metasomatic processes in ancient mantle wedge environments (see Scambelluri et al. 2010; see Fig. 9.18).

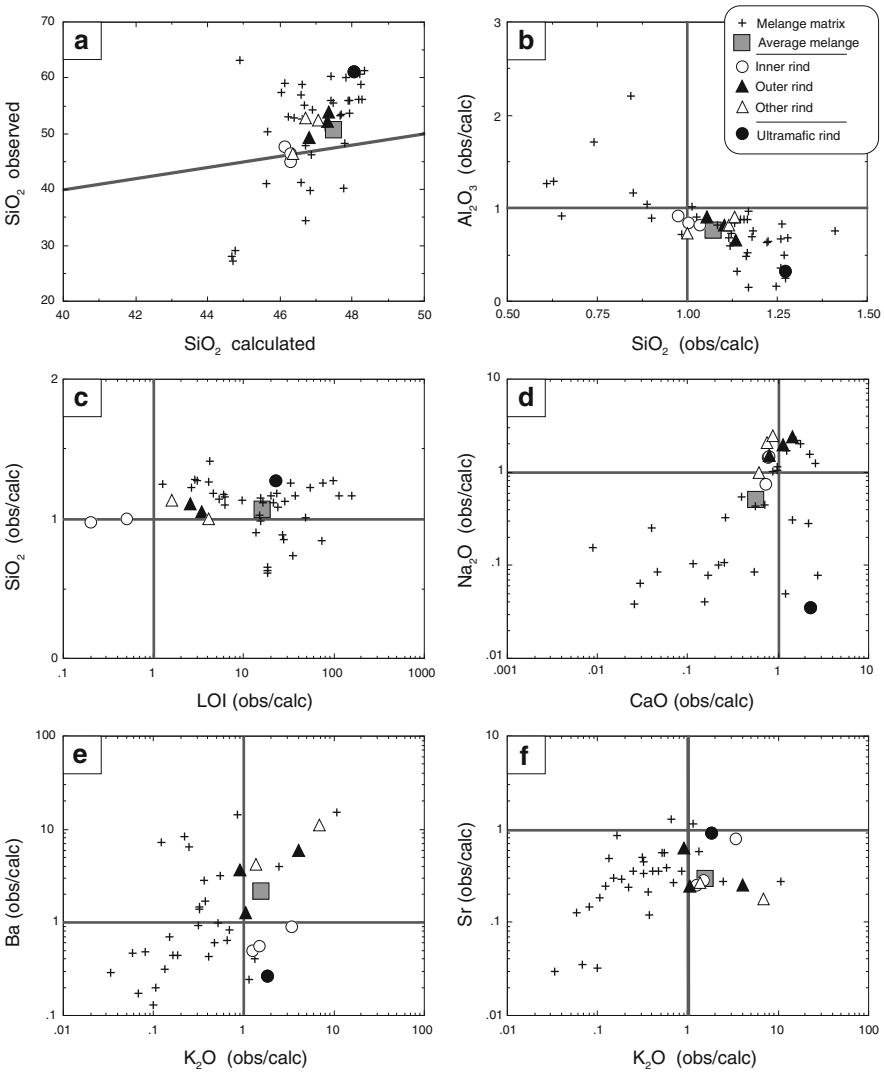

Fig. 9.17 Demonstration of metasomatism in subduction mélange zones, with examples from Bebout and Barton (2002) (see other studies of mélange "hybrid rocks" by Spandler et al. 2008; Miller et al. 2009; Marocchi et al. 2010). In these plots (**a**–**f**), measured concentrations of various elements (and LOI), in Catalina Schist amphibolite-grade mélange matrix samples, are compared with the concentrations calculated for each sample using a Cr-Al_2O_3 mixing reference frame (i.e., calculating mixing proportions of mafic and ultramafic rocks assuming relative immobility of Cr and Al in the metamorphic fluids). In these calculations, mafic rocks are the Al-rich mixing component, and the ultramafic rocks are highly enriched in Cr. Based on these calculations, SiO_2 and LOI (mostly H_2O) show significant additions, whereas Na, Ba, and Sr show depletion relative to the concentrations due only to simple mixing. Some nearly monomineralic chlorite schists have extremely high Cr and Al_2O_3 concentrations, reflecting extensive volume strain (resulting from removal of most other elements not residing in chlorite), accommodated by fluid infiltration traced by the O isotope behavior within the mélange unit

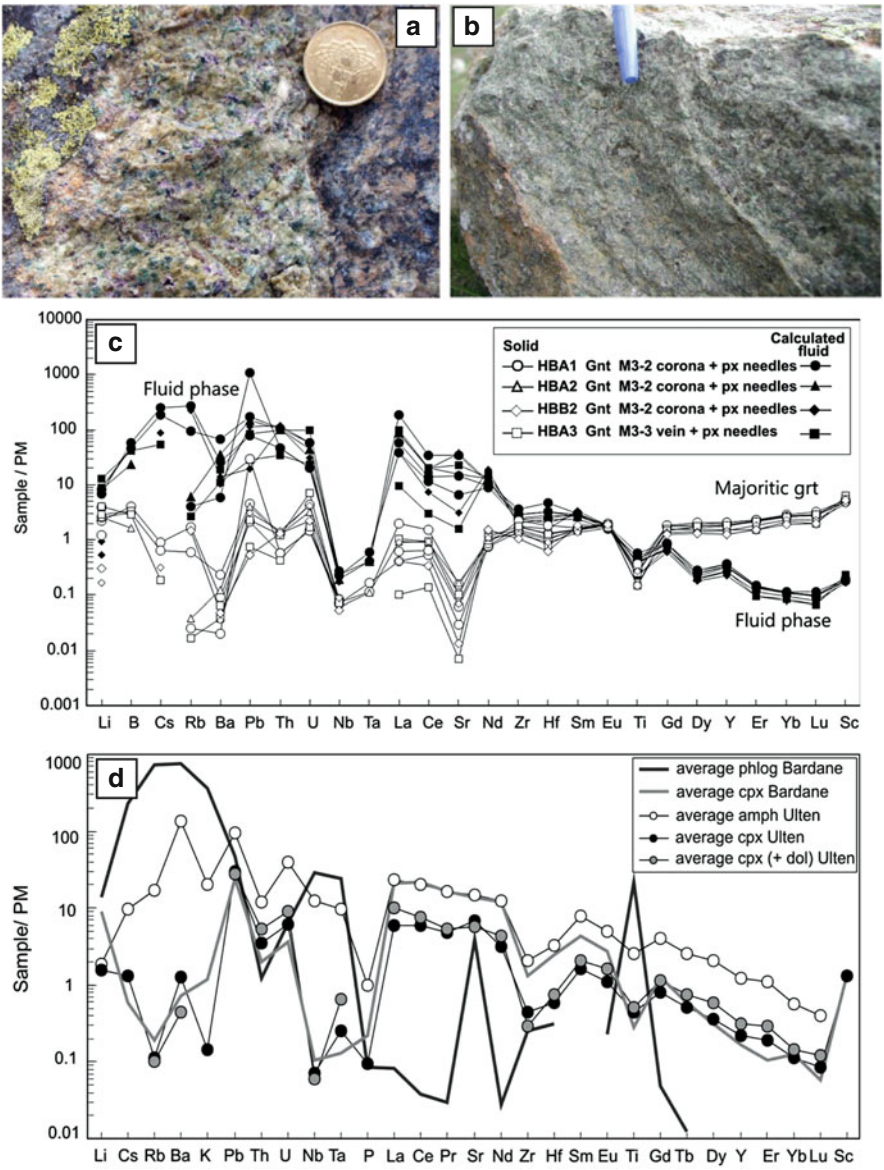

Fig. 9.18 Example of a geochemical study of peridotites believed to represent ancient mantle wedge environments. (**a**) and (**b**) Field photographs of garnet peridotites from the Ulten Zone, Italian Alps (from Scambelluri et al. 2010; also see Scambelluri et al. 2006; Malaspina et al. 2009). (**a**) Coronitic garnet peridotites. The coarse porphyroclastic texture of this rock is inherited from shallow spinel-facies crystallization. Spinel grains (*black*) are contoured by *light pink* garnet coronas formed during low-strain recrystallization of the mantle peridotite; (**b**) Mylonitic garnet + amphibole peridotite. The main foliation dips from the *top left* to the *bottom right* of the photograph. It consists of amphibole and fine-grained garnet associated with olivine, clinopyroxene, and orthopyroxene. (**c**) Calculated fluid compositions in equilibrium with M3-3 and M3-2 stage majorite using $D_{fluid/garnet}$ from Kessel et al. (2005a). (**d**) Comparison of the trace element compositions of the major trace element mineral repositories from the peak assemblages in Bardane (clinopyroxene and phlogopite) and Ulten Zone (clinopyroxene and amphibole)

In such rocks, enrichment in the concentrations of some trace elements, and calculations of fluid compositions, using published partition coefficients, indicate the mobility of "fluids" with chemical characteristics not unlike those thought to be liberated from devolatilizing slabs (e.g., in some cases, with particular enrichments in Li, B, and LILE such as Cs, Rb, Ba, Pb, Th, and U; see Fig. 9.18c). The calculated fluids show other features commonly associated with crustal subduction inputs, including negative Nb–Ta anomalies and steep LREE–HREE patterns.

9.6.3.5 Element Mobility as Inferred from Metamorphic Studies

The research to date on element mobility, based on study of HP and UHP metamorphic rocks, allows some preliminary conclusions to be made.

Extents of Devolatilization in Forearcs

It appears that, in the relatively cool subduction zones, subducting sediments (and probably also oceanic crustal rocks) can largely retain their inventories of even the more fluid-mobile elements, to at least 90 km (Lago di Cignana; Busigny et al. 2003; Bebout et al. 2011). In cases where young, warm oceanic lithosphere is being subducted (e.g., Cascadia; Kirby et al. 1996), during ridge-trench encounters, and in the Archean (see Martin 1986), higher geothermal gradients may generate greater forearc devolatilization leading to greater loss of fluid and fluid-mobile elements to the mantle wedge. The data for HP and UHP mafic eclogites in Fig. 9.16 indicate that a number of the elements, of greatest interest to those studying volcanic arcs, are actually enriched in subducting metabasaltic rocks rather than lost, certainly arguing against any strong depletions related to prograde devolatilization to depths of up to ~90 km.

Mass-Balance of Forearc Slab/Sediment Element Loss and Mantle Wedge Element Additions

It is as yet unclear whether it is possible to lose small amounts of fluids and trace elements in forearcs, over large volumes of subducting rocks, to produce the fluid and trace element budget in the forearc mantle wedge. This mantle wedge fluid and element budget is partly delivered to beneath arcs via slab corner convection and partly fluxed toward the surface in serpentinite seamounts and associated pore fluids. Such loss could easily be obscured by the large protolith heterogeneity incorporated into any study of trace element loss. In studies comparing higher-grade rocks with lower-grade or unmetamorphosed equivalents, only the extremely fluid-mobile elements (B, Cs, As, Sb, for the Catalina Schist metasedimentary suite) show a clear record of whole-rock loss. A mass-balance of this type, involving calculation of element loss using published partition coefficients, and

evaluating the extents of loss that could be achieved without observing them, has not yet been conducted (see the brief consideration of this problem for B and Be and B/Be of released fluids in Bebout et al. 1993; the analysis of the Catalina Schist LILE systematics by Zack et al. 2001).

Veining Records of Local- or Large-Scale Mass Transfer

Veins in many cases appear to reflect only local-scale element redistribution and it is unknown whether larger-scale removal of fluid-mobile elements can occur in subducting slabs. Although there is, in some cases, clear demonstration that fluid-rock interactions were relatively local-scale in relatively closed systems (e.g. Philippot and Selverstone 1991; Getty and Selverstone 1994; see also Scambelluri and Philippot 2001), some open system behavior may occur at/or near peak P-T conditions or along the prograde P-T path. Relatively small fluid fluxes, within large masses of chemically similar rock, can be difficult to document using trace elements and stable isotopes. Tracts of rock, that contain vein systems in local equilibrium with host-rocks (Sadofsky and Bebout 2004), do not preclude infiltration by externally-derived fluids transporting mass over large distances. Over large volumes of subducting sedimentary and mafic rocks, relatively small fluid flux could be significant in transporting fluid-mobile elements into the mantle wedge. There is a developing consensus that the majority of examples of larger-scale fluid flux are for zones of structural weakness. Fluid and element flux, strongly concentrated in small parts of the system (e.g., fractures and mélange zones), could result in the disproportionate influence of these zones on the chemical characteristics of any fluids traversing the slab-mantle interface beneath volcanic arcs (see examples of fluid flow and extensive metasomatism highly localized along fracture systems in Austrheim and Prestvik 2008; John et al. 2010; Beinlich et al. 2010b).

Possible Significance of Mélange Formation at the Slab-Mantle Interface

The scarcity of subduction-zone mélange exposures has made it difficult to evaluate the volumetric significance of such domains at depth along the slab-mantle interface. However, as noted earlier, if fluid flow at sub-arc depths is highly channelized along mélange zones (and fractures), such zones could exert disproportionate influence on the chemical/isotopic compositions of the fluids ascending from the slab-mantle interface into the mantle wedge. These fluids could possess hybridized mafic, sedimentary, and ultramafic signatures that crudely reflect the gross proportions of these lithologies. Mélange processes could produce high-variance mineral assemblages, such as nearly monomineralic chlorite- and talc-schists, stabilizing a large hydrous reservoir (and any chemical/isotopic signatures inherited during mixing) to depths greater than those typical for dehydration of normal mafic, sedimentary, and ultramafic compositions (see Bebout 1991b; Bebout and Barton 2002; Spandler et al. 2008).

9.6.4 *Formation of Magmatic Arcs and the Compatibility of the Volcanic Arc and Metamorphic Records of Subduction Zone Mass Transfer*

Arc volcanism is perhaps the most spectacular product of subduction and, as noted above, a grand-scale example of metasomatic transfer, involving metasomatism in subducting slabs, ascent of slab-derived "fluids" through a highly dynamic and chemically reactive flow path in the mantle wedge (perhaps also involving diapiric mass advection; Castro et al. 2010), fluxing of partial melting from the ultramafic melt source, then melt ascent, and, lastly, AFC processes in the hanging-wall lithosphere (see van Keken 2003). Interestingly, although much attention is paid to the characterization of slab additions to arc magmatism, the bulk of the mass mobilized in volcanic arcs is the product of mantle wedge melting (Plank and Langmuir 1988). The voluminous volcanic arc geochemistry database provides a rich set of hypotheses, regarding slab and mantle wedge metasomatism and subduction-zone cycling, that can evaluated through a combination of field-based, theoretical, and experimental studies. In general, the seafloor sediments and altered oceanic basalts subducting into modern convergent margins are enriched in the same chemical species thought to be enriched in subduction-related lavas by fluids released by subducting rocks and ascending into the mantle wedge (e.g., Rb, Cs, Ba, B, and Li, in addition to Th, U, Pb, ^{10}Be, and the LREE; see Elliott 2003; Morris and Ryan 2003; see Fig. 9.19). Attempts to quantify this slab-to-mantle chemical flux rely on a modest number of experimental studies investigating the partitioning of these and other elements among minerals and various types of fluid (alkali-chloride aqueous fluids, hydrous silicate melts, and transitional supercritical liquids; Brenan et al., 1995a,b, 1998; Hermann et al. 2006; Manning 2004; Kessel et al. 2005a, b). Although it appears that aqueous fluids are the dominant fluid type released by subducting sediment and basalt in forearc regions (Hermann et al. 2006; see P-T diagram with wet- and dehydration-melting solidi in Fig. 9.5), the supercritical liquids and hydrous silicate melts may be more important beneath volcanic fronts and across volcanic arcs (e.g., for transporting Be, Th; Elliott 2003; Morris and Ryan 2003).

The element mobility in aqueous fluids documented for various HP/UHP suites representing ancient forearcs is, in general, compatible with what is inferred as the slab component in studies of volcanic arcs. Unfortunately, however, it is not possible to directly infer element mobility at subarc and greater depths from these studies of fluid release and mass transfer in ancient forearcs. The most common theme in the studies of forearc suites is that of SiO_2 mobility, but a number of other major and trace element studies show particular evidence for mobilization at the forearc P-T conditions (B, Na, LILE, perhaps Li; see Bebout 2007a). Metasomatic alteration of slab and sediment in forearcs, related to this transfer of aqueous fluids and dissolved solutes, can become important in altering the chemical/isotopic compositions of subducting oceanic crust and sediments contributing to volcanic arc magmatism at greater depths (i.e., the rocks that at greater depths release solutes into "fluids" entering the subarc mantle wedge). Studies of forearc devolatilization of sedimentary rocks

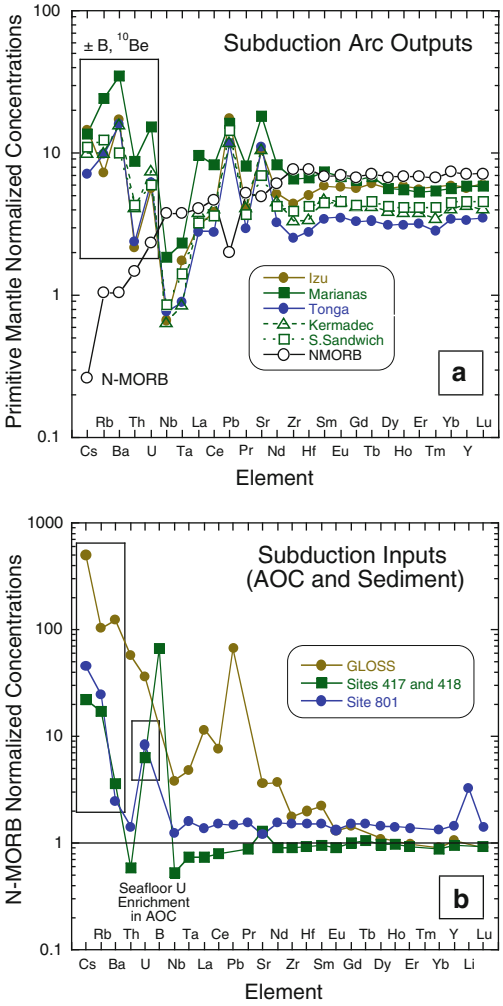

Fig. 9.19 The volcanic arc outputs (**a**) and AOC and sediment inputs (**b**) from subduction-zone cycling, showing the inheritance of non-magmatic trace element signatures in seafloor basalt related to interactions with seawater, and the GLOSS (globally subducting sediment) composite from Plank and Langmuir (1998). Data are normalized to primitive mantle or N-MORB, both from Hofmann (1988). Elements are ordered to the left in terms of increasing incompatibility during mantle melting (tendency to partition into melts) during mantle melting. Data for AOC are from Staudigel (2003) and Kelley et al. (2003). The *boxes* on (**a**) and (**b**) indicate elements that are enriched in both arc volcanic rocks (outputs of subduction) and seafloor sediments and basalts (inputs of subduction). Transfer, to the mantle wedge, of elements enriched in the subducting materials depends on the relative partitioning of the elements into fluids during fluid release from the slab

(Bebout et al. 1999, 2007; Busigny et al. 2003; Bebout et al. 2011) appear to have documented retention of B and Cs to depths of nearly 90 km, implying that most of the inventory of these elements subducted in sedimentary lithologies is available for addition to volcanic arcs and the deeper mantle. Documentation of element mobility

in fluids in forearcs is important as these fluids could ascend into the forearc mantle wedge, hydrating and otherwise metasomatizing ultramafic rocks that are later entrained by mantle convection to subarc and greater depths.

9.6.5 Production of Deep-Mantle Geochemical Heterogeneity and Compatibility with the Record of Metasomatism in HP and UHP Metamorphic Suites

Many geochemical studies of ocean island basalt (OIB) invoke the presence, in mantle source regions, of subducted slabs chemically modified by metamorphism (e.g., loss of Pb and U; Kelley et al. 2005; Hart and Staudigel 1989; Chauvel et al. 1995; Bach et al. 2003). As discussed by Hofmann (2003), it has become relatively routine to associate certain geochemical signatures of the deep mantle (HIMU, EM-1, EM-2, and others), sampled by ocean island basalts, relative to the depleted mantle signature associated with MORB, with varying combinations of variably processed oceanic sediment, oceanic lithosphere, and oceanic island and plateau materials that have conceivably experienced considerable isotopic decay during long-term residence in the deep mantle (see recent discussions by Kelley et al. 2005; Stracke et al. 2003, 2005). The degree to which records of metasomatic change in HP and UHP metamorphic rocks are compatible with inferred metamorphic change to produce these deep mantle signatures was considered by Bebout (2007a) and will be only briefly discussed here (see the discussion of mantle metasomatism in Chap. 12).

9.6.5.1 HIMU

The HIMU mantle signature is generally regarded as reflecting an igneous crustal precursor. The EM-type OIB is interpretated as tracing subducted oceanic crust together with minor amounts of sediment of varying composition. Some workers have concluded that, in order to produce precursors to HIMU, it is necessary for subducting AOC to lose large fractions of its Pb and U inventory, relative to Th, then age in the mantle for varying periods of time (Kelley et al. 2005; Bach et al. 2003; Stracke et al. 2003). This loss, if it occurs beneath volcanic arcs, can explain the complementary large enrichments in these elements in volcanic arc lavas (Chauvel et al. 1995; Fig. 9.19a; cf. Kelley et al. 2005). A similar relationship exists for the Rb-Sr isotope system, for which significant loss of Rb from AOC is generally invoked in order to produce viable precursor compositions for the HIMU source (Bach et al. 2003; Stracke et al. 2003). In fact, depending on the assumptions employed regarding the composition of the subducting oceanic crust, the Rb, Pb, and U losses that are required represent nearly the full undoing of the Pb-U-Rb enrichment that occurs on the seafloor (see composition of AOC in Fig. 9.19b). An oceanic crustal composition unaffected by seafloor alteration, and aged to varying degrees in the mantle, appears to more successfully reproduce the HIMU source

composition (see Hauri and Hart 2003). The data for Pb, U, Ce, Nb, Th, Rb, and Sr, and the REE in HP and UHP rocks lead to the following conclusions relevant for consideration of the formation of HIMU signatures:

1. Obvious losses of Pb and U, relative to Ce, Nb, and Th, occur in only a small number of HP and UHP metabasaltic and metagabbroic rocks, and it appears that the Pb and U enrichments, related to seafloor alteration, are largely preserved to ~90 km (see Fig. 9.16c–e). For a number of samples, Pb enrichment appears to have occurred during subduction-zone metamorphism (see John et al. 2004; Fig. 9.16c).
2. Hints of increases in Th/U, at relatively constant Th concentration, for some metamafic rocks point to possible U loss in some samples (Fig. 9.16e). Thorium loss beneath volcanic arcs is largely dominated by the subducting sediments, which have Th concentrations far higher than those of MORB and AOC (see discussions by Plank 2005; Plank et al. 2002; Plank and Langmuir 1998; Fig. 9.16e). Although relatively few data for Th and U exist for only a few subduction-zone metasedimentary suites, a comparison of metasedimentary Th-Th/U for the Catalina Schist, Franciscan Complex, and the Western Baja Terrane, with compositions of seafloor sediments (Plank and Langmuir 1998; Ben Othman et al. 1989), indicates little or no effect of HP metamorphism on these compositions, even in rocks which experienced epidote-amphibolite-facies metamorphism. In the Catalina Schist, only partially melted, amphibolite-facies metasedimentary rocks have Th-Th/U compositions that deviate from more normal compositions similar to those of seafloor sediment (see Fig. 9.16e; cf. Plank and Langmuir 1998). This could conceivably be due to the removal of low-Th/U "fluids" (aqueous fluids or silicate melts; also see Sorensen et al. 2005). The production of mélange zones, in which coeval metasomatic and mechanical mixing produces hybridized rock compositions, represents another means of decoupling Pb, Th, and U during subduction-zone metamorphism (see Breeding et al. 2004; King et al. 2007).
3. A comparison of the Rb/Sr of AOC with that for the HP and UHP metamafic rocks, many of which had AOC protoliths, demonstrates that this ratio overlaps almost completely with the ratios of their seafloor protoliths (Bebout 2007a). The Group IID eclogites of John et al. (2004) show some shift to lower Nd concentrations and higher Sm/Nd, seemingly reflecting loss of LREE relative to MREE. Whereas other metabasaltic rocks, including some rinds on blocks in melange, appear to show Nd enrichment, relative to Sm, resulting in a decrease in Sm/Nd (see Fig. 9.16f). AOC represents a viable precursor for HIMU OIB sources only if its Rb/Sr is reduced to near its level before hydrothermal alteration on the seafloor. Sm/Nd would need to be slightly decreased in order for AOC to produce the HIMU compositions (see Stracke et al. 2003).

9.6.5.2 EM-1 and EM-2

Various sediment types are called upon as important precursor lithologies, in addition to oceanic crust, for the EM-1 and EM-2 mantle components (see Eisele et al. 2002; discussions by Hofmann 2003 and Stracke et al. 2003, 2005), to produce the radiogenic isotope patterns, and (particularly for EM-1) contribute to higher

proportions of Ba relative to Th, Nb, and La (Weaver 1991). Barium is very efficiently retained in the metasedimentary suites indicating its retention to depths approaching 90 km (Bebout et al. 2007, 2011). In the Catalina Schist metasedimentary suite, whole-rock Ba/K is uniform across the wide range of metamorphic grade, as is whole-rock Ba/Th, Ba/Nb, and Ba/La (Bebout et al. 1999, 2007), similar to what is seen in the Franciscan and Western Baja Terrane metasedimentary rocks (Sadofsky and Bebout 2003).

9.6.5.3 Metamorphic Contributions to the Production of Deep Mantle Geochemical Reservoirs

As discussed above, the work thus far on metamorphic geochemistry in subduction zones has mostly been conducted on suites representing subduction to $\leq$100 km (forearcs) in fluid-rock regimes dominantly involving relatively dilute aqueous fluids (Fig. 9.5; cf. Hermann et al. 2006). It remains unknown whether certain element losses, from subducting rocks in the subarc to greater depth range, can produce appropriate chemically fractionated residues conveyed into the deeper mantle (Fig. 9.1), particularly as silicate melts or supercritical liquids derived in sediments and/or oceanic crust become more important agents of transfer from these lithologies during their transit beneath volcanic arcs (i.e., at >100 km depths).

9.6.6 Volatiles Metasomatism in Subduction Zones: Inputs and Volcanic Outputs of Carbon in the Central America Margin

Recent studies of volcanic degassing at margins, for which subduction inputs are relatively well-known, afford estimates of recycling efficiencies and consideration of the factors governing these efficiencies (see Fig. 9.20). Li and Bebout (2005) provided a detailed dataset with C and N concentrations and isotopic compositions in this sediment section and speculated regarding the input fluxes of C and N into this margin. Also, employing noble gas data from Central America volcanic gases, de Leeuw et al. (2007) estimated the return flux for CO_2. Comparing this flux with the input flux of Li and Bebout (2005) suggested a 10–20% return efficiency in the volcanic gases. For each of the gas samples, de Leeuw et al. (2007) estimated proportions of mantle, organic, and carbonate proportions (see Fig. 9.20b, c). Comparing these proportions with the known lithology of the subducting sediment section, they suggested variations in fluid flow geometries and fluxes from the various subducting lithologies (particularly the deeper, nearly pure carbonate part of the section and the more shallow hemipelagic sediments at shallower levels).

Metasomatic processes could dictate the degree to which C is liberated from subducting sediments and oceanic crust. Kerrick and Connolly (2001) and Gorman

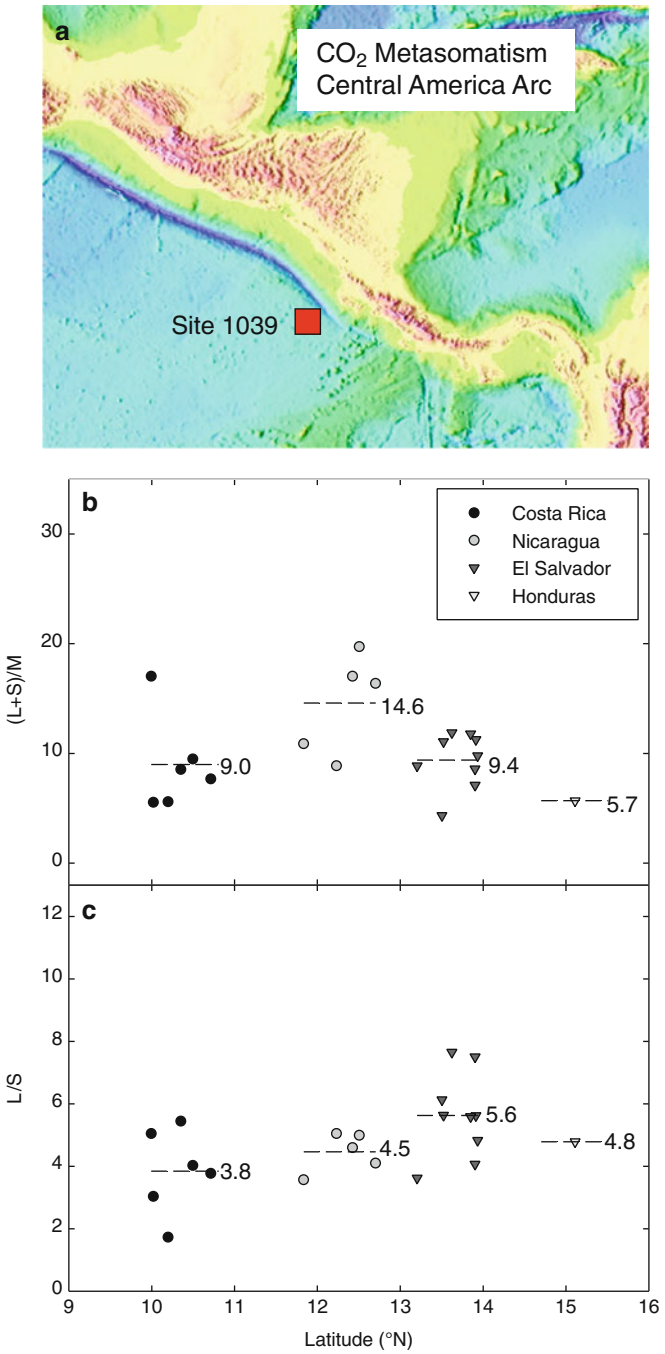

Fig. 9.20 Arc volcano degassing of CO_2 for Central America vs. subduction inputs. (**a**) Bathymetric/topographic map of Central America (*cooler colors* indicating *greater* water depths; *warmer colors* indicating *higher* elevations above sea level), showing the trench and magmatic volcanic arc, and the drilling location for ODP Site 1039, drilled into the sediment section just outboard of the trench and soon to subduct into this margin. Li and Bebout (2005) provided a

et al. (2006) tested two scenarios regarding the fluid infiltration behavior affecting the decarbonation history of subducting pure and impure carbonate rocks and thus the efficiency with which CO_2 is entrained to great depths in subduction zones. Kerrick and Connolly (2001) calculated the devolatilization histories of subducting carbonates assuming no infiltration by an H_2O-rich fluid but allowing any fluid generated by devolatilization reactions to leave the rocks. This scenario resulted in little or no devolatilization in all but the most impure carbonate lithologies and predicted that, under such conditions, the large majority of the carbonate initially subducted in such rocks would survive metamorphism in the forearc, even beyond subarc depths, and would be entrained to greater depths in the mantle. Gorman et al. (2006) allowed for varying degrees of infiltration of the carbonates at the slab-mantle interface by H_2O-rich fluids generated by dehydration reactions in the sub-crustal, ultramafic part of the subducting slab. In that scenario, far more extensive decarbonation was driven by the dilution of the fluid phase by the H_2O in these infiltrating fluids. This latter scenario is worth considering as a means of extensively metasomatizing the slab-mantle interface, with the fluid flux enhanced along fractures and mélange zones, leading to extensive metasomatic alteration. John et al. (2004) suggested that fluids from sub-crustal slab ultramafic rocks infiltrated mafic rocks at UHP conditions, leading to metasomatic element enrichments and depletion (e.g., see the REE fractionation outlined in Fig. 9.16). Variations in the flux of sub-crustally-derived H_2O-rich fluids could be an additional factor in influencing variations in the CO_2 flux along subduction margins such as Central America. Carbonate assemblages in garnet peridotites from the Ulten Zone, believed to represent a paleo-mantle wedge, could reflect infiltration by CO_2-bearing fluids liberated in a subducting slab/sediment section (see Sapienza et al. 2009; also see Scambelluri et al. 2010).

Recent evaluation of the extent of devolatilization during the prograde metamorphism of the Schistes Lustres metasedimentary suite, and UHP metasedimentary rocks at Lago di Cignana, indicates little decarbonation and related C isotope shift (Bebout et al. 2010; see the smaller dataset for carbonates in Busigny et al. 2003). This finding is consistent with the calculations by Kerrick and Connolly (2001) in which very little decarbonation occurred in most carbonate-bearing lithologies to depths beneath the volcanic arcs (and beyond).

Fig. 9.20 (continued) detailed dataset with C and N concentrations and isotopic compositions in this sediment section and speculated regarding the input fluxes of C and N into this margin. Variations in (**b**) slab (calcareous and organic) to mantle-derived CO_2 ((L + S)/M ratio), and (**c**) slab-derived calcareous to organic C (L/S ratio) for the volcanic output in Central America as a function of latitude (from de Leeuw et al. 2007). El Salvador and Honduras data (de Leeuw et al. 2007) are compared with volatiles data for Costa Rica and Nicaragua as reported by Shaw et al. (2003), for which the (L + S)/M and L/S ratios have been recalculated with $\delta^{13}C$ values of organic and marine carbonate endmembers (from Li and Bebout 2005). *Symbols* represent the average ratio at each sample location. *Dashed lines* represent average ratios for each country. For this margin, using the inputs from Li and Bebout (2005), de Leeuw et al. (2007) estimated 10–20% volcanic arc return of subducted C and attributed the imbalance to incomplete decarbonation, fluid flow patterns, and varying forearc underplating of sediment

This conclusion has direct relevance to considerations of the C flux in ancient and modern subduction zones and its influence on deep-mantle (and atmospheric) C content.

9.7 Suggested Future Directions of Research on Subduction Zone Metasomatism

The following section discusses some key issues, related to subduction zone metasomatism, that warrant further attention, if possible integrating experimental, theoretical, field petrologic and geochemical, and geophysical perspectives.

9.7.1 HP and UHP Records of Subduction-Zone Metasomatic Processes

As discussed above, one gloomy perspective might be that, in our studies of metasomatism in HP and UHP suites, we have characterized only the relatively minor metasomatism in forearcs, involving relatively dilute aqueous fluids, relative to the metasomatism at greater depths (subarc and beyond) likely involving melts or supercritical liquids with far higher solute loads (see Hermann et al. 2006). Studies of forearc devolatilization appear to document the relative retention of the even more fluid-mobile elements nearly to subduction depths beneath volcanic fronts (Bebout et al. 1999, 2007, 2011; Busigny et al. 2003). The element mobility observed in the veins investigated in studies of forearc suites could reflect very minor removal of the elements but over large volumes of subducting rocks, resulting in a relatively small overall element flux. Thus, again, there is a great need to undertake a detailed geochemical study of fluids and related metasomatism in UHP suites that experienced P-T conditions of subarcs and greater depths (the P-T diagram in Fig. 9.5 shows some candidates for work of this type). One of the obstacles to undertaking the detailed geochemical work on suites peak-metamorphosed at greater than 100 km is that they tend to have been overprinted more extensively during exhumation than a number of the lower-P suites.

9.7.2 Physicochemical Characteristics of Subduction-Zone "Fluids" Contributing to Volcanic Arc Magmatism

Badly needed are additional experimental studies of solubility and melting of mafic, sedimentary, ultramafic, and hybridized compositions, following up on work by

Manning (2004) and Hermann et al. (2006), in particular exploring the realm of P-T in which silicate melts and supercritical liquids (above the second critical points) are the important agents of mass transfer (see also Spandler et al. 2007; Hermann and Spandler 2008). This work should continue to be focused on both simplified systems (for which it is easier to extract detailed information regarding complexing of solutes in various fluid types; e.g., Manning 2004; Tropper and Manning 2004, 2005; Manning et al. 2010) and more complex systems with compositions approximating those of natural subduction-related bulk compositions (e.g., Keppler 1996; Johnson and Plank 1999; Kessel et al. 2005a, b; Hermann et al. 2006; Spandler et al. 2007; Hermann and Spandler 2008).

9.7.3 Relationships of Seismicity with Fluid Flow and Hydration/Dehydration (and Other Reactions)

A number of researchers have investigated the possible relations between seismicity and fluid flow and hydration/dehydration (and other reactions) over a wide range of depths in subduction zones, in subducting slabs and in mantle wedge environments (Kirby et al. 1996; Peacock and Hyndman 1999; Hyndman and Peacock 2003; Hacker et al. 2003a, b; Abers et al. 2006; John and Schenk 2006; Andersen and Austrheim 2006; Rondenay et al. 2008; Peacock 2009; see Chap. 13). Future research should further evaluate the extent to which devolatilization reactions and related fluid and mass transfer can affect rheology, for example, leading to earthquake generation and more broadly, contributing to degrees of mechanical coupling along the slab-mantle interface. One example of the possible effects of fluid flow and related mass transfer on deep subduction zone rheology, discussed by Peacock and Hyndman (1999), is the stabilization through hydration/metasomatism of talc-rich mineral assemblages at the slab-mantle interface. These authors suggested that serpentine minerals, talc, and brucite would exhibit slab-sliding behavior and that their presence along the subduction thrust could control the downdip limit of earthquakes in some subduction zones.

9.7.4 Role of Hydrated Sub-Crustal Ultramafic Rocks inSubducting Slabs

Depending on its volume and hydration state, subducting hydrated ultramafic rocks in slabs could profoundly influence the subduction budgets of not only H_2O (see Ranero et al. 2005; Hacker 2008; van Keken et al. 2011), but also a number of other components thought to be enriched in serpentinites during fluid-rock interactions involving seawater. It is thus extremely important to identify ways to evaluate the volume of hydrated material being subducted along with their hydration state and chemical composition.

9.7.5 Role of Hydrated Serpentinized Ultramafic Rocks in Mantle Wedges

Mantle wedge ultramafic rocks, hydrated in forearcs, could be transported downward to depths beneath volcanic arcs, or beyond, and, when dehydrated, could figure prominently in H_2O cycling and element transport at depth in convergent margins (Scambelluri et al. 2004a, b; also see recent discussion by Straub and Layne 2008; Deschamps et al. 2010). Additional work should be conducted to determine the major and trace element and isotopic compositions of mantle wedge serpentinites from fossil subduction zones, in order to determine the magnitude of this chemical/isotopic flux.

9.7.6 The Nature of the "Subduction Channel"

Recently, a number of authors have proposed that melange zones represent zones of complex mechanical mixing, and coeval metasomatism, at the interface between subducting slabs and sediments and the overlying mantle wedge (see Bebout and Barton 1989, 2002; Sorensen and Grossman 1989; Spandler et al. 2008). Study of HP/UHP exposures, such as that at Monviso, Italy, emphasizes that the "subduction channel" is a zone of extremely heterogeneous structures and lithology, in which rocks with disparate bulk compositions and metamorphic P-T history can be juxtaposed over a very wide range of scales (see Angiboust et al. 2011). Additional study should investigate the physical and chemical properties of field exposures of these lithologies and evaluate whether they contribute to the low-seismic velocity signatures at/or near the top of subducting slabs (see Abers 2000, 2005; Hacker et al. 2003a, b) and affect the rheology of the slab-mantle interface (Peacock and Hyndman 1999).

Acknowledgements Most of the author's research presented in this chapter was funded by the National Science Foundation, recently by NSF grants EAR-0711355 and EAR-1119264. The author also acknowledges collaborations and discussions with Eizo Nakamura and other colleagues at the Pheasant Memorial Laboratory, Institute for Study of the Earth's Interior (ISEI; Okayama University, Misasa, Japan), and financial support from the ISEI and the Japanese government (most recently, the COE-21 program). This chapter benefited greatly from constructive reviews by Marco Scambelluri and Reiner Klemd and assistance from the book editors D. Harlov and H. Austrheim.

References

Abers GA (2000) Hydrated subducted crust at 100–250 km depth. Earth Planet Sci Lett 176: 323–330

Abers GA (2005) Seismic low-velocity layer at the top of subducting slabs: observations, predictions, and systematics. Phys Earth Planet Inter 149:7–29

Abers GA, van Keken PE, Kneller EA, Ferris A, Stachnik JC (2006) The thermal structure of subduction zones constrained by seismic imaging: implications for slab dehydration and wedge flow. Earth Planet Sci Lett 241:387–397

Agard P, Monie P, Jolivet L, Goffe B (2002) Exhumation of the Schistes Lustres complex: in situ laser probe $^{40}Ar/^{39}Ar$ constraints and implications for the Western Alps. J Metamorph Geol 20:599–618

Alt JC, Teagle DAH (2003) Hydrothermal alteration of upper oceanic crust formed at a fast-spreading ridge: mineral, chemical, and isotopic evidence from ODP Site 801. Chem Geol 201:191–211

Andersen TB, Austrheim H (2006) Fossil earthquakes recorded by pseudotachylytes in mantle peridotite from the Alpine subduction complex of Corsica. Earth Planet Sci Lett 242:58–72

Angiboust S, Langdon R, Agard P, Waters D, Chopin C (2011) Eclogitization of the Monviso ophiolite (W. Alps) and implications on subduction dynamics. J Metamorph Geol. doi:10.1111/j.1525-1314.2011.00951.x

Arculus RJ, Lapierre H, Jaillard E (1999) Geochemical window into subduction and accretion processes: Raspas metamorphic complex, Ecuador. Geology 27:547–550

Austrheim H, Prestvik T (2008) Rodingitization and hydration of the oceanic lithosphere as developed in the Leka ophiolite, north-central Norway. Lithos 104:177–198

Ayers JC, Watson EB (1991) Solubility of apatite, monazite, zircon, and rutile in supercritical aqueous fluids with implications for subduction zone geochemistry. Philos Trans Roy Soc Lond 335:365–375

Bach W, Peucker-Ehrenbrink B, Hart SR, Blusztajn JS (2003) Geochemistry of hydrothermally altered oceanic crust: DSDP/ODP Hole 504B – implications for seawater-crust exchange budgets and Sr- and Pb-isotopic evolution of the mantle. Geochem Geophys Geosyst 4 (8904). doi:10.1029/2002GC000419

Barton MD, Bebout GE, Sorensen SS (1988) Isotopic constraints on the geochemical evolution of an ultramafic subduction zone melange: Catalina Schist terrane, California (abstr.). EOS Trans Am Geophys Un 68:1525

Barton MD, Ilchik RP, Marikos MA (1991) Metasomatism. Mineral. Soc., Am Rev Mineral Geochem 26: 321–349

Bebout GE (1989) Geological and geochemical investigations of fluid flow and mass transfer during subduction-zone metamorphism. Ph.D. thesis, University of California, Los Angeles, 370pp

Bebout GE (1991a) Geometry and mechanisms of fluid flow at 15 to 45 kilometer depths in an early Cretaceous accretionary complex. Geophys Res Lett 18:923–926

Bebout GE (1991b) Field-based evidence for devolatilization in subduction zones: implications for arc magmatism. Science 251:413–416

Bebout GE (1997) Nitrogen isotope tracers of high-temperature fluid-rock interactions: case study of the Catalina Schist, California. Earth Planet Sci Lett 151:77–90

Bebout GE (2007a) Metamorphic chemical geodynamics in subduction zones. Earth Planet Sci Lett 260:373–393

Bebout GE (2007b) Trace element and isotopic fluxes/subducted slab. In: Turekian KK, Holland HD, Rudnick R (eds) Treat Geochem. Elsevier, pp 1–50, online only

Bebout GE, Agard P, Kobayashi K, Moriguti T, Nakamura E (2011) Devolatilization history and trace element mobility in deeply subducted sedimentary rocks: SIMS evidence from Western Alps HP/UHP suites (abstract). In: Proceedings of the Fall Meeting, American Geophysical Union, San Francisco

Bebout GE, Anderson LD, Agard P, Bastoni C, Sills G, Damon A (2010) Extents of decarbonation in HP/UHP Western Alps metacarbonates and implications for subduction zone carbon cycling (abstract). In: Proceedings of the Fall Meeting, American. Geophysical Union, San Francisco

Bebout GE, Barton MD (1989) Fluid flow and metasomatism in a subduction zone hydrothermal system: Catalina Schist Terrane, California. Geology 17:976–980
Bebout GE, Barton MD (1993) Metasomatism during subduction: products and possible paths in the Catalina Schist, California. Chem Geol 108:61–92
Bebout GE, Barton MD (2002) Tectonic and metasomatic mixing in a high-T, subduction-zone mélange – insights into the geochemical evolution of the slab-mantle interface. Chem Geol 187:79–106
Bebout GE, Bebout AE, Graham CM (2007) Cycling of B, Li, and LILE (K, Cs, Rb, Ba, Sr) into subduction zones: SIMS evidence from micas in high-P/T metasedimentary rocks. Chem Geol 239:284–304
Bebout GE, Ryan JG, Leeman WP (1993) B-Be systematics in subduction-related metamorphic rocks: characterization of the subducted component. Geochim Cosmochim Acta 57:2227–2237
Bebout GE, Ryan JG, Leeman WP, Bebout AE (1999) Fractionation of trace elements during subduction-zone metamorphism: impact of convergent margin thermal evolution. Earth Planet Sci Lett 171:63–81
Becker H, Carlson RW, Jochum KP (2002) Trace element fractionation during dehydration of eclogites from high-pressure terranes and the implications for element fluxes in subduction zones. Chem Geol 163:65–99
Beinlich A, Austrheim H, Glodny J, Erambert M, Andersen TB (2010a) CO_2 sequestration and extreme Mg depletion in serpentinized peridotite clasts from the Devonian Solund basin, SW-Norway. Geochim Cosmochim Acta 74:6935–6964
Beinlich A, Klemd R, John R, Gao J (2010b) Trace-element mobilization during Ca-metasomatism along a major fluid conduit: eclogitization of blueschist as a consequence of fluid-rock interaction. Geochim Cosmochim Acta 74:1892–1922
Ben Othman D, White WM, Patchett J (1989) The geochemistry of marine sediments, island arc magma genesis, and crust-mantle recycling. Earth Planet Sci Lett 94:1–21
Benton LD, Ryan JG, Tera F (2001) Boron isotope systematics of slab fluids as inferred from a serpentinite seamount, Mariana forearc. Earth Planet Sci Lett 187:273–282
Benton LD, Ryan JG, Savov IP (2004) Lithium abundance and isotope systematics of forearc serpentinites, Conical Seamount, Mariana forearc: insights into the mechanics of slab-mantle exchange during subduction. Geochem Geophys Geosyst 5(8):Q08J12. doi:10.1029/2004GC000708
Boles JR, Ramseyer K (1988) Albitization of plagioclase and vitrinite reflectance as paleothermal indicators, San Joakin Basin. In: Studies of the geology of the San Joakin Basin. Soc. Econ. Paleo. Min, Los Angeles, pp 129–139
Breeding CM, Ague JJ (2002) Slab-derived fluids and quartz-vein formation in an accretionary prism, Otago Schist, New Zealand. Geology 30:499–502
Breeding CM, Ague JJ, Brocker M (2004) Fluid-metasedimentary interactions in subduction zone mélange: implications for the chemical composition of arc magmas. Geology 32:1041–1044
Brenan JM, Shaw HF, Ryerson FJ (1995a) Experimental evidence for the origin of lead enrichment in convergent margin magmas. Nature 378:54–56
Brenan JM, Shaw HF, Ryerson FJ, Phinney DL (1995b) Mineral-aqueous fluid partitioning of trace elements at 900°C and 2.0 GPa: constraints on the trace element geochemistry of mantle and deep crustal fluids. Geochim Cosmochim Acta 59:3331–3350
Brenan JM, Shaw HF, Phinney DL, Ryerson FJ (1994) Rutile-aqueous fluid partitioning of Nb, Ta, Hf, Zr, U, and Th: implications for high field strength element depletions in island-arc basalts. Earth Planet Sci Lett 128:327–339
Brenan JM, Ryerson FJ, Shaw HF (1998) The role of aqueous fluids in the slab-to-mantle transfer of boron, beryllium, and lithium during subduction; experiments and models. Geochim Cosmochim Acta 62:3337–3347
Brown KM, Saffer DM, Bekins BA (2001) Smectite diagenesis, pore-water freshening, and fluid flow at the toe of the Nankai wedge. Earth Planet Sci Lett 194:97–109

Bulle F, Bröcker M, Gärtner C, Keasling A (2010) Geochemistry and geochronology of HP mélanges from Tinos and Andros, Cycladic blueschist belt, Greece. Lithos 117:68–81

Busigny V, Cartigny P, Philippot P, Ader M, Javoy M (2003) Massive recycling of nitrogen and other fluid-mobile elements (K, Rb, Cs, H) in a cold slab environment: evidence from HP to UHP oceanic metasediments of the Schistes Lustres nappe (western Alps, Europe). Earth Planet Sci Lett 215:27–42

Carr MJ, Feigenson MD, Patino LC, Walker JA (2003) Volcanism and geochemistry in Central America: progress and problems. In: Eiler J (ed) Inside the subduction factory, vol 138, Geophysical monograph. American Geophysical Union, Washington, DC, pp 153–174

Castro A, Gerya T, Garcia-Casco A, Fernandez C, Diaz-Alvarado J, Moreno-Ventas I, Low I (2010) Melting relations of MORB-sediment mélanges in underplated mantle wedge plumes: implications for the origin of Cordilleran-type batholiths. J Petrol 51(6):1267–1295

Chalot-Prat F (2005) An undeformed ophiolite in the Alps: field and geochemical evidence for a link between volcanism and shallow plate processes. In: Natland GR, Presnall DC, Anderson DL (eds) Plates, plumes, and paradigms, vol 388, Geological Society of America Special Papers. Geological Society of America, Boulder, pp 751–780

Chalot-Prat F, Ganne J, Lombard A (2003) No significant element transfer from the oceanic plate to the mantle wedge during subduction and exhumation of the Tethys lithosphere (Western Alps). Lithos 69:69–103

Chauvel C, Goldstein SL, Hofmann AW (1995) Hydration and dehydration of oceanic crust controls Pb evolution in the mantle. Chem Geol 126:65–75

Clift PD, Vannucchi P, Morgan JP (2009) Crustal redistribution, crust-mantle recycling and Phanerozoic evolution. Earth Sci Rev 97:80–104

de Leeuw GAM, Hilton DR, Fischer TP, Walker JA (2007) The He-CO_2 isotope and relative abundance characteristics of geothermal fluids in El Salvador and Honduras: new constraints on volatile mass balance of the Central American volcanic arc. Earth Planet Sci Lett 258:132–146

Deschamps F, Guillot S, Godard M, Chauvel C, Andreani M, Hattori K (2010) In situ characterization of serpentinites from forearc mantle wedges: timing of serpentinization and behavior of fluid-mobile elements in subduction zones. Chem Geol 269:262–277

Dumitru TA (1991) Effects of subduction parameters on geothermal gradients in forearcs, with an application to Franciscan subduction in California. J Geophys Res 96(B2):621–641

Eiler JM, Carr MJ, Reagan M, Stolper E (2005) Oxygen isotope constraints on the sources of Central American arc lavas. Geochem Geophys Geosyst 6(2005):Q07007. doi:10.1029/2004GC000804

Eisele J, Sharma M, Galer SJG, Blichert-Toft J, Devey CW, Hofmann AW (2002) The role of sediment recycling in EM-1 inferred from Os, Pb, Hf, Nd, Sr isotope and trace element systematics of the Pitcairn hotspot. Earth Planet Sci Lett 196:197–212

Elderfield H, Kastner M, Martin JB (1990) Compositions and sources of fluids in sediments of the Peru subduction zone. J Geophys Res 95:8819–8827

Elliott T (2003) Tracers of the slab. In: Eiler J (ed) Inside the subduction factory, vol 138, Geophysical monograph. American Geophysical Union, Washington, DC, pp 23–45

Fisher DM (1996) Fabrics and veins in the forearc: a record of cyclic fluid flow at depths of $<$15 km. In: Bebout GE, Scholl DW, Kirby SH, Platt JP (eds) Subduction: top to bottom, vol 96, Geophysical Monograph. American Geophysical Union, Washington, DC, pp 75–89

Franz L, Romer RL, Klemd R, Schmid R, Oberhansli R, Wagner T, Shuwen D (2001) Eclogite-facies quartz veins within metabasites of the Dabie Shan (eastern China): pressure-temperature-time-deformation path, composition of the fluid phase and fluid flow during exhumation of high-pressure rocks. Contrib Mineral Petrol 141:322–346

Frezzotti M, Selverstone J, Sharp ZD, Compagnoni R (2011) Carbonate dissolution during subduction revealed by diamond-bearing rocks from the Alps. Nat Geosci. doi:10.1038/NGEO1246

Fu B, Zheng Y-F, Touret JLR (2002) Petrological, isotopic and fluid inclusion studies of eclogites from Sujiahe, NW Dabie Shan (China). Chem Geol 187:107–128

Fukao Y, Hori S, Ukawa M (1983) A seismological constraint on the depth of basalt-eclogite transition in a subducting oecanic crust. Nature 303:413–415

Fyfe WS, Kerrich R (1985) Fluids and thrusting. Chem Geol 49:353–362

Gao J, Klemd R (2001) Primary fluids entrapped at blueschist to eclogite transition: evidence from the Tianshan meta-subduction complex in northwestern China. Contrib Mineral Petrol 142:1–14

Garcia-Casco A, Lazaro C, Rojas-Agramonte Y, Kroner A, Torres-Roldan RL, Nunez K, Neubauer F, Millan G, Blanco-Quintero I (2008) Partial melting and counterclockwise P-T path of subducted oceanic crust (Sierra del Convento Melange, Cuba). J Petrol 49:129–161. doi:10.1093/petrology/egm074

George R, Turner S, Morris M, Plank T, Hawkesworth C, Ryan J (2005) Pressure-temperature-time paths of sediment recycling beneath the Tonga-Kermadec arc. Earth Planet Sci Lett 233:195–211

Getty SR, Selverstone J (1994) Stable isotopic and trace element evidence for restricted fluid migration in 2 GPa eclogites. J Metamorph Geol 12:747–760

Giaramita MJ, Sorensen SS (1994) Primary fluids in low-temperature eclogites: evidence from two subduction complexes (Dominican Republic, and California, USA). Contrib Mineral Petrol 117:279–292

Gill JB (1981) Orogenic andesites and plate tectonics. Springer, Berlin, p 390

Godon A, Jendrzejewski N, Castrec-Rouelle Dia A, Pineau F, Boulegue J, Javoy M (2004) Origin and evolution of fluids from mud volcanoes in the Barbados accretionary complex. Geochim Cosmochim Acta 68:2153–2165

Gorman PJ, Kerrick DM, Connolly JAD (2006) Modeling open system metamorphic decarbonation of subducting slabs. Geochem Geophys Geosyst 7(4):Q04007. doi:10.1029/2005GC001125

Grove M, Bebout GE (1995) Cretaceous tectonic evolution of coastal southern California: insights from the Catalina Schist. Tectonics 14:1290–1308

Grove M, Bebout GE, Jacobson CE, Barth AP, Kimbrough DL, King RL, Zou H, Lovera OM, Mahoney BJ, Gehrels GE (2008) The Catalina Schist: evidence for mid-Cretaceous subduction erosion of southwestern North America. In: Draut AE, Clift PD, Scholl DW (eds) Formation and applications of the sedimentary record in arc collision zones, vol 436, Geological Society of America Special paper. Geological Society of America, Boulder, pp 335–361

Hacker BR (2006) Pressures and temperatures of ultrahigh-pressure metamorphism: implications for UHP tectonics and H_2O in subducting slabs. Int Geol Rev 48:1053–1066

Hacker BR (2008) H_2O subduction beyond arcs. Geochem Geophys Geosyst 9(3):Q03001. doi:10.1029/2007GC001707

Hacker BR, Abers GA, Peacock SM (2003a) Subduction factory 1. Theoretical mineralogy, densities, seismic wave speeds, and H_2O contents. J Geophys Res 108(B1):2029. doi:10.1029/2001JB001127

Hacker BR, Luffi P, Lutkov V, Minaev V, Ratschbacher L, Plank T, Ducea M, Patino-Douce A, McWilliams M, Metcalf J (2005) Near-ultrahigh pressure processing of continental crust: miocene crustal xenoliths from the Pamir. J Petrol 46:1661–1687

Hacker BR, Peacock SM, Abers GA, Holloway SD (2003b) Subduction factory 2. Are intermediate-depth earthquakes in subducting slabs linked to metamorphic dehydration reactions? J Geophys Res 108(B1):2030. doi:10.1029/2001JB001129

Hart SR, Staudigel H (1989) Isotopic characterization and identification of recycled components. In: Hart SR, Gulen L (eds) Crust/mantle recycling at convergence zones, NATO (N. Atlantic Treaty Org.), ASI (Adv. Stud. Inst.) Ser., Kluwer, pp 15–28

Hauri EH, Hart SR (2003) Re-Os isotope systematics of HIMU and EMII oceanic island basalts from the South Pacific Ocean. Earth Planet Sci Lett 114:353–371

Helffrich GR (1996) Subducted lithospheric velocity structure: observations and mineralogical inferences. In: Bebout GE, Scholl DW, Kirby SH, Platt JP (eds) Subduction: top to bottom, vol 96, Geophysical monograph. American Geophysical Union, Washington, Dc, pp 215–222

Helffrich G, Abers GA (1997) Slab low-velocity layer in the eastern Aleutian subduction zone. Geophys J Int 130:640–648

Helffrich GR, Stein S, Wood BJ (1989) Subduction zone thermal structure and mineralogy and their relationship to seismic wave reflections and conversions at the slab/mantle interface. J Geophys Res 94:753–763

Hermann J, Spandler CJ (2008) Sediment melts at sub-arc depths: an experimental study. J Petrol 49:717–740

Hermann J, Spandler C, Hack A, Korsakov AV (2006) Aqueous fluids and hydrous melts in high-pressure and ultra-high pressure rocks: implications for element transfer in subduction zones. Lithos 92:399–417

Hilton DR, Fischer TP, Marty B (2002) Noble gases and volatile recycling at subduction zones. In: Porcelli D et al (eds) Noble Gases in geochemistry and cosmochemistry, vol 47, Reviews in mineralogy and geocheminstry. Mineralogical Society of America, Washington, DC, pp 319–370

Hori S, Inoue H, Fukao Y, Ukawa M (1985) Seismic detection of the untransformed "basaltic" oceanic crust subducting into the mantle. Geophys J Roy Astr Soc 83:169–197

Hofmann AW (1988) Chemical differentiation of the Earth: the relationship between mantle, continental crust, and oceanic crust. Earth Planet Sci Lett 90:297–314

Hofmann AW (2003) Sampling mantle heterogeneity through oceanic basalts: isotopes and trace elements. Treat Geochem 2:61–101

Hulme SM, Wheat CG, Fryer P, Mottl MJ (2010) Pore water chemistry of the Mariana serpentinite mud volcanoes: a window to the seismogenic zone. Geochem Geophys Geosyst 11:Q01X09. doi:10.1029/2009GC002674

Hyndman RD, Peacock SM (2003) Serpentinization of the forearc mantle. Earth Planet Sci Lett 212:417–432

Jarrard RD (2003) Subduction fluxes of water, carbon dioxide, chlorine, and potassium. Geochem Geophys Geosyst 5. doi:10.1029/2002GC000392

John T, Gussone NC, Beinlich A, Halama R, Bebout GE, Podladchikov YY, Magna T (2010) Pulse-like channelled long-distance fluid flow in subducting slabs. In: Abstracts for AGU Fall Meeting, San Francisco

John T, Schenk V (2003) Partial eclogitisation of gabbroic rocks in a late Precambrian subduction zone (Zambia): progade metamorphism triggered by fluid infiltration. Contrib Mineral Petrol 146:174–191. doi:10.1007/s00410-003-0492-8

John T, Schenk V (2006) Interrelations between intermediate-depth earthquakes and fluid flow within subducting oceanic plates: constraints from eclogite facies pseudotachylytes. Geology 34(7):557–560

John T, Scherer EE, Haase K, Schenk V (2004) Trace element fractionation during fluid-induced eclogitization in a subducting slab: trace element and Lu-Hf-Sm-Nd isotope systematics. Earth Planet Sci Lett 227:441–456

Johnson MC, Plank T (1999) Dehydration and melting experiments constrain the fate of subducted sediments. Geochem Geophys Geosyst 1 (Art. no. 1999GC000014)

Kastner M, Elderfield H, Martin JB (1991) Fluids in convergent margins: what do we know about their composition, origin, role in diagenesis and importance for oceanic chemical fluxes? Philos Trans R Soc Lond 335:243–259

Kay SM, Godoy E, Kurtz A (2005) Episodic arc migration, crustal thickening, subduction erosion, and magmatism in the south-central Andes. Geol Soc Am Bull 117:67–88

Kelemen PB, Rilling JL, Parmentier EM, Mehl L, Hacker BR (2003) Thermal structure due to solidstate flow in the mantle wedge. In: Eiler J (ed) Inside the subduction factory, vol 138, Geophysical monograph. American Geophysical Union, Washington, DC, pp 293–311

Kelley KA, Plank T, Farr L, Ludden J, Staudigel H (2005) Subduction cycling of U, Th, and Pb. Earth Planet Sci Lett 234:369–383

Kelley KA, Plank T, Ludden J, Staudigel H (2003) The composition of altered oceanic crust and ODP Sites 801 and 1149. Geochem Geophys Geosyst 4:8910. doi:10.1029/2002GC000435

Keppler H (1996) Constraints from partitioning experiments on the composition of subduction-zone fluids. Nature 380:237–240
Kerrick DM, Connolly JAD (2001) Metamorphic devolatilization of subducted marine sediments and the transport of volatiles into the Earth's mantle. Nature 411:293–296
Kessel R, Schmidt MW, Ulmer P, Pettke T (2005a) Trace element signature of subduction-zone fluids, melts and supercritical fluids at 120–180 km depths. Nature 437(29):724–727
Kessel R, Ulmer P, Pettke T, Schmidt MW, Thompson AB (2005b) The water-basalt system at 4 to 6 GPa: phase relations and second critical endpoint in a K-free eclogite at 700 to 1400°C. Earth Planet Sci Lett 237:873–892
Kincaid C, Sacks IS (1997) Thermal and dynamical evolution of the upper mantle in subduction zones. J Geophys Res 102:12295–12315
King RL, Bebout GE, Grove M, Moriguti T, Nakamura E (2007) Boron and lead isotope signatures of subduction-zone melange formation: hybridization and fractionation along the slab-mantle interface beneath volcanic fronts. Chem Geol. doi:10.1016/j.chemgeo.2007.01.009
King RL, Bebout GE, Kobayashi K, Nakamura E, van der Klauw SNGC (2004) Ultrahigh-pressure metabasaltic garnets as probes into deep subduction-zone chemical cycling. Geochem Geophys Geosyst 5:Q12J14. doi:10.1029/2004GC000746
King RL, Bebout GE, Moriguti T, Nakamura E (2006) Elemental mixing systematics and Sr-Nd isotope geochemistry of mélange formation: obstacles to identification of fluid sources to arc volcanics. Earth Planet Sci Lett 246:288–304
Kirby S, Engdahl ER, Denlinger R (1996) Intraslab earthquakes and arc volcanism: dual expressions of crustal and upper mantle metamorphism in subducting slabs. In: Bebout GE, Scholl DW, Kirby SH, Platt JP (eds) Subduction: top to bottom, vol 96, Geophysical monograph. American Geophysical Union, Washington, DC, pp 195–214
Kvenvolden KA (1993) Gas hydrates – geological perspective and global change. Rev Geophys 31 (2):173–187
Li L, Bebout GE (2005) Carbon and nitrogen geochemistry of sediments in the Central American convergent margin: insights regarding paleoproductivity and carbon and nitrogen subduction fluxes. J Geophys Res 110:B11202. doi:10.1029/2004JB003276
Maekawa H, Shozui M, Ishii T, Fryer P, Pearce JA (1993) Blueschist metamorphism in an active subduction zone. Nature 364:520–523
Malaspina N, Hermann J, Scambelluri M (2009) Fluid/mineral interaction in UHP garnet peridotite. Lithos 107(1–2):38–52
Manning CE (1994) The solubility of quartz in H_2O in the lower crust and upper mantle. Geochim Cosmochim Acta 58:4831–4839
Manning CE (1998) Fluid composition at the blueschist-eclogite transition in the model system Na_2O-MgO-Al_2O_3-SiO_2-H_2O-HCl. Schweiz Miner Petrog 78:225–242
Manning CE (2004) The chemistry of subduction-zone fluids. Earth Planet Sci Lett 223:1–16
Manning CE, Antignano A, Lin HA (2010) Premelting polymerization of crustal and mantle fluids, as indicated by the solubility of albite + paragonite + quartz in H_2O at 1 GPa and 350–620°C. Earth Planet Sci Lett 292:325–336
Marocchi M, Hermann J, Tropper P, Bargossi GM, Mair V (2010) Amphibole and phlogopite in "hybrid" metasomatic bands monitor trace element transfer at the interface between felsic and ultramafic rocks (Eastern Alps, Italy). Lithos 117:135–148
Martin H (1986) Effect of steeper Archean geothermal gradient on geochemistry of subduction-zone magmas. Geology 14:753–756
Massone H-J, Kopp J (2005) A low-variance mineral assemblage with talc and phengite in an eclogite from the Saxonian Erzgebirge, Central Europe, and its P-T evolution. J Petrol 46:355–375
Marschall HR (2005) Lithium, beryllium, and boron in high-pressure metamorphic rocks from Syrox (Greece). Ph.D. dissertation, Universitat Heidelberg, p 411

Matsuzawa T, Umino N, Hasegawa A, Takagi A (1986) Upper mantle velocity structure estimated from PS-converted wave beneath the north-eastern Japan Arc. Geophys J Roy Astr Soc 86: 767–787

McDonough WF, Sun SS (1995) The composition of the Earth. Chem Geol 120:223–253

Miller DM, Goldstein SL, Langmuir CH (1994) Cerium/lead and lead isotope ratios in arc magmas and the enrichment of lead in the continents. Nature 368:514–520

Miller DP, Marschall HR, Schumacher JC (2009) Metasomatic formation and petrology of blueschist-facies hybrid rocks from Syros (Greece): implications for reactions at the slab-mantle interface. Lithos 107:53–67

Moore DE, Liou JG, King B-K (1981) Chemical modifications accompanying blueschist facies metamorphism of Franciscan conglomerates, Diablo Range, California. Chem Geol 33:237–263

Moore GF, Taira A, Klaus A et al (2001) New insights into deformation and fluid flow processes in the Nankai Trough accretionary prism: results of Ocean Drilling Program Let 190. Geochem Geophys Geosyst 2, 25 Oct 2001, 2001GC0000166

Moore JC, Vrolijk P (1992) Fluids in accretionary prisms. Rev Geophys 30:113–135

Morad S (1988) Albitized microcline grains of post-depositional and probable detrital origins in Brottom Formation sandstones (Upper Proterozoic), Sparagmite Region of southern Norway. Geol Mag 125:229–239

Morris JD, Ryan JG (2003) Subduction zone processes and implications for changing composition of the upper and lower mantle. Treat Geochem 2:451–470

Mottl MJ, Wheat CG, Fryer P, Gharib J, Martin JB (2004) Chemistry of springs across the Mariana forearc shows progressive devolatilization of the subducting slab. Geochim Cosmochim Acta 68:4915–4933

Nadeau S, Philippot P, Pineau F (1993) Fluid inclusion and mineral isotopic compositions (H-C-O) in eclogitic rocks as tracers of local fluid migration during high-pressure metamorphism. Earth Planet Sci Lett 114:431–448

Nelson BK (1995) Fluid flow in subduction zones: evidence from Nd- and Sr-isotope variations in metabasalts of the Franciscan Complex, California. Contrib Mineral Petrol 119:246–262

Nesbitt HW, Young GM (1982) Early Proterozoic climates and plate motions inferred from major element chemistry of lutites. Nature 299:715–717

Newton RC, Manning CE (2008) Thermodynamics of SiO_2-H_2O fluid near the upper critical end point from quartz solubility measurements at 10 kbar. Earth Planet Sci Lett 274:241–249

Peacock SM (1992) Blueschist-facies metamorphism, shear heating, and P–T–t paths in subduction shear zones. J Geophys Res 97:17693–17707

Peacock SM et al (1996) Thermal and petrologic structure of subduction zones. In: Bebout GE (ed) Subduction: top to bottom, vol 96, Geophysical monograph. American Geophysical Union, Washington, DC, pp 119–133

Peacock SM et al (2003) Thermal structure and metamorphic evolution of subducting slabs. In: Eiler J (ed) Inside the subduction factory, vol 138, Geophysical monograph. American Geophysical Union, Washington, DC, pp 7–22

Peacock SM (2009) Thermal and metamorphic environment of subduction zone episodic tremor and slip. J Geophys Res 114:B00A07. doi:10.1029/2008JB005978

Peacock SM, Hyndman RD (1999) Hydrous minerals in the mantle wedge and the maximum depth of subduction zone earthquakes. Geophys Res Lett 26:2517–2520

Peacock SM, van Keken PE, Holloway SD, Hacker BR, Abers GA, Fergason RL (2005) Thermal structure of the Costa Rica-Nicaragua subduction zone. Phys Earth Planet Int 149:187–200

Pearce JA, Peate DW (1995) Tectonic implications of the composition of volcanic arc magmas. Annu Rev Earth Planet Sci 23:251–285

Penniston-Dorland SC, Bebout GE, van Pogge van Strandmann PAE, Elliott T, Sorensen SS (2011) Lithium and its isotopes as tracers of subduction zone fluids and metasomatic processes: evidence from the Catalina Schist, California, USA. Geochim Cosmochim Acta. doi:10.1016/j.gca.2011.10.038

Penniston-Dorland SC, Sorensen SS, Ash RD, Khadke SV (2010) Lithium isotopes as a tracer of fluids in a subduction zone mélange: Franciscan Complex, CA. Earth Planet Sci Lett 292:181–190
Philippot P, Selverstone J (1991) Trace-element-rich brines in eclogitic veins: implications for fluid compositions and transport during subduction. Contrib Mineral Petrol 106:417–430
Plank T (2005) Constraints from thorium/lanthanum on sediment recycling at subduction zones and the evolution of the continents. J Petrol 46:921–944
Plank T, Balzer V, Carr M (2002) Nicaraguan volcanoes record paleoceano-graphic changes accompanying closure of the Panama gateway. Geology 30:1087–1090
Plank T, Cooper LB, Manning CE (2009) Emerging geothermometers for estimating slab surface temperatures. Nat Geosci 2. doi:10.1038/NGEO614
Plank T, Langmuir CH (1988) An evaluation of the global variations in the major element chemistry of arc basalts. Earth Planet Sci Lett 90:349–370
Plank T, Langmuir CH (1998) The chemical composition of subducting sediment and its consequences for the crust and mantle. Chem Geol 145:325–394
Putnis A, John T (2010) Replacement processes in the Earth's crust. Elements 6:159–164
Ranero CR, Villasenor A, Phipps Morgan J, Weinrebe W (2005) Relationship between bend-faulting at trenches and intermediate-depth seismicity. Geochem Geophys Geosyst 6(12): Q12002. doi:10.1029/2005GC000997
Rea DK, Ruff LJ (1996) Composition and mass flux of sedimentary materials entering the World's subduction zones: implications for global sediment budgets, great earthquakes, and volcanism. Earth Planet Sci Lett 140:1–12
Rondenay S, Abers GA, van Keken PE (2008) Seismic imaging of subduction zone metamor-phism. Geology 36:275–278
Rupke LH, Morgan JP, Hort M, Connolly JAD (2002) Are the regional differences in Central American arc lavas due to differing basaltic versus peridotitic slab sources of fluids? Geology 30:1035–1038
Rupke LH, Morgan JP, Hort M, Connolly JAD (2004) Serpentine and the subduction zone water cycle. Earth Planet Sci Lett 223:17–34
Ryan J, Morris J, Bebout G, Leeman B, Tera F (1996) Describing chemical fluxes in subduction zones: insights from "depth-profiling" studies of arc and forearc rocks. In: Bebout GE, Scholl DW, Kirby SH, Platt JP (eds) Subduction: top to bottom, vol 96, Geophysical monograph. American Geophysical Union, Washington, DC, pp 263–268
Sadofsky SJ, Bebout GE (2003) Record of forearc devolatilization in low-T, high-P/T metasedimentary suites: significance for models of convergent margin chemical cycling. Geochem Geophys Geosyst 4(4):9003. doi:10.1029/2002GC000412
Sadofsky SJ, Bebout GE (2004) Field and isotopic evidence for fluid mobility in the Franciscan Complex: forearc paleohydrogeology to depths of 30 km. Int Geol Rev 46:1053–1088
Saha A, Basu AR, Wakabayashi J, Wortman GL (2005) Geochemical evidence for a subducted infant arc in Franciscan high-grade-metamorphic tectonic blocks. Geol Soc Am Bull 117:1318–1335
Sakakibara M, Umeki M, Cartwright I (2007) Isotopic evidence for channeled fluid flow in low-grade metamorphosed Jurassic accretionary complex in the Northern Chichibu belt, western Shikoku. Jpn J Metamorph Geol 25:383–400
Sample JC, Reid MR (1998) Contrasting hydrogeologic regimes along strike-slip and thrust faults in the Oregon convergent margin: evidence from the chemistry of syntectonic carbonate cements and veins. Geol Soc Am Bull 110:48–59
Sapienza GT, Scambelluri M, Braga R (2009) Dolomite-bearing orogenic garnet peridotites witness fluid-mediated carbon recycling in a mantle wedge (Ulten Zone, Eastern Alps, Italy). Contrib Mineral Petrol 158:401–420
Savov IP, Ryan JG, D'Antonio M, Kelley K, Mattie P (2005) Geochemistry of serpentinized peridotites from the Mariana forearc Conical Seamount, ODP Leg 125: implications for the elemental recycling at subduction zones. Geochem Geophys Geosyst 6(4):Q04J15. doi:10.1029/2004GC000777

Scambelluri M, Bottazzi P, Trommsdorff V, Vannucci R, Hermann J, Gomez-Pugnaire MT, Lopez-Sanchez Vizcaíno V (2002) Incompatible element-rich fluids released by antigorite breakdown in deeply subducted mantle. Earth Planet Sci Lett 192:457–470

Scambelluri M, Fiebig J, Malaspina N, Muntener O, Pettke T (2004a) Serpentinite subduction: implications for fluid processes and trace-element recycling. Int Geol Rev 46:595–613

Scambelluri M, Hermann J, Morten L, Rampone E (2006) Melt- versus fluid-induced metasomatism in spinel to garnet wedge peridotites (Ulten Zone, Eastern Italian Alps): clues from trace element and Li abundances. Contrib Mineral Petrol. doi:10.1007/s00410-006-0064-9

Scambelluri M, Muntener O, Ottolini L, Pettke T, Vannucci R (2004b) The fate of B, Cl, and Li in the subducted oceanic mantle and in the antigorite breakdown fluids. Earth Planet Sci Lett 222:217–234

Scambelluri M, Philippot P (2001) Deep fluids in subduction zones. Lithos 55:213–227

Scambelluri M, Philippot P, Pennacchioni G (1998) Salt-rich aqueous fluids formed during eclogitization of metabasites in the Alpine continental crust (Austroalpine Mt. Emilius unit, Italian western Alps). Lithos 43:151–161

Scambelluri M, Van Roermund HLM, Pettke T (2010) Mantle wedge peridotites: fossil reservoirs of deep subduction zone processes: inferences from high and ultrahigh-pressure rocks from Bardana (Western Norway) and Ulten (Italian Alps). Lithos 120:186–201

Schmidt MW, Poli S (2003) Generation of mobile components during subduction of oceanic crust. Treat Geochem 3:567–591

Schmidt MW, Vielzeuf D, Auzanneau E (2004) Melting and dissolution of subducting crust at high pressures: the key role of white mica. Earth Planet Sci Lett 228:65–84

Scholl DW, von Huene R (2009) Crustal recycling at modern subduction zones applied to the past–issues of growth and preservation of continental basement, mantle geochemistry, and supercontinent reconstruction. In: Hatcher RD Jr, Carlson MP, McBride JH, Martinez Catalan JR (eds) The 4D framework of continental crust, Geological Society of America, Special Paper 327:371–404

Shaw AM, Hilton DR, Fischer TP, Walker JA, Alvarado GE (2003) Contrasting He–C relationships in Nicaragua and Costa Rica: insights into C cycling through subduction zones. Earth Planet Sci Lett 214:499–513

Shen, B, Jacobsen B, Lee C-YA, Yin Q-Z, Morton DM (2009) The Mg isotopic systematics of granitoids in continental arcs and implications for the role of chemical weathering in crust formation. Proc Nat Acad Sci, 106(49):29652–20657

Solomon EA, Kastner M, Robertson G (2006) Barium cycling at the Costa Rica convergent margin. In: Morris JM, Villinger HW, Klaus A (eds) Proceedings of ODP scientific results 205:1–21. Online: http://www-odp.tamu.edu/publications/205_SR/210/210.htm. doi:10.2973/odp.proc.sr.205.210.2006

Sorensen SS, Barton MD (1987) Metasomatism and partial melting in a subduction complex, Catalina Schist, southern California. Geology 15:115–118

Sorensen SS, Grossman JN (1989) Enrichment of trace elements in garnet amphibolites from a paleo-subduction zone: Catalina Schist, southern California. Geochim Cosmochim Acta 53:3155–3178

Sorensen SS, Grossman JN, Perfit MR (1997) Phengite-hosted LILE-enrichment in eclogite and related rocks: implications for fluid-mediated mass transfer in subduction zones and arc magma genesis. J Petrol 38:3–34

Sorensen SS, Sisson VB, Harlow GE, Ave Lallement HG (2010) Element residence and transport during subduction-zone metasomatism: evidence from a jadeitite-serpentinite contact. Guatemala Int Geol Rev 52(9):899–940

Sorensen SS, Sisson VB, Ave Lallement HG (2005) Geochemical evidence for possible trench provenance and fluid-rock histories, Cordillera de la Costa eclogite belt, Venezuela. In: Ave Lallement HG, Sisson VB (eds) Carribean-South American plate interactions, Venezuela. Geological Society of America, Special Paper 394:173–192

Spandler C, Hermann J, Arculus R, Mavrogenes J (2003) Redistribution of trace elements during prograde metamorphism from lawsonite blueschist to eclogite facies; implications for deep subduction processes. Contrib Mineral Petrol. doi:10.1007/s00410-003-495-5, online article

Spandler C, Hermann J, Arculus R, Mavrogenes J (2004) Geochemical heterogeneity and elemental mobility in deeply subducted oceanic crust; insights from high-pressure mafic rocks from New Caledonia. Chem Geol 206:21–42

Spandler C, Hermann J, Faure K, Mavrogenes JA, Arculus RJ (2008) The importance of talc and chlorite "hybrid" rocks for volatile recycling through subduction zones; evidence from the high-pressure subduction mélange of New Caledonia. Contrib Mineral Petrol 155:181–198

Spandler C, Mavrogenes J, Hermann J (2007) Experimental constraints on element mobility from subducted sediments using high-P synthetic fluid/melt inclusions. Chem Geol 239:228–249

Staudigel H (2003) Hydrothermal alteration processes in the oceanic crust. Treat Geochem 3:511–535

Staudigel H, Plank T, White WM, Schminke H-U (1996) Geochemical fluxes during seafloor alteration of the upper oceanic crust: DSDP sites 417 and 418. In: Bebout GE, Scholl DW, Kirby SH, Platt JP (eds) Subduction: top to bottom, vol 96, Geophysical monograph. American Geophysical Union, Washington, DC, pp 19–38

Stern RJ (1991) Role of subduction erosion in the generation of Andean magmas. Geology 19:78–81

Stern RJ (2002) Subduction zones. Rev Geophys 40(4):1012. doi:10.1029/2001RG000108

Stracke A, Bizimis M, Salters VJM (2003) Recycling oceanic crust: quantitative constraints. Geochem Geophys Geosyst 4:8003. doi:10.1029/2001GC000223

Stracke A, Hofmann AW, Hart SR (2005) FOZO, HIMU, and the rest of the mantle zoo. Geochem Geophys Geosyst 6:Q05007. doi:10.1029/2004GC000824

Straub SM, Layne GD (2008) Decoupling of fluids and fluid-mobile elements during shallow subduction: evidence from halogen-rich andesite melt inclusions from the Izu arc volcanic front. Geochem Geophys Geosyst 4(7):9003. doi:10.1029/2002GC000349

Sun SS, McDonough WF (1989) Chemical and isotopic systematics of oceanic basalts: implications for mantle composition and processes. In: Saunders AD, Norry MJ (eds) Magmatism in the ocean basins, vol 42, Geological Society Special publications. Geological Society, London, pp 313–345

Syracuse EM, van Keken PE, Abers GA (2010) The global range of subduction zone thermal models. Phys Earth Planet In 183:73–90

Tenore-Nortrup J, Bebout GE (1993) Metasomatism of gabbroic and dioritic cobbles in blueschist facies metaconglomerates: sources and sinks for high-P/T metamorphic fluids (abstract). EOS Transactions, American Geophysical Union 74: 331

Tropper P, Manning CE (2004) Paragonite stability at 700°C in the presence of H_2O-NaCl fluids: constraints on H_2O activity and implications for high pressure metamorphism. Contrib Mineral Petrol 147:740–749

Tropper P, Manning CE (2005) Very low solubility of rutile in H_2O at high pressure and temperature, and its implications for Ti mobility in subduction zones. Am Mineral 90:502–505

van Keken PE (2003) The structure and dynamics of the mantle wedge. Earth Planet Sci Lett 215:323–338

van Keken PE, Hacker BR, Syracuse EM, Abers GA (2011) Subduction factory: 4. Depth-dependent flux of H2O from subducting slabs worldwide. J Geophys Res 116. doi:10.1029/2010JB007922

van Keken PE, Kiefer B, Peacock SM (2002) High-resolution models of subduction zones: implications for mineral dehydration reactions and the transport of water into the deep mantle. Geochem Geophys Geosyst 3:1056. doi:10.1029/2001GC000256

Vielzeuf D, Schmidt MW (2001) Melting relations in hydrous systems revisited: application to metapelites, metagreywackes and metabasalts. Contrib Mineral Petrol 141:251–267

von Huene R, Scholl DW (1991) Observations at convergent margins concerning sediment subduction, subduction erosion, and the growth of continental crust. Rev Geophys 29 (3):279–316

Vrolijk P (1987) Paleohydrogeology and fluid evolution of the Kodiak accretionary complex. Alaska. Ph.D. thesis, University of California, Santa Cruz

Vrolijk P (1990) On the mechanical role of smectite in subduction zones. Geology 18:703–707

Vrolijk P, Chambers SR, Gieskes JM, O'Neil JR (1990) 13. Stable isotope ratios of interstitial fluids from the northern Barbados accretionary prism, ODP Leg 110. In: Moore JC, Mascle A et al (eds) Proceedings of ODP scientific results 110, pp 189–205. Available online at: http://www-odp.tamu.edu/publications/110_SR/110TOC.HTM. doi:10.2973/odp.proc.sr.110.137.1990

Wada I, Wang K (2009) Common depth of slab-mantle decoupling: reconciling diversity and uniformity of subduction zones. Geochem Geophys Geosyst 10:Q10009. doi:10.1029/2009GC002570

Weaver BL (1991) The origin of ocean island basalt end-member compositions: trace element and isotopic constraints. Earth Planet Sci Lett 104:381–397

Widmer T, Thompson AB (2001) Local origin of high pressure vein material in eclogite facies rocks of the Zermatt-Saas zone, Switzerland. Am J Sci 301:627–656

You C-F, Castillo PR, Gieskes JM, Chan LH, Spivack AJ (1996) Trace element behavior in hydrothermal experiments: implications for fluid processes at shallow depths in subduction zones. Earth Planet Sci Lett 140:41–52

You C-F, Gieskes JM, Lee T, Yui T-F, Chen H-W (2004) Geochemistry of mud volcano fluids in the Taiwan accretionary prism. Appl Geochem 19:695–707

Zack T, Foley SF, Rivers T (2002) Equilibrium and disequilibrium trace element partitioning in hydrous eclogites (Trescolmen, Central Alps). J Petrol 43:1947–1974

Zack T, Rivers T, Foley SF (2001) Cs-Rb-Ba systematics in phengite and amphibole: an assessment of fluid mobility at 2.0 GPa in eclogites from Trescolmen, Central Alps. Contrib Mineral Petrol 140:651–669

Zack T, Tomascak PB, Rudnick RL, Dalpe C, McDonough WF (2003) Extremely light Li in orogenic eclogites: the role of isotope fractionation during dehydration in subducted oceanic crust. Earth Planet Sci Lett 208:279–290

Zheng Y, Kastner, M (1997) 12. Pore-fluid trace metal concentrations: implications for fluid-rock interactions in the Barbados accretionary prism. In: Shipley TH, Ogawa Y, Blum P, Bahr JM (eds) Proceedings of the Ocean Drilling Program Scientific Results 156:163–170. Available online at: http://www-odp.tamu.edu/publications/156_SR/156TOC.HTM. doi:10.2973/odp.proc.sr.156.021.1997

Zheng Y-F, Fu B, Gong B, Li L (2003) Stable isotope geochemistry of ultrahigh pressure metamorphic rocks from the Dabie-Sulu orogen in China: implications for geodynamics and fluid regime. Earth Sci Rev 62:105–161

Zheng Y-F, Xia Q-X, Chen R-X, Gao X-Y (2011) Partial melting, fluid supercriticality and element mobility in ultrahigh-pressure metamorphic rocks during continental collision. Earth Sci Rev 107:342–374

Chapter 10
Metasomatism During High-Pressure Metamorphism: Eclogites and Blueschist-Facies Rocks

Reiner Klemd

Abstract High-pressure (HP) and ultrahigh-pressure (UHP) metamorphic rocks, which represent parts of ancient subducted slabs, are the obvious target for obtaining constraints on the P-T conditions, composition, and type of slab-derived fluids responsible for metasomatism in subduction zone environments since they are the only direct witnesses of such processes. Usually, solute-poor, aqueous fluids, derived by prograde HP metamorphic devolatilisation reactions in subducted slabs, are made responsible for the trace element transfer between the slab and mantle wedge, both of which may have been metasomatised (modification of bulk rock composition) in due process. At deeper levels in subduction zones at UHP conditions, dense, solute-rich transitional fluids (intermediate between hydrous silicate melts and aqueous fluids), or hydrous silicate melts are thought to become more important with regards to element mobilization and transport. Nonetheless, when considering the petrological and fluid inclusion evidence, it seems reasonable to generally assume that solute-poor aqueous fluids (solute <~30 wt.% of fluid) mainly dominate the fluid budget during HP metamorphism of oceanic and continental crust in subduction zones (70–40 km depth). This is supported by experimental data favoring an aqueous fluid under HP conditions in cold subduction zones. These fluids are regarded by some researchers as being relatively inefficient in mobilizing and transporting elements, as, for instance, has been suggested by experimentally derived fluid-mineral partitioning data. This is consistent with some geochemical studies of HP veins, which suggest a locally highly-restricted fluid flow and thus only localized (small-scale) diffusive element transport. Similar conclusions of only short-distance fluid-mediated mass transport have also been

R. Klemd (✉)
GeoZentrum Nordbayern, Universität Erlangen-Nürnberg, Schlossgarten 5a, Erlangen 91054, Germany
e-mail: klemd@geol.uni-erlangen.de

D.E. Harlov and H. Austrheim, *Metasomatism and the Chemical Transformation of Rock*, Lecture Notes in Earth System Sciences,
DOI 10.1007/978-3-642-28394-9_10,

reached by some stable isotope studies in various HP terrains and many fluid inclusion studies. However, significant trace element changes have been reported for metasomatic depletion haloes surrounding eclogite-facies dehydration veins, which constitute major conduits of channelized high fluid flow during prograde HP-metamorphism or for zones of high fluid-rock ratios and fluid flow. Consequently, understanding of the metasomatic processes leading to the mobilization and redistribution of major and trace elements within subduction zone rocks is crucial for (quantitatively) evaluating bulk compositional changes, which occurred under HP and UHP conditions.

10.1 Introduction

Arc magmas, generated within subduction zone settings, exhibit a characteristic geochemical signature with elevated concentrations of relatively fluid- and melt-mobile elements such as the large-ion lithophile elements (LILE) and the light rare earth elements (LREE), and low concentrations of the high field strength elements (HFSE) and the heavy rare earth elements (HREE) (e.g. Gill 1981; McCulloch and Gamble 1991). There is general agreement among researchers that this characteristic is caused by additions of 'fluids' and or/melts derived from the subducted slab, thereby fluxing the melting in the overlying metasomatized mantle wedge to generate arc magmas (e.g., Chap. 9). These fluids or melts are considered to have been liberated during high-pressure (HP) to ultrahigh-pressure (UHP) metamorphism in the (variably hydrothermally altered) subducted oceanic lithosphere (Fig. 10.1). Neglecting the expulsion of large volumes of pore water during initial subduction, solute-poor aqueous fluids derived by prograde HP metamorphic devolatilization reactions are usually held responsible for the trace element transfer between the slab and mantle wedge, with both of these environments showing significant metasomatism (modification of bulk rock composition; Tatsumi and Eggins (1995); Peacock 1990; Schmidt and Poli 1998; Manning 2004; Hacker 2008). At deeper levels in the subduction zones, at UHP conditions, dense solute-rich transitional fluids (intermediate between hydrous silicate melts and aqueous fluids) or hydrous silicate melts are thought to become more important agents of element mobilization and transport (e.g. Kessel et al. 2005a; Hermann et al. 2006; Bebout 2007a, b; Hack et al. 2007; Klimm et al. 2008; Plank et al. 2009). An understanding of the metasomatic processes leading to the mobilization and redistribution of major and trace elements within subduction zone rocks is crucial for (quantitatively) evaluating bulk compositional changes which occurred under HP and UHP conditions. HP and UHP rocks, representing parts of ancient subducted slabs, are obvious targets for the study of P-T conditions as well as composition and type of slab-derived fluids responsible for metasomatism in subduction zone environments as these rocks are the only direct witnesses of such processes. This chapter focuses mainly on characterizing

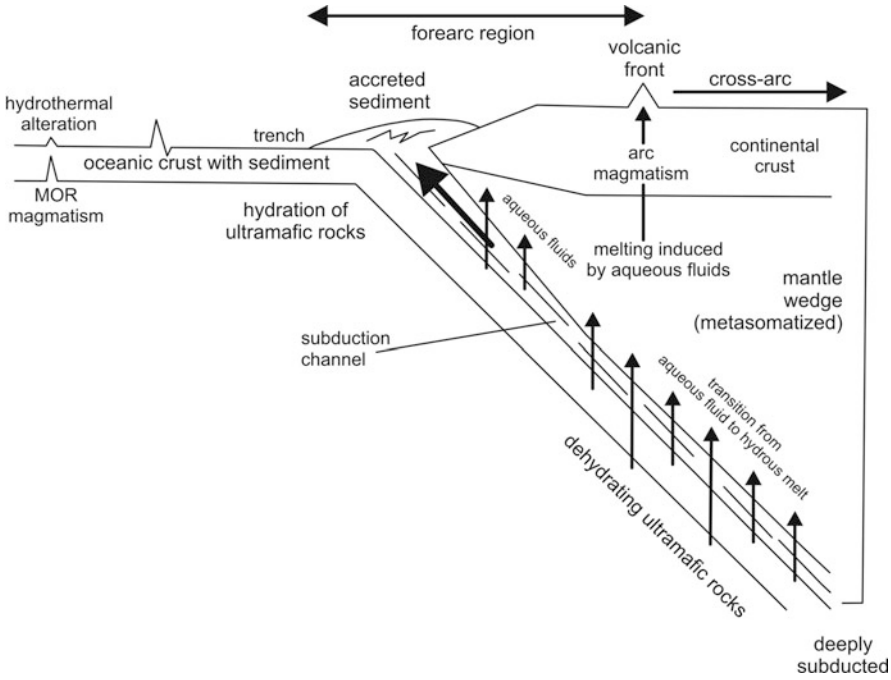

Fig. 10.1 Simplified sketch of a cold ocean-continent subduction zone (Modified after Bebout 2007a). The *arrows* pointing out possible pathways of fluids, which were derived during subduction zone metamorphism. The fluid phase responsible for (de)hydration and metasomatism of the upper oceanic lithosphere and the overlying mantle wedge under HP and UHP conditions is illustrated as a solute-poor aqueous fluid phase (see text for details)

the composition of the fluid phase liberated during prograde-dehydration reactions and its impact on rock compositional changes (metasomatism) during fluid-rock interaction. Furthermore, it reports on recent studies of compositional (metasomatic) changes in various HP to UHP meta-sedimentary, meta-igneous, and meta-ultramafic rock types derived from former subducted oceanic lithosphere and continental crust.

10.2 Protolith Lithologies of HP and UHP Rocks

The protoliths of HP and UHP rocks, from ancient oceanic subduction zones, are generally thought to reflect either the upper part of the oceanic lithosphere consisting of a thin veneer of sediments, or a 5–7 km thick section of igneous rocks dominated by MORB volcanics, gabbroic intrusions, and a depleted

peridotite upper mantle section (e.g. Karson 2002). HP and UHP rocks from subducted continental crust also contain a large variety of protolith rocks such as sediments, granitoids, and volcanic rocks (e.g. Rumble et al. 2003). In contrast with the oceanic lithosphere, the investigated continental crust, which underwent HP and UHP metamorphism, did not undergo large-scale hydration processes, more localized events appear to be more common (e.g. Rumble et al. 2003; Zheng 2009). Nearly all information, regarding the fluid phase and associated metasomatism during UHP metamorphism, stems from formerly subducted continental crust, since up to the present time no oceanic crust has been reported to have been exhumed from depths below ~80 km (e.g. Agard et al. 2009). Possible exceptions occur when the exhumation of oceanic slabs is directly related to the cessation of continental subduction processes (Agard et al. 2009; cf. Lü et al. 2009).

The following sections provide a short introduction regarding the different lithological units that serve as source rocks for the 'metasomatizing' fluids (or melts) associated with HP and UHP conditions in oceanic and continental subduction zones.

10.2.1 Oceanic Lithosphere

Several geological, geochemical, and petrological investigations, either on drill cores from the uppermost portion of the oceanic crust or from ophiolites (obducted oceanic crust), coupled with seismic studies of the oceanic crust, provide a general picture of its composition and structure (e.g. Karson 2002 and references herein). Trench sediment packages derived from the uppermost part of the oceanic crust are often not accreted in the forearc but instead subducted to great depths, along with forearc crust, by 'subduction erosion' (Rutland 1971; von Huene and Scholl 1991; Ranero and von Huene 2000; Scholl and von Huene 2007). The thickness of the sediment layers between the overlying mantle wedge and the subducting slab varies between 200 and 500 m, although they can be up to several kms thick (Plank and Langmuir 1998; Plank et al. 2007). The average "globally subducting sediments" (GLOSS) consists of the dominant 'terrigeneous' component (~76 wt.%), carbonates (~7% wt.%), opal (~10 wt.%), and mineral-bound fluids (~7 wt.%), however large variations have been reported in individual subduction zones (e.g. Rea and Ruff 1996; Plank and Langmuir 1998). The igneous oceanic crust, which is overlain by the thin pelagic sediment veneer, forms the next lower unit in the oceanic crustal section. It consists of a ~ 1–2 km thick upper layer of pillow basalts, underlain by a 1–2 km thick sheeted dike complex. The lowest unit consists of a 3–5 km thick gabbroic complex geochemically similar to the sheeted dike complex. The oceanic crustal section is then completed by the lowermost ultramafic unit composed of harzburgite, lherzolite, and dunite (e.g. Karson 2002). This oceanic crustal section is thought to have mainly formed at fast-spreading centers such as those in the Pacific Ocean. At very slow-spreading centers (e.g. mid-Atlantic ridge), the oceanic crust may have units with varying thicknesses or may even lack certain layers such as extrusive rocks (e.g. Bach et al. 2001; Bach and Früh-Green 2010).

10.2.1.1 Alteration of the Oceanic Crust

It is important to understand the alteration processes leading to chemical compositional diversity in subducted oceanic crust. Difficulties associated with distinguishing the chemical differences or modifications imposed on the protoliths of subducted oceanic crust include magmatism on the one hand, and seawater-rock interaction on the other (e.g. Staudigel 2003). In order to establish metasomatic changes related to fluid-rock interaction in subduction zones, major and trace element compositions in HP and UHP rocks, representing paleo-subduction zones, are often compared with those of oceanic crustal rocks that have not undergone subduction. This approach is complicated by the wide range of tectonic settings and origins, and thus varying chemical compositions, of the sedimentary and igneous oceanic protoliths of subduction-related HP and UHP rocks. In the following sections, I will discuss some studies which illuminate the problems pertaining to bulk rock chemical changes related either to seafloor alteration or subduction-related metasomatism during bulk rock metamorphism. For a more detailed overview see Chaps. 8 and 9 as well as Bebout (2007a, b) and references therein.

The nature and extent of fluid-rock interaction processes in oceanic crust are, to a large degree, responsible for the chemical heterogeneities, even within the same rock units, of the oceanic crust (see Staudigel 2003 for an extensive discussion). In general, the related alteration decreases in intensity towards the mid to lower parts of the oceanic crust (e.g. Gillis and Robinson 1990; Staudigel 2003). Consequently, the lower part of the oceanic crustal section contains fewer volatile-rich minerals than the upper part (e.g. Wallmann 2001). Therefore, most of the fluid released, during prograde metamorphism of subducting oceanic crust, is believed to be derived from the upper part of the oceanic crustal section.

Alteration of the Upper Oceanic Crust

The alteration/hydration of the upper part of the oceanic lithosphere by seawater-rock interaction has been outlined in many studies (e.g. Muehlenbachs 1986; Alt 1995; Staudigel et al. 1995; Cartwright and Barnicoat 1999). The upper crust (0–600 m) shows mainly a non-pervasive, low-grade alteration (at temperatures $< 100°C$), which usually occurs at reducing conditions and low water–rock ratios, but can be oxidizing at high water–rock ratios. The net fluxes between seawater and oceanic crust are, with the exception of black smoker water fluxes, relatively low (e.g. Staudigel et al. 1996; Staudigel 2003). However, some major (Si, Al, Mg, Ca, Na and K) and some trace elements (Sr, Cs, Ba, LREE's) may experience considerable large-scale redistribution (cf. Staudigel et al. 1996; Bebout 2007b). During low-temperature alteration, the upper crust generally experiences a gain of K_2O, Rb, Cs, and, to a lesser extent, Ba, and a depletion of SiO_2 while $\delta^{18}O_{V\text{-}SMOW}$ values increase to values $> +5.7‰$ (the value of the original magmatic value; e.g.

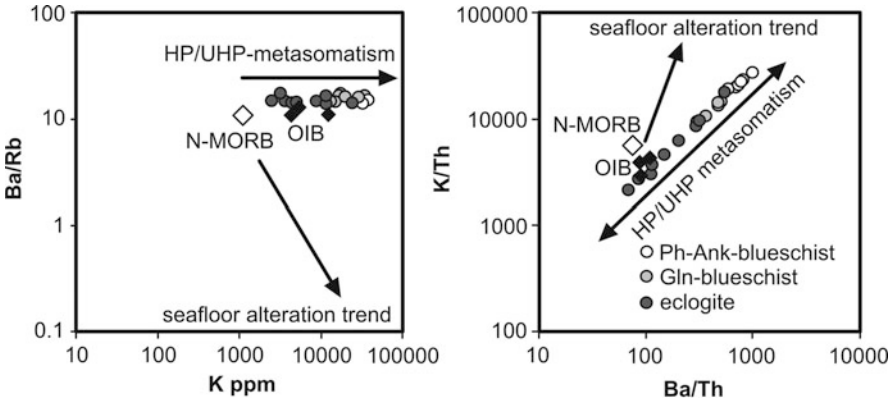

Fig. 10.2 Ba/Rb versus K and K/Th versus Ba/Th diagrams, which differentiate between metasomatism during seafloor-seawater alteration and HP metasomatism in blueschists and eclogites from western Tianshan (China) (Modified after van der Straaten et al. 2008)

Spooner et al. 1974; Gregory and Taylor 1981; Muehlenbachs 1986; Stakes and Taylor; 1992; Alt 1994, 1995; Staudigel et al. 1995; Bach et al. 2001; Bebout 2007a, b). In the deeper part of the oceanic crust, usually between the sheeted dikes and the pillows, alteration temperatures increase to $> 100°C$ while water–rock ratios decrease and the primary mineral assemblage of the basalt is typically pervasively replaced by a greenschist-facies alteration assemblage (Gregory and Taylor 1981; Alt 1995; Staudigel 2003). However, gabbros are generally altered/hydrated along veins and their alteration halos (e.g. Bach et al. 2001). Coarse-grained gabbros, in many cases, show only alteration along grain boundaries. Despite these features, the $\delta^{18}O$ values in the deeper part of the crust are $\leq 5.7‰$, while Na_2O is gained and CaO lost (e.g. Spooner et al. 1974; Gregory and Taylor 1981; Muehlenbachs 1986; Stakes and Taylor; 1992; Alt 1994, 1995; Staudigel et al. 1995; Bach et al. 2001). Bebout (2007a, b) reported on the relationship between LILE and Th in various HP and UHP metamorphic mafic rock suites and compared them to altered oceanic basalts. He concluded that it is virtually impossible to distinguish seafloor-related changes in K, Rb, and Ce concentrations from those resulting from HP and UHP metamorphism in subduction zones. However, the relative Ba gain during seafloor alteration is much smaller than that of K and Rb (Bebout 2007b). For example, van der Straaten et al. (2008) used this argument to characterize LILE and transition element enrichments produced during exhumation of bulk rock eclogitic pillow lavas from the Chinese Tianshan as a consequence of fluid-rock interaction under retrograde HP conditions and not of seafloor alteration (Fig. 10.2). This conclusion was further supported by apparent losses of LREE and HREE, which would not have occurred during seawater alteration. The comparison of blueschists and eclogites from northern New Caledonia, with their presumed igneous protoliths (Spandler et al. 2004), also provided evidence for the loss of LILE and B during this transformation. These elements showed evidence of relative fluid immobility in the majority of samples, subsequent to seafloor alteration

(Spandler et al. 2004). By comparing eclogites and their gabbro protoliths from central Zambia, John et al. (2004) proposed that the fractionation of LREE from HREE and HFSE occurred during eclogitization and was thus not the result of seafloor-alteration or magmatism. In addition, Gao et al. (2007) reported the small-scale mobilization of the HFS elements Ti, Nb, and Ta during the transformation of blueschist to eclogite, thereby excluding the pre-metamorphic, seafloor-related, trace element changes.

In general, it is thought that between 2 and 3 wt.% H_2O is added to the upper oceanic crust during interaction with seawater, which is less than that observed in HP oceanic crustal rocks such as H_2O-rich blueschists (e.g. Peacock 1990, 1993; Bebout 1996; Staudigel et al. 1996; Miller et al. 2002). The additional H_2O may stem from an enhanced fluid and element reflux during the early stages of subduction at shallow levels of accretionary prisms and subduction zones where large amounts of pore waters and connate brines are driven off by diagenetic processes (Fig. 10.1; e.g. Moore and Vrolijk 1992; Wallmann 2001; Rüpke et al. 2002).

Alteration of the Lower Oceanic Crust

Little is known regarding seafloor alteration/hydration of the ultramafic section of the oceanic crust. However, the ultramafic rocks of the oceanic crust may loose up to 15 wt.% MgO during pervasive, marine weathering (Snow and Dick 1995). Ranero et al. (2003) further suggested significant hydration and alteration of the lower extrusive crust and the first few kms of the upper mantle along large deep-reaching fracture-zones as a result of bending-related faulting in trenches prior to subduction. In addition, serpentinized peridotites of a slow spreading mid-ocean ridge are interpreted to have undergone massive replacement by talc under static conditions, which required either the removal of Mg from or the addition of Si into the system (MAR 15°N; Bach et al. 2006). These authors suggested that the talc-altered rocks were Si-metasomatized and that the Si was derived from the gabbro-seawater interaction or the breakdown of pyroxene deeper in the basement. In addition, extensive talc-(hematite/magnetite-sulphide) veins occur in the basement of this mid-ocean ridge (Bach et al. 2006). Scambelluri et al. (2001) showed that the seafloor alteration (serpentinization) of peridotites from Erro-Tobbio (Western Alps) caused considerable increase in water-localized CaO loss and a gain of Cl, Sr, and alkali elements while the REE were fairly immobile. Li et al. (2004) also worked on peridotites (Zermatt-Saas, Western Alps) serpentinized during seafloor hydrothermal alteration. They reported that this process caused massive hydration and oxidation without any major metasomatic change in the major element concentrations, apart from a loss of CaO, causing localized Ca-metasomatism of mafic dykes (rodingitization). Iyer et al. (2008) and Austrheim and Prestvik (2008) reported the mobility of Ca, K, Na, Fe, Mn, Ti, V, Ba, Rb, and Cs, at grain size to regional scale, during seafloor serpentinization and chloritization of ultramafic rocks from the Leka Ophiolite Compex (Norway). These authors suggested that Fe and Mn can be transported even out of the system, thereby constraining the

global ocean chemical budget and producing ocean floor ore deposits. Furthermore, Malaspina et al. (2006a) presented a petrological and geochemical study of UHP eclogites from Dabie Shan (China). They proposed a metasomatic overprint of the eclogites based on bulk rock major and trace element compositions. Comparing the chemical composition of the eclogites with that of their assumed protolith basalts, these authors established a strong depletion in SiO_2 and alkalies and a gain in FeO and MgO. This was interpreted to reflect an element exchange with nearby ultramafic rocks, prior to subduction, during infiltration of Si-depleted and Mg-enriched fluids liberated in the course of serpentinization of the ultramafic rocks.

In summary, numerous studies have shown that, apart from a gain in H_2O and certain mobile elements, no large-scale mobilization of the majority of trace and major elements occurred as a result of seafloor alteration processes prior to subduction. However, special care has to be taken when distinguishing bulk rock compositional changes involving certain relatively mobile elements such as Si, K, Ca, Fe, Mn, Mg, Ba, Rb, Ce, Cs and B in slab lithologies, caused by seawater–rock alteration, from those caused by HP and UHP metamorphism.

10.2.2 Continental Crust

Continental crust which has been metamorphosed under subduction-related HP and UHP metamorphic conditions often contains interlayered metamorphosed sediments such as quartzite, marble, mica schist, gneiss and concordant layers of eclogite and granitic gneiss in the meta-sedimentary sequences that resemble basaltic sills or lava flows and granites, respectively (e.g. Liou et al. 1998; Rumble et al. 2003). Eclogites from the European Hercynides and the European Alps display an oceanic affinity whereas those from the Caledonides (Scandinavia) and the Dabie Shan-Sulu orogenic belt (China) exhibit continental features (e.g. Griffin and Brueckner 1985; Stosch and Lugmair 1990; Miller and Thöni 1995; Jahn 1999; Rumble et al. 2003). Study of the 'continental' eclogites suggests that large blocks of continental crust were subducted to mantle depths. However, eclogites with MORB-affinities, which are interlayered with thick sequences of continental sedimentary rocks, suggest tectonic juxtaposition rather than simultaneous HP and UHP metamorphism of oceanic and continental rocks (for discussion and references, see Jahn 1999 and Rumble et al. 2003). The purely continental crust does not experience large-scale hydration prior to subduction owing to the absence of an interaction with seawater (e.g. Rumble et al. 2003). This is documented for example by the conservation of gabbroic textures and primary igneous minerals and intergranular coesite in eclogite from the Sulu orogen (China). These features are interpreted to be due to a lack of fluid to facilitate equilibration during peak and retrograde metamorphism (see Rumble et al. 2003; Zheng et al. 2003). These results are supported by the presence of high- and low-$\delta^{18}O$ in marbles reflecting pristine protolith and pre-metamorphic alteration respectively (Rumble et al. 2000). On the other hand, anhydrous granulites in the Caledonides (Scandinavia) were eclogitized

by localized introduction of an external fluid under HP and UHP conditions (e.g. Austrheim 1987; Austrheim and Engvik 1997; Engvik et al. 2000, 2001). The fluid necessary for eclogitization of 'dry' rocks such as these granulites is postulated to have been partly derived by internal processes (cf. Miller et al. 2002) such as the devolatilization of sheet silicate-rich sediments (e.g. Chopin 1984; Schertl et al. 1991). In addition, fluids liberated at depth, from dehydrating subducting oceanic crust, could migrate back along the subduction zone to hydrate the forearc region, i.e. continental margin (e.g. Moore and Vrolijk 1992; Miller et al. 2002; Gerya et al. 2002; King et al. 2006; van der Straaten et al. 2008). However, using Sm–Nd whole rock and Sr isotope data, Vrijmoed et al. (2006) showed that externally-derived crustal fluids, from the surrounding host-rock gneisses, infiltrated the Svartberget peridotite body (Western Norway), and created a network of websterite and garnetite veins under UHP conditions in a continental subduction zone.

10.3 Modeling of the Thermal Evolution of Subduction Zones

Thermal modeling and surface heat-flow measurements suggest that HP and UHP metamorphism is accompanied by relatively low temperatures in subduction zones (Ernst 1970; 1972; Maruyama et al. 1996) a fact that was confirmed by the discovery of blueschists in a serpentinite seamount in the forearc of the active Mariana subduction zone during deep ocean drilling (Maekawa et al. 1993). Early two-dimensional numerical models of heat transfer in subduction zones, done in order to determine specific P-T paths for the subducting slab and the overlying mantle wedge, suggested subarc temperatures below 600°C at ca. 100 km depth for the slab-wedge interface in 'cold' subduction zones and the absence of high shear stress (e.g. Peacock 1990; Peacock et al. 1994; Peacock and Wang 1997). In such 'cold' subduction zones, relatively old oceanic crust follows a P-T path with a low-geothermal gradient of ca. 5–7°C/km (Fig. 10.3) thereby crossing the blueschist to eclogite transition for the basaltic part of the slab at ~100 km depth. Due to the subduction of younger oceanic crust and/or a high shear stress, a higher geothermal gradient of ca. 13–15°C/km was calculated for 'warm' or 'hot' subduction zones. Thus, the blueschist to eclogite transition for basaltic rocks in hot subduction zones occurs at much shallower depths of < 50 km. Here, the partial melting of lithologies, such as basalts, pelites, and granites, due to the crossing of their wet solidi, is possible, depending on the degree of H_2O saturation in the slab (Fig. 10.3). At pressures above 20 kbar, H_2O occurs mainly as crystallographically-bound H_2O in the oceanic crust. Thus the solidus may not be H_2O-saturated and the amount of partial melting could be rather small (cf. Peacock et al. 2005; Kimura et al. 2009). More recent modeling, using non-Newtonian rheologies, indicates that temperatures at the slab-mantle interface are higher than previously anticipated (Fig. 10.4) in hot subduction zones at the deeper levels (about 800°C at 100 km depth; see van Keken et al. 2002; van Keken 2003; Kelemen et al. 2003; Rüpke et al. 2004; Peacock et al. 2005; Abers et al. 2006; Arcay et al. 2007; Kimura et al.

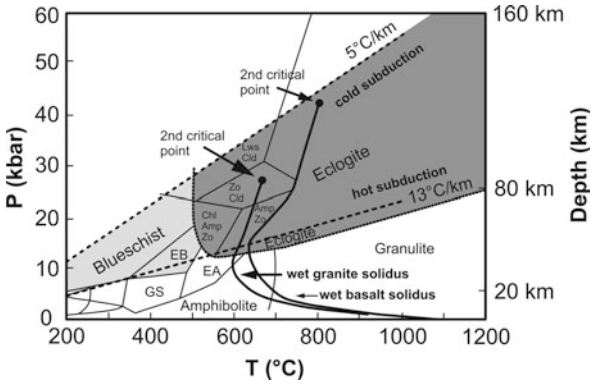

Fig. 10.3 Metamorphic facies and stability fields of hydrous minerals under eclogite-facies conditions. *Dashed lines* represent geothermal gradients in cold (5°C/km) and hot (13°C/km) subduction zones (modified after Peacock and Wang 1999). *Solid lines* represent wet solidi for basaltic (Schmidt and Poli 1998) and granitic (Huang and Wyllie 1981; Holtz et al. 2001) bulk rock compositions. *Shaded area* represents the stability field of eclogites. Second critical points are after Hermann et al. (2006). *GS* Greenschist-facies, *EB* Epidote-blueschist-facies, *EA* Epidote-amphibolite-facies. Mineral abbreviations follow Kretz (1983)

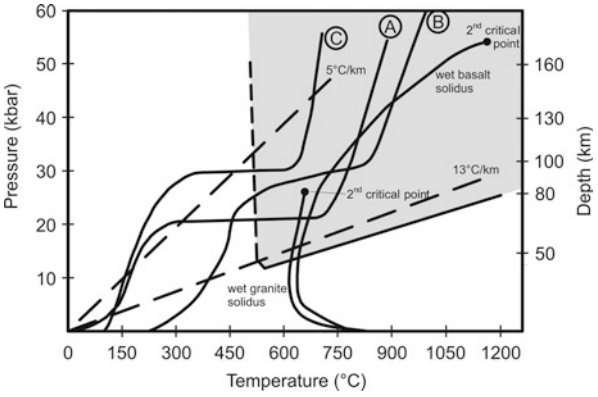

Fig. 10.4 P-T diagram showing the predicted P-T trajectories for the Tohoku (Japan) (C; Kimura et al. 2009), Cascadia (Canada) (B; Kimura et al. 2009) and Honshu (Japan) (A; van Keken et al. 2002) subduction slab interfaces when using high-resolution finite element models employing non-Newtonian rheologies as examples for cold and hot subduction zones. *Shaded area* represents the eclogite stability field. The wet basalt solidus and the second critical point are after Schmidt and Poli (1998) and Kessel et al. (2005b). The wet granite solidus is after Huang and Wyllie (1981) and Holtz et al. (2001). The second critical point is extrapolated by Hermann et al. (2006) from the critical curve of Bureau and Keppler (1999). In addition, two geothermal gradients of 5°C/km and 13°C/km are shown by the *dashed lines*

2009; Syracuse et al. 2010). Preliminary slab-surface geothermometry from different subduction zones also predicts high slab-fluid temperatures in the range of 725–950°C at such depths (Plank et al. 2009). However, exhumed oceanic crust,

with the exception of UHP eclogites and meta-sediments from the Tianshan (China) and the Lago di Cignana (Italy) (see below), usually shows maximum pressures of about 23 kbar (~ 80 km) and peak temperatures of mostly $< 650°C$ (Hermann et al. 2000; Guillot et al. 2001; Hacker et al. 2003b; Agard et al. 2009) while continental crust, with pressures in excess of 27 kbar, has peak temperatures of mostly $> 650°C$ (Chopin 1984; Parkinson and Katayama 1999; Massonne 1999, 2003; and Lardeaux et al. 2001; Ghiribelli et al. 2002; van Roermund et al. 2002).

10.4 Generation of Fluids During Subduction

The increase in pressure and temperature during subduction is the driving force behind devolatilization-reaction processes in subducting slabs (e.g. Peacock 1990). Fluid release, during metamorphic devolatilization of subducting slabs, is a continuous process that takes place over depths of 10–300 km (Fig. 10.1; Poli and Schmidt 2002). This chapter is concerned with fluids and fluid compositions responsible for metasomatism in subducting slabs at depths of 50 to about 135 km, the latter depth representing approximately the maximum depth of slabs beneath volcanic arcs (Syracuse and Abers 2006; Syracuse et al. 2010). As the dominant subducted volatile, H_2O is a vital component in all types of subduction-zone fluids (e.g. Manning 2004; Hacker 2008). Moreover, according to Kerrick and Connolly (2001a, b), the release of CO_2 during decarbonation of subducting oceanic crust is negligiable along cold and intermediate geotherms and rather limited along high-temperature P-T paths of subducting slabs. Therefore, in the present contribution, H_2O is regarded as the dominant fluid phase responsible for the majority of metasomatic changes imposed on HP and UHP rocks.

According to Schmidt and Poli (2003), two different fluid-producing regimes can be distinguished in subducting oceanic crust at the P-T conditions of interest. All rocks of the subducted oceanic crust first undergo a stage where high dehydration rates occur under low to medium pressures and low temperatures ($P < 25$ kbar $T < 600°C$). In this first regime, on a P-T diagram, the dehydration reaction curves are frequently perpendicular to the subduction geotherms. In the second regime, medium to low dehydration rates occur at medium to high pressures and low temperatures ($P = 25$–100 kbar; $T = 500$–$850°C$). In this case, dehydration reaction curves are often subparallel to P-T trajectories.

Subducted continental slabs have often been excluded when discussing fluid sources and the composition of fluid-rock interaction and metasomatism during HP and UHP metamorphism in subduction-zone environments (cf. Poli and Schmidt 2002; Schmidt and Poli 2003; Hacker 2003a; Hacker et al. 2003b). As discussed above, this is probably due to the different properties of continental and oceanic crust prior to subduction, as continental crust entering subduction zones is generally less hydrated than oceanic crust (e.g. Austrheim 1987; Jackson et al. 2004; Rumble et al. 2000, 2003; Zheng et al. 2003). This general lack of fluid during UHP metamorphism of subducting continental crust does not allow for large-scale

metasomatism of the overlying mantle wedge and is thus consistent with the general absence of arc magmatism in continental collision zones (e.g. Rumble et al. 2003; Zheng 2009).

In the following sections, I will discuss the generation of fluids in subducting oceanic lithosphere. For simplicity these are treated here as altered terrigeneous sediments, basalts, and serpentinized peridotite.

10.4.1 Dehydration of Terrigeneous Sediments and Continental Crust

The thin sediment veneer on top of the slab dehydrates first, followed by the altered oceanic crust and then the lithospheric mantle (e.g. Rüpke et al. 2002; Kimura et al. 2009). The absolute amount of hydrous mineral phases, the main source of H_2O, depends on the modal abundance of quartz, which strongly varies between terrigeneous sediments and more felsic continental crust (Schmidt and Poli 2003). Most crystallograpically-bound water (as OH^-) is released from terrigeneous sediments and continental crust during continuous dehydration reactions at HP-LT ($< 650°C$) metamorphism. Ignoring the structural hydroxyl and molecular water in nominally anhydrous minerals, (e.g. Chen et al. 2007; Gose et al. 2009; Su et al. 2009) the most important minerals containing (crystallographically-bound) H_2O in both terrigeneous sediments and continental crust, under HP conditions, are phengite and biotite, both of which contain up to 5 wt.% H_2O. The modal abundance of these micas depends on the K_2O content of their respective host rock (Schmidt and Poli 2003; Hacker 2008). Other important carrier minerals of bound H_2O, especially in meta-pelites, are talc, chloritoid, chlorite, lawsonite, and amphibole (e.g. Poli and Schmidt 2002; Hermann 2002; Kimura et al. 2009). Biotite reacts to garnet and phengite at pressures above 25–30 kbar unless the bulk rock composition of the host rock is Mg-rich (Poli and Schmidt 2002; Hermann 2002). Phengite on the other hand is often stable throughout the prograde and retrograde evolution of HP and UHP rocks even at $aH_2O << 1$ (Domanik and Holloway 1996, 2000; Ono 1998).

Change in the absolute H_2O content of meta-sediment during prograde subduction-zone metamorphism can best be described in the context of the behavior of terrigeneous sediments and the fluid regimes outlined by Schmidt and Poli (2003). In hot subduction zones, significant amounts of H_2O are released during shallow depth diagenesis, and shallow-level forearc devolatilization, and, hence, unavailable for release during UHP metamorphism. In addition, melting of terrigeneous sediments occurs under UHP conditions > 27 kbar and temperatures $>650°C$ (see below; Schmidt et al. 2004). In contrast, during cold subduction, significant amounts of aqueous-rich fluids can be released at HP and UHP conditions and melting may or may not occur depending on H_2O saturation of the solidus (Fig. 10.4). Kimura et al. (2009) modeled the fluid evolution for

terrigeneous sediments in a cold subduction zone (Tohoku, NE Japan). They observed that the largest drop in the absolute amount of H_2O content, from about 4.3 wt.% to 1.75 wt.%, occurred at about 30 kbar, thus corresponding to the breakdown of hydrous silicate minerals such as amphibole, lawsonite (depending on the CaO content of the host rock), and chlorite. Phengite remains stable at up to 60 kbar, and this is able to transport a significant amount of H_2O into the deeper mantle. However, due to the minor volume of sediment in comparison to altered basalts and serpentinized peridotites of the oceanic lithosphere, the absolute amount of sediment-derived H_2O is by far less than that derived from the latter rock types.

10.4.2 Dehydration of (Altered) Basalts

Blueschist-facies meta-basalts in the first dehydration regime of Schmidt and Poli (2003) are usually regarded as fully hydrated whereas the related coarser-grained gabbros display variable hydration (e.g. Wallmann 2001; John and Schenk 2003). Most P-T trajectories calculated for various subduction-slab interfaces, for both cold and hot subduction zones, reveal that meta-basalts are characterized by the hydrous mineral assemblage sodic-calcic amphibole (~2 wt.% H_2O), chlorite (~12 wt.% H_2O), phengite (~4 wt.% H_2O), paragonite (~5 wt.% H_2O), lawsonite (~11 wt.% H_2O), and/or zoisite/epidote (~2 wt.% H_2O) at pressures below about 25 kbar (Evans 1990; Schmidt and Poli 2003; Fig. 10.5). At the onset of blueschist-facies metamorphism, the meta-basalts contain about 6 wt.% H_2O (Schmidt and Poli 2003). With increasing temperature, lawsonite reacts to zoisite while chlorite breaks down to garnet (Schmidt and Poli 1998). However, a major fluid pulse is released when the blueschist, still containing up to 3–4 wt.% H_2O, transforms into eclogite which usually contains <1 wt.% H_2O (Peacock 1993). Thus, hydrated basalts may lose up to 4 wt.% H_2O due to dehydration reactions during blueschist-facies metamorphism (Figs. 10.3, 10.5). Typical prograde dehydration reactions observed in meta-basalts at the blueschist-eclogite transition are (e.g. Evans 1990; Manning and Bohlen 1991; Gao and Klemd 2001):

$$clinozoisite + titanite => garnet + rutile + quartz + H_2O \quad (10.1)$$

$$glaucophane + titanite => omphacite + rutile + quartz + H_2O \quad (10.2)$$

$$clinozoisite + glaucophane => garnet + clinopyroxene + quartz + H_2O \quad (10.3)$$

$$glaucophane + paragonite => garnet + clinopyroxene + quartz + H_2O. \quad (10.4)$$

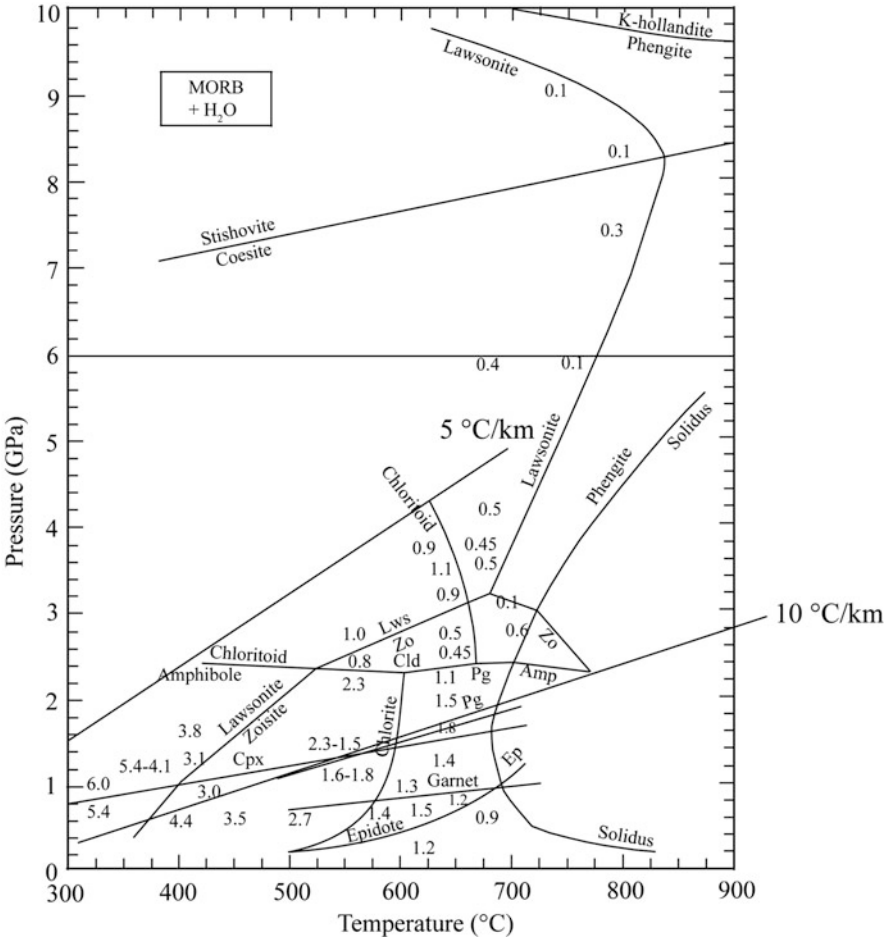

Fig. 10.5 Major phase stabilities and maximum H_2O contents (in wt.%) in hydrous phases in MORB (Modified after Schmidt and Poli 1998, 2003). In addition two geothermal gradients of 5°C/km and 10°C/km are shown by the *dashed lines*. Mineral abbreviations follow Kretz (1983)

The latter two dehydration reactions have steep negative P-T slopes between 14 and 20 kbar, at 550–600°C, corresponding with the release of large amounts of H_2O and a volume reduction at the blueschist-eclogite transition (for discussion see Gao and Klemd 2001; Feineman et al. 2007 and John et al. 2008). In meta-basalts, the stability of amphibole, which may change in composition from more sodic (aluminous) to more calcic with increasing temperature (Schmidt and Poli 1998), is however calculated to lie far above 25 kbar in H_2O-saturated systems and in mixed H_2O–CO_2 fluid systems (e.g. Kerrick and Connolly 2001a; Peacock et al. 2005; Kimura et al. 2009). At UHP conditions, amphibole and zoisite may react to stabilize Mg-rich chloritoid (7.5 wt.% H_2O) along P-T paths in cold subduction zones under H_2O-saturated conditions (Fig. 10.5):

$$amphibole + zoisite = chloritoid + clinopyroxene + quartz + H_2O. \quad (10.5)$$

Chloritoid, and also lawsonite, are, however, rarely observed in natural UHP eclogites and their stability in meta-basalts at the UHP conditions is disputed (Hacker et al. 2003b; Hacker 2006; cf. Zack et al. 2004; Lü et al. 2009). It appears that their occurrence is restricted to relatively low temperatures in very-cold subduction regimes (Zack et al. 2004; Lü et al. 2009; Brovarone et al. 2011; Fig. 10.5). Although lawsonite and chloritoid, in addition to phengite, can be present in the UHP dehydration regime (24–100 kbar at temperatures between 500°C and 800°C), relatively little fluid is produced because of small dehydration fluxes relating to the fact that the (continuous) dehydration reactions are subparallel to most calculated P-T paths and are thus crossed over a wide depth range (Schmidt and Poli 2003). Above about 25 kbar, a maximum amount of 1.5 wt.% H_2O is thought to occur as crystallographically-bound H_2O in hydrous minerals (Fig. 10.5). The final breakdown of lawsonite and phengite in the stishovite stability field marks the end of major dehydration in subducting meta-basalts (Fig. 10.5). Although in very-low temperature subduction zones, phengite and lawsonite can be preserved through the prograde and retrograde P-T evolution of HP and UHP meta-basalts (see Schmidt and Poli 2003; Hermann et al. 2006; Angiboust and Agard 2010; Brovarone et al. 2011)

10.4.3 Dehydration of Serpentinized Upper Lithospheric Mantle

As discussed earlier, subducted oceanic lithosphere includes upper-mantle ultramafic rock consisting of harzburgite, lherzolite, and dunite (e.g. Karson 2002). Ocean-floor serpentinization appears to be a common feature in the ultramafic part of the subducting slab and can be described by the hydration reaction:

$$enstatite + forsterite + H_2O => serpentine + magnetite + H_2 \quad (10.6)$$

Although it is impossible to determine the exact amount of serpentinization, it is suggested that lithospheric bend faulting at the outer rise creates channels for seawater to serpentinize the cold (<600°C) ultramafic rocks in the subducting slabs (Rüpke et al. 2002; Ranero et al. 2003). Ranero et al. (2003) suggested that bending-related faulting of the incoming plate at the Middle America trench creates a pervasive tectonic fabric which cuts across the crust and extends into the mantle. These authors assumed a maximum amount of 30% serpentinization of the uppermost mantle, which occurs during hydration along these fault systems near the trench. Larger-scale serpentinization would create a low-density upper lithospheric mantle which would result in slab buoyancy strongly affecting the dynamics of the subduction (Schmid et al. 2003). Schmidt and Poli (1998) estimated a maximum bound H_2O-content of about 11 wt.%, in hydrous phases, in metamorphosed

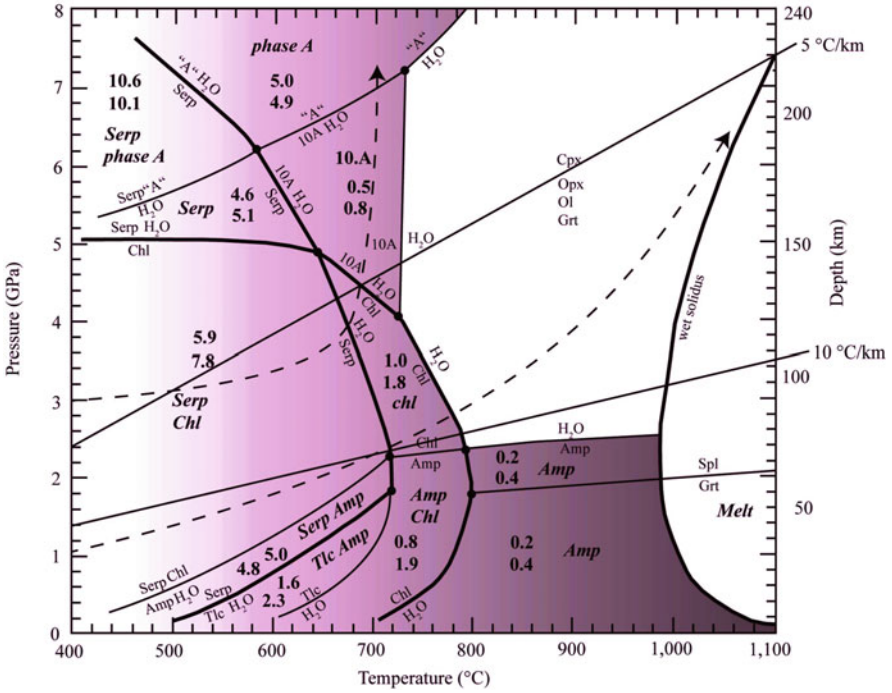

Fig. 10.6 Phase diagram showing major phase stability boundaries for H_2O-saturated average mantle peridotite and maximum mineral-bound H_2O contents (in wt.%; Modified after Schmidt and Poli 1998, 2003). The *shaded field* displays stability fields of hydrous phases. In addition two geothermal gradients of 5°C/km and 10°C/km are shown by the *dashed lines*. Serpentinized peridotite, following a P-T path in a cold subduction zone (*stippled line*) will not dehydrate below about 40 kbar (~ 130 km). Phase A is ($Mg_7Si_2O_8(OH)_6$, 11.8 wt.% H_2O). Mineral abbreviations follow Kretz (1983)

harzburgites by undertaking mass balance calculations using modal abundances and bulk rock chemical compositions. Serpentine (~12 wt.% H_2O) and chlorite (~12 wt. % H_2O) dominate the water budget of hydrated peridotite to about 50 kbar (Fig. 10.6). Serpentine is the dominant hydrous mineral at pressures of up to 70 kbar and temperatures < 700°C whereas chlorite, talc, and amphibole can occur as minor hydrous phases at these P-T conditions (Fig. 10.6). At temperatures above about 700°C and pressures of up to 21 kbar, serpentine reacts to talc + olivine + H_2O. At higher pressures (> 21 kbar) and temperatures (>650°C), serpentine reacts to chlorite + olivine + orthopyroxene + H_2O (Fig. 10.6; Schmidt and Poli 1998; Padron-Navarta et al. 2010). However, depending on the temperature, bulk rock chemistry, and it's Al-Cr content, serpentine is stable up to >20 kbar throughout almost all subduction-slab P-T trajectories (geothermal gradients < 10°C/km; Fig. 10.6; Schmidt and Poli 1998; Bromiley and Pawley 2003; Padron-Navarta et al. 2010). Thus the serpentinized peridotite unit produces significant amounts of fluid only at depths greater than about 70 km where the rest

of the oceanic crust had already undergone significant dehydration (see above). In contrast, sediments are suggested to have lost more than two-thirds of their mineral-bound H_2O by about 50 km depth (Rüpke et al. 2002). It should further be noted that serpentinites, which follow P-T paths in cold subduction zones (5°C/km), will not dehydrate at < 40–45 kbar (~130 km; Fig. 10.6). However, calculated phase diagrams (cf. Scambelluri et al. 2004; Hacker 2008) for H_2O-saturated oceanic peridotite show somewhat different experimentally determined upper thermal stabilities for serpentine than those reported above (Fig. 10.6; Schmidt and Poli 1998). For example, a complete prograde P-T path in a hot subduction zone was constructed using natural oceanic mantle samples, starting with low-grade chrysotile-bearing oceanic serpentinites (P < 2.5 kbar at T < 300°C; Northern Appennine and Erro-Tobbio, Italy), going up to HP antigorite serpentinites (P = 20–25 Kbar at T = 500–650°C; Erro-Tobio, Italy and Betic Cordillera, Spain), and ending with olivine-orthopyroxene-chlorite harzburgites (P > 25 kbar at T > 650°C; Betic Cordillera, Spain), (see Scambelluri et al. 2004 and references therein). Two main dehydration events are displayed by partial antigorite dewatering during formation of metamorphic olivine, followed by the complete breakdown of antigorite to olivine, orthopyroxene, and fluid at temperatures > 650°C. However, the calculated phase diagrams may have suffered from the lack of appropriate thermodynamic data sets and solution models for Al in the serpentine (cf. Padron-Navarta et al. 2010).

10.4.4 Generation of Melts and Fluids During Exhumation of HP and UHP Rocks

A major problem when investigating exhumed HP and UHP subduction-related rocks is that oceanic crust usually exhumes as small boudins or layers in buoyant serpentinized peridotite or meta-sediments from maximum depths of about 80 km (Gerya et al. 2002; for compilation of data see Agard et al. 2009). Thus, up to now, more intact subducted oceanic crust from depths of 100 to 135 km (estimated depth of subducting slabs beneath volcanic arcs Syracuse and Abers 2006; see also Fig. 10.1) has not yet been found (cf. Angiboust and Agard 2010). Most information regarding the properties and behavior of hydrous melt and/or fluid phase, during exhumation from UHP to HP conditions, comes from exhumed continental rocks. Partial melting may occur during decompression in felsic rocks exhumed from these depths (see Fig. 10.7). Phengite in felsic continental crust will be stable throughout the prograde and retrograde metamorphic evolution in cold slabs during simultaneous cooling and decompression of UHP rocks, as is the case in Doira Maira (Italy) (for discussion see Hermann et al. 2006). On the other hand, in hot continental UHP slabs, temperatures at peak conditions are > 700°C and thus, during isothermal exhumation, dehydration melting of phengite should take place under HP conditions as is the case in the Dabie-Sulu orogeny (China)

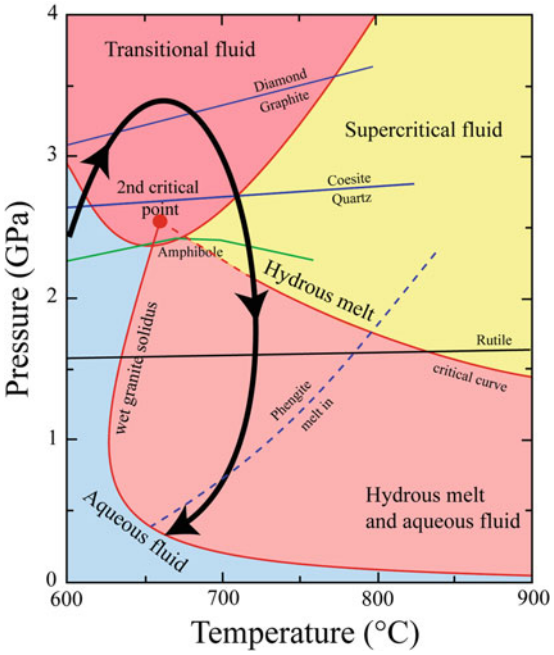

Fig. 10.7 P-T path of UHP meta-granites from the Dabie Shan (China) displaying dehydration melting during exhumation (Modified after Xia et al. 2010). The phengite dehydration melting curve (*stippled*) is shown for a pelitic bulk rock composition (after Vielzeuf and Holloway 1988). The wet granite solidus is after Huang and Wyllie (1981) and Holtz et al. (2001) and the second critical point is extrapolated by Hermann et al. (2006) from the critical curve of Bureau and Keppler (1999). The compositional character of the fluid phase above the second critical point follows the definition of Hermann et al. (2006) (for details see text and caption of Fig. 10.8)

(e.g. Nakamura and Hirajima 2000; Hermann et al. 2006; Xia et al. 2010; Fig. 10.7) and in the Greenland Caledonides (Lang and Gilotti 2007). In the absence of phengite, no evidence was found for the former presence of a retrograde aqueous fluid in equilibrium with a hydrous melt in ultrahigh-pressure OH-rich topaz-bearing quartzites from the Sulu terrane (China) (Frezzotti et al. 2007). However, even if dehydration melting of phengite occurs during the exhumation of UHP rocks, this process is often difficult to demonstrate because many UHP fluid (flow) features and textures, as well as mineralogical and metasomatic changes established during HP-UHP metamorphism, are overprinted or annealed due to the abundant availability of fluids along the slab-wedge interface (subduction channel; e.g. Gerya et al. 2002) along which these rocks are exhumed (e.g. Hermann et al. 2006; van der Straaten et al. 2008). Pervasive fluid flow along the slab-wedge transition zone is possible due to retrograde mineral reactions, which have a positive volume change (Konrad-Schmolke et al. 2011). Also, exhumation to lower levels in subduction zones often leads to rehydration of dry eclogites and the formation of retrograde veins. The latter is interpreted by mass balance considerations to be the result of

large-scale element transport (e.g. Miller et al. 2002: van der Straaten et al. 2008). For example, van der Straaten et al. (2008) investigated chemical changes associated with blueschist-facies rehydration of eclogites during exhumation in the Tianshan orogen (NW-China). These authors suggested that the infiltrating fluids, that hydrated the eclogites, were released, during dehydration of the serpentinized parts of the upper mantle in the downgoing slab, and migrated up-dip into exhuming HP rocks along the slab-wedge interface. Furthermore, in Alpine Corsica, the coexistence of lawsonite-bearing blueschists and eclogites as pods and lenses in retrograded epidote-blueschist- and greenschist-facies host rocks indicate that much of the lawsonite-breakdown, which released large amounts of H_2O ($>$ 3 wt.%), occurred during exhumation (Brovarone et al. 2011; see also Angiboust and Agard 2010).

10.5 Fluid Flow Under HP and UHP Metamorphism

Large volumes of crystallographically-bound fluid (especially H_2O) are subducted in altered oceanic crust and upper mantle lithosphere (e.g. Peacock 1990; Hacker 2008). Much of the crystallographically-bound H_2O in oceanic, as well as in continental crust, is previously released, at shallower levels in forearcs, during continuous dehydration reactions throughout HP-LT ($<$650°C) metamorphism. For example, altered, K_2O-poor oceanic basalt and upper lithospheric peridotite have little or insignificant amounts of H_2O accessible during UHP conditions in hot subduction zones, based on scaling of subducted H_2O with bulk K_2O. In contrast, terrigeneous clay-rich sediments and continental crust may stabilize significant amounts of water in phengite throughout UHP conditions unless melting occurs (e.g. Hacker 2008). Because of the presence of serpentine, amphibole, talc, and chlorite, mafic and ultramafic igneous rocks are best suited for containing the H_2O available under UHP conditions at about 30 kbar in cold subduction zones. Continental crust and terrigeneous sediments similarly convey significant amounts of H_2O in phengite, amphibole, chloritoid, and lawsonite under these conditions (e.g. Schmidt and Poli 2003; Kimura et al. 2009). However, the primary source of H_2O from the dehydrating slab is serpentine between ~120 km depth and below. Thus, significant amounts of released aqueous fluids are accessible under HP and UHP conditions during cold subduction whereas, in the case of hot subduction, aqueous fluids are mainly released during HP dehydration or even lower-grade metamorphic conditions. Furthermore, in hot subduction zones, partial melting of altered oceanic crust and terrigeneous sediments occurs under HP and UHP condition $>$ 10 kbar and temperatures $>$ 650°C (see Fig. 10.4; Schmidt et al. 2004). Therefore, at higher temperatures ($>$ about 650°C hot subduction), partial melting occurs while at lower temperatures ($<$ about 650°C cold subduction) an aqueous fluid prevails during subduction (Fig. 10.4). When temperature conditions during HP and UHP metamorphism in cold and hot slabs exceed the stability limit of the hydrous minerals in the various rock types, water and other volatiles are liberated and create fluid

overpressures as a result of their larger volume in comparism to the porosity created by the devolatilization reaction (Hacker 1997). Fluid overpressure creates local hydrofractures which form a small-scale, permeable-fracture network (see Miller et al. 2003; Zack and John 2007). Fluid flow along grain boundaries through an interconnected porosity is known as 'pervasive' flow while flow along high-permeability zones such as cracks, faults and shear zones is termed 'channeled' or 'focused' (e.g. Ague 2003a, cf. Oliver 1996). However, internally-buffered localized networks on a microscopic scale do not permit pervasive or focused fluid flow on a mesoscopic to macroscopic scale, since the dihedral angle between water and mafic silicates exceeds 60° under HP and low-temperature conditions (< 30 kbar < 700°C, e.g. Mibe et al. 2003). An interconnected vein network can therefore only form if a sufficient volume of fluid is continuously liberated, (for instance by fluid pooling (e.g. Balashov and Yardley 1998)), in order to overcome the lithostatic pressure leading to dehydration embrittlement and hydrofracturing (Watson and Brenan 1987; Ague 2003a; Miller et al. 2003). Pathways formed by these processes tend to focus fluid flow, as predicted by fluid mechanics (Davies 1999; Miller et al. 2003). The process of focused fluid flow results in the formation of HP veins (see below) which may be subject to multiple opening and sealing (crack-and-seal mechanism) related to pulse-like fluid flow owing to the high lithostatic pressure at greater depths (Philippot 1987; Philippot and Selverstone 1991; Connolly 1997; Davies 1999; John and Schenk 2006). Continuous fluid release causing dehydration embrittlement may also be linked with intermediate-depth intraslab earthquakes in subduction zones (Green and Houston 1995; Kirby et al. 1996; Hacker et al. 2003b). However, in comparison with hot subduction zones, dehydration embrittlement occurs at greater depths in cold subduction zones (e.g. Kimura et al. 2009). If sufficient volumes of fluid are released, the fluid phase migrates away from the site of their liberation, along gradients in fluid pressure, either up-dip into the subduction zone channel or into the overlying mantle wedge (Manning 1998; Hacker et al. 2003b; Miller et al. 2003; see also Chap. 14). Depending on their total volume and composition, these fluids can potentially metasomatize the infiltrated rock unit (Zack and John 2007). The scale and quantities of fluid flow in HP and UHP rocks are still a matter of discussion (see below). Oliver (1996) defined fluid-rock interaction lacking a significant contribution from externally-derived fluids as a closed rock-fluid system. Whereby closed system fluid behavior is restricted to localized fluid flow in microcracks and cracks (without a fluid-connectivity) and occurs over a large range of strain rates and small fluxes. He restricted larger, mesoscopic to macroscopic scale, pervasive fluid flow to open system flow along channels in heterogeneous rocks at high strain rates and moderate to high fluid fluxes. Thus, the generation and the advective transport of aqueous fluids, and thereby trace elements, on a larger scale during HP-UHP conditions in subduction zones can be achieved mainly by focused fluid flow along hydrofractures or large shear zones, which could connect isolated fluid phases in oceanic and/or continental crust (Davies 1999; Bruhn et al. 2000; Zack and John 2007). For example, Breeding et al. (2003, 2004) suggested mélange-type tectonic contacts between the subducting slabs and overlying mantle wedges (subduction

channels) as conduits of major fluxes (also see Bebout and Barton 1989, 2002). On the other hand, Davies (1999) regarded hydrofracturing to be the more important process because the influence of shear deformation on aqueous fluid connectivity seems to be rather limited at geological strain rates. In contrast, some researchers favor convective circulation of fluids in order to explain the generation and transport of aqueous fluid, and thereby trace elements, on a larger scale during HP-UHP metamorphism (e.g. Philippot 1993; Rubatto and Hermann 2003; Spandler and Hermann 2006; Xiong et al. 2009). Zack and John (2007) pointed out that a convective circulation of fluids can only be obtained by means of a hydrostatic gradient in fluid pressure, which can only be achieved due to overlying highly permeable rocks with low-permeability rocks (also see Walther and Orville 1982; Etheridge et al. 1983). Usually, this is not the case in subducting slabs associated with HP and UHP conditions, as high permeabilities rarely occur under such conditions. Kummer and Spinelli (2008) confirmed by numerical modeling that, due to low permeabilities, significant fluid convection ceases beyond 16 km into subduction zones. Another significant argument against fluid convection in deep levels of subduction zones is the need for fluid flow downward against vertical lithostatic pressure-gradients despite the buoyancy of the fluid phase (e.g. Oliver 1996; Ague 2003a).

10.6 Composition and Type of Fluids Creating Metasomatism During HP and UHP Conditions

The composition and types of fluid responsible for metasomatic changes during HP and UHP metamorphism are largely unknown, and only inferred, due to the impossibility of collecting pristine HP-UHP fluids from subduction zone environments. In general, there are two main approaches to obtain information on the composition and type of fluid phase present during HP and UHP conditions and thus responsible for metasomatism in rocks from former subduction zones: (1) experimental studies, and (2) investigation of natural rocks.

10.6.1 Experimental Investigations of Composition and Type of Fluid

Three distinct types of fluid, buffered by a certain mineral assemblage, may occur under HP and UHP conditions in subducting slabs and will be discussed in this chapter. These are aqueous fluids, hydrous melts, and ‘transitional’ fluids. Transitional fluids represent a complete miscibility between a hydrous melt and an aqueous fluid above a second critical endpoint (Shen and Keppler 1997; Bureau and Keppler 1999; Stalder et al. 2000, 2001; Manning 2004; Kessel et al. 2005b;

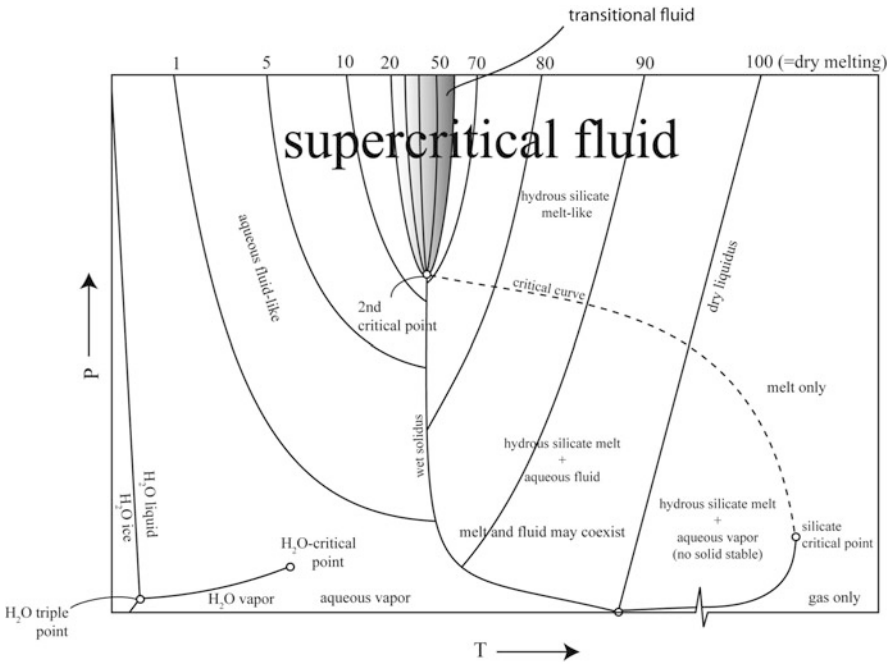

Fig. 10.8 Generalized P-T phase diagram representing a simple binary (silicate + H_2O) system (Modified after Stalder et al. 2001; Ferrando et al. 2005; Hermann et al. 2006). The mineral-buffered fluid composition shows the total dissolved solid in wt.%. At pressures above the second critical point, the compositional character of the mineral-buffered, supercritical fluid ranges from the lower temperature 'aqueous fluid-like' to the higher temperature 'hydrous silicate melt-like' region which are connected by a 'transitional' solute-rich fluid (*shaded area*). However, it should be noted that the different compositional regions are not separated by phase transitions (cf. Hermann et al. 2006)

Hermann et al. 2006; Hack et al. 2007; Klimm et al. 2008). Phase relations in hydrous systems have been experimentally investigated for various silicate-H_2O systems. Mineral solubility data for felsic rocks suggest that, at a certain temperature and pressure, the water-saturated solidus is terminated by the second critical point above which the composition of a solid-buffered, supercritical fluid distinctly varies between a solute-poor aqueous fluid and a solute-rich hydrous melt (e.g. Stalder et al. 2001; Manning 2004; Hermann et al. 2006; Fig. 10.8). There is considerable discussion regarding the existence of a true solidus under these conditions or whether a hydrous silicate melt shows a full miscibility between melt and aqueous fluid. In the literature, transitional fluids are often termed as 'supercritical' fluids, which is imprecise and ambiguous. This is because the term 'supercritical fluid' also describes aqueous fluids or hydrous melts (any stable single fluid phase above a critical curve or point is supercritical), which are stable over a wide P-T range and not just at HP and UHP conditions (for discussion see Manning 2004; Hermann et al. 2006; Hayden and Manning 2011). As suggested by

Hermann et al. (2006), the following terms for fluids buffered by a mineral assemblage are preferred: 'aqueous fluid' for an H_2O-rich fluid phase with less than ~30 wt.% solutes, 'hydrous melt' for a fluid phase with $\geq$ 65 wt.% solutes and 'transitional (solute-rich) fluid phase' in between. All of these fluid phases are supercritical over a large range of P-T conditions (Figs. 10.7, 10.8). The P-T conditions of the second critical point vary from about 25 to 35 kbar at ~700°C and 40 to 60 kbar at about 700 to 1,400°C for a haplogranite- and MORB-H_2O system, respectively (Bureau and Keppler 1999; Spandler et al. 2007; Kessel et al. 2005b; for discussion Hermann et al. 2006 and Klimm et al. 2008; Figs. 10.4, 10.7, 10.8). Thus the exact location of the second critical point strongly depends on the bulk rock chemical composition of the particular rock sample. Up to now only very limited experimental data are available for constraining the P-T position of this point for different bulk rock compositions. This is especially the case for the system basalt + H_2O. However, experimental data at 30 ± 5 Kbar and 700 ± 50°C, concerning the second critical point for meta-pelitic or meta-granitic rocks, suggest that (supercritical) transitional fluids can be expected in continental crust, which has suffered UHP conditions in relatively cold subduction zones (Figs. 10.4, 10.7; also see Hermann et al. 2006; Klimm et al. 2008; Xia et al. 2010). In contrast, the possible presence of transitional fluids in HP and UHP oceanic crust (MORB-like) is problematic. The critical curve, and thus the second critical point of (K-free) mafic (ultramafic) systems, lie at pressures and temperatures of ca. 35 Kbar at ~800°C (Lambert and Wyllie 1972; Mibe et al. 2011) but may occur at much higher pressures $>$ 50 kbar at temperatures $>$ 1,000°C (Fig. 10.4; Kessel et al. 2005b). The second critical point for peridotites lies at even higher pressures (Green 1973). As yet no oceanic crust has ever been recovered from such UHP depths. Thus, it appears that exhumed mafic rock systems remain subcritical to these pressures and temperatures. High-resolution, finite-element thermal models predict P-T paths for HP and UHP oceanic crustal rocks in cold subduction zones to be characterized by the presence of solute-poor aqueous fluids and the absence of partial melting. Whereas, in hot subduction zones at high enough temperatures ($>$ 650°C) and pressures ($\geq$ 20 kbar), hydrous melts may occur rather than transitional fluids (Fig. 10.4). Several experimental studies (for a detailed review see Hermann et al. 2006) on natural rocks have been undertaken under HP and UHP conditions in order to study the behavior of major and trace elements during fluid-saturated melting of greywackes and pelitic bulk compositions, which would produce rhyolitic to granitic melts (e.g. Hermann and Green 2001; Schmidt et al. 2004; Spandler et al. 2007; Hermann and Spandler 2008); of basaltic rocks, which would produce haplogranitic-rhyolitic to trondhjemitic-andesitic melts (e.g. Green and Ringwood 1968; Prouteau et al. 2001; Kessel et al. 2005b; Klimm et al. 2008); and of peridotites, which should produce basaltic melts (e.g. Green et al. 1987; Kawamoto and Holloway 1997). Generally, the H_2O content in the melts increases with increasing pressure and decreasing temperature under UHP metamorphic conditions (Hermann 2003; Hermann et al. 2006). Under UHP conditions, felsic and mafic rocks, despite their different bulk compositions, contain similar mineral assemblages of garnet, clinopyroxene, phengite, coesite, and accessory rutile,

zircon, and apatite (with widely varying modal proportions; see Schmidt et al. 2004; Hermann et al. 2006). Hydrous melts, coexisting with this mineral assemblage, will contain relatively elevated concentrations of fluid-mobile elements (e.g. LILE, LREE) and low HFSE and HREE concentrations (cf. Hermann et al. 2006). Experimental studies on aqueous fluid, in equilibrium with silicate-rich rocks, are scarce because aqueous fluids cannot be quenched. However, mineral solubility-experimental studies, based on weight loss of single minerals and predicted thermodynamic properties, can be used for complex systems (Manning 1994, 1998, 2004; Hayden and Manning 2011). For example, Manning (1998) predicted H_2O-rich fluids, liberated during the blueschist-eclogite transition, would have solute-poor Si-, Na-, and Al-dominated compositions. Furthermore, several different experimental methods can be used to obtain information on trace element partitioning between aqueous fluids and hydrous melts. These involve the buffering of the aqueous fluids by solids in separate capsules (Green and Adams 2003) or in diamond cells (Stalder et al. 1998; Johnson and Plank 1999; Tenthorey and Hermann 2004; Kessel et al. 2005a, b) or in a hydrothermal piston-cylinder (Ayers and Watson 1993; Spandler et al. 2007). Each of these approaches indicates that certain LREE, LILE and Sr are relatively enriched in the aqueous solute-poor liquid at HP and UHP and temperatures below about 700°C (for a detailed discussion see Hermann et al. 2006). However, the experimental data, obtained by these different methods, often provide contradicting results, as was pointed out by Hermann et al. (2006). For example, experimental investigations on rutile solubility in pure H_2O fluids obtained by Audetat and Keppler (2005), using hydrothermal diamond anvil cells, and Tropper and Manning (2005), using hydrothermal piston-cylinder weight-loss techniques, show significantly lower solubilities than those previously reported for similar P-T conditions by (Ayers and Watson 1993), who used hydrothermal piston-cylinder techniques.

10.6.2 Investigations of Natural Rocks

Several approaches can be undertaken when investigating natural rocks in order to obtain information regarding the type and composition of fluids responsible for metasomatic changes in the slab during HP to UHP conditions.

10.6.2.1 Fluid Composition: Evidence from Fluid Inclusion Studies

Several decades ago, one of the major issues when investigating HP and UHP metamorphism was the possible presence and behavior of a free fluid phase (e.g. Essene and Fyfe 1967; Okrusch et al. 1978). More recently, the question rather concerns the fluid type, namely whether a solute-poor aqueous fluid, a hydrous melt, and/or a transitional fluid was present and responsible for metasomatic changes in the host rocks during HP and UHP metamorphism. Peak-metamorphic

mineral assemblages, and their preserved 'fluid' and melt inclusions in blueschist- and eclogite-facies rocks, have been utilized by many researchers to constrain subduction zone metasomatism, as fluid inclusions may deliver the only direct information on the composition, type, and P-T conditions of slab-derived fluids. Fluid inclusions can potentially provide the only pristine samples of such fluids and/or solids trapped in cavities generally smaller than 100 μm. Thus, in order to obtain constraints on the P-V-T-X properties of the fluid present at the time of trapping, petrographic and microthermometric investigations as well as special analytical techniques, such as laser Raman spectroscopy and laser ablation-inductively coupled plasma-mass spectrometry (LA-ICP-MS) of fluid inclusions, must be employed. A detailed outline of the textural occurrences of, and methods for investigating, fluid inclusions in HP and UHP rocks is beyond the scope of this chapter and the reader is referred to reviews by Roedder (1984), Touret and Frezzotti (2003), Klemd (2004), and Ferrando et al. (2005), which provide both a detailed overview of this topic and a discussion of the results of several case studies. In this chapter, the results of those studies are discussed that are relevant to defining the composition and behavior of the fluid phase responsible for the metasomatic changes in subduction-related host rocks at HP to UHP conditions.

Several fluid inclusion studies of syn-metamorphic HP to UHP vein minerals and matrix minerals of the surrounding host rocks revealed a large variety of fluid compositions. Reported compositions of prograde and peak metamorphic fluid inclusions include aqueous low-salinity fluids (e.g. Klemd 1989; Giaramita and Sorensen 1994; Vallis and Scambelluri 1996; El-Shazly and Sisson 1999; Franz et al. 2001; Gao and Klemd 2001; Gao et al. 2007), high-salinity aqueous fluids, and/or CO_2-N_2- or N_2-rich fluids (e.g. Andersen et al. 1989; Selverstone et al. 1992; Philippot 1993; Klemd et al. 1992, 1995; Scambelluri et al. 1997, 1998; Xiao et al. 2000, 2002; Fu et al. 2001, 2002, 2003; Mukherjee and Sachan 2009). Furthermore polyphase solid inclusions, with considerable amounts of hydrous alumino-silicate phases, carbonates, sulfides, and sometimes diamond or carbon phases, have been described (e.g. Stöckhert et al. 2001, 2009; van Roermund et al. 2002; Dobrzhinetskaya et al. 2003; Carswell and van Roermund 2005; Ferrando et al. 2005, 2009; Hwang et al. 2001, 2003, 2005; Korsakov and Hermann 2006; Vrijmoed et al. 2006; Malaspina et al. 2006a; Frezzotti et al. 2007; Lang and Gilotti 2007; Zhang et al. 2008). The presence of a fluid, as well as its exact composition, is of primary importance when considering P-T estimates and quantitative phase diagrams such as P-T pseudosections (phase diagrams that are constructed for the specific chemical composition of a rock) (e.g. Chap. 3). The composition and type of fluid phase is important when assessing it's capability to transport and mobilize major and trace elements during HP and UHP metamorphism in subduction zones. However, significant differences exist not only regarding fluid composition but also regarding the type of fluid that caused element mobilization and transport under eclogite-facies conditions.

The following section, detailing two representative natural case studies, provides an overview of typical fluid inclusions characteristic of eclogite-facies rocks, and hopefully sheds some light on the composition and type of fluids responsible for metasomatism in subduction-related HP and UHP rocks (for more detailed case studies see Klemd 2004).

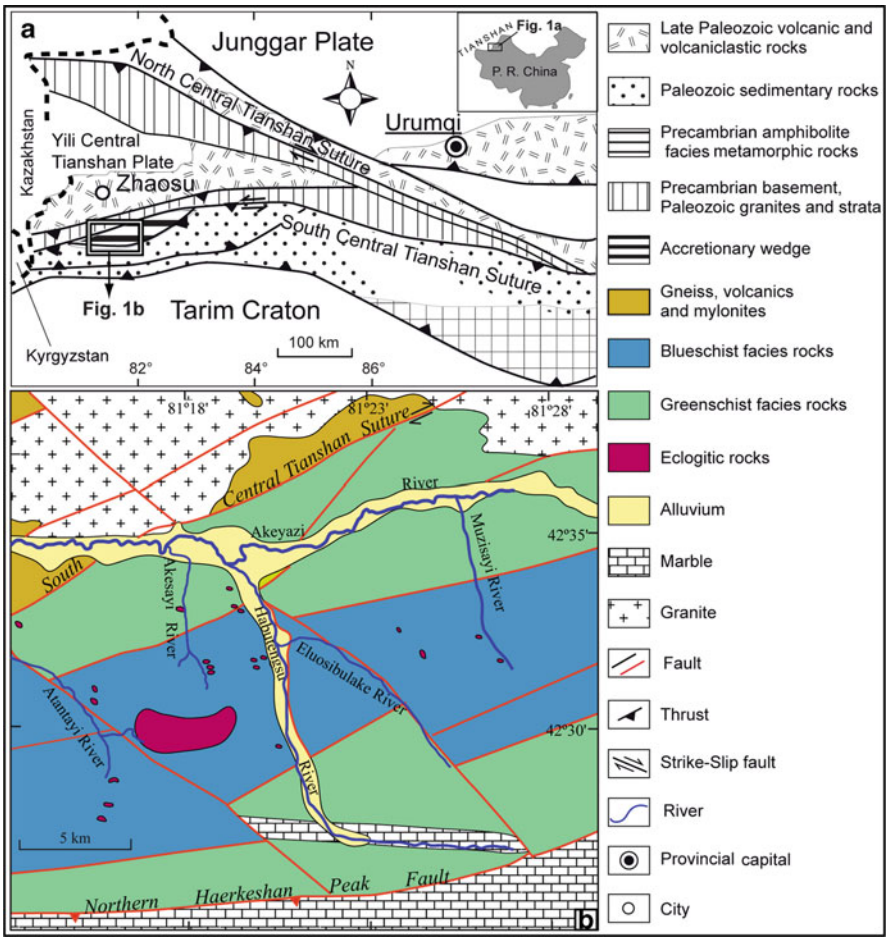

Fig. 10.9 Geological map of the western Tianshan HP-LT metamorphic belt in northwestern China (Modified after Gao et al. 1995, 1999). (**a**) Regional geological map, (**b**) local geological map, and (**c**) detailed geological map including the eclogite localities

Tianshan Subduction Complex, NW-China

The western Tianshan HP-LT metamorphic belt in northwestern China occurs along a suture between the Yili (Central Tianshan) and the Tarim blocks (Fig. 10.9a). It is mainly composed of blueschist-, eclogite-, and greenschist-facies meta-sedimentary rocks and some mafic meta-volcanic rocks with N-MORB, E-MORB, OIB and arc basalt affinities (Gao and Klemd 2003; John et al. 2008). Blueschists occur within greenschist-facies meta-sediments as small discrete bodies, lenses, bands, and thick layers. Eclogites, often preserving primary igneous textures such as pillows (Fig. 10.10), are interlayered with the blueschist layers as pods, boudins, thin layers, or massive blocks (Fig. 10.9b, c). Most eclogites

Fig. 10.10 Blueschist-facies pillow basalts showing eclogitization (*green*) in places (see *arrow*) in the Chinese western Tianshan (NW China)

underwent peak metamorphism on a regional scale, estimated to have ranged between 480°C and 580°C at 14–23 kbar (Gao et al. 1999; Klemd et al. 2002; Wei et al. 2003; Lin and Enami 2006; Lü et al. 2007). UHP peak metamorphic conditions for some eclogites were reported and are somewhat controversial (e.g. Zhang et al. 2003; Klemd 2003). UHP conditions of 25–27 kbar at 420–520°C, confirmed by the presence of coesite, were reported for a single eclogite boudin (Lü et al. 2009) entirely enclosed in HP and UHP meta-pelitic-felsic schists. These country rock schists come from the same locality and show variable peak metamorphic conditions as derived by pseudosection modeling of 28–32 kbar at 550–570°C, 22–24 kbar at 480–550°C, and 21–23 kbar at 530–550°C (Lü et al. 2008; Wei et al. 2009). Other eclogite boudins from this locality show pressures from 18 to 25 kbar at temperatures between 400°C and 600°C (Lü et al. 2007). It is tempting to relate the exhumation of the HP and UHP eclogite boudins to the enclosing buoyant meta-sediments as was suggested for eclogites from the Western Alps (Agard et al. 2009). This explanation is supported by the intimate interlayering, on a meter-scale, of HP and UHP eclogites (Lü et al. 2007, 2008, 2009), which may have been incorporated at different depths by the buoyant meta-sediments during their exhumation within the subduction channel as is indicated by sharp blueschist to eclogite transitions (Fig. 10.11). However, the peak metamorphic P-T estimates from UHP meta-sediments and eclogites all lie on a lower geothermal gradient, and thus on a colder P-T path at the slab-wedge interface, than the HP meta-sediments and eclogites (Fig. 10.12). This suggests that the slab-subduction angle steepened sharply ('kinking') at a depth greater than approximately 90 km (Klemd et al. 2011). Because of the low temperatures at HP and UHP conditions, as well as during exhumation, none of the samples show prograde or retrograde melting, despite post-peak almost isothermal decompression and the widespread presence of phengite

Fig. 10.11 Intimate interlayering of prograde blueschist and eclogite layers on a cm-scale from the Chinese western Tianshan (NW China)

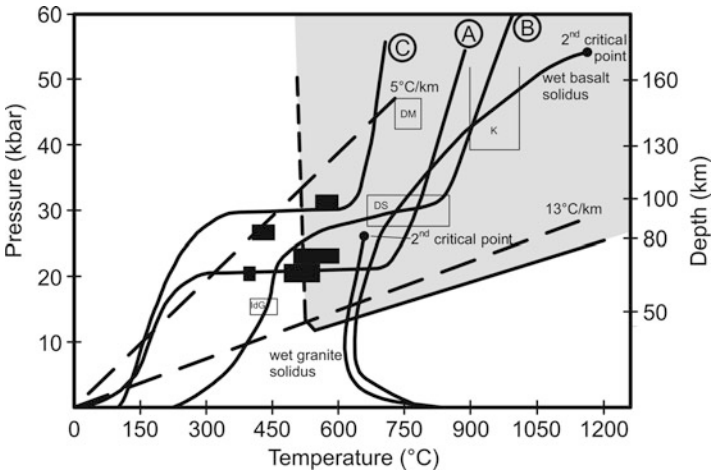

Fig. 10.12 Peak P-T conditions of some natural HP and UHP occurrences. Furthermore, the diagram shows calculated P-T paths for slab mantle wedge interfaces representative for cold and hot subduction zones. In addition the position of the wet solidi for basalts and meta-sediments, as well as geotherms of 5°C/km and 13°C/km, are shown (see text for details and captions of Fig. 10.4 for references). In order to compare natural HP and UHP occurrences from cold and warm subduction zones, P-T data for the Tianshan (China) (*black rectangles*) were taken from Gao et al. (1999), Klemd et al. (2002), Wei et al. (2003, 2009) and Lü et al. (2007, 2008, 2009), for the Kokchetav massif (Russian Federation) (K) from Shatsky et al. (1995, 1999), for Dabie-Sulu (China) (DS) from Zheng et al. (2003), for Doira Maira (Italy) (DM) from Hermann (2003), and for Ile de Groix (France) (*white rectangles*) from Bosse et al. (2002). It is evident that the Tianshan (China) P-T data plot on two different trajectories

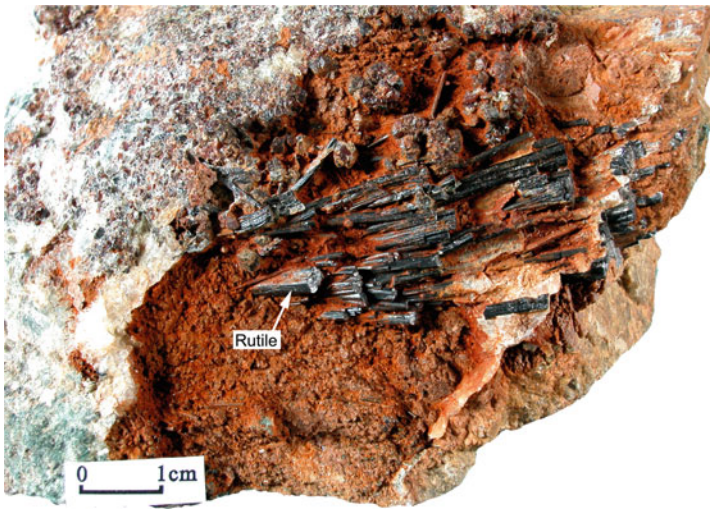

Fig. 10.13 Fibrous rutile in a segregation surrounded by a metasomatic depletion halo (eclogite) in blueschist host rock from the western Tianshan (NW China)

(Klemd et al. 2002, 2011; van der Straaten et al. 2008; Wei et al. 2009). The timing of peak metamorphism is constrained by the multi-point Lu–Hf isochron ages from four HP rocks with consistent garnet-growth ages of ca. 315 Ma (Klemd et al. 2011), which are in agreement, within error, with the U-Pb ages of metamorphic zircon rims of ca. 320 Ma in eclogites (Su et al. 2010) and Sm-Nd isochron data (omphacite-glaucophane-garnet-whole rock) yielding a Carboniferous age of 343 ± 44 Ma (Gao and Klemd 2003). White mica ^{40}Ar-^{39}Ar and Rb-Sr ages cluster at 311 Ma, interpreted to date exhumation of the HP rocks (Klemd et al. 2005). Fluid inclusion investigations were undertaken on omphacite in externally-derived transport and locally-derived dehydration HP veins (for details of the vein terminology see below) as well as on segregations and matrix omphacite from the HP rocks (Gao and Klemd 2001; Gao et al. 2007). Primary, tubular, two-phase fluid inclusions in omphacite from locally formed dehydration veins and the associated metasomatic eclogite dehydration halo, contain a predominantly low-salinity aqueous fluid with a maximum salinity of 7.4 wt.% NaCl equivalent in a NaCl-KCl-H_2O dominant system (Gao and Klemd 2001). Similar texturally primary inclusions were observed in fibrous omphacite and in omphacite inclusions in garnet from the segregation, which is surrounded by a depletion aureole, and contains cm-sized rutile crystals (Fig. 10.13; see also Gao et al. 2007). Maximum salinities are up to 4.5 wt.% NaCl equivalent in a NaCl-KCl-H_2O dominant system. Primary fluid inclusions in omphacite, from the over 10 m long externally-derived transport veins and the host rocks, showed almost identical salinities of up to 4.5 NaCl wt.% equivalent. The presence of primary low-salinity inclusions in omphacite from the HP veins and host eclogite constrains the entrapment of these fluid inclusions to peak metamorphic conditions. In fluid inclusions from some samples, solid

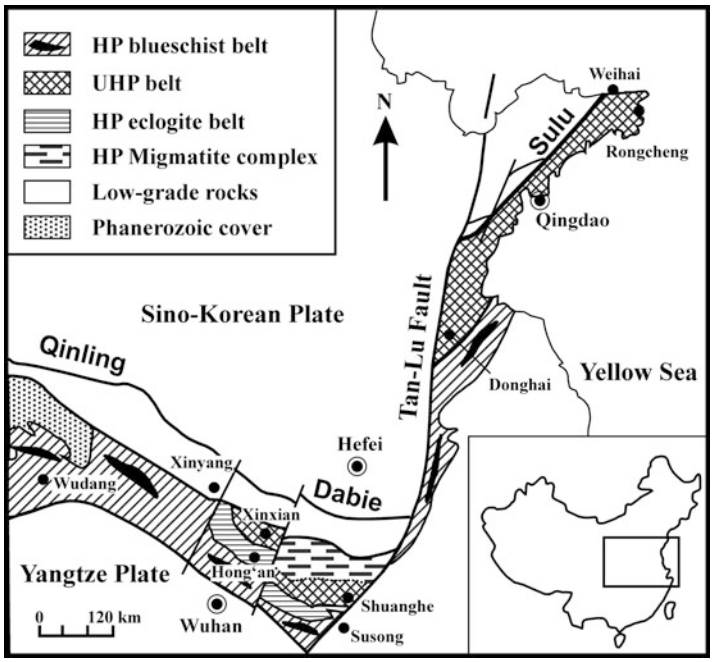

Fig. 10.14 Geological map of the Dabie-Sulu terranes (central-eastern China) (Modified after Zheng et al. 2003)

inclusions, which constitute less than 10% of the inclusion volume, were identified as carbonates by means of laser Raman spectroscopy. These carbonates may be the result of back reactions between the host omphacite and the low-salinity aqueous fluid with minor CO_2 (e.g. Heinrich and Gottschalk 1995) or were accidentally trapped. However, in fluid inclusions without carbonates, the gas bubble and liquid revealed no CO_2 by laser Raman spectroscopic investigations (Gao and Klemd 2001). Thus CO_2 activities seem to have been low in the aqueous fluid phase present during peak metamorphic conditions. This is consistent with thermodynamic modeling using internal consistent thermodynamic datasets (Gao et al. 2007).

In summary, peak metamorphic aqueous fluids, interpreted to have been derived during dehydration of the host blueschist, have a low-salinity aqueous composition. Fluid inclusion data and oxygen isotope data for dehydration veins and segregations favor a local fluid source and thus a small-scale derivation for the aqueous fluids from dehydration in situ.

Dabie Shan and Sulu Terranes in China

The Dabie-Sulu terranes constitute the eastern part of a Triassic suture between the Sino-Korean and Yangtse cratons. The HP-UHP metamorphic terrane extents from

Qinling to Dabieshan crosscutting the Tanlu fault to the Sulu region (Fig. 10.14; Hacker et al. 1998, 2000; Eide and Liou 2000; Ayers et al. 2002; Liu and Ye 2004; Liu et al. 2006a, b). The eastern part of this metamorphic terrane was displaced more than 500 km by the NNE-SSW trending sinistral strike-slip Tan-Lu fault (Xu et al. 1992). Recent geochronological studies on the HP and UHP rocks give ages of between 240 Ma and 220 Ma for the peak metamorphic event (e.g. Hacker et al. 2000; Ayers et al. 2002). The central UHP belt is terminated to the north by a HP-HT migmatitic zone and to the south by a HP-LT blueschist-facies zone. The UHP unit mainly consists of felsic gneiss, orthogneiss, marble, jadeite quartzite, minor eclogite, and garnet clinopyroxenite layers and lenses as well as associated ultramafic rocks (Fig. 10.14). Principally three metamorphic stages were distinguished: (1) peak UHP conditions at $>$ 28 kbars and temperatures ranging from about 700°C to 900°C; (2) a retrograde eclogite-facies recrystallization stage at 12–24 kbar and temperatures ranging from 600°C to 750°C; (3) a retrograde amphibolites-facies stage at 6–10 kbar and temperatures ranging from 450°C to 600°C, and in places (4) a granulite-facies stage is observed with pressures ranging from 8 to 14 kbar at temperatures between 750°C and 850°C (for a more detailed discussion of the petrology and references see Zheng et al. 2003). The extremely low-$\delta^{18}O$, whole-rock signature in some of the HP and UHP eclogites and garnet clinopyroxenites from the Dabie-Sulu terranes (China) is interpreted to be due to interaction of meteoric fluids with the pre-metamorphic protolith of the eclogites and garnet clinopyroxenites before continental subduction (for discussion and extensive reference list see Zheng et al. 2003).

The first fluid inclusion study on coesite-bearing UHP-eclogites from Central Dabie Shan (China), involving several eclogite-facies minerals such as kyanite, omphacite, and clinozoisite, revealed the presence of NaCl $\pm$ $CaCl_2$ $\pm$ $MgCl_2$-rich brines without significant CO_2-contents, in texturally primary and secondary aqueous as well as CH_4-N_2-rich inclusions (Cong and Touret 1993). Since then, several fluid inclusion studies, mostly combined with oxygen isotope investigation, on the HP and UHP rocks of the Dabie Shan and Sulu terranes have followed (e.g. You et al. 1996; Xiao et al. 2000, 2001, 2006; Franz et al. 2001; Fu et al. 2001, 2002, 2003; Schmid et al. 2003; Ferrando et al. 2005; Malaspina et al. 2006a; Frezzotti et al. 2007; Ni et al. 2008; Zhang et al. 2008). The aim of these fluid inclusion studies was to search for possible relics of a pre-metamorphic fluid in eclogite-facies minerals such as garnet, omphacite, kyanite, and epidote-group minerals. Several generations of primary fluid inclusions were interpreted either as early pre-peak metamorphic low-salinity inclusions ($<$ 14 wt.% NaCl equivalent) or syn-peak metamorphic aqueous inclusions with a wide variety of salinities ($>$ 14 wt.% NaCl equivalent to halite saturation) and N_2 $\pm$ CO_2 $\pm$ CH_4-rich inclusions (e.g. Fu et al. 2001, 2002, 2003; Xiao et al. 2001, 2002, 2006; Franz et al. 2001; Ni et al. 2008). In addition, primary polyphase solid inclusions with various silicates $\pm$ salts $\pm$ fluid, interpreted to have been present during peak metamorphism, have increasingly been observed (Fig. 10.15; Ferrando et al. 2005; Malaspina et al. 2006a; Frezzotti et al. 2007; Zhang et al. 2008). No difference in composition or density was reported for individual samples among the aqueous and gaseous inclusion fluids in the peak-metamorphic minerals that were

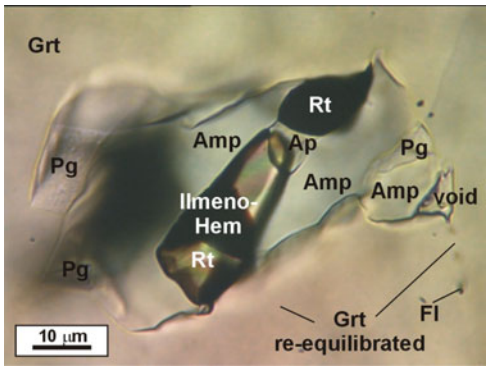

Fig. 10.15 Photomicrograph of polyphase inclusions within kyanite-phengite-bearing eclogite from Hushan (Sulu terrane China; courtesy of S. Ferrando). The inclusions in garnet consist of amphibole, paragonite, rutile with ilmenite-hematite lamella and apatite. Abbreviations follow Kretz (1983)

investigated. However, it should be noted that all primary aqueous and gaseous inclusion fluids underwent a density modification because *none* of the calculated fluid isochors correlate with peak metamorphic conditions.

In order to assign primary inclusion fluids to certain rock types, Fu et al. (2002, 2003) reported that high-$\delta^{18}O$ HP and UHP eclogites and clinopyroxenites exhibit primary fluid inclusions with high-salinity brines. Low, initial, melting temperatures $< -35.5°C$ indicate the presence of divalent ions such as Ca^{2+}, Mg^{2+}, and Fe^{2+} besides Na and K. Moreover N_2-rich inclusions are associated with the high-salinity brines. In contrast, low $\delta^{18}O$ HP and UHP eclogites have low-salinity inclusions with up to two accidentally trapped solid inclusions in quartz inclusions in epidote-group minerals and in the cores of clinozoisite porphyroblasts. These low-salinity inclusions have high initial-melting temperatures $> -20°C$ thereby indicating a NaCl- and KCl-dominant system. Consequently the authors assumed a correlation between $\delta^{18}O$ values and fluid salinity. They concluded that peak metamorphic fluids in high $\delta^{18}O$ HP and UHP eclogites are $CaCl_2$-$MgCl_2$-dominated high-salinity brines while NaCl-dominated low-salinity brines occur in low $\delta^{18}O$ HP and UHP rocks. Because of the extremely low $\delta^{18}O$ values for some of these rocks, Fu et al. (2003) suggested that the low-salinity fluids in clinozoisite may be remnants of meteoric water that had interacted with the protoliths of the HP rocks prior to plate subduction and was subsequently modified during peak metamorphic conditions. However, Zheng (2009) proposed that the aqueous and gaseous inclusion fluids were residues of UHP metamorphic fluids possibly derived from pore fluids of the sedimentary precursor rocks. In contrast, Frezotti et al. (2007) (see also Wu et al. 2009) interpreted the high $CaCl_2$-dominant brines they observed in UHP topaz-kyanite quartzites as being externally derived (probably from the mafic and ultramafic wall rocks) during the earliest stages of decompression. NaCl-dominated brines were considered to have dominated the final stages of exhumation under eclogite-facies conditions while low-salinity aqueous fluids and CO_2-rich fluids were externally derived under sub-eclogite-facies retrograde conditions.

Primary polyphase solid inclusions in UHP minerals contain several hydrous alkali-alumino-silicate mineral phases such as amphibole, paragonite, muscovite and chlorite as well as minor phases such as phosphates, sulphates, sulfides, oxides,

chlorides, and the (former) presence of H_2O (Fig. 10.15; Ferrando et al. 2005; Malaspina et al. 2006a; Frezzotti et al. 2007; Zhang et al. 2008). Based on fluid inclusion textures and their daughter minerals Ferrando et al. (2005) calculated the fluid composition for polyphase solid–fluid inclusions in kyanite and garnet for UHP quartzite and eclogite. For quartzites these fluids consisted of 24 wt.% SiO_2, 30 wt.% Al_2O_3, 9 wt.% CaO, 5 wt.% K_2O, 3 wt.% Na_2O, 11 wt.% SO_3, and 18 wt.% H_2O with traces of TiO_2, Fe_2O_3, FeO, MgO, BaO, P_2O_5, Cl-, and F and $(CO_3)^{2-}$and for eclogites 26 wt.% SiO_2, 21 wt.% TiO_2, 20 wt.% Al_2O_3, 2 wt.% MgO, 4 wt.% FeO, 6 wt.% Fe_2O_3, 7 wt.% CaO, 3 wt.% P_2O_5, 7 wt.% H_2O, and 1 wt.% Cl with traces of ZnO, MnO, K_2O, SO_3, and F. These solutes reflect the chemical composition of their respective host rock. Thus, fluids in eclogites contain considerabley higher amounts of Mg^{2+}, $Fe^{2+/3+}$, Ti^{4+}, P^{5+}, and Na^+ than those in the quartzites. However the estimated fluid composition is only semi-quantitative due to the problems of unambiguously distinguishing true daughter minerals from those formed by back reactions with the host mineral or solid inclusions trapped accidently (e.g. Heinrich and Gottschalk 1995; Svensen et al. 1999; Franz et al. 2001). A further uncertainty is the precise amount of water present during trapping (e.g. Ferrando et al. 2005).

Malaspina et al. (2006b, 2009) investigated fluid inclusions in garnet-orthopyroxenites, hosted by UHP gneisses from the UHP Maowu Ultramafic Complex in the Dabie Shan (China). Former garnet-harzburgite was inferred to have been metasomatized to a garnet-orthopyroxenite at peak UHP conditions (~40 kbar, 750 $\pm$ 50°C) due to the infiltration of a silica- and incompatible trace element-rich fluid phase (hydrous melt) originally from the associated crustal rocks. Primary polyphase solid inclusions within peak metamorphic garnet of the garnet-orthopyroxenite have constant volume ratios of infilling mineral phases. Homogenization of these inclusions in piston cylinder experiments, at conditions near those of peak metamorphism, demonstrated that the polyphase inclusions stem from homogeneous solute-rich aqueous fluids. These are characterized by high LREE- and LILE-contents and positive anomalies of Cs, Ba, Pb, and high U/Th (Malaspina et al. 2006b, 2009). The polyphase inclusions were interpreted to be remnants of a LILE- and LREE-enriched residual fluid liberated during metasomatism of the former garnet-harzburgite by the crustal-derived hydrous melt. The trace element pattern of these inclusions is very similar to that of polyphase inclusions in an UHP wedge-type peridotite from Sulu (China) (Malaspina et al. 2009).

In summary, the presence of a discrete and free fluid phase in subducting host rocks, during HP and UHP metamorphism, was substantiated by the finding of HP syn-peak metamorphic, low- to high-salinity, aqueous fluid inclusions and/or gaseous, CO_2-N_2-rich inclusions and UHP polyphase solid inclusions in eclogite-facies minerals in veins or in the matrix of these rocks. However, peak metamorphic transitional fluids or hydrous melts (preserved as polyphase inclusions) do not dominate the fluid budget during UHP conditions in all continentally-drived UHP suites. Primary fluid inclusions in omphacite from coesite-bearing UHP eclogites located in the Tso Morari Complex (NW-Himalaya, China) contain aqueous, high-salinity brines and gaseous, N_2-CH_4-rich inclusions. These are considered to represent prograde and peak metamorphic fluids (Mukherjee and Sachan 2009).

10.6.3 Bulk-Compositional Metasomatic Changes in Subduction-Related HP-UHP Rocks

The majority of bulk-compositional geochemical studies on HP and UHP rocks simply focus on changes in whole-rock chemical compositions, sometimes in combination with single mineral analyses, thereby constraining the relative solubilities of elements in fluids derived from dehydration reactions. Exhumed meta-mafic lithologies usually occur either in a mélange-type matrix of serpentinites (or more silicified ultramafic rocks) and/or pelitic-felsic meta-sediments with variable scales (e.g. Sorensen 1988; 1997; Gao et al. 1995, 1999; Bebout and Barton 2002; Gao and Klemd 2003; Agard et al. 2005; Agard 2006; King et al. 2006, 2007; Spandler and Hermann 2006; van der Straaten et al. 2008; El Korh et al. 2009), or as larger, more coherent, (often) undeformed blocks without an intimately associated mélange-type matrix (e.g. Klemd 1989; Klemd et al. 1991; Widmer and Thompson 2001; Brunsmann et al. 2001; Rubatto and Hermann 2003; Chalot-Prat et al. 2003; John et al. 2004; King et al. 2004; Molina et al. 2004).

In general, meta-mafic rocks in mélanges from former slab-mantle interfaces (subduction channels) display extensive fluid-rock interaction, which is, for instance, displayed by metasomatic 'rinds' along the rim of such blocks (Sorensen 1988; 1997; Bebout and Barton 2002; Saha et al. 2005). Sorensen (1988) deduced that the bulk of mass transfer was accomplished by aqueous fluids rather than by melts. On investigating trace element mobility during devolatilization in several meta-sedimentary units of the Catalina schist (California) Bebout et al. (1999, 2007a, b) and Bebout and Barton (2002) came to the conclusion that some trace elements (Cs, B, As, Sb and N) were enriched in fluids associated with meta-sediments which had experienced relatively warm subduction (see above), whilst trace element mobility was restricted in fluids related to meta-sediments which had undergone a cold subduction. In addition, in a geochemical study of meta-mafic, meta-peridotite, and meta-sedimentary rocks from the Western Alps and Ile de Groix (France), which had equilibrated under different metamorphic grades, Chalot-Prat et al. (2003) and El Korh et al. (2009), respectively, postulated the absence of large bulk rock compositional changes during prograde metamorphism. These authors suggested that, due to the (almost) absence of metasomatism during HP metamorphism, the fluid phase released during prograde dehydration must have been solute-poor. Based on the study of bulk rock major and trace element behavior at different metamorphic grades in HP meta-mafic and meta-pelitic rocks from New Caledonia, Spandler et al. (2003) furthermore suggested that, up to eclogite-facies conditions, trace elements are not significantly released during prograde metamorphism. They proposed a decoupling of fluid and trace element release during HP conditions since trace elements are considered to be retained by newly formed major and accessory minerals during prograde mineral breakdown reactions at depths of up to 150 km. The solute-poor fluid, released during dehydration of the meta-mafic rocks, was interpreted to be the cause of partial melting of the overlying sedimentary rocks, which could have produced a solute-rich fluid or hydrous

Fig. 10.16 Major mélange zone (subduction channel) containing ultramafic and mafic blocks from Syros (Greece) (cf. Bröcker and Keasling 2006). Large eclogite-facies meta-mafic block in sheared serpentinite (Courtesy of M. Bröcker)

granitic melt (Spandler et al. 2003). In addition, by comparing whole-rock concentrations from various HP and UHP meta-basaltic rocks from less coherent mélange-type environments (Sorensen et al. 1997; Saha et al. 2005; Spandler et al. 2004; King et al. 2006) and more coherent localities (King et al. 2004) with their assumed protolith rocks (hydrothermally altered seafloor basalts), Bebout (2007a, Fig. 10.4) concluded that only minor compositional changes had occurred as a result of HP and UHP metamorphism. Nonetheless, with regard to all these studies it should be kept in mind that, in many cases, the protolith rocks have a very heterogeneous trace element composition and thus any trace element change, which occurred during HP to UHP metamorphism, will be obscured by these features (cf. Bebout 2007b).

Some of the most coherent mafic blueschist-eclogite-facies sequences (Fig. 10.9) occur in tectonic mélanges on a km-scale (e.g. Gao et al. 1995, 1999; Breeding et al. 2004). Breeding et al. (2004) suggested that fluids, released by dehydration of subducting slabs, may react with metamorphosed ultramafic-mafic rocks in mélange zones near slab-mantle interfaces (Fig. 10.16; also see Bebout and Barton 1989). In their study of HP-rocks from Syros (Greece) they observed that such fluids preferentially (>90%) leach LILE, U and Pb during infiltration and reaction with the meta-sedimentary portion of the subducted oceanic crust. Also, John et al. (2004), working on eclogites and their gabbro protolith from central Zambia, observed a large fractionation of LREE from HREE and HFSE during prograde metamorphism. These authors suggested that the fluids released during metamorphism of the serpentinized lithospheric mantle were responsible for triggering the gabbro-eclogite transitions and mobilization of the LREE. They interpreted the eclogitization and LRRE fractionation as resulting from high

fluid-rock ratios during channelized fluid flow through the lower part of the oceanic crust. Fluid-assisted mobilization of HFSE in chlorite-bearing harzburgite, from the Cerro del Amirez Ultramafic Massif (Spain), was demonstrated, using field and geochemical evidence, as the product of HP dehydration of an antigorite-bearing serpentinite (Garrido et al. 2005). These authors provided further geochemical evidence that during dehydration, suggested to have occurred in a relatively warm subduction zone, liberated fluids were enriched in LILE, LREE, and MREE, relative to HFSE, and had left the serpentinite in an aqueous fluid during dehydration. This conclusion is corroborated by LA-ICPMS studies on aqueous fluid inclusions, produced by the breakdown of antigorite, in the Almirez olivine, which show a strong enrichment of LILE and LREE relative to Nb (Scambelluri et al. 2004).

Stable isotope work on the Doira-Maira whiteschists (Western Alps) has suggested that these rocks originated from metasomatizing fluids liberated from the subducting oceanic lithosphere (Sharp et al. 1993). Sharp et al. (1993) concluded, from the stability of pyrope and coesite during prograde dehydration, that the a(H_2O) must have been reduced to 0.4–0.75 at 700–750°C due to the presence of a melt-phase. In a more recent Cl isotope study, Sharp and Barnes (2004) suggested a high-salinity aqueous fluid, liberated by dehydration of serpentinized peridotite during subduction, as being responsible for the extreme Mg-enrichment of the whiteschists. Schertl and Schreyer (2008), conducting a mass balance calculation between whiteschists and granitic/orthogneiss protoliths, established strong enrichment in Mg and loss of Na, Ca, Fe, Cu, P, Rb, Ba, and Sr due to infiltration of Mg-rich solutions during UHP metamorphism, consistent with the proposal of Compagnoni and Hirajima (2001) based on study of zoned garnets. REE, on the other hand, are considered to have been rather immobile during this process (Grevel et al. 2009). Ferrando et al. (2009) compared whole-rock major and trace element data for whiteschists and granitoid protoliths. They suggested a gain of Mg and a loss of alkalis, Ca, Fe, and P from the whiteschists, proposing that these changes were caused by the influx of a Mg-enriched fluid leaching alkalies, Ca, and LILE during UHP conditions.

A somewhat different approach involves metasomatic changes associated with single minerals such as garnet or omphacite (e.g. King et al. 2004; Morishita et al. 2007). For example, such studies employ in situ high-resolution trace element geochemistry in order to evaluate prograde reaction histories as displayed by chemical zoning patterns of garnet. This is of considerable importance because garnet often preserves prograde and peak metamorphic major and, especially, trace element patterns due to their very slow diffusion rates even in HP rocks (e.g. John et al. 2008). King et al. (2004), studying trace element zoning and mineral inclusions in UHP meta-basaltic garnet from Lago di Cignana (Italy), established the liberation of certain trace element-enriched fluids during the prograde breakdown of clinozoisite and titanite. This method supplies no information regarding the scale of fluid mobilization.

In summary, it can be ascertained that, in general, the observed lack of significant bulk rock compositional changes in meta-basalts, meta-sediments, and meta-peridotites

indicates that the fluids released during prograde HP metamorphism of oceanic and continental crust are relatively solute-poor, whereas the fluids present during UHP metamorphism of continental crust appear to be relatively solute-rich. This is in accordance with experimentally derived fluid-mineral partition coefficients (e.g. Manning 2004; Hermann et al. 2006). Nonetheless, several studies showed that the solute-poor aqueous fluids are highly enriched in certain elements such as LILE and LREE when compared to HFSE or HREE (e.g. John et al. 2004; Garrido et al. 2005). In this context, it should be noted that only small amounts of the solute-poor aqueous fluid, released during prograde dehydration, will be accessible for a short time (Poli and Schmidt 2002) and, thus, that fluid-rock interaction is initially only possible over a short flow distance due to (very) low fluid-rock ratios. If these small amounts of fluid were able to mobilize trace elements, it would not be detectable in the trace element budget of the donator rock (cf. Liebscher 2004; Zack and John 2007). Thus, relatively unchanged bulk rock compositions provide only limited information regarding the composition of a fluid liberated during prograde dehydration, as was shown by simple Rayleigh distillation calculations (Zack and John 2007). Consequently, bulk rock compositional investigations allow a rather ambiguous insight into the actual composition of the fluid phase responsible for metasomatism during HP and UHP conditions in subduction zones.

10.6.4 Metasomatic Changes Evidenced by HP-UHP Veins

HP and UHP eclogite-facies veins (Fig. 10.17), cross-cutting metamorphosed oceanic lithospheric rocks, are believed to represent former pathways of migrating fluids in subduction zones (e.g. Holland 1979; Bebout and Barton 1989, 1993; Philippot and Selverstone 1991; Selverstone et al. 1992; Nadeau et al. 1993; Becker et al. 1999, 2000; Franz et al. 2001; Gao and Klemd 2001; Widmer and Thompson 2001; Rubatto and Hermann 2003; John et al. 2008; John and Schenk 2006; Vrijmoed et al. 2006, 2009; Spandler and Hermann 2006; Gao et al. 2007; Zhang et al. 2008; Scambelluri and Van Roermund 2008; Beinlich et al. 2010). Prograde or peak eclogite-facies veins may contain high-variance mineral assemblages including omphacite, garnet, kyanite, quartz, phengite, zoisite, and accessory minerals such as rutile, titanite, zircon, allanite, and apatite while retrograde veins may still contain HP minerals but also chlorite, actinolite, albite, quartz, and calcite (e.g. Bebout and Barton 1989, 1993; Miller et al. 2002; van der Straaten et al. 2008; Wu et al. 2009). Thus, prograde and retrograde veins provide important information regarding the composition of fluids and resulting metasomatic changes during fluid-rock interaction under HP to UHP conditions and during exhumation processes. Eclogite-facies veins, derived by prograde dehydration, are usually relatively small and range in size from mms to cms (e.g. Philippot and Selverstone 1991; Becker et al. 1999; Scambelluri and Van Roermund 2008), although much larger veins ranging to meter scales have also been reported (e.g. Castelli et al. 1998; Gao and Klemd 2001; Widmer and Thompson 2001; Vrijmoed et al. 2006, 2009; Gao et al.

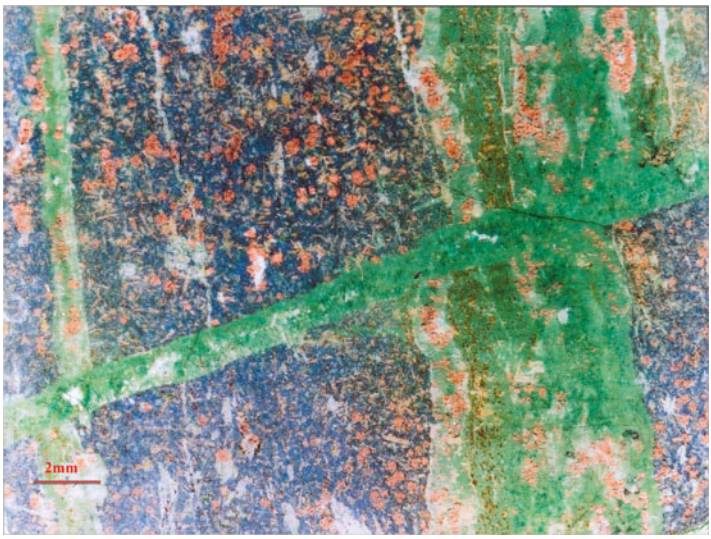

Fig. 10.17 Network of externally-derived HP veins consisting of omphacite, garnet, quartz, apatite, and carbonate along the median line. The veins typically show crack seal behavior. The younger ones crosscut the older ones, which may show some displacement (western Tianshan, China). Note the sharp interfaces of the veins with the surrounding blueschist and lack evidence for host-rock dehydration (Modified after John et al. 2008). The vein network characteristically displays the channelized fluid flow

2007; John et al. 2008; Beinlich et al. 2010). Generally two different types of HP and UHP veins can be distinguished (John et al. 2008) and will be discussed here: (1) Veins formed by a local source ('dehydration' veins) mainly displaying restricted fluid flow or short-distance (mm- to cm-scale) diffusive transport of solutes and closed system behavior and (2) Veins derived from an external source ('transport' veins) usually indicating long-distance (m- to km-scale) advective transport of solutes and showing open system behavior.

10.6.4.1 Metasomatic Changes Associated with 'Dehydration' Veins

An example of the first vein type, representing a local fluid source liberated during prograde dehydration at the blueschist-eclogite transition, was first documented from the Tianshan Mountains in northwestern China by Gao and Klemd (2001). These authors described an interconnected network of veins filled with HP eclogite-facies minerals such as fibrous omphacite and garnet. In places these veins are surrounded by metasomatic depletion halos where the blueschist host rock was gradually transformed into eclogite. Thus, the transition from blueschist- to eclogites-facies parageneses occurs as dehydration aureoles around these HP veins. The eclogitization of the former blueschist host rock is interpreted to have occurred as the result of dissolution of the blueschist-facies mineral assemblage and direct precipitation of the eclogite-facies product phases. During this process all

dissolved elements are probably in local equilibrium with the fluid. The composition of the precipitating product phases are believed to reflect the prevailing pressure and temperature during fluid infiltration and therefore provide evidence that vein formation took place during eclogite-facies conditions (e.g. Putnis 2002; Putnis 2009; Putnis and Austrheim 2010; Putnis and John 2010). Because the O isotope compositions of the vein and wall rock are similar, the dehydration halo (eclogite) is interpreted to result from the in situ dehydration of the blueschist host rock. The veins are thus classified as dehydration veins (Gao and Klemd 2001). The major element vein composition indicates that Si-, Na-, and Ca-rich fluids were liberated during dehydration of the blueschist. Brunsmann et al. (2000, 2001) investigated the trace element budget of HP mm- to cm-wide zoisite and clinozoisite segregations and vein-like bodies and the immediate meta-basaltic host rock from the Tauern Window (Austria). They found that mobilization of LREE is displayed by a decreasing element content towards the segregations. Based on mass balance calculations for certain LREE, the composition of the fluid, from which the minerals in the segregation had precipitated, was calculated. During formation of the segregation, the rare earth elements La to Tb were geochemically decoupled from Dy to Lu. The fluid composition shows LREE enrichment with $(La/Sm)_N = 3.7$ (Brunsmann et al. 2001). These authors also calculated individual REE contents in the fluid phase, which range from Eu $= 2.4 \pm 1.1$ ppm up to Ce $= 90 \pm 20$ ppm with a total REE concentration of 190 ± 50 ppm. Brunsmann et al. (2001) concluded that their data prove leaching and mobilization of certain LREE only over a few cms whereas their mass balance calculations suggest mobilization of certain LREE at larger scales. Widmer and Thompson (2001) investigated kyanite-quartz-bearing veins formed during the blueschist-eclogite facies transition within meta-basaltic rocks from the Western Alps. These veins are up to several meters in length and up to 20 cm wide and contain omphacite or chloritoid in addition to quartz and kyanite. These authors observed distinct cm-sized Al_2O_3 and SiO_2 metasomatic depletion haloes in the wall rocks adjacent to the veins that they interpreted to have resulted from contact with the veins. Widmer and Thompson (2001) interpreted the veins to be the result of local segregation and not to represent extensive large-scale dehydration channels. Similar short-distance element transport was observed during the blueschist-eclogite-facies transformation in meta-basalts from the Tianshan orogen (NW-China) (Gao et al. 2007). A segregation with cm-sized, needle-like, rutile crystals is surrounded by a metasomatic depletion aureole, a relationship indicative of short-distance diffusion element transport (Fig. 10.13). Gao et al. (2007) interpreted the large size of the needle-like rutile crystals in the segregation to be the result of unhindered growth from a Ti-, Nb-, and Ta-supersaturated solution in an open fluid-filled cavity under hydrostatic conditions. In the eclogite host of the segregation, the Ti contents of garnet and omphacite, the modal abundances of garnet, zoisite, rutile, and titanite, and the bulk rock Ti, Nb, Ta, and HREE contents decrease towards the segregation (Figs. 10.18a, b), suggesting that these elements were leached and mobilized from the host rock during the blueschist-eclogite transformation. The change in modal proportions of HP minerals requires element exchange by transport in a fluid phase, which is the dominant mechanism over solid-

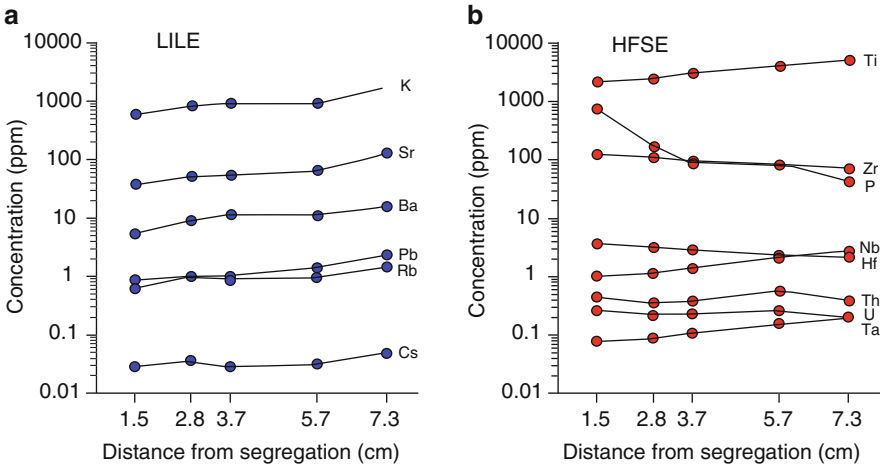

Fig. 10.18 Chemical composition of the segregation depletion halo along a profile with variable distance to the segregation. (**a**) LILE and (**b**) HFSE (Modified after Gao et al. 2007)

state diffusion, in order to redistribute chemical constituents under HP conditions (e.g. Putnis 2002; Putnis 2009; Putnis and Austrheim 2010; Putnis and John 2010). A mass balance calculation was conducted in order to establish whether the change in element concentrations is a result of dilution or rather scavenging. When undertaking mass balance calculations, an immobile geochemical frame must be established (Gresens 1967; Ague 2003b). This is often difficult due to heterogeneous bulk chemistry and mineral distribution in the host rocks. Gao et al. (2007) used the average host rock as the reference rock and the samples along the profile were analyzed and used for the mass balance calculation. Zirconium and Hf were chosen as immobile elements because zircon grains are absent in the segregation yet present in the host rock where they showed no evidence of corrosion. Apart from Zr and Hf, all elements show a relative mass loss (Fig. 10.19). For example, Ti, Nb, and Ta were mobilized during dehydration of the blueschist host and thus fractionated from Zr and Hf. The calculated loss of Ti, Nb, and LILE gradually increases towards the segregation from ~20% to ~75%, which indicates that these elements were more efficiently leached closer to the segregation (Fig. 10.19). Major elements, such as Si, Al, Fe, and Ca, show a mass loss between ~34% and ~60%. Thus, during dehydration, most elements were scavenged and then mobilized over several cms from the metasomatized host rock into the segregation (Fig. 10.19). Furthermore, Spandler and Hermann (2006) investigated the petrology and geochemistry of HP veins formed during prograde HP metamorphism in the Pouebo Eclogite Mélange of northern Caledonia (Spain). Using isotopic and geochemical data, the authors interpreted the protolith of the HP rocks to be seafloor-altered MORB that had undergone HP metamorphism in a subduction zone. The HP veins are surrounded by a metasomatic depletion aureole, which was taken as evidence that they had formed as a result of local prolonged fluid circulation. The fluid was interpreted to

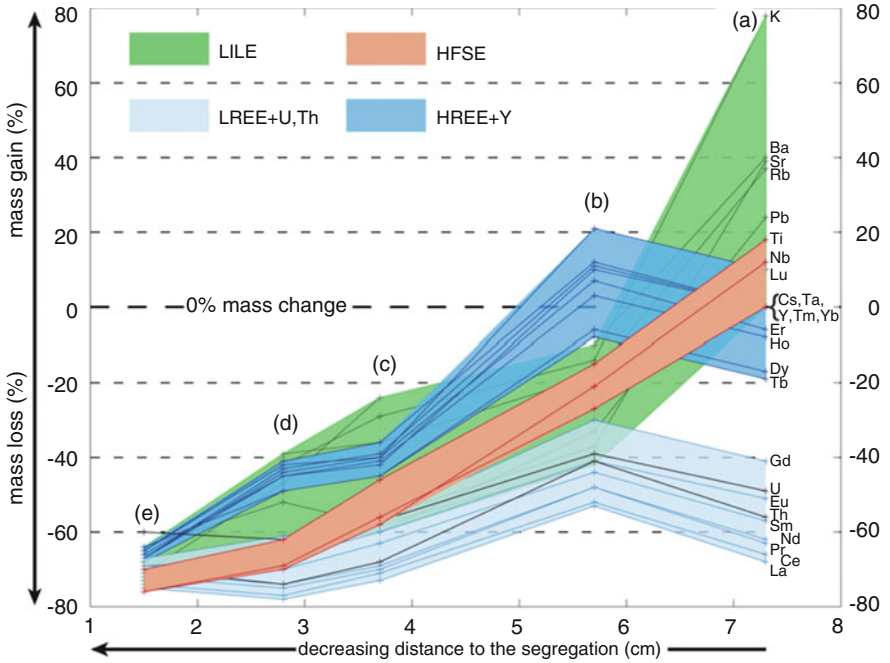

Fig. 10.19 Concentration ratio diagram showing mass loss at the metasomatic segregation halo (sample TS33-5R). Estimate of the concentration ratio for immobile elements (r inv) indicated by the *thick horizontal dashed line* (0% mass change). Apart from Zr and Hf (immobile geochemical frame), all other elements are leached from the blueschist host and then mobilized into the segregation thereby exhibiting the fluid-mediated diffusive mass transport.. For reasons of simplicity only trace elements are shown. They form several groups of similarly behaving elements, such as LILE, HFSE, LREE + U, Th, and HREE + Y (Modified after Gao et al. 2007)

have been liberated during prograde dehydration of blueschist-facies rocks. Their mass balance calculation requires a small additional external input of trace elements from meta-sediments during peak eclogite-facies metamorphism. Spandler and Hermann (2006) argue that a high fluid flux, which was able to mobilize significant element concentrations including HREE and HFSE (cf. Spandler et al. 2003) in deeply subducted crust, is due to episodic microfracturing and mineral precipitation, mainly in a closed system. They further suggested these trapped fluids can be transported/subducted down to the arc source regions.

10.6.4.2 Metasomatic Changes Associated with 'Transport' Veins

In the Tianshan orogen (China), Gao et al. (2007) described >10 m long HP veins containing omphacite, phengite, quartz, ankerite, rutile, and apatite cross-cutting, not only blueschist, but also eclogite, meta-quartzite, and meta-pelite and are

therefore not restricted to the site of dehydration. These veins were thus interpreted as representing externally derived transport veins. The sharp interfaces between the rutile-bearing veins and the host eclogite, and the lack of a (metasomatic) dehydration halo, indicate an external source for the fluid from which the minerals of this 'transport vein' were precipitated. Textural and geochemical data for the vein minerals indicate that a Ti-, Nb-, and Ta–rich fluid phase was transported over distances of at least the meter-scale during channel-controlled, relatively high fluid fluxes. Based on experimental data (e.g. Bright and Readey 1987; Brenan 1993; van Baalen 1993; Antignano and Manning 2008), the authors suggested that complex-forming ligands enhanced the Ti, Nb and Ta solubilities and thus may have been responsible for keeping these elements in solution. Furthermore, changes in the fluid composition may have precipitated rutile and fractionated Ti, Nb, and Ta from LILE and LREE. Gao et al. (2007) further speculated that the vein-forming fluid may have been derived from a source, such as the metasomatic depletion aureoles surrounding the dehydration veins. John et al. (2008) reported on an interconnected network of eclogite-facies vein systems (from the same locality) that cross-cut blueschist textures, exhibit sharp interfaces with the surrounding host rock, and lack evidence for host rock dehydration, thereby indicating infiltration of a fluid phase from an external source rock. They were also construed to be transport veins (Fig. 10.17). The infiltrating fluids were also interpreted to have triggered the eclogitization of the blueschist host. The solute poor, vein-forming fluid scavenged between 40% and 80% of all trace elements, involving a loss of LILE and LREE, almost double the loss of the HREE and HFSE as indicated by mass balance calculations (John et al. 2008). The authors came to the conclusion that fluid-rock ratios, fluid compositions, and the non steady-state character of the fluid flow, rather than the mineral assemblages and equilibrium partition coefficients, mainly control trace element mobilities in an open system such as dehydrating oceanic crust during subduction. Also in the Tianshan (China), Beinlich et al. (2010) investigated an eclogite-facies vein that cross cuts massive blueschists and exhibits indications for both fluid infiltration from an external source as well as in situ dehydration of the immediate wall rock. The cross cutting vein can be traced throughout the entire outcrop (ca. 3×3m) and neither start nor termination is exposed within the investigated area, indicating that fluid flow occurred on a greater scale (Fig. 10.20). Samples from the vein, the surrounding eclogitic metasomatic halo, and the unaltered blueschist host rock were analyzed in order to constrain the processes leading to eclogite formation around the vein and to gain knowledge on the behavior of trace elements (Fig. 10.20). Petrologic and geochemical evidence suggests that the formation of both the vein and the metasomatic eclogite aureole surrounding the vein was caused by fluid infiltration under HP metamorphic conditions. The combination of whole rock and mineral trace element data, with mass balance calculations, displays substantial differences between the unaltered host rock and the part which was metasomatized by fluid-rock interaction. These differences include depletion of LILE and Li of up to 60% relative to their concentrations in the unaltered host rock, an extreme enrichment of CaO ($\sim$ 115%) in the altered parts Sr, and Pb ($>$ 300%) in the altered parts of the vein-

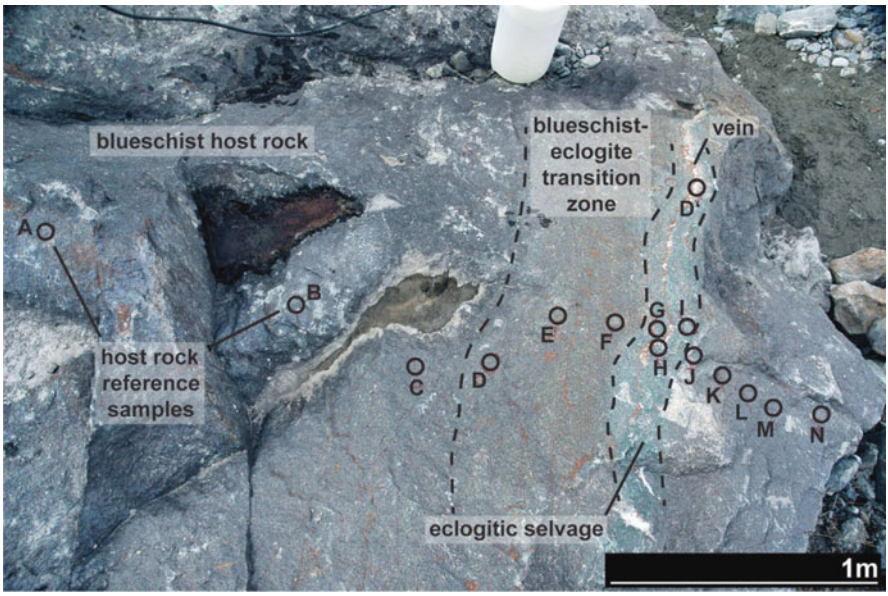

Fig. 10.20 Sample location showing the blueschist host rock, the blueschist transition zone, the metasomatic halo (eclogitic selvage), and vein. *Circles* show drilled and studied sample locations (Modified after Beinlich et al. 2010)

wall rock system, and redistribution of HREE, from partly replaced rutile and recrystallized titanite, in the blueschist-eclogite transition zone, into newly grown garnet rims in the eclogite aureole surrounding the vein. The authors further observed the transformation of high Nb/Ta rutile into low Nb/Ta titanite and the decoupling of Zr and Hf from Nb and Ta. The latter are depleted by ~30% relative to the unaltered blueschist host rock whereas the former are depleted by only ~10%. The transformation of Ca-poor blueschist (6–7 wt.% CaO) into Ca-rich eclogite (up to 14 wt.% CaO) was caused by the infiltration of a Ca-rich fluid requiring large fluid volumes (200 m^3 per m^3 of rock). The mobilization of trace elements was attributed to partitioning of these elements into the passing fluid phase as a result of dissolution-reprecipitation processes during the course of eclogitization. The reactivity of the precursor mineral assemblage, and the chemical gradients between the reacting and passing fluid of the conduit, are mainly responsible for the diffusive trace element mobilization in these samples. In the context of metasomatized mantle wedge melting, as a possible source of volcanic arc magmas, the suite of trace elements mobilized, during fluid-induced eclogitization of the reactive wall rock, resembles that in island arc magmas, showing strong enrichment of LIL elements, strong depletions in HFS elements, and intermediate concentrations of REE. Molina et al. (2004) investigated eclogite-facies vein systems with metasomatic amphibole-eclogite sequences in the Marun-Keu complex (Polar Urals, Russian Federation). These authors established significant bulk rock compositional changes in the wall rock, a net mass-exchange between the wall rock and vein

fluids, Rb/Sr disequilibria throughout the vein-wall rock system, and a significant temperature increase during the growth of the mineral sequence. They interpreted these features as a consequence of fracture-related metamorphism resulting from large-scale migration of hot disequilibrium fluids during HP metamorphism. Franz et al. (2001) investigated HP quartz veins within HP meta-basites from the Dabie Shan (eastern China). Mineral assemblages from these veins incorporate quartz, kyanite, paragonite, talc, zoisite, ankerite, paragonite, garnet, omphacite, and rutile (up to 5 cm in length). The initial Pb isotopic composition of the rutile encompasses the whole range of isotopic compositional characteristics of old basement rocks from the Dabie Shan (China) and may thus originate from contrasting sources. This indicates open system behavior for the fluid from which the HP veins were precipitated.

Vrijmoed et al. (2006, 2009), working in the northernmost UHP metamorphic domain in the Western Gneiss Region of Norway, discovered a fine-grained, Fe–Ti type garnet-peridotite body at Svartberget cross-cut by a network of systematically-orientated, coarse-grained, garnet-phlogopite, websterite and garnetite veins on the meter-scale. The P-T conditions estimated for the formation of the websterite veins are about 55 kbar at 800°C. Textural and mineralogical evidence from polyphase, (microdiamond-bearing), solid inclusions (see above), Sm–Nd whole rock, and Sr isotope data suggest that supercritical (above the second critical point) C–O–H rich fluids were externally derived from crustal host-rock sources infiltrating the Svartberget body during the Caledonian subduction at UHP conditions. This result is in contrast with the reported conservation of low oxygen isotope signatures in continental UHP rocks from the Dabie-Sulu terrane (China). It indicates a virtually closed system with the absence of external fluid infiltration and the widespread absence of an aqueous liquid phase during UHP conditions (e.g. Rumble et al. 2003; Zheng et al. 2003).

In summary, these studies suggest that (aqueous) fluids in HP and UHP rocks, moving along zones of high permeability, are able to scavenge elements, despite low solubilities during dehydration, and, thus, to metasomatize host rocks. They subsequently contradict studies claiming small-scale fluid recycling or decoupling of trace elements and fluid (e.g. Scambelluri and Philippot 2001; Spandler et al. 2003; Spandler and Hermann 2006).

10.7 Discussion

The composition of the eclogite-facies fluid, and its metasomatic impact on the host rocks, is highly variable in different eclogite-facies terranes. Several fluid inclusion studies show that a solute-poor aqueous fluid phase, with possible additions of N_2 and CO_2 and/or a separate N_2-CO_2 fluid phase, seems to be the dominant fluid phase prevailing under HP conditions (e.g. Andersen et al. 1989; Klemd 1989; Klemd et al. 1992, 1995; Giaramita and Sorensen 1994; Vallis and Scambelluri 1996; El-Shazly and Sisson 1999; Franz et al. 2001; Gao and Klemd 2001; Scambelluri

et al. 2004; Gao et al. 2007). However, on investigating HP eclogite-facies rocks and veins ($P \leq 20$ kbar, $T < 625°C$) from the European Alps, Phillipot and Selverstone (1991) and Selverstone et al. (1992) reported the occurrence of primary, very high-salinity brine inclusions containing abundant chlorides, such as halite and sylvite, as well as several silicate and other solid daughter minerals, thus displaying some of the characteristics of polyphase solid inclusions. Nonetheless, when considering the petrological and fluid inclusion evidence, it seems reasonable to generally assume that solute-poor aqueous fluids ($< \sim 30$ wt.% solutes) generally dominate the fluid budget during HP metamorphism of oceanic and continental crust in subduction zones (70–40 km depth). This is supported by experimental data favoring an aqueous fluid under HP conditions in cold subduction zones (e.g. Hermann et al. 2006; Manning 2004).

These fluids are regarded, by some researchers, as being relatively inefficient in mobilizing and transporting elements, as for instance is suggested by experimentally derived fluid-mineral partitioning data (for discussion and references see Manning 2004 and Hermann et al. 2006). This is consistent with some geochemical studies of HP veins (e.g. Brunsmann et al. 2001; Widmer and Thompson 2001; Spandler et al. 2003; Hermann et al. 2006; Gao et al. 2007), which suggest a locally highly restricted pervasive fluid flow and, thus, only localized (small-scale) element transport. Similar conclusions of only short-distance fluid transport were also reached by some stable isotope studies in various HP terrains (e.g. Getty and Selverstone 1994; Nadeau et al. 1993; Barnicoat and Cartwright 1995; Henry et al. 1996; Cartwright and Barnicoat 1999; Busigny et al. 2003) and many fluid inclusion studies (e.g. Scambelluri and Philippot 2001; Touret and Frezzotti 2003; Klemd 2004). Even, within single continental collision orogens, such as the Dabie-Sulu (eastern China), fluid inclusion and stable isotope investigations revealed strong fluid activity gradients due to buffering by the respective host rock which had apparently persisted during UHP metamorphism (e.g. Ferrando et al. 2005; Hwang et al. 2006; Frezzotti et al. 2007; Zheng 2009). This supports other fluid inclusion studies on HP oceanic crustal rocks worldwide (e.g. Philippot and Selverstone 1991; Selverstone et al. 1992; Klemd et al. 1992, 1995; cf. discussion in Klemd 2004). Such fluid gradients suggest local fluid production and/or internal buffering and seem to support limited fluid flow on a relatively small-scale during eclogite-facies metamorphism. On the basis of these fluid inclusion studies and small-scale isotope heterogeneities, Scambelluri and Philippot (2001) proposed that the fluids mostly remain entrapped in the subducting rocks and are only released into the overlying mantle at depths greater than those revealed by most exposed eclogites (>120 km).

In contrast to these results, HP vein studies (e.g. Franz et al. 2001; Molina et al. 2004; Gao et al. 2007; John et al. 2008; Beinlich et al. 2010) as well as isotope studies (Bebout and Barton 1989; Bebout 1991, 1997; Nelson 1995) demonstrate that fluid flow under eclogite-facies conditions also involves large-scale (meter- to km-scale) mobilization and advective transport of elements by aqueous fluids in an open system. Significant trace element changes were reported for metasomatic depletion haloes surrounding eclogite-facies dehydration veins, which constitute

major conduits of high fluid flow during prograde HP-metamorphism (e.g. Molina et al. 2004; John et al. 2008; Beinlich et al. 2010), or for zones of high fluid-rock ratios and fluid flow (e.g. Breeding et al. 2004; John et al. 2004). Consequently, these solute-poor aqueous fluids are able to scavenge and transport major and trace elements on a meso- to macroscopic scale during prograde HP metamorphism. The potential of these fluids to mobilize and transport trace elements, such as HFSE, is suggested to be related to complex-forming ligands such as Na-Si-Al polymers and F, which may enhance solubilities in the fluid phase (e.g. Manning 2004; Rapp et al. 2010). The first direct observation of silicate polymers in high-density fluids was made by Mysen (1998) who described aqueous silica dimers and trimers associated with felsic melts. The presence and importance of silica polymerization was confirmed by phase equilibrium and in situ studies under HP conditions (e.g. Zhang and Frantz 2000; Zotov and Keppler 2000, 2002; Newton and Manning 2002). In addition, changes in the coordination of certain trace elements, such as Ti, are suggested to promote complexation with other elements already present in aqueous fluids (van Sijl et al. 2010). In summary, significant metasomatic trace element changes produced during prograde HP metamorphism in subduction zones will mainly occur at high fluid-rock ratios and high fluid fluxes along meso- to macroscopic localized fracture systems (e.g. Bebout 1991; Bebout and Barton 1993, 2002; Breeding et al. 2003, 2004; John et al. 2004). Consequently, fluid inclusion studies and isotope studies on undeformed rocks are ambiguous with regards to the scale of fluid flow and element transport.

Under UHP conditions, (supercritical) hydrous melts and transitional fluids appear to be the dominant fluid phase as is indicated by recent experimental studies, at least under relatively warm subduction zone conditions (e.g. Kessel et al. 2005b; Klimm et al. 2008). This conclusion is strongly supported by the above reported fluid inclusion investigations on former subducted continental crust. Primary (fluid) inclusions in peak metamorphic minerals are usually polyphase solid inclusions (cf. Mukherjee and Sachan 2009) and are considered to either represent (supercritical) transitional fluids (e.g. Stöckhert et al. 2001, 2009; Ferrando et al. 2005, 2009; Hwang et al. 2005; Malaspina et al. 2006b, 2009; Frezzotti et al. 2007; Zhang et al. 2008) or (supercritical) hydrous silicate melts (e.g. Hwang et al. 2001, 2003; Korsakov and Hermann 2006), both of which seem to be a more efficient agent for element transport (e.g. Hermann et al. 2006). Thus polyphase solid inclusions are construed to be remnants of transitional fluids or hydrous silicate melts derived by dehydration melting of the subducting host rock under UHP conditions in both cold and hot subduction zones (Fig. 10.7). In addition, the presence of silicate melts is supported by experimental evidence since polyphase inclusions in eclogite-facies garnets, from various subduction-related complexes, re-homogenize into hydrous silicate or carbonate melts under UHP metamorphism (Perchuk et al. 2008). A critical factor is the former presence of transitional fluids and hydrous melts in exhumed oceanic crust, since calculated P-T paths, at least for cold subduction zones (Fig. 10.4), do not crosscut the water-saturated basalt solidus or lie above the second critical point, which only occurs at pressures $>$ 50 kbar, from were oceanic crust has never been reported to return (e.g. Agard et al. 2009). Further, fluid

inclusion and geochemical studies of UHP meta-pelitic or felsic rocks from oceanic subduction zones could shed more light on the composition and type of transitional fluid in these rocks. For example the meta-sediments of the Lago di Ciagnana (Western Alps) display pressures of up to 28 kbar at about 600°C (Reinecke 1998). Thus temperatures and pressures may be too low to reach the water-saturated solidus and the second critical point respectively (Fig. 10.4). Therefore, fluid inclusion investigations should reveal solute-poor aqueous fluids. However, the UHP felsitic schists from the Tianshan (China) have pressures higher than 32 kbar at about 570°C (Wei et al. 2009) and may lie very close or even in the field where transitional fluids are to be expected (Fig. 10.7)

10.8 Summary

Most mineral-bound H_2O, the dominant fluid component in subduction zones to depths of about 120 km, is released in oceanic and continental crust during continuous dehydration reactions associated with HP-LT (< 650°C) metamorphism. The thin sediment veneer on top of the slab dehydrates first, followed by the altered oceanic crust, and then the lithospheric mantle. Altered oceanic basalt and upper lithospheric mantle have little or no significant amounts of H_2O available during UHP conditions in warm subducting slabs, whereas terrigeneous clay-rich sediments and continental crust have significant amounts of accessible water (stabilized in phengite) during UHP conditions, unless melting occurs. In cool subduction zones, mafic (troctolite) and ultramafic igneous rocks are best suited for contributing H_2O available under UHP conditions at about 30 kbar. However, continental crust and terrigeneous sediments also have significant amounts of H_2O on hand due to the presence of phengite, amphibole, chloritoid, and lawsonite. Thus, significant amounts of released aqueous-rich fluid are accessible under HP and UHP conditions during cold subduction, whereas in warmer subduction zones aqueous fluids are mainly released during HP dehydration. In warmer subduction zones, partial melting of altered oceanic crust and terrigeneous sediments occurs under HP and UHP conditions > 10 kbar and temperatures > 650°C. Three distinct types of fluids, buffered by the mineral assemblage of the respective host rock, are thought to be responsible for metasomatism during HP and UHP metamorphism. They are solute-poor aqueous fluids ($<$ ~30 wt.% of solutes), hydrous melts ($H_2O < 35$ wt.%), and transitional fluids, the latter showing a complete miscibility between a hydrous melt and an aqueous fluid above the second critical endpoint. Fluids, responsible for metasomatism in oceanic crust under HP-LT conditions (< 600–650°C), are, in general, low-solute ($\sim < 30$ wt.%) aqueous fluids buffered by an eclogite-facies mineral assemblage. At higher temperatures (> 650°C) partial melting occurs in oceanic crust as well as in continental crust. Under UHP conditions, the fluid phase, buffered by the mineral assemblage of oceanic mafic and ultramafic crustal rocks, is a solute-poor aqueous fluid, whereas a fluid, buffered by the mineral assemblage in meta-sediments, is either a solute-poor

aqueous fluid or, depending on the bulk rock composition of the meta-sediments, a transitional fluid with between ~ 30 and < ~ 65 wt.% solutes. The composition of the fluid phase, present during UHP metamorphism of continental crust, usually is either a transitional fluid or a hydrous melt, depending on the peak P-T conditions experienced by the host rocks. The solute-poor, aqueous fluids, which dominate the fluid budget during HP metamorphism, produce significant, metasomatically-induced trace element changes in the depletion haloes surrounding eclogite-facies veins as well as zones of high fluid-rock ratios and fluid flow, such as subduction channels in oceanic crustal rocks. HP veins, in some cases, represent major conduits of channeled, high fluid flow during prograde (and retrograde) HP-metamorphism and are suggested to be the result of hydrofracturing. Furthermore, extensive fluid flow along (hydro)fractures could represent one possibility of overcoming fluid gradients in HP and UHP continental crust resulting in the creation of large-scale, high-permeability pathways for channelized externally derived fluids. Thus, solute-poor aqueous fluids are responsible for mobilizing and transporting major and trace elements along such zones of high permeability during prograde and retrograde HP metamorphism. This transport is possibly due to complex-forming ligands and F, which may enhance the solubilities in the fluid phase. Concurrently, transitional and/hydrous melts seem to be more important under UHP conditions. However, significant metasomatic trace element change, produced during prograde HP and UHP metamorphism in subduction zones, will mainly occur under high fluid-rock ratios and macroscopic channelized fluid flow. Finally, much more experimental, petrological and geochemical investigation of UHP oceanic and continental crust is necessary to further prove this type of fluid flow as well as further determine the composition and type of fluids responsible for metasomatism under such UHP conditions.

Acknowledgment I would like to thank Jun Gao, Timm John, and Craig E. Manning for fruitful discussions on all aspects of 'subduction metsomatism'. In addition, Timm John is thanked for critical comments on a previous version of the manuscript. I further appreciate helpful suggestions and comments of the reviewers Gray E. Bebout and Berhard W. Evans, which clearly helped to improve the manuscript. Andrea Friese, Melanie Meyer, and Anja Josties are thanked for preparing the line drawings. Michael Bröcker and Simona Ferrando generously provided Figs. 10.16 and 10.15, respectively. Mimi Klemd is thanked for editorial comments and semantic suggestions. Dan Harlov and Hakon Austrheim are thanked for editorial handling and comments.

References

Abers GA, Van Keken PE, Kneller EA, Ferris A, Stachni JC (2006) The thermal structure of subduction zones constrained by seismic imaging: implications for slab dehydration and wedge flow. Earth Planet Sci Lett 241:387–397

Agard P, Monie P, Gerber W, Omrani J, Molinaro M, Meyer B, Labrousse L, Vrielynck B, Jolivet L, Yamato P (2006) Transient, synobduction exhumation of Zagros Blueschists Inferred from P-T, deformation, time, and kinematic constraints: implications for Neotethyan wedge dynamics. J Geophys Res 111:B11401. doi:10.1029/2005JB004103

Agard P, Omrani J, Jolivet L, Mouthereau F (2005) Convergence history across Zagros (Iran): constraints from collisional and earlier deformation. Int J Earth Sci 94:401–419

Agard P, Yamato P, Jolivet L, Burov E (2009) Exhumation of oceanic blueschists and eclogites in subduction zones: timing and mechanisms. Earth Sci Rev 92:53–79

Ague JJ (2003a) Fluid flow in the deep crust. In: Rudnick RL (ed) Treatise on geochemistry, Chap. 3.06. Elsevier, Amsterdam

Ague JJ (2003b) Fluid infiltration and transport of major, minor, and trace elements during regional metamorphism of carbonate rocks, Wepawaug Schist, Connecticut, USA. Am J Sci 303:753–816

Alt JC (1994) A sulfur isotopic profile through the troodos ophiolite, Cyprus: primary composition and the effects of seawater hydrothermal alteration. Geochim Cosmochim Acta 58:1825–1840

Alt JC (1995) Sulfur isotopic profile through the oceanic crust: sulfur mobility and seawater-crustal sulfur exchange during hydrothermal alteration. Geology 23:585–588

Andersen T, Burke E, Austrheim H (1989) Nitrogen-bearing, aqueous fluid inclusions in some eclogites from the western gneiss region of the Norwegian Caledonides. Contrib Mineral Petrol 103:153–156

Angiboust S, Agard P (2010) Initial water budget: the key to detaching large volumes of eclogitized oceanic crust along the subduction channel? Lithos 120:453–474

Antignano A, Manning CE (2008) Rutile solubility in H_2O, H_2O-SiO_2 and H_2O $NaAlSi_3O_8$ fluids at 0.7–2.0 GPa and 700–1000°C: implications for mobility of nominally insoluble elements. Chem Geol 255:283–293

Arcay D, Tric E, Doin MP (2007) Slab surface temperature in subduction zones: influence of the interpolate decoupling depth and upper plate thinning processes. Earth Planet Sci Lett 255:324–338

Audetat A, Keppler H (2005) Solubility of rutile in subduction zone fluids, as determined by experiments in the hydrothermal diamond anvil cell. Earth Planet Sci Lett 232:393–402

Austrheim H (1987) Eclogitization of lower crustal granulites by fluid migration through shear zones. Earth Planet Sci Lett 81:221–232

Austrheim H, Engvik AK (1997) Fluid transport, deformation and metamorphism at depth in a collision zone. In: Jamtveit B, Yardley BWD (eds) Fluid flow and transport in rocks. Chapman and Hall, London

Austrheim H, Prestvik T (2008) Rodingitization and hydration of the oceanic lithosphere as developed in the Leka Ophiolite, North-Central Norway. Lithos 104:177–198

Ayers JC, Watson EB (1993) Rutile solubility and mobility in supercritical fluids. Contrib Mineral Petrol 114:321–330

Ayers JC, Dunkle S, Gao S, Miller CF (2002) Constraints on timing of peak and retrograde metamorphism in the Dabie Shan ultrahigh-pressure metamorphic belt, East-Central China, using U-Th-Pb dating of zircon and monazite. Chem Geol 186:315–331

Bach W, Früh-Green GL (2010) Alteration of the oceanic lithosphere and implications for seafloor processes. Elements 6:173–178

Bach W, Alt JC, Niu Y, Humphris SE, Erzinger J, Dick HJ (2001) The geochemical consequences of late-stage low-grade alteration of lower ocean crust at the SW Indian Ridge: results from ODP Hole 735B (Leg 176). Geochim Cosmochim Acta 65:3267–3287

Bach W, Paulick H, Garrido CJ, Ildefonse B, Meurer WP, Humphris SE (2006) Unraveling the sequence of serpentinization reactions: petrography, mineral chemistry, and petrophysics of serpentinites from MAR 15_N (ODP Leg 209, Site 1274). Geophys Res Lett 33:L13306. doi:10.1029/2006GL025681

Balashov V, Yardley BWD (1998) Modeling metamorphic fluid flow with rection-compaction-permeability feedbacks. Am J Sci 298:410–470

Barnicoat AC, Cartwright I (1995) Focused fluid flow during subduction: oxygen isotope data from high-pressure ophiolites of the Western Alps. Earth Planet Sci Lett 132:53–61

Bebout GE (1991) Geometry and mechanisms of fluid flow at 15 to 45 km depths in an early cretaceous accretionary complex. Geophys Res Lett 18:923–926

Bebout GE (1996) Volatile transfer and recycling at convergent margins: mass balance and sinsights from high-P/P metamorphic rocks. Am Geophys Union Monogr 96:179–194
Bebout GE (1997) Nitrogen isotope tracers of high-temperature fluid-rock interactions: case study of the Catalina Schist, California. Earth Planet Sci Lett 151:77–90
Bebout GE (2007a) Metamorphic chemical geodynamics of subduction zones. Earth Planet Sci Lett 260:373–393
Bebout GE (2007b) Trace element and isotopic fluxes/subducted slab. Treatise on geochemistry. In: Rudnick RL (ed) Treatise on geochemistry, Chap. 3.06. Elsevier, Amsterdam
Bebout GE, Barton MD (1989) Fluid flow and metasomatism in a subduction zone hydrothermal system: Catalina Schist Terrane, California. Geology 17:976–980
Bebout GE, Barton MD (1993) Metasomatism during subduction: products and possible paths in the Catalina Schist, California. Chem Geol 108:61–92
Bebout GE, Barton MD (2002) Tectonic and metasomatic mixing in a high-T, subduction-zone mélange-insights into the geochemical evolution of the slab-mantle interface. Chem Geol 187:79–106
Bebout GE, Ryan JG, Leeman WP, Bebout AE (1999) Fractionation of trace elements by subduction-zone metamorphism; effect of convergent-margin thermal evolution. Earth Planet Sci Lett 171:63–81
Becker H, Jochum KP, Carlson RW (1999) Constraints from highpressure veins in eclogites on the composition of hydrous fluids in subduction zones. Chem Geol 160:291–308
Becker H, Jochum KP, Carlson RW (2000) Trace element fractionation during dehydration of eclogites from high-pressure terranes and the implications for element fluxes in subduction zones. Chem Geol 163:65–99
Beinlich A, Klemd R, John T, Gao J (2010) Trace element mobilization during Ca-metasomatism along a major fluid conduit: eclogitization of blueschist as a consequence of fluid-rock interaction. Geochim Cosmochim Acta 74:1892–1922
Bosse V, Ballevre M, Vidal O (2002) Ductile thrusting recorded by the garnet isograd from blueschist-facies metapelites of the Ile de Groix, Armorican Massif, France. J Petrol 43:485–510
Breeding CM, Ague JJ, Bröcker M, Bolton EW (2003) Blueschist preservation in a retrograded, high-pressure, low-temperature metamorphic Terrane, Tinos, Greece: implications for fluid flow paths in subduction zones. Geochem Geophys Geosyst. doi:10.1029/2002GC000380
Breeding CM, Ague JJ, Bröcker M (2004) Fluid-metasedimentary rock interactions in subduction-zone mélange: implications for the chemical composition of arc magmas. Geology 32:1041–1044
Brenan JM (1993) Partitioning of fluorine and chlorine between apatite and aqueous fluid at high pressure and temperature: implications for the F and Cl content of high P-T fluids. Earth Planet Sci Lett 117:251–263
Bright E, Readey DW (1987) Dissolution kinetics of TiO_2 in HF-HCl solutions. J Am Ceram Soc 70:900–906
Bröcker M, Keasling A (2006) Ionprobe U-Pb zircon ages from the high-pressure/low-temperature mélange of Syros, Greece: age diversity and the importance of pre-Eocene subduction. J Metamorph Geol 24:615–631
Bromiley GD, Pawley AR (2003) The stability of antigorite in the systems $MgO–SiO_2–H_2O$ (MSH) and $MgO–Al_2O_3–SiO_2–H_2O$ (MASH): the effects of Al^3 substitution on high-pressure stability. Am Mineral 88:99–108
Brovarone AV, Groppo C, Hetenyi G, Compagnoni R, Malavielle EJ (2011) Coexistence of lawsonite-bearing eclogite and blueschist: phase equilibria modelling of Alpine Corsica metabasalts and petrological evolution of subducting slabs. J Metamorph Geol 29:583–600
Bruhn D, Groebner N, Kohlstedt DL (2000) An interconnected network of core-forming melts produced by shear deformation. Nature 403:883–886
Brunsmann A, Franz G, Erzinger J, Landwehr D (2000) Zoisite- and clinozoisite segregations in metabasites (Tauern Window, Austria) as evidence for high-pressure fluid-rock interaction. J Metamorph Geol 18:1–21

Brunsmann A, Franz G, Erzinger J (2001) REE mobilization during small-scale high-pressure fluid–rock interaction and zoisite/fluid partitioning of La to Eu. Geochim Cosmochim Acta 65:559–570

Bureau H, Keppler H (1999) Complete miscibility between silicate melts and hydrous fluids in the upper mantle: experimental evidence and geochemical implications. Earth Planet Sci Lett 165:187–196

Busigny V, Cartigny P, Philippot P, Ader M, Javoy M (2003) Massive recycling of nitrogen and other fluid mobile elements (K, Rb, Cs, H) in a cold slab environment: evidence from HP to UHP oceanic metasediments of the Schists Lustrés Nappe (Western Alps, Europe). Earth Planet Sci Lett 215:27–42

Carswell DA, Van Roermund HLM (2005) On multi-phase mineral inclusions associated with microdiamond formation in mantle-derived peridotite lens at Bardane on Fjørtoft, West Norway. Eur J Mineral 17:31–42

Cartwright I, Barnicoat AC (1999) Stable isotope geochemistry of Alpine ophiolites: a window to ocean-floor hydrothermal alteration and constraints on fluid–rock interaction during high-pressure metamorphism. Int J Earth Sci 88:219–235

Castelli D, Rolfo F, Compagnoni R, Xu S (1998) Metamorphic veins with kyanite, zoisite and quartz in the Zhu-Jia-Chong Eclogite, Dabie Shan, China. Isl Arc 7:159–173

Chalot-Prat F, Ganne J, Lombard A (2003) No significant element transfer from the oceanic plate to the mantle wedge during subduction and exhumation of the Tethys Lithosphere (Western Alps). Lithos 69:69–103

Chen RX, Zheng YF, Gong B, Zhao ZF, Gao TS, Chen B, Wu YB (2007) Origin of retrograde fluid in ultrahigh-pressure metamorphic rocks: constraints from mineral hydrogen isotope and water content changes in Eclogite–Gneiss transitions in the Sulu Orogen. Geochim Cosmochim Acta 71:2299–2325

Chopin C (1984) Coesite and pure pyrope in high-grade blueschists of the Western Alps: a first record and some consequences. Contrib Mineral Petrol 86:107–118

Compagnoni R, Hirajima T (2001) Superzoned garnets in the coesite-bearing Brossasco-Isasca unit. Dora-maira massif, Western Alps, and the origin of whiteschists. Lithos 57:219–236

Cong Y, Touret JLR (1993) Fluid inclusions in eclogites from Dabie Mountains, eastern China. Terra Abstr 1:475

Connolly JAD (1997) Devolatilization-generated fluid pressure and deformation propagated fluid flow during prograde regional metamorphism. J Geophys Res 102:18149–18173

Davies JH (1999) The role of hydraulic fractures and intermediate-depth earthquakes in generating subduction-zone magmatism. Nature 398:142–145

Dobrzhinetskaya LF, Green HW, Bozhilov NK, Mitchell TE, Dickerson RM (2003) Crystallization environment of Kazakhstan Microdiamond: evidence from nanometric inclusions and mineral associations. J Metamorph Geol 21:425–437

Domanik KJ, Holloway JR (1996) The stability and composition of phengitic muscovite and associated phases from 5.5 to 11 GPa: implications for deeply subducted sediments. Geochim Cosmochim Acta 60:4133–4150

Domanik KJ, Holloway JR (2000) Experimental synthesis and phase relations of Phengitic Muscovite from 6.5 to 11 GPa in a Calcareous Metapelite from the Dabie Mountains, China. Lithos 52:51–77

Eide EA, Liou JG (2000) Lithos high-pressure blueschists and eclogites in Hong'an: a framework for addressing the evolution of high- and ultrahigh-pressure rocks in Central China. Lithos 52:1–22

El Korh A, Schmidt ST, Ulianov A, Potel S (2009) Trace element partitioning in HP–LT metamorphic assemblages during subduction-related metamorphism, Ile de Groix, France: a detailed LA-ICPMS study. J Petrol 50:1107–1148

El-Shazly AK, Sisson VB (1999) Retrograde evolution of eclogite facies rocks from NE Oman: evidence from fluid inclusions and petrological data. Chem Geol 154:193–223

Engvik AK, Austrheim H, Andersen TB (2000) Structural, mineralogical and petrophysical effects on deep crustal rocks of fluid-limited polymetamorphism, Western Gneiss Region, Norway. J Geol Soc Lond 157:121–134

Engvik AK, Austrheim H, Erambert M (2001) Interaction between fluid flow, fracturing and mineral growth during eclogitization, an example from the Sunnfjord Area, Western Gneiss Region, Norway. Lithos 57:111–141

Ernst WG (1970) Tectonic contact between the Franciscan Mélange and the Great Valley Sequence—crustal expression of a late Mesozoic benioff zone. J Geophys Res 75:886–902

Ernst WG (1972) Occurrence and mineralogic evolution of blueschist belts with time. Am J Sci 272:657–668

Essene EJ, Fyfe WS (1967) Omphacite in Californian metamorphic rocks. Contrib Mineral Petrol 15:1–23

Etheridge MA, Wall VJ, Vernon RH (1983) The role of the fluid phase during regional metamorphism and deformation. J Metamorph Geol 1:205–226

Evans BW (1990) Phase relations of epidote-blueschists. Lithos 25:3–23

Feineman MD, Ryerson FJ, DePaolo DJ, Plank T (2007) Zoisite-aqueous fluid trace element partitioning with implications for subduction zone fluid composition. Chem Geol 239:250–265

Ferrando S, Frezzotti ML, Dallai L, Compagnoni R (2005) Multiphase solid inclusions in UHP rocks (Su-Lu, China): remnants of supercritical silicate-rich aqueous fluids released during continental subduction. Chem Geol 223:82–92

Ferrando S, Frezzotti ML, Petrelli M, Compagnoni R (2009) Metasomatism of continental crust during subduction: the UHP whiteschists from the Southern Dora-Maira Massif (Italian Western Alps. J Metamorph Geol 27:739–757

Franz L, Romer RL, Klemd R, Schmid R, Oberhänsli R, Wagner T (2001) Eclogite-facies quartz veins within metabasites of the Dabie Shan (Eastern China): pressure–temperature–time–deformation path, composition of the fluid phase and fluid flow during exhumation of high-pressure rocks. Contrib Mineral Petrol 141:322–346

Frezzotti ML, Ferrando S, Dallai L, Compagnoni R (2007) Intermediate alkali–alumino-silicate aqueous solutions released by deeply subducted continental crust: fluid evolution in UHP OH-Rich topaz–kyanite quartzites from Donghai (Sulu, China). J Petrol 48:1219–1241

Fu B, Touret JLR, Zheng YF (2001) Fluid inclusions in coesite bearing eclogites and jadeite quartzite at Shuanghe, Dabie Shan (China). J Metamorph Geol 19:529–545

Fu B, Zheng YF, Touret JLR (2002) Petrological, isotopic and fluid inclusion studies of eclogites from Sujiahe, NW Dabie Shan (China). Chem Geol 187:107–128

Fu B, Touret JLR, Zheng YF (2003) Remnants of premetamorphic fl uid and oxygen isotopic signatures in eclogites and garnet clinopyroxenite from the Dabie Sulu terrane, eastern China. J Metamorph Geol 21:561–578

Gao J, Klemd R (2001) Primary fluids entrapped at blueschist to eclogite transition: evidence from the Tianshan meta-subduction complex in Northwestern China. Contrib Mineral Petrol 142:1–14

Gao J, Klemd R (2003) Formation of HP-LT rocks and their tectonic implications in the western Tianshan Orogen, NW China: geochemical and age constraints. Lithos 66:1–22

Gao J, He G, Li M, Xiao X, Tang Y, Wang J, Zhao M (1995) The mineralogy, petrology, metamorphic PTDt trajectory and exhumation mechanism of blueschists, South Tianshan, Northwestern China. Tectonophysics 250:151–168

Gao J, Klemd R, Zhang L, Wang Z, Xiao X (1999) P-T path of high-pressure/low temperature rocks and tectonic implications in the western Tianshan Mountains, NW China. J Metamorph Geol 17:621–636

Gao J, John T, Klemd R, Xiong X (2007) Mobilization of Ti-Nb-Ta during subduction: evidence from rutile-bearing dehydration segregations and veins hosted in eclogite, Tianshan, NW China. Geochim Cosmochim Acta 71:4974–4996

Garrido CJ, Sánchez-Vizcaíno VL, Gómez-Pugnaire MT, Trommsdorff V, Alard O, Bodinier J, Godard M (2005) Enrichment of HFSE in Chlorite-Harzburgite produced by high-pressure

dehydration of Antigorite-Serpentinite: implications for subduction magmatism. Geochem Geophys Geosyst. doi:10.1029/2004GC000791
Gerya T, Stöckhert B, Perchuk AL (2002) Exhumation of high-pressure metamorphic rocks in a subduction channel: a numerical simulation. Tectonics 21:1–15
Getty SR, Selverstone J (1994) Stable isotopic and trace element evidence for restricted fluid migration in 2 GPa eclogites. J Metamorph Geol 12:747–760
Ghiribelli B, Frezzotti ML, Palmeri R (2002) Coesite in eclogites of the Lanterman Range (Antarctica): evidence from textural and Raman studies. Eur J Mineral 14:355–360
Giaramita MJ, Sorensen SS (1994) Primary fluids in low-temperature eclogites: evidence from two subduction complexes (Dominican Republic and California, USA). Contrib Mineral Petrol 117:279–292
Gill JB (1981) Orogenic andesites and plate tectonics. Springer, Berlin
Gillis KM, Robinson PT (1990) Patterns and processes of alteration in the lavas and dykes of the Troodos ophiolite, Cyprus. J Geophys Res 21:523–21
Gose J, Schmädicke E, Beran A (2009) Water in enstatite from Mid-Atlantik Ridge peridotite: evidence for the water content of suboceanic Mantle ? Geology 37:543–546
Green DH (1973) Experimental melting studies on a model upper mantle composition at high pressure under water-saturated and water-undersaturated conditions. Earth Planet Sci Lett 19:37–53
Green TH, Adam J (2003) Experimentally-determined trace element characteristics of aqueous fluid from dehydrated mafic oceanic crust at 3.0 GPa, 650–700°C. Eur J Mineral 15:815–830
Green HW, Houston H (1995) The mechanics of deep earthquakes. Ann Rev Earth Planet Sci 23:169–213
Green TH, Ringwood AE (1968) Genesis of the calc-alkaline igneous rock suite. Contrib Mineral Petrol 18:105–162
Green DH, Fallon TJ, Taylor WR (1987) Mantle-derived magmas – roles of variable source peridotite and variable C–H–O fluid compositions. In: Myson BO (ed) Magmatic processes: physiochemical principles, The geochemical society special publication. Geochemical Society, Pennsylvania, pp 139–154
Gregory R, Taylor H (1981) An oxygen isotope profile in a section of cretaceous oceanic crust, Samail Ophiolite, Oman: evidence for δO buffering of the oceans by deep (>5 km) seawater-hydrothermal circulation at mid-ocean ridges. J Geophys Res 86:2737–2755
Gresens RL (1967) Composition-volume relationships of metasomatism. Chem Geol 2:47–65
Grevel C, Schreyer W, Grevel KD, Schertl HP, Willner AP (2009) REE distribution, mobilization and fractionation in the coesite-bearing 'pyrope quartzite' and related rocks of the Dora-Maira Massif, Western Alps. Eur J Mineral 21:1225–1250
Griffin WL, Brueckner HK (1985) REE, Rb-Sr and Sm-Nd studies of Norwegian eclogites. Chem Geol 52:249–271
Guillot S, Agbossoumonde Y, Menot RP (2001) Metamorphic evolution of Neoproterozoic eclogites from south Togo (West Africa). Earth Planet Sci Lett 33:227–244
Hack AC, Thompson AB, Aertz M (2007) Phase relations involving hydrous silicate melts, aqueous fluids, and minerals. Rev Mineral Geochem 65:129–185
Hacker BR (1997) Diagenesis and fault valve seismicity of crustal faults. J Geophys Res. doi:10.1029/97JB02025
Hacker BR (2003) Subduction factory. 2. Are intermediate-depth earthquakes in subducting slabs linked to metamorphic dehydration reactions? J Geophys Res 108:2055–2071
Hacker BR (2006) Pressures and temperatures of ultrahigh-pressure metamorphism: implications for UHP tectonics and H_2O in subducting slabs. Int Geol Rev 48:1053–1066
Hacker BR (2008) H_2O subduction beyond arcs. Geochem Geophys Geosyst. doi:10.1029/2007GC001707
Hacker BR, Ratschbacher L, Webb LE, Ireland T, Walker D, Shuwen D (1998) U/Pb zircon ages constrain the architecture of the ultrahigh-pressure Qinling–Dabie Orogen, China. Earth Planet Sci Lett 161:215–230

Hacker BR, Ratschbacher L, Webb LE, McWilliams M, Ireland T, Dong S, Calvert A, Wenk HR (2000) Exhumation of the ultrahigh-pressure continental crust in East-Central China: late Triassic-early Jurassic Extension. J Geophys Res 105:13339–13364

Hacker BR, Abers GA, Peacock SM (2003) Subduction factory 1. Theoretical mineralogy, densities, seismic wave speeds and H_2O contents. J Geophys Res 108:2029–2054

Hayden LA, Manning CE (2011) Rutile solubility in supercritical $NaAlSi_3O_8$–H_2O fluids. Chem Geol 284:74–81

Heinrich W, Gottschalk M (1995) Metamorphic reactions between fluid inclusions and mineral hosts. I. Progress of the reaction Calcite + Quartz = Wollastonite + CO_2 in natural Wollastonite-hosted fluid inclusions. Contrib Mineral Petrol 122:51–61

Henry C, Burkhard M, Goffé B (1996) Evolution of synmetamorphic veins and their wallrocks through a Western Alps Transect: no evidence for large-scale fluid flow. Stable isotope, major- and trace element systematic. Chem Geol 127:81–109

Hermann J (2002) Experimental constraints on phase relations in subducted continental crust. Contrib Mineral Petrol 143:219–235

Hermann J (2003) Experimental evidence for diamond-facies metamorphism in the Dora Maira Massif. Lithos 70:163–182

Hermann J, Green DH (2001) Experimental constraints on high pressure melting in subducted crust. Earth Planet Sci Lett 188:149–186

Hermann J, Spandler C (2008) Sediment melts at sub-arc depths: an experimental study. J Petrol 49:717–740

Hermann J, Müntener O, Scambelluri M (2000) The importance of serpentinite mylonites for subduction and exhumation of oceanic crust. Tectonophysics 327:225–238

Hermann J, Spandler C, Hack A, Korsakov AV (2006) Aqueous fluids and hydrous melts in high-pressure and ultrahigh pressure rocks: implications for element transfer in subduction zones. Lithos 92:399–417

Holland TJB (1979) High water activities in the generation of high-pressure kyanite eclogites of the Tauern Window, Austria. J Geol 87:1–27

Holtz F, Becker A, Freise M, Johannes W (2001) The water undersaturated and dry Qz–Ab–Or system revisited. Experimental results at very low water activities and geological implications. Contrib Mineral Petrol 141:347–357

Huang WL, Wyllie PJ (1981) Phase relationships of S-type granite with H_2O to 35 kbar: muscovite granite from Harney Peak, South Dakota. J Geophys Res 86:10515–10529

Hwang SL, Shen P, Chu HT, Yui TF, Lin CC (2001) Genesis of microdiamonds from melt and associated multiphase inclusions in garnet of ultrahigh-pressure gneiss from Erzgebirge, Germany. Earth Planet Sci Lett 188:9–15

Hwang SL, Shen P, Yui TF, Chu HT (2003) Metal–sulfur–COH silicate fluid mediated diamond nucleation in Kokchetav ultrahigh-pressure gneiss. Eur J Mineral 15:503–511

Hwang SL, Shen P, Chu HT, Yui TF, Liou JG, Sobolev NV, Shatsky VS (2005) Crust-derived potassic fluid in metamorphic microdiamond. Earth Planet Sci Lett 231:295–306

Hwang SL, Chu HT, Yui TF, Shen P, Schertl HP, Liou JG, Sobolev NV (2006) Nanometer-Size P/K-rich silica glass (former melt) inclusions in microdiamond from the gneisses of Kokchetav and Erzgebirge Massifs: diversified characteristics of the formation media of metamorphic microdiamond in UHP rocks due to host-rock buffering. Earth Planet Sci Lett 243:94–106

Iyer K, Austrheim H, John T, Jamtveit B (2008) Serpentinization of the oceanic lithosphere and some geochemical consequences: constraints from the Leka Ophiolite Complex, Norway. Chem Geol 249:66–90

Jackson JA, Austrheim H, McKenzie D, Priestley K (2004) Metastability, mechanical strength, and the support of mountain belts. Geology 32:625–628

Jahn BM (1999) Sm-Nd isotope tracer study of UHP metamorphic rocks: implications for continental subduction and collisional tectonics. Int Geol Rev 41:859–885

John T, Schenk V (2003) Partial eclogitization of gabbroic rocks in a late Precambrian subduction zone (Zambia): prograde metamorphism triggered by fluid infiltration. Contrib Mineral Petrol 146:174–191

John T, Schenk V (2006) Interrelations between intermediate-depth earthquakes and fluid flow within subducting oceanic plates: constraints from eclogite-facies Pseudotachylytes. Geology 34:557–560

John T, Scherer EE, Haase K, Schenk V (2004) Trace element fractionation during fluid-induced eclogitization in a subducting slab: trace element and Lu-Hf-Sm-Nd isotope systematics. Earth Planet Sci Lett 227:441–456

John T, Klemd R, Gao J, Garbe-Schönberg CD (2008) Trace element mobilization in slabs due to non steady-state fluid-rock interaction: constraints from an eclogite-facies transport vein in blueschist (Tianshan, China). Lithos 103:1–24

Johnson MC, Plank T (1999) Dehydration and melting experiments constrain the fate of subducted sediments. Geochem Geophys Geosyst 1. doi:1999GC000014

Karson JA (2002) Geologic structure of the uppermost oceanic crust created at fast- to intermediate-rate spreading centres. Earth Planet Sci 30:347–384

Kawamoto T, Holloway JR (1997) Melting temperature and partial melt chemistry of H_2O-saturated mantle peridotite to 11 gigapascals. Science 276:240–243

Kelemen PB, Rilling JL, Parmentier EM, Mehl L, Hacker BR (2003) Thermal structure due to solid-state flow in the mantle wedge beneath arcs. Am Geophys Union Monogr 138:293–311

Kerrick DM, Connolly JAD (2001a) Metamorphic devolatilization of subducted oceanic metabasalts: implications for seismicity, arc magmatism and volatile recycling. Earth Planet Sci Lett 189:19–29

Kerrick DM, Connolly JAD (2001b) Metamorphic devolatilization of subducted marine sediments and the transport of volatiles into the Earth's mantle. Nature 411:293–296

Kessel R, Ulmer P, Pettke T, Schmidt MW, Thompson AB (2005a) The water-basalt system at 4 to 6 GPa: phase relations and second critical endpoint in a K-free eclogite at 700 to 1400°C. Earth Planet Sci Lett 273:873–892

Kessel R, Schmidt MW, Ulmer P, Pettke T (2005b) Trace element signature of subduction-zone fluids, melts and supercritical liquids at 120–180 km depth. Nature 437:724–727

Kimura JI, Hacker BR, van Keken PE, Kawabata H, Yoshida T, Stern RJ (2009) Arc basalt simulator version 2 m, a simulation for slab dehydration and fluid-fluxed mantle melting for arc basalts: modeling scheme and application. Geochem Geophys Geosyst 10. doi:10.1029/2008GC002217

King RL, Bebout GE, Kobayashi K, Nakamura E, Van der Klauw SNGC (2004) Ultrahigh-pressure metabasaltic garnets as probes into deep subduction zone chemical cycling. Geochem Geophys Geosyst 5. doi:10.1029/2004GC000746

King RL, Bebout GE, Moriguti T, Nakamura E (2006) Elemental mixing systematics and Sr–Nd isotope geochemistry of mélange formation: obstacles to identification of fluid sources to arc volcanic. Earth Planet Sci Lett 246:288–304

King RL, Bebout GE, Grove M, Moriguti T, Nakamura E (2007) Boron and lead isotope signatures of subduction-zone mélange formation: hybridization and fractionation along the slab–mantle interface beneath volcanic arcs. Chem Geol 239:305–322

Kirby S, Engdahl ER, Denlinger R (1996) Intermediate-depth intraslab earthquakes and arc volcanism as physical expressions of crustal and uppermost mantle metamorphism in subducting slabs. Am Geophys Union Monogr 96:195–214

Klemd R (1989) P-T evolution and fluid inclusion characteristics of retrograded eclogites, Münchberg gneiss complex, Germany. Contrib Mineral Petrol 102:221–229

Klemd R (2003) Ultrahigh-pressure metamorphism in eclogites from the western tianshan high-pressure belt (Xinjiang, western China). Am Mineral 88:1153–1156

Klemd R (2004) Fluid inclusions in epidote minerals and fluid development in epidote-bearing rocks. Rev Mineral Geochem 56:197–234

Klemd R, Matthes S, Okrusch M (1991) High-pressure relics in meta-sediments intercalated with the Weissenstein eclogite, Münchberg gneiss complex, Bavaria. Contrib Mineral Petrol 107:328–342

Klemd R, van den Kerkhof AM, Horn EE (1992) High-density CO-N_2 inclusions in eclogite-facies metasediments of the Münchberg gneiss complex, SE Germany. Contrib Mineral Petrol 111:409–441

Klemd R, Bröcker M, Schramm J (1995) Characterisation of amphibolite-facies fluids of variscan eclogites from the Orlica-Snieznik Dome (Sudetes, SW Poland). Chem Geol 119:101–113
Klemd R, Schröter FC, Will TM, Gao J (2002) P-T evolution of glaucophane omphacite bearing HP-LT rocks in the Western Tianshan Orogen, NW China: New Evidence for 'Alpine-type' Zectonics. J Metamorph Geol 20:239–254
Klemd R, Bröcker M, Hacker BR, Gao J, Gans P, Wemmer K (2005) New age constraints on the metamorphic evolution of the high-pressure/low-temperature belt in the western Tianshan Mountains, NW China. J Geol 113:157–168
Klemd R, John T, Scherer EE, Rondenay S, Gao J (2011) Changes in dip of subducted slabs at depth: petrological and geochronological evidence from HP-UHP rocks (Tianshan, NW-China). Earth Planet Sci Lett 310:9–20
Klimm K, Blundy JD, Green TH (2008) Trace element partitioning and accessory phase saturation during H_2O-saturated melting of basalt with implications for subduction zone chemical fluxes. J Petrol 49:523–553
Konrad-Schmolke M, O'Brien PJ, Zack T (2011) Fluid migration above a subducted slab—constraints on amount, pathways and major element mobility from partially overprinted eclogite-facies rocks (Sesia Zone, Western Alps). J Petrol 52:457–486
Korsakov AV, Hermann J (2006) Silicate and carbonate melt inclusions associated with diamonds in deeply subducted carbonate rocks. Earth Planet Sci Lett 241:104–118
Kretz R (1983) Symbols for rock forming minerals. Am Mineral 68:277–279
Kummer T, Spinelli GA (2008) Hydrothermal circulation in subducting crust reduces subduction zone temperatures. Geology 36:91–94
Lambert IB, Wyllie PJ (1972) Melting of gabbro (Quartz Eclogite) with excess water to 35 kilobars with geological applications. J Geol 80:693–708
Lang HM, Gilotti JA (2007) Partial melting of metapelites at ultrahigh-pressure conditions, Greenland Caledonides. J Metamorph Geol 25:129–147
Lardeaux JM, Ledru P, Daniel I, Duchene S (2001) The Variscan French Massif Central – a new addition to the ultra-high pressure metamorphic 'Club': exhumation processes and geodynamic consequences. Tectonophysics 332:143–167
Li XP, Rahn M, Bucher K (2004) Serpentinites of the Zermatt-Saas ophiolite complex and their texture evolution. J Metamorph Geol 22:159–177
Liebscher A (2004) Decoupling of fluid and trace element release in subducting slab? Comment on "redistribution of trace elements during prograde metamorphism from lawsonite blueschist to eclogite facies; implications for deep subduction-zone processes". Contrib Mineral Petrol 148:502–502
Lin W, Enami M (2006) Prograde pressure-temperature path of jadeite-bearing eclogites and associated high-pressure/low-temperature rocks from western Tianshan. Isl Arc 15:483–502
Liou J, Zhang RY, Ernst WG, Rumble D, Maruyama S (1998) High-pressure minerals from deeply subducted metamorphic rocks. Rev Mineral Geochem 37:33–96
Liu J, Ye K (2004) Transformation of garnet epidote amphibolite to eclogite, western Dabie Mountains, China. J Metamorph Geol 22:383–394
Liu FL, Gerdes A, Liou JG, Xue HM, Liang FH (2006a) Shrimp U-Pb zircon dating from Sulu-Dabie Dolomitic marble, Eastern China: constraints on prograde, ultrahigh-pressure and retrograde metamorphic ages. J Metamorph Geol 24:569–589
Liu JB, Ye K, Sun M (2006b) Exhumation P–T path of UHP eclogites in the Hong'an area, Western Dabie Mountains, China. Lithos 89:154–173
Lü Z, Zhang LF, Qü JF, Li HF (2007) Petrology and metamorphic P-T path of eclogites from Habutengsu, southwestern Tianshan, Xinjiang. Acta Petrol Sinica 23:1617–1626
Lü Z, Zhang LF, Du J, Bucher K (2008) Coesite inclusions in garnet from eclogitic rocks in western Tianshan, northwest China: convincing proof of UHP metamorphism. Am Mineral 93:1845–1850
Lü Z, Zhang LF, Du J, Bucher K (2009) Petrology of coesite-bearing eclogite from Habutengsu Valley, western Tianshan, NW China and its tectonometamorphic implication. J Metamorph Geol 27:773–789

Maekawa H, Shozul M, Ishll T, Fryer P, Pearce JA (1993) Blueschist metamorphism in an active subduction zone. Nature 364:520–523
Malaspina N, Hermann J, Scambelluri M, Compagnoni R (2006a) Polyphase inclusions in Garnet–Orthopyroxenite (Dabie Shan, China) as monitors for metasomatism and fluid-related trace element transfer in subduction zone peridotite. Earth Planet Sci Lett 249:173–187
Malaspina N, Hermann J, Scambelluri M, Compagnoni R (2006b) Multistage metasomatism in ultrahigh-pressure mafic rocks from the north dabie complex (China). Lithos 90:19–42
Malaspina N, Hermann F, Scambelluri M (2009) Fluid/mineral Interaction in UHP garnet peridotite. Lithos 10:38–52
Manning CE (1994) The solubility of quartz in the lower crust and upper mantle. Geochim Cosmochim Acta 58:4831–4839
Manning CE (1998) Fluid composition at the blueschist–eclogite transition in the model system Na_2O-MgO-Al_2O_3-SiO_2-H_2O-HCl. Schweiz Miner Petrogr Mitt 78:225–242
Manning CE (2004) The chemistry of subduction-zone fluids. Earth Planet Sci Lett 223:1–16
Manning CE, Bohlen SR (1991) The reaction titanite + kyanite = anorthite + rutile and titanite-rutile barometry in eclogites. Contrib Mineral Petrol 109:1–9
Maruyama S, Liou J, Terabayashi M (1996) Blueschists and eclogites of the world and their exhumation. Int Geol Rev 38:485–594
Massonne HJ (1999) A new occurrence of microdiamonds in quartzofeldspathic rocks of the Saxonian Erzgebirge, Germany, and their metamorphic evolution. In: Proceedings of 7th international Kimberlite conference, Cape Town, pp 533–539
Massonne HJ (2003) A comparison of the evolution of diamondiferous quartz-rich rocks from the Saxonian Erzgebirge and the Kokchetav Massif: are so-called diamondiferous gneisses magmatic rocks? Earth Planet Sci Lett 216:347–364
McCulloch MT, Gamble JA (1991) Geochemical and geodynamical constraints on subduction zone magmatism. Earth Planet Sci Lett 102:358–374
Mibe K, Yoshino T, Ono S, Yasuda A, Fujii T (2003) Connectivity of aqueous fluid in eclogite and its implications for fluid migration in the Earth's interior. J Geophys Res 108:2295–3006
Mibe K, Kawamoto T, Matsukake KN, Fei Y, Ono S (2011) Slab melting versus slab dehydration in subduction-zone magmatism. PNAS. doi:10.1073/pnas.1010968108
Miller C, Thöni M (1995) Origin of eclogites from the Austroalpine Otztal basement (Tirol, Austria): geochemistry and Sm-Nd vs. Rb-Sr systematic. Chem Geol 122:199–225
Miller JA, Buick IS, Cartwright I, Barnicoat A (2002) Fluid processes during the exhumation of high-P metamorphic belts. Min Mag 66:93–119
Miller SA, Van Der Zee W, Olgaard DL, Connolly JAD (2003) A fluid-pressure feedback model of dehydration reactions: experiments, modelling, and application to subduction zones. Tectonophysics 370:241–251
Molina JF, Poli S, Austrheim HJG, Rusin A (2004) Eclogite facies vein systems in the Marun-Keu complex (Polar Urals, Russia): textural, chemical and thermally constraints for patterns of fluid flow in the lower crust. Contrib Mineral Petrol 147:487–504
Moore JC, Vrolijk P (1992) Fluids in accretionary prisms. Rev Geophys 30:113–135
Morishita T, Arai S, Ishida Y (2007) Trace element compositions of jadeite (+Omphacite) in Jadeitites from the Itoigawa-Ohmi District, Japan: implications for fluid processes in subduction zones. Isl Arc 16:40–56
Muehlenbachs K (1986) Alteration of the oceanic crust and the ^{18}O history of seawater. Rev Mineral 16:425–445
Mukherjee BK, Sachan HK (2009) Fluids in coesite-bearing rocks of the Tso Morari Complex, NW Himalaya: evidence for entrapment during peak metamorphism and subsequent uplift. Geol Mag 146:876–889
Mysen BO (1998) Interaction between aqueous fluid and silicate melt in the pressure and temperatures regime of the Earth's crust and upper mantle. N Jahrb Miner Abh 172:227–244
Nadeau S, Philippot P, Pineau F (1993) Fluid inclusion and mineral isotopic compositions (H–O–C) in eclogitic rocks as tracers of local fluid migration during high-pressure metamorphism. Earth Planet Sci Lett 114:431–448

Nakamura D, Hirajima T (2000) Granulite-facies overprinting of ultrahigh-pressure metamorphic rocks northeastern Su-Lu region, eastern china. J Petrol 41:563–582
Nelson BK (1995) Fluid flow in subduction zones: evidence from Nd- and Sr-isotope variations in metabasalts of the Franciscan complex, California. Contrib Mineral Petrol 119:247–262
Newton RC, Manning CE (2002) Solubility of enstatite + forsterite in H_2O at deep crust/upper mantle conditions: 4 to 15 kbar and 700 to 900°C. Geochim Cosmochim Acta 66:4165–4176
Ni P, Zhu X, Wang R, Shen K, Zhang Z, Qiu J, Huang J (2008) Constraining ultrahigh-pressure (UHP) metamorphism and titanium ore formation from an infrared microthermometric study of fluid inclusions in Rutile from Donghai UHP Eclogites, Eastern China. Geol Soc Am Bull 120:1296–1304
Okrusch M, Seidel E, Davies EN (1978) The assemblage jadeite-quartz in the glaucophane rocks of Sifnos. N Jahrb Miner Abh 132:284–308
Oliver NHS (1996) Review and classification of structural controls on fluid flow during regional metamorphism. J Metamorph Geol 14:477–492
Ono S (1998) Stability limits of hydrous minerals in sediment and mid-ocean ridge basalt compositions: implications for water transport in subduction zones. J Geophys Res. doi:10.1029/98JB01351
Padron-Navarta JA, Hermann J, Garrido ECJ, Sanchez-Vizcaıno VL, Gomez-Pugnaire MT (2010) An experimental investigation of antigorite dehydration in natural silica-enriched serpentinite. Contrib Mineral Petrol 159:25–42
Parkinson CD, Katayama I (1999) Metamorphic microdiamond and coesite from Sulawesi, Indonesia: Evidence of deep subduction as SE Sundaland Margin. EOS Trans Am Geophy Union 80:F1181
Peacock SM (1990) Fluid processes in subduction zones. Science 248:329–337
Peacock SM (1993) The importance of blueschist–eclogite dehydration reactions in subducting oceanic crust. Geol Soc Am Bull 105:684–694
Peacock SM, Wang K (1999) Seismic consequences of warm versus cool subduction metamorphism: examples from southwest and northeast Japan. Science 286:937–939
Peacock SM, Rushmer T, Thompson AB (1994) Partial melting of subducting oceanic crust. Earth Planet Sci Lett 121:227–244
Peacock SM, Van Keken PE, Holloway SD, Hacker BR, Abers GA, Fergason RL (2005) Thermal structure of the Costa Rica – Nicaragua subduction zone. Phys Earth Planet Int 149:187–200
Perchuk AL, Burchard M, Maresch VM, Schertl HL (2008) Melting of hydrous and carbonate mineral inclusions in garnet host during ultrahigh pressure experiments. Lithos 103:25–45
Philippot P (1987) "Crack Seal" vein geometry in eclogitic rocks. Geodin Acta 1:171–181
Philippot P (1993) Fluid–melt-rock interaction in mafic eclogites and coesite-bearing metasediments: constraints on volatile recycling during subduction. Chem Geol 108:93–112
Philippot P, Selverstone J (1991) Trace element rich brines in eclogitic veins: implications for fluid composition and transport during subduction. Contrib Mineral Petrol 106:417–430
Plank T, Langmuir CH (1998) The chemical composition of subducting sediments and its consequences for the crust and mantle. Chem Geol 145:325–394
Plank T, Kelley KA, Murray RW, Stern LQ (2007) Chemical composition of sediments subducting at the Izu-Bonin trench. Geochem Geophys Geosys. doi:10.1029/2006GC001444
Plank T, Cooper LB, Manning CE (2009) Emerging geothermometers for estimating slab surface temperatures. Nat Geosci. doi:10.1038/ngeo614
Poli S, Schmidt MW (2002) Petrology of subducted slabs. Ann Rev Earth Planet Sci 30:207–235
Prouteau G, Scaillet B, Pichavant M, Maury R (2001) Evidence for mantle metasomatism by hydrous silicate meltrs derived from subducted oceanic crust. Nature 410:197–200
Putnis A (2002) Mineral replacement reactions: from macroscopic observations to microscopic mechanisms. Mineral Mag 66:689–708
Putnis A (2009) Mineral replacement reactions. In: Oelkers EH, Schott J (eds) Thermodynamics and kinetics of water-rock interaction, vol 70, Reviews in Mineralogy and Geochemistry. Mineralogical Society of America, Chantilly, pp 87–124

Putnis A, Austrheim H (2010) Fluid induced processes: metasomatism and metamorphism. Geofluids 10:254–269
Putnis A, John T (2010) Replacement processes in the Earth's crust. Elements 6:159–164
Ranero CR, Von Huene R (2000) Subduction erosion along the Middle America convergent margin. Nature 404:748–752
Ranero CR, Morgan JP, McIntosh K, Reichert C (2003) Bending-related faulting and mantle serpentinization at the Middle America trench. Nature 425:367–373
Rapp JF, Klemme S, Butler IB, Harley SL (2010) Extremely high solubility of rutile in chloride and fuoride-bearing metamorphic fluids: an experimental investigation. Geology 38:323–326
Rea DK, Ruff LJ (1996) Composition and mass flux of sediment entering the world's subduction zones: implications for global sediment budgets, great earthquakes, and volcanism. Earth Planet Sci Lett 140:1–12
Reinecke T (1998) Prograde high- to ultrahigh-pressure metamorphism and exhumation of oceanic sediments at Lago di Cignana, Zermatt-Saas Zone, Western Alps. Lithos 42:147–190
Roedder E (1984) Fluid inclusions. Rev Mineral 12:1–677
Rubatto D, Hermann J (2003) Zircon formation during fluid circulation in eclogites (Monviso, Western Alps): implications for Zr and Hf budget in subduction zones. Geochim Cosmochim Acta 67:2173–2187
Rumble D III, Wang Q, Zhang R (2000) Stable isotope geochemistry of marbles from the coesite UHP terrains of Dabieshan and Sulu, China. Lithos 52:79–95
Rumble D, Liou J, Jahn BM (2003) Continental crust subduction and ultrahigh pressure metamorphism. In: Holland HD, Turekian KK (eds) Treatise on geochemistry. Elsevier, Amsterdam
Rüpke LH, Morgan JP, Hort M, Connolly JAD (2002) Are the regional variations in Central American arclavas due to differing basaltic versus peridotitic slab sources of fluids. Geology 30:1035–1038
Rüpke LH, Morgan JP, Hort M, Connolly JAD (2004) Serpentine and the subduction zone water cycle. Earth Planet Sci Lett 22:17–34
Rutland RWR (1971) Andean orogeny and ocean floor spreading. Nature 233:252–255
Saha A, Basu AR, Wakabayashi J, Wortman GL (2005) Geochemical evidence for a subducted infant arc in Franciscan high-grade-metamorphic tectonic blocks. Geol Soc Am Bull 117:1318–1335
Scambelluri M, Philippot P (2001) Deep fluids in subduction zones. Lithos 55:213–227
Scambelluri M, Van Roermund HLM (2008) Majoritic garnets monitor deep subduction fluid flow and mantle dynamics. Geology 36:59–62
Scambelluri M, Piccardo GB, Philippot P, Robbiano A, Negretti L (1997) High salinity fluid inclusions formed from recycled seawater in deeply subducted Alpine serpentinite. Earth Planet Sci Lett 148:485–499
Scambelluri M, Pennacchioni G, Philippot P (1998) Salt-rich aqueous fluids formed during eclogitization of metabasites in the Alpine continental crust (Austroalpine Mt. Emilius Unit, Italian Western Alps). Lithos 43:151–167
Scambelluri M, Bottazzi P, Trommsdorff V, Vannucci R, Hermann J, Gomez-Pugnaire MT, Vizcaino VLS (2001) Incompatible element-rich fluids released by antigorite breakdown in deeply subducted mantle. Earth Planet Sci Lett 192:457–470
Scambelluri M, Fiebig J, Malaspina N, Müntener O, Pettke T (2004) Serpentinite subduction: implications for fluid processes and trace element recycling. Int Geol Rev 46:595–613
Schertl HP, Schreyer W (2008) Geochemistry of coesite-bearing "Pyrope Quartzite" and related rocks from the Dora-Maira Massif, Western Alps. Eur J Mineral 20:791–809
Schertl HP, Schreyer W, Chopin C (1991) The pyrope-coesite rocks and their country rocks at Parigi, Dora Maira Massif, Western Alps: detailed petrography, mineral chemistry and PT-path. Contrib Mineral Petrol 108:1–21
Schmid R, Klemd R, Franz L, Oberhänsli R, Dong S (2003) UHP metamorphism and associated fluid evolution: a case study in the bixiling area (Dabie Shan, China). Beih Eur J Miner 15:175

Schmidt MW, Poli S (1998) Experimentally based water budgets for dehydrating slabs and consequences for arc magma generation. Earth Planet Sci Lett 163:361–379

Schmidt MW, Poli S (2003) Generation of mobile components during subduction of oceanic crust. In: Rudnick RL, Holland HD, Turekian KK (eds) Treatise on geochemistry. Elsevier, Amsterdam

Schmidt MW, Vielzeuf D, Auzanneau E (2004) Melting and dissolution of subducting crust at high pressures: the key role of White Mica. Earth Planet Sci Lett 228:65–84

Scholl WS, von Huene R (2007) Crustal recycling at modern subduction zones applied to the past-issues of growth and preservation of continental basement, mantle geochemistry, and supercontinent reconstruction. Geol Soc Am Mem 200:9–32

Selverstone J, Franz G, Thomas S, Getty S (1992) Fluid variability in 2 GPa eclogites as an indicator of fluid behaviour during subduction. Contrib Mineral Petrol 112:341–357

Sharp ZD, Barnes JD (2004) Water-soluble chlorides in massive seafloor serpentinites: a source of chloride in subduction zones. Earth Planet Sci Lett 226:243–254

Sharp ZD, Essene EJ, Hunziker JC (1993) Stable isotope geochemistry and phase equilibria of coesite-bearing whiteschists, Dora-Maira Massif, Western Alps. Contrib Mineral Petrol 114:1–12

Shatsky VS, Sobolev NV, Vavilov MA (1995) Diamond-bearing metamorphic rocks of the Kokchetav Massif (Northern Kazakhstan). In: Coleman RG, Wang X (eds) Ultrahigh pressure metamorphism. Cambridge University Press, Cambridge

Shatsky VS, Jagoutz E, Sobolev NV, Kozmenko OA, Parkhomenko VS, Troesch M (1999) Geochemistry and age of ultrahigh pressure metamorphic rocks from the Kokchetav Massif (Northern Kazakhstan). Contrib Mineral Petrol 137:185–205

Shen AH, Keppler H (1997) Direct observation of complete miscibility the albite-H_2O system. Nature 385:710–712

Snow JE, Dick HJB (1995) Pervasive magnesium loss by marine weathering of peridotite. Geochim Cosmochim Acta 59:4219–4235

Sorensen SS (1988) Petrology of amphibolite-facies mafic and ultramafic rocks from the Catalina Schist, Southern California: metasomatism and migmatization in a subduction zone metamorphic setting. J Metamorph Geol 6:405–435

Sorensen SS, Grossman JN, Perfit MR (1997) Phengite-Hosted LILE enrichment in eclogite and related rocks: implications for fluid-mediated mass transfer in subduction zones and arc magma genesis. J Petrol 38:3–34

Spandler C, Hermann J (2006) High-pressure veins in eclogite from New Caledonia and their significance for fluid migration in subduction zones. Lithos 89:135–153

Spandler C, Hermann J, Arculus R, Mavrogenes J (2003) Redistribution of trace elements during prograde metamorphism from Lawsonite Blueschist to eclogite facies; implications for deep subduction zone processes. Contrib Mineral Petrol 146:205–222

Spandler C, Hermann J, Arculus R, Mavrogenes J (2004) Geochemical heterogeneity and element mobility in deeply subducted oceanic crust; insights from high-pressure mafic rocks from New Caledonia. Chem Geol 206:21–42

Spandler C, Mavrogenes J, Hermann J (2007) Experimental constraints on element mobility from subducted sediments using High-P synthetic fluid/melt inclusions. Chem Geol 239:228–249

Spooner ETC, Beckinsale RD, Fyfe WS, Smewing JD (1974) O^{18} enriched ophiolitic metabasic rocks from E. Liguria (Italy), Pindos (Greece), and Troodos (Cyprus). Contrib Mineral Petrol 47:41–62

Stakes D, Taylor H (1992) The Northern Samail Ophiolite: an oxygen isotope, microprobe, and field study. J Geophys Res 97:70443–7080

Stalder R, Foley SF, Brey GP, Horn I (1998) Mineral-aqueous fluid partitioning of trace elements at 900–1200°C and 3.0–5.7 GPa: new experimental data for garnet, clinopyroxene, and rutile, and implications for mantle metasomatism. Geochim Cosmochim Acta 62:1781–1801

Stalder R, Ulmer P, Thompson AB, Günther D (2000) Experimental approach to constrain second critical end points in Fluid/Silicate systems: near-solidus fluids and melts in the system Albite-H_2O. Am Mineral 85:68–77

Stalder R, Ulmer P, Thompson AB, Günther D (2001) High pressure fluids in the system $MgO–SiO_2–H_2O$ under upper mantle conditions. Contrib Mineral Petrol 140:607–618

Staudigel H (2003) Hydrothermal alteration processes in the oceanic crust. In: Rudnick RL, Holland HD, Turekian KK (eds) Treatise on geochemistry. Elsevier, Amsterdam

Staudigel H, Davies GR, Hart SR, Marchant KM, Smith BM (1995) Large scale isotopic Sr, Nd and O ssotopic anatomy of altered oceanic crust: DSDP/ODP sites417/418. Earth Planet Sci Lett 130:169–185

Staudigel H, Plank T, White B, Schmincke HU (1996) Geochemical fluxes during seafloor alteration of the basaltic upper oceanic crust: DSDP sites 417 and 418. Am Geophys Union Monogr 96:19–38

Stöckhert B, Duyster J, Trepmann C, Massonne HJ (2001) Microdiamond daughter crystals precipitated from supercritical COH + silicate fluids included in garnet, Erzgebirge, Germany. Geology 29:391–394

Stöckhert B, Trepmann CA, Massonne HJ (2009) Decrepitated UHP fluid inclusions: about diverse phase assemblages and extreme decompression rates (Erzgebirge, Germany). J Metamorph Geol 27:673

Stosch HG, Lugmair GW (1990) Geochemistry and evolution of the MORB-type eclogites from the Münchberg Massif, southern Germany. Earth Planet Sci Lett 99:230–249

Su W, Zhang M, Redfern SAT, Gao J, Klemd R (2009) OH in zoned amphiboles of eclogite from the western Tianshan, NW-China. Int J Earth Sci 98:1299–1309

Su W, Gao J, Klemd R, Li J, Zhang X, Li X, Chen N, Zhang L (2010) U-Pb zircon geochronology of Tianshan eclogites in NW China: implication for the collision between the Yili and Tarim blocks of the southwestern Altaids. Eur J Mineral 22:473–478

Svensen H, Jamtveit B, Yardley BWD, Engvik AK, Austrheim H, Broman C (1999) Lead and bromine enrichment in eclogite-facies fluids: extreme fractionation during lower- crustal hydration. Geology 27:467–470

Syracuse EM, Abers GA (2006) Global compilation of variations in slab depth beneath arc volcanoes and implications. Geochem Geophys Geosys. doi:10.1029/2005GC001045

Syracuse EM, van Keken PE, Abers GA (2010) The global range of subduction zone thermal models. Phys Earth Planet Int 51:1761–1782

Tatsumi Y, Eggins SM (1995) Subduction zone magmatism. Blackwell, Cambridge

Tenthorey E, Hermann J (2004) Composition of fluids during serpentinite breakdown in subduction zones: evidence for limited boron mobility. Geology 32:865–868

Touret JLR, Frezzotti ML (2003) Fluid inclusions in high pressure and ultrahigh pressure metamorphic rocks. In: Carswell DA, Compagnoni R (eds) Ultrahigh pressure metamorphism. Eötvös University Press, Budapest

Tropper P, Manning CE (2005) Very low solubility of Rutile in H_2O at high pressure and temperature and its implications for Ti mobility in subduction zones. Am Mineral 90:502–505

Vallis F, Scambelluri M (1996) Redistribution of high-pressure fluids during retrograde metamorphism of eclogite-facies rocks (Voltri Massif, Italian West Alps). Lithos 39:81–92

Van Baalen MR (1993) Titanium mobility in metamorphic systems: a review. Chem Geol 110:233–249

Van der Straaten F, Schenk V, John T, Gao J (2008) Blueschist-Facies rehydration of eclogites (Tian Shan, NW China): implications for fluid-rock interaction in the subduction channel. Chem Geol 255:195–219

Van Keken PE (2003) The structure and dynamics of the mantle wedge. Earth Planet Sci Lett 215:323–338

Van Keken PE, Kiefer B, Peacock SM (2002) High-resolution models of subduction zones: implications for mineral dehydration reactions and the transport of water into the deep mantle. Geochem Geophys Geosyst 3. doi:10.1029/2001GC000256

Van Roermund HLM, Carswell DA, Drury MR, Heijboer TC (2002) Microdiamond in a megacrystic garnet websterite pod from Bardane on the Island of Fjørtoft, Werstern Norway: evidence for diamond formation in mantle rocks during deep continental subduction. Geology 30:959–962

Van Sijl J, Allan NL, Davies GR, van Westrenen W (2010) Titanium in subduction zone fluids: frist insights from *ab initio* molecular metadynamics simulations. Geochim Cosmochim Acta 74:2797–2810

Vielzeuf D, Holloway JR (1988) Experimental determination of the fluid-absent melting relations in the Pelitic System. Contrib Mineral Petrol 98:257–276

Von Huene R, Scholl DW (1991) Observations at convergent margins concerning sediment subduction, subduction erosion, and the growth of continental crust. Rev Geophys 29:279–316

Vrijmoed JC, Van Roermund HLM, Davies GR (2006) Evidence for diamond-grade ultra-high pressure metamorphism and fluid interaction in the Svartberget Fe–Ti Garnet Peridotite–Websterite Body, Western Gneiss Region, Norway. Mineral Petrol 88:381–405

Vrijmoed JC, Podladchikov YY, Andersen TB, Hartz EH (2009) An alternative model for ultra-high pressure in the Svartberget Fe-Ti garnet-peridotite, Western Gneiss Region, Norway. Eur J Mineral 21:1119–1133

Wallmann K (2001) The geological water cycle and the evolution of Marine $\delta^{18}O$ values. Geochim Cosmochim Acta 65:2469–2485

Walther JV, Orville PM (1982) Volatile production and transport in regional metamorphism. Contrib Mineral Petrol 79:252–257

Watson EB, Brenan JM (1987) Fluids in the lithosphere, 1. Experimentally determined wetting characteristics of CO_2-H_2O fluids and their implications for fluid transport, host-rock physical properties, and fluid inclusion formation. Earth Planet Sci Lett 85:497–515

Wei C, Powell R, Zhang L (2003) Eclogites from the South Tianshan, NW China: petrological characteristic and calculated mineral equilibria in the Na_2O-CaO-FeO MgO-Al_2O_3-SiO_2-H_2O system. J Metamorph Geol 21:163–179

Wei C, Wang CGL, Zhang L, Song S (2009) Metamorphism of high/ultrahigh-pressure pelitic–felsic schist in the South Tianshan Orogen, NW China: phase equilibria and P–T path. J Petrol 50:1973–1991

Widmer T, Thompson AB (2001) Local origin of high pressure vein material in eclogite facies rocks of the Zermatt–Saas Zone, Switzerland. Am J Sci 301:627–656

Wu YB, Gao S, Zhang HF, Yang SH, Liu XC, Jiao WF, Liu YS, Yuan HL, Gong HY, He MC (2009) U-Pb Age, trace element, and Hf-Isotope compositions of zircon in a quartz vein from eclogite in the Western Dabie Mountains: constraints on fluid flow during early exhumation of ultrahigh-pressure rocks. Am Mineral 94:303–312

Xia QX, Zheng YF, Hu Z (2010) Trace elements in Zircon and coexisting minerals from Low-T/UHP Metagranite in the Dabie Orogen: implications for action of supercritical fluid during continental subduction-zone metamorphism. Lithos 114:385–412

Xiao YL, Hoefs J, van den Kerkhof AM, Fiebig J, Zheng Y (2000) Fluid history of UHP metamorphism in Dabie Shan, China: a fluid inclusion and oxygen isotope study on the coesite-bearing eclogite from Bixiling. Contrib Mineral Petrol 139:1–16

Xiao YL, Hoefs J, van den Kerkhof AM, Li S (2001) Geochemical constraints of the eclogite and granulite facies metamorphism as recognized in the Raobazhi complex from North Dabie Shan, China. J Metamorph Geol 19:3–19

Xiao YL, Hoefs J, Van den Kerkhof AM, Simon K, Fiebig J, Zheng YF (2002) Fluid evolution during HP and UHP metamorphism in Dabie Shan, China: constraints from mineral chemistry, fluid inclusions and stable isotopes. J Petrol 43:1505–1527

Xiao YL, Zhang Z, Hoefs J, Van den Kerkhof AM (2006) Ultrahigh-pressure metamorphic rocks from the Chinese continental scientific drilling project: II oxygen isotope and fluid inclusion distributions through vertical sections. Contrib Mineral Petrol 152:443–458

Xiong X, Keppler H, Audétat A, Gudfinnsson G, Sun W, Song M, Xiao W, Yuan L (2009) Experimental constraints on Rutile saturation during partial melting of metabasalt at the amphibolite to eclogite transition, with applications to TTG Genesis. Am Mineral 94:1175–1186

Xu S, Okay AI, Ji S, Sengör AMC, Su W, Liu Y, Jiang L (1992) Diamond from the Dabie Shan metamorphic rocks and its implication for tectonic setting. Science 256:80–82

You Z, Han Y, Yang W, Zhang Z, Wie B, Liu R (1996) The high-pressure and ultra-high-pressure metamorphic belt in the East Quinling and Dabie Mountains. China University of Geoscience Press, Wuhan

Zack T, John T (2007) An evaluation of reactive fluid flow and trace element mobility in subducting slabs. Chem Geol 239:199–216

Zack T, Rivers T, Brumm R, Kronz A (2004) Cold subduction of oceanic crust: implications from a lawsonite eclogite from the Dominican Republic. Eur J Mineral 16:909–916

Zhang YG, Frantz JD (2000) Enstatite-forsterite-water equilibria at elevated temperatures and pressures. Am Mineral 85:918–925

Zhang LF, Ellis D, Williams S, Jiang WB (2003) Ultrahigh-pressure metamorphism in eclogites from the western Tianshan, China - Reply. Am Miner 88:1157–1160

Zhang ZM, Shen K, Sun WD, Liu YS, Liou JG, Shi C, Wang JL (2008) Fluids in deeply subducted continental crust: petrology, mineral chemistry and fluid inclusion of UHP metamorphic veins from the Sulu Orogen, Eastern China. Geochim Cosmochim Acta 72:3200–3228

Zheng YF (2009) Fluid regime in continental subduction zones: petrological insights from ultrahigh-pressure metamorphic rocks. J Geol Soc 166:763–782

Zheng YF, Fu B, Gong B, Li L (2003) Stable isotope geochemistry of ultrahigh pressure metamorphic rocks from the Dabie-Sulu orogen in China: implications for geodynamics and fluid regime. Earth Sci Rev 62:105–161

Zotov N, Keppler H (2000) N-Situ Raman Spectra of dissolved silica species in aqueous fluids to 900°C and 14 kbar. Am Mineral 85:600–604

Zotov Z, Keppler H (2002) Silica speciation in aqueous fluids at high pressures and high temperatures. Chem Geol 184:71–82

Chapter 11
Prograde, Peak and Retrograde Metamorphic Fluids and Associated Metasomatism in Upper Amphibolite to Granulite Facies Transition Zones

J.L.R. Touret and T.G. Nijland

Abstract Granulites constitute a major part of the (lower) continental crust, occurring on a regional scale in many metamorphic belts. Their origin is generally discussed in terms of vapour-absent melting and fluid-assisted dehydration. This last model is notably supported by the occurrence of two immiscible free fluids at peak- and retrograde conditions, viz. CO_2 and highly saline brines. Evidence includes fluid remnants preserved in mineral inclusions, but also large scale metasomatic effects. The current paper discusses the presence and action of these fluids in granulites, with special attention to amphibolite to granulite facies transition zones (e.g. the Bamble sector, south Norway). Metasomatic effects induced by fluid percolation at different scales and stages include: (1) Control of state variables (H_2O activity or O_2 fugacity), regional oxidation and so-called 'granulite facies' islands. (2) Small scale metasomatism at mineral intergrain boundaries (e.g. K-feldspar microveins and/or myrmekites). (3) Large scale metasomatism at the amphibolite to granulite facies transition zone, evidenced by: (a) Incipient charnockites, (b) Metasomatic redistribution of elements traditionally considered as immobile (e.g. Zr, Th, REE), (c) Peak metamorphic to retrograde bulk chemical processes (scapolitization, albitization), (d) Long distance action of granulite fluids. The importance and widespread occurrence of these effects call for large fluid quantities stored in the lower crust at peak metamorphic conditions, later expelled towards shallower crustal levels during retrogradation. Fluid origin, only briefly discussed in this paper, is complicated, not unique. Some fluids are crustal, either far remnants of sedimentary waters (brines) or linked to metamorphic/melt reactions. But, especially for high-temperature granulites, the greatest amount, notably for CO_2, is issued from the upper mantle, which contain also the same fluid remnants as those found in the lower crust.

J.L.R. Touret (✉)
Musée de Minéralogie, Mines-ParisTech, 60 Boulevard St. Michel, Paris 75006, France
e-mail: jtouret@ensmp.fr

T.G. Nijland
TNO, P.O. Box 49, AA Delft 2600, The Netherlands

D.E. Harlov and H. Austrheim, *Metasomatism and the Chemical Transformation of Rock*, Lecture Notes in Earth System Sciences,
DOI 10.1007/978-3-642-28394-9_11,

11.1 Introduction

Granulites constitute a major part of the (lower) continental crust and are spread, on a regional scale, in many metamorphic belts, especially in Precambrian shield areas. They are typically characterized by water-free (pyroxene, garnet) or water-poor mineral assemblages. Though water-poor, granulites are by no means fluid-free rocks. Since the early 1970s, it has been claimed, notably by the senior author, that two immiscible free fluids are present at peak conditions, viz. CO_2 and highly saline brines (e.g. Touret 1985). These findings were in line with early suggestions by D.S. Korzhinskii, first proposed in 1940 and elaborated in a series of papers culminating in his 1959 English language treatise *Physicochemical basis of the analysis of the paragenesis of minerals*. Korzhinskii explained charnockite/granulite-forming mineral reactions by variation in chemical potentials, such as a high μK_2O for the formation of K-feldspar and a low μH_2O for the stabilisation of anhydrous mineral assemblages. He concluded that such variations are due to processes of fluid-rock interaction. This line of research has since been developed by many Russian geologists, on the basis of field observations, theory and experiments (see e.g. reviews by Perchuk and Gerya 1992, 1993). This model can be designed as *fluid-assisted metamorphism*. Fluids play an active role, being able to dissolve, transport and deliver chemical element to form minerals. In contrast, many Western geologists researchers have been inclined to favour a *vapour-absent* or *fluid-absent model* (*fluid-absent metamorphism*; Thompson 1983). In this model, no free fluid is present at peak metamorphic conditions, all fluid components (e.g. H_2O for water-bearing mineral phases) are either bound in mineral structures or dissolved in melts. Though the presence of fluids during granulite facies metamorphism is still debated (e.g. Rigby and Droop 2011), it is clear, at least for present authors, that the so-called granulite controversy, which has lasted for more than 40 years now, has come to an end. Nobody denies that dehydration melting, the major process involved in vapour-absent models, is of major importance for the formation of many granulite facies terrains. But, as discussed in Sect. 11.3 of this chapter, dehydration melting is quite compatible with the occurrence of different low H_2O-activity fluids. Two major fluids are found in granulites, viz. CO_2 and brines. An impressive set of arguments demonstrates that these occur in granulites at both peak and retrograde metamorphic conditions. They differ radically in terms of transport properties and the ability to dissolve solid phases (Newton and Manning 2010). Their occurrence, however, implies that large-scale, fluid-assisted mass transport of elements, called *metasomatism* by Naumann (1826), could occur. The relative roles of metamorphic versus metasomatic effects have been discussed since, e.g. Goldschmidt (1922), Ramberg (1951, 1952), Korzhinskii (1959) and Putnis and Austrheim (2010). However, if such metasomatic effects do exist, they provide (additional) proof of the reality of these fluids. Consequently, understanding the role and significance of theses fluids is of major importance for the formation of the continental crust. To do so, it is necessary to first consider the position of granulites in a vertical section of the continental crust. Subsequently,

major evidence for the presence and action of fluids during granulite facies metamorphism will be presented and discussed as a basis for an integral understanding of granulite formation, paying special attention to the amphibolite to granulite facies transition zones. As the Bamble sector, southern Norway, provides one of the best records of fluids in granulites, we will describe it in several parts of this chapter, incorporating crucial and salient observations from other granulite facies terranes.

11.2 Background: A Granulite Continental Lower Crust

Compared to high pressure rocks within the eclogite facies, high temperature rocks comprise various types of granulites, from the (relatively) low pressure varieties (LP, P > about 5 kb, T > about 750°C) to high temperature (HT) and ultra-high temperature (UHT) types, which can reach temperatures covering part of the magmatic range (> 1,000°C). Most common are intermediate granulites, with T about 700–800°C, P = 7–8 kb, occurring notably in large, regional-scale complexes (e.g. Harley 1993). Granulites, characterized primarily by water-deficient mineral assemblages (orthopyroxenes, clinopyroxenes, garnets; Fig. 11.1) are transitional to amphibolite facies rocks, notably the granitic migmatites, which are themselves the most commonly occurring igneous rocks in the continental crust. A great number of data, including P-T mineral estimates, LILE and trace element geochemistry as well as geophysical density and electrical conductivity measurements, suggest that the amphibolite and granulite facies correspond broadly to a vertical section of the continental crust (Beloussov 1966; Rudnick and Fountain 1995).

Granitic migmatites are the most common rock type in the middle crust between approximately 5 km, the typical level of emplacement of most granites, and about 20 km (e.g. Guillot et al. 1995). The lower crust down to the Moho (generally at a depth of about 40 km under the majority of the continental cratons) is the domain of granulites. This implies that the latter constitute about one third of the entire continental land mass. Only small parts of this huge domain have reached the Earth's surface through orogenic uplift, often suffering intense deformation and retrogression. Granulites were for a long time considered as petrographical oddities, restricted to few exotic countries (India, Madagascar; e.g. Lacroix 1910). For instance, in Rinne's 1928 textbook, which served as the standard reference for all French petrologists until the late 1950s, the name charnockite is hardly mentioned (orthopyroxene-bearing granite). Granulites, to which Rinne devoted only two whole pages of description, are presented in a very confusing way. They are considered as purely magmatic rocks and defined as muscovite-bearing granites, following the French tradition of that time. However, at the same time, examples are given of typical granulites in current sense such as the Sri Lankan graphite-bearing granulites, as well as of textural features such as platy quartz that are typical for Saxonian granulites. Recognition of the geological

Fig. 11.1 Example of typical granulite facies orthopyroxene-bearing veins at Hove, Tromøy, Bamble sector, Norway

importance of granulites occurred in the late 1970s, when it was progressively realized that the average composition of the continental crust was less magmatic (granitic) than had been assumed since the nineteenth century, but instead metamorphic, with remnants of supracrustal (i.e. sediments and eruptive rocks) that survived at the highest metamorphic grades. In the same period, deep crustal granulites were recognized amongst xenoliths from active volcanoes, in addition to a greater number of upper mantle rocks (e.g. Lovering and White 1969; Nixon 1987; Amundsen et al. 1988; Kovacs and Szabo 2005; Montanini and Harlov 2006), confirming the observations a century before from the French Massif Central (gneiss à pyroxène; Lacroix 1893). They document a systematic change in the composition of the granulite lower crust with depth (Bohlen and Mezger 1989; Bohlen 1991). The upper part is purely metamorphic, corresponding to regionally exposed granulite complexes, whereas recrystallized magmatic rocks, mostly gabbroic in composition (two pyroxene-granulites), dominate the lower part down to the upper mantle (Moho). The source of these gabbroic rocks is upper mantle plagioclase- or spinel-lherzolites residing at depths not exceeding 60–70 km. The timing of the emplacement of these magmas is often close to peak metamorphism, e.g. the French Massif Central (Vielzeuf and Pin 1989). Such intrusions provide the required heat for HT and UHT-metamorphism. As will be discussed below, we believe that they also play a key role in establishing the fluid regime in this part of the crust.

The transition zone between amphibolite and granulite facies rocks is quite complicated. It is marked by a number of prograde mineral isograds, corresponding to the (dis)appearance of diagnostic minerals, e.g. muscovite-out, biotite-out, orthopyroxene-in, cordierite-in, garnet-in, in terranes like the Adirondacks, US

(Engel and Engel 1958, 1960), Broken Hill, Australia (Binns 1964), the Bamble sector, Norway (Touret 1971; Nijland and Maijer 1993) and the classical granulites from Saxony (Rötzler 1992) or even osumilite-in in UHT granulites, like Rogaland, Norway (Tobi et al. 1985). Other index minerals in progressive granulite facies metamorphism include the more localized occurrence of minerals like sapphirine, spinel + quartz, kornerupine, etc. Additional petrological indicators that can be used include the degree of partial melting, the occurrence of quartz-garnet symplectites in some mobilisates, etc. However, the interpretation of these features in terms of variable P and T is even more difficult than that of the mineral reactions, though the latter is far from being straight forward (Chap. 3). Most minerals are complex solid solutions connected to each other by multivariant equilibria. The large number of chemical and physical variables affecting an isograd can lead to complicated map patterns with intersecting isograds (Fig. 11.2). In some cases, it is hard to identify whether these isograds are prograde (transition amphibolite to granulite) or retrograde (retrogressed granulite). Identification is only possible if the relationships between the consumed phases and the product phases are unambiguous. In some areas, the amphibolite to granulite facies transition is considered to be a retrograde feature (e.g. the Limpopo belt; Van Reenen 1986; Ungava orogen, Canada; St Onge and Lucas 1995). The complex nature of the granulite facies is clear on a conventional P-T diagram (Fig. 11.3). Whereas the boundaries separating high pressure facies (blueschist and eclogite) from high temperature facies (greenschist, amphibolite and granulite) are relatively well defined, boundaries delimiting the granulite facies are never represented by a sharp line, but by a rather broad, diffuse band.

On a regional scale, it is clear that temperature plays an important role in the amphibolite to granulite transition. Overall, temperature tends to be higher in granulites than in neighbouring amphibolites. In detail, however, the situation is often much more complicated, as illustrated by the case of the Bamble sector, southern Norway (Fig. 11.2). Here, mineral isograds differ grossly from isotherms, maximum temperatures (above 800°C, typical for most intermediate pressure granulites) being reached in a dome situated in the northern part of the granulite core east of the town of Arendal extending in this direction within the neighbouring amphibolite (Nijland and Maijer 1993). This situation is by no means exceptional. Even if it has been rarely documented in detail, it is our experience, from various field studies in Finland, Sweden and the Variscan belt that it occurs in many granulite facies terranes worldwide. It is for this reason that, on Fig. 11.3, we have represented the granulite and amphibolite fields as partly overlapping (shaded area on Fig. 11.3). In this zone, another variable of state is required to initiate and control the transition from amphibolite to granulite facies mineral assemblages. This variable is P_{H2O} as most reactions involve dehydration. It is significantly lower than lithostatic pressure in the granulite facies terrane, whilst nearly equal to the lithostatic pressure in the amphibolite domain.

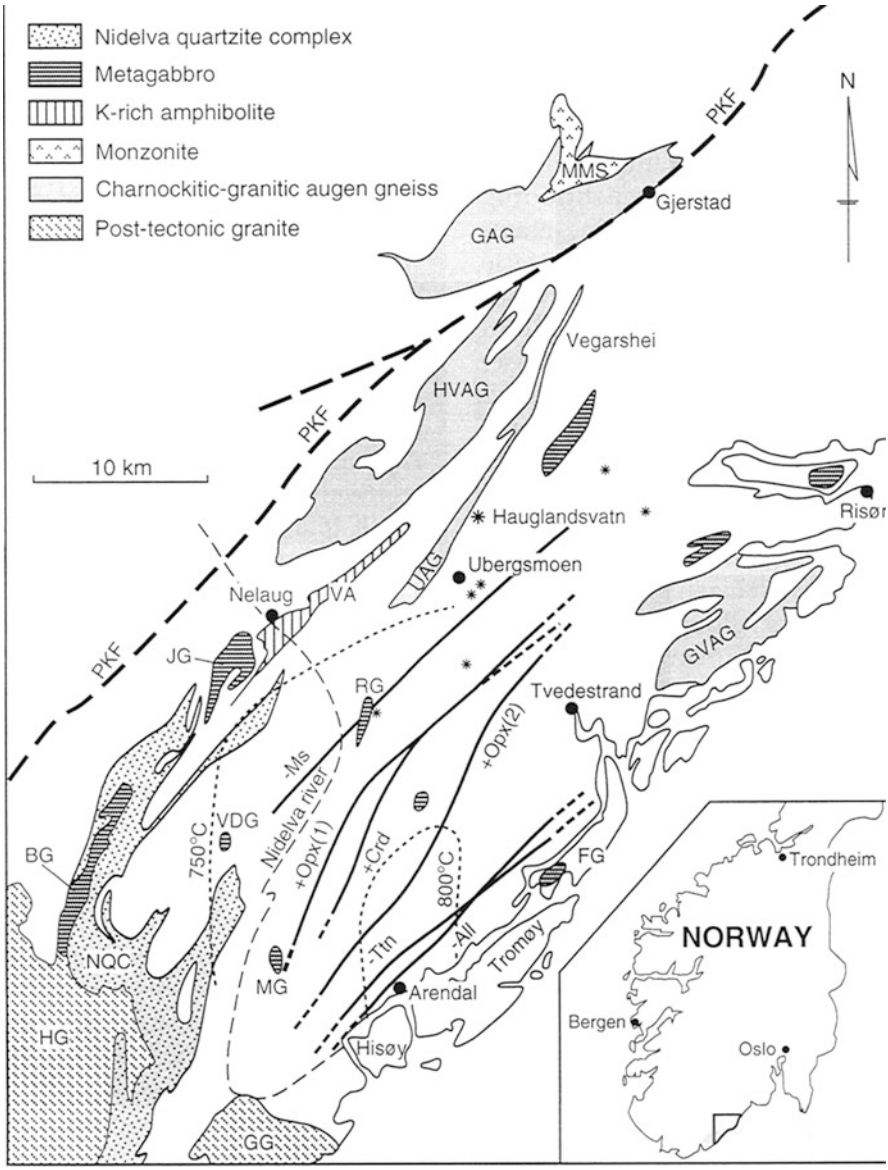

Fig. 11.2 Generalized metamorphic map of the Bamble sector, south Norway (Nijland et al. 1998), indicating metamorphic isograds (continuous lines, + = appearance, - = disappearance of diagnostic minerals; +Opx(1): in basic rocks, +Opx(2): in metapelites) and isotherms (*dashed lines*), as well as so-called granulite facies islands (*stars*; see text). Geological units: *BG* Blengsvatn gabbro, *FG* Flosta gabbro, *GAG* Gjerstad augen gneiss, *GG* Grimstad granite, *GVAG* Gjeving augen gneiss, *HG* Herefoss granite, *HVAG* Hovdefjell-Vegårshei augen gneiss, *JG* Jomåsknutene gabbro, *MG* Messel gabbro, *MMS* Morkheia monzonite suite, *NQC* Nidelva quartzite complex, *PKF* Porsgrunn-Kristiansand fault, *RG* Ripåsen gabbro, *VA* Vimme amphibolite, *VDG* Vestre Dale gabbro

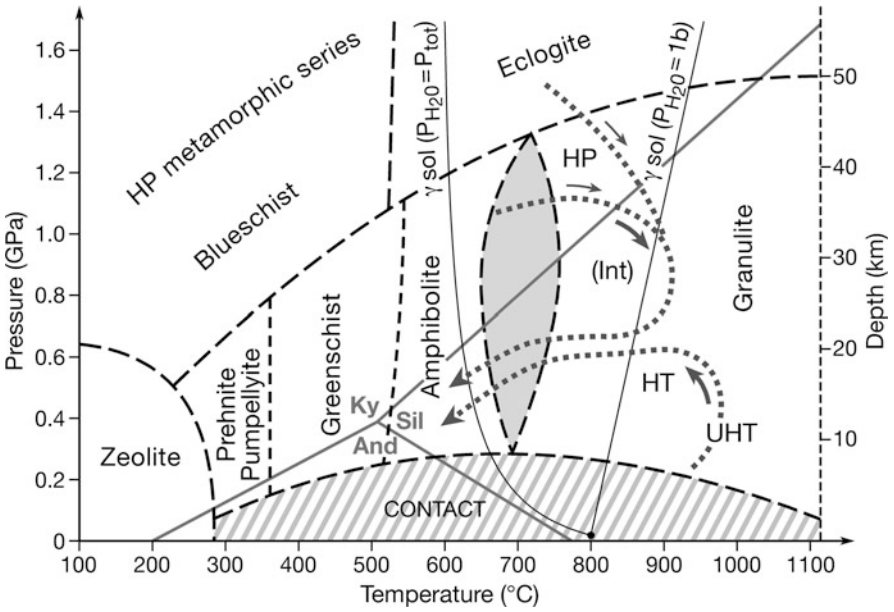

Fig. 11.3 Major metamorphic facies in P-T space for $P_{H2O} = P_{Total,}$ except in granulite; this explains the partial overlap of amphibolite and granulite facies, indicated as a *shaded area* on the figure. In this portion of an amphibolite to granulite facies transition zone is not explained by an increase of temperature but by a decrease of P_{H2O} relative to P_{Total}. Subdivisions of the granulite facies are indicated as *HP* high pressure, *HT* and *UHT* high to ultrahigh temperature, and Int-Intermediate. *Dots* with *arrows* indicate typical P-T paths, either clockwise (in HP-granulites) or anticlockwise (in HT-UHT-granulites)

11.3 Granulites: Vapour-Absent Melting or Fluid-Assisted Dehydration?

P-T conditions for both upper amphibolite and granulite facies rocks are all above the hydrous granite minimum melting curve. These rocks are the source of crustal granites (typically S-types) which, when formed in the amphibolite facies domain, are H_2O-saturated and crystallize rapidly above the migmatite source (midcrustal granites). Water undersaturated lower crustal granites, on the other hand, may rise to higher levels, reaching the upper crust or even the Earth's surface in the form of rhyolite eruptions (Clemens 2006). Being able to dissolve and transport fluids, notably H_2O, these granitic magmas obviously can play an important role for regulating the fluid regime at peak metamorphic conditions. Following a seminal paper by W.S. Fyfe (1973) on the Lewisian complex in Scotland, a first, purely magmatic model was proposed for the formation of granulites, in line with ideas prevailing during the first half of the twentieth century (see above). This model was later extended to many other terranes including Broken Hill, Australia (Phillips 1980),

New England, US (Tracy and Robinson 1983) and Namaqualand, South Africa (Waters 1988).

The model of vapour-absent (dehydration) melting involves breakdown of hydrous phases such as muscovite, biotite and amphibole, releasing water as well as other interstitial fluids (e.g. Le Breton and Thompson 1988). The released water is partitioned into melts and subsequently removed by melt extraction. In this hypothesis, granulites are restites, with no fluids remaining at peak metamorphic conditions (e.g. Vielzeuf et al. 1990). This model is supported by a number of microstructural, experimental, and theoretical investigations (e.g. Thompson 1982; Brown and White 2008). Being purely magmatic, it does not leave much room for any large scale metasomatic processes. Only limited diffusion metasomatism on the millimetre to centimetre scales between coexisting phases of contrasting compositions, permitted by high metamorphic temperatures, is possible. These include corona textures, spectacular in some high temperature (HT) granulites, but even more developed in high pressure metamorphic rocks (HP granulites, eclogites). For this reason, also because they are well discussed in the literature (e.g. Yardley 1989; Harley 1989), as well as in Chaps. 5 and 10 of this volume, these textures will only be marginally considered in this chapter. Moreover, at least in some cases, including the coronitic gabbros of southern Norway (formerly referred to as hyperites), compelling evidence suggest that in some of these gabbros the coronas are caused by interaction with residual melts, rather than being of metasomatic origin (Joesten 1986; De Haas et al. 2002).

The discovery of low water activity fluids (CO_2, concentrated brines) included in many granulite minerals (Touret 1971, 1972, 1973; Figs. 11.4, 11.5), combined with theoretical and experimental work done by D.S. Korzhinskhii and his followers (e.g. Aranovich et al. 1987) has led the other model for granulite genesis, namely *fluid-assisted dehydration* (e.g. Janardhan et al. 1979; Newton et al. 1980). Under the influence of these low water activity fluids, hydrous mineral such as muscovite, biotite, amphiboles breakdown to granulite mineral assemblages whilst producing water. The water produced becomes diluted. This model does not negate partial melting at all. In fact, partial melting is an efficient way to produce some of these low water activity fluids such as CO_2, either due to preferential dissolution of H_2O into granitic melts (Kadik et al. 1972), reaction of graphite (former organic matter) with H_2O (Touret and Dietvorst 1983) or possibly residual brines. There is no doubt that some melts are extracted leaving behind residual granulites, especially in zones of intense shearing and deformation. However, the astonishing preservation of delicate sedimentary structures such as graded or cross bedding, mudcracks and conglomerates in quartzitic sediments in the transition zone (Nijland et al. 1993) and even in migmatitic quartzo-feldspathic gneisses where partial melts remained in situ (e.g. Selås gneisses, Touret 1966) shows that, even in the most structurally complicated terranes, strain-free domains exist, in which post-crystalline deformation is virtually absent. These features illustrate the metasomatic character of the amphibolite-granulite transition, namely mineralogical changes at nearly constant volume without melting. This is illustrated by an impressive series of features including granulite oxidation states, grain boundary microtextures and

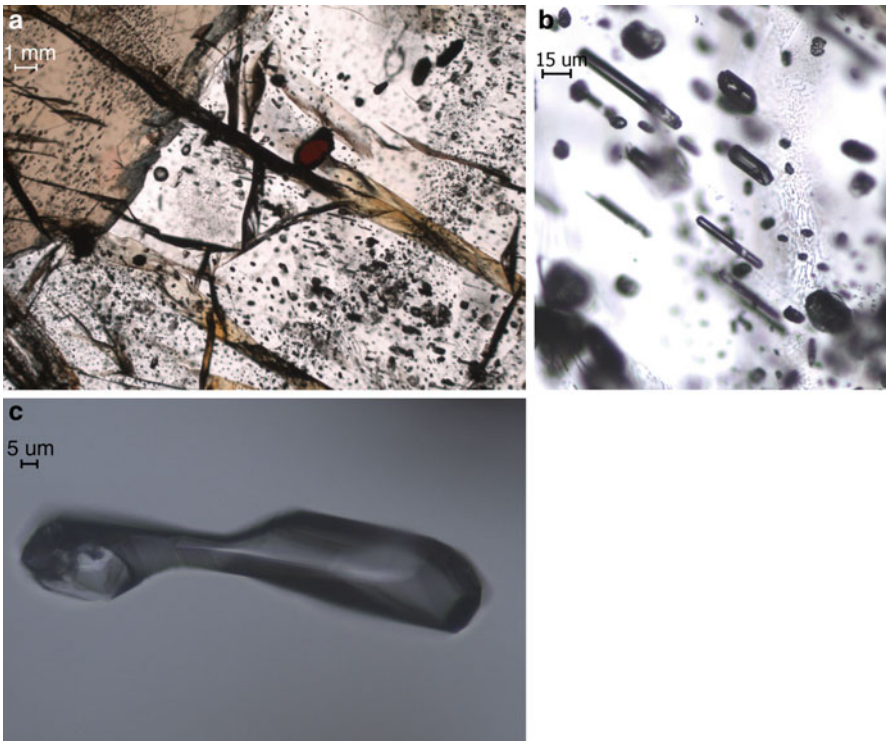

Fig. 11.4 Examples of CO_2-rich fluid inclusions in sapphirine-bearing granulites from central Sri Lanka (Bolder-Schrijver et al. 2000). (**a**): Overall view of major rock-forming minerals in thick section with garnet to the *right* and orthopyroxene to the *left*. (**b**): Array of tubular primary inclusions in garnet; *dark* inclusions are filled by high-density CO_2, *white* inclusions are daughter crystals of magnesite; detail of CO_2-inclusion in garnet

incipient charnockites (see below). The scale and extent of these features requires infiltration (percolation) metasomatism in the sense of Korzhinskii (1959, 1968). It also requires a number of necessary conditions, some of them at odds with commonly accepted hypotheses, notably by advocates of vapour-absent models:

- A significant quantity of fluids is present in the lower granulite crust (and in the underlying mantle) at peak metamorphic conditions.
- These fluids are able move through the rock masses, at a level where, classically, no fluid movement is supposed to occur, except along rare, discrete shear zones (Etheridge et al. 1983).
- The fluids can have a profound geochemical action, either in the control of some variables of states (first of all P_{H2O}) or in dissolution and transport of chemical components involved in metasomatic reactions and mineral genesis.

Except for the minute remnants preserved as fluid inclusions in minerals, most deep fluids have left the rock system before eventual uplift and exposure at the

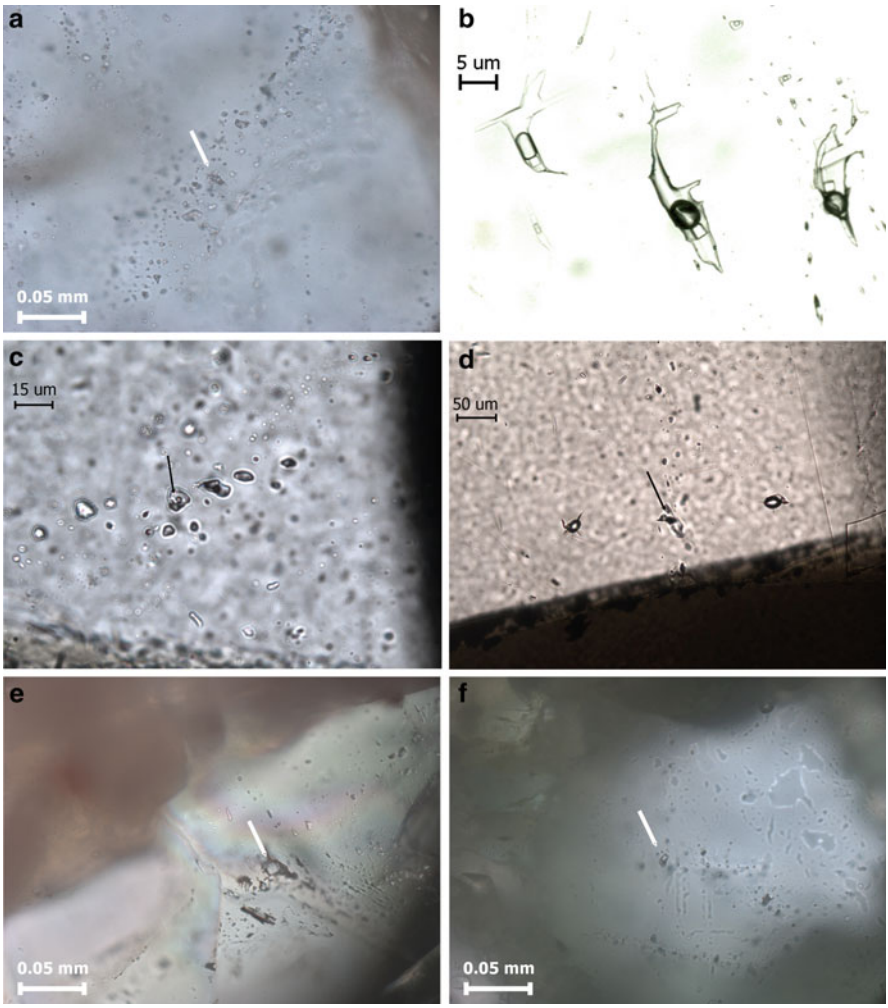

Fig. 11.5 Examples of brines inclusions in granulites and associated rocks from the Bamble sector, Norway. (**a**): brine inclusion from a so-called granulite facies island, Hauglandsvatn (Nijland et al. 1998). (**b**): brine inclusion in quartz-actinolite rock. (**c**,**d**): brine inclusions in cordierite-anthophyllite rock hosting giant myrmekites from Åkland with C a squeezed brine inclusion in cordierite accompanied by small solid inclusions of zircon and D in quartz blebs in cordierite. (**e**): brine in apatite from the former Lykkens mine, Kragerø. (**f**): brine inclusion in scapolite in rutile-scapolite-pargasite rock from Ødegårdens Verk

Earth's surface. But, as discussed in detail below, the existence and abundance of fluids in granulite facies is documented by the numerous traces that they have left in the rocks. Description of these features is the core of this chapter. However, it is first necessary to justify the presence of these fluids, as they are critical for the existence of metasomatic processes at this deep level of the continental crust.

11.4 Free Fluid Phase During Granulite Metamorphism

11.4.1 Fluid Inclusion Data

The revolutionary idea that some free fluids can exist at peak metamorphic granulite conditions, at a temperature of 800–1,000°C and a depth of many 10s of kilometres, come primarily from fluid inclusion data, first described in southern Norway (Touret 1971), then in virtually all granulite facies terrains (Newton 1989). Ignoring minor components such as N_2 or CH_4, found in some high grade terranes, two types of fluids are systematically observed:

- Pure CO_2 of variable density (Fig. 11.4), reaching more than 1.1 g cm^{-3} in the case of ultradense inclusions as described by Van den Kerkhof and Olsen (1990) from the Colorado Front Range, USA, from many localities in India including Dodabetta (Touret and Hansteen 1988; Srikantappa et al. 1992), Nuliyam, Kerala (Fonarev et al. 2001), eastern Ghats (Mohan et al. 2003), Salem area south of the Shevaroy Hills (Santosh and Tsunogae 2003), Nagercoil (Santosh et al. 2003) and the Chottanagpur complex (Mishraa et al. 2007), as well as the Napier complex, Antarctica (Tsunogae et al. 2002), In Ouzzal, Algeria (Cuney et al. 2007) and the Gandese charnockites, southern Tibet (Zhang et al. 2011).
- Highly saline aqueous inclusions (brines; Fig. 11.5), typically with 20–30 mol% equivalent NaCl, approaching pure salt in a few extreme cases (Touret 1985; Frost and Touret 1989). In the literature, brine inclusions are much less frequently reported than CO_2-bearing ones. However, brines also occur in classic granulite areas from which up to recent only CO_2-bearing ones have been described, like southern India (Srikantappa and Arash Zargar 2009). It is noteworthy that rather similar fluids have also been encountered in rocks from deeper levels in the mantle (Izraeli et al. 2001; Klein-BenDavid et al. 2004).

It has been argued that the CO_2 (brines were not considered at this time) represents late fluids, unrelated to granulite metamorphism (Lamb et al. 1987). It is true that both fluids are constantly found during all the steps of retrograde metamorphic evolution. In fact, recent detailed investigations of the Bamble sector rocks (Sørensen 2007) show that they act as a sort of shield, protecting high grade mineral assemblages against surficial retrogression. Traces of this superficial retrogression, due to encounters with surface waters during the final stages of uplift, are quite widespread. This retrogression is, for example, responsible for the fact that French petrologists have ignored until very recently that the southern Vosges and Massif Central are typical granulite provinces. They considered only relatively late, intrusive granites, that make up only a small fraction of the exposed rocks.

But, as discussed in many papers (Coolen 1980, 1982; Touret and Hartel 1990; Santosh 1992; Santosh et al. 1991), the reality of synmetamorphic granulite fluids can hardly be questioned. Their existence is proven by a set of three, concordant arguments: synchronism of inclusion formation and mineral crystallization (primary inclusions), concordance between CO_2 density (isochores) and P-T mineral

data, and fluid compositions in agreement with those predicted from mineral assemblages (Touret 2009). Contrary to conventional wisdom, quartz is not the best mineral host in granulites. Other minerals (garnet, feldspars) may contain many more, larger and better preserved inclusions than the neighbouring quartz (Srikantappa et al. 1992).

Not only fluid inclusions demonstrate the presence of a free fluid phase during granulite facies metamorphism. Mineral assemblages may also indicate the former presence of free CO_2 and/or saline solutions. This holds notably for CO_2-scapolite-bearing granulites (Goldsmith 1976; Aitken 1983; Moecher and Essene 1990, 1992; Moecher 1993) which have been described from a number of granulite terranes, including SW Finland (Parras 1958), Furua, Tanzania (Coolen 1980, 1982; Hoefs et al. 1981), the Aldan shield, Siberia (Perchuk et al. 1985), Fiordland, New Zealand (Bradshaw 1989) and the Kohistan arc, NW Himalayas (Yoshino and Satish-Kumar 2001). Though once considered as common (e.g. Turner and Verhoogen 1960), the number of documented occurrences is relatively small, possibly indicating that most CO_2-bearing scapolites were destroyed during uplift, leading to liberation of CO_2 during this stage of evolution.

Anyone studying fluid inclusions will immediately find that if remnants of both CO_2 and brines can be found in most granulites, their relative abundance and state of preservation are rather different. CO_2 may occur as large, spectacular inclusions several tens of micrometres in size and often negative-shaped (Fig. 11.4). Most granulite complexes show post-metamorphic P-T paths with generally isobaric cooling, i.e. roughly parallel to high density CO_2 isochores, favouring the preservation of CO_2 inclusions (cf. Touret and Huizenga 2011) (Fig. 11.6). Brines, on the other hand, occur only in minute inclusions of only a few micrometres, with an irregular cavity often squeezed around one of several solids (halides) (so-called collapsed inclusions; Touret 2001) (Fig. 11.5). The steeper brine isochores cause these inclusions to be constantly underpressed and transposed until final decompression, which typically occurs at temperatures of about 300–350°C (Fig. 11.6).

11.4.2 Deep Fluids Can Move Through the Rocks

Permeability estimates of the lower crustal conditions are very low (Fyfe et al. 1978), which is apparently incompatible with large fluid movements through these rocks. Nevertheless, focussed fluid flow has been demonstrated to occur at all levels (e.g. Ague 2003 and references therein). The absence of large fluid movements in the lower crust does not comply with some common observations on fluid inclusions. Most granulites contain numerous trails of secondary inclusions, most of them CO_2, trapped over a wide P-T range. Detailed observations on the CO_2 density evolution show that it follows the inferred P-T path closely, with a density increase for relatively late inclusions in the case of isobaric cooling and a density decrease in the case of isothermal decompression (Touret 2001). This indicates that significant quantities of dense CO_2 were able to move through the rocks through

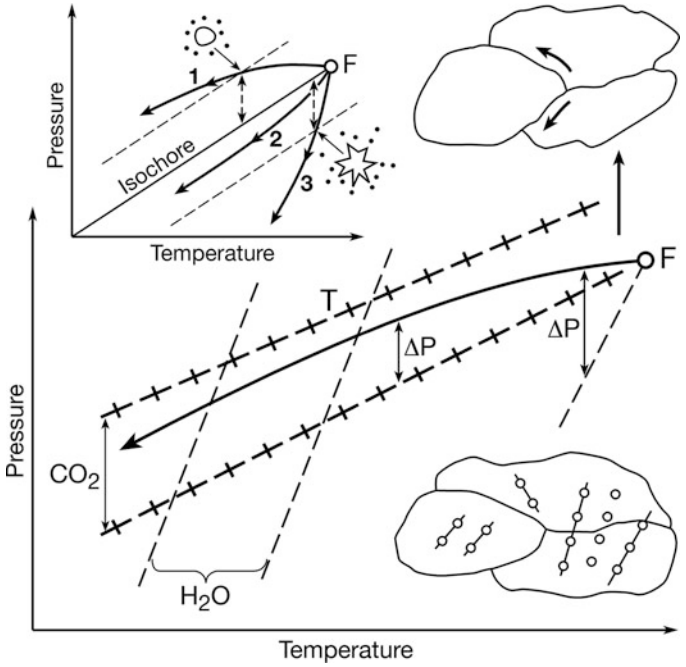

Fig. 11.6 Diagram illustrating how deep fluid inclusions can (or cannot) reach the Earth's surface. *Crosses* and *dashed lines*: relevant CO_2 and H_2O isochores, respectively; *solid lines* (with *arrow*): postmetamorphic P-T paths. At any temperature, the distance between both lines defines a pressure difference (ΔP) which, when exceeding the strength of a mineral host, leads to inclusion rupture, either by implosion (collapsed inclusions; path 1 (insert)) or explosion (decrepitation; path 3 (insert)). If a P-T path remains close to an isochore (path 2 (insert)), inclusions may remain undisturbed until the surface. On the insert, F indicates an inclusion formation at peak P-T conditions, whereas the grain sketches show typical ways of fluid migration through rocks at high P-T: H_2O moves along interstitial grain boundaries; CO_2 moves through successive generations of microfractures, forming trails of secondary inclusions

a system of microfractures, which were successively opened and then healed after a short period of time (*fluid-induced fracturing*, Putnis and Austrheim 2010, Chap. 5). In many cases, most inclusions belonging to the same fracture represent a group of synchronous inclusions (GSI), i.e. they have formed at almost the same time, as shown by the same homogenisation temperature with a typical variation of only a few degrees Celsius (Touret 2001).

Healing occurred at nearly constant temperature by the solubility change induced by surface tension effects in very narrow cavities (Lemmlein 1951). Most fluids initially contained in the open crack are expelled during this healing, causing the formation of another microcrack in the neighbourhood. But, due to the large wetting angle of CO_2 (Holness 1992; Watson and Brenan 1987; Gibert et al. 1998), some inclusions will remain regularly aligned in the plane of the former fissure, forming the typical trail that we see today. It is much more difficult for CO_2

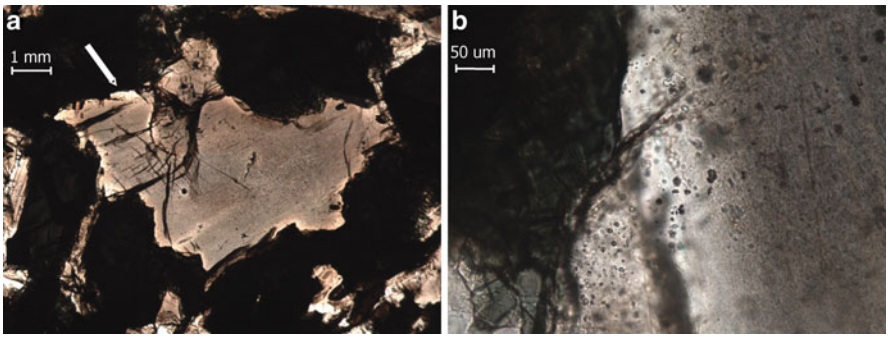

Fig. 11.7 Metagabbro from the Anápolis-Itauçu complex, Brazil: *Left*: Magmatic plagioclase appearing *grey* with along its margin clear white metamorphic plagioclase (*arrow*). *Right*: detail of the recrystallized margin with CO_2 fluid inclusions appearing as *black dots*

than H_2O to travel along grain boundaries, as noted by many authors (e.g. Watson and Brenan 1987). It is, however, to a limited extent not impossible as is illustrated by many granulite facies metagabbroic rocks. In many of deep-seated gabbroic and anorthositic intrusions transformed into two-pyroxene granulites during metamorphism, magmatic feldspars are still present, as indicated by numerous inclusions of ilmenites and other Fe-Ti oxides. A good example is the metagabbro shown in Fig. 11.7, from the Anápolis-Itauçu complex in central Brazil, a key locality for the characterization of UHT granulite metamorphism (Harley 2008). In this metagabbro, magmatic plagioclases, coeval with granulite metamorphism are very dark, due to a great number of minute opaque ilmenite inclusions (Della Giustina et al. 2010) (Fig. 11.7a). In contrast, recrystallized metamorphic plagioclase, formed along the borders or major fractures of magmatic crystals, is very clear and free of solid inclusions. It contains a number of minute, primary CO_2 inclusions, which only occasionally grade into the periphery of the magmatic plagioclase in the form of very small, pseudo-secondary trails (Fig 11.7b). It is interesting to note that the Anápolis-Itauçu case is precisely a case of *fluid-resaturation* of an initially dry, CO_2-undersaturated, mineral assemblage (Table 4 in Rigby and Droop 2011). This shows that CO_2-rich fluids, which are normally much less mobile than brines at intergrain boundaries (see below), can move to a certain extent along grain boundaries, provided that fluid movement is accompanied by sufficient recrystallization of the mineral host. Also granitic melts may, to some extent, dissolve CO_2 (Eggler and Kadik 1979). This implies that migmatic leucosomes may provide a transport medium (e.g. Frost and Frost 1987). The occurrence of dense CO_2 inclusions in granites contemporaneous with granulite facies metamorphism (Santosh et al. 2005) shows that this may be of significance in at least some granulite terrains.

Brines move in a very different way than CO_2 (cf. Gibert et al. 1998). During typical post-metamorphic granulite isobaric cooling paths, brine inclusions behave differently than CO_2 inclusions due to the different slopes of the H_2O and CO_2 isochores (Fig. 11.6). Also, the very small wetting angle of brines prohibits the

formation of secondary trails, in contrast to CO_2. Compared to CO_2, brines exhibit high mobility along grain boundaries, as evidenced by the numerous traces that they have left within rocks. With this respect, it is interesting to recall the so-called catastrophic textures described by Trommsdorff and Skippen (1986). These consist of a sudden increase in the mineral grain size, sometimes by one or two orders of magnitude, at places where concentrated brines, originating from fluid immiscibility, occur in high grade rocks. This role of brines, i.e. favouring large crystal sizes, illustrates the large capacity of element transport of this medium, quite different in this respect of the more *inert* CO_2 fluids (Newton and Manning 2010).

11.5 Metasomatic Effects Induced by Fluid Percolation

The fact that CO_2 and brines may have been present at granulite conditions and able to move through rock masses, notably during the early stages of post-peak metamorphic uplift, implies that they can induce large-scale metasomatic effects. This requires that mineral solubilities are high enough at the P-T conditions of interest to cause mineral transformations through dissolution-recrystallization/reprecipitation processes (Putnis 2002, 2009, Chap. 5). Solubilities of rock-forming minerals in CO_2 are generally very low. For example, quartz solubilities can only be measured in H_2O + CO_2 fluids, not in pure CO_2 (Novgorodov 1977; Newton and Manning 2010). The CO_2 fluid can only act as a neutral component in the overall fluid. The primary silicate solvent in the fluid is the H_2O component. However, the presence of alkali carbonates, such as nahcolite, $NaHCO_3$, in carbonic inclusions from several terrains, e.g. In Ouzzal, Algeria (Cuney et al. 2007), demonstrates the capability of this fluid to transport alkali, as well as trace elements commonly associated with carbonates, such as REE (e.g. Kontak and Morteani 1983), with a preference of the HREE over the LREE (Hellman et al. 1979; Humphries 1984; Michard and Albarède 1986).

In contrast to CO_2, mineral solubilities can be quite high in brines, as documented by the ongoing work of the UCLA group (Newton and Manning 2002, 2006, 2007, 2008, 2010). Presence of NaCl in the fluid will enhance solubility of phases like monazite and xenotime (Tropper et al. 2011). If P and T variations are large enough, – a necessary condition for some minerals to be dissolved and others to be precipitated–, metasomatic processes may leave their tracks within rocks. The mechanism behind mineral re-equilibration in these metasomatic reactions is covered extensively by Putnis (2002, 2009), Putnis and Austrheim (2010) as well as in Chap. 5 of this book. There are many lines of evidence for metasomatic alteration in granulite facies rocks, which can occur on all scales, from minute structures at intergranular boundaries to larger scale replacement of entire rock masses. Previously, they have either been ignored or considered to be limited to a few odd areas. Nowadays, such metasomatic effects have been documented from many areas and are especially obvious in the amphibolite to granulite facies transition zone.

Evidence for metasomatism will be described in an order which reflects an increasing scale of alteration:

- Control of state variables (H_2O activity or O_2 fugacity).
- Small scale metasomatism at intergranular boundaries (myrmekites, K-feldspar microveins)
- Large scale prograde and retrograde metasomatism in the amphibolite to granulite facies transition zone:
  - Incipient charnockites
  - Metasomatic redistribution of elements traditionally considered as *immobile* (e.g. Zr, Th, REE)
  - Peak metamorphic to retrograde bulk chemical processes (scapolitization, albitization)
- Long distance action of granulite fluids by fluid focussing in shear zones.

11.5.1 Control of the Variables of States, Regional Oxidation, and Granulite Facies Islands

One of the most obvious effects of granulite facies fluids is the control of some variables of state, first of all the partial pressure of H_2O, which for low values (typically up to about 0.3 of P_{Total}) is compatible with granulite facies mineral assemblages. This can be realized by the presence of a low H_2O activity fluid phase, rapidly released during prograde metamorphism (Chap. 14), as argued above either CO_2-rich fluids or concentrated brines. The widespread occurrence of CO_2 within the rock masses, not exclusively along grain boundaries, suggests that, within granulite domains, a low H_2O activity is mainly due to dilution by CO_2. The scarcity of adequate mineral reactions, as well as required CO_2 amounts, requires an external origin for this fluid. Demand for an external source is illustrated by the Bamble sector, south Norway, in which CO_2-bearing fluids are a prominent feature, but which is almost devoid of carbonate rocks whose decarbonation could have provided free CO_2. Many arguments, including C- or He-isotopes (e.g. Pineau et al. 1981; Dunai and Touret 1993; Santosh et al. 1993), can be made that the source is mainly the mantle (see discussion in Touret 2009). This CO_2-rich fluid is then transported into the lower crust by synmetamorphic intrusions during peak metamorphic granulite facies conditions (e.g. Frost et al. 1989; Farquhar and Chacko 1991; Hansen et al. 1995). These intrusions contribute to the high temperatures reached during granulite facies metamorphism, especially for HT or UHT-types (Kelsey 2008; Touret 2009). It had been argued that infiltration by CO_2-rich fluids should lead to the deposition of large quantities of graphite (Lamb and Valley 1984, see also discussion in Touret 2009). This may account for some of the major graphite deposits found worldwide, e.g. in the Adirondacks, New York State, USA (Ticonderoga; Luke et al. 1998) and Sri Lanka (Katz 1987). On a smaller

scale, graphite-bearing hydrothermal veins in New Hampshire, USA, have been ascribed to the reduction of infiltrating CO_2-rich fluids that resulted in local granulite facies hot spots (Chamberlain and Rumble 1989; Rumble et al. 1989). The reducing trends are, however, rarely evident. CO_2 itself has some oxidizing capacity (Frost 1991) and its introduction at high temperature will, on the contrary, result in a high degree of oxidation, typical for many granulite terranes (Harlov 2000). This has notably been demonstrated along a traverse of Archean lower crust in southern India including the Shevaroy Hills, southern India (Harlov et al. 1997; Harlov and Hansen 2005). Other examples include the granulite facies rocks of the Bamble sector, south Norway, where magnetite-hematite and ferrosilite-magnetite-quartz oxygen barometers show that peak metamorphic oxidation states were well above fayalite-magnetite-quartz buffer (Harlov 1992, 2000). Considerations on the buffering capacity of the oxygen fugacity of the C-H-O system (Huizenga 2005; Huizenga and Touret, 2012) show that this high degree of oxidation can be understood if CO_2 is introduced into the rock system at high, magmatic or submagmatic temperatures, well above the graphite stability curve. Except in a few cases, i.e. the above mentioned graphite deposits, the fluids will not re-equilibrate during retrogression; firstly, because of the difficulty for graphite to nucleate; secondly, because most of the free fluids probably leave the rock system during the first stages of the retrogression, at temperatures still too high for graphite to crystallize. Recent modelling by J.M. Huizenga on the C-O system shows that if CO_2 is introduced in completely dry rocks (hence the absence of H^+), the quantity of graphite which can be deposited is extremely small, leaving excess oxygen which can then be responsible large scale oxidation effects (Huizenga and Touret, 2012). It should be also noted that, in addition to CO_2, fluids may introduce other oxidizing components such as SO_2 (Cameron and Hattori 1994; Harlov et al. 1997; see also discussion in Newton and Manning 2005). The presence of SO_2-bearing fluids in (some) granulites is also indicated by assemblages of sulfate scapolites, reported from, amongst others, Ghana (Von Knorring and Kennedy 1958), xenoliths in deep seated pipes from eastern Australia (Lovering and White 1964) and the Kohistan arc, NW Himalayas (Yoshino and Satish-Kumar 2001).

As far as the stability of granulite mineral assemblages is concerned, the role of brines is significantly different. An important feature is the development of so-called granulite facies islands, i.e. scattered, isolated occurrences of granulite facies rocks well beyond the orthopyroxene-in isograds for both basic and felsic rocks in the amphibolite to granulite facies transition zone of the Bamble sector, southern Norway (Nijland et al. 1998) (Fig. 11.2). The occurrences are not related to magmatic intrusions that might have provided a local additional heat source. They have up to now been only documented in this terrain, but likely occur in other amphibolite to granulite facies transition zones too. These granulite facies islands are characterized by diagnostic granulite facies minerals like orthopyroxene + K-feldspar (Fig. 11.8) and sapphirine + quartz in ordinary metapelitic rocks. This common bulk chemistry distinguishes these granulite facies islands from granulite facies mineral assemblages that may occur in very Mg-rich lithologies like cordierite-orthoamphibole rocks (e.g. Munz 1990; Visser and Senior 1990) or

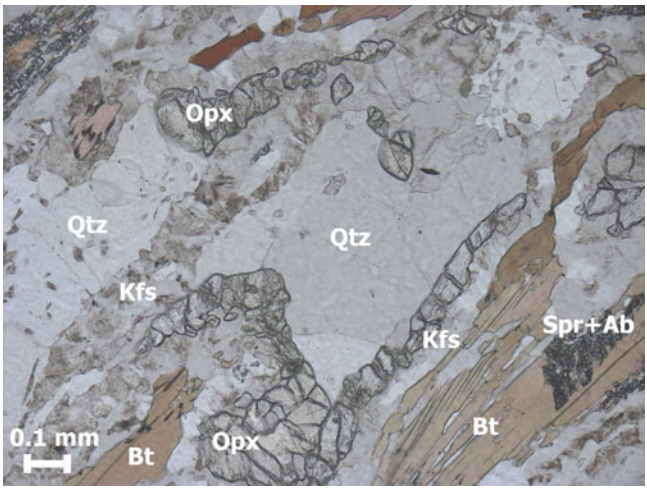

Fig. 11.8 Orthopyroxene-K-feldspar coronas between biotite and quartz, formed in response to saline brines, Hauglandsvatn, Bamble, Norway (See Nijland et al. 1998)

Mg-rich assemblages in scapolitized metagabbros (Engvik and Austrheim 2010; Engvik et al. 2011). In the latter, the Mg-rich bulk chemistry apparently plays a role in stabilizing granulite facies assemblages to lower temperature. The presence of B may also serve to stabilize typical granulite facies minerals, such as kornerupine, to considerably lower temperature, as demonstrated by kornerupine + andalusite assemblages (Girault 1952; Grew et al. 1990). In the case of common metapelites from the Bamble sector, low a_{H2O} fluids are probably responsible for the formation of such granulite facies islands, characterized by low-Al orthopyroxene + K-feldspar coronas between biotite and quartz (Fig. 11.8) and spinel ± corundum + albite/oligoclase symplectites at the expense of biotite and sillimanite (which have subsequently been partially replaced by sapphirine ± albite/oligoclase symplectites) (Nijland et al. 1998). Brines are closely associated with the anhydrous assemblages (Fig. 11.5) and regarded the cause behind the formation of these granulite facies islands. Current fluid inclusions studies indicate salinities of c. 25 wt% NaCl, which are too low to stabilize low-Al orthopyroxene + K-feldspar assemblages. However, daughter minerals like halite are not taken into account in this salinity estimate from heating-freezing data implying that this salinity estimate represents the lower limits of synmetamorphic salinity. The low Al-content of the orthopyroxene and presence of low Ca-plagioclase fits with observations by Perchuk and Gerya (1995) that these Al- and Ca-contents decrease with alkali activity.

This raises further questions concerning the nature of fluids involved in other examples of anomaleous formation of granulite facies assemblages. Examples of such assemblages include orthopyroxene + andalusite symplectites at expense of cordierite in granulites from the Arunta block, Australia (Ballèvre et al. 1997) and the retrograde formation of sapphirine at the expense of spinel in quartz-rich

granulites from the Sharyzhalgay complex, Siberia (Podlesskii and Kurdyukov 1992).

The action of brines in controlling mineral stabilities is not limited to peak metamorphic conditions. Brines may exert their influence during cooling and uplift. The Ubergsmoen augen gneiss is a syntectonic granitic-charnockitic intrusion in the Bamble area, with a fluid inclusion population dominated by H_2O and CO_2, respectively (Touret 1985). It generally shows a postmagmatic evolution of orthopyroxene + clinopyroxene → hornblende + garnet → hastingsite + biotite. The later assemblage is in particular abundant in white pinkish granitic zones between fresh, greenish charnockitic varieties, and is accompanied by late trails of aqueous fluid inclusions. The zones might be termed decharnockitization. In one section, however, the late stage evolution is different, with the hastingite + biotite being overgrown by new, coarser grained coronas of garnet, with contemporaneous replacement of plagioclase by aggregates of scapolite and carbonate.

Associated with this assemblage (and different from other samples), are small fluid inclusions, generally about 5 μm and occurring in trails, often ending near larger, irregular shaped empty inclusions; sporadically, a salt cube, without fluid, is present in the latter inclusions. Inclusions, saturated with NaCl at room temperature have final melting temperatures between −4.7°C and −27.8°C, homogenizing to liquid between 122.3°C and 188.7°C (Nijland and Touret 2000). Fluid inclusion textures, the large spread in freezing point depression, and the relatively low homogenization temperatures indicate that the inclusions likely reflect reset samples of the original fluid that was contained in the larger, now decrepitated inclusions. This fluid was saturated with NaCl and possibly with other salts. The close spatial relationship between brine inclusions and a late anhydrous assemblage demonstrates that, as in prograde granulite facies metamorphism, brines with reduced water activity may provoke *progressive dehydration* during retrograde cooling and uplift in upper greenschist – lower amphibolite facies and give rise to *apparently* high grade mineral assemblages (Nijland and Touret 2000).

The example above illustrates that peak metamorphic granulite facies fluids may stay present during the post-peak metamorphic evolution, instead of being expelled. This holds for both brines and CO_2. Salient examples include the formation of calcite + quartz symplectites after wollastonite in the granulite facies Rogaland area, south Norway (Fig. 11.9); similar symplectites have been described by Harley and Santosh (1995) from Kerala, south India.

11.5.2 K-Feldspar Microveins and Myrmekites

K-feldspar microveins at the boundary between quartz and feldspar in granulite facies rocks were already noted by Coolen (1980), then described in India (Hansen et al. 1984) and subsequently in a series of Russian and Finnish granulite facies rocks (Perchuk and Gerya 1992, 1993, 1995). Similar K-feldspar microtextures have subsequently been found in many other mafic granulites (Franz and Harlov 1998;

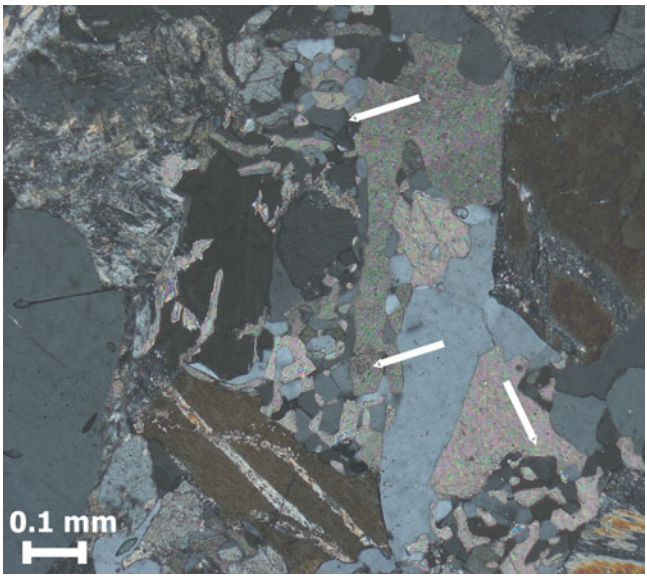

Fig. 11.9 Post-peak metamorphic effect of CO_2: calcite + quartz symplectites (indicated by *arrows*) after wollastonite in a hedenbergite-scapolite-wollastonite-quartz rock from the Asheimvatn, Rogaland, Norway

Harlov et al. 1998; Safonov 1999; Parfenova and Guseva 2000; Harlov and Wirth 2000; Harlov and Förster 2002; Montanini and Harlov 2006; Hansen and Harlov 2007). K-feldspar in the veins often has high Ba-contents (Hansen et al. 1995; Franz and Harlov 1998) and may contain relatively high albite contents. Different microtextures occur (Harlov et al. 1998; Sukumaran and Ravindra Kumar 2000; Harlov and Wirth 2000; Harlov and Förster 2002; Montanini and Harlov 2006; Hansen and Harlov 2007) (Figs. 11.10–11.13). These include:

- Rods, blebs, and irregular patches of antiperthite in randomly scattered plagioclase grains.
- Microveins along quartz-plagioclase and plagioclase-plagioclase grain boundaries or other minerals grain boundaries (pyroxene, opaque, etc.) or transecting these (Figs. 11.10 and 11.13).
- Myrmekites, which are vermicular intergrowths with Ca-rich plagioclase along (mainly) K-feldspar grain boundaries (Figs. 11.11–11.13).
- Occasional microperthitic discrete anhedral grains.

It is interesting to note that, despite their ubiquitous character, these intergranular microveins had remained largely unnoticed, until fluid inclusion studies indicated the possible occurrence of intergranular fluids at these deep levels.

Among all these microstructural features, myrmekites are the most common and obvious. They are also quite abundant in granites, especially when deformation has facilitated the introduction of external fluids (Simpson and Wintsch 1989). Myrmekites in granulites deserve special attention for several reasons:

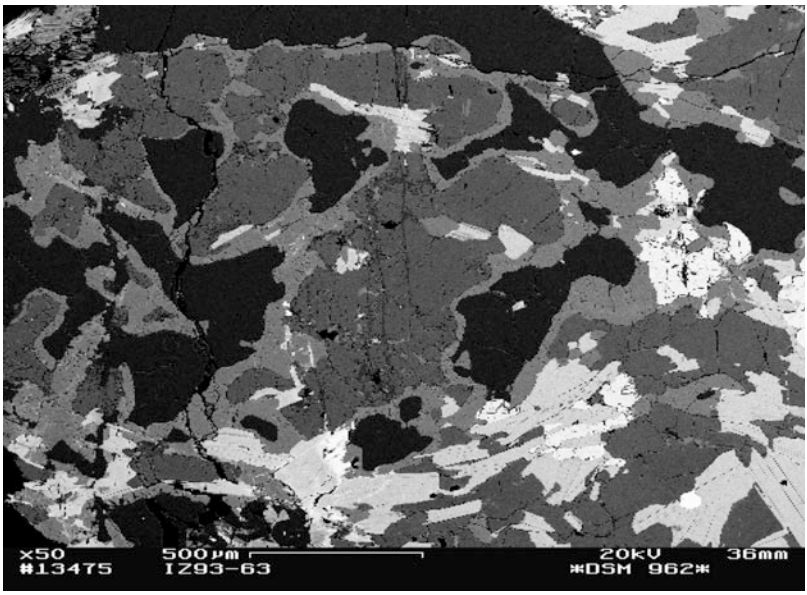

Fig. 11.10 Examples of K-feldspar microveins in granulites from a localized dehydration zone from the Seward peninsula, Alaska (Harlov and Förster 2002)

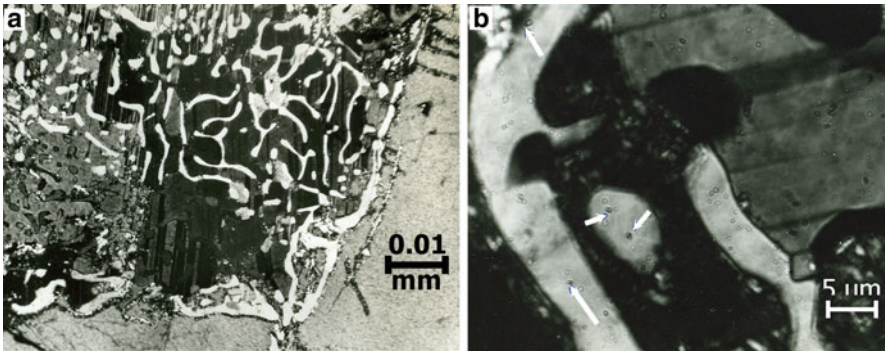

Fig. 11.11 Giant myrmekites in plagioclase at the contact with cordierite in cordierite-anthophyllite rocks from Åkland, Bamble sector, Norway (**a**). (**b**): detail, with *arrows* indicating minute brine fluid inclusions

– They are best developed along the margins of large K-feldspar phenocrysts in magmatic granulites (charnockites), especially when these rocks show evidence of high temperature deformation (so-called *charnockitic augen gneisses*), e.g. Hovdefjell and Ubergsmoen in southern Norway (Figs. 11.2 and 11.12a) or Ansignan, Massif de l'Agly, French Pyrénées (Fonteilles 1970) (Fig. 11.14). In these rocks, static mineral recrystallization (*granulite texture*; cf. Vernon 2004)

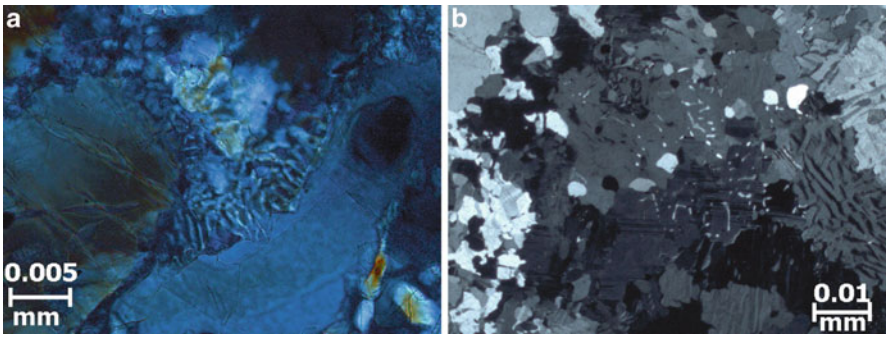

Fig. 11.12 Myrmekites in magmatic granulites (charnockites and related rocks). (**a**): Charnockitic augen gneiss, Hovdefjell summit, Bamble sector, Norway. Along the boundary of a large, plastically deformed K-feldspar phenocryst (augen), a continuous myrmakite layer grades into a granulated groundmass towards the *top* of the figure. Secondary muscovite (and biotite) adjacent to the myrmekite (see Fig 11.14). (**b**): Myrmekite (*centre*) in an entirely recrystallized, undeformed garnet granulite, commercially distributed as ornamental stone under the name Kashmir White, (India); large, undeformed mesoperthite crystals occur to the *right* and *bottom* and typical groundmass granulite texture to the *right*

postdates high temperature plastic deformation, occurring first in the ground mass of the rocks and eventually in the augen. In such cases, any sign of plastic deformation are erased (Fig. 11.12b). This type of re-equilibrated texture can only occur in high temperature granulite facies environments, demonstrating that the formation of myrmekites in granulites occurred at high temperature, close or equal to peak metamorphic conditions. The myrmekites should be considered as part of the characteristic granulite facies mineral assemblage instead of late phenomena as often assumed, especially in granitic rocks.

– Myrmekites occur preferentially (but not exclusively) in K-feldspar bearing rocks. For instance, in the Ansignan charnockite, they are much more abundant in the garnet-bearing marginal charnockitic variety than in the orthopyroxene-bearing enderbitic core. However, they may also be found, sometimes in a most spectacular way, in rocks virtually free of K-feldspar. An example is the cordierite-anthophyllite rock (often replaced by phlogopite or actinolite) from the Bamble sector, southern Norway, shown in Fig. 11.11. These well known rock varieties, remarkable by the gem quality and the large size (up to 1 dm) of most of their rock forming minerals, may contain spectacular myrmekites at the contact between cordierite and quartz. These rocks contain great numbers of small brine inclusions, either in the cordierite or, most typically, in quartz blebs within the cordierite (Fig. 11.5c, d). The origin of these cordierite-anthophyllite rocks has been much debated, as shown later (§ 11.5.5). In the case of most possible precursor, brines are a more than a likely premetamorphic fluid, and the brines found in inclusions probably represent far remnants from these hydrothermal fluids.
– In charnockites, charnockitic augen gneiss and related rock types, myrmekites are closely associated with feldspar microveins on the scale of single intergrain

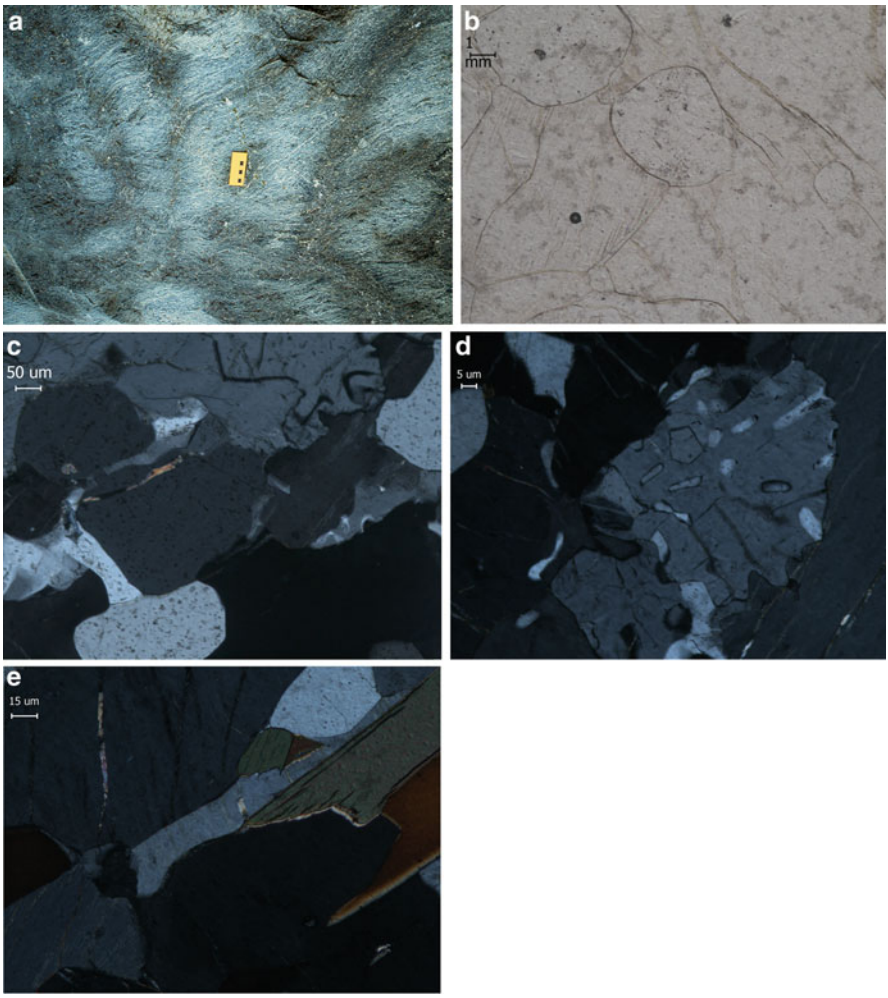

Fig. 11.13 Network of incipient charnockite veins crosscutting the foliation of garnet-bearing pelitic gneisses, Kurunegala, Sri Lanka. The incipient charnockite shows K-feldspar microveins and myrmekite (Sample provided by L.L. Perchuk, 96 Per 4, see Perchuk et al. 2000). (**a**): Field occurrence (Photo courtesy A. Kröner), with *greenish* charnockite and *light grey* pelitic gneisses. **b**–**e**: Microscopic features (**b** plain polarized light, **c**–**e** cross polarized light). (**b**): massive part of an incipient charnockite vein made up by mesorthites and rounded quartz crystals containing minute fluid inclusions (appearing as *black dots*). (**c**): myrmekites (*right*) adjacent to K-feldspar microveins (*left*) along the boundary of large mesoperthite crystal. (**d**): detail of myrmekite. (**e**): detail of K-feldspar microvein, in this case extending along biotite interfaces

boundaries (Harlov and Wirth 2000). They occur in such a way that they have to be considered as complementary processes. A good example of this can be found in so-called *incipient charnockite* from Kurunegala, Sri Lanka (Perchuk et al. 2000), described in detail in Fig. 11.13. Here, in the middle, massive part of

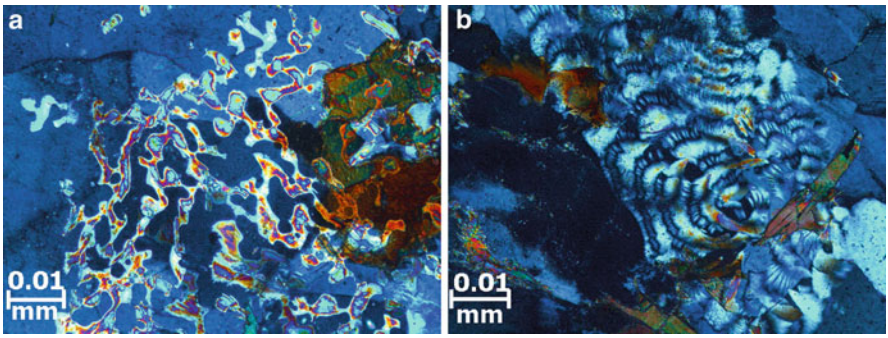

Fig. 11.14 Muscovitization of K-feldspar microveins in the Ansignan charnockite, Massif de l'Agly, French Pyrénées. (**a**): Network of muscovite, first partially replacing K-feldspar microveins (*upper left corner*), subsequently overgrowing the remaining mineral assemblage. (**b**): Detail of circular arrangement of platy muscovite crystals, possibly reminiscent of former myrmekite textures

an incipient charnockite vein contains mostly mesoperthites and quartz (Fig. 11.13b), with small amounts of orthopyroxene and biotite. Myrmekites and K-feldspar microveins occur along the same boundary of large mesoperthite crystals, at a distance of a few millimetres or less (Fig. 11.13c). Whereas myrmekites only occur at or in the mesoperthites (Fig. 11.13d), the K-feldspar microveins have developed at different mineral interfaces, either feldspar, quartz or even biotite (Fig. 11.13e). As in the case of the cordierite-anthophyllite samples, the role of brines is indicated by the fact that, when a K-feldspar microvein is in contact with or very near a quartz grain (Fig. 11.13c), the quartz contains many small, collapsed brine inclusions. If enough fluid remains available after formation of the microveins, K-feldspar may eventually be replaced by muscovite or, in relatively Fe-rich environments, by biotite. For example in the Ansignan charnockite, muscovite occurs in spectacular networks superimposed on the original mineral assemblage (Fig. 11.14a) and in circular aggregates which suggest pseudomorphism of former myrmekitic textures (Fig. 11.14b).

So much has been written on myrmekites, that any interpretation will immediately lead to some controversy. Our observations fit best with the early interpretation of myrmekites by Becke (1908), the first one ever proposed after these structures had been discovered under the microscope. Here K-feldspar is replaced by intergrowths of plagioclase + quartz under the influence of Na- and Ca-bearing aqueous solutions, according to the reaction (Simpson and Wintsch 2007):

$$1.25\,KAlSiO_8 + 0.25\,Na^+ + 0.25\,Ca^{2+} \rightarrow Na_{0.75}Ca_{0.25}Al_{1.25}Si_{2.75}O_8 + 1.25\,K^+ + SiO_2$$

This reaction releases K^+, which immediately reprecipitates in the form of alkali feldspar, as it is less mobile in solution than Na^+ or Ca^{2+}. The fact that this represents the formation of a new mineral, not, as in the case of myrmekite,

the replacement of a pre-existing mineral phase, is indicated by the fact that the K-feldspar microveins are developed between quite different minerals, including biotite (Fig. 11.13e). Silica liberated during myrmekite formation is less mobile than the K-feldspar. This is shown by the frequent occurrence of small quartz grains, all with the same optical orientation, around the myrmekite domains (Fig. 11.13c). It gives the impression of silica-rich solutions penetrating the rocks on the scale of a few mineral grains.

11.5.3 Incipient Charnockites

Ever since charnockite was first defined by T.H. Holland from the tombstone of Calcutta's founder Job Charnock (Holland 1900), its genesis has been debated between proponents of either a metamorphic or an igneous origin (e.g. Quensel 1952; Pichamuthu 1953; Klimov et al. 1964; Harley 1989; Newton 1992a,b; Kilpatrick and Ellis 1992; Abramov and Kurdyukov 1997; Frost and Frost 2008). As early as 1960, C.S. Pichamuthu (1960, 1961) reported the local transformation of biotite and amphibole gneisses into charnockite in Mysore state, southern India. His observation raised no marked interest until the 1980s, when it was realized that some of these incipient charnockites, in most cases irregular patches of decimetre to metre size, did not only occur in a variety of protoliths, ranging from metavolcanics to metapelites and gneisses, but also often occurred along a regular fracture network (Fig. 11.13a), suggesting that they represented fossil fluid pathways (Friend 1981). This distinguishes them from igneous charnockites occurring in anorthosite-mangerite-charnockite-granite suites. Incipient charnockites have since been found in many areas including southern India and Sri Lanka (e.g. Janardhan et al. 1979, 1982; Park and Dash 1984; Hansen et al. 1984, 1987; Raith and Srikantappa 1993), the Seward Peninsula, Alaska (Harlov and Förster 2002) and SW Sweden (Harlov et al. 2006; Fig. 11.15). Fluid inclusion data document the general occurrence of CO_2-rich fluid inclusions in the charnockite only, not in the surrounding amphibolite facies rocks (e.g. Sri Lanka, Perchuk et al. 2000, SW Sweden, Harlov et al. 2006). But the other granulite fluid (brines) can also be present, especially in granitic intrusions. This is notably the case for the well-known Closepet granite in the Indian Dharwar craton (Srikantappa and Malathi 2008; see also Słaby et al. 2011). Brine-loaded incipient charnockites (Srikantappa and Arash Zargar 2009) occur in the lower part of the granite. These brines were presumably expelled from underlying massive igneous charnockites.

Data from all incipient charnockite localities, whether with a metasedimentary (metapelitic) or magmatic precursor, clearly demonstrate the progressive nature of the metasomatic transformation from precursor to charnockite (Fig. 11.16). In detail, this can be quite complicated. Knudsen and Lidwin (1996) interpreted enderbitic veins on Tromøy and Havsøya in the Bamble sector, southern Norway, as intrusive, and described the formation of dehydration bands along these veins as being due to the infiltration of $CO_2 \pm N_2$ from the veins (Fig. 11.17). Vander

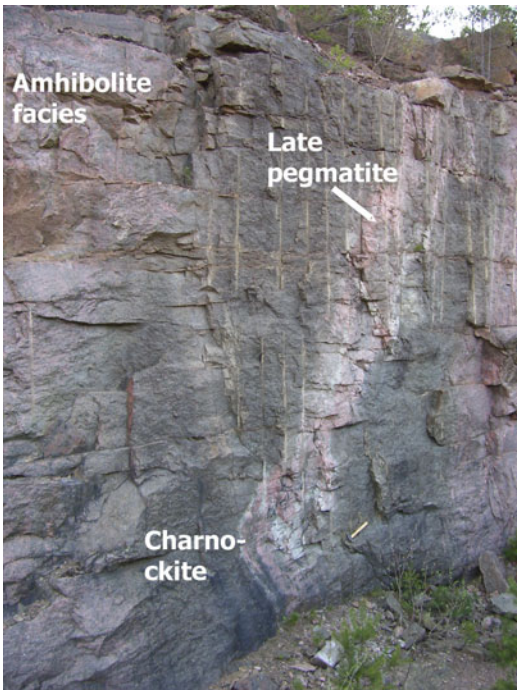

Fig. 11.15 Incipient charnockites in the Söndrum quarry (Stenhyggeriet), Halmstad, SW Sweden (cf. Harlov et al. 2006)

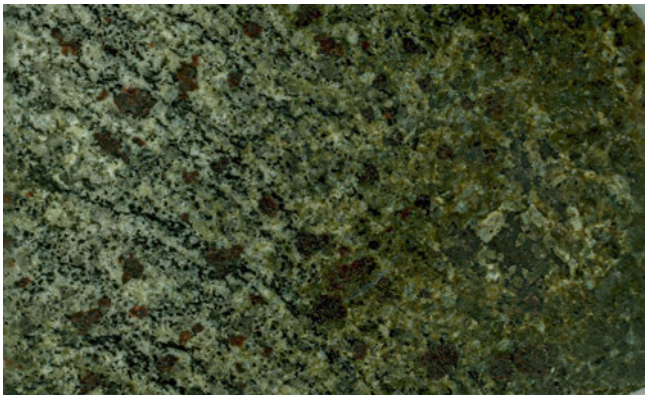

Fig. 11.16 At the scale of the hand specimen, progressive transformation of garnet-biotite gneisses (*left*) into coarse-grained, homogeneous charnockite (*right*) (*Arrested charnockite formation*; Raith and Srikantappa 1993) (Sample 04JT3, courtesy M. Raith; width of picture 8 cm)

Auwera (1993) described the formation of dehydration bands at the margins of amphibolites against charnockites, with element mobility and continuous changes in solid solution compositions over the bands. In this case, element mobility is

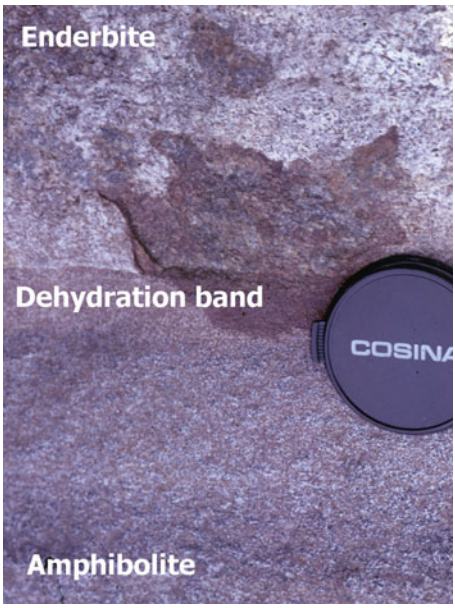

Fig. 11.17 Dehydration band along the margin of amphibolite against enderbite on Tromøy, Bamble sector, Norway

considered to be a diffusional process rather than an infiltration process. The diffusional process was considered to be controlled by the chemical potential of SiO_2 rather than that of H_2O.

Following Korzhinskii's (Korzhinskii 1962) notion of the importance of the chemical potential of K_2O, Perchuk and Gerya (1992) developed the concept of charnockitization of amphibolite facies rocks being dependent on the infiltration of one or both metasomatizing agents, CO_2 or K_2O, a notion also proposed by Stähle et al. (1987). In the case of CO_2, this involved generalized reactions like tschermakite + quartz + CO_2-fluid → anorthite + enstatite + CO_2-H_2O-fluid, i.e. in which the CO_2 component is not consumed. In case of K_2O, reactions like pargasite + quartz + K_2O (in fluid) → K-feldspar + enstatite + diopside + H_2O-fluid containing Na_2O are involved. These reactions illustrate several important aspects regarding incipient charnockitization:

- In all cases, dehydration is accompanied by the formation of new feldspars.
- In the case of CO_2, the active agent promoting dehydration is not consumed in the reaction, but remains available, thus capable of promoting charnockitization/enderbitization elsewhere after transport.
- In many cases, actual metasomatism occurs. K_2O is introduced and consumed in the reactions, resulting in evident changes in the bulk rock compositions.

The later is not limited to K_2O. Bulk chemical analysis of incipient charnockites show that, compared to the original amphibole-bearing gneiss, the former show an increase in not only K_2O but also Na_2O and SiO_2, and a decrease in MgO, FeO and especially CaO (Hansen et al. 1987; Stähle et al. 1987). The loss of CaO, probably

due to the incongruent dissolution of hornblende (Newton pers. com. 2011) and may be explained by its high solubility in concentrated NaCl solutions (Newton and Manning 2007).

For those interested in the history of geology and its concepts, it is tempting to speculate how the recent results regarding to the formation of feldspars discussed above would have figured in the great debate in the 1940s and 1950s between the so-called *soaks* and *pontiffs* (Young 2002). The soaks, a nickname coined by N.L. Bowen, favouring formation of granites by diffusion in the solid state (Bugge 1945), denominated as granitization (Read 1957), the pontiffs headed by E. Niggli a magmatic origin. A major difference with the current hypotheses is, however, that whereas true solid state diffusion must be extremely limited to a scale not exceeding few millimetres at most, element transport resulting in charnockite formation in the amphibolite to granulite transition zone must occur on a much longer scale on the order of metres to killometres. This type of K-feldspar formation may not be limited to incipient charnockites. Baltybaev et al. (2010) presented evidence for the regional formation of large K-feldspar crystals in migmatitic quartz-feldspar leucosomes after solidification and deformation of these leucosomes.

The metasomatic origin of incipient charnockites does by no means imply that they have systematically escaped melting. In a very detailed study of the Kurunegala (Sri Lanka) occurrence shown in Fig. 11.13, Perchuk et al. (2000) concluded that gneisses had been metasomatically altered along shear zones with minimum melting for the post metasomatic composition (700–750°C, 6 kb, a_{H2O} 0.52–0.59) due to the influx of an external fluid with both CO_2 and a supercritical brine component. These observations would imply that in this case supposedly magmatic charnockites can then be produced in situ, without showing any sign of restitic material along the edge of the molten zone.

11.5.4 Metasomatic Redistribution of Elements Traditionally Considered as Immobile

Until a decade ago, widespread opinion considered REE, Th and U-bearing accessory minerals in high grade rocks, notably phosphates and zircon, to be non-reactive and recording magmatic phenomena only. For this reason, they are widely used for dating, each successive layer, if occurring, being ascertained to successive episodes of magmatic growth. This is in marked contrast to observations that minerals like monazite and xenotime may be formed at sub-greenschist facies conditions (Sestri-Voltaggio zone, Liguria, Italy, Cabella et al. 2001; Bukowiec, Carpathians, Poland, Budzyn et al. 2005; Malopolska block, Poland, Stanislawska and Michalik 2008) or even in diagenetic environments (Welsh basin; Evans and Zalasiewicz 1996). Meanwhile, it has been known for a long time that many granulite zircons show rounded, almost eroded shapes. These are often explained by multiple resorption and interaction with extracted melts (Tichomirova et al. 2005). However, several

studies have shown that in many cases Zr-bearing minerals can be quite mobile during granulite facies metamorphism, through dissolution-reprecipitation processes (Harlov and Dunkley 2010, Schutesky della Giustina et al. 2011). Some observations show that distances of mobility can reach at least the outcrop scale, such as the case of ilmenite-zircon veinlets occurring in granulite facies metamorphosed pegmatite in Rogaland, south Norway (Wielens 1979).

Also in Rogaland, Bingen (1989) demonstrated that granulite facies metamorphism may result in the redistribution of supposedly immobile elements, manifest by a regional allanite-out isograd; over the amphibolite to granulite facies transition zone, REE, U and Th are redistributed between accessory phases (Bingen et al. 1996). Similar observations with regard to the redistribution of REE in minerals as a function of metamorphic grade have been made along a traverse of amphibolite to granulite facies Archean lower crust in the Dharwar craton, southern India (Hansen and Harlov 2007). During the last decade, it has become clear that dissolution-reprecipitation processes, assisted by brines, might affect accessory phases under P-T conditions relevant to granulite facies metamorphism (Harlov et al. 2002, 2005; Harlov and Förster 2003). However, these do not explain typical zonation textures in for example monazite and zircon with respect to Th, U and Pb. Recent experiments at Potsdam (Harlov and Hetherington 2010; Harlov et al. 2011) have shown that at the relevant P-T conditions (900°C, 1,000 MPa and 600°C, 500 MPa, respectively), alkali-bearing fluids are able to explain these textures, resulting in pseudomorphic (partial) replacement and redistribution of elements by coupled dissolution-reprecipitation processes, the grain boundary fluid essentially acting as catalyst. The metasomatized monazite is apparently completely recrystallized, with a pristine appearance. This mechanism provides an alternative explanation to melt extraction. Experimental fluids consisted of NaOH, KOH, a water glass-like compound $Na_2Si_2O_5$ or NaF, with addition of a few more 'traditional' fluid components (HCl, $CaCl_2$ and $Ca(OH)_2$) in case of zircon (Harlov and Dunkley 2010). The exact nature of these fluids is still an open question. As a matter of fact, they represent a key problem with regard to fully understanding processes occurring in the lower crust. Their presence would, however, have far reaching consequences. Not only does it explain the remarkable abundance of monazite in some granulite terrains, – monazite-bearing sands are a major source of thorium along the southern coast of Madagascar-, but it again implies that dating the external layer of a monazite, xenotime or zircon crystal does not necessarily relate to the last magmatic event, but might well reflect metasomatic action. Another interesting consequence of such fluids would be their high capability to transport silica. Metasomatic granulite veins, like in the Seguin subdomain of the Grenville province, for which granulite facies infiltration of SiO_2, Na_2O and Al_2O_3 has been documented (Zaleski and Pattison 1993) might be an interesting case for future research. These fluids have not yet been found in fluid inclusions, though, as indicated at the beginning of this paper, it can not be excluded that they correspond to some 'low salinity' aqueous inclusions occasionally found in granulites, but generally considered not to be related to granulite facies metamorphism because of their incompatibility with the granulite mineral assemblage.

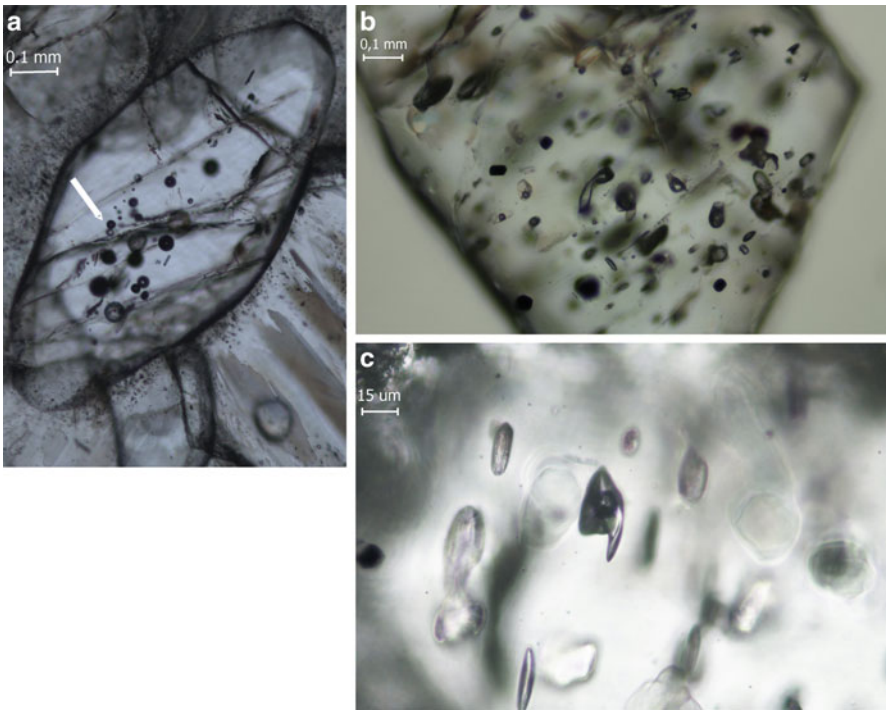

Fig. 11.18 Fluid inclusions in carbonatites: (**a**): CO_2-inclusions in apatite from Kovdor, Kola peninsula. Russia. (**b**): Overall view of an apatite crystal from the Kerimasi carbonatite, completely crowded with primary inclusions. These correspond to three immiscible fluid/melts: carbonatite melt, Mg- and Fe-rich peralkaline silicate melt, and (*arrow*) C-O-H-S alkaline fluid (Guzmics et al. 2011). (**c**): detail of the biphase (liquid-vapour) alkaline fluid (C-O-H-S- Na and K components, T. Guzmics pers. com. 2010)

Though synmetamorphic alkaline intrusions in granulite facies terrains have not been documented, it is interesting to note that comparable fluids (alkali-bearing and alkaline aqueous solutions) occur in some carbonatites, notably at the transition between calcium- and natrocarbonatites (Fig. 11.18). The inclusions shown in Fig. 11.18, in apatite from the Kerimasi (Tanzania) calciocarbonatite contain a C-O-H-S alkali-bearing fluid (Guzmics et al. 2011), only partly analyzed at present. However, at first sight, estimated compositions are in broad agreement with fluids used by D. Harlov and co-workers in their experiments. As observed by Guzmics et al. (2011), these alkali-bearing aqueous fluids occur in the Kerimasi carbonatite at an early magmatic stage as a result of immiscibility from a Mg- and Fe-peralkaline silicate melt, itself the result of unmixing from a Ca-rich, P-, S- and alkali-bearing carbonatite melt (Fig. 11.18). These types of multiple immiscibilities, only detectable by a thorough investigation of melt and fluid inclusions, are probably much more widespread than commonly realized. They are likely to be a major source of melt and fluid production in the mantle. It is interesting in this respect to note that

highly siliceous alkali-bearing fluids have been produced experimentally in synthetic fluid inclusions (Wilkinson et al. 1996).

Southern Madagascar, a well known, classical granulite province, is a good example to illustrate U, Th and REE-mobility under granulite facies conditions. It has been metamorphosed about 580–600 Ma ago, at the same time as the larger part of east Africa, Sri Lanka, and the most southern part of India (Pan-African orogeny, e.g. Paquette et al. 1994). The fact that all these regions are among the world's largest producers of gemstones is certainly not a coincidence (e.g. Dahanayake and Ranasinghe 1981). It indicates that typical granulite-facies P-T conditions (high temperature, relatively low pressure, low water activity fluids) are ideal for creating gem varieties of ordinary minerals like zoisite (tanzanite) and garnet (tsavorite). In the region of Tranomaro, in the southeasternmost part of Madagascar, a number of carbonate-rich metasedimentary layers occur, partly transformed into pyroxene-rich rocks. These pyroxenites also contain garnet; therefore, they are commonly described as skarns (Moine et al. 1985). However, like in the Arendal region of the Bamble sector, southern Norway, they are not a product of contact metamorphism due to a granitic intrusion, but the result of regional granulite facies metamorphism, at a temperature of about 800–850°C and a pressure of 4–5 kb (Moine et al. 1985). Some marbles and, to a lesser extent, skarns are enriched in U, Th, Zr and REE. Locally, they form deposits of economical value, being the source of urano-thorianite minerals abundant in placers along the southeastern coast of Madagascar (Rakotondrazafy et al. 1996). Boulvais et al. (2000) showed how, across a meter-scale profile at the marble-pyroxenite contact, REE-contents increase markedly towards the skarns, e.g. La from 19.8 ppm in the most distant sample to 129 ppm in marble at the pyroxenite contact. These authors concluded that this element distribution was caused by the infiltration of a fluid at peak metamorphic conditions. Fluid inclusion studies show this fluid to be CO_2-rich ($X_{CO2} > O.8$; Ramambazafy et al. 1998). It is interesting to note that fluid infiltration was not recognizable from C- and O isotopic signatures, because of the persistence of large isotopic variations predating granulite facies metamorphism.

11.5.5 Peak Metamorphic to Retrograde Bulk Chemical Processes (Scapolitization, Albitization)

Lower crustal granulites now exposed at the Earth's surface must have experienced a complicated uplift history, during which a number of retrograde features may have happened. If still hot granulites are thrusted on low-grade, H_2O-rich metamorphic terranes, it may lead to widespread retrogradation and various types of retrograde isograds (e.g. orthopyroxene to anthophyllite), as described by D. Van Reenen and co-workers in the Limpopo complex of southern Africa (Van Reenen 1986; Van Schalkwyk and Van Reenen 1992; Van Reenen et al. 2011). In general, however, both peak and retrograde metamorphic evolution of

amphibolite and granulite facies terranes involve regional scale metasomatic processes, provoked by the infiltration of notably Na (± Cl)-rich fluids (albitization and scapolitization), K-rich fluids or possibly Mg-rich fluids, giving rise to the formation of particular lithologies. Mg-rich cordierite-orthoamphibole rocks have already been mentioned. These high temperature analogues of the high pressure orthoamphibole-kyanite-talc schists (*whiteschists*, Schreyer 1974) occur in various settings within regional amphibolite-granulite facies terrains and high temperature contact metamorphic aureoles. The question whether synmetamorphic metasomatism is involved is still debated. An origin due to Mg metasomatism has been proposed for these rocks by several workers (Eskola 1914; Tilley 1937; Oen 1968). Alternative origins proposed include low temperature alteration of mafic volcanics (Vallance 1967; Reinhardt 1987; Smith et al. 1992; Visser 1995; Hinchey and Carr 2007), sediments derived from altered or weathered volcanics (Robinson and Jaffe 1969), weathered greywacke (Owen and Greenough 1995), meta-evaporites (Touret 1979; Nijland et al. 1993), products of metamorphism at very high oxygen fugacities (Cameron and Hattori 1994) or retrogressed granulites (Van Reenen 1986). Probably, different genetic types exist.

Scapolitization and albitization, on both a local as well as a regional scale, have been observed in several amphibolite and granulite facies terrains (for a more detailed discussion, see Chaps. 4 and 7). Both processes clearly involve chemical mass transfer by fluids, notably brines. Both processes may be contemporaneous. This is, for example, the case in the amphibolite facies Mary Kathleen fold belt, Mt. Isa inlier, Queensland, Australia where albitization and scapolitization of calc-silicate rocks occur at peak metamorphic conditions (560–630°C, 3–4 kb; Oliver and Wall 1987; Oliver et al. 1990, 1994; Oliver 1995). In other areas, they show close spatial relationships, but follow each other in time. This is the case in the amphibolite to granulite facies transition zone of the Bamble sector, southern Norway (Putnis and Austrheim 2010; Engvik et al. 2011). Albitization and scapolitization occur in metasedimentary complexes dominated by quartzites intruded by gabbroic magmas (the Nidelva Quartzite Complex in the Froland area and Coastal Quartzite Complex in the Kragerø area). However, whereas scapolitization likely occurred at or near peak metamorphic conditions (Visser et al. 1999, Engvik and Austrheim 2010), spatially associated albitization has occurred during cooling and uplift.

In the Bamble sector, scapolitization in the form of Cl-rich scapolite mainly affects the gabbros and related amphibolites in the amphibolite facies portion of the amphibolite to granulite facies transition zone (Brøgger and Reusch 1875; Brøgger 1934; Green 1956). The role of fluids during the transformation of plagioclase to scapolite has already been shown in 1899 by W.J. Judd in a paper inspired by H.C. Sorby, which contains one of the first microscopic descriptions of fluid inclusions in rocks (Fig. 11.19). Judd was not able to identify precisely the fluid composition, but the strong contrast between liquid and vapour bubble in his drawings (Fig. 11.19c), as well as the occurrence of minute cubic solids in the inclusions clearly indicate that he had found a highly saline aqueous solution. Another element frequently found in or associated to brines is boron; its presence is suggested by the frequent

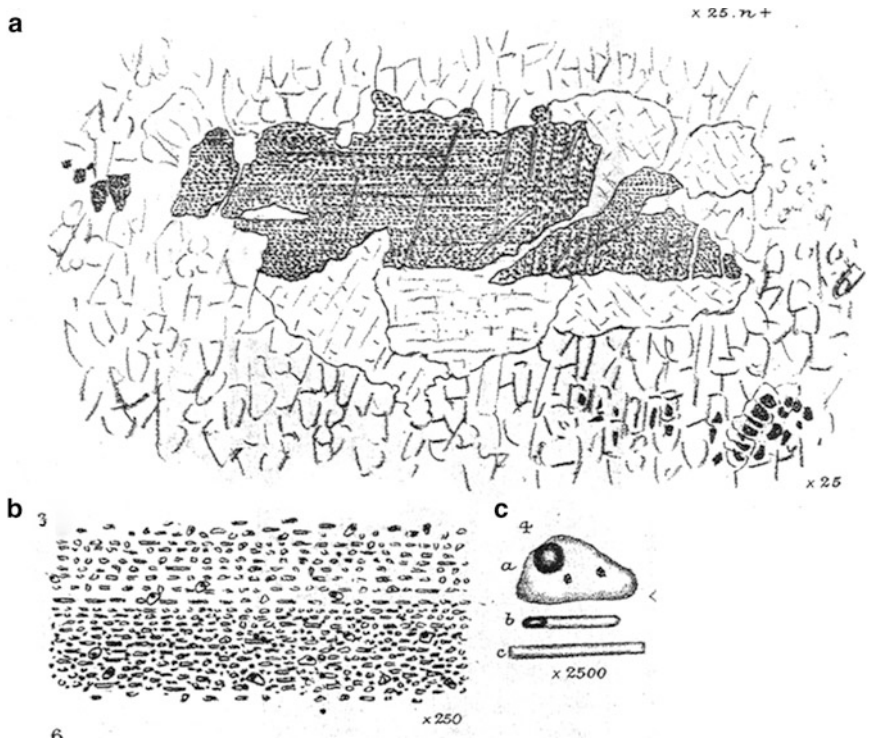

Fig. 11.19 Judd's (1889) '.. *plagioclase feldspar converted into scapolite*'; (**a**): cloudy plagioclase (*grey*) partly surrounded by scapolite (*clear*). (**b**): plagioclase containing myriads of fluid inclusions. (**c**): detail of the inclusions

occurrence of tourmaline in scapolite veins (Fig. 11.20). These veins contain the rare tri-octahedral Al-rich sodium mica preiswerkite (Visser et al. 1999), a mineral usually found in HP metamorphic rocks (e.g. Godard and Smith 1999; Wang et al. 2000), but in this case indicative of high Na^+ activity in the fluid. Scapolitization in southern Norway is generally accompanied by the formation of local apatite-enstatite-phlogopite veins (Lieftink et al. 1994; Engvik et al. 2009). This illustrates the economic importance of metasomatism. At one time, the Ødegårdens Verk deposit in the Bamble municipality constituted the largest phosphate mine in Europe, exploited by the Compagnie Française de Mines de Bamle and the Norwegian Bamle Apatit AS (Bugge 1965, 1978). Associated with scapolitization are also significant enrichments of rutile (Korneliussen et al. 1992; Fig. 11.21). Other local metasomatic effects accompanying scapolitization include the formation of sapphirine in scapolitized gabbro (Engvik and Austrheim 2010; Engvik et al. 2011). The widespread formation of Cl-rich scapolite (up to X_{Cl} up to 0.94; Lieftink et al. 1993), which itself contains brine inclusions (Fig. 11.5f), demonstrate the movement of saline fluids. Chlorapatite and Cl-bearing amphibole formed by (exchange

Fig. 11.20 Example of preiswerkite and tourmaline-bearing scapolite veins at Blengsvatn, Bamble sector, Norway (cf. Visser et al. 1999)

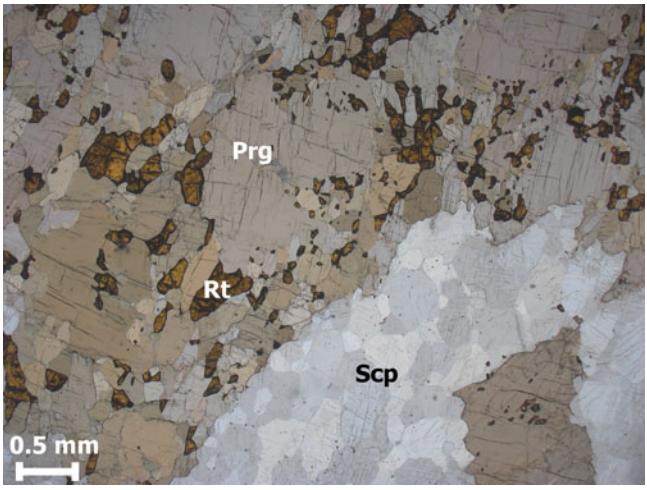

Fig. 11.21 Rutile-scapolite-pargasite rock from Ødegårdens Verk, Bamble sector, South Norway, illustrating the enrichment in rutile associated with scapolitization

with) these fluids have $\delta^{37}Cl$ isotopic signatures comparable to modern sea water (Eggenkamp and Schuiling 1995).

Albitization is well known as a diagenetic phenomenon in sedimentary basins (e.g. Boles 1982), as a subsolidus alteration of granites (e.g. Baker 1985; Boulvais et al. 2007), or as alteration of basalts (e.g. Rehtijärvi and Saastamoinen 1985). Regional scale albitization during cooling and uplift is prominent in several terrains. Besides from the Proterozoic Mary Kathleen fold belt, Australia, it is know for example from the Proterozoic Kongsberg (Jøsang 1966; Munz et al. 1994, 1995) and Bamble sectors of southern Norway (Brøgger 1934; Bugge 1965; Elliott 1966; Nijland and Touret 2001; Engvik et al. 2008). In the latter, albitization occurs on a regional scale (Fig. 11.22). Though called albitization, in many cases spectacular albite + actinolite (hedenbergite) ± quartz assemblages are formed, for example in the Bamble sector. In many cases, albitization spreads from central veins that are filled with actinolite (± hedenbergite) (Fig. 11.23). Albitization is accompanied by enrichment in Ti, in the form of abundant titanite and rutile (Watson 1912; Nijland and Touret 2001). The presence of an albite-component in fluids enhances the solubility of rutile (Hayden and Manning 2011). Initial stages often preserve original sedimentary or igneous textures on the meso-scale, as illustrated for example by a graphic pegmatite from Mjåvatn, Norway (Nijland and Touret 2001). Here, plagioclase is replaced by albite, and quartz by actinolite/clinopyroxene intergrowths, whilst the original graphic texture is apparently preserved (Fig. 11.24). On the microscale, however, the original grain boundaries are not preserved. In this case, albitization is evidently accompanied by the leaching of silica. The comparable process of episyenitization, a term originally coined by Lacroix (1920) to describe dequartzification, i.e. the subsolidus leaching of quartz from granitic rocks, has been documented in several cases under greenschist to lower amphibolite facies conditions. In most cases, dequartzification is accompanied by albitization (e.g. Cathelineau 1985, 1986; Petersson and Eliasson 1997; Boulvais et al. 2007). Interestingly, in the Bamble sector, albitite occurrences are often accompanied by the formation of hydrothermal quartz pipes up to several metres in diameter, consisting of very clear quartz and up to several decimetres long (by a 0.5–1 mm diameter) actinolite crystals.

Restoration of volatiles in granulites requires the formation of a new metamorphic plumbing network in response to deformation, including processes such as strain partitioning channeling fluid flow and fluid overpressure initiating fracturing (Etheridge et al. 1983; Yardley 1997; Oliver and Bons 2001). Munz et al. (1995) studied fluid inclusions in albitized rocks from the Modum amphibolite facies terrain, south Norway, which show methane-dominated hydrocarbons and low K, Na-Ca-Cl brines with $Ca/Na < 1$ and Br/Cl ratios comparable to modern seawater. These authors interpreted these as evidence for deep infiltration of fluids from sedimentary basins.

In the case of Mjåvatn, mentioned above, fluid inclusions in the albitite-actinolite-clinopyroxene assemblage show brines with c. 25 wt% NaCl (Nijland and Touret 2001). Ordinary amphibolitized metagabbro (i.e. not affected by the formation of albite-actinolite assemblages) from the area show, besides high density CO_2-

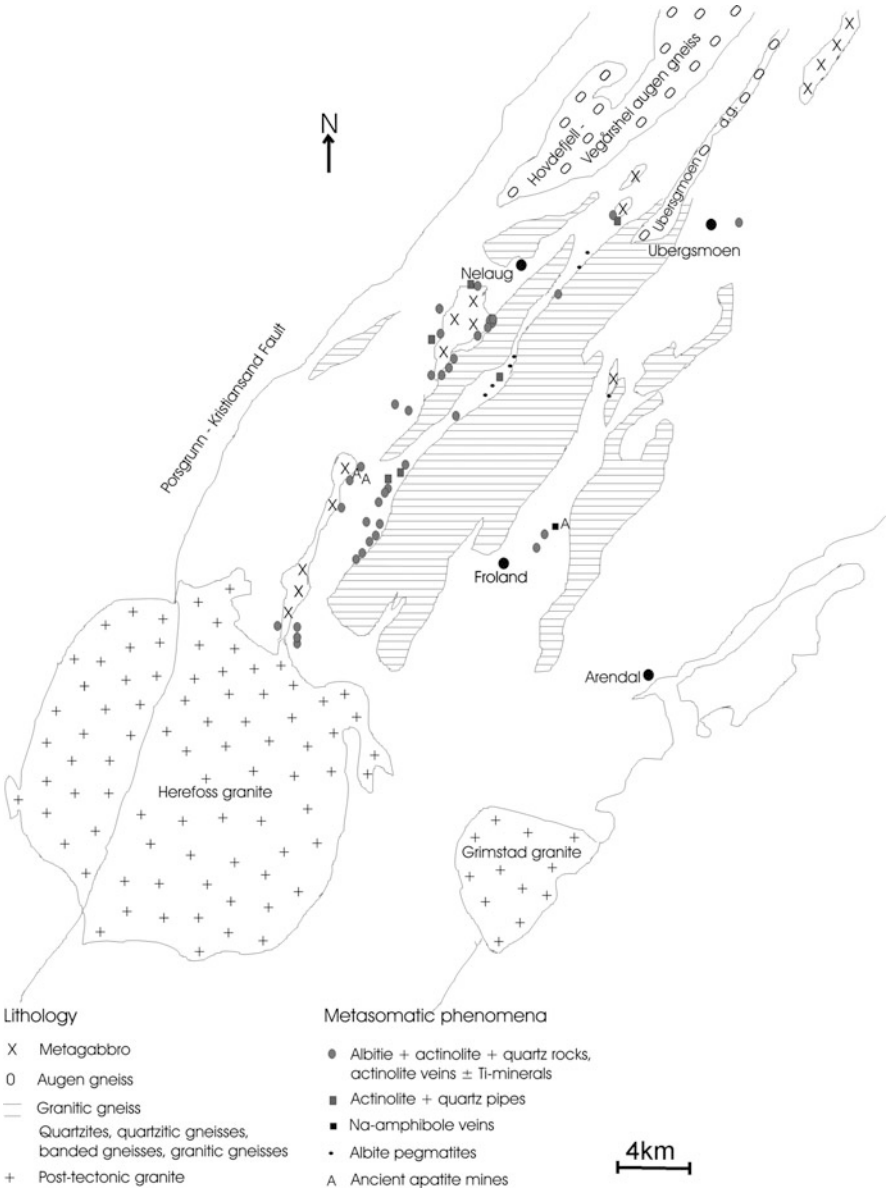

Fig. 11.22 Regional distribution of metasomatic and magmatic albitites in the Froland area of the Bamble sector, South Norway

N_2 and low density N_2 fluid inclusions, NaCl brine inclusions as well (Dam 1995). This might suggest that infiltration of brines starts prior to the formation of albite-actinolite assemblages. Albite-actinolite assemblages are generally considered to be formed at 350–450°C, but albitization may actually start at higher temperatures.

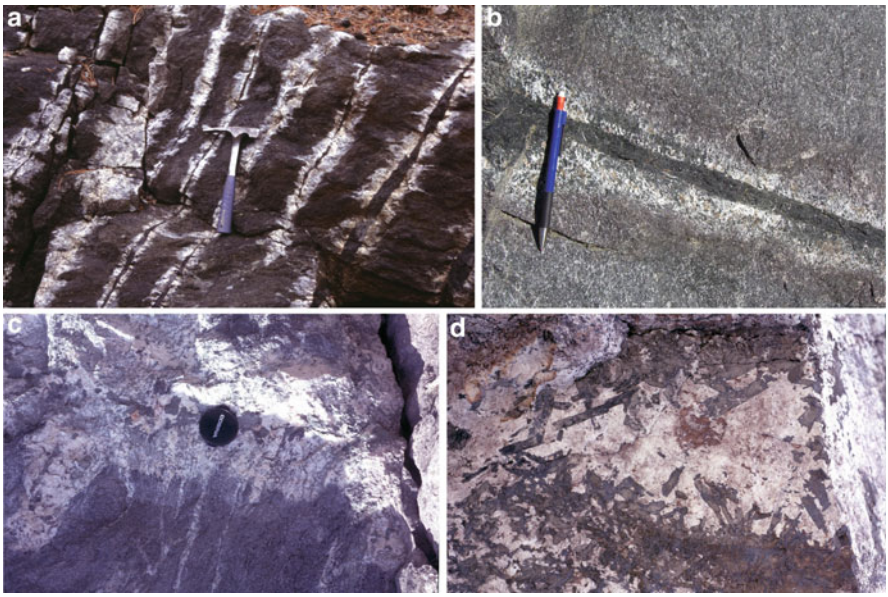

Fig. 11.23 Examples of albitization in the Bamble sector, Norway: (**a**, **b**): spreading from central veins filled by actinolite (**a**): Barlindåsen and (**b**): Kleivane). (**c**, **d**): progressive albitization of gneisses, finally resulting in coarse grained albite-clinopyroxene rock (Mjåvatn); both pictures are from the same, continuous outcrop

Fig. 11.24 Replacement of graphic pegmatite by albite + actinolite/clinopyroxene from Mjåvatn, Bamble sector, Norway (cf. Nijland and Touret 2001)

TEM-studies show that actinolites from metasomatic albitite rocks in the Bamble sector exhibit cummingtonite exsolution lamellae, indicating formation above the cummingtonite solvus, ca. 620°C at $P_{Fluid} = 2$ kb (Ter Haar 1988). This relatively

high temperature initiation for the albitization process may be supported by the fact that metasomatic albitites are accompanied by magmatic-hydrothermal pegmatitic dykes or veins, like clinopyroxene-bearing albite pegmatites in the Bamble sector (Bodart 1968; Morshuis 1991) or magmatic-hydrothermal albite-actinolite-apatite rocks in the Mary Kathleen fold belt, Australia (Mark and Foster 2000). In the Froland area of the Bamble sector, where albitization is best developed, it affects both metasediments and metagabbros, in particular along their contacts. In addition, it occurs along late joints. It may be speculated that synmetamorphic saline fluids were collected at the lithological contacts during cooling and uplift.

From an economic geological point of view, it is worth noting that albitization (and dequartzification) is, in several cases, accompanied by the U mineralizations (e.g. Hoeve 1974; Hålenius and Smellie 1983; Lobato et al. 1983; Poty et al. 1986; Porto da Silveira et al. 1991; Respaut et al. 1991), Cu and Au (Frietsch et al. 1997), Fe (Nuutilainen 1968), Ti (e.g. Watson 1912; Force 1991; Korneliussen et al. 1992) or apatite (Bugge 1922; Nijland and Maijer 1991).

11.5.6 Long Distance Action of Granulite Fluids

If granulite fluids leave behind a wealth of traces on the single mineral or hand specimen scale, their long distance action, namely the possibility to transport elements without noticeable modification of the rock structure, is much more difficult to assess. Besides localized evidence of granulite facies fluids, as discussed above, a number of arguments suggest that these fluids could scavenge some elements at peak metamorphic conditions, subsequently transporting and redistributing them during retrograde stages. Such a hypothesis is notably supported by the fact that many medium to high grade metamorphic areas, like India, Madagascar and Norway, contain shear zones of the regional scale, typically over 100 km by 10 km (Newton 1990; Pili et al. 1997, 1999), in which up to 20% of the country rocks are replaced by massive calcite and/or dolomite (e.g. Dahlgren et al. 1993; Newton and Manning 2002; Fig. 11.25). Carbonate formation occurred at 500–700°C and the uniform carbon isotopic signature ($\delta^{13}C$ about −7‰) clearly points to a primary mantle origin. A great number of gold deposits are associated with this type of environment (Archean epigenetic gold deposits, e.g. Eisenlohr et al. 1989). With this respect, it is interesting to note that many granulite terranes, on a regional scale, appear to be strongly depleted in gold (e.g. Bamble, Norway and the Lewisian, Scotland; Cameron 1989a,b, 1994). One may speculate that brines have scavenged some elements during granulite facies metamorphism, notably Au or U (Cameron 1988; Chi et al. 2006; Cuney and Kyzer 2009) and transported them, such that they finally end up being deposited in late shear zones.

A similar mechanism had been proposed to scavenge all LILE from the lower crust. This is based on the assumption that the lower crust was depleted in heat producing elements, notably K or Rb, a notion first put forward by Ramberg (1951, 1952) and Heier (1965, 1973). As a matter of fact, this supposed depletion had been

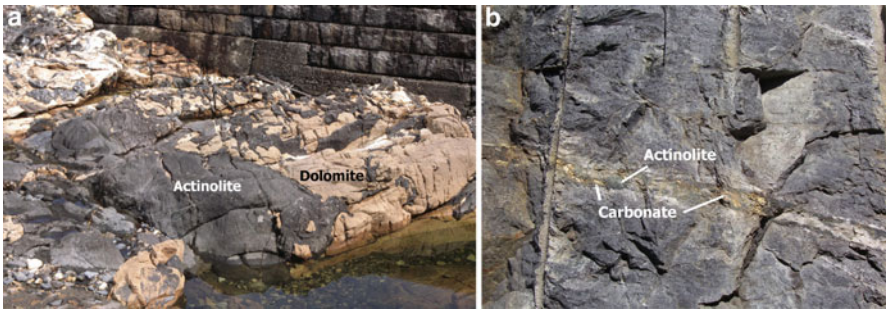

Fig. 11.25 (**a**): Dolomite-actinolite rocks at Kammerfoss, Bamble sector, Norway (cf. Dahlgren et al. 1993; note concrete blocks for scale). (**b**): carbonate-actinolite vein at Kleivane, Bamble sector, Norway (width of vein about 6–8 cm)

a key argument for the vapour-absent melting model of granulite metamorphism, i.e. LILE being supposedly removed by anatectic melts (Fyfe 1973). More detailed studies have shown that the picture is much more complicated (Touret 1996). LILE depletion is not systematic but rather variable within granulite facies terranes (e.g. Moine et al. 1972; Rudnick et al. 1985). In some granulites, many minerals are actually LILE-enriched (Villaseca et al. 2007). Some, notably associated magmatic rocks, such as charnockites, may also be LILE-enriched. In some areas where this depletion exists, like the southern part of the Bamble sector, once taken as the most typical and extreme example of granulite facies LILE-depletion (Field et al. 1980), it has been shown that this depletion is related to the initial whole rock composition. Whereas several supracrustal rocks are not depleted at all (Moine et al. 1972), LILE-depletion of igneous rocks is a premetamorphic feature preserved during high grade metamorphism (Knudsen and Andersen 1999). Similar igneous, premetamorphic LILE-depletion was proposed by Rollinson and Tarney (2005). However, several other studies have demonstrated LILE and HFSE mobility during incipient charnockitization (e.g. Raith and Srikantappa 1993), which may affect granulite facies terrains in general (Hansen and Harlov 2007).

It seems finally that the only elements which can be transported over long distances outside of the granulite domain are those which are relatively soluble at granulite facies conditions and may remain in solution over a wide range of P-T conditions. Gold, U and some REE are good candidates, in contrast to alkali (K or Na) that are rapidly redistributed in the host rocks. Major minerals deposited from fluids during retrogradation are silica (quartz) and carbonates, in such quantities that the fluid source at peak conditions must have been very large indeed. It is likely that fluids remaining after mineral deposition may even reach the hydrosphere and atmosphere, with important climatic consequences (Touret and Huizenga 2012). The compositional similarities between these fluids and those occurring at peak conditions indicate a common source, namely late fluids collected in shear zones from peak metamorphic fluids under decreasing P-T conditions. The extent of these retrograde phenomena shows indeed that amount of *water undersaturated* fluid at

peak metamorphic P-T conditions must have been very great indeed, orders of magnitude more than the minute remnants now preserved in fluid inclusions.

11.6 Conclusions

The metamorphic transition from amphibolite to granulite facies is traditionally regarded as a transition from wet to dry rocks. In reality, granulites are all but fluid-free. Research over the past decades has shown two free fluid phases being present in granulites, i.e. CO_2 and highly saline brines. The transition from amphibolite to granulite facies does not only reflect an increase in temperature, but also a transition from a H_2O-dominated metamorphic facies to a CO_2 and brine-dominated one. The two fluids present in granulite facies rocks are immiscible under granulite facies P-T conditions (Bowers and Helgeson 1983; Johnson 1991; Shmulovich and Graham 2004). They also have rather different transport properties and effects on the solubilities of minerals and elements. Their presence, however, implies that fluid-assisted reactions may occur, including removal and introduction of specific elements (metasomatism). Discussing the origin of these fluids is outside of the scope of this current review. However, it has been recently discussed at some length by Touret (2009) and Touret and Huizenga (2012), who basically conclude that CO_2 is dominantly, if not exclusively, mantle-derived. As deduced from coupled He-CO_2 fluxes, CO_2 flux from the mantle is too low to generate a regional scale amphibolite to granulite facies transition (O'Nions and Oxburgh 1988). The other granulite facies fluid, brines, is an essential companion. The question of their origin is more complicated. Some brines are probably locally derived, remnants of original sedimentary pore waters (Yardley and Graham 2002), which may have been possibly progressively concentrated during metamorphism (Kullerud 1996; Markl et al. 1998). Others, like CO_2, may have been introduced from the underlying mantle by intrusions at peak metamorphic conditions (e.g. Hansen et al. 1995). These may ultimately be derived from remnants of subducted crust (Newton et al. 1998). Like for CO_2, the carbonatite connexion cannot be excluded for brines. Brines and carbonatite melts are among the most typical inclusions found in diamonds (Klein-BenDavid et al. 2004; Araujo et al. 2009), in which part of the brines may be of juvenile mantle origin instead of oceanic crust incorporated in the mantle (Burgess et al. 2009). If CO_2 derives from the breakdown of metasomatic carbonate melts in the mantle, akin to carbonatites (Touret 2009), it seems probable that at least some brines also have this origin. In all cases, it should be realized that fluids, whether locally generated or introduced, may mix or change composition by reactive transport.

The widespread occurrence of metasomatic features does not preclude that, in the same areas and often within close range, pre-metamorphic features, such as whole rock chemistry reflecting surficial weathering like lateritization (Bol et al. 1989) or premetamorphic albitization (Owen et al. 2003), sedimentary structures (Nijland et al. 1993) and/or regional pre-metamorphic carbon and oxygen isotopic

trends in carbonates and graphites from metasediments (Broekmans et al. 1994; Bol et al. 1995; Boulvais et al. 1998) are still present, having survived both devolatilization and the action of granulite facies fluids. They have also survived melt extraction, another important process occurring widely in the middle and lower continental crust (Brown and White 2008). Overall, the lower continental crust appears to be a rather complicated domain, in which highly transformed and well-preserved rocks occur side by side, sometimes on the scale of the outcrop or even the hand specimen. Tracing the contributions from the different processes relating to granulite genesis and metasomatism during the transition from amphibolite to granulite facies will be a great challenge for future work.

Acknowledgements Successive versions of this paper have benefited from comments and/or discussions and/or (in)formal reviews by H. Austrheim T. Andersen, M. Cuney, D.E. Harlov, W.L. Griffin, R.C. Newton, D. Rumble and O. Safonov, as well as by careful editorial work by the editors of this volume. The senior author wants to acknowledge the constant support and inspiration he has got from Bob Newton during more than 40 years, as well as the technical support of the ENS team (C. Chopin, E. Charon) for a number of microphotographs.

References

Abramov SS, Kurdyukov EB (1997) The origin of charnockite-enderbite complexes by magmatic replacement: geochemical evidence. Geochem Int 35:219–226

Ague JJ (2003) Fluid flow in the deep crust. In: Rudnick RL (ed) Treatise on geochemistry, vol 3, The crust. Elsevier, Amsterdam, pp 195–228

Aitken BG (1983) T-X_{CO2} stability relations and phase equilibria of a calcic carbonate scapolite. Geochim Cosmochim Acta 47:351–362

Amundsen HEF, Griffin WL, O'Reilly SY (1988) The nature of the lithosphere beneath north-western Spitsbergen: xenolith evidence. In: Kristoffersen Y (ed) Progress in studies of the lithosphere in Norway, vol. 3, Norges Geologiske Undersøkelse Special Publication. Norges Geologiske Undersøkelse, Trondheim pp 58–65

Aranovich LY, Shmulovich KI, Fedkin VV (1987) The H_2O and CO_2 regime in regional metamorphism. Int Geol Rev 29:1379–1401

Araujo DP, Griffin WL, O'Reilly SY (2009) Mantle melts, metasomatism and diamond formation: insights from melt inclusions in xenoliths from Diavik, Slave craton. Lithos 112(suppl 2):675–682

Baker JH (1985) Rare earth and other trace element mobility accompanying albitization in a Proterozoic granite, W Bergslagen, Sweden. Mineral Mag 49:107–115

Ballèvre M, Hensen BJ, Reynard B (1997) Orthopyroxene-andalusite symplectites replacing cordierite in granulites from the Strangways range (Arunta block, central Australia): a new twist to the pressure-temperature history. Geology 25:215–218

Baltybaev SK, Levchenkov OA, Glebovitskii VA, Rizvanova NG, Yakubovich OV, Fedoseenko AM (2010) Timing of the regional postmigmatitic K-feldspar mineralization on the base of U-Pb dating of monazite (metamorphic complex of the northern Ladoga region). Doklady Earth Sci 430:186–189

Becke F (1908) Ueber Myrmekite. Schweiz Mineral Petrograph Mitt 27:377–390

Beloussov VV (1966) Modern concepts of the structure and development of the earth's crust and the upper mantle of continents. J Geol Soc Lond 122:293–314

Bingen B (1989) Geochemistry of Sveconorwegian augen gneisses from SW Norway at the amphibolite-granulite transition. Norsk Geol Tidsskr 69:177–189

Bingen B, Demaiffe D, Hertogen J (1996) Redistribution of rare earth elements, thorium, and uranium over accessory minerals in the course of amphibolite to granulite metamorphism: the role of apatite and monazite in orthogneisses from southwestern Norway. Geochim Cosmochim Acta 60:1341–1354

Binns RA (1964) Zones of progressive regional metamorphism in the Willyama complex, Broken Hill district, New South Wales. J Geol Soc Aust 11:283–330

Bodart DE (1968) On the paragenesis of albitites. Norsk Geol Tidsskr 48:269–280

Bohlen SR (1991) On the formation of granulites. J Metamorph Geol 9:223–229

Bohlen SR, Mezger K (1989) Origin of granulite terranes and the formation of the lowermost continental crust. Science 244:326–329

Bol LCGM, Maijer C, Jansen JBH (1989) Premetamorphic lateritization in Proterozoic metabasites of Rogaland, SW Norway. Contrib Mineral Petrol 103:299–309

Bol LCGM, Nijland TG, Sauter PCC, Jansen JBH, Valley JW (1995) Preservation of premetamorphic oxygen and carbon isotopic trends in granulite facies marbles from Rogaland, SW Norway. Am J Sci 295:1179–1219

Bolder-Schrijver L, Kriegsman L, Touret JLR (2000) Primary carbonate/CO_2 inclusions in sapphirine-bearing granulites from central Sri Lanka. J Metamorph Geol 18:259–269

Boles JR (1982) Active albitization of plagioclase, Gulf Coast Tertiary. Am J Sci 282:165–180

Boulvais P, Fourcade S, Gruau G, Moine B, Cuney M (1998) Persistence of pre-metamorphic C and O isotopic signatures in marbles subject to Pan-African granulite-facies metamorphism and U-Th mineralization (Tranomaro, southeast Madagascar). Chem Geol 150:247–262

Boulvais P, Fourcade S, Moine B, Gruau G, Cuney M (2000) Rare-earth elements distribution in granulite-facies marbles: a witness of fluid-rock interaction. Lithos 53:117–126

Boulvais P, Ruffet G, Cornichet J, Mermet M (2007) Cretaceous albitization and dequartzification of Hercynian peraluminous granite in the Salvezines massif (French Pyrénées). Lithos 93: 89–106

Bowers TS, Helgeson HC (1983) Calculation of the thermodynamic and geochemical consequences of nonideal mixing in the system H_2O-CO_2-NaCl on phase relations in geologic systems: metamorphic equilibria at high pressures and temperatures. Am Mineral 68: 1059–1075

Bradshaw JY (1989) Early Cretaceous vein-related garnet granulite in Fiordland, southwest New Zealand: a case for infiltration of mantle-derived CO_2-rich fluids. J Geol 97:697–717

Broekmans MATM, Nijland TG, Jansen JBH (1994) Are stable isotopic trends in amphibolite to granulite facies transitions metamorphic or diagenetic ? – an answer for the Arendal area (Bamble sector, SE Norway) from Mid-Proterozoic carbon-bearing rocks. Am J Sci 294: 1135–1165

Brøgger WC (1934) On several Archaean rocks from the south coast of Norway. II the South Norwegian hyperites and their metamorphism, vol 1, Det Norske Videnskaps-Akademi i Oslo Skrifter, Matematisk-Naturvidenskapelig Klasse. I kommisjon hos J. Dybwad, Oslo

Brøgger WC, Reusch HH (1875) Vorkommen des Apatit in Norwegen. Z deutsch geol Gesell 27:646–702

Brown M, White RW (2008) Processes in granulite metamorphism. J Metamorph Geol 26: 121–124

Budzyn B, Michalik M, Malata T, Poprawa P (2005) Primary and secondary monazite in a calcitized gneiss clast from Bukowiec (the Silesian unit, western outer Carpathians). Mineral Pol 36:161–165

Bugge A (1965) Iakttagelser fra rektangelbladet Kragerö og den store grunnfjellbreksje. vol 229, Norges Geologiske Undersøkelse Bulletin, Norges Geologiske Undersøkelse, Trondheim

Bugge C (1922) Statens apatitdrift i rationeringstiden, vol 110, Norges Geologiske Undersøkelse Bulletin, Norges Geologiske Undersøkelse, Trondheim

Bugge JAW (1945) The geological importance of diffusion in the solid state. vol 13, Norske Videnskaps-Akademi i Oslo Skrifter, Matematisk-Naturvidenskapelig Klasse, Det Norske Videnskaps-Akademi, Oslo

Bugge JAW (1978) Kongsberg – Bamble complex. In: Bowie SHO, Kvalheim A, Haslam MW (eds) Mineral deposits of Europe, vol 1, Northwest Europe. Institution of Mining and Metallurgy and Mineralogical Society, London, pp 213–217

Burgess R, Cartigny P, Harrison D, Hobson E, Harris J (2009) Volatile composition of microinclusions in diamonds from the Panda kimberlite, Canada: implications for chemical and isotopic heterogeneity in the mantle. Geochim Cosmochim Acta 73:1779–1794

Cabella R, Luccheti G, Marescotti P (2001) Authigenic monazite and xenotime from pelitic metacherts in pumpellyite-actinolite-facies conditions, Sestri-Voltaggio zone, central Liguria, Italy. Can Mineral 39:717–727

Cameron EM (1988) Archean gold: relation to granulite formation and redox zoning in the crust. Geology 16:109–112

Cameron EM (1989a) Derivation of gold by oxidative metamorphism of a deep ductile shear zone. Part 1. Conceptual model. J Geochem Explor 31:135–147

Cameron EM (1989b) Derivation of gold by oxidative metamorphism of a deep ductile shear zone. Part 2. Evidence from the Bamble belt, south Norway. J Geochem Explor 31:149–169

Cameron EM (1994) Depletion of gold and LILE in the lower crust: Lewisian complex, Scotland. J Geol Soc Lond 151:747–775

Cameron EM, Hattori K (1994) Highly oxidized deep metamorphic zones: occurrence and origin. Mineral Mag 58A:142–143

Cathelineau M (1985) Épisénitisation ou déquartzification hydrothermale: une typologie basée sur les successions minérales et sur le comportement différentiel de Si, Na et K. Comptes Rendus de l'Académie des Sciences Paris, série II 300:677–680

Cathelineau M (1986) The hydrothermal alkali metasomatism effects on granitic rocks: quartz dissolution and related subsolidus changes. J Petrol 27:945–965

Chamberlain CP, Rumble D III (1989) The influence of fluids on the thermal history of a metamorphic terrain: new Hampshire, USA. In: Daly JS, Cliff RA, Yardley BWD (eds) Evolution of metamorphic belts, vol 43, Geological Society Special Publication. Blackwell Science, Oxford, pp 203–213

Chi G, Dube B, Williamson K, Williams-Jones AE (2006) Formation of the campbell-red lake gold deposit by H_2O-poor, CO_2-dominated fluids. Miner Deposita 40:726–741

Clemens JD (2006) Melting of the continental crust: fluid regimes, melting reactions and source-rock fertility. In: Brown M, Rushmer T (eds) Evolution and differentiation of the continental crust. Cambridge University Press, Cambridge, pp 297–331

Coolen JJMMM (1980) Chemical petrology of the Furua granulite complex, southern Tanzania. Ph.D. thesis, GUA Papers of Geology vol 13, GUA Papers of Geology, Free University, Amsterdam

Coolen JJMMM (1982) Carbonic fluid inclusions in granulites from Tanzania: a comparison of geobarometric methods based on fluid density and mineral chemistry. Chem Geol 37:59–77

Cuney M, Coulibaly Y, Boiron MC (2007) High-density early CO_2 fluids in the ultrahigh temperature granulites of Ihouhaouene (In Ouzzal, Algeria). Lithos 96:402–414

Cuney M, Kyzer K (2009) Recent and not-so-recent developments in uranium deposits and implication for exploration. Mineralogical Association of Canada Short Course Series vol 39, Mineralogical Association of Canada Short Course Series, Mineralogical Association of Canada, Ottawa

Dahanayake K, Ranasinghe AP (1981) Source rocks of gem minerals. a case study from Sri Lanka. Miner Deposita 16:103–111

Dahlgren S, Bogoch R, Magaritz M, Michard A (1993) Hydrothermal dolomite marbles associated with charnockitic magmatism in Proterozoic Bamble shear belt, south Norway. Contrib Mineral Petrol 113:394–409

Dam BP (1995) Geodynamics in the Bamble area during Gothian- and Sveconorwegian times, vol 117, Geologica Ultraiectina, Utrecht University, Utrecht

Della Giustina MES, Pimental MM, Ferreira Filho CF, Maia de Hollanda MHB (2010) Dating coeval mafic magmatism and ultrahigh-temperature metamorphism in the Anápolis-Itauçu Complex, central Brazil. In: Della Giustina MES (ed) Geocronologia e significado tectônico de rochas máficas de alto grau metamórfico da Faixa Brasília. Ph.D. thesis, Universidade de Brasília, Brasília, pp 18–56

De Haas GJLM, Nijland TG, Valbracht PJ, Maijer C, Verschure R, Andersen T (2002) Magmatic versus metamorphic origin of olivine-plagioclase coronas. Contrib Mineral Petrol 143:537–550

Dunai TJ, Touret JLR (1993) A noble-gas study of a granulite sample from the Nilgiri Hills, southern India: implications for granulite formation. Earth Planet Sci Lett 119:271–281

Eggenkamp HGM, Schuiling RD (1995) δ^{37}Cl variations in selected minerals: a possible tool for exploration. J Geochem Explor 55:249–255

Eggler DH, Kadik AA (1979) The system $NaAlSi_3O_8$-H_2O-CO_2 to 20 kbars pressure: 1. Compositional and thermodynamic relations of liquids and vapors coexisting with albite. Am Mineral 64:1036–1048

Eisenlohr BN, Groves D, Partington GA (1989) Crustal-scale shear zones and their significance to Archaean gold mineralization in western Australia. Miner Deposita 24:1–8

Elliott RB (1966) The association of amphibolite and albitite, Kragerö, south Norway. Geol Mag 103:1–7

Engel AEJ, Engel CG (1958) Progressive metamorphism and granitization of the major paragneiss, northwest Adirondack Mountains, New York. I. Bull Geol Soc Am 69:1369–1414

Engel AEJ, Engel CG (1960) Progressive metamorphism and granitization of the major paragneiss, northwest Adirondack Mountains, New York. II. Bull Geol Soc Am 71:1–58

Engvik AK, Austrheim H (2010) Formation of sapphirine and corundum in scapolitised and Mg-metasomatised gabbro. Terra Nova 22:166–171

Engvik AK, Golla-Schindler U, Berndt J, Austrheim H, Putnis A (2009) Intragranular replacement of chlorapatite by hydroxy-fluor-apatite during metasomatism. Lithos 112:236–246

Engvik AK, Mezger K, Wortelkamp S, Bast R, Corfu F, Korneliussen A, Ihlen P, Bingen B, Austrheim H (2011) Metasomatism of gabbro-mineral replacement and element mobilization during the Sveconorwegian metamorphic event. J Metamorph Geol 29:399–423

Engvik AK, Putnis A, Fitzgerald JD, Austrheim H (2008) Albitization of granitic rocks: the mechanism of replacement of oligoclase by albite. Can Mineral 46:1401–1415

Eskola P (1914) On the petrology of the Orijärvi region in southwestern Finland, vol 40, Commision Géologique de Finlande Bulletin, ommision Géologique de Finlande, Helsinki

Etheridge MA, Wall VJ, Vernon RH (1983) The role of the fluid phase during regional metamorphism and deformation. J Metamorph Geol 1:205–226

Evans J, Zalasiewicz J (1996) U-Pb, Pb-Pb and Sm-Nd dating of authigenic monazite: implications for the diagenetic evolution of the Welsh basin. Earth Planet Sci Lett 144:421–433

Farquhar J, Chacko T (1991) Isotopic evidence for involvement of CO_2-bearing magmas in granulite formation. Nature 354:60–63

Field D, Drury SA, Cooper DC (1980) Rare-earth and LIL element fractionation in high grade charnockitic gneisses, south Norway. Lithos 13:281–289

Fonarev VI, Santosh M, Filimorov MB, Vasiukova OV (2001) Pressure-temperature fluid history and exhumation path of a Gondwana fragment: Trivandrum granulite block, southern India. Gondwana Res 4:615–616

Fonteilles M (1970) Géologie des terrains métamorphiques et granitiques du Massif de l'Agly (Pyrénées Orientales). Bulletin B R G M Sect IV 3:21–72

Force ER (1991) Geology of titanium-mineral deposits, vol 259, Geological society of america special paper. Geological Society of America, Boulder

Franz L, Harlov DE (1998) High grade K-feldspar veining in granulites from the Ivrea-Verbano zone, northern Italy: fluid flow in the lower crust and implications for granulite facies genesis. J Geol 106:455–472

Friend CRL (1981) Charnockite and granite formation and influx of CO_2 at Kabbaldurga. Nature 294:550–552
Frietsch R, Tuisku P, Martinsson O, Perdahl JA (1997) Early Proterozoic Cu-(Au) and Fe ore deposits associated with regional Na-Cl metasomatism in northern Fennoscandia. Ore Geol Rev 12:1–34
Frost BR (1991) Introduction to oxygen fugacity and its petrologic importance. In: Lindsley DH (ed) Oxide minerals: petrologic and magnetic significance, vol 25, Reviews in mineralogy. Mineralogical Society of America, Washington, DC, pp 1–9
Frost BR, Frost CD (1987) CO_2, melts and granulite metamorphism. Nature 327:503–506
Frost BR, Frost CD (2008) On charnockites. Gondwana Res 13:30–44
Frost BR, Frost CD, Touret JLR (1989) Magmas as a source of heat and fluids in granulite metamorphism. In: Bridgwater D (ed) Fluid movements-element transport and the composition of the deep crust. Kluwer, Dordrecht, pp 1–18
Frost BR, Touret J (1989) Magmatic CO_2 and saline melts from the Sybille monzosyenite, Laramie anorthosite complex, Wyoming. Contrib Mineral Petrol 103:178–186
Fyfe WS (1973) The granulite facies, partial melting and the Archean crust. Philos Trans R Soc Lond A273:457–461
Fyfe WS, Prince NJ, Thompson AB (1978) Fluids in the Earth's crust. Elsevier, Amsterdam
Girault JP (1952) Kornerupine from Lac Ste-Marie, Quebec, Canada. Am Mineral 37:531–541
Gibert F, Guillaume D, Laporte D (1998) Importance of fluid immiscibility in the H_2O-NaCl-CO_2 system and selective CO_2 entrapment in granulites: experimental phase diagram at 5–7 kbar, 900°C and wetting textures. Eur J Mineral 10:1109–1123
Godard G, Smith D (1999) Preiswerkite and Na-(Mg, Fe)-margarite in eclogites. Contrib Mineral Petrol 136:20–32
Goldschmidt VM (1922) On the metasomatic processes in silicate rocks. Econ Geol 17:105–123
Goldsmith JR (1976) Scapolites, granulites, and volatiles in the lower crust. Geol Soc Am Bull 87:161–168
Green JC (1956) Geology of the Storkollen-Blankenberg area, Kragerö, Norway. Nor Geol Tidsskr 36:89–140
Grew ES, Chernosky JH, Werding G, Abraham K, Marquez N, Hinthorne JR (1990) Chemistry of kornerupine and associated minerals, wet chemical, ion microprobe, and X-ray study emphasizing Li, Be, B, and F contents. J Petrol 31:1025–1070
Guillot S, Le Fort P, Pecher A, Roy Barman M, Apphrahamian J (1995) Contact metamorphism and depth of emplacement of the Manaslu granite (central Nepal): implications for Himalayan orogenesis. Tectonophysics 241:99–119
Guzmics T, Mitchell R, Szabó C, Berkesi M, Milke R, Abart R (2011) Carbonatite melt inclusions in coexisting magnetite, apatite and monticellite in Kerimasi calciocarbonatite, Tanzania: melt inclusions and petrogenesis. Contrib Mineral Petrol 161:177–196
Hålenius U, Smellie JAT (1983) Mineralisations of the Arjeplog-Arvidsjaur-Sorsele uranium province: mineralogical studies of selected uranium occurrences. N Jahrb Mineral Abh 147:229–252
Hansen EC, Harlov DE (2007) Whole rock, phosphate, and silicate compositions across an amphibolite- to granulite-facies transition, Tamil Nadu, India. J Petrol 48:1641–1680
Hansen EC, Janardhan AS, Newton RC, Prame WKBN, Ravindra Kumar GR (1987) Arrested charnockite formation in southern India and Sri Lanka. Contrib Mineral Petrol 96:225–244
Hansen EC, Newton RC, Janardhan AS (1984) Fluid inclusions in rocks from amphibolite-facies gneiss to charnockite progression in southern Karnataka, India: direct evidence concerning the fluids of granulite metamorphism. J Metamorph Geol 2:249–264
Hansen EC, Newton RC, Janardhan AS, Lindenberg S (1995) Differentiation of late Archean crust in the eastern Dharwar craton, south India. J Geol 103:629–651
Harley SL (1989) The origin of granulites: a metamorphic perspective. Geol Mag 126:215–247
Harley SL (1993) Proterozoic granulite terranes. In: Condie KC (ed) Proterozoic crustal growth. Elsevier, Amsterdam, pp 301–359

Harley SL (2008) Refining the P-T records of UHT crustal metamorphism. J Metamorph Geol 26:125–154

Harley SL, Santosh M (1995) Wollastonite at Nuliyam, Kerala, southern India: a reassessment of CO_2-infiltration and charnockite formation at a classic locality. Contrib Mineral Petrol 120:83–94

Harlov DE (1992) Comparative oxygen barometry in granulites, Bamble sector, SE Norway. J Geol 100:447–464

Harlov DE (2000) Titaniferous magnetite-ilmenite thermometry/titaniferous magnetite-ilmenite-orthopyroxene-quartz oxygen barometry in orthopyroxene-bearing granulite facies gneisses, Bamble sector, SE Norway: implications for the role of high grade CO_2-rich fluids during granulite genesis. Contrib Mineral Petrol 139:180–197

Harlov DE, Dunkley D (2010) Experimental high-grade alteration of zircon using akali- and Ca-bearing solutions: resetting geochronometer during metasomatism. AGU Fall meeting, San Francisco, abstract V41D-2301

Harlov DE, Förster HJ (2002) High-grade fluid metasomatism on both a local and a regional scale: the Seward peninsula, Alaska, and the Val Strona di Omegna, Ivrea-Verbano zone, northern Italy. Part I: petrography and silicate mineral chemistry. J Petrol 43:769–799

Harlov DE, Förster HJ (2003) Fluid-induced nucleation of (Y + REE)-phosphate minerals within apatite: nature and experiment. Part II. Fluorapatite. Am Mineral 88:1209–1229

Harlov D, Förster HJ, Nijland TG (2002) Fluid-induced nucleation of (Y + REE)-phosphate minerals within apatite: nature and experiment. Part I. Chlorapatite. Am Mineral 87:245–261

Harlov DE, Hansen EC (2005) Oxide and sulphide isograds along a late Archean, deep-crustal profile in Tamil Nadu, south India. J Metamorph Geol 23:241–259

Harlov DE, Hansen EC, Bigler C (1998) Petrologic evidence for K-feldspar metasomatism in granulite facies rocks. Chem Geol 151:373–386

Harlov DE, Hetherington CJ (2010) Partial high-grade alteration of monazite using alkali-bearing fluids: experiment and nature. Am Mineral 95:1105–1108

Harlov DE, Johansson L, Van den Kerkhof A, Förster HJ (2006) The role of advective fluid flow and diffusion during localized, solid-state dehydration: Söndrum Stenhuggeriet, Halmstad, SW Sweden. J Petrol 47:3–33

Harlov DE, Newton RC, Hansen EC, Janardhan AS (1997) Oxide and sulphide minerals in highly oxidized, Rb-depleted, Archaean granulites of the Shevaroy Hills massif, south India: oxidation states and the role of metamorphic fluids. J Metamorph Geol 15:701–717

Harlov DE, Wirth R (2000) K-feldspar-quartz and K-feldspar-plagioclase phase boundary interactions in garnet-orthopyroxene gneisses from the Val Strona di Omegna, Ivrea-Verbano zone, northern Italy: a case for high grade emplacement under relatively dry conditions. Contrib Mineral Petrol 140:148–162

Harlov DE, Wirth R, Förster HJ (2005) An experimental study of dissolution-reprecipitation in fluorapatite: fluid infiltration and the formation of monazite. Contrib Mineral Petrol 150:268–286

Harlov DE, Wirth R, Hetherington C (2011) Fluid-mediated partial alteration of monazite: the role of coupled dissolution-reprecipitation during apparent solid-state element mass transfer. Contrib Mineral Petrol 162:329–348

Hayden LA, Manning CE (2011) Rutile solubility in supercritical $NaAlSi_3O_8$-H_2O fluids. Chem Geol 284:74–81

Heier KS (1965) Metamorphism and the chemical differentiation of the crust. GFF 87:249–256

Heier KS (1973) Geochemistry of granulite facies rocks and problems of their origin. Philos Trans R Soc Lond A273:429–442

Hellman PL, Smith RE, Henderson P (1979) The mobility of the rare earth elements: evidence and implications from selected terrains effected by burial metamorphism. Contrib Mineral Petrol 71:23–44

Hinchey AM, Carr SD (2007) Protolith composition of cordierite-gedrite basement rocks and garnet amphibolite of the Bearpaw Lake area of the Thor-Odin dome, Monashee complex, British Columbia, Canada. Can Mineral 45:607–629

Hoefs J, Coolen JJM, Touret J (1981) The sulfur and carbon isotope composition of scapolite-rich granulites from southern Tanzania. Contrib Mineral Petrol 78:332–336
Hoeve J (1974) Soda metasomatism and radioactive mineralization in the Västervik area, south-eastern Sweden. Ph.D. thesis, Free University, Amsterdam
Holland TH (1900) The charnockite series, a group of Archean hypersthenic rocks in peninsular India. vol 28, Memoir of the Geological Survey of India, Geological Survey of India, Kolkata, pp 192-249
Holness MB (1992) Equilibrium dihedral angles in the system quartz-CO_2-H_2O-NaCl at 800°C and 1–15 kb – The effects of pressure and fluid composition on the permeability of quartzites. Earth Planet Sci Lett 114:171–184
Huizenga JM (2005) COH, an excel spreadsheet for composition calculations in the C-O-H fluid system. Comput Geosci 31:797–800
Huizenga JM, Touret JLR (2012) Granulites, CO_2 and graphite. Gondwana Research, submitted
Humphries S (1984) The mobility of the rare earth elements in the crust. In: Henderson P (ed) Rare earth geochemistry. Elsevier, Amsterdam, pp 317–342
Izraeli ES, Harris JW, Navon O (2001) Brine inclusions in diamonds; a new upper mantle fluid. Earth Planet Sci Lett 187:323–332
Janardhan AS, Newton RC, Hansen EC (1982) The transformation of amphibolite facies gneiss to charnockite in southern Karnataka and northern Tamil Nadu, India. Contrib Mineral Petrol 79:130–149
Janardhan AS, Newton RC, Smith JV (1979) Ancient crustal metamorphism at low P_{H2O}: charnockite formation at Kabbaldurga, south India. Nature 278:511–514
Joesten R (1986) The role of magmatic reaction, diffusion and annealing in the evolution of coronitic microstructure in troctolitic gabbro from Risör, Norway. Mineral Mag 50:441–467
Johnson EL (1991) Experimentally determined limits for H_2O-CO_2-NaCl immiscibility in granulites. Geology 19:925–928
Jøsang O (1966) Geologiske og petrografiske undersøkelser i Modumfeltet, vol 235, Norges Geologiske Undersøkelse Bulletin, Norges Geologiske Undersøkelse, Trondheim
Judd JW (1889) On the processes by which a plagioclase feldspar is converted into scapolite. Mineral Mag 8:186–198
Kadik AA, Lukanin OA, Lebedev YB, Korovushkina EY (1972) Solubility of H_2O and CO_2 in granite and basalts at high pressures. Geochem Int 9:1041–1050
Katz MB (1987) Graphite deposits of Sri Lanka: a consequence of granulite facies metamorphism. Miner Deposita 22:18–25
Kelsey DE (2008) On ultra-high temperature crustal metamorphism. Gondwana Res 13:1–29
Kilpatrick JA, Ellis DJ (1992) C-type magmas: igneous charnockites and their extrusive equivalents. Trans R Soc Edin Earth Sci 83:155–164
Klein-BenDavid O, Izraeli ES, Hauri E, Navon O (2004) Mantle fluid evolution – a tale of one diamond. Lithos 77:243–253
Klimov LV, Ravich MG, Solovjev DS (1964) East Antarctic charnockites. In: Proceedings of the 22nd international geological congress, vol 13, Proceedings of the 22nd international geological congress, New Delhi, pp 79–85
Knudsen TL, Andersen T (1999) Petrology and geochemistry of the Tromøy gneiss complex, south Norway, an alleged exampled of Proterozoic depleted lower continental crust. J Petrol 40:909–933
Knudsen TL, Lidwin A (1996) Magmatic CO_2, brine and nitrogen inclusions in Sveconorwegian enderbitic dehydration veins and a gabbro from the Bamble sector, southern Norway. Eur J Mineral 8:1041–1064
Korneliussen A, Dormann P, Erambert M, Furuhaug L, Mathiesen CO (1992) Rutilforekomster tilknyttet eklogitt-bergarter på Vestlandet of metasomatiske omvandlede bergarter of metasedimenter i Bamble-Arendal regionen. report 92.234, Norges Geologiske Undersøkelse, Trondheim

Kontak DJ, Morteani G (1983) On the geochemical fractionation of rare earth elements during the formation of Ca-minerals and its application to problems of the genesis of ore deposits. In: Augustithis SS (ed) Trace elements in petrogenesis: the significance of trace elements in solving petrogenetic problems and controversies. Theophrastus Publications S.A, Athens, pp 147–791

Korzhinskii DS (1940) Factors in mineral equilibria and mineralogical depth facies. Trudy Akademii Nauk SSSR, Moscow

Korzhinskii DS (1959) Physicochemical basis of the analysis of the paragenesis of minerals. Consultant Bureau, New York

Korzhinskii DS (1962) The role of alkalinity in the formation of charnockitic gneisses. In: Precambrian geology and petrology: general and regional problems. vol 5. Trudy Vostochono-Sibirskogo Geologicheskogo Institute, Geological Series Izd-vo Akademii nauk SSSR, Moskva, pp 50–61

Korzhinskii DS (1968) The theory of metasomatic zoning. Miner Deposita 3:222–231

Kovacs I, Szabó C (2005) Petrology and geochemistry of granulite xenoliths beneath the Nógrád-Gömör volcanic field, Carpathian-Pannonian region (N-Hungary S-Slovakia). Mineral Petrol 85:269–290

Kullerud K (1996) Chlorine-rich amphiboles: interplay between amphibole composition and an evolving fluid. Eur J Mineral 8:355–370

Lacroix A (1893) Les enclaves des roches volcaniques. Ann Acad Mâcon 10:17–697

Lacroix A (1910) Sur l'existence à la Côte d'Ivoire d'une série pétrographique comparable à celle de la charnockite. CR Acad Sci II 150:18–22

Lacroix A (1920) Les roches éruptive du Crétacé pyrénéen et la nomenclature des roches éruptives modifiées. CR Acad Sci II 170:690–695

Lamb W, Valley JW (1984) Metamorphism of reduced granulites in low-CO_2 vapour-free environment. Nature 312:56–58

Lamb WM, Valley JW, Brown PE (1987) Post-metamorphic CO_2-rich inclusions in granulites. Contrib Mineral Petrol 96:485–494

Le Breton N, Thompson AB (1988) Fluid-absent (dehydration) melting of biotites in metapelites in the early stages of crustal anatexis. Contrib Mineral Petrol 99:226–237

Lemmlein GG (1951) The fissure-healing process in crystals and changes in cavity shape in secondary liquid inclusions. Dokl Akad Nauk SSSR 1(78):685–688 (in Russian)

Lieftink DJ, Nijland TG, Maijer C (1993) Cl-rich scapolite from Ødegårdens Verk, Bamble, Norway. Nor Geol Tidsskr 73:55–57

Lieftink DJ, Nijland TG, Maijer C (1994) The behavior of rare-earth elements in high temperature Cl-bearing aqueous fluids: results from the Ødegårdens Verk natural laboratory. Can Mineral 32:149–158

Lobato LM, Forman JMA, Fyfe WS, Kerrich R, Barnett RL (1983) Uranium enrichment in Archaean crustal basement associated with overthrusting. Nature 303:235–237

Lovering JF, White AJR (1964) The significance of primary scapolite in granulitic inclusions from deep-seated pipes. J Petrol 5:195–218

Lovering JF, White AJR (1969) Granulitic and eclogitic inclusions from basic pipes at Delegate, Australia. Contrib Mineral Petrol 21:9–52

Luke FJ, Pasteris JD, Wopenka B, Rodas M, Barrenechea JF (1998) Natural fluid-deposited graphite: mineralogical characteristics and mechanisms of formation. Am J Sci 298:471–498

Mark G, Foster DRW (2000) Magmatic-hydrothermal albite-actinolite-apatite-rich rocks from the Cloncurry district, NW Queensland, Australia. Lithos 51:223–245

Markl G, Ferry J, Bucher K (1998) Formation of saline brines and salt in the lower crust by hydration reactions in partially retrogressed granulites from the Lofoten islands, Norway. Am J Sci 298:705–757

Michard A, Albarède F (1986) The REE content of some hydrothermal fluids. Chem Geol 55:51–60

Mishraa B, Saravanana CS, Bhattacharyaa A, Goona S, Mahatoa S, Bernhard HJ (2007) Implications of super dense carbonic and hypersaline fluid inclusions in granites from the Ranchi area, Chottanagpur gneissic complex, Eastern India. Gondwana Res 11:504–515

Moecher DP (1993) Scapolite phase equilibria and carbon isotopes – constraints on the nature and distribution of CO2 in the lower continental crust. Chem Geol 108:163–174
Moecher DP, Essene EJ (1990) Scapolite phase equilibria: additional constraints on the role of CO_2 in granulite genesis. In: Vielzeuf D, Vidal P (eds) Granulites and crustal evolution. Kluwer, Dordrecht, pp 385–396
Moecher DP, Essene EJ (1992) Calculation of CO_2 activities using scapolite phase equilibria: constraints on the presence and composition of a fluid phase during high-grade metamorphism. Contrib Mineral Petrol 108:219–240
Mohan A, Singh PK, Sachan HK (2003) High-density carbonic fluid inclusions in charnockites from eastern Ghats, India: petrologic implications. J Asian Earth Sci 22:101–113
Moine B, De la Roche H, Touret J (1972) Structures géochimique et zonéographie métamorphique dans le Précambrien catazonal du sud de la Norvège. Sci Terre 17:131–164
Moine B, Rakotondratsima C, Cuney M (1985) Les pyroxénites à uranothorianite de sud-est de Madagascar: conditions physico-chimiques de la métasomatose. Bull Minéral 108:325–340
Montanini A, Harlov D (2006) Petrology and mineralogy of granulite-facies mafic xenoliths (Sardinia, Italy): evidence for KCl metasomatism in the lower crust. Lithos 92:588–608
Morshuis J (1991) Albietpegmatieten in Bamble (zuid-Noorwegen). Unpublished M.Sc. thesis, Utrecht University, Utrecht
Munz IA (1990) Whiteschists and orthoamphibole-cordierite rocks and the P-T-t path of the Modum complex, south Norway. Lithos 24:181–200
Munz IA, Wayne D, Austrheim H (1994) Retrograde fluid infiltration in the high-grade Modum complex, south Norway: evidence for age, source and REE mobility. Contrib Mineral Petrol 116:32–46
Munz IA, Yardley BWD, Banks DA, Wayne D (1995) Deep penetration of sedimentary fluids in basement rocks from southern Norway: evidence from hydrocarbon and brine inclusions in quartz veins. Geochim Cosmochim Acta 59:239–254
Naumann CF (1826) Lehrbuch der mineralogie. Engelman, Leipzig
Newton RC (1989) Metamorphic fluids in the deep crust. Annu Rev Earth Planet Sci 17:385–412
Newton RC (1990) Fluids and shear zones in the deep crust. Tectonophysics 182:21–37
Newton RC (1992a) An overview of charnockite. Precambrian Res 55:399–405
Newton RC (1992b) Charnockitic alteration: evidence for CO_2 infiltration in granulite facies metamorphism. J Metamorph Geol 10:383–400
Newton RC, Aranovich LY, Hansen EC, Vandenheuvel BA (1998) Hypersaline fluids in precambrian deep-crustal metamorphism. Precambrian Res 91:41–63
Newton RC, Manning CE (2002) Experimental determination of calcite solubility in H_2O-NaCl solutions at deep crust/upper mantle pressures and temperatures: implications for metasomatic processes in shear zones. Am Mineral 87:1401–1409
Newton RC, Manning CE (2005) Solubility of anhydrite, $CaSO_4$, in NaCl-H_2O solutions at high pressures and temperatures: applications to fluid-rock interaction. J Petrol 46:701–716
Newton RC, Manning CE (2006) Solubilities of corundum, wollastonite quartz in H_2O-NaCl solutions at 800°C and 10 kbar: interaction of simple minerals with brines at high pressure and temperature. Geochim Cosmochim Acta 70:5571–5582
Newton RC, Manning CE (2007) Solubility of grossular, $Ca_3Al_2Si_3O_{12}$, in H_2O-NaCl solutions at 800°C and 10 kbar, and the stability of garnet in the system $CaSiO_3$-Al_2O_3-H_2O-NaCl. Geochim Cosmochim Acta 71:5191–5202
Newton RC, Manning CE (2008) Solubility of corundum in the system Al_2O_3-SiO_2-H_2O-NaCl at 800°C and 10 kbar. Chem Geol 249:250–261
Newton RC, Manning CE (2010) Role of saline fluids in deep-crustal and upper-mantle metasomatism: insights from experimental studies. Geofluids 10:58–72
Newton RC, Smith JV, Windley BF (1980) Carbonic metamorphism, granulites and crustal growth. Nature 288:45–50

Nijland TG, Maijer C (1991) Primary sedimentary structures and infiltration metamorphism in the Håvatn-Bårlindåsen-Tellaugstjern area, Froland. In: Abstract of the 2nd SNF Excursion, Bamble

Nijland TG, Maijer C (1993) The regional amphibolite to granulite facies transition at Arendal, Norway: evidence for a thermal dome. N Jahrb Mineral Abh. 165:191–221

Nijland TG, Maijer C, Senior A, Verschure RH (1993) Primary sedimentary structures and composition of the high-grade metamorphic Nidelva quartzite complex (Bamble, Norway), and the origin of nodular gneisses. In: Proceedings of the Koninklijke Nederlandse Akademie van Wetenschappen 96:217–232

Nijland TG, Touret JLR (2000) Brine control of 'apparent' metamorphic grade: a case from the Ubergsmoen augen gneiss, south Norway. In: Volume of abstracts, 24th nordic geological winter Meeting, Trondheim, pp 126–127

Nijland TG, Touret JLR (2001) Replacement of graphic pegmatite by graphic albite-actinolite-clinopyroxene intergrowths (Mjåvatn, southern Norway). Eur J Mineral 13:41–50

Nijland TG, Touret JLR, Visser D (1998) Anomalously low temperature orthopyroxene, spinel and sapphirine occurrences in metasediments from the Bamble amphibolite to granulite facies transition zone (South Norway): possible evidence for localized action of saline fluids. J Geology 106:575–590

Nixon PH (1987) Mantle xenoliths. Wiley, New York

Novgorodov PG (1977) On the solubility of quartz in H_2O + CO_2 and H_2O + NaCl at 700 °C and 1.5 kb pressure. Geochem Int 14:191–193

Nuutilainen J (1968) On the geology of the Misi ore province, northern Finland, vol 96, Annales Academia Scientiae Fennicae, series A III. Suomalainen tiedeakatemie, Helsinki

Oen IS (1968) Magnesium-metasomatism in basic hornfelses near Farminhao, Viseu district (northern Portugal). Chem Geol 3:249–279

Oliver NHS (1995) Hydrothermal history of the Mary Kathleen fold belt, Mt. Isa block, Queensland. Aust J Earth Sci 42:267–280

Oliver NHS, Bons PD (2001) Mechanism of fluid flow and fluid-rock interaction in fossil metamorphic hydrothermal systems inferred from vein-wallrock patterns, geometry and microstructure. Geofluids 1:137–162

Oliver NHS, Rawling TJ, Cartwright I, Pearson PJ (1994) High temperature fluid-rock interaction and scapolitization in a large extension-related hydrothermal system, Mary Kathleen, Australia. J Petrol 35:1455–1491

Oliver NHS, Valenta RK, Wall VJ (1990) The effect of heterogeneous stress and strain on metamorphic fluid flow, Mary, Kathleen, Australia, and a model for large-scale fluid circulation. J Metamorph Geol 8:311–331

Oliver N, Wall V (1987) Metamorphic plumbing system in Proterozoic calc-silicates, Queensland, Australia. Geology 15:793–796

O'Nions RK, Oxburgh ER (1988) Helium, volatile fluxes and the development of continental crust. Earth Planet Sci Lett 90:331–347

Owen JV, Greenough JD (1995) Petrology of cordierite + gedrite-bearing sodic granulite from the Grenvillian Long Range inlier, New Foundland. Can J Earth Sci 32:1035–1045

Owen JV, Longstaffe FJ, Greenough JD (2003) Petrology of sapphirine granulite and associated sodic gneisses from the Indian head range, Newfoundland. Lithos 68:91–114

Paquette JL, Nédélec A, Moine B, Rakotondrazafy M (1994) U-Pb single zircon Pb evaporation, and Sm-Nd isotopic study of a granulite domain in SE Madagascar. J Geol 102:523–538

Parfenova OV, Guseva EV (2000) Feldspars of enderbite-charnockite complexes as indicators of alkalinity during the charnockitization of schists. Geochem Int 38:856–866

Park AF, Dash B (1984) Charnockite and related neosome development in the eastern Ghats, Orissa, India: petrographic evidence. Trans R Soc Edin Earth Sci 75:341–352

Parras K (1958) On the charnockites in the light of a highly metamorphic rock complex in southwestern Finland. Bulletin de la Commission Géoloqiue de Finlande, vol 181, Commision Géologique du Finlande Bulletin, Commision Géologique du Finlande, Helsinki

Perchuk LL, Aranovich LY, Podlesskii KK, Lavrenteva IV, Gerasimov VY, Fedkin VV, Kitsul VI, Karsakov LP, Berdnikov NV (1985) Precambrian granulites of the Aldan shield, eastern Siberia, USSR. J Metamorph Geol 3:265–310

Perchuk LL, Gerya TV (1992) The fluid regime of metamorphism and the charnockite reaction in granulites: a review. Int Geol Rev 34:1–58

Perchuk LL, Gerya TV (1993) Fluid control of charnockitization. Chem Geol 108:175–186

Perchuk LL, Gerya TV (1995) Evidence for potassium mobility in the charnockitization of gneisses. Dokl Rossiiskoi Akad Nauk 331:86–91

Perchuk LL, Safonov OG, Gerya TV, Fu B, Harlov DE (2000) Mobility of components in metasomatic transformation and partial melting of gneisses: an example from Sri Lanka. Contrib Mineral Petrol 140:212–232

Petersson J, Eliasson T (1997) Mineral evolution and element mobility during episyenitization (dequartzification) and albitization in the postkinematic Bohus granite, southwest Sweden. Lithos 42:123–146

Phillips GN (1980) Water activity changes across an amphibolite-granulite facies transition, Broken Hill, Australia. Contrib Mineral Petrol 75:377–386

Pichamuthu CS (1953) The charnockite problem. Mysore Geologists' Association, Bangalore

Pichamuthu CS (1960) Charnockite in the making. Nature 188:135–136

Pichamuthu CS (1961) Transformation of peninsular gneisses into charnockites in Mysore state. J Geol Soc India 2:46–49

Pili E, Sheppard SMF, Lardeaux JM (1999) Fluid-rock interaction in the granulites of Madagascar and lithospheric-scale transfer of fluids. Gondwana Res 2:341–350

Pili E, Sheppard SMF, Lardeaux JM, Martelat JE, Nicollet C (1997) Fluid flow vs. scale of shear zones in the lower continental crust and the granulite paradox. Geology 25:15–18

Pineau F, Javoy M, Behar F, Touret JLR (1981) La géochimie isotopique du faciès granulite du Bamble (Norvège) et l'origine des fluides carbonés dans la croûte profonde. Bull Minéral 104:630–641

Podlesskii KK, Kurdyukov YB (1992) The association sapphirine + quartz in the Chogar and Sharyzhalgay complexes, east Siberia. Int Geol Rev 34:611–616

Porto da Silveira CL, Schorscher HD, Mickeley N (1991) The geochemistry of albitization and related uranium mineralization, Espinhares, Paraiba (P), Brazil. J Geochem Explor 40:329–347

Poty B, Leroy J, Cathelineau M, Cuney M, Friedrich M, Lespinasse M, Turpin L (1986) Uranium deposits spatially related to granites in the french part of the hercynian orogen. In: Fuchs HD (ed) Vein type uranium deposits. IAEA, Vienna, TEC-DOC 361 pp 215–246

Putnis A (2002) Mineral replacement reactions: from macroscopic observations to microscopic mechanisms. Mineral Mag 66:689–708

Putnis A (2009) Mineral replacement reactions. Thermodynamics and kinetics of water-rock interaction. vol 70, Reviews in mineralogy and geochemistry, Mineralogical Society of America, Washington, DC, pp. 87-124

Putnis A, Austrheim H (2010) Fluid-induced processes: metasomatism and metamorphism. Geofluids 10:254–269

Quensel P (1952) The charnockite series of the Varberg district on the south-western coast of Sweden. Ark Mineral Geol 1:227–332

Raith M, Srikantappa C (1993) Arrested charnockite formation at Kottavattam, southern India. J Metamorph Geol 11:815–832

Rakotondrazafy AFM, Moine B, Cuney M (1996) Mode of formation of hibonite ($CaAl_{12}O_{19}$) within the U-Th skarns from the granulites of SE Madagascar. Contrib Mineral Petrol 123:190–201

Ramambazafy A, Moine B, Rakotondrazafy M, Cuney M (1998) Signification des fluides carboniques dans les granulites et skarns du Sud-Est de Madagascar. CR Acad Sci IIa 327:743–748

Ramberg H (1951) Remarks on the average chemical composition of granulite and amphibilite-to-epidote amphibolite facies gneisses in west Greenland. Medd Dan Geol Foren 12:27–34

Ramberg H (1952) The origin of metamorphic and metasomatic rocks. University of Chicago Press, Chicago

Read HH (1957) The granite controversy. Thomas Murby, London
Rehtijärvi P, Saastamoinen J (1985) Tectonized actinolite-albite rocks from the Outokumpu district, Finland: field and geochemical evidence for mafic extrusive origin. Bull Geol Soc Finland 57:47–54
Reinhardt J (1987) Cordierite-anthophyllite rocks from north-west Queensland, Australia: metamorphosed magnesian pelites. J Metamorph Geol 5:451–472
Respaut JP, Cathelineau M, Lancelot JR (1991) Multistage evolution of the Pierres-Plantées uranium ore deposit (Margeride, France): evidence from mineralogy and U-Pb systematics. Eur J Mineral 3:85–103
Rigby MJ, Droop GTR (2011) Fluid-absent melting versus CO_2 streaming during the formation of metapelitic granulites: a review of insights from the cordierite fluid monitor. In: Van Reenen DD, Kramers JD, McCourt S, Perchuk LL (eds) Origin and evolution of Precambrian high-grade gneiss terranes, with special emphasis of Limpopo complex of southern Africa, vol 207, Geological Society of America Memoir. Geological Society of America, Boulder, pp 39–60
Rinne F (1928) La science des roches. 3rd French edition, 8th German edition: (trans: Bertrand L). J. Lamarre, Paris, 616 pp
Robinson P, Jaffe HW (1969) Aluminous enclaves in gedrite-cordierite gneiss from southwestern New Hampshire. Am J Sci 267:389–421
Rollinson HR, Tarney J (2005) Adakites – the key to understanding LILE depletion in granulites. Lithos 79:61–81
Rötzler J (1992) Zur petrogenese im sächsischen Granulitgebirge. Geotektonische Forschungen 72:1–114
Rudnick R, Fountain DM (1995) Nature and composition of the continental crust: a lower crustal perspective. Rev Geophys 33:267–309
Rudnick RL, McLennan SM, Taylor SR (1985) Large ion lithophile elements in rocks from high pressure granulite-facies terrains. Geochim Cosmochim Acta 49:1645–1655
Rumble D III, Chamberlain CP, Zeitler PK, Barreiro B (1989) Hydrothermal graphite veins and Acadian granulite metamorphism, new Hampshire, USA. In: Bridgwater D (ed) Fluid movements – element transport and the composition of the deep crust. Kluwer, Dordrecht, pp 117–119
Safonov OG (1999) The role of alkalis in the formation of coronitic textures in metamangerites and metaanorthosites from the Adirondack complex, United States. Petrology 7:102–121
Santosh M (1992) Carbonic fluids in granulites: cause or consequence ? J Geol Soc India 39:375–399
Santosh M, Jackson DH, Harris NBW (1993) The significance of channel and fluid-inclusion CO_2 in cordierite: evidence from carbon isotopes. J Petrol 34:233–258
Santosh M, Jackson DH, Harris NBW, Mattey DP (1991) Carbonic fluid inclusions in south Indian granulites: evidence for entrapment during charnockite formation. Contrib Mineral Petrol 108:318–330
Santosh M, Tagawa M, Taguchi S, Yoshikura S (2003) The Nagercoil granulite block, southern India: petrology, fluid inclusions and exhumation history. J Asian Earth Sci 22:131–155
Santosh M, Tanaka K, Yoshimura Y (2005) Carbonic fluid inclusions in ultrahigh-temperature granitoids from Southern India. CR Geosci 337:327–335
Santosh M, Tsunogae T (2003) Extremely high-density pure CO_2 fluid inclusions in a garnet granulite from southern India. J Geol 111:1–16
Schreyer W (1974) Whiteschist, a new type of metamorphic rock formed at high pressures. Geol Rundsch 63:597–609
Giustina MESD, Martins Pimentel M, Ferreira Filho CF, Fuck RA, Andrade S (2011) U-Pb-Hf-trace element systematics and geochronology of zircon from a granulite-facies metamorphosed mafic–ultramafic layered complex in central Brazil. Precambrian Res 189:176–192
Shmulovich KI, Graham CM (2004) An experimental study of phase equilibria in the systems H_2O-CO_2-$CaCl_2$ and H_2O-CO_2-NaCl at high pressures and temperatures (500–800°C, 0.5–0.9 GPa): geological and geophysical applications. Contrib Mineral Petrol 146:450–462
Simpson C, Wintsch RP (1989) Evidence for deformation-induced K-feldspar replacement by myrmekite. J Metamorph Geol 7:261–275

Słaby E, Martin H, Hamada M, Schmigielski M, Domonik A, Götze J, Hoefs J, Hałas S, Simon K, Devidal JL, Moyen JF, Jayananda M (2011) Evidence in Archaean alkali feldspar megacrysts for high-temperature interaction with mantle fluids. J Petrol (58:67–98)

Smith MS, Dymek RF, Schneidermann JS (1992) Implications of trace element geochemistry for the origin of cordierite-orthoamphibole rocks from Orijärvi, SW Finland. J Geol 100:543–559

Sørensen BE (2007) Metamorphic refinement of quartz under influence of fluids during exhumation with reference to the metamorphic/metasomatic evolution observed in amphibolites. Ph.D. thesis, NTNU, Trondheim

Srikantappa C, Arash Zargar S (2009) First report on the halite-bearing fluid inclusions in the Precambrian granulites around Halaguru, Dharwar craton, India. Indian Mineral 43:77–80

Srikantappa C, Malathi MN (2008) Solid inclusions of magmatic halite and CO_2-H_2O inclusions in closepet granite from Ramanagaram, Dharwar craton, India. Indian Mineral 42:84–98

Srikantappa C, Raith M, Touret JLR (1992) Synmetamorphic high-density carbonic fluids in the lower crust: evidence from the Nilgiri granulites, southern India. J Petrol 33:733–760

Stanislawska M, Michalik M (2008) Xenotime-(Y) veins in a Neoproterozoic metamudstone (Malopolska block, S Poland). Mineralogia 39:105–113

Stähle HJ, Raith M, Hoernes S, Delfs A (1987) Element mobility during incipient granulite formation at Kabbaldurga, southern India. J Petrol 28:803–834

St Onge MR, Lucas SB (1995) Large-scale fluid infiltration, metasomatism and re-equilibration of Archaean basement granulites during Palaeoproterozoic thrust belt construction, Ungava orogen, Canada. J Metamorph Geol 13:509–535

Sukumaran S, Ravindra Kumar GR (2000) K-feldspar metasomatism in granulite-facies rocks of Palghat region, Kerala: evidence and implications of brines in charnockite-forming metamorphism. Curr Sci 79:1594–1958

Ter Haar JH (1988) De sub-solidus geschiedenis van actinoliet uit een actinoliet-amfibool (Alb.-Act.-Qtz.) gesteente van Bamble, SE-Noorwegen. Unpublished M.Sc. thesis, Utrecht University, Utrecht

Thompson AB (1982) Dehydration melting of pelitic rocks and the generation of H_2O undersaturated granitic liquids. Am J Sci 282:1567–1595

Thompson AB (1983) Fluid-absent metamorphism. J Geol Soc Lond 140:533–547

Tichomirova M, Whitehouse MJ, Nasdala L (2005) Resorption, growth, solid-state recrystallization and annealing of granulite facies zircon – a case study from the central Erzgebirge, Bohemian massif. Lithos 82:25–50

Tilley CE (1937) Anthophyllite-cordierite granulites in the Lizard. Geol Mag 74:300–309

Tobi AC, Hermans GAEM, Maijer C, Jansen JBH (1985) Metamorphic zoning in the high-grade Proterozoic of Rogaland-Vest Agder. In: Tobi AC, Touret JLR (eds) The deep Proterozoic crust in the North Atlantic provinces. Reidel, Dordrecht, pp 499–516

Touret JLR (1966) Sur l'origine supracrustale des gneiss rubanés de Selås (formation de Bamble, Norvège méridionale). CR Acad Sci 262:9–12

Touret JLR (1971) Le faciès granulite en Norvège méridionale. II Les inclusions fluides. Lithos 4:423–436

Touret JLR (1972) Le faciès granulite en Norvège méridionale et les inclusions fluides: paragneiss et quartzites. Science de la Terre 17:179–193

Touret JLR (1973) Minerais de fer-titane, roches plutoniques et zonéographie métamorphique dans le sud de la Norvège. In: Raguin Colloquium E (ed) Les roches plutoniques dans leurs rapports avec les gîtes minéraux. Masson, Paris, pp 249–260

Touret JLR (1979) Les roches à tourmaline-cordiérite-disthène de Bjordammen (Norvège méridionale) sont-elles liées a d'anciennes évaporites ? Sci Terre 23:95–97

Touret JLR (1985) Fluid regime in southern Norway: the record of fluid inclusions. In: Tobi AC, Touret JLR (eds) The deep Proterozoic crust in the North Atlantic provinces. Reidel, Dordrecht, pp 517–549

Touret JLR (1996) LILE-depletion in granulites: myth or reality ? In: Demaiffe D (ed) Petrology and geochemistry of magmatic suites of rocks in the continental and oceanic crusts. Université Libre de Bruxelles, Brussels & Royal Museum for Central Africa, Tervuren, pp 53–72

Touret JLR (2001) Fluids in metamorphic rocks. Lithos 55:1–25

Touret JLR (2009) Mantle to lower-crust fluid/melt transfer through granulite metamorphism. Russ Geol Geophys 50:1–11

Touret JLR, Dietvorst P (1983) Fluid inclusions in high-grade anatectic metamorphites. J Geol Soc Lond 140:635–649

Touret JLR, Hansteen TH (1988) Geothermobarometry and fluid inclusions in a rock from the DoddaBetta charnockite complex. Rend Soc Ital Mineral Petrol vol 43. pp 65–82

Touret JLR, Hartel THD (1990) Synmetamorphic fluid inclusions in granulites. In: Vielzeuf D, Vidal P (eds) Granulites and crustal evolution. Reidel, Dordrecht, pp 397–417

Touret JLR, Huizenga JM (2011) Fluids in granulites. In: Van Reenen DD, Kramers JD, McCourt S, Perchuk LL (eds) Origin and evolution of Precambrian high-grade gneiss terranes, with special emphasis on the Limpopo complex of southern Africa, vol 207, Geological Society of America Memoir. Geological Society of America, Boulder, pp 25–37

Touret JLR, Huizenga JM (2012) Fluid-assisted granulite metamorphism: a continental journey. Gondwana Res 21:224–235

Tracy RJ, Robinson P (1983) Acadian migmatite types in pelitic rocks of central Massachusetts. In: Atherton MP, Gribble CD (eds) Migmatites, melting and metamorphism. Shiva, Nantwich, pp 163–173

Trommsdorff V, Skippen G (1986) Vapour loss ('boiling') as a mechanism for fluid evolution in metamorphic rocks. Contrib Mineral Petrol 94:317–322

Tropper P, Manning CE, Harlov DE (2011) Solubility of $CePO_4$ monazite and YPO_4 xenotime in H_2O and H_2O-NaCl at 800°C and 1 GPa: implications for REE and Y transport during high-grade metamorphism. Lithos 282:58–66

Tsunogae T, Santosh M, Osanai Y, Owada M, Toyoshima T (2002) Very high-density carbonic fluid inclusions in sapphirine-bearing granulites from Tonagh island in the Napier complex, Antarctica: implications for CO_2 infiltration during ultrahigh-T ($T > 1100$°C) metamorphism. Contrib Mineral Petrol 143:279–299

Turner FJ, Verhoogen J (1960) Igneous and metamorphic petrology, 2nd edn. McGraw Hill, New York

Vallance TG (1967) Mafic rock alteration and isochemical development of some cordierite-anthophyllite rocks. J Petrol 8:84–96

VanderAuwera J (1993) Diffusion controlled growth of pyroxene-bearing margins on amphibolite bands in the granulite facies of Rogaland (southwestern Norway): implications for granulite formation. Contrib Mineral Petrol 114:203–220

Van den Kerkhof AM, Olsen SN (1990) A natural example of superdense CO_2 inclusions: microthermometry and Raman analysis. Geochim Cosmochim Acta 54:895–901

Vernon RH (2004) A practical guide to rock microstructures. Cambridge University Press, Cambridge

Van Reenen DD (1986) Hydration of cordierite and hypersthene and a description of the retrograde orthoamphibole isograd in the Limpopo belt, South Africa. Am Mineral 71:900–915

Van Reenen DD, Smit CA, Perchuk LL, Roering C, Boshoff R (2011) Thrust exhumation of the Neoarchean UHT Southern Marginal Zone, Limpopo complex: convergence of decompression-cooling paths in the hanging wall and prograde P-T paths in the footwall. In: Van Reenen DD, Kramers JD, McCourt S, Perchuk LL (eds) Origin and evolution of Precambrian high-grade gneiss terranes, with special emphasis on the Limpopo complex of southern Africa, vol 207, Geological Society of America Memoir. Geological Society of America, Boulder, pp 189–212

Van Schalkwyk JF, Van Reenen DD (1992) High-temperature hydration of ultramafic granulites from the southern marginal zone of the Limpopo belt by infiltration of CO_2-rich fluid. Precambrian Res 55:337–352

Vielzeuf D, Pin C (1989) Geodynamic implications of granitic rocks in the Hercynian belt. In: Daly JS, Cliff RA, Yardley BWD (eds) Evolution of metamorphic belts. Geological Society London Special Publication, vol 43, Geological Society London Special publication. Blackwell Science, Oxford, pp. 343–348

Vielzeuf D, Clemens JD, Pin C, Moinet E (1990) Granites, granulites, and crustal differentiation. In: Vielzeuf D, Vidal P (eds) Granulites and crustal evolution. Kluwer, Dordrecht, pp 59–83

Villaseca C, Orejana D, Paterson BA (2007) Zr-LREE rich minerals in residual peraluminous granulites, another factor in the origin of low Zr-LREE granitic melts. Lithos 96:375–386
Visser D (1995) Kornerupine in a biotite-spinel-garnet schist near Böylefossbru, Bamble sector, south Norway: implications for early and late metamorphic fluid activity. N Jahrb Mineral Abh. 169:1–34
Visser D, Nijland TG, Lieftink DJ, Maijer C (1999) The occurrence of preiswerkite in a tourmaline-biotite-scapolite rock (Blengsvatn, Bamble, Norway). Am Mineral 84:977–982
Visser D, Senior A (1990) Aluminous reaction textures in orthoamphibole bearing rocks: the P-T path of the high grade Proterozoic of the Bamble sector, south Norway. J Metamorph Geol 8:231–246
Von Knorring O, Kennedy WQ (1958) The mineral paragenesis and metamorphic states of garnet-hornblende-pyroxene-scapolite-gneiss from Ghana (Gold Coast). Mineral Mag 31:846–859
Wang RC, Xu SJ, Xu SJ (2000) First occurrence of preiswerkite in the Dabie Shan UHP metamorphic belt. Chinese Sci Bull 45–8:748–750
Waters DJ (1988) Partial melting and the formation of granulite facies assemblages in Namaqualand, South Africa. J Metamorph Geol 6:387–404
Watson EB, Brenan JM (1987) Fluids in the lithosphere 1. Experimentally determined wetting characteristics of CO_2-H_2O fluids and their implication for fluid transport, host-rock physical properties and fluid inclusion formation. Earth Planet Sci Lett 85:497–515
Watson LT (1912) Krageroite, a rutile-bearing rock from Kragerö, Norway. Am J Sci 24:509–514
Wielens JBW (1979) Morphology and U-Pb ages of zircons from the high-grade metamorphic Precambrian in the Sirdal-Ørsdal area, SW Norway. ZWO Laboratory for Isotope Geology, vol 4, Verhandeling ZWO Laboratory for Isotope Geology, ZWO Laboratory for Isotope Geology, Amsterdam
Wilkinson JJ, Nolan J, Rankin AH (1996) Silicothermal fluid: a novel medium for mass transport in the lithosphere. Geology 24:1059–1062
Yardley BWD (1989) An introduction to metamorphic petrology. Longman, Harlow
Yardley BWD (1997) The evolution of fluids through the metamorphic cycle. In: Jamtveit B, Yardley BWD (eds) Fluid flow and transport in rocks. Mechanisms and effects. Chapman & Hall, London, pp 99–121
Yardley BWD, Graham JT (2002) The origins of salinity in metamorphic fluids. Geofluids 2:249–256
Yoshino T, Satish-Kumar M (2001) Origin of scapolite in deep-seated metagabbros of the Kohistan arc, NW Himalayas. Contrib Mineral Petrol 140:511–531
Young DA (2002) Norman Levi Bowen (1887–1956) and igneous rock diversity. In: Oldroyd DR (ed) The earth inside and out: some major contributions to geology in the twentieth century, vol 192, Geological Society Special Publication. Geological Society, London, pp 99–111
Zaleski I, Pattison DRM (1993) Metasomatism in the generation of granulite veins: mass balance, mass transfer, and reference frames. J Petrol 34:1303–1323
Zhang Z, Shen K, Santosh M, Dong X (2011) High density carbonic fluids in a slab window: evidence from the Gangdese charnockite, Lhasa terrane, southern Tibet. J Asian Earth Sci 42:515–524

Chapter 12
Mantle Metasomatism

Suzanne Y. O'Reilly and W.L. Griffin

Abstract Mantle metasomatism is a relatively recent concept introduced in the early 1970s when detailed studies of lithospheric mantle rock fragments (xenoliths), brought to the surface of in basaltic to kimberlitic magmas, became widespread. Two main types of metasomatism were defined: modal (or patent) metasomatism describes the introduction of new minerals; cryptic metasomatism describes changes in composition of pre-existing minerals without formation of new phases. A new type of metasomatism is introduced here, stealth metasomatism; this process involves the addition of new phases (e.g. garnet and/or clinopyroxene), but is a "deceptive" metasomatic process that adds phases indistinguishable mineralogically from common mantle peridotite phases. The recognition of stealth metasomatism reflects the increasing awareness of the importance of refertilisation by metasomatic fluid fronts in determining the composition of mantle domains. Tectonically exposed peridotite massifs provide an opportunity to study spatial relationships of metasomatic processes on a metre to kilometre scale.

The nature of mantle fluids can be determined from the nature of fluid inclusions in mantle minerals and indirectly from changes in the chemical (especially trace-element) compositions of mantle minerals. Metasomatic fluids in off-craton regions cover a vast spectrum from silicate to carbonate magmas containing varying types and abundances of dissolved fluids and solutes including brines, C-O-H species and sulfur-bearing components. Fluid inclusions in diamond and deep xenoliths reveal the presence of high-density fluids with carbonatitic and hydro-silicic and/or saline-brine end-members. The deep cratonic xenolith data also reinforce the importance of highly mobile melts spanning the kimberlite-carbonatite spectrum and that may become immiscible with changing conditions.

S.Y. O'Reilly (✉) • W.L. Griffin
ARC Centre of Excellence for Core to Crust Fluid Systems and GEMOC National Key Centre, Department of Earth and Planetary Sciences, Macquarie University, Sydney NSW 2109, Australia
e-mail: sue.oreilly@mq.edu.au

D.E. Harlov and H. Austrheim, *Metasomatism and the Chemical Transformation of Rock*, Lecture Notes in Earth System Sciences,
DOI 10.1007/978-3-642-28394-9_12,

A critical conceptual advance in understanding Earth's geodynamic behaviour is emerging from understanding the linkage between mantle metasomatism and the physical properties of mantle domains recorded by geophysical data. For example, metasomatic refertilisation of cratonic lithospheric mantle increases its density, lowers its seismic velocity and strongly affects its rheology. Introduction of heat-producing elements (U, Th, K) increases heat production, and the key to understanding electromagnetic signals from mantle domains may be closely related to fluid distribution and type (e.g. carbonatitic) and its residence in or between grains.

The lithospheric mantle is a palimpsest recording the multiple fluid events that have affected each domain since it formed. These events, involving different fluids and compositions, have repeatedly overprinted variably depleted original mantle wall-rocks. This produces a complex, essentially ubiquitously metasomatised lithospheric mantle, heterogeneous on scales of microns to terranes and perhaps leaving little or no "primary" mantle wall-rock. Decoding this complex record by identifying significant episodes and processes is a key to reconstructing lithosphere evolution and the nature and origin of the volatile flux from the deep Earth through time.

12.1 Introduction

Direct evidence for metasomatic processes in the subcontinental lithospheric mantle (SCLM) is provided by mantle rocks in two very different geological situations. The first comprises xenoliths and xenocrysts entrained in a spectrum of magmatic rocks. Kimberlitic and related magmas typically sample ancient cratonic lithospheric keels, which are thick (150–250 km), relatively depleted, and complexly metasomatised. Alkali basalts and related magmas mainly sample thinner, more fertile Phanerozoic (off-craton) tectonic domains, or regions where older SCLM has been thinned (e.g. the North China Craton; see review by Griffin et al. 1998a). The other type of occurrence ("ultramafic massifs", ophiolites and some ocean-floor peridotites) comprises fragments of the upper mantle that have been tectonically exposed or emplaced into the crust.

The ultramafic massifs and ophiolites have the advantage of exposing large volumes of upper mantle material so that rock-type relationships can be defined; intrusive magmatic relationships (e.g. veins, dyking) and the effects of fluid infiltration can be traced coherently over scales of metres to kilometres. However, the deformation associated with tectonic emplacement can obscure essential information. Xenoliths (and xenocrysts) are smaller samples, and relationships between rock types are *seldom visible*. However, they can also provide fragments of relatively unaltered lithospheric mantle, as they generally reach the surface within a maximum of 50 h after their entrainment in the host magma (see review by O'Reilly and Griffin 2010a). Some idea of their original spatial context can be derived from geothermobarometry, which involves the use of mineral compositions to calculate the pressure and temperature at the level where the xenoliths were sampled. This approach assumes equilibrium among the mineral phases, and requires careful

attention to issues such as the compositional homogeneity of individual phases, and microstructural criteria for equilibrium.

In early studies of metasomatism in mantle-derived xenoliths, considerable discussion took place about which geochemical effects had been imposed while the samples were in the mantle, and which reflected interaction with the host magma during transport or during residence in slow-cooling volcanic necks. The latter effects would involve infiltration of the melts or exsolved fluids into the xenolith along cracks or grain boundaries, processes that commonly are petrographically obvious. However, enough ambiguity remained to exercise the minds of many researchers. Since the introduction of microanalytical techniques for both major and trace elements, the primary minerals of the xenoliths can be analysed and grain-boundary effects can be minimised. Condie et al. (2004) used these techniques to identify the grain-boundary residence of a range of "diagnostic" trace elements in spinel lherzolite xenoliths. In modern, high-precision analysis of isotopic compositions and very low-level element abundances, care is taken to remove secondary contaminants by acid-leaching techniques. A recent detailed investigation is described by Huang et al. (2011).

Indirect evidence of mantle metasomatism can be provided by the trace-element and isotopic characteristics of small-volume magmas (e.g. alkali basalts) that have interacted with low-temperature, low-degree melts in their passage through the lithosphere (e.g. Menzies et al. 1983; Wilson and Downes 1991; Zhang et al. 2001; Zhang et al. 2008; O'Reilly et al. 2009).

The *geophysical signatures* of metasomatised mantle domains can be recognised in some regions by seismic and gravity responses (reflecting mineralogy and composition, hence density), by high heat flow (reflecting high contents of K-U-Th), and by magnetotelluric signals that may indicate dispersed grain-boundary fluids (see Sect. 12.8).

12.1.1 Lithospheric Mantle Rock Types

Important rock types in the lithospheric mantle are defined below. Nixon (1987) gives a comprehensive treatment and Fig. 12.1 illustrates the terminology for ultramafic rock types after Streckeisen (1979).

Peridotite mantle wall-rocks (over 95% by volume) are ultramafic (olivine-dominated) in composition and may contain orthopyroxene (harzburgites), clinopyroxene (wehrlites), or orthopyroxene + clinopyroxene (lherzolites) as well as an aluminous phase (garnet, spinel or plagioclase depending on the pressure-temperature environment; garnet and spinel, ranging from hercynite to chromite, may coexist).

Eclogites are clinopyroxene + garnet rocks, mafic in bulk composition and equilibrated under high-pressure and low geothermal gradient conditions in the lithospheric mantle. They may represent subducted crustal material (e.g. Jacob 2004) or igneous intrusions (Griffin and O'Reilly 2007).

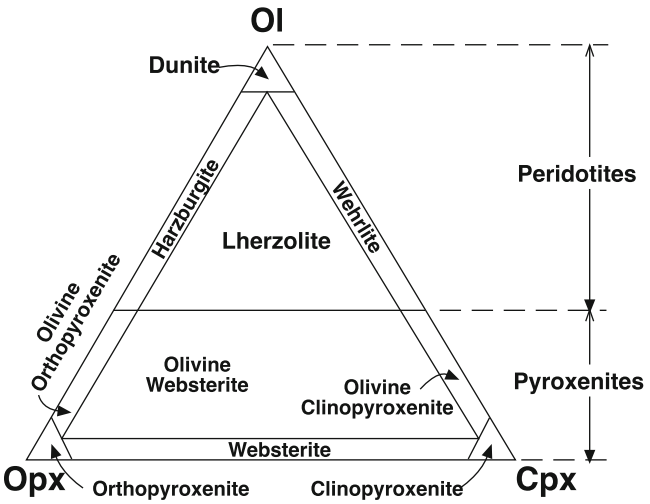

Fig. 12.1 Modal definition of major rock types in the lithospheric mantle (After Streckeisen (1979))

Pyroxenites are mafic in composition and represent frozen basaltic magmas, cumulates and fractionates, most commonly intruded into young (Phanerozoic) mantle domains, or more rarely into high levels in cratonic regions. By analogy they may be the lower-pressure/higher temperature equivalents of some types of eclogites from the cratonic mantle. A recent review is provided by Downes (2007).

12.1.2 Types of Mantle Metasomatism: Nomenclature

Mantle metasomatism refers to compositional changes in the mantle wall-rock due to interaction with mantle fluids (*sensu lato*). Lloyd and Bailey (1973) were the first to identify mantle metasomatism, applying a term ("metasomatism") that previously had been used to describe crustal processes (e.g. Goldschmidt 1922; Korzhinski 1936). They attributed the mineralogy and composition of amphibole-bearing peridotite xenoliths from the Eifel and Uganda basaltic provinces to metasomatism by "alkali element-enriched volatile fluxes from a degassing lower mantle".

The term *"modal" mantle metasomatism* was introduced by Harte (1983) to describe "the presence of minerals additional to those seen commonly in peridotites". Such minerals include amphibole, mica, carbonates, apatite, sulfides, titanite, ilmenite and zircon.

Dawson (1984) used the term *"cryptic" metasomatism* to describe changes in the composition (especially trace-element abundances) of existing phases without the addition of new phases. Dawson (1984) also used the term "patent" to refer to

Harte's "modal" metasomatism, but *"modal"* and *"cryptic"* have become widely used for two end-member types of mantle metasomatism.

However, more recent studies have brought recognition that the presence of garnet and clinopyroxene in the cratonic lithospheric mantle, and abundant clinopyroxene (±spinel) in cratonic or younger lithospheric mantle domains, commonly reflects refertilisation of more refractory protoliths. This refertilisation has involved the addition of basaltic components (major elements such as Ca, Al, Fe, Ti, trace elements, including Sr, Zr, and rare-earth elements (REE)). As this process represents the addition of new phases it could be regarded as a variety of "modal" metasomatism, but the phases involved (garnet and clinopyroxene) are part of the common four-phase assemblage of mantle peridotites.

We will refer to this refertilisation process as *"stealth metasomatism"* because of the "deceptive" nature of the process, which adds phases that are new to the rock, but indistinguishable mineralogically from common peridotite phases. The failure to recognise this type of metasomatism until the last decade has led to a fundamental misinterpretation of key mantle processes. Work on the importance and the ubiquity of this refertilisation process is shedding new light on the nature of the processes that generated Archean lithospheric mantle, and on its later geochemical evolution (see summary by Griffin et al. 2009) through repeated metasomatic episodes.

12.1.3 Types of Fluids

The examples of mantle metasomatism discussed below involve an enormous variety of fluid types: silicate melts ranging from mafic to ultramafic; carbonatite melts; sulfide melts; C-O-H fluids ranging from water to CH_4 and CO_2; dense brines and hydrosilicic fluids; and hydrocarbon-bearing fluids. Many of these appear to be miscible with one another under some environmental conditions, and immiscible under others. There is evidence of the coexistence and interaction of different fluid types within single volumes of the mantle, on short time scales. The complexity of mantle metasomatic processes is far from understood at present, and offers abundant opportunities for innovative research.

12.2 How Fluids Move Through the Mantle

There are two main ways that fluids can move in the mantle: grain-boundary infiltration and crack propagation. Once the fluid has arrived at a reaction site, intra-granular diffusion, along with dissolution and reprecipitation, become the rate-limiting steps (e.g. van Orman et al. 2001, 2002), and may preserve compositional gradients (zoned minerals) that provide a wealth of information on the rates of processes (see Sect. 12.6 and Chap. 14).

Fig. 12.2 Dyke of eclogite in tectonically exposed peridotite (Almklovdalen, Norway) showing intrusive relationship with straight contacts

12.2.1 Crack Propagation

Crack propagation allows for almost instantaneous movement of significant volumes of fluid, and is the major mechanism for larger-scale intrusion in the mantle and for magma ascent. The triggering of crack propagation due to fluid overpressure provides a robust pathway for the transport of metasomatic fluids and melts over significant distances and has the secondary effect of creating at least a transient porosity that may temporarily enhance diffusion.

Evidence for transient brittle fracture of mantle rocks, caused by fluid pressure, is found in both exposed peridotite massifs and mantle xenoliths. Wilshire and Kirby (1989) described straight-sided dikes cross-cutting other structures in peridotite massifs. Similar relationships are seen in the massifs of western Norway (Fig. 12.2), where eclogite dykes have straight sides (and a metasomatic halo; see below). A study of over 4,000 mantle-derived peridotite and pyroxenite xenoliths in basaltic flows, dykes, sills, and cinder cones from Australia and Spitsbergen (O'Reilly, unpublished data; Skjelkvåle et al. 1989) shows that xenoliths are typically angular to subangular and many show polygonal and facetted shapes. Most spinel lherzolite xenoliths from alkali basalts, when subjected to mild hydraulic stress, split along planar surfaces in up to three different orientations, suggesting that pre-existing planes of weakness were present in the original upper-mantle wall rock. Xenoliths from kimberlites more commonly have rounded shapes that reflect tumbling of originally angular fragments during a turbulent ascent, leading to the use of the term "nodules" for xenoliths in kimberlites and more rarely in basalts.

Many metasomatised xenoliths contain planar veins of secondary phases such as amphibole and mica (less than 0.1 mm to more than 10 cm wide; Fig. 12.3). Cross-cutting planar veins oriented in up to three directions have been reported from

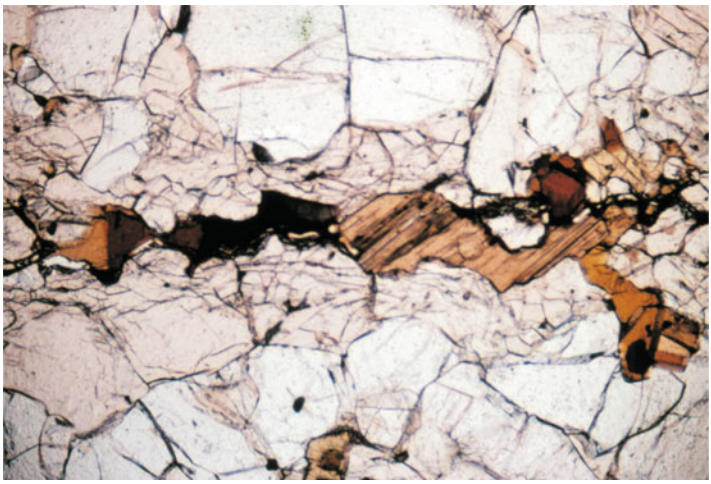

Fig 12.3 Amphibole-rich veinlet in spinel-peridotite xenolith. Width of image 11 mm

several localities world-wide (e.g. Wilshire et al. 1980, 1991; Skjelkvåle et al. 1989; O'Reilly and Griffin 2010a; Fig. 12.4). Other evidence for crack-filling fluids within the mantle is provided by planar arrays of fluid inclusions within mineral grains of xenoliths. These arrays represent fractures that filled with fluids. The fluids were trapped as inclusions with shapes that have proceeded from amoeboid to negative-crystal forms as the host grain recrystallised to reduce the surface free energy of the crack (Roedder 1984).

12.2.2 Grain-Boundary Infiltration

Infiltration of fluids along grain boundaries causes cryptic metasomatism and can cause stealth metasomatism by reaction with the minerals of the pre-existing mantle wall-rock. However, grain boundary infiltration is driven by interfacial energy. It is a relatively slow process and cannot move large quantities of fluid on a short timescale.

The rate of grain-boundary infiltration is highly dependent on the composition of the fluid. Carbonate and silicate melts (basaltic to komatiitic compositions) have low wetting angles with olivine grain boundaries. Such fluids can form a continuous 3-dimensional network (Fig. 12.5). The low interfacial energy drives fluid penetration into non-porous rock even in the absence of any pressure gradient (Watson and Brenan 1987; Watson et al. 1990). Such energy-driven infiltration can drive a fluid front up to 20–50 m per year, and thus can be an important mechanism for pervasive metasomatism such as that recorded in the Lherz and Ronda massifs (e.g. Bodinier et al. 1990, 2004 ; Le Roux et al. 2007; see Sect. 12.4).

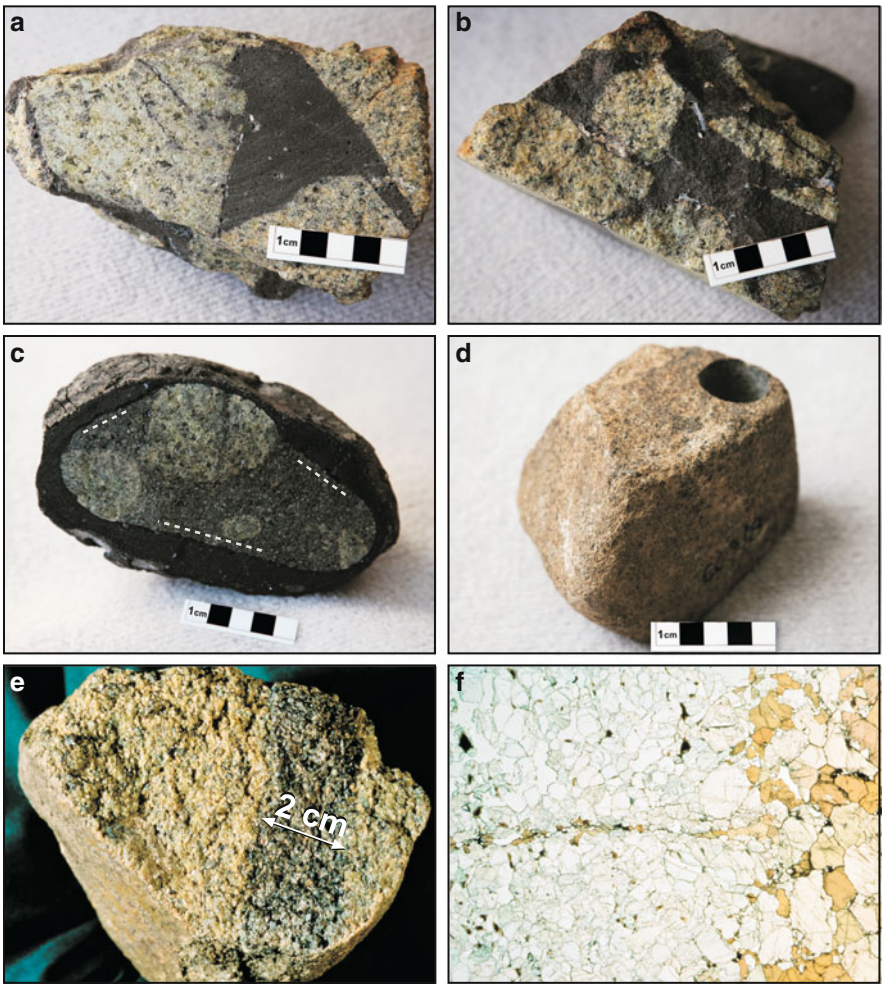

Fig. 12.4 Typical mantle xenoliths in alkali basalts, showing the sharp planar facets that testify to brittle fracture in the lithospheric mantle. Width of photomicrograph in Fig. 12.4f is ca 1 mm (Reproduced from O'Reilly and Griffin (2010a), Blackwell)

In contrast to carbonate and silicate melts, H_2O–CO_2 fluids have a high wetting angle with olivine grain boundaries and tend to form isolated pores at grain boundaries (Watson et al. 1990; Fig. 12.5). An unusual example of this is seen in volatile-rich peridotites from western Victoria, Australia (O'Reilly 1987) where high-pressure "vesicles" form part of the polygonal equilibrium microstructural fabric along with olivine and minor pyroxene (Fig. 12.6). Smaller fluid inclusions within the mineral grains are high-density CO_2, and it seems probable that the vesicles were filled with the same type of fluid. Watson et al. (1990) demonstrated that C-O-H fluids cannot form grain-boundary films in the uppermost mantle and

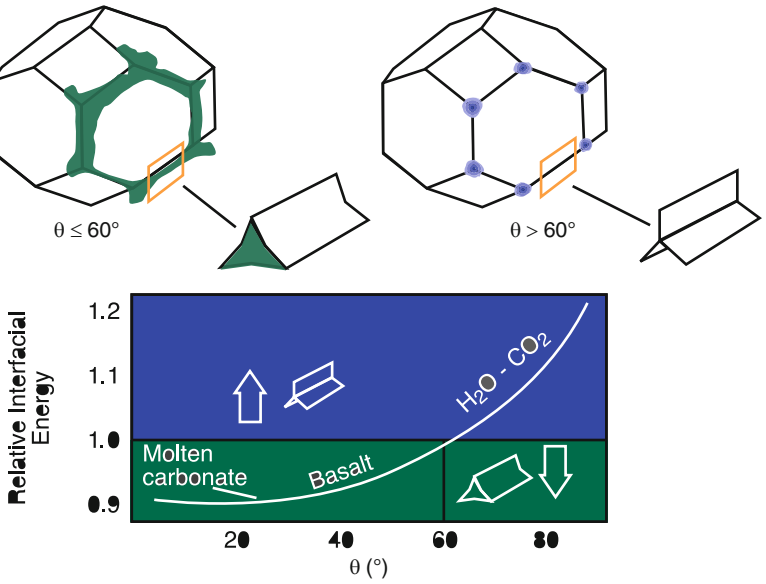

Fig. 12.5 Effect of interfacial energy (θ) on fluid geometry in granular aggregates (after Watson et al. (1990)). If the $\theta > 60°$, the fluid/melt forms discrete polyhedral blebs at grain corners. If $\theta < 60°$, the fluid wets all grain boundaries, forming a 3-dimensional connected film. The composition of the fluid/melt determines the interfacial energy. Carbonate and basalt melts (*sensu lato*, including a wide range of mafic and ultratramafic melt compositions) have low interfacial energies and will infiltrate grain boundaries easily. CO_2- and H_2O-rich fluids have high interfacial energies and form discrete blebs at grain triple junctions in mantle rocks

could form an interconnected phase only under restricted conditions, for example if a water-dominant fluid exists at pressures higher than 30 kb at temperatures just below the solidus.

In summary, movement of fluid in the mantle is achieved by two main processes: (1) geologically instantaneous, lithosphere-scale transport by crack propagation and (2) grain boundary infiltration, which is effective for carbonate and basaltic (sensu lato) melts, but not for H_2O–CO_2 fluids, on time and length scales appropriate for metasomatic fronts recorded in exposed peridotite massifs. Combinations of these two mechanisms can produce widely dispersed domains of metasomatised mantle.

12.3 Dating Metasomatic Events in the Mantle

Most isotopic systems are not suitable for dating of metasomatic events in the mantle, because the high temperatures allow equilibration of the daughter isotopes between minerals and on the whole-rock scale. Where “ages” have been obtained on coexisting minerals of high-T xenoliths, these commonly record the age of the eruption, whereas older ages may appear in low-T xenoliths. These effects are illustrated by Sm-Nd dating of garnet websterite xenoliths (pyroxenes + garnet

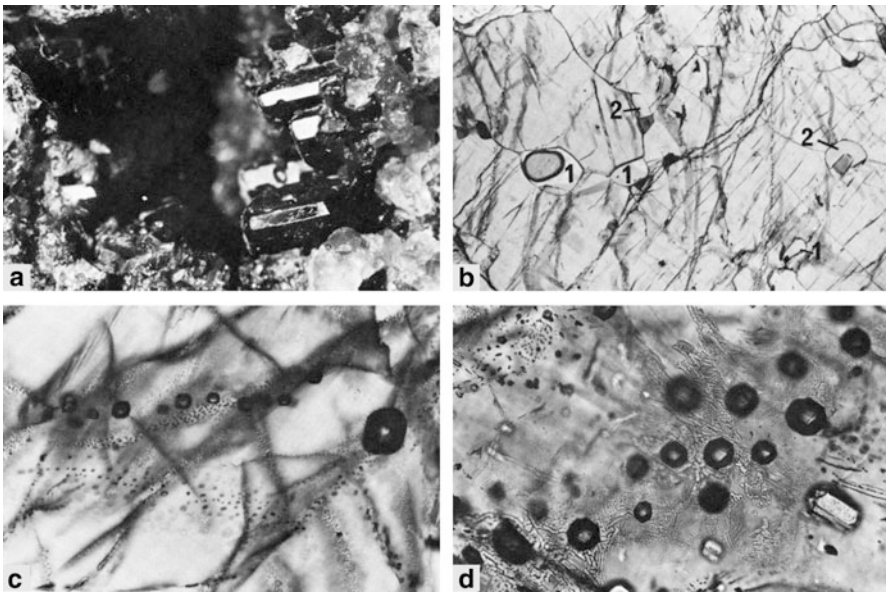

Fig. 12.6 Evidence of fluids in *upper-mantle* xenoliths (after Andersen et al. (1984)). (**a**) open vug (1 cm across) lined with euhedral amphibole crystals. (**b**) polygonal cavities ("1") as part of the granoblastic structure. Those labeled "2" have amphibole crystals projecting from their walls. Width of photo 3.5 mm. (**c**) large fluid inclusions (liquid CO_2-dominated) have *negative-crystal* form. *Smaller spherical ones* are arrayed along planes representing healed fractures. (**d**) *large negative-crystal* CO_2 inclusions, associated with planes of secondary fluid inclusions produced by decrepitation of *larger ones*. Dendritic microstructure shows early stages of crack healing

$\pm$ plag + whole-rock) from basalt diatremes in SE Australia (Chen et al. 1998; Griffin and O'Reilly, unpublished data). These pyroxenites originated as cumulates of complex high-Al clinopyroxenes (Griffin et al. 1984) and have recrystallised and equilibrated over a range of T from 850°C to 1,100°C. In the Lake Bullenmerri maar (age <1 Ma) two pyroxenites, equilibrated at 1,050–1,100°C give two mineral ages of 27 $\pm$ 7 and 32 $\pm$ 14 Ma, significantly older than the age of the eruption (<1 Ma). In the Delegate pipe, two pyroxenites, equilibrated at 1,060–1,100°C, give ages of 146 $\pm$ 9 and 160 $\pm$ 4 Ma, close to the time of eruption (150–160 Ma); clinopyroxene-orthopyroxene-plagioclase xenoliths, from the same pipe, equilibrated at ca 850°C, give ages of 200 $\pm$ 14 Ma. These data suggest that the isotopic equilibration of $^{143}Nd/^{144}Nd$ between garnet and pyroxene can be continuous at T $\geq$ 1,100°C, and quasi-continuous at T down to 850–900°C. None of these "ages" is likely to record the real timing of a crystallisation event. Similarly, such techniques are unlikely to provide real ages for metasomatic events in the mantle.

By contrast, the U-Pb system of zircon has proven to be quite resistant to thermal resetting. In recent years, techniques for extracting minute amounts of zircon from metasomatised mantle peridotites, and the use of *in situ* analysis of both U-Pb ages and Hf-isotope compositions in single grains, have advanced rapidly. There are now

many examples of peridotite xenoliths and massif peridotites that contain several discrete age populations of zircon. The ages of these populations commonly can be correlated with the ages of events in the overlying crust (e.g. Zheng et al. 2006, 2008a, b), providing links between crustal tectonics and the movement of metasomatic fluids in the lithosphere.

The Re-Os systematics of mantle peridotites are controlled by sulfides (Alard et al. 2000), which can move through the mantle as melts, and commonly accompany other types of metasomatic processes. Since most peridotite samples contain multiple generations of sulfide minerals, whole-rock Re-Os model ages are unlikely to date any real event. However, the development of techniques for the *in situ* analysis of the Os-isotope composition of sulfides (Alard et al. 2002; Pearson et al. 2002) has made it possible to obtain model ages for single grains of sulfide in mantle peridotites. Although isotopic mixing between different generations of sulfide melts seems probable, individual xenoliths (or massif samples) commonly contain several distinct sulfide age populations. Where detailed studies have been done, these populations appear to be linked to events in the overlying crust, suggesting that the sulfide melts, like the fluids that deposit zircons in mantle peridotites, move through the lithosphere in response to large-scale tectonic events. For example, in xenoliths from the Kaapvaal craton, the oldest sulfide model ages from each terrane correspond to the age of the oldest known crust of that terrane, while other age peaks can be correlated with craton suturing and with later magmatic episodes (Griffin et al. 2004).

12.4 Metasomatism in Peridotite Massifs in Orogenic Belts

To understand the origin of the lithospheric mantle, it is essential to recognise which aspects of its composition are primary, and which have been imposed by metasomatic processes. Over the last decade there has been a growing recognition that "primary" phases such as clinopyroxene and garnet in mantle-derived lherzolites probably have been metasomatically added (*stealth metasomatism*) to the sub-continental lithospheric mantle, and that the original sub-continental lithospheric mantle was significantly more depleted in elements such as Ca, Al and Fe.

Some of the most compelling evidence for a new view of mantle metasomatism is coming from exposed mantle fragments – the peridotite massifs – where rock-type relationships are most visible, offering a means of testing genetic models. In this section we review two key examples of metasomatic processes in massifs, to see how major- and trace-element patterns are affected.

12.4.1 The Lherz Massif

The Lherz peridotite massif of the French Pyrenees (ca 1.5 km^2 in outcrop) is the type locality of *lherzolite* (olivine + opx + cpx ± spinel ± garnet); within the

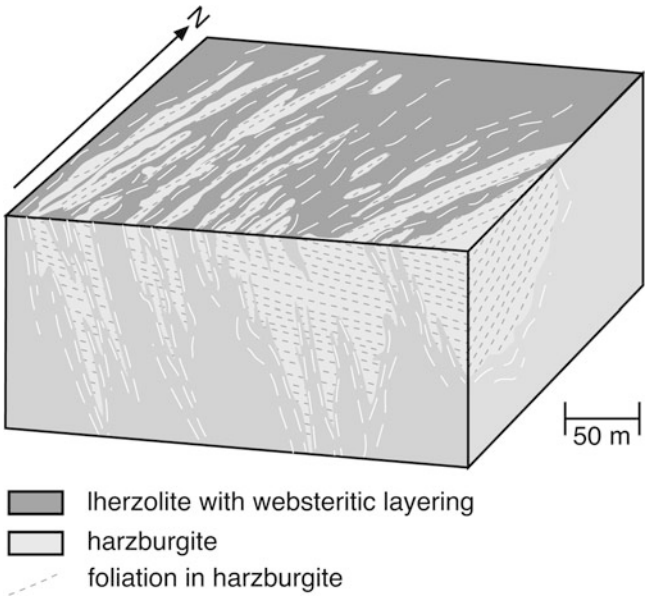

Fig. 12.7 Block diagram showing relationships between primary harzburgite and secondary lherzolite in the Lherz peridotite massif (After Le Roux et al. (2007)

massif, thin layers of spinel harzburgite (1–3% cpx; locally dunite) are interleaved with the dominant lherzolite (9–25% cpx). Several studies of this massif have concluded that the lherzolite, which has a mean composition near that expected for the Primitive Upper Mantle (PUM), was the primary mantle rock (McDonough and Sun 1995), and that the harzburgites represent zones from which melt had been extracted. Others have suggested that the two rock types were tectonically interleaved (Bodinier and Godard 2003). However, a recent series of studies by researchers from the University of Montpellier (Bodinier et al. 1990; Le Roux et al. 2007, 2009) has overturned this model. Their detailed structural mapping shows that the harzburgite lenses throughout the massif have a constant foliation and lineation, which is cross-cut by the lherzolites and interlayered websterites (Fig. 12.7). These observations imply that a body of refractory harzburgite was largely replaced by the lherzolite, in a metasomatic process that has dramatically changed the composition of this mantle volume without the introduction of obviously metasomatic phases (an excellent example of *stealth metasomatism*).

Away from their contacts with the lherzolite, the harzburgite lenses are enriched in LREE/HREE, whereas the lherzolites have low LREE/HREE. This observation alone indicates that the harzburgites do not represent partial-melting residues of the lherzolites. Detailed geochemical sampling across harzburgite bodies shows abrupt fluctuations in the abundances of many trace elements in pyroxenes (*cryptic metasomatism*), including rapid increases, then decreases, in LREE/HREE (Fig. 12.8). This type of enrichment of highly incompatible elements at melt

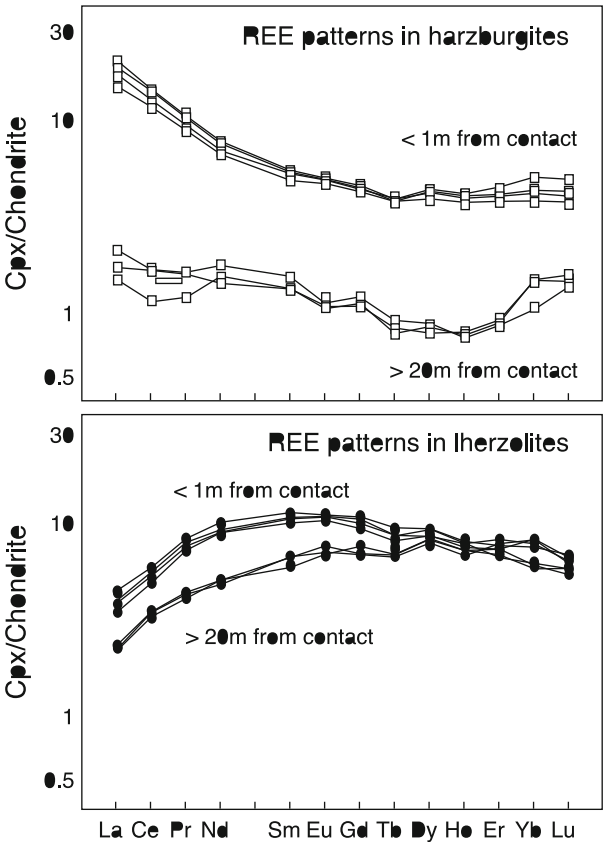

Fig. 12.8 REE mobility during transformation of harzburgite to lherzolite in the Lherz massif (After Le Roux et al. (2007)). Harzburgites, distant from contacts, show mild LREE enrichment from a previous metasomatic episode. Fluids infiltrating in advance of the lherzolite front bring extreme LREE enrichment. Modal metasomatism to produce lherzolite carries the LREE-depleted signature of the infiltrating melt

infiltration fronts reflects the segregation and infiltration of small, probably volatile-rich, melt fractions that separate from the advancing melt front, and precede it through the protolith (Vernières et al. 1997; the "percolative fractional crystallisation" of Harte et al. 1993).

The *stealth metasomatism* that produced the lherzolites reflects the arrival of the melt front itself. It reacted with the pre-existing harzburgite, dumping large amounts of some major elements (Ca, Al, Si) and minor elements (Ti, Na). This has occurred largely at the expense of olivine and Mg. The mean Mg# drops from ca 92 in the harzburgites to ca 90.5 in the lherzolites. Calcium is well-correlated with Al in both the harzburgites and the lherzolites, but with different trends (Fig. 12.9a). Iron contents are negatively correlated with Al in the harzburgites, but not in the lherzolites. The average harzburgite and lherzolite differ by only 0.2 wt% in FeO.

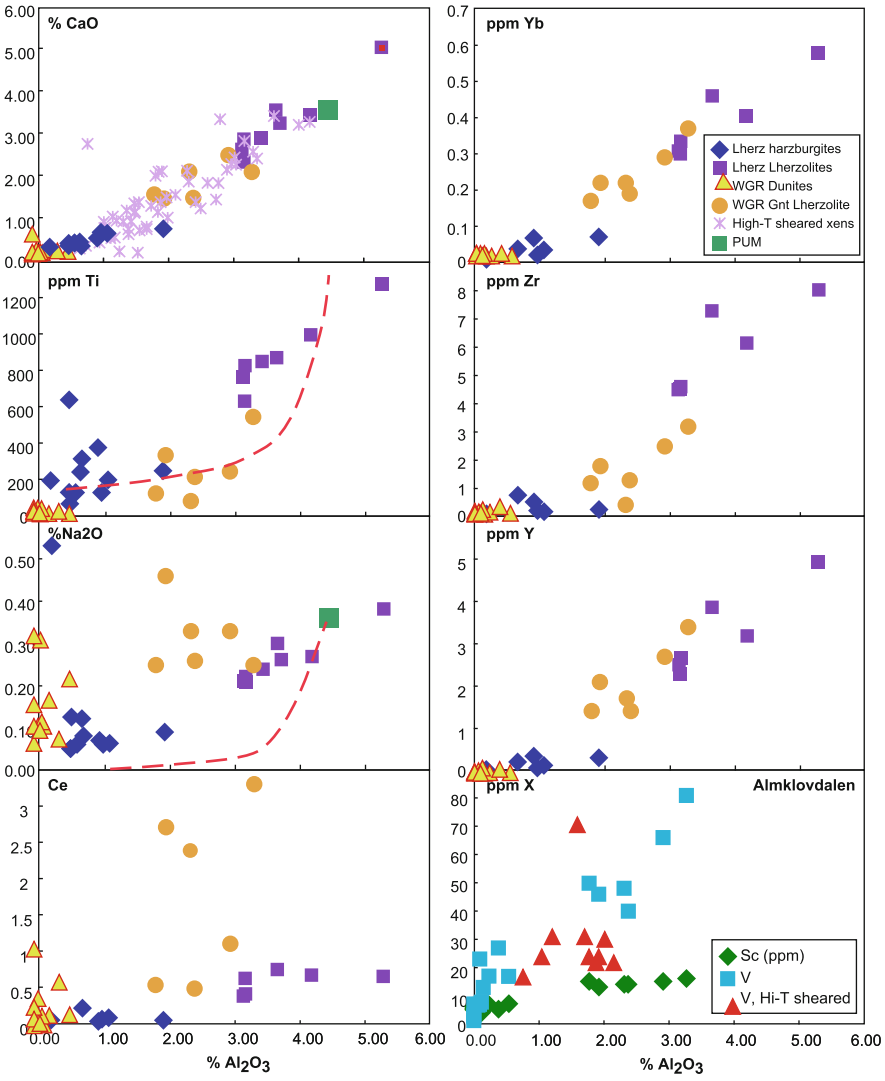

Fig. 12.9 Element correlation plots showing harzburgite-lherzolite relations at Lherz (Data from Le Roux et al. (2007)), dunite-lherzolite relations at Almklovdalen, Western Gneiss Region (Data from Beyer et al. (2006)), and sheared lherzolite xenoliths from southern Africa (Data compilation). Dashed lines show distributions expected from removal of melts from a primitive mantle (pum).

The enrichment in Ca, Al, Si, Ti, and Na suggests that the metasomatising agents were silicate melts with moderate Fe contents. These may be represented by the websteritic dikes and veins found throughout the lherzolites (Le Roux et al. 2007). This enrichment trend thus extends from the highly depleted rocks toward the composition of the Primitive Upper Mantle (Fig. 12.9). Similar arrays have traditionally been interpreted as representing the progressive removal of basaltic

components from fertile (PUM-like) primary mantle, through partial melting processes (e.g. Boyd 1989).

The metasomatism also has strongly affected the abundances of most trace elements (Fig. 12.9). In the harzburgites, elements such as Yb, Sr, Zr and Y are present at very low levels, and their abundances are not correlated with Al or Ca. In the lherzolites, all of these elements occur at much higher abundances (typically ten times those in the harzburgites), and most show strong correlations with Al and/or Ca. This pattern suggests that these trace elements had been essentially removed during the partial-melting processes that left harzburgite residues with 0–2% Al_2O_3. The enrichment of the trace elements in the lherzolites is consistent with mixing between the harzburgites and silicate melts such as the websterite dikes that are associated with the lherzolites (Le Roux et al. 2007).

12.4.2 The Almklovdalen Massif

The Almklovdalen peridotite massif covers an area of >15 km^2 and is several hundred metres thick. It is the largest of at least 100 bodies scattered throughout the Western Gneiss Region of Norway (Brueckner et al. 2010). Unlike the Lherz massif, Almklovdalen is dominated by dunites and clinopyroxene-free harzburgites. The dunites are highly magnesian ($Fo_{93–94}$) and are extensively quarried for refractory material. The garnet peridotite bodies, within the dunite, are small and scattered, and are intimately associated with lenses and dikes of eclogite and garnet websterite (Medaris and Brueckner 2003; Beyer et al. 2006). Contact relations between the dunites and the lherzolites commonly are partly obscured by shearing and late hydration, but appear to be sharp on a scale of centimeters. Re-Os dating of sulfide minerals and whole-rock samples has shown that the dunites are Archean ($\geq$3 Ga) whereas the garnet lherzolites formed in Mesoproterozoic time (ca 1.6 Ga; Beyer et al. 2004). The massif is interpreted as a fragment of Laurentian sub-continental lithospheric mantle that was entrained in the Baltic continental crust as it was subducted beneath the Laurentian continent during the Caledonian (440–400 Ma) HP-UHP event (Brueckner et al. 2010).

The Almklovdalen dunites are more depleted than the Lherz harzburgites. Most have $<0.5\%$ Al_2O_3 and the mine-run average has 0.14% Al_2O_3 and $<0.1\%$ CaO. This extreme depletion has been ascribed to high-degree melting at pressures of 3–5 GPa, possibly in rising plumes (Beyer et al. 2006; Griffin et al. 2009). The garnet peridotites typically contain 1.5–3% CaO, and display an excellent correlation between Ca and Al (Fig. 12.9), similar to that in the Lherz massif. The FeO contents of the dunites are significantly lower than those of the Lherz harzburgites. This difference between depleted rocks in Archean and Proterozoic sub-continental lithospheric mantle is observed worldwide (Griffin et al. 1998b, 2009). The garnet peridotites show a strong correlation between Al and Fe, trending toward the values seen in Lherz lherzolites. As at Lherz, the lherzolites have much higher Ti contents than the dunites, but the Al-Ti correlation is weaker than in the Lherz peridotites.

As at Lherz, the enrichment process can be modelled in terms of mixing between the dunites and the pyroxene-rich rocks (eclogites and websterites) that are spatially associated with the garnet peridotites (Beyer et al. 2006).

The behaviour of some trace elements (Fig. 12.9) during the metasomatism is more complex than that seen in Lherz. The dunites show a range of Sr and Ce, uncorrelated with Al. The contents of these elements in the lherzolites are much higher, but poorly correlated with Al or Ca. On the other hand, Y, Yb, and Zr (and other MREE and HREE, not shown) show strong correlations with Al and Ca, with trends similar to those seen at Lherz. Some elements, such as V, Sc, and Ga, have been regarded as "stable" elements, on the assumption that they respond to partial melting but are less affected by metasomatism (e.g. Canil 2002, 2004; Lee et al. 2003), and thus can be used to interpret the origins of mantle-derived peridotites. However, these elements also show low values in the dunites and strong correlations with Al and Ca (Fig. 12.9) in the lherzolites. It is clear that they have been added to the ultra-depleted protoliths during the metasomatic process, and are highly mobile during this type of metasomatism.

12.5 Cratonic Sub-Continental Lithospheric Mantle (SCLM): Xenolith Evidence for Metasomatism

Several compositional types of metasomatism have been recognised in suites of mantle-derived xenoliths in kimberlites, corresponding to different fluid types and different levels of the cratonic lithosphere. Many studies have focused on obvious examples of modal metasomatism – phlogopite peridotites, MARID (Mica (phlogopite) – Amphibole (K-richterite) – Rutile – Ilmenite – Diopside) rocks and pyroxenites (see below). However, it has become apparent that stealth metasomatism, as observed in the peridotite massifs, is widespread and has played a major role in determining the composition of cratonic SCLM. The evidence for this interpretation comes largely from studies of zoned minerals in peridotites. These examples must represent samples of *recently* metasomatised SCLM (i.e. ≈ contemporaneous with eruption of the host magma), because the chemical gradients within such grains would be obliterated by intragranular diffusion on time scales of a few Ma, even at relatively low T (800–1,000°C). However, these examples show us the types of processes that may have altered the SCLM repeatedly over billions of years.

12.5.1 High-T Sheared Lherzolites

Many kimberlites, particularly in southern Africa, carry garnet-lherzolite xenoliths with fluidal porphyroclastic ("sheared") microstructures (Fig. 12.10). P-T estimates typically yield temperatures of 1,300–1,400°C at depths of 150–180 km. These

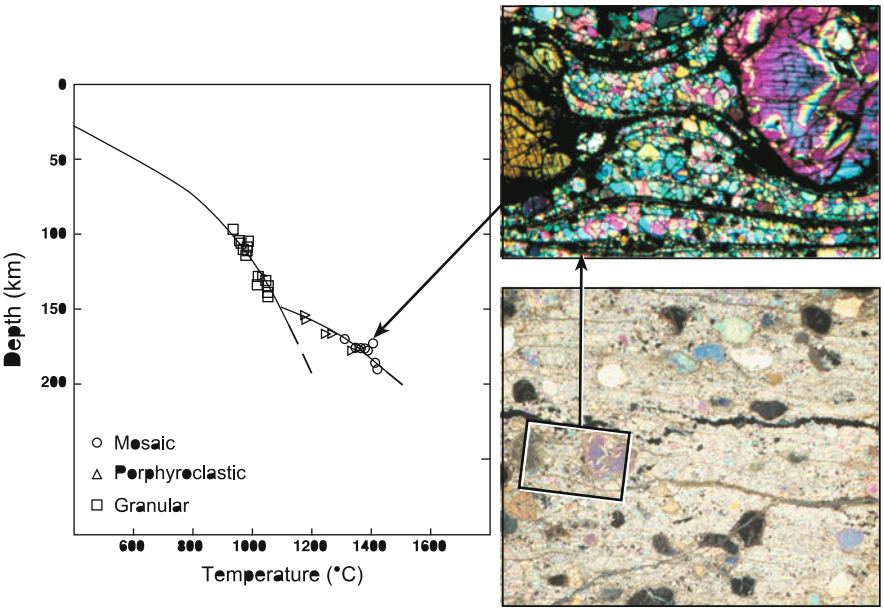

Fig. 12.10 P-T estimates for granular and sheared lherzolite xenoliths from Lesotho define a "kinked" geotherm (After Boyd and Nixon (1973)). Photomicrographs show views of sheared xenolith PHN1611. *Upper photo* is 0.5 mm long

conditions lie well above the continuation of a typical cratonic geotherm, suggesting a "kinked" geotherm consistent with thermal events near the base of the SCLM (Fig. 12.10). Experiments and theoretical annealing models (Mercier 1979) demonstrate that the disequilibrium microstructures of these xenoliths could not be preserved for more than tens of years at the temperatures recorded by their mineral chemistry. This implies that the deformation was essentially contemporaneous with the entrainment of the xenoliths in their host kimberlite. The sheared xenoliths are fertile in terms of basaltic components (Mg# $\leq$ 91; high Ca, Al, Ti; chondritic REE patterns). The bulk compositions of some samples approximate estimates of the Primitive Upper Mantle, in contrast to the more refractory compositions of the lower-T granular peridotites from the same kimberlites (see below).

These xenoliths were originally thought to be possible samples of the undepleted convecting asthenosphere (Boyd and Nixon 1973). However, detailed studies of zoning in their minerals (Smith and Boyd 1987; Smith et al. 1991, 1993; Griffin et al. 1996) have demonstrated that the sheared xenoliths represent fragments of strongly metasomatised lithospheric mantle. Garnet porphyroblasts commonly have rims that are strongly enriched in Fe, Ti, Y and Zr relative to the cores (Fig. 12.11). These zoning profiles can be modelled as the result of an overgrowth, followed by annealing and diffusion over periods from a few days to hundreds of years prior to eruption. Smith and Boyd (1987) derived similar estimates from the

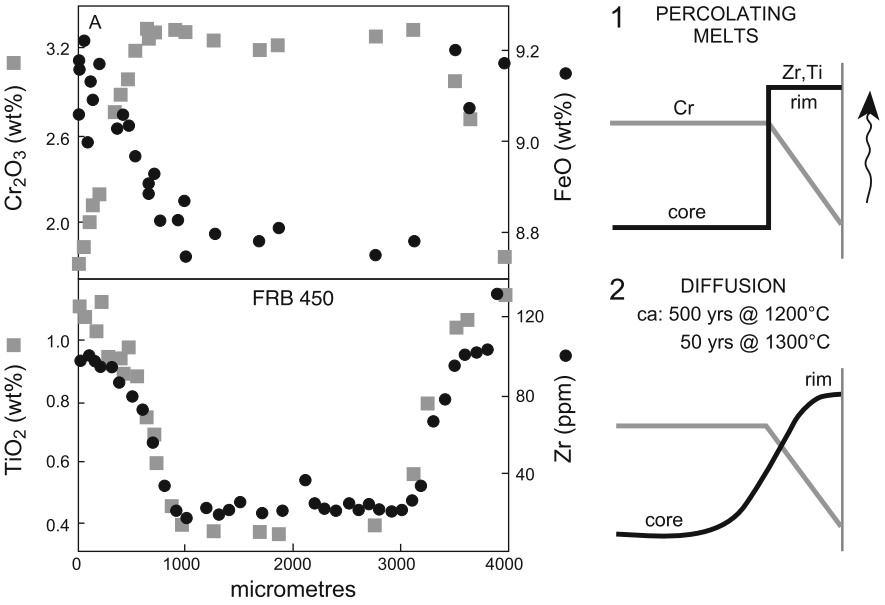

Fig. 12.11 Zoning in a garnet from sheared lherzolite xenolith FRB450, and a model. (*1*) Instantaneous overgrowth of a garnet rim high in Zr and Ti, but low in Cr. (*2*) Diffusional modification of Zr and Ti profile. Chromium diffuses much more slowly, if at all (After Griffin et al. (1996)).

chemical gradients between Fe-rich and Fe-poor domains, juxtaposed by the shearing, within single xenoliths.

These observations indicate that the rims of the garnets represent a metasomatic addition of garnet to a more depleted protolith. Simple geometric estimates imply that at least 50% of the garnet was added by this stealth metasomatism. Correlations between the modal abundances of garnet and clinopyroxene (Fig. 12.12) therefore suggest that at least 50% of the clinopyroxene in the rocks also was added. The whole-rock compositions of sheared xenoliths from Africa plot along the same Ca-Al correlation trend as the metasomatic lherzolites of the Lherz and Almklovdalen massifs (Fig. 12.9). The addition of so much Ca, Al, Fe, and Na to the original protolith strongly suggests that the metasomatic agent, as in the massif examples discussed above, was a mafic melt.

12.5.2 Granular Xenoliths: Metasomatism at Shallower Levels

The high-T sheared lherzolite xenoliths described above are derived from depths corresponding to the base of the depleted SCLM. However, the overwhelming majority of mantle-derived xenoliths in kimberlites are coarser-grained and have

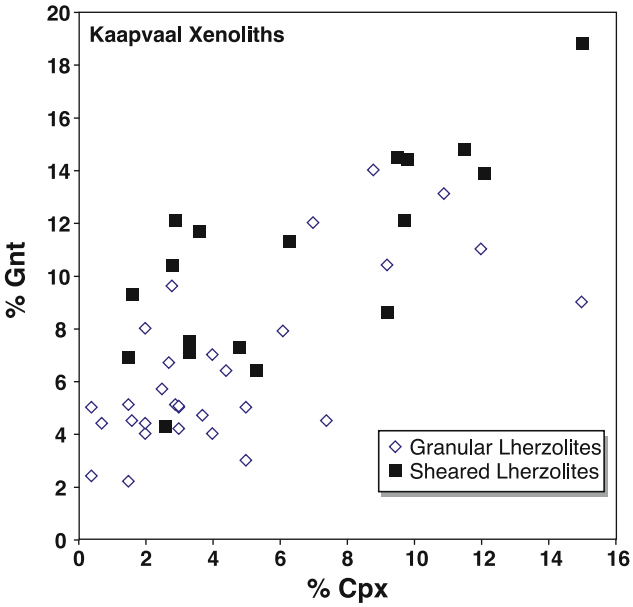

Fig. 12.12 Correlations between modal abundances of garnet and clinopyroxene in sheared and granular xenoliths from southern Africa (Authors' unpublished compilation)

microstructures that suggest long-term equilibrium among the major minerals (Boyd and Mertzman 1987). Their compositions range from highly magnesian (Mg# 93–95) dunites and harzburgites to fertile (Mg# $\leq$ 90) lherzolites. These lherzolites contain garnet at depths greater than ca 90 km, and spinel at shallower depths. Chromite is stable in the depleted rocks to at least 100 km depth. In large xenolith suites, such as those from the dumps at diamond mines in the Kimberley area of South Africa, dunite-harzburgite ($\pm$chromite) xenoliths are abundant but little-studied, partly because we have no good way to determine their precise depths of origin. Modelling of geophysical data (gravity, geoid, seismic) suggests that such depleted rocks make up most of the shallower SCLM beneath the cratonic areas (Afonso et al. 2008; Griffin et al. 2009), and that the relative abundance of fertile rocks increases with depth. This structure is difficult to explain through models that produce the dunite-harzburgites by progressive melting of the lherzolites, but is consistent with a metasomatic refertilisation process driven from the bottom up. Several types of xenoliths and xenocrysts in kimberlites offer clues to the nature of these processes.

12.5.2.1 Harzburgite Metasomatism: The First Steps

The peridotitic xenoliths from the kimberlites of the Kimberley area are probably the most intensively studied xenolith suite in the world. Much of the work has concentrated on the ubiquitous garnet lherzolites, but the dumps from the diamond

mines also contain a high proportion of more depleted rocks, including garnet-free dunites and harzburgites. The harzburgites, and most lherzolites, have high orthopyroxene/olivine relative to similar rocks from kimberlites in Siberia, North America, or other places in Africa (Griffin et al. 1998b).

Banas et al. (2009) have shown that olivine inclusions in diamonds from the Kaapvaal kimberlites have highly magnesian compositions ($>Fo_{94}$), implying that the diamonds grew in rocks (dunites) that had been melt-depleted to beyond the point of orthopyroxene depletion. This suggests that the orthopyroxene now present in the harzburgites and lherzolites probably represents the first stage of metasomatic refertilisation of the depleted SCLM. Kelemen et al. (1998) and Bell et al. (2005) have suggested that this addition of SiO_2 could reflect the penetration of fluids derived from subducting slabs, which could relate this metasomatism to the processes of Archean craton assembly.

Many kimberlite-borne xenoliths of harzburgite (clinopyroxene-free) contain small amounts of garnet, which typically is a low-Ca chrome pyrope (<1–4% CaO, 2–20% Cr_2O_3). These "G10" garnets (e.g. Dawson and Stephens 1975; summary in Malkovets et al. 2007) are used as "indicator minerals" in diamond exploration programs, because of the recognised association (at least in the Kaapvaal and Siberian cratons) between such garnets and the presence of diamond in a kimberlite. G10 garnets have unusual sinuous REE patterns, with low contents of both light and heavy REE, but relatively high contents of the mid-range REE from Nd to Eu (Fig. 12.13). These patterns have been attributed to the metasomatic modification of a pre-existing garnet, which would originally have had low LREE/HREE because the large ions of the LREE are preferentially excluded by the garnet lattice (e.g. Stachel and Harris 1997; Banas et al. 2009; references therein). However, this model would require the retention of garnet in a highly depleted residue, even at the high degrees of melting (>50%) required to reach Mg# >94 (e.g. Banas et al. 2009).

An alternative possibility is that the garnet itself is entirely a metasomatic phase, precipitated directly from a metasomatic fluid percolating through an extremely depleted garnet-free dunite (or harzburgite) protolith. Calculations based on experimentally-determined fluid/garnet distribution coefficients require a metasomatic fluid that was extremely enriched in LREE relative to HREE (Fig. 12.13). The growing garnet would be depleted in HREE because these elements were very low in the fluid; the lightest REE would be rejected by the garnet lattice, and the MREE would be relatively enriched, giving the sinuous patterns. Mg-rich carbonatite-like fluids with this predicted trace-element pattern recently have been found as inclusions in coated diamonds from kimberlites in the Slave Craton of northern Canada (Klein-BenDavid et al. 2007; Araujo et al. 2009a; Fig. 12.13)

These observations provide a link between diamond-forming fluids (on which more below), the most important diamond-indicator mineral, and the initial modification of highly depleted SCLM protoliths. Malkovets et al. (2007) have suggested that the metasomatism reflects the introduction of reduced, methane-rich asthenosphere-derived fluids into the relatively more oxidising lithosphere, inducing reactions such as (schematically):

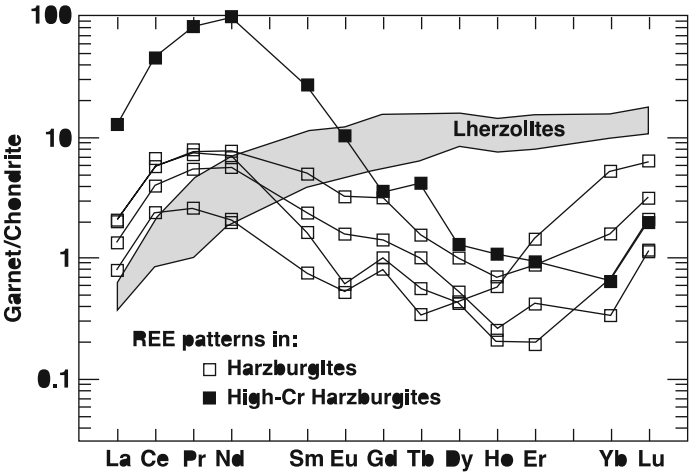

Fig. 12.13 Sinuous REE patterns in low-Ca Cr-pyrope garnets (After Stachel and Harris (1997). *Dark field* shows patterns of garnets in lherzolite xenoliths (Authors' unpublished compilation)

$$\mathrm{Fe^{3+}(Al-rich\ chromite)} + \mathrm{Opx} + \mathrm{CH_4(fluid)} \rightarrow \mathrm{C\ (diamond\ or\ graphite)} + \mathrm{low-Ca\ garnet} + \mathrm{Fe^{2+}(garnet} \pm \mathrm{residual\ Cr-rich\ chromite)} + \mathrm{H_2O}$$

The H_2O-rich fluid produced by such reactions would react in turn with other components of the mantle wall-rocks, producing low-degree partial melting, and other types of metasomatic effects.

12.5.2.2 Harzburgite to Lherzolite: And Sometimes Back Again

The zoned minerals in the high-T sheared lherzolite xenoliths, described above, carry the signature of a metasomatic process that fortuitously was captured (by entrainment of the xenolith in an erupting kimberlite) before it could be erased by intragranular diffusion. The overwhelming majority of lower-T, cratonic, peridotite xenoliths have granoblastic microstructures and homogeneous minerals, and retain no direct evidence of the processes that have produced them. However, a number of studies (Schulze 1995; Smith et al. 1991; Griffin et al. 1999c) have described garnet-harzburgite xenoliths containing zoned garnets that provide information on the metasomatic processes. In each case, the cores of the garnets resemble the low-Ca "G10" garnets described above, and are zoned toward more Ca-rich rims.

One intensively studied suite of such xenoliths includes six harzburgites (some phlogopite-bearing) from the Wesselton kimberlite, (South Africa) (Griffin et al. 1999a). These rocks were metasomatically modified at T $\approx$ 1,000°C and depths of 110–120 km. Garnet cores have sinuous REE patterns. Rimward increases in Ca (with Cr and Mg decreasing) are accompanied by increases in Zr, Y, Ti, and HREE

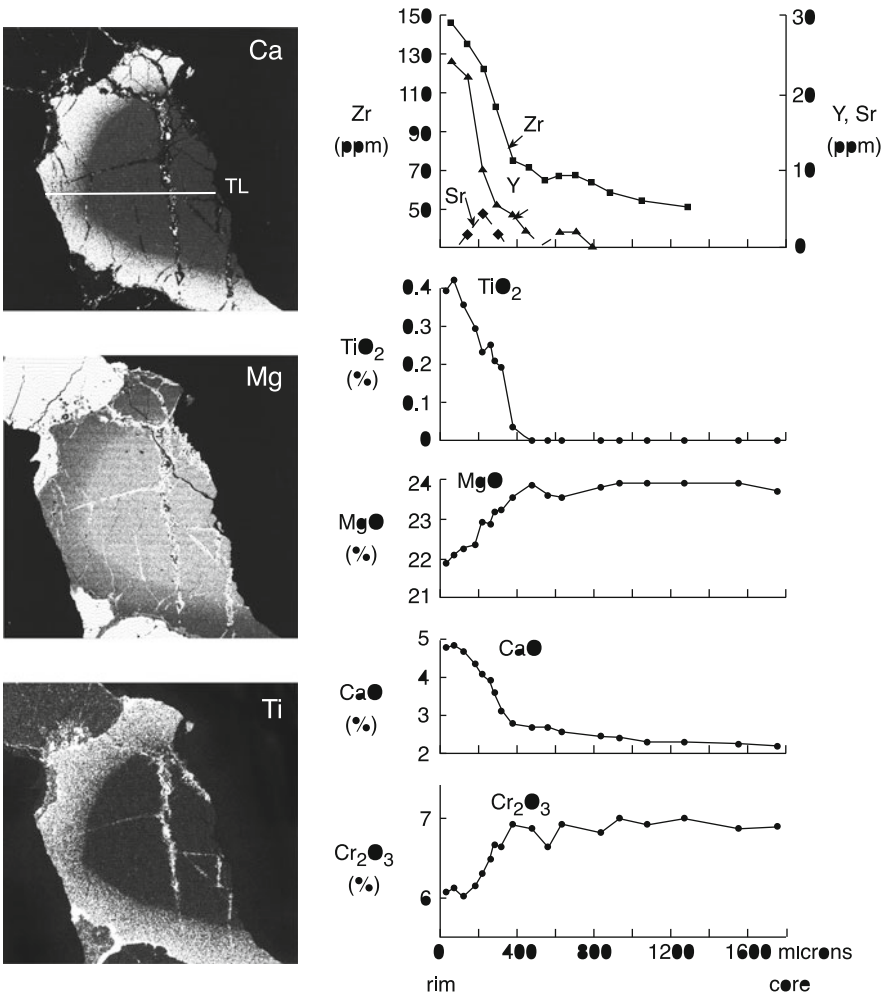

Fig. 12.14 Zoning profiles along line TL (length 1,800 μm) in Ca image and element maps of a garnet grain in a garnet harzburgite xenolith from the Wesselton kimberlite, South Africa (After Griffin et al. (1999a)). Y can be used as a prexy for the HREE.

(Fig. 12.14). Late replacement rims show a reversal of the zoning to garnet with lower Ca but high Mg, Ti, and HREE. The zoning profiles can be modelled in terms of a three-stage metasomatic process (Fig. 12.15): (a) inward diffusion of Ca, Zr, Y, and HREE from a fluid depleted in Ti, Ga, and Y, over periods of 10,000–30,000 years; (b) formation of overgrowths high in Ca, Zr, Y, HREE, and Ti, followed by annealing over several thousand years; and (c) growth of late lower-Ca garnet rims shortly before kimberlite eruption. McCammon et al. (2001) used Mossbauer spectroscopy to measure the oxidation state of Fe in the garnets, and found increases in $Fe^{3+}/Fe(T)$ from core to rim to secondary rim. Oxygen fugacities,

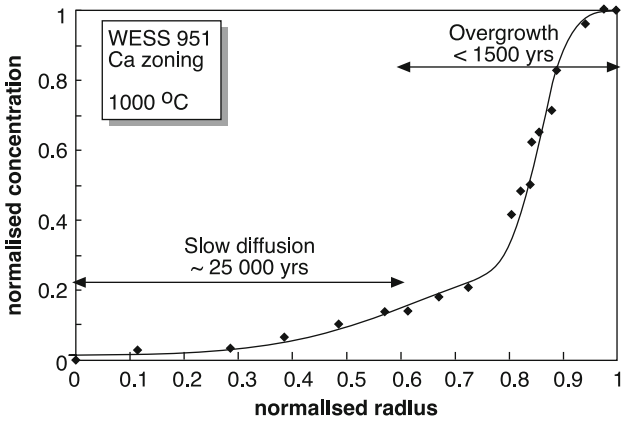

Fig. 12.15 Two-stage diffusion modelling of zoning profile shown in Fig. 12.14

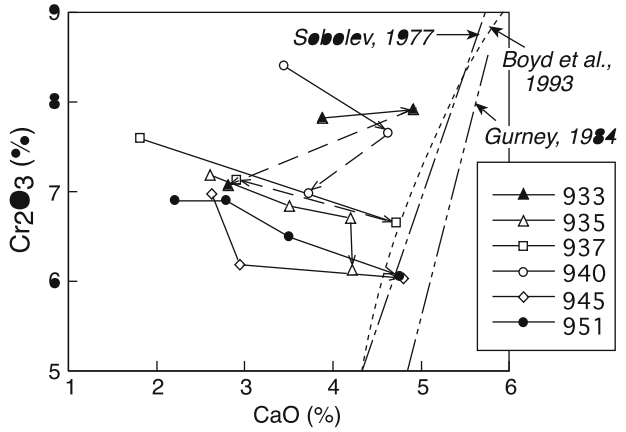

Fig. 12.16 Ca-Cr plot showing zoning in garnets from Wesselton harzburgites, with three definitions of the harzburgite-lherzolite boundary (After Griffin et al. (1999a))

calculated using the garnet-olivine-orthopyroxene oxybarometer, increase by approximately one log-bar unit (relative to QFM) from garnet cores to secondary rims, implying a rise in fO_2 from the initial protolith, through stages (a) to (c).

The effect of stages (a + b) is to convert the harzburgite garnets to compositions typical of lherzolitic garnets (Fig. 12.16), but without significant change in Mg#. This suggests either that the fluids carried little Fe or Mg, or that they had thoroughly equilibrated with the olivine and orthopyroxene of the harzburgitic wall-rocks. The high Zr/Y, Zr/Ti, and Zr/Ca of the fluids in stage (a) suggest the presence of phlogopite and garnet in the surrounding matrix, leading to the development of concentration fronts in the percolating fluid. Microstructures suggest that overgrowths of stage (b) coincide with the precipitation of phlogopite in the rocks. The source of these fluids is presumed to be a silicate melt. Infiltration of these

melts may have produced the lherzolites with lower Mg# that also occur in this xenolith suite. This scenario is a direct analogue to the Lherz model described above, i.e. a melt-percolation front that is preceded by volatile-rich fluids producing (in this case) cryptic metasomatism (enrichment of pre-existing garnet), stealth metasomatism (garnet overgrowths), and, finally, modal metasomatism (phlogopite, clinopyroxene, garnet).

12.5.3 Modal Metasomatism in Cratonic Xenolith Suites

12.5.3.1 Phlogopite-Related Metasomatism of Peridotites

The introduction of phlogopite is the first step in a process of progressive *modal* metasomatism that has been widely studied in cratonic xenoliths, especially from kimberlites in South Africa and China. Erlank et al. (1987) defined a sequence of progressive metasomatism from garnet-phlogopite peridotite (GPP) through phlogopite peridotite (PP, garnet-free) to phlogopite + K-richterite peridotite (PKP, garnet-free), and, finally, to wehrlite (clinopyroxene-olivine-phlogopite). This metasomatism was originally ascribed to an H_2O-rich fluid. Waters and Erlank (1988) subsequently argued for a volatile-rich alkaline melt.

Van Achterbergh et al. (2001) studied a similar sequence in xenoliths from the Letlhakane kimberlite (Botswana), in which the reactions were especially clear because the garnets in the rocks were progressively pseudomorphed by the secondary phases, allowing for the tracking of mass balances through the steps of the metasomatic process. The initial protolith is represented by clinopyroxene-free harzburgites carrying minor garnet, with trace-element patterns indicative of previous cryptic metasomatism (see above). The pseudomorphing reaction was defined as

$$\text{Fluid}_1 + \text{garnet} \rightarrow \text{phlogopite} + \text{clinopyroxene} + \text{Cr} - \text{spinel} + \text{Fluid}_2.$$

A continuous decrease in the modal abundance of orthopyroxene through the sequence defined a second reaction:

$$\text{Fluid}_1 + \text{orthopyroxene} \rightarrow \text{olivine} + \text{clinopyroxene} + \text{Fluid}_2.$$

Mass-balance models showed that large amounts of Sr, Na, K, LREE and HFSE (Zr, Ti, Nb) were introduced into the whole-rock system, while Al, Cr, Fe and garnet-compatible trace elements (V, Y, Sc, HREE) were removed. Importantly, the loss of Al from the whole-rock system could be directly tied to the metasomatic process. The metasomatism was accompanied by a rise in T (from 850–1,050°C to >1,200°C, based on Ti contents of phlogopite) and the authors concluded that the fluids probably emanated from an alkaline mafic melt in nearby magma conduits.

12.5.3.2 MARID and Related Rocks

Kimberlites, especially those of southern Africa, also carry a distinctive suite of phlogopite-rich xenoliths that lack olivine. Early workers commonly referred to these as "glimmerites". Dawson and Smith (1977) defined a MARID (Mica (phlogopite) – Amphibole (K-richterite) – Rutile – Ilmenite – Diopside) suite but cautioned that not all phlogopite-rich rocks are necessarily MARID. In a valiant attempt to sort out the nomenclature, Grégoire et al. (2002) used mineralogy, major- and trace-element geochemistry, and isotopic data to distinguish MARID rocks from mica pyroxenites (no K-richterite) and glimmerites (>90% phlogopite), and then grouped the latter two suites as PIC (Pyroxene – Ilmenite – Cpx ± minor rutile). They noted that the bulk compositions of these rocks were strongly controlled by the modal abundances of different minerals, and took this as evidence for a cumulate origin (as argued by Williams 1932; Aoki 1974; Sweeney et al. 1993, and others), although monomineralic banding also is a characteristic feature of metasomatic processes (e.g. Korzhinski 1936). Modelling of the fluids in equilibrium with the clinopyroxene of each group shows that the parental melts of MARID rocks resemble the (ca. 100–170 Ma) Group 2 kimberlites of the Kaapvaal Craton, whereas the PIC melts are more similar to Group 1 (<100 Ma, >200 Ma) kimberlites. The Sr-Nd isotopic signatures of these two kimberlite types are significantly different, and the signatures of MARID and PIC rocks are consistent with the proposed genetic relationship.

Choukroun et al. (2005) used in situ LAM-ICPMS (Laser ablation microprobe – Inductively coupled plasma mass spectrometry) techniques to analyse the Hf-isotope composition of rutile grains in MARID rocks. The data show very large spreads in $^{176}Hf/^{177}Hf$ even within single grains, suggesting interaction between asthenosphere-derived melts and ancient (>3.2 Ga) SCLM. A similar model has been used to explain the Sr-Nd isotopic compositions of Group 2 kimberlites (Grégoire et al. 2002). Choukroun et al. (2005) also reported a $^{206}Pb/^{238}U$ age of 112 ± 4 Ma for a large zircon in a MARID rock. Similar ages have been reported by Konzett et al. (2000), providing a further link between MARID and Group 2 kimberlites. The rutile data also suggest later modification of the MARID rocks by metasomatic fluids carrying extremely radiogenic Hf, probably derived from the metasomatic breakdown of old garnets. Thus even if the MARID rocks are magmatic in origin, they have seen their share of metasomatic modification.

12.5.4 Distribution of Metasomatic Styles: Chemical Tomography

Relatively few kimberlites carry the extensive and spatially representative xenolith suites needed for detailed investigations of mantle processes. A single kimberlite may carry xenoliths from only a restricted depth range, and many xenoliths disaggregate during transport. However, most kimberlites carry abundant xenocrysts of pyrope garnet derived from the mantle wall-rocks, and these contain

several types of information on the composition of the SCLM, and on metasomatic processes. Detailed correlations between the major- and trace-element patterns of garnets in different types of xenoliths (Griffin et al. 1999c, 2002; Grégoire et al. 2003) provide a template for recognising, in suites of garnet xenocrysts, the chemical fingerprints of a range of processes. Relationships between elements such as Zr, Y and Ti are especially useful, because they allow distinction between melt-related metasomatism (as seen in the high-T sheared xenoliths) and fluid-related metasomatism (often associated with phlogopite) (Fig. 12.17). Thus garnets from melt-metasomatised peridotites tend to have high Ti contents, and strong correlations between Ti, Y and Zr, whereas garnets affected by fluid-related metasomatism (phlogopite-associated) tend to have low to moderate contents of Y and Ti, but high Zr. Alkali basalts may carry fertile garnet peridotite xenoliths, which may be samples of relatively undepleted mantle (see below). The garnets of these xenoliths have low contents of Ti and Zr, but high contents of Y (and HREE).

However, we want to understand not only the presence or absence of these processes, but their spatial distribution in the mantle. Fortunately, the partitioning of Ni between olivine and garnet is strongly temperature-dependant. Most of the Ni resides in the olivine, which in typical mantle peridotites has 2,900 $\pm$ 100 ppm Ni, whereas the Ni content of the coexisting garnet varies from <10 to >150 ppm, levels that are easily measured by PIXE (proton-induced X-ray emission) or LAM-ICPMS. This Ni-in-garnet thermometer has been empirically calibrated (Griffin et al. 1989; Ryan et al. 1996) using well-equilibrated garnet-peridotite xenoliths for which P-T estimates can be derived using experimentally-calibrated thermobarometers. Thus we can estimate the temperature at which a given xenocryst resided in the mantle. Projection of this T to a local geotherm can then provide a depth estimate. This geotherm can be established from P-T estimates on xenoliths (Fig. 12.10), or derived from suites of garnet xenocrysts by a more complex procedure (Ryan et al. 1996).

The garnet xenocrysts carry several types of useful information (Griffin et al. 1999c, 2002). Their major-element compositions reflect the rock type from which they were derived. Their trace-element patterns reflect metasomatic processes. The composition of the coexisting olivine can be calculated (Gaul et al. 2000), and their Y contents can be used to estimate the Al_2O_3 content of their original host rock (a good measure of its fertility; Griffin et al. 1999b). When a large suite of garnet analyses (major and trace elements) is available from a single area, the distribution of different types of geochemical signatures gives a picture of the variation in rock types and processes with depth ("chemical tomography"; Griffin et al. 2003; O'Reilly and Griffin 2006).

The chemical tomography section derived from xenocrysts in the Group 1 (ca 90 Ma) kimberlites of the Kimberley area (Fig. 12.18), shows a thick section of depleted rocks (garnet harzburgites, garnet lherzolites with low Y, Zr, Ti). Melt-related ("stealth") metasomatism is especially prominent near the base of the depleted section (170–190 km: O'Reilly and Griffin 2010b), but is still important up to 130–140 km. A population of garnets that can be recognised as depleted grains overprinted by fluid-related metasomatism is concentrated between 130 and

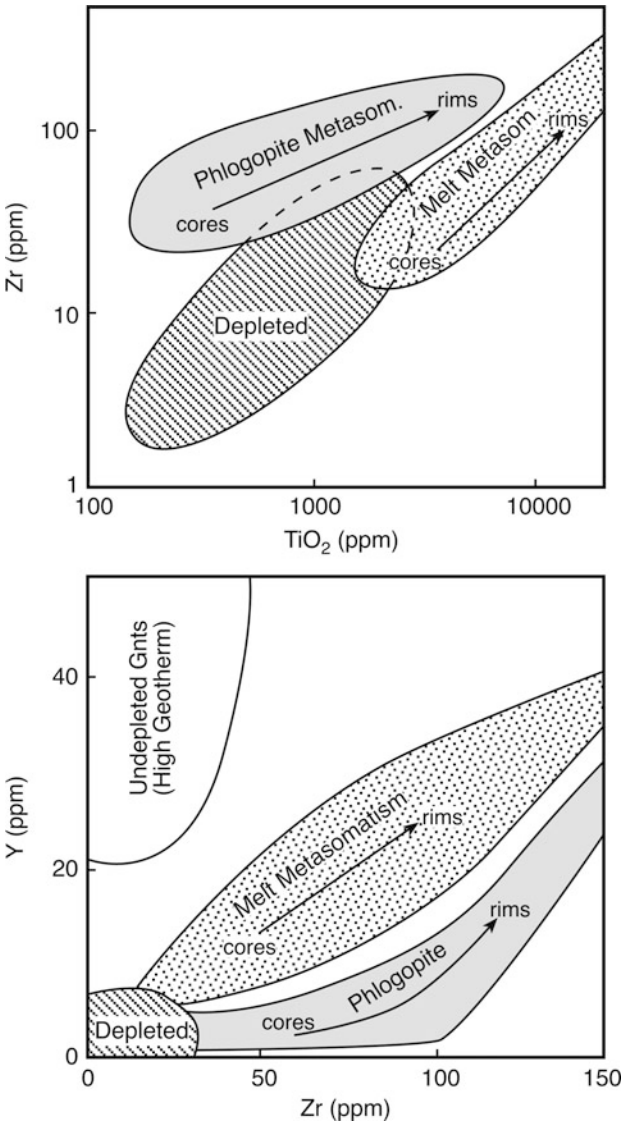

Fig. 12.17 Trace-element signatures of Cr-pyrope garnets affected by melt depletion ("depleted") and different types of metasomatic processes. Melt metasomatism is typical of high-T peridotites, while phlogopite-related metasomatism is typical of lower-T peridotites (After Griffin and Ryan (1995))

170 km depth. At levels above ca 120 km, fertile lherzolites, reflecting mainly fluid-related metasomatism, completely dominate the sampled section. The drop in mean X_{Mg} of olivine at depths >160 km reflects the introduction of Fe characteristic of melt-related metasomatism. A smaller drop in X_{Mg} in the 100–120 km depth

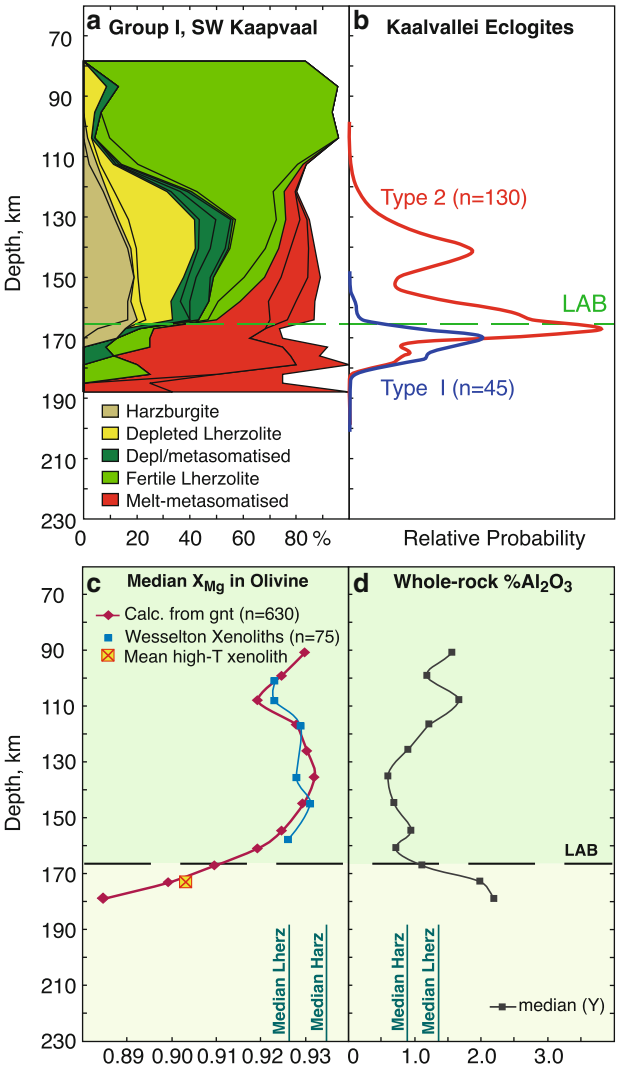

Fig. 12.18 Chemical Tomography section of the mantle beneath the Kimberley area, South Africa, 80–100 Ma ago, constructed from Cr-pyrope garnet concentrates and xenoliths. (**a**) distribution of rock types and metasomatic processes; (**b**) distribution of eclogites; (**c**) distribution of median Mg# of olivine, comparing values calculated from garnets Gaul et al. (2000) with data from xenoliths; (**d**) distribution of whole-rock Al_2O_3 contents (a measure of fertility), calculated from the Y contents of Cr-Pyrope garnets (After Griffin et al. 2003; Griffin and O'Reilly (2007))

interval reflects the intense fluid-related metasomatism at these depths, and correlates with a rise in calculated whole-rock Al contents.

It is clear that this mantle section has been thoroughly modified over time by the infiltration of fluids and melts. However, the chemical tomography approach relies

on analysis of garnet – most (all?) of which is itself a metasomatic phase, at least in ancient SCLM. Rocks that have not been affected by garnet-producing metasomatism, or those that were metasomatised to the point where garnet disappeared, will be invisible to this technique, and the proportion of garnet-free depleted rocks (the initial protolith) probably is relatively high, as is illustrated by the abundance of garnet-free peridotites on the Kimberley dumps, and by geophysical modelling (Afonso et al. 2008; Griffin et al. 2009).

The distribution of eclogites in these chemical tomography sections has been mapped by deriving T estimates for clinopyroxene-garnet pairs at different P, and projecting this locus to a known geotherm, derived as discussed above; it may give an indication of the sources of metasomatic fluids. In most sections studied, eclogites are tightly clustered at the base of the depleted SCLM, or at sharp breaks in SCLM stratigraphy (Griffin and O'Reilly 2007). Many studies have regarded cratonic eclogite xenoliths as samples of subducted oceanic crust, although this is incompatible with microstructural evidence for complex exsolution, which shows that many eclogites originated as high-T magmatic rocks (Griffin and O'Reilly 2007; Greau et al. 2011; references therein). The strong spatial correlation between eclogites and melt-related metasomatism of the peridotites is unlikely to be a coincidence. We suggest that the crystallising melts that produced the eclogites, and fluids expelled during this crystallisation, may also have been the agents of metasomatism in the deep lithosphere.

12.5.5 Discussion: Progressive Melting Versus Refertilisation in the SCLM

The linear geochemical trends observed in both massifs and large xenolith suites (Fig. 12.19) have long been interpreted as reflecting progressive depletion by removal of melts. This assumption has, for example, underlain several attempts to estimate the composition of the primitive upper mantle (e.g. Boyd 1989). However, numerical modelling (Niu 1997) shows that the extraction of partial melts from a primitive upper mantle composition will produce concave-upward trends in plots of incompatible elements (e.g. Ti, Na) vs more compatible ones (e.g. Al, Mg), because the incompatible elements are more rapidly depleted relative to compatible ones as melt is extracted (Fig. 12.9). The linear trends that dominate the massif and xenolith datasets, thus, are consistent with mixing relationships, but not with partial melting.

The observations on peridotite massifs and xenolith suites reviewed here make it abundantly clear that most of our SCLM samples have a history involving depletion by the (often extreme) removal of partial melts, followed by metasomatic refertilisation. The entire range of xenolith compositions from the SCLM can be observed on a scale of meters within massifs such as Lherz or Almklovdalen (Fig. 12.9), and clearly is related to reaction between depleted peridotite wall-rocks and infiltrating melts (mafic to ultramafic) and fluids.

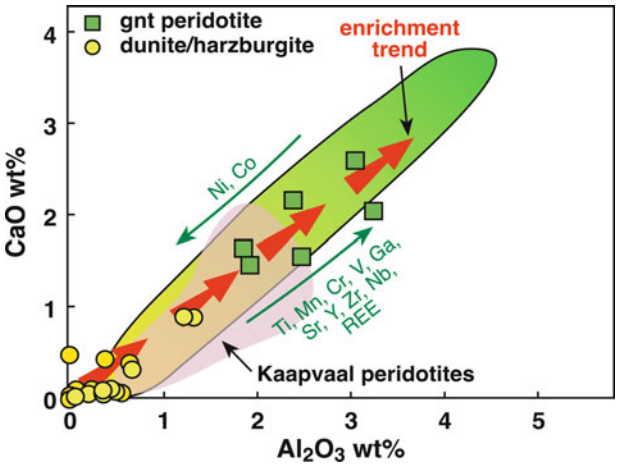

Fig 12.19 Illustration of the enrichment trend (seen here in CaO and Al_2O_3 space) due to metasomatic addition to depleted lithospheric mantle. Also shown are the changes in minor and trace element compositions (After Griffin et al. (2009)). This refertilisation trend mimics the path for inferred depletion, but is in the opposite sense.

It is important to note that trace elements are introduced or removed by these refertilisation processes, to at least the same extent as the major elements, producing large changes in trace-element patterns and abundance. This process includes elements such as HREE, V, Sc that are commonly used to "see through" metasomatic effects; they cannot be used to evaluate the "origins" of mantle rocks. The focus of this discussion has been on the peridotite wall-rocks, but these processes will affect any pre-existing rocks that get in the way of the fluids, including eclogites, pyroxenites and related rocks, so that great care (and scepticism) are needed to interpret their origins from such data.

If the protolith and the metasomatising agent have had different histories and sources, they are likely to be isotopically different (in almost any radiogenic system), so great care also is required in interpreting isotopic data where stealth metasomatism has been active. In some cases this can be obvious. For example in Lherz and other Pyreneean massifs, $^{87}Sr/^{86}Sr$ is negatively correlated with Al_2O_3, while $^{143}Nd/^{144}Nd$ is positively correlated, which is inconsistent with a partial-melting process (Bodinier et al. 1990; Le Roux et al. 2007, 2009). In both massifs (including Lherz) and some xenolith suites, $^{187}Os/^{186}Os$ is positively correlated with Al_2O_3 contents, and this relationship has been assigned an age significance (the "Aluminochron" approach; Reisberg and Lorand 1995) on the assumption that the variable Al_2O_3 contents reflect different degrees of partial melting. However, more recent work (e.g. Le Roux et al. 2007) has made it obvious that this relationship simply reflects mixing between an older SCLM protolith (low $^{187}Os/^{186}Os$) and metasomatic fluids/melts from the convecting mantle (higher $^{187}Os/^{186}Os$).

12.6 Off-Craton SCLM: Xenolith Evidence for Metasomatism

Xenolithic samples of the lithospheric mantle from off-craton regions are found worldwide, mainly in alkali-basalt (sensu lato) host rocks, and provide ubiquitous evidence of an almost overwhelming variety of metasomatic effects. Most of these regions are tectonically young, dominantly in Phanerozoic terrains. Examples include xenolith suites from the western USA (Nielson et al. 1993; Wilshire and Shervais 1975), Spitsbergen (Amundsen et al. 1987), the Massif Central of France (e.g. Downes and Dupuy 1987; Downes et al. 2003) and eastern China (e.g. Xu et al. 2000; Zheng et al. 2007). This section cannot address the details of all these studies, but presents an overview of the range of metasomatic types represented and the processes and mechanisms involved.

Several early benchmark studies of off-craton metasomatised mantle xenoliths (Frey and Green 1974; Wilshire and Shervais 1975; Frey and Prinz 1978) described mantle metasomatism beneath western Victoria (Australia), the Western USA, and the San Carlos locality (Arizona, USA) respectively, in terms of the introduction of a basanite-type melt into refractory mantle peridotite. Wilshire and Shervais (1975) distinguished two major types of mantle xenoliths, the Cr-diopside series (Type I of Frey and Prinz 1978) which is now universally recognised as representing the pre-existing mantle wall-rock, and the Al-augite series (Type II of Frey and Prinz 1978), now recognised as infiltrated basaltic magmatic products frozen in the mantle.

Subsequent early studies recognised the importance of $CO_2 \pm H_2O \pm Cl$ as major metasomatic agents (e.g. Menzies and Wass 1983; Roden et al. 1984; Stosch and Seck 1980). Taylor and Green (1988) explored C-O-H fluids more widely, including the effects of percolation of reducing fluids such as CH_4. Integrated studies of "text-book" sample suites, such as those from western Victoria, have allowed the unravelling of multiple episodes of metasomatic overprints, the characterisation of the different types of metasomatic fluids responsible for specific episodes, and in some cases, correlation with intrusive magmatic events and tectonism.

12.6.1 Eastern Australia

Although there are myriad accounts of off-craton metasomatism, the studies from eastern Australia, which represent a >4,000 km traverse of mantle samples, are still the most comprehensive and integrated examples of such a large region of the Earth's mantle over a time span of about 100 Ma (up to the present). The metasomatised xenoliths from southeastern Australia incorporate the whole range of chemical interactions observed globally in off-craton suites, and contains some unique xenolith suites in which multiple episodes can be clearly delineated (modally and geochemically). These also illustrate a remarkable geochemical

provinciality in the lithospheric mantle, which can be correlated with the geochemical signatures of the alkali basalts that ascended through these domains (e.g. Zhang et al. 2001). They thus provide unparalleled evidence for the large-scale imprint of off-craton metasomatism, analogous to the intensively studied samples from the Kaapvaal Craton.

12.6.1.1 Xenolith Types

The young volcanoes and maars of western Victoria are the source of a remarkable variety of mantle xenoliths that show a varied palette of metasomatic effects in peridotitic xenoliths (spinel peridotites and lherzolites), and in abundant pyroxenites that represent frozen intruded basaltic magmas, their cumulates and/or fractionates. These basaltic products have infiltrated the spinel-lherzolite facies of the lithospheric mantle (30–65 km depth range). In many off-craton areas lithospheric thickness ranges up to about 100 km depth, but in E. Australia only a few garnet peridotite samples have been found, and these were derived only from depths of $\leq$65 km. There are two main types of pyroxenites (a garnet pyroxenite suite and a wehrlite suite) representing metasomatic events at different times. The pyroxenites occur as veins and dykes, as discrete xenoliths, and as straight-sided veins or mainly linear contacts in composite xenoliths.

The spinel peridotites are mainly lherzolites, and range from cryptically metasomatised samples to those showing weak to strong modal metasomatism. Modal metasomatism is reflected in the development of volatile-bearing phases such as apatite, amphibole and mica, carbonate, and sulfides, all accompanied by abundant CO_2-rich fluid inclusions (e.g. Andersen et al. 1984). These phases can occur singly or in any combination. Zircon has not been observed in these xenoliths, but has been documented in other basalt-borne xenolith suites (e.g. Zheng et al. 2006, 2008a, b). The modally metasomatised xenoliths show a range of microstuctures and veining relationships (e.g. O'Reilly 1987). Some veined and composite xenoliths show geochemical gradients from the vein contact into the peridotite wall-rock over a scale of up to 20 cm (limited by xenolith size). Similar relationships have been documented from other mantle domains (e.g. Dish Hill, California, USA (Nielson et al. 1993)).

12.6.1.2 The Importance of Apatite

Abundant apatite is widespread in xenoliths from western Victoria and from other Phanerozoic localities (O'Reilly and Griffin 2000) and its abundance in off – craton mantle may be greatly underestimated. It occurs as dispersed polygonal grains or as veins, and may locally comprise up to 10% by volume of the mode. Apatite is especially important for understanding the geochemical budget of the metasomatised mantle. It is the main residence of volatiles such as Cl and F, and is a major site for the REE, U, Th, and Sr. The metasomatic agents that deposited

apatite commonly also crystallised trace-element-rich metasomatic phases such as amphibole and mica (± carbonate), and deposited or enriched the local clinopyroxene. Two types of apatite have been identified: a carbonate-bearing hydroxychlorapatite unique to this petrogenesis, and a hydroxy-fluor apatite. These two types reflect metasomatic agents of different origins.

Apatite is important in terms of heat production and heat flow in the mantle. The measured U and Th contents of mantle apatite average 60 and 200 ppm, respectively. Just 0.5% apatite would dominate heat production in the mantle. Metasomatised mantle may also contain amphibole and mica with K_2O and clinopyroxene with detectable U and Th. In lithospheric mantle with a thickness of 70 km, this type of metasomatism would result in a mantle heat flow contribution of about 12 mWm^{-2}, a significant proportion of the total "normal" mantle heat flow of about 18 mWm^{-2}.

12.6.1.3 Apatite-Amphibole Suite

A very distinctive suite of apatite-amphibole xenoliths occurs globally as fragments, and occurs in abundance as a representative suite at the Kiama locality (New South Wales, Eastern Australia; Wass 1979; Wass et al. 1980; Wass and Rogers 1980; O'Reilly 1987; O'Reilly and Griffin 2000). The xenoliths contain abundant amphibole and apatite, Al-augite (commonly Fe-rich), rare highly altered olivine, magnesian ilmenite, Mg- and Al-rich titanomagnetite, carbonate, rare rutile and sulfides (chalcopyrite, pyrrhotite, pyrite, and pentlandite). Modes range from monomineralic rocks to those showing the complete mineral assemblage, and layering occurs on all scales from <1 to 20 cm (limited by xenolith size).

This suite has been interpreted as fragments of a metasomatised upper-mantle volume veined and infiltrated by a fractionated magma of kimberlitic affinity. It is significant because it has close compositional links with the MARID-suite xenoliths (Sect. 12.6.3 above) found in kimberlites (e.g. Dawson and Smith 1977). It indicates that similar processes and similar fluids can affect cratonic and off-cratonic mantle, although the products are mineralogically distinctive because of the different pressure-temperature regimes.

Analogous xenoliths have been recorded from other alkali basaltic provinces, including the Western Eifel, Germany (Duda and Schmincke 1985), Alaska (Francis 1976; Menzies and Murthy 1980), and numerous other localities summarised by O'Reilly (1987). The global distribution, the ubiquity, and the highly trace-element-enriched nature of the parent melt/fluid phase identifies it as a powerful and widespread metasomatic agent.

12.6.1.4 Multiple Metasomatic Events

Isotopic and trace-element data for the xenolith suite from western Victoria (O'Reilly and Griffin 1988; Griffin et al. 1988) indicate that there have been at

least three distinct metasomatic events. Two of these can be correlated spatially and geochemically with the infiltration of mafic silicate melts that carried varying amounts of dissolved carbonate and sulfide components. Stealth metasomatism is also seen in the introduction of clinopyroxene and/or orthopyroxene (Yaxley et al. 1998).

The oldest recognisable metasomatism in these samples is related to melts now seen as re-equilibrated garnet pyroxenites. These have low εNd and high $^{87}Sr/^{86}Sr$, typical of a component of recycled crust. They are isotopically similar to the amphibole and mica that have been introduced into the mantle wall-rocks. Modelling of the Nd and Sr isotopic data indicates that the equilibration of the garnet-bearing metapyroxenites, and thus probably the metasomatism, occurred at least 300–500 Ma ago. The wehrlitic pyroxenite xenolith suite, in contrast, is a younger event and has Sr and Nd isotopic compositions lying along the Nd-Sr mantle array. They overlap the western Victorian basalts erupted from about 60 Ma ago to the present. The third distinctive metasomatic episode introduced abundant apatite (and possibly a new generation of amphibole and mica) that locally overprinted the previous metasomatic events, leaving an isotopic signature of present-day εSr and $\varepsilon Nd = 0$. Further trace-element work by laser-ablation ICPMS on these samples (Powell et al. 2004) confirmed carbonatitic fluids and silicate melts as the dominant fluid sources.

This pattern of two main end-members of metasomatic agents (carbonatitic and silicate melts) recurs in many off-craton regions (e.g. Powell and O'Reilly 2007; Zheng et al. 2007) and in some of the rare examples of well-studied oceanic mantle regions (e.g. Hauri et al. 1993; Coltorti et al. 1999). Coltorti et al. (1999) devised a simple discrimination diagram based on the ratio La/Yb plotted against Ti/Eu (Fig. 12.20). It clearly shows that both carbonatitic and silicate melts are globally active as metasomatic agents in off-craton mantle.

12.6.2 Mantle Chromatography

Hofmann (1986) suggested that the mantle could function as a chromatographic column, fractionating elements in an infiltrating fluid by exchange with the wall-rocks; this concept was developed in detail by Navon and Stolper (1987). It remained for modern micro-analysis techniques (such as PIXE and LAM-ICPMS), mostly in application to off-craton xenoliths, to produce strong evidence in support of this concept.

The first study of the spatial distribution and residence sites of trace elements in such modally metasomatised xenoliths was carried out by O'Reilly et al. (1991) using *in situ* PIXE techniques. This detailed analysis demonstrated that the metasomatism observed is due to the infiltration of fluids released by the crystallising silicate melts. It also confirmed that mantle metasomatism is an open system process. Thus, the bulk distribution coefficient between the rock and percolating fluid, is determined by the mineral assemblage. The modal composition is

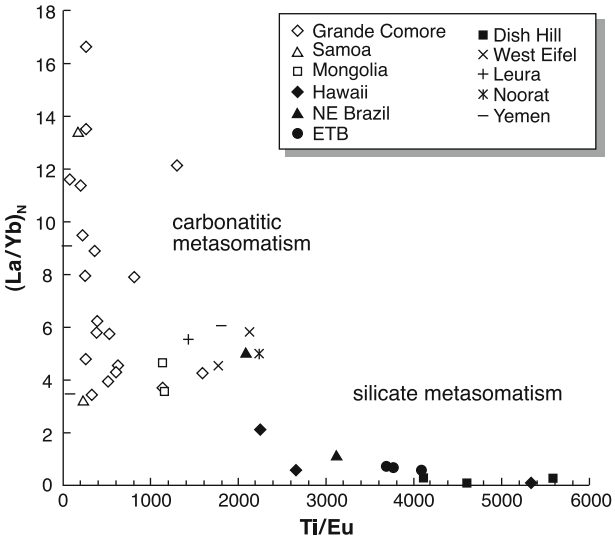

Fig. 12.20 Plot of La/Yb against Ti/Eu in clinopyroxenes from mantle peridotites, showing discrimination of carbonatitic and silicate metasomatism (After Coltorti et al. (1999))

especially crucial where different phases have widely different abilities to accept individual elements. Cryptic metasomatism can only result in trace-element enrichment up to the levels controlled by the K_D value for clinopyroxene/fluid. The presence of high levels of large-ion-lithophile and high-field-strength elements requires modal metasomatism to provide specific, metasomatically introduced, acceptor minerals. In particular, high levels of rare-earth elements, Sr, U, and Th require apatite, high K and Ba requires mica and/or amphibole, and high Nb and Ta require amphibole or mica.

O'Reilly et al. (1991) also presented a model showing progressive changes in wall-rock modal assemblage and trace-element content as a basaltic vein crystallises and expels dissolved fluids. These fluids successively change in composition with distance from the vein, due to exchange reactions and mineral crystallisation (Fig. 12.21). Although other examples may vary in specific mineral assemblage and fluid composition, this process and principle is universal and individual rock volumes may be multiply overprinted through time.

The widespread use of LAM-ICPMS analysis in the last decade has produced many studies of a wide spectrum of trace elements in metasomatised xenoliths from many localities worldwide. Pioneering studies by Xu et al. (2000) and Grégoire et al. (2000a) documented the wide range of trace-element patterns in the minerals of metasomatised mantle xenoliths from eastern China and the Kerguelen Islands (Fig. 12.22), and showed the sensitivity of clinopyroxene trace-element patterns to the chemical nature of the metasomatising agent. These, and the many subsequent studies, emphasise the complexity of mantle fluid processes, and the multiple overprinting (and in some cases, depletion by partial melting) of mantle domains.

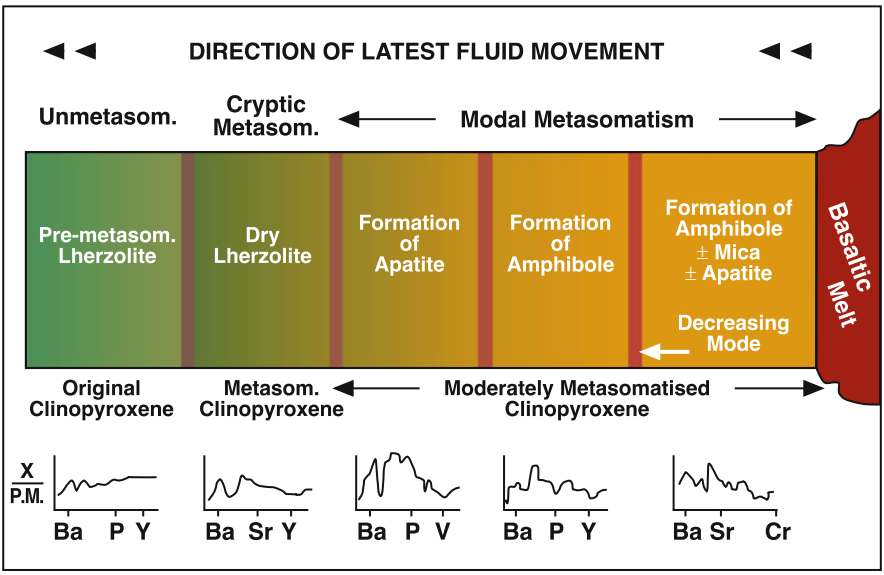

Fig. 12.21 Cartoon illustrating the formation of successive zones of distinctive metasomatic character as fluids are released from silicate melts and interact with adjacent mantle wall-rock, i.e., chromatographic effect of Navon and Stolper (1987). Trace-element patterns are normalised to Primitive Mantle (McDonough and Sun 1995). All source data are given in O'Reilly and Griffin (1988a)

They confirmed the known range of metasomatising agents originally identified petrographically, and provided their geochemical fingerprints.

Moine et al. (2001) showed that the change in the composition of fluids expelled from veins provides a mechanism to separate Ti from the other high-field-strength elements (Nb, Ta, Zr, Hf). Veins in peridotite xenoliths, from the Kerguelen mantle, represent a high degree of crystallisation of highly alkalic basaltic melts, which expelled small volumes of fluids greatly enriched in H_2O compared with the parent melts. Amphiboles in thin veins have significantly lower Ti and higher Nb, Ta, Zr, and Hf contents than those in the thick veins because of the differences in K_D of these HFSE elements in water-poor and water-rich fluids. Powell et al. (2004) also emphasised the significance of a water-rich component as a metasomatising agent enhancing the partitioning of Zr and Hf into clinopyroxene and amphibole relative to REE and LILE. This mechanism can explain the significant positive anomalies for Zr and Hf observed in some metasomatised whole-rock xenoliths.

Vernières et al. (1997) and Bodinier et al. (1990) further refined the chromatographic model and added the complexity (but common reality) that the advective heat from percolating fluids may generate low-degree melt fractions from previously metasomatised peridotites. The infiltrating fluids then can mix with these new melts to produce hybrid metasomatic agents with distinctive effects.

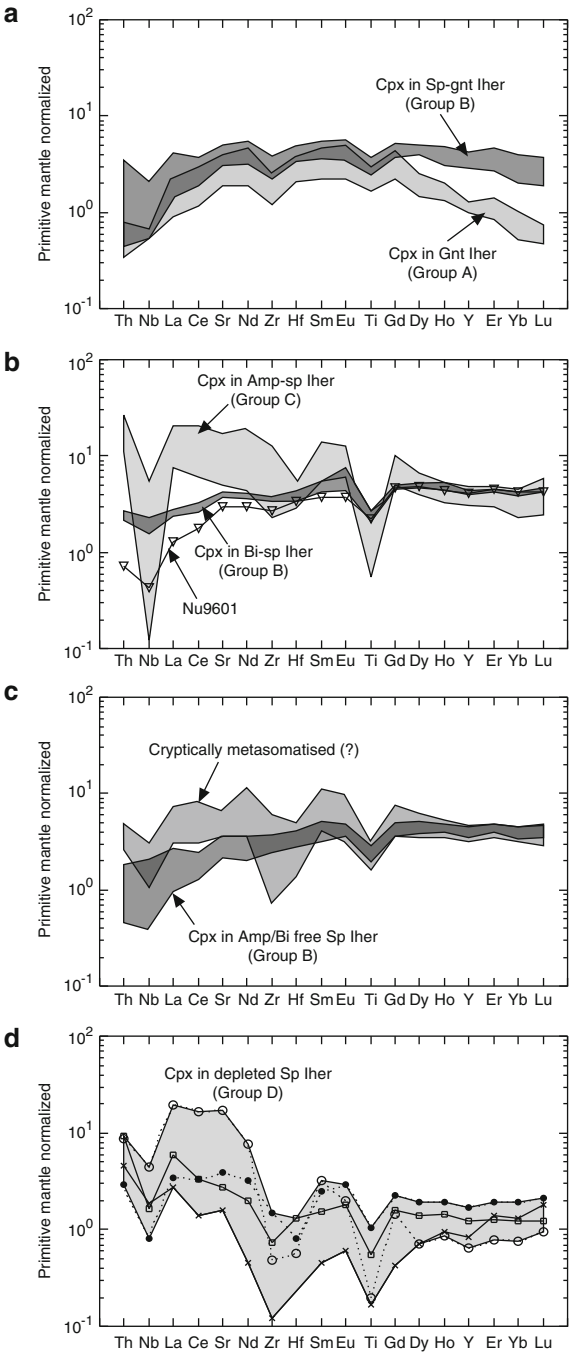

Fig. 12.22 Trace-element patterns of clinopyroxene in spinel peridotite xenoliths from the Nushan volcano, E. China, showing a wide range of LREE enrichment reflecting different styles and degrees of metasomatism (After Xu et al. (2000)).

12.6.3 Oceanic Environments

Metasomatism in the oceanic mantle, including oceanic plateaus, has not been studied as much as that in sub-continental regions. However, most available studies (e.g. Hauri et al. 1993; Coltorti et al. 1999; Grégoire et al. 2000a, b; Kogarko et al. 2001; Moine et al. 2004; Dixon et al. 2008) indicate that, in general, oceanic mantle metasomatism shows a similar compositional range in both the agents and the metasomatic products to those documented for continental off-craton regions.

Metasomatism in the mantle overlying modern subduction zones is even more sparsely characterized. Some recent studies indicate some similarities (e.g. Ishimaru et al. 2007) but also some differences. Differences in amphibole compositions have been recognised between intraplate and subduction-zone mantle (Coltorti et al. 2007). Native metals have been found in some xenoliths from subduction zones (Ishimaru et al. 2009). The style of metasomatism recorded in xenoliths from the subduction-related volcanism on Lihir Island in the island arc region of Papua New Guinea (Grégoire et al. 2001) is unusual. The metasomatic products in the Lihir xenoliths include fibrous orthopyroxene, Fe-Ni sulfides, olivine, clinopyroxene, amphibole, mica and magnetite. The resultant metasomatic fingerprint is enriched in HREE, MREE and LILE although the apparent lack of change in HFSE suggests a significant hydrous component, consistent with inferred slab-melt compositions, and compositional similarities to some metasomatised regions in the continental mantle. However, the appearance of metasomatic orthopyroxene appears to be related to subduction environments. This has been proposed as an explanation for the anomalously high orthopyroxene contents of xenoliths from the Archean SCLM of the Western Terrane of the Kaapvaal Craton. An unusual occurrence of armalcolite (an intermediate member of the ferropseudobrookite ($FeTi_2O_5$–$MgTi_2O_5$) solid solution series that can accommodate significant LILE and HFSE elements) was recorded in the Kerguelen mantle (Grégoire et al. 2000b) and provides a link to the MARID xenolith suite beneath the cratons (e.g. Haggerty 1987).

Bonadiman et al. (2005) described an unusual suite of spinel peridotite xenoliths in basalts on the island of Sal in the Cape Verde Islands off N. Africa. These have the unusually low FeO contents typical of Archean SCLM (Griffin et al. 1999b, 2009), and a style of metasomatism similar to that seen in kimberlite-borne xenoliths from cratonic areas. The authors concluded that these rocks were derived from a fragment of cratonic SCLM embedded in the oceanic lithosphere. This was disputed by Shaw et al. (2006), who regarded the xenolith compositions as the result of alteration by reaction with the host lavas. However, Coltorti et al. (2010) demonstrated that the xenoliths contain sulfide minerals with Archean and Proterozoic Re-Os model ages. O'Reilly et al. (2009) have shown that this part of the Cape Verde archipelago, and other parts of the ocean floor between N. Africa and the Mid-Atlantic Ridge, are underlain by shallow volumes of high-Vs mantle, with the seismic fingerprint of cratonic SCLM. The correlation between the geochemical data and the seismic data makes it probable that these mantle volumes do, in fact,

represent buoyant fragments of the N. Africa SCLM left in the Atlantic basin during its opening, as proposed by Bonadiman et al. (2005). This, in turn, would support the argument that the major-element compositions are Archean in origin, and that the observed metasomatism took place in the SCLM, rather than in the host basalt.

12.6.4 Summary of Off-Craton Mantle Metasomatism and Global Perspective

In summary, fluids ranging from silicate to carbonate magmas and containing varying types and quantities of dissolved fluids, including brines, C-O-H species and S-bearing phases, have actively infiltrated mantle regions throughout the evolution of the off-craton subcontinental and the oceanic mantle. The overall similarity between subduction-related and off-craton intraplate continental mantle metasomatism is predictable, as the sources of metasomatic melts and fluids throughout the evolution of the mantle must have included past subduction environments (e.g. Griffin et al. 1988). These fluids have metasomatically overprinted pre-existing, variably depleted mantle wall-rocks, resulting in a complex, heterogeneous and essentially ubiquitously metasomatised lithospheric mantle that is compositionally variable spatially and temporally. Such repetitive invasions of melts and fluids have produced mantle domains that are variable on all scales from microns to terranes.

However, there is a provinciality of mantle domains on the scale of 10s to 100s of kilometers, that is recognisable in the trace-element and isotopic fingerprints of small-volume magmas, such as alkali basalts, that have passed through such mantle domains before eruption. As these magmas traverse the lithospheric mantle, advective heating causes small volumes of melts enriched in highly incompatible elements to form from the low-melting-point fraction of any previously metasomatised mantle (Sleep 1988; Foley et al. 1999). These mix into the ascending basaltic magmas, imparting distinctive geochemical fingerprints (Leeman 1982; Menzies et al. 1983; Menzies and Wass 1983; Griffin et al. 1988; O'Reilly et al. 1988; Zhang et al. 2001). This process is directly analogous to that observed in the exposed mantle massifs (Bodinier 1988; Bodinier and Godard 2003; Bodinier et al. 2004) and interpreted as examples of reactive porous flow, in which the percolating metasomatic agent mixes with small fractions of partial melts from the previously enriched mantle wall-rock.

The provinciality produced by these processes is well-demonstrated in the natural laboratory of the eastern Australian basaltic provinces, which were extruded mainly from 100 Ma to the present along a strike length of >4,000 km; many carry xenoliths from the underlying mantle (Zhang et al. 2001). Comparisons of the trace-element and isotopic characteristics of the low-volume alkali basalts, and the spatially-related mantle xenoliths, demonstrate a one-to-one correlation of distinctive fingerprints, ranging from those indicating old recycled crust, to young

subduction regimes, to plume signatures. Since the alkali basalts formed as partial melts of asthenospheric mantle, below the lithosphere that they subsequently sampled as xenoliths, this provides evidence of the significant geochemical role played by the contamination of such magmas by low-degree lithospheric melts. These lithospheric melts in turn record ancient to modern geodynamic processes.

12.7 Samples of Metasomatic Fluids

12.7.1 Cratonic Fluids: Information from Diamonds

We have some unique insights into the nature of metasomatic fluids affecting the cratonic SCLM, thanks to the world's desire for diamonds. Depletion of the cratonic SCLM to dunite-harzburgite would have removed any primary C, especially at the relatively high fO_2 described above. The presence of diamonds (or graphite) in the peridotites implies the introduction of C via mantle fluids. Diamonds therefore are themselves a metasomatic phase, and during their growth they may trap micron-scale inclusions of the fluids from which they grew. Gem-quality diamonds contain few such inclusions, but diamonds that show evidence of rapid growth (fibrous diamonds, framesite, boart) may contain up to 1% by volume of syngenetic high-density fluids ± daughter minerals. The small size of the inclusions, coupled with the high strength of the diamond lattice, allows them to survive transport to the surface, providing us with "time capsules" and a window on processes in the deep lithosphere.

Numerous studies of the high-density fluids (HDF) included in fibrous diamonds have defined two compositional arrays, extending between carbonatitic and hydrosilicic or saline-brine "end-members" (Fig. 12.23; see review by Klein-BenDavid et al. 2007). More recently the carbonatitic end-member has been divided into high-Mg and low-Mg varieties (Klein-BenDavid et al. 2009; Weiss et al. 2009). These studies have used EMPA techniques, which analyse the major-element compositions of the fluids. Recent studies of daughter minerals in sub-micron inclusions (e.g. Wirth et al. 2009) have identified a wide range of phases rich in alkali metals, alkaline earths, halogens and water, consistent with crystallisation from extremely concentrated fluids.

Early trace-element data on diamonds came from NAA analysis (Schrauder and Navon 1994; references therein) or isotope-dilution analysis of the residues of burned diamonds (Akagi and Masuda 1988). More recently, LAM-ICPMS techniques have made it possible to quantitatively analyse many elements *in situ* (pits 50–100 mm diameter, 30–50 μm deep; Rege et al. 2005), or to ablate larger volumes for off-line analysis by ICPMS (McNeill et al. 2009). Initial analyses (Rege et al. 2005, 2008) of fibrous diamonds and diamondites (aggregates of fine-grained diamonds) yielded trace-element patterns that are very similar to those of low-degree mantle melts such as kimberlite and carbonatite (Fig. 12.24). Analyses

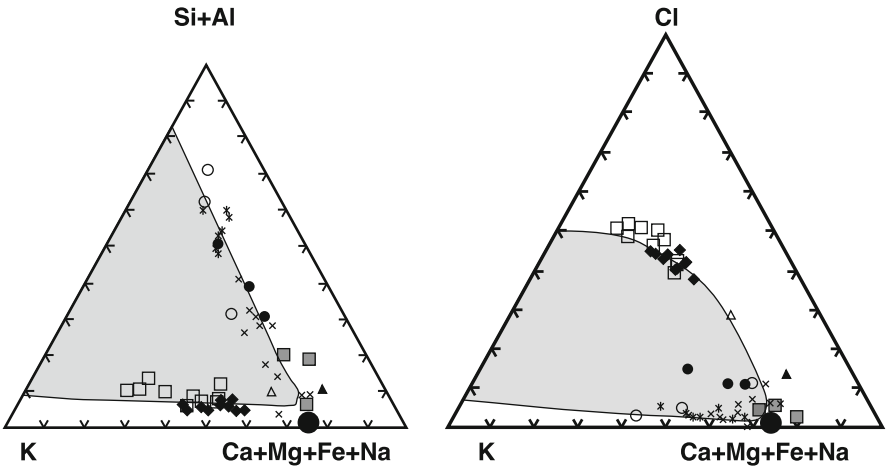

Fig. 12.23 Compositions of fluid inclusions in fibrous diamonds, showing the immiscibility gap between carbonate-silicate mixtures and carbonate-brine mixtures (After Klein-BenDavid et al. (2009)).

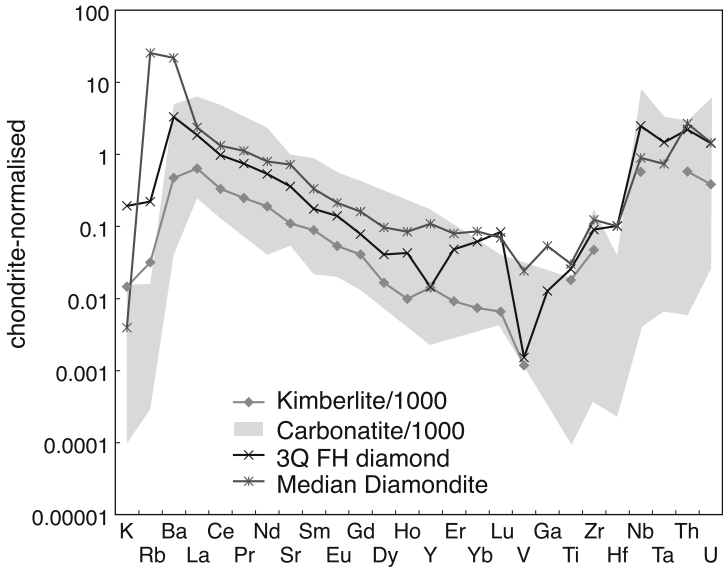

Fig. 12.24 Trace-element patterns of diamondites and fibrous diamonds (3Q HF), compared with those of kimberlites and carbonatites (After Rege et al. (2010)).

of fibrous diamonds in which the fluid inclusions had been studied by EMPA (Weiss et al. 2008, 2009) have shown that the several varieties of HDF have very similar trace-element patterns, despite their large differences in major-element composition.

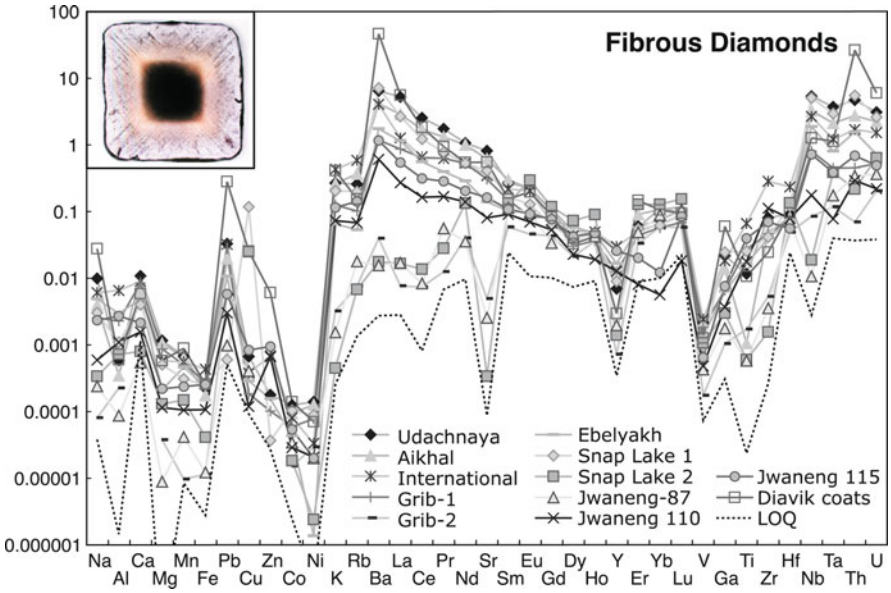

Fig. 12.25 LAM-ICPMS analyses of fibrous diamonds. Inset shows a zoned fibrous diamond from Siberia. Analyses of the inclusion-rich cores of such diamonds show the patterns with extreme LREE enrichment. Analyses of their rims, and of most monocrystalline diamonds, show the LREE-depleted patterns (After Rege et al. (2010))

However, as more analytical data have accumulated on both fibrous and monocrystalline (gem) diamonds, it has become apparent that there are some significant variations in diamond trace-element patterns. Zedgenizov et al. (2007, 2009) and Rege et al. (2010) have described zoned fibrous diamonds from Yakutia in which inclusion-rich cores have LREE-enriched trace-element patterns, like most fibrous diamonds, but the relatively inclusion-poor rims have patterns with strong depletion in LREE, and deep negative anomalies in Sr and Y (Fig. 12.25). The LREE-depleted pattern is also typical of some sub-suites of fibrous diamonds (from the Jwaneng, Grib, and Snap Lake kimberlites; Fig. 12.25) and of most monocrystalline diamonds. On the other end of this spectrum, the fibrous, inclusion-rich coats on diamonds from the Diavik mines in northern Canada are extremely enriched in LREE and Ba, compared to other fibrous diamonds.

The occurrence of these two types of patterns, even within single stones, suggests radical changes in fluid composition during diamond crystallisation. Rege et al. (2010) have argued that these changes reflect the development of immiscibility between a carbonatitic end-member (extremely enriched in LREE $\pm$ Ba, Zr/Hf_{CN} and $Nb/Ta_{CN} > 1$) and a more (hydro) silicic one (depleted in LREE, $Nb/Ta_{CN} < 1$) (see Fig. 12.26a). One implication from this model is that most monocrystalline diamonds have crystallised from the more silicic end-member. The projected carbonatitic end-member is very similar to the fluids required to produce G10 garnets in depleted harzburgites (see above; Fig. 12.26b, c).

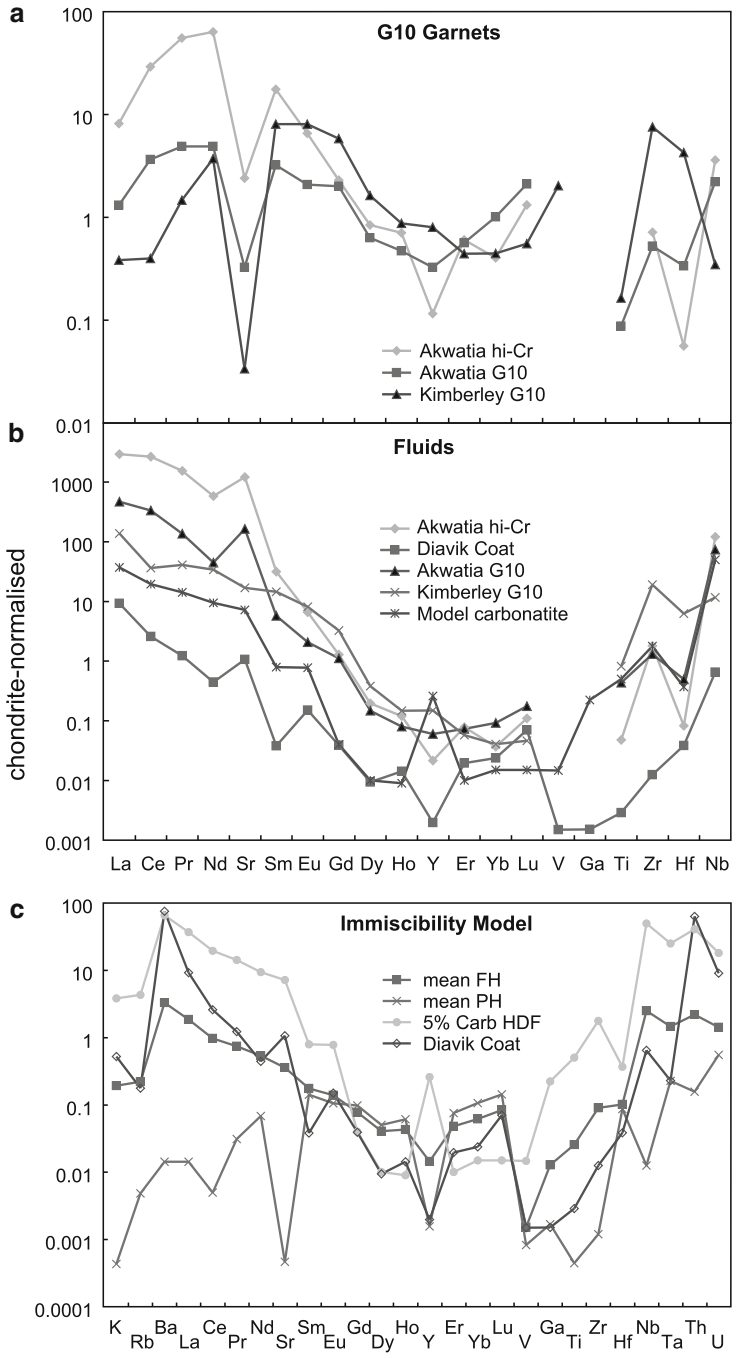

Fig. 12.26 Diamonds, fluids and "G-10" garnets. (**a**) Mean trace-element patterns for some G-10 garnet populations (Data from Stachel and Harris (1997)). (**b**) Fluids in equilibrium with the garnets in a, as well as carbonatites and coats on some Diavik diamonds (Data from Araujo et al. (2009b)). (**c**) Model for generating fluids such as those in (**b**). The fluid precipitating fibrous

12.7.2 Cratonic Fluids: Information from Trapped Melts

Melt inclusions containing carbonate and carbonate-silicate phases have been reported in mantle xenoliths derived from various depths. They have been explained either by entrapment of mantle fluids (Pyle and Haggerty 1994; Schiano et al. 1994; Bali et al. 2002; van Achterbergh et al. 2001, 2004; Rosatelli et al. 2007; Guzmics et al. 2008) or by infiltration of the rising host magma (e.g. Golovin and Sharygin 2007; Golovin et al. 2008; Sharygin et al. 2008). Some carbonate-silicate associations have been interpreted as immiscible pairs formed in the upper mantle (Pyle and Haggerty 1994; Kogarko et al. 2001) or the result of quenching during the ascent of xenoliths in the magma (van Achterbergh et al. 2004; Rosatelli et al. 2007). Melting experiments on carbonated mantle rocks show that such melts can exist in the mantle over a continuous compositional range from carbonatitic to kimberlitic in composition, at varying temperature and pressure (Yaxley et al. 1998; Hammouda 2003; Yaxley and Brey 2004; Dasgupta and Hirschmann 2007; Gudfinnsson and Presnall 2005; Brey et al. 2008). These melts are likely to differentiate during percolation in the mantle through wall-rock interaction, fractionation, and immiscibility.

The A154 kimberlite in the Diavik mine (Slave Craton, Canada) contains xenoliths of megacrystalline lherzolite, found mainly as single crystals (up to >25 cm in diameter) of Cr-diopside with inclusions of garnet, olivine and orthopyroxene. This mineral assemblage yields P-T estimates of 1,200–1,250°C at 60 kb, corresponding to the base of the SCLM in this area (Griffin et al. 1999d; van Achterbergh et al. 2004). Some of the Cr-diopside megacrysts contain abundant rounded inclusions, 0.2–2.5 mm in diameter; microstructures identify them as trapped melts, still liquid at the time of kimberlite eruption (Fig. 12.27). Phenocrysts and spectacular quench crystals of calcite, olivine and mica are set in carbonatitic (50–97% carbonate) to Ca-Mg-silicic (10–50% carbonate) to Mg-silicic (ultramafic, <10% dispersed carbonate) matrices. Within single inclusions, irregular volumes of the carbonatite and the Mg-silicate melts appear to have unmixed from a common predecessor. Calculated bulk compositions of the more silicic melts are similar to those of the host kimberlites (Fig. 12.28). The inclusions appear to have originated as veins of kimberlite-related material, and to have been isolated from one another by recrystallisation and necking-down as the cracks healed, even as immiscibility between carbonate and silicate melts was developing.

This evidence of silicate-carbonatite immiscibility echoes the suggestion of immiscibility derived from the analysis of diamonds, and there is still another connection to diamonds. The Cr-diopside adjacent to the melt inclusions is enriched in LREE, Ba, alkali elements, HFSE, Th, and U, apparently by fluids escaping from

Fig. 12.26 (continued) diamonds (mean FH) evolves to the point where it separates into two immiscible fluids. One (95%) is hydro-silicic and has a pattern similar to most peridotitic diamonds (mean PH) and the other (5%) is a carbonatitic HDF, with a pattern similar to the coats on Diavik diamonds (After Rege et al. (2010)).

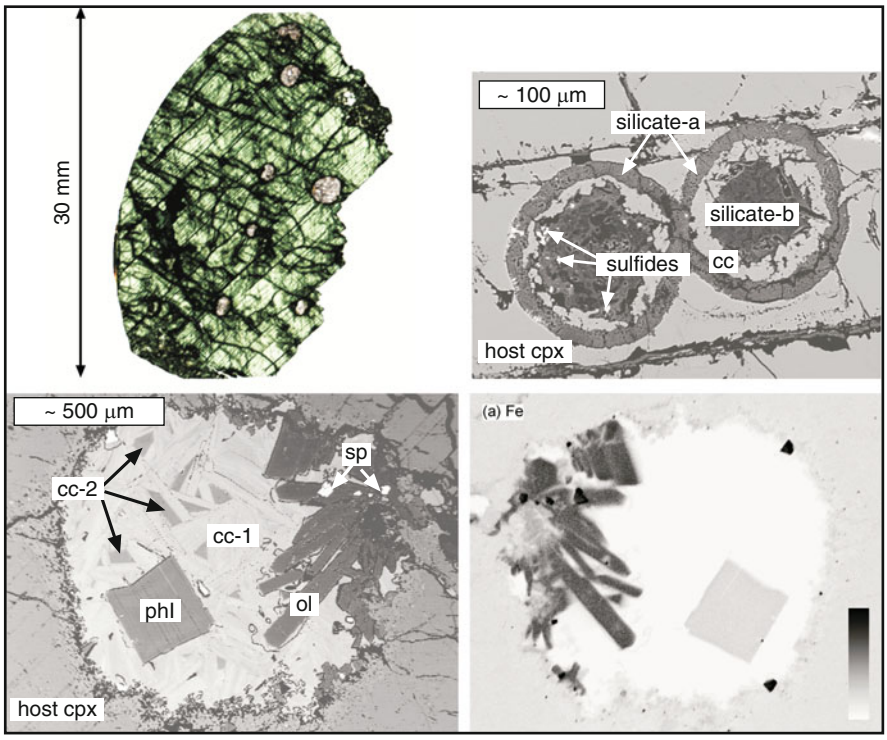

Fig. 12.27 Inclusions of carbonatitic and silicic melts trapped in the Cr-diopside of megacrystalline lherzolite xenoliths from the A154 kimberlite, Slave Craton, Canada. Quench crystals of a Sr-rich carbonate and olivine show that these inclusions were molten at the time of kimberlite eruption, but that the melts had penetrated the pyroxene long enough before the eruption that the pyroxene was able to partially recrystallise and trap the melt inclusions. The lower two frames are mirror images at the same scale (After van Achterbergh et al. (2004)).

the trapped melts. The compositions of these fluids, calculated using experimentally-derived clinopyroxene/fluid partition coefficients, are strongly enriched in the incompatible elements relative to the trapped melts, and are essentially identical to fluids trapped in the opaque coats found on many Diavik diamonds.

12.7.3 Fluid Samples in Off-Craton Xenoliths

The metasomatised mantle samples from western Victoria (Sect. 12.6.1) include rock types that may contain up to 3 vol% of *fluids* trapped at high pressure (O'Reilly 1987). The fluid-filled cavities range from fluid inclusions (1–100 μm across) to vugs up to 1.5 cm across which may be lined with high-pressure phases (e.g. Andersen et al. 1984). As discussed above, the larger cavities form an integral

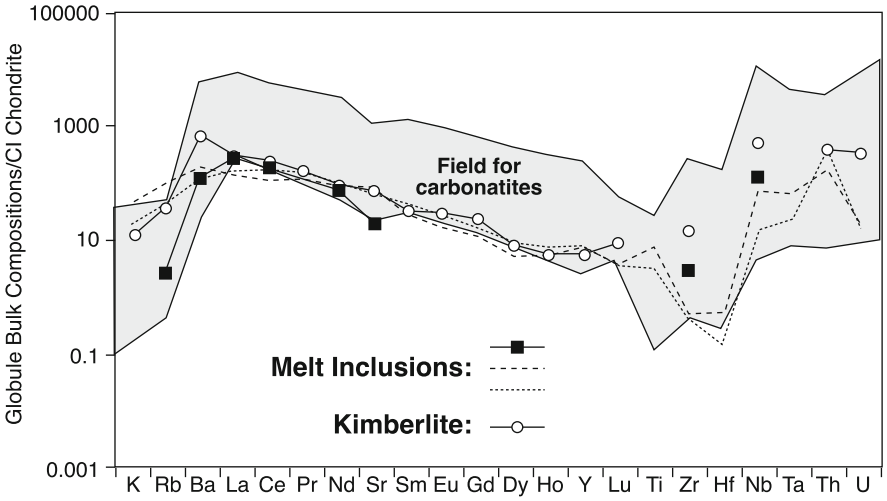

Fig. 12.28 Bulk compositions of melt inclusions trapped in Cr-diopside (see Fig 12.27), showing that the more silicic melts are similar in composition to kimberlites (After Araujo et al. (2009a). The carbonatite field is from Nelson et al. (1988) and Kogarko et al. (2001) and kimberlite composition is from Graham et al. (1999))

part of the granoblastic microstructure (Fig. 12.6). Microthermometry and Raman laser microprobe analysis show that the relict fluids are dominantly CO_2. However, OH-, CO_2-, and Cl-bearing phases lining the walls of fluid inclusions and cavities are inferred to have formed by reaction, implying the presence of up to 15% H_2O and small amounts of Cl in the fluids (Andersen et al. 1984). Mass spectrometric analyses (O'Reilly et al. 1990) showed the presence of small quantities of He, COS, SO_2, N_2, O_2, Ar, H_2S, and hydrocarbons. The $^3He/^4He$ ratios are 7–10 times atmospheric. Matsumoto et al. (1998) showed $^{20}Ne/^{22}Ne$ and $^{21}Ne/^{22}Ne$ ratios are linearly correlated and plot on the well-established MORB-line, $^{40}Ar/^{36}Ar$ ratios are relatively high and excesses in ^{129}Xe and ^{136}Xe, with respect to atmospheric Xe, are correlated. In addition, ^3He to ^{22}Ne ratios are close to those of a solar component, reinforcing the view that the Earth contains primordial He and Ne of solar composition.

Some xenolith samples (pyroxenite veins and adjacent peridotites) contain abundant metasomatic sulfides (Andersen et al. 1987), commonly in several generations. These sulfides clearly were trapped as melts (Fig. 12.29). They are the major hosts for Pt-group elements, and allow Re-Os dating of metasomatic events (see Sect. 12.3).

12.7.4 Summary and a Cartoon Model

The observations from xenoliths and diamonds suggest that the deeper parts of the cratonic SCLM may be locally or periodically awash with highly mobile

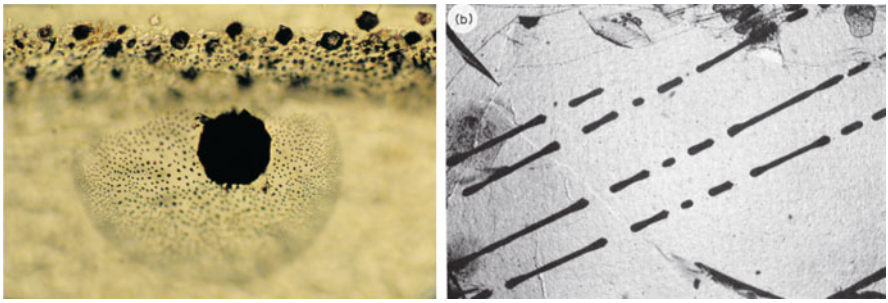

Fig. 12.29 Photomicrographs of inclusions of sulfide melts, trapped in pyroxene from pyroxenite xenoliths from SE Australia. *Left panel* shows a single large inclusion that has expanded and fractured the pyroxene, sending molten sulfide and CO_2 into the crack, which has recrystallised to trap a swarm of microinclusions. *Right panel* shows sulfide melts that originally were trapped as elongate hollow rods filled with liquid CO_2, and then necked down to hollow spheres (After Andersen et al. (1987))

low-volume melts in the kimberlite-carbonatite spectrum (e.g. Rudnick et al. 1993). These melts might be generated by low-degree partial melting, induced by mild thermal pulses and/or delivery of fluids from crystallising magmas (e.g. eclogites) near the base of the SCLM. Immiscibility can develop within such melts, leading to more end-member types of compositions. These may in turn exsolve fluids, perhaps giving rise to the whole spectrum of high density fluids found as inclusions in diamonds.

Detailed studies in peridotite massifs (e.g. Lherz; Le Roux et al. 2007, 2009) show that fronts of cryptic metasomatism, induced by fluids, may move faster than the front of stealth or modal metasomatism, induced by the melts from which the fluids separated. Malkovets et al. (2007) presented a cartoon-model (Fig. 12.30) illustrating how this sort of evolution could explain some of the correlations between metasomatic signatures in cratonic xenoliths and the genesis (and destruction) of diamonds. The inevitable overprinting of early fluid metasomatism by subsequent melt metasomatism, and the overprinting of one metasomatic event by later ones, helps to explain the extraordinary complexity of geochemical signatures in the cratonic SCLM. It also should serve as a caution against the interpretation of any given SCLM composition, except perhaps the most depleted, as representing a "primary" composition on which models might be built.

12.8 Scale and Distribution of Metasomatic Domains and Geodynamic Significance

Metasomatism affects not only the geochemical characteristics of the lithospheric mantle, but also its physical parameters. Geophysical techniques can be used, in some cases, to evaluate the size and distribution of metasomatised domains in the mantle.

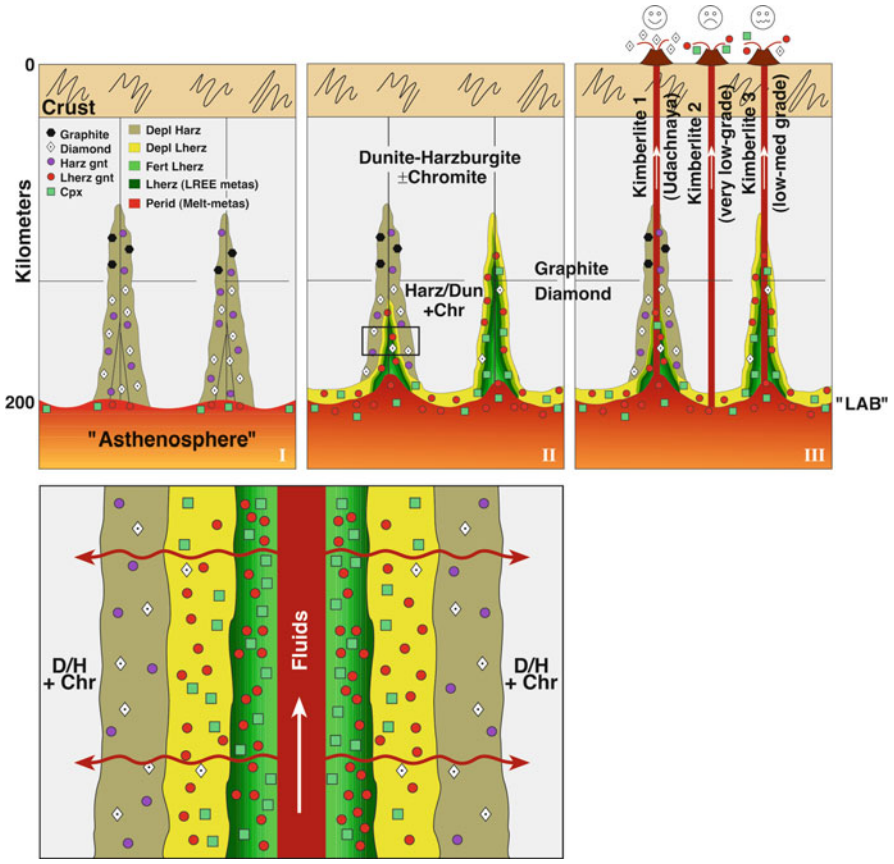

Fig. 12.30 Cartoon illustrating a model for the early stages of cratonic metasomatism (After Malkovets et al. (2007)). (I) Primitive Archean SCLM, consisting of relatively oxidised harzburgite/dunite, is metasomatised by Si-bearing CH_4-rich fluids brought in by low-degree melts from the underlying "asthenosphere". Precipitation of diamond/graphite ± harzburgitic garnet near fluid conduits. Melt-related metasomatism near the lithosphere-asthenosphere boundary (LAB) converts some harzburgites to lherzolite by addition of Ca, Fe, and Al. (II) Continued input of melts/fluids. Reduced harzburgite does not precipitate diamond/graphite. Melt-related metasomatism refertilises harzburgite to lherzolite at the base of the lithosphere and along conduits (weakly in *left* conduit, more extensively in *right* conduit). Relict harzburgitic diamonds in lherzolites. (III) Kimberlite eruption; *high-grade* pipes sample remnants of Stage-A modified mantle. Barren pipes sample least-metasomatised mantle and lack both harzburgitic garnets and diamonds. Some *low-grade* pipes sample highly metasomatised mantle with relict diamonds. The *lower panel* shows a detail of the melt conduit and the progressive metasomatism of the wall rocks, first by CH_4-rich fluids expelled from the melts, and then by the melts themselves. *Dun* dunite, *Harz* harzburgite, *Lherz* lherzolite, *Fert* (re)-fertilised, *Perid* peridotite, *Cpx* clinopyroxene, *Gnt* garnet, *Chr* chromite, *LREE* light rare earth elements, *metas* metasomatised.

12.8.1 Geophysical Signatures of Metasomatism

12.8.1.1 Density, Seismic Response and Rheology

Primitive Archean lithospheric mantle is highly magnesian and has a relatively low density (~3.31 g/cm^3) compared to fertile mantle (~3.37 g/cm^3). The particular elastic properties of olivine are such that magnesian compositions, though less dense, have higher seismic velocities than denser, more Fe-rich compositions (Anderson 1989). Such contrasts in seismic response become measurable if metasomatised regions are on the scale of tens to hundreds of kilometers. Geophysical modellers commonly interpret lateral variations in seismic velocity in terms of temperature variations, but up to 20% of the observed range in S-wave velocity at depths of 100–175 km in the continental mantle can be attributed to compositional differences (e.g. Deen et al. 2006).

Coherence analysis of the relationship between Bouguer gravity (a reflection of lithospheric density) and surface topography can be used to determine the Effective Elastic Thickness (T*e*) of the lithosphere, a measure of mantle rheology. Regional studies where xenolith data help to define the mantle composition show that tectonothermally younger, more fertile SCLM has a lower T*e* than older, more depleted SCLM (Poudjom Djomani et al. 1999). On a smaller scale, strong gradients in T*e* correlate well with zones of kimberlite intrusion and metasomatised mantle, and with inferred translithospheric faults and sutures (Poudjom Djomani et al. 2003, 2005). These observations suggest that metasomatic refertilisation of the cratonic SCLM not only increases its density, but strongly affects its rheology.

12.8.1.2 Thermal Effects

There are two main thermal effects of mantle metasomatism. *The first* is the simple advective movement of heat caused by the hotter metasomatising fluids penetrating upward through mantle. These transfer heat along their mantle pathways until thermal equilibration causes "heat death" (Spera 1984) as a result of geochemical transfer (cryptic metasomatism) and/or crystallisation (modal or stealth metasomatism). Intrusion of magmas into the lithospheric mantle can significantly raise the geothermal gradient, giving a transient heat pulse and producing a "kinked" geotherm (Fig. 12.10). *The second* effect is the influx of heat-producing elements (K, U, Th) that accompanies some types of metasomatic enrichment. The heat produced by radioactive decay of these elements could raise the local heat flow by 50–70% compared to the normal reduced mantle heat flow (e.g. O'Reilly and Griffin 2000).

12.8.1.3 Electrical Effects

The origins of electromagnetic responses in the lithospheric mantle have not yet been satisfactorily identified (see Chap. 13). Geophysical interpretations have commonly invoked interconnecting graphite films (Jones et al. 2001) but there is no supporting evidence for this from petrographic studies of xenolith suites. A recent global 3-D model of Earth's electrical conductivity (Kelbert et al. 2009) reveals significant spatial variations, especially in the transition zone (410–670 km depth). High values correlate with domains of high seismic velocity where subducted slabs have ponded at, or penetrated through, the transition zone and are interpreted as reflecting high water contents. However, an anomalously high-conductivity domain beneath the Slave Craton, Canada, (Jones et al. 2001) coincides with mantle rock types (sampled as xenoliths in kimberlites) that are very refractory and dry. Magnetotelluric data along a geophysical traverse across China and Siberia (Yuan 1996) have identified a highly conductive region that correlates with the seismic low-velocity zone immediately below the lithosphere. It is interpreted as indicating the presence of ubiquitous low-volume melts at the top of the asthenosphere. Interconnecting carbonate films (Gaillard et al. 2008) are also highly conductive. Experiments have shown that carbonatite melts in olivine aggregates have low intergranular energies and thus can wet grain boundaries in mantle rocks. The key to understanding the electromagnetic signals in the mantle lies in unravelling the nature of fluids and their distribution and thus is closely connected with a full understanding of metasomatic processes and fluid movement in the mantle.

12.8.2 Size and Distribution of Metasomatic Domains: The Kaapvaal Example

Most of our information about the cratonic SCLM is derived from xenoliths and xenocrysts in kimberlites – but how representative is the sample? As discussed above, the movement of large volumes of fluid through the SCLM requires crack propagation, which will tend to follow earlier lines of weakness (old sutures, translithospheric faults) where available. Zones, once metasomatised, are likely to be the loci of fluid movement during subsequent episodes. The refertilisation process will result in lower seismic velocities in the metasomatised zones, and this will be amplified where significant K-U-Th have been added, raising the local heat production. These effects allow a broad-scale analysis of the distribution of metasomatised *vs* relict parts of the SCLM, where high-resolution data are available. An excellent example is given by the images from the Kaapvaal Seismic project (Fouch et al. 2004; James et al. 2001 and references therein).

Figure 12.31 shows the distribution of shear-wave velocity (Vs) along a NE-SW traverse across South Africa at 200 km depth. In this image, high velocities are shown in red to white tones, and low velocities in blue to black tones. A

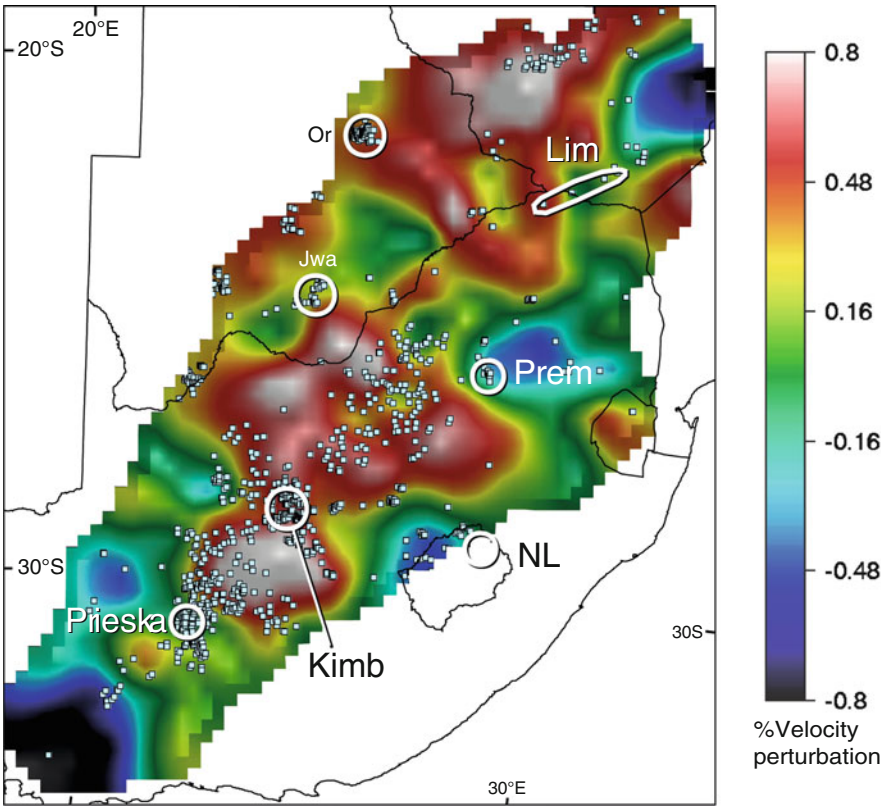

Fig. 12.31 Detailed Vs tomography along a 1,000-km traverse at 200 km depth across the SW part of the Kalahari craton of southern Africa (Begg et al. 2009), with locations of kimberlites (Faure 2006). *Circles* and *oval mark* locations of well-studied xenolith and xenocryst suites. *Lim* Limpopo Belt, *Prem* Premier (Cullinan) Mine, *NL* northern Lesotho, *Kimb* Kimberley area, *Or* Orapa area, *Jwa* Jwaneng area, Prieska area lies across the craton margin. These suites clearly do not sample the highest-velocity (most depleted) parts of the SCLM root

major low-velocity area underlies the Bushveld layered intrusion, suggesting that the mantle has been intensively refertilised. This is consistent with xenolith evidence that this mantle volume has an unusually high Fe content (Hoal 2004). The other low-velocity volumes form an anastomosing network enclosing blobs of high-velocity material, interpreted as relict depleted dunite/harzburgite (Deen et al. 2006; Griffin et al. 2009; Begg et al. 2009).

The kimberlite intrusions are concentrated in the low-Vs areas, and generally avoid the high-Vs volumes. This suggests that the kimberlites (low-volume melts) are following the same paths used by earlier generations of metasomatising fluids. It also implies that the kimberlites (and especially those from which most xenolith data are derived) have sampled the most strongly metasomatised parts of the cratonic root, and their suites of entrained xenoliths thus give a biased picture of mantle composition (Bell et al. 2005; Griffin et al. 2009).

12.9 Concluding Observations

The metasomatised lithospheric mantle is a palimpsest, recording the multiple fluid events that have affected that domain since it formed. Reading this complex record and tracking specific episodes and processes is a key to reconstructing lithosphere evolution through time, and also the nature of the volatile flux from the deep Earth over time. Understanding mantle metasomatism requires understanding processes at different time scales over the 4.5 billion years since the Earth formed, and length scales ranging from nano- to global (from fluid pathways and geochemical gradients at all scales, to planetary scale convection and fluid movement).

Early work in mantle metasomatism laid an impressive foundation of accurate and meticulous observation of mineral and rock-type relationships, followed by electron microprobe geochemical data that showed the spatial relationships of compositional variations within and between mineral grains. Experimental studies have significantly enhanced our understanding of metasomatic processes and their pressure-temperature conditions. The technology explosion since the electron microprobe became a widespread tool has enabled *in situ* analysis of trace elements and a range of isotopic systems, as well as a range of imaging and spectroscopic techniques that can analyse volatile phases and define the microstructures of metasomatised mantle rocks.

Future progress in understanding mantle metasomatism, and its significance in shaping the Earth system, will stem from advances in dating mantle processes, improved characterisation of their redox conditions, and the current new wave of isotopic methodologies, including analysis of stable metal isotopes and other new isotopic systems, as well as the ability to analyse elements at increasingly lower abundances. Coupling these geochemical groundtruths with new geodynamic modelling using mineral physics for exploring nanoscale fluid flow mechanisms and interpreting the physical-property data (seismic, magnetotelluric) at large scales will bring a new dimension. However, detailed observations based on field, hand-specimen, and petrographic work must remain a key part of any such studies.

Acknowledgments The concepts and data presented in this review have evolved over several decades through collaborations with many valued colleagues and students, most of whom appear as authors and coauthors on the articles cited here. We would especially like to acknowledge Chris Ryan, whose development of the PIXE geoanalytical techniques provided geochemists with their first tool for rapid, quantitative in situ microanalysis of trace elements, and Norman Pearson, who over these years has developed many of the other *in situ* microanalysis techniques that now are pushing geochemical research into the future. He also has contributed greatly to the conceptual advances in understanding metasomatic processes that stemmed from the application of these geochemical techniques. The draft manuscript was improved by thoughtful reviews from Michel Gregoire and Hilary Downes and the editorial work of Daniel Harlov and Håkon Austrheim. This is publication 780 from the GEMOC National Key Centre (www.GEMOC.mq.edu.au), and publication 5 from the ARC Centre of Excellence for Core to Crust Fluid Systems (www.CCFS.mq.edu.au).

Glossary

This list gives definitions of terms commonly encountered in discussions of mantle metasomatism; some of these terms are used differently in other types of geochemical and mantle studies.

Asthenosphere The convecting portion of the Earth's mantle; source of most mafic to ultramafic magmas, and reduced C-O-H fluids.

Depleted In the context of mantle metasomatism, *depleted* refers to rocks that are depleted in basaltic components – principally the major elements such as Ca, Al, Fe, and Ti. Depleted peridotites and their constituent minerals are highly magnesian; olivine typically is $Fo_{93–95}$. Such compositions are also referred to as *refractory* because of their inferred origin as residues from the partial melting of more fertile primitive mantle.

Enriched In the context of mantle metasomatism, *enriched* refers to the addition of trace elements such as Sr, Ba, Zr, and rare-earth elements (REE) which can be highly mobile in the mantle rock-fluid systems. Mantle rocks that are *depleted* (as defined by major element compositions), can also be *enriched* if they have undergone cryptic metasomatism.

Fertile Refers to peridotites (typically lherzolites) with relatively high contents of basaltic components including major elements such as Ca, Al, Fe, and Ti and which also have significant trace-element abundances (but not necessarily as high as those for *enriched* compositions). Olivine is typically in the range $Fo_{86–90}$. These rocks can represent cooled asthenosphere under regions of tectonic thinning or rifting, or originally depleted lithospheric mantle compositions that have been refertilised by metasomatism.

Fluid A volatile phase that would not form a rock on cooling or crystallisation. Mantle fluids include C-O-H phases such as H_2O, CO_2, CH_4, and brines (high-density fluids, or HDF). At mantle pressures, such phases exist in the mantle in the liquid rather than vapour state.

Lithosphere The upper non-convecting part of the Earth, including the crust and the underlying subcontinental lithospheric mantle (SCLM).

Mantle Throughout this Chapter the term "mantle" refers to "lithospheric mantle" unless otherwise specified.

Melt A fluid phase that could form a rock on crystallisation. Mantle melts form a spectrum of compositions with overlaps and transitions. Low-degree melts range from carbonatite to kimberlite. High-degree melts range from basalt (sensu lato) to komatiite. Mantle carbonate and silicate melts can transport fluids and sulfide melts as dissolved components that become immiscible on fractionation and cooling.

References

Afonso JC, Fernandez M, Ranalli G, Griffin WL, Connolly JAD (2008) Integrated geophysical-petrological modeling of the lithosphere and sublithospheric upper mantle: methodology and applications. Geochem Geophys Geosyst. doi:10.1029/2007GC001834

Akagi T, Masuda A (1988) Isotopic and chemical evidence for a relationship between kimberlite and Zaire cubic diamonds. Nature 336:665–667

Alard O, Griffin WL, Lorand JP, Jackson SE, O'Reilly SY (2000) Non-chondritic distribution of the highly siderophile elements in mantle sulfides. Nature 407:891–894

Alard O, Griffin WL, Pearson NJ, Lorand J-P, O'Reilly SY (2002) New insights into the Re-Os systematics of subcontinental lithospheric mantle from in-situ analysis of sulfides. Earth Planet Sci Lett 203:651–663

Amundsen HEF, Griffin WL, O'Reilly SY (1987) The lower crust and upper mantle beneath northwestern Spitsbergen: evidence from xenoliths and geophysics. Tectonophysics 139: 169–185

Andersen T, O'Reilly SY, Griffin WL (1984) The trapped fluid phase in the upper mantle xenoliths from Victoria. Contrib Mineral Petrol 88:72–85

Andersen T, Griffin WL, O'Reilly SY (1987) Primary sulphide melt inclusions in mantle-derived megacrysts and pyroxenites. Lithos 20:279–294

Anderson DL (1989) Theory of the Earth. Blackwell Scientific, Boston

Aoki KI (1974) Phlogopites and potassic richterites from mica nodules in South African kimberlites. Contrib Mineral Petrol 48:1–7

Araujo DP, Griffin WL, O'Reilly SY (2009a) Mantle melts, metasomatism and diamond formation: insights from melt inclusions in xenoliths from Diavik, Slave Craton. Lithos 112(Suppl 2):675–682

Araujo DP, Griffin WL, O'Reilly SY, Grant KJ, Ireland T, Holden P, van Achterberg E (2009b) Microinclusions in monocrystalline octahedral diamonds and coated diamonds from Diavik, Slave Craton: clues to diamond genesis. Lithos 112 (Suppl 2):724–735

Bali E, Czabo C, Vaselli O, Tørøk K (2002) Significance of silicate melt pockets in upper mantle xenoliths from the Bakony-Balaton Highland Volcanic Field, Western Hungary. Lithos 61:79–102

Banas A, Stachel T, Phillips D, Shimizu N, Viljoen KS, Harris JW (2009) Ancient metasomatism recorded by ultra-depleted garnet inclusions in diamonds from DeBeers Pool, South Africa. Lithos 112 (Suppl 2):736–746

Begg GC, Griffin WL, Natapov LM, O'Reilly SY, Grand SP, O'Neill CJ, Hronsky JMA, Poudjom Djomani Y, Swain CJ, Deen T, Bowden P (2009) The lithospheric architecture of Africa: Seismic tomography, mantle petrology and tectonic evolution. Geosphere 5:23–50

Bell DR, Gregoire M, Grove TL, Chatterjee N, Carlson RW, Buseck PR (2005) Silica and volatile-element metasomatism of Archean mantle: a xenolith-scale example from the Kaapvaal Craton. Contrib Mineral Petrol 150:251–267

Beyer EE, Brueckner HK, Griffin WL, O'Reilly SY, Graham S (2004) Archean mantle fragments in Proterozoic crust, Western Gneiss Region, Norway. Geology 32:609–612

Beyer EE, Griffin WL, O'Reilly SY (2006) Transformation of Archean lithospheric mantle by refertilisation: evidence from exposed peridotites in the Western Gneiss Region, Norway. J Petrol 47:1611–1636

Bodinier JL (1988) Geochemistry and petrogenesis of the Lanzo peridotite body, western Alps. Tectonophysics 149:67–88

Bodinier JL, Godard M (2003) Orogenic ophiolitic and abyssal peridotites. In: Carlson RW (ed) Treatise on geochemistry – the mantle and core. Elsevier, New York, pp 103–170

Bodinier JL, Vasseur G, Vernieres J, Dupuy CF (1990) Mechanisms of mantle metasomatism: geochemical evidence from the lherz orogenic peridotite. J Petrol 31:597–628

Bodinier JL, Menzies MA, Shimizu N, Frey FA, McPherson E (2004) Silicate, hydrous and carbonate metasomatism at Lherz, France: contemporaneous derivatives of silicate melt-harzburgite reaction. J Petrol 45:299–320

Bonadiman CL, Beccaluva L, Coltorti M, Siena F (2005) Kimberlite-like metasomatism and 'garnet signature' in spinel-peridotite xenoliths from Sal, Cape Verde archipelago: relics of a subcontinental mantle domain within the Atlantic Oceanic lithosphere? J Petrol 46:2465–2493
Boyd FR (1989) Compositional distinction between oceanic and cratonic lithosphere. Earth Planet Sci Lett 96:15–26
Boyd FR, Mertzman SA (1987) Composition and structure of the Kaapvaal lithosphere, southern Africa. In: Mysen BO (ed) Magmatic processes: physicochemical principles, vol 1, The Geochemical Society, Special Publication. Geochemical Society, University Park
Boyd FR, Nixon PH (1973) Origin of the ilmenite-siicate nodules in kimberlites from Lesotho and South Africa. In: Nixon PH (ed) Lesotho kimberlites. Lesotho National Development Corporation, Maseru
Brey GP, Bulatov VK, Girnis AV, Lahaye Y (2008) Experimental melting of carbonated peridotite at 6–10 GPa. J Petrol 49:797–821
Brueckner HK, Carswell DA, Griffin WL, Medaris LG Jr, van Roermund HLM, Cuthbert SJ (2010) The mantle and crustal evolution of two garnet peridotite suites from the Western Gneiss Region, Norwegian Caledonides. Lithos 117:1–19
Canil D (2002) Vanadium in peridotites, mantle redox and tectonic environments: Archean to present. Earth Planet Sci Lett 195:75–90
Canil D (2004) Mildly incompatible elements in peridotites and the origins of mantle lithosphere. Lithos 77:375–393
Chen YD, O'Reilly SY, Griffin WL, Krogh TE (1998) Combined U-Pb dating and Sm-Nd studies on lower crustal and mantle xenoliths from the Delegate Basaltic Pipes, Southeastern Australia. Contrib Mineral Petrol 130:154–161
Choukroun M, O'Reilly SY, Griffin WL, Pearson NJ, Dawson JB (2005) Hf isotopes of MARID rutile trace metasomatic processes in the lithospheric mantle. Geology 33:45–48
Coltorti M, Bonadiman C, Hinton RW, Siena F, Upton BGJ (1999) Carbonatite metasomatism of the oceanic upper mantle: evidence from clinopyroxenes and glasses in ultramafic xenoliths of Grande Comore, Indian Ocean. J Petrol 40:133–165
Coltorti M, Bonadiman C, Faccini B, Gregoire M, O'Reilly SY, Powell W (2007) Discrimination of suprasubduction and intraplate amphiboles from mantle xenoliths in alkaline and calc-alkaline magmas: implications for Nb and Ti anomalies and slab recycling. Lithos 92:68–84
Coltorti M, Bonadiman C, O'Reilly SY, Griffin WL, Pearson NJ (2010) Buoyant ancient continental mantle embedded in oceanic lithosphere (Sal island, Cape Verde Archipelago). Lithos 120:222–233
Condie KC, Cox JC, O'Reilly SY, Griffin WL, Kerrich R (2004) Distribution of high field strength and rare earth elements in mantle and lower crustal xenoliths from the southwestern United States: the role of grain-boundary phases. Geochim Cosmochim Acta 68:3919–3942
Dasgupta R, Hirschmann MM (2007) A modified iterative sandwich method for determination of near-solidus partial melt compositions. II. Application to determination of near-solidus melt compositions of carbonated peridotite. Contrib Mineral Petrol 154:647–661
Dawson JB (1984) Contrasting types of upper mantle metasomatism. In: Kornprobst J (ed) Kimberlites II: the mantle and crust-mantle relationships. Elsevier, Amsterdam
Dawson JB, Smith JV (1977) The MARID (mica-amphibole-rutile-ilmenite-diopside) suite of xenoliths in kimberlites. Geochim Cosmochim Acta 41:309–323
Dawson JB, Stephens WE (1975) Statistical classification of garnets from kimberlite and associated xenoliths. J Geol 83:589–607
Deen T, Griffin WL, Begg G, O'Reilly SY, Natapov LM (2006) Thermal and compositional structure of the subcontinental lithospheric mantle: derivation from shear-wave seismic tomography. Geochem Geophys Geosyst. doi:10.1029/2005GC001164
Dixon J, Clague DA, Cousens B, Monsalve ML, Uhl J (2008) Carbonatite and silicate melt metasomatism of the mantle surrounding the Hawaiian plume: evidence from volatiles, trace elements, and radiogenic isotopes in rejuvenated-stage lavas from Niihau, Hawaii. Geochem Geophys Geosyst. doi:10.1029/2008GC002076

Downes H (2007) Origin and significance of spinel and garnet pyroxenites in the shallow lithospheric mantle: ultramafic massifs in orogenic belts in Western Europe and NW Africa. Lithos 99:1–24

Downes H, Dupuy C (1987) Textural, isotopic and REE variations in spinel peridotite xenoliths, Massif Central, France. Earth Planet Sci Lett 82:121–135

Downes H, Reichow MK, Mason PR, Beard AD, Thirlwall MF (2003) Mantle domains in the lithosphere beneath the French Massif Central: trace element and isotopic evidence from mantle clinopyroxenes. Chem Geol 200:71–87

Duda A, Schmincke H-U (1985) Polybaric differentiation of alkali basaltic magmas: evidence from green-core clinopyroxene (Eifel. FRG). Contrib Mineral Petrol 91:340–353

Erlank AJ, Waters FG, Hawkesworth CJ, Haggerty SE, Allsopp HL, Rickard RS, Menzies M (1987) Evidence for mantle metasomatism in peridotite nodules from the Kimberley pipes, South Africa. In: Menzies M, Hawkesworth CJ (eds) Mantle metasomatism. Academic, London

Faure S (2006) World kimberlites database version 2006–2. Montreal, Que. Consortium de Recherche en Exploration Minerale CONSOREM, Universite du Quebec a Montreal. www.consorem.ca

Foley SF, Musselwhite DS, Van Der Laan SR (1999) Melt compositions from ultramafic vein assemblages in the lithospheric mantle: a comparison of cratonic and non-cratonic settings. In: Gurney JJ, Gurney JL, Pascoe MD, Richardson SH (eds) Proceedings of the 7th international kimberlite conference. Red Roof Design, Cape Town

Fouch MJ, James DE, VanDecar JC, van der Lee S, The Kaapvaal Seismic Group (2004) Mantle seismic structure beneath the Kaapvaal and Zimbabwe Cratons. S Afr J Geol 107:33–44

Francis DM (1976) Amphibole pyoxenite xenoliths cumulate or replacement phenomena from the upper mantle, Nunivak Island, Alaska. Contrib Mineral Petrol 58:51–61

Frey FA, Green DH (1974) The mineralogy, geochemistry and origin of lherzolite inclusions in Victorian basanites. Geochim Cosmochim Acta 38:1023–1059

Frey FA, Prinz M (1978) Ultramafic inclusions from San Carlos, Arizona: petrologic and geochemical data bearing on their petrogenesis. Earth Planet Sci Lett 38:129–176

Gaillard F, Malki M, Iacono-Marziano G, Pichavant M, Scaillet B (2008) Carbonatite melts and electrical conductivity in the asthenosphere. Science 322:1363–1365

Gaul OF, Griffin WL, O'Reilly SY, Pearson NJ (2000) Mapping olivine composition in the lithospheric mantle. Earth Planet Sci Lett 182:223–235

Goldschmidt VM (1922) On the metasomatic processes in silicate rocks. Econ Geol 17:105–123

Golovin AV, Sharygin VV (2007) Petrogenetic analysis of fluid and melt inclusions in minerals from mantle xenoliths from the Bele pipe basanites (North Minusa depression). Russ Geol Geophys 48:811–824

Golovin A, Sharygin I, Korsakov A, Kamenetsky V, Pokhilenko N (2008) Alkali- and Cl-enriched carbonate–silicate melt inclusions in sheared lherzolite xenoliths from unaltered kimberlites of the Udachnaya-East pipe (Yakutia). In: Abstract 9th international kimberlite conference, Frankfurt

Graham I, Burgess JL, Bryan D, Ravenscoft PJ, Thomas E, Doyle BJ, Hopkins R, Armstrong K (1999) Exploration history and geology of the diavik kimberlites, Lac de Gras, Northwest Territories, Canada. In: Gurney JJ, Gurney JL, Pascoe MD, Richardson SH (eds) Proceedings of the 7th international kimberlite conference. Red Roof Design, Cape Town

Greau Y, Huang J-X, Griffin WL, Renac C, Alard O, O'Reilly SY (2011) Type I eclogites from Roberts Victor Kimberlites: products of extensive mantle metasomatism. Geochim Cosmochim Acta 75:6927–6954

Grégoire M, Moine BN, O'Reilly SY, Cottin JY, Giret A (2000a) Trace element residence and partitioning in mantle xenoliths metasomatized by highly alkaline, silicate- and carbonate-rich melts (Kerguelen Islands, Indian Ocean). J Petrol 41:477–509

Grégoire M, Lorand JP, O'Reilly SY, Cottin JY (2000b) Armalcolite-bearing, Ti-rich metasomatic assemblages in harzburgitic xenoliths from the Kerguelen Islands: implications for the oceanic mantle budget of high-field strength elements. Geochim Cosmochim Acta 64:673–694

Grégoire M, McInnes BIA, O'Reilly SY (2001) Hydrous metasomatism of oceanic sub-arc mantle, Lihir, Papua New Guinea Part 2. Trace element characteristics of slab-derived fluids. Lithos 59:91–108

Grégoire M, Bell DR, Le Roex AP (2002) Trace element geochemistry of phlogopite-rich mafic mantle xenoliths: their classification and their relationship to phlogopite-bearing peridotites and kimberlites revisited. Contrib Mineral Petrol 142:603–625

Grégoire M, Bell DR, Le Roex AP (2003) Garnet lherzolites from the Kaapvaal Craton (South Africa): trace element evidence for a metasomatic history. J Petrol 44:629–657

Griffin WL, Ryan CG (1995) Trace elements in indicator minerals: area selection and target evaluation in diamond exploration. J Geochem Explor 53:311–337

Griffin WL, O'Reilly SY (2007) Cratonic lithospheric mantle: is anything subducted? Episodes 30:43–53

Griffin WL, Wass SY, Hollis JD (1984) Ultramafic xenoliths from Bullenmerri and Gnotuk maars, Victoria, Australia: petrology of a subcontinental crust-mantle transition. J Petrol 25:53–87

Griffin WL, O'Reilly SY, Stabel A (1988) Mantle metasomatism beneath western Victoria, Australia: II. Isotopic geochemistry of Cr-diopside lherzolites and Al-augite pyroxenites. Geochim Cosmochim Acta 52:449–459

Griffin WL, Ryan CG, Cousens DC, Sie SH, Suter GF (1989) Ni in Cr-pyrope garnets: a new geothermometer. Contrib Mineral Petrol 103:199–202

Griffin WL, Smith D, Ryan CG, O'Reilly SY, Win TT (1996) Trace element zoning in mantle minerals: metasomatism and thermal events in the upper mantle. Can Mineral 34:1179–1193

Griffin WL, Zhang A, O'Reilly SY, Ryan CG (1998a) Phanerozoic evolution of the lithosphere beneath the Sino-Korean Craton. In: Flower M, Chung SL, Lo CH, Lee TY (eds) Mantle dynamics and plate interactions in East Asia, vol 27, Geodynamics. American Geophysical Union, Washington, DC

Griffin WL, O'Reilly SY, Ryan CG, Gaul O, Ionov D (1998b) Secular variation in the composition of subcontinental lithospheric mantle. In: Braun J, Dooley JC, Goleby BR, van der Hilst RD, Klootwijk CT (eds) Structure and evolution of the Australian Continent, vol 26, Geodynamics. American Geophysical Union, Washington, DC

Griffin WL, Shee SR, Ryan CG, Win TT, Wyatt BA (1999a) Harzburgite to lherzolite and back again: metasomatic processes in ultramafic xenoliths from the Wesselton kimberlite, Kimberley, South Africa. Contrib Mineral Petrol 134:232–250

Griffin WL, O'Reilly SY, Ryan CG (1999b) The composition and origin of subcontinental lithospheric mantle. In: Fei Y, Bertka CM, Mysen BO (eds) Mantle petrology: field observations and high-pressure experimentation: a tribute to Francis R. (Joe) Boyd, vol 6, Geochemical Society Special Publication. Geochemical Society, Houston

Griffin WL, Fisher NI, Friedman JH, Ryan CG, O'Reilly SY (1999c) Cr-pyrope garnets in the lithospheric mantle. I. Compositional systematics and relations to tectonic setting. J Petrol 40:679–704

Griffin WL, Doyle BJ, Ryan CG, Pearson NJ, O'Reilly SY, Natapov L, Kivi K, Kretschmar U, Ward J (1999d). Lithosphere structure and mantle terranes: slave Craton, Canada. In: Proceedings of the 7th international kimberlite conference. Red Roof Design, Cape Town

Griffin WL, Fisher NI, Friedman JH, O'Reilly SY, Ryan CG (2002) Cr-pyrope garnets in the lithospheric mantle. II. Compositional populations and their distribution in time and space. Geochem Geophys Geosyst 3:1073

Griffin WL, O'Reilly SY, Natapov LM, Ryan CG (2003) The evolution of lithospheric mantle beneath the Kalahari Craton and its margins. Lithos 71:215–241

Griffin WL, Graham S, O'Reilly SY, Pearson NJ (2004) Lithosphere evolution beneath the Kaapvaal Craton. Re-Os systematics of sulfides in mantle-derived peridotites. Chem Geol 208:89–118

Griffin WL, O'Reilly SY, Afonso JC, Begg G (2009) The composition and evolution of lithospheric mantle: a re-evaluation and its tectonic implications. J Petrol 50:1185–1204

Gudfinnsson GH, Presnall DC (2005) Continuous gradations among primary carbonatitic, kimberlitic, melilititic, basaltic, picritic, and komatiitic melts in equilibrium with garnet lherzolite at 3–8 GPa. J Petrol 46:1645–1659

Guzmics T, Zajacz K, Kodolánul JZ, Halter WE, Szabo C (2008) LA-ICP-MS study of apatite- and K feldspar-hosted primary carbonatite melt inclusions in clinopyroxenite xenoliths from lamprophyres, Hungary: implications for significance of carbonatite melts in the Earth's mantle. Geochim Cosmochim Acta 72:1864–1886

Haggerty SE (1987) Metasomatic mineral titanates in upper mantle xenoliths. In: Nixon PH (ed) Mantle xenoliths. Wiley, Chicago

Hammouda T (2003) High-pressure melting of carbonated eclogite and experimental constraints on carbon recycling and storage in the mantle. Earth Planet Sci Lett 214:357–368

Harte B (1983) Mantle peridotites and processes: the kimberlite sample. In: Hawkesworth CJ, Norry MJ (eds) Continental basalts and their xenoliths. Shiva, Nantwich

Harte B, Hunter RH, Kinny PD (1993) Melt geometry, movement and crystallization, in relation to mantle dykes, veins and metasomatism. Philos Trans R Soc Lond A342:1–21

Hauri EH, Shimizu N, Dieu JJ, Hart SR (1993) Evidence for hotspot-related carbonatite metasomatism in the oceanic upper mantle. Nature 365:221–227

Hoal K (2004) Samples of Proterozoic iron-enriched mantle from the Premier kimberlite. Lithos 71:259–272

Hofmann A (1986) Nb in Hawaiian magmas: constraints on source composition and evolution. Chem Geol 57:17–30

Huang JX, Griffin WL, Greau Y, O'Reilly SY (2011) Seeking the primary compositions of mantle xenoliths: isotopic and elemental consequences of sequential leaching treatments on an eclogite suite. Chem Geol (submitted, 3/2011)

Ishimaru S, Arai S, Ishida Y, Shirasaka M, Okrugin VM (2007) Melting and multi-stage metasomatism in the mantle wedge beneath a frontal arc inferred from highly depleted peridotite xenoliths from the Avacha Volcano, Southern Kamchatka. J Petrol 48:395–433

Ishimaru S, Arai S, Shukuno H (2009) Metal-saturated peridotite in the mantle wedge inferred from metal-bearing peridotite xenoliths from Avacha volcano, Kamchatka. Earth Planet Sci Lett 284:352–360

Jacob DE (2004) Nature and origin of eclogite xenoliths. Lithos 77:295–316

James DE, Fouch MJ, Van Decar JC, van der Lee S, Kaapvaal Seismic Group (2001) Tectospheric structure beneath southern Africa. Geophys Res Lett 28:2485–2488

Jones AG, Ferguson IJ, Chave AD, Evans RL, McNeice GW (2001) Electric lithosphere of the slave craton. Geology 29:423–426

Kelemen PB, Hart SR, Bernstein S (1998) Silica enrichment in the continental lithosphere via melt/rock reaction. Earth Planet Sci Lett 164:387–406

Kelbert A, Schultz A, Egbert G (2009) Global electromagnetic induction constraints on transition-zone water content variations. Nature 460:1003–1006

Klein-BenDavid O, Izraeli ES, Hauri E, Navon O (2007) Fluid inclusions in diamonds from the Diavik mine, Canada and the evolution of diamond-forming fluids. Geochim Cosmochim Acta 71:243–253

Klein-BenDavid O, Logvinova AM, Schrauder M, Spetius ZV, Weiss Y, Hauri E, Kaminsky FV, Sobolev NV, Navon O (2009) High-Mg carbonatitic microinclusions in some Yakutian diamonds: a new type of diamond-forming fluid. Lithos 112(Suppl 2):648–659

Kogarko LN, Kurat G, Ntaflos T (2001) Carbonate metasomatism of the oceanic mantle beneath Fernando de Noronha Island, Brazil. Contrib Mineral Petrol 140:577–587

Konzett J, Armstrong RA, Gunther D (2000) Modal metasomatism in the Kaapvaal craton lithosphere: constraints on timing and genesis from U-Pb zircon dating of metasomatised peridotites and MARID-type xenoliths. Contrib Mineral Petrol 139:704–719

Korzhinski DS (1936) Mobility and inertness of components in metasomatism. Izv Akad Nauk SSSR Ser Geol 1:58–60
Lee CT, Brandon AD, Norman M (2003) Vanadium in peridotites as a proxy for paleo-fO2 during partial melting: prospects, limitations and implications. Geochim Cosmochim Acta 67:3045–3064
Leeman WP (1982) Tectonic and magmatic significance of strontium isotopic variations in Cenozoic volcanic rocks from the western United States. Geol Soc Am Bull 93:487–503
Le Roux V, Bodinier JL, Thomassi A, Alard O, Dautria JM, Vauchez A, Riches AJV (2007) The Lherz spinel lherzolite: refertilised rather than pristine mantle. Earth Planet Sci Lett 259:599–612
Le Roux V, Bodinier JL, Alard O, O'Reilly SY, Griffin WL (2009) Isotopic decoupling of Hf, Nd and Sr during porous melt flow: a case study in the Lherz peridotites (Pyrenees). Earth Planet Sci Lett 29:76–85
Lloyd FE, Bailey DK (1973) Light element metasomatism of the continental mantle: the evidence and the consequences. Phys Chem Earth 9:389–416
McCammon CA, Griffin WL, Shee SR, O'Neill HSC (2001) Oxidation during metasomatism in ultramafic xenoliths from the Wesselton kimberlite, South Africa. Contrib Mineral Petrol 141:287–296
McDonough WF, Sun SS (1995) The composition of the Earth. Chem Geol 120:223–253
McNeill JCR, Klein-BenDavid O, Nowell GM, Pearson DG, Ottley CJ (2009) Quantitative analysis of trace element concentrations in some gem-quality diamonds. J Phys Condens Matter 21:1–13
Malkovets VG, Griffin WL, O'Reilly SY, Wood BJ (2007) Diamond, subcalcic garnet and mantle metasomatism: kimberlite sampling patterns define the link. Geology 35:339–342
Matsumoto T, Honda M, McDougall I, O'Reilly SY (1998) Noble gases in anhydrous lherzolites from the Newer Volcanics, southeastern Australia: a MORB-like reservoir in the subcontinental mantle. Geochim Cosmochim Acta 62:2521–2533
Medaris LG, Brueckner HK (2003) Excursion to the Almklovdalen peridotite. In: Carswell DA (ed) Guidebook to the field excursions in the Nordfjord–Stadlandet–Almklovdalen area. Norges Geologiske Undersøkelse, Trondheim
Menzies M, Murthy VR (1980) Nd and Sr isotope geochemistry of hydrous mantle nodules and their host and their host alkali basalts: implications for local heterogeneities in metasomatically veined mantle. Earth Planet Sci Lett 46:323–324
Menzies MA, Leeman WP, Hawkesworth CJ (1983) Isotope geochemistry of Cenozoic volcanic rocks reveals mantle heterogeneity below western USA. Nature 303:205–209
Menzies M, Wass SY (1983) CO_2-rich mantle below eastern Australia: rare earth element, Sr and Nd isotopic study of Cenozoic alkaline magmas and apatite-rich xenoliths, Southern Highlands Province, New South Wales, Australia. Earth Planet Sci Lett 65:287–302
Mercier JC (1979) Peridotites, xenoliths and the dynamics of kimberlite intrusion. In: Boyd FJ, Meyer HOA (eds) The mantle sample: inclusions in kimberlites and other volcanics. In: Proceedings of the 2nd international kimberlite conference. American Geophysical Union, Washington, DC
Moine BM, Gregoire M, O'Reilly SY, Sheppard SMF, Cottin JY (2001) High field strength element fractionation in the upper mantle: evidence from amphibole-rich composite mantle xenoliths from the Kerguelen Islands (Indian Ocean). J Petrol 42:2145–2167
Moine BM, Gregoire M, O'Reilly SY, Delpech G, Sheppard SMF, Lorand JP, Renac C, Giret A, Cottin JY (2004) Carbonatite melt in oceanic upper mantle beneath the Kerguelen Plateau. Lithos 75:239–252
Navon O, Stolper E (1987) Geochemical consequences of melt percolation: the upper mantle as a chromatographic column. J Geol 95:285–307
Nelson DR, Chivas AR, Chappell B, McCulloch MT (1988) Geochemical and isotopic systematics in carbonatites and implications for the evolution of ocean-island sources. Geochim Cosmochim Acta 52:1–17

Nielson JE, Budahn JR, Unruh DM, Wilshire HG (1993) Actualistic models of mantle metasomatism documented in a composite xenolith from Dish Hill, California. Geochimica Cosmochimica Acta 57:105–121

Nixon PH (1987) Mantle xenoliths. Wiley, Chichester

Niu Y (1997) Mantle melting and melt extraction processes beneath ocean ridges: evidence from abyssal peridotites. J Petrol 38:1047–1074

O'Reilly SY (1987) Volatile-rich mantle beneath Eastern Australia. In: Nixon PH (ed) Mantle xenoliths. Wiley, Chichester

O'Reilly SY, Griffin WL (1988) Mantle metasomatism beneath western Victoria, Australia, I: metasomatic processes in Cr-diopside lherzolites. Geochim Cosmochim Acta 52:433–447

O'Reilly SY, Griffin WL (2000) Apatite in the mantle: implications for metasomatic processes and high heat production in Phanerozoic mantle. Lithos 53:217–232

O'Reilly SY, Griffin WL (2006) Imaging chemical and thermal heterogeneity in the subcontinental lithospheric mantle with garnets and xenoliths: geophysical implications. Tectonophysics 416:289–309

O'Reilly SY, Griffin WL (2010a) The continental lithosphere-asthenosphere boundary: can we sample it? Lithos 102:1–13

O'Reilly SY, Griffin WL (2010b) Rates of magma ascent: constraints from mantle-derived xenoliths. In: Dosseto A, Turner S, Van Orman J (eds) Timescales of magmatic processes: from core to atmosphere. Blackwell , Chichester

O'Reilly SY, Griffin WL, Stabel A (1988) Evolution of Phanerozoic eastern Australian lithosphere: isotope evidence for magmatic and tectonic underplating. J Petrol, Special vol: 89–108

O'Reilly SY, Griffin WL, Segelstad TV (1990) The nature and role of fluids in the upper mantle: evidence in xenoliths from Victoria, Australia. In: Herbert HK, Ho SE (eds) Conference on stable isotopes and fluid processes in mineralisation. Geology Department and University Extension, The University of Western Australia, Perth

O'Reilly SY, Griffin WL, Ryan CG (1991) Residence of trace elements in metasomatized spinel lherzolite xenoliths: a proton-microprobe study. Contrib Mineral Petrol 109:98–113

O'Reilly SY, Zhang M, Griffin WL, Begg G, Hronsky J (2009) Ultradeep continental roots and their oceanic remnants: a solution to the geochemical "crustal reservoir" problem? Lithos 112:1043–1054

Pearson NJ, Alard O, Griffin WL, Jackson SE, O'Reilly SY (2002) In situ measurement of Re-Os isotopes in mantle sulfides by laser ablation multi-collector inductively-coupled mass spectrometry: analytical methods and preliminary results. Geochim Cosmochim Acta 66:1037–1050

Poudjom Djomani YH, Fairhead JD, Griffin WL (1999) The flexural rigidity of Fennoscandia: reflection of the tectonothermal age of the lithospheric mantle. Earth Planet Sci Lett 174:139–154

Poudjom Djomani Y, Griffin WL, O'Reilly SY, Natapov L, Erinchek Y, Hronsky J (2003) Upper mantle structure beneath Eastern Siberia? Evidence from gravity modelling and mantle petrology. Geochem Geophys Geosyst 4:1–21

Poudjom Djomani Y, Griffin WL, O'Reilly SY, Natapov L, Pearson NJ, Doyle BJ (2005) Variations of the effective elastic thickness (Te) and structure of the lithosphere beneath the Slave Province, Canada. Aust Soc Explor Geophys 35:266–271

Powell W, Zhang M, O'Reilly SY, Tiepolo M (2004) Mantle amphibole trace-element and isotopic signatures trace multiple mantle metasomatic episodes in lithospheric mantle, western Victoria, Australia. Lithos 75:141–171

Powell W, O'Reilly SY (2007) Sulfide mobility in mantle fluids beneath eastern Australia: implications for metasomatic processes and mantle Re-Os chronology. Lithos 94:132–147

Pyle JM, Haggerty SE (1994) Silicate-carbonate liquid immiscibility in upper-mantle eclogites: implications for natrosilicic and carbonatitic conjugate melts. Contrib Mineral Petrol 58:2997–3011

Rege S, Jackson SJ, Griffin WL, Davies RM, Pearson NJ, O'Reilly SY (2005) Quantitative trace element analysis of diamond by laser ablation inductively coupled plasma mass spectrometry. J Anal Atom Spectrom 20:601–610

Rege S, Griffin WL, Kurat G, Jackson SE, Pearson NJ, O'Reilly SY (2008) Trace element chemistry of diamondites: crystallisation of diamond from kimberlite-carbonatite melts. Lithos 106:39–54

Rege S, Griffin WL, Pearson NJ, Araujo D, Zedgenizov D, O'Reilly SY (2010) Trace-element patterns of fibrous and monocrystalline diamonds: insights into mantle fluids. Lithos 118:313–337

Reisberg L, Lorand JP (1995) Longevity of subcontinental mantle lithosphere from osmiuym isotope systematics in orogenic peridottite massifs. Nature 376:159–162

Roden MF, Frey FA, Francis DM (1984) An example of consequent mantle metasomatism in peridotite inclusions from Nunivak Island, Alaska. J Petrol 25:546–577

Roedder E (1984) Fluid inclusions. Rev Mineral 12:3–10

Rosatelli G, Stoppa F, Jones AP (2007) Intrusive calcite-carbonatite occurrence from Mt Vulture volcano, southern Italy. Mineral Mag 64:615–624

Rudnick RL, McDonough WF, Chappell BW (1993) Carbonatite metasomatism in the northern Tanzanian mantle: petrographic and geochemical characteristics. Earth Planet Sci Lett 114:463–475

Ryan CG, Griffin WL, Pearson NJ (1996) Garnet Geotherms: a technique for derivation of P-T data from Cr-pyrope garnets. J Geophys Res 101:5611–5625

Schiano P, Clocchiatti R, Shimizu N, Weis D, Mattielli N (1994) Cogenetic silica-rich and carbonate-rich melts trapped in mantle minerals in Kerguelen ultramafic xenoliths: implications for metasomatism in the oceanic upper mantle. Earth Planet Sci Lett 123:167–178

Schrauder M, Navon O (1994) Hydrous and carbonatitic mantle fluids in fibrous diamonds from Jwaneng, Botswana. Geochim Cosmochim Acta 58:761–771

Schulze DJ (1995) Low-Ca garnet harzburgites from Kimberly, South Africa: abundance and bearing on the structure and evolution of the lithosphere. J Geophys Res 100:12513–12526

Sharygin IS, Golovin AV, Pokhilenko NP (2008) Melt pockets in sheared garnet lherzolite xenoliths from the Udachnaya-Eastern kimberlite pipe (Yakutia, Russia). In: Abstracts 9th international kimberlite conference, Frankfurt

Shaw CSJ, Heidelachm F, Dingwell DB (2006) The origin of reaction textures in mantle peridotite xenoliths from Sal Island, Cape Verde: the case for "metasomatism" by the host lava. Contrib Mineral Petrol 151:681–697

Skjelkvåle BL, Amundsen HEF, O'Reilly SY, Griffin WL, Gjelsvik T (1989) A primitive alkali basaltic stratovolcano and associated eruptive centres, NW Spitsbergen: volcanology, origin and tectonic significance. J Volcanol Geoth Res 37:1–19

Sleep NH (1988) Tapping of melt by veins and dikes. J Geophys Res 93:10255–10272

Smith D, Boyd FR (1987) Compositional heterogeneities in a high-temperature lherzolite nodule and implications for mantle processes. In: Nixon PH (ed) Mantle xenoliths. Wiley, New York

Smith D, Griffin WL (2005) Navajo garnetites and rock-water interactions in the mantle below the Colorado Plateau, Southwestern United States. J Petrol 46:1901–1924

Smith D, Griffin WL, Ryan CG, Cousens DR, Sie SH, Suter GF (1991) Trace-element zoning of garnets from The Thumb: a guide to mantle processes. Contrib Mineral Petrol 107:60–79

Smith D, Griffin WL, Ryan CG (1993) Compositional evolution of high-temperature sheared lherzolite PHN1611. Geochim Cosmochim Acta 57:605–613

Spera FJ (1984) Carbon dioxide in petrogenesis III: role of volatiles in the ascent of alkaline magma with special reference to xenolith-bearing mafic lavas. Contrib Mineral Petrol 88:217–232

Stachel T, Harris JW (1997) Diamond precipitation and mantle metasomatism – evidence from the trace element chemistry of silicate inclusions in diamonds from Akwatia, Ghana. Contrib Mineral Petrol 129:143–154

Stosch HG, Seck HA (1980) Geochemistry and mineralogy of two spinel peridotite suites from Dreiser Weiher, West Germany. Geochim Cosmochim Acta 44:457–470

Streckeisen A (1979) Classification and nomenclature of volcanic rocks, lamprophyres, carbonatites, and melilitic rocks: recommendations and suggestions of the IUGS Subcommission on the systematics of igneous rocks. Geology 7:331–335

Sweeney RJ, Thompson AB, Ulmer P (1993) Phase relations of a natural MARID composition and implications for MARID genesis, lithospheric melting and mantle metasomatism. Contrib Mineral Petrol 115:225–241

Taylor WR, Green DH (1988) Measurement of reduced peridotite-C-O-H solidus and implications for redox melting of the mantle. Nature 332:349–352

Van Achterbergh E, Griffin WL, Stiefenhofer J (2001) Metasomatism in mantle xenoliths from the Letlhakane kimberlites: estimation of element fluxes. Contrib Mineral Petrol 141:397–414

Van Achterbergh E, Griffin WL, O'Reilly SY, Ryan CG, Pearson NJ, Kivi K, Doyle BJ (2004) Melt inclusions from the deep Slave lithosphere: implications for the origin and evolution of mantle-derived carbonatite and kimberlite. Lithos 76:461–474

Van Orman JA, Grove TL, Shimizu N (2001) Rare earth element diffusion in diopside: influence of temperature, pressure and ionic radius, and an elastic model for diffusion in silicates. Contrib Mineral Petrol 141:687–703

Van Orman JA, Grove TL, Shimizu N, Layne GD (2002) Rare earth element diffusion in a natural pyrope single crystal at 2.8 GPa. Contrib Mineral Petrol 142:416–424

Vernières J, Godard M, Bodinier JL (1997) A plate model for the simulation of trace element fractionation during partial melting and magma transport in the earth's upper mantle. J Geophys Res 102:24771–24784

Wass SY (1979) Fractional crystallization in the mantle of late-stage kimberlite liquids – evidence in xenoliths from the Kiama area, NSW, Australia. In: Boyd FR, Meyer HOA (eds) The mantle sample: inclusions in kimberlites and other volcanics. Proceedings of the 2nd international kimberlite conference, vol 2. American Geophysical Union, Washington, DC

Wass SY, Rogers N (1980) Mantle metasomatism by kimberlitic/carbonatitic fluids – precursor to continental alkali volcanism. Geochim Cosmochim Acta 144:1811–1823

Wass SY, Henderson P, Elliott C (1980) Chemical heterogeneity and metasomatism in the upper mantle – evidence from rare earth and other elements in apatite-rich xenoliths in basaltic rocks from eastern Australia. Philos Trans R Soc Lond A297:333–346

Waters FG, Erlank AJ (1988) Assessment of the vertical extent and distribution of mantle metasomatism below Kimberley, South Africa. J Petrol, Special vol: 185–204

Watson EB, Brenan JM (1987) Fluids in the lithosphere, 1. Experimentally-determined wetting characteristics of CO_2-H_2O fluids and their implications for fluid transport, host-rock physical properties and fluid inclusion formation. Earth Planet Sci Lett 85:497–515

Watson EB, Brenan JM, Baker DR (1990) Distribution of fluids in the mantle. In: Menzies MA (ed) Continental mantle. Clarendon, Oxford, UK

Weiss Y, Griffin WL, Elhlou S, Navon O (2008) Comparison between LA-ICP-MS and EPMA analysis of trace elements in diamond. Chem Geol 252:158–168

Weiss Y, Kessel R, Griffin WL, Kiflawi I, Klein-BenDavid O, Bell DR, Harris J, Navon O (2009) A new model for the evolution of diamond forming fluids: evidence from microinclusion-bearing diamonds from Kankan, Guinea. Lithos 112(Suppl 2):660–674

Williams AF (1932) The genesis of the diamond. Ernest Benn Ltd, London

Wilshire HG, Kirby SH (1989) Dikes, joints and faults in the upper mantle. Tectonophysics 161:23–31

Wilshire HG, Shervais JW (1975) Al-augite and Cr-diopside ultramafic xenoliths in basaltic rocks from western United States. Phys Chem Earth 9:257–272

Wilshire HG, Nielson-Pike JE, Meyer CE, Schwarzman EC (1980) Amphibole-rich veins in lherzolite xenoliths, Dish Hill and Deadman Lake, California. Am J Sci 280A:576–593

Wilshire HG, McGuire AV, Noller JS, Turrin BD (1991) Petrology of lower crustal and upper mantle xenoliths from the Cima volcanic field, California. J Petrol 32:169–200

Wilson M, Downes H (1991) Tertiary – quaternary extension-related alkaline magmatism in Western and Central Europe. J Petrol 32:811–849

Wirth R, Kaminsky F, Matsyuk S, Schreiber A (2009) Unusual micro- and nano-inclusions in diamonds from the Juina area, Brazil. Earth Planet Sci Lett 286:292–303

Xu X, O'Reilly SY, Griffin WL, Zhou XM (2000) Genesis of young lithospheric mantle in southeastern China: a LAM-ICPMS trace element study. J Petrol 41:111–148

Yaxley GM, Green DH, Kamenetsky V (1998) Carbonatite metasomatism in the southeastern Australian lithosphere. J Petrol 39:1917–1930

Yaxley GM, Brey GP (2004) Phase relations of carbonate-bearing eclogite assemblages from 2.5 to 5.5 GPa: implications for petrogenesis of carbonatites. Contrib Mineral Petrol 146:606–619

Yuan X (1996) Velocity structure of the qinling lithosphere and mushroom cloud model. Sci China SerD 39:235–244

Zedgenizov DA, Rege S, Griffin WL, Kagi H, Shatsky VS (2007) Compositional variations of micro-inclusions in fluid-bearing diamonds from Udachnaya kimberlite pipe as revealed by LA-ICP-MS. Chem Geol 240:151–162

Zedgenizov DA, Ragozin AL, Shatsky VS, Araujo DP, Griffin WL, Kagi H (2009) Mg-Fe-rich carbonate-silicate high-density fluids in cuboid diamonds from the Internationalnaya kimberlite pipe (Yakutia). Lithos 112 (Suppl 2):638–647

Zhang M, Stephenson PJ, O'Reilly SY, McCulloch MT, Norman M (2001) Petrogenesis and geodynamic implications of Late Cenozoic basalts in North Queensland, Australia: trace-element and Sr-Nd-Pb isotope evidence. J Petrol 42:685–719

Zhang M, O'Reilly SY, Wang KL, Hronsky J, Griffin WL (2008) Flood basalts and metallogeny: the lithospheric mantle connection. Earth Sci Rev 86:145–174

Zheng JP, Griffin WL, O'Reilly SY, Zhang M, Pearson N (2006) Zircons in mantle xenoliths record the Triassic Yangtze-North China continental collision. Earth Planet Sci Lett 247:130–142

Zheng JP, Griffin WL, O'Reilly SY, Yu C, Zhang HF, Pearson NJ, Zhang M (2007) Mechanism and timing of lithospheric modification and replacement beneath the eastern North China Craton: peridotitic xenoliths from the 100 Ma Fuxin basalts and a regional synthesis. Geochim Cosmochim Acta 71:5203–5225

Zheng JP, Sun M, Griffin WL, Zhou MF, Zhao GC, Robinson P, Tang HY, Zhang ZH (2008a) Age and geochemistry of contrasting peridotite types in the Dabie UHP belt, eastern China: petrogenetic and geodynamic implications. Chem Geol 247:282–304

Zheng JP, Griffin WL, O'Reilly SY, Hu BQ, Zhang M, Pearson NJ, Lu FX, Wang FZ (2008b) Continental collision and accretion recorded in the deep lithosphere of central China. Earth Planet Sci Lett 269:496–506

Chapter 13
Mapping the Distribution of Fluids in the Crust and Lithospheric Mantle Utilizing Geophysical Methods

Martyn Unsworth and Stéphane Rondenay

Abstract Geophysical imaging provides a unique perspective on metasomatism, because it allows the present day fluid distribution in the Earth's crust and upper mantle to be mapped. This is in contrast to geological studies that investigate mid-crustal rocks have been exhumed and fluids associated with metasomatism are absent. The primary geophysical methods that can be used are (a) electromagnetic methods that image electrical resistivity and (b) seismic methods that can measure the seismic velocity and related quantities such as Poisson's ratio and seismic anisotropy. For studies of depths in excess of a few kilometres, the most effective electromagnetic method is magnetotellurics (MT) which uses natural electromagnetic signals as an energy source. The electrical resistivity of crustal rocks is sensitive to the quantity, salinity and degree of interconnection of aqueous fluids. Partial melt and hydrogen diffusion can also cause low electrical resistivity. The effects of fluid and/or water on seismic observables are assessed by rock and mineral physics studies. These studies show that the presence of water generally reduces the seismic velocities of rocks and minerals. The water can be present as a fluid, in hydrous minerals, or as hydrogen point defects in nominally anhydrous minerals. Water can further modify seismic properties such as the Poisson's ratio, the quality factor, and anisotropy. A variety of seismic analysis methods are employed to measure these effects in situ in the crust and lithospheric mantle and include seismic tomography, seismic reflection, passive-source converted and scattered wave imaging, and shear-wave splitting analysis. A combination of magnetotelluric and seismic data has proven an effective tool to study the fluid

M. Unsworth (✉)
University of Alberta, Edmonton, AB T6G 2J1, Canada
e-mail: unsworth@UAlberta.ca

S. Rondenay
University of Bergen, Bergen 5020, Norway

Massachusetts Institute of Technology, Cambridge, MA 02139, USA
e-mail: rondenay@geo.uib.no

D.E. Harlov and H. Austrheim, *Metasomatism and the Chemical Transformation of Rock*, Lecture Notes in Earth System Sciences,
DOI 10.1007/978-3-642-28394-9_13,

distribution in zones of active tectonics such as the Cascadia subduction zone. In this location fluids can be detected as they diffuse upwards from the subducting slab and hydrate the mantle wedge. In a continent-continent collision, such as the Tibetan Plateau, a pervasive zone of partial melting and aqueous fluids was detected at mid-crustal depths over a significant part of the Tibetan Plateau. These geophysical methods have also been used to study past metasomatism ancient plate boundaries preserved in Archean and Proterozoic aged lithosphere.

13.1 Introduction

Metasomatism occurs in the crust and upper mantle and causes a profound change in the composition of rocks. The presence of even small amounts of aqueous or magmatic fluids often controls the rate of metamorphic reactions. Most of our knowledge of metamorphic and metasomatic processes is based on geochemical studies of these rocks when they have been exhumed and exposed at the surface. This means that the process of metasomatism is being studied in ancient orogens, when the fluids are no longer present, except in isolated fluid inclusions. Being able to observe the fluids that cause metasomatism in real time is essential to understanding how this process occurs. Geophysics allows us to map in situ fluid distributions in real time, because the presence of fluids can significantly change the physical properties of a rock, primarily electrical resistivity and seismic velocity. Subsurface variations in these properties can be measured with surface based geophysical data. Electromagnetic methods can image electrical resistivity and seismic methods can image seismic velocities and related quantities such as Poisson's ratio.

In this chapter the physical basis for using geophysical observations to map the present day fluid distribution in the crust and upper mantle is described. This includes (1) an understanding of how the presence of fluids changes the properties of the rock, (2) how to measure these properties from the surface with geophysical imaging, and (3) a number of case studies that illustrate how geophysical data can determine the fluid distribution in locations where metasomatism is occurring. Metasomatism changes the mineralogy of crustal and upper mantle rocks in a permanent way, which can provide evidence of past metasomatism. Examples of this type of observation are also discussed.

13.2 Electromagnetic Methods

13.2.1 Electrical Resistivity of Rocks

The electrical resistivity, or reciprocal conductivity, of a rock contains information about its composition and structure. To understand the resistivity of crustal and

upper mantle rocks, it is first necessary to consider the resistivity of the minerals that make up these rocks.

The electrical resistivity of a pure mineral depends on two factors: (1) the density of charge carriers, typically electrons or ions and (2) the ease with which these charge carriers can move through the mineral (mobility). An extreme example is Cu, which has a very high density of charge carriers (electrons) that are weakly attached to atoms in the lattice and move very easily, resulting in a very low electrical resistivity ($\rho = 10^{-10}$ Ωm). In contrast, in diamond the C atoms are rigidly attached to the crystal lattice and cannot easily move through the crystal to carry electric current. This makes the electrical resistivity of diamond very high, typically more than 10^{10} Ωm.

Pure materials are only found locally in the Earth, with most rocks consisting of a complex mixture of materials. Thus to calculate the overall resistivity of a rock, the resistivity of the constituents must be considered, along with their geometric distribution. A common situation in the crust and upper mantle is for the rock to be characterized by two phases. The bulk of the rock comprises mineral grains that have a very high resistivity, while the pore space is occupied by a second phase that has a low resistivity. Even if the second phase is volumetrically small, it can significantly influence the overall resistivity of the rock. This is a common occurrence with, for example, saline aqueous fluids or melt occupying the space between the grains. Other conducting phases can be present and include sulphides or graphite. Note that this is in contrast to seismic velocity where contrasts in velocities are smaller.

The focus of this chapter is on the detection of metasomatizing fluids, so the emphasis will be on crustal rocks containing saline fluids and partial melts. In this case the overall resistivity of the rock is dominated by (a) the resistivity of the fluid, (b) the amount of fluid, and (c) the geometric distribution of the fluid. These factors are reviewed below.

13.2.1.1 Resistivity of Aqueous Fluids

First, the electrical resistivity of saline fluids as a function of composition, pressure and temperature, is reviewed. As the salinity increases the number of charge carriers (anions and cations) increases and the resistivity decreases. A number of empirical equations have been developed to characterize this behaviour (Block 2001; Meju 2000). At low salinities the increase in conductivity with salinity is nearly linear.

To interpret crustal resistivity values observed at mid and lower crustal depths, it is important to consider effects of temperature on the resistivity of aqueous fluids. Temperature effects are summarized in Figs. 13.1 and 13.2, based on the studies of Ussher et al. (2000) and Nesbitt (1993). The results of Ussher et al. (2000) are based on the original data of Ucok et al. (1980). At all temperatures, increasing salinity produces a monotonic decrease in resistivity as more charge carriers become

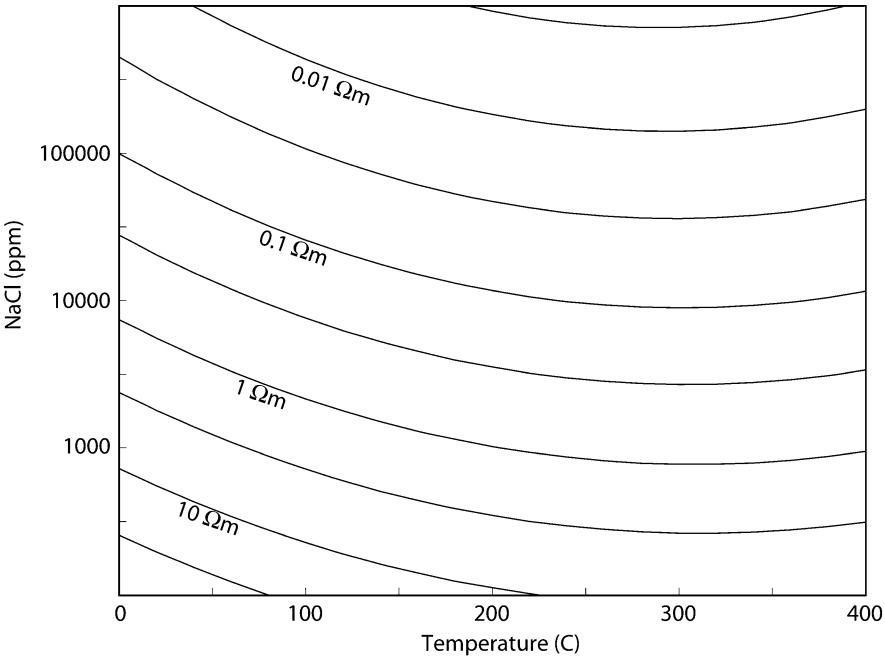

Fig. 13.1 Contour plot of electrical resistivity as a function of salinity and temperature for saline crustal fluids (Adapted from Ussher et al. (2000))

available. At constant salinity, increasing temperatures (0–300°C) causes a decrease in resistivity as fluid viscosity decreases and the ions are able to move more easily through the solution. Above 300°C an increase in resistivity is observed and this effect is correlated with decreasing solution density. The decreased density causes an increase in ion pairing that reduces the density of available charge carriers (Nesbitt 1993).

Pressure also influences the electrical resistivity of the aqueous fluid. A detailed summary of the pressure temperature dependence of resistivity is described by Quist and Marshall (1968) and number of similar studies. Nesbitt (1993) summarizes information about aqueous fluid resistivity, with specific application to conditions found in the Earth's crust. Figure 13.2 illustrates the combined effects of temperature and pressure on a KCl solution of varying concentrations based on the data of Nesbitt (1993). Below 300°C, the resistivity decreases with increasing temperature and pressure has very little effect. The lowest resistivity occurs around 300°C. At temperatures above 300°C pressure has a significant influence on resistivity because of the resistivity density correlation described above. Note that in this range, increasing pressure decreases the resistivity by increasing the solution density.

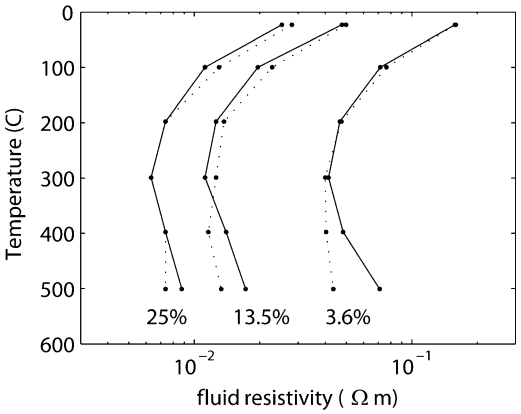

Fig. 13.2 Effect of temperature and pressure on the resistivity of a KCl solution (Adapted from Fig. 1 in Nesbitt (1993)). For each salinity value, two pressures are shown (*continuous curve* = 1Kbar; *dashed curve* = 3Kbar). Percentage values indicate salinity.

In interpreting crustal resistivity values measured with magnetotelluric data, it is important to understand depth variations in fluid resistivity due to simultaneous increases in both pressure and temperature. Figure 13.3a shows this effect for a geothermal gradient of 30°C per km and a lithostatic pressure gradient (25 MPa per km or 0.25 kb per km).

Salts are not the only source of dissolved ions in crustal aqueous fluids. Carbon is widely observed in the Earth's crust in a variety of forms, including diamond, graphite, hydrocarbons, and carbon dioxide. Carbon dioxide will dissolve in water to form H^+ and HCO_3^- ions that will act as charge carriers and lower the electrical resistivity of the fluid. Nesbitt (1993) summarizes data that show that an increase in CO_2 concentration will lower the resistivity of the solution (Fig. 13.3b). Note that the electrical resistivity of these solutions exhibits a greater temperature dependence than salt solutions. As with salt solutions, increasing temperature causes a decrease in resistivity up to a temperature of 300°C, after which the resistivity increases.

Of course, many aqueous solutions contain both dissolved salts and carbon dioxide. The synthesis of Nesbitt (1993) suggests that at upper crustal levels, the salt will dominate the fluid resistivity, while in the mid-crust the dissolved CO_2 will dominate the fluid resistivity under lithostatic conditions.

In summary, it can be seen that aqueous fluids will have resistivities in the range 0.01–10 Ωm. Knowledge of the fluid composition, either from well measurements or fluid inclusions, plus thermal and pressure gradients, are also needed to give a more precise estimate of the fluid resistivity.

13.2.1.2 Electrical Resistivity of Partial Melts

Under certain conditions, the presence of aqueous fluids can cause partial melting. As the partial melts migrate, they can cause metasomatism in both the crust and

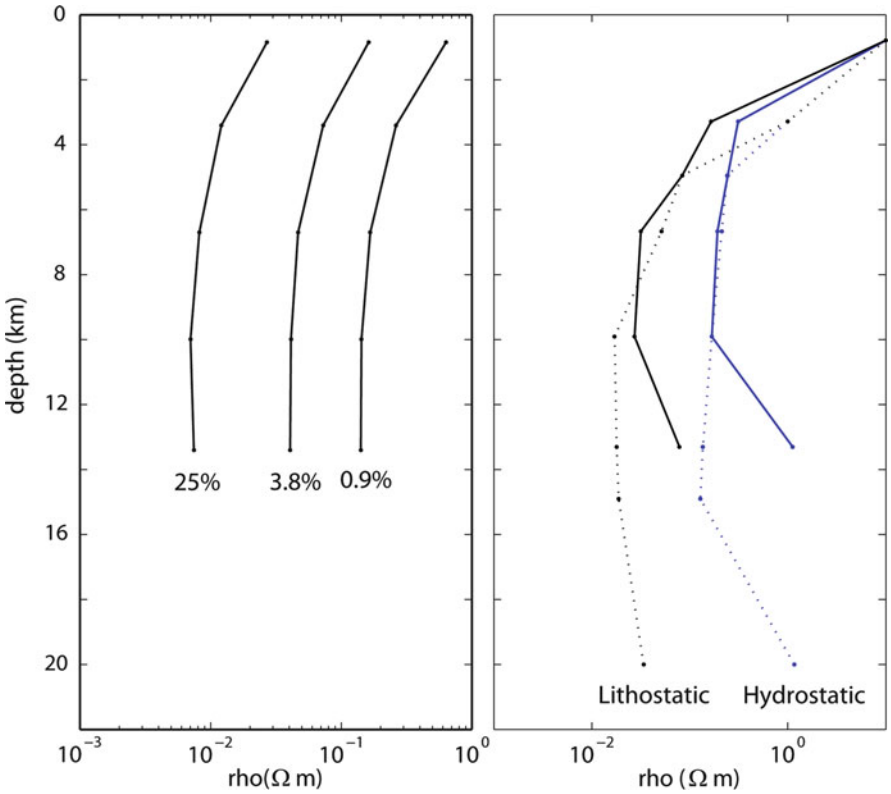

Fig. 13.3 Variation of resistivity as a function of depth for an aqueous fluid containing (**a**) KCl and (**b**) $KHCO_3$ solution assuming geothermal gradients of 20°C/km (*solid curve*) and 30°C/km (*dashed curve*) (Based on data from Nesbitt (1993)). Percentage values indicate salinity.

upper mantle (Prouteau et al. 2001). Partial melt has a low resistivity, since the ions can move relatively easily through the liquid. The resistivity of the melt depends on the amount of dissolved water and the petrology, and is generally in the range 1–0.1 Ωm (Wannamaker 1986; Li et al. 2003).

13.2.1.3 Resistivity of Whole Rock for Various Pore Fluid Distributions

As described above, in a typical rock, the low resistivity phase dominates the bulk resistivity of the sample, even if the minor phase occupies a very small fraction of the whole rock. The second factor that controls the overall resistivity is the geometric distribution of a low resistivity minor phase, such as a free fluid

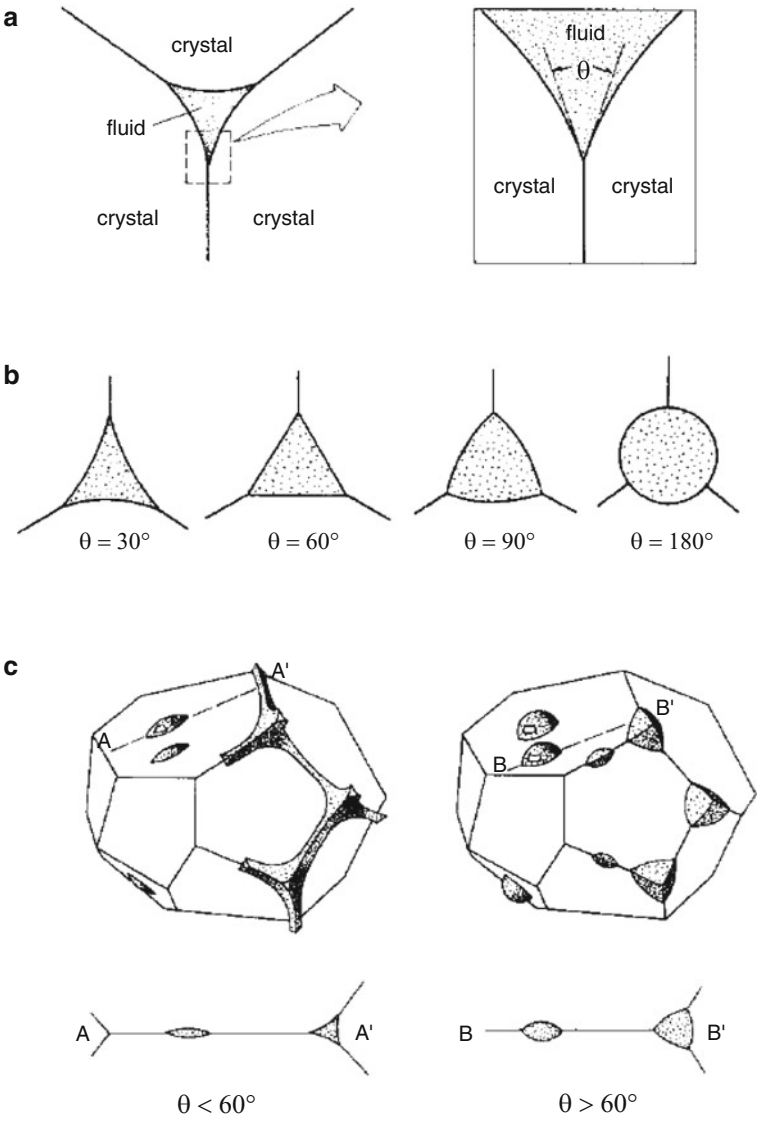

Fig. 13.4 Illustration of the effect of the dihedral angle (θ) on the fluid distribution in a porous rock (Adapted from Watson and Brenan 1987). For $\theta > 60°$ the fluid will be distributed as isolated inclusions, while for $\theta < 60°$ it will be distributed in tubes along the grain boundaries

phase. This effect is illustrated in Fig. 13.4. If the fluid is located in isolated pores, it will not form an interconnected network that can effectively conduct electricity. In contrast, if the fluid is distributed in tubes along the grain boundaries then a continuous network exists that will conduct electric current.

Thus it is important to be able to predict the distribution of a fluid in a host rock. This depends on the relative surface energy of the fluid and the mineral crystals, and can be visualized through the dihedral or wetting angle as shown in Fig. 13.4. Laboratory data for aqueous fluids and partial melts are reviewed in the following sections.

It can be shown that, with a low dihedral angle, the pore fluid will effectively wet all grain boundaries, while at high values, the fluid will be located in isolated inclusions. At low fluid fractions (<1%), a dihedral angle $\theta = 60^\circ$ represents the boundary between these fluid distributions. At higher fluid fractions this angle may increase slightly (Watson and Brenan 1987). The dihedral angle is very important as it controls many of the properties of the rock. A low dihedral angle produces interconnection that will result in a low resistivity. It will also allow fluids to migrate rapidly through the rock matrix, which is very significant in the context of metasomatism. Interconnection of the fluids will also reduce the strength of the rock.

Dihedral Angles of Aqueous Fluids in Crustal and Upper Mantle Rocks

Watson and Brenan (1987) studied the dihedral angles of H_2O–CO_2 fluids in synthetic rock samples at temperatures of 950–1,150°C and pressures of 1 GPa = 10 Kbar, corresponding to lower crustal conditions. The study showed that under these conditions, the dihedral angle for pure water in a quartz matrix was 57° and 65° for pure water in an olivine matrix. The addition of CO_2 caused a marked increase to values around 90° in both lithologies. Thus crustal fluids containing significant amounts of CO_2 are unlikely to be interconnected at mid and lower crustal conditions. In contrast, the addition of solutes caused a reduction in dihedral angle below 60° indicating that saline fluids could form an interconnected network along the grain edges. Additional studies of dihedral angles in crustal fluids are presented by Brenan and Watson (1988).

The study of dihedral angles in fluid saturated crustal rocks was extended by Holness (1992) and (1993) to consider a range of pressures and temperatures. Holness (1992) showed that at 800°C there was a strong pressure control on the dihedral angle. Holness (1993) confirmed that dihedral angles greater than 60° were present over a broad range of pressure and temperature conditions as shown in Fig. 13.5. This study also confirmed that the presence of CO_2 raises the dihedral angle, while dissolved salts can dramatically lower the dihedral angle. It should also be noted that when multiple fluids are present, they can become immiscible (Gibert et al. 1998).

In summary, it appears that fluids can be interconnected in two distinct pressure-temperature windows. The first occurs at temperatures close to the melting point, and the second at the lower temperatures found in regions with a geothermal gradient typical of a craton.

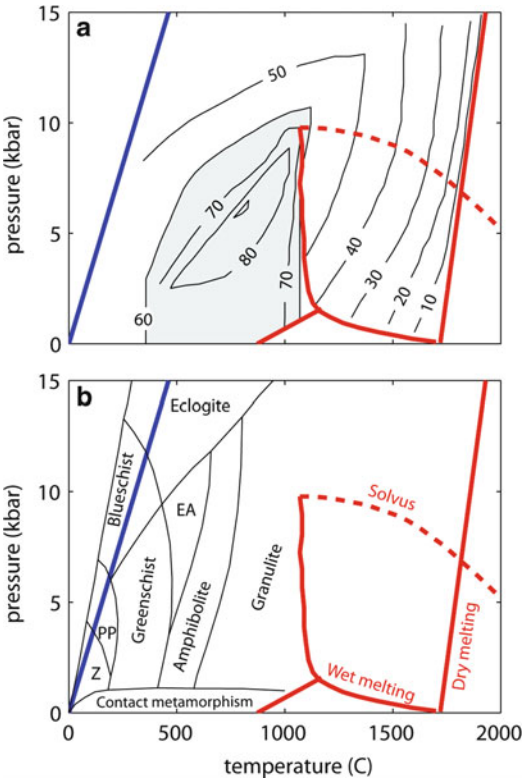

Fig. 13.5 (**a**) Plot of dihedral angle as a function of temperature and pressure (Taken from Fig. 6 in Holness 1993). Lower dihedral angles are expected if the water has a high salinity. (**b**) Metamorphic facies. *Blue line* denotes a cratonic geothermal gradient. *PP* Prehenite-pumpellyite, *EA* Epidote-amphibolite, *Z* zeolite

Dihedral Angles of Partial Melts in Crustal and Upper Mantle Rocks

A number of laboratory studies have investigated the dihedral angles found in partial melts. ten Grotenhuis et al. (2005) studied basaltic melts and showed that effective interconnection occurred, implying a dihedral angle below 60°. Holness (2006) studied the melt-solid dihedral angles in field samples and reported the following values: plagioclase (25°), clinopyroxene (38°), olivine (29°), quartz (18°), and leucite (20°). Mamaus et al. (2004) studied partial melts with a more felsic (SiO_2-rich) composition and showed a median value for dihedral angles of 50°. This study also showed that anisotropy of the olivine required a melt fraction of 0.3% for interconnection to occur. Their study raised questions about the ability of silica-rich melts to act as metasomatizing fluids. This is because the melt was unable to infiltrate a rock at low melt fraction.

It should be noted that fluid distributions measured in the laboratory may not be representative of those found in regions undergoing active deformation. Shear will redistribute the fluid and can often generate a higher degree of interconnection than found in undeformed samples. Laboratory studies of this effect include both rocks containing aqueous fluids (Tullis et al. 1996) and partial melts (Hasalová et al. 2008; Schulmann et al. 2008).

13.2.1.4 Bulk Resistivity of Rocks Containing Fluids

Having considered the typical situation of a high conductivity fluid permeating a matrix of low conductivity grains, we can now consider the bulk resistivity of the rock. This analysis will consider both aqueous fluids and the partial melts. The type of fluid present depends on temperature and composition of the rocks. In dry rocks, a temperature of 1,100°C may be needed to initiate melting, and the fluids will be partial melts. If the rocks are water saturated then melting will begin at lower temperatures and a range of fluids can be expected with aqueous fluids trending into partial melts.

A number of empirical relationships have been developed to predict the bulk resistivity of a fluid bearing rock. These equations use the terms described in previous sections. The bulk resistivity is primarily dependent on the fluid resistivity and the fluid geometry (degree of interconnection).

Archie's Law is an empirical relationship that was originally developed for the interpretation of resistivity logs measured in water saturated sedimentary rocks (Archie 1942). It was developed to allow resistivity measured by well logging to be used to infer the type of fluid present in the surrounding rock layers. The physical basis was the fact that hydrocarbons have a much higher resistivity than water. Archie's Law states that the bulk resistivity ρ of a fluid saturated rock can be written as

$$\rho = C\rho_w \Phi^{-m}$$

where ρ_w is the resistivity of the fluid, Φ is the porosity, and m is a constant, termed the cementation factor, that depends on the fluid distribution (interconnectivity of the pores). Values of m in the range 1–1.3 correspond to a fluid that is well connected, equivalent to a dihedral angle $\theta < 60°$. Values of $m = 2$, or greater, correspond to a fluid located in isolated pores, with $\theta > 60°$. C is an empirical constant, typically close to 1. It should be noted that the resistivity of the rock matrix does not appear in the equation, since it is assumed that the fluid is much more conductive than the mineral grains and all electrical conduction occurs through the pore fluid. Archie's Law also assumes that no clay minerals are present in the rock, as these would provide an alternate pathway for electric current flow and invalidate Archie's Law as a way of converting bulk resistivity into an estimate of porosity (Worthington 1993). A more general form of Archie's Law considers the case of partial saturation, and it has also been adapted to model three phase systems (Glover et al. 2000).

Archies Law was developed for the analysis of sedimentary rocks containing aqueous pore fluids. It has been successfully applied to rocks where the fluid is a partial melt. Owing to the difficulties of working with molten rocks, very few experimental studies of the resistivity of partial melts have been reported. Roberts and Tyburczy (1999) investigated a mixture of olivine and MORB, with the melt fraction being controlled by the temperature. This study showed that Archie's Law could be used to understand the bulk resistivity of partial melts with $C = 0.73$ and $m = 0.98$, implying a good interconnection of the grain boundary melt. The approach of Roberts and Tyburczy (1999) has the complication that the melt composition varied with temperature, and only a limited range of melt fractions

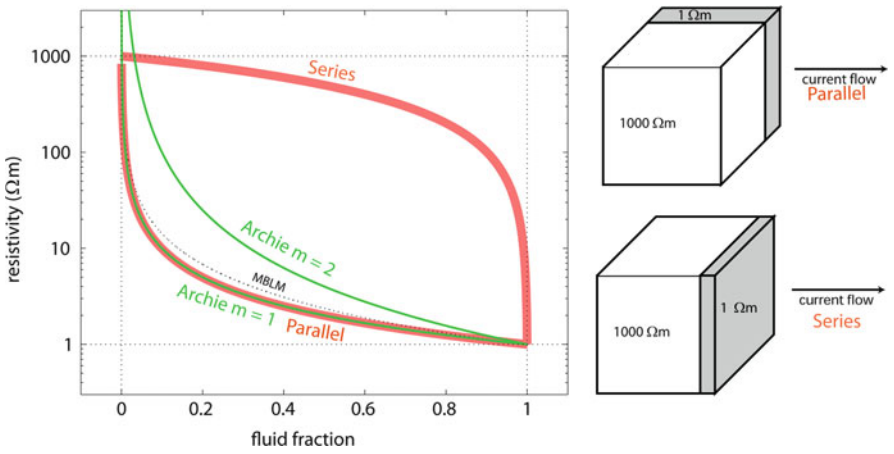

Fig. 13.6 Plot of bulk resistivity as a function of porosity for a rock containing a pore fluid with resistivity 1 Ωm and with mineral grains with a resistivity 1,000 Ωm. Series and parallel curves show maximum and minimum resistivities possible for a given fluid content. Fluid is shown in *grey* in panels on the *right*. *Green curves* show values for Archie's Law with m = 1 and 2. Note that m = 1 is essentially the same as the parallel circuit with the best possible interconnection. Also note that Archie's Law is incorrect at low fluid fractions when conduction through the mineral grains becomes significant

could be considered. A novel approach to this problem was presented by ten Grotenhuis et al. (2005) who studied the melt geometry in a synthetic olivine sample at atmospheric pressure, with the melt fraction controlled by the addition of glass. Analysis of quenched samples showed that effective interconnection occurs at melt fractions in the range 1–10%. The resistivity of the samples was well described by Archies Law with constant C = 1.47 and cementation factor m = 1.3, which represents a lower degree of interconnection than in the study of Roberts and Tyburczy (1999). The discovery of the crustal low resistivity zone beneath Southern Tibet has motivated new studies of the physical properties of partial melts. Laboratory studies by Gaillard (2004) showed that the resistivity of hydrous granitic melts at the appropriate pressures and temperatures were in "perfect agreement with those inferred from MT data" beneath Southern Tibet.

Other empirical equations and models have been developed to model the bulk resistivity of a rock consisting of a conductive fluid and a resistive matrix. The modified block layer model (MBLM) model was developed by Partzsch et al. (2000) and assumes effective interconnection of the pore fluid. This model explicitly considers conduction through the mineral grains. This becomes important at higher temperatures since it causes the ion mobility in the rock matrix to increase and contribute to the overall resistivity of the rock. The bulk resistivities predicted by MBLM and Archie's Law are illustrated in Fig. 13.6. Also shown are the maximum and minimum possible resistivities, assuming that the fluid is distributed in sheets parallel (ρ_{par}) and perpendicular (ρ_{perp}) to the electric current flow. Note that ρ_{par} (Φ) and Archie's Law, with a cementation factor m = 1, give virtually

identical curves, since both assume effective interconnection of the low resistivity fluid phase. These results are similar to those for the MBLM.

Figure 13.6 also shows that Archie's Law, with $m = 2$, predicts a higher resistivity at a given value of Φ than with $m = 1$. This is because interconnection is less effective with m = 2 and more fluid is needed to produce the same network at $m = 2$. This figure also shows the limitations of Archie's Law, since the $m = 2$ curve predicts a resistivity greater than the rock matrix at low values of Φ, which is clearly non-physical. In these models, the conducting phase can be aqueous fluids or partial melts. The models can be applied to rocks containing a small amount of a low resistivity phase such as graphite or disseminated sulphide minerals.

Some authors have suggested that surface conduction mechanisms occurring along grain boundaries may control the bulk resistivity of crustal and upper mantle rocks (ten Grotenhuis et al. 2004). In this scenario, low resistivity anomalies could be due to regions with smaller grain size, and not an enhanced fluid content as suggested above.

13.2.1.5 Electrical Anisotropy

A range of field and laboratory studies suggest that both crustal and upper mantle rocks can exhibit electrical anisotropy (Wannamaker 2005). In the case of crustal rocks, this occurs when the rock contains a low resistivity phase that is distributed anisotropically in the rock. For example, graphite is commonly found in fractures in rocks that have undergone extensive deformation. This produces electrical anisotropy that has been measured both with borehole logging (Eisel and Haak 1999) and with magnetotelluric surveys (Kellett et al. 1992; Heise and Pous 2003). A similar effect can occur when crustal rocks contain fluids that are present in fractures that are not uniformly distributed.

There is significant evidence that the upper mantle can be electrically anisotropic and different mechanisms have been proposed as an explanation (Gatzemeier and Moorkamp 2004).

(a) One explanation proposes that in the upper mantle, free water can dissociate into ions which act as charge carriers to transport electric current. The diffusion of H ions, along grain boundaries, has been proposed as an explanation for spatial variations in upper mantle conductivity (Karato 1990). Since olivine grains are preferentially oriented by shearing during upper mantle flow, this may cause electrical anisotropy (Simpson 2001; Simpson and Tommasi 2005).
(b) Another explanation, for upper mantle anisotropy, suggested that in the roots of the Archean Superior Craton, was caused by graphite deposited by metasomatism (Kellett et al. 1992; Mareschal et al. 1995).
(c) Finally it has been proposed that anisotropic distribution of partial melt could cause electrical anisotropy in the upper mantle, specifically in the asthenosphere. However, the study of Gatzemeier and Moorkamp (2004) suggested that this could not explain the anisotropy observed beneath Germany.

It should be noted that magnetotelluric (MT) measurements cannot determine the length scale of the anisotropy if it is less than the skin depth of the MT signals. It can also be very difficult to distinguish between heterogeneous isotropic resistivity structures and anisotropic resistivity structures. This requires high quality MT datasets with a high spatial density of measurements. It has been shown that measurements of the vertical magnetic field are very useful in this respect (Brasse et al. 2009).

13.2.1.6 Non-Uniqueness in Interpreting Electrical Resistivity Measurements

Finally it should be stressed that there is an inherent non-uniqueness in interpreting the electrical resistivity of crustal and mantle rocks. The laboratory studies listed above, and empirical observations derived from them, can be considered a forward calculation, i.e. starting from a particular rock and fluid composition, the overall electrical resistivity of the rock can be predicted. In contrast, the inverse problem is much more complicated since an observed resistivity for a particular rock layer must be interpreted in terms of composition. This process is inherently non-unique at many levels as there are multiple causes for low resistivity (aqueous fluids, melt, H ion diffusion etc.). A clear example of this is the ongoing debate over the reason for the high conductivities observed in the lower crust. The available evidence has been taken to support both graphite or aqueous fluids as an explanation for the elevated conductivity (Yardley and Valley 1997; Wannamaker 2000). This is discussed in detail later in this chapter.

13.2.2 Measuring the Electrical Resistivity of the Earth at Depth

The results described in the previous section were based on laboratory measurements of the electrical resistivity of rocks. These studies are typically made on samples a few centimetres across.

Measuring the resistivity of in situ rocks is much more challenging, since indirect methods must be employed. These can be divided into (a) well-logging that measures resistivity of the rocks within a few metres of a borehole, and (b) geophysical studies that sample volumes up to depths of hundreds of kilometres with a horizontal extent of tens of kilometres. Resistivity log data can provide a valuable check on resistivity models derived from geophysical studies, and vice versa.

During well-logging, the resistivity of the subsurface rocks can be measured with a range of tools that use either galvanic or inductive coupling (Ellis and Singer 2008). Resistivity measurements, made by well-logging, have the advantage that the measurement is made with the tool relatively close to the rocks being studied. However, it does not provide measurements of a large volume away from the borehole and is inherently limited by the depth extent of the well.

Thus, measuring the resistivity of rocks under in situ conditions at depth in the crust or upper mantle requires the use of geophysical imaging, which is the focus of the following section.

For shallow investigations of subsurface electrical resistivity, methods using direct electrical current are very effective. These methods inject current into the ground with metal stakes and can give multi-dimensional images of near surface resistivity structure. However, they are inherently limited in their depth of penetration because the electrode spacing must be comparable to the depth of investigation. Sounding to depths in excess of 1 km becomes logistically complicated. In contrast, the depth of investigation with electromagnetic methods can be varied by simply changing the frequency of the signal. Systems, using a small transmitter, can image the crust to depth of a few kilometres, and some controlled source methods may reach mid-crustal depths (Strack et al. 1990). However, for deeper imaging, naturally occurring low frequency EM signals represent the ideal choice. This is the geophysical imaging technique called magnetotellurics (MT), which is the most suitable for studies of crustal and upper mantle resistivity (Simpson and Bahr 2005).

In magnetotelluric exploration, natural EM signals are used to probe the electrical resistivity of the subsurface. These waves are generated by global lightning activity (>1 Hz) and by magnetospheric variations caused by time-varying interactions between the solar wind and the geomagnetic field (<1 Hz). Figure 13.7 shows electromagnetic waves with two frequencies incident on the surface of the Earth. Most of the energy is reflected back into the atmosphere, but a small fraction enters the Earth and diffuses downwards. The depth to which the EM signal penetrates is controlled by the skin depth, which is defined in metres as:

$$\delta = 503\sqrt{\frac{\rho}{f}}$$

where the electromagnetic signal has a frequency f and the Earth has a uniform resistivity, ρ. This equation is illustrated in Fig. 13.8. Note that as the frequency is decreased, the depth of penetration (δ) increases. Thus a measurement of the depth variation in resistivity can be made by simply measuring natural electromagnetic signals over a range of frequencies. Similarly, it can be seen that the depth of penetration of signal, at a given frequency, will vary according to the subsurface resistivity. Low resistivity rocks can greatly limit the depth of investigation with MT.

When the incident, reflected, and transmitted waves are analysed, it can be shown that a simple equation can be derived for the resistivity of the Earth. Suppose the horizontal surface components of the electric and magnetic fields are E_x and H_y at a frequency f. The apparent resistivity (ρ_a) is defined as

$$\rho_a = \frac{1}{2\pi\mu f}\left|\frac{E_x}{H_y}\right|^2$$

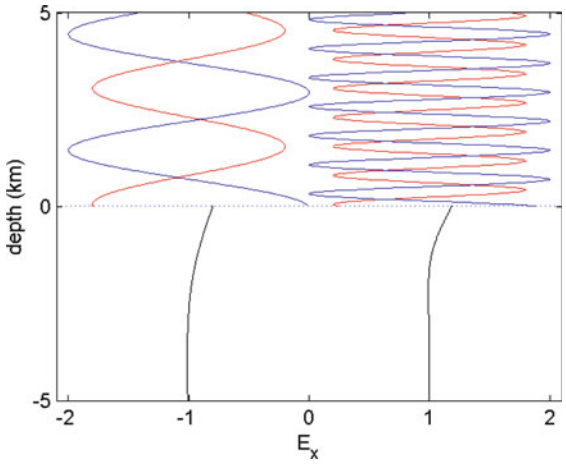

Fig. 13.7 Schematic diagram showing how the magnetotelluric method measures the resistivity of the Earth. A low frequency electromagnetic wave is incident on the Earth's surface (*blue*). Most of the energy is reflected (*red*) but a small proportion is transmitted into the Earth (*black*). The mode of propagation in the Earth is by diffusion. Note that the lower frequency signal penetrates deeper into the Earth than the high frequency signal. An animated version of this can be found at http://www.ualberta.ca/~unsworth/MT/MT.html

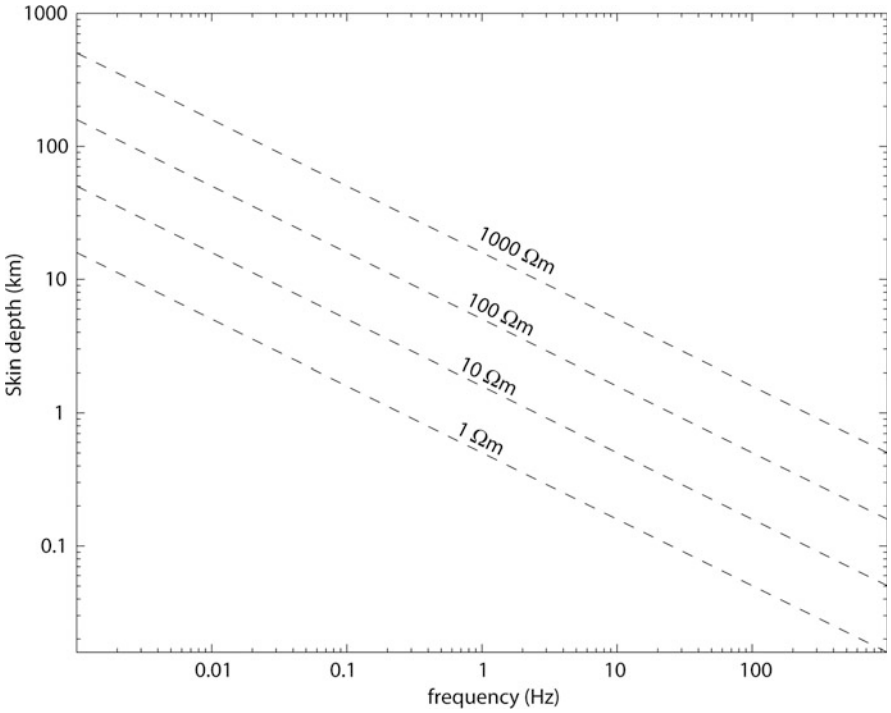

Fig. 13.8 (**a**) Skin depth (δ) as a function of frequency for uniform halfspaces with conductivity of 1,000, 100, 10, and 1 Ωm

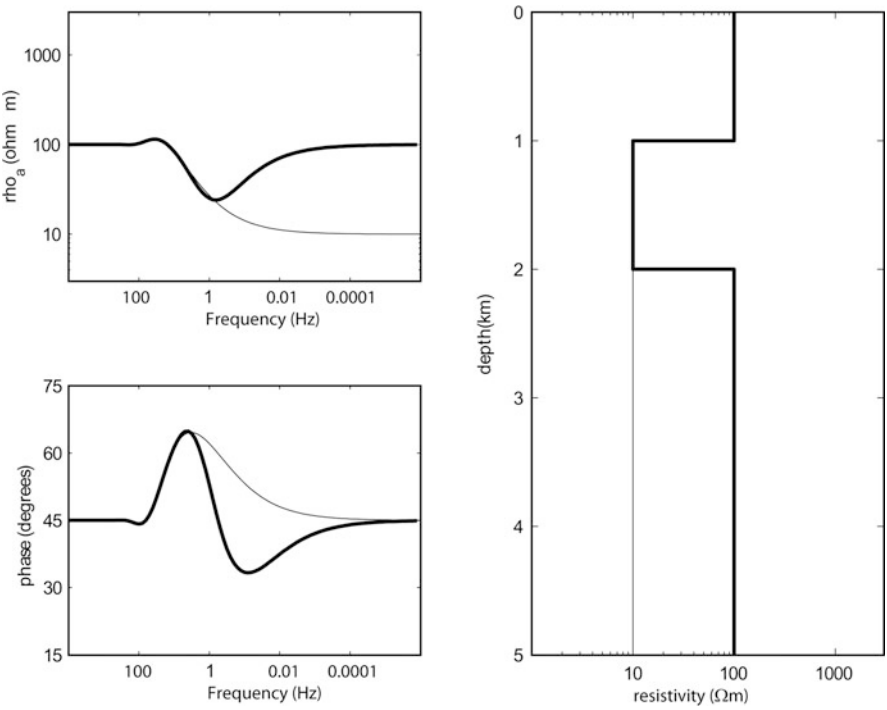

Fig. 13.9 Apparent resistivity and phase that would be measured at the surface over a 2-layer and 3-layer resistivity model

The apparent resistivity represents an average resistivity from the surface to a depth equal to the skin depth, δ. μ is the magnetic permeability, usually taken to be the free space value. Note that this only requires surface measurements of the electromagnetic fields to image resistivity at depth. More details of the MT method are described by Unsworth (2010).

13.2.2.1 MT Responses of a Layered Earth

The resistivity of the Earth usually varies with depth, so the equation for apparent resistivity is rarely applicable. To understand how MT can measure depth variation of resistivity, consider the case of a two-layer resistivity model shown in Fig. 13.9 (thin line). This will show how the measured apparent resistivity is related to the subsurface resistivity structure. In Fig. 13.9, the apparent resistivity is plotted as a function of signal frequency. Note that frequency decreases to the right, which corresponds to increasing depth of penetration in the Earth. At the highest frequencies ($f > 100$ Hz), the EM signals are attenuated before they ever reach the interface at a depth of 1 km. Thus, the apparent resistivity is the average resistivity over the region in which the EM signals travel, which is equal to the true resistivity of the upper layer (100 Ωm).

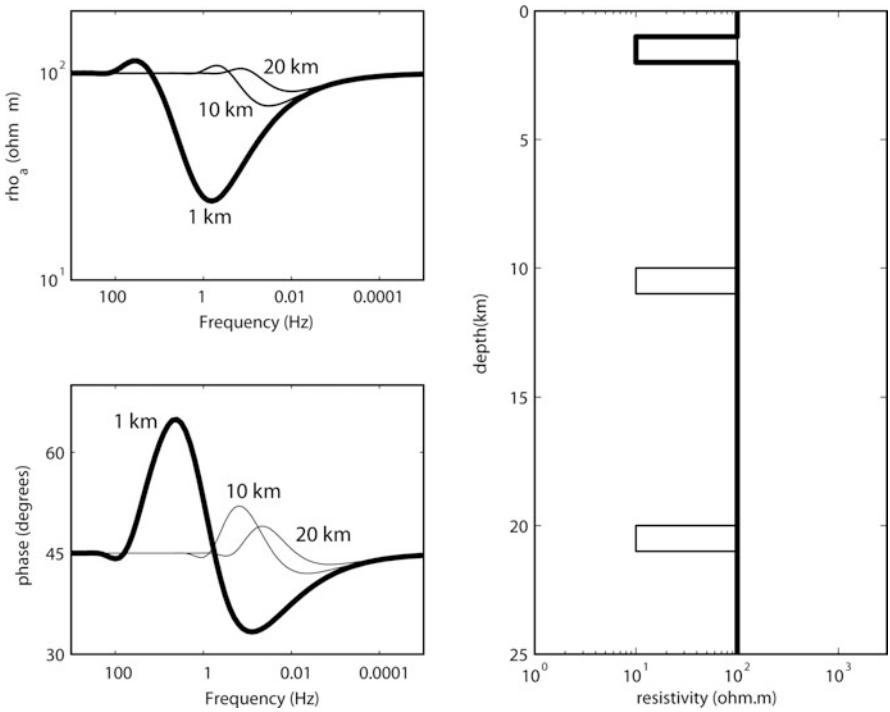

Fig. 13.10 Apparent resistivity and phase measured at the surface for a three layer Earth. The *top of the conductive layer* moves from 1 to 20 km depth. Note that as the layer moves deeper, the response becomes smaller

As the frequency decreases, the skin depth increases and signals will sample the lower layer. At these frequencies, the apparent resistivity represents an average of the two layers and it decreases with decreasing frequency. In the model in Fig. 13.9, this occurs at f ~30 Hz. As the frequency is further decreased, the skin depth increases and the depth of penetration becomes much greater than the layer thickness. This means that the apparent resistivity is dominated by the resistivity of the lower layer and the apparent resistivity asymptotically approaches the value of the lower half space resistivity (10 Ωm). The plot in Fig. 13.9 also shows the magnetotelluric phase. This quantity is the phase difference between the electric and magnetic fields and is sensitive to changes in resistivity with depth.

Figure 13.9 also shows a 3-layer model (thick line) with an increase in resistivity at a depth of 2 km. Note that apparent resistivity, as a function of frequency, shows a qualitative similarity to the variation of true resistivity with depth. In this model the second layer (1–2 km depth) can be considered a conductor, which is a relative term.

Figure 13.10 shows a set of 3-layer resistivity models where the depth to the top of the layer increases. This illustrates another important aspect of MT exploration

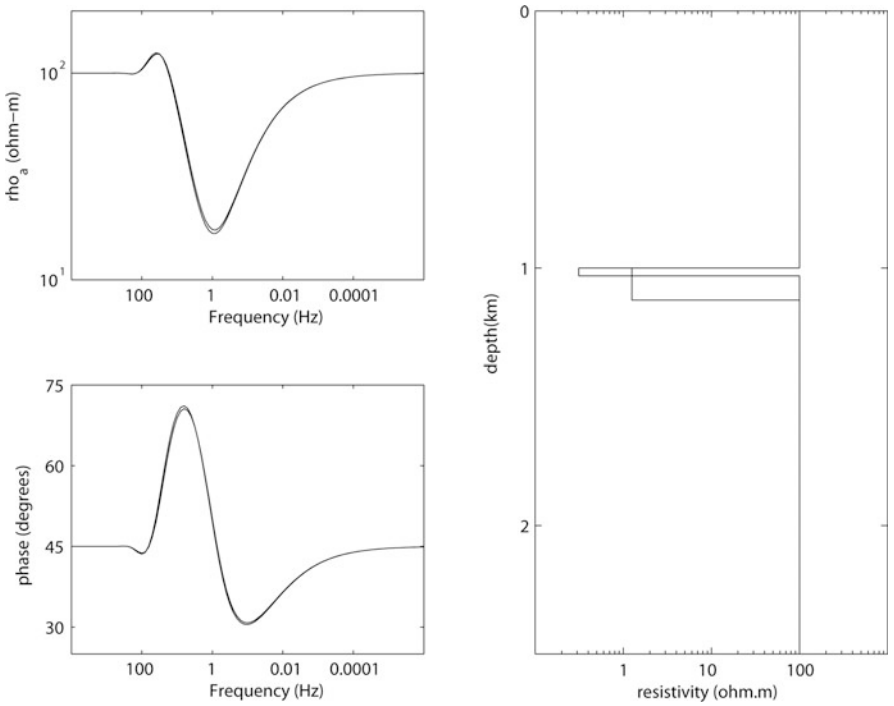

Fig. 13.11 Apparent resistivity for two resistivity models with a conductive layer at a depth of 1 km. Both models have the same conductance and give a very similar apparent resistivity and phase response

since it shows that the effect of a conductive layer on surface measurements becomes smaller as the depth of the layer increases.

The final example of MT responses illustrates a very important concept, as shown in Fig. 13.11. This figure shows a pair of resistivity models, each with a conductor at 1 km. The layers all have the same conductance, which is defined as the product of conductivity and thickness. In this example the conductance is 100 S. Note that the MT apparent resistivity curves are virtually identical for all models. Consider now the case of interpreting MT data collected over an unknown structure. With even a small amount of noise in the data, it would not be possible to distinguish between these models.

Comparing Figs. 13.10 and 13.11 shows both the ability and limitations of MT data to image the geometry and properties of conductive layers in the Earth. Remember that conductors, or zones of low resistivity, are typically associated with zones of aqueous fluids. MT is sensitive to the depth to the top of the layer and also to the conductance of the layer. However, MT cannot separately determine the

thickness and conductivity of the layer. This should not be seen as a limitation of the MT method. Rather by understanding exactly what can be resolved with MT will allow it to be used more effectively.

13.2.2.2 MT Responses of 2-D and 3-D Earth Structures

The examples above show how a 1-D resistivity model can be investigated with MT. Most MT data are not 1-D and show aspects of 2-D and 3-D subsurface resistivity structure. Over a 1-D Earth, the same apparent resistivity will be measured regardless of the direction in which the electric and magnetic fields are measured. However, if the Earth has a 2-D resistivity structure, then the apparent resistivity will vary with azimuth. In the case of a location where the subsurface resistivity varies in 2-D, it can be shown that electric current parallel and perpendicular to the strike direction are independent (so called TE and TM modes). A number of tests can be applied to MT data to determine if 2-D analysis is appropriate. If a 2-D approach is appropriate, then 2-D inversion can be applied to a profile of stations using a number of well-tested inversion algorithms that will run quickly on a desktop computer (Rodi and Mackie 2001). A number of 2-D inversion models are presented later in this chapter. If the subsurface is characterized by a 3-D resistivity model, then a grid of MT stations may be needed to accurately define the structure. Inversion of such a dataset is much more computationally demanding than in the 2-D scenario and a number of algorithms are now available (Siripunvaraporn et al. 2005).

13.2.3 Magnetotelluric Data Collection

MT instruments are passive and record time variations in the Earth's magnetic field (H_x, H_y, H_z) and horizontal electric field (E_x, E_y). As described earlier, the skin depth phenomenon means that deeper investigation requires that lower frequencies are measured. For shallow exploration of the upper crust, instruments using induction coil magnetometers can be used to record data in the frequency range 1,000–0.001 Hz (so called broadband magnetotelluric instruments, available from commercial manufacturers). The system layout is sketched in Fig. 13.12. Broadband MT data collection typically requires 1–2 days recording per station. Deeper investigation uses long-period MT (LMT) with a fluxgate magnetic sensor and provides data in the frequency range 1–0.0001 Hz. Additional details about MT field techniques and data analysis are described by Simpson and Bahr (2005) and Unsworth (2010).

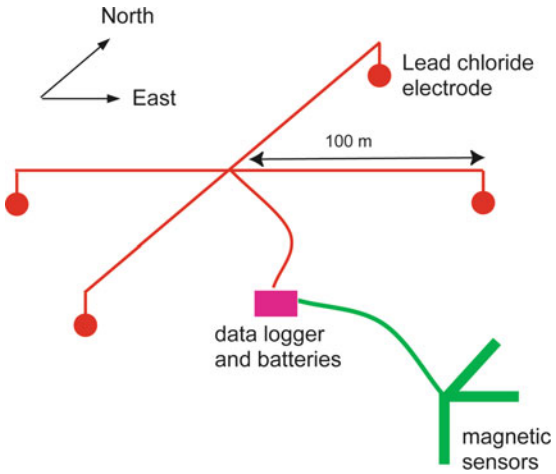

Fig. 13.12 Typical setup for broadband MT data collection. Electric fields are measured with a pair of dipoles that are connected to the Earth with non-polarizing electrodes. Magnetic fields are measured with induction coils that are buried to prevent motion

13.3 Seismic Methods

13.3.1 Variations of Seismic Properties as a Function of Fluid Content, Hydration Alteration and Water in Anhydrous Minerals

This section reviews the effects of metasomatism on seismic properties and observables. Once again, we treat metasomatism in the most general framework. That is, we take it to denote any form of interaction between water and minerals or rocks. In this framework, water can either be present as a free fluid in fractured and/or porous media, as structurally bound water (H_2O) or hydroxyl (OH) in hydrous minerals, or as H point defects in the structure of nominally anhydrous minerals. All of these occurrences of water change the response of materials to seismic waves that travel through them.

Relevant seismic observables discussed in this section include:

1. The velocities of compressional (P) waves, V_p, and shear (S) waves, V_s. In the crust and upper mantle, rocks have average velocities that range between 3.2–4.9 km/s for V_s, and 5.8–9.1 km/s for V_p (Dziewonski and Anderson 1981). Lower velocities can be found in parts of the uppermost crust that are weathered and/or fractured.
2. The Poisson's ratio, ν (sometimes also denoted by the symbol σ), which is the ratio of transverse contraction strain to the longitudinal extension strain in the direction of an applied stretching force. Typical values of Poisson's ratio for crustal and upper mantle rocks range between ~0.10 and 0.40 (Christensen 1996). The Poisson's ratio is related to V_p and V_s, or the V_p/V_s ratio, through the following expression: $\nu = 0.5[1-1/((V_p/V_s)^2 - 1)]$. An average value of

$\nu = 0.25$ = Poisson Solid ($V_p/V_s = 1.732$) is often considered typical for crustal and upper mantle rocks.

3. The seismic impedance, which is the product of seismic velocity and density, $I_p = \rho V_p$ for P-waves, and $I_s = \rho V_s$ for S-waves. The reflection coefficient at sharp seismic interfaces is proportional to the seismic impedance.
4. Seismic attenuation, which denotes the loss in seismic energy due to anelastic effects and scattering. Attenuation is defined by the quality factor $Q = 2\pi E/\Delta E$, or its inverse Q^{-1}, where ΔE represents the loss of seismic energy per unit cycle and E denotes the elastic energy stored in the system. Estimated values of Q, for the crust and upper mantle, range between the lowest values of ~30–40 for Q_S (S-wave attenuation) in the asthenosphere to values of several thousands in low-attenuation regions (e.g., Cammarano and Romanowicz 2008).
5. Seismic anisotropy, which is manifested by a variation in seismic velocity as a function of the propagation/polarization direction of seismic waves travelling though a given material. Anisotropy is commonly associated with the preferential orientation of fractures or mineral fabric. The magnitude of anisotropy is measured by taking the normalized difference between the maximum and minimum velocities for a given type of seismic wave, $(V_{max} - V_{min})/V_{mean}$, and can range from several percents to tens of percents depending on the mineral or mineral aggregate (Mainprice and Ildefonse 2009).

As we will discuss below, there exist two main approaches to determine the effects of water on seismic properties of materials: laboratory measurements and theoretical methods. We rely on results from these approaches to give an overview of how seismic properties are modified by hydrous fluids, hydrous minerals, and water in nominally anhydrous minerals.

13.3.1.1 Hydrous Fluids

As the term indicates, hydrous fluids refer to volatiles (in our case H_2O or aqueous solutions) in liquid form that occupy the voids present throughout a host rock. This situation is relevant to our discussion as the circulation of these fluids often stems from, or leads to, the occurrence of metasomatic reactions. It leads to the coexistence between a material that is porous and/or fractured (the matrix) and a fluid that fills its open spaces. This affects the seismic properties of subsurface materials in several ways when compared to dry, unfractured rocks. First, the presence of open fractures can reduce the stiffness of the rock. This effect is amplified when pore pressure is increased relative to confining pressure. Second, seismic energy may be absorbed through fluid displacement. The presence of interstitial fluid in fractured rocks at depth can thus have the following effects on seismic properties: a decrease in seismic velocities (V_p and V_s); a modification of the Poisson's ratio (or V_p/V_s ratio) of the composite material; an increase in the attenuation of seismic waves; and anisotropic behaviour if the fluid is present in fractures that are preferentially oriented.

Methodologies for Quantifying Physical Properties

Many approaches have been used to estimate the effects of porous fluids on the seismic properties of fractured materials. These can be grossly categorised into theoretical, numerical, and experimental approaches. They represent an active field of research, in large part driven by hydrocarbon exploration. Here, we provide a brief summary of these approaches, and we will discuss their results and their solid Earth implications in the next section.

Theoretical methods use thermodynamic and mechanical principles to establish relationships between elastic parameters and state variables that describe the fractured medium, e.g., fracture/pore density, geometry of the voids, properties of the solid matrix and the pore fluid. They include methods based on (1) effective medium theory, such as self-consistent approaches, which consider the minimum energy state at solid-solid and solid–liquid interfaces (e.g., O'Connell and Budiansky 1974, 1977; Schmeling 1985); and (2) poroelastic theory, which is based on continuum mechanics and seeks to estimate the seismic response of composite materials by linearly integrating the effects of the various components (see, e.g., Berryman 1995 for a review).

Numerical approaches seek to determine the effects of porous fluids by modelling a seismic wavefield propagating though materials containing predetermined asperities and fluid properties. For example, Hammond and Humphreys (2000a, b) used a finite-difference approach to look at the effects of partial melts on seismic velocities and attenuation for various pore shapes and concentrations.

Experimental methods measure seismic properties on samples of natural or synthesized rocks. Measurements on saturated porous rocks have been conducted largely in the context of hydrocarbon reservoirs, but the results can be easily extrapolated to deeper crustal rocks (see, e.g., Murphy 1985; Winkler and Murphy 1995, and references therein). Christensen (1984) made some measurements, specifically on oceanic basalts, to further characterize the effects of pore-fluid pressure on seismic properties. Constraints on the effects of water at greater depths in the lower crust and uppermost mantle (e.g., in subduction environments) can also be deduced from experiments on samples placed under high pressure-temperature conditions to investigate the effects of melt and/or fluids at the grain interface (e.g., Gribb and Cooper 2000; Aizawa et al. 2008).

Effects on Seismic Properties

Given the wide range of approaches described above and their various results, it is difficult to formulate a unified description of how aqueous liquids affect seismic properties. That is, there is no single expression or graph that can summarize the relationship between values of water content and seismic properties (e.g., velocities, attenuation, or anisotropy). Still, a generalisation of these results shows that an increase in water content has the following effects: (1) it tends to

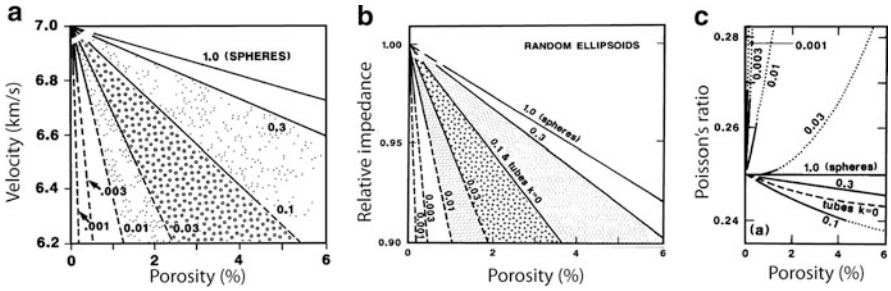

Fig. 13.13 Effects of porous fluids on seismic velocities for porosities ranging between 0% and 6% and pore aspect ratios (ratio of short to long axis) between 1.0 and 0.001. (**a**) P-wave velocity. (**b**) P-seismic impedance, relative to the unfractured (zero porosity) medium. (**c**) Poisson's ratio (Figures are from Hyndman and Klemperer (1989), and Hyndman and Shearer (1989))

reduce the stiffness of the rock, thereby reducing seismic velocities; (2) depending on the aspect ratio of the fractures/voids, it can either increase or reduce the Poisson's ratio (or V_p/V_s ratio); (3) it can increase the attenuation of seismic waves; and (4) it can cause seismic anisotropy. In the remainder of this section, we highlight some notable results that will help put some numbers on these general statements.

The perturbation in seismic velocities and V_p/V_s ratio associated with water-filled fractures is well summarized in papers by Hyndman and Shearer (1989) and Hyndman and Klemperer (1989), which seek to explain the high reflectivity and low velocities observed in the lower continental crust by controlled-source seismic investigations. These papers use the self-consistent approach described in Schmeling (1985) to calculate variations in V_p, seismic impedance I_p, and Poisson's ratio as a function of various pore aspect ratios (ratio of short to long axis), for rocks that are saturated with liquid water and porosities in the range 0–6%. Their results, which are summarized in Fig. 13.13, show that increased porosity systematically decreases the velocities, and that this effect is exacerbated as the pore aspect ratio becomes smaller, i.e., for long disk-shape voids that become equivalent to a network of thin, water-filled fractures (Fig. 13.13a). Since both V_p and density decrease with increased porosity, equivalent trends are observed for seismic impedances, noting that relatively small liquid fractions can cause impedance contrasts in excess of 5% relative to unfractured material – something that may yield important seismic reflections. Finally, while both V_p and V_s decrease systematically with increasing concentration of porous water, the Poisson's ratio (or V_p/V_s ratio) takes on different trends depending on the fractures' aspect ratios and the differential pressure (i.e., confining pressure minus pore pressure). It stays constant or decreases for aspect ratios between 0.3 and 1, and increases for smaller aspect ratios where thin water-filled fractures can preferentially reduce the resistance to shear. Experimental results indicate that these effects (reduction in V_p, V_s, and increase in V_p/V_s ratio) are amplified when pore pressure is increased relative to a constant confining pressure (Christensen 1984).

Three processes can lead to the attenuation and dispersion of seismic waves in saturated porous media: grain boundary sliding, liquid squirt between contiguous connected pores or fractures, and bulk fluid displacement (O'Connell and Budiansky 1977; Winkler and Murphy 1995; Wiens et al. 2008). Theoretical and numerical analyses suggest that the first two processes have relaxation time scales (i.e., range of frequencies where attenuation is maximum, between the unrelaxed and relaxed states) that are significantly higher than the central frequency of common seismic waves for both passive and active source applications (Hammond and Humphreys 2000a; Wiens et al. 2008). On the other hand, recent experimental results suggest that the first and third processes, grain boundary sliding and bulk fluid displacement, may cause attenuation in the frequency range of seismic waves, although the magnitude of these effects is still poorly constrained (see, e.g., Aizawa et al. 2008; and Wiens et al. 2008, and references therein for a review).

Aligned, fluid-filled fractures cause P and S seismic waves whose particle motion is in the plane of the fractures to travel faster than those whose particle motion is perpendicular to that plane, thus resulting in seismic anisotropy (see, e.g., Crampin and Booth 1985; Dunn and Toomey 2001; Fouch and Rondenay 2006). The magnitude of the anisotropy depends on the density of aligned fractures and on the combined properties of the solid and the fluid. A larger fracture density increases anisotropy, whereas the properties of the fluid control the overall bulk modulus of the medium. A formal theoretical treatment of the effects of fluid-filled cracks on seismic anisotropy is presented by Berryman (2007). These results show that such fractured media can have anywhere between several percent to tens of percent V_p and V_s anisotropy.

13.3.1.2 Hydrous Minerals

Hydrous minerals comprise water as part of their standard chemical structure. They are highly relevant to our discussion on metasomatism because they are both a main source of water carried and fluxed into the upper mantle by subduction zones, and a product of metasomatic alteration (see, e.g., Hyndman 1988; Hyndman and Peacock 2003; Grove et al. 2006; Chen et al. 2009). They tend to exhibit lower seismic velocities and higher seismic anisotropy than associated dry phases due to the inherent weakness of H bonds in their chemical structure and to the sheeted structure common to many species. Hydrous minerals can also cause seismic attenuation, though this effect is still poorly constrained (see, e.g., Pozgay et al. 2009). Here, we will discuss common hydrous minerals that are stable at relatively low temperatures in the crust and/or lithospheric upper-mantle, such as amphiboles, lawsonite, chlorite, and serpentine. We will also discuss accessory minerals associated with alteration reactions (e.g., talc and brucite), as these can produce highly anomalous seismic properties. Lastly, we will briefly discuss high-pressure hydrous phases (e.g., alphabet phases) that have the potential to carry water at great depth in the mantle transition zone and the lower mantle.

Methods for Quantifying Physical Properties

Once again, there exist three categories of approaches used to estimate the effect of hydration/alteration on the seismic properties of minerals and rocks: experimental measurements, theoretical calculations, and hybrid methods.

Experimental approaches are conducted either on natural and synthetic rock samples that are subjected to pressures and temperatures representative of conditions at depth (e.g., Birch 1960; Christensen 1966, 1984, 2004; Ito 1990; Kono et al. 2007), or on single crystals (e.g., Kumazawa and Anderson 1969; Frisillo and Barsch 1972; Schilling et al. 2003; Hilairet et al. 2006). Theoretical approaches, on the other hand, seek to estimate the elastic constants of hydrous minerals through first-principles quantum mechanical calculation (e.g., Reynard et al. 2007; Mainprice et al. 2008), or through atomistic simulations based on semi-empirical interatomic potentials that reproduce the structure of minerals (e.g., Auzende et al. 2006). Hybrid methods combine these two approaches, using experimentally-derived seismic properties of single minerals to compute the properties of rocks at depth. The mineral properties are extrapolated to high P-T conditions with thermodynamic equations, then combined with mixing laws to represent the desired assemblage (e.g., Bina and Helffrich 1992; Helffrich 1996; Hacker et al. 2003a).

Effects on Seismic Properties

Over the last 50 years, experiments and calculations have been conducted on many hydrous mineral and mineral assemblages to characterise their seismic properties. Due to the large quantity of material published on this topic over the years, it is not possible to review all of these results here. Thus we will focus the discussion on a few key results that pertain to hydrous minerals or rocks that play an important role in the context of subduction zones, as these represent the main point of entry of water into the Earth's mantle. Specifically, we will investigate the properties of the secondary alteration minerals serpentine and chlorite, as well at those of hydrated oceanic basalts. For more complete reviews, readers are referred to papers by Christensen (2004), Hacker et al. (2003a, b), and especially Mainprice and Ildefonse (2009).

The first two hydrous minerals that we shall discuss are serpentine and chlorite, which are common alteration minerals of lithospheric rocks. Serpentine is most commonly found as the hydrous alteration product of mantle peridotites, with peridotites transforming entirely into serpentinite and accessory minerals (e.g., talc, brucite, magnetite) if enough water is available, e.g. in saturated conditions. The formation of chlorite, on the other hand, is associated with the alteration of pyroxenes, amphiboles, and biotite, and is limited by the availability of Al in the crust and uppermost mantle. The top panels of Fig. 13.14 show the phase diagram of a hydrated lherzolite (a variety of peridotite) and the seismic properties corresponding to its various phases as a function of pressure and temperature (P-T)

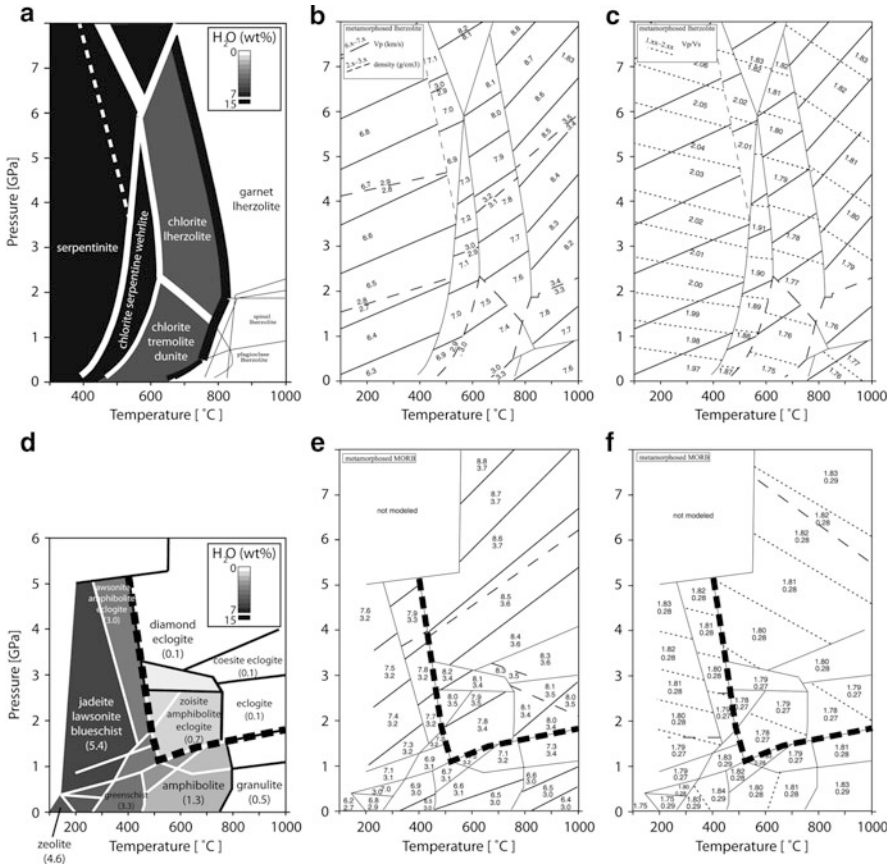

Fig. 13.14 Phase diagrams of hydrated rocks and their seismic properties as a function of pressure and temperature, calculated by the method of Hacker et al. (2003a). *Top row*: Phase diagram of lherzolite (**a**), with corresponding P-wave velocities and densities (**b**), and V_p/V_s ratios (**c**). *Bottom row*: Phase diagram of hydrated mid-ocean ridge basalt (**d**), with corresponding velocities and densities (**e**), and V_p/V_s and Poisson's ratio (**f**). The *thick dashed line* in panels (**d–e**) denotes the transformation into eclogite (Figures are modified from Hacker et al. (2003a))

conditions. These diagrams were obtained with the hybrid method of Hacker et al. (2003a) and outline the P-T conditions under which serpentine and chlorite are stable. We note that as the pressure increases, the water content of the rock decreases and that this decrease is accompanied by sharp, localised increases in seismic velocities and decreases in V_p/V_s ratio. The results of Fig. 13.14 are consistent with constraints obtained by experimental measurements, such as those of Christensen (2004) for antigorite (see Fig. 13.15), which is the variety of serpentine containing 13.0 wt.% H_20 that remains stable at the highest temperatures (see also, Hilairet et al. 2006).

Because of their layered structure, the alteration minerals serpentine, chlorite and their associated accessory minerals exhibit strong seismic anisotropy. Theoretical

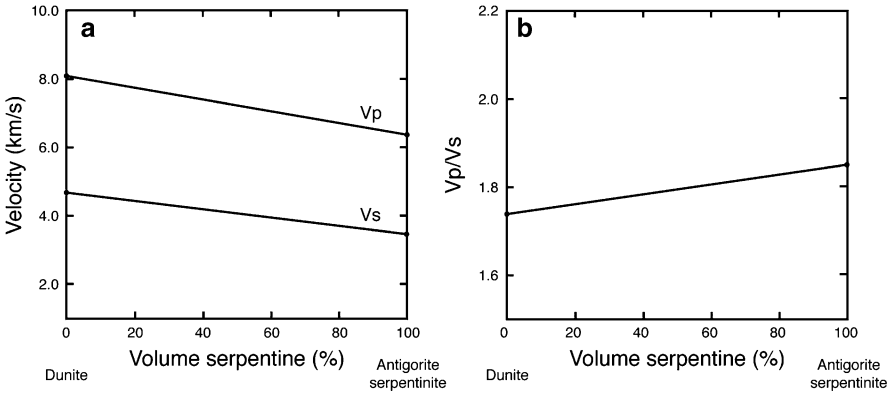

Fig. 13.15 Experimental results showing variations in (**a**) seismic velocities and (**b**) Vp/Vs ratio as a function of the degree of serpentinization, for the antigorite form of serpentine (Modified from Christensen 2004)

calculations for single minerals and experimental measurements on mono-mineralic aggregates have provided valuable estimates of anisotropic properties for several hydrous minerals (see Mainprice and Ildefonse 2009, and references therein). These include antigorite (71% V_p, 68% V_s), clinochlore and chlorite (35% V_p, 76% V_s), and talc (65% V_p, 68% V_s). Such large values suggest that strong seismic anisotropy may be observed for parts of the lithosphere and upper mantle that have undergone extensive hydrous alteration. However, this will only be the case if the hydrous minerals in real rocks exhibit a preferred crystallographic orientation when deformed under in situ P-T conditions, such that the bulk anisotropy is strong enough to yield detectable signals (e.g., Christensen 2004). Although the existence of such preferred orientation remains an open question, a handful of experimental studies, conducted on serpentine, have shown that crystals do indeed tend to align when aggregates are subjected to stresses similar to those found at convergent margins (Kern et al. 1997; Katayama et al. 2009; Bezacier et al. 2010a).

The second type of mineral assemblage we shall discuss is hydrated metabasalt, which is one of the main constituents of the oceanic crust and thus a major source of fluid input in subduction zones (see, e.g., Hacker et al. 2003a; Rondenay et al. 2008). At near surface P-T conditions, the main hydrous minerals in these rocks are chlorites and zeolites, which give the rock a ~5% H_2O content by weight. At intermediate P-T conditions, where chlorite remains stable, a significant portion of the mineral-bound water is also carried by amphiboles, which have been shown to exhibit strong seismic anisotropy (see, e.g., Bezacier et al. 2010b), and by lawsonite. The evolution of the water content and seismic velocities of hydrated metabasalts with increasing P-T conditions, as calculated by Hacker et al. (2003a) is shown in the bottom panels of Fig. 13.14. We observe that the water content progressively decreases with increasing P-T until the eclogite-facies is reached. We also observe that phase transformations are associated with significant changes in seismic properties. In particular, the transformation from lawsonite, blueschist,

or granulite into eclogite translates into seismic velocity increases of up to ~12% Though these transformations do not necessarily occur at a precise subduction depth, as demonstrated by field observations of ultra-high pressure rocks (e.g., Austrheim et al. 1997), we may still be able to observe them in the seismic response. Note, also, that since they do not take into account the effects of pore-fluid pressure, the graphs of Hacker et al. (2003a) should be used with caution when interpreting seismic images of crustal segments that are potentially overpressured (see, e.g., Shelly et al. 2006; Audet et al. 2009).

We conclude this section on hydrous minerals by briefly discussing the stability of the minerals already discussed, which are generally stable to depths of ~200 km, as well as those that remain stable to much greater depths. The latter include the following minerals (see reviews in Williams and Hemley 2001; and Mainprice and Ildefonse 2009): clinohumite, which can be stable to mantle transition zone depths; hydrous ringwoodite and hydrous wadsleyite, both of which are found in the mantle transition zone; and dense hydrous magnesium silicates of the so-called alphabet series such as phase A (stable in the upper mantle), superhydrous phase B (stable in the transition zone), and phase D (stable to lower mantle depths). The seismic properties of many of these high-pressure phases have only been calculated theoretically, and generally exhibit small to moderate deviations from the properties of anhydrous mantle rocks (see, e.g., Mainprice and Ildefonse 2009). Even if some of these phases could remain undetectable by virtue of their seismic properties, they may still play an important role in the nucleation of deep earthquakes in subduction zones – another important seismic observable. Indeed, the dehydration reactions of hydrous minerals carried in cold subducted slabs (e.g., serpentine, chlorite, and lawsonite at shallow and intermediate depths; clinohumite, phase A, and superhydrous phase B at greater depth) are believed to trigger intraslab earthquakes. Another possible cause of intraslab seismicity is the rapid transformation of metastable, dry granulite to eclogite by additions of hydrous fluids (see, e.g., Jackson et al. 2004). In these models, earthquakes are caused by changes in the stress field related to densification reactions and/or by a reduction in friction coefficients due to the flux of released fluids into existing fractures – processes that are generally described as dehydration embrittlement (see, e.g., Green and Houston 1995; Hacker et al. 2003b).

13.3.1.3 Water in Nominally Anhydrous Minerals

As pressure and temperature increase with greater depth, and away from cold anomalies caused by subducted slabs, it becomes less and less likely to encounter liquid water or hydrous minerals. Water may still be present in these environments, though, with the introduction of H^+ cations as point defects in the structure of nominally anhydrous minerals. This phenomenon produces a weak H. . .O atomic bond that enhances anelasticity, reduces velocities, and has the potential to modify the anisotropic parameters. In this section, we will discuss the effects of water in olivine, the main anhydrous mineral phase in the upper mantle.

Methods for Quantifying Physical Properties

The main approach used in quantifying the effects of H point defects in nominally anhydrous minerals is a combination of experimental and analytical methods. In experimental methods, samples comprising single crystals of olivine or olivine-rich aggregates are subjected to deformation under high P-T conditions to measure the rheological properties and the dominant crystal orientation (e.g., Jackson et al. 1992; Jung and Karato 2001). From these experimental results, one can derive analytical expressions relating seismic properties, in particular anelastic relaxation and seismic anisotropy, to the concentration of absorbed water (see, e.g., Karato 1995; Karato and Jung 1998; and reviews by Karato 2003, 2006).

Effects on Seismic Properties

The introduction of water as H point defects in nominally anhydrous minerals, in particular olivine at upper mantle P-T conditions, has two main effects on the seismic properties of mantle rocks: (1) enhancement of anelasticity, which in turn causes modification of seismic velocities, and (2) modification of the crystal preferred orientation in deformed aggregates, which causes a realignment of the principal axes of seismic anisotropy.

Anelastic relaxation occurs as a result of intragranular processes, whereby H enhances dislocation and diffusion creep. Through grain-boundary processes, H increases grain-boundary mobility (Karato 2003). These processes result in enhanced seismic attenuation Q^{-1}, which can in turn translate into velocity reductions through the following expression (Minster and Anderson 1981; Karato 2003):

$$V(\omega, T, P, C_{OH}) = V_{\infty}(T, P)\left[1 - \frac{1}{2}\cot\left(\frac{\pi\alpha}{2}\right)Q^{-1}(\omega, T, P, C_{OH})\right], \tag{13.1}$$

where $V(\omega, T, P, C_{OH})$ is the seismic velocity as a function of frequency ω, temperature T, pressure P, and concentration of water in the form of hydroxyl C_{OH}. $V_{\infty}(T,P)$ is the unrelaxed seismic velocity at infinite frequency, and α is a parameter that describes the frequency dependence of attenuation and has been shown experimentally to take values between 0.1 and 0.3. The attenuation dependence on water concentration follows the proportionality relationship (Karato 2003):

$$Q^{-1}(\omega, T, P, C_{OH}) \propto \exp\left(-\alpha\frac{H^*}{RT_{eff}}\right), \tag{13.2}$$

with

$$T_{eff} = T \cdot \xi, \tag{13.3}$$

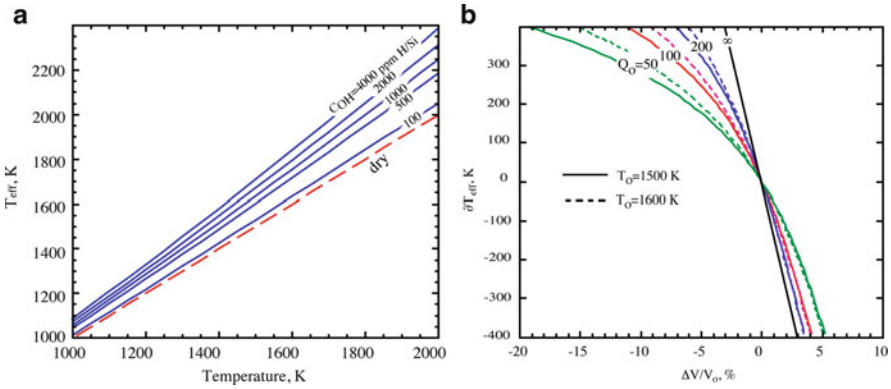

Fig. 13.16 Effects of water in nominally anhydrous minerals on seismic velocities. (**a**) Rheologically effective temperature, as a function of actual temperature, for various concentrations of water in olivine. (**b**) Velocity anomaly as a function of perturbation in rheologically effective temperature, for various values of the initial attenuation coefficient and temperatures (Q_0, T_0). For example, at $T_0 = 1{,}600$ K, the addition of 4,000 ppm H/Si (~0.03 wt.% water) raises the effective temperature by ~250 K (panel a), which can lead to a velocity perturbation of −3.2% for an initial (dry) attenuation coefficient $Q_0 \sim 200$ (panel b; see Karato 2003, his Fig. 13.2 for values of Q_0) (Figures are modified from Karato (2003))

and

$$\xi = \frac{1}{\left[1 - (RT/H^*) \cdot \log\left(A_w \cdot C_{OH}^r / A_d\right)\right]}, \tag{13.4}$$

where H^* is the activation enthalpy, R is the ideal gas constant, and T_{eff} is the rheologically effective temperature that incorporates the effects of water concentration through quantity ξ. The latter depends mainly on C_{OH} elevated to the power r, where r is an experimentally derived constant that depends on the process and takes on values between ~0.7 and 2.3 (see Karato 2006; his Table 1). Finally, A_w and A_d are constants that are independent of pressure and temperature (Karato and Jung 2003). Figure 13.16 illustrates these relationships. We see from the right panel of Fig. 13.16 that small concentrations of water (i.e., between 800 ppm H/Si and 3,000 ppm H/Si, which are reasonable estimates for typical oceanic asthenosphere and mantle wedge, respectively; see Karato 2003) are sufficient to generate seismic velocity perturbations of several percents.

Rheological experiments conducted on single crystals and aggregates of olivine have also shown that the addition of water causes the intragranular and grain-boundary effects discussed above to be enhanced along preferential crystallographic directions (e.g., Karato 1995; Jung and Karato 2001). Jung and Karato (2001) showed that these effects can have a dramatic effect on the deformation fabric of mantle olivines, as the crystallographic axis [001] becomes aligned with the maximum shear direction instead of axis [100] in dry samples. This leads to the existence of different types of olivine fabrics as a function of water concentration

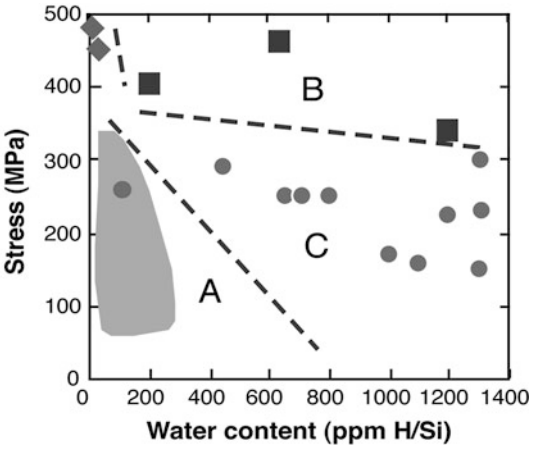

Fig. 13.17 Effects of water content and shear stress on the crystallographic orientation of olivine. *Symbols* and shaded area represent experimental results (see Jung and Karato 2001). *Dashed lines* define the fields corresponding to types A, B, and C fabrics. For a shear wave traveling perpendicularly to the shear plane, the fast polarization direction is parallel to the maximum shear direction in types A and C fabrics, while it is perpendicular to this direction in type B fabric. (Figure from Karato (2003))

and ambient shear stress (see Fig. 13.17). Type-A fabric corresponds to the most commonly assumed state for dry olivine, with its crystallographic axis [100] aligned subparallel to the shear direction and plane (010) subparallel to the shear plane. Type-B fabric is found for wet olivine under high shear stress conditions, and has its axis [001] aligned subparallel to the shear direction and plane (010) subparallel to the shear plane. Type-C fabric corresponds to wet olivine under low-stress conditions, and has its axis [001] aligned subparallel to the shear direction and plane (100) subparallel to the shear plane. One can fully appreciate the effects of these fabrics on seismic anisotropy when analyzing S waves that propagate perpendicularly to the shear plane (i.e., parallel to one of the crystallographic axes) and considering known elastic properties of olivine crystals (see, e.g., Babuška and Cara 1991). In this framework, S waves will observe a fast polarization direction parallel to the shear direction for types A and C. Conversely, for type-B fabric, the fast polarization direction will be perpendicular to the shear direction. There is, thus, a possible 90° ambiguity in the fast axis of anisotropy between dry and wet olivine aggregates.

13.3.1.4 Partial Melt

As discussed in Sect. 13.2.1, partial melt is directly linked to metasomatic processes. For example, melt alters the composition of rocks with which it comes in contact (including source rocks), rocks through which the melt migrates, and host

rocks in which it crystallises. Moreover, melt can be caused by the addition of water to dry rocks and it can thus facilitate the transport of this water through the mantle and the lithosphere. Compositional variations due to partial melt extraction can cause observable changes in seismic properties, such as S-wave velocity perturbations of the order of 0.1 km/s for the range of values of Fe depletion in the source region of melts (e.g., Lee 2003). However, the main effects of partial melt are related to the viscoelastic response of the liquid–solid mixture (see, e.g., Wiens et al. 2008; and references therein). As such, the same approaches used to estimate the effects of water on observable seismic properties and to measure those in situ, which were described in Sect. 13.3.1.1, can be applied to liquid partial melt in a solid rock matrix. The pore space volume and geometry are defined by grain boundary topology, and they control the magnitude of seismic velocity and Q reduction. As in the case of aqueous fluids, experimental and theoretical methods suggest that melt fractions ranging between $\ll 1\%$ to several percent can produce large reductions in velocity and increases in attenuation (10s percent and more; see, e.g., Gribb and Cooper 2000; Takei 2002; Faul et al. 2004; Takei and Holtzman 2009a, b, c).

13.3.2 Seismic Methods for Imaging Fluids (Free and Mineral Bound) in the Deep Crust and Upper Mantle

After reviewing how seismic properties are affected by rock-water interactions, we now turn our attention to the seismic methods that are commonly used to observe these properties in situ, for rocks of the crust and upper mantle. We provide a brief discussion of each method that provides a qualitative understanding of the physical principles on which they are based and an appreciation of their resolving power.

13.3.2.1 Seismic Tomography

Tomographic approaches rely on the properties of transmitted seismic waves to produce images of volumetric seismic velocity anomalies (V_p, V_s) or seismic attenuation (Q_p, Q_s) of the subsurface. One of the most common tomographic approaches is based on the inversion of body-wave travel times to recover velocity variations (or perturbations) through a 3-D gridded volume (see, e.g., Nolet 2008 for a review of this and other approaches involving surface waves). Attenuation tomography, on the other hand, is performed by estimating attenuation parameters on individual ray paths by spectral analysis of P and S waveforms, and then inverting these data for Q perturbations through a 3-D grid (see, e.g., Stachnik et al. 2004). The reader should also be aware of recently developed techniques that yield improved resolution of subsurface structure, which include full seismic waveform inversion (e.g., Brenders and Pratt 2007; Tape et al. 2010), and

tomographic methods based on the cross-correlation of ambient seismic noise (e.g., Shapiro et al. 2005).

Due in part to the inherent trade-off between smoothness and error misfit that characterises inverse approaches, tomographic images tend to produce spatially smooth images that are not particularly sensitive to sharp velocity boundaries. The spatial resolution of tomographic images can be defined as the smallest size perturbation that can be imaged accurately. It depends on a number of parameters such as the seismic ray coverage through the imaged volume (which in turn depends on the source and receiver coverage), the magnitude of the anomalies, and the frequency content of the seismic signal. For adequate coverage, the resolution is proportional to the quantity $\sqrt{\lambda \cdot l}$, where λ is the wavelength of the signal and l is the length of the ray.

Travel-time tomography approaches, that seek to image seismic structure in the crust and upper mantle at regional scales, can use controlled sources (e.g., long-range refraction/wide-angle profiles), local earthquake sources, or teleseismic sources. The spatial resolution afforded by P-wave models is of the order of a few km to 10s of kilometres for controlled source applications (depending on the source/receiver density and depth), ~10–35 km for local earthquake source applications, and ~50–70 km for teleseismic approaches.

13.3.2.2 Seismic Reflection

Seismic reflection is a controlled-source technique that relies on recordings of near-offset seismic body-waves that are reflected at sharp discontinuities in material properties in the subsurface. These recordings are corrected for differential travel-times as a function of offset and stacked to increase their signal-to-noise ratio. The signals are mapped to depth using a range of possible techniques involving varying degrees of sophistication (from simple 1-D time-depth conversions to more involved 2-D or 3-D back projection-migration operators) to form vertical profiles of seismic discontinuities of the crust and uppermost mantle. The strength of the imaged reflectors is proportional to the seismic impedance contrasts at the discontinuities and to the thickness of the discontinuities, i.e., where a discontinuity can either be perfectly sharp or gradational over a finite thickness. Spatial resolution can thus be defined, here, as either the maximum gradient thickness that a discontinuity must have to produce an observable reflection, or as the minimum separation for two perfectly sharp discontinuities to be distinguishable. A commonly used rule of thumb suggests that this quantity is of the order of $\lambda/4$, though complete separation between two discontinuities is achieved at $\lambda/2$, where λ is the wavelength of the signal (see, e.g., Levander et al. 2006). For a typical frequency range of ~10–50 Hz in crustal seismic studies, the value of λ for P-waves ranges between ~508 and 116 m in the upper crust (for $V_p = 5.8$ km/s), ~700–140 m in the lower crust (for $V_p = 7.0$ km/s), and ~810–162 m in the upper mantle (for $V_p = 8.1$ km/s).

13.3.2.3 Passive-Source Converted and Scattered Wave Imaging

Methods in this section exploit the phenomenon of scattering and conversion of teleseismic waves at sharp discontinuities of the subsurface. They are similar to reflection methods in the type of structure they image, but complement these methods in terms of their probing depth since they illuminate the structures from below instead of from the surface. Another key difference is that these passive imaging techniques rely principally on P-to-S converted waves in the coda of P-waves (and also on S-to-P conversions in the percusory signal of S waves) to identify discontinuities. As in the case of reflection imaging, the recorded traces are source-normalised and stacked to increase the signal-to-noise ratio. The mapping to depth is done either in 1-D below single stations or array of receivers, in an approach commonly referred to as receiver function (RF) imaging, or using back-projection migration operators that can image structures in 2-D and 3-D below arrays of receivers (see, e.g., Vinnik 1977; Langston 1979; Dueker and Sheehan 1997; Bostock and Rondenay 1999; Levander et al. 2006; and for a review, see Rondenay 2009). In their applications to direct imaging, these approaches produce profiles highlighting discontinuities from the lower crust to the mantle transition zone. The amplitude of these signals is more sensitive to rapid changes in V_s than to density perturbations, as the latter have more influence on reflection coefficients than on transmission coefficients (see, e.g., Rychert et al. 2007). Spatial resolution is defined in the same way as in reflection seismic, though with a value that is now twice as large ($\lambda/2$ rather than $\lambda/4$) given that the process involves transmission instead of reflection (see Rondenay 2009). The maximum frequency of signals analysed is typically between 0.3 and 1.5 Hz, yielding spatial resolutions of ~6.7–1.3 km in the lower crust ($V_s = 4.0$ km/s), and ~7.8–1.6 km in the uppermost mantle ($V_s = 4.7$ km/s). RF signals can also be inverted to obtain layered velocity models of the crust (Ammon et al. 1990), and for estimating the average Poisson's ratio of the crust (Zhu and Kanamori 2000).

13.3.2.4 Shear-Wave Splitting Analysis

This category of approaches is used to characterize seismic anisotropy in the subsurface. It exploits the phenomenon whereby shear waves, that travel through anisotropic media, are split into two quasi-S waves that are polarized along the principal axes of anisotropy and thus travel at different velocities – a phenomenon similar to optical birefringence (for reviews on the topic see Silver 1996; Savage 1999; and Fouch and Rondenay 2006). Shear-wave splitting analysis consists of applying an operator to split shear waves recorded at the surface (commonly S and SKS waves) to recover the directions of the principal axes of anisotropy and the strength of the anisotropy. The method generally assumes hexagonal anisotropy with a horizontal axis of symmetry, and returns two parameters: the azimuth of the fast polarization axis ϕ, and the time shift between the two split waves δt, which is

representative of the strength of anisotropy (product of percent anisotropy and thickness of the anisotropic layer). Values of anisotropic parameters are usually given for single stations using multiple events. The lateral resolution below the stations is defined by the Fresnel zone of the seismic rays that are analysed (e.g., 90 km radius at 120 km depth of a vertically incident SKS wave with 12 s dominant period; see Fouch and Rondenay 2006). Conversely, the method is insensitive to the depth extent and vertical position of the anisotropic layer, since it measures a path-integrated process. It is still possible to obtain constraints on the depth of anisotropy, though. This is done, for example, by interpreting shear-wave splitting results in conjunction with surface waves sampling a region of interest from various azimuths (see, e.g., Chen et al. 2007).

This completes our review of the resistivity and seismic properties of crustal and upper mantle rocks that can detect fluids that cause metasomatism in the Earth. We now proceed with case studies that will illustrate the applicability of geophysical approaches to detect metasomatism in different geodynamic environments.

13.4 Mid-Ocean Ridges

Hydrothermal circulation of seawater causes extensive serpentinization of the newly formed oceanic crust at the global mid-ocean ridge system. It has been estimated that this causes a 20–30% volume increase (Bach and Früh-Green 2010). Hydrothermal circulation within the oceanic crust at a mid-ocean ridge has been imaged with EM geophysical data, primarily using a system of transmitters and receivers. Hydration of the ocean plate also occurs as it bends and enters a subduction zone. Seismic imaging of faulting has defined this process in Central America and shown that the fluids circulate deep enough to hydrate both the oceanic crust and the mantle (Ranero et al. 2003). Magnetotelluric profiles collected onshore and offshore Costa Rica have imaged the deep circulation of the hydrothermal fluids (Worzewski et al. 2010).

13.5 Subduction Zones

Subduction zones are important in the global tectonic cycle because of their role in transporting fluids from the surface of the Earth into the crust and upper mantle. This provides a link between the Earth's hydrosphere, lithosphere, and biosphere. The significance of fluids in controlling the properties and evolution of the lithosphere cannot be overstated (Wannamaker 2010). Water is transported in the subducting plate as both (1) free water within sediments and the ocean crust and (2) as hydrated minerals in the oceanic crust (e.g., amphiboles) and in the upper mantle (e.g., serpentine; see Fig. 13.18). This water is released in the subduction zone over a depth range that extends from the surface to at least 200 km (Hyndman

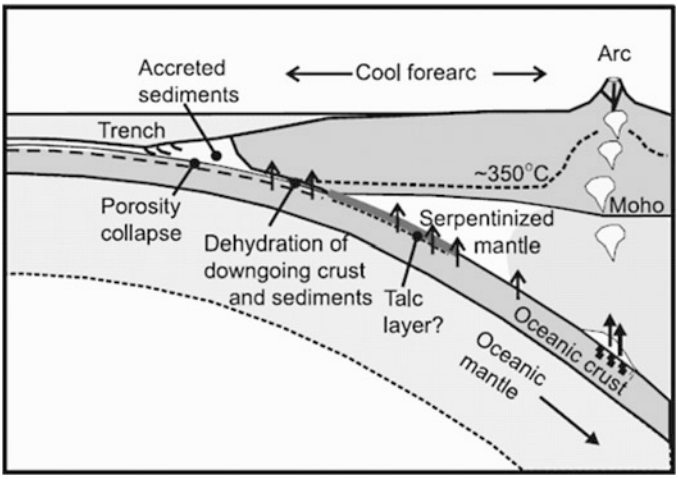

Fig. 13.18 Schematic of fluid flux in a subduction zone, based on Fig. 13.1 from Hyndman and Peacock (2003)

and Peacock 2003). Some recent studies suggest that significant water may be transported as far as the mantle transition zone (Bercovici and Karato 2003; Booker et al. 2004)

This release of fluids controls the processes that occur in the subduction zone. For example compression of the seafloor sediments causes porosity collapse that expels water as the accretionary wedge develops. Deeper in the lithosphere, increasing temperature and pressure in the downgoing slab drives prograde metamorphic reactions that generate fluids (e.g. basalt to eclogite in the slab, plus others). These fluids migrate upwards and can cause retrograde metamorphic reactions in the colder part of the mantle wedge, e.g. addition of water to the mantle wedge converts peridotite into serpentinite. The release of water at greater depths (i.e., ~100 km) causes a lowering in the melting point of the mantle and triggers melting that supplies the volcanic arc. This is a key part of the mechanism that has led to the development of a felsic crust and the presence of continents on the surface of the Earth (O'Neill et al. 2007).

Geophysical imaging has played a significant role in the development of the view of subduction zones summarized above. This is because the presence of fluids can change the seismic velocity and electrical resistivity of rocks. Seismic and magnetotelluric surveys have contributed in two distinct ways: (1) they are able to detect fluids within a subduction zone, and (2) they can also detect the changes that occur in rocks as they undergo metamorphism. These geophysical studies have also allowed the first steps to be made towards quantifying the rate of fluid flux into the lithosphere (Hyndman and Peacock 2003). The Cascadia subduction zone is one of the best studied subduction zones in the world and will be the focus of this section. References to studies of other subduction zones are included to keep the discussion as general as possible.

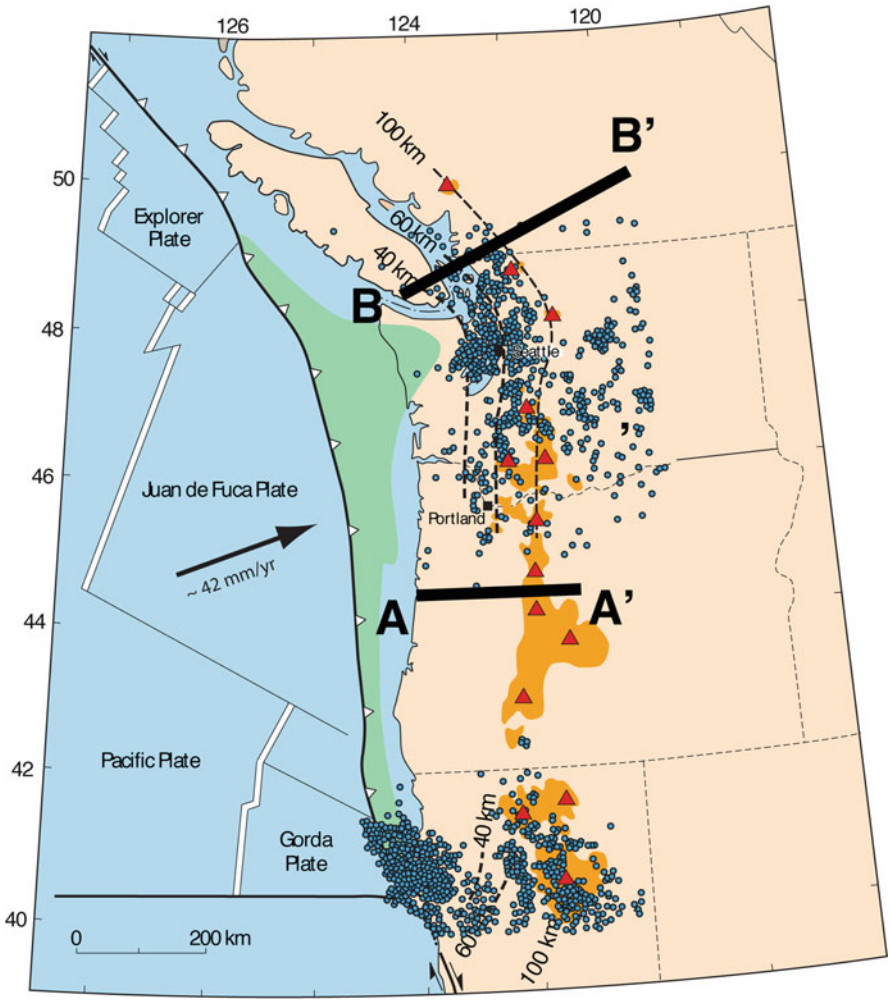

Fig. 13.19 Simplified tectonic map of the Cascadia subduction zone. Line A-A' and B-B' indicate the location of geophysical profiles discussed in the text. *Blue circles* denote earthquakes and *red triangles* indicate the locations of Quaternary arc volcanoes. (Figure is modified from Romanyuk et al. (1998))

13.5.1 Tectonic Setting and Geophysical Studies of the Cascadia Subduction Zone

The Cascadia Subduction Zone (CSZ), which is shown in Fig. 13.19, extends along the west coast of North America, from southern British Columbia to northern California. In the CSZ, the Juan de Fuca plate subducts beneath North America at a rate of 35–45 mm/year in a NE direction (DeMets et al. 1994). Along the trench,

the subducting plate is very young (i.e., 6–10 Million year; Wilson 2002), placing it at the warm end of the spectrum of plate thermal structures (Hacker et al. 2003b; Hyndman and Wang 1993; Kirby et al. 1996). It is among the youngest subducting plates on the planet to produce a continuous volcanic arc, with Quaternary volcanoes that extend along nearly the entire length of the subduction zone. A Wadati-Benioff zone is observed between 40 and 90 km depth in the northern CSZ, north of 47°N, suggesting a slab dip steepening from 10° to 30° in that region. Conversely, intra-slab seismicity is conspicuously absent in Oregon for reasons that are not well understood (e.g., Wells et al. 2002). Yet, active volcanism, magnetotelluric analyses and seismic images support the existence of a dehydrating slab that is continuous to at least 150–200 km depth beneath the central CSZ (e.g., Rasmussen and Humphreys 1988; Wannamaker et al. 1989; Rondenay et al. 2001). Below, we briefly summarize the types of MT and seismic investigations that have been undertaken across Cascadia over the last three decades.

Kurtz et al. (1986, 1990) presented one of the first MT studies of a subduction zone with a profile crossing southern Vancouver Island. Though it yielded compelling evidence for the existence of fluid-rich zones in the system, it has been shown that such MT onshore data may be strongly influenced by the presence of nearby oceans, as these are the largest conductors found on the surface of the Earth. Thus, MT profiles that combine both onshore and offshore MT data, such as the one discussed below, have the potential to image onshore resistivity structures more reliably than a profile with just onshore data (Evans et al. 2002).

The EMSLAB project was the first major effort to apply magnetotellurics to study a subduction zone from the oceanic plate to the continental interior. The survey used an east–west transect in central Oregon that was more than 1,000 km long. Wannamaker et al. (1989) described the resistivity model derived by forward modelling both the onshore and offshore MT data (see Fig. 13.20). Since the Vancouver Island and EMSLAB studies from the 1980, new images of the Cascadia subduction zone have been published by several authors (Aprea et al. 1998; Vanyan 2002). This has included the first long-period MT data capable of imaging the lower crust and upper mantle of the Cascadia Subduction zone across southern British Columbia (Soyer and Unsworth 2006; see Fig. 13.21). Previous studies used only broadband MT data that were limited in the depth of penetration.

Cascadia has been studied seismically using a wide variety of approaches, including imaging with off-shore and on-shore controlled source data, and analyses of broadband data from permanent stations or dense networks. Controlled-source studies provide images of seismic discontinuities and volumetric anomalies in the 0–50 km range. They have been conducted across the accretionary wedge and forearc mantle wedge in southern British Columbia (Green et al. 1986; Clowes et al. 1987; Calvert 1996, 2004), Washington state (Flueh et al. 1998; Preston et al. 2003), and in Oregon (Tréhu et al. 1994). Other controlled-source transects were designed to investigate the volcanic arc (e.g., Leaver et al. 1984; Tréhu et al. 1994; Miller et al. 1997). Regional 3-D velocity models, based on active-source and local earthquake data, have provided detailed crustal structure across large portions of the Cascadia subduction zone (Parsons et al. 2005; Ramachandran et al. 2006).

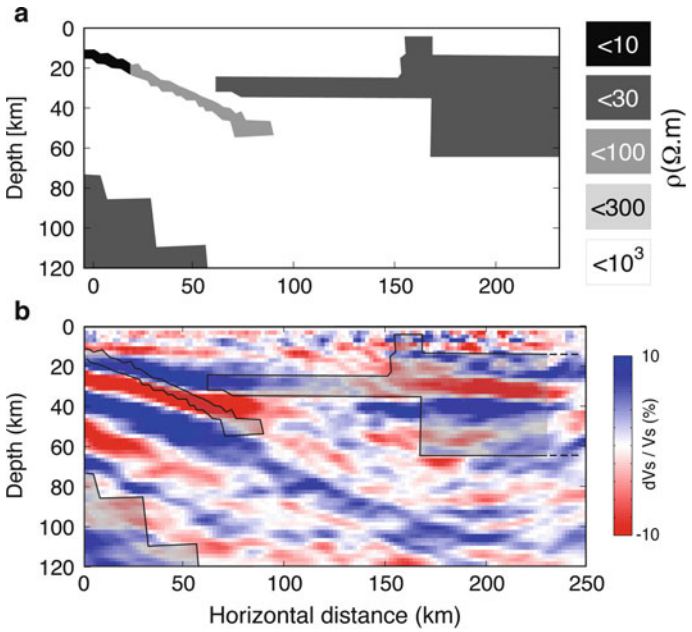

Fig. 13.20 Comparison of MT and seismic results across central Oregon – profile A-A' in Fig. 13.19. (**a**) Resistivity model derived from forward modelling of MT data recorded as part of the EMSLAB project (Wannamaker et al. 1989). (**b**) Seismic discontinuity profile derived from inversion of teleseismic scattered waves (Rondenay et al. 2001). *Shaded* area indicates the projection of conductive features superimposed on the seismic image

Broadband seismic studies have yielded tomographic velocity models of the entire Cascadia subduction zone between 0 and 400 km depth (Rasmussen and Humphreys 1988; VanDecar 1991; Bostock and VanDecar 1995; Zhao et al. 2001; Xue and Allen 2007; Roth et al. 2008), and high-resolution profiles of seismic discontinuities in the 0–150 km range across southern British Columbia, Washington and central Oregon (Rondenay et al. 2001; Nicholson et al. 2005; Abers et al. 2009). Individual broadband stations have also been used to analyse velocity and anisotropy structure beneath the region (Langston 1977, 1979; Cassidy and Bostock 1996; Park et al. 2004).

13.5.2 Subducted Crust and Slab Dehydration

The MT study of Kurtz et al. (1986, 1990) revealed an eastward dipping zone of low resistivity beneath southern Vancouver Island that was inferred to represent the uppermost part of the subducting Juan de Fuca Plate. The low resistivity zone was coincident with a dipping set of reflectors, the E-horizon of Green et al. (1986). Active source seismic studies have shown that both the low resistivity layer and

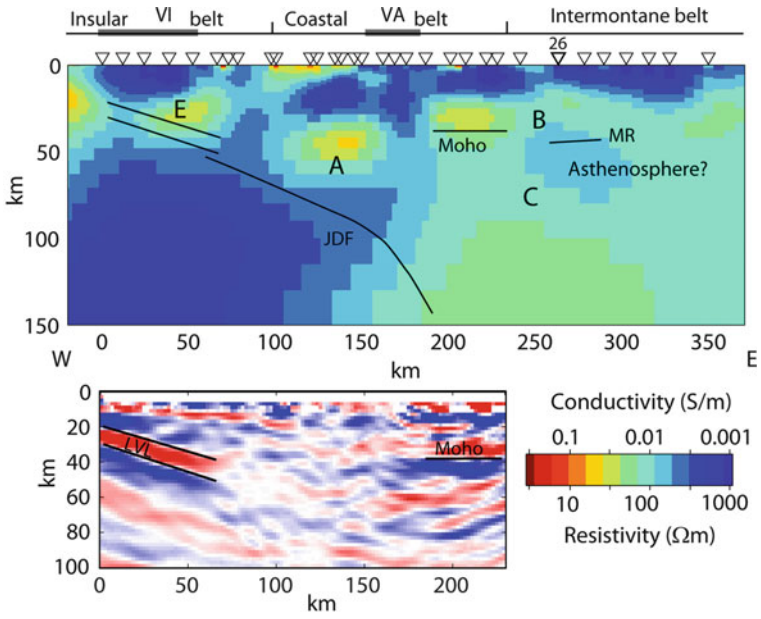

Fig. 13.21 Comparison of MT and seismic results across southern British Columbia – profile B-B' in Fig 13.19. (**a**) Resistivity model for Cascadia Subduction Zone derived from inversion of the magnetotelluric data (Soyer and Unsworth 2006). (**b**) Seismic discontinuity profile derived from inversion of teleseismic scattered waves (Nicholson et al. 2005). *Black lines* in both panels show the interpretation of imaged features

reflectors are located in the overriding North American Plate some 10 km above the subduction thrust in the crust, reflecting fluids derived from the Juan de Fuca Plate that are trapped by an impermeable layer at a temperature of around 400°C (Hyndman 1988). The observed resistivity can be explained by a 1–2% porosity filled with saline fluids. A debate has continued about the exact origin of the E-horizon with Calvert and Clowes (1990) proposing it to be a shear zone associated with subcreted sediments because the fluids alone could not explain the strength of the reflections.

At the regional scale, recent high-resolution seismic profiles based on teleseismic scattered waves suggest that the subducted crust is represented by a thin, low-velocity layer that extends from ~20 km depth beneath the coast to ~40 km depth beneath the forearc basin (Rondenay et al. 2001; Nicholson et al. 2005; Abers et al. 2009). The spatial extent of this low-velocity layer appears to coincide with dipping conductive structures detected by Wannamaker et al. (1989) in central Oregon (see Fig. 13.20), and by Soyer and Unsworth (2006) in southern British Columbia (see Fig. 13.21). Note that in each figure, both the low-velocity layer and the dipping conductor appear to terminate where the Juan de Fuca plate comes in contact with the mantle wedge. These results have raised new questions about the exact location of the dipping electrical features, but regardless of whether

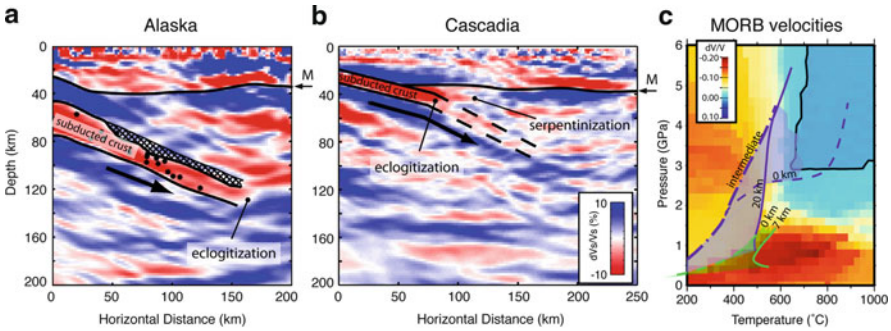

Fig. 13.22 Seismic imaging of slab dehydration reactions. Comparison between seismic profiles of (**a**) an older, thus cooler subducted slab in southern Alaska, and (**b**) a younger, thus warmer subducted slab in Cascadia. (**c**) Estimated P-T paths of both subducted crusts (Cascadia in *green*, Alaska in *purple*) superimposed on velocity perturbations of metamorphosed mid-ocean ridge basalts (MORB). The P-T paths are calculated by running geodynamic models, and denote temperatures at the subduction interface (*dashed lines*), the subducted Moho (*solid line*), and, for Alaska, the depth of minimum crustal temperature (*dash-dot line*). Velocity perturbations are estimated following Hacker and Abers (2004), and Hacker (2008). They are slightly different than the plots described in Sect. 13.3.1.2 because a different approach is used to calculate mineral modes (Figures are modified from Rondenay et al. (2008))

the conductive layer is situated at the top of the subducted slab or above the subduction interface, it is clearly the product of progressive dehydration of the subducted oceanic slab. Our first concern is thus to address slab dehydration.

The spatial extent of slab dehydration has been inferred through (1) the mapping of intraslab seismicity (e.g., Hacker et al. 2003b; Rüpke et al. 2004; Brudzinski et al. 2007), (2) the characterization of low-velocity layers by waveform modelling (e.g., Abers 2005), and (3) direct seismic imaging (e.g., Rondenay et al. 2008). Although all these approaches provide important complementary constraints on this process, here we will focus on the last one. In their study, Rondenay et al. (2008) compared the seismic profiles of two thermally distinct subduction zones, Cascadia and Alaska, and used constraints from geodynamic and petrological models to interpret the seismic images in terms of dehydration reactions. They found that the low-velocity dipping layer is associated with hydrated basalts, that its termination can be explained by the transformation of these basalts into eclogite, and that the depth of this transformation is dependent on the thermal state (age) of the slab. Thus older, colder slabs (e.g., Alaska) possess subducted crusts that persist as low-velocity layers to much greater depths than those of younger, warmer slabs (e.g., Cascadia). Figure 13.22 shows a comparison between the two imaged slabs and their thermal state as a function of increasing P-T conditions. These results, which generally agree with those from other approaches mentioned above, indicate that high-resolution seismic profiling can image robustly where dehydration reactions take place.

13.5.3 Flux of Fluids into the Overriding Crust

As the subducting slab dehydrates, fluids flux into the subducting crust and potentially into the overlying portions of the subduction system. In regions where the slab is in direct contact with the overriding crust, fluids may thus form a channel that runs parallel to the interface – either above or beneath the interface. The dipping conductive layers mentioned in the previous section (Kurtz et al. 1986; Wannamaker et al. 1989; Soyer and Unsworth 2006) may represent a direct evidence of these channels. Recent seismic results have also shown evidence for such channels in the form of sharp seismic discontinuities across southern British Columbia and Washington state (e.g., Audet et al. 2009; Abers et al. 2009). As mentioned in the previous section, some authors have suggested that this channel is formed in the overriding crust above the subduction interface (e.g., Hyndman 1988). Conversely, the receiver function study of Audet et al. (2009), which detects a dipping layer with an anomalously high Poisson's ratio, suggests a layer of overpressured hydrous fluids trapped under a sealed plate boundary at the subduction interface. This channel would comprise the entire column of the subducted crust.

The existence of fluids, potentially trapped at the subduction interface, is believed to play an important role in the recently discovered process of episodic tremor and slip (ETS). ETS are recurrent bursts of non-volcanic tremors that are accompanied by aseismic slip events occurring down-dip of the locked segment of the subduction interface (see, e.g., Rogers and Dragert 2003). They have been observed in the subduction zones of Cascadia, Japan, Alaska, Mexico, and Costa Rica (Rogers and Dragert 2003; Obara et al. 2004; Peterson and Christensen 2009; Payero et al. 2008; Brown et al. 2009). Although their exact cause is still unknown, it has been widely believed since their discovery by Obara (2002), that tremors are related to the presence of free fluids in the vicinity of the subduction interface, i.e., fluid flux from the slab and/or high pore-fluid pressure in the subducted crust (e.g., Shelly et al. 2006; Audet et al. 2009). In this scenario, the tremors may be associated with the movement of fluids (e.g., hydrofracturing) or to a modification of the stress conditions at the subduction interface. The recent study of Abers et al. (2009) across Washington state clearly shows a direct correlation between the lateral (trench-normal) extent of the tremors and that of the dipping low-velocity channel at the top of the subducted slab. This result, in conjunction with a similar conductive structure inferred from MT, suggests that seismic and MT analyses can help directly image the source region of ETS.

13.5.4 Flux of Fluids into the Mantle Wedge

Down dip of the intersection between the top of the subducted slab and the base of the overriding crust, fluids are fluxed from the slab into the mantle wedge. In the upper corner of the mantle wedge, where temperatures are cooler, water-rich fluids

cause alteration of mantle peridotites into serpentine and associated accessory minerals (see Sect. 13.3.1.2; and the review by Hyndman and Peacock 2003). At greater depth, in the warm circulating portion of the mantle wedge, the influx of water-rich fluids trigger partial melting of mantle peridotites by lowering their melting temperature (see, e.g., Grove et al. 2006). Here, we will focus on the effects of water on the hydration-alteration of the mantle wedge. For a comprehensive review about geophysical observation of magma distribution in subduction zones, the reader is referred to Wiens et al. (2008).

Kamiya and Kobayashi (2000) presented one of the first direct geophysical observations of serpentine alteration in the mantle wedge using P- and S-wave tomography across central Japan. They interpreted a localized region with a high V_p/V_s ratio (>0.3) in the corner of the mantle wedge (20–45 km depth) as being due to the presence of serpentinite. Similar observations were made soon after in Cascadia with tomographic models (Zhao et al. 2001), high-resolution profiles based on teleseismic scattered waves (Bostock et al. 2002), and controlled source seismic surveys (Brocher et al. 2003). These seismic results were further supported by the magnetotelluric study of Soyer and Unsworth (2006), who observe a low resistivity zone 'A' that was shown to be required by the data (see Fig. 13.21). Other magnetotelluric studies of subduction zones that revealed how fluids are transported to depth, then released to cause metamorphism include those in Mexico (Jodicke et al. 2006), and Costa Rica (Worzewski et al. 2010). Mantle wedge serpentinization can also be observed by potential field methods. For example, Blakely et al. (2005) suggest that the forearc mantle wedges in Cascadia and Alaska both exhibit negative gravity anomalies associated with serpentine, combined with positive magnetic anomalies due to magnetite, which itself is an accessory mineral of serpentinization.

In the Cascadia profiles, derived from teleseismic scattered waves, the presence of serpentine has been inferred from an anomalous response of the continental Moho (see Bostock et al. 2002). In most of these profiles, a clear Moho is observed on the east side of the sections with a characteristic increase in velocity from crust to mantle. However above the mantle wedge, an anomalous structure is observed with either a very weak Moho in southern British Columbia and central Washington (see Fig. 13.21 between model offsets of 70 and 170 km; see, also, Abers et al. 2009), or even a reversed polarity Moho in central Oregon (Bostock et al. 2002; see also Figs. 13.20b and 13.22b between 50 and 130 km model offsets). This implies that there is either a minimal or inverted velocity contrast between the crust and mantle, with the mantle here exhibiting anomalously low velocities. Brocher et al. (2003) notes that this same Moho behaviour is observed in the form of an absent or muted Moho reflection (P_mP) below refraction lines that sample the forearc along the entire length of the CSZ.

Bostock et al. (2002) used constraints from thermal models and petrological results to interpret this unusual Moho response as due to serpentine. First, thermal models show that the weak or inverted Moho is present directly above the portion of the mantle wedge where temperatures are below ~650°C, the maximum temperature at which serpentine is stable (see Sect. 13.3.1.2). Second, they show that an

inverted Moho implies an upper-mantle S-wave velocity $\leq$3.25 km/s, which implies a level of serpentinization of 50–60% based on petrological results. Christensen (2004) later pointed out that these conclusions were based on measurements for lizardite, a lower temperature variety of serpentine. Instead, if one considers results for antigorite (the variety of serpentine stable at the highest temperature, see Sect. 13.3.1.2 and Fig. 13.14), velocities cannot be lowered to 3.25 km/s by serpentine alone and thus an additional mechanism is required, for example, high pore pressures (Christensen 2004).

A global compilation of seismic anisotropy measurements in subduction zones by Long and Silver (2008) suggests that the introduction of water in the cold corner of the mantle wedge may lead to observable type-B fabric (see Sect. 13.3.1.3). This process is manifested by a trench-parallel fast axis of seismic anisotropy observed in many subduction zones. Experimental measurements by Katayama et al. (2009) indicate that a trench-parallel fast axis can also result from crystal-preferred orientation of deformed serpentine in subduction zones characterized by steeply dipping slabs. However, in Cascadia the fast axis is trench-perpendicular in all portions of the system and appears to stem mainly from the response of the sub-slab asthenosphere to absolute slab motion (Currie et al. 2004); a somewhat unusual observation that may be associated to the exceptionally young age of the subducted slab (Long and Silver 2008).

In terms of MT response, serpentinite can locally lower the resistivity of crustal and upper mantle rocks, compared to unmetamorphosed peridotite. This resistivity reduction occurs mainly through increased porosity, with additional conduction occurring through mineral phases such as magnetite (Stetsky and Brace 1973). Thus the low mantle resistivity observed in the Cascadia mantle forearc requires the presence of aqueous fluids, associated with ongoing metamorphism. A simple estimation of the fluid content can be made with Archie's Law, provided that the pore fluid resistivity can be estimated. Nesbitt (1993) showed that crustal pore fluid resistivity is generally in the range 0.3–0.03 Ωm. However, it should be remembered that MT gives a robust constraint on conductance, not the individual conductivity and thickness that make up a given conductance. This is illustrated for a range of fluid resistivities and cementation factors in Fig. 13.23. As expected, the same conductance can be accounted for by a porosity that decreases as the layer thickness increases. This non-uniqueness can be addressed by noting that the thickness of the mantle wedge is defined by seismic constraints at around 20 km. The value of the cementation factor, m, is likely close to unity since saline fluids will be interconnected, giving Φ in the range 0.0002–0.002 depending on the value ρ_f chosen.

13.6 Metasomatism in the Stable Continental Lithosphere

The continental lithosphere is generally viewed as a dry environment, though mounting geological and geophysical observations suggest that some parts are or have been affected by circulating fluids. This is to be expected considering that

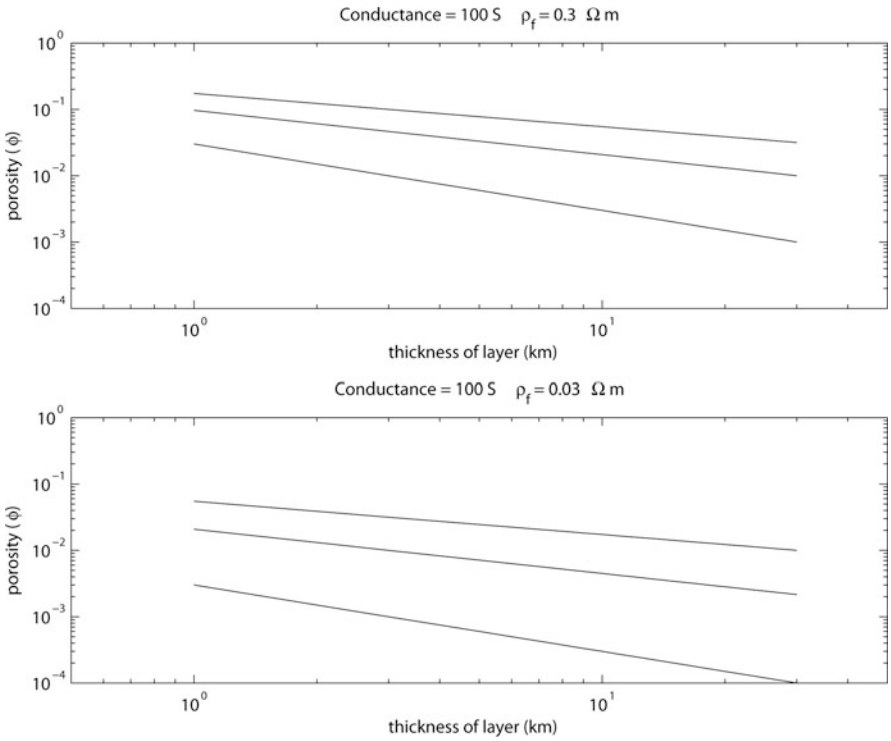

Fig. 13.23 Thickness and porosity combinations required to explain a 100 S conductor in the forearc mantle wedge. *Upper* and *lower* panels are for a pore fluid resistivity of 0.3 Ωm and 0.03 Ω m respectively. In each panel, the three curves are for cementation factors of m = 1, 1.5, and 2 in Archie's Law

subduction plays a key role in the formation of the continental crust and lithospheric mantle, both through arc volcanism and terrane accretion. Moreover, the introduction of fluids can be facilitated by post-stabilization events such as lithospheric delamination or plume interaction, as these place the lithosphere in contact with more fertile and hydrated mantle.

In this section, we will discuss the effects of water on the crust and lithospheric mantle. Instead of concentrating on one specific region, as we did in the previous section, we will focus the discussion on two main types of continental environments: (1) the lower continental crust, especially that of Phanerozoic age, which exhibits higher electrical conductivity and seismic reflectivity than the upper crust, and lower seismic velocities than those predicted by laboratory analyses of dry xenoliths; and (2) the lithospheric mantle of Archean cratons, which has been shown to contain regions of mineral alteration associated with the subduction-accretion events that played a role in their initial assembly.

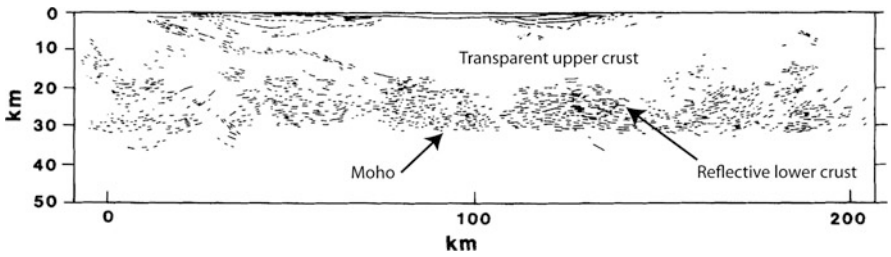

Fig. 13.24 Example of a seismic reflection profile across the southwest continental shelf of the British Isles, showing a reflective lower crust and a transparent upper crust (Modified from Matthews 1986)

13.6.1 Phanerozoic Crust

Phanerozoic crust is relatively young and formed in the last ~542 Ma. It is usually found along the periphery of continents, and is underlain by a lithospheric mantle of moderate thickness that transitions to asthenosphere at an average depth of ~100 km. Like all other types of continental crusts, Phanerozoic crust has been extensively studied by both geological and geophysical means. Geophysical observations have long found that the lower Phanerozoic crust was somewhat atypical in that it is characterized by a combination of (1) high electrical conductivity, (2) enhanced seismic reflectivity compared to the higher crust, and (3) lower seismic velocities than those predicted by experimental measurement on dry xenoliths. Here, we explore how these properties can be explained by the presence of fluids in the lower crust.

Through a compilation of MT observations, Hyndman and Klemperer (1989) observed that Phanerozoic lower crust has an average electrical resistivity of 20–30 Ωm, much lower than predicted values of 10,000–100,000 Ωm for dry lower-crustal rocks. They also noted that this average value is significantly lower than that for lower crust of Proterozoic and Archean ages (~500 Ωm); though from these observations, it is clear that most lower continental crust appears more conductive than laboratory measurements predict. Such low conductivities can be due either to interconnected porous fluids, or an interconnected conductive phase such as graphite (Jones and Ferguson 2001).

From a seismological standpoint, Phanerozoic lower crust exhibits two distinctive characteristics (Hyndman and Shearer 1989; Hyndman and Klemperer 1989). First, it is generally more reflective than the upper crust (see Fig. 13.24). It has been proposed that this is due to the presence of lenses rich in porous fluids (Hyndman and Shearer 1989; Suetnova et al. 1994); to a composition made of alternating metamorphic rocks with differing acoustic impedances (Christensen 1989); or to a combination of the two. Second, Phanerozoic lower crust has lower seismic velocities than those predicted by lab measurements made on mafic rocks (i.e., ~6.6–6.75 km/s compared to predicted

velocities of >7.00 km/s; Hyndman and Klemperer 1989). This could be simply explained by assuming that Phanerozoic lower crust is composed primarily of intermediate composition rocks that exhibit lower seismic velocities. However, analyses of deep crustal xenoliths recovered at the surface tend to indicate a predominantly mafic composition (see Hyndman and Klemperer 1989; and references therein). Alternatively, the low velocities could be due to the presence of a fluid phase, i.e., either an aqueous fluid or a partial melt. Though since the temperatures are relatively low in the lower-crust of stable continental settings (lower than the vapour-saturated solidus), the most likely candidate here would be an aqueous fluid.

Although the electrical and seismic characteristics of Phanerozoic lower crust can be explained in several ways, the model that best explains all the observations is the presence of a saline aqueous fluid in interconnected pores. Calculations made by Hyndman and Shearer (1989) and Hyndman and Klemperer (1989), based on the effective medium theory implementation of Schmeling (1985), suggest that these observations can be explained by only 1–2% porous water. Their model considers water in intergranular pores as opposed to actual fractures, since an extensive network of open fractures is unlikely under high-pressure conditions corresponding to lower crustal depths. As seen in Sects. 13.2 and 13.3, the important parameters for estimating the electrical and seismic properties are the porosity, as well as the dihedral angle and aspect ratio of the pores. For their estimates, Hyndman and Shearer (1989) use an average dihedral angle of ~60°, Archie's Law exponents between 1.5 and 2, and pore aspect ratios of 0.03–0.1, all of which are based on experimental results. Thus, for an average resistivity of 20–30 Ωm, they find that a porosity of 0.5–3% is needed if the fluid has a salinity equivalent to that of seawater. As for seismic observations, impedance contrasts of 5–10% as those observed require 1–4% porosity (Hyndman and Shearer 1989; Fig. 13.13b), and velocity reductions of 5% can be explained by 1–2% porosity (Hyndman and Klemperer 1989; Fig. 13.13a).

As described above, possible fluid sources include dehydration from underlying subducted slabs or mantle devolatilization processes, which may inject fluids throughout the entire crustal column. This raises an important question, though, as to why these inferred fluids are confined to the lower crust. Hyndman and Shearer (1989) suggest that the minimum depth is constrained by a temperature of 350–400°C, which may mark an impermeable horizon formed by a hydration reaction (at the top of greenschist facies conditions) or silica precipitation. Porous water may thus remain trapped under this boundary over geological time. The fact that equivalent properties may not be found in Precambrian lower-crust is attributed to potential tectonothermal events that dehydrate the lower crust by prograde metamorphic reactions. However, relict metasomatism may still be found deeper in the thick lithospheric roots of Archean cratons as discussed in the next section.

13.6.2 Archean Cratons

Archean cratons often form the nuclei of Precambrian continental shields. They are generally thought of as highly stable entities whose longevity is attributed to the combined effects of their deep, coherent lithospheric roots (i.e., tectosphere, Jordan 1978) and the protection afforded by neighboring Proterozoic orogens (see, e.g., Lenardic et al. 2000, 2003). As in the case of the crust, water may be introduced into the cratonic lithosphere during its assembly and through alteration processes that occur after its stabilization.

Let us first consider the assembly stage. Geological and geochemical mapping of crustal lithologies suggest that Archean provinces were assembled through tectonic processes similar to, although perhaps more vigorous than, those that have been active during Phanerozoic times (see, e.g., Helmstaedt and Schulze 1989; Calvert et al. 1995; Albarède 1998, and references therein). Mechanisms invoked for their assembly include imbrication of island arcs and oceanic plateaus, and possible accretions to even older proto-cratonic nuclei (see, e.g., Ludden and Hubert 1986; de Wit et al. 1992; Albarède 1998). These mechanisms are driven by subduction. Thus water-rich fluid is introduced both by dehydration of the subducted slabs and by advection of hydrated terranes from the near surface into the deep structure of the lithosphere.

After their assembly and stabilization, some Archean cratons have experienced only limited reworking, such as kimberlite injection and/or local interactions with mantle plumes (e.g., Superior craton; Rondenay et al. 2000). Conversely, other cratons were deeply modified by large-scale events, such as lithospheric delamination (e.g., North China Craton; Gao et al. 2002). All of these alteration processes, whether local or regional, have the potential to inject water-rich fluids into the lithosphere by putting it directly in contact with more fertile/hydrated mantle that either replaces the delaminated lithosphere or intrudes it.

Given the involvement of water in processes of cratonic assembly and evolution, it is likely that signs of water circulation should remain visible in the cratonic lithosphere over geological time scales. Here, we discuss a recent geophysical study carried out in the Slave craton that supports this hypothesis. The Slave province is a small Archean craton located in the northwest corner of the Canadian Shield (Fig. 13.25). Exposed lithologies mainly comprise Late Archean (2.73–2.58 Ga) supracrustal and plutonic rocks, although the craton also hosts some of the oldest dated rocks on Earth, the ~4.03 Ga Acasta gneisses (Bowring et al. 1989, 1990). The Slave craton is flanked by two Proterozoic orogens, the Thelon orogen to the east and the Wopmay orogen to the west. The Slave craton is an attractive scientific target because it is well exposed and preserved, and because its underlying mantle is sampled by more than 150 kimberlite pipes (Heaman et al. 1997) that provide petrological constraints on the entire lithospheric column. The Slave craton has been the subject of extensive geophysical investigations (e.g., Bostock 1997, 1998; Bank et al. 2000; Jones and Ferguson 2001; Jones et al. 2001; Snyder et al. 2003,

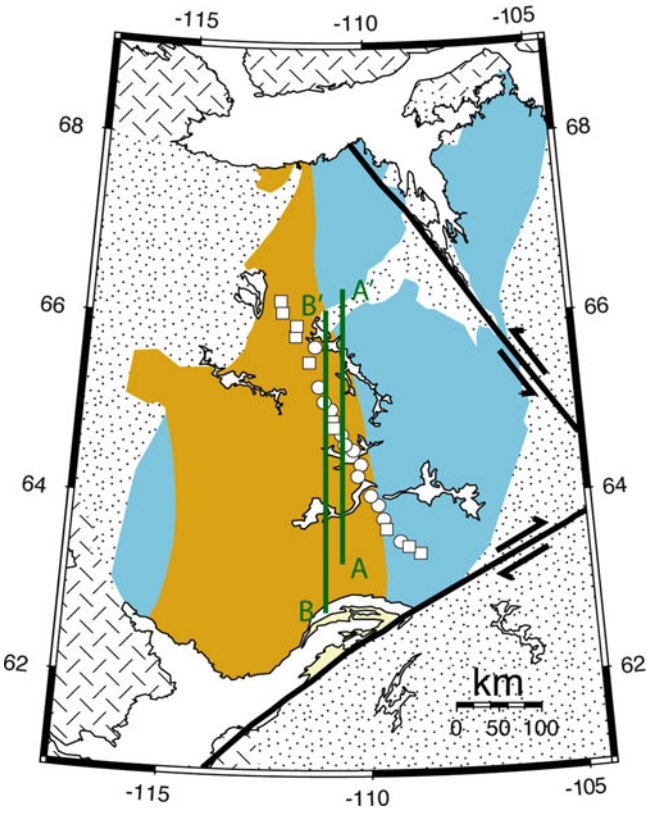

Fig. 13.25 Map of the Slave craton. *Color shaded* region denotes the exposed area of the craton, with *orange shading* showing the outline of the older Central Slave Basement Complex (4.03–2.83 Ga). *White squares* and *circles* denote seismic stations. *Black* solid lines are major faults. Projection lines of the seismic (A-A') and resistivity (B-B') profiles are indicated in *green* (Figure modified from Chen et al. (2009))

2004; Chen et al. 2007, 2009; Mercier et al. 2008). For the purpose of this discussion, we will focus on results from magnetotelluric and seismic receiver function studies.

Magnetotellurics studies of the Slave craton were among the first to clearly detect an electrical Moho, in the form of a sudden drop in resistivity from ~50,000 to ~5,000 Ωm occurring at 35.5 km depth (Jones and Ferguson 2001; Jones et al. 2001). According to Jones and Ferguson (2001), the enhanced visibility of the electrical Moho is attributed to the fact that the Slave Craton does not exhibit the conductive lower crust often found in other environments (see Sect. 13.6.1). This indicates that the crust here has probably been heated and dehydrated, as suggested by the hypothesis of Hyndman and Shearer (1989). Such resistive crust has the benefit of enhancing the sensitivity of MT data to the resistivity of

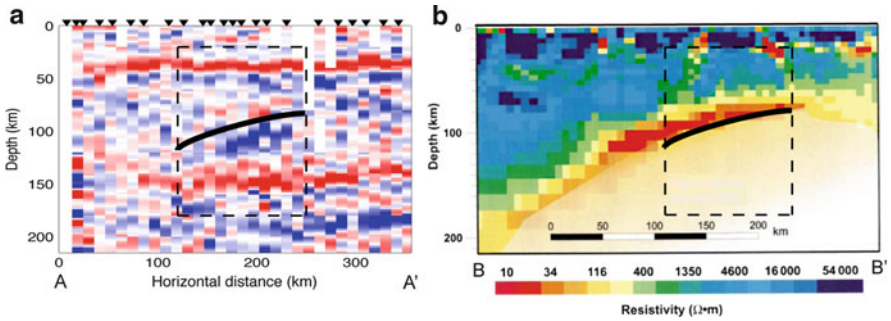

Fig. 13.26 Comparison of seismic and resistivity profiles across the central Slave craton. (**a**) Receiver function profile, *colour coded* such that *red*/*blue* represent positive/negative discontinuities in seismic velocities Vs, where a positive discontinuity represents a downward slow-to-fast transition, and a negative discontinuity represents a downward fast-to-slow transition. (**b**) Resistivity profile, with *colour scale* indicating values of electrical resistivity. See Fig. 13.25 for projection lines. The coincident seismic/electrical anomaly is indicated by a *thick black line*, in the area outlined by the *dashed box* (Figure modified from Chen et al. (2009))

the underlying mantle structures. This has allowed Jones et al. (2001) to image a strong, south-southwest dipping conductor, centred at ~100 km depth, in the cratonic lithosphere beneath the central Slave Craton. The transition from mantle rocks to the conductor marks a sharp reduction in resistivity from 1,000–10,000 Ωm to ~15 Ωm. According to these authors, the low resistivity layer is best explained by the presence of an interconnected conductive phase, most likely graphite.

In terms of seismic constraints, several recent analyses based on converted teleseismic waves and surface waves have shown evidence for a seismic discontinuity located at the same depth as the conductive anomaly described above (Chen et al. 2007, 2009; Moorkamp et al. 2007, 2010). In particular, the receiver function profile of Chen et al. (2009) images a dipping seismic discontinuity that overlaps almost exactly with the conductor detected by Jones et al. (2001). The seismic discontinuity marks a rapid decrease in seismic velocity (9–21%) with depth. A comparison of the two profiles is shown in Fig. 13.26.

In trying to interpret the coincident electrical and seismic anomalies, Chen et al. (2009) showed that they probably do not have a unique physical origin. Indeed, the most likely candidate would be the presence of a fluid or melt at depth, but P-T conditions at 100 km depth impede the prolonged existence of either fluids or melts. Instead, these authors suggest that the anomalies are related to the same process, metasomatism, but that different metasomatic alteration/deposition products cause the two anomalies. That is, hydrated minerals cause the seismic velocity reduction, and graphite causes the conductive anomaly. This hypothesis is supported by petrological analyses of mantle xenoliths sampling the anomalous region, which suggest that hydrous fluids were introduced at that depth and caused metasomatic alteration at the time of

cratonic assembly (Aulbach et al. 2007). Relying on additional evidence from diamond ages, Chen et al. (2009) suggest that this metasomatic front is associated with a subduction event that took place during paleo-Archean time (~3.5 Gyr ago) and contributed to the assembly of the lithospheric block now forming the central Slave craton. The study of Chen et al. (2009) thus presents compelling evidence that relict metasomatism can be preserved over billions of years in the cratonic lithosphere, and that combined geophysical analyses can image the affected regions.

13.7 Fluids Generated in Collision Zones

Collision zones occur in a range of tectonic settings including continent-continent collisions and arc continent collisions. In both situations, the relative buoyancy of the continental crust prevents its subduction and a region of thickening crust develops.

In an arc continent collision, such as Taiwan, the buoyant continental crust does not enter the subduction zone and a region of thickened crust develops. In the crustal root, elevated temperature and pressure causes prograde metamorphic reactions that generate fluids. Mineralization provides evidence for past fluid flow in major fault zones (Lewis et al. 2007). Magnetotelluric studies have provided evidence that this fluid flow continues today with a major conductive zone detected beneath Central Taiwan and originating in the crustal root (Fig. 13.27 and Bertrand et al. 2009). Similar tectonic processes occur beneath the South Island of New Zealand and have also formed a crustal root. The magnetotelluric results of Wannamaker et al. (2002), shown in Fig. 13.27, also show evidence of fluid generation in the crustal root, with transport upwards to the surface. These fluids clearly cause metasomatism at higher crustal levels. In both these collision zones, upper crustal material is progressively buried, and then exhumed through erosion. It has been suggested that most of the fluids are generated beneath the Southern Alps as crustal material is being exhumed (Vry et al. 2010). Figure 13.27 shows that MT is a powerful tool for imaging the pattern of fluid generation beneath an active orogen in real time. Studies to the north in the Malborough sound area have shown how fluids may play a role in the development of the orogen (Wannamaker et al. 2009).

In a continent-continent collision, such as the India-Asian collision a large region of thickened crust has formed the Himalaya and Tibetan Plateau. In places this exceeds 80 km in thickness. Radiogenic heat production in the thickened crust causes prograde metamorphism and ultimately crustal melting (Beaumont et al. 2001). These melts can tunnel horizontally and form an interconnected layer extending over a horizontal distance for 100s of kilometres. Geophysical data has given the strongest evidence for this melt layer. Seismic reflection data showed that

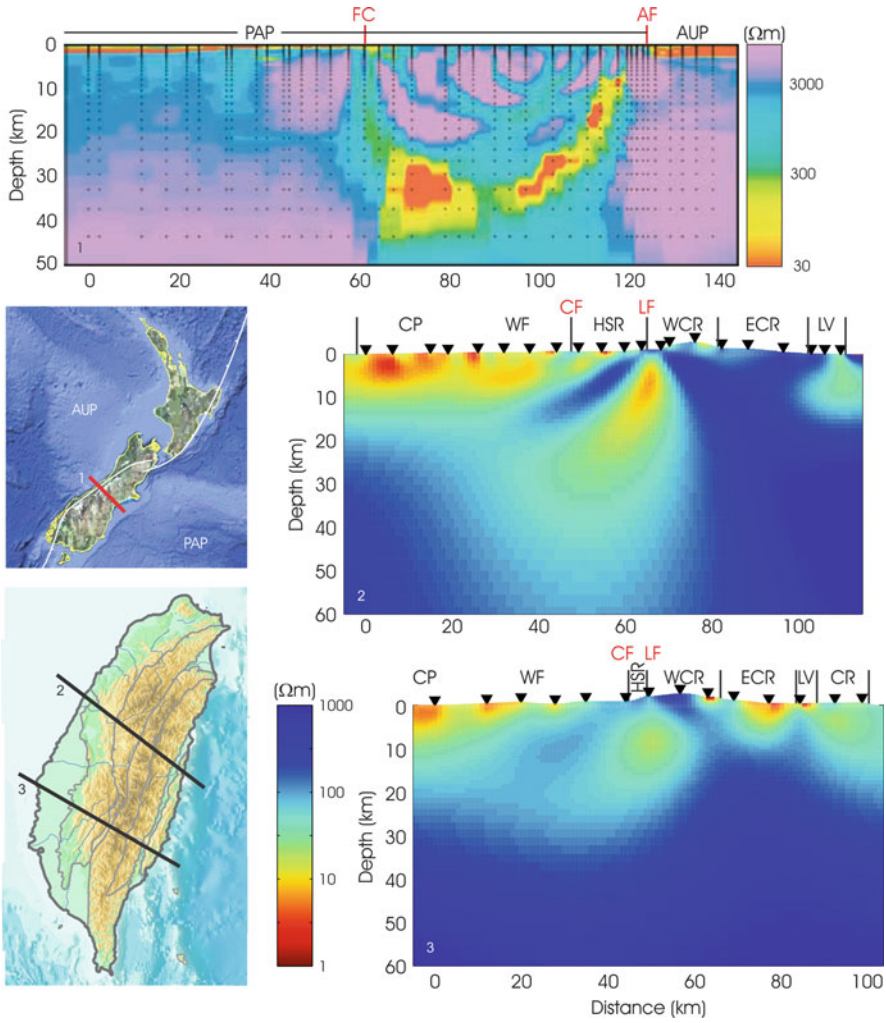

Fig. 13.27 Resistivity models of (1) New Zealand from Wannamaker et al., (2002), (2) Central Taiwan from Bertrand et al., (2009), and (3) Southern Taiwan from Bertrand (2010). In the *upper* two panels, note the zone of low resistivity extending from depths of 20–30 km to the surface, which is inferred to be a region of fluids generated by prograde metamorphism in the thickened crustal root. In Taiwan this reaches the surface at the Lishan Fault (LF) and in New Zealand this occurs beneath the Alpine Fault (AF). Note that the resistivity model of New Zealand is reversed east–west, to emphasize the similarity with Taiwan

it has a low velocity (Brown et al. 1996) and magnetotelluric data reveal a low resistivity that has been used to infer a fluid content of 5–12% (Unsworth et al. 2005) (Fig. 13.28).

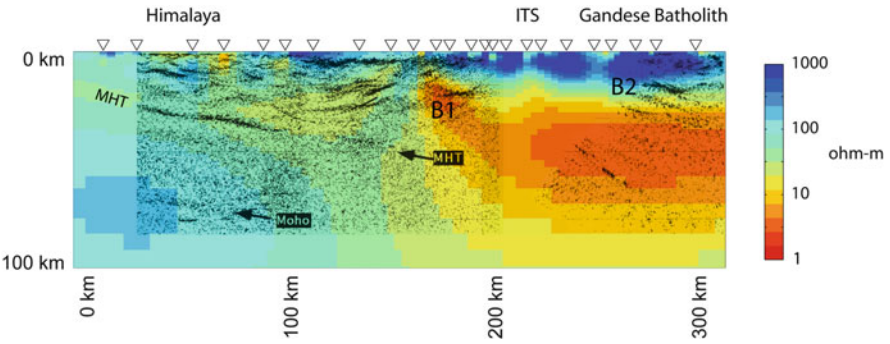

Fig. 13.28 Geophysical image of the crust below the Himalayas and southern Tibetan Plateau. *Black lines* show seismic reflection data (Nelson et al. 1996) with the Main Himalayan Thrust (MHT) interpreted as the upper surface of the underthrust Indian Plate. Triangles indicate locations where magnetotelluric (MT) data was recorded. *Colours* show electrical resistivity determined by MT exploration along the same transect (Unsworth et al. 2005). *Blues* and *green* represent the resistivity values typical of dry, cold crust and upper mantle. *Red* regions have anomalously low resistivity suggesting the presence of a fluid phase such as partial melt and/or aqueous fluids. ITS = Indus-Tsangpo suture (defines the plate boundary at the surface). B1 and B2 are seismic bright spots that are interpreted as concentrations of fluids

13.8 Conclusions

Seismic and magnetotelluric exploration are powerful tools to image fluid distribution in the crust and upper mantle. The analysis presented in this chapter shows that quantitative estimates of fluid content can be derived from both methods. As joint inversion techniques are developed to simultaneously invert both datasets, more detailed images of metasomatizing fluids will be obtained.

Acknowledgements The authors thank Michael Bostock and Nik Christensen for their reviews, and numerous colleagues for discussions on this topic over the year. We also thank the Editors for their great patience in waiting for this chapter.

References

Abers GA (2005) Seismic low-velocity layer at the top of subducting slabs beneath volcanic arcs: observations, predictions, and systematics. Phys Earth Planet Inter 149:7–29

Abers GA, MacKenzie LS, Rondenay S, Zhang Z, Wech AG, Creager KC (2009) Imaging the source region of Cascadia tremor and intermediate-depth earthquakes. Geology 37:1119–1122. doi:10.1130/G30143A.1

Aizawa Y, Barnhoorn A, Faul UH, Gerald JDF, Jackson I, Kovács I (2008) Seismic properties of Anita Bay dunite: an exploratory study of the influence of water. J Petrol 49(4):841–855. doi:10.1093/petrology/egn007

Albarède F (1998) The growth of continental crust. Tectonophysics 296:1–14

Ammon CJ, Randall GE, Zandt G (1990) On the non-uniqueness of receiver function inversions. J Geophys Res 95:15303–15319

Aprea CM, Unsworth MJ, Booker JR (1998) Resistivity structure of the Olympic mountains and Puget Lowlands. Geophys Res Lett 25:109–112

Archie GE (1942) The electrical resistivity log as an aid in determining some reservoir characteristics. Trans Am Inst Min Metall Pet Eng 146:54–62

Audet P, Bostock MG, Christensen NI, Peacock SM (2009) Seismic evidence for overpressured subducted oceanic crust and megathrust fault sealing. Nature 457:76–78. doi:10.1038/nature07650

Aulbach S, Pearson NJ, O'Reilly SY, Doyle BJ (2007) Origins of xenolithic eclogites and pyroxenites from the central Slave Craton, Canada. J Petrol 48(10):1843–1873. doi:10.1093/petrology/egm041

Austrheim H, Erambert M, Engvik AK (1997) Processing of crust in the root of the Caledonian continental collision zone: the role of eclogitization. Tectonophysics 273:129–153

Auzende AL, Pellenq RJM, Devouard B, Baronnet A, Grauby O (2006) Atomistic calculations of structural and elastic properties of serpentine minerals: the case of lizardite. Phys Chem Miner 33:266–275. doi:10.1007/s00269-006-0078-x

Babuška V, Cara M (1991) Seismic anisotropy in the earth. Kluwer, Dodrecht, 217pp

Bach W, Früh-Green G (2010) Alteration of the oceanic lithosphere and implications for seafloor processes. Elements 6:173–178

Bank CG, Bostock MG, Ellis R, Cassidy J (2000) A reconnaissance teleseismic study of the upper mantle and transition zone beneath the Archean Slave Craton in Northwest Canada. Tectonophysics 319(3):151–166

Beaumont C, Jamieson RA, Nguyen BH, Lee B (2001) Himalayan tectonics explained by extrusion of a low-viscosity crustal channel coupled to focused surface denudation. Nature 414:738–742

Bercovici D, Karato S (2003) Whole mantle convection and the transition-zone water filter. Nature 425:39–44

Berryman JG (1995) Mixture theories for rock properties. In: Ahrens TJ (ed) Rock physics and phase relations: a handbook of physics constants, vol 3, AGU reference shelf. AGU, Washington, DC, pp 205–228

Berryman JG (2007) Seismic waves in rocks with fluids and fractures. Geophys J Int 171:954–974. doi:10.1111/j.1365-246X.2007.03563.x

Bertrand EA (2010) MT study of the Taiwan arc-continent collision, Ph.D. thesis, University of Alberta, Edmonton

Bertrand EA, Unsworth MJ, Chiang CW, Chen CS, Chen CC, Wu F, Turkoglu E, Hsu HK, Hill G (2009) Magnetotelluric studies of the arc-continent collision in Central Taiwan. Geology 37:711–714

Bezacier L, Reynard B, Bass JD, Sanchez-Valle C, de Moortèle BV (2010a) Elasticity of antigorite, seismic detection of serpentinites, and anisotropy in subduction zones. Earth Planet Sci Lett 289:198–208. doi:10.1016/j/epsl.2009.11.009

Bezacier L, Reynard B, Bass JD, Wang J, Mainprice D (2010b) Elasticity of glaucophane, seismic velocities and anisotropy of the subducted oceanic crust. Tectonophysics 494:201–210. doi:10.1016/j.tecto.2010.09.011

Bina CR, Helffrich GR (1992) Calculation of elastic properties from thermodynamic equation of state principles. Annu Rev Earth Planet Sci 20:527–552

Birch F (1960) The velocity of compressional waves in rocks to 10 kilobars, Part 1. J Geophys Res 65(4):1083–1102

Blakely RJ, Brocher TM, Wells RE (2005) Subduction-zone magnetic anomalies and implications for hydrated forearc mantle. Geology 33(6):445–448

Block D (2001) Water resistivity Atlas of Western Canada Abstract, Paper presented at Rock the Foundation Convention of Canadian Society of Petroleum Geologists, Calgary, 18–22 June 2001

Booker JR, Favetto A, Pomposiello MC (2004) Low electrical resistivity associated with plunging of the Nazca flat slab beneath Argentina. Nature 429:399–403
Bostock MG (1997) Anisotropic upper-mantle stratigraphy and architecture of the Slave craton. Nature 390:392–395
Bostock MG (1998) Mantle stratigraphy and evolution of the Slave province. J Geophys Res 103 (B9):21183–21200
Bostock MG, Rondenay S (1999) Migration of scattered teleseismic body waves. Geophys J Int 137:732–746
Bostock MG, VanDecar JC (1995) Upper-mantle structure of the northern Cascadia subduction zone. Can J Earth Sci 32:1–12
Bostock MG, Hyndman RD, Rondenay S, Peacock SM (2002) An inverted continental moho and serpentinization of the forearc mantle. Nature 417:536–538
Bowring SA, Williams IS, Compston W (1989) 3.96 Ga gneisses from the Slave province, Northwest-Territories, Canada. Geology 17(11):971–975
Bowring SA, Housh TB, Isachsen CE (1990) The Acasta gneisses: remnant of Earth's early crust. In: Newsom HE, Jones JH (eds) Origin of the Earth. Oxford University Press, Oxford, UK, pp 319–343
Brasse H, Kapinos Li Y, Mutschard SW, Eydam D (2009) Structural electrical aniostropy in the crust at the south-Central Chilean continental margin as inferred from geomagnetic transfer functions. Phys Earth Planet Inter 173:7–16
Brenan JM, Watson EB (1988) Fluids in the lithosphere, 2. Experimental constraints on CO2 transport in dunite and quartzite at elevated P-T conditions with implications for mantle and crustal decarbonation processes. Earth Planet Sci Lett 91:141–158
Brenders AJ, Pratt RG (2007) Full waveform tomography for lithospheric imaging: results from a blind test in a realistic crustal model. Geophys J Int 168:133–151. doi:10.1111/j.1365-246X.2006.03,156.x
Brocher T, Parsons T, Trehu AM, Snelson CM, Fisher MA (2003) Seismic evidence for widespread serpentinized forearc upper mantle along the Cascadia margin. Geology 31(3):267–270
Brown LD, Zhao W, Nelson KD, Hauck M, Alsdorf D, Ross A, Cogan M, Clark M, Liu X, Che J (1996) Bright spots, structure and magmatism in southern Tibet from INDEPTH seismic reflection profiling. Science 274:1688–1690
Brown JR, Beroza GC, Ide S, Ohta K, Shelly DR, Schwartz SY, Rabbel W, Thorwart M, Kao H (2009) Deep low-frequency earthquakes in tremor localize to the plate interface in multiple subduction zones. Geophys Res Lett 36:L19306. doi:10.1029/2009GL040027
Brudzinski MR, Thurber CH, Hacker BR, Engdahl ER (2007) Global prevalence of double Benioff zones. Science 316:1472–1474. doi:10.1126/science.1139204
Calvert AJ (1996) Seismic reflection constraints on imbrication and underplating of the northern Cascadia convergent margin. Can J Earth Sci 33:1294–1307
Calvert AJ (2004) Seismic reflection imaging of two megathrust shear zones in the northern Cascadia subduction zone. Nature 428:163–167. doi:10.1038/nature02372
Calvert AJ, Clowes RM (1990) Deep, high-amplitude reflections from a major shear zone above the subducting Juan de Fuca plate. Geology 18:1091–1094
Calvert AJ, Sawyer EW, Davis WJ, Ludden JN (1995) Archaean subduction inferred from seismic images of a mantle suture in the Superior Province. Nature 375:670–673
Cammarano F, Romanowicz B (2008) Radial profiles of seismic attenuation in the upper mantle based on physical models. Geophys J Int 175:116–134. doi:10.1111/j.1365-246X.2008.03863.x
Cassidy JF, Bostock MG (1996) Shear-wave splitting above the subducting Juan de Fuca plate. Geophys Res Lett 23:941–944
Chen CW, Rondenay S, Weeraratne D, Snyder DB (2007) New constraints on the upper mantle structure of the slave craton from rayleigh wave inversion. Geophys Res Lett 34:L10301. doi:10.1029/2007GL029535

Chen CW, Rondenay S, Evans RL, Snyder DB (2009) Geophysical detection of relict metasomatism from an Archean (ca 3.5 Ga) subduction zone. Science 326:1089–1091. doi:10.1126/science.1178477

Christensen NI (1966) Elasticity of ultrabasic rocks. J Geophys Res 71(24):5921–5931

Christensen NI (1984) Pore pressure and oceanic crustal seismic structure. Geophys J R Astr Soc 79:411–423

Christensen NI (1989) Reflective and seismic properties of the deep continental crust. J Geophys Res 94:17793–17804

Christensen NI (1996) Poisson's ratio and crustal seismology. J Geophys Res 101:3139–3156

Christensen NI (2004) Serpentinites, peridotites, and seismology. Int Geol Rev 46:795–816

Clowes RM, Brandon MT, Green AG, Yorath CJ, Sutherland Brown A, Kanasewich ER, Spencer C (1987) Lithoprobe-southern Vancouver Island: cenozoic subduction complex imaged by deep seismic reflections. Can J Earth Sci 24:31–51

Crampin S, Booth DC (1985) Shear-wave polarizations near the North Anatolian Fault – II. Interpretation in terms of crack-induced anisotropy. Geophys J R Astr Soc 83:75–92

Currie CA, Cassidy JF, Hyndman RD, Bostock MG (2004) Shear wave anisotropy beneath the Cascadia subduction zone and western North American craton. Geophys J Int 157:341–353. doi:10.1111/j.1365-246X.2004.02175.x

de Wit M, Roehring C, Hart RJ, Armstrong RA, de Ronde CEJ, Green RWE, Tredoux M, Peberdy E, Hart RA (1992) Formation of an Archaean continent. Nature 357:553–562

DeMets C, Gordon RG, Argus DF, Stein S (1994) Effect of recent revisions to the geomagnetic reversal time-scale on estimates of current plate motions. Geophys Res Lett 21(20):2191–2194

Dueker KG, Sheehan AF (1997) Mantle discontinuity structure from midpoint stacks of converted p to s waves across the Yellowstone hotspot track. J Geophys Res 102:8313–8327

Dunn RA, Toomey DR (2001) Crack-induced seismic anisotropy in the oceanic crust across the East Pacific rise (9°30′N). Earth Planet Sci Lett 189:9–17

Dziewonski AM, Anderson DL (1981) Preliminary reference earth model. Phys Earth Planet Inter 25:297–356

Eisel M, Haak V (1999) Macro-anisotropy of the electrical conductivity of the crust: a magnetotelluric study of the German continental deep drilling site (KTB). Geophys J Int 136:109–122

Ellis DV, Singer JM (2008) Well logging for Earth scientists, 2nd edn. Springer, Berlin. ISBN 978-1-4020-3738-2

Evans RL, Chave AD, Booker JR (2002) On the importance of offshore data for magnetotelluric studies of ocean-continent subduction systems. Geophys Res Lett 29(9):1302. doi:10.1029/2001GL013960

Faul UH, Gerald JDF, Jackson I (2004) Shear wave attenuation and dispersion in melt-bearing olivine polycrystals: 2. Microstructural interpretation and seismological implications. J Geophys Res 109:B06202. doi:10.1029/2003JB002407

Flueh ER, Fisher MA, Bialas J, Childs JR, Klaeschen D, Kukowski N, Parsons T, Scholl DW, ten Brink U, Tréhu AM, Vidal N (1998) New seismic images of the Cascadia subduction zone from cruise SO108 – ORWELL. Tectonophysics 293:69–84

Fouch MJ, Rondenay S (2006) Seismic anisotropy beneath stable continental interiors. Phys Earth Planet In 158:292–320

Frisillo AL, Barsch GR (1972) Measurement of single-crystal elastic constants of bronzite as a function of pressure and temperature. J Geophys Res 77(32):6360–6384

Gaillard F (2004) Laboratory measurements of electrical conductivity of hydrous and dry silicic melts under pressure. Earth Planet Sci Lett 218:215–228

Gao S, Rudnick RL, Carlson RW, McDonough WF, Liu YS (2002) Re-Os evidence for replacement of ancient mantle lithosphere beneath the North China craton. Earth Planet Sci Lett 198:307–322

Gatzemeier A, Moorkamp M (2004) 3D modelling of electrical anisotropy from electromagnetic array data: hypothesis testing for different upper mantle conduction mechanisms. Phys Earth Planet Inter 149:225–242

Gibert F, Guillaume D, Laporte D (1998) Importance of fluid immiscibility in the H2O- NaCl-CO2 system and selective CO2 entrapment in granulites: experimental phase diagram at 5–7 kbar, 900°C and wetting textures. Eur J Mineral 10:1109–1123

Glover P, Hole MJ, Pous J (2000) A modified Archie's Law for two conducting phases. Earth Planet Sci Lett 180:369–383

Green HW, Houston H (1995) The mechanics of deep earthquakes. Annu Rev Earth Planet Sci 23:169–213

Green AG, Clowes RM, Yorath CJ, Spencer C, Kanasewich ER, Brandon MT, Sutherland Brown A (1986) Seismic reflection imaging of the subducting Juan de Fuca plate. Nature 319:210–213

Gribb TT, Cooper RF (2000) The effect of an equilibrated melt phase on the shear creep and attenuation behavior of polycrystalline olivine. Geophys Res Lett 27(15):2341–2344

Grove TL, Chatterjee N, Parman SW, Médard E (2006) The influence of H2O on mantle wedge melting. Earth Planet Sci Lett 249:74–89

Hacker BR (2008) H_2O subduction beneath arcs. Geochem Geophys Geosyst 9. doi:10.1029/2007GC001707

Hacker BR, Abers GA (2004) Subduction factory 3. An excel worksheet and macro for calculating the densities, seismic wave speeds, and H2O contents of minerals and rocks at pressure and temperature. Geochem Geophys Geosyst 5:Q01005. doi:10.1029/2003GC000614

Hacker B, Abers G, Peacock S (2003a) Subduction factory 1: theoretical mineralogy, density, seismic wave-speeds, and H2O content. J Geophys Res 108(B1):2029. doi:10.1029/2001JB001127

Hacker BR, Peacock SM, Abers GA, Holloway SD (2003b) Subduction factory 2. Are intermediate-depth earthquakes in subducting slabs linked to metamorphic dehydration reactions? J Geophys Res 108(B1):2030. doi:10.1029/2001JB001129

Hammond WC, Humphreys ED (2000a) Upper mantle seismic wave attenuation: effects of realistic partial melt distribution. J Geophys Res 105:10987–10999

Hammond WC, Humphreys ED (2000b) Upper mantle seismic wave velocity: effects of realistic partial melt geometries. J Geophys Res 105:10975–10986

Hasalová P, Schulmann K, Lexa O, Štípská P, Hrouda F, Ulrich S, Haloda J, Týcová P (2008) Origin of migmatites by deformation-enhanced melt infiltration of orthogneiss: a new model based on quantitative microstructural analysis. J Metamorph Geol 26:29–53

Heaman LM, Kjarsgaard RA, Creaser RA, Cookenboo HO, Kretschmar U (1997) Multiple episodes of kimberlite magmatism in the Slave province, North America. In: Lithoprobe report vol 56, Lithoprobe Secretariat, Vancouver, pp 14–17

Heise W, Pous J (2003) Anomalous phases exceeding 90^o in magnetotellurics: anisotropic model studies and a field example. Geophys J Int 155:308–318

Helffrich GR (1996) Subducted lithospheric slab velocity structure: observations and mineralogical inferences. In: Bebout G, Scholl D, Kirby S, Platt J (eds) Subduction top to bottom, vol 96, AGU geophysical monograph. AGU, Washington, DC, pp 215–222

Helmstaedt H, Schulze DJ (1989) Southern African kimberlites and their mantle sample: implications for Archean tectonic and lithosphere evolution. In: Ross J (ed) Kimberlites and related rocks, vol 1, Their composition, occurrence, origin, and emplacement. Blackwell, Carlton, pp 358–368

Hilairet N, Daniel I, Reynard B (2006) Equation of state of antigorite, stability field of serpentines, and seismicity in subduction zones. Geophys Res Lett 33:L02302. doi:10.1029/2005GL024728

Holness MB (1992) Equilibrium dihedral angles in the system quartz-CO2–H2O-NaCl at 800°C and 1–15 kbar: the effects of pressure and fluid composition on the permeability of quartzites. Earth Planet Sci Lett 114:171–184

Holness MB (1993) Temperature and pressure dependence of quartz-aqueous fluid dihedral angles: the control of adsorbed H_2O on the permeability of quartzites. Earth Planet Sci Lett 117:363–377
Holness MB (2006) Melt-solid dihedral angles of common minerals in natural rocks. J Petrol 47(4):791–800
Hyndman RD (1988) Dipping seismic reflectors, electrically conductive zones, and trapped water in the crust over a subducting plate. J Geophys Res 93:13391–13405
Hyndman RD, Klemperer SL (1989) Lower-crustal porosity from electrical measurements and inferences about composition from seismic velocities. Geophys Res Lett 16(3):255–258
Hyndman RD, Peacock SM (2003) Serpentinization of the forearc mantle. Earth Planet Sci Lett 212:417–432
Hyndman RD, Shearer PM (1989) Water in the lower continental crust: modelling magnetotelluric and seismic reflection results. Geophys J Int 98:343–365
Hyndman RD, Wang K (1993) Thermal constraints on the zone of major thrust earthquake failure: the Cascadia subduction zone. J Geophys Res 98:2039–2060
Ito K (1990) Effects of H_2O on elastic velocities in ultrabasic rocks at 900°C under 1 GPa. Phys Earth Planet Inter 61:260–268
Jackson I, Paterson MS, Gerald JDF (1992) Seismic wave dispersion and attenuation in Åheim dunite: an experimental study. Geophys J Int 108:517–534
Jackson JA, Austrheim H, McKenzie D, Priestley K (2004) Metastability, mechanical strength, and the support of mountain belts. Geology 32(7):625–628
Jodicke H, Jording A, Ferrari L, Arzate J, Mezger K, Rupke L (2006) Fluid release from the subducted Cocos Plate and partial melting of the crust deduced from magnetotelluric studies in Southern Mexico: implications for the generation of volcanism and subduction dynamics. J Geophys Res 111:B08102. doi:10.1029/2005JB003739
Jones AG, Ferguson IJ (2001) The electric Moho. Nature 409:331–333
Jones AG, Ferguson IJ, Chave AD, Evans RL, McNeice GW (2001) Electric lithosphere of the Slave craton. Geology 29(5):423–426
Jordan TH (1978) Composition and development of the continental tectosphere. Nature 274:544–548
Jung H, Karato S (2001) Water-induced fabric transitions in olivine. Science 293:1460–1463
Kamiya S, Kobayashi Y (2000) Seismological evidence for the existence of serpentinized wedge mantle. Geophys Res Lett 27(6):819–822
Karato S (1990) The role of hydrogen in the electrical conductivity of the upper mantle. Nature 347:272–273
Karato S (1995) Effects of water on seismic wave velocities in the upper mantle. Proc Jpn Acad 71:61–66
Karato S (2003) Mapping water content in the upper mantle. In: Eiler JM (ed) Inside the subduction factory, vol 138, AGU geophysical monograph. AGU, Washington, DC, pp 135–152
Karato S (2006) Remote sensing of hydrogen in Earth's mantle. Rev Mineral Geochem 62:343–375. doi:10.2138/rmg.2006.62.15
Karato S, Jung H (1998) Water, partial melting and the origin of the seismic low velocity and high attenuation zone in the upper mantle. Earth Planet Sci Lett 157:193–207
Karato S, Jung H (2003) Effects of pressure on high-temperature dislocation creep in olivine. Philos Mag 83(3):401–414. doi:10.1080/0141861021000025829
Katayama I, Hirauchi K, Michibayashi K, Ando J (2009) Trench-parallel anisotropy produced by serpentine deformation in the hydrated mantle wedge. Nature 461:1114–1117. doi:10.1038/nature08513
Kellett RL, Mareschal M, Kurtz RD (1992) A model of lower crustal electrical anisotropy for the Pontiac Subprovince of the Canadian shield. Geophys J Int 111:141–150
Kern H, Liu B, Popp T (1997) Relation between anisotropy of P and S wave velocities and anisotropy of attenuation in serpentinite and amphibolite. J Geophys Res 102:3051–3065

Kirby S, Engdahl ER, Denlinger R (1996) Intermediate-depth intraslab earthquakes and arc volcanism as physical expressions of crustal and uppermost mantle metamorphism in subducting slabs. In: Bebout G, Scholl D, Kirby S, Platt J (eds) Subduction top to bottom, vol 96, AGU geophysical monograph. AGU, Washington, DC, pp 195–214

Kono Y, Ishikawa M, Arima M (2007) Effect of H2O released by dehydration of serpentine and chlorite on compressional wave velocities of peridotites at 1 GPa and up to 1000°C. Phys Earth Planet Inter 161:215–223. doi:10.1016/j.pepi.2007.02.005

Kumazawa M, Anderson OL (1969) Elastic moduli, pressure derivatives, and temperature derivatives of single-crystal olivine and single-crystal forsterite. J Geophys Res 74 (25):5961–5972

Kurtz RD, Delaurier JM, Gupta JC (1986) A magnetotelluric sounding across Vancouver Island detects the subducting Juan-de-Fuca plate. Nature 321:596–599

Kurtz RD, Delaurier JM, Gupta JC (1990) The electrical-conductivity distribution beneath Vancouver Island – a region of active plate subduction. J Geophys Res 95:10929–10946

Langston CA (1977) Corvallis, Oregon, crustal and upper mantle receiver structure from teleseismic p and s waves. Bull Seismol Soc Am 67(3):713–724

Langston CA (1979) Structure under Mount Rainier, Washington, inferred from teleseismic body waves. J Geophys Res 84:4749–4762

Leaver DS, Mooney WD, Kohler WM (1984) A seismic refraction study of the Oregon Cascades. J Geophys Res 89:3121–3134

Lee CTA (2003) Compositional variations of density and seismic velocities in natural peridotites at STP conditions: implications for seismic imaging of compositional heterogeneities in the upper mantle. J Geophys Res 108:2441. doi:10.1029/2003JB002413

Lenardic A, Moresi L, Mühlhaus H (2000) The role of mobile belts for the longevity of deep cratonic lithosphere: the crumple zone model. Geophys Res Lett 27(8):1235–1238

Lenardic A, Moresi LN, Mühlhaus H (2003) Longevity and stabilty of cratonic lithosphere: insights from numerical simulations of coupled mantle convection and continental tectonics. J Geophys Res 108(B6):2303. doi:10.1029/2002JB001859

Levander A, Niu F, Lee CTA, Cheng X (2006) Imag(in)ing the continental lithosphere. Tectonophysics 416:167–185. doi:10.1016/j/tecto.2005.11.018

Lewis C, Ray D, Chiu KK (2007) Primary geologic sources of arsenic in the Chianan plain (blackfoot disease area) and the Lanyang plain of Taiwan. Int Geol Rev 49:947–961

Li S, Unsworth MJ, Booker JR, Wei W, Tan H, Jones AG (2003) Partial melt or aqueous fluid in the mid-crust of Southern Tibet? Constraints from INDEPTH magnetotelluric data. Geophys J Int 153:289–304

Long MD, Silver PG (2008) The subduction zone flow field from seismic anisotropy: a global view. Science 319:315–318. doi:10.1126/science.1150809

Ludden J, Hubert C (1986) Geologic evolution of the late Archean Abitibi greenstone belt of Canada. Geology 14:707–711

Mainprice D, Ildefonse B (2009) Seismic anisotropy of subduction zone minerals – contribution of hydrous phases. In: Lallemand S, Funiciello F (eds) Subduction zone geodynamics. Springer, Berlin/Heidelberg, pp 63–84

Mainprice D, Le Page Y, Rodgers J, Jouanna P (2008) Ab initio elastic properties of talc from 0 to 12 GPa: interpretation of seismic velocities at mantle pressures and prediction of auxetic behaviour at low pressure. Earth Planet Sci Lett 274:327–338. doi:10.1016/j.epsl.2008.07.047

Mamaus J, Laporte D, Schiano P (2004) Dihedral angle measurements and infiltration property of SiO2 rich melts in mantle peridotite assemblages. Contrib Mineral Petrol 148:1–12

Mareschal M, Kellett RL, Kurtz RD, Ludden JN, Ji S, Bailey RC (1995) Archaean cratonic roots, mantle shear zones and deep electrical anisotropy. Nature 375:134–137

Matthews DH (1986) Seismic reflections from the lower crust around Britain. In: Dawson JB, Carswell DA, Hall J, Wedepohl KH (eds) The nature of the lower continental crust, vol 24, Special publication. Geological Society, London, pp 11–24

Meju MA (2000) Geoelectric investigation of old/abandoned, covered landfill sites in urban areas: model development with a genetic diagnosis approach. J Appl Geophys 44:115–150

Mercier JP, Bostock MG, Audet P, Gaherty JB, Garnero EJ, Revenaugh J (2008) The teleseismic signature of fossil subduction: Northwestern Canada. J Geophys Res 113:B04308. doi:10.1029/2007JB005127

Miller KC, Keller GR, Gridley JM, Luetgert JH, Mooney WD, Thybo H (1997) Crustal structure along the west flank of the Cascades, western Washington. J Geophys Res 102:17857–17873

Minster JB, Anderson DL (1981) A model of dislocation-controlled rheology for the mantle. Philos Trans R Soc Lond A 299:319–356

Moorkamp M, Jones AG, Eaton DW (2007) Joint inversion of teleseismic receiver functions and magnetotelluric data using a genetic algorithm: are seismic velocities and electrical conductivities compatible? Geophys Res Lett 34:L16311. doi:10.1029/2007GL030519

Moorkamp M, Jones AG, Fishwick S (2010) Joint inversion of receiver functions, surface wave dispersion, and magnetotelluric data. J Geophys Res 115:B04318. doi:10.1029/2009JB006369

Murphy WF (1985) Sonic and ultrasonic velocities: theory versus experiment. Geophys Res Lett 12(2):85–88

Nelson KD, Zhao W, Brown LD, Kuo J, Che J, Liu X, Klemperer SL, Makovsky Y, Meissner R, Mechie J, Kind R, Wenzel F, Ni J, Nablek J, Leshou C, Tan H, Wei W, Jones AG, Booker JR, Unsworth MJ, Kidd WSF, Hauck M, Alsdorf D, Ross A, Cogan M, Wu C, Sandvol E, Edwards M (1996) Partially molten Middle Crust Beneath Southern Tibet: synthesis of project INDEPTH results. Science 274:1684–1686

Nesbitt B (1993) Electrical resistivities of crustal fluids. J Geophys Res 98:4301–4310

Nicholson T, Bostock M, Cassidy J (2005) New constraints on subduction zone structure in northern Cascadia. Geophys J Int 161(3):849–859

Nolet G (2008) A breviary of seismic tomography. Cambridge University Press, Cambridge, UK

O'Connell RJ, Budiansky B (1974) Seismic velocities in dry and saturated cracked solids. J Geophys Res 79(35):5412–5426

O'Connell RJ, Budiansky B (1977) Viscoelastic properties of fluid-saturated cracked solids. J Geophys Res 82(36):5719–5735

O'Neill C, Jellinek AM, Lenardic A (2007) Conditions for the onset of plate tectonics on terrestrial planets and moons. Earth Planet Sci Lett 261:20–32

Obara K (2002) Nonvolcanic deep tremor associated with subduction in Southwest Japan. Science 296:1679–1681

Obara K, Hirose H, Yamamizu F, Kasahara K (2004) Episodic slow slip events accompanied by non-volcanic tremors in southwest Japan subduction zone. Geophys Res Lett 23:L23602. doi:10.1029/2004GL020848

Park J, Yuan H, Levin V (2004) Subduction zone anisotropy beneath Corvallis, Oregon: a serpentinite skid mark of trench-parallel terrane migration? J Geophys Res 109:B10306. doi:10.1029/2003JB002718

Parsons T, Blakely RJ, Brocher TM, Christensen NI et al (2005) Crustal structure of the Cascadia fore arc of Washington. USGS professional paper 1661-D, USGS, Denver, 45 pp

Partzsch GM, Schilling FR, Arndt J (2000) The influence of partial melting on the electrical behavior of crustal rocks: laboratory examinations, model calculations and geological interpretations. Tectonophysics 317:189–203

Payero JS, Kostoglodov V, Shapiro N, Mikumo T, Iglesias A, Perez-Campos X, Clayton RW (2008) Nonvolcanic tremor observed in the Mexican subduction zone. Geophys Res Lett 35: L07305. doi:10.1029/2007GL032877

Peterson CL, Christensen DH (2009) Possible relationship between nonvolcanic tremor and the 1998–2001 slow slip event, south central Alaska. J Geophys Res 114:B06302. doi:10.1029/2008JB006096

Pozgay SH, Wiens DA, Conder JA, Shiobara H, Sugioka H (2009) Seismic attenuation tomography of the Mariana subduction system: implications for thermal structure, volatile distribution,

and slow spreading dynamics. Geochem Geophys Geosyst 10(4):Q04X05. doi:10.1029/2008GC002313
Preston LA, Creager KC, Crosson RS, Brocher TM, Tréhu AM (2003) Intraslab earthquakes: dehydration of the Cascadia slab. Science 302:1197–1200
Prouteau G, Scaillet B, Pichavant M, Maury R (2001) Evidence for mantle metasomatism by hydrous silicic melts derived from subducted oceanic crust. Nature 410:197–200
Quist AS, Marshall WL (1968) Electrical conductances of aqueous sodium chloride solutions from 0–800°C and at pressures to 4000 Bars. J Phys Chem 72:684–703
Ramachandran K, Hyndman RD, Brocher TM (2006) Regional P wave velocity structure of the Northern Cascadia subduction zone. J Geophys Res 111:B12301. doi:10.1029/2005JB004108
Ranero CR, Morgan JP, McIntosh K, Reichert C (2003) Bending-related faulting and mantle serpentenization at the Middle America trench. Nature 425:367–373
Rasmussen J, Humphreys E (1988) Tomographic image of the Juan de Fuca plate beneath Washington and western Oregon using teleseismic P-wave travel times. Geophys Res Lett 15:1417–1420
Reynard B, Hilairet N, Balan E, Lazzeri M (2007) Elasticity of serpentines and extensive serpentinization in subduction zones. Geophys Res Lett 34:L13307. doi:10.1029/2007GL030176
Roberts JJ, Tyburczy JA (1999) Partial-melt electrical conductivity: influence of melt composition. J Geophys Res 104:7055–7065
Rodi W, Mackie RL (2001) Nonlinear conjugate gradients algorithm for 2-D magnetotelluric inversion. Geophysics 66:174–187
Rogers G, Dragert H (2003) Episodic tremor and slip on the Cascadia subduction zone: the chatter of silent slip. Science 300:1942–1943
Romanyuk TV, Blakely R, Mooney WD (1998) The Cascadia subduction zone: two contrasting models of lithospheric structure. Phys Chem Earth 23(3):297–301
Rondenay S (2009) Upper mantle imaging with array recordings of converted and scattered teleseismic waves. Surv Geophys 30:377–405. doi:10.1007/s10712-009-9071-5
Rondenay S, Bostock MG, Hearn TM, White DJ, Ellis RM (2000) Lithospheric assembly and modification of the SE Canadian Shield: Abitibi-Grenville teleseismic experiment. J Geophys Res 105(B6):13735–13754
Rondenay S, Bostock MG, Shragge J (2000) Multiparameter two-dimensional inversion of scattered teleseismic body waves, 3, application to the Cascadia 1993 data set. J Geophys Res 106:30795–30808
Rondenay S, Abers GA, van Keken PE (2008) Seismic imaging of subduction zone metamorphism. Geology 36:275–278
Roth JB, Fouch MJ, James DE, Carlson RW (2008) Three-dimensional seismic velocity structure of the northwestern United States. Geophys Res Lett 35:L15304. doi:10.1029/2008GL034669
Rüpke LH, Morgan JP, Hort M, Connolly JA (2004) Serpentine and the subduction zone water cycle. Earth Planet Sci Lett 223:17–34
Rychert CA, Rondenay S, Fischer KM (2007) P-to-S and S-to-P imaging of a sharp lithosphere-asthenosphere boundary beneath eastern North America. J Geophys Res 112(B8):B08314. doi:10.1029/2007GL029535
Savage MK (1999) Seismic anisotropy and mantle deformation: what have we learned from shear wave splitting? Rev Geophys 37(1):65–106
Schilling FR, Sinogeikin SV, Bass JD (2003) Single-crystal elastic properties of lawsonite and their variation with temperature. Phys Earth Planet Inter 136:107–118. doi:10.1016/S0031-9201(03), 00024-4
Schmeling H (1985) Numerical models on the influence of partial melt on elastic, anelastic and electric properties of rocks. Part I: elasticity and anelasticity. Phys Earth Planet Inter 41:34–57
Schulmann K, Martelat JE, Ulrich S, Lexa O, Štípská P, Becker JK (2008) Evolution of microstructure and melt topology in partially molten granitic mylonite: implications for rheology of felsic middle crust. J Geophys Res 113:B10406

Shapiro NM, Campillo M, Stehly L, Ritzwoller MH (2005) High-resolution surface-wave tomography from ambient seismic noise. Science 307:1615–1618. doi:10.1126/science.1108339

Shelly DR, Beroza GC, Ide S, Nakamula S (2006) Low-frequency earthquakes in Shikoku, Japan, and their relationship to episodic tremor and slip. Nature 442:188–191. doi:10.1038/nature04931

Silver PG (1996) Seismic anisotropy beneath the continents: probing the depths of geology. Annu Rev Earth Planet Sci 24:385–432

Simpson F (2001) Resistance to mantle flow inferred from the electromagnetic strike of the Australian upper mantle. Nature 412:632–635

Simpson F, Bahr K (2005) Practical magnetotellurics. Cambridge University Press, Cambridge, UK

Simpson F, Tommasi A (2005) Hydrogen diffusivity and electrical anisotropy of a peridotite mantle. Geophys J Int 160:1092–1102

Siripunvaraporn W, Egbert GD, Lenbury Y, Uyeshima M (2005) Three dimensional magnetotelluric inversion: data subspace method. Phys Earth Planet Inter 150:3–14

Snyder DB, Bostock MG, Lockhart GD (2003) Two anisotropic layers in the Slave craton. Lithos 71:529–539

Snyder DB, Rondenay S, Bostock MG, Lockhart GD (2004) Mapping the mantle lithosphere for diamond potential. Lithos 77:859–872

Soyer W, Unsworth M (2006) Deep electrical structure of the northern Cascadia (British Columbia, Canada) subduction zone: implications for the distribution of fluids. Geology 34(1):53–56. doi:10.1130/G21951.1

Stachnik J, Abers G, Christensen D (2004) Seismic attenuation and mantle wedge temperatures in the Alaska subduction zone. J Geophys Res 109:B10304. doi:10.1029/2004JB003018

Stetsky RM, Brace WF (1973) Electrical conductivity of serpentinized rocks to 6 kilobars. J Geophys Res 78:7614–7621

Strack KM, Luschen E, Kotz AW (1990) Long-offset transient electromagnetic (LOTEM) depth soundings applied to crustal studies in the Black Forest and Swabian Alb, Federal Republic of Germany. Geophysics 55:834–842

Suetnova EI, Carbonell R, Smithson SB (1994) Bright seismic reflections and fluid movement by porous flow in the lower crust. Earth Planet Sci Lett 126:161–169

Takei Y (2002) Effect of pore geometry on V_P/V_S: from equilibrium geometry to crack. J Geophys Res 107:2043. doi:10.1029/2001JB000522

Takei Y, Holtzman BK (2009a) Viscous constitutive relations of solid-liquid composites in terms of grain boundary contiguity: 1. Grain boundary diffusion control models. J Geophys Res 114:B06205. doi:10.1029/2008JB005850

Takei Y, Holtzman BK (2009b) Viscous constitutive relations of solid-liquid composites in terms of grain boundary contiguity: 2. Compositional model for small melt fractions. J Geophys Res 114:B06206. doi:10.1029/2008JB005851

Takei Y, Holtzman BK (2009c) Viscous constitutive relations of solid-liquid composites in terms of grain boundary contiguity: 3. Causes and consequences of viscous anisotropy. J Geophys Res 114:B06207. doi:10.1029/2008JB005852

Tape C, Liu Q, Maggi A, Tromp J (2010) Seismic tomography of the southern California crust based on spectral-element and adjoint methods. Geophys J Int 180:433–462. doi:10.1111/j.1365-246X.2009.04429.x

ten Grotenhuis SM, Drury MR, Peach CJ, Spiers CJ (2004) Electrical properties of fine-grained olivine: evidence for grain boundary transport. J Geophys Res 109:B06203. doi:10.1029/2003JB002799

ten Grotenhuis SM, Drury MR, Spiers CJ, Peach CJ (2005) Melt distribution in olivine rocks based on electrical conductivity measurements. J Geophys Res 110:B12201. doi:10.1029/2004JB003462

Tréhu AM, Asudeh I, Brocher TM, Luetgert JH, Mooney WD, Nabelek JL, Nakamura Y (1994) Crustal architecture of the Cascadia forearc. Science 266:237–243

Tullis J, Yund R, Farver J (1996) Deformation enhanced fluid distribution in feldspar aggregates and implications for ductile shear zones. Geology 24:63–66
Ucok H, Ershaghi I, Olhoeft G (1980) Electrical resistivity of geothermal brines. J Petrol Technol 32:717–727, June 1980
Unsworth MJ (2010) Geophysics 424 class notes at University of Alberta. http://www.ualberta.ca/~unsworth/UA-classes/424/424index.html
Unsworth MJ, Jones AG, Wei W, Marquis G, Gokarn S, Spratt J (2005) Crustal rheology of the Himalaya and Southern Tibet inferred from magnetotelluric data. Nature 438:78–81. doi:10.1038/nature04154
Ussher G, Harvey C, Johnstone R, Anderson E (2000) Understanding the resistivities observed in Geothermal systems. In: Proceedings World Geothermal Congress, Kyushu
VanDecar JC (1991) Upper-mantle structure of the Cascadia subduction zone from non-linear teleseismic travel-time inversion. Ph.D. thesis, University of Washington, Seattle
Vanyan L (2002) A geoelectric model of the Cascadia Subduction zone. Izv Phys Solid Earth 38:816–845
Vinnik L (1977) Detection of waves converted from P to SV in the mantle. Phys Earth Planet Inter 15:39–45
Vry J, Powell R, Golden KM, Petersen K (2010) The role of exhumation in metamorphic dehydration and fluid production. Nat Geosci 3:31–35
Wannamaker PE (1986) Electrical conductivity of water- undersaturated crustal melting. J Geophys Res 91:6321–6327
Wannamaker PE (2000) Comment on "The petrologic case for a dry lower crust" by BWD Yardley and JW Valley. J Geophys Res 105(B3):6057–6064
Wannamaker PE (2005) Anisotropy versus heterogeneity in continental solid earth electromagnetic studies: fundamental response characteristics and implications for physiochemical state. Surv Geophys 26:733–765
Wannamaker PE (2010) Water from stone. Nat Geosci 3:10–11
Wannamaker PE, Booker JR, Jones AG, Chave AD, Filloux JH, Waff HS, Law LK (1989) Resistivity cross section through the Juan de Fuca subduction system and its tectonic implications. J Geophys Res 94:14127–14144
Wannamaker PE, Jiracek GR, Stodt JA, Caldwell TG, Gonzalez V, McKnight J, Porter AD (2002) Fluid generation and pathways beneath an active compressional orogen, the New Zealand Southern Alps, inferred from magnetotelluric data. J Geophys Res 107. doi:2001JB000186
Wannamaker PE, Caldwell TG, Jiracek GR, Maris V, Hill GJ, Ogawa Y, Bibby HM, Bennie SL, Heise W (2009) Fluid and deformation regime at an advancing subduction system at Marlborough, New Zealand. Nature 460:733–737
Watson E, Brenan JM (1987) Fluids in the lithosphere, 1. Experimentally determined wetting characteristics of CO2-H2O fluids and their implications for fluid transport, host-rock physical properties and fluid inclusion formation. Earth Planet Sci Lett 85:497–515
Wells RE, Blakely RJ, Weaver CS (2002) Cascadia microplate models and within-slab earthquakes. In: Kirby S,Wang K, Dunlop S (eds) The Cascadia subduction zone and related subduction systems – Seismic structure, intraslab earthquakes and processes, and earthquake hazards, Open-File Report, vol 02–328, US Geological Survey, Menlo Park, pp 17–23
Wiens DA, Conder JA, Faul UH (2008) The seismic structure and dynamics of the mantle wedge. Annu Rev Earth Planet Sci 36:421–455
Williams Q, Hemley RJ (2001) Hydrogen in the deep earth. Annu Rev Earth Planet Sci 29:365–418
Wilson DS (2002) The Juan de Fuca plate and slab: Isochron structure and Cenozoic plate motions. In: Kirby S, Wang K, Dunlop S (eds) The Cascadia subduction zone and related subduction systems – Seismic structure, intraslab earthquakes and processes, and earthquake hazards, Open-File Report, vol 02–328, US Geological Survey, Menlo Park, pp 9–12

Winkler KW, Murphy WF (1995) Acoustic velocity and attenuation in porous rocks. In: Ahrens TJ (ed) Rock physics and phase relations: a handbook of physics constants, vol 3, AGU reference shelf. AGU, Washington, DC, pp 20–34

Worthington PF (1993) The uses and abuses of the Archie equations, 1: the formation factor-porosity relationship. J Appl Geophys 30:215–228

Worzewski T, Jegen M, Kopp H, Brasse H, Castillo WT, Magnetotelluric image of the fluid cycle in the Costa Rican subduction zone, Nature Geoscience, 4, 108–111, 2010.

Xue M, Allen RM (2007) The fate of the Juan de Fuca plate: implications for a Yellowstone plume head. Earth Planet Sci Lett 264:266–276. doi:10.1016/j.epsl.2007.09.047

Yardley B, Valley J (1997) The petrologic case for a dry lower crust. J Geophys Res 102:12173–12185

Zhao D, Wang K, Rogers GC, Peacock SM (2001) Tomographic image of low P velocity anomalies above slab in northern Cascadia subduction zone. Earth Planet Space 53:285–293

Zhu L, Kanamori H (2000) Moho depth variation in southern California from teleseismic receiver functions. J Geophys Res 105:2969–2980

Chapter 14
A Hydromechanical Model for Lower Crustal Fluid Flow

J.A.D. Connolly and Y.Y. Podladchikov

Abstract Metamorphic devolatilization generates fluids at, or near, lithostatic pressure. These fluids are ultimately expelled by compaction. It is doubtful that fluid generation and compaction operate on the same time scale at low metamorphic grade, even in rocks that are deforming by ductile mechanisms in response to tectonic stress. However, thermally-activated viscous compaction may dominate fluid flow patterns at moderate to high metamorphic grades. Compaction-driven fluid flow organizes into self-propagating domains of fluid-filled porosity that correspond to steady-state wave solutions of the governing equations. The effective rheology for compaction processes in heterogeneous rocks is dictated by the weakest lithology. Geological compaction literature invariably assumes linear viscous mechanisms; but lower crustal rocks may well be characterized by non-linear (power-law) viscous mechanisms. The steady-state solutions and scales derived here are general with respect to the dependence of the viscous rheology on effective pressure. These solutions are exploited to predict the geometry and properties of the waves as a function of rock rheology and the rate of metamorphic fluid production. In the viscous limit, wavelength is controlled by a hydrodynamic length scale δ, which varies inversely with temperature, and/or the rheological length scale for thermal activation of viscous deformation l_A, which is on the order of a kilometer. At high temperature, such that $\delta < l_A$, waves are spherical. With falling temperature, as $\delta \to l_A$, waves flatten to sill-like structures. If the fluid overpressures associated with viscous wave propagation reach the conditions for plastic failure, then compaction induces channelized fluid flow. The channeling is caused by vertically elongated porosity waves that nucleate with characteristic spacing δ. Because δ increases with falling temperature, this mechanism is amplified towards the surface. Porosity wave passage is associated with pressure

J.A.D. Connolly (✉)
Department of Earth Sciences, Swiss Federal Institute of Technology, Zurich 8092, Switzerland

Y.Y. Podladchikov
Geophysics Institute, University of Lausanne, Lausanne 6617, Switzerland

D.E. Harlov and H. Austrheim, *Metasomatism and the Chemical Transformation of Rock*, Lecture Notes in Earth System Sciences,
DOI 10.1007/978-3-642-28394-9_14,

anomalies that generate an oscillatory lateral component to the fluid flux that is comparable to the vertical component. As the vertical component may be orders of magnitude greater than time-averaged metamorphic fluxes, porosity waves are a potentially important agent for metasomatism. The time and spatial scales of these mechanisms depend on the initial state that is perturbed by the metamorphic process. Average fluxes place an upper limit on the spatial scale and a lower limit on the time scale, but the scales are otherwise unbounded. Thus, inversion of natural fluid flow patterns offers the greatest hope for constraining the compaction scales. Porosity waves are a self-localizing mechanism for deformation and fluid flow. In nature these mechanisms are superimposed on patterns induced by far-field stress and pre-existing heterogeneities.

14.1 Introduction

The volume change associated with isobaric metamorphic devolatilization is usually positive, consequently devolatilization has a tendency to generate high pressure pore fluids. This generality has led to the notion that high fluid pressures are the ultimate cause of metamorphic fluid flow. A simple experiment with a well-shaken bottle of soda pop (i.e., a sweet, carbonated, beverage) demonstrates that this notion is ill conceived. Once the bottle is opened some pop is lost, but, after a short time, flow ceases leaving most of the initial pop in the bottle. In the metamorphic analogy, the bottle is the porous rock matrix and the pop is its pore fluid. How then is this pore fluid expelled? As early as 1911, Goldschmidt (1954) realized that fluid expulsion could only occur if the rock compacts and squeezes the pore fluid out. The compaction process is a form of deformation that, usually, is driven by the weight of the overlying rock. In this case, the downward flow of the rock matrix, in response to gravity, is responsible for the upward flow of the less dense pore fluid. Compaction driven fluid flow is complex because it is inseparable from rock deformation and because the hydraulic properties that limit fluid flow through the rock matrix, such as permeability and porosity, are dynamic. This chapter outlines a physical model for the compaction process in the Earth's lower crust. While the specifics of this chapter are of direct relevance only to continental crust, the concepts apply to oceanic crust as well.

Metamorphic devolatilization usually results in a significant decrease in the volume of the residual solid, e.g., serpentine dehydration causes a reduction in the solid volume in excess of 10%. Without compaction, this change in volume would be preserved as grain-scale porosity. Thus, the near absence of grain-scale porosity in exhumed metamorphic rocks (Norton and Knapp 1977) is unequivocal evidence for irreversible compaction. Despite this evidence, irreversible compaction is almost universally disregarded in quantitative models of metamorphic fluid flow. This neglect is reasonable provided the fluid flow of interest occurs on a short time scale compared to the time scale for compaction. Because viscous compaction is thermally-activated, neglecting compaction becomes more problematic, but not

necessarily invalid, with increasing metamorphic grade. Likewise, although compaction is an appealing explanation for ubiquitous evidence of high fluid pressure during metamorphism (e.g., Etheridge et al. 1984; Sibson 1992; McCuaig and Kerrich 1998; Simpson 1998; Cox 2005; Rubinstein et al. 2007; Peng et al. 2008; Scarpa et al. 2008; Padron-Navarta et al. 2010), high fluid pressures cannot be explained unless metamorphic systems are poorly drained. However, if metamorphic systems are poorly drained, high fluid pressures may simply be a consequence of ephemeral fluid production. This argument is not brought forward to justify the neglect of compaction in modeling metamorphic fluid flow, but rather to emphasize that the conditions at which compaction becomes important are uncertain. An intriguing set of observations (Young and Rumble 1993; van Haren et al. 1996; Graham et al. 1998) indicate that localized fluid-rock interaction at amphibolite-facies conditions occurred on a time scale of 10^3–10^5 y during much longer (~10^7 y) regional metamorphic events. An explanation for the limited duration of fluid-rock interaction is that compaction sealed the rocks on the 10^3–10^5 y time scale. Transiently high metamorphic permeability on similar time scales (Ingebritsen and Manning 2010) and geophysically observable sub-Himalyan densification on a time scale of < 1 My at eclogite facies conditions (Hetenyi et al. 2007) provide additional evidence that compaction is an efficient process at moderate metamorphic temperatures. Compaction is synonymous with fluid expulsion, thus if metamorphic fluid flow is compaction dominated, exotic fluid sources and crustal scale fluid recirculation should have limited impact on the metamorphic fluid budget (Walther and Orville 1982). That metamorphic fluid fluxes, inferred from field studies (e.g., Ferry 1994; Skelton 1996; Wing and Ferry 2007; Manning and Ingebritsen 1999), are comparable to the vertically integrated metamorphic fluid production (Walther and Orville 1982; Yardley 1983; Connolly and Thompson 1989) is suggestive that metamorphic flow regimes are indeed compaction dominated.

The assumption of classical metamorphic petrology, that fluid pressure is equal to the total pressure, implies that rocks compact in response to negligible effective pressure, i.e., that rocks have no strength. In this limit, compaction driven flow of a low-density fluid can only be upward (Walther and Orville 1982). A surprising feature of compaction-driven fluid flow in rocks of finite strength is that a perturbation, e.g., a metamorphic devolatilization reaction, to a uniform flow regime induces a regime in which fluid flow occurs by the propagation of domains of fluid-filled porosity (Richter and McKenzie 1984; Scott and Stevenson 1986; Suetnova et al. 1994; Wiggins and Spiegelman 1995; Connolly 1997). The properties of these domains closely approximate steady-state wave solutions to the equations that describe fluid flow in compacting media (Barcilon and Richter 1986; Barcilon and Lovera 1989). In this porosity wave propagated flow regime, while the overall tendency is to drive fluid upward or, in the presence of tectonic stress, toward low mean stress (Connolly and Podladchikov 2004), lateral fluid flow occurs on the time and spatial scales of the steady-state waves. In a homogeneous crust that is not subject to tectonic forcing, such waves would be the primary mechanism of metamorphic fluid flow. This idealization is far from reality, but

the steady-state wave solutions define background patterns upon which the effects of lithological heterogeneity and tectonic deformation are imposed. Consequently, the spatial and temporal scales of the compaction process limit the extent to which perturbations may influence the idealized compaction-driven flow regime. For example, a transient shear zone may induce both lateral and downward fluid flow (Austrheim 1987; Sibson 1992), but it can only do so on time and spatial scales shorter than those for compaction (Connolly 2010). Understanding the time and length scales of steady-state wave solutions to the compaction equations is thus essential to understanding lower crustal fluid flow, even if the flow is not dominated by compaction.

The physical explanation for the existence of porosity waves requires only an elementary understanding of the driving forces and constitutive relations that govern fluid flow, but the derivation of the steady-state solutions involves cumbersome math (Barcilon and Richter 1986; Barcilon and Lovera 1989). The intent here is to avoid this math, which is summarized in the Appendix, and to focus on the physical constraints that influence the steady-state solutions. The first part of this Chapter reviews the rheological and hydraulic concepts relevant to the compaction process. Large scale modeling of metamorphic fluid flow inevitably invokes a steady-state hydraulic regime to define the pre-metamorphic state. This initial steady state is critical to model outcomes because it determines the response of the system to the metamorphic perturbation. Unfortunately, because metamorphism is the most probable source of lower crustal fluids, the assumption of an initial steady state leaves much to be desired. In truth, in the modeling of metamorphic fluid flow, less is known about the initial state than is known about the metamorphic state. The second part of this Chapter draws attention to the uncertainties inherent in defining the pre-metamorphic lower crustal hydraulic regime, and the final part details the expected scales and patterns of compaction-driven flow as function of initial conditions and rheology.

14.2 Compaction Pressures and Rheologic and Hydraulic Constitutive Relations

In compaction problems, fluid is distinguished from the solid phase(s) by its shear strength; specifically the fluid is defined as a phase that cannot support deviatoric stress. This definition has the implication that on the time scale relevant for compaction, fluid pressure is uniform throughout the connected porosity at the scale of the solid grains and is independent of the solid pressure. The term porosity is used here to mean only this connected porosity; rocks may contain porosity that is not interconnected, but because this porosity does not influence fluid flow it is of little interest. Further, it is assumed that the porosity is always filled by fluid, i.e., porosity is simply the volume fraction of fluid in the solid matrix. Although the word porosity conjures up an image of grain-scale structures, it may apply to

substantially larger features, such as fractures, provided these features are small in comparison to the length scale for fluid flow.

Compaction is formally the change in porosity caused by dilational (volume changing) strain of a solid matrix, i.e., the isotropic component of the strain tensor. It follows from the Curie principle that compaction can only be a direct function of invariant characteristics of the stress state. From Terzhaghi's effective stress concept, the simplest invariant is the effective pressure, i.e., the difference between total pressure and fluid pressure, which is assumed here to be the sole cause of compaction. The total pressure can be decomposed into components due to the fluid and solid as

$$p = (1 - \phi)p_s + \phi p_f \tag{14.1}$$

where ϕ is porosity and subscripts s and f denote solid and fluid, respectively (see Table 14.1 for notation). Making use of Eq. 14.1, and observing that mean stress, $\bar{\sigma}$, and pressure are formally equivalent, effective pressure is

$$p_e \equiv \bar{\sigma} - p_f = (1 - \phi)(p_s - p_f). \tag{14.2}$$

Because high fluid pressures may lead to negative effective pressures, it is sometimes convenient to describe compaction processes in terms of fluid overpressure, which is defined here as $-p_e$.

Darcy's law (e.g., McKenzie 1984) relates the volumetric fluid flux relative

$$\mathbf{q} = -(1 - \phi)\frac{k}{\mu}(\nabla p_f - \rho_f g \mathbf{u}_z) \tag{14.3}$$

through a porous matrix to the difference between the actual fluid pressure gradient and the hydrostatic pressure gradient of the fluid ($\rho_f g \mathbf{u}_z$), where k is the hydraulic permeability of the solid matrix, ρ_f and μ are the density and shear viscosity of the fluid, and $\mathbf{u}_z$ is a downward directed unit vector. It is often useful to characterize the dynamics of fluid flow by the macroscopic velocity, $\mathbf{v}$, of the fluid rather than flux. As the fluid flux is the product of the fluid velocity and porosity, any expression in terms of flux can be converted to one in terms of velocity via

$$\mathbf{v} = \mathbf{q}/\phi \tag{14.4}$$

Fluid flux is a vector, which is typically negative (upward) for a downward directed depth coordinate. This is a potential source of confusion in that a large upward flux is, numerically, less than a small flux. To minimize such confusion, the magnitude of a vectorial quantity, indicated by italics (e.g., q for flux $\mathbf{q}$ and v for velocity $\mathbf{v}$), is used when direction is evident. Darcy's law relates flux to pressure gradients rather than pressure. This has the implication that a high-pressure fluid need not flow provided its pressure gradient is hydrostatic.

Table 14.1 Frequently used symbols

Symbol	Meaning
A	Coefficient of viscous flow, Eqs. 14.11 and 14.12
c_ϕ	Geometric and grain-size dependent factor in the permeability function, Eq. 14.17
c_σ	Geometric factor in the compaction rate function, Eq. 14.16
D	Pre-exponential term in Arrhenius dependence of A, Eqs. 14.12 and 14.14
e	Base of natural logarithms (2.718...)
g	Magnitude of gravitational acceleration
k; k_0	Permeability, Eq. 14.17; background value
l_A	Viscous e-fold length, Eq. 14.15
n_ϕ	Porosity exponent in the permeability function, Eq. 14.17
n_σ	Stress exponent in the viscous flow law, Eq. 14.11
$O(n)$	Literally, "of the order of magnitude of n"
p; p_e; p_f; p_s	Total pressure, Eq. 14.1; effective pressure, $p - p_f$, Eq. 14.2; fluid pressure; solid pressure
$\mathbf{q}$; q; q_0;$\bar{q}$	Fluid flux, Eqs. 14.3, 14.5, 14.8, and 14.37; fluid flux magnitude; background value; time-averaged value
q_e	Time-averaged fluid flux (magnitude) associated with a 1-d wave, Eq. 14.25
Q	Activation energy for viscous deformation of the solid matrix
R	Universal gas constant
R	Viscosity contrast
T	Temperature, K
$\mathbf{u}_z$	A downward directed unit vector
V_e; V_e^{1d}	Fluid volume associated with a wave, Eq. 14.27; 1-d volume, Eq. 14.26
v; v_0; v_ϕ	Fluid speed; background value; wave speed, Eq. 14.56
z	Depth coordinate, positive downward
$\dot{\varepsilon}$	Shear strain rate, Eq. 14.11
$\dot{\varepsilon}_\phi$	Compaction rate, Eq. 14.16
δ; δ_d	Viscous compaction length, Eq. 14.23; decompaction length for decompaction-weakening, Eq. 14.30
$\Delta\rho$; $\Delta\sigma$	$\rho_s - \rho_f$; differential stress
η	Solid shear viscosity
λ	Wavelength
μ	Fluid shear viscosity
ϕ; ϕ_0	Porosity (hydraulically connected); background value
ρ_s; ρ_f	Solid density; fluid density
$\bar{\sigma}$; σ_y	Mean stress (p), Eq. 14.38; tensile yield stress
τ	Compaction time scale, δ/v_0, Eq. 14.24
∇; $\nabla\cdot$	Gradient ($\partial/\partial z$ in 1-d); divergence ($\partial/\partial z$ in 1-d)

In compaction problems, it is useful to reformulate Darcy's law in terms of the effective pressure responsible for compaction as

$$\mathbf{q} = -(1-\phi)\frac{k}{\mu}(\nabla\bar{\sigma} - \nabla p_e - \rho_f \mathbf{g}\mathbf{u}_z). \tag{14.5}$$

For the classical $p = p_f$ metamorphic model (i.e., $\nabla p_e = 0$), this form demonstrates that the direction of fluid flow is a function of the mean stress gradient, which may

be influenced by tectonic processes. These effects complicate discussion because they depend on the specifics of the tectonically-induced stress field. To eliminate this complication, it is assumed that the mean stress gradient is due entirely to the vertical load, i.e., that pressure is lithostatic. Tectonic stress affects the direction of compaction driven flow, but does not affect the compaction mechanism, thus the lithostatic assumption is not essential to any of the phenomena discussed here. Making the additional assumptions that solid density is not strongly variable and that porosity is small (i.e., $1 - \phi \approx 1$), total and effective pressures are

$$p \approx p_s \approx \rho_s g z \tag{14.6}$$

$$p_e \approx \rho_s g z - p_f, \tag{14.7}$$

where ρ_s is the density of the solid matrix and z is depth. Rearranging Eq. 14.7 to give fluid pressure in terms of effective pressure, Darcy's law then simplifies to

$$\mathbf{q} = \frac{k}{\mu}(\nabla p_e - \Delta\rho g \mathbf{u}_z). \tag{14.8}$$

At near surface conditions, fluid pressures are near hydrostatic, i.e., $\nabla p_e \approx \Delta\rho g \mathbf{u}_z$, and small perturbations in pressure can cause fluids to flow in any direction. This regime is often referred to as one of normal fluid pressure, whereas at conditions of lithostatic fluid pressure, in which case $\nabla p_e = 0$,

$$q = k\Delta\rho g/\mu \tag{14.9}$$

and flux is vertical and essentially controlled by permeability.

Equations 14.3 and 14.4, give the fluid velocity and flux relative to the reference frame of the solid, but in geological compaction problems solid velocities are finite relative to the Earth's surface. It is assumed here that the solid velocity is negligible. This assumption is justified in the small porosity limit (Connolly and Podladchikov 2007). The Appendix provides a more rigorous treatment that does not neglect solid velocity.

14.2.1 Rheology

Just as in the case of non-dilational rheology, the endmember compaction rheologies are elastic, plastic, and viscous. Strictly elastic, plastic, and viscous describe, respectively, reversible time-independent, irreversible time-independent, and irreversible time-dependent deformation (Hill 1950). In the geological literature these terms, particularly plastic, are often confused with terms such as ductile and brittle that describe deformation style. In geological materials, the origin of ductile behavior is most commonly viscous rheology, but may also be a plastic

mechanism, while brittle deformation is a manifestation of plasticity and is usually localized (Ranalli 1995).

Elastic compaction and fluid expulsion results from both solid (β_s) and fluid (β_f) compressibilities and a peculiar component referred to as pore compressibility that is a property of the fluid–rock aggregate (Gueguen et al. 2004). Although pore compressibility dominates the compaction of poorly consolidated sediments, in rocks with porosities below a few percent, pore compressibilities become comparable to the solid compressibility, which is $O(10^{-11})$ Pa^{-1} (Wong et al. 2004; the notation $O(n)$, which means, literally, "of the order of magnitude of n", is used extensively in this chapter because of our concern with scales based on highly uncertain parameters). Thus, for lower crustal rocks, the elastic compaction caused by a change in effective pressure Δp_e is

$$\Delta\phi/\phi \approx -\beta_s \Delta p_e. \tag{14.10}$$

From Eq. 14.10, a reduction in p_f from lithostatic to hydrostatic conditions at 20 km depth ($\Delta p_e = \Delta\rho g z$) decreases by 0.4% of its initial value. As fluid compressibilities are roughly an order of magnitude greater than solid compressibility at the conditions of the lower crust (Walther and Orville 1982), the net fluid expulsion necessary to effect the pressure drop is only ~4.4% of the fluid mass initially present in the porosity. Thus, at typical lower crustal conditions, elastic dilational strain can be neglected as a mechanism for lower crustal fluid expulsion. In this regard it is important to distinguish fluid expulsion from fluid flow as, particularly in the non-compacting limit, thermoelastic expansivity of the fluid may create pressure gradients responsible for fluid circulation (e.g., Hanson 1997; Staude et al. 2009; Nabelek 2009).

Excepting irreversible phase transformations, viscous and plastic bulk strains in rocks are caused by microscopic shear deformation that eliminates porosity. Plastic rheologies are complex, but fortunately only cataclastic and Mohr-Coulomb plastic rheologies are of relevance here. Cataclasis (Wong et al. 2004), the crushing of grains in response to increasing load, is a well-known phenomenon in sedimentary basins where it gives rise to an exponential decay of porosity with depth (Athy 1930; Connolly and Podladchikov 2000). Crushing is inescapable once stress concentrations approach the ultimate strength of the solid material (Hill 1950), which is itself 10% of the shear modulus of the solid. Thus, the role of cataclastic compaction must be acknowledged once stress concentrations are $O(1)$ GPa. In sedimentary rocks, the requisite stress concentrations are caused by irregular grain contacts. These asperities are gradually eliminated during compaction, leading to strain-hardening. In sediments, this strain-hardening typically limits cataclastic compaction to rocks with porosities in excess of a few percent (Hunt 1990; Powley 1990). Cataclasis is thus unlikely in lower crustal metamorphic rocks unless effective pressures are exceptionally large.

Although brittle failure is usually thought of as a mechanism for accommodating shear strain, positive dilational strain (i.e., dilatancy) is an inescapable consequence of non-associated plastic (brittle) failure. If an imposed differential stress is large in

comparison to the tensile strength of the rock matrix, brittle failure may limit fluid pressure to sublithostatic values (Sibson 2004, cf. Rozhko et al. 2007). Given that rock tensile strengths rarely exceed 50 MPa, and may be near zero, in some circumstances truly lithostatic fluid pressures may only be possible in the absence of significant differential stress, whereupon fluid pressure is limited by hydrofracturing, which occurs when the fluid overpressure exceeds tensile strength.

Viscous compaction is unimportant at surface conditions, but, because it is a thermally activated mechanism, it becomes inevitable with increasing temperature. The viscous rheology of the crust is usually described by a power-law constitutive relationship of the form (e.g., Kohlstedt et al. 1995; Ranalli 1995)

$$\dot{\varepsilon} = A|\Delta\sigma|^{n_\sigma - 1}\Delta\sigma, \tag{14.11}$$

where $\dot{\varepsilon}$ is the strain rate in response to differential stress $\Delta\sigma$, n_σ is the stress exponent, and A is the coefficient of viscous flow. The coefficient A is a temperature dependent material property that may also be sensitive to grain size (e.g., pressure solution creep) and chemical factors (e.g., the chemical potential of oxygen and/or water). These latter dependencies are uncertain and therefore disregarded in large-scale modeling, but the temperature dependence is usually retained and described by the Arrhenius relation

$$A = D\exp\left(\frac{-Q}{\mathrm{R}T}\right), \tag{14.12}$$

where Q is the activation energy for the viscous mechanism, and D is a material property that is independent of temperature. To provide a simple model for the viscous rheology of the lower crust, D is parameterized here in terms of the strain-rate, stress, temperature, and depth of the brittle-ductile transition, i.e., the depth at which viscous mechanisms become capable of accommodating tectonic strain rates (Kohlstedt et al. 1995). In compressional settings, at this depth, z_{BD}, assuming $\sigma_2 = (\sigma_1 + \sigma_3)/2$ and the hydrostatic fluid pressure, the Mohr-Coulomb rheology of the upper crust defines the differential stress as (Petrini and Podladchikov 2000)

$$\Delta\sigma_{\mathrm{BD}} = gz_{\mathrm{BD}}\frac{\rho_{\mathrm{f}}(3\sin\theta - 1) - 2\rho_{\mathrm{UC}}\sin\theta}{\sin\theta - 1} \tag{14.13}$$

where, by Byerlee's law, the internal angle of friction $\theta = \pi/6$ (Ranalli 1995) and ρ_{UC} is the density of upper crustal rock. For $\rho_{\mathrm{f}}/\rho_{\mathrm{UC}} = 0.3$, Eq. 14.13 simplifies to $\Delta\sigma_{\mathrm{BD}} = 1.7\rho_{\mathrm{UC}}gz_{\mathrm{BD}}$. Substituting this estimate for $\Delta\sigma$ in Eq. 14.11 and making use of Eq. 14.12

$$D = \frac{\dot{\varepsilon}_{\mathrm{BD}}}{(1.7z_{\mathrm{BD}}\rho_{\mathrm{UC}}g)^{n_\sigma}}\exp\left(\frac{Q}{\mathrm{R}T_{\mathrm{BD}}}\right). \tag{14.14}$$

The validity of this parameterization hinges on whether Eqs. 14.11 and 14.12 provide an adequate description of the ductile mechanism, but does not require or imply that metamorphism occurs in a compressional tectonic setting or that the brittle-ductile transition during metamorphism occurs at the conditions chosen for the parameterization. Activation energies and stress exponents are relatively well known from rock deformation experiments. Typical values for crustal rocks are in the range $n_\sigma = 2.5 - 4$ and $Q = 150 - 400$ kJ/mol. The depth, temperature, and strain rate at the base of the seismogenic zone, which is usually considered to correspond to the brittle portion of the crust (Sibson 1986; Scholz 1988; Zoback and Townend 2001), are $z_{BD} \approx 3 - 20$ km, $T_{BD} \approx 623 - 723$ K and $\dot{\varepsilon}_{BD} \approx 10^{-12}$ to 10^{-16} s^{-1}, but these ranges are not independent due to autocorrelation (Liotta and Ranalli 1999; Ranalli and Rybach 2005). The values $n_\sigma = 3$, $Q = 250$ kJ/mol, $T_{BD} = 623$ K, $\dot{\varepsilon}_{BD} = 10^{-15}$ s^{-1}, $z_{BD} = 15$ km, and $\rho_{UC} = 2{,}700$ kg/m^3 are taken here to represent a plausible, but by no means unique, condition for the brittle-ductile transition.

It is often useful to characterize the variation in viscous rheology due to the increase in temperature with depth in terms of a depth interval rather than a temperature change. For this purpose, differentiation of Eq. 14.12, with respect to depth, yields the desired measure

$$l_A = A \Big/ \frac{\partial A}{\partial z} = \frac{RT^2}{Q \frac{\partial T}{\partial z}}, \tag{14.15}$$

which is the change in depth necessary to increase strain rates by a factor of e (2.718...). For the parameter choices specified above, the viscous e-fold length l_A is $O(1)$ km at the conditions of lower crustal metamorphism (Fig. 14.1). In the upper crust, pressure solution gives rise to a linear viscous ($n_\sigma = 1$) rheology that is characterized by activation energies in the range 20 –40 kJ/mol (Rutter 1983; Spiers and Schutjens 1990; Shimizu 1995; Connolly and Podladchikov 2000). From Eq. 14.15, such small activation energies increase l_A by an order of magnitude, implying a weak depth dependence that is inconsistent with the restricted depth range and temperature dependence of the seismogenic zone (Sibson 1986; Scholz 1988; Ranalli and Rybach 2005). Thus, it is unlikely that pressure solution is the viscous mechanism responsible for the brittle-ductile transition.

For a material that deforms by viscous creep according to Eq. 14.11, the compaction rate (Wilkinson and Ashby 1975) is

$$\dot{\varepsilon}_\phi = \frac{1}{\phi}\frac{\mathrm{d}\phi}{\mathrm{d}t} = -c_\sigma \frac{(1-\phi)^2}{\left(1-\phi^{1/n_\sigma}\right)^{n_\sigma}} A |p_e|^{n_\sigma - 1} p_e \approx -c_\sigma A |p_e|^{n_\sigma - 1} p_e, \tag{14.16}$$

where the approximate form, which is adopted hereafter, applies in the small-porosity limit. The geometric factor $c_\sigma = n_\sigma^{-n_\sigma}(3/2)^{n_\sigma+1}$ follows rigorously only for spherical pore geometry. At the level of accuracy required here, this geometric

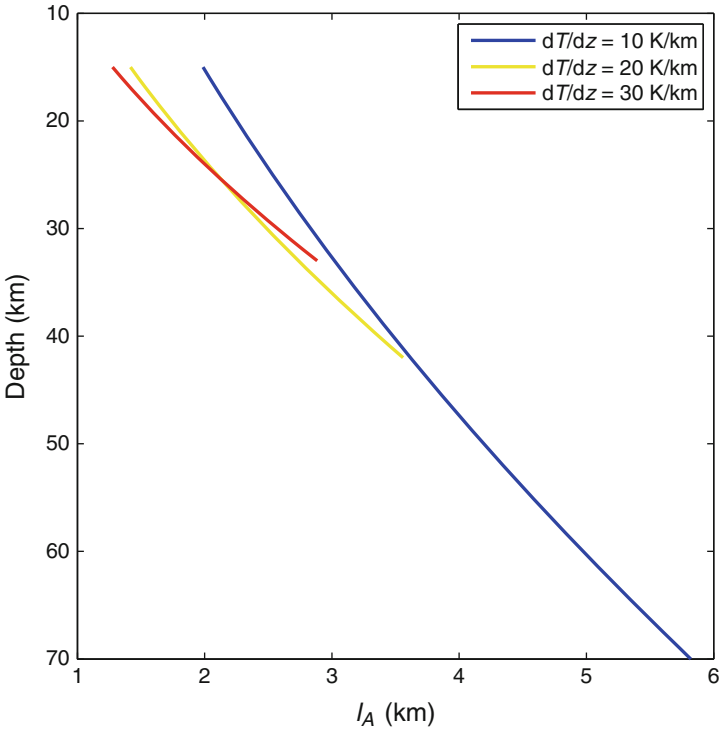

Fig. 14.1 The viscous e-fold length l_A is the characteristic length scale for variation in the ductile rheology of the lower crust with depth due to thermal activation (Eq. 14.15). For a given stress, strain rates increase 10-fold over a depth interval $\Delta z = 2.3\ l_A$. The viscous e-fold length is computed for the indicated geotherms, a reference temperature of 623 K at 15 km depth, and an activation energy of $Q = 250$ kJ/mol. Experimentally determined activation energies for dislocation creep in silicate minerals are in the range 135–400 kJ/mol (e.g., Paterson and Luan 1990; Ranalli 1995). Variation within this range affects l_A by less than a factor of two

assumption is an unimportant source of variability. For the specific case of $n_\sigma = 3$, $c_\sigma = 3/16$.

The dependence of the viscous compaction rate on effective pressure has a number of implications for compaction processes during metamorphism. Most notably the viscous mechanism cannot operate at the $p_\mathrm{f} = p$ condition generally assumed in metamorphic petrology. Thus, dilational strain, caused by a metamorphic reaction that initiates at $p_\mathrm{f} = p$, must be accommodated by elastic mechanisms until the induced stresses become large enough to activate viscous or plastic deformation. As these elastic strains are insignificant, during this incipient stage metamorphism is effectively isochoric rather than isobaric.

The assumption that the viscous mechanism is non-linear is not essential to any subsequent argumentation; it is adopted because it is widely accepted and general. Relations for the special case of linear viscous rheology are obtained from the relations for the non-linear case by observing that, when $n_\sigma = 1$, viscosity is $1/(3A)$. Both

compaction and macroscopic shear deformation are accomplished by microscopic shear. Thus, if a rock is simultaneously subject to both modes of deformation, then they must be accommodated by the same microscopic mechanism. This mechanism is determined by the largest of the stresses responsible for the deformation, $|\Delta\sigma|$ or $|p_e|$, with the result that, if the stresses are of different magnitude, the viscous response to the inferior stress is approximately linear and determined by effective viscosity resulting from the deformation induced by the superior stress. Regardless of magnitude, far-field tectonic stress facilitates compaction by lowering the effective viscosity of the solid matrix (Tumarkina et al. 2011).

14.2.2 Permeability

Although the hydraulic permeability of rocks is extraordinarily variable, it is well established from both theoretical studies and empirical observation (Wark and Watson 1998; Xiao et al. 2006) that the permeability of a given rock will vary as a strong function of its connected porosity. Typically, a power-law relationship is assumed such that if the permeability is k_0 at porosity ϕ_0, then

$$k = k_0(\phi/\phi_0)^{n_\phi} = c_\phi \phi^{n_\phi}. \tag{14.17}$$

In its second form, Eq. 14.17 separates the variability of permeability into a component related to its porosity dependence and a coefficient, c_ϕ, which is a function of pore geometry and proportional to the square of the matrix grain size. From analysis of in situ rock permeability, Neuzil (1994) shows that pore geometry and grain size give rise to variations in permeability that span eight orders of magnitude, but that porosity dependence is approximately cubic. This cubic dependence, i.e., $n_\phi = 3$, is adopted here and is predicted from theory irrespective of whether flow is intergranular or fracture controlled (Norton and Knapp 1977; Gavrilenko and Gueguen 1993). Higher exponents are observed in rocks where the degree of hydraulic connectivity varies strongly with porosity (Zhu et al. 1995; Zhu et al. 1999).

14.2.3 Porosity

Given a steady source at depth, it is conceivable that crustal rocks could adjust their permeability to accommodate this flux at lithostatic pressure (Connolly and Thompson 1989). While such a model is problematic, as it implies rocks have no strength, it provides the only basis for assuming that the lower crust has a tendency to evolve towards a state with homogeneous permeability. Unfortunately, this tenuous argument does not extend to porosity given that different lithologies may have the same permeability with drastically different porosities (Neuzil 1994;

Thompson and Connolly 1990). Thus, the only certainty about lower crustal porosity is that it is spatially and temporally variable. An upper bound on lower crustal porosities of $O(10^{-2})$ is provided by the sensitivity of geophysical measurements, but there is no lower bound. On the basis of isotopic diffusion profiles, Skelton et al. (2000) infer background porosities, i.e., the porosity in non-reactive metaphyllites about a metabasite undergoing devolatilization at greenschist facies conditions, in the range of $\phi_0 \sim 10^{-3}$ to 10^{-6}. These are consistent with grain scale porosities in the range 10^{-3} to 10^{-6} measured in exhumed metamorphic rocks (Norton and Knapp 1977). This variability has non-trivial consequences because, discounting the influence of phase changes on intrinsic material properties, the impact of metamorphic reactions on the mechanical properties of the crust is determined by the relative change in porosity via the constitutive relations for permeability (Eq. 14.17) and rheology (Eq. 14.16), e.g., an increase in porosity of 10^{-3} has no significant influence on permeability if it occurs in rocks with an initial porosity of 10^{-2}, but if the initial porosity is 10^{-6}, permeability increases by nine orders of magnitude.

Hydraulically connected porosities of $< O(10^{-2})$ may seem implausible to a reader familiar with percolation theory models of rock permeability (Gueguen and Palciauskas 1994); however such models assume static pore structure. In natural systems, experimental, theoretical, and numerical evidence suggests that textural equilibration may maintain hydraulic connectivity to vanishingly small porosities (Cheadle et al. 2004; cf., Holness and Siklos 2000 and Price et al. 2006). As remarked earlier (Sect. 14.1), the term porosity is used here to denote any hydraulically connected textural features (e.g., cracks) present on a spatial scale significantly less than the, as yet to be defined, compaction length scale. Thus, even if a percolation threshold is relevant to the expulsion process, porosity may take on any value between zero and unity. Evidence for high metamorphic fluid pressures, in combination with low fluid production rates, provides an indirect argument that these porosities are small at the onset of metamorphism. For example, theoretical porosity-permeability models (Connolly et al. 2009) imply that for $O(1)$ mm grain size, the porosity necessary to conduct a plausible $O(10^{-13})$ m/s devolatilization-generated fluid flux (Connolly and Thompson 1989) at lithostatic pressure, is $O(10^{-5})$.

Whether rocks exist that have no hydraulically connected porosity is, to a certain degree, a metaphysical question. Viscous compaction may completely eliminate microcrack connectivity (Gratier et al. 2003; Tenthorey and Cox 2006), but, in texturally equilibrated rocks, grain-scale viscous compaction reduces porosity asymptotically with time. Similarly, chemical cementation and retrograde hydration require the ingress of a fluid phase and therefore are unlikely to completely eliminate porosity. Even seemingly pristine igneous rocks have detectable hydraulic connectivity (Norton and Knapp 1977). Regardless of whether rocks with no hydraulically connected porosity exist, it is certainly possible that devolatilization may occur in a setting in which the surrounding rocks have such low permeabilities that viscous dilational mechanisms become ineffective on the geological time scale. The compaction time scale, discussed subsequently (Sect. 14.5.2), can be used to assess when the viscous mechanism becomes ineffective. In this limit, elastic or

plastic dilational mechanisms must be responsible for fluid flow. Elastic and plastic mechanisms do not require finite hydraulic connectivity and are therefore also capable of explaining fluid flow into truly impermeable rocks (Connolly and Podladchikov 1998), but these mechanisms introduce complexities that are beyond the scope of this Chapter.

14.3 The Lower Crustal Hydrologic Regime

Conventional wisdom holds that continental crust can be divided into two hydrologic regimes, an upper crustal regime in which fluid pressures are near hydrostatic and a lower crustal regime in which fluid pressures are lithostatic (Fig. 14.2a). Direct (e.g., Huenges et al. 1997) and geophysical observations (e.g., Zoback and Townend 2001) confirm the existence of the upper regime and suggest that it can extend to depths of 10–15 km, while fluid inclusion data and deformation styles support the existence of the lower regime, at least during episodes of regional metamorphism (e.g., Etheridge et al. 1984; Sibson 1992; Cox 2005). The observation that fluid overpressures develop at a eustatic compaction front at ~ 3–4 km depth in many sedimentary basins suggests that compaction can establish a steady-state connection between the hydrostatic and lithostatic regimes. However, this steady-state is only possible in conjunction with sedimentation, because sediment burial is necessary to compensate for upward propagation of the compaction front (Connolly and Podladchikov 2000). Given that steady burial is not a characteristic continental process, a steady-state connection between the hydrologic regimes is improbable.

In active metamorphic settings, the transition between hydraulic regimes can be explained by both the compacting and non-compacting limiting cases. In the compacting case, thermally activated viscous compaction reduces permeability to levels at which drainage to the upper crust cannot keep pace with expulsion and/or metamorphic fluid production. This scenario is the basis for the false notion that the transition to lithostatic fluid pressure is coincident with the brittle-ductile transition. Assuming hydrostatic fluid pressures are characteristic of the upper crust, at the brittle-ductile transition the effective pressure responsible for compaction is comparable to the differential stress that drives tectonic deformation (Connolly and Podladchikov 2004). From Eqs. 14.11 and 14.16, the compaction rate at the transition is therefore comparable to the tectonic strain rate. Thus, for a tectonic strain rate of 10^{-15} s^{-1}, compaction at the brittle-ductile transition requires $2.3c_\sigma/\dot{\varepsilon} \sim 388$ My to reduce porosity by an order of magnitude. As this time scale is greater than the time scale for heat-conduction limited metamorphism, compaction at the depth of the brittle-ductile transition is an ineffective means of regulating metamorphic fluid pressure unless metamorphism is coeval with anomalously high rates of tectonic deformation. This generality applies to the expulsion process, but the healing of microcrack controlled permeability in shear zones is an indirect mechanism by which localized compaction at shallow crustal levels, and short time scales, may generate hydraulic seals (Gratier et al. 2003; Tenthorey and Cox 2006). These seals

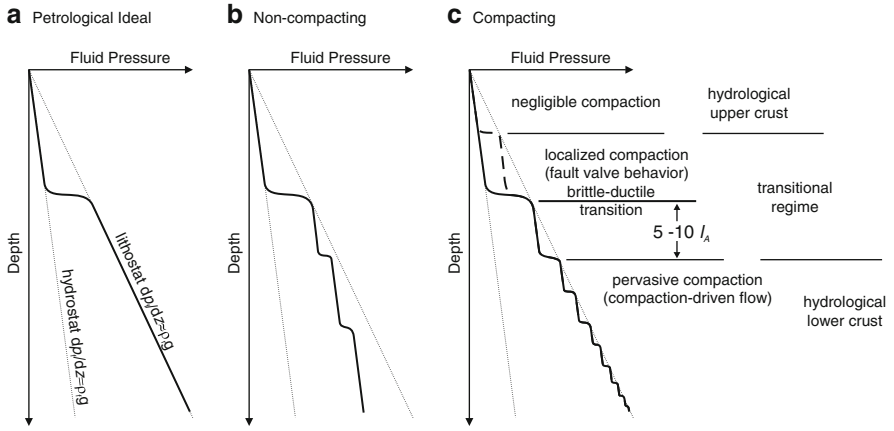

Fig. 14.2 Three models for fluid pressure in the crust. The petrological lithostatic fluid pressure model (**a**) is hydrologically untenable unless permeability is uniform throughout the lower crust and the fluid originates from a steady sub-crustal source. In the non-compacting scenario (**b**) drainage of lower crustal rocks is limited by the least permeable horizon. In the absence of short-term effects related to fluid production, this horizon, i.e., top-seal, would mark the closest approach to lithostatic fluid pressure. Above this horizon fluid pressures would be near hydrostatic. While below the horizon fluid pressure would increase step wise across low permeability seals (Etheridge et al. 1984; Gold and Soter 1985; Hunt 1990; Powley 1990). The superposition of thermally activated compaction on the non-compacting scenario gives rise to three hydrologic regimes (**c**). An upper crustal regime in which faulting maintains such high permeabilities that negligible deviation from hydrostatic fluid pressure is adequate to drive fluid circulation (Zoback and Townend 2001) is limited at depth by the conditions at which localized compaction becomes an effective mechanism for sealing fault-generated permeability (Gratier et al. 2003; Tenthorey and Cox 2006). At greater depths, pervasive compaction and/or metamorphic fluid production may generate transient fluid overpressure that is periodically relieved by faulting (Sibson 1992). At the brittle-ductile transition (i.e., the base of the seismogenic zone) it is improbable that pervasive compaction can keep pace with metamorphic fluid production; thus the transitional hydrologic regime is likely to persist over an interval that extends ~10 l_A below the brittle-ductile transition. Beneath the transitional regime, pervasive compaction is capable of generating hydraulic seals and fluid, if present, is at near lithostatic pressure. Within this lower-most regime, fluid flow is truly compaction-driven. In the absence of fluid production, the tendency of both time and depth is to decrease the wavelength of the fluid pressure compartments resulting in a near-steady regime approximating the petrological ideal. Barring the possibility of a sub-crustal fluid source, the flux in this near steady regime must decrease with depth. Thus the magnitude of the perturbation caused by metamorphic devolatilization to the lower crustal regime is dependent on its depth

may cause fluid overpressure to develop as consequence of local fluid production or deeper expulsion processes (Cox 2005). Viscous compaction rates increase by a factor of e with an increase in depth of $\Delta z \sim l_A$, thus the depth at which compaction operates pervasively on the metamorphic time scale must lie at least several viscous e-fold lengths (Fig. 14.1) below the brittle-ductile transition, but the exact depth is dependent on the rate of metamorphism.

In the non-compacting limit (Fig. 14.2b), lithostatic fluid pressure is generated when metamorphic fluid production overwhelms drainage capacity. A complication

in this scenario is that if fluid pressures are lithostatic throughout the lower crust, then either fluxes are uniform and vertical throughout the lower crust or permeability must be a function of flux rather than porosity. The physical absurdity of either case leads to the conclusion that a heterogeneous permeability structure is the only plausible model for the non-compacting limit. In this case (Fig. 14.2c), fluid pressures cannot be uniformly lithostatic, but approach lithostatic values at low-permeability seals (e.g., Etheridge et al. 1984). The resulting compartmentalized fluid pressure profile is identical to the compartmentalization observed in sedimentary basins (Hunt 1990; Powley 1990). Even in the non-compacting limit, brittle failure permits permeability to increase to accommodate vertical fluxes, but, given the variability of natural permeability with lithology, the permeability of a seal-forming lithology may be orders of magnitude lower than in the intervening rocks. If such seals exist, then, in the absence of metamorphic fluid production, the lower crust may achieve a quasi-steady state with near uniform vertical fluxes in which the closest approach to lithostatic fluid pressure occurs at the uppermost seal. Beneath each seal, Darcy's law requires that the fluid pressure gradient must be nearly hydrostatic, despite large absolute fluid pressures. The time scale for reaching this steady state is dictated by the high-permeability rocks, whereas the effective permeability of the lower crust is defined by the permeability of the top seal. As the vertical flux in this scenario must degrade with time, the number of effective seals must likewise decrease.

As a crustal model, the non-compacting limit has the virtue that it acknowledges the enormous variability of permeability with lithology and it has features that are consistent with both direct and indirect observation. In the former category, results from the Kola deep drilling project suggest the development of fluid compartmentalization at ~8 km depth within the crust (Zharikov et al. 2003). While in the latter category, the existence of permeable horizons with sublithostatic fluid pressure are essential to explain the lateral fluid flow so often inferred in metamorphic studies (Ferry and Gerdes 1998; Wing and Ferry 2007; Staude et al. 2009). Counter-intuitively, the non-compacting scenario is consistent with the idea that the brittle-ductile transition is coincident with the transition in crustal hydrologic regimes if faulting in the brittle domain is responsible for the high permeability of the upper crust (Zoback and Townend 2001).

Thermal activation of viscous compaction dictates the degree to which the compacting or non-compacting scenario is relevant to nature. As the non-compacting limit is broadly consistent with the upper crustal hydrologic regime, it is simplest to develop a conceptual model for the lower crust by considering how depth-dependent viscosity would perturb the non-compacting limit. The primary effect of depth-dependent viscosity would be to reduce the effective pressures sustained within, and therefore the vertical extent of, compartments with depth. Additionally, compaction would provide a source for fluxes, permitting pressurization of seals independently of the top seal. These two effects would lead to a decrease in the wavelength of fluid compartments with depth and lithostatically pressured seals throughout the lower crust, i.e., a pressure profile that would approximate the classical model of lithostatic fluid pressure at depth (Fig. 14.2c).

The absence of any uncontrived steady state for the lower crustal hydrologic regime poses a fundamental limitation to modeling metamorphic fluid flow in that the initial conditions for such models are unconstrained. Thus, by adjusting an arbitrary model parameter, such as the background fluid flux, the modeler has complete control on the impact of metamorphic fluid production on crustal fluid flow. This has the implication that forward modeling of metamorphic fluid flow has little predictive power and that hypothesis testing, based entirely upon modeling, is suspect. The utility of forward models is that they can be used to predict patterns. The comparison of these patterns with natural observations then provides a basis for inverting the parameters and the initial conditions of the metamorphic environments.

14.4 Metamorphic Fluid Production and Dilational Strain

A first order constraint on metamorphic fluid production follows from the observation that between low and high metamorphic grades typical crustal rocks lose ~ 5% of their mass as a consequence of devolitalization (Shaw 1956). For crustal thicknesses of l_c ~ 35–70 km, this implies time-integrated fluxes of the order

$$\hat{q} = \frac{w\rho_r l_c}{\rho_f} \sim O\left(10^4\right)\mathrm{m} \tag{14.18}$$

where w is the weight fraction of the volatiles released during metamorphism. This estimate is comparable to, or greater than, integrated fluxes derived from field studies (e.g., Ferry 1994; Skelton 1996; Wing and Ferry 2007; Staude et al. 2009) suggesting that, at least from a mass balance perspective, there is no necessity to invoke convection cells or exotic fluid sources to explain typical metamorphic fluxes. Introducing the assumptions that fluid expulsion keeps pace with metamorphic fluid production and that the duration of metamorphism is dictated by the heat conduction time scale ($\tau_{met} \sim l_c^2/\kappa$, where κ is thermal diffusivity, $O(10^{-6})$ m^2/s for crustal rocks), time-averaged fluxes are of the order

$$\bar{q} = \frac{w\rho_r \kappa}{\rho_f l_c} \sim O\left(10^{-12}\right)\mathrm{m/s}. \tag{14.19}$$

By introducing an additional assumption about the pressure gradient responsible for the average flux, Darcy's law can be inverted for time-averaged permeability (Ingebritsen and Manning 1999). The simplicity of this logic is seductive, but because metamorphic fluxes are dynamic such averages are misleading. For example, Fulton et al. (2009) reject the contention of Ague et al. (1998) that dehydration generated fluid overpressures may trigger faulting. The fallacy of the argumentation being that, by definition, the average permeability is the permeability necessary to accommodate metamorphic fluxes at lithostatic pressure, thus it is unsurprising that a dynamic metamorphic flux is inadequate to generate overpressures if this

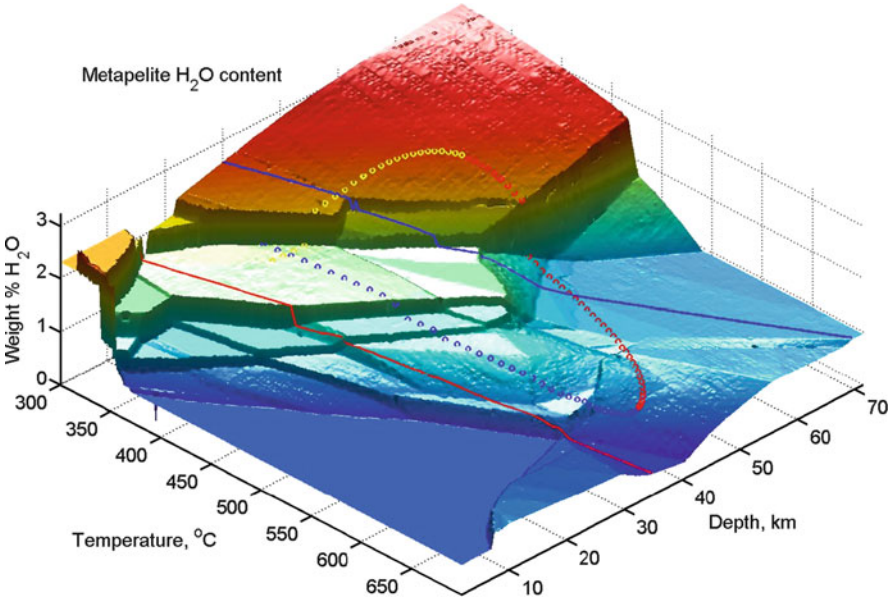

Fig. 14.3 Water-content for an average pelitic sediment composition (Plank and Langmuir 1998) as a function of temperature and pressure, computed assuming equilibrium with a pure H_2O fluid. Red and blue lines indicate hot (20°C/km) and cold (10°C/km) metamorphic geotherms. The increase in water-content at temperatures > 600°C is due to melting that occurs because the model assumes water-saturation. This melting does not occur if the water released by low temperature processes is expelled (Modified from Connolly 2010)

permeability is assumed as an initial condition. From the point of view of understanding dynamic flow, average permeability has no utility unless permeability is a static property. However, it would be fortuitous if this static permeability were exactly the permeability necessary to conduct metamorphic fluxes at lithostatic pressure. Thus, the pertinent issue to understanding lower crustal fluid flow is not the average permeability of the lower crust, but rather the background permeability that characterizes the environment prior to the onset of the flow perturbation of interest.

To illustrate the variability of metamorphic fluid production, consider equilibrium dehydration of a pelitic rock (Fig. 14.3). In the closed system limit, the classical lithostatic fluid pressure model requires that volume changes associated with devolatilization must be instantaneous. In the context of this model, the instantaneous dilational strain is a function of pressure and temperature and can be decomposed into components representing fluid and solid volumetric production rates (Fig. 14.4). The rates are broadly consistent with the expectation that metamorphic devolatilization is associated with a reduction in solid volume, but an increase in total volume; a behavior that would increase fluid pressure and drive dilational deformation in real systems. If hydrofracture provides an instantaneous dilational mechanism then the equilibrium model can be realized for the general case. Exceptions to this generality occur at the extremes of the metamorphic

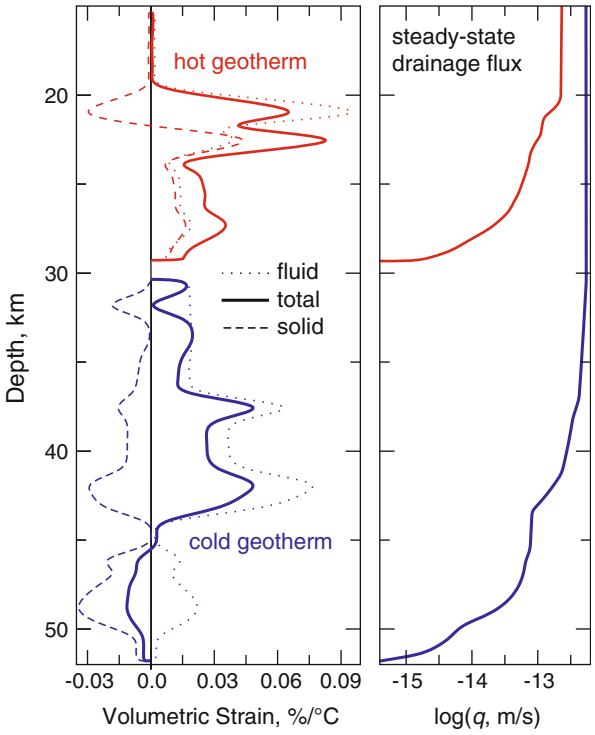

Fig. 14.4 Dehydration induced, isobaric strain, and steady-state fluid fluxes as a function of depth for the metamorphic model depicted in Fig. 14.3. The strain is resolved into the components due to fluid and solid production and corrected for the effect of thermal expansivity. Fluid and solid production rates are the product of the corresponding component of the isobaric strain multiplied by the metamorphic heating rate. The steady-state drainage flux q is the vertically integrated fluid production rate computed for a heating rate of 3°C/My. This is the flux required for drainage to balance fluid production. For the hot geotherm, the curves are terminated at the onset of melting because the melting process is dependent on the dynamics of fluid expulsion (Modified from Connolly 2010)

spectrum, i.e., at low temperature and high pressure or high temperature and low pressure. In the former case, the net volume change may be negative, an effect that would generate sub-lithostatic fluid pressures and therefore cause reaction rates to be limited by relatively slow viscous compaction mechanisms. In contrast, along high geothermal gradients the solid volume may increase (Fig. 14.4) during devolatilization requiring a more complex dilational deformation process than the hydrofracture mechanism assumed here.

Under the assumption that fluids are expelled upwards as rapidly as they are produced, metamorphic fluxes are the vertically integrated fluid production rate, i.e., the component of the dilational strain rate attributed to fluid generation. Taking a heating rate of 3 K/My and assuming consistent heat-conduction controlled metamorphism (England and Thompson 1984), fluid fluxes estimated in this way for both cool and warm geothermal conditions are comparable to the average flux deduced earlier (Fig. 14.4). However, the more detailed model illustrates that fluxes

must vary by orders of magnitude with depth. These fluxes place an upper bound on the effective permeability of the lower crust, because it would be impossible to generate elevated fluid pressure at a higher permeability. Unfortunately, there is little reason to expect that background permeabilities will be conveniently close to this upper bound, although they may well correlate with rates of metamorphism. This latter issue is topical because recent studies (Oliver et al. 2000; Dewey 2005; Ague and Baxter 2007; Warren et al. 2011) suggest that at least some episodes of regional metamorphism occur on time scales one to two orders of magnitude shorter than implied by the heat conduction time scale.

14.5 Fluid Flow in Compacting Media: Porosity Waves

Evidence that metamorphic devolatilization occurs at elevated fluid pressure leaves little doubt that devolatilization perturbs the pre-metamorphic hydrologic regime. In rigid rock, the dilational strain required for reaction progress is eliminated if the fluid is simultaneously drained by hydraulic diffusion. However, if the rocks initially contain fluid at or near lithostatic pressure, then, from Darcy's law, the fluid pressure gradient required for this drainage must be supralithostatic and is therefore inconsistent with the existence of lithostatic fluid pressure during metamorphism. If the definition of rigid is relaxed to allow for brittle failure at insignificant overpressure, the coupling between reaction rate and pressure is eliminated, but so too are the fluid overpressures that would be capable of explaining increased fluid drainage. Thus, without compaction, the effect of brittle failure is to generate a horizon of elevated porosity, filled by near lithostatically pressured fluid, sandwiched between relatively impermeable unreacted rocks. The horizon is analogous to a wet sponge in that it releases fluid only if it is squeezed. The weight of the overlying rocks acts as the agent for squeezing by, what has been argued here to be, predominantly, viscous compaction. The rate at which the fluid is drained is fundamentally limited by the permeability of the overlying rocks, but because these rocks are also deformable this permeability is dynamic. As noted earlier, the peculiar feature of fluid flow in this scenario is that it occurs in waves of fluid-filled porosity. An idealized 1-d, constant viscosity, model is employed here to explain why these waves form, after which the model is extended to account for more complex rheology and multidimensional effects.

14.5.1 Porosity Waves in Viscous Rock, Why?

For simplicity consider a constant volume devolatilization reaction that initiates at depth within an otherwise uniform rock subject to some small background fluid flux q_0 (Fig. 14.5). Initially, since the reaction is isochoric it does not perturb the background flux, but it does increase the porosity from ϕ_0 to ϕ_1 by reducing the solid volume. This porosity change increases the permeability within the reacted

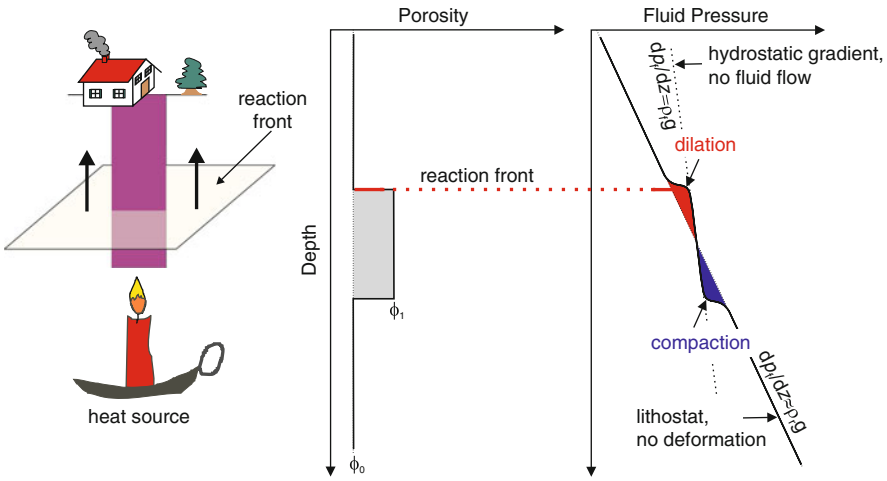

Fig. 14.5 Conceptual model of an isochoric metamorphic devolatilization reaction. The unreacted rock has porosity ϕ_0 and conducts the flux q_0. The reaction leaves a region of elevated porosity ϕ_1 in its wake. This high porosity region has a permeability $(\phi_1/\phi_0)^3$ times greater than in the unreacted rock (for $n_\phi = 3$ in Eq. 14.17). Because there are no dilational effects associated with an isochoric reaction, the flux in the permeable reacted region must initially be the same as the background flux. For this to be true Darcy's law requires that the effective pressure gradient in the reacted rocks must be $\Delta\rho g/(\phi_1/\phi_0)^3$; thus a factor of 2 increase in porosity reduces the fluid pressure gradient to within 12.5% of the hydrostatic gradient. As the vertical extent of the reacted rocks becomes larger with time, this condition causes finite effective pressure anomalies that lead to fluid expulsion. Non-isochoric reactions lead to a similar scenario, but with asymmetric pressure anomalies (Connolly 1997) (Modified from Connolly 2010)

rocks by a factor of $(\phi_1/\phi_0)^3$ (for $n_\phi = 3$ in Eq. 14.17). From Darcy's law, if fluid flux is constant then an increase in permeability must be compensated by a reduction in the fluid pressure gradient. Thus, an order of magnitude increase in permeability is sufficient to cause the fluid pressure gradient to relax to essentially hydrostatic values within the reacted rock. In turn, this relaxation gives rise to an effective pressure gradient such that pore fluids are overpressured above the center of the reacted zone and underpressured below it (Fig. 14.5). These pressure anomalies induce transient perturbations to the fluid flux above and below the reacted zone, but because the anomalies are antisymmetric there is no net drainage of fluid from the reacted layer as long as deformation is insignificant. However, the magnitude of the pressure anomalies must grow in proportion to the vertical extent of the reacted rocks with the result that deformation becomes inevitable. This deformation is manifest as compaction at the base of the reacted rocks and dilation at their top and has the effect of propagating the reaction-generated porosity upward (Fig. 14.6a). If the rate of propagation is high enough, then this mechanism can generate an isolated domain, or wave, of porosity that separates from the reaction front. Alternatively if the domain moves too slowly to detach from the source a wave train develops. The isolated wave and wave train correspond to steady-state solitary (Richter and McKenzie 1984; Barcilon and Richter 1986) and periodic (Sumita et al. 1996; Connolly and Podladchikov 1998) wave solutions of the

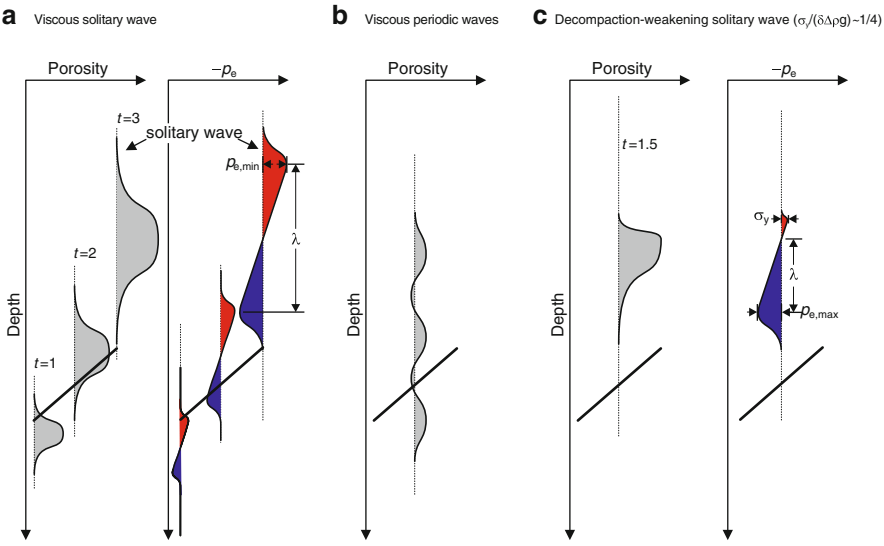

Fig. 14.6 Time evolution of reaction-generated porosity and fluid overpressure, $p_f - p$, profiles in a viscous solid matrix. For each profile the baseline is indicated by a vertical dotted line that corresponds to the background porosity, ϕ_0, or zero overpressure. In the symmetric viscous case (**a**), the magnitude of the fluid pressure anomalies within the reaction-generated porosity is proportional to the vertical extent of the high porosity. Thus, the anomalies grow as the reaction front advances upward until they become large enough to cause significant deformation. Thereafter, compaction at the base of the high porosity region squeezes fluid upward to the upper portion of the high porosity region where it is accommodated by dilational deformation. This process has the effect of propagating the reaction-generated porosity upward. The high porosity region detaches from the source when the compaction rate at the base becomes comparable to the fluid production rate giving rise to a solitary wave that propagates independently of its source (Richter and McKenzie 1984; Connolly 1997). For the solitary wave to be stable it must propagate with speed $v_\phi > n_\phi v_0$ (Appendix, Eq. 14.54). If the source is too weak to sustain a wave with this speed then a periodic wave train forms that is unable to separate from the source (**b**). These periodic waves dissipate if the source is exhausted. If the fluid overpressures are large enough to induce embrittlement, decompaction becomes viscoplastic (**c**), but the compaction remains viscous. In this case, the lower portion of the solitary wave is unchanged from the symmetric viscous case, but hydrofracturing acts as homeostat that regulates the overpressures in the *upper* portion of the wave. The scenarios depicted here assume that the speed at which the reaction front propagates upward is not much greater than the speed of fluid flow v_0 through the unperturbed matrix, in the alternative, fast devolatilization scenario (Sect. 14.5.3) waves detach from the source only after the cessation of devolatilization

equations that govern two-phase flow in an infinite viscous matrix (Fig. 14.6b and Appendix). In the case of the solitary wave solution, the steady state consists of a single isolated wave that propagates without dissipating. Because of its solitary character, this steady state can plausibly be realized in nature and has been verified in analog experiments (Scott et al. 1986). Additionally, numerical experiments have shown that solitary waves are resistant to perturbations, e.g., if two waves collide they regain their initial form after the collision (Richter and McKenzie 1984; Scott and Stevenson 1986). In contrast, the periodic steady state consists of an infinite

wave train, which cannot be realized in nature. Thus, although a finite periodic wave train, in close proximity to the infinite steady state, may develop in response to a fluid source, once the source is exhausted the finite wave train will spread and dissipate to smooth flow.

14.5.1.1 Why Don't Solitary Waves Dissipate?

It is natural to wonder why steady-state wave solutions exist at all. The origin of the phenomenon is the non-linear relation between porosity and permeability (e.g., Eq. 14.17) that permits flow perturbations to grow into shocks that propagate more rapidly than the fluid flows by hydraulic diffusion (Spiegelman 1993). This phenomenon is most easily explained for a matrix with no strength (i.e., the classical metamorphic model) in which case fluid pressure is lithostatic and fluid flux and velocity are solely a function of porosity. Consider then a situation in which a region with a large flux ($\mathbf{q}_1 = \mathbf{v}_1\phi_1$) is overlain by a region with a small flux ($\mathbf{q}_0 = \mathbf{v}_0\phi_0$) and that the regions are, initially, connected by a region in which the porosity decreases upward (Fig. 14.7a). From Eqs. 14.9 to 14.17, in terms of the fluid velocity in the low porosity region, the fluid velocity at any other porosity is

$$\mathbf{v} = \mathbf{v}_0(\phi/\phi_0)^{n_\phi - 1}. \tag{14.20}$$

At any point where the porosity gradient is finite and decreases in the direction of flow, the divergence of the flux (i.e., the difference between the flux into and out of an infinitesimal volume) is also finite. This divergence must be manifest by an increase in porosity, i.e., dilational strain, which leads to a steepening of the porosity gradient and, ultimately, the formation of a porosity shock (i.e., a self-propagating step in the porosity profile, Fig. 14.7b). Because the shock is moving more rapidly than the fluid in front of shock, in a reference frame that moves with the shock, the flux from the unperturbed matrix must be directed toward the shock. Consequently, as the shock propagates it gains fluid volume at the rate $q_1 - q_0$ from the low porosity region. As the porosity behind the shock is constant, conservation of the fluid volume requires that the shock velocity satisfies

$$\mathbf{v}_\phi = (\mathbf{q}_1 - \mathbf{q}_0)/(\phi_1 - \phi_0), \tag{14.21}$$

or, making use of Eq. 14.20,

$$\mathbf{v}_\phi = \mathbf{v}_0(1 - (\phi_0/\phi_1)^{n_\phi})/(\phi_1/\phi_0 - 1). \tag{14.22}$$

From Eq. 14.22, the smallest discrepancy between the velocity of the shock, and that of the fluid behind the shock, occurs in the limit that the shock is small, i.e., $\phi_1 \to \phi_0$. The solitary porosity wave represents a steady state in which the finite strength of the matrix balances the tendency of fluid flow to steepen the porosity profile. Although the solitary wave is more complex than the simple shock, the

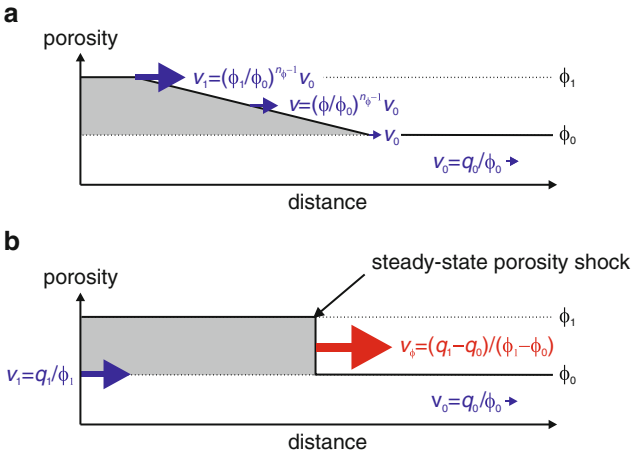

Fig. 14.7 Formation of a porosity shock during fluid flow through an inviscid matrix (i.e., the classical metamorphic model). If the matrix is inviscid, then fluid pressure must be lithostatic and fluid velocity is solely a function of porosity. Consequently, if porosity decreases in the direction of flow, fluid in the high porosity direction catches up to the fluid in the low porosity region. This process increases the porosity gradient until it becomes infinite. At which point, the resulting step in the porosity profile corresponds to a porosity shock. In a reference frame that moves with the shock, the fluid flux from the unperturbed matrix is negative; thus the shock must travel more rapidly than the fluid behind it (Eq. 14.22). The minimum discrepancy between the fluid and shock velocities occurs when the porosity behind the shock is only infinitesimally larger than the background value. In this case, the velocity of the shock is $n_\phi v_0$, and corresponds to the minimum velocity at which the solitary wave solution is stable in a matrix with a finite viscosity (Appendix, Eq. 14.54)

solitary wave must have the same properties as the simple shock at the conditions where it connects to the unperturbed porosity. At this point the fluid velocity is $\mathbf{v}_0$ and, from Eq. 14.22, the velocity of the simple shock is $n_\phi \mathbf{v}_0$. Thus, a requirement for the existence of steady-state solitary porosity waves is that they move ~ n_ϕ times faster than the flow through the unperturbed matrix (Appendix, Eq. 14.54). As in the simple shock, the solitary wave catches up with fluid flow through the background porosity with the consequence that a geochemical signal from the wave source may become diluted with time. The magnitude of this effect can be quantified (Spiegelman and Elliott 1993), but it is insignificant for large amplitude waves, i.e., $\phi_{max} >> \phi_0$.

14.5.2 One-Dimensional Isothermal Waves: How Big, How Fast, and How Much?

In the limit of a small perturbation to steady fluid flow through a uniform fluid-filled porosity, compaction phenomena develop on a natural length scale known as the viscous compaction length (McKenzie 1984). For a power-law viscous matrix this scale (Appendix, Eq. 14.63) is

$$\delta = \phi_0^{\frac{n_\phi - 1}{n_\sigma + 1}} \sqrt[n_\sigma + 1]{\left(\frac{2}{n_\sigma + 1}\right)^{n_\sigma} \frac{c_\phi}{c_\sigma A \mu (\Delta\rho g)^{n_\sigma - 1}}}, \tag{14.23}$$

The compaction length is an estimate of the depth interval over which the matrix can sustain a non-lithostatic pressure gradient and, as such, it is unsurprising that it increases both with the strength ($\propto 1/A$, Eq. 14.16) of the matrix and the ease with which fluid flows through it ($\propto c_\phi/\mu$). The speed of fluid flow at lithostatic fluid pressure through the unperturbed matrix, $v_0 \approx c_\phi \phi_0^{n_\phi - 1} \Delta\rho g/\mu$ (Eqs. 14.4 and 14.9), provides a natural scale for the speed of compaction processes. From this speed the compaction time scale (δ/v_0) is

$$\tau = \phi_0^{\frac{n_\sigma(1 - n_\phi)}{n_\sigma + 1}} \sqrt[n_\sigma + 1]{\left(\frac{\mu}{c_\phi (\Delta\rho g)^2}\right)^{n_\sigma} \Big/ A}, \tag{14.24}$$

The compaction scales given by Eqs. 14.23 and 14.24 separate the porosity ϕ_0 of the fluid-rock aggregate from material properties (A, $\Delta\rho$, μ, c_ϕ) that are, at least in principle, measurable quantities. In metamorphic problems this porosity is an unknown property of the initial state. The challenge presented by metamorphic fluid expulsion is to find observations that constrain the compaction scales and thereby this initial state. Because the compaction scales are formulated in terms of the initial state they represent, for $n_\sigma > 1$ and $n_\phi > 1$, a lower bound on the length scale and an upper bound on the time scale for fluid expulsion.

Given the uncertainties in the material properties involved in the compaction scales, it may be preferable to use observational constraints to infer the magnitudes of these scales. To this end, background flux q_0, which is presumably less than the time-averaged metamorphic flux, provides a useful proxy for the hydraulic material properties. Taking the observations of Young and Rumble (1993), van Haren et al. (1996), and Graham et al. (1998) to be indicative of compaction time scales O(10^4) y at amphibolite facies conditions ($T = 773 - 923$ K), in conjunction with a plausible estimate for $v_0 = q_0/\phi_0$ of 10^{-10} m/s, the compaction length ($\delta = \tau v_0$) consistent with these observations is 31 m. Clearly, it would be preferable to have direct observational constraints on the compaction length scale, as might be provided by variation in the pressures ($O(2\delta\Delta\rho g)$) recorded by syn-metamorphic fluid inclusions or, as discussed subsequently, by the length scale ($O(\delta)$) for lateral fluid flow. However, taken at face value, an $O(10^4)$ y time scale and an $O(10^2)$ m length scale implies a viscous rheology roughly three orders of magnitude weaker than given by Eq. 14.14 for tectonic strain rates $O(10^{-15})$ s^{-1}. A discrepancy of this magnitude can be explained if fluid expulsion is contemporaneous with pulses of intense tectonic deformation that lower the effective viscosity of the crust; an explanation consistent with a non-uniformitarian model of deformation and metamorphism (Oliver et al. 2000; Dewey 2005; Ague and Baxter 2007).

There is no fundamental principle that dictates a steady-state balance between metamorphic fluid production and transport, but for the range of conditions

investigated by numerical simulations of metamorphic compaction-driven fluid flow (Connolly 1997; Connolly 2010) such a balance does develop locally. A requirement for this balance is that the time-averaged flux associated with the passage of a wave must be greater than or equal to the vertically integrated production, $\bar{q}$, because a wave with $q_e < \bar{q}$ would be unable to separate from its source. This time-averaged flux is

$$q_e = \frac{v_\phi}{\lambda} V_e^{1d} \tag{14.25}$$

where λ and v_ϕ are the length and speed of the wave, and

$$V_e^{1d} = \int_{-\lambda/2}^{\lambda/2} (\phi - \phi_0) dz \tag{14.26}$$

is the fluid volume associated with the wave, which in one dimension has units of length. If $q_e > \bar{q}$, then the waves must be separated by a depth interval of

$$\Delta z = \lambda(q_e/\bar{q} - 1)$$

In 1-d numerical simulations, the transient dynamics of wave separation are such that $q_e/\bar{q}$ is typically < 2 (Connolly 1997). This result suggests that, to a first approximation, the properties of waves expected in metamorphic environments can be predicted from the steady-state solitary wave solution to the compaction equations (Fig. 14.8). The solitary wave solution does not exist for values of $q_e/q_0 < 2$ (Appendix, Eq. 14.53), thus weak sources, or strong background fluxes, will generate periodic waves that degenerate to uniform flow once the source is exhausted. Periodic solutions to the compaction equations exist for all conditions; however numerical (Richter and McKenzie 1984; Scott and Stevenson 1986; Wiggins and Spiegelman 1995; Connolly 1997) and analog (Scott et al. 1986) simulations suggest that the solitary wave solution is the stable solution whenever it is a possible solution. The reason for this stability is unclear, but is most probably related to the fact that the solitary wave is the more effective expulsion mechanism and therefore maximizes the rate of dissipation of gravitational potential energy.

Because the matrix recovers to the background porosity asymptotically in a steady-state solitary wave (for $n_\sigma \geq 1$), the wavelength of the true steady state is infinite (Appendix, Eq. 14.59). For practical purposes, it is desirable to define an effective wavelength, which defines the extent of the wave that includes the bulk of the anomalous porosity. Two non-arbitrary measures of wavelength are the distance between the points of minimum and maximum effective pressure (λ) and twice the second moment of the porosity distribution within the wave (λ_1, Fig. 14.8c), the former value being roughly half the latter. Comparison of the excess volume obtained by integrating the porosity over these intervals to the total excess volume obtained by integrating over infinite space (dashed curve, Fig. 14.8d) shows that,

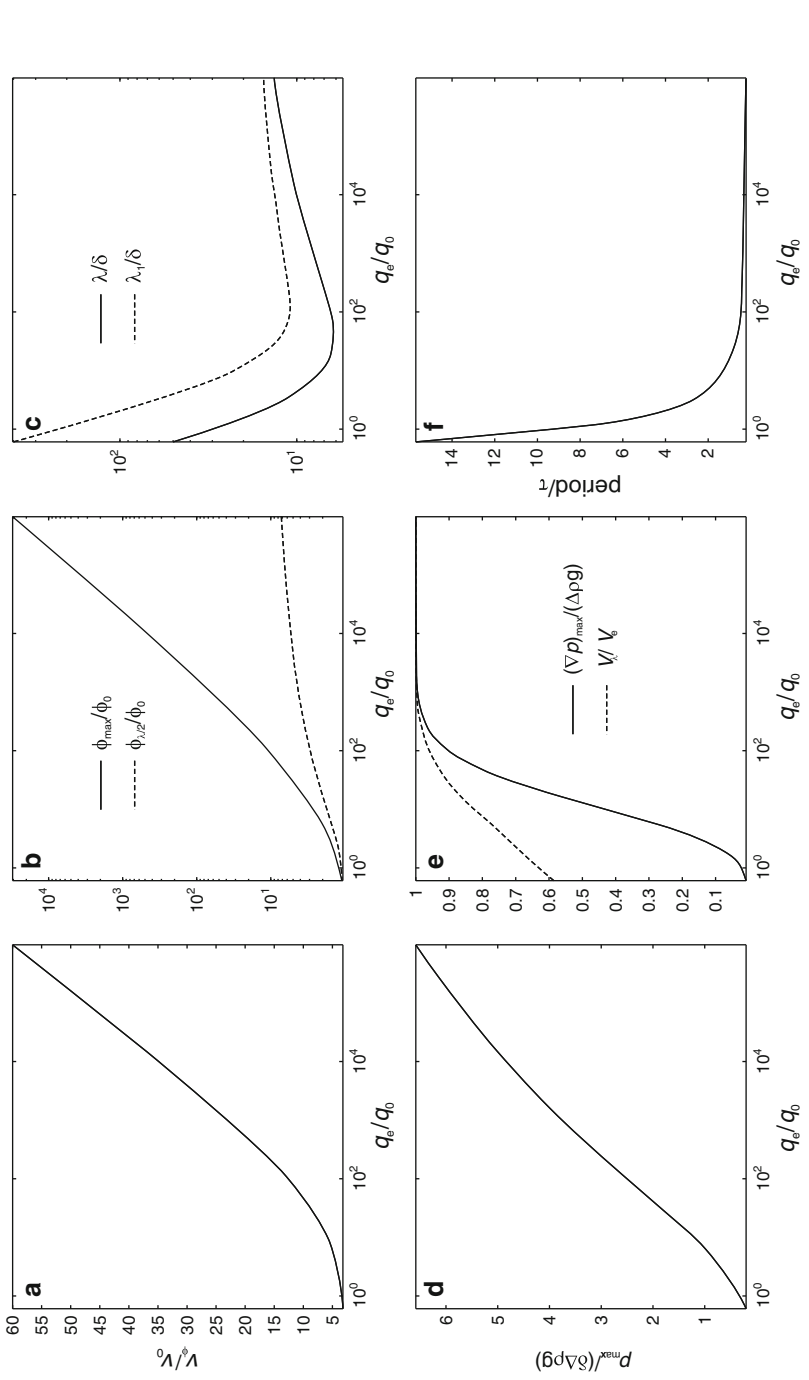

Fig. 14.8 Steady-state 1-d solitary wave properties (for $n_\sigma = n_\phi = 3$) as a function of the excess fluid flux q_e, which is the time-averaged flux associated with the passage of a porosity wave estimated as the product of the wave period and its excess volume. The power law exponent does not influence the speed-amplitude relation, but wavelength increases inversely with n_σ. (**a**) Wave speed, v_ϕ. (**b**) Maximum porosity ϕ_{max}, and porosity at the depth of maximum effective pressure within a wave (Fig. 14.6a). (**c**) Two measures of the spatial extent of solitary waves: λ is the depth interval between the minimum and maximum effective pressure (Fig. 14.6a), and λ_1 is the second moment of the porosity distribution. (**d**) Maximum effective pressure within the wave. (**e**) Maximum effective pressure gradient ($\phi = \phi_{max}$, $p_e = 0$) and the fraction of the total excess volume of the wave that occurs within the depth interval $\pm\,\lambda/2$ around ϕ_{max}. (**f**) Wave period, λ/v_ϕ

even at the minimum q_e for solitary wave stability, >80% of the porosity of a wave occurs within a distance of $\pm\ \lambda/2$ from its center. Accordingly, λ is adopted here as the measure of wavelength rather than the more conservative measure λ_1. The solitary wave period, λ/v_ϕ, is the time required for a wave to travel its wavelength.

To illustrate the quantitative implications of the solitary wave solution, consider the initial condition $\phi_0 = 10^{-4}$, $q_0 = 10^{-14}$ m/s, $\tau = 10$ ky, and $\delta = 31$ m, which, as discussed previously, is chosen to be consistent with the timing of fluid-rock interaction during amphibolite facies metamorphism (Young and Rumble 1993; van Haren et al. 1996; and Graham et al. 1998). From this condition, and the properties of the solitary wave steady state (Fig. 14.8), the waves required to conduct a typical metamorphic flux $\bar{q} = 10^{-12}$ m/s (i.e., $q_e/q_0 = \bar{q}/q_0 = 10^2$) have $\lambda = 200$ m, $\phi_{max} = 1.0{\cdot}10^{-3}$, travel at $v_\phi = 39$ m/ky, and are associated with fluid pressure anomalies of 1.4 MPa. These pressure anomalies are small enough that a viscous dilational mechanism for wave propagation is plausible. The sensitivity of this result is demonstrated by considering the effect increasing $\bar{q}$ to 10^{-10} m/s, which is consistent with the rate for Dalradian regional metamorphism inferred by Ague and Baxter (2007). For this increased flux, $\lambda = 320$ m, $\phi_{max} = 55{\cdot}10^{-3}$, $v_\phi = 110$ m/ky, and $p_{max} = 2.9$ MPa; the most prominent difference being the large increase in porosity.

14.5.3 *Fast Versus Slow Devolatilization and Complex Fluid Sources*

The knife-edge sharp, constant volume, devolatilization reaction used so far for purposes of illustration may seem unrealistic, but it captures the essence of the fluid expulsion problem, which is not how fluid is released, but rather how it escapes. The key to predicting the waves that are likely to evolve in response to more complex devolatilization processes is to obtain plausible estimates for both the background flux that the system is capable of accommodating without appreciable dilational deformation and the excess flux generated by devolatilization that must be accommodated by porosity waves.

The relationships between porosity wave speed and excess flux (Fig. 14.8a) and between excess flux and wave amplitude (Fig. 14.8b) indicate that extraordinarily large porosities are required to generate waves that travel more than two orders of magnitude faster than the speed of the fluid flow in the unperturbed matrix. As the analytical formulation ignores large porosity effects that lead to a further weakening of the dependence of speed on amplitude, it is reasonable to conclude that if natural porosity waves exist, then they do not propagate at speeds $>> v_0$. Given that a porosity wave can only escape from a devolatilization reaction front if it travels faster than the front, these considerations imply that the wave nucleation scenario outlined in Sect. 14.5.1 represents the limiting case of slow devolatilization, wherein the devolatilization front propagates at speeds that are comparable

to or less than v_0. In the alternative fast devolatilization scenario, devolatilization generates a high porosity source region. Porosity waves cannot escape from this source until lithological heterogeneity or geodynamic factors hinder the advance of the devolatilization front. If it is assumed that the material properties of the reacted and unreacted rocks do not differ significantly, then the porosity increase within the source region decreases the time scale for intra-source fluid expulsion (Eq. 14.24). This increase in efficiency has the consequence that the excess flux delivered to the upper boundary of the source region is independent of the processes in the unreacted rocks, which compact on a longer time scale. If the porosity, ϕ_1, within the source is $>> \phi_0$, then this excess flux is $\sim q_0(\phi_1/\phi_0)^{n_\phi}$ and the waves that ultimately evolve from the source can be expected to carry a flux that is greater than, but comparable to this flux. Spiegelman (1993) demonstrated that in the waves which nucleate at the boundary between the source and unreacted rocks are not true solitary waves. However, for large porosity contrasts, i.e., $\phi_1 >> \phi_0$, the distinction is not important and is diminished still further in models that account for the elastic compressibility of the fluid (Connolly and Podladchikov 1998).

The dehydration model presented earlier suggests that in nature devolatilization may occur by many reactions simultaneously over a depth interval of several kilometers (Fig. 14.3). The increase in porosity caused by these reactions increases the compaction length within such an interval, an effect that will tend to blur the influence of individual reactions. Thus the characteristics of waves that would evolve above such an interval can be anticipated by equating the excess flux to either the vertically integrated fluid production in the slow devolatilization limit, or to $q_0(\phi_1/\phi_0)^{n_\phi}$ in the fast limit.

A reaction with a finite isobaric volume change leads to a coupling between devolatilization kinetics, temperature, and fluid pressure, but this coupling does not hinder the evolution of porosity waves (Connolly 1997). Finite volume change reactions also influence the initial pressure distribution, but regardless of this distribution, deformation will cause the system to evolve toward a state in which effective pressures are low or negative at the top of the reacted region. For example, a reaction with a positive (isobaric) volume change may initially generate fluid overpressure throughout the reacted rocks, with the result that hydraulic diffusion drives fluid both upward and downward from the reaction front. Thus the flux within the reacted rocks is not constrained by symmetry. However, provided the permeability within the reacted rocks is much higher than in the surroundings, the fluid pressure gradient will approach the hydrostatic value. Thus, the greatest overpressures will occur at the top of the reacted column. This distribution must lead to higher rates of dilational deformation at the top of the column and, ultimately, underpressured porosity at depth.

Despite the complexities that may influence the kinetics of individual devolatilization reactions, there is reason to believe that overall rates of metamorphic devolatilization do not differ greatly from those predicted by equilibrium models. Specifically, if rocks cannot sustain large fluid overpressures then the thermal overstepping of the equilibrium conditions is likely to be the primary manifestation of disequilibrium. As reaction kinetics are typically an exponential function of

temperature (Rubie and Thompson 1985), moderate thermal overstepping should accelerate kinetics to the point at which they become limited by the rate of energy input as would be the case for an equilibrium system. This logic assumes that rocks cannot support large elastic stresses. That this assumption is not a universal truth has been demonstrated in experiments on reactive systems in which a fluid inclusion achieves a non-hydrostatic equilibrium with its surroundings (Kerschhofer et al. 1998; Mosenfelder et al. 2000; Milke et al. 2009). Vrijmoed et al. (2009) argue that strength contrasts in rocks are capable of generating large scale fluid inclusions that sustain pressures far above the lithostatic load. An effect of this nature has been invoked to explain the seemingly metastable persistence of volatile-bearing rocks (Padron-Navarta et al. 2011).

14.5.4 Multidimensional Viscous Porosity Waves

The 3-d expression of the 1-d porosity wave just discussed corresponds to a sill-like structure (Fig. 14.9b). However in two and three dimensions both numerical (Scott and Stevenson 1986; Stevenson 1989; Wiggins and Spiegelman 1995) and analytical (Barcilon and Lovera 1989) models show that 1-d solitary waves are unstable with respect to circular and spherical solitary waves. This instability is demonstrated numerically for fluid flow from a high porosity region, an analogy for a metamorphic fluid source, by introducing random noise into the initial porosity distribution (Fig. 14.9a). Although the 2-d waves (Fig. 14.9c) appear significantly different from the 1-d waves (Fig. 14.9b) that evolve from the initial porosity distribution without noise, it emerges that their properties are well approximated by applying radial symmetry to the porosity distribution of the 1-d solitary wave solution (Connolly and Podladchikov 2007). Thus, 1-d and 2-d solitary waves have an essentially equivalent relation between amplitude and speed. Although untested, it is assumed that the same approximation can be made in 3-d by applying spherical symmetry to the 1-d porosity distribution. That the 2-d approximation is nearly exact in the limit that the maximum porosity is $> 10\ \phi_0$ is verified by comparing the relationship between wave velocity and amplitude in analytic (Fig. 14.8) and numerical results (Fig. 14.9). The reason for the increased speed of 2-d waves compared to 1-d waves emanating from a comparable source is primarily the effect of a weak spatial focusing of the source flux in the 2-d case. The most important distinction between planar and circular waves is the existence of strong lateral pressure gradients associated with the dipolar pressure field of circular waves (Figs. 14.9d and 14.10a). Thus, in contrast to the unidirectional fluid flow of planar waves, fluid flow in circular waves is characterized by a circular pattern in which lateral fluxes are of comparable magnitude (Scott 1988; Connolly 2010). The circular pattern develops in the reference frame of the wave (Fig. 14.10a), but, in the reference frame of the solid matrix, passage of a wave is marked first by fluxes with a lateral component away from the vertical axis of the wave, followed by a period in which the lateral component is directed toward the axis. During this oscillation, the vertical component of the flux is always upward.

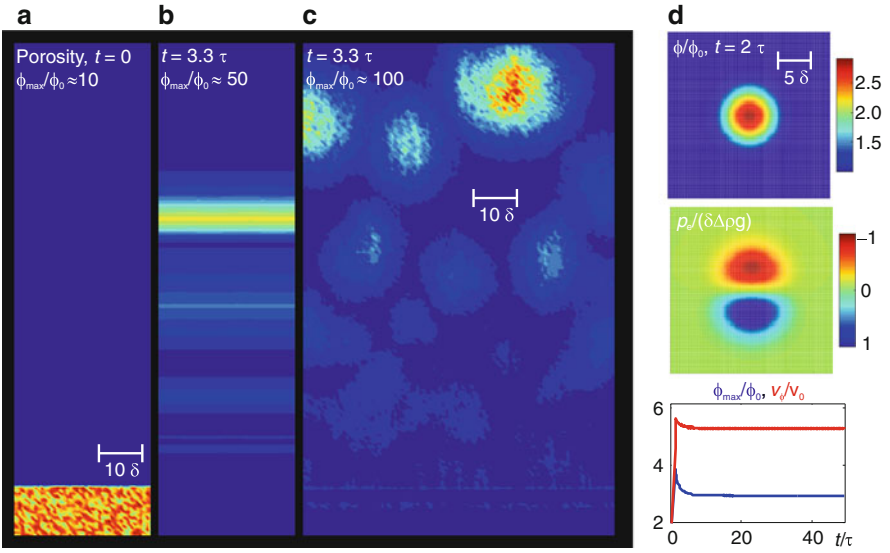

Fig. 14.9 Two-dimensional numerical simulations of porosity waves initiating from high porosity horizons that differ only in that in one case random noise is added to the initial porosity distribution. The simulations are for a Newtonian matrix ($n_\sigma = 1$, $n_\phi = 3$). If the initial porosity is perfectly smooth, 1-d sill-like waves nucleate from the source (**b**). However, if white noise is added to the initial porosity distribution as depicted in (**a**), the 1-d waves become unstable with respect to circular 2-d waves (**c**). The 2-d waves cause spatial focusing of the source flux. Consequently the 2-d waves have larger amplitudes and higher velocities than 1-d waves initiating from a similar source. Numerical simulations have also shown that the stable viscous solitary wave geometry in 3-d is spherical (Wiggins and Spiegelman 1995). (**d**) A numerical simulation of a 2-d wave nucleated from a small circular source region, illustrating the dipolar effective pressure field and the short duration of transient effects (i.e., the wave has essentially reached a steady state by $t/\tau \sim 2$). Wave properties along the vertical axis of 2-d waves, with $\phi_{max}/\phi_0 > 10$, are indistinguishable from those predicted for 1-d waves with the same amplitude (Connolly and Podladchikov 2007)

14.5.5 Porosity Waves in an Upward Strengthening Crust

The preceding discussion has ignored the temperature dependence of the viscous rheology, which is responsible for the upward strengthening of the lower crust. From Eq. 14.12, the compaction length and time scales increase exponentially with decreasing temperature towards the Earth's surface, increasing by a factor of $(n_\sigma + 1)^{-1}$, for a decrease in depth comparable to the viscous e-fold length l_A (Eq. 14.15, Fig. 14.1). This effect makes achievement of true steady-state waves a mathematical impossibility because the compaction scales vary between the top and bottom of a wave (Connolly 1997). The strength of this variation can be assessed by comparing the steady-state wavelength λ to l_A. If $\lambda << l_A$, then the rheological variation within the wave is weak and a quasi-steady state may arise such that at any point in time the properties of the wave closely approximate the

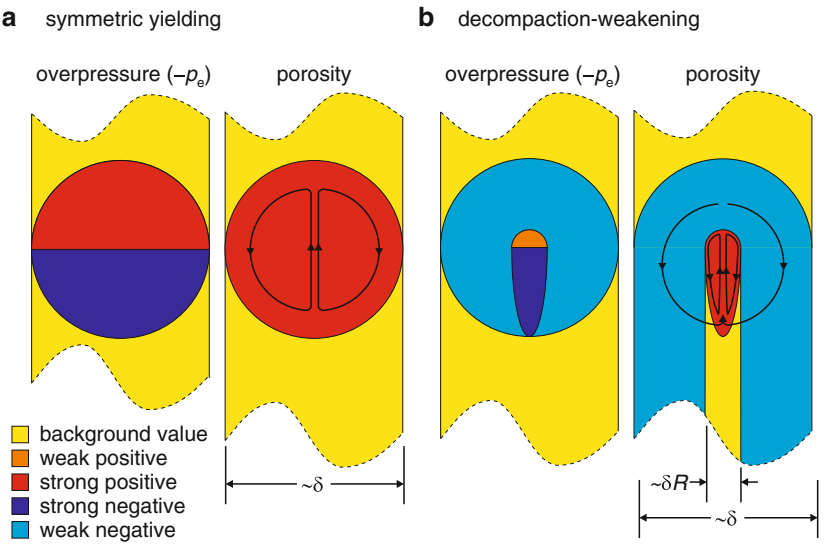

Fig. 14.10 Illustration of the scaling arguments used to relate the solitary wave solution in the symmetric viscous case (**a**) to the solitary waves that develop in a matrix with decompaction weakening (**b**). *Colors* indicate regions of the matrix that are characterized by weakly and strongly depressed or elevated values of overpressure and porosity. Approximate fluid flow paths, relative to a reference frame that moves with the porosity wave, are shown in the porosity map. The true paths do not close because the wave is subject to a small fluid flux from the background porosity (Fig. 14.7). This discrepancy is insignificant in large amplitude waves. In the reference frame of the solid, the vertical component of compaction driven fluxes is upward. In the symmetric case, the pressure distribution associated with a porosity wave is an antisymmetric dipole that induces balanced fluid circulation so the wave has no tendency to gain or lose mass (Fig. 14.11d). With decompaction weakening, fluid underpressures and compaction develop on the length scale δ as in the symmetric viscous case, whereas decompaction and overpressure develop on the shorter length scale δR. Thus, decompaction generates an elevated region of porosity and pressure analogous to the *upper* hemisphere of the symmetric viscous case, but on this shorter length scale. Restoration of this elevated porosity occurs on the length scale δ, which causes the compacting portion of the wave to develop a semi-ellipsoidal geometry. Fluid underpressure in the compacting region relaxes on the length scale δ causing compaction of the matrix in advance of the wave as well as in laterally adjacent portions of the matrix that have not been perturbed by decompaction. The asymmetric pressure distribution causes unbalanced fluid circulation, with the result that the wave gains mass from the matrix as it propagates, this imbalance is indicated schematically by the outermost, unclosed, flow path

steady state. In this regime, waves slow and spread as they propagate upward. In the limit $\lambda \rightarrow l_A$ this quasi-steady state becomes infeasible because compaction within a wave occurs much more rapidly than decompaction. At this point, the local compaction length scale becomes meaningless for compaction processes in the vertical direction, and l_A determines the vertical length scale (Connolly and Podladchikov 1998). In the absence of strong lateral thermal gradients, as assumed here, the local compaction length dictates the scale of lateral processes, thus,

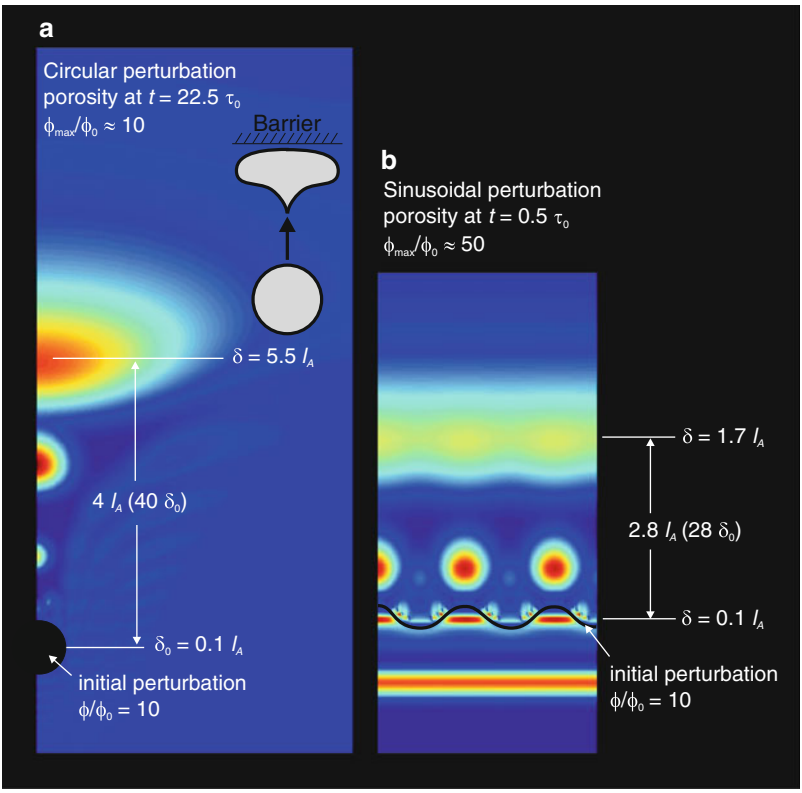

Fig. 14.11 Two-dimensional numerical simulations of viscous porosity waves in a rock matrix that strengthens upward due to thermal activation on the length scale l_A (Fig. 14.1). This effect causes the local compaction length δ to increase upward from its initial value δ_0; the simulations are for Newtonian rheology ($n_\sigma = n_\phi = 3$). (**a**) If the source is at depth such that $\delta_0 < l_A$, the quasi-steady state waves mimic the circular viscous steady-state, but spread as they rise upward until their wavelength approaches l_A at which point the waves flatten to oblate ellipsoids with vertical length scale l_A and horizontal length scale δ. The wave velocities decay exponentially upward on the length scale l_A. (**b**) Waves are generated from a high porosity layer with a sinusoidal upper boundary at depth such that $\delta_0 < l_A$. This simulation demonstrates that the effect of thermal activation is to restabilize 1-d solitary waves when wavelength approaches l_A (Modified from Connolly and Podladchikov (1998))

thermal activation gives rise to an intrinsic anisotropy to compaction-driven fluid flow.

The consequences of thermal activation for the 2- and 3-d viscous solitary wave solutions is demonstrated by a numerical experiment in which upward propagating waves are induced from a circular source (Fig. 14.11a) . At the initial depth, the waves are small in comparison to l_A and approximate the circular 2-d steady state. As the waves migrate upward their wavelength becomes comparable to l_A and they flatten to ellipsoidal structures with the horizontal length scale controlled by the local value of δ and the vertical length scale limited by l_A. A second numerical

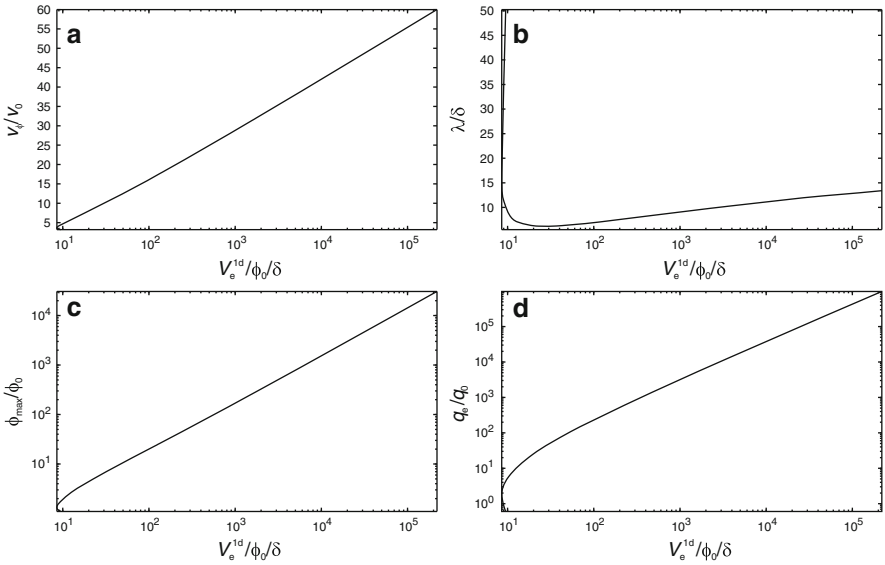

Fig. 14.12 Steady-state 1-d solitary wave properties in a power law ($n_\sigma = n_\phi = 3$) viscous matrix as a function of the excess volume (V_e^{1d}, Eq. 14.26). These properties can be used to predict quasi-steady state wave evolution in upward strengthening rocks as a function of the local compaction length. See text for discussion

experiment, in which waves initiating from a horizontal source are destabilized by a perturbation, shows that the effect of thermal activation is to restabilize 1-d planar waves (Fig. 14.11b). To show that this process is relevant to crustal fluid flow it is necessary to show that the wavelength of quasi-steady state waves will approach the l_A at the brittle-ductile transition (Fig. 14.1). This cannot be established from wave properties expressed as a function of excess flux because this flux decays as waves slow. However, quasi-steady state waves may conserve the excess fluid volume

$$V_e = \int\int\int (\phi - \phi_0) \mathrm{d}x\mathrm{d}y\mathrm{d}z \tag{14.27}$$

and therefore wave evolution can be predicted as a function of V_e (Fig. 14.12) provided $\lambda < l_A$. There are two complications in such predictions. The more difficult is that if waves evolve from 3-d structures, it is necessary to account for lateral variations in porosity. To avoid this complexity, the waves are approximated here as 1-dimensional. This approximation has the consequence that waves lengthen more rapidly than they would if 3-d geometry were taken into consideration. The second complication is that the dimensionless excess volume has a minimum at $V_e^{1d}/\delta/\phi_0 \sim 8$ (Fig 14.13a), thus a wave that initiates with $V_e^{1d}/\delta/\phi_0 > 8$ and broadens upward due to thermal activation cannot increase its wavelength above $\lambda_{max} \sim 17\ \delta$, the wavelength at $V_e^{1d}/\delta/\phi_0 \sim 8$, and must decay to the dissipative periodic solution as it propagates above this point, i.e., at $v_\phi \approx 3.5\, v_0$, slightly above the minimum velocity at which the solitary solution is stable. Returning to the

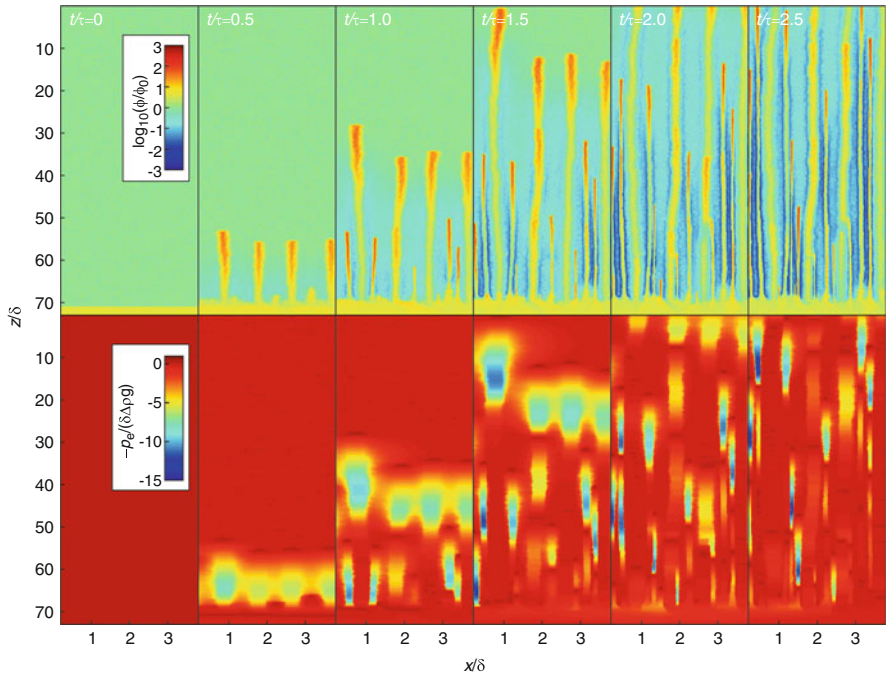

Fig. 14.13 Two-dimensional numerical simulation of fluid flow through a matrix with decompaction weakening ($R = 0.03$) as it evolves from a layer with elevated porosity of thickness 60 δ that is bounded from above and below by regions with an order of magnitude lower porosity. *Upper panels* show porosity in the uppermost portion of the layer and in the overlying region. *Lower panels* show the corresponding distribution of fluid overpressure. Initial waves ($t = \tau/2$) form with characteristic spacing identical to the viscous compaction length and leave a trail of slightly elevated porosity, flanked by a fluid depleted matrix. Depletion of the matrix reduces the local compaction length scale for the initiation of subsequent waves ($t = \tau$). These waves collect within the trails of the initial waves, so that at 30 –40 δ from the initial obstruction, flow is again channelized on the length scale δ. By analogy with the 3-d viscous case (Wiggins and Spiegelman 1995), it is presumed that the 3-d expression of the channels would be pipe-like structures. However, in the presence of far field stress, kinematic effects would flatten the tubes in the direction of the minimum horizontal stress (Modified from Connolly and Podladchikov (2007))

amphibolite-facies example (Sect. 14.5.2), if thermal activation is the sole source of variability in the compaction scales, then from Eqs. 14.12, 14.23, and, 14.24 then the compaction scales can be expressed as a function of temperature by

$$\delta = \delta_0 \exp\left[\frac{Q}{n_\sigma + 1}\frac{T_0 - T}{TT_0}\right] \tag{14.28}$$

and

$$\tau = \tau_0 \exp\left[\frac{Q}{n_\sigma + 1}\frac{T_0 - T}{TT_0}\right], \tag{14.29}$$

where T_0 is the temperature at which the scales are δ_0 and τ_0. For $Q = 250$ kJ/mol, $n_\sigma = 3$, $\delta_0 = 31$ m, and $\tau_0 = 10$ ky, and estimating the temperature of the amphibolite facies metamorphism as $T_0 = 848$ K; the initial length and time scales increase to 780 m and 250 ky at the temperature of the brittle-ductile transition (~ 623 K). For $q_e/q_0 = \bar{q}/q_0 = 10^2$, from the initial wave speed $v_\phi/v_0 = 12.2$ (Fig. 14.8a), $V_e^{1d}/\delta_0/\phi_0 = 49$ (Fig. 14.12a) and, if $V_e^{1d}$and ϕ_0 are constant, then at the brittle-ductile transition $V_e^{1d}/\delta_1/\phi_0 = \left(V_e^{1d}/\delta_0/\phi_0\right)(\delta_0/\delta_1) = 2.0$. This value is below the minimum in $V_e^{1d}/\delta/\phi_0$, so in this case the wave would reach λ_{max} below the brittle-ductile transition, at which point it would begin to evolve toward the periodic wave solution. For the case $q_e/q_0 = \bar{q}/q_0 = 10^4$, the initial wave has $v_\phi/v_0 = 36$ and $V_e^{1d}/\delta_0/\phi_0 = 3400$, so at the brittle-ductile transition $V_e^{1d}/\delta_1/\phi_0 = 140$. From this value of $V_e^{1d}/\delta/\phi_0$ (Fig. 14.12), the quasi-steady state wave has $v_\phi/v_0 = 18$, $\lambda/\delta_1 = 7.2$, $\phi_{max}/\phi_0 = 28$, and $q_e/q_0 = 67$. As this wavelength (5,600 m) exceeds l_A it may be concluded that the flow processes would cease to be controlled by the viscous steady-state at greater depth. For this particular case, the overpressure associated with the wave (~50 MPa) near the brittle-ductile transition might be sufficient to provoke a change from viscous to plastic dilational deformation. In the absence of such a change, viscous waves are expected to die at depth, with smaller waves dying at greater depth. Death, in this context, means simply that the behavior of the system cannot be predicted in terms of the steady state. What can be predicted is that in its death throes a viscous wave will produce a sub-horizontal fluid-rich domain, with thickness comparable to l_A beneath the brittle-ductile transition.

14.5.6 Hydrofracture and Decompaction-Weakening

The viscous porosity wave mechanism requires overpressures of the same magnitude as the effective pressures that cause compaction ($\sim\lambda\Delta\rho g/2$). If these overpressures are greater than rock tensile strength, they induce plastic dilational strain by macroscopic or microscopic hydrofracturing, the latter manifestation being favored at high temperature (Hill 1950). Returning to the schematic devolatilization scenario considered in the viscous case (Fig. 14.6a), the greatest overpressures must occur at the top of the reacted horizon, thus repeated hydrofracturing will propagate porosity into the overlying rocks. Provided the hydrofracturing occurs on a length scale that is small in comparison to the viscous compaction length δ, the rate of propagation is limited by the rate at which compaction at depth supplies fluid to the hydrofracture front. Thus, in 1-d there is a steady state in which fluid driven upward through a porous domain, by viscous compaction at depth, is accommodated by hydrofracturing at overpressures that are much smaller than the effective pressures required for compaction (Fig. 14.6c). The difficulty in quantifying this steady-state is that it is dependent on details of the hydrofracture mechanism (Rozhko et al. 2007). An approximation that circumvents

this complexity is to assume that the effect of plasticity is to reduce the effective viscosity of rocks undergoing decompaction. The assumption is justified if hydrofracture and viscous dilation occur in tandem, because the effective behavior is then viscous; but characterizing this behavior by a single parameter is ad-hoc. For present purposes, the parameter chosen to characterize a relative weakening in decompaction is

$$R = \sqrt[n_\sigma+1]{A/A_\mathrm{d}}$$

where A_d is the coefficient of viscous flow during decompaction, i.e., $R < 1$. The reason for using R rather than A_d to characterize decompaction-weakening is that R is the proportionality constant that relates the length scales for decompaction and compaction, i.e., the decompaction length is $\delta_\mathrm{d} = R\delta$. If decompaction weakening maintains fluid overpressures near the tensile strength σ_y, then R is related to σ_y by

$$\sigma_\mathrm{y} = \delta_\mathrm{d}\Delta\rho g = R\delta\Delta\rho g. \tag{14.30}$$

Equation 14.30 results in a parameterization that is consistent with the expectation that overpressure is limited by the rock tensile strength, but it does not justify the formulation.

In the 1-d case, the existence of a solitary wave solution for a matrix with decompaction-weakening requires only that it is possible to connect the viscous solitary wave solution for the decompacting region, with length scale $R\delta$, with the viscous solution for the compacting region, with length scale δ. Because the relationship between wave velocity and amplitude is independent of the coefficient of viscous flow (Eq. 14.55, Appendix), this connection is possible in 1-d and identical to the viscous solitary wave solution except that the overpressured portion of the wave scales as $R\delta$ rather than δ. Compaction is the rate limiting process for the combined solution, with the result that the time scale for the steady state is unchanged from the viscous case. Moreover, for strong manifestations of plasticity, i.e., $R << 1$, the extent of the overpressured portion of the wave is insignificant, with the result that the wave solution for decompaction-weakening is well approximated by the lower half of the viscous solution. In numerical simulations, such waves appear as self-propagating fluid compartments within which fluid pressure rises along a hydrostatic gradient to pressures slightly above the lithostat (Connolly and Podladchikov 2000).

Decompaction-weakening results in a rheology in which rocks weaken in the direction of compaction-driven flow. This effect is the opposite of thermal activation in the viscous case, which leads to flattening of porosity waves (Fig. 14.11). Thus, decompaction-weakening causes waves to elongate in the direction of flow inducing channelization (Fig. 14.13). The channels are generated by tube-like porosity waves of extraordinary amplitude and speed that leave a trail of incompletely compacted porosity in their wake. These trails act as preferential pathways for subsequent fluid flow, and develop initially with spacing ~ δ and width ~ $R\delta$, a

geometry that amplifies the source fluid flux by a factor of ~ $4/R^2$. This pattern of fluid flow corresponds to that inferred in greenschist-facies rocks by Skelton et al (2000), who propose that the flow was episodic and propagated by microcracking. Similar flow patterns have also been inferred in asthenospheric systems (Jagoutz et al. 2006; Bouilhol et al. 2009; Bouilhol et al. 2011).

The tube-like waves are propagated by a region of overpressure that decompacts the matrix on the length scale "$R\delta$" (Fig. 14.13). A much larger region of underpressure of length scale δ, beneath the overpressured region, is necessary for compaction to expel fluid at the rate required to fill the porosity created by decompaction. This asymmetric pressure distribution induces unbalanced fluid circulation (Fig. 14.10b), which causes the waves to gain fluid by draining the porosity of the surrounding matrix. The gain in fluid obviates a steady state, but the speed-amplitude relation of the waves is essentially identical to the symmetric viscous case suggesting a quasi-steady state. This quasi-steady state can be explained by observing that if decompaction is much more rapid than compaction, then the decompacting region will develop with the characteristics of the upper hemisphere of the 2- or 3-d viscous solution on the length scale $R\delta$. Compaction restores the porosity generated by decompaction on the length scale δ, thus the compacting region will approximate the lower half of a prolate ellipsoid (Fig. 14.10b). The associated fluid volume is $R^2V_e^0/2$, where V_e^0 is the fluid volume of the 3-d spherical viscous solution (Eq. 14.27), which is approximated by applying spherical symmetry to the porosity distribution of the 1-d viscous solution. For R in the range $10^{1/2}$– 10^3 this model has been verified by comparison with numerical simulations for linear viscous rheology ($n_\sigma = 1$, Connolly and Podladchikov 2007). These simulations also show that, in the absence of thermal effects, wave amplitude grows as

$$\partial\phi_{\max}/\partial t \approx \phi_0 \Big/ \left(\tau R^{3/4}\right). \tag{14.31}$$

and that the speed-amplitude relation of waves is essentially identical to the steady solitary wave solution in a viscous matrix without decompaction-weakening if the simple viscous matrix is characterized by the $AR^{n_\sigma+1}$. This latter result implies that the effective time-scale for compaction-driven fluid flow in a decompaction-weakening matrix is dictated by the viscous response of the weak, overpressured, rocks, i.e., the effective time-scale is

$$\tau_d \approx \tau R. \tag{14.32}$$

Given the ad-hoc nature of the parameterization further quantification is unwarranted, but the role of plastic yielding should increase with falling temperature because δ is strongly dependent on temperature, but yield strength is weakly temperature dependent. Thus, a decompaction-weakening rheology causes compaction-driven fluid flow to become increasingly focused towards the surface, the antithesis of the behavior of the symmetric viscous case.

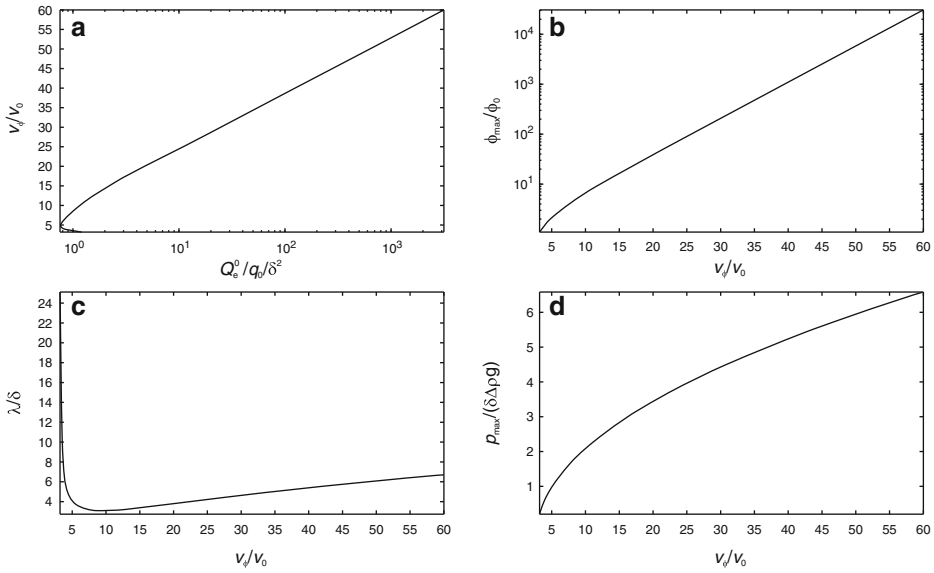

Fig. 14.14 Quasi-steady state solitary wave properties (for $n_\sigma = n_\phi = 3$) for a decompaction-weakening viscous rheology as a function of Q_e^0. For $R << 1$, the volumetric rate of fluid transport by a wave is $Q_e \approx Q_e^0 R^2$. Equating this rate to the source flux that is focused into the wave, $Q_s \approx 4\bar{q}\delta^2$, yields the value of $Q_e^0/\delta^2 q_0$(i.e., $4\bar{q}/R^2 q_0$). This value is appropriate to predict the properties of the 3-d tube-like waves that would nucleate from a dehydrating horizon

Decompaction weakening causes fluid flow within a horizontal source region to be focused into tube-like channels of width $R\delta$ with a characteristic spacing δ. The properties of the waves responsible for channel formation can be predicted as a function of R and fluid production within the source region if, as before, a balance between fluid transport and production is assumed. The symmetry of the quasi-steady state is such that for $R << 1$ the rate of fluid transport, by a wave, is $Q_e \approx Q_e^0 R^2$, where $Q_e^0 = V_e^0 v_\phi/\lambda/2$ is half the rate for the viscous rheology ($R = 1$). Approximating the area drained by a channel as a square of area $4\delta^2$, the vertically-integrated fluid production rate within the source region is $Q_s \approx 4\bar{q}\delta^2$. Equating Q_e and Q_s, rearranging the result, and dividing through by q_0 to make the result non-dimensional, yields

$$\frac{Q_e^0}{\delta^2 q_0} \approx \frac{4\bar{q}}{R^2 q_0}. \tag{14.33}$$

Given Q_e^0 from Eq. 14.33, wave speed, amplitude, and wavelength, which are independent of R, are recovered from the properties of the steady-state (Fig. 14.14). In the absence of experimental or theoretical constraints, field evidence of channelized fluid flow can be used to infer the R values necessary to explain

channelization by decompaction weakening. Channelization patterns are difficult to discern at low metamorphic grades, but at higher temperatures patterns associated incipient charnockitization (Stahle et al. 1987) and pervasive melt migration (Jagoutz et al. 2006; Bouilhol et al. 2009; Bouilhol et al. 2011) are broadly consistent with $R \sim O(10^{-1})$. Adopting this value for the scales of the amphibolite facies example considered previously ($\delta = 31$ m and $\tau = 10$ ky), a miniscule flux perturbation of $\bar{q}/q_0 = 2$ ($Q_e^0/\delta^2/q_0 = 800$) is adequate to generate a wave that travels with speed $v_\phi = 51\ \delta/\tau = 160$ m/ky, vertical dimension $\lambda = 6\delta = 190$ m, horizontal dimension $R\lambda = 19$ m, $\phi_{max} = 0.7$, $p_{max} = 4$ MPa ($\sim\lambda\Delta\rho g$), and $p_{min} = -0.4$ MPa ($\sim R\lambda\Delta\rho g$). Although the amplitude of this wave violates the small-porosity approximation used to derive the steady-state properties, it demonstrates the extraordinary efficacy of 3-d focusing. In nature, such instabilities would be likely to provoke an alternative transport mechanism such as fracture-controlled flow.

14.6 Adding Details

The suggestion that lower crustal fluid flow is accomplished by the propagation of fluid-rich domains that correspond to some esoteric solution of the compaction equations cries for evidence and provokes the suspicion in the minds of field-based geologists that they are being sold a geological analog to the proverbial spherical cow of theoretical physics. The model is the mathematical consequence of a set of essential assumptions that are, at least individually, accepted in geoscience; the purpose of this Chapter is to draw attention to this consequence rather than to prove that it corresponds to reality. If there is a spherical cow to be found, then it must be lurking among these assumptions. The assumptions are: (1) that when a fluid is present its pressure is near lithostatic; (2) that flow is governed by Darcy's law; (3) that permeability is continuous and a strong function of connected porosity; and (4) that compaction occurs by a viscous mechanism (e.g., dislocation or pressure-solution creep) in response to effective pressure. In rejecting the model, it behooves the skeptic to decide which of these assumptions is false. The fourth assumption is treacherous at small porosities because omnipresent elastic mechanisms may limit viscous response (Connolly and Podladchikov 1998; Bercovici et al. 2001). However, if these assumptions are accepted, the consequence is that fluid flow must be episodic and accompanied by oscillations in fluid pressure, even in an idealized homogeneous crust perturbed by an idealized devolatilization reaction. As a prediction, this result is mundane because there is no geologic evidence to the contrary; its value is only that it offers a consistent explanation for such phenomena that, in principle, can be tested against observation. The purpose of modeling is not to emulate the complexity of nature, rather to explain it. For this reason, the models presented here sacrifice detail, but it is undeniable that the details of natural systems will influence fluid flow. A comprehensive discussion of this influence is

impractical; however, it is appropriate to consider some circumstances when the effect of such details can be neglected or anticipated.

14.6.1 Large-Scale Lateral Fluid Flow

Metamorphic devolatilization reactions have the capacity to produce high porosity layers, within which the compaction length, δ_1, may be orders of magnitude greater than it is in the surrounding rocks. In principle such a layer has the capacity to conduct lateral fluxes on the length scale δ_1; however, in the absence of external forcing, the pressure gradients responsible for lateral fluxes are limited by the spacing of the porosity waves that effect drainage through the low porosity surroundings. This spacing is dictated by the compaction length in the unperturbed matrix, which therefore determines the length scale for lateral fluid flow (Figs. 14.9 and 14.13). It seems probable that large-scale lateral fluid flow inferred from metamorphic field studies (e.g., Ferry and Gerdes 1998; Skelton 1996; Wing and Ferry 2007) is induced by external perturbations, such as drainage caused by tectonically-induced dilatant shear zones (Sibson 1992) or mean stress variations caused by folding (Schmalholz and Podladchikov 1999; Mancktelow 2008). The strength of these perturbations increases rock strength, thus they are likely to become important under the same conditions that embrittlement may cause a decompaction-weakening rheology (Sect. 14.5.6). Because decompaction weakening reduces the time-scale for dynamic drainage by porosity waves through the unperturbed matrix, the influence of an externally imposed drain will be dependent on the relative magnitudes of the time scale for within-layer flow

$$\tau_1 = \tau_0 \left(\frac{\phi_0}{\phi_1} \right) \phi_0^{\frac{n_\sigma \left(n_\phi - 1 \right)}{n_\sigma + 1}} \tag{14.34}$$

and the effective time scale τ_d (Eq. 14.32) for dynamic drainage by decompaction weakening, such that the process that operates on the shorter time-scale will dominate (Fig. 14.15). For the case $\tau_1 = \tau_d$, numerical simulation of fluid flow caused by the intersection of a permeable fracture zone with a metamorphic reaction front (Fig. 5 of Connolly 2010) shows that lateral flow occurs toward the fracture zone on the length scale δ_1 for $t < \tau_d$, but occurs only on the shorter length scale δ_0, and is independent of the fracture zone, at $t > \tau_d$. It is of course possible that a reaction generates a highly permeable layer that is sealed from above by a different, impermeable, lithology. In this case, the lateral flow can occur on the length scale δ_1. As evidence for large-scale lateral flow appears to come primarily from low and moderate grade metamorphic rocks, a more probable explanation for the phenomenon is that the flow occurs at conditions such that $\delta < l_A$. Under such conditions (Fig. 14.11), the vertical scale for compaction driven flow is l_A, but the horizontal length scale is the local value of δ, which increases exponentially with falling temperature.

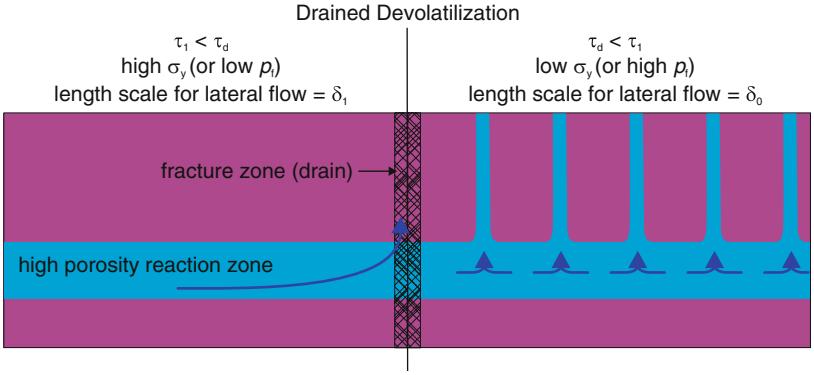

Fig. 14.15 Schematic of the influence of a drain (e.g., a permeable fracture zone) on fluid flow within a high porosity horizon generated by a devolatilization reaction. If the compaction time and length scales in the unperturbed matrix are τ_0 and δ_0, and the porosity in the horizon is ϕ_1, then the corresponding scales within the horizon are, for $n_\sigma = n_\phi = 3$, $\delta_1 = (\phi_1/\phi_0)^{1/2}\delta_0 > \delta_0$ and $\tau_1 = (\phi_0/\phi_1)^{3/2}\tau_0 < \tau_0$. Thus, in the absence of decompaction weakening, the drain will draw fluid from the layer on the length scale δ_1 (as depicted to the left of the drain) because the time scale (τ_1) for within layer flow is shorter than the time scale (τ_0) for the development of dynamic drainage within the unreacted matrix in response to high fluid pressure. If tensile yield strength is $< \delta_0\Delta\rho g$, then decompaction weakening reduces the time scale for the development of dynamic drainage to $\tau_d = \sigma_y/(\delta_0\Delta\rho g)\tau_0$. Thus, decompaction weakening may lead to circumstances (i.e., $\tau_d < \tau_1$) in which dynamic drainage dominates and the length scale for lateral fluid within the layer is limited by the compaction length (δ_0) in the unreacted rocks

14.6.2 Lithological Heterogeneity

There are two limiting cases for lithological heterogeneity. The trivial case is that the heterogeneity occurs on length scales that are $>> \delta$. In this case (Fig. 14.16a), the time and length scales relevant for each lithology individually dictate compaction phenomena. The alternative is that the heterogeneities are small, relative to the compaction length, in any of the individual lithologies. To illustrate this case (Fig. 14.16b), suppose a vertical sequence of two alternating lithologies in which the layering is thin compared to the compaction length in either layer and that the compaction length in one layer is so much larger than in the other layer that is effectively infinite (i.e., the lithology is rigid). If a porosity wave impinges on such a sequence, the fluid pressure gradient within the rigid layer must rise to supra-lithostatic values to conduct the excess flux carried by the wave, but within the soft layers dilation will cause the fluid pressure gradient to relax to near hydrostatic values in regions of elevated porosity. The result is to create a stepped fluid pressure profile that maintains a balance between compaction and dilation on the compaction time and length scales of the soft lithology. An implication of this behavior is that the effective rheology for compaction processes in the lower crust is dictated by the rheology of the weakest lithology. In contrast, crustal strength in response to tectonically imposed deformation may be controlled by the strongest lithology, i.e., in the case of homogeneous thickening or thinning.

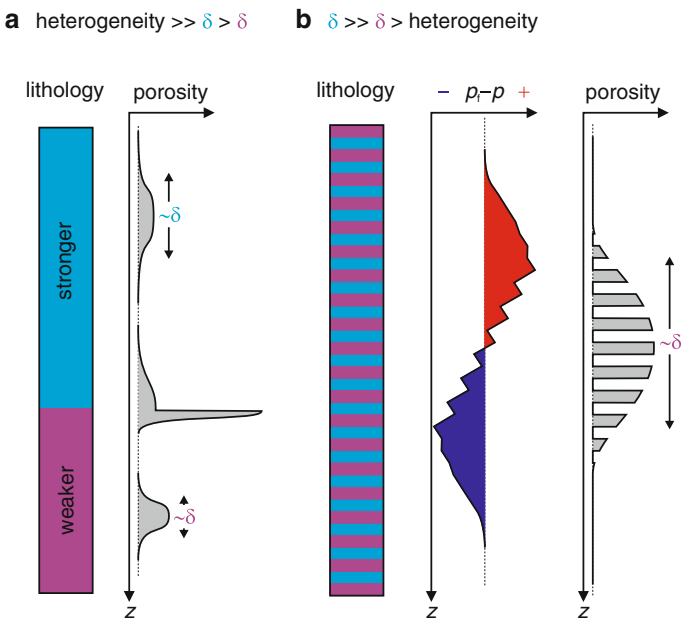

Fig. 14.16 Schematic of the influence of lithological layering on the propogation of a solitary porosity wave through a viscous matrix. If the layers are thick, compared to the compaction length, within each layer (**a**), the wave adopts its shape and speed according to the local compaction time and length scales. If the layers are thin compared to the compaction length in either lithology, but the compaction length is much greater in one lithology than it is in the other (**b**), then the properties of the wave are limited by the compaction scales in the weaker lithology. The effective pressure profile is drawn so that the fluid pressure gradient in the large porosity weak layers is near hydrostatic, and that fluid pressure gradient necessary to conduct the excess flux within the intervening rigid layers is supralithostatic and constant. In reality, because the excess flux varies locally within a solitary wave, the supralithostatic gradients in the rigid layer would decrease toward the tails of the wave

14.6.3 Non-Lithostatic Stress

Compaction-driven flow responds to tectonic stress through its dependence on the mean stress gradient (Eq. 14.5), but local deformation and/or lithological heterogeneity may give rise to strong variations in the far-field stress (Schmalholz and Podladchikov 1999; Mancktelow 2008). As in the case of lithological heterogeneity in a lithostatic crust, the influence of these variations depends upon whether they occur on a spatial scale that is large or small compared to the compaction length scale. Small scale variations will affect local flow patterns, but will not influence the overall tendency of compaction to drive fluid toward low mean stress (strictly in the direction of $\rho_f \mathbf{g}\mathbf{u}_z - \nabla\bar{\sigma}$, which is vertical in the lithostatic limit). These variations may distort the geometry of the porosity waves that develop in the non-lithostatic case. But because the effective pressure necessary for compaction can only be

achieved by having hydraulic connectivity on the compaction length scale, the distortions are likely to be primarily kinematic.

Large scale tectonic perturbations to the lithostatic mean stress gradient can, in general, be expected to have relatively minor influence on the rate and direction of compaction-driven fluid flow. The greatest influence on rate is realized during extension. In such a setting, the relaxation of differential stress in the brittle crust, which may be comparable to half the vertical load (Ranalli 1995), will relax over an $O(l_A)$ vertical interval (Connolly and Podladchikov 2004), potentially increasing the mean stress gradient responsible for, and accelerating, compaction-driven fluid flow. Perhaps more importantly, this effect will be amplified within, and favor the formation of, vertically elongated hydraulic domains such as the porosity waves predicted for the decompaction-weakening rheology (Sect. 14.5.6). The greatest influence on direction is realized in compression. During tectonic compression, the brittle crust supports differential stresses that are approximately twice the lithostatic load (Petrini and Podladchikov 2000; Mancktelow 2008). The relaxation of this stress gives rise to a negative mean stress gradient that may cause downward directed compaction-driven fluid flow on an $O(l_A)$ scale (Connolly and Podladchikov 2004). The inversion also creates a barrier to upward directed compaction driven flow. This barrier is most effective within vertically elongated hydraulic domains; thus, in contrast to the extensional case, compression may favor the formation of slow moving, horizontal, hydraulic domains such as the porosity waves predicted for compaction-driven flow in upward strengthening viscous rocks (Sect. 14.5.5).

In the lithostatic limit, rocks can sustain fluid overpressures comparable to their tensile strength. Thus, decompaction can occur by viscous mechanisms as assumed in the porosity wave models presented here. However, in the presence of large differential stresses, rocks will fail by plastic mechanisms before the fluid overpressure necessary for viscous dilational mechanisms can develop (Sibson 2000; Rozhko et al. 2007). As differential stresses are expected to grow towards the brittle-ductile transition, plastic failure will limit the viscous porosity wave mechanism to greater depths in non-lithostatic settings. Whether truly brittle deformation can be propagated upward by viscous compaction at depth, as implied by the viscous decompaction-weakening model advocated here, remains to be demonstrated.

14.7 Concluding Remarks

At near surface conditions, tectonic deformation maintains permeable fracture systems that, under most circumstances, permit drainage of crustal fluids with negligible fluid overpressure (e.g., Zoback and Townend 2001). In this regime, fluid flow is largely independent of the stress state of the rock matrix and weak perturbations induced by topography or fluid density variations may give rise to complex flow patterns (e.g., Ingebritsen et al. 2006). The base of the seismogenic

zone, at temperatures of ~ 623 K, defines the brittle-ductile transition (Sibson 1986; Scholz 1988), but evidence for the involvement of high pressure fluids in faulting (e.g., Sibson 2009; Cox and Ruming 2004; Miller et al. 2004) indicates that fluid overpressures develop above the brittle-ductile transition on the inter-seismic time scale. This short-term cyclicity reflects the role of localized compaction in sealing faults and fractures (Gratier et al. 2003; Tenthorey and Cox 2006). But at the brittle-ductile transition the time scale for fluid expulsion ($> 2.3\ c_\sigma/\dot{\varepsilon}_{\text{tectonic}} \sim O(10^8)$ y) is slow with respect to metamorphic fluid production. Thus, the brittle-ductile transition lies within a transitional hydrological regime in which compaction-driven fluid flow is gradually superimposed on the upper crustal regime. Within this transitional regime, the efficiency of compaction increases exponentially with depth on the $O(1)$ km scale of the viscous e-fold length (Fig. 14.1). Because the efficiency of compaction must be measured relative to rates of fluid production or drainage, it is not possible to make a general statement about the depth or temperature at which metamorphic fluid flow will become dominated by compaction.

Even if recent challenges (e.g., Oliver et al. 2000; Dewey 2005; Ague and Baxter 2007) to the paradigm of heat-conduction limited metamorphism (England and Thompson 1984) are acknowledged, the development of high fluid pressures indicates that metamorphic environments must be characterized by extraordinarily low permeability. Metamorphic fluid expulsion is not necessarily efficient (Warren et al. 2011), but efficient fluid expulsion from poorly drained rocks requires a dynamic mechanism in which the dilational deformation responsible for increasing permeability is balanced by a compaction mechanism at depth responsible for maintaining high fluid pressure. An essential feature of such a mechanism is that, irrespective of the mean-stress gradient, hydraulic connectivity must be maintained over a vertical interval that is large enough to generate the effective pressures necessary to drive the deformation. Both self-propagating domains of fluid-filled fractures (Gold and Soter 1985) and individual hydrofractures (Rubin 1995; Nakashima 1995; Okamoto and Tsuchiya 2009) have been proposed as the mechanism for such flow. These models suppose that the fractures are closed at depth, i.e., compacted, by the elastic response of the matrix. As a consequence, the fractures propagate at high speeds, $O(1)$ m/s, and have km-scale vertical dimensions. The porosity wave mechanism, reviewed here, may also be manifest as interconnected fractures, provided the individual fractures are small in comparison to the viscous compaction length, but differs from elastic fracture models in that compaction is viscous. A satisfying feature of the viscous mechanism is that it can operate on the grain-scale, thereby explaining the pervasive compaction evident in metamorphic rocks. If viewed as competing mechanisms, the mechanism that requires the smallest vertical extent necessary to accommodate fluid production will dominate. The albeit highly uncertain $O(100)$ m estimate for the viscous compaction length, obtained here for amphibolite-facies conditions, indicates that porosity waves can meet this criterion for dominance.

The relatively minor role of compaction in many near surface environments makes large scale hydrological modeling of the upper crust possible (e.g., Ingebritsen et al. 2006). Possible in this context means that a stable initial condition can be

envisioned in which fluid and rock coexist. In contrast, the lower crust is an environment in which fluids are mechanically and, potentially, thermodynamically unstable (Connolly and Thompson 1989). Thus there is no time-invariant initial condition from which it is possible to assess the impact of the metamorphic process, which is itself the most likely source of lower crustal fluids. The assertion that the lower crust has an intrinsic background permeability towards which transient permeability decays is logically specious, because it is based on time-averaged metamorphic fluxes. However, permeabilities inferred from time-averaged fluid fluxes do provide an upper limit on the background permeability that characterizes the local environment of a metamorphic process in time and space (Ingebritsen and Manning 2010). The time and length scales for viscous compaction have been formulated to emphasize this limitation by separating material properties of the solid and fluid, from two transient properties of the initial state, namely porosity and the hypothetical background flux necessary to maintain lithostatic fluid pressure. If the time-averaged flux is used in place of the background flux, then the result provides only upper and lower limits on the compaction length and time scales. Consequently, forward models are unlikely to reveal the scales of fluid flow in lower crustal systems, but observations of natural patterns may ultimately provide a useful parameterization of these scales. These scales are fundamental limits for flow phenomena that are independent of stress state within the solid matrix. Thus, the scales are constrained by the duration and extent of lateral (e.g., Ferry and Gerdes 1998; Wing and Ferry 2007; Staude et al. 2009) or downward (e.g., Austrheim 1987; McCaig et al. 1990; Wickham et al. 1993; Upton et al. 1995; Cartwright and Buick 1999; Read and Cartwright 2000; Gleeson et al. 2000; Yardley et al. 2000; Munz et al. 2002; Gleeson et al. 2003) fluid flow.

The role of compaction in metamorphic fluid flow is extraordinarily uncertain, but ignoring this uncertainty in models of metamorphic fluid flow does not make the models any more certain. Compaction is a good news, bad news story. The bad news is that the details of lower crustal flow may be influenced by unknowable details. The good news is that compaction driven fluid flow has a tendency to self-organize. Self-organization eliminates the dependence on details that are present on spatial or temporal scales that are smaller than the compaction length and time scales. Porosity waves are the mechanism for this self-organization, through which dilational deformation is localized in either time and/or space to create pathways for fluid expulsion. Although, this dilational deformation may be manifest as plastic failure, its rate is limited by the compaction process necessary to maintain elevated fluid pressures. At metamorphic conditions, the compaction process is unequivocally viscous. The porosity waves that form in a matrix that compacts by viscous mechanisms are generally solitary waves that, once formed, are independent of their source. This chapter has outlined a simple method of predicting the geometry, size, and speed of such waves under the assumption that fluid drainage keeps pace with fluid production. If this assumption were true throughout the metamorphic column then the time-averaged permeability would be identical to that obtained by assuming uniform fluid flow. In fact, the assumption is demonstrably untrue on a crustal scale for the viscous case, because the waves slow towards the brittle-ductile transition,

an effect that leads to fluid accumulation. Of course, the activation of other drainage mechanisms may maintain the assumed steady state, but the inconsistency serves to demonstrate that characterizing a dynamic system by a time-averaged dependent property, such as permeability, has no predictive value.

In the viscous limit, the models summarized here predict that lower crustal porosity waves will create fluid-rich horizons, with thickness comparable to l_A, beneath the brittle-ductile transition (Sect. 14.5.5). Geophysical evidence for such horizons is common (Suetnova et al. 1994; Hammer and Clowes 1996; Ozel et al. 1999; Liotta and Ranalli 1999; Makovsky and Klemperer 1999; Vanyan and Gliko 1999; Stern et al. 2001; Jiracek et al. 2007). Coupled with external forcing, the horizons may function as conduits for the large-scale lateral fluid flow responsible for some types of hydrothermal mineralization and as reservoirs for fluid-driven seismicity (e.g., Cox 2005). Paradoxically, although these horizons reflect upward strengthening of the ductile crust with respect to dilational processes, they may reduce the shear strength of the crust precisely at depths where the crust is presumed to be strong. Fluid flow within this interval of the crust is likely to be further complicated by the influence of tectonic stress developed in the brittle crust (Sect. 14.6.3). To make matters still worse, elastic compaction mechanisms become competitive at this depth (e.g., Fig. 14.15 of Connolly and Podladchikov 1998). Elastic compaction rheology also has wave solutions that form in response to high fluid pressures (Rice 1992), but unlike viscous waves, elastic waves cannot detach from their source and propagate as transient shocks accompanied by fluid pressure surges. Thus, the stagnation of mid-crustal viscous porosity waves may be accompanied by high velocity, low amplitude surges of fluid into the upper crust (Connolly and Podladchikov 1998). This type of flow pattern is consistent with the timing of aftershocks during crustal faulting (Miller et al. 2004). Because elastic waves can propagate through a matrix with no prior hydraulic connectivity, elastic compaction may also be an important mechanism at the onset of metamorphism. Viscoelastic porosity wave solutions exist in the zero-porosity limit (Connolly and Podladchikov 1998), but their relevance to metamorphic fluid expulsion has yet to be explored.

Porosity waves are a mechanism capable of bridging the extremes between pervasive and fully segregated fluid flow. The metasomatic effect of fluid infiltration is maximized between these extremes when the flow is strongly focused into channels, but not fully segregated. A decompaction-weakening matrix rheology, in which the matrix yields more readily under negative effective pressure than it does under positive pressures, can explain channeling (Sect. 14.5.6). The origin of this rheology is attributed to the asymmetric role of cohesion during dilation (Connolly and Podladchikov 2007). The expression of plastic yielding is temperature-dependent, tending toward the ductile and brittle limits at, respectively, high and low temperatures (Hill 1950). Thus at high temperatures decompaction-weakening is capable of inducing channelized fluid flow in completely ductile rocks (Bouilhol et al. 2011). Reactive transport instability (Daines and Kohlstedt 1994; Aharonov et al. 1997) and shear-enhanced segregation (Holtzman and Kohlstedt 2007) are alternative mechanisms for inducing channelization in ductile rocks. In nature any

mechanism of channelization may be associated with metasomatism, but the reactive transport instability is implicitly metasomatic. A limitation to the reactive transport instability is that the net solubility of the matrix in the fluid must increase in the direction of fluid flow. The key distinction between the flow patterns generated by decompaction-weakening and other focusing mechanisms, is that in the case of decompaction-weakening fluid is circulated into and out of the matrix, whereas reactive transport and shear-enhanced segregation are associated with unidirectional flow. When considered in tandem, mechanical and reactive transport instabilities are mutually reinforcing (Spiegelman et al. 2001; Liang et al. 2010).

Acknowledgements This paper was improved by outstanding, although not necessarily laudatory, reviews by Stephen F. Cox, Yves Gueguen, Peter O. Koons and Peter I. Nabelek. I am grateful to Dan Harlov and Hakon Austrheim for their extraordinary patience and judicious editing. The work presented here was supported by Swiss National Science Foundation grant 200021_130411.

Appendix: Steady-State Porosity Waves in a Viscous Matrix

This appendix presents a steady-state wave solution for flow of an incompressible fluid through a viscous matrix composed of incompressible solid grains. Geological compaction literature invariably assumes Newtonian behavior for the viscous mechanism; however, lower crustal environments may well be characterized by power-law viscous rheology (e.g., Kohlstedt et al. 1995). Accordingly, the solution derived here is general with respect to the dependence of the viscous rheology on effective pressure. Aside from this modification, the mathematical formulation of the governing compaction equations is identical to that of Connolly and Podladchikov (2000, 2007).

Conservation of solid and fluid mass requires

$$\frac{\partial(1-\phi)}{\partial t} + \nabla \cdot ((1-\phi)\mathbf{v}_\mathrm{s}) = 0 \tag{14.35}$$

and

$$\frac{\partial \phi}{\partial t} + \nabla \cdot (\phi \mathbf{v}_\mathrm{f}) = 0, \tag{14.36}$$

where subscripts f and s distinguish the velocities, $\mathbf{v}$, of the fluid and matrix. From Darcy's law, force balance between the matrix and fluid requires

$$\mathbf{q} = \phi(\mathbf{v}_\mathrm{f} - \mathbf{v}_\mathrm{s}) = -\frac{k}{\mu}(\nabla p_\mathrm{f} - \rho_\mathrm{f} g \mathbf{u}_z). \tag{14.37}$$

In one-dimensional compaction of a vertical column, mean stress is identical to the load

$$\bar{\sigma} = \int_0^z ((1-\phi)\rho_s + \phi\rho_f) g \mathbf{u}_z dz. \tag{14.38}$$

Thus, in terms of effective pressure, $p_e = \bar{\sigma} - p_f$, Eq. 14.37 is

$$\phi(\mathbf{v}_f - \mathbf{v}_s) = \frac{k}{\mu}(\nabla p_e - (1-\phi)\Delta\rho g \mathbf{u}_z). \tag{14.39}$$

The divergence of the total volumetric flux of matter is the sum of Eqs. 14.35 and 14.36

$$\nabla \cdot (\mathbf{v}_s + \phi(\mathbf{v}_f - \mathbf{v}_s)) = 0, \tag{14.40}$$

and substituting Eq. 14.39 into Eq. 14.40

$$\nabla \cdot \left(\mathbf{v}_s + \frac{k}{\mu}(\nabla p_e - (1-\phi)\Delta\rho g \mathbf{u}_z) \right) = 0. \tag{14.41}$$

Matrix rheology is introduced with Eq. 14.16 by observing that the divergence of the solid velocity is the dilational strain rate of the matrix

$$\nabla \cdot \mathbf{v}_s = \frac{\phi}{1-\phi}\dot{\varepsilon}_\phi = -c_\alpha f_\phi A |p_e|^{n_\sigma - 1} p_e \tag{14.42}$$

where $f_\phi = \phi(1-\phi)/\left(1-\phi^{1/n_\sigma}\right)^{n_\sigma}$ (Wilkinson and Ashby 1975). As the functional form of Eq. 14.42 may vary depending on the magnitude of the porosity and the viscous mechanism (Ashby 1988), the subsequent analysis assumes f_ϕ is an unspecified function of porosity.

To avoid the unnecessary complication associated with the use of vector notation for a one-dimensional problem, in the remainder of this analysis vector quantities are represented by signed scalars and the gradient and divergence operators are replaced by $\partial/\partial z$. Supposing the existence of a steady state solution in which fluid explusion is accomplished by waves that propagate with unchanging form through a matrix with background porosity ϕ_0 filled by fluid at zero effective pressure, then, in a reference frame that travels with the wave, integration of Eq. 14.35 gives the matrix velocity as

$$v_s = v_\infty \frac{1-\phi_0}{1-\phi} \tag{14.43}$$

where v_∞ is the solid velocity in the limits $\phi \to \phi_0$ and $p_e \to 0$, i.e., at infinite distance from the wave. After substitution of Eq. 14.43, the integrated form of Eq. 14.41 can be rearranged to

$$\frac{\partial p_e}{\partial z} = \left(q_t - v_\infty \frac{1-\phi_0}{1-\phi} \right) \frac{\mu}{k} + (1-\phi)\Delta\rho g \tag{14.44}$$

where $q_t = \phi v_f + (1-\phi)v_s$ is the constant, total, volumetric flux of matter through the column, which evaluates in the limit $\phi \to \phi_0$ and $p_e \to 0$ as

$$q_t = v_\infty - (1-\phi_0)\frac{k_0}{\mu}\Delta\rho g \tag{14.45}$$

where k_0 is the permeability at ϕ_0. Thus, Eq. 14.44 can be rewritten

$$\frac{\partial p_e}{\partial z} = \Delta\rho g \left(1 - \phi - (1-\phi_0)\frac{k_0}{k} \right) - v_\infty \frac{\mu}{k} \frac{\phi - \phi_0}{1-\phi}. \tag{14.46}$$

Likewise, substitution of Eq. 14.43 into Eq. 14.42 yields

$$\frac{\partial \phi}{\partial z} = -\frac{(1-\phi)^2}{1-\phi_0} f_\phi \frac{c_\sigma A |p_e|^{n_\sigma - 1} p_e}{v_\infty} \tag{14.47}$$

If permeability is an, as yet unspecified, function of porosity, then Eqs. 14.46 and 14.47 form a closed system of two ordinary differential equations in two unknown functions, ϕ and p_e. As v_∞ is the solid velocity at infinite distance from a steady-state wave, if the reference frame is changed to that of the unperturbed matrix, the phase velocity of the wave is $v_\phi = -v_\infty$.

For notational simplicity Eqs. 14.46 and 14.47 are now rewritten as

$$\frac{\partial p_e}{\partial z} = f_1 \tag{14.48}$$

$$\frac{\partial \phi}{\partial z} = f_2 \frac{c_\sigma A}{v_\phi} |p_e|^{n_\sigma - 1} p_e \tag{14.49}$$

where f_1 is the dependence of Eq. 14.46 on ϕ and v_ϕ, and f_2 isolates the dependence of Eq. 14.47 on ϕ. Combining Eqs. 14.48 and 14.49 to eliminate z, and rearranging, yields

$$0 = \frac{c_\sigma A}{v_\phi} |p_e|^{n_\sigma - 1} p_e \mathrm{d}p_e - \frac{f_1}{f_2} \mathrm{d}\phi, \tag{14.50}$$

which must be satisfied by the ϕ-p_e trajectory of any steady-state solution. Defining a function H such that

$$H \equiv -\int \frac{f_1}{f_2} \mathrm{d}\phi, \tag{14.51}$$

the integral of Eq. 14.50 yields a function

$$U \equiv \frac{c_\sigma A}{v_\phi} \frac{|p_e|^{n_\sigma - 1} p_e^2}{n_\sigma + 1} + H \tag{14.52}$$

whose ϕ-p_e contours explicitly define the ϕ-p_e trajectory for all steady-state solutions as a function v_ϕ. Because U increases monotonically, and symmetrically, with positive or negative p_e at constant ϕ, and H is independent of p_e, the stationary points of U must occur at $p_e = 0$ and correspond to extrema in H, i.e., the real roots of $\partial H/\partial\phi = -f_1/f_2 = 0$. Moreover, as f_2 must be finite if the matrix is coherent, the roots of $\partial H/\partial\phi = 0$ are identical to the roots of $f_1 = 0$. Therefore ϕ_0 is always a stationary point, with the character of a focal point if $\partial f_1/\partial\phi < 0$ and that of a saddle point if $\partial f_1/\partial\phi > 0$. When ϕ_0 is a focal point, the steady-state wave solutions correspond to periodic waves that oscillate between two values of porosity on either side of ϕ_0, characterized by equal H, at which p_e vanishes (Fig. 14.6b). The case of greater interest is a solitary wave (Fig. 14.6a), in which the porosity rises from ϕ_0 to a maximum, at which $H(\phi_{max}) = H(\phi_0)$, and then returns to ϕ_0. This solution requires both the existence of a focal point at $\phi > \phi_0$ and that ϕ_0 is a saddle point. For the rheological constitutive relation employed here (Eq. 14.42), the first condition is always met when ϕ_0 is a saddle point. Thus, the critical velocity for the existence of the solitary wave solution, i.e., the bifurcation at which ϕ_0 switches from focal to saddle point, is

$$v_\phi^{crit} = -\frac{k_0}{\mu}(1-\phi_0)\Delta\rho g\left(\frac{(1-\phi_0)}{k_0}\left.\frac{\partial k}{\partial\phi}\right|_{\phi=\phi_0} - 1\right), \tag{14.53}$$

which is obtained by solving $\partial f_1/\partial\phi = 0$ for v_ϕ. Substituting the explicit function for permeability given by Eq. 14.17 into Eq. 14.53 yields

$$v_\phi^{crit} = -\frac{k_0}{\phi_0\mu}(1-\phi_0)\Delta\rho g\big((1-\phi_0)n_\phi - \phi_0\big) = v_0\big((1-\phi_0)n_\phi - \phi_0\big). \tag{14.54}$$

Equation 14.54 implies that, in the small-porosity limit, the minimum speed at which steady solitary waves exist is n_ϕ times the speed of the fluid through the unperturbed matrix.

The relation between solitary wave amplitude (maximum porosity) and v_ϕ is obtained by solving

$$H(\phi_{\max}) - H(\phi_0) = -\int_{\phi_0}^{\phi_{\max}} \frac{f_1}{f_2} \mathrm{d}\phi = 0. \tag{14.55}$$

The resulting expressions are cumbersome, but, in the small-porosity limit of Eqs. 14.17 and 14.42, the solution of Eq. 14.55 is

$$v_\phi = -\frac{c_\phi \phi_0^{n_\phi - 1} \Delta\rho g}{\mu} (n_\phi - 1) \frac{\phi_0^{n_\phi} + \phi_{\max}^{n_\phi} \left[n_\phi \ln\left(\frac{\phi_{\max}}{\phi_0}\right) - 1 \right]}{\phi_0^{n_\phi - 1} \left[n_\phi \phi_{\max} - \phi_0 (n_\phi - 1) \right] - \phi_{\max}^{n_\phi}}. \tag{14.56}$$

From Eq. 14.56 it follows that $n_\phi > 1$ is a necessary condition for the existence of solitary waves. Equation 14.56 also has the surprising implication that amplitude is not a function of n_σ, for large porosity the function f_ϕ, in the exact form of Eq. 14.42, gives rise to a weak dependence of amplitude on n_σ. For a solitary wave with specified phase velocity, the effective pressure is obtained as an explicit function of ϕ from the definite integral of Eq. 14.50, which can be rearranged to

$$p_e = \pm \sqrt[n_\sigma + 1]{(n_\sigma + 1) \frac{v_\phi}{c_\sigma A} \int_{\phi_0}^{\phi} \frac{f_1}{f_2} \mathrm{d}\phi}, \tag{14.57}$$

where the signs have been dropped in view of the symmetry of the solution. And finally, substituting Eq. 14.57 into Eq. 14.47, inverting the result, and integrating yields the depth coordinate relative to the center of a wave as a function of ϕ

$$z = \pm \sqrt[n_\sigma + 1]{\frac{v_\phi}{c_\sigma A (n_\sigma + 1)^{n_\sigma}}} \int_{\phi_{\max}}^{\phi} \frac{1}{f_2} \left(\int_{\phi_0}^{\phi} \frac{f_1}{f_2} \mathrm{d}\phi \right)^{-\frac{n_\sigma}{n_\sigma + 1}} \mathrm{d}\phi. \tag{14.58}$$

To demonstrate that $z \to \pm\infty$ as $\phi \to \phi_0$, the inner integral and its factor in Eq. 14.58 are approximated by the first non-zero terms of Taylor series expansions about $\phi = \phi_0$ to obtain

$$z \approx \pm \left(\frac{v_\phi}{c_\sigma A f_2|_{\phi=\phi_0}} \left(\frac{n_\sigma + 1}{2} \frac{\partial f_1}{\partial \phi}\bigg|_{\phi=\phi_0} \right)^{-n_\sigma} \right)^{\frac{1}{n_\sigma + 1}} \int_{\Phi}^{0} \Phi^{-\frac{2n_\sigma}{n_\sigma + 1}} \mathrm{d}\Phi \tag{14.59}$$

where $\Phi = \phi - \phi_0$. In the limit $\Phi \to 0$, the integral in Eq. 14.59 is finite only if $n_\sigma < 1$, from which it is concluded that solitary waves have infinite wavelength in a linear or shear thinning viscous matrix, but may have finite wavelength in the peculiar case of a shear thickening viscous matrix. Rewriting the integral in Eq. 14.59 in terms of $\mathrm{d}\ln\phi$, and differentiating yields

$$\frac{\partial z}{\partial \ln \Phi} \approx \left(\Phi^{1-n_\sigma} \frac{v_\phi}{c_\sigma A f_2|_{\phi=\phi_0}} \left(\frac{n_\sigma + 1}{2} \frac{\partial f_1}{\partial \phi}\bigg|_{\phi=\phi_0} \right)^{-n_\sigma} \right)^{\frac{1}{n_\sigma+1}} \tag{14.60}$$

the depth interval over which porosity decays from eϕ_0 to ϕ_0 within a porosity wave. This interval is taken here as the characteristic length scale for variations in porosity, i.e., the viscous compaction length. The derivative on the right-hand side of Eq. 14.60,

$$\frac{\partial f_1}{\partial \phi}\bigg|_{\phi=\phi_0} = \Delta\rho g \left(\frac{(1-\phi_0)}{k_0} \frac{\partial k}{\partial \phi}\bigg|_{\phi=\phi_0} - 1 \right) + \frac{v_\phi \mu}{k_0(1-\phi_0)}, \tag{14.61}$$

is zero at $v_\phi = v_\phi^{\text{crit}}$, but decreases monotonically with v_ϕ; thus dropping the first term in Eq. 14.61, substituting $v_\phi = v_\phi^{\text{crit}}$ and $\Phi = (\text{e} - 1)\ \phi_0$ in Eq. 14.60, and expanding f_2 at ϕ_0 as$(1-\phi_0) f_\phi|_{\phi=\phi_0}$yields

$$\delta = \left[\left((\text{e}-1)\phi_0 \Delta\rho g \left([1-\phi_0] \frac{\partial k}{\partial \phi}\bigg|_{\phi=\phi_0} - k_0 \right) \right)^{1-n_\sigma} \left(\frac{2k_0}{n_\sigma + 1} \right)^{n_\sigma} \frac{1}{c_\sigma A \mu f_\phi|_{\phi=\phi_0}} \right]^{\frac{1}{n_\sigma+1}}, \tag{14.62}$$

a length scale that provides a lower bound on wavelength. For a linear-viscous matrix with shear viscosity $\eta = 1/(3A)$, the constitutive relation given by Eq. 14.42, and the small-porosity limit, Eq. 14.62 simplifies to

$$\delta = \sqrt{\frac{4}{3} \frac{\eta}{\phi_0} \frac{k_0}{\mu}}$$

which, accounting for differences in the formulation of the bulk viscosity of the matrix, is identical to the viscous compaction length of McKenzie (1984). For a non-linear viscous matrix, making use of constitutive relations given by Eqs. 14.17 and 14.42, in the small-porosity limit the compaction length is

$$\delta = C \phi_0^{\frac{n_\phi - 1}{n_\sigma + 1}} \sqrt[n_\sigma+1]{\left(\frac{2}{n_\sigma + 1} \right)^{n_\sigma} \frac{c_\phi}{c_\sigma A \mu (\Delta\rho g)^{n_\sigma - 1}}}, \tag{14.63}$$

where

$$C = \sqrt[n_\sigma+1]{\left[n_\phi (\text{e}-1) \right]^{1-n_\sigma}}. \tag{14.64}$$

The factor C represents two non-general assumptions of the analysis: that the phase velocity is $n_\phi v_0$; and that the porosity decay is from $e\phi_0$ to ϕ_0. In the spirit of dimensional analysis, this factor (~2.27 for $n_\sigma = n_\phi = 3$) is neglected in the text.

References

Ague JJ, Baxter EF (2007) Brief thermal pulses during mountain building recorded by Sr diffusion in apatite and multicomponent diffusion in garnet. Earth Planet Sci Lett 261:500–516. doi:10.1016/j.epsl.2007.07.017

Ague JJ, Park J, Rye DM (1998) Regional metamorphic dehydration and seismic hazard. Geophys Res Lett 25:4221–4224

Aharonov E, Spiegelman M, Kelemen P (1997) Three-dimensional flow and reaction in porous media: implications for the earth's mantle and sedimentary basins. J Geophys Res 102:14821–14833

Ashby MF (1988) The modeling of hot isostatic pressing. In: Garvare T (ed) Proceedings hip: hot isostatic pressing – theories and applications. Centek, Lulea, pp 29–40

Athy LF (1930) Density, porosity and compaction of sedimentary rocks. Bull Am Assoc Pet Geol 14:1–24

Austrheim H (1987) Eclogitization of lower crustal granulites by fluid migration through shear zones. Earth Planet Sci Lett 81:221–232. doi:10.1016/0012-821X(87)90158-0

Barcilon V, Lovera OM (1989) Solitary waves in magma dynamics. J Fluid Mech 204:121–133

Barcilon V, Richter FM (1986) Nonlinear-waves in compacting media. J Fluid Mech 164:429–448

Bercovici D, Ricard Y, Schubert G (2001) A two-phase model for compaction and damage 1. General theory. J Geophys Res 106:8887–8906

Bouilhol P, Burg JP, Bodinier JL, Schmidt MW, Dawood H, Hussain S (2009) Magma and fluid percolation in arc to forearc mantle: evidence from Sapat (Kohistan, Northern Pakistan). Lithos 107:17–37. doi:10.1016/j.lithos.2008.07.004

Bouilhol P, Connolly JAD, Burg JP (2011) Geological evidence and modeling of melt migration by porosity waves in the sub-arc mantle of Kohistan (Pakistan). Geology 39:1091–1094. doi:10.1130/G32219.1

Cartwright I, Buick IS (1999) The flow of surface-derived fluids through alice springs age middle-crustal ductile shear zones, Reynolds Range, Central Australia. J Metamorph Geol 17:397–414

Cheadle MJ, Elliott MT, McKenzie D (2004) Percolation threshold and permeability of crystallizing igneous rocks: the importance of textural equilibrium. Geology 32:757–760. doi:10.1130/g20495.1

Connolly JAD (1997) Devolatilization-generated fluid pressure and deformation-propagated fluid flow during prograde regional metamorphism. J Geophys Res 102:18149–18173

Connolly JAD (2010) The mechanics of metamorphic fluid expulsion. Elements 6:165–172. doi:10.2113/gselements.6.3.165

Connolly JAD, Podladchikov YY (1998) Compaction-driven fluid flow in viscoelastic rock. Geodinamica Acta 11:55–84

Connolly JAD, Podladchikov YY (2000) Temperature-dependent viscoelastic compaction and compartmentalization in sedimentary basins. Tectonophysics 324:137–168

Connolly JAD, Podladchikov YY (2004) Fluid flow in compressive tectonic settings: implications for mid-crustal seismic reflectors and downward fluid migration. J Geophys Res 109:B04201. doi:10.1029/2003JB002822

Connolly JAD, Podladchikov YY (2007) Decompaction weakening and channeling instability in ductile porous media: implications for asthenospheric melt segregation. J Geophys Res 112: B10205. doi:10.1029/2005jb004213

Connolly JAD, Thompson AB (1989) Fluid and enthalpy production during regional metamorphism. Contrib Mineral Petrol 102:346–366
Connolly JAD, Schmidt MW, Solferino G, Bagdassarov N (2009) Permeability of asthenospheric mantle and melt extraction rates at mid-ocean ridges. Nature 462:209–212. doi:10.1038/nature08517
Cox SF (2005) Coupling between deformation, fluid pressures and fluid flow in ore-producing hydrothermal environments. In: Economic geology 100th anniversary volume, Denver, pp 39–75
Cox SF, Ruming K (2004) The St Ives mesothermal gold system, Western Australia – a case of golden aftershocks? J Struct Geol 26:1109–1125. doi:10.1016/j.jsg.2003.11.025
Daines MJ, Kohlstedt DL (1994) The transition from porous to channelized flow due to melt/rock reaction during melt migration. Geophys Res Lett 21:145–148
Dewey JF (2005) Orogeny can be very short. Proc Natl Acad Sci USA 102:15286–15293. doi:10.1073/pnas.0505516102
England PC, Thompson AB (1984) Pressure temperature time paths of regional metamorphism. 1. Heat-transfer during the evolution of regions of thickened continental-crust. J Petrol 25:894–928
Etheridge MA, Wall VJ, Cox SF, Vernon RH (1984) High fluid pressures during regional metamorphism and deformation – implications for mass-transport and deformation mechanisms. J Geophys Res 89:4344–4358
Ferry JM (1994) Overview of the petrologic record of fluid-flow during regional metamorphism in Northern New-England. Am J Sci 294:905–988
Ferry JM, Gerdes ML (1998) Chemically reactive fluid flow during metamorphism. Annu Rev Earth Planet Sci 26:255–287
Fulton PM, Saffer DM, Bekins BA (2009) A critical evaluation of crustal dehydration as the cause of an overpressured and weak San Andreas Fault. Earth Planet Sci Lett 284:447–454. doi:10.1016/j.epsl.2009.05.009
Gavrilenko P, Gueguen Y (1993) Fluid overpressures and pressure solution in the crust. Tectonophysics 21:91–110
Gleeson SA, Yardley BWD, Boyce AJ, Fallick AE, Munz LA (2000) From basin to basement: the movement of surface fluids into the crust. J Geochem Explor 69:527–531
Gleeson SA, Yardley BWD, Munz IA, Boyce AJ (2003) Infiltration of basinal fluids into high-grade basement, South Norway: sources and behaviour of waters and brines. Geofluids 3:33–48
Gold T, Soter S (1985) Fluid ascent through the solid lithosphere and its relation to earthquakes. Pure Appl Geophys 122:492–530
Goldschmidt VM (1954) Geochemistry. Clarendon, Oxford, p 730
Graham CM, Valley JW, Eiler JM, Wada H (1998) Timescales and mechanisms of fluid infiltration in a marble: an ion microprobe study. Contrib Mineral Petrol 132:371–389
Gratier JP, Favreau P, Renard F (2003) Modeling fluid transfer along California faults when integrating pressure solution crack sealing and compaction processes. J Geophys Res 108. doi:10.1029/2001jb000380
Gueguen Y, Palciauskas VV (1994) Introduction to the physics of rocks. Princeton University Press, Princeton, p 194
Gueguen Y, Dormieux L, Bouteca M (2004) Fundamentals of poromechanics. In: Gueguen Y, Bouteca M (eds) Mechanics of fluid-saturated rocks. Elsevier Academic, Burlington, pp 55–79
Hammer PTC, Clowes RM (1996) Seismic reflection investigations of the mount cayley bright spot: a midcrustal reflector beneath the Coast Mountains, British Columbia. J Geophys Res 101:20119–20131
Hanson RB (1997) Hydrodynamics of regional metamorphism doe to continental collision. Econ Geol Bull Soc Econ Geol 92:880–891

Hetenyi G, Cattin R, Brunet F, Bollinger L, Vergne J, Nabelek J, Diament M (2007) Density distribution of the india plate beneath the Tibetan Plateau: geophysical and petrological constraints on the kinetics of lower-crustal eclogitization. Earth Planet Sci Lett 264:226–244. doi:10.1016/j.epst.2007.09.036

Hill R (1950) The mathematical theory of plasticity. Clarendon, Oxford, p 356

Holness MB, Siklos STC (2000) The rates and extent of textural equilibration in high-temperature fluid-bearing systems. Chem Geol 162:137–153. doi:10.1016/s0009-2541(99)00124-2

Holtzman BK, Kohlstedt DL (2007) Stress-driven melt segregation and strain partitioning in partially molten rocks: effects of stress and strain. J Petrol 48:2379–2406. doi:10.1093/petrology/egm065

Huenges E, Erzinger J, Kuck J, Engeser B, Kessels W (1997) The permeable crust: geohydraulic properties down to 9101 m depth. J Geophys Res 102:18255–18265

Hunt JM (1990) Generation and migration of petroleum from abnormally pressured fluid compartments. Am Assoc Pet Geol 74:1–12

Ingebritsen SE, Manning CE (1999) Geological implications of a permeability-depth curve for the continental crust. Geology 27:1107–1110

Ingebritsen SE, Manning CE (2010) Permeability of the continental crust: dynamic variations inferred from seismicity and metamorphism. Geofluids 10:193–205. doi:10.1111/j.1468-8123.2010.00278.x

Ingebritsen SE, Sanford WE, Neuzil C (2006) Groundwater in geologic processes. Cambridge University Press, Cambridge

Jagoutz O, Muntener O, Burg JP, Ulmer P, Jagoutz E (2006) Lower continental crust formation through focused flow in km-scale melt conduits: the zoned ultramafic bodies of the Chilas complex in the Kohistan Island Arc (NW Pakistan). Earth Planet Sci Lett 242:320–342

Jiracek GR, Gonzalez VM, Caldwell TG, Wannamaker PE, Kilb D (2007) Seismogenic, electrically conductive, and fluid zones at continental plate boundaries in New Zealand, Himalaya, and California-USA. Geophys Monogr Ser 175:347–369. doi:10.1029/175GM18

Kerschhofer L, Dupas C, Liu M, Sharp TG, Durham WB, Rubie DC (1998) Polymorphic transformations between olivine, wadsleyite and ringwoodite: mechanisms of intracrystalline nucleation and the role of elastic strain. Mineral Mag 62:617–638

Kohlstedt DL, Evans B, Mackwell SJ (1995) Strength of the lithosphere – constraints imposed by laboratory experiments. J Geophys Res 100:17587–17602

Liang Y, Schiemenz A, Hesse MA, Parmentier EM, Hesthaven JS (2010) High-porosity channels for melt migration in the mantle: top is the dunite and bottom is the harzburgite and lherzolite. Geophys Res Lett 37:L15306. doi:10.1029/2010gl044162

Liotta D, Ranalli G (1999) Correlation between seismic reflectivity and rheology in extended lithosphere: southern Tuscany, Inner Northern Apennines, Italy. Tectonophysics 315:109–122

Makovsky Y, Klemperer SL (1999) Measuring the seismic properties of tibetan bright spats: evidence for free aqueous fluids in the Tibetan middle crust. J Geophys Res 104:10795–10825

Mancktelow NS (2008) Tectonic pressure: theoretical concepts and modelled examples. Lithos 103:149–177. doi:10.1016/j.lithos.2007.09.013

Manning CE, Ingebritsen SE (1999) Permeability of the continental crust: implications of geothermal data and metamorphic systems. Rev Geophys 37:127–150

McCaig AM, Wickham SM, Taylor HP (1990) Deep fluid circulation in alpine shear zones, Pyrenees, France – field and oxygen isotope studies. Contrib Mineral Petrol 106:41–60

McCuaig TC, Kerrich R (1998) P-T-t-deformation-fluid characteristics of lode gold deposits: evidence from alteration systematics. Ore Geol Rev 12:381–453

McKenzie D (1984) The generation and compaction of partially molten rock. J Petrol 2:713–765

Milke R, Abart R, Kunze K, Koch-Muller M, Schmid D, Ulmer P (2009) Matrix rheology effects on reaction rim growth i: evidence from orthopyroxene rim growth experiments. J Metamorph Geol 27:71–82. doi:10.1111/j.1525-1314.2008.00804.x

Miller SA, Collettini C, Chiaraluce L, Cocco M, Barchi M, Kaus BJP (2004) Aftershocks driven by a high-pressure CO_2 source at depth. Nature 427:724–727. doi:10.1038/nature02251

Mosenfelder JL, Connolly JAD, Rubie DC, Liu M (2000) Strength of (Mg, Fe)2SiO4 wadsleyite determined by relaxation of transformation stress. Phys Earth Planet Inter 120:63–78
Munz IA, Yardley BWD, Gleeson SA (2002) Petroleum infiltration of high-grade basement, South Norway: pressure-temperature-time-composition (P-T-t-X) constraints. Geofluids 2:41–53
Nabelek PI (2009) Numerical simulation of kinetically-controlled calc-silicate reactions and fluid flow with transient permeability around crystallizing plutons. Am J Sci 309:517–548. doi:10.2475/07.2009.01
Nakashima Y (1995) Transport model of buoyant metamorphic fluid by hydrofracturing in leaky rock. J Metamorph Geol 13:727–736
Neuzil CE (1994) How permeable are clays and shales? Water Resour Res 30:145–150
Norton D, Knapp R (1977) Transport phenomena in hydrothermal systems – nature of porosity. Am J Sci 277:913–936
Okamoto A, Tsuchiya N (2009) Velocity of vertical fluid ascent within vein-forming fractures. Geology 37:563–566. doi:10.1130/g25680a.1
Oliver GJH, Chen F, Buchwaldt R, Hegner E (2000) Fast tectonometamorphism and exhumation in the type area of the Barrovian and Buchan zones. Geology 28:459–462
Ozel O, Iwasaki T, Moriya T, Sakai S, Maeda T, Piao C, Yoshii T, Tsukada S, Ito A, Suzuki M, Yamazaki A, Miyamachi H (1999) Crustal structure of Central Japan and its petrological implications. Geophys J Int 138:257–274
Padron-Navarta JA, Tommasi A, Garrido CJ, Sanchez-Vizcaino VL, Gomez-Pugnaire MT, Jabaloy A, Vauchez A (2010) Fluid transfer into the wedge controlled by high-pressure hydrofracturing in the cold top-slab mantle. Earth Planet Sci Lett 297:271–286. doi:10.1016/j.epsl.2010.06.029
Padron-Navarta JA, Sanchez-Vizcaino VL, Garrido CJ, Gomez-Pugnaire MT (2011) Metamorphic record of high-pressure dehydration of antigorite serpentinite to chlorite harzburgite in a subduction setting (Cerro del Almirez, Nevado-Filabride Complex, Southern Spain). J Petrol 52:2047–2078. doi:10.1093/petrology/egr039
Paterson MS, Luan FC (1990) Quartzite rheology under geological conditions. In: Knipe RJ, Rutter EH (eds) Deformation mechanisms, rheology and tectonics, vol 54. The Geological Society, London, pp 299–307
Peng ZG, Vidale JE, Creager KC, Rubinstein JL, Gomberg J, Bodin P (2008) Strong tremor near Parkfield, CA, excited by the 2002 Denali fault earthquake. Geophys Res Lett 35. doi:10.1029/2008gl036080
Petrini K, Podladchikov Y (2000) Lithospheric pressure-depth relationship in compressive regions of thickened crust. J Metamorph Geol 18:67–78
Plank T, Langmuir CH (1998) The chemical composition of subducting sediment and its consequences for the crust and mantle. Chem Geol 145:325–394
Powley DE (1990) Pressures and hydrogeology in petroleum basins. Earth Sci Rev 29:215–226
Price JD, Wark DA, Watson EB, Smith AM (2006) Grain-scale permeabilities of faceted polycrystalline aggregates. Geofluids 6:302–318. doi:10.1111/j.1468-8123.2006.00149.x
Ranalli G (1995) Rheology of the earth. Springer, New York
Ranalli G, Rybach L (2005) Heat flow, heat transfer and lithosphere rheology in geothermal areas: features and examples. J Volcanol Geotherm Res 148:3–19. doi:10.1016/j.jvolgeores.2005.04.010
Read CM, Cartwright I (2000) Meteoric fluid infiltration in the middle crust during shearing: examples from the Arunta Inlier, Central Australia. J Geochem Explor 69:333–337
Rice JR (1992) Fault stress states, pore pressure distributions, and the weakness of the San Andreas Fault. In: Evans B, Wong T-F (eds) Fault mechanics and transport properties of rocks. Academic, New York, pp 475–503
Richter FM, McKenzie D (1984) Dynamical models for melt segregation from a deformable rock matrix. J Geol 92:729–740
Rozhko AY, Podladchikov YY, Renard F (2007) Failure patterns caused by localized rise in pore-fluid overpressure and effective strength of rocks. Geophys Res Lett 34:L22304. doi:10.1029/2007gl031696

Rubie DC, Thompson AB (1985) Kinetics of metamorphic reactions. In: Thompson AB, Rubie DC (eds) Metamorphic reactions kinetics, textures, and deformation, vol 4. Springer, New York, pp 291

Rubin RM (1995) Propagation of magma-filled cracks. Annu Rev Earth Planet Sci 23:287–336

Rubinstein JL, Vidale JE, Gomberg J, Bodin P, Creager KC, Malone SD (2007) Non-volcanic tremor driven by large transient shear stresses. Nature 448:579–582. doi:10.1038/nature06017

Rutter EH (1983) Pressure solution in nature, theory and experiment. J Geol Soc Lond 140:725–740

Scarpa R, Amoruso A, Crescentini L, Fischione C, Formisano LA, La Rocca M, Tronca F (2008) Slow earthquakes and low frequency tremor along the Apennines, Italy. Ann Geophys 51:527–538

Schmalholz SM, Podladchikov Y (1999) Buckling versus folding: importance of viscoelasticity. Geophys Res Lett 26:2641–2644

Scholz CH (1988) The brittle-plastic transition and the depth of seismic faulting. Geol Rundsch 77:319–328

Scott DR (1988) The competition between percolation and circulation in a deformable porous-medium. J Geophys Res 93:6451–6462

Scott DR, Stevenson DJ (1986) Magma ascent by porous flow. J Geophys Res 91:9283–9296

Scott DR, Stevenson DJ, Whitehead JA (1986) Observations of solitary waves in a viscously deformable pipe. Nature 319:759–761

Shaw DM (1956) Geochemistry of pelite rocks, iii, major elements and general geochemistry. Geol Soc Am Bull 67:919–934

Shimizu I (1995) Kinetics of pressure solution creep in quartz; theoretical considerations. Tectonophysics 245:121–134

Sibson RH (1986) Earthquakes and rock deformation in crustal fault zones. Annu Rev Earth Planet Sci 14:149–175

Sibson RH (1992) Fault-valve behavior and the hydrostatic lithostatic fluid pressure interface. Earth Sci Rev 32:141–144

Sibson RH (2000) Tectonic controls on maximum sustainable overpressure: fluid redistribution from stress transitions. J Geochem Explor 69:471–475

Sibson RH (2004) Controls on maximum fluid overpressure defining conditions for mesozonal mineralisation. J Struct Geol 26:1127–1136. doi:10.1016/j.jsg.2003.11.003

Sibson RH (2009) Rupturing in overpressured crust during compressional inversion-the case from NE Honshu, Japan. Tectonophysics 473:404–416. doi:10.1016/j.tecto.2009.03.016

Simpson GDH (1998) Dehydration-related deformation during regional metamorphism, NW Sardinia, Italy. J Metamorph Geol 16:457–472

Skelton ADL (1996) The timing and direction of metamorphic fluid flow in Vermont. Contrib Mineral Petrol 125:75–84

Skelton ADL, Valley JW, Graham CM, Bickle MJ, Fallick AE (2000) The correlation of reaction and isotope fronts and the mechanism of metamorphic fluid flow. Contrib Mineral Petrol 138:364–375

Spiegelman M (1993) Flow in deformable porous-media. 1. Simple analysis. J Fluid Mech 247:17–38

Spiegelman M, Elliott T (1993) Consequences of melt transport for uranium series disequilibrium in young lavas. Earth Planet Sci Lett 118:1–20

Spiegelman M, Kelemen PB, Aharonov E (2001) Causes and consequences of flow organization during melt transport: the reaction infiltration instability in compactible media. J Geophys Res 106:2061–2077

Spiers CJ, Schutjens PMTM (1990) Densification of crystalline aggregates by diffusional creep. J Geolo Soc Spec Publ 54:215–227

Stahle HJ, Raith M, Hoernes S, Delfs A (1987) Element mobility during incipient granulite formation at kabbaldurga, Southern India. J Petrol 28:803–834

Staude S, Bons PD, Markl G (2009) Hydrothermal vein formation by extension-driven dewatering of the middle crust: an example from SW Germany. Earth Planet Sci Lett 286:387–395. doi:10.1016/j.epsl.2009.07.012

Stern T, Kleffmann S, Okaya D, Scherwath M, Bannister S (2001) Low seismic-wave speeds and enhanced fluid pressure beneath the Southern Alps of New Zealand. Geology 29:679–682

Stevenson D (1989) Spontaneous small-scale melt segregation in partial melts undergoing deformation. Geophys Res Lett 16:1067–1070

Suetnova EI, Carbonell R, Smithson SB (1994) Bright seismic reflections and fluid movement by porous flow in the lower crust. Earth Planet Sci Lett 126:161–169. doi:10.1016/0012-821x(94)90248-8

Sumita I, Yoshida S, Kumazawa M, Hamano Y (1996) A model for sedimentary compaction of a viscous medium and its application to inner-core growth. Geophys J Int 124:502–524

Tenthorey E, Cox SF (2006) Cohesive strengthening of fault zones during the interseismic period: an experimental study. J Geophys Res 111:B09202. doi:10.1029/2005jb004122

Thompson AB, Connolly JAD (1990) Metamorphic fluids and anomalous porosities in the lower crust. Tectonophysics 182:47–55

Tumarkina E, Misra S, Burlini L, Connolly JAD (2011) An experimental study of the role of shear deformation on partial melting of a synthetic metapelite. Tectonophysics 503:92–99. doi:10.1016/j.tecto.2010.12.004

Upton P, Koons PO, Chamberlain CP (1995) Penetration of deformation-driven meteoric water into ductile rocks: isotopic and model observations from the Southern Alps, New Zealand. N Z J Geol Geophys 38:535–543

van Haren JLM, Ague JJ, Rye DM (1996) Oxygen isotope record of fluid infiltration and mass transfer during regional metamorphism of pelitic schist, Connecticut, USA. Geochim et Cosmochim Acta 60:3487–3504

Vanyan LL, Gliko AO (1999) Seismic and electromagnetic evidence of dehydration as a free water source in the reactivated crust. Geophys J Int 137:159–162

Vrijmoed JC, Podladchikov YY, Andersen TB, Hartz EH (2009) An alternative model for ultra-high pressure in the Svartberget Fe-Ti Garnet-Peridotite, Western Gneiss Region, Norway. Eur J Mineral 21:1119–1133. doi:10.1127/0935-1221/2009/0021-1985

Walther JV, Orville PM (1982) Volatile production and transport in regional metamorphism. Contrib Mineral Petrol 79:252–257

Wark DA, Watson EB (1998) Grain-scale permeabilities of texturally equilibrated, monomineralic rocks. Earth Planet Sci Lett 164:591–605

Warren CJ, Smye AJ, Kelley SP, Sherlock SC (2011) Using white mica $^{40}Ar/^{39}Ar$ data as a tracer for fluid flow and permeability under high-p conditions: Tauern Window, Eastern Alps. J Metamorph Geol. doi:10.1111/j.1525-1314.2011.00956.x

Wickham SM, Peters MT, Fricke HC, Oneil JR (1993) Identification of magmatic and meteoric fluid sources and upward-moving and downward-moving infiltration fronts in a metamorphic core complex. Geology 21:81–84

Wiggins C, Spiegelman M (1995) Magma migration and magmatic solitary waves in 3-d. Geophys Res Lett 22:1289–1292

Wilkinson DS, Ashby MF (1975) Pressure sintering by power law creep. Acta Metall 23:1277–1285

Wing BA, Ferry JM (2007) Magnitude and geometry of reactive fluid flow from direct inversion of spatial patterns of geochemical alteration. Am J Sci 307:793–832. doi:10.2475/05.2007.02

Wong TF, Christian D, Menendez B (2004) Mechanical compaction. In: Gueguen Y, Bouteca M (eds) Mechanics of fluid-saturated rocks. Elsevier Academic, Burlington, pp 55–79

Xiao XH, Evans B, Bernabe Y (2006) Permeability evolution during non-linear viscous creep of calcite rocks. Pure Appl Geophys 163:2071–2102. doi:10.1007/s00024-006-0115-1

Yardley BWD (1983) Quartz veins and devolatilization during metamorphism. J Geol Soc 140:657–663

Yardley B, Gleeson S, Bruce S, Banks D (2000) Origin of retrograde fluids in metamorphic rocks. J Geochem Explor 69:281–285

Young ED, Rumble D (1993) The origin of correlated variations in insitu O^{18}/O^{16} and elemental concentrations in metamorphic garnet from southeastern Vermont, USA. Geochim et Cosmochim Acta 57:2585–2597. doi:10.1016/0016-7037(93)90419-w

Zharikov AV, Vitovtova VM, Shmonov VM, Grafchikov AA (2003) Permeability of the rocks from the Kola superdeep borehole at high temperature and pressure: implication to fluid dynamics in the continental crust. Tectonophysics 370:177–191. doi:10.1016/s0040-1951(03)00185-9

Zhu W, David C, T-f W (1995) Network modeling of permeability evolution during cementation and hot isostatic pressing. J Geophys Res 100:15451–15464

Zhu W, Evans B, Bernabe Y (1999) Densification and permeability reduction in hot-pressed calcite: a kinetic model. J Geophys Res 104:25501–25511

Zoback MD, Townend J (2001) Implications of hydrostatic pore pressures and high crustal strength for the deformation of intraplate lithosphere. Tectonophysics 336:19–30

Chapter 15
Metasomatism in the Early Solar System: The Record from Chondritic Meteorites

Adrian J. Brearley and Alexander N. Krot

Abstract Mineralogic, petrologic, and isotopic studies of chondritic meteorites have revealed a significant body of evidence of metasomatic processes during the earliest stages of Solar System evolution. The exact nature of these processes, as well as the conditions and environments where metasomatism occurred, are still the subject of vigorous debate. The interaction of aqueous fluids with early Solar System solids affected different chondrite groups to different degrees: even within a single chondrite group the effects of metasomatism can be highly variable. Among the carbonaceous chondrite groups, the CV (Vigarano-type) and CO (Ornans-type) chondrites show the best documented evidence of metasomatic effects. In the oxidized subgroup of the CV chondrites, Ca-Al-rich Inclusions (CAIs), Amoeboid Olivine Aggregates (AOAs), chondrules, and matrix have all been extensively affected by Fe-alkali-halogen metasomatism, that has resulted in the formation of a wide range of secondary, dominantly anhydrous minerals, including grossular, andradite, wollastonite, monticellite, anorthite, forsterite, ferroan olivine, corundum, Na-melilite, nepheline, sodalite, wadalite, Al-diopside, kushiroite, ferroan diopside – hedenbergite pyroxenes, ilmenite, phosphates, magnetite, awaruite, tetrataenite, and Fe,Ni sulfides. Hydrous phases are much rarer, but include, margarite, vesuvianite, and kaolinite. The mineral assemblages that form are highly dependent on the primary mineralogy of the host object: distinct mineral assemblages are produced by alteration of CAIs, chondrules, and matrix, for example. Nebular and asteroidal scenarios for these metasomatic effects have been extensively discussed in the literature for the metasomatism observed in the

A.J. Brearley (✉)
Department of Earth and Planetary Sciences, MSC03-2040, University of New Mexico, Albuquerque, NM 87131, USA
e-mail: brearley@unm.edu

A.N. Krot
Hawai'i Institute of Geophysics and Planetology, School of Ocean, Earth Science and Technology, University of Hawai'i at Mānoa, Honolulu, HI 96822, USA

D.E. Harlov and H. Austrheim, *Metasomatism and the Chemical Transformation of Rock*, Lecture Notes in Earth System Sciences,
DOI 10.1007/978-3-642-28394-9_15,

CV chondrites. Oxygen isotopic studies of the secondary minerals in CV chondrites, such as fayalite, magnetite and Ca, Fe-rich silicates, indicate formation at relatively low temperatures (<550 K) from aqueous solutions, consistent with an asteroidal environment. On the other hand, primary minerals in CAIs show oxygen isotopic heterogeneity, with melilite and anorthite exhibiting heavy isotope enrichments compared with spinel, hibonite, Al,Ti-diopside, and forsterite. The origin of this selective isotopic exchange is still the subject of debate; it may have occurred by gas–solid or gas–melt exchange in the solar nebula or by isotopic exchange with a ^{16}O-depleted fluid in an asteroidal environment. The CO chondrites show significant evidence of metasomatic events, but the degree and extent of metasomatism is much less than that for the CV chondrites. Calcium-rich phases, such as melilite, plagioclase, and glassy mesostasis in CAIs, AOAs and chondrules have been affected the most and have been replaced by fine-grained alteration products. Although the secondary minerals in CO chondrites have not been characterized in as much detail as the CV chondrites, nepheline, sodalite, ilmenite, ferroan olivine, and ferroan diopside – hedenbergite pyroxenes have all been positively identified. Collectively the data indicate that Fe-alkali metasomatism has also affected the CO chondrites, but the involvement of halogens is much less extensive. Although the alteration of CAIs, AOAs and chondrules is extremely heterogeneous in CO chondrites, there is a general correlation between the degree of metasomatism and metamorphism, indicating that the metasomatism occurred dominantly within an asteroidal environment. However, some rare CAIs in type 3.0 CO chondrites and chondrules in higher petrologic CO3 subtypes contain metasomatic effects that may be best explained by alteration prior to asteroidal accretion. In comparison, the ordinary chondrites (H, L, and LL) show minimal evidence of metasomatic effects. Only a few unequilibrated ordinary chondrites show evidence of highly localized and minimal development of nepheline, sodalite, and scapolite that occurs only with chondrules that contain Al-rich phases such as plagioclase. The most extensively metasomatized ordinary chondrite is Tieschitz (H3.6), which contains a highly unusual component of matrix consisting of veins of nepheline and albite interstitial to chondrules. Chondrule glass in this meteorite has been leached extensively of alkalis and Al, indicating extensive interaction with an aqueous fluid. Finally, new evidence is coming to light which suggests that some more highly metamorphosed ordinary chondrites may have undergone metasomatism, indicated by partial albitization of plagioclase, formation of ferroan olivine replacing low-Ca pyroxene and remobilization of phosphate minerals. These limited data suggest that mineral-fluid interactions in the ordinary chondrites occurred late in the metamorphic history of these meteorites. Metasomatic effects may be much more extensively developed in the ordinary chondrites, but are cryptic in nature and have yet to be recognized. Research on the role of fluids in the geologic evolution of the ordinary chondrite parent bodies is therefore still in its infancy.

15.1 Introduction

15.1.1 Background

Chondritic meteorites (chondrites) represent a tangible record of astrophysical and geologic processes that occurred during the very earliest stages of solar system history. Hence, they provide a unique glimpse of the sequence of early solar system events starting with the formation of the first solids to the accretion and geologic evolution of small solar system bodies. These events occurred over a remarkably short timescale, spanning <25 Ma, resulting in a complex and sometimes perplexing evolutionary history for these objects. Of key importance for understanding the genesis of chondritic meteorites is constraining the role that water played in their chemical, mineralogical, and isotopic evolution. Although it has been recognized for more than 150 years that water, in the form of hydrous minerals, is present in chondrites, it is only in the last 20 years that the widespread effects of water have been fully appreciated. The evidence for alteration comes in two main forms; low temperature hydrothermal alteration, with widespread development of hydrous minerals, and metasomatism involving the formation of mainly anhydrous phases. In the case of metasomatism, the evidence for the involvement of water is sometimes cryptic and consequently this area of research is the subject of lively and stimulating debate. In addition to hydrothermal alteration and metasomatism, some chondrites have clearly experienced thermal metamorphism. A key question in the debate over the importance of water in chondrite evolution is the relationship between metamorphism and metasomatism.

At the core of research on chondrites is the fundamental objective of improving our understanding of the processes that occurred as the Sun and planets were forming 4,567 Ga ago. It is widely accepted that formation of the planetary bodies in our solar system occurred within a disk of dust and gas that surrounded the proto-Sun (the so-called protoplanetary disk or solar nebula). Chondritic meteorites contain a record of these very early processes and, hence, can place constraints on physical and chemical conditions within the protoplanetary disk; information that provides ground truth for astrophysical models of early solar system evolution (e.g., Shu et al. 2001; Desch and Connolly 2002; Ciesla 2005; Desch et al. 2005). Few chondrites, however, contain a pristine record of these early solar system processes – so called secondary processes that include aqueous alteration, metamorphism, and metasomatism have all acted to modify this very early record to different degrees. Chondrites are rocks that represent lithified samples of materials that originate from small asteroidal bodies from within the main Asteroid belt ~ 3 AU (astronomical units) from the Sun. Although some of the secondary processing of chondritic meteorites may have occurred prior to formation (accretion) of these asteroidal parent bodies (e.g., Bischoff 1998; Brearley 2003), much of the evidence indicates that this processing occurred largely after accretion. Our ability to use meteorites to provide us with information about the stage of solar system evolution prior to the formation of planetary bodies requires a comprehensive understanding

of how secondary processes may have affected this primary record. Hence, the study of metasomatic and metamorphic effects in chondrites has to be an integral component of any effort to decipher the full cosmochemical evolution of chondritic materials.

In this chapter, we review the evidence for metasomatism in chondrites and examine the link between metasomatism and metamorphism in these meteorites. Research on the metasomatic effects present in chondritic meteorites is aimed at addressing several different questions, some shared in common with studies of terrestrial metasomatism, but some that are unique to chondrites. These questions include: (1) When and where did metasomatism occur? (2) How long did metasomatism last? (3) What are the mineralogical, isotopic, and cosmochemical effects of metasomatism? (4) How did metasomatism modify the primary (nebular) record contained in chondritic meteorites? (5) On what scale did metasomatism occur? (6) What is the source and composition of the metasomatizing fluids? (7) Are the effects of metasomatism heterogeneously developed within chondrites? (8) Were metasomatism and metamorphism linked? (9) What were the physical and chemical conditions under which metasomatism occurred? and (10) How did metasomatism contribute to the geologic evolution of small solar system bodies? The answers to many of these questions are far from resolved and continue to be an area of active research in planetary science.

15.1.2 Chondritic Meteorites: Classification and Terminology

Chondrites, so called because they contain distinctive mm-sized silicate spherules called chondrules (Greek – Khondros = grain), are heterogeneous aggregates of materials that formed in different locations and under different conditions within the protoplanetary disk. Detailed information on the characteristics and classification of chondritic meteorites can be found in several recent review papers (e.g., Krot et al. 2003; Scott and Krot 2005a; Weisberg et al. 2006; Krot et al. 2009). Here we only provide a basic overview of chondrites in order to provide a context for the following discussion of metasomatism and metamorphism. We first define some terms that are commonly used in the meteoritics and cosmochemical literature to avoid confusion.

The three major, distinct components of chondrites are chondrules, refractory inclusions [Calcium-Aluminum-rich Inclusions (CAIs) and amoeboid olivine aggregates (AOAs)] and matrix, but other components such as sulfides, Fe,Ni metal, and carbonaceous materials also occur in varying abundances in different chondrites (Fig. 15.1). Chondrules are ultramafic silicate spherules that have textures indicative of rapid crystallization from a melt and appear to have once been molten droplets that cooled and crystallized rapidly (e.g., Jones et al. 2005). Mineralogically, they are dominated by phenocrysts of olivine ($(Mg,Fe)_2SiO_4$), low-Ca pyroxene (enstatite, $MgSiO_3$), and an interstitial mesostasis that represents residual quenched melt. Low Ni, Fe-metal grains (kamacite,~$Fe_{95}Ni_5$) and sulfide

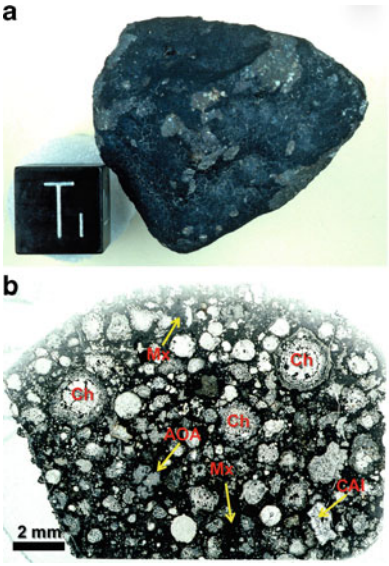

Fig. 15.1 (*Upper image*) Photograph of a single stone of the Allende CV3 carbonaceous chondrite, showing the presence of a dark fractured fusion crust over a significant proportion of its surface. A 1 cm^3 is shown for scale. The interior of the stone is revealed where the fusion crust is absent. (*Lower image*) Optical micrograph (transmitted light) of a thin section of the Allende CV3 chondrite showing the characteristic textures and components of chondritic meteorites. The thin section contains abundant, millimeter-sized, rounded to subrounded chondrules (Ch) set in a dark fine-grained matrix (Mx) that acts as a groundmass to the chondrules. Rarer refractory inclusions, Ca,Al-rich inclusions (CAIs) and amoeboid olivine aggregates (AOAs) are also distributed throughout the thin section. Opaque phases such as metals, oxides, sulfides, and carbides also occur, but are indistinguishable from the fine-grained matrix (Mx) in this transmitted light image. The matrix is extremely fine-grained and appears opaque in the image where the thin section is a typical 30 μm in thickness. However, in the *upper part* of the image the thin section is thinner (~10 μm) and the matrix is translucent in this region.

(troilite, FeS) also occur in many chondrules. Chondrules are ultramafic to mafic in composition with Mg, Si, and Fe as the major elements with Fe occurring as both Fe^0 and Fe^{2+} in the primary nebular mineralogy of chondrules. Refractory inclusions are a heterogeneous group of extremely complex objects whose mineralogy is dominated by highly refractory minerals rich in Ca, Al, and Ti, such as corundum (Al_2O_3), hibonite ($CaAl_{12}O_{19}$), melilite (åkermanite, $Ca_2MgSi_2O_7$ – gehlenite, $Ca_2Al_2SiO_7$ solid solution), anorthite ($CaAl_2Si_2O_8$), spinel ($MgAl_2O_4$), perovskite ($CaTiO_3$), Ca,Al,Ti-rich pyroxenes ($Ca(Mg,Al,Ti)(Si,Al)_2O_6$), and forsteritic olivine ($(Mg)_2SiO_4$). Ca-Al-rich inclusions are the oldest known solids from the early solar system with ages of 4,567–4,568 Ma (Amelin et al. 2002) and formed in solar nebular region(s) with a very high ambient temperature (> 1,350 K) by a variety of high-temperature processes including condensation, evaporation, and melting (MacPherson 2003; MacPherson et al. 1988; MacPherson et al. 2005). Chondrules, CAIs, and other macroscopic

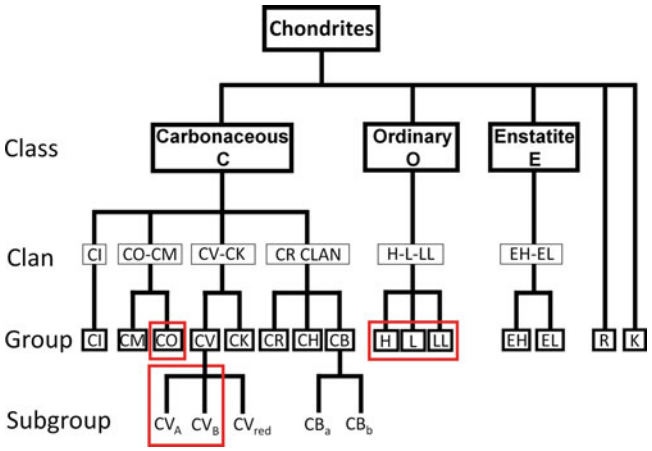

Fig. 15.2 Classification scheme for chondritic meteorites (After Weisberg et al. 2006). Chondritic meteorites can be classified into three major classes, the Carbonaceous (C), Ordinary (O) and Enstatite (E) chondrites. These groups can be further broken down into clans, which represent meteorites with similar affinities. Based on a variety of petrographic, compositional and isotopic characteristics, these clans can be further divided into 15 different distinct chondrite groups. Some of the groups can be further divided into subgroups as indicated. The meteorite groups or subgroups, in which metasomatic effects have been identified definitively, are *outlined* in *red boxes*. These are the CV_A and CV_B subgroups, the CO group and the Ordinary chondrite group

components of chondrites are embedded in a fine-grained micron to submicron matrix that appears opaque in thin sections of typical 30 μm thickness. In the least altered chondrites, the matrix is a complex disequilibrium assemblage of silicates (amorphous and crystalline), sulfides, metals, oxides, and carbonaceous materials. The matrix is also the host of presolar grains that occur at the part per million (ppm) level in chondritic meteorites. Compositionally, matrix is generally enriched in Fe relative to chondrules and has higher volatile element contents (Scott et al. 1988; Brearley 1996; Scott and Krot 2005b; Huss et al. 2005).

Chondrites are grouped into three major classes, the carbonaceous (C), ordinary (O), and enstatite (E), based on their bulk chemistry, oxygen isotopic compositions, oxidation state, and petrographic characteristics. These three classes are further divided into different groups which are closely related (Fig. 15.2). For the C chondrites, eight different groups have been recognized with the designations CI, CM, CO, CV, CR, CK, CH, and CB, the letter following the C corresponding to the first letter of the type meteorites for that group, e.g., Ivuna (I), Mighei (M), etc.. For the O chondrites, just three groups have been recognized, H (high total Fe), L (low total Fe) and LL (low total Fe and low metallic Fe), and for the enstatite chondrites, there are two groups, the EL (low Fe) and EH (high Fe). In order to denote the fact that chondrites have experienced aqueous alteration and thermal metamorphism, Van Schmus and Wood (1967) proposed an additional designation to the C, O and E

chondrite classification. This scheme adds a number between 1 and 6 to the group designation, defining the so-called petrologic type of a meteorite. Van Schmus and Wood (1967) defined type 3 chondrites as the petrologic type which had undergone no aqueous alteration or thermal metamorphism, i.e. whose nebular record was the most pristine. Increasing degrees of metamorphism are denoted by increasing petrologic type from 4 to 6 and aqueous alteration increases in degree from petrologic type 2–1. The petrologic classification scheme has evolved as more detailed studies of larger numbers of chondrites have been carried out. Most notably, we now know that type 3 chondrites actually show a range of thermal metamorphism, resulting in a further subdivision into types 3.0–3.9. Most recently, very subtle changes, as a result of low degrees of metamorphism, have been recognized, adding a further decimal place onto the classification scheme for meteorites between petrologic types 3.0 and 3.2, i.e., 3.00, 3.01, etc. (Grossman and Brearley 2005).

At present, evidence of metasomatism is restricted to only a handful of individual chondrite groups, and not all members of these chondrite groups exhibit metasomatism. In this chapter, we focus on metasomatic effects in the CV3 and CO3 carbonaceous chondrites and the ordinary chondrites. The CV3 chondrites show the most extensive and well-documented evidence of metasomatism, with more mild effects being apparent in the CO3 chondrites. The ordinary chondrites show comparatively limited evidence of metasomatism, however, there is some evidence that metasomatism occurred over a wider range of temperatures than in the carbonaceous chondrite groups.

15.1.3 Metasomatism in Chondrites: Unique Samples, Unique Problems

The study of metasomatism in chondrites shares aspects in common with studies of terrestrial metasomatism, but there are also notable differences. A problem unique to chondrites is the issue of the environment where elemental mass transport took place. A long standing debate in the meteoritics literature concerns the question of whether metasomatism occurred when the components of chondrites were free floating in the protoplanetary disk, prior to accretion, or whether metasomatism occurred after these components were assembled together into asteroidal parent bodies (e.g., Krot et al. 1995; Brearley 2003). These different environments are commonly referred to as nebular and parent body environments, respectively, but the terms pre-accretionary or post-accretionary processes are also commonly used in the literature. Obviously the processes and conditions that could have operated in these two distinct environments are quite different, one involving gas-solid interactions at very low total gas pressure ($<10^{-3}$ bar) dominated by hydrogen and much smaller partial gas pressures and the second involving fluids at higher

pressures (a few bars to 10s of bars). Although in most cases the evidence for asteroidal metasomatism is unequivocal, in other cases there is certainly ambiguity.

An additional problem is the fact that meteorites are essentially delivered by stochastic processes to Earth, and, hence, even the most basic information about the geologic context of these samples is completely absent. It is commonly assumed that meteorites of the same groups, e.g., CV chondrites, originate from the same asteroidal parent body, and, thus, share at least some basic relationship. However, even this basic assumption has not yet been demonstrated for any single type of meteorite. In addition, meteorite-asteroid connections are still poorly understood (e.g., Burbine et al. 2002). The lack of any information about the field relationships between different meteorites of the same type is a similar problem to that posed by terrestrial mantle xenoliths, except that at least we know the planetary body and the general location that mantle xenoliths originate from. Part of the debate over whether metasomatism occurred in the solar nebula or on asteroidal parent bodies comes from the lack of knowledge of larger scale field relationships.

A significant difference between metasomatism in chondrites and terrestrial metasomatism is the scale on which metasomatism operates. The issue of the lack of any field relationships poses some interesting problems for constraining the maximum length scales over which metasomatism occurs in chondrites. An upper limit of the length scale is provided by the maximum radius of the potential parent asteroids of chondritic meteorites, which is of the order of 10s of kilometers (Grimm and McSween 1989; Young et al. 1999; McSween et al. 2002). In reality, for all but the most fluid-mobile elements, the length scales of metasomatism in chondrites are likely to be of the order of 10s of microns to millimeters (see for example, Putnis and Austrheim 2010). The focus of this review will, however, largely be on metasomatic effects that are observable on the scale of a petrologic thin section or less. Metasomatism on this scale is rarely, if ever, described in the terrestrial environment. However, the unique characteristics of chondritic meteorites are such that the mineralogical effects of metasomatism are clearly visible on the scale of 10s to 100s of microns. There is evidence that the geochemical and isotopic effects of metasomatism occur over larger scales, but because of the lack of field relationships between different samples, as noted earlier, these scales are very difficult to constrain. They could, however, certainly be of the order of meters to 10s of meters.

The micrometasomatism (in comparison with terrestrial metasomatism) observed in most chondrites is the result of the highly heterogeneous character of the materials that constitute these meteorites. The principal components of chondrites, chondrules, CAIs, and matrix have very different compositions and mineral constituents, which are far from equilibrium in petrologic type 3 chondrites. The term ‘cosmic conglomerate’ has been used to describe chondrites and is a useful description because it conveys the idea that chondrites are a mixture of materials with very different histories that were mixed together during

the process of accretion into asteroids. Metasomatic processes in chondrites, that occurred on asteroidal parent bodies, involve the exchange of elements between these different components, i.e. each component is effectively acting as a distinct rock type. The length scales of mass transport for different elements are controlled by elemental solubilities and geochemical reactions between the fluid and solid and are variable. For some elements, the length scales of metasomatism are of the order of a few 10s of microns, but for highly fluid mobile elements, such as the alkalis and halogens, may be much longer and result in changes to the bulk rock chemistry.

15.1.4 Aqueous Alteration, Metasomatism, and Thermal Metamorphism in Chondritic Meteorites

As presented in detail below there is a considerable body of evidence that demonstrates that aqueous fluids played an important role in the evolution of the chondritic meteorites. However, the terminology used to describe the interaction of aqueous fluids with chondrites is confusing and used interchangeably in different contexts. For example, the terms aqueous alteration, metasomatism and fluid-assisted metamorphism are often used to describe these processes, with no clear definition of exactly what is meant. Here we attempt to provide working definitions of the terms aqueous alteration, metasomatism, and metamorphism to provide a framework for discussing mineral-fluid interactions in chondrites and the possible relationships between fluids and metamorphism.

Aqueous alteration and metasomatism can usefully be defined as processes in which significant mass transport involving a fluid phase occurs and the fluid is the primary agent that drives replacement or alteration of pre-existing primary phases by secondary alteration products. Such processes therefore involve very significant changes in the structure and/or composition of primary phases. However, aqueous alteration in chondritic meteorites can be differentiated from metasomatism, based on the characteristics of the phases that are formed. For example, aqueous alteration can be defined as a process that results in the formation of phyllosilicates as the dominant reaction product, whereas metasomatic processes result in the formation of largely anhydrous phases. Zolotov et al. (2006) have used thermodynamic calculations to identify reactions which define the boundary between these two different processes. Above 100°C, ferroan olivine (Fa_{4-47}) becomes the dominant stable phase, rather than phyllosilicates, in the presence of aqueous fluids at low water/rock (W/R) ratios (<0.1), in carbonaceous chondrite matrices. This reaction boundary varies in temperature depending on the W/R ratio, but still represents a very useful criterion for defining the regimes of aqueous alteration vs. metasomatism in chondrites. However, because this

boundary is sensitive to the intrinsic variables of the particular system under study (i.e. W/R ratio, aH_2O in the fluid, etc.), it does mean that the temperature boundary between aqueous alteration and metasomatism is not a fixed value, unlike transitions that are based on solid–solid reactions.

Metamorphism, as it pertains to chondritic meteorites, involves two major processes, which differentiate it from metasomatism. First, it involves (1) the chemical equilibration of different components of a chondrite that formed under very different conditions and by different processes and (2) it involves thermally-driven recrystallization of components with very different primary grain sizes to attain textural equilibrium. The principal process dominating (1) is elemental exchange between a fine-grained, dominantly silicate, FeO-rich matrix and coarser-grained, Mg-rich chondrule silicates, but also involves significant other more subtle effects involving minor and trace elements. The rate-controlling step for process (1) is volume diffusion of elements within the major silicate phases, olivine, and low-Ca pyroxene, whereas for process (2) the rate-controlling step is grain boundary, intercrystalline diffusion.

The presence of an aqueous fluid during metamorphism modifies the response of the host chondrite in several major ways. First, it provides a medium for elemental mass transport between different components and hence significantly increases the rates of grain boundary diffusion. This will facilitate more rapid recrystallization during the metamorphic process. Second, many primary nebular phases that are metastable at low temperatures, in a fluid-absent system, are unstable in the presence of an aqueous fluid. An aqueous fluid will therefore act as both a reactant and a catalyst to drive breakdown reactions of these primary mineral phases, in addition to acting as a mass transfer medium. The behavior of primary phases in the presence of an aqueous fluid at metamorphic temperatures is also variable: some phases, such as forsteritic olivine, may have compositions that are unstable in the presence of an aqueous fluid and undergo complex coupled dissolution and reprecipitation reactions involving other phases. The final products of such reactants may be the formation of olivine with a different composition (e.g., fayalite (Fe_2SiO_4) or ferroan olivine). Other primary phases, particularly Ca-bearing phases such as melilite, anorthite, and glassy mesostasis undergo complete decomposition in reactions that involve significant redistribution of elements by the fluid phase during the reaction.

We suggest then that the term fluid-assisted metamorphism is a term that best describes the coupling of both metamorphic processes (i.e. volume diffusion and recrystallization of individual grains) with metasomatic processes (fluid-driven breakdown of primary phases, dissolution of primary phases). Mass transport that, in a dry metamorphic system, is controlled by volume and grain boundary diffusion becomes much more complex when water is present as a reactant, catalyst, and mass transfer agent. However, a key issue for chondritic meteorites is whether metamorphism and metasomatism are actually coupled, i.e. was fluid present during the entire period of metamorphism or was it present for only limited periods of time, either during heating or possibly during post-peak metamorphic conditions.

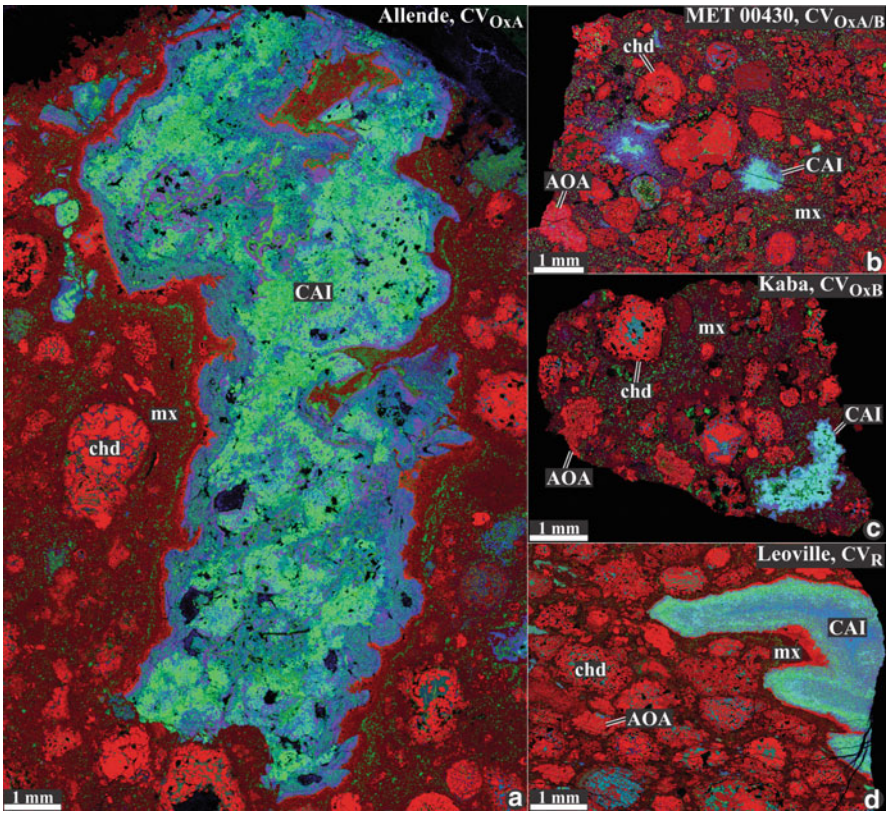

Fig. 15.3 Combined elemental maps in Mg (*red*), Ca (*green*), and Al K_α (*blue*) x-rays of the CV carbonaceous chondrites (**a**) Allende (CV_{OxA}), (**b**) MET 00430 ($CV_{OxA/B}$), (**c**) Kaba (CV_{OxB}), and (**d**) Leoville (CV_R). The CV chondrites contains large Ca,Al-rich inclusions (CAI), amoeboid olivine aggregates (AOA), and chondrules (chd), and interstitial fine-grained matrix (mx). Matrices in Kaba and MET 00430 are hydrated. Matrices in Leoville and Allende are anhydrous. Matrices of the oxidized CV chondrites contain abundant secondary ferroan diopside–hedenbergite pyroxenes (*green spots*). Secondary pyroxenes are less common in the Leoville matrix. This image of the Allende meteorite is not representative. Large CAIs are generally relatively rare (After Weisberg et al. 2006); Figure from Meteorites and the Early Solar System II edited by Dante s. Lauretta and Haryy Y. McSween Jr.© The Arizona Board of Regents. Reprinted by permission of the University of Arizona Press.

15.2 Metasomatic Alteration of CV Carbonaceous Chondrites

15.2.1 Classification of CV (Vigarano-Type) Carbonaceous Chondrites

The CV (Vigarano-type) carbonaceous chondrites are characterized by (1) mm-size chondrules with mainly porphyritic textures, most of which are Mg-rich (type I); (2) high matrix/chondrule ratios (0.5–1.2); and (3) high abundance of mm to cm-

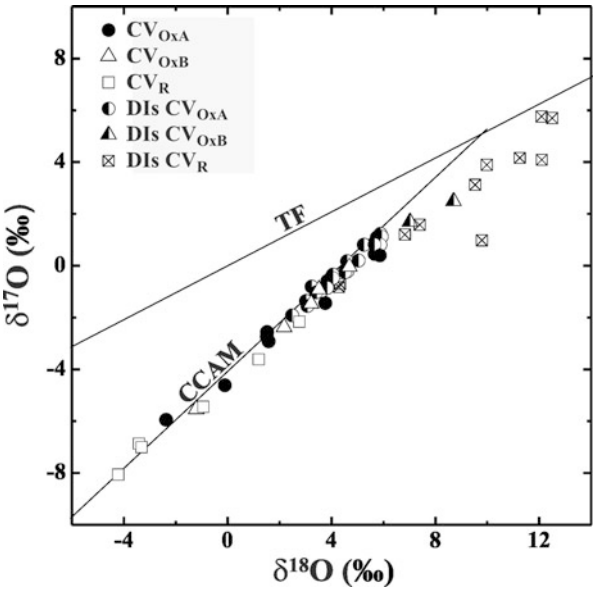

Fig. 15.4 Oxygen isotopic compositions of whole-rock samples of the CV_{OxA}, CV_{OxB}, and CV_R chondrites and CV chondrite lithic clasts (dark inclusions, DIs). The terrestrial fractionation line (TF) and carbonaceous chondrite anhydrous mineral line (CCAM) are shown for reference (Data from Clayton and Mayeda 1999)

sized CAIs and AOAs (McSween 1977a; MacPherson et al. 1988). The CV chondrites are a highly diverse group of meteorites (Fig. 15.3) that was originally divided into oxidized (CV_{Ox}) and reduced (CV_R) subgroups, based principally on modal metal/magnetite ratios and Ni content of metal and sulfides (McSween 1977a). Subsequently, Weisberg et al. (1997) subdivided the oxidized CVs into the Allende-like (CV_{OxA}) and Bali-like (CV_{OxB}) subgroups. Matrix/chondrule ratios increase in the order CV_R (0.5–0.6) – CV_{OxA} (0.6–0.7) – $CV3_{OxB}$ (0.7–1.2); metal/magnetite ratios decrease in the same order (McSween 1977a; Simon et al. 1995). Oxygen isotopic compositions of the CV chondrites show a wide range along a slope of ~1 on the three isotope diagram, with the CV_{OxB} chondrites being slightly ^{16}O-depleted relative to the CV_R and CV_{OxA} chondrites (Fig. 15.4)

There are also significant mineralogical differences between the CV subgroups, which are largely secondary and resulted from alteration and thermal metamorphism and which affected, to various degrees, all CV chondrite components (e.g., Krot et al. 1995, 1998a and references therein). Secondary minerals resulting from metasomatic processes in the CV chondrite group are summarized in Table 15.1.

The CV_{OxB} chondrites (e.g., Kaba, Bali) experienced a moderate degree of alteration and minor thermal metamorphism. Matrices of the CV_{OxB} chondrites are very fine-grained and contain abundant phyllosilicates, magnetite (Fe_3O_4), fine-grained ($<1-2$ μm) ferroan olivine ($(Fe,Mg)_2SiO_4$, $Fa_{\sim 50}$), coarser grains (>10 μm) of nearly pure fayalite (Fe_2SiO_4, Fa_{90-100}), nodules of ferroan diopside – hedenbergite pyroxenes ($(CaMg)_2Si_2O_6$-$(CaFe)_2Si_2O_6$ $Fs_{10-50}Wo_{48-50}$) ± andradite ($Ca_3Fe_2Si_3O_{12}$), and Fe,Ni sulfides (troilite (FeS), pyrrhotite $(Fe,Ni)_{1-x}S$), and pentlandite $(Fe,Ni)_9S_8$)) (Fig. 15.5a).

The CV_{OxA} chondrites (e.g., Allende, ALH 84128) are more extensively altered and metamorphosed than the CV_{OxB} chondrites, but contain very minor phyllosilicates, secondary nepheline ($(Na,K)_2Al_2Si_2O_8$), sodalite ($Na_4Al_3Si_3O_{12}Cl$),

Table 15.1 Compilation of minerals formed by secondary metasomatic processes in chondritic meteorites

Silicates	Formula	Meteorite type
ferroan olivine	$(Fe,Mg)_2SiO_4$, $Fa_{\sim 50}$	CV, CO, OC
fayalite	Fe_2SiO_4, Fa_{90-100}	CV
kirschsteinite	$CaFeSiO_4$	CV
diopside − hedenbergite	$(CaMg)_2Si_2O_6$-$(CaFe)_2Si_2O_6$	CV,CO
wollastonite	$CaSiO_3$	CV
andradite	$Ca_3Fe_2Si_3O_{12}$	CV,CO
grossular	$Ca_3Al_2Si_3O_{12}$	CV,CO
monticellite	$CaMgSiO_4$	CV,CO
anorthite	$CaAl_2Si_2O_8$	CV
albite	$NaAlSi_3O_8$	OC
nepheline	$(Na,K)_2Al_2Si_2O_8$	CV,CO
sodalite	$Na_4Al_3Si_3O_{12}Cl$	CV,CO,OC
scapolite	$Na_4A1_3Si_9O_{24}Cl$	OC
Na-melilite	$(CaNa)_2(Al,Mg)(AlSi)_2O_7$	CV
wadalite	$Ca_6Al_5Si_2O_{16}Cl_3$	CV
kushiroite	$CaAl_2SiO_6$	CV
vesuvianite	$Ca_{10}(Mg,Fe)_2Al_4(SiO_4)_5(Si_2O_7)_2(OH,F)_4$	CV
kaolinite	$Al_2Si_2O_5(OH)_4$	CV
margarite	$CaAl_2(Al_2Si_2)O_{10}(OH)_2)$	CV
Na-phlogopite	$Na(Mg,Fe,Mn)_3Si_3AlO_{10}(F,OH)_2$	CV
saponite	$(½Ca,Na)_{0.33}(Mg,Fe)_3(Si,Al)_4O_{10}(OH)_2{\cdot}4H_2O)$	CV
Ca-amphiboles	$Ca_2(Mg,Fe)_5Si_8O_{22}(OH)_2$	CV
talc	$Mg_3Si_4O_{10}(OH)_2$	CV
Oxides		
magnetite	Fe_3O_4	CV
ilmenite	$FeTiO_3$	CV
corundum	Al_2O_3	CV
Metals		
awaruite	Ni_3Fe	CV
tetrataenite	FeNi	CV
Sulfides		
troilite	FeS	CV,CO
pyrrhotite	$(Fe,Ni)_{1-x}S$	CV
pentlandite	$(Fe,Ni)_9\ S_8$	CV
Phosphates		
graftonite	$(Fe, Mn, Ca)_3(PO_4)_2$	CO

ferroan olivine, ferroan diopside −hedenbergite pyroxenes ($Fs_{10-45}Wo_{48-50}$), andradite, Fe,Ni sulfides, magnetite and Ni-rich metal (awaruite (Ni_3Fe), tetrataenite (FeNi)) are common instead. Matrices of the CV_{OxA} chondrites are coarser-grained than those in the CV_{OxB} chondrites and consist of ferroan olivine ($Fa_{\sim 50}$), nodules of Ca,Fe-pyroxenes ± andradite, nepheline, and Fe,Ni sulfides (Fig. 15.5b,c). Some oxidized CVs (e.g., MET 00430) are mineralogically intermediate between the CV_{OxB} and CV_{OxA} chondrites (Fig. 15.5b). Others (e.g., Mokoia) are breccias

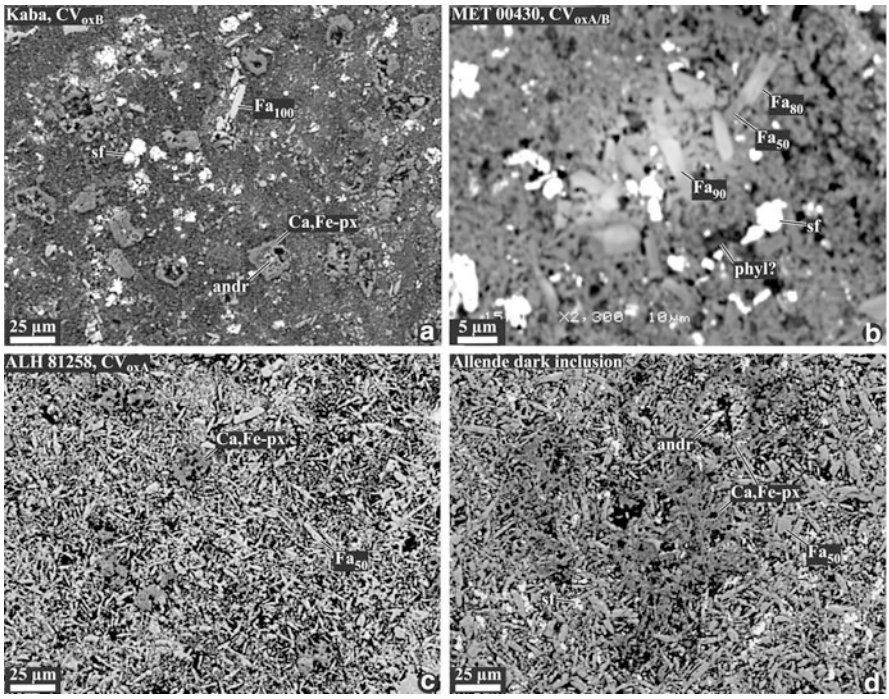

Fig. 15.5 Backscattered electron (BSE) images of matrices in the oxidized CV chondrites (**a**–**c**) and Allende dark inclusion (**d**). Matrix in Kaba (CV_{OxB}) contains nearly pure fayalite (~Fa_{100}) and very fine-grained groundmass largely composed of ferroan olivine (~Fa_{50}), phyllosilicates, and Fe, Ni sulfides (sf). Matrix in MET 00430 ($CV_{OxA/B}$) contains relatively coarse fayalite grains showing inverse compositional zoning ($Fa_{80–50}$); finer grained, lath-shaped ferroan olivine (~Fa_{50}); magnetite; sulfides; and phyllosilicates(?). Matrix in ALH 81258 (CV_{OxA}) and the Allende dark inclusion consists mainly of relatively coarse-grained, lath-shaped, compositionally uniform ferroan olivine (~Fa_{50}). All CV matrices contain nodules of ferroan diopside – hedenbergite pyroxenes (~$Fs_{10–50}Wo_{48–50}$) (Ca,Fe-px) ± andradite (andr) (From Krot et al. 2006). Figures a-d from Meteorites and the Early Solar System II edited by Dante s. Lauretta and Haryy Y. McSween Jr.© The Arizona Board of Regents. Reprinted by permission of the University of Arizona Press.

containing fragments of the CV_{OxA} and CV_{OxB} materials (Krot et al. 1998a). The CV_{OxA} clasts in the Mokoia breccia experienced aqueous alteration that overprints "anhydrous", Allende-like alteration; phyllosilicates replace nepheline and sodalite (Kimura and Ikeda 1998).

The CV_R chondrites (e.g., Efremovka, Leoville) experienced a smaller degree of secondary alteration and thermal metamorphism than the CV_{OxA} chondrites. Phyllosilicates and fayalite are rare. Ferroan olivine, Ca,Fe-rich pyroxenes, nepheline, magnetite, and Fe,Ni sulfides are common. The CV_R chondrite breccia Vigarano contains clasts of both CV_{OxB} and CV_{OxA} materials (Krot et al. 2000a).

In addition to the oxidized and reduced subgroups, CV chondrites often contain chondritic lithic clasts (named "dark inclusions"), which are chemically and petrographically similar to their host meteorites (Fig. 15.5d), but in general experienced

more extensive alteration (e.g., Fruland et al. 1978; Kurat et al. 1989; Johnson et al. 1990; Buchanan et al. 1997; Krot et al. 1997a, 1998a, b, 1999, 2001).

Based on the mineralogy, petrography, and bulk chemical and oxygen isotopic compositions, it is inferred that the CV_{OxA}, CV_{OxB}, and CV_R subgroups and CV dark inclusions may represent different lithologic varieties of a single asteroidal body (Krot et al. 1998a); multiple CV parent asteroids may not be excluded, however (e.g., Jogo et al. 2010). In particular, as discussed by Krot et al. (1995), the bulk chemical compositions of CV chondrites exhibit significant variability, more than is observed in any other chondrite group. These differences are most apparent in the volatile elements, which are distinctly different between the oxidized and reduced subgroups. The available data for CV chondrites show, for example, that Na, Mn, and Fe are all enriched in the oxidized group (Krot et al. 1995), consistent with the fact that this group of CV chondrites has experienced considerable aqueous alteration and metasomatism, as discussed in the following sections. These data indicate that, for this subgroup of meteorites at least, secondary alteration was not isochemical.

15.2.2 Metasomatic Alteration of the CV Chondrite Components: Mineralogy and Petrography

15.2.2.1 Alteration of Refractory Inclusions

Alteration of Refractory Inclusions in CV_{OxB} Chondrites

Refractory inclusions (CAIs and AOAs) in the CV_{OxB} chondrites experienced a low degree of alteration in the presence of aqueous solutions. Primary melilite and anorthite are partially replaced by Al-rich phyllosilicates, whereas Al,Ti-diopside and forsterite are overgrown by ferroan olivine (Fa_{50-80}), and ferroan diopside – hedenbergite (Fig. 15.6). Occasionally, subhedral and euhedral fayalite grains (Fa_{100}) occur in void space inside aqueously altered fine-grained CAIs (Fig. 15.6d). Neither fayalite nor hedenbergite show evidence for replacement by phyllosilicates, suggesting precipitation of fayalite and hedenbergite from an aqueous solution, e.g.,

$$2\ Fe^{2+}{}_{(aq)} + SiO_{2(aq)} + 2\ H_2O_{(g)} = Fe_2SiO_{4(s)} + 2\ H_{2(g)} \tag{15.1}$$

$$3\ Ca^{2+}{}_{(aq)} + 3\ Fe^{2+}{}_{(aq)} + 6\ SiO_{2(aq)} + 6\ H_2O_{(g)} = 3\ CaFeSi_2O_{6(s)} + 3\ Fe^{2+}{}_{(aq)} + 6\ H_{2(g)} \tag{15.2}$$

where aq = aqueous, g = gas, and s = solid.

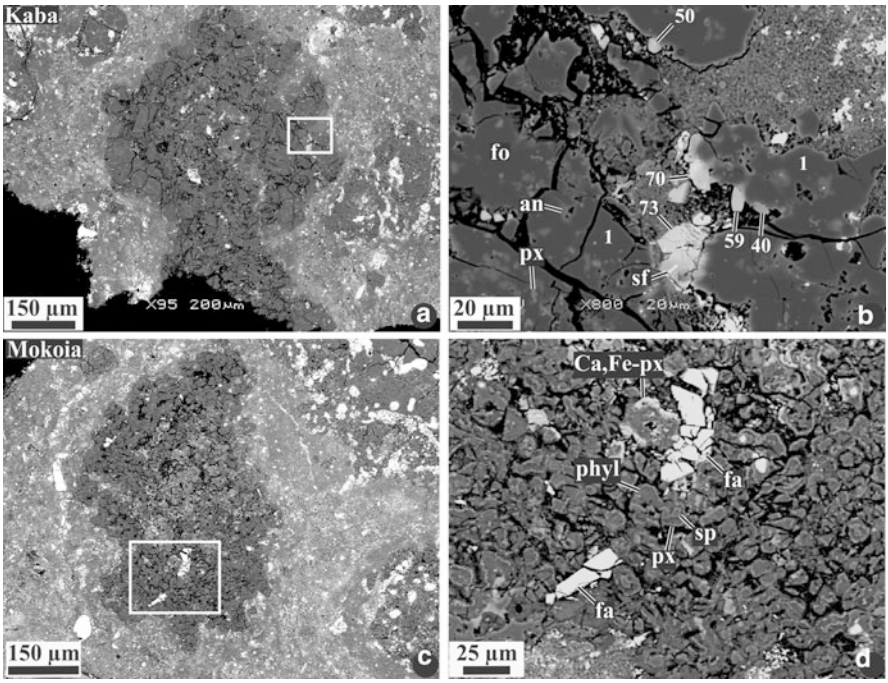

Fig. 15.6 BSE images of an aqueously altered AOA from Kaba (CV_{OxB}) (**a**, **b**) and a fine-grained spinel-rich CAI from Mokoia (CV_{OxB}) (**c**, **d**). Regions *outlined* in (**a**) and (**c**) are shown in detail in (**b**) and (**d**), respectively. The AOA consists of forsterite with tiny inclusions of Al-diopside (px) and anorthite (an). Forsterite grains (fo, $Fa_{<1}$) are overgrown by secondary ferroan olivines with different fayalite contents (40−73). Some of the ferroan olivines contain inclusions of Fe,Ni sulfides (sf). The CAI consists of numerous concentrically-zoned objects composed of spinel (sp) surrounded by phyllosilicates (phyl) and Al,Ti-diopside (px). The phyllosilicates probably replaced primary melilite and/or anorthite. Euhedral fayalite grains occur between these bodies. Ferroan diopside − hedenbergite pyroxenes (Ca,Fe-px) overgrow Al,Ti-diopside

Alteration of Refractory Inclusions in CV_{OxA} Chondrites

In contrast to the CV_{OxB} CAIs, and AOAs, refractory inclusions in the CV_{OxA} chondrites contain a large variety of secondary minerals, which are mostly anhydrous: grossular ($Ca_3Al_2Si_3O_{12}$), wollastonite ($CaSiO_3$), monticellite ($CaMgSiO_4$), anorthite, forsterite, corundum (Al_2O_3), Na-melilite ($(CaNa)_2(Al,Mg)(AlSi)_2O_7$), nepheline, sodalite, wadalite ($Ca_6Al_5Si_2O_{16}Cl_3$), Al-diopside ($Ca(Mg,Al)(Si,Al)_2O_6$), kushiroite ($CaAl_2SiO_6$), andradite, ferroan diopside − hedenbergite pyroxenes ($Fs_{10-45}Wo_{48-50}$), ilmenite ($FeTiO_3$), phosphates, magnetite, awaruite, tetrataenite, and Fe,Ni sulfides (e.g., Hutcheon and Newton 1981; Hashimoto and Grossman 1987; McGuire and Hashimoto 1989; Lin et al. 2005; Fagan et al. 2007; Ushikubo et al. 2007; Ford and Brearley 2008, 2010; Ishii et al. 2010; Krot et al. 2007, 2008, 2010). The hydrated minerals (vesuvianite $Ca_{10}(Mg,Fe)_2Al_4(SiO_4)_5(Si_2O_7)_2(OH,F)_4$), kaolinite $Al_2Si_2O_5(OH)_4$, and margarite

$CaAl_2(Al_2Si_2)O_{10}(OH)_2$) are minor. However, they provide clear evidence for the involvement of a fluid phase in the alteration (Ford and Brearley 2010).

Melilite and anorthite are the major primary CAI minerals susceptible to alteration; åkermanitic melilite is generally more altered than gehlenitic melilite. Both the degree of alteration and secondary mineralogies depend on the texture, primary mineralogy, and chemical composition of CAIs, all of which are highly variable[1] (e.g., MacPherson et al. 1988 and references therein). Type B CAIs containing åkermanite-rich melilite, porous fine-grained CAIs, and fluffy Type A CAIs and are typically more extensively altered than CTA CAIs (e.g., McGuire and Hashimoto 1989). Below we illustrate the major characteristics of secondary mineralization in several types of Allende CAIs.[2]

Grossular is one of the major secondary minerals replacing melilite and anorthite in Allende CAIs. There are two main occurrences and mineral assemblages of grossular: (1) coarse subhedral and anhedral grains associated with monticellite, wollastonite, forsterite, Na-melilite, and ± wadalite and replacing åkermanitic melilite and anorthite in the cores of Type B and C CAIs (Figs. 15.7–15.10), and (2) fine-grained grossular associated with secondary anorthite and Al-diopside that forms veins crosscutting gehlenitic melilite mantles in Type B1 CAIs (Figs. 15.11–15.14) and gehlenitic melilite in Type A CAIs (Fig. 15.15) (see also Fagan et al. 2007; Krot et al. 2007, 2010). The coarse-grained grossular-bearing assemblages are either crosscut by the grossular-bearing veins (Fig. 15.12) or there is a continuous transition between them (Krot et al. 2010).

The mineralogy of grossular-bearing veins that crosscut the melilite mantles of Allende Type B1 CAIs, depends on the chemical composition of the host melilite. The abundance of Mg-bearing minerals (Al-diopside and monticellite) in veins increase, whereas the abundance of secondary anorthite and margarite(?)[3] and the Mg content in grossular decrease with increasing åkermanite content of the melilite (Figs. 15.11–15.14).

In addition to these two main occurrences of grossular, primary anorthite, in the cores of Allende Type B CAIs, is crosscut by veins of grossular associated with secondary, Na-rich (up to 7 wt.% Na_2O), Mg-poor (<0.5 wt.% MgO) melilite, ±wadalite, and ± kushiroite (Fig. 15.16a–c). Occasionally, the secondary Na-melilite forms oriented inclusions inside anorthite (Fig. 15.16d) or coarse euhedral grains growing into an open space inside the anorthite crystals

[1] Based on the textures and mineralogy, six major types of CAIs are recognized in CV chondrites (e.g., MacPherson et al. 1988): fine-grained (1) spinel-rich (porous aggregates of concentrically-zoned objects having a spinel ($MgAl_2O_4$) ± hibonite ($CaAl_{12}O_{19}$) ± perovskite ($CaTiO_3$) core surrounded by layers of melilite/anorthite and Al,Ti-diopside), and coarse-grained: (2) fluffy Type A (FTA, irregularly-shaped, melilite-rich), (3) compact Type A (CTA, igneous, melilite-rich), (4) Type B1 (igneous, rich in pyroxene and anorthite, with a melilite mantle), (5) Type B2 (igneous, rich in Al,Ti-diopside and anorthite, unmantled), and (6) Type C (igneous, anorthite-rich).

[2] CAIs in other CV_{OxA} chondrites have not been systematically studied yet.

[3] Identified tentatively based on the textural similarity to margarite described by Ford and Brearley (2010).

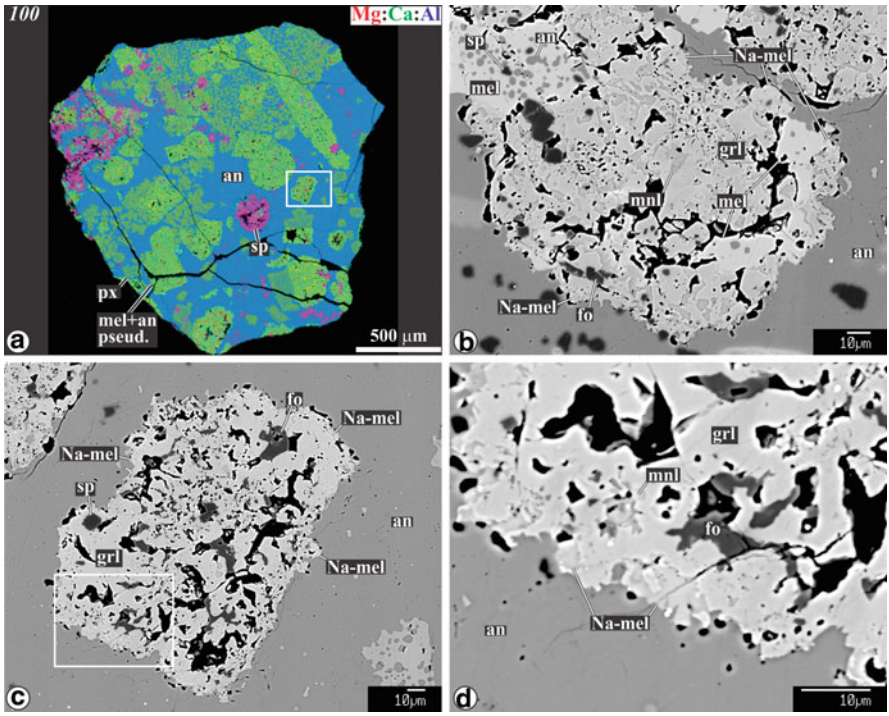

Fig. 15.7 Combined x-ray elemental maps in (**a**) Mg (*red*), Ca (*green*), and Al (*blue*) and (**b**–**d**) BSE images of a Type C CAI fragment *100* from Allende (CV_{OxA}). Regions *outlined* in (**a**) and (**c**) are shown in detail in (**b**) and (**d**), respectively. The CAI is composed of Al,Ti-diopside (px), åkermanitic ($Åk_{\sim 60}$) melilite (mel), and spinel (sp) embedded in anorthite (an) groundmass. Melilite grains, with abundant inclusions of anorthite (named "lacy melilite" by Wark 1987), are almost completely pseudomorphed by a porous aggregate of grossular (grl), monticellite (mnl), and forsterite (fo). Secondary Na-rich, Mg-poor melilite (Na-mel) occurs at the boundaries with anorthite (From Krot et al. 2007)

(Fig. 15.16e, f). The individual Na-melilite grains are compositionally zoned and show a range of Na_2O contents (1–7 wt.%). Since primary anorthite grains in Type B CAIs are Na- and Mg-free and lack any porosity, these observations indicate that the secondary minerals precipitated from a fluid phase into the opened spaces formed as a result of dissolution of primary anorthite.

There is a zoned distribution of secondary Na- and Cl-bearing minerals (nepheline, sodalite, wadalite, and Na-melilite) in Allende Type B1 CAIs, easily recognizable in the combined x-ray elemental maps showing Cl (red), Na (green), and Al Kα (blue) (Figs. 15.8, 15.11, 15.13). In these maps, nepheline, sodalite, and wadalite appear green, yellow, and red, respectively.[4] Nepheline and sodalite occur in the peripheral portions of CAIs where, together with ferroan olivine,

[4] Na-melilite usually contains ~1–3 wt.% Na_2O and can be recognized clearly only in BSE images.

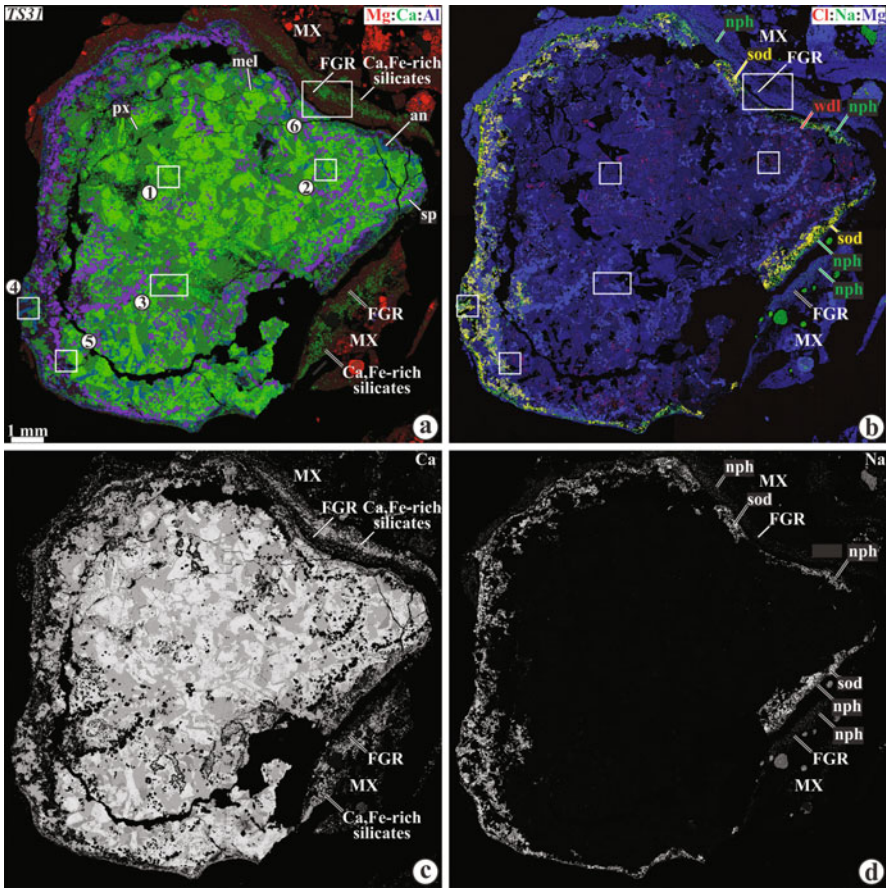

Fig. 15.8 Combined x-ray elemental maps in (**a**) Mg (*red*), Ca (*green*), and Al (*blue*), and (**b**) Cl (*red*), Na (*green*), and Mg (*blue*), and elemental maps in (**c**) Ca and (**d**) Na of a Type B2 CAI *TS31* from Allende. Regions *outlined* and numbered in (**a**) are shown in detail in Figs. 15.9, 15.10, and 15.17. The CAI shows a zoned distribution of secondary Na- and Cl-bearing minerals. Nepheline and sodalite occur in its outer portion, whereas wadalite occurs exclusively in the CAI core. The CAI is surrounded by a fine-grained rim containing abundant inclusions of nepheline and Ca,Fe-silicates (mainly ferroan diopside – hedenbergite pyroxenes) and a massive layer of Ca,Fe-silicates (ferroan diopside – hedenbergite pyroxenes, andradite, wollastonite; see Fig. 15.17). *an* anorthite, *FGR* fine-grained rim, *mel* melilite, *MX* matrix, *nph* nepheline, *px* Al,Ti-diopside; *sod* sodalite, *sp* spinel, *wdl* wadalite

hedenbergite, andradite, secondary anorthite, grossular, margarite, kaolinite, and vesuvianite, they replace gehlenitic melilite and primary anorthite. Wadalite and Na-melilite occur almost exclusively in CAI cores where they replace åkermanitic melilite and anorthite. Co-existing sodalite and wadalite or Na-melilite are exceptionally rare (Figs. 15.9c–e, 15.16); no evidence for corrosion relationships between these minerals has been observed.

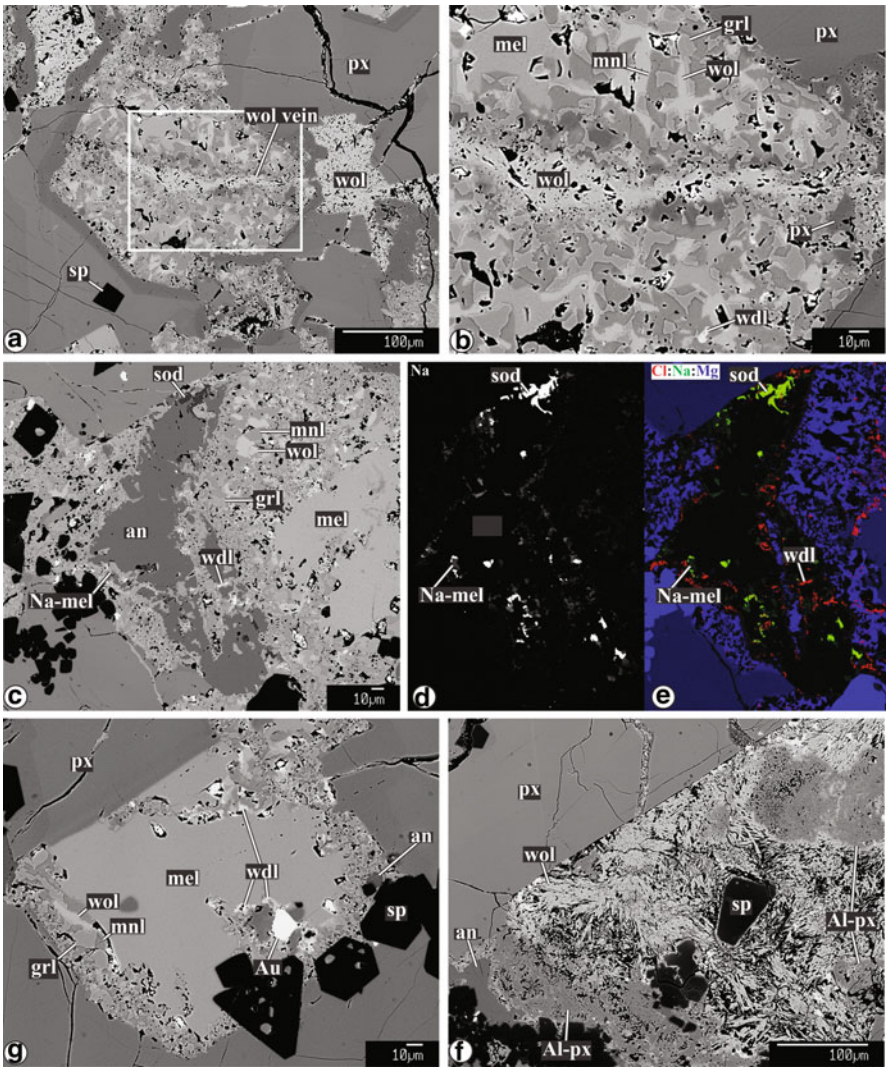

Fig. 15.9 BSE images (**a**, **b**, **c**, **f**), elemental map of Na (**d**), and combined elemental map of Cl (*red*), Na (*green*), and Mg (*blue*) (**e**) of a central portion of a Type B2 CAI *TS31*. (**a**–**b**, **c**–**e**), and (**f**–**g**) correspond to regions 1, 2, and 3, in Fig. 15.8, respectively. Melilite is replaced to various degrees by grossular, monticellite, wollastonite, and wadalite. The replaced melilite shown in (**a**) is crosscut by a wollastonite vein. Some regions consist entirely of needle-shaped wollastonite and Al- and Fe-bearing high-Ca pyroxenes (see (**a**) and (**g**)). Occasionally, anorthite is crosscut by veins of grossular, monticellite, Na-rich, Mg-poor melilite, wadalite, and sodalite (see (**c**–**e**)). *an* anorthite, *Al-px* Al- and Fe-bearing high-Ca pyroxene, *grl* grossular, *mel* melilite, *mnl* monticellite, *Na-mel* Na-rich, Mg-poor melilite; *px* Al,Ti-diopside; *sod* sodalite, *sp* spinel, *wdl* wadalite, *wol* wollastonite

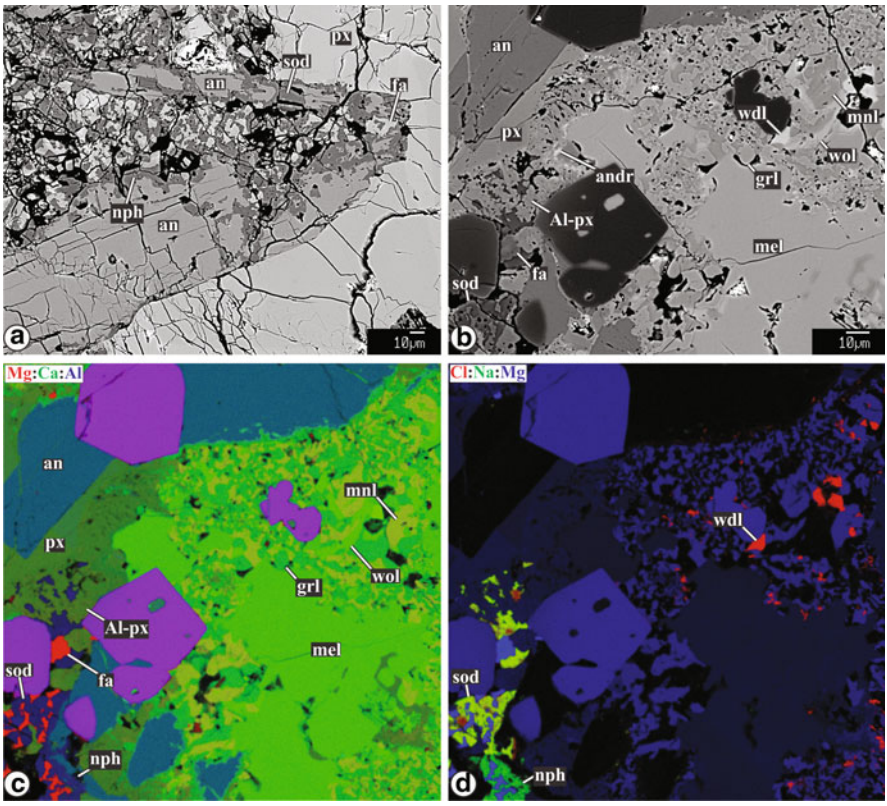

Fig. 15.10 BSE images (**a**, **b**) and combined x-ray elemental maps in Mg (*red*), Ca (*green*), and Al (*blue*) (**c**), and Cl (*red*), Na (*green*), and Mg (*blue*) (**d**) of a peripheral portion of a Type B2 CAI *TS31*. (**a**) and (**b**–**d**) correspond to regions 4 and 5 in Fig. 15.8, respectively. Anorthite and melilite in the outermost portion of the CAI are replaced by nepheline, sodalite, Al- and Fe-bearing high-Ca pyroxene, ferroan olivine, and andradite. Towards the CAI core, melilite and, to a smaller degree, anorthite are replaced by grossular, monticellite, wollastonite, and wadalite. *Al-px* Al- and Fe-bearing high-Ca pyroxene, *an* anorthite, *andr* andradite, *fa* ferroan olivine, *grl* grossular *mel* melilite; *mnl* monticellite, *nph* nepheline *px* Al,Ti-diopside; *sod* sodalite, *sp* spinel, *wdl* wadalite, *wol* wollastonite

A zoned distribution of secondary minerals has also been described in Allende fine-grained CAIs (McGuire and Hashimoto 1989). The center zones of these inclusions contain mostly of secondary nepheline, needle-shaped crystals of anorthite (could also be margarite(?), Ford and Brearley 2010), and ferroan diopside – hedenbergite pyroxenes (~$Fs_{10-40}Wo_{50}$); sodalite, grossular, ferroan olivine, and ilmenite are minor. In addition to the secondary minerals which occur in the central zone, the intermediate zone is characterized by the presence of secondary hedenbergite ($Fs_{45-50}Wo_{50}$) and andradite partially filling voids. The outermost zone consists mostly of intergrown ferroan olivine and nepheline with small ilmenite grains enclosed; nepheline and sodalite are minor. The observed zoning

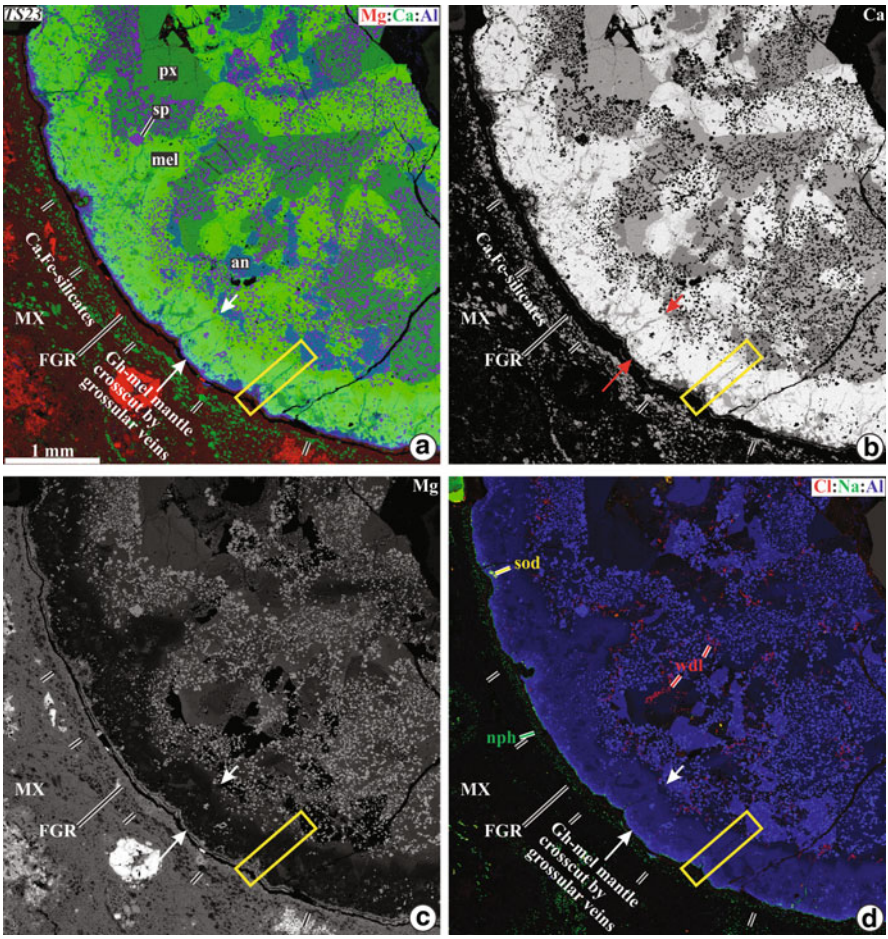

Fig. 15.11 Combined x-ray elemental maps in Mg (*red*), Ca (*green*), and Al (*blue*) (**a**), and Cl (*red*), Na (*green*), and Al (*blue*) (**d**), and elemental maps in Ca (**b**) and Mg (**c**) of a Type B1 CAI *TS23* from Allende. Region *outlined* in yellow is shown in detail in Fig. 15.12. The CAI has a zoned distribution of secondary Na- and Cl-bearing minerals: nepheline and sodalite occur in its outermost portion; wadalite occurs exclusively in the CAI core. The mantle is crosscut by grossular veins showing depletion in Ca (see (**b**)). The CAI is surrounded by a fine-grained rim containing abundant inclusions of nepheline and a massive layer of Ca,Fe-silicates (ferroan diopside – hedenbergite pyroxenes, andradite, and wollastonite; see Fig. 15.17). *an* anorthite, *FGR* fine-grained rim, *mel* melilite, *MX* matrix, *nph* nepheline, *px* Al,Ti-diopside; *sod* sodalite, *sp* spinel, *wdl* wadalite

in the distribution of secondary minerals in Allende fine-grained CAIs is partly due to the primary mineralogical zoning observed in many fine-grained CAIs from the CV_R chondrites Efremovka and Leoville (Krot et al. 2004a). The CAI cores are enriched in anorthite, whereas the CAI mantles contain a high abundance of melilite. The primary mineralogical zoning of the fine-grained CAIs is attributed

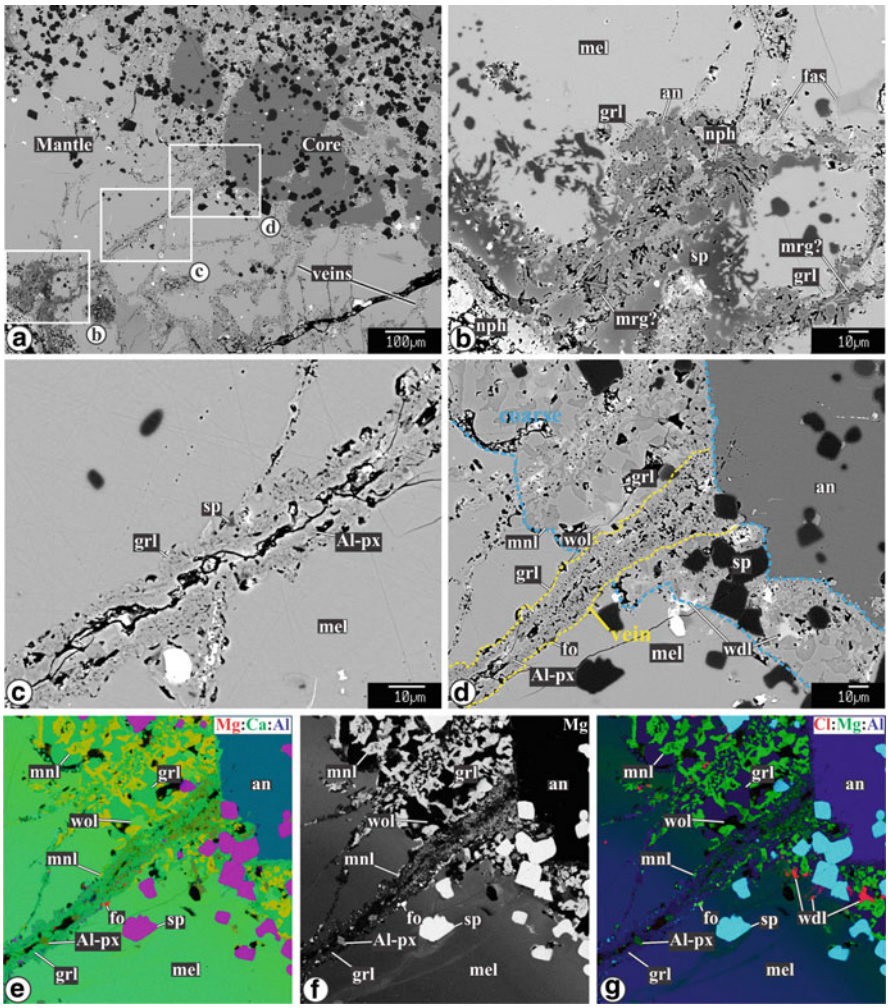

Fig. 15.12 BSE images (**a**–**d**), elemental map in Mg (**d**), and combined x-ray elemental maps in Mg (*red*), Ca (*green*) and Al (*blue*) (**c**), and Cl (*red*), Mg (*green*), and Al (*blue*) (**e**) of a grossular vein crosscutting the melilite mantle of a Type B1 CAI *TS23* (see Fig. 15.11). Åkermanite content in melilite increases towards the CAI core. The vein shows mineralogical zoning that correlates with the chemical composition of the host melilite and its position from the CAI edge. Near the CAI edge, it consists mainly of anorthite, elongated crystals of possibly margarite (tentatively identified), and grossular. Closer to the CAI core, the vein is composed largely of grossular, Al-diopside, and minor forsterite. The abundance of Al-diopside increases, whereas the Mg content in grossular from the vein decreases towards the CAI core. At the inner part of the mantle, composed of åkermanitic melilite, the vein crosscuts a coarse-grained assemblage of grossular, monticellite, wollastonite, and wadalite. The coarse-grained grossular is Mg-poor. *Al-px* Al-diopside, *an* anorthite, *fo* forsterite, *grl* grossular, *mel* melilite, *mnl* monticellite, *mrg?* margarite (tentatively identified), *nph* nepheline, *px* Al,Ti-pyroxene; *sp* spinel, *wdl* wadalite

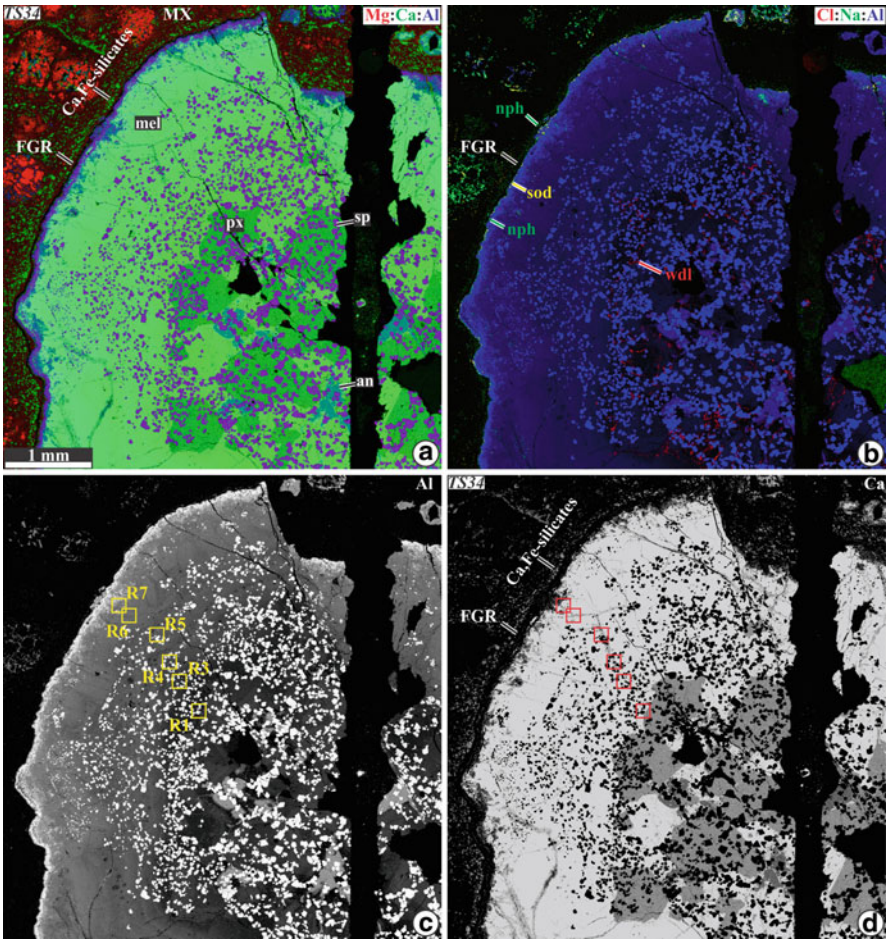

Fig. 15.13 Combined x-ray elemental maps in Mg (*red*), Ca (*green*), and Al (*blue*) (**a**), and Cl (*red*), Na (*green*), and Mg (*blue*) (**b**), and elemental maps in Al (**c**) and Ca (**d**) of a Type B1 CAI *TS34* from Allende. Regions *outlined* and numbered in (**c**) are shown in detail in Fig. 15.14. The CAI shows a zoned distribution of secondary Na- and Cl-bearing minerals. Nepheline and sodalite occur in its outermost portion. Wadalite occurs exclusively in the CAI core. The mantle is crosscut by numerous grossular veins showing depletion in Ca (see (**d**)). The CAI is surrounded by a fine-grained rim containing abundant inclusions of nepheline and a layer of Ca,Fe-silicates (ferroan diopside – hedenbergite pyroxenes, andradite, and wollastonite). *an* anorthite, *FGR* fine-grained rim, *mel* melilite, *MX* matrix, *nph* nepheline, *px* Al,Ti-diopside; *sod* sodalite, *sp* spinel, *wdl* wadalite

to their multistage thermal processing in the solar nebula prior to alteration (Krot et al. 2004a).

Coarse-grained and fine-grained CAIs in the CV_{OxA} chondrites are typically surrounded by fine-grained, matrix-like rims containing nodules of ferroan diopside – hedenbergite pyroxenes ($Fs_{10-50}Wo_{45-50}$) ± andradite and nepheline

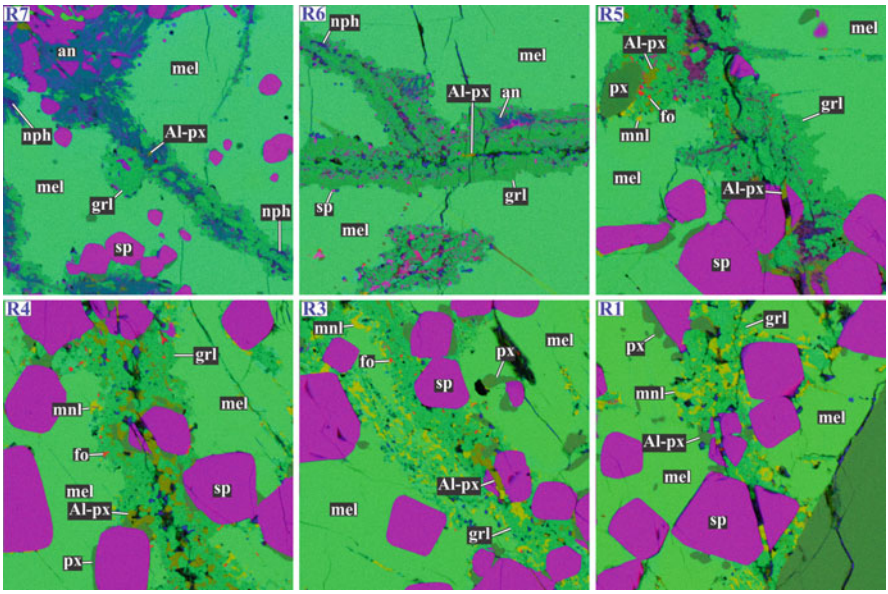

Fig. 15.14 Combined x-ray elemental maps in Mg (*red*), Ca (*green*), and Al (*blue*) of a vein crosscutting the melilite mantle of a Type B1 CAI *TS34* (see Fig. 15.13). Åkermanite content in melilite increases towards the CAI core (from R7 to R1). The mineralogy of the vein correlates with composition of the host melilite. The abundance of Mg–bearing minerals (Al-diopside and monticellite) increases, whereas Mg content in grossular decreases towards the CAI core. *Al-px* Al-diopside, *an* anorthite, *fo* forsterite *grl* grossular, *mel* melilite, *mnl* monticellite, *nph* nepheline, *px* Al,Ti-pyroxene; *sp* spinel

with needle-shaped inclusions of ferroan olivine (Figs. 15.8, 15.11, 15.13, 15.15). A discontinuous layer of Ca,Fe-silicates (ferroan diopside – hedenbergite pyroxenes, wollastonite and andradite are minor) occurs between the fine-grained rims and the neighboring Allende matrix (Fig. 15.17).

Based on the bulk chemical compositions and primary and secondary mineralogies of the CV_{OxA} CAIs, it is inferred that they experienced open-system metasomatic alteration: Si, Na, Fe, and Mg were introduced, whereas Ca and Al were lost from or redistributed within the CAIs (Hashimoto and Grossman 1987; McGuire and Hashimoto 1989; Ford and Brearley 2008; Krot et al. 2010). Hashimoto and Grossman (1987) and McGuire and Hashimoto (1989) suggested that open-system alteration of the Allende CAIs occurred in the protoplanetary disk at temperatures less than 1,000°K and higher than solar H_2O/H ratio ($\sim 5 \times 10^{-4}$). Under these conditions, Ca is more volatile than Si due to the formation of gaseous Ca-hydroxides (Hashimoto and Wood 1986). This interpretation, however, is inconsistent with mass-balance calculations (Ford and Brearley 2008) indicating that Ca lost from CAIs was used to form a layer of secondary Ca,Fe silicates between the fine-grained rims and the neighboring Allende matrix. The presence

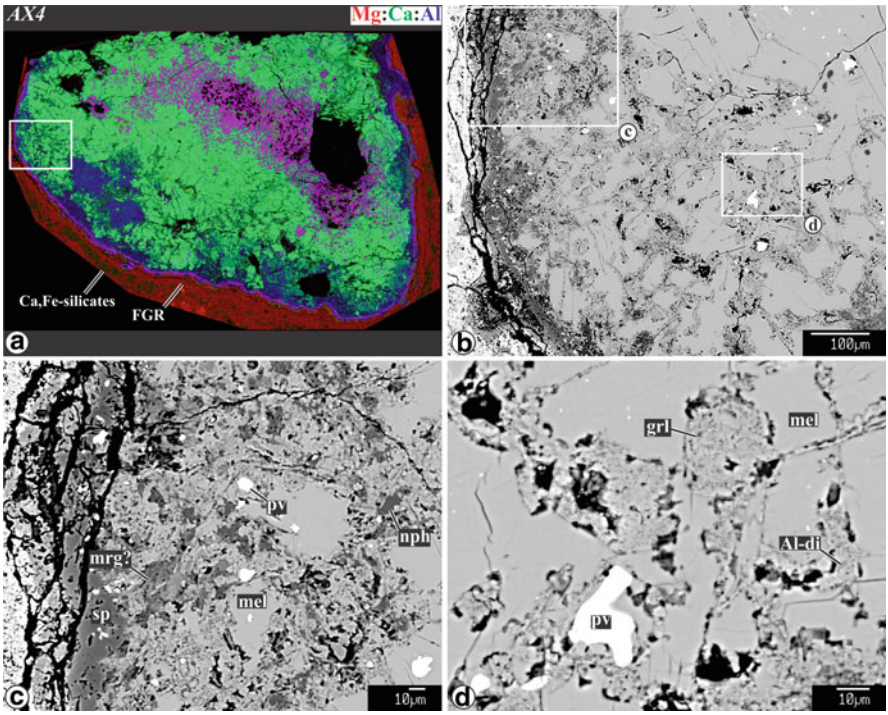

Fig. 15.15 Combined x-ray elemental maps in Mg (*red*), Ca (*green*), and Al (*blue*) (**a**) and BSE images (**b**–**d**) of a compact Type A CAI *AX4* from Axtell (CV_{OxA}). Regions *outlined* in (**a**–**b**) are shown in detail in (**b**–**d**). The CAI consists mainly of melilite (mel), spinel (sp), and minor perovskite (pv). The outer portion of *AX4* is crosscut by a network of veins composed of fine-grained grossular (grl), Al-diopside (Al-px), nepheline (nph), and elongated crystals of possibly margarite (mrg?, tentatively identified). The CAI is surrounded by a fine-grained rim containing abundant inclusions of nepheline and a layer of Ca,Fe-silicates (ferroan diopside – hedenbergite pyroxenes, andradite, and wollastonite)

of abundant nepheline grains in the fine-grained rims around CAIs also suggests that the host CAIs may have experienced partial loss of Al.

The replacement of melilite and anorthite by grossular, monticellite, and wollastonite in Allende CAIs during open-system alteration can be described by the following reactions:

$$(Ca_2MgSi_2O_7 + Ca_2Al_2SiO_7)_{ss} + SiO_{2(aq)} = Ca_3Al_2Si_3O_{12(s)} + CaMgSiO_{4(s)} \quad (15.3)$$

$$(2\,Ca_2MgSi_2O_7 + Ca_2Al_2SiO_7)_{ss} + SiO_{2(aq)} + 4\,H_{2(g)} = Ca_3Al_2Si_3O_{12(s)} + 2\,CaMgSiO_{4(s)} + CaSiO_{3(s)} + 4\,H_2O_{(g)} \quad (15.4)$$

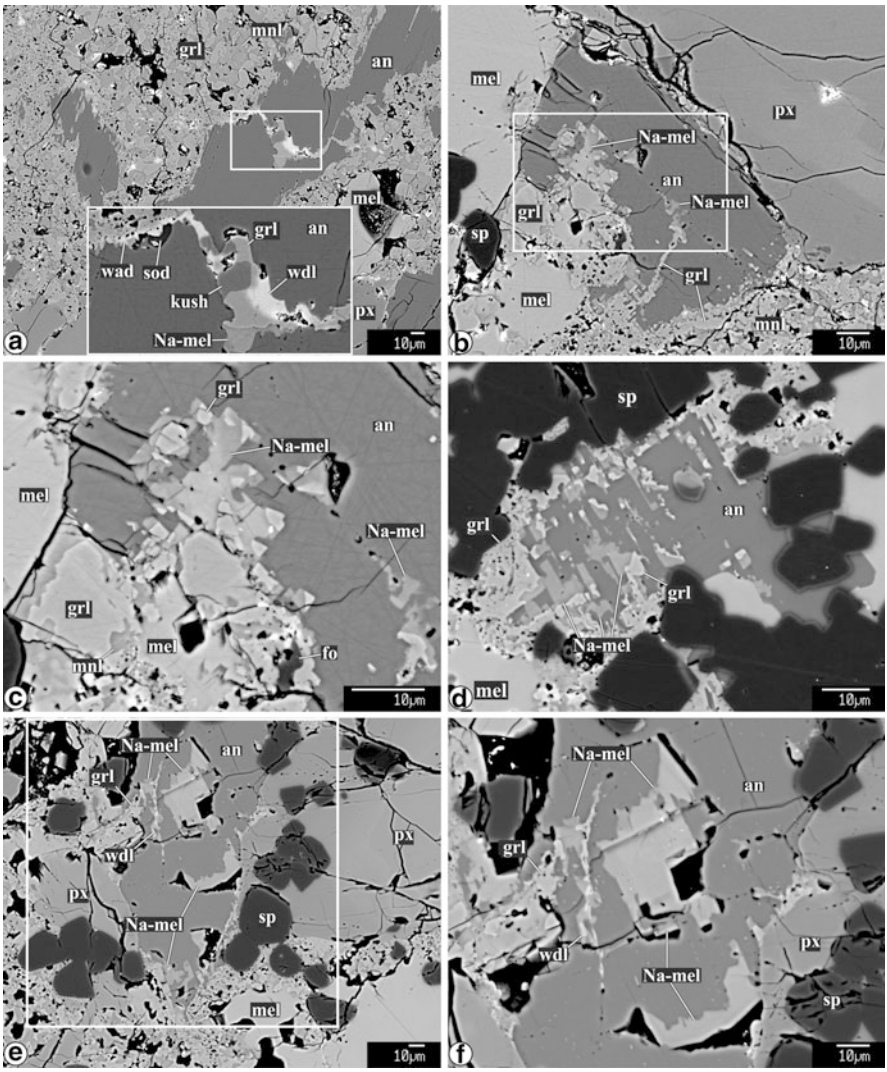

Fig. 15.16 BSE images of altered regions in central portions of the Allende Type B1 CAIs *TS23* (**a**–**c**), *3529Z* (**d**), and *Big-Al* (**e**, **f**). Regions *outlined* in (**a**) and (**e**) are shown in detail in (**b**) and (**f**), respectively. Melilite is replaced mainly by grossular, monticellite, and wadalite. Secondary Al-diopside and wollastonite are less abundant. Secondary forsterite and corundum are minor. Anorthite is crosscut by veins of Na-melilite, grossular, ± kushiroite, and ± wadalite. All minerals in veins are typically Mg-poor. Na-melilite ± grossular also form oriented inclusions in anorthite (see (**d**)) and coarse subhedral crystals (see (**f**)). Na-melilite grains are typically chemically-zoned, which is observed as variations in brightness of Na-melilite in BSE images. *an* anorthite, *grl* grossular, *kush* kushiroite, *mel* melilite, *mnl* monticellite, *Na-mel* Na-melilite, *nph* nepheline, *px* Al,Ti-diopside; *sod* sodalite, *sp* spinel, *wdl* wadalite

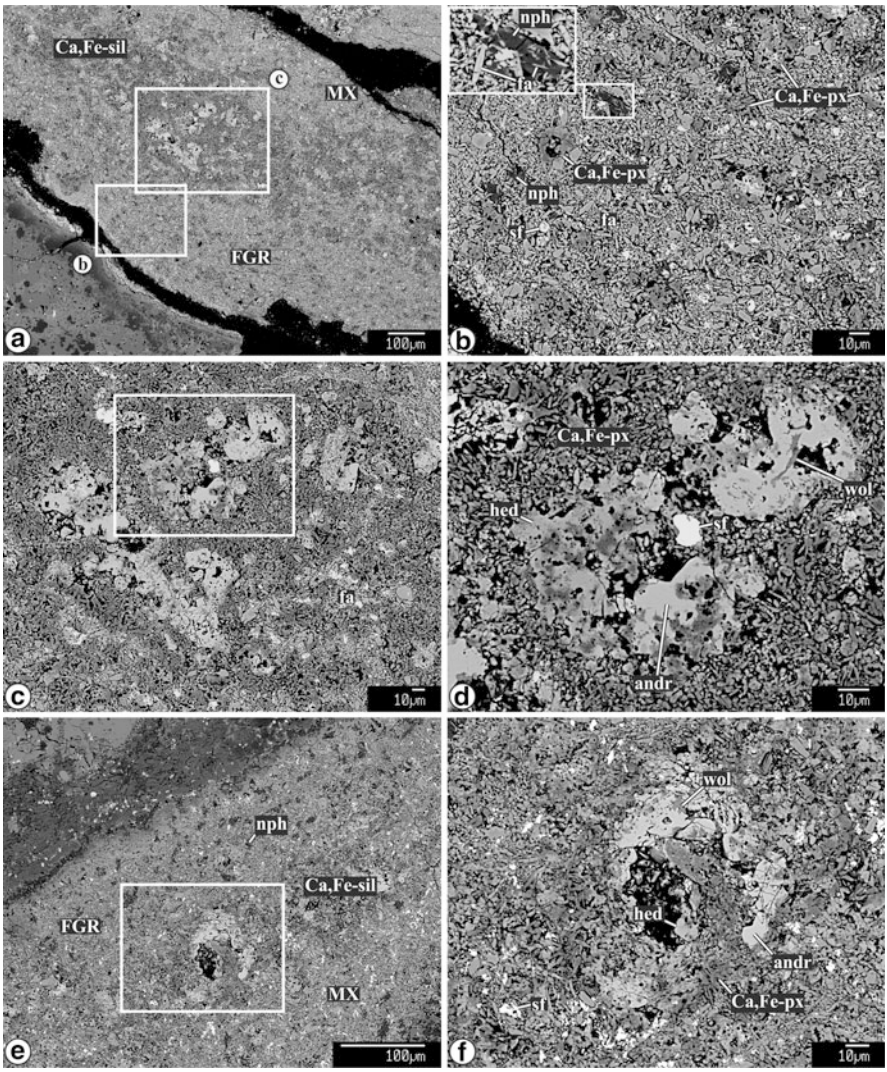

Fig. 15.17 BSE images of the peripheral portions of a Type B2 CAI *TS31* (**a**–**d**), region 6 (see Fig. 15.8) and of a Type B1 CAI *TS23* (**e**, **f**). Regions *outlined* in (**a**) are shown in detail in (**b**) and (**c**); regions *outlined* in (**c**) and (**e**) are shown in detail in (**d**) and (**f**), respectively. The peripheral portions of *TS31* and *TS23* are surrounded by a fine-grained rim (FGR), a layer of Ca,Fe-rich silicates (ferroan diopside – hedenbergite pyroxenes (Ca,Fe-px), andradite (andr) and wollastonite (wol)), and matrix (MX). The fine-grained rims consists of ferroan olivine (fa), nepheline (nph) with needle-shaped inclusions of ferroan olivine (see inset in (**b**)), nodules of ferroan diopside – hedenbergite pyroxenes, and Fe,Ni sulfides (sf)

where ss = solid solution. In contrast, the pseudomorphic replacement of melilite, by abundant inclusions of anorthite in Type C CAIs by grossular, monticellite, and ± forsterite (Fig. 15.7), may be due to closed-system metamorphic reactions (Krot et al. 2007), e.g.,

$$(3\ Ca_2MgSi_2O_7 + Ca_2Al_2SiO_7)_{ss} + CaAl_2Si_2O_{8(s)} = 2\ Ca_3Al_2Si_3O_{12(s)} + 3\ CaMgSiO_{4(s)} \quad (15.5)$$

$$(3\ Ca_2MgSi_2O_7 + Ca_2Al_2SiO_7)_{ss} + 2\ CaAl_2Si_2O_{8(s)} = 3\ Ca_3Al_2Si_3O_{12(s)} + CaMgSiO_{4(s)} + Mg_2SiO_{4(s)} \quad (15.6)$$

$$(2\ MgSi_2O_7 + Ca_2Al_2SiO_7)_{ss} + CaAl_2Si_2O_{8(s)} = 2\ Ca_3Al_2Si_3O_{12(s)} + 4\ CaMgSiO_{4(s)} + CaSiO_{3(s)} \quad (15.7)$$

Åkermanitic melilite in Type B and Type C CAIs in Allende usually contains up to 0.3 wt.% Na_2O, suggesting crystallization from a Na-bearing melt (Beckett and Stolper 2000; Beckett et al. 2000). Sodium released from alteration of this melilite could have been used to form secondary, Na-rich melilite around altered melilite-anorthite regions (Fig. 15.7). An external source of Na for Na-melilite in Type B CAIs (Fig. 15.16), which experienced open-system alteration, cannot be excluded.

15.2.3 Alteration of Chondrules and Matrices

Chondrules and matrices are believed to be genetically related chondritic components, which experienced brief heating events, possibly by shock waves, in the protoplanetary disk ~1–3 Ma after the formation of refractory inclusions (e.g., Desch et al. 2005; Scott and Krot 2005a and references therein). Most chondrules were incompletely melted during these heating events, whereas a significant fraction of fine-grained matrix materials was probably vaporized and recondensed (Brearley 1993; Abreu and Brearley 2010). Because chondrules and matrices in CV chondrites appear to have been affected by the same alteration processes,[5] they are discussed together.

[5] We note, however, that there are significant differences in both the style and the degree of alteration processes, which affected chondrules and matrices in the CV_{OxA}, CV_{OxB} and CV_R chondrites (e.g., Housley and Cirlin 1983; Ikeda and Kimura 1995; Keller and Buseck 1990a; Keller and McKay 1993; Keller et al. 1994; Kimura and Ikeda 1995, 1998; Brearley 1997b; Krot et al. 1997a, 1998a, b, 2004b; Choi et al. 2000).

15.2.3.1 Alteration of Chondrules and Matrices in Cb_{oxb} Chondrites

Chondrules in Kaba (CV_{OxB}) and Mokoia (a breccia containing clasts of the CV_{OxB} and CV_{OxA} lithologies) experienced aqueous alteration to various degrees. The anorthite-normative glassy mesostasis, high-Ca pyroxenes and low-Ca pyroxenes in magnesian porphyritic (type I) chondrules are extensively replaced by Ca-poor phyllosilicates, Na-phlogopite ($Na(Mg,Fe,Mn)_3Si_3AlO_{10}(F,OH)_2$) and saponite ($(½Ca,Na)_{0.33}(Mg,Fe)_3(Si,Al)_4O_{10}(OH)_2{\cdot}4H_2O$) (Fig. 15.18a; Keller and Buseck 1990a; Kimura and Ikeda 1998). A thin layer of diopside ($Fs_{9-35}Wo_{\leq 1}$) often separates altered portions of low-Ca pyroxene grains from saponite (Fig. 15.18a). On the basis of the compositional differences between the primary chondrule minerals and the secondary phyllosilicates, it is inferred that Si, Al, Mg, Fe, Na, and Ca were mobile during the alteration with most of the Ca was removed from the chondrules (Krot et al. 1998a, b).

Fe,Ni metal nodules in type I chondrules are pseudomorphically replaced by Cr-bearing magnetite and Fe,Ni sulfides with or without significant volume change (Fig. 15.18a, b); the latter reaction may require removal of a fraction of Fe by an aqueous solution, e.g.,

$$3\ Fe_{(s)} + 4\ H_2O_{(l,g)} = Fe_3O_{4(s)} + 4\ H_{2(g)} \tag{15.8}$$

$$4\ Fe_{(s)} + 4\ H_2O_{(l,g)} = Fe_3O_{4(s)} + Fe^{2+}{}_{(aq)} + 4\ H_{2(g)} \tag{15.9}$$

Some of the magnetite-sulfide nodules are overgrown by compositionally pure magnetite, suggesting precipitation from an aqueous solution (Fig. 15.18c, d):

$$3\ Fe^{2+}{}_{(aq)} + 4\ H_2O_{(l,g)} = Fe_3O_{4(s)} + 4\ H_{2(g)} \tag{15.10}$$

Rare, relict Fe,Ni metal grains found inside forsteritic olivine phenocrysts are surrounded by ferroan olivine (Fa_{21-54}) halos (Fig. 15.18b), suggesting introduction of Fe and loss of Mg from forsterite.

Chromium-poor magnetite is often replaced by coarse fayalite grains (Fa_{95-100}) and fine-grained Al-poor ferroan diopside – hedenbergite pyroxenes ($Fs_{10-50}Wo_{50}$), suggesting addition of Si and Ca (Fig. 15.18b–d). The fayalite grains are poor in Cr_2O_3 (<0.04 wt.%) and rich in MnO (up to 1.5 wt.%). Although the Ca could have been transported as a volatile hydroxide (e.g. Hashimoto and Wood 1986; Hashimoto and Grossman 1987), the volatility of Si is not known to be enhanced in similar fashion, because it has no known thermodynamically stable hydroxides (Hashimoto and Wood 1986). Therefore, since both elements are absent in magnetite, the most likely mechanism of mass transport for these elements to form the new Fe- and Ca-Fe silicates appears to be transport via an aqueous solution, e.g.,

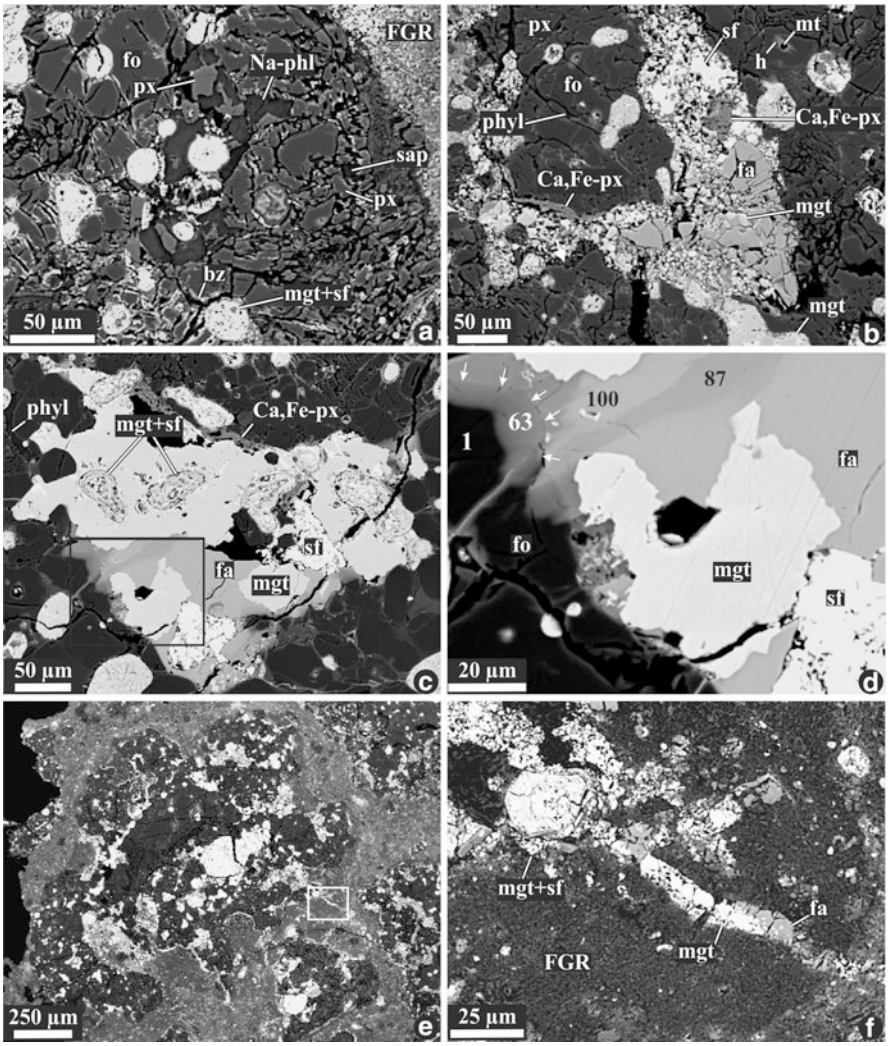

Fig. 15.18 BSE images of type I chondrules in the CV_{OxB} chondrites Kaba (**a**) and Mokoia (**b**−**f**). Regions *outlined* in (**c**) and (**e**) are shown in detail in (**d**) and (**f**), respectively. (**a**) Chondrule mesostasis and high-Ca pyroxenes (cpx) are replaced by Na-phlogopite (Na-phl). Low-Ca pyroxene (px) near the chondrule edge is replaced by bronzitic pyroxene (bz) and saponite (sap). Fe,Ni metal nodules are replaced by magnetite (mgt) and Fe,Ni sulfides (sf). Tiny relict Fe,Ni metal grains (mt) in forsteritic olivine (fo) phenocrysts are surrounded by halos of ferroan olivine (**h**). (**b**) Fe,Ni metal nodules inside the chondrule are replaced by magnetite and Fe,Ni sulfides. Magnetite is replaced by fayalite (fa), and ferroan diopside − hedenbergite pyroxenes (Ca,Fe-px). Chondrule mesostasis is replaced by phyllosilicates (phyl). (**c**, **d**) Fe,Ni metal nodules are pseudomorphed by Cr-bearing magnetite and Fe,Ni sulfides and overgrown by Cr-free magnetite, which is replaced by pure fayalite (Fa_{100}). Forsterite phenocrysts (Fa_1) are partly pseudomorphed by ferroan olivine (Fa_{63}). An outline of one of the replaced phenocrysts is indicated by *arrows*. Fayalite is crosscut by a vein of ferroan olivine (Fa_{87}) suggesting forsterite is the source of Mg. (**e**, **f**) Fine-grained rim (FGR) around the chondrule is crosscut by fayalite-magnetite veins, which start at the Fe,Ni sulfide + magnetite nodules in the peripheral part of the chondrule, suggesting in situ alteration (From Krot et al. 1998a, 2006). Figures b, d, e and f from Meteorites and the Early Solar System II edited by Dante s. Lauretta and Haryy Y. McSween Jr.© The Arizona Board of Regents. Reprinted by permission of the University of Arizona Press.

$$2\ Fe_3O_{4(s)} + 3\ SiO_{2(aq)} + 2\ H_{2(g)} = 3\ Fe_2SiO_{4(s)} + 2\ H_2O_{(g)} \quad (15.11)$$

$$2\ Fe_3O_{4(s)} + 6\ SiO_{2(aq)} + 3\ Ca^{2+}{}_{(aq)} + 2\ H_{2(g)} = 3\ CaFeSi_2O_{6(s)} + 3\ Fe^{2+}{}_{(aq)} + 2\ H_2O_{(g)} \quad (15.12)$$

$$5\ Fe_3O_{4(s)} + 9\ SiO_{2(aq)} + 9\ Ca^{2+}{}_{(aq)} + 2\ H_2(g) = 3\ Ca_3Fe_2Si_3O_{12(s)} + 9\ Fe^{2+}{}_{(aq)} + 2\ H_2O_{(g)} \quad (15.13)$$

The proposed mechanism of alteration is consistent with the petrographic and mineralogical observations: fayalite, ferroan diopside – hedenbergite pyroxenes, and andradite coexist with phyllosilicates and show no evidence for corrosion or replacement by phyllosilicates. This mechanism can also explain the observed fractionation of the refractory elements Ca and Al in ferroan diopside – hedenbergite pyroxenes and andradite and the moderately volatile Mn and Cr in fayalite. These fractionations may have resulted from differences in the solubility of these elements in aqueous solutions.

Some of the fayalite grains appear to be corroded by ferroan diopside – hedenbergite pyroxenes (Fig. 15.18c; see also Fig. 4 in Krot et al. 1998b):

$$Fe_2SiO_{4(s)} + Ca^{2+}{}_{(aq)} + SiO_{2(aq)} = CaFeSi_2O_{6(s)} + Fe^{2+}{}_{(aq)} \quad (15.14)$$

Occasionally, ferroan olivines pseudomorphically replace forsteritic olivine phenocrysts. There is a sharp compositional boundary between the ferroan olivine (Fa_{63}) and the replaced forsterite (Fa_1), as shown in Fig. 15.18c, d. The neighboring fayalite (Fa_{100}), replacing magnetite-sulfide grains, shows enrichment in a forsterite component (up to Fa_{87}) along the boundary and along the crosscutting veins. This suggests that Mg, released during replacement of forsterite, diffused into the fayalite. The Fe-Mg interdiffusion in forsterite and fayalite most likely took place in the presence of aqueous solutions, e.g.,

$$Fe^{2+}{}_{(aq)} + Mg_2SiO_{4(s)} + H_2O_{(l,g)} = (Fe,Mg)_2SiO_{4(s)} + Mg^{2+}{}_{(aq)} + H_{2(g)} \quad (15.15)$$

$$Mg^{2+}{}_{(aq)} + Fe_2SiO_{4(s)} + H_2O_{(l,g)} = (Fe,Mg)_2SiO_{4(s)} + Fe^{2+}{}_{(aq)} + H_{2(g)} \quad (15.16)$$

A similar formation mechanism may explain the origin of ferroan olivine halos around relict metal inclusions inside forsteritic olivine phenocrysts (Fig. 15.18b), and the inversely-zoned ferroan olivine grains in chondrules and matrices in some of the CV_{OxB} chondrites (Figs. 15.5b, 15.19a, b; see also Fig. 8 in Krot et al. 2004b). The supporting argument in favor of this mechanism comes from aqueously-altered dark inclusions in the reduced CV chondrite Efremovka, where ferroan olivine ($Fa_{\sim 50}$) and phyllosilicates replace chondrule forsteritic phenocrysts, resulting in

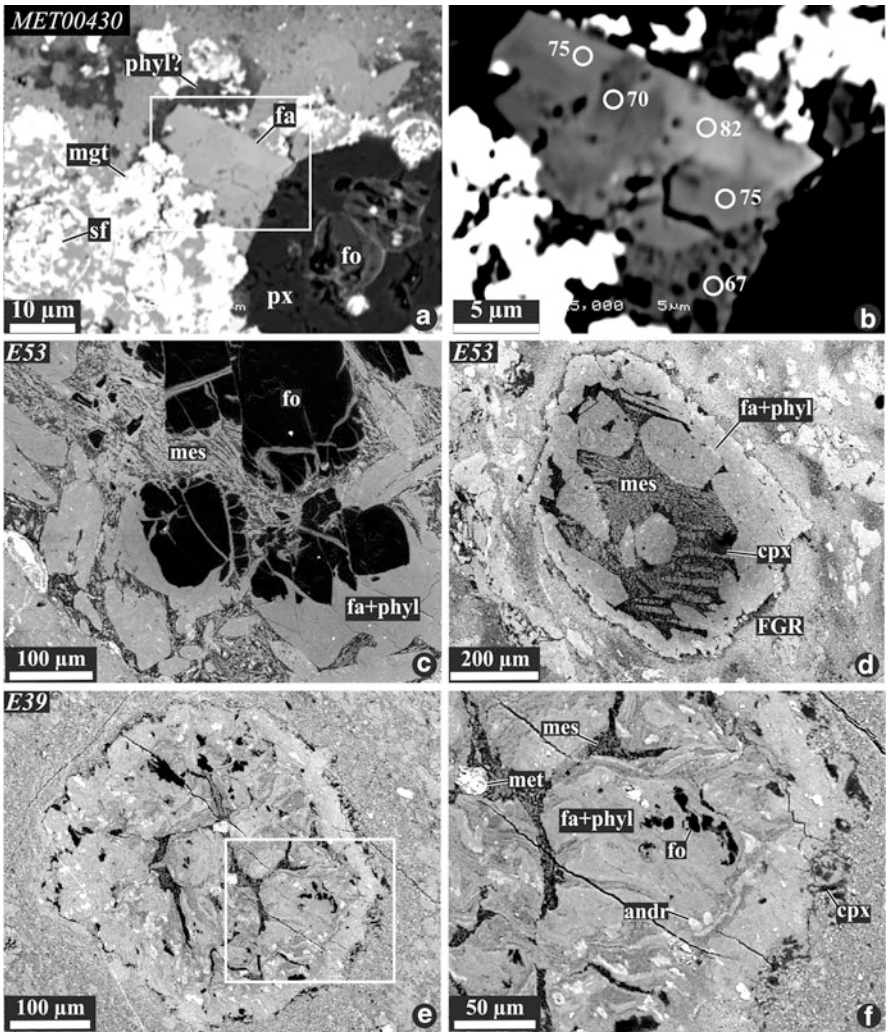

Fig. 15.19 BSE images of type I chondrules in MET 00430 ($CV_{OxA/OxB}$) (**a**, **b**) and dark inclusions *E53* (**c**, **d**) and E39 (**e**, **f**) in Efremovka (CV_R). Regions *outlined* in (**a**) and (**e**) are shown in detail in (**b**) and (**f**), respectively. (**a**, **b**) Ferroan olivine (fa) replaces magnetite (mgt) – sulfide (sf) nodules in the peripheral part of the chondrule. Low-Ca pyroxene (px) is overgrown by a euhedral grain of ferroan olivine, which shows complex chemical zoning (numbers in (**b**) correspond to fayalite contents in olivine), suggesting dissolution of ferrous olivine and precipitation of more forsteritic olivine from a fluid phase. (**c**, **d**) Chondrule phenocrysts and fine-grained mesostasis are pseudomorphed to a various degree by a mixture of ferroan olivine and phyllosilicates (phyl). High-Ca pyroxenes (cpx) are relict. (**e**, **f**) Chondrule phenocrysts and mesostasis are nearly completely replaced by a fine-grained mixture of ferroan olivine, phyllosilicates, and andradite (andr). Forsteritic olivine and high-Ca pyroxenes are relict (From Krot et al. 1999, 2004b)

a sharp compositional boundary between the primary forsterite and secondary ferroan olivine + phyllosilicates (Fig. 15.19c–f; Krot et al. 1999)

The CV_{OxB} chondrules are typically surrounded by fine-grained rims composed of submicron-sized grains of ferroan olivine and saponite. Some of the rims are crosscut by fayalite-magnetite-sulfide veins, which typically start at the opaque nodules in peripheral parts of the chondrules and occasionally extend into the neighboring matrix, indicative of in situ formation (Fig. 15.18e, f).

Matrices in the CV_{OxB} chondrites consist almost entirely of secondary minerals resulting from secondary alteration involving aqueous fluids (Fig. 15.5a; see also Fig. 2 in Krot et al. 1998a). These include micron-sized lath-shaped crystals of ferroan olivine (Fa_{20-40}), coarser grained ferroan olivine fragments (Fa_{10-85}), large grains (up to 200 μm) of nearly pure fayalite (Fa_{95-100}), and concentrically-zoned nodules (15–30 μm in diameter) of ferroan diopside – hedenbergite pyroxenes ($Fs_{10-50}Wo_{\sim 50}$) ± andradite, and saponite (Keller and Buseck 1990a; Keller and McKay 1993; Keller et al. 1994; Krot et al. 1998a). Magnetite occurs sparsely. Fe, Ni sulfides are common. Nepheline, sodalite, and Fe,Ni metal are generally absent.

15.2.3.2 Alteration of Chondrules and Matrices in Cb_{oxa} Chondrites and CV Dark Inclusions

Chondrules in the CV_{OxA} chondrites experienced a different style of alteration than those in CV_{OxB} chondrites. In addition to magnetite, Fe,Ni sulfides, and ferroan diopside – hedenbergite pyroxenes, the major secondary minerals in CV_{OxA} chondrules include ferroan olivine (Fa_{30-50}), nepheline, sodalite, Ni-rich metal (awaruite and tetrataenite), magnetite, and Fe,Ni sulfides (troilite, pyrrhotite, and pentlandite). Andradite, wollastonite, grossular, and kirschsteinite ($CaFeSiO_4$) are minor. Phyllosilicates are very minor. Pure fayalite is absent (Ikeda and Kimura 1995; Kimura and Ikeda 1995; Brearley 1997a; Krot et al. 1997a, 1998a, b).

There are several textural occurrences of secondary ferroan olivine in the CV_{OxA} chondrules (1–4) and matrices (4): (1) halos around relict Ni-rich metal grains inside forsteritic olivine, (2) veins and rims around forsteritic olivine (Fig. 15.20c, d; see also Figs. 1–2 in Kimura and Ikeda 1995; Hua et al. 1988; Weinbruch et al. 1990), (3) a replacement product of Mg-rich, low-Ca pyroxene phenocrysts and magnetite nodules (Figs. 15.20b–d, 4; see also Figs. 1–5 in Kimura and Ikeda 1995), and (4) lath-shaped grains (Fig. 15.5). In addition, forsteritic olivine grains in chondrules are enriched in FeO along grains boundaries; the degree of enrichment increases towards chondrule peripheries.

Glassy mesostasis and plagioclase in the CV_{OxA} chondrules are mainly replaced by nepheline and sodalite (see Figs. 1.4–6 in Kimura and Ikeda 1995). Hedenbergite, andradite, grossular, kirschsteinite, and wollastonite are minor. They often occur intimately intergrown with nepheline and sodalite (Kimura and Ikeda 1995). In addition, ferroan diopside – hedenbergite pyroxenes and andradite occur as the replacement products of opaque nodules in chondrules (Fig. 15.20), as rims around altered chondrules (Fig. 8 in Krot et al. 1998b), and as rounded nodules in

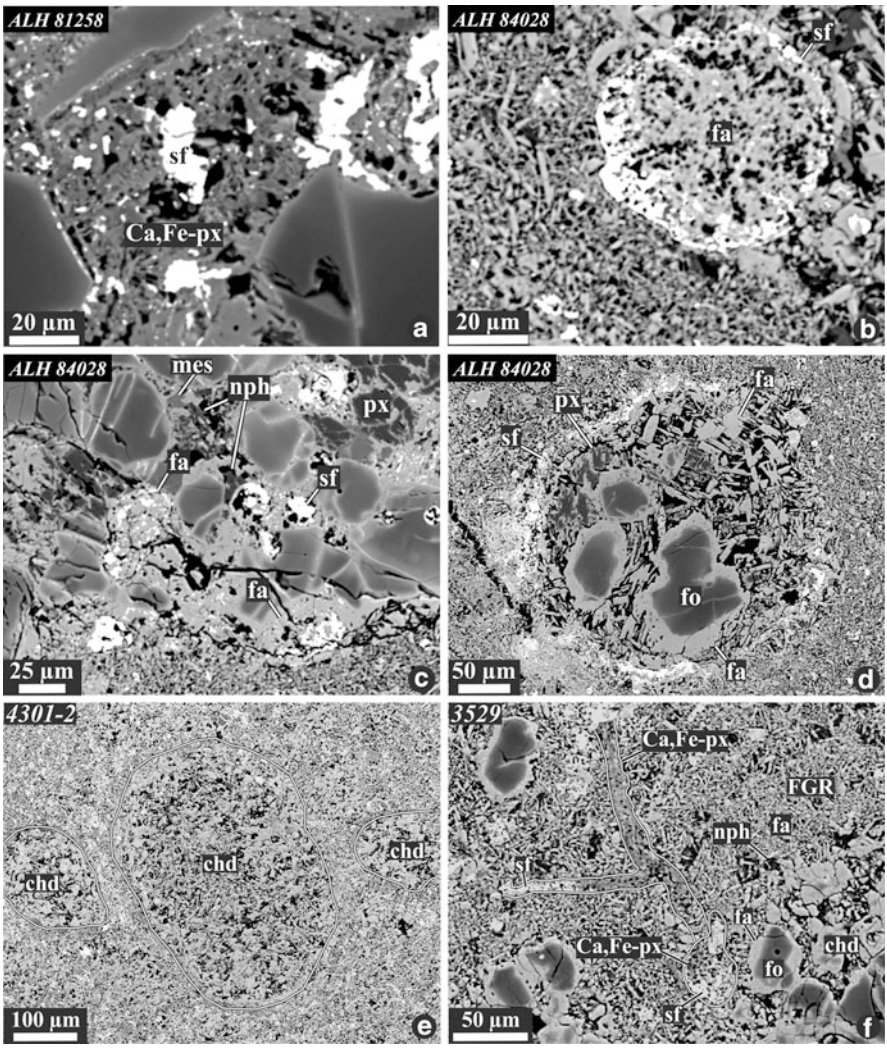

Fig. 15.20 BSE images of altered chondrules in ALH 81258 (CV_{OxA}) (**a**), ALH 84028 (CV_{OxA}) (**b**–**d**), and dark inclusions *4301-2* (**e**) and *3529* (**f**) from Allende (CV_{OxA}). (**a**–**d**) Opaque nodules are pseudomorphed by ferroan olivine (fa), ferroan diopside – hedenbergite pyroxenes (Ca,Fe-px), and Fe,Ni sulfides (sf). Low-Ca pyroxene phenocrysts (px) are replaced by ferroan olivine. Chondrule mesostasis (mes) is replaced mainly by nepheline (nph). Forsteritic olivine phenocrysts (fo) show enrichment in fayalite contents near their edges and along the fractures. (**e**, **f**) Chondrules extensively replaced by ferroan olivine and nepheline. Chondrule shown in (**e**) is surrounded by a fine-grained rim (FGR) composed of lath-shaped ferroan olivine and nepheline. The rim is crosscut by a vein composed of ferroan diopside – hedenbergite pyroxenes and Fe,Ni sulfides. The vein starts at an opaque nodule (*outlined*) replaced by ferroan diopside – hedenbergite pyroxenes, ferroan olivine, and Fe,Ni sulfides. Figures a-f from Meteorites and the Early Solar System II edited by Dante s. Lauretta and Haryy Y. McSween Jr.© The Arizona Board of Regents. Reprinted by permission of the University of Arizona Press.

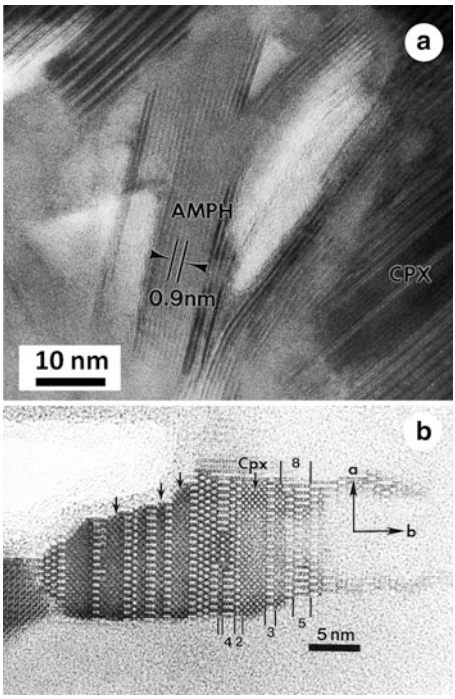

Fig. 15.21 Transmission electron micrographs of hydrous phases in lowCa pyroxene-bearing chondrules from Allende. (**a**) bright field TEM image of elongate amphibole (Amph) crystals that have partially replaced clinoenstatite (Cpx). (**b**) High resolution TEM image of a region of clinoenstatite (Cpx) imaged down the c-axis. The clinoenstatite (remnant Cpx is *arrowed*) has been partially replaced by lamellae of amphiboles (double chain) and disordered biobyriboles with chain widths that vary from 3 up to 8. The development of these phases is a transitional step in the transformation of the enstatite to talc. Although these hydrous phases occur in minor amounts, they are widespread within all clinoenstatite-bearing chondrules (From Brearley 1997b)

the matrix (Fig. 15.5c, d). Hydrated minerals (Ca-rich amphiboles ($Ca_2(Mg, Fe)_5Si_8O_{22}(OH)_2$), talc ($Mg_3Si_4O_{10}(OH)_2$), and disordered biopyriboles), replacing low-Ca pyroxene phenocrysts in chondrules, are very minor (Fig. 15.21), but are found in every porphyritic olivine-pyroxene chondrule studied by transmission electron microscopy (Brearley 1997b). High-Ca pyroxenes typically show no evidence for alteration (Ikeda and Kimura 1995).

The degree of alteration is variable among chondrules, reflecting variations in their textures, primary mineralogies, and chemical compositions (Ikeda and Kimura 1995; Kimura and Ikeda 1995). The peripheral parts of chondrules are always more altered than their cores. Some chondrules show a zoned distribution of Na and Ca. The former is concentrated in the peripheral parts, whereas the latter is mainly present in the cores (Fig. 15.22).

The chemical compositions of primary and secondary minerals in chondrules indicate that during alteration, Na, K, Fe, and Cl were introduced into chondrules, whereas Ca and Si were removed from or redistributed within chondrules (Ikeda and Kimura 1995; Kimura and Ikeda 1995; Krot et al. 1998b), e.g.,

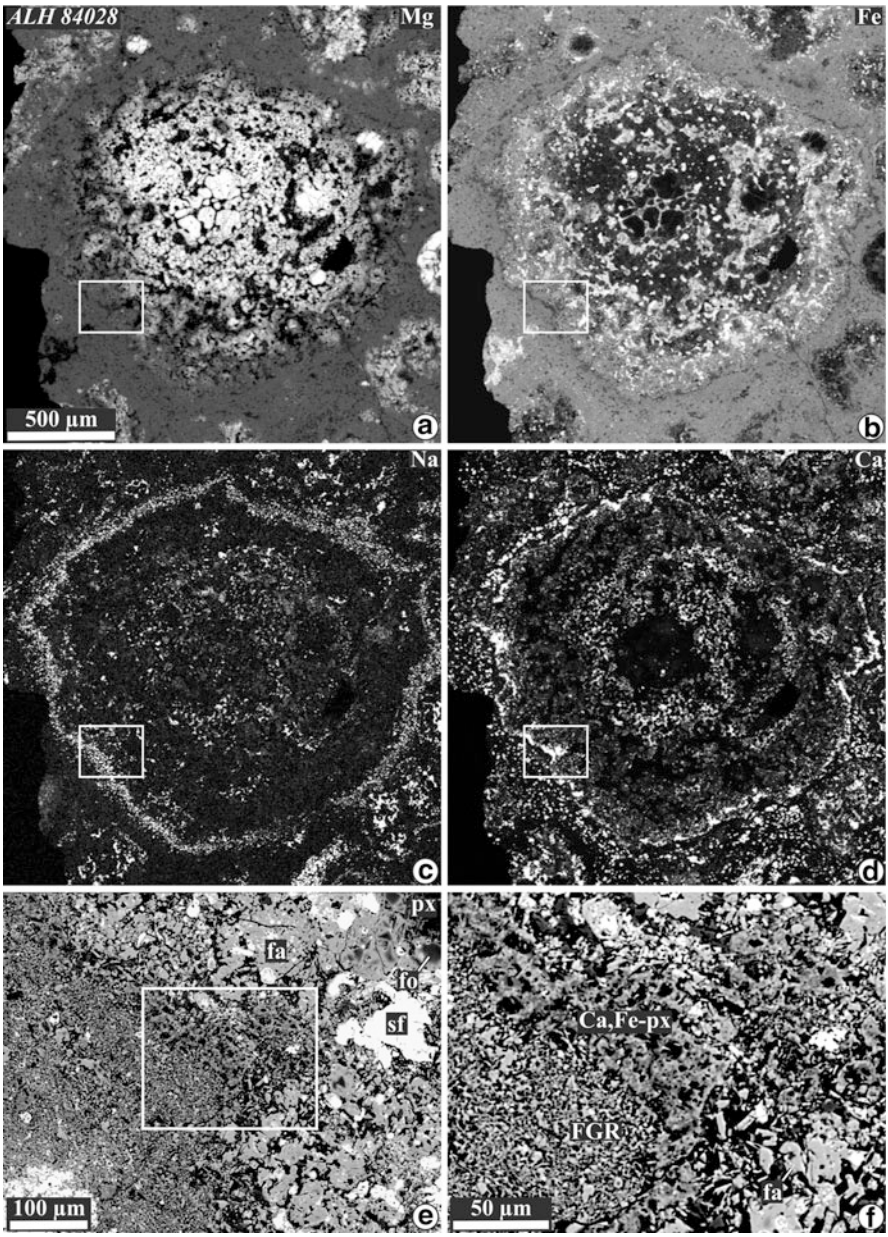

Fig. 15.22 X-ray elemental maps in Mg (**a**), Fe (**b**), Na (**c**), and Ca Kα (**d**) and BSE images (**e**, **f**) of a type I chondrule in ALH 84028 (CV_{OxA}). Chondrule consists of forsteritic olivine (ol) and magnesian, low-Ca pyroxene (px) phenocrysts, diopsidic pyroxene, anorthitic mesostasis, and opaque nodules. Low-Ca pyroxene and opaque nodules are replaced to various degrees by ferroan olivine (fa). The outer portion of the chondrule is surrounded by a layer of ferroan diopside – hedenbergite pyroxenes (Ca,Fe-px), enclosing relict grains of olivine and diopsidic pyroxene. The chondrule is surrounded by a fine-grained rim (FGR) composed of ferroan olivine and nepheline (From Krot et al. 1998b)

$$2(CaAl_2Si_2O_8 - NaAlSi_2O_8)_{ss} + 4\ Na^+{}_{(aq)} + 4\ H_{2(g)} = 3\ Na_2Al_2Si_2O_{8(s)} + 2\ Ca^{2+}{}_{(aq)} + 2\ SiO_{2(aq)} + 4\ H_2O_{(g)} \quad (15.17)$$

The released Ca and Si were used to form secondary Ca-rich minerals inside chondrules, rims around chondrules, and ferroan diopside – hedenbergite pyroxenes ± andradite nodules in matrix.

Chondrules and matrices in the Allende dark inclusions show very similar alteration features to those in the host meteorite. The alteration, however, is generally more extensive (Fruland et al. 1978; Kurat et al. 1989; Johnson et al. 1990; Kojima and Tomeoka 1996; Buchanan et al. 1997; Krot et al. 1997a, 1998a, b, 2001; Weisberg and Prinz 1998). Most chondrules in the Allende dark inclusions are nearly completely pseudomorphed by ferroan olivine (Fa_{35-45}) and nepheline[6]; low-Ca pyroxene grains are generally absent (Figs. 15.20e, f, 15.23a, 15.24a, b). Opaque nodules in chondrules are replaced by ferroan olivine, ferroan diopside, and Fe,Ni sulfides; magnetite is absent. Fine-grained rims and matrices around chondrule pseudomorphs are often crosscut by veins composed of ferroan olivine, ferroan diopside – hedenbergite pyroxenes, and Fe,Ni sulfides (Figs. 15.20f, 15.23a, see also Fig. 12a in Krot et al. 1998b). Ferroan olivines in Allende dark inclusions have, on average, lower fayalite contents than those in the neighboring Allende matrix (Fa_{41-44} vs. $Fa_{\sim 50}$) (Krot et al. 2001).

Most dark inclusions in Allende are surrounded by Ca-rich rims, which are mineralogically similar to the Ca-rich rims outside fine-grained rims around Allende CAIs (Fig. 15.17) and are composed of ferroan diopside – hedenbergite pyroxenes, wollastonite, andradite, and kirschsteinite (Figs. 15.23, 15.24). The rims have variable widths and are often mineralogically zoned (Fig. 15.24c, d). The innermost layer consists of ferroan diopside ($Fs_{10-15}Wo_{48-50}$) followed by a layer of nearly pure hedenbergite ($Fs_{45-50}Wo_{48-50}$). The central zone of the rim is composed of wollastonite, andradite, and minor kirschsteinite. Wollastonite and kirschsteinite appear to replace andradite. The outermost layer consists of ferroan diopside – hedenbergite pyroxenes ($Fs_{15-35}Wo_{48-50}$). The Ca-rich veins, crosscutting dark inclusions, are commonly connected to the rims, but do not extend into the Allende matrix (Fig. 15.23a). The rims are typically intergrown with the Allende matrix olivines and enclose fragments of chondrules and regions of Allende-like matrix material (Fig. 15.24e, f). The peripheral portions of the rimmed dark inclusions are depleted to various degrees in Ca; the degree of Ca depletion correlates with the rim thicknesses (Fig. 15.23a, d, g). Abundant nodules of ferroan diopside – hedenbergite pyroxenes, wollastonite, and andradite are also observed in the neighboring Allende matrix (Fig. 15.23a, d, g). These observations indicate that the Ca removed from the dark inclusions was re-deposited at the interface with the Allende host.

[6] In the Efremovka (CV_R) dark inclusions, chondrules are pseudomorphed by a fine-grained mixture of ferroan olivine, phyllosilicates, and, occasionally, andradite (Figs. 15.19e–f; Krot et al. 1999).

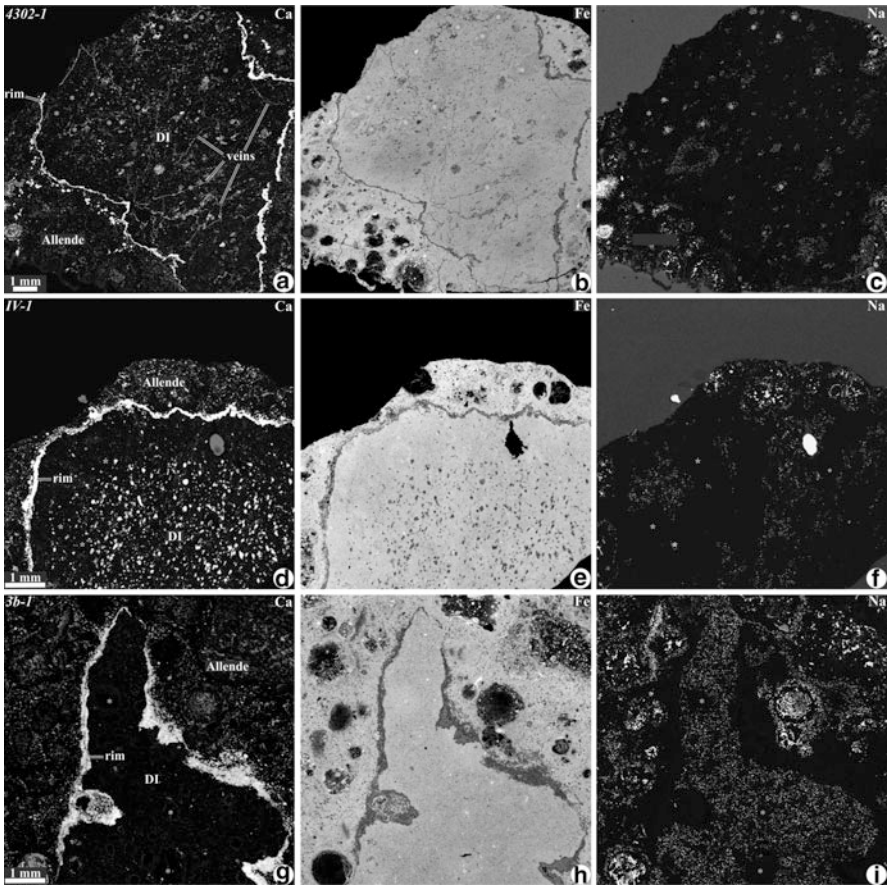

Fig. 15.23 X-ray elemental maps in Ca (**a**, **d**, **g**), Fe (**b**, **e**, **h**), and Na (**c**, **f**, **i**) of the heavily-altered chondrite lithic clasts (dark inclusions, DI) *4302-1* (**a**–**c**), *IV-1* (**d**–**f**), and *3b-1* (**g**–**i**) from Allende (CV_{OxA}). The dark inclusions consist entirely of secondary minerals (ferroan olivine, nepheline, sodalite, and Fe,Ni sulfides) and contain chondrule pseudomorphs (indicated by *yellow stars*), which are depleted in Ca (see Fig. 15.20e). Chondrule pseudomorphs in *4302-1* contain abundant nepheline and minor sodalite. The matrix in *4302-1* is depleted in Na. Chondrule pseudomorphs in *3b-1* are depleted in Na, whereas its matrix is uniformly enriched in Na. No apparent correlation between Na-bearing minerals and chondrule pseudomorphs is observed in *IV-1*. Ferroan olivines in the dark inclusions are less fayalitic than those in the neighboring Allende matrix (Fa_{41-44} vs. Fa_{47}). A continuous rim of Ca,Fe-silicates (ferroan diopside – hedenbergite pyroxenes, wollastonite, andradite, and kirschsteinite) surrounds the inclusions. In addition, *4301-2* is crosscut by multiple veins of ferroan diopside pyroxenes. There is a progressive depletion in Ca from *4301-2* to *IV-1* to *3b-1*. The Ca depletion is zoned in such a way that the Ca concentration is the lowest near the rim and increases towards the core of the inclusions (After Krot et al. 2001)

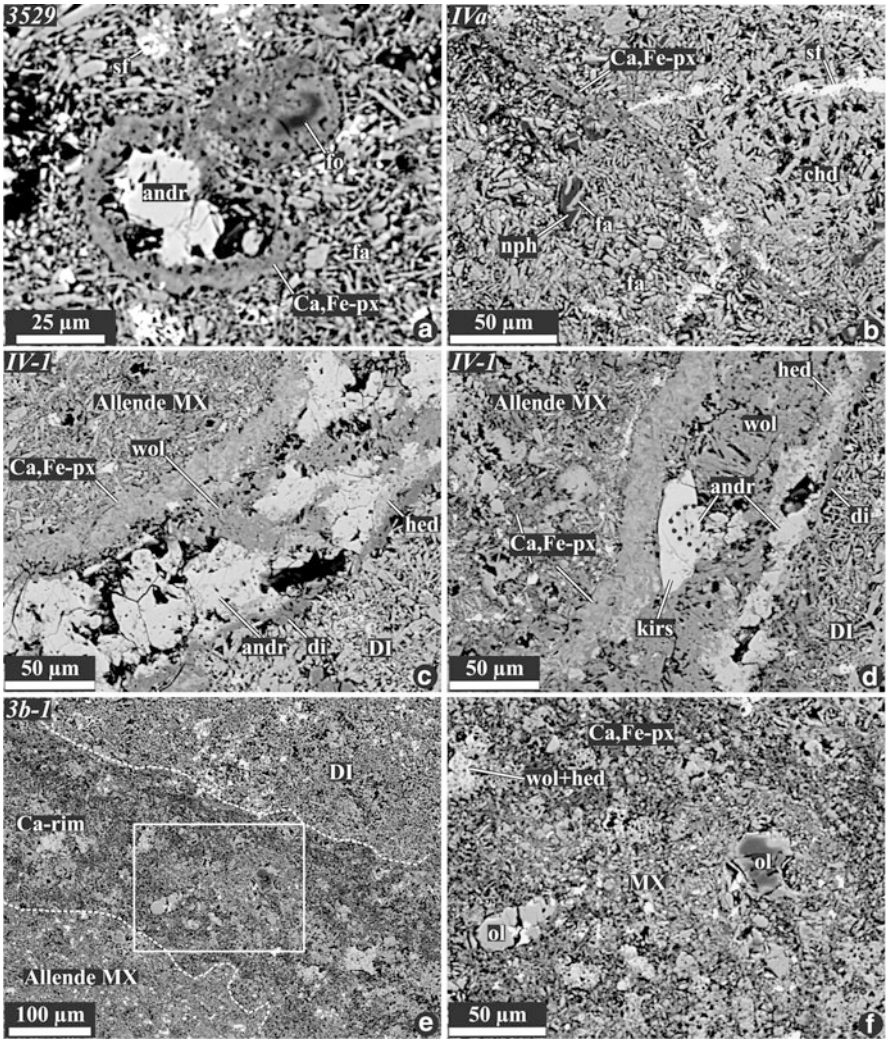

Fig. 15.24 BSE images of the Allende dark inclusions (DI) *3529* (**a**), *IV-a* (**b**), *IV-1* (**c**, **d**), and *3b-1* (**e**, **f**). The dark inclusions contain relatively coarse-grained chondrule pseudomorphs (chd) and finer-grained matrix; both are almost entirely composed of secondary minerals: ferroan olivine (fa), nepheline (nph), Fe,Ni sulfides, Ca,Fe-pyroxenes (Ca,Fe-px), and andradite (andr). There are three main occurrences of the Ca,Fe-pyroxenes: (1) concentrically-zoned nodules with cores often containing massive andradite, and, occasionally, relict forsteritic olivine (**a**); (2) veins crosscutting fine-grained matrix (**b**); and (3) rims separating the dark inclusions from the Allende matrix (MX) (**c**–**f**). The rims are often mineralogically-zoned (**c**, **d**). The innermost layer consists of ferroan diopside (di, $Fs_{10-15}Wo_{48-50}$). It is followed by a layer of hedenbergite (hed, $Fs_{48-50}Wo_{48-50}$). The central zone of the rim is composed mainly of wollastonite (wol) and andradite. Kirschsteinite (kirs) is rare. The central zone is followed by a thick layer of ferroan diopside – hedenbergite pyroxenes (Ca,Fe-px, $Fs_{15-35}Wo_{48-50}$). Occasionally, the rims entrap chondrule fragments and regions of the Allende matrix (**e**, **f**), suggesting in situ formation (From Krot et al. 1998b, 1999)

15.2.3.3 Nebular Versus Asteroidal Models of Alteration of CV_{oxa} Chondrules, Matrices and Dark Inclusions

Nebular and asteroidal models have been proposed to explain the origin of secondary minerals in chondrules, matrices, and dark inclusions in CV_{OxA} chondrites (e.g., Housley and Cirlin 1983; Johnson et al. 1990; Weinbruch et al. 1990; Kojima and Tomeoka 1996; Brearley and Prinz 1996; Buchanan et al. 1997; Dohmen et al. 1998; Brearley 1997a; Krot et al. 1997a, 2004b).

The nebular scenario involves condensation from a hot (>1,450 K), highly oxidizing nebular gas produced by evaporation of local nebular regions with high (silicate dust + water ice)/gas ratios (e.g., Weinbruch et al. 1990; Johnson et al. 1990; Dohmen et al. 1998). This mechanism, however, is inconsistent with (1) the petrographic observations described above (e.g., postaccretionary formation of ferroan olivine and ferroan diopside – hedenbergite pyroxene veins, chondrule pseudomorphs, and Ca-rich rims around Allende dark inclusions); (2) the presence of abundant, randomly oriented (i.e., not crystallographically controlled) inclusions (< 100 nm) of pentlandite, poorly-graphitized carbon (PGC), chromite ($FeCr_2O_4$), and ilmenite in ferroan olivine and ferroan diopside – hedenbergite pyroxenes in the matrix and dark inclusions in Allende[7] (Brearley and Prinz 1996; Brearley 1997a) (Fig. 15.25a, b); (3) the large mass-dependent fractionation of oxygen isotopes in secondary fayalite, magnetite, ferroan diopside – hedenbergite pyroxenes, wollastonite, and andradite (see Sect. 15.2.5); (4) the prolonged duration of the CV alteration (see Sect. 15.2.7); and (5) the thermodynamic analysis of high-temperature condensation of ferroan olivine (Fedkin and Grossman 2010).

Kojima and Tomeoka (1996) and Krot et al. (1995) suggested that fibrous ferroan olivine, in Allende dark inclusions, formed by progressive aqueous alteration and subsequent dehydration of the phyllosilicates during thermal metamorphism on the CV parent asteroid. Subsequently, Krot et al. (1997a) applied this mechanism to explain the origin of secondary ferroan olivine in chondrules and matrices of CV chondrites. This mechanism is consistent with (1) the microstructures of matrix olivine in Allende, which are similar to those described in dehydrated phyllosilicates in CM chondrites (Akai 1988), and include voids, inclusions of pentlandite and PGC (Brearley and Prinz 1996; Brearley 1997a; Fig. 15.25a, b); (2) the presence of phyllosilicates associated with ferroan olivine in the Efremovka dark inclusions (Krot et al. 1997a); and (3) the presence of hydrous silicates in the Allende chondrules, which appear to have formed prior to or contemporaneously with ferroan olivine (Brearley 1997b). However, this mechanism appears to be inconsistent with the lack

[7] The formation of PGC is a thermodynamically irreversible process, which results from annealing of graphitizeable carbons. In nature these are complex hydrocarbons, such as kerogens, which are formed at low temperatures (Buseck and Huang 1985). In the classical condensation sequence, graphitic carbon does not become stable until temperatures reach 600 K at a total pressure of 10^{-3} atm (Hayatsu et al. 1980), ~500−600 K below the condensation temperature of diopside. These observations indicate ferroan olivine and ferroan diopside – hedenbergite pyroxenes must have formed after formation of the low temperature carbonaceous material.

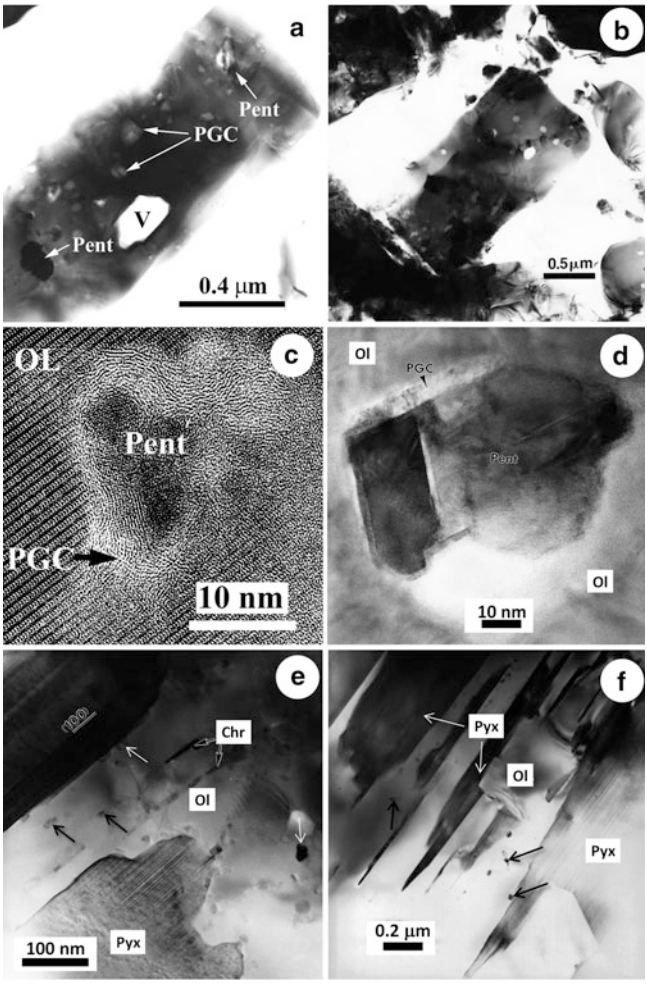

Fig. 15.25 Transmission electron microscope (TEM) images of microstructures in the Allende matrix, and dark inclusion olivines and fayalitic olivine replacing enstatite in chondrules. Figures (**a, c** and **d**) are from Brearley (1999). (**a**) Bright field TEM image of typical matrix olivine in Allende containing abundant inclusions of poorly graphitized carbon (PGC), pentlandite (Pent), as well as voids (V). (**b**) Bright field TEM image of typical olivine in an Allende dark inclusion which also contains abundant inclusions of poorly graphitized carbon, pentlandite, and voids. (**c**) High resolution TEM image of an inclusion of pentlandite (Pent) rimmed by poorly graphitized carbon (PGC) in a matrix olivine (OL) from Allende (From Brearley 1999). (**d**) High resolution TEM image of a faceted pentlandite (Pent) inclusion within olivine (OL) in an Allende dark inclusion. The pentlandite is rimmed by poorly graphitized carbon (PGC) with a higher degree of order than those observed in Allende matrix olivines. (**e**) Bright field TEM image of fayalitic olivine (Ol) replacing twinned clinoenstatite (Pyx) from a porphyritic pyroxene chondrule in Allende. The replacement occurs preferentially parallel to (100) enstatite. The product fayalite contains abundant fine-grained inclusions of chromite (Chr) that are distributed throughout the fayalite and at the interface between the olivine and the enstatite (*arrowed*). (**f**) Bright field TEM

of mass-dependent fractionation of oxygen isotopes in bulk CV chondrites (Fig. 15.4), which would be expected for extensively aqueously-altered and dehydrated meteorites (e.g., metamorphosed CI/CM chondrites) (Clayton and Mayeda 1999). In addition, it does not explain (1) the steep compositional gradients between the ferroan olivine rims and their host chondrules in Allende; (2) the microstructures of ferroan olivine replacing low-Ca pyroxenes, which are consistent with solid-state replacement reactions (Brearley 1997a) (Fig. 15.25c, d); (3) the common occurrences of ferroan olivine in the aqueously-altered and virtually unmetamorphosed CV_{OxB} chondrites (Krot et al. 1998a, b; Bonal et al. 2007); and (4) the formation of secondary ferroan diopside – hedenbergite pyroxenes, andradite, wollastonite, and kirschsteinite coexisting with ferroan olivine in the Allende chondrules and dark inclusions.

Subsequently, Krot et al. (1998a, b, 2000a, 2001, 2004b) suggested that CV_{OxA} chondrites experienced fluid-assisted thermal metamorphism, which resulted in dissolution of primary minerals, mobilization of Ca, Si, Fe, Mg, Mn, Na, K, and S by a fluid phase (aqueous solution), replacement of the primary minerals in chondrules and matrices by the secondary minerals, and direct precipitation of the secondary minerals from a fluid. According to this model, ferroan olivine formed during this process via several mechanisms. These include replacement of magnetite nodules (Reaction 15.18), replacement of magnesian pyroxene (Reaction 15.19), Fe-Mg exchange between olivine and fluid (Reactions 15.20, 15.21), and by direct precipitation from a fluid (Reaction 15.22):

$$2\,Fe_3O_{4(s)} + 3\,SiO_{2(aq)} + 6\,Mg^{2+}{}_{(aq)} + 2\,H_{2(g)} = 3(Fe,Mg)_2SiO_{4(s)} + 2\,H_2O_{(g)} \quad (15.18)$$

$$Fe^{2+}{}_{(aq)} + MgSiO_{3(s)} + H_2O_{(l,g)} = (Fe,Mg)_2SiO_{4(s)} + H_{2(g)} \quad (15.19)$$

$$Fe^{2+}{}_{(aq)} + Mg_2SiO_{4(s)} + H_2O_{(l,g)} = (Fe,Mg)_2SiO_{4(s)} + Mg^{2+}{}_{(aq)} + H_{2(g)} \quad (15.20)$$

$$Mg^{2+}{}_{(aq)} + Fe_2SiO_{4(s)} + H_2O_{(l,g)} = (Fe,Mg)_2SiO_{4(s)} + Fe^{2+}{}_{(aq)} + H_{2(g)} \quad (15.21)$$

$$Fe^{2+}{}_{(aq)} + Mg^{2+}{}_{(aq)} + SiO_{2(aq)} = (Fe,Mg)_2SiO_{4(s)} \quad (15.22)$$

Dehydration of phyllosilicates appears to have played only a minor role. Growth of ferroan olivine, in the presence of fluid released during dehydration of phyllosilicates, seems more likely (Krot et al. 2004b).

The proposed different mechanisms for the origin of ferroan olivine in Allende are supported by microstructural differences of several textural occurrences of ferroan olivine (Brearley 1997a). For example, (1) platy or lath-shaped matrix olivines and

Fig. 15.25 (continued) image of a region of enstatite in a pyroxene-rich chondrule that has been partially replaced by fayalite. Elongate remnants of pyroxene (Pyx) are present surrounded by fayalite (OL), with interfaces parallel to (100) enstatite. As in (**e**), very fine-grained inclusions of chromite (*arrowed*) are present throughout the fayalitic olivine

olivines in Allende dark inclusions often contain numerous voids, planar dislocations parallel to the direction of elongation of the grain (Fig. 15.25a–d). They also contain submicron inclusions of chromite, ilmenite, pentlandite, and PGC, none of which appears to have a crystallographic orientation relationship with the host olivine. (2) Ferroan olivine veins, crosscutting forsteritic chondrule olivines, frequently contain abundant chromite and/or hercynitic spinel, occasionally crystallographically oriented with respect to the olivine. The ferroan olivine within the veins is typically in crystallographic continuity with the forsteritic host olivine, but the vein olivine appears strained and contains abundant closely spaced planar defects on (100). (3) Ferroan olivine, replacing low-Ca pyroxene, typically consists of crystallographically continuous regions of olivine, which can extend for several microns or more and is essentially unstrained and free of defects (Fig. 15.25d, e). The olivine contains inclusions of chromite and relict enstatite; the former often decorate subgrain boundaries with the ferroan olivine or occur at the interface between the fayalite and enstatite (Fig. 15.25d, e). There is no evidence of crystallographic orientation relationships between the ferroan olivine and enstatite.

The Allende dark inclusions appear to have experienced at least two stages of alteration after lithification and aggregation in the presence of an aqueous solution (Krot et al. 2001). One episode of alteration resulted in replacement of primary chondrule minerals by secondary ferroan olivine, nepheline, sodalite, and Ni-rich sulfides. Calcium, removed from the chondrules, was redeposited as ferroan diopside – hedenbergite pyroxene veins and inclusions in the matrix, and as rims around chondrules. Following this alteration, the dark inclusions were excavated from their original location (most likely the CV3 asteroidal body) and incorporated into the host Allende. The last episode of alteration took place in situ and resulted in dissolution of secondary Ca,Fe silicates in the dark inclusions and re-deposition of Ca-bearing minerals as rims around dark inclusions at the interfaces with the Allende host (Krot et al. 2001).

15.2.4 Thermal Metamorphism of CV Chondrites

Although it is generally accepted that CV chondrites experienced thermal metamorphism on their parent asteroid, there is no agreement on metamorphic grades and peak metamorphic temperatures reached by individual members of this very diverse group of meteorites (e.g., Guimon et al. 1995; Huss and Lewis 1994a, b, 1995; Huss et al. 1996; Krot et al. 1995 and references therein; Bonal et al. 2006). An additional complexity comes from the fact that most CV chondrites are breccias containing fragments of oxidized and reduced CV subgroups/lithologies that experienced various degrees of aqueous alteration and thermal metamorphism (Krot et al. 1995, 1998a, 2000a); in some cases (e.g., Mokoia), aqueous alteration postdates thermal metamorphism (Tomeoka and Buseck 1990; Krot et al. 1998a).

The most recent and comprehensive study of the metamorphic classification of CV chondrites was reported by Bonal et al. (2006), who used the maturity of

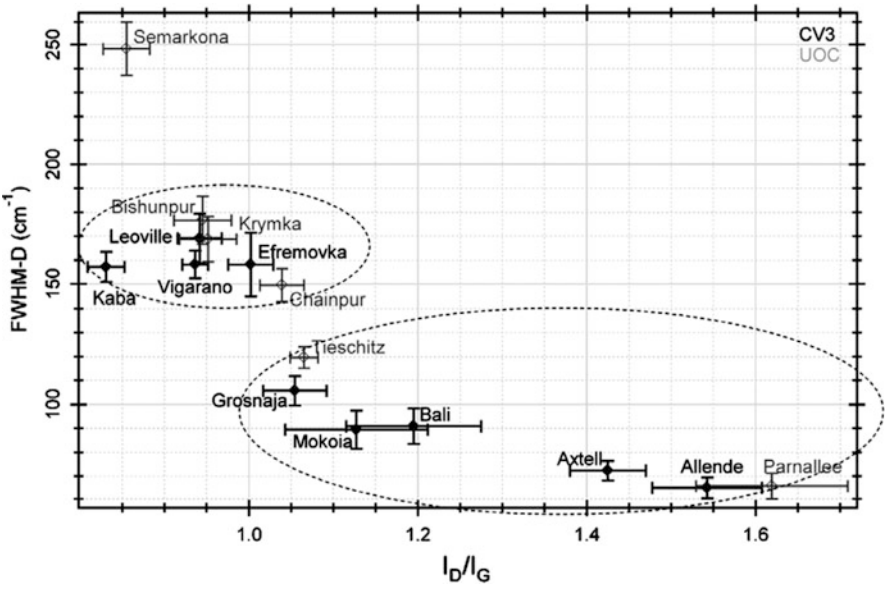

Fig. 15.26 Spectral parameters of Raman bands of carbonaceous materials in chondrite meteorites: FWHM-D (full width at half maximum of D-band) versus I_D/I_G (intensity of D-band/intensity of G-band). Averages (*points*) and standard deviations (*bars*) are plotted for unequilibrated ordinary chondrites (UOC, *grey dots*) and for CV3 chondrites (*black dots*) (From Bonal et al. 2006)

organic matter in CV matrices, determined by Raman spectroscopy, as a metamorphic tracer (Fig. 15.26). The reported petrologic types of CV chondrites are the following: Allende > Axtell (>3.6) > Bali ~ Mokoia > Grosnaja (~3.6) >> Efremovka > Vigarano ~ Leoville (3.1−3.4) > Kaba (~3.1). This metamorphic classification is generally consistent with whole-rock noble gas abundances (Fig. 15.27), the abundance of presolar grains (Huss and Lewis 1995), and petrologic observations (e.g., Fe-Mg zoning in forsteritic olivine phenocrysts in type I chondrules).

There are several estimates for peak metamorphic temperatures reached by CV chondrites. Assuming that ferroan olivine in the Allende matrix and dark inclusions formed by dehydration of saponite[8] (Kojima and Tomeoka 1996; Krot et al. 1997a), Buchanan et al. (1997) estimated the peak metamorphic temperature of Allende and Allende dark inclusions as high as 800–900°C, corresponding to approximately granulite facies grade of metamorphism. The upper limit on the peak metamorphic temperature experienced by Allende can be inferred from the common presence of grossular in altered CAIs and chondrules (see above): grossular decomposes to

[8] The origin of ferroan olivine in the CV matrices, as a result of the dehydration of phyllosilicates, was later challenged by Krot et al. (2004b). For additional arguments against this mechanism see Brearley and Prinz (1996), Brearley (1997a), and Clayton and Mayeda (1999).

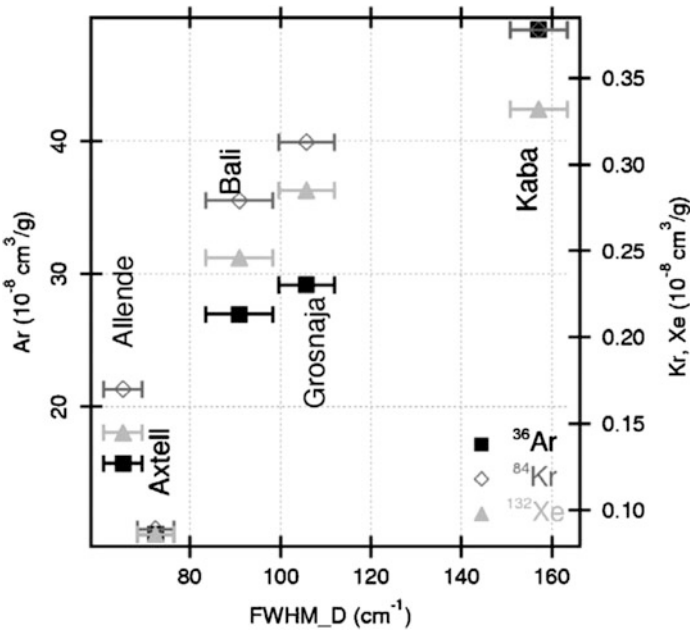

Fig. 15.27 Concentration of trapped planetary noble gases in the CV_{OxA} (Allende, Grosnaja) and CV_{OxB} (Bali, Kaba) chondrites versus Raman spectral parameter FWHM-D. The abundance of noble gases decreases with an increase in the degree of thermal metamorphism (From Bonal et al. 2006)

wollastonite, gehlenite and anorthite at 798°C (Huckenholz et al. 1974). On the basis of a thermodynamic analysis of the closed-system replacement reaction of melilite + anorthite by grossular, monticellite, ±forsterite, and ± wollastonite in the Allende Type C CAIs, Krot et al. (2007) inferred a peak metamorphic temperature for Allende of < 700°C (Fig. 15.28). Asimilar estimate comes from the presence of pentlandite in Allende matrix olivines, which is unstable above 610°C (Brearley 1997a). Temperatures in the range of 500–600°C, for the maximum metamorphic temperatures of Allende, come from several different types of geothermometry. For example, Cody et al. (2008) estimated temperatures of 554 ± 25°C using the exciton intensity of insoluble organic material (IOM), and Busemann et al. (2007) reported temperatures of 674 ± 118°C and 515 ± 120°C, using calibrations of the microRaman width parameters Γ_D cm^{-1} and Γ_G cm^{-1}, respectively, from IOM. Similarly, Huss and Lewis (1995) suggested maximum temperatures of 600°C, based on the abundance of presolar grains in Allende. Nevertheless, the maximum metamorphic temperatures experienced by Allende are certainly the subject of considerable debate. For example, Rietmeijer and Mackinnon (1985) and Bonal et al. (2007) argued for metamorphic temperatures of ~330°C, also based on studies of ordering in graphitic material in Allende. Although there are clearly issues that need to be resolved regarding the thermal

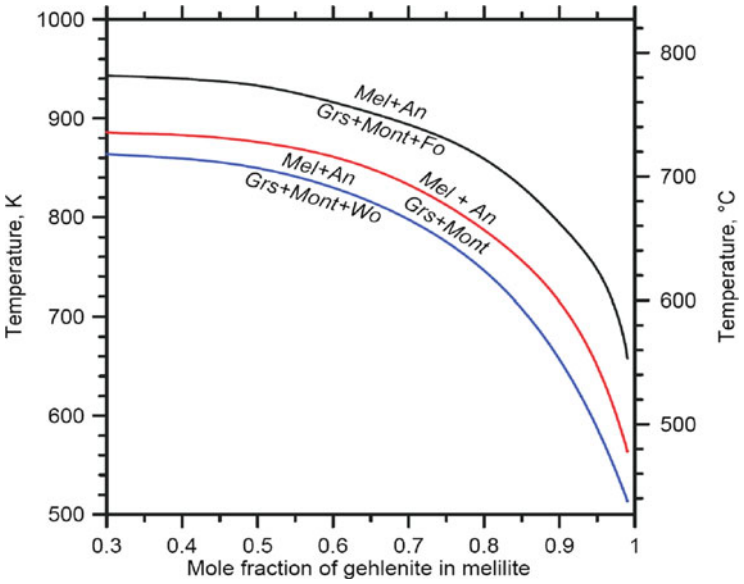

Fig. 15.28 Equilibrium calculations illustrating the formation temperature of grossular, monticellite, and forsterite or wollastonite by replacement of melilite and anorthite (From Krot et al. 2007)

history of Allende, the bulk of the current data favor maximum metamorphic temperatures in the range 500–700°C.

15.2.5 Oxygen Isotopic Compositions of CV Chondrites, Dark Inclusions, and Secondary Minerals

15.2.5.1 Whole-Rock Oxygen Isotopic Compositions of CV Chondrites and Dark Inclusions

Bulk oxygen isotopic compositions of CV chondrites and CV dark inclusions, reported by Clayton and Mayeda (1999), are plotted in Fig. 15.4. In contrast to aqueously-altered meteorites, such as CI, CM, and CR chondrites, and some of the dark inclusions in the CV_R and CV_{OxB} chondrites, the whole-rock samples of the reduced and oxidized CV chondrites and most of the Allende dark inclusions plot along the Carbonaceous Chondrite Anhydrous Mineral (CCAM) line with a slope of ~ 1, and hence show no clear evidence for mass-dependent fractionation of oxygen isotopes associated with the alteration. These observations are interpreted as being the result of isotopic exchange between ^{16}O-rich solids and ^{16}O-poor gases in the high-temperature regions of the solar nebula (Clayton and Mayeda 1999). At the same time, the whole-rock oxygen isotopic compositions of CV_{oxB} and Allende

dark inclusions tend to be isotopically heavier than the CV_R and CV_{OxA} meteorites reflecting either a sampling problem (CV chondrites are characterized by the presence of large ^{16}O-rich CAIs and AOAs) or alteration processes that did not cause significant fractionation of the bulk oxygen isotopic composition of these meteorites along a mass-dependent fractionation line with a slope of ~ 0.5 (Clayton and Mayeda 1999). Since the whole-rock oxygen isotopic compositions of altered meteorites primarily depend on W/R ratio, rather than temperature and the degree or duration of alteration (Clayton and Mayeda 1999), these observations may indicate that alteration of CV chondrites and Allende dark inclusions took place in the presence of a relatively small amount of water that was largely consumed during the alteration. This interpretation is consistent with thermodynamic analysis of the secondary mineralization in CV chondrites (e.g., Krot et al. 1998a, b, 2001; Zolotov et al. 2006), summarized in Sect. 15.2.6.

15.2.5.2 Oxygen Isotopic Compositions of Secondary Minerals in CV Chondrites

Oxygen Isotopic Compositions of Fayalite and Magnetite in CV_{OxB} Chondrites

Fayalite, replacing magnetite-sulfide nodules in type I chondrules in CV_{OxB} chondrites, shows large ($\delta^{18}O$ ~ 20‰) mass-dependent fractionation of oxygen isotopes (Fig. 15.29), consistent with its low-temperature formation in the presence of aqueous solutions (Hutcheon et al. 1998; Choi et al. 2000; Hua et al. 2005; Zolotov et al. 2006). Because of the large uncertainty associated with the reported SIMS (secondary ion mass spectrometer) measurements, it is unclear whether these minerals are in isotopic equilibrium, and whether their oxygen isotopic compositions can be used for constraining the temperature of alteration. Oxygen isotopic compositions of Ca,Fe-pyroxenes, andradite, wollastonite, and phyllosilicates in CV_{OxB} chondrites have not been reported yet.

Oxygen Isotopic Compositions of Ca,Fe-Silicates and Magnetite in CV_{OxA}Chondrites

Oxygen isotope compositions of the secondary Ca,Fe-pyroxenes, andradite, and wollastonite, in and around Allende CAIs and dark inclusions and in Allende matrix, plot parallel to the terrestrial fractionation line with a large (~20‰) range in $\delta^{18}O$, comparable with the range reported for magnetites and fayalites in the CV_{OxB} chondrites (Fig. 15.29). This suggests relatively low temperatures for their formation in the presence of aqueous solutions (Krot et al. 1998a, b; Brearley and Shearer 2000; Zolotov et al. 2006; Cosarinsky et al. 2008). The $\Delta^{17}O$ values of these minerals are indistinguishable, within the uncertainty of the SIMS measurements, from the reported values of magnetite and fayalite in CV_{OxB} chondrites (-2.5 ± 2.6‰ vs. -1.2 ± 1.9‰, respectively; Fig. 15.29b, d). The mass-

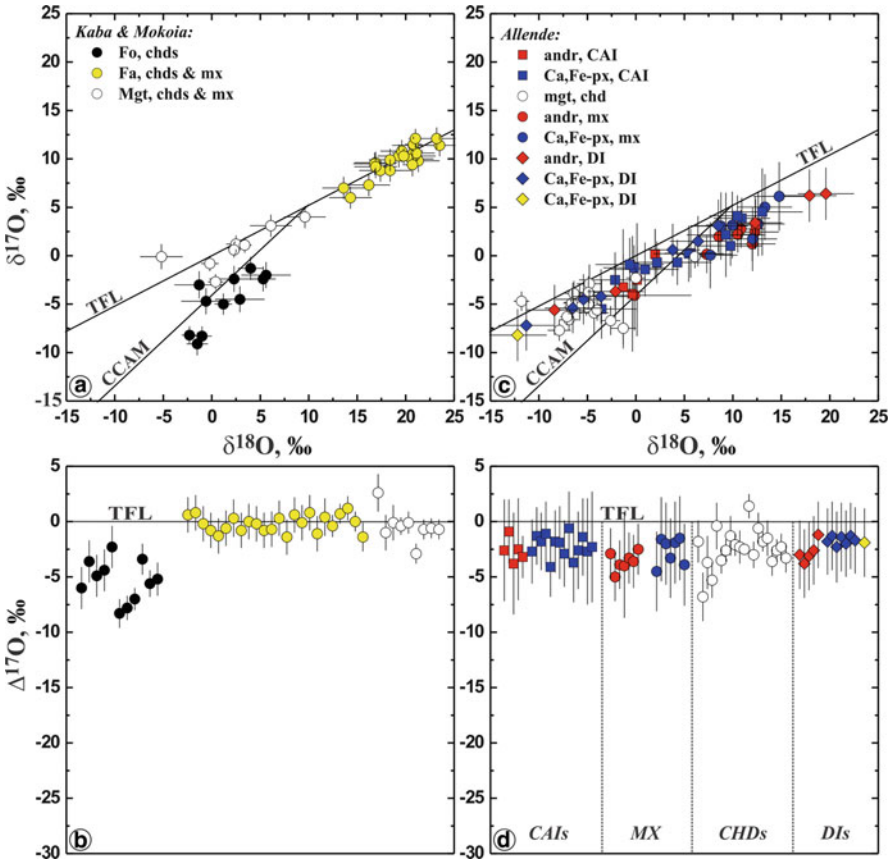

Fig. 15.29 Oxygen isotopic compositions of secondary magnetite (mgt) and fayalite (fa) and primary forsteritic olivine (fo) in type I chondrules in Kaba and Mokoia (CV_{OxB}), and of secondary magnetite, ferroan diopside – hedenbergite pyroxenes (Ca,Fe-px), wollastonite (wol), and andradite (andr) in various Allende (CV_{OxA}) components (chondrules, matrices, and rims around CAI's) and Allende dark inclusions (DI) (Data from Choi et al. 2000; Krot et al. 2000b; Hua et al. 2005; and Cosarinsky et al. 2008). In (**a**), the data are plotted on a three-isotope oxygen diagram. In (**b**), the same data are plotted as deviations from the terrestrial fractionation line (TFL), $\Delta^{17}O$ ($= \delta^{17}O - 0.52\times\delta^{18}O$). Magnetite and fayalite in the CV_{OxB} chondrites differ in $\delta^{18}O$ by ~ 20‰, suggesting formation at low temperatures. Compositions of forsteritic olivine in type I chondrules plot along the CCAM line and are not in isotopic equilibrium with the secondary minerals. The compositions of secondary magnetite and Ca,Fe-rich silicates in Allende tend to be slightly ^{16}O-enriched ($\Delta^{17}O = -2.5 \pm 2.6$‰ vs. -1.2 ± 1.9‰; they are indistinguishable within uncertainty of the measurements) relative to those of fayalite and magnetite in CV_{OxB} chondrites, but show a similarly large spread in $\delta^{18}O$ values, suggesting a similar formation mechanism. The terrestrial fractionation line and Carbonaceous Chondrite Anhydrous Mineral line (CCAM) are shown for reference. Error bars are 1σ

dependent fractionation line defined by the secondary Ca,Fe-rich silicates coincides with the Allende mass-fractionation line based on the whole-rock isotopic compositions of Allende chondrules which experienced Fe-alkali metasomatic

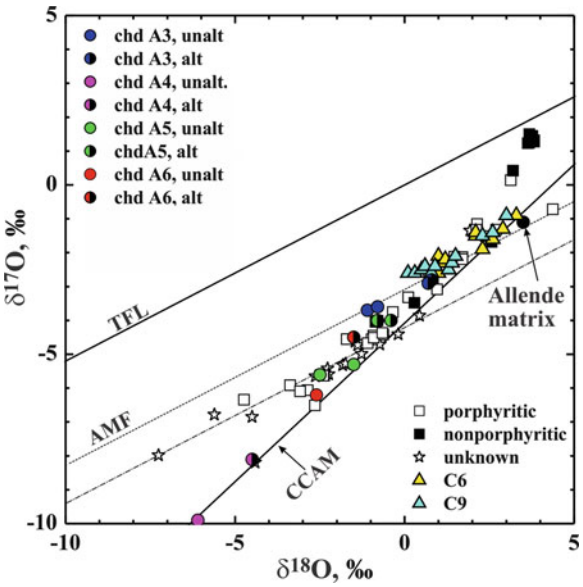

Fig. 15.30 Bulk oxygen isotopic compositions of Allende chondrules and of unaltered and altered regions in Allende chondrules. C6 and C9 represent compositions of different regions within individual chondrules. *AMF* Allende Mass Fractionation line (Ash et al. 1999). *Dash-dotted line* = line fitting bulk compositional data for small altered chondrules analyzed by Jabeen et al. (1998b). The reason for the discrepancy between the Ash et al. (1999) and Jabeen et al. (1998b) data is unknown. Data are from Clayton et al. (1983), Rubin et al. (1990), Jabeen et al. (1998b), and Ash et al. (1999). The terrestrial fractionation line (TFL) and Carbonaceous Chondrite Anhydrous Mineral line (CCAM) are shown for reference

alteration (Fig. 15.30; Jabeen et al. Jabeen et al. 1998a, b; 1999; Ash et al. 1999; Young et al. 1999). These observations, together with the mineralogical and petrographic studies reviewed above and thermodynamic analysis (see Sect. 15.2.6), support formation of the secondary Ca,Fe-silicates, fayalite, magnetite, and alkali-rich minerals (nepheline, sodalite, wadalite, Na-melilite) in all CV chondrite components by interaction with an isotopically heavy, ^{16}O-depleted reservoir on the CV parent body.

Oxygen Isotopic Compositions of Melilite, Anorthite, and Secondary Minerals in CV_{OxA} CAIs

The mineralogically pristine CAIs in primitive (unmetamorphosed) chondrites (e.g., CR2, CO3.0) have uniformly ^{16}O-rich compositions ($\Delta^{17}O \sim -25‰$), indicating formation in an ^{16}O-rich gaseous reservoir (e.g., Itoh et al. 2004; Makide et al. 2009). In contrast, most CAIs in CV chondrites show oxygen isotopic heterogeneity. Melilite and anorthite are ^{16}O-depleted ($\Delta^{17}O > -10‰$) compared to spinel,

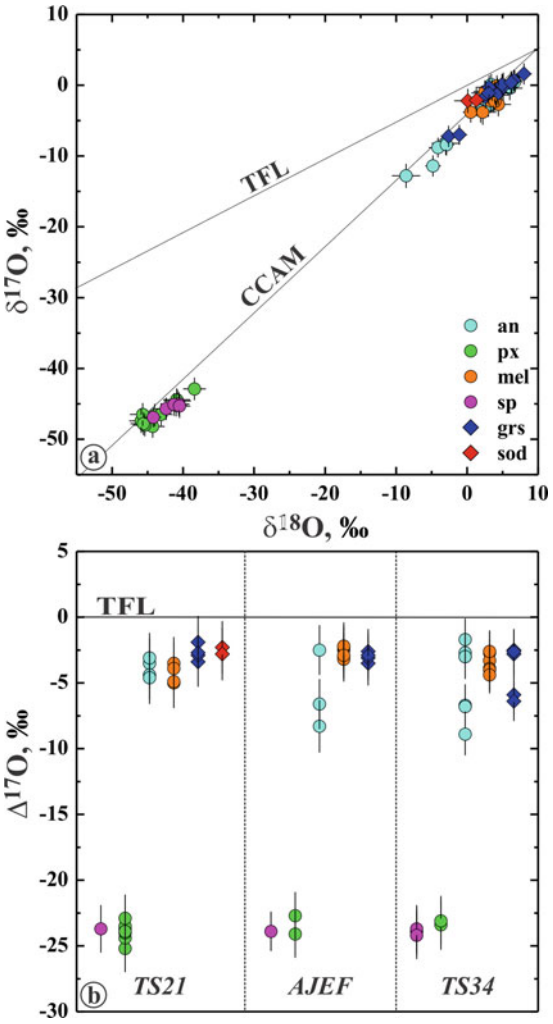

Fig. 15.31 Oxygen isotopic compositions of primary (anorthite, an, melilite, mel, Al,Ti-diopside, px, and spinel, sp) and secondary (grossular, grl and sodalite, sod) minerals in the Allende Type B1 CAIs *AJEF*, *TS21*, and *TS34*. In (**a**), the data are plotted on a three-isotope oxygen diagram. In (**b**), the same data are plotted as deviations from the terrestrial fractionation line, $\Delta^{17}O$. Spinel and Al,Ti-diopside have ^{16}O-rich compositions, whereas anorthite, Al,Ti-diopside, grossular, and sodalite are similarly ^{16}O-depleted (Data from Krot et al. 2010). The terrestrial fractionation line (TFL) and Carbonaceous Chondrite Anhydrous Mineral line (CCAM) are shown for reference

hibonite, Al,Ti-diopside, and forsterite, which have largely retained their original ^{16}O-rich ($\Delta^{17}O \sim -25‰$) compositions (Fig. 15.31; see also Yurimoto et al. 2008 and references therein). Because some melilite and anorthite grains in CV CAIs preserve ^{16}O-rich compositions (e.g., Yurimoto et al. 1998; Kim et al. 2002; Ito et al. 2004; Fagan et al. 2004; Aléon et al. 2005; Krot et al. 2008), oxygen isotopic exchange, between originally ^{16}O-rich CAIs and a ^{16}O-depleted external reservoir, is required.

Several mechanisms have been proposed to explain the nature of the selective isotopic exchange in the CV CAIs; however, they either have some problems or require experimental confirmation. (1) High-temperature gas–solid exchange in the solar nebula (Clayton et al. 1977) is inconsistent with the measured oxygen

self-diffusion in melilite, anorthite, diopside, and spinel (Yurimoto et al. 1989; Ryerson et al. 1989; Ryerson and McKeegan 1994). (2) Isotopic exchange between ^{16}O-rich CAI melt and ^{16}O-poor nebular gas either during CAI melting or crystallization is inconsistent with the inferred crystallization sequence of the CAI melts (e.g., Stolper 1982; Stolper and Paque 1986). (3) Yurimoto et al. (1998) suggested that isotopic exchange occurred during disequilibrium melting. Experimental confirmation of this hypothesis is, however, currently absent. (4) Recently, Wasson et al. (2001) and Itoh et al. (2004) reported a correlation between ^{16}O depletion in melilite in CO chondrite CAIs with the petrologic type (3.0−3.8) of the host meteorite. There is also a correlation between the petrologic type of the host meteorite and the degree of alteration resulting in replacement of melilite and anorthite by nepheline, sodalite, andradite, and hedenbergite in CAIs and chondrules from CO chondrites (Tomeoka et al. 1992; Kojima et al. 1995; Russell et al. 1998). Based on these observations, Wasson et al. (2001) hypothesized that the oxygen-isotope composition of melilite from CAIs in metamorphosed CO chondrites resulted from fluid–rock interaction on the CO parent asteroid (see also section 15.2.5). Because the style of alteration of CO and CV chondrites appears to be similar (aqueous/hydrothermal alteration followed by thermal metamorphism) and there is an apparent correlation between the degree of alteration of CV chondrites and their petrologic types (e.g., Krot et al. 1995, 1998a, b; Bonal et al. 2006), the metasomatic alteration of CV CAIs may have been responsible for at least part of the oxygen isotopic exchange in melilite and anorthite. The similar ^{16}O-depleted compositions of melilite, anorthite, and secondary grossular, sodalite, Na-melilite, monticellite, and kushiroite in Allende CAIs (Fig. 15.31; Krot et al. unpublished) are consistent with this hypothesis. The common presence of ^{16}O-rich melilite and/or anorthite in CAIs from Kaba (petrologic type 3.1, Nagashima et al. 2007) and Efremovka (petrologic type 3.1–3.4, Fagan et al. 2004; Aléon et al. 2005; Krot et al. 2008; Nagashima et al. 2010) and the exceptionally rare presence of ^{16}O-rich melilite or anorthite in CAIs from Allende (petrologic type >3.6) supports this suggestion. Experimental data on oxygen-isotope self-diffusion in melilite and anorthite, under hydrothermal conditions, are required to test this hypothesis.

15.2.6 Physico-Chemical Conditions of Metasomatic Alteration of CV Chondrites and Allende Dark Inclusions

15.2.6.1 Physico-Chemical Conditions of Alteration of CV Chondrites

It is inferred that CV chondrites experienced fluid-rock interactions during progressive metamorphism of a heterogeneous mixture of hydrous (probably ices) and anhydrous materials (e.g., Krot et al. 1995, 1998a). Crucial information on the physico-chemical conditions present during the alteration of CV chondrites comes from petrographic studies of the aqueously-altered type I chondrules in CV_{OxB}

chondrites, in which primary anorthitic mesostases and low-Ca pyroxene phenocrysts are replaced to various degrees by Ca-poor, Mg- and Al-rich phyllosilicates, saponite, and Na-phlogopite. Metal nodules in these chondrules are oxidized to magnetite that is replaced mainly by fayalite and Ca,Fe-silicates (Ca,Fe-pyroxenes and andradite). These observations suggest the alteration took place at relatively low temperatures in an environment enriched in H_2O (either a liquid or a vapor) capable of redistributing Ca, Fe, Mg, Si, and Al at least on a local (100s of microns) scale. On the basis of mineralogical observations, thermodynamic analysis of phase relations in the Si-Fe-Ca-O-H system, and the large oxygen isotopic fractionation of coexisting magnetite, fayalite, and Ca,Fe-silicates in CV_{OxB} chondrites, it is inferred that these minerals formed contemporaneously with phyllosilicates at relatively low temperatures ($<350°C$) in the presence of aqueous solutions (Krot et al. 1998b). The common presence of phyllosilicates in the CV_{OxB} chondrites and nearly complete absence of hydrous minerals in the CV_{OxA} chondrites suggest that aqueous alteration in the CV parent asteroid occurred at progressively increasing temperatures and was followed by thermal metamorphism resulting in a loss of aqueous solutions and dehydration of phyllosilicates in the CV_{OxA} chondrites.

Thermodynamic modeling of aqueous alteration in a multisystem compositionally similar to the CV chondrites (Petaev and MFeenko 1997) shows that there are two distinct stages in the alteration process. At low W/R ratios $<0.2–0.3$, no aqueous solution is present in the system, because all the water is consumed by oxidation and hydration reactions.[9] Hydrogen, released by these reactions, forms large volumes of a gaseous phase that contains trace amounts of volatile anionic elements (H, O, S, Cl, and C). At this stage, aqueous alteration could proceed as an isochemical process without appreciable redistribution of cationic elements. At higher W/R ratios, an aqueous solution coexists with the altered rock and is capable of redistributing cationic elements such as Na, Ca, Mg, Fe, Si, and Al among the textural components of the CV chondrites.

Liquid water or an aqueous solution could be present in the interior of the CV parent asteroid only over a limited temperature range. According to the equation of state for water (e.g., Naumov et al. 1971), liquid water coexists with water vapor in the temperature range $0.01-374.15°C$, providing the total pressure in the system is equal or higher than the pressure of saturated water steam at given temperature. At temperatures $> 374.15°C$, an aqueous solution is unstable regardless of the total pressure. At lower temperatures, an upper temperature limit on the stability of an aqueous solution is pressure dependent. Lithostatic pressures in small asteroidal bodies are negligible compared to those created by gases released during fluid–rock interaction and filling the porous spaces (Grimm and McSween 1989). An upper limit on the pressure that the parent body can sustain depends upon the

[9] The water/rock ratio depends upon the Fe^{2+}/Fe^0 ratio in the precursor material. If the CV_R chondrites are the primary precursor materials of the CV_{OxB} chondrites, an aqueous solution in equilibrium with a partially altered CV chondrite should appear at a lower water/rock ratio (<0.1).

tensile strength of the rocks. If the CV chondrite tensile strength is ~ 100 bars, it places an upper temperature limit of ~ 310°C on the presence of an aqueous solution on the CV chondrite parent body. The pressure in the interior of the CV parent body could have been low initially, but release of abundant hydrogen during the early stage of aqueous alteration should have increased the pressure to its upper limit of ~ 100 bars by the time an aqueous solution appears in equilibrium with partially altered rock. Mineralogical observations (see Sect. 15.2.2), and a wide range of oxygen isotopic compositions of secondary minerals (see Sect. 15.2.5.2), indicate that complete equilibrium during alteration has not been reached, although equilibrium could have been approached on a local scale.

Mineral reactions describing the stability of magnetite, fayalite, hedenbergite, andradite, and kirschsteinite in the Si-Fe-Ca-H-O system in the presence of an aqueous solution and gaseous phase, which are in equilibrium, are as follows:

$$2\ Fe_3O_{4(s)} + 3\ SiO_{2(aq)} + 2\ H_{2(g)} = 3\ Fe_2SiO_{4(s)} + 2\ H_2O_{(g)} \tag{15.23}$$

$$\begin{aligned} 2\ Fe_3O_{4(s)} + 6\ SiO_{2(aq)} + 3\ {Ca^{2+}}_{(aq)} + 2\ H_{2(g)} \\ = 3\ CaFeSi_2O_{6(s)} + 3\ {Fe^{2+}}_{(aq)} + 2\ H_2O_{(g)} \end{aligned} \tag{15.24}$$

$$Fe_2SiO_{4(s)} + {Ca^{2+}}_{(aq)} + SiO_{2(aq)} = CaFeSi_2O_{6(s)} + {Fe^{2+}}_{(aq)} \tag{15.25}$$

$$\begin{aligned} 9\ CaFeSi_2O_{6(s)} + 4\ H_2O_{(g)} = 3\ Ca_3Fe_2Si_3O_{12(s)} + Fe_3O_{4(s)} \\ + 9\ SiO_{2(aq)} + 4\ H_{2(g)} \end{aligned} \tag{15.26}$$

$$\begin{aligned} 5\ Fe_2SiO_{4(s)} + 6\ {Ca^{2+}}_{(aq)} + SiO_{2(aq)} + 2\ H_2O_{(g)} \\ = 2\ Ca_3Fe_2Si_3O_{12(s)} + 6\ {Fe^{2+}}_{(aq)} + 2\ H_{2(g)} \end{aligned} \tag{15.27}$$

$$\begin{aligned} 5\ Fe_3O_{4(s)} + 9\ SiO_{2(aq)} + 9\ {Ca^{2+}}_{(aq)} + 2\ H_{2(g)} \\ = 3\ Ca_3Fe_2Si_3O_{12(s)} + 9\ {Fe^{2+}}_{(aq)} + 2\ H_2O_{(g)} \end{aligned} \tag{15.28}$$

$$Fe_2SiO_{4(s)} + {Ca^{2+}}_{(aq)} = FeCaSiO_{4(s)} + {Fe^{2+}}_{(aq)} \tag{15.29}$$

$$FeCaSiO_{4(s)} + SiO_{2(aq)} = FeCaSi_2O_{6(s)} \tag{15.30}$$

$$\begin{aligned} 2\ Fe_3O_{4(s)} + 3\ SiO_{2(aq)} + 3\ {Ca^{2+}}_{(aq)} + 2\ H_{2(g)} \\ = 3\ CaFeSiO_{4(s)} + 3\ {Fe^{2+}}_{(aq)} + 2\ H_2O_{(g)} \end{aligned} \tag{15.31}$$

$$9\ CaFeSiO_{4(s)} + 4\ H_2O_{(g)} = 3\ Ca_3Fe_2Si_3O_{12(s)} + Fe_3O_{4(s)} + 4\ H_{2(g)} \tag{15.32}$$

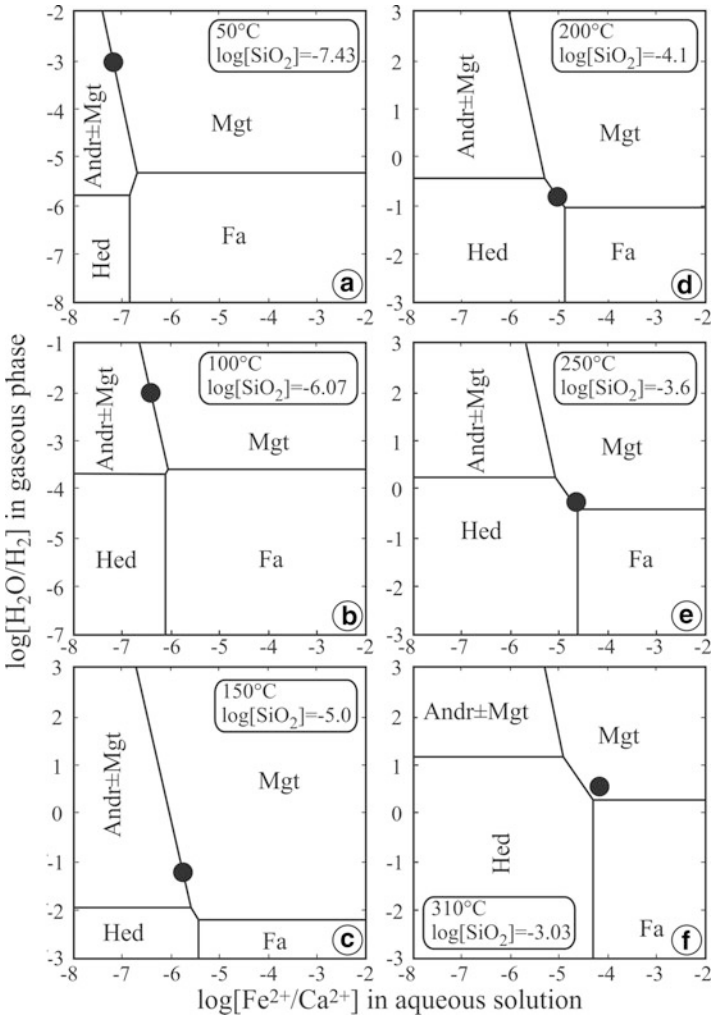

Fig. 15.32 Phase relations among hedenbergite (Hed), andradite (Andr), fayalite (Fa), and magnetite (Mgt) in the Si-Fe-Ca-O-H system at different temperatures. *Solid circles* show compositions of aqueous solutions and gaseous phases equilibrated with the Kaba matrix at corresponding temperatures (Petaev and MFeenko 1997). Values of log[SiO_2] are from Petaev and MFeenko (1997). Andradite in the upper left fields of all diagrams is the only mineral equilibrated with magnetite and fayalite. Magnetite shown in addition to andradite, is an excess phase included to account for the mass-balance of the reaction 9Hed ↔ 3Andr + Mgt (from Krot et al. 1998b)

Phase relations among the Ca,Fe-silicates, described by Reactions 15.23−15.32, are shown in Fig. 15.32 at different temperatures as functions of the Fe^{2+}/Ca^{2+} ratio of the aqueous solution and the H_2O/H_2 ratio of the gaseous phase. The activities of SiO_2 shown in the plots are those of an aqueous solution equilibrated with the Kaba

matrix at corresponding temperatures and a total pressure of 100 bar (Petaev and MFeenko 1997). There are four stability fields in the diagrams for the Si-Fe-Ca-O-H system. Fayalite is stable in equilibrium with a relatively reducing gaseous phase (low $\log[H_2O/H_2]$ values) and a Fe^{2+}-rich aqueous solution (high $\log[Fe^{2+}/Ca^{2+}]$ values). Hedenbergite can be formed in the presence of a Ca^{2+}-rich aqueous solution and reducing gaseous phase. Magnetite requires an oxidizing gaseous phase and a Fe^{2+}-rich aqueous solution. Andradite would be the only mineral equilibrated with an oxidizing gaseous phase and a Ca^{2+}-rich aqueous solution. Magnetite shown in the upper left fields of all diagrams, in addition to andradite, is an excess phase included to account for the mass-balance of Reaction 15.26.

Temperature increase tends to enlarge the hedenbergite stability field at the expense of all other minerals. There is also an important change in the topology of the phase diagrams at some temperature slightly above 100°C. At lower temperatures, the stability fields of magnetite and hedenbergite are separated by the assemblage fayalite and andradite, which may replace one another by Reaction 15.27. In this case, the phase boundary that separates the stability fields of hedenbergite and andradite ± magnetite (Reaction 15.26) is ambiguous and may be valid only if magnetite is in excess. On the contrary, at higher temperature, fayalite and andradite are separated by hedenbergite and magnetite (cf. Reaction 15.24). As a result, fayalite and andradite cannot coexist if equilibrium in the system is maintained. Kirschsteinite is metastable relative to hedenbergite at all temperatures due to the high activity of SiO_2 in the aqueous solution equilibrated with the Kaba matrix.

To apply the calculated phase diagrams to the analysis of alteration processes in the CV3 chondrites, one needs to know variations in the intensive parameters during the alteration process, i.e. temperature, pressure, and values of $\log[Fe^{2+}/Ca^{2+}]$ and $\log[H_2O/H_2]$. Values of the $\log[Fe^{2+}/Ca^{2+}]$ for the aqueous solution and $\log[H_2O/H_2]$ for the gaseous phase, equilibrated with the Kaba matrix (Petaev and MFeenko 1997), are shown in the diagrams by solid circles. These are assumed to be representative of the aqueous alteration conditions on the CV3 chondrite parent body. If complete equilibrium among the Ca,Fe-silicates, gaseous phase and aqueous solution could be attained in the CV3 chondrite parent body, then the low-temperature (<200°C) mineral assemblage would consist of magnetite and andradite. When temperature reaches ~200°C andradite and a portion of magnetite will be replaced by hedenbergite by Reaction 15.26 until andradite or magnetite completely disappear. The assemblage of andradite, hedenbergite and magnetite would mean that Reaction 15.26 has not gone to completion. At ~250°C, the compositions of the gaseous phase and aqueous solution plot in the magnetite stability field very close to the invariant point of the three phase mineral assemblage of hedenbergite, magnetite, and fayalite, implying that fayalite could replace magnetite by Reaction 15.23. At higher temperatures, the compositions of the gaseous phase and aqueous solution move away from the invariant point along the fayalite-magnetite phase boundary. This may result in substitution of fayalite for hedenbergite by Reaction 15.25.

The major portion of the aqueous solution was probably contained in the matrix pore space. It is not unreasonable to expect that the chemical composition of a major portion of this aqueous solution, which is in reactive contact with the matrix, would be more or less homogeneous due to the fine grain size of the matrix, its overall homogeneity, and close contact between the matrix minerals and the aqueous solution. However, some portions of the aqueous solution, which are in reactive contact with Fe- or Ca-rich components such as ferroan olivine, magnetite, chondrule mesostases, and CAIs, could be locally enriched in Fe or Ca, respectively, due to the high concentrations of these elements in the solid phases. Whether an aqueous solution will be homogeneous throughout the rock or not depends upon the efficiency of mixing of different portions of the aqueous solution. If large amounts of an aqueous solution move (flow) through a rock, then thorough mixing of different portions of an aqueous solution could be expected, such that the aqueous solution will be compositionally homogeneous. However, if only small amounts of an aqueous solution are present in the porous space of a rock (or an aqueous solution percolates through the rock at a rate, which is much slower than the diffusional exchange of cations through the aqueous solution among compositionally different phases), then strong compositional gradients, among portions of an aqueous solution equilibrated with different minerals, may develop. Such compositional gradients would exist in the system until complete equilibrium between the aqueous solution and all minerals is achieved. In the case of CV chondrites, bulk oxygen isotopic compositions suggest that only a limited amount of liquid water has exchanged oxygen with anhydrous precursor materials (Clayton and Mayeda 1999). It is inferred that there was no extensive flow of an aqueous solution and that efficient mixing of aqueous solutions did not occur, resulting in large local chemical gradients (e.g., abundance of Ca^{2+}, Fe^{2+}, and Mg^{2+}) in the aqueous solution (Krot et al. 1998b). Since an aqueous solution is a highly conductive medium, large concentration gradients of Ca^{2+} and Fe^{2+} ions will result in diffusional fluxes of these cations through the aqueous solution which would tend to homogenize it. In such a scenario, the replacement of magnetite by Ca,Fe-silicates is caused by electrochemical reactions that take place on a local scale under conditions of very high Ca^{2+}/Fe^{2+} ratios in the aqueous solution.

More recent equilibrium calculations in the water-chondrite system (Zolotov et al. 2006; Jogo et al. 2009) show that fayalite forms at temperatures between 60°C and 200°C, W/R ratio of 0.07−0.18, $f\mathrm{H_2}/f\mathrm{H_2O}$ of 30−4,000, and a pressure that exceeds that of water saturation (Fig. 15.33). The pressure excess is attributed to H_2 gas formed through the oxidation of Fe,Ni metal by water. At a higher W/R ratio, fayalite can be stable at slightly higher temperatures. Pure fayalite (Fa_{100}) forms at lower temperatures such that the fayalite number decreases with increasing temperature. Under reducing conditions (lower W/R and higher $f\mathrm{H_2}/f\mathrm{H_2O}$ ratios), magnetite is absent from fayalite-bearing assemblages. Equilibrium calculations imply that fayalite can form as a rare and transient mineral during the aqueous to metamorphic transition in parent asteroids.

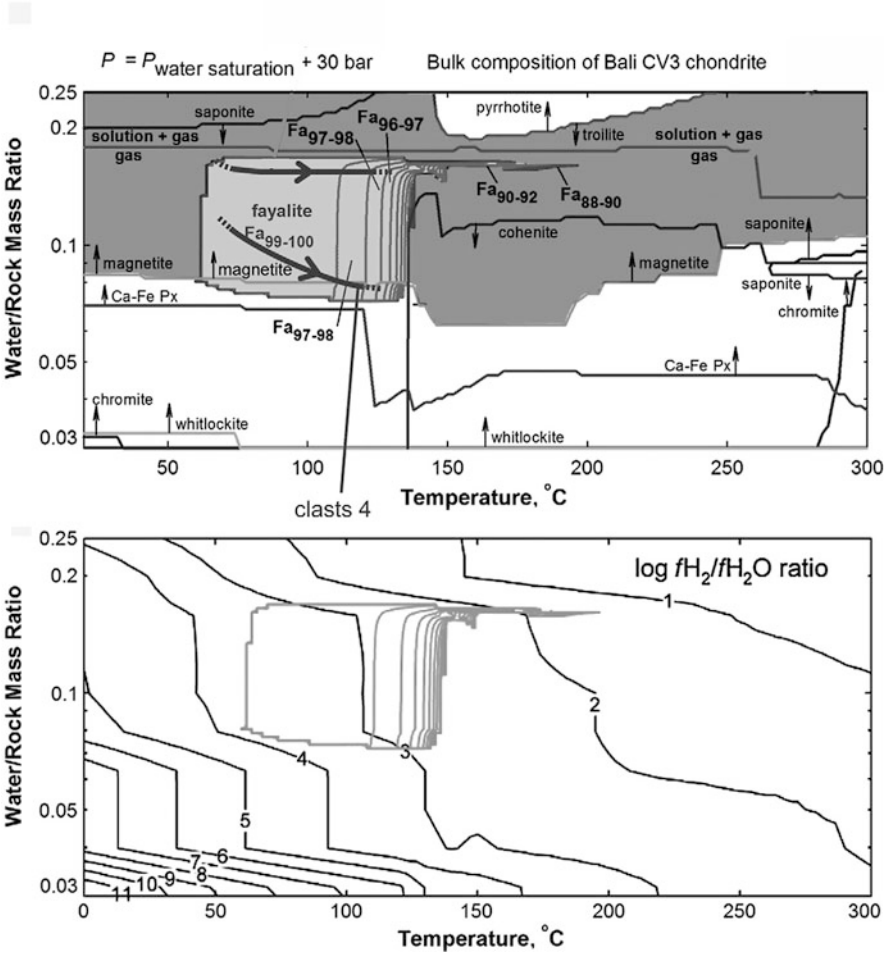

Fig. 15.33 The equilibrium mineralogy formed through alteration of a CV_{OxB}-like bulk composition at total pressure (P) of 30 bar above pressure of water saturation as a function of temperature and bulk water/rock (W/R) mass ratio. (**a**) The *dark gray curve* shows the boundary between aqueous and metamorphic conditions. The closed *light-gray* fields show conditions where fayalite is present in equilibrium mineral assemblages. In each field, the fayalite content of ferroan olivine is indicated. Other *curves* with *arrows* represent boundaries of stability for some minerals present in the calculated equilibrium assemblage. Minerals are present to the side of the *curve* where each *arrow* points. The *light gray* field represents the coexistence of fayalite, troilite, and magnetite. (**b**) The fH_2/fH_2O ratio represents redox conditions in the water-chondrite system ($\log fO_2 = -2 \log(fH_2/fH_2O) - \log K$, where K is the equilibrium constant of the H_2O dissociation reaction) for the calculations presented in (**a**). High W/R ratios and elevated temperature are characterized by lower fH_2/fH_2O ratios, which correspond to more oxidizing conditions. The *dark gray curve* shows the fayalite stability field. Fayalite forms at moderately reduced conditions that are characterized by an excess of H_2 in the system (at fH_2/fH_2O from 30 to 4,000) (From Jogo et al. 2009)

15.2.6.2 Growth of Ca-Rich Rims Around Allende Dark Inclusions

Petrographic observations described above (see Sect. 15.2.3.2) indicate that Ca-rich rims around Allende dark inclusions grew *in situ*, at the interface between the dark inclusions and the host Allende. Because the growth of the Ca-rich rims requires significant mass transport (re-mobilization) of Ca, Fe, Si, and Mg, aqueous solutions must have played an important role in this process. This is supported by the laboratory experiments of Jones and Brearley (2006) showing a rapid mobilization of Ca during low-temperature (~200°C) aqueous alteration of Allende.

The mineralogical reactions observed in the Ca-rich rims, i.e. replacement of andradite by hedenbergite and wollastonite (Fig. 15.24d), and the rare overgrowths of andradite by kirschsteinite and wollastonite (Fig. 15.24c), can be described by the chemical Reactions 15.33 and 15.34, respectively:

$$\begin{aligned} &Ca_3Fe_2Si_3O_{12(s)} + 2\ SiO_{2(aq)} + H_{2(g)} \\ &\quad = 2\ CaFeSi_2O_{6(s)} + CaSiO_{3(s)} + H_2O_{(g)} \end{aligned} \tag{15.33}$$

$$Ca_3Fe_2Si_3O_{12(s)} + H_{2(g)} = 2\ CaFeSiO_{4(s)} + CaSiO_{3(s)} + H_2O_{(g)} \tag{15.34}$$

Additional constraints could be placed on the stability fields of andradite and hedenbergite by reactions describing the substitution of these minerals by fayalite or magnetite in the Fe^{2+}-rich portion of the system (Reactions 15.25, 15.27, 15.28) or by wollastonite under Ca^{2+}-rich conditions (Reactions 15.35, 15.36):

$$\begin{aligned} &Ca_3Fe_2Si_3O_{12(s)} + 2\ SiO_{2(aq)} + 2\ Ca^{2+}{}_{(aq)} + H_{2(g)} \\ &\quad = 5\ CaSiO_{3(s)} + 2\ Fe^{2+}{}_{(aq)} + H_2O_{(g)} \end{aligned} \tag{15.35}$$

$$CaFeSi_2O_{6(s)} + Ca^{2+}{}_{(aq)} = 2\ CaSiO_{3(s)} + Fe^{2+}{}_{(aq)} \tag{15.36}$$

We note that there is no evidence for the newly-formed magnetite and fayalitic olivine in the Ca-rich rims. Finally, the lack of magnetite, which does not replace fayalitic olivine in the dark inclusions, Ca-rich rims around them, and the Allende matrix adjacent to the rims (but could by Reaction 15.23), places an upper limit on the H_2O/H_2 ratios characteristic of the rim-forming reactions.

The phase relations described by Reactions 15.23, 15.25, 15.27, 15.28, 15.33−15.36 are shown in Fig. 15.34 at temperatures of 200°C and 250°C as a function of the Fe^{2+}/Ca^{2+} ratio of an aqueous solution and the H_2O/H_2 ratio of a gaseous phase.[10] The activities of SiO_2 shown in Fig. 15.34 are those of an aqueous

[10] Magnesium is excluded from thermodynamic analysis by the addition of the activity terms for fayalite and hedenbergite dissolved in the olivine and pyroxene solid solutions, respectively. The ideal models of Fe-Mg exchange in olivine are used.

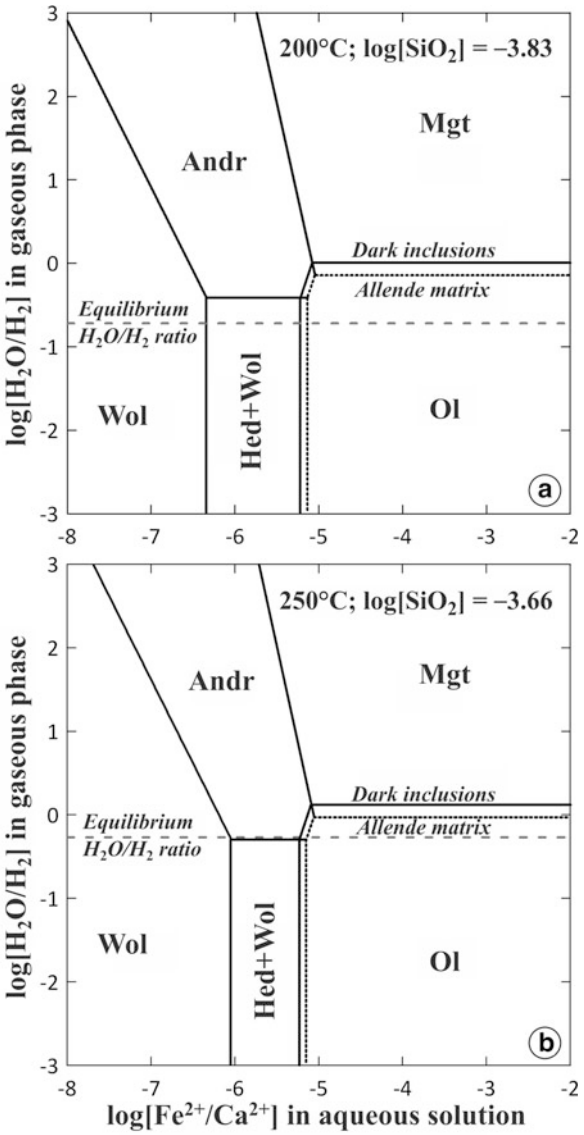

Fig. 15.34 Phase relations among Ca, Fe-rich minerals in the Fe-Ca-Si-O-H system at (**a**) 200°C and (**b**) 250°C. *Andr* andradite, *Hed* hedenbergite, *Mgt* magnetite, *Wol* wollastonite, *Ol* olivine. Stability fields of olivines in the dark inclusions (Fa_{40}) and the Allende host (Fa_{50}) are shown by *solid* and *dotted lines*, respectively. Hedenbergite in the lower middle fields of both diagrams is the only mineral equilibrated with fayalitic olivine. Wollastonite, shown in addition to hedenbergite, is an excessive phase included to account for the observed breakdown of andradite to wollastonite and hedenbergite by Reaction 15.33. *Dashed lines* show H_2O/H_2 ratios of the gaseous phases equilibrated with the aqueous solutions. At a temperature of ~250°C, olivines from both the dark inclusions and Allende are in equilibrium with andradite, whereas at ~200°C the equilibrium mineral assemblage consists of fayalitic olivine and hedenbergite (From Krot et al. 2001)

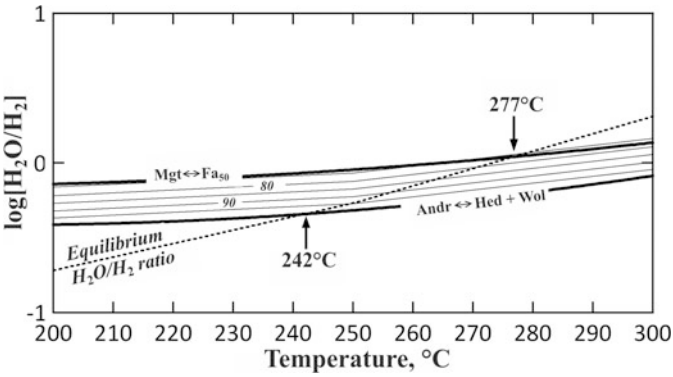

Fig. 15.35 Temperature stability of Ca,Fe-rich silicates in the Fe-Ca-Si-O-H system: *Andr* andradite, Fa_{50} Allende matrix olivine, *Hed* hedenbergite, *Mgt* magnetite, *Wol* wollastonite. *Thin lines* show the phase boundaries of Reaction 15.33 (Andr = Hed + Wol) at different hedenbergite contents in pyroxenes indicated by numbers. *Dotted line* shows variations of the equilibrium H_2O/H_2 ratios in the gaseous phase. Intersection of the *dotted line* with the andradite–hedenbergite–wollastonite phase boundary at 242°C defines the lower temperature limit of andradite stability. At temperatures above 277°C, Allende matrix olivine becomes unstable and must be replaced by magnetite if equilibrium among the gaseous phase, aqueous solution and solid phases is to be maintained (From Krot et al. 2001)

solution equilibrated with the Allende matrix at corresponding temperatures and a total pressure of 100 bars. In the phase diagrams, X_{Fa} values[11] of 0.5 and 0.4 are used as representative of the matrix olivines in the Allende host and central zones of the Allende dark inclusions, respectively. Since andradite in the central zones of the Ca-rich rims coexists with essentially pure hedenbergite, $X_{Hed} = 1.0$ is used.

There are five stability fields in the diagrams of the Ca-Fe-Si-O-H system (Fig. 15.34). Ferroan olivine is stable in equilibrium with a relatively reducing gaseous phase and Fe^{2+}-rich aqueous solution. Wollastonite is stable in the presence of a Ca^{2+}-rich aqueous solution regardless of the redox conditions. Magnetite requires an oxidizing gaseous phase and Fe^{2+}-rich aqueous solution. The stability fields of andradite and hedenbergite are squeezed between those of wollastonite from the Ca-rich end of the diagrams, and magnetite and ferroan olivine from the Fe-rich end. Wollastonite and hedenbergite (as an excess phase) in the lower middle fields of both diagrams, is included to account for the decomposition of andradite by Reaction 15.33. Kirschsteinite is unstable relative to hedenbergite at all temperatures due to the high concentration of SiO_2 in the aqueous solution.

The temperature increase from 200°C to 250°C enlarges the stability field of wollastonite at the expense of andradite and hedenbergite, but has little effect on the other phase boundaries (Fig. 15.34). The only important difference between the diagrams is the value of the equilibrium H_2O/H_2 ratio in the gaseous phase, which

[11] X_{Fa} and X_{Hed} = Fe/(Fe + Mg) in ferroan olivine and ferroan diopside – hedenbergite pyroxene, respectively.

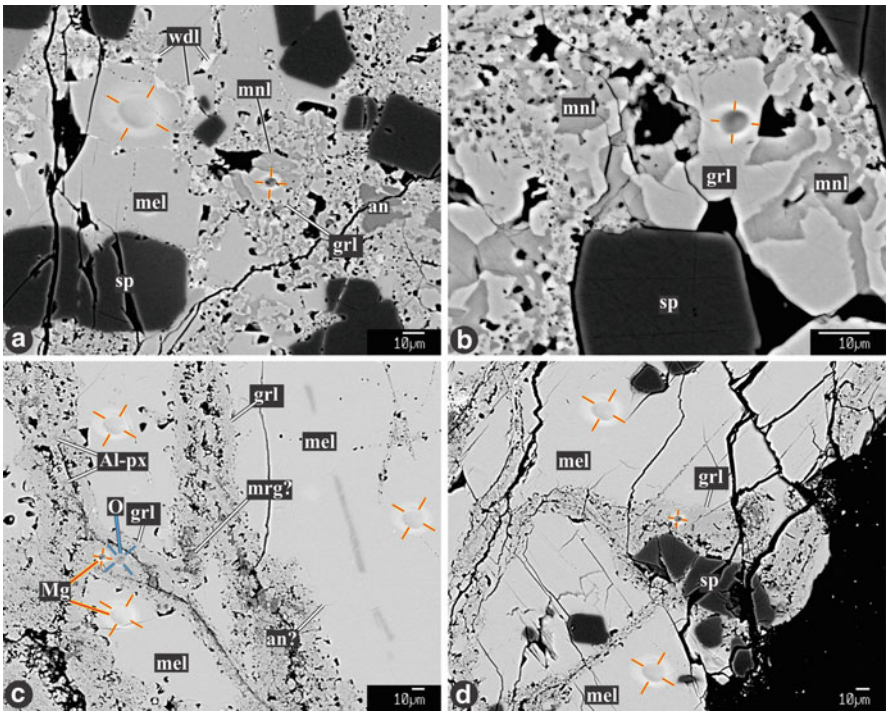

Fig. 15.36 BSE images of core (**a**, **b**) and mantle (**c**, **d**) regions of a Type B CAI *TS34* from Allende. In the CAI core, åkermanitic melilite is replaced by grossular associated with abundant monticellite and wadalite. In the CAI mantle, gehlenitic melilite is crosscut by veins composed largely of grossular. Al-diopside and elongated crystals (margarite?) are minor. *Yellow-orange* and *blue-cyan lines* indicate regions sputtered during oxygen- and Mg-isotope measurements. *Al-px* aluminum-diopside, *an* anorthite, *mel* melilite, *mnl* monticellite, *mrg(?)* margarite(?), *sp* spinel, *wdl* wadalite

has a significant effect on Reaction 15.33. At 250°C, the gaseous phase is oxidizing enough to stabilize andradite. At 200°C, if equilibrium in the Ca-Fe-Si-O-H system is maintained, andradite would breakdown to hedenbergite and wollastonite.

The temperature at which andradite, hedenbergite, and wollastonite are stable altogether can be found by plotting the H_2O/H_2 ratios from both Reaction 15.33 and the gaseous phase equilibrated with the aqueous solution in the log $[H_2O/H_2]$ versus temperature plot (Fig. 15.35). This plot also shows an H_2O/H_2 ratio from Reaction 15.23. Pure hedenbergite coexists with andradite, wollastonite, and ferroan olivine (Fa_{50}) at 242°C. A decrease in X_{Hed} in pyroxene moves the phase boundary of Reaction 15.33 towards higher temperatures until the maximum stability temperature (277°C) for ferroan olivine (Fa_{50}) is reached. Since the Allende dark inclusions, the Ca-rich rims around them, and the Allende matrix adjacent to the rims lack magnetite, this temperature places an upper limit on the rim-forming event. It also

defines a minimum X_{Hed} value for pyroxene of ~ 0.75, which can be in equilibrium with andradite, wollastonite, and the Allende matrix olivines.

Because the sizes of the mineral stability fields shown in Fig. 15.34, strongly depends on the log [SiO_2], whereas the equilibrium H_2O/H_2 ratios in the gaseous phase depends only upon temperature and total pressure in the system, the estimated temperatures of the andradite − hedenbergite + wollastonite and magnetite − olivine phase boundaries (Fig. 15.35) are very sensitive to the accepted log [SiO_2] values. An increase in log [SiO_2] will move the andradite − hedenbergite + wollastonite and magnetite−olivine phase boundaries toward a higher H_2O/H_2 ratios in Fig. 15.35. This will result in an increase of the estimated temperatures for andradite − hedenbergite + wollastonite and olivine−magnetite equilibria. However, the temperature cannot exceed 310°C, which is the upper temperature limit for the existence of an aqueous solution at 100 bar (see above).

Mineralogical observations indicate that the Ca-rich rims coexist with the matrix olivines in the host Allende and Allende dark inclusions, which have different compositions (~ Fa_{50} and Fa_{40}, respectively). The stability fields of olivine with fayalite contents of 40 and 50 are plotted in Fig. 15.35. Although the sizes of these stability fields change slightly with temperature, the offset between Fa_{40} − hedenbergite and Fa_{50} − hedenbergite, and Fa_{40} − andradite and Fa_{50} − andradite phase boundaries remains the same. This means that if equilibrium among minerals and aqueous solutions is locally maintained, the aqueous solution equilibrated with an assemblage of ferroan olivine and ferroan diopside-hedenbergite pyroxene in the dark inclusions would have a Fe^{2+}/Ca^{2+} ratio lower by a factor of about 1.2 than that in the host Allende. These compositional gradients will set up the diffusional fluxes of Ca^{2+} ions from the dark inclusions towards the host Allende and Fe^{2+} ions in the opposite direction, which will drive the reactive system towards equilibrium. We note that the compositional gradients and diffusional exchange of Ca and Fe between the solutions could exist only if the solutions are stagnant in the pores of the host Allende matrix and the Allende dark inclusions. Mixing of the solutions with slightly different compositions at the Allende matrix−dark inclusion interface will increase the concentrations of both Ca^{2+} and Fe^{2+} ions above the solubility limit of a Ca,Fe-rich phase, which will precipitate in the cavities along the interface as a rim. It is inferred that the higher concentration of Fe^{2+} ions in an aqueous solution equilibrated with the host Allende matrix and acted as a geochemical barrier for Ca^{2+} ions dissolved from the dark inclusions. Precipitation of Ca-rich minerals depleted the solution in both Ca^{2+} and Fe^{2+} ions at the Allende matrix−dark inclusion interface. Subsequently these ions can be supplied to the solution again from the dark inclusions and Allende matrix.

Rim formation will continue until matrix olivines in the dark inclusion and Allende matrix become equilibrated, or the Ca-rich objects in the dark inclusions are exhausted, or when the aqueous solution dries out or is lost from the system. Petrographic observations indicate that neither complete exhaustion of the dark inclusions in Ca, nor complete equilibrium between the dark inclusions and Allende matrix, has been achieved. As a result, the growth of the Ca-rich rims was probably terminated by the disappearance of the aqueous solution.

15.2.7 *Dating of Metasomatic Alteration and Thermal Metamorphism of CV Chondrites*

15.2.7.1 ^{26}Al-^{26} Mg Dating of Secondary Nepheline, Sodalite, Anorthite, and Grossular

^{26}Al is a short-lived radionuclide that undergoes β decay to ^{26} Mg with a half-life of ~0.72 Ma. Excess ^{26} Mg (^{26} Mg*) can be detected by SIMS or by other mass spectrometric techniques in bulk samples or mineral fractions (e.g., inductively-coupled plasma mass-spectrometry, ICP-MS). If ^{26} Mg* is derived from the *in situ* decay of ^{26}Al, then the data points plotted as δ^{26} Mg (‰ deviation from the terrestrial ^{26} Mg/^{24} Mg ratio of 0.13932) against the ^{27}Al/^{24} Mg ratio will define a straight line (Al-Mg isochron) with the slope proportional to ^{26}Al/^{27}Al at the time of Al-Mg isotope system closure. The solar system initial ^{26}Al/^{27}Al ratio, called the "canonical" and estimated from high-precision measurements of CAIs, the oldest Solar System solids[12] (Amelin et al. 2002, 2010), is ~5.25 × 10^{-5} (Jacobsen et al. 2008). The difference in the initial ^{26}Al/^{27}Al ratios between the unknown sample and the canonical ^{26}Al/^{27}Al ratio in CAIs corresponds to their relative formation age:

$$\Delta t_{\text{sample}-\text{CAI}}(\text{Ma}) = 1/\lambda \times \ln\left[\left(^{26}\text{Al}/^{27}\text{Al}\right)_{\text{CAI}}/\left(^{26}\text{Al}/^{27}\text{Al}\right)_{\text{sample}}\right] \qquad (15.37)$$

where $\lambda = \ln 2/0.72$ is the ^{26}Al decay constant.

Secondary nepheline, sodalite, anorthite, and grossular (minerals with high Al/Mg ratios suitable for measurements by SIMS) in most of the coarse-grained CAIs from CV_{OxA} chondrites show no evidence for resolvable ^{26} Mg*, suggesting their formation took place at least several half-lives of ^{26}Al after crystallization of the primary minerals in the host CAIs (e.g., Hutcheon and Newton 1981; Hsu et al. 2006; Fagan et al. 2007; Jacobsen et al. 2008).

Variable excesses of ^{26} Mg, corresponding to a range of $(^{26}\text{Al}/^{27}\text{Al})_0$ ratios from $<4 \times 10^{-7}$ to $(5-6) \times 10^{-5}$, were reported in nepheline and sodalite replacing melilite and/or anorthite in a fine-grained spinel-rich CAI (Brigham et al. 1986), and in fine-grained grossular replacing gehlenitic melilite in coarse-grained Type A and Type B CAIs (Fagan et al. 2007; Ushikubo et al. 2007; Krot et al. 2010). MacPherson et al. (1995) and Fagan et al. (2007) interpreted these data as evidence for the early, nebular formation of nepheline, sodalite, and grossular that continued over an extended (several Ma) period of time, possibly on the CV parent asteroid.

This interpretation was questioned by Krot et al. (2010) who described coarse-grained grossular with large ^{26} Mg* and fine-grained grossular without resolvable ^{26} Mg* in a single Allende CAI, TS34. The coarse grossular grains, coexisting with

[12] ^{207}Pb-^{206}Pb absolute age of a forsterite-bearing Type B CAI from Allende corrected for ^{238}U/^{235}U ratio is 4567.22 ± 0.21 Ma (Amelin et al. 2010). This age can be considered as the age of the Solar System.

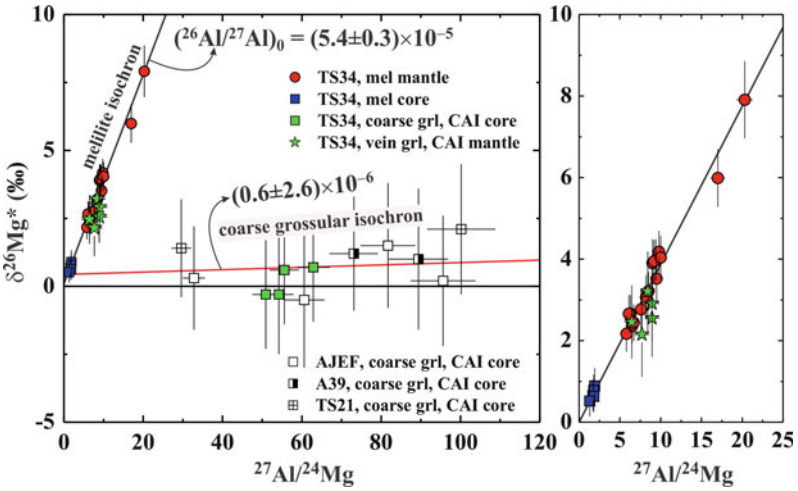

Fig. 15.37 Aluminum-Mg isochron diagram of primary melilite (mel) and secondary grossular (grl) in the Allende Type B CAIs *TS34*, *AJEF*, *A39*, and *TS21*. Region *outlined* in (**a**) is shown in detail in (**b**). Magnesium isotopic compositions of melilite grains in *TS34* define an isochron with a slope of $(5.4 \pm 0.3) \times 10^{-5}$. Coarse grossular replacing åkermanitic melilite in CAI cores and associated with abundant monticellite has a high Al/Mg ratio and no resolvable excess of ^{26} Mg (^{26} Mg*). The upper limit on $(^{26}Al/^{27}Al)_0$ is 3.2×10^{-6} (isochron is forced through åkermanitic melilite). Grossular in the veins replaces gehlenitic melilite of the CAI mantles and is associated with minor Al-diopside. This grossular has a low Al/Mg ratio and shows ^{26} Mg* corresponding to the canonical $(^{26}Al/^{27}Al)_0$ of ~5×10^{-5}. Magnesium isotopic compositions of both types of grossular were inherited from those of melilite of the host CAIs, suggesting grossular formation occurred after nearly complete decay of ^{26}Al, ≥2.9 Ma after crystallization of primary CAI minerals (From Krot et al. 2010)

monticellite and replacing åkermanitic melilite in TS34 (Fig. 15.36), have high Al/Mg ratios (40−120) and no resolvable ^{26} Mg*. An upper limit on $(^{26}Al/^{27}Al)_0$ is 3.2×10^{-6} (Fig. 15.37). Whereas the fine-grained grossular, coexisting with Al-diopside in veins replacing gehlenitic melilite in TS34, has a low Al/Mg ratio (5−10) and large ^{26} Mg* corresponding to $(^{26}Al/^{27}Al)_0$ of ~5×10^{-5} (Fig. 15.37). Both types of grossular have isotopically heavy Mg (δ^{25} Mg ~ 5−6‰), similar to the composition of the melilite they replace, indicating that the Mg-isotopic composition of grossular (and probably other secondary minerals replacing melilite) were inherited from the host melilite (Fig. 15.38). This interpretation may explain variable $(^{26}Al/^{27}Al)_0$ previously reported for secondary anorthite, nepheline, sodalite, and grossular in CV CAIs (Brigham et al. 1986; Ushikubo et al. 2007; Fagan et al. 2007). Krot et al. (2010) suggested that grossular, and other secondary minerals closely associated with it in CV chondrites (e.g., monticellite, wollastonite, forsterite, Na-melilite, Al-diopside, wadalite, corundum, margarite, kaolinite, vesuvianite), formed after the nearly complete decay of ^{26}Al at ≥ 2.9 Ma after crystallization of the primary CAI minerals.

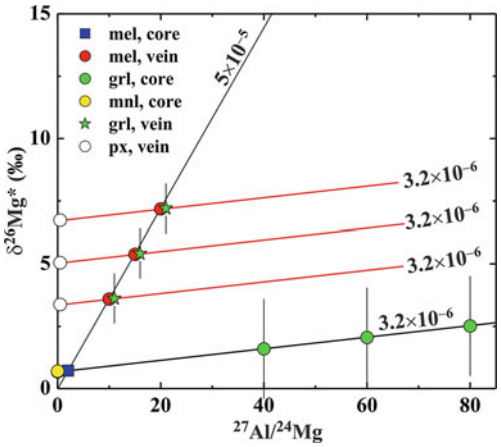

Fig. 15.38 Cartoon explaining contemporaneous formation of grossular with large and without resolvable ^{26} Mg* in the Type B CAI *TS34* (see Fig. 15.37). Formation of secondary Al- and/or Mg-bearing minerals (grossular, monticellite, Al-diopside) replacing primary melilite resulted in Al/Mg fractionation. Magnesium isotopic compositions of the secondary minerals were inherited from the host melilite at the time of their formation. To construct a proper isochron representing the age of alteration, Mg-isotopic compositions of secondary minerals, and the primary minerals replaced by them, need to be considered together. For example, åkermanitic melilite in the *TS34* core is replaced by monticellite and Mg-poor grossular. Within uncertainty of SIMS measurements, ~2‰, no observable excess is found in this grossular. An isochron with a slope of 3.2×10^{-6}, representing an upper limit for Mg-poor grossular, is constructed using data for monticellite and åkermanitic melilite. Gehlenitic melilite in the *TS34* mantle is replaced by Mg-rich grossular and Al-diopside, which is minor. The Al/Mg ratio in this grossular is nearly identical to this ratio in the host melilite and, therefore, correlates with the Al/Mg ratio. A set of *isochron lines* with a slope 3.2×10^{-6} are constructed for the Mg-rich grossular, gehlenitic melilite, and Al-diopside (all have variable Mg-isotopic compositions). Both types of grossular formed after nearly complete decay of ^{26}Al, $\geq$2.9 Ma after crystallization of primary CAI minerals. *grl* grossular, *mel* melilite, *mnl* monticellite, *px* Al-diopside

15.2.7.2 ^{53}Mn-^{53}Cr Dating of Secondary Fayalite

^{53}Mn is a short-lived radionuclide that β-decays to ^{53}Cr with a half-life of ~3.7 Ma. The excess of ^{53}Cr (^{53}Cr*), relative to the terrestrial ^{53}Cr/^{52}Cr ratio of 0.113458, can be detected by SIMS in individual minerals having high Mn/Cr ratios ($\geq$100). If ^{53}Cr* is derived from the *in situ* decay of ^{53}Mn, then the data points, plotted as δ^{53}Cr (‰ deviation from the terrestrial ^{53}Cr/^{52}Cr ratio) against the ^{55}Mn/^{52}Cr ratio will define a straight line (Mn-Cr isochron) with the slope proportional to the ^{53}Mn/^{55}Mn ratio at the time of isotope closure of the Mn-Cr system. The relative ages of the two samples, 1 and 2, are then calculated from their ^{53}Mn/^{55}Mn ratios:

$$\Delta t_{1-2}(\mathrm{Ma}) = 1/\lambda \times \ln\left[\left(^{53}\mathrm{Mn}/^{55}\mathrm{Mn}\right)_2 / \ln\left(^{53}\mathrm{Mn}/^{55}\mathrm{Mn}\right)_1\right] \qquad (15.38)$$

where $\lambda = \ln 2/3.7$ is the ^{53}Mn decay constant.

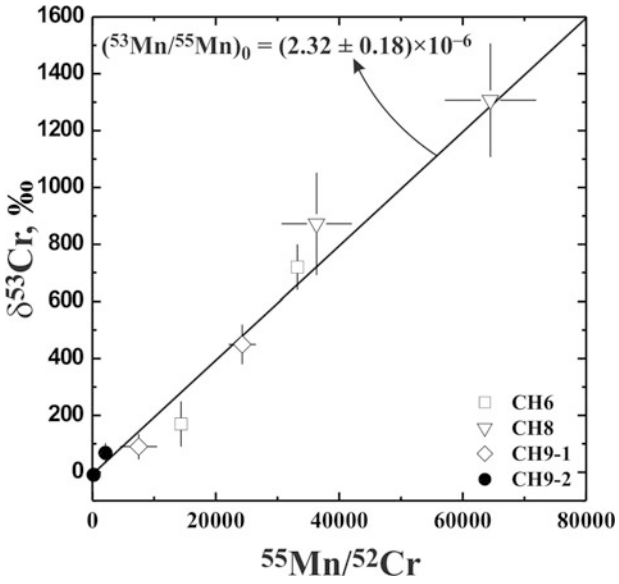

Fig. 15.39 A ^{53}Mn-^{53}Cr evolution diagram for four fayalite grains in three magnesian porphyritic chondrules from Mokoia (CV_{OxB}). The slope of the *line* fitted to the data yield the initial $^{53}Mn/^{55}Mn$ ratio at the time of fayalite formation, of $(2.32 \pm 0.18) \times 10^{-6}$. Errors are two standard deviations. (Data from Hutcheon et al. (1998))

Due to the uncertainty of the solar system initial $^{53}Mn/^{55}Mn$ ratio (estimates range from 0.84×10^{-5} (Lugmair and Shukolyukov 1998) to 4.4×10^{-5} (Birck and Allègre 1988)), the Mn-Cr ages are given relative to the $(^{53}Mn/^{55}Mn)_0$ ratio in angrite North West Africa 4801, $(0.96 \pm 0.04) \times 10^{-6}$ (Shukolyukov et al. 2009), which has an absolute Pb-Pb age of 4558.0 ± 0.13 Ma (Amelin and Irving 2007).

High MnO contents (up to 1.5 wt.%) in secondary fayalite, and the nearly complete absence of Cr (Mn/Cr ratios range up to 2×10^6), favor Cr isotopic measurements of fayalite to constrain its crystallization time (Hutcheon et al. 1998; Hua et al. 2005; Jogo et al. 2009, 2010). Hutcheon et al. (1998) measured Cr-isotopic compositions of fayalite replacing magnetite-sulfide nodules within type I chondrules from Mokoia (CV_{OxB}). Hua et al. (2005) reported Cr-isotopic measurements of fayalite associated with magnetite and sulfides in the Kaba (CV_{OxB}) matrix. Jogo et al. (2009, 2010) measured the Cr-isotopic compositions of fayalite in chondrules and matrices from the Vigarano (CV_R breccia), Asuka 881317 (CV_R breccia), Meteorite Hills (MET) 00430, and MET 01074 ($CV_{OxA/B}$) meteorites. The fayalite grains' large $^{53}Cr^*$, correlated with $^{55}Mn/^{52}Cr$ ratios, are indicative of the *in situ* decay of ^{53}Mn (Fig. 15.39). The inferred initial $^{53}Mn/^{55}Mn$ ratios for fayalite in Mokoia, Kaba, Vigarano, Asuka 881317, MET 00430 and MET 01074 are (2.3 ± 0.2), (2.3 ± 0.4), (2.3 ± 0.5), (1.9 ± 0.5), (1.4 ± 0.5), and $(1.6 \pm 0.8) \times 10^{-6}$, respectively (errors are 2 σ). These ratios correspond to a possible range of absolute ages from ~4,561 to 4,564 Ma, which may represent the duration of fayalite formation on the CV parent asteroid or duration of closure of Mn-Cr isotope systematics in different CV chondrites.

15.2.7.3 ^{129}I-^{129}Xe Dating of Alteration of CV Chondrite Components

^{129}I is a short-lived radionuclide that β-decays to ^{129}Xe with a half-life of 15.7 Ma. If no Xe losses have occurred, the ratio of radiogenic ^{129}Xe (^{129*}Xe) to ^{127}I equals the value for the initial I (^{129}I/^{127}I) at the time of isotopic closure. The analytical technique behind I-Xe dating involves neutron irradiation in a reactor, which converts a fraction of ^{127}I to ^{128*}Xe [^{127}I (n, $\gamma\beta$) $\rightarrow$ ^{128*}Xe]. Correlated quantities of the two I derived Xe isotopes (^{129*}Xe and ^{128*}Xe) are released in a stepwise pyrolysis and measured by an ion counting mass spectrometry. The simplicity of this technique is enhanced by including, in the irradiation, a meteorite standard of known age with the relative I-Xe age then given by the relative slopes of the isochrons (Swindle and Podosek 1988). Typically, the ratio of ^{129}Xe to some Xe isotope not produced in the irradiation, such as ^{130}Xe or ^{132}Xe, is plotted against the ratio of ^{128}Xe to that same isotope. If the ^{128*}Xe and ^{129*}Xe are both derived from I of uniform isotopic composition, then the data points will define a straight line (I-Xe isochron), with the slope proportional to the ^{129}I/^{127}I ratio present the last time the Xe isotopes were in equilibrium. The I-Xe isochron is thus a two-component mixture of trapped and I-derived Xe. The trapped Xe component is confined to lie at the lower end of this isochron and to represent a typical "planetary" composition (Lavielle and Marti 1992). Therefore, I-Xe ages are calculated directly from the differences in the isochron slopes $(^{129*}\mathrm{Xe}/^{128*}\mathrm{Xe})_{\mathrm{sample}}$ with that of the standard $(^{129*}\mathrm{Xe}/^{128*}\mathrm{Xe})_{\mathrm{standard}}$ (Shallowater aubrite or Bjurböle L4 ordinary chondrite; Bjurböle predates Shallowater by 460 Ka, Brazzle et al. 1999):

$$\Delta t_{\mathrm{sample-Shallowater}}(\mathrm{Ma}) = 1/\lambda \times \ln\left[\left(^{129}\mathrm{I}/^{127}\mathrm{I}\right)_{\mathrm{Shallowater}} / \left(^{129}\mathrm{I}/^{127}\mathrm{I}\right)_{\mathrm{sample}}\right] \tag{15.39}$$

where $\lambda = \ln 2/15.7$ is the ^{129}I decay constant; negative/positive values correspond to older/younger ages than Shallowater.

Because I is a mobile element, I-Xe chronometry has been shown to be a promising technique for dating secondary alteration processes that is capable of resolving age differences of a few hundred thousand years between closure times of different mineral phases from the same meteorite (e.g., Swindle 1998; Brazzle et al. 1999; Pravdivtseva et al. 2003a).

^{129}I-^{129}Xe Dating of Alteration of CAIs and Chondrules in CV_{OxA} Chondrites

I-Xe isotope data for the coarse-grained and fine-grained CAIs in Allende, which experienced Fe-alkali metasomatic alteration, encompass a spread of $\geq$10 Ma, suggesting an asteroidal setting during alteration (Swindle et al. 1988). On the basis of the strong correlation of I with Cl in two fine-grained CAIs analyzed by Kirschbaum (1988), together with the fact that sodalite was the only significant

Cl-bearing mineral known in these CAIs, it was inferred that sodalite is the major I-carrier phase. However, the recent discovery of another Cl-bearing mineral, wadalite, in the Allende coarse-grained CAIs (Ishii et al. 2010) may imply that wadalite is another potential I-carrier phase in the Allende fine-grained CAIs as well.

The Xe isotope measurements (Pravdivtseva et al. 2003a) indicate that heavily-altered fine-grained CAIs in Allende define isochrons with ages between 3.1 ± 0.2 and 3.7 ± 0.2 Ma younger than Shallowater (Fig. 15.40). The CAIs have nearly identical release profiles for radiogenic ^{129*}Xe and ^{128*}Xe, suggesting the same I carrier(s) for both.

Although Allende chondrules often contain large fractions of radiogenic Xe, and an I-Xe association suggestive for chronometry, they rarely yield isochrons that are well-defined at the level of precision provided by the isotopic data. Among nine chondrules studied by Swindle et al. (1983), eight have a pattern of increasing model age with each incrementally increased temperature step. This was attributed to relatively slow cooling (~10−20°C/Ma using the lower release temperatures (600−1,100°C) or 50−300°C/Ma using release temperatures above 1,300°C) or the monotonic (with release temperature) relaxation of other conditions during thermal metamorphism or alteration (Swindle et al. 1983; Nichols et al. 1990). One chondrule gave a well-defined isochron with an apparent age of 0.53 ± 0.15 Ma younger than the Bjurböle whole rock age standard (Swindle et al. 1983), and I-Xe ages from four different chondrules gave ages ranging from −0.37 ± 0.16 Ma to 1.54 ± 0.07 Ma, relative to Bjurböle (Nichols et al. 1990).

^{129}I-^{129}Xe Dating of Alteration of CV Dark Inclusions

Xenon isotope compositions were measured in bulk samples from 17 Allende dark inclusions (Pravdivtseva et al. 2003b). All dark inclusions yielded similar release profiles with two major peaks, suggesting two major I carriers (sodalite, and wadalite(?)), and well-defined I-Xe isochrons with ages ranging from 0.5 ± 0.3 to 2.8 ± 0.3 Ma older than the Shallowater internal standard (Fig. 15.41). The I-Xe ages of the dark inclusions are interpreted as the time of their early alteration prior to incorporation into Allende. The younger I-Xe ages of the fine-grained CAIs may reflect metasomatic alteration of the Allende host, which could have occurred contemporaneously with the second stage alteration of the Allende dark inclusions. The lack of evidence for the disturbance of the I-Xe system in the Allende dark inclusions suggests that the fluid responsible for the alteration of the Allende CAIs must have been in equilibrium with the I- and Xe-bearing phases of the dark inclusions, so the latter were not affected by the second stage of alteration.

Xenon isotope compositions were measured in bulk samples of six dark inclusions from CV_R chondrites (Swindle et al. 1998; Krot et al. 1999; Pravdivtseva et al. 2003b). The I carriers in the dark inclusions have not been identified. The I-Xe

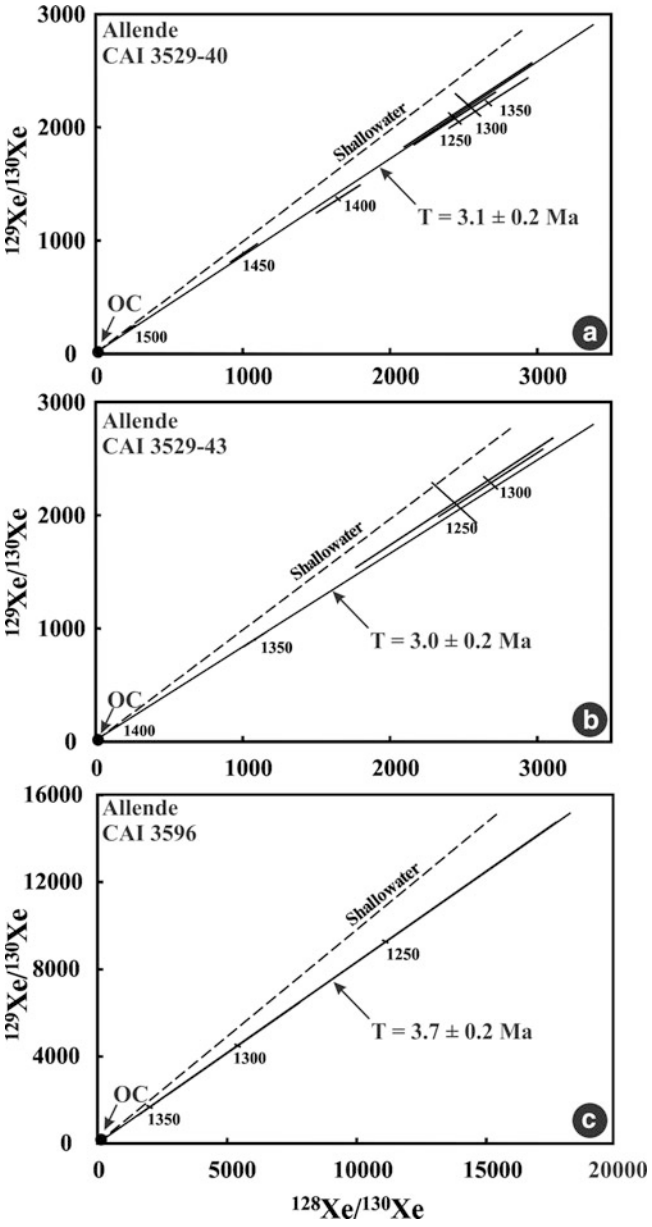

Fig. 15.40 ^{129}I-^{129}Xe evolution diagrams for fine-grained CAIs in Allende (From Pravdivtseva et al. 2003a). I-Xe ages are relative to Shallowater. The contribution from the trapped Xe component is within experimental uncertainty consistent with the "planetary" OC-Xe (From Lavielle and Marti 1992)

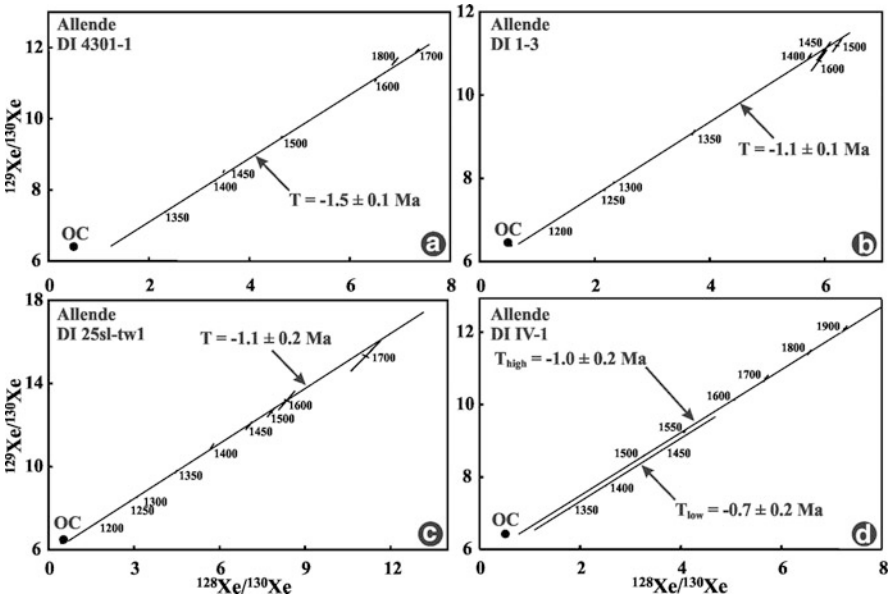

Fig. 15.41 ^{129}I-^{129}Xe evolution diagrams for the Allende dark inclusions *4301-1*, *1-3*, *25 s1-tw1*, and *IV-1*. I-Xe ages are relative to the Shallowater internal standard. Two isochrons plotted for the dark inclusion *IV-1* correspond to low- and high-temperature Xe released. All isochrons suggest a "sub-planetary" trapped component (From Pravdivtseva et al. 2003b)

ages of the dark inclusions range from -4.9 ± 1.8 to 9.5 ± 2.3 Ma relative to Shallowater and are generally younger than those from the Allende dark inclusions.

To summarize, the I-Xe ages of the CV dark inclusions span ~14 Ma, suggesting a long period of metasomatic alteration and thermal metamorphism, most likely on the CV parent asteroid.

15.3 Metasomatic Alteration of CO Carbonaceous Chondrites

15.3.1 Overview

Although the effects of metasomatism in CO chondrites have been known for many years, (Kurat and Kracher 1980; Palme and Wlotzka 1981), it is only relatively recently that the extent of these effects has been fully appreciated (e.g., Jones 1997; Russell et al. 1998; Tomeoka and Itoh 2004). There is now a considerable body of evidence for Fe-alkali metasomatism also affecting chondrules, CAIs, and AOAs in CO chondrites, which has resulted in the formation of secondary minerals (see Table 15.1). Compared with the CV chondrites, the CO carbonaceous chondrites are particularly notable, because of the small size of their constituent components

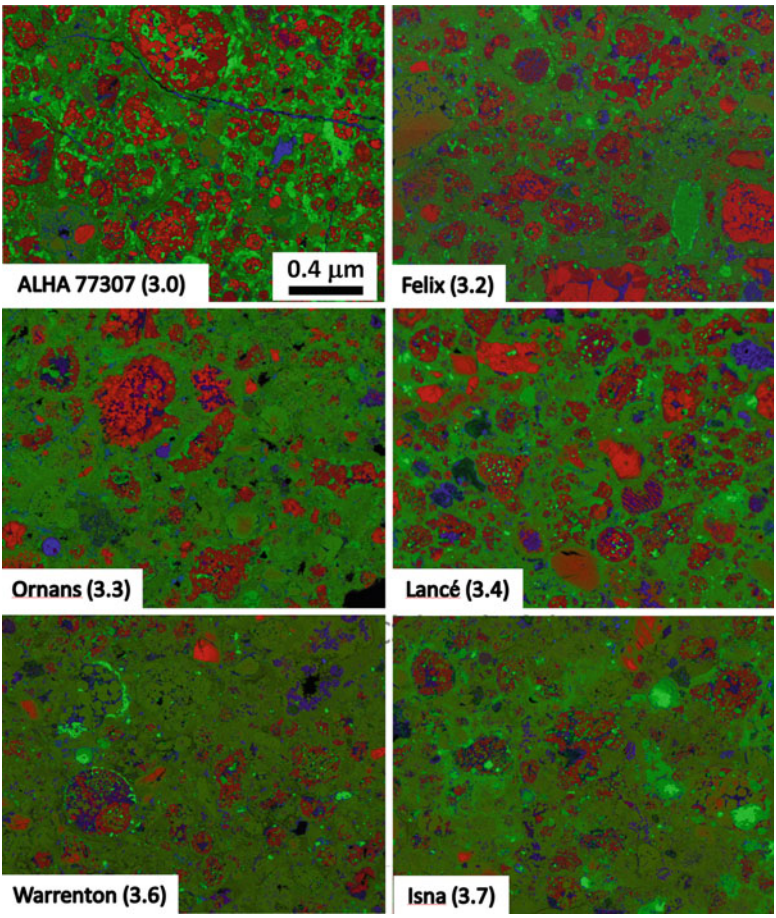

Fig. 15.42 Combined x-ray elemental maps in Mg (*red*), Fe (*green*), and Ca (*blue*) showing the progressive compositional equilibration of Mg-rich silicates in chondrules with the FeO-rich matrix in a sequence of CO3 chondrites from petrologic type 3.0 (ALHA 77307) to type 3.7 (Isna). The images show that in ALHA 77307 Mg-rich chondrule silicates are abundant and clearly defined. The bright red grains are olivine and the duller red are low-Ca pyroxene. By petrologic type 3.3/3.4 the chondrule silicates, particularly olivine have begun to equilibrate with the matrix and are less abundant. By petrologic types 3.6 and 3.7, almost no Mg-rich silicates, except low-Ca pyroxene remain. Olivine has almost fully equilibrated with the matrix resulting in compositions that are more FeO-rich. Scale for all the images is identical to that shown in the image for ALHA 77307

(Fig. 15.42). For example, Rubin (1989) found that the mean apparent diameter of chondrules in CO chondrites is 148 μm compared with, for example, 910 μm in the CV3 chondrites (Paque and Cuzzi 1997) or 300 μm (H), 400 μm (L) and 570 μm (LL) in the ordinary chondrites (Rubin 2010). However, it is apparent that despite the small size of these components and consequent higher susceptibility to alteration, the effects of metasomatism are much less well developed than in the

oxidized CV3 chondrites. The metasomatic events that affected the CO chondrites were clearly either of shorter duration or involved less metasomatizing fluid than the CV3 chondrites. Certainly in comparison with the CV3 chondrites, our understanding of the effects of metasomatism in the CO chondrites is in its infancy, and there is still much to be learned about essentially all aspects of the metasomatic processes. This includes details of the mechanisms of the metasomatic reactions, the timing of the metasomatism, and the stable isotopic composition of the alteration products.

Despite the limited understanding of metasomatism in this group, the CO chondrites are of particular importance, because they are the only carbonaceous chondrite group that exhibits a well-defined metamorphic sequence among its members. At present, this metamorphic sequence extends only from petrologic type 3.00 to petrologic 3.7 (or 3.8 depending on which scheme is used to assign petrologic type – see below); no type 4 or higher CO3 chondrites have yet been found. Although there is some disagreement as to the relative ranking of individual CO chondrites within the metamorphic sequence (e.g., McSween 1977b; Scott and Jones 1990; Sears et al. 1991; Chizmadia et al. 2002; Grossman and Brearley 2005; Bonal et al. 2007; Kimura et al. 2008), there is a widespread consensus that this sequence represents the result of parent body metamorphism. Using the well-established sequence of metamorphic effects, observed in CO chondrites, has allowed researchers to suggest a correlation between increasing metasomatism and metamorphism (see Sect. 15.3.5). For the following discussion, we follow the recommendation of Greenwood and Franchi (2004), and use the petrologic subtypes proposed by Scott and Jones (1990).

15.3.2 Metasomatism in CO Chondrites: Bulk Physical, Chemical and Isotopic Characteristics

In this section, we discuss only bulk, physical, chemical, and isotopic characteristics of the CO chondrites that provide evidence of changes through the petrologic sequence indicative of metasomatism. We discuss the detailed parameters relating to metamorphism in Sect. 15.3.4. Rubin et al. (1985), Rubin (1998), and Greenwood and Franchi (2004) have investigated a variety of different characteristics of this group of meteorites, which provide useful and interesting constraints on the behavior of the CO chondrites through the metamorphic sequence. Each of these different parameters provides a different perspective on the kinds of processes that affected this group of meteorites.

Greenwood and Franchi (2004) examined the bulk oxygen isotopic compositions of CO chondrites and found that through petrologic types 3.1–3.4, there are subtle changes in the oxygen isotopic composition, specifically in $\Delta^{17}O$, which increases in correlation with increasing degrees of metamorphism (Fig. 15.43). However, this systematic change does not continue to higher petrologic types. This evidence was

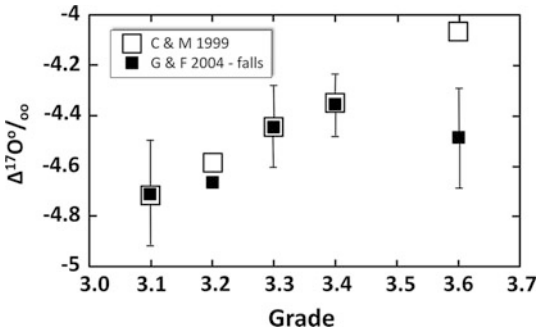

Fig. 15.43 Bulk oxygen isotopic composition of CO3 chondrites (After Greenwood and Franchi 2004 (G&F)). Diagram shows bulk $\Delta^{17}O$ versus metamorphic grade (petrologic type) for CO3 chondrite falls. Data from Clayton and Mayeda (1999) (C&M) are also shown. Through the lower petrologic types there is a systematic increase in $\Delta^{17}O$, which Greenwood and Franchi (2004) have interpreted as being indicative of interaction with aqueous fluids

used by Greenwood and Franchi (2004) to argue that metamorphism of the CO chondrites occurred in the presence of an aqueous fluid. For low petrologic types, they argued that the change in $\Delta^{17}O$ was caused by the progressive formation of phyllosilicates and the destruction of ^{16}O-poor melilite in CAIs (see mineralogical effects below).

Although the oxygen isotopic data indicate that an aqueous fluid was present during thermal metamorphism, these fluids did not cause any apparent changes in the bulk rock composition of the CO chondrites. Bulk major, minor, and trace element compositions for CO chondrites (Kallemeyn and Wasson 1981) show no systematic variations with increasing petrologic type. These data indicate that the processes that affected this group of meteorites were isochemical in character or of too limited extent to affect the bulk chemical compositions of these meteorites.

15.3.3 Metasomatic Alteration of CO Chondrite Components

15.3.3.1 Mineralogy and Petrography

Metasomatic Effects in CAIs in CO Chondrites

CAIs have been widely recognized and described in CO chondrites by a number of workers (Ikeda 1982; Fahey et al. 1994; Holmberg and Hashimoto 1992; Tomeoka et al. 1992; Kojima et al. 1995). However, the most comprehensive study has been performed by Russell et al. (1998) who studied CAIs in a suite of CO chondrites spanning the range of petrologic types from 3.0 to 3.7. The abundance of CAIs in individual CO chondrites is approximately 1 vol.% and is independent of petrologic type. Three major groups of CAIs occur in CO chondrites: (1) melilite-rich

inclusions (Type A), often containing spinel/hercynite, perovskite, and occasionally hibonite; (2) spinel-pyroxene inclusions, which rarely contain perovskite, and (3) hibonite-rich inclusions. Other rarer types of inclusions such as hibonite-pyroxene spherules, rimmed melilite, anorthite-bearing, and grossite-bearing inclusions also occur (Kojima et al. 1995; Russell et al. 1998). Like chondrules in CO chondrites, CAIs are also significantly smaller than their counterparts in CV3 chondrites, with a maximum dimension of 500 μm or less.

Secondary alteration effects have been described in CO CAIs by a large number of authors (Ikeda 1982; Fahey et al. 1994; Holmberg and Hashimoto 1992; Tomeoka et al. 1992; Kojima et al. 1995; Russell et al. 1998; Wasson et al. 2001; Itoh et al. 2004), but extremely detailed studies, such as those that have been carried out for the CV3 chondrites, are generally lacking. The extent of alteration of CAIs in the CO chondrites is heterogeneous within an individual chondrite but is generally correlated with the extent of thermal metamorphism (Kojima et al. 1995; Russell et al. 1998; Itoh et al. 2004). In low petrologic subtypes, alteration is minimal, but with increasing degrees of metamorphism, metasomatic effects increase to the extent that in some cases all the primary components of the CAIs have either been replaced or have had their compositions modified. The complete replacement of all primary CAI phases is certainly facilitated by the smaller size and finer grained nature of CO CAIs in comparison with CV3 CAIs. Russell et al. (1998) found that with increasing petrologic type, the melilite-rich inclusions appear to decrease in abundance and spinel-rich inclusions apparently show an increase.

Several key trends are observed in the alteration of CAIs in CO chondrites as a function of petrologic type (Kojima et al. 1995; Russell et al. 1998; Wasson et al. 2001; Itoh et al. 2004). Alteration of CO CAIs is dominated by the replacement of primary melilite, which is typically fine-grained (~10 μm) in melilite-rich CAIs. Melilite in type 3.0 CO chondrites shows no evidence of alteration, but in higher petrologic types shows progressively more advanced degrees of replacement from the exterior of the inclusion inwards. By petrologic type 3.4, melilite-rich inclusions are rare. Russell et al. (1998) indicated that melilite-bearing inclusions are absent in higher petrologic types, because melilite has been completely replaced. However, this observation is at odds with our own observations of melilite-bearing inclusions in types 3.5−3.7 CO chondrites (Figs. 15.44−15.47), suggesting that metasomatic alteration may be heterogeneously developed even within a single chondrite. The replacement products of melilite in CAIs are dominated by fine-grained nepheline, pyroxene and troilite. There is certainly also evidence of the presence of a Na- and Cl-bearing phase, possibly sodalite. In some melilite-rich inclusions in Kainsaz and Ornans, Wasson et al. (2001) documented hedenbergite and andradite intergrown on the submicron scale with nepheline and Itoh et al. (2004) described small grains of graftonite ($[Fe,Mn,Ca]_3[PO_4]_2$), surrounding nodules of spinel and diopside in an inclusion in Kainsaz. The only other minor Ca-rich phase that has rarely been described in CO CAIs is Fe-bearing monticellite in Felix (CO3.2) (Greenwood et al. 1992) and Yamato 82050 (Kojima et al. 1995). However, because of the fine-grained nature of the alteration products in many melilite-bearing CAIs, the details

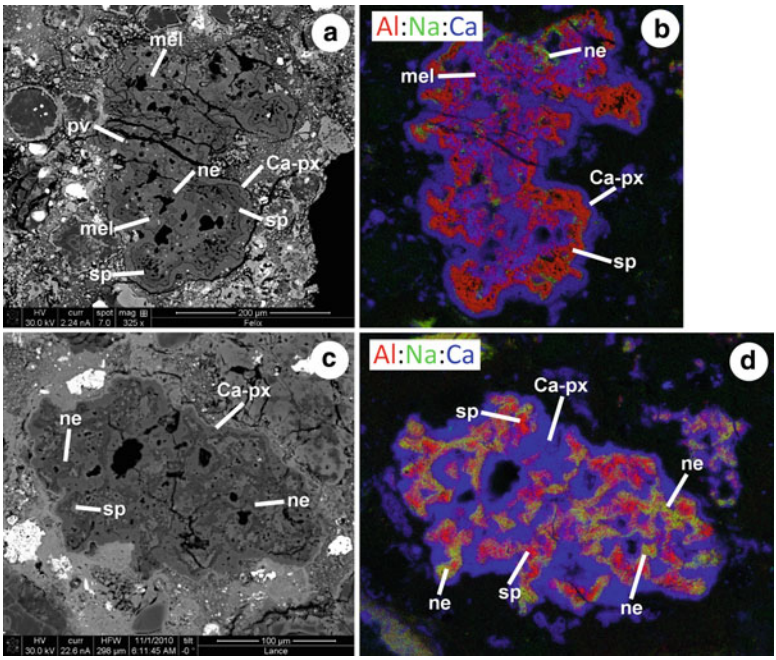

Fig. 15.44 BSE images (**a**, **c**) and combined x-ray elemental maps in Al (*red*), Na (*green*), and Ca (*blue*) (**b**, **d**) illustrating metasomatic alteration in two melilite-bearing CAIs in Felix (CO3.2) and Lancé (CO3.4). (**a**, **b**) A porous, weakly altered melilite-bearing CAI in Felix. The inclusion consists largely of an irregular core of spinel (sp) and Ca-pyroxene (Ca-px), with localized regions of melilite (mel). The inclusion has a continuous rim of Ca-pyroxene. Small grains of perovskite (pv) are present largely within the spinel. The purple regions in (**b**) are areas of melilite which locally shows replacement by a Na-rich phase, possibly nepheline (ne). (**c**) A relatively heavily altered spinel-pyroxene inclusion from Lancé. The inclusion has a continuous rim of Ca-rich pyroxene with an interior of Ca-rich pyroxene (Ca-px), spinel (sp), and nepheline (Ne). Spinel (*red* in (**d**)) is distributed as relatively small grains that are surrounded by regions of nepheline that is probably the replacement product of melilite. No remaining melilite is detectable in the inclusion, indicating that the CAI has been extensively altered, compared with the CAI in Felix

of the secondary phases are still not well understood. Figures 15.44–15.47 show examples of alteration of melilite-bearing CAIs in CO chondrites, ranging from petrologic subtype 3.3–3.7. In these CAIs, melilite has been partially replaced by extremely fine-grained nepheline, both around the periphery of the inclusion and in the interior. Even in Warrenton (CO3.6), melilite is still present but has been quite extensively, but variably replaced. Figure 15.46 shows, for example, a melilite-bearing inclusion in which distinct regions of fine-grained alteration products have replaced melilite, but significant regions of unaltered melilite remain. Russell et al. (1998) also found that unaltered melilite in CO CAIs shows a progressive increase in Fe content from 0.08 wt.% in Allan Hills (ALH) 77307 (CO3.0) to up to ~0.71 wt.% in ALH 82101 (CO3.3). Although rare in CO chondrites, anorthite-bearing CAIs also show evidence of secondary alteration. Kojima et al. (1995)

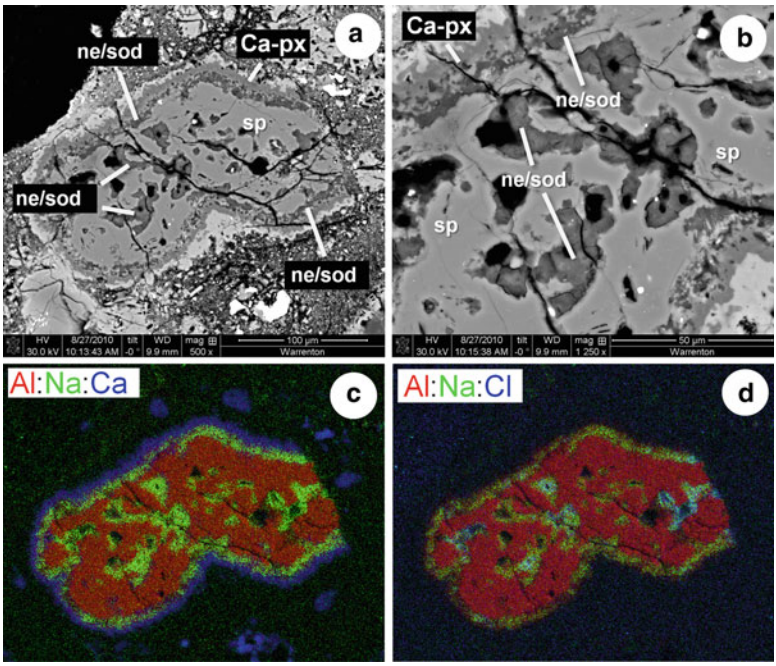

Fig. 15.45 BSE images (**a**, **b**) and combined x-ray elemental maps (**c**, **d**) of a spinel-rich CAI in Warrenton (CO3.6) showing the characteristic effects of metasomatism. (**a**) The central core of the CAI is made up of massive spinel (sp), which is enriched in Fe due to metamorphic exchange with the matrix. Nepheline, probably intergrown with sodalite (ne/sod), possibly a replacement product of melilite, is present in a narrow rim around the central spinel core of the inclusion and in irregular regions within the CAI interior. The CAI has a continuous rim of diopside (Ca-px). The outer most rim (*bright*) on the CAI is a layer of ferroan olivine. (**b**) Close up image of irregular regions of replacement within the spinel. The replacement phases consist of extremely fine-grained nepheline, which, based on x-ray maps (**d**) indicating the localized presence of Cl, is intergrown on a fine scale with sodalite. However, positive identification of sodalite in CAIs in Warrenton has yet to be confirmed. (**c**) Combined x-ray elemental map in Al (*red*), Na (*green*), and Ca (*blue*), showing the distribution of nepheline along the periphery of the central spinel grain and in irregular regions within the CAI interior. (**d**) Combined x-ray elemental map in Al (*red*), Na (*green*), and Cl (*blue*). The presence of sodalite is indicated locally by the *pale blue* coloration within some of the irregular regions of alteration within the core of the inclusion

found that, in anorthite-pyroxene inclusions in Yamato (Y) 81020, nepheline has almost completely replaced primary anorthite. This contrasts with a highly unusual anorthite-bearing inclusion in Isna (CO3.7), where anorthite has been partial replaced by nepheline (Fig. 15.48) and shows evidence of elemental exchange (Ca and Mg for Na and Fe).

Kojima et al. (1995) have documented in detail the earliest stages of alteration of CAIs in Y-82050 (CO3.1). CAIs in this chondrite show considerable variability in their degree of alteration and contain secondary nepheline abundances from <5 to 60 vol.%, with large inclusions containing a lower volume percent of nepheline.

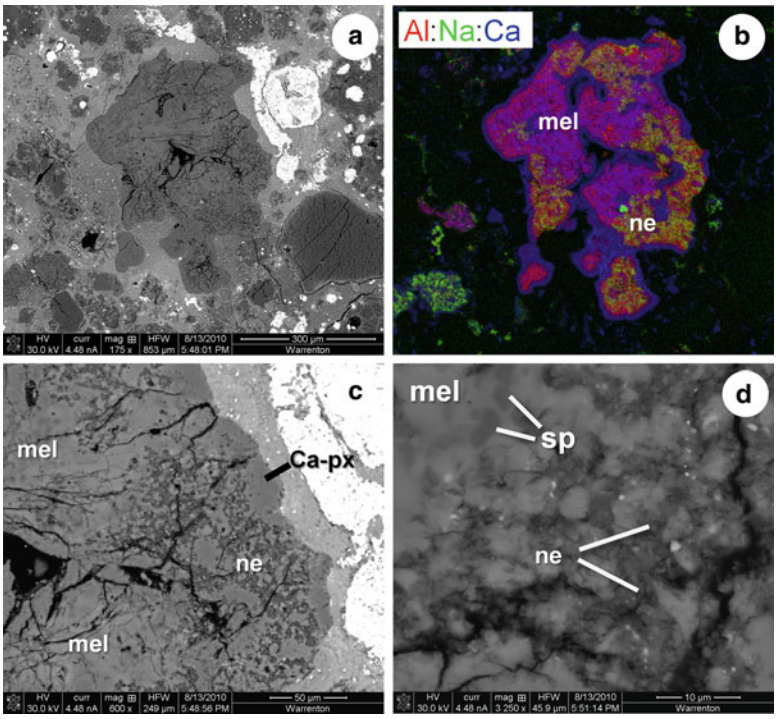

Fig. 15.46 BSE images (**a**, **c**, **d**) and a combined x-ray elemental map (**b**) of alteration in a compact melilite-bearing inclusion from Warrenton (CO3.6). (**a**) Overview of the full CAI showing *irregular-shaped pockets* of alteration (ne) in melilite (mel) in the interior of the CAI and a narrow zone of alteration on the peripheral region of the CAI just inside a Ca-rich pyroxene (Ca-px) rim. (**b**) Combined x-ray elemental map in Al (*red*), Na (*green*), and Ca (*blue*) showing the distribution of nepheline within the inclusion. A narrow zone of nepheline is present around the entire periphery of the inclusions and as irregular pockets in the interior of the inclusion. (**c**, **d**) Close-up of alteration on the edge and interior of the CAI. The pockets of alteration are highly irregular in shape and appear to consist of an intergrowth of fine-grained phases, dominantly nepheline and sodalite, some with a fibrous morphology. There is no evidence of any crystallographic control on the development of the alteration products. The dark regions in each of the areas of alteration appear to be pores that have developed during alteration

Porous aggregates of nepheline containing fine-grained troilite grains (<1 μm) have irregular contacts with melilite, anorthite, and Al-Ti diopside, indicative of a replacement relationship. Similar nepheline-troilite associations have also been described by Tomeoka et al. (1992) in Y-791717. Electron microprobe analyses show the presence of low concentrations of Cl in the porous nepheline, which Kojima et al. (1995) suggested is indicative of the presence of sodalite intergrown with the nepheline.

In CO chondrites, both coarse and fine-grained spinel-rich inclusions are present (Kojima et al. 1995; Russell et al. 1998). In each type of inclusion, a thin, usually continuous, layer of diopside (2−10 μm) is present (e.g., Figs. 15.44, 15.45) on the

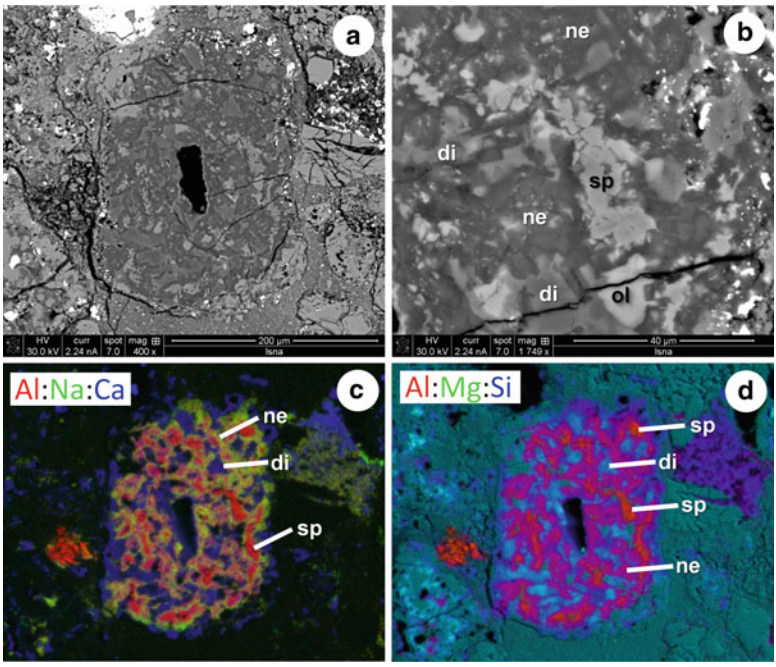

Fig. 15.47 BSE images (**a**, **b**) and combined x-ray elemental maps (**c**, **d**) showing advanced alteration of a CAI from Isna (CO3.7). (**a**) Overview of the full CAI showing the complex characteristics of the alteration. The inclusion was originally probably a melilite-bearing CAI, but the melilite has been completely replaced. Irregularly-shaped, corroded relicts of primary phases occur within the inclusion. (**b**) Close-up of the right hand side of the altered inclusion. The bright grains are primary spinel (sp) grains that are now hercynitic in composition due to Mg-Fe exchange, as well as some rare olivines (ol) that are also now Fe-rich. Relicts of diopside (di), which show evidence of Mg-Fe zoning and have a corroded appearance, occur embedded within fine-grained nepheline (ne). (**c**) Combined x-ray elemental map in Al (*red*), Na (*green*), and Ca (*blue*) showing the distribution of phases within the inclusion. Spinel grains (*red*), diopside (*blue*), and nepheline (*yellow*) are distributed throughout the inclusion. (**d**) Combined x-ray elemental map in Al (*red*), Mg (*green*), and Si (*blue*) illustrates the textural relationships between the three major phases. Spinel (*orange*) and irregularly-shaped diopside grains (*blue*) occur in a complex intergrowth with nepheline (*purple*)

rim of the inclusion. In higher petrologic type CO3 chondrites, a thin layer of nepheline is present immediately inside the diopside rim (Figs. 15.44, 15.45). The response of fine-grained spinel inclusions to thermal metamorphism/metasomatism is somewhat different than in melilite-rich inclusions. In these inclusions, spinel and diopside occur intergrown with secondary nepheline, but minor hedenbergite, grossular, and andradite also occur along with FeS. Russell et al. (1998) noted that, due to their fine-grained characteristics, essentially all the primary phases in fine-grained spinel-rich inclusions had either been altered to secondary phases or have undergone compositional changes. Further details of the effects of alteration have been provided by Itoh et al. (2004). They found that, in fine-grained CAIs from

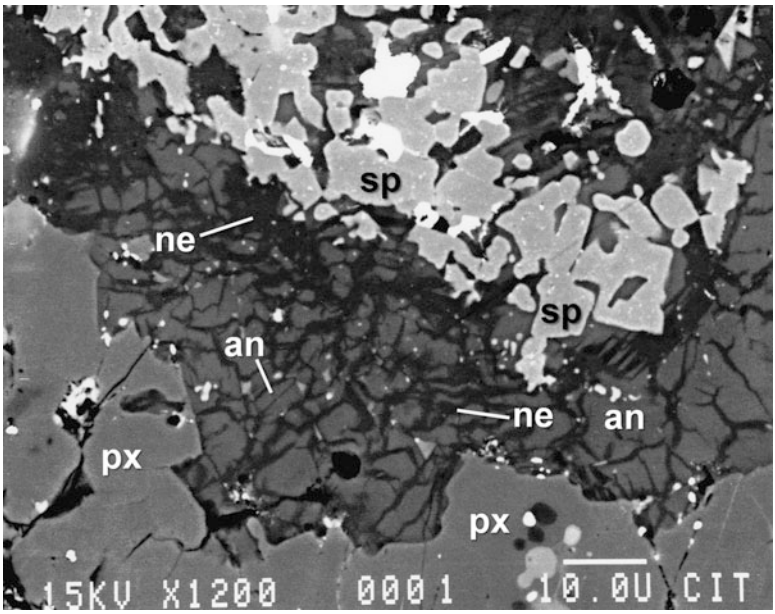

Fig. 15.48 BSE image of a heavily altered anorthite-bearing CAI from Isna (CO3.7) (From Russell et al. 1998). Primary anorthite (an) has been variably replaced along fractures and cleavage planes by secondary nepheline (ne). Pyroxene (px – lower) is unaltered. The bright grains distributed through the CAI are grains of spinel (sp) that have undergone Fe-enrichment during metamorphism and are now fully equilibrated. Image courtesy of Sara Russell

Kainsaz (CO3.2), diopside commonly exhibits a porous texture or is intergrown with alteration phases along grain boundaries. Such porous diopside is not observed in similar CAIs from Y-81020 (CO3.0) suggesting that the texture is the result of interaction with an aqueous fluid. Compositionally the porous diopside in Kainsaz has lower Al_2O_3 contents than non-porous diopside, evidence that alteration affects both the texture and chemical composition of the diopside.

Russell et al. (1998) found that the behavior of hibonite-rich inclusions through the petrologic sequence in CO3 chondrites is less systematic than melilite-bearing inclusions. Unlike melilite, hibonite occurs in all CO chondrites from petrologic type 3.0 to 3.7 and only shows evidence of alteration to hercynitic spinel in some chondrites. The presence of unreacted hibonite in CAIs in Isna (CO3.7) demonstrates that hibonite can survive thermal metamorphism/metasomatism.

The FeO content of spinels and perovskites in all types of CAIs also increases with increasing petrologic type such that perovskite is progressively replaced by ilmenite. Fe enrichment in spinel grains occurs preferentially from the exterior of the inclusions inwards and adjacent to fractures or cracks in the inclusions, with zoning developing in individual grains for intermediate petrologic types (Kojima et al. 1995; Russell et al. 1998). By petrologic type 3.4, spinels have a

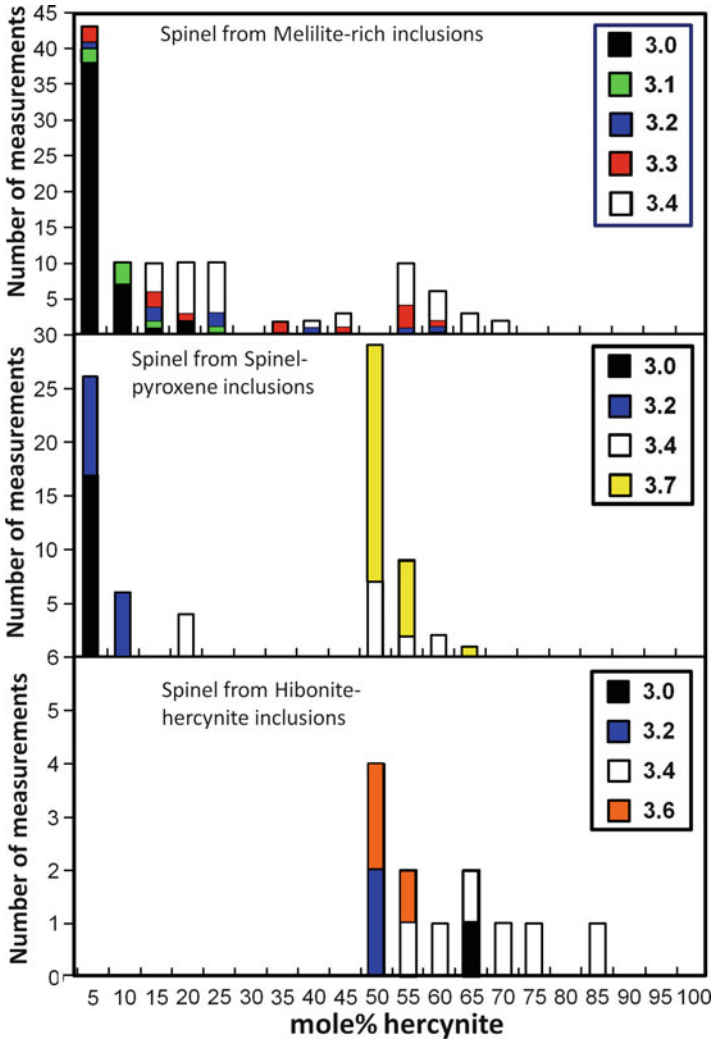

Fig. 15.49 Histograms showing the hercynite content of spinel (mol%) as a function of petrologic type in three major types of CAIs in CO3 chondrites (After Russell et al. 1998). For low petrologic types each inclusion type is dominated by pure Mg-spinel. As petrologic type increases and metamorphic equilibration begins to occur, the hercynite content of the spinels increases and the range of compositions within the individual chondrites increases as compositional zoning develops. By petrologic type 3.4, the spinels in all CAI types are much more Fe-rich and generally show narrower ranges in composition, indicative of almost complete compositional equilibration with a Fe-rich reservoir, i.e. the matrix of the chondrite

composition of ~50 mol% hercynite, and by type 3.7 they are fully equilibrated (Figs. 15.47, 15.48) due to Mg-Fe exchange with the Fe-rich matrix. The progressive compositional equilibration of spinel in different CAI types, through the

petrologic sequence in the CO3 chondrites, as documented by Russell et al. (1998), is shown in Fig. 15.49.

These data clearly show that there are significant differences between the alteration observed in CAIs in CV3 chondrites and those in the CO chondrites. The extensive development of Ca-rich pyroxene, garnet, and wollastonite in altered CV3 CAIs is essentially absent in the alteration products of CO3 CAIs. The alteration in CO chondrites is dominated by the formation of nepheline with only extremely limited, and in some cases indirect, evidence of the development of sodalite.

Metasomatic Effects in AOAs in CO Chondrites

Like in other carbonaceous chondrites, amoeboid olivine aggregates (AOA) are the dominant type of refractory inclusions in CO3 chondrites. Amoeboid olivine aggregates in CO chondrites range in size from ~20 μm to 1 mm, with olivine grain sizes of 2 − 10 μm (Chizmadia et al. 2002). Their fine-grained characteristics therefore make them highly susceptible to metasomatic alteration. Kojima et al. (1995) and Chizmadia et al. (2002) have provided important details on the alteration present in CO AOAs. Kojima et al. (1995) described the mineralogy of AOAs in the three CO chondrites, Y-81020 (CO3.0), Y-82050 (CO3.1) and Y-790992 (CO3.3−3.5). Chizmadia et al. (2002) examined AOAs in a more extensive suite of 7 CO chondrites ranging from petrologic type 3.0 to 3.8. The observations show that the primary mineralogy of AOAs in the type 3.0 CO chondrites consists of abundant forsteritic olivine, with lesser amounts of interstitial anorthite and diopside. Fe,Ni metal and troilite are also present. According to the observations of Kojima et al. (1995), anorthite is common in AOAs in Y-81020, but decreases in abundance in higher petrologic types, being replaced by nepheline. Although Chizmadia et al. (2002) did not report any evidence of nepheline in the suite of AOAs that they studied, Rubin (1998) found veins of nepheline in AOAs in Kainsaz. Krot et al. (2004c) reported nepheline in AOAs in Warrenton (CO3.6). Nevertheless, the progressive alteration of anorthite by nepheline in AOAs, described by Kojima et al. (1995), is not apparent in the mineralogical modal abundance data reported by Chizmadia et al. (2002). Further studies of the relationship between anorthite and nepheline in CO AOAs is needed in order to clarify this issue, but certainly would be expected based on observations from chondrules.

Metasomatic Effects in Chondrules in CO Chondrites

A significant number of different studies have been carried out on chondrules in CO3 chondrites that have revealed evidence of interaction with aqueous fluids on a localized scale (e.g., Kurat and Kracher 1980; Palme and Wlotzka 1981; Jones 1997; Jones and Brearley 1994; Itoh and Tomeoka 1998, 2003; Tomeoka and Itoh

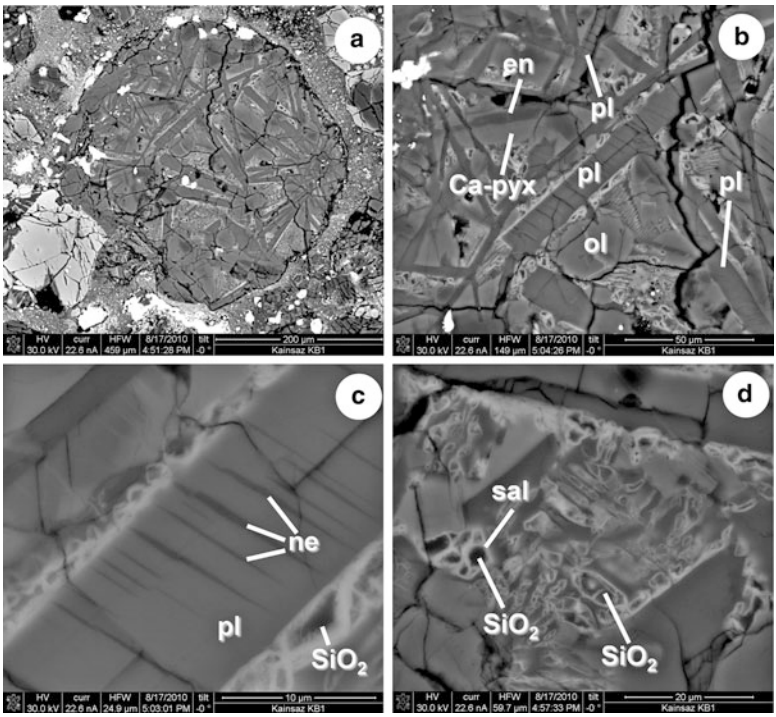

Fig. 15.50 BSE images of a plagioclase-rich chondrule from Kainsaz (CO3.2). (**a**) The chondrule is dominated by abundant laths of plagioclase with rarer phenocrysts of olivine and enstatite and interstitial mesostasis, shown in detail in (**b–d**). The bright grains are Fe,Ni metal. (**b**) Close-up showing textural characteristics of the chondrule. The central lath of plagioclase (pl) contains crystallographically-oriented lamellae of nepheline (*dark lines*). Enstatite phenocrysts (en) with a fibrous morphology occur overgrown by Ca-rich pyroxene (Ca-pyx). Subhedral phenocrysts of olivine (ol) are also present associated with the plagioclase. (**c**) High magnification image of a plagioclase lath that contains an irregular distribution of crystallographically–oriented nepheline lamellae (ne). The lamellae are locally offset, probably due to the presence of twin planes within the plagioclase. (**d**) Close-up of a complex region of mesostasis. The *dark*, irregularly shaped grains are crystals of silica (SiO_2), that have been partially replaced on their edges and along fractures by salitic pyroxene (sal) during metasomatic alteration

2004). These metasomatic effects are apparent in both the primary chondrule silicates and chondrule mesostasis, as discussed below.

Metasomatic alteration in CO chondrules involving Na- and Fe-bearing fluids is apparent in rare plagioclase-rich chondrules and plagioclase-bearing type I chondrules (Kurat and Kracher 1980; Palme and Wlotzka 1981; Ikeda 1982; Jones and Brearley 1994; Jones 1997; Tomeoka and Itoh 2004; Wick 2010). Kurat and Kracher (1980) first described plagioclase-rich chondrules in Lancé (CO3.4) as basaltic clasts, based on their mineralogical and textural characteristics. They have since been recognized in several other CO chondrites, including Ornans (CO3.3) (Palme and Wlotzka 1981), Kainsaz (CO3.2), and the paired chondrites

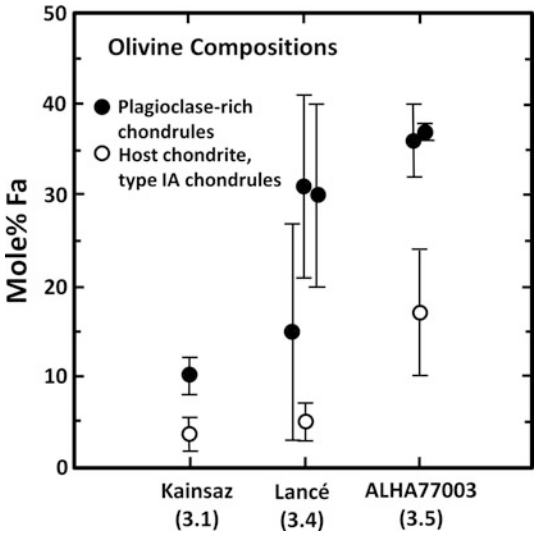

Fig. 15.51 Compositions of olivines in plagioclase-rich chondrules and typical type IA chondrules in Kainsaz (CO3.2), Lancé (CO3.4), and ALHA 77003 (CO3.5). In all three chondrites, the olivines in the plagioclase-rich and type IA chondrules are considered to be forsteritic in composition prior to Fe-enrichment. However, the Fe-enrichment in olivine in the plagioclase-rich chondrules is significantly higher than that observed in the type IA chondrules, indicating that the enrichment cannot be explained simply by parent body metamorphic exchange of Mg and Fe between the matrix and chondrule olivines (From Jones 1997)

ALH 77003 and ALH 83108 (CO3.6). Jones (1997) conducted a survey of 13 CO chondrites in 19 thin sections and found a total of just 9 of these chondrules in 4 chondrites. These objects consist of abundant primary anorthite laths (An_{80-90}), orthopyroxene, and augite with a basaltic texture, in addition to olivine, Fe,Ni metal, troilite, and a mesostasis consisting of silica and glass (Fig. 15.50).

In these chondrules, Fe-alkali metasomatism dominates the style of alteration, with no evidence of introduction of Cl. Laths of plagioclase (Fig. 15.50a–c) have been partially replaced by nepheline with a very characteristic alteration texture, similar to that observed in CV3 chondrites (Kimura and Ikeda 1998; MacPherson 2003). Individual laths of plagioclase contain crystallographically-oriented lamellae of nepheline with variable widths and distributions through the feldspar grains (Fig. 15.50c) (Kurat and Kracher 1980; Palme and Wlotzka 1981; Jones 1997). Silica, in the mesostasis of these chondrules, shows variable and complex replacement textures as a result of the formation of ferrosalitic pyroxene (Fig. 15.50d). In some cases, this replacement is complete and no primary silica remains in the chondrule. Primary olivine (inferred to be forsteritic in composition) has also undergone significant enrichment in FeO, but in each chondrite, this enrichment is significantly higher than the typical Fe enrichment in normal type I chondrules (Fig. 15.51), and is commonly attributed to Mg-Fe exchange during thermal metamorphism.

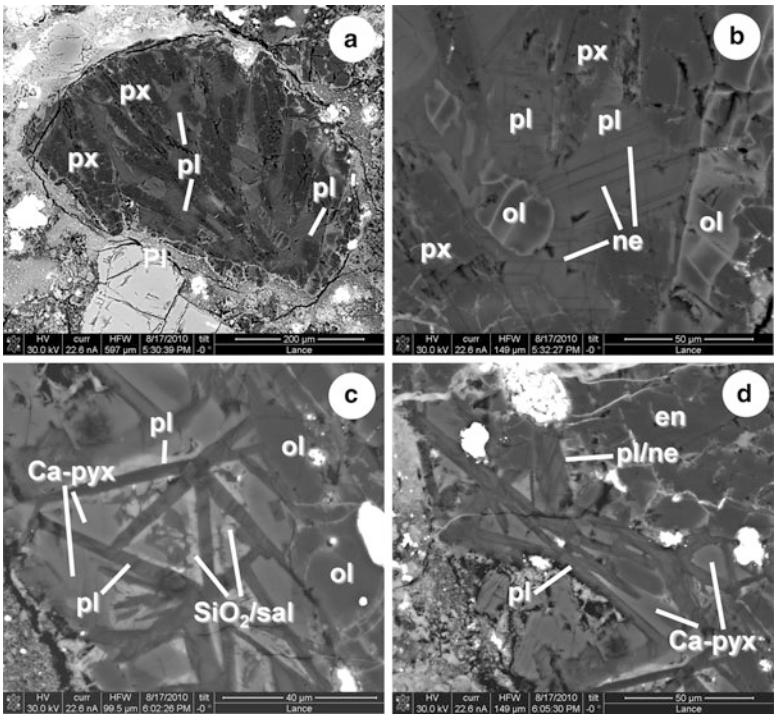

Fig. 15.52 BSE images of metasomatic alteration effects in plagioclase-bearing chondrules in Lancé (CO3.4). (**a**) Porphyritic enstatite-rich (px) chondrule containing numerous interstitial grains of plagioclase (pl). (**b**) Close up of interstitial plagioclase grains between enstatite (px) and olivine (ol). The olivine (ol) shows evidence of Mg-Fe zoning that results from thermal metamorphism. The fine, *linear dark lines* that occur in the plagioclase crystals are thought to be lamellae of nepheline (ne), based on their resemblance to coarser-grained nepheline lamellae in chondrules in, e.g., Kainsaz (CO3.2) (Fig. 15.51). (**c**) Close up of a region from a plagioclase-bearing chondrule that contains a high abundance of plagioclase laths with interstitial Ca-rich pyroxene (Ca-pyx) and silica that has been partially to completely replaced by salitic pyroxene (SiO_2/sal). The individual plagioclase laths contain randomly distributed, crystallographically-oriented lamellae of a darker (lower Z) phase, which electron microprobe analyses indicate are nepheline. Small phenocrysts of olivine are also present. (**d**) High magnification close-up image of an additional region of plagioclase laths in a plagioclase-bearing chondrule showing the heterogeneous development of lamellae of nepheline with plagioclase laths (pl/ne). Ca-rich pyroxene occurs commonly interstitially to the plagioclase laths along with larger phenocrysts of enstatite (en)

Primary plagioclase also occurs relatively commonly in type I chondrules from CO3 chondrites and has also been replaced, to various degrees, by nepheline (Fig. 15.52a–d). The development of nepheline as a replacement product of plagioclase, was first recognized by Ikeda (1982) and has subsequently been described in detail by Tomeoka and Itoh (2004), who also examined the alteration behavior of chondrule mesostasis. Based on observations of chondrules from 7 CO chondrites, ranging from petrologic subtype 3.0 to 3.7, Tomeoka and Itoh (2004) were able to examine alteration of these components as function of increasing

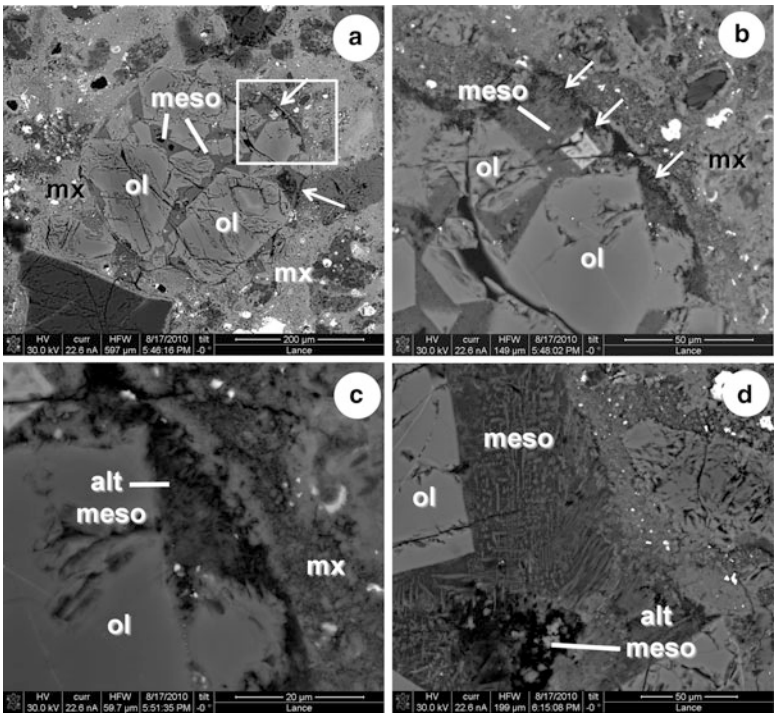

Fig. 15.53 BSE images showing the effects of metasomatism on mesostasis in a type IIA chondrule in the Lancé CO3.4 chondrite. (**a**) Low magnification BSE image of a typical type IIA chondrule in Lancé, embedded within a fine-grained matrix (mx). The chondrule consists of ferroan olivine (ol) grains, some showing compositional zoning with interstitial glassy mesostasis (meso). In several places on the periphery of the chondrule (*arrows*), the mesostasis is in direct contact with the matrix, where it shows evidence of darkening and the development of porosity as shown in (**b**)). (**b**) Close-up of boxed region in (**a**) showing porous, altered mesostasis (*arrowed*), present where the mesostasis (*meso*) is juxtaposed against the fine-grained matrix. (**c**) High magnification image of a region of altered mesostasis (*alt meso*) in contact with mesostasis, showing porosity where the glass has been leached and altered to a porous material containing a very fine-grained fibrous phase. (**d**) Region of unaltered mesostasis (*meso*) that consists of abundant quench crystallites of high-Ca pyroxene. The lower part of the image contains a pocket of highly porous altered mesostasis (*alt meso*) that contains extremely fine-grained, Na-rich alteration products

petrologic type. They restricted their study to chondrules in the size range 100−350 μm, to minimize possible size effects on the degree of alteration exhibited by different chondrules.

Primary plagioclase phenocrysts and mesostasis glass in type I chondrules from low petrologic type CO chondrites, such as Y-81020 (CO3.0), show essentially no evidence of alteration, even when they are in contact with the fine-grained matrix. However, by petrologic subtype 3.2 (Kainsaz), ~62% of the chondrules show evidence of minor alteration in their mesostases (Tomeoka and Itoh 2004). Mesostases show an enrichment in Na_2O, reaching as high as 10 wt.%, where the

glass has been replaced by a fine-grained, porous aggregate of nepheline. Plagioclase phenocrysts show the same alteration textures as described above for plagioclase-rich chondrules, with lamellae of nepheline, 0.5–2 μm in width. The alteration commences on the exterior of the chondrule, initially where mesostasis is in contact with the fine-grained matrix and progresses into the interior. Similar features are observed in FeO-rich, porphyritic, olivine chondrules (type IIA) except that leaching of the glass, leaving a network of Ca-rich pyroxene quench crystals, is also observed (Fig. 15.53a–d). However, a common feature of the alteration is that although the degree of alteration increases progressively as petrologic type increases, there is still significant variability in the degree of alteration within individual chondrules, within the same chondrite. In low petrologic type chondrites (~3.2), chondrules, with completely unaltered glass, are present in contact with the fine-grained matrix, as well as chondrules which show distinct evidence of replacement of plagioclase and mesostasis by nepheline. As petrologic type increases, the percentage of chondrules which show evidence of replacement of mesostasis glass increases to >90% in types 3.4–3.5 and the abundance and thickness of nepheline lamellae replacing primary plagioclase also increases. In the highest petrologic subtype, 3.7, all chondrules show some evidence of alteration to nepheline and the grain size of nepheline has also increased. Further, troilite blebs are more commonly associated with nepheline than in lower petrologic type CO3 chondrites. Although extensive replacement of primary plagioclase has occurred, unaltered plagioclase is present, particularly in the cores of chondrules. Tomeoka and Itoh (2004) also observed that fine-grained diopside crystals in the mesostasis glass have been converted to hedenbergite and sometimes nepheline by petrologic type 3.7. Finally, at this most advanced stage of alteration, evidence of partial replacement of enstatite phenocrysts by FeO-rich olivine is present, dominantly along their peripheral regions.

The compositions of glass in type I chondrules in low petrologic type CO chondrites are relatively low in Na and K, but enriched in Ca. However, the formation of nepheline as a replacement for glass, causes a significant increase in the alkali content of the mesostasis that correlates with metamorphic type (Fig. 15.54) (Tomeoka and Itoh 2004).

A characteristic feature of metasomatic alteration of chondrules in the Allende subgroup of the oxidized CV3 chondrites, is the presence of ferroan olivine overgrowths on forsteritic olivine grains in chondrules and isolated forsteritic olivine grains (e.g., Fig. 15.20c, d). Ferroan olivine is also found replacing low-Ca pyroxene in many chondrules in Allende. Similar features are also observed in some CO3 chondrites, particularly those of higher petrologic type. Kerridge (1972) first noted the presence of ferroan olivine veins in a chondrule in Warrenton (CO3.6), which he attributed to the transport of Fe into the chondrule by an aqueous fluid. More recently, Tomeoka and Itoh (2004) have also observed replacement of enstatite in chondrules in Warrenton by ferroan olivine, a process they attributed to metasomatic alteration. In fact, the replacement of enstatite by ferroan olivine is present in other CO chondrites such as Ornans (CO3.3) (Fig. 15.55a, b) as well as Warrenton and can be quite extensive, comparable in some cases to that observed in some pyroxene-bearing chondrules in Allende. Although this phenomenon has not been widely recognized or studied in CO3 chondrites, our observations indicate that

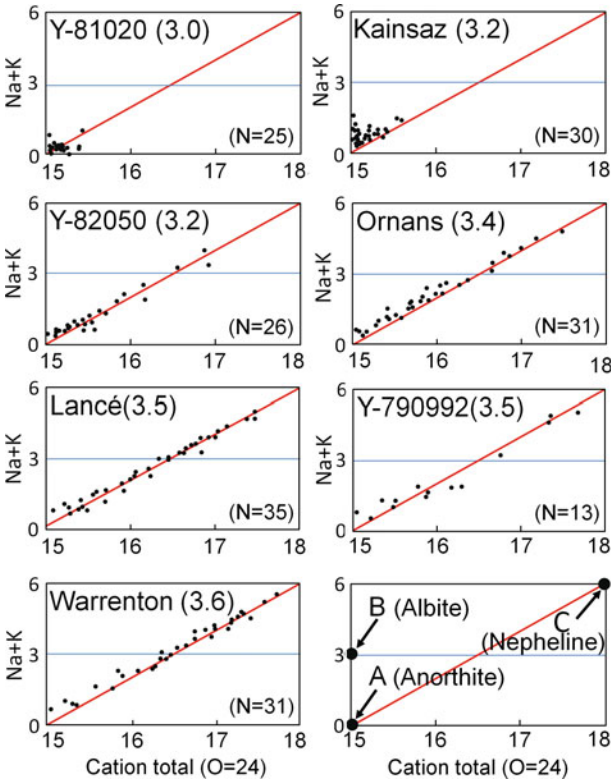

Fig. 15.54 Plots of cation total per 24 [O] versus Na + K for plagioclase mesostasis in plagioclase-bearing chondrules in several different CO3 chondrites (After Tomeoka and Itoh 2004). As illustrated in the lower right hand diagram, point A represents the composition of anorthite, point B is albite, and point C is nepheline. The diagrams show that in low petrologic type CO3 chondrites, such as Y-81020, the plagioclase is anorthitic in composition, but with increasing petrologic type, as the degree of nephelinitization of plagioclase increases, the range of Na + K ratios increases. Individual electron microprobe analyses represent fine-scale mixtures of nepheline and plagioclase that extend along the mixing line between the compositions of anorthite and nepheline. As petrologic type increases, the distribution of analyses shifts towards the composition of nepheline and away from the anorthite

the degree of alteration is not so obviously correlated to thermal metamorphism. In Allende, the overgrowth of ferroan olivine as continuous rims and, in some cases, platy olivines onto forsteritic olivine grains, in chondrules and isolated grains in the matrix, is common. Similar features also occur in Felix (CO3.2) as shown in Fig. 15.55c and d, where a large isolated forsteritic olivine grain has a continuous overgrowth of fayalitic olivine around it. As shown in Fig. 15.55d, the interface between the forsteritic olivine grain and the fayalite is extremely sharp (c.f. Fig. 15.20d shows more advanced overgrowths in ALH 84028 (CV_{OxA})). Many of the fayalitic olivine grains in the overgrowth have a platy morphology comparable to that of olivines in the matrices of CV_{OxA} chondrites and have grown with their long axis normal to the interface with the olivine.

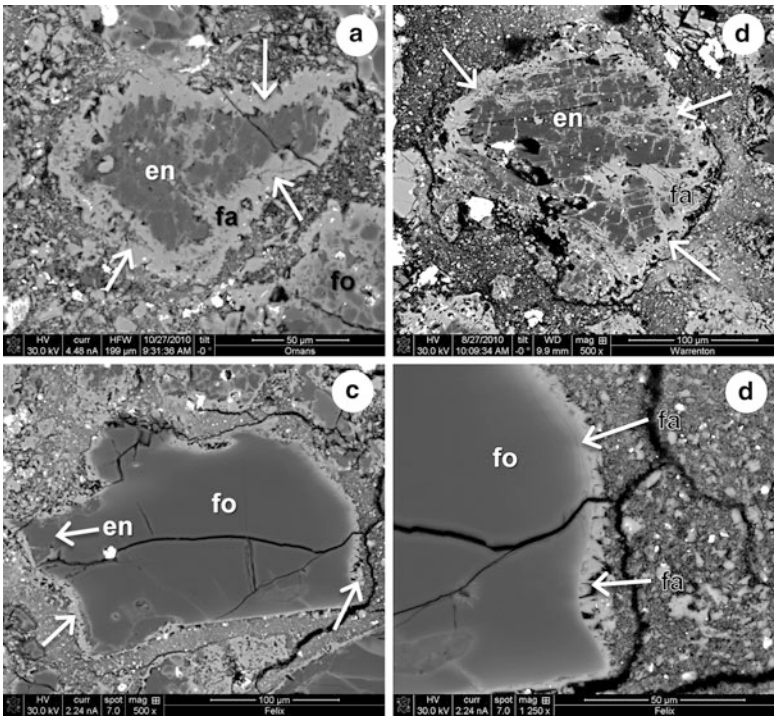

Fig. 15.55 BSE images of occurrences of ferroan olivine in CO3 chondrites. (**a**) Enstatite (en) grain in Ornans (3.3) that has been partially replaced by ferroan olivine (fa). The ferroan olivine occurs as an overgrowth around the entire periphery of enstatite, forming a continuous rim (*arrowed*). Enstatite in the interior of the grain has also been partially replaced by ferroan olivine. (**b**) Porphyritic pyroxene chondrule in Warrenton (3.6) in which enstatite been extensively replaced around its periphery (*arrowed*) and interior by fayalitic olivine. In the interior of the grain, replacement of the pyroxene has occurred along contraction cracks in the enstatite. (**c**) Large isolated forsteritic olivine (fo) with associated minor enstatite that has been overgrown by a rim of ferroan olivine (*arrowed*) around the entire periphery of the grain in Felix (3.2). (**d**) Close-up of the edge of the olivine grain shown in (**c**) showing the sharp interface between the forsteritic olivine and the ferroan olivine overgrowth. In several regions of the overgrowth the ferroan olivine occurs as platy olivine grains that are oriented with their elongation direction normal to the interface with the forsteritic olivine grains

15.3.3.2 Effects of Metasomatic Alteration on Al-Mg and O-Isotope Systematics of CO Refractory Inclusions

Aluminum-Magnesium-Isotope Systematics

The effects of metasomatism coupled with metamorphism on the isotopic composition of CAIs in CO chondrites are currently not well constrained and appear to be complex. Russell et al. (1998) measured the Al-Mg isotope systematics of 38 CAIs

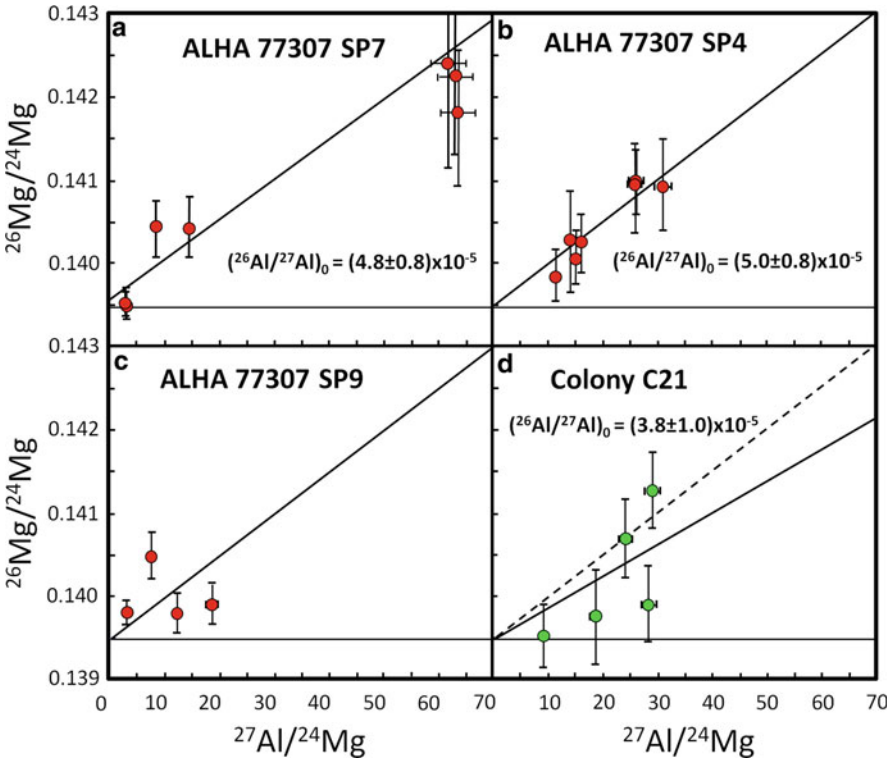

Fig. 15.56 Al-Mg isotope systematics for four different melilite-bearing CAIs from ALHA 77307 (CO3.0) and Colony (CO3.0), measured by ion microprobe (After Russell et al. 1998). (**a**) Inclusion from ALHA 77307 that shows a well-behaved isochron with a very good correlation between ^{26} Mg/^{24} Mg and ^{27}Al/^{24} Mg indicative of in situ decay of ^{26}Al. (**b**) Further inclusion from ALHA 77307 that also shows a well behaved isochron. (**c**) CAI from ALHA 77307 that shows a poorly defined isochron, but does show evidence of a ^{26} Mg* excess indicative of in situ decay of ^{26}Al. The *dashed line* represents $(^{26}Al/^{27}Al)_0 = 5.0 \times 10^{-5}$. (**d**) CAI from Colony that also shows a disturbed Mg-Al isochron indicated by the poor correlation between ^{26} Mg/^{24} Mg and ^{27}Al/^{24} Mg

from several CO chondrites using the ion microprobe. Their data show that in low petrologic type CO chondrites such as ALHA 77307 and Colony, CAIs, with well-behaved Al-Mg-isotope isochrons (Fig. 15.56), coexist with inclusions, which clearly have disturbed isotopic systematics, particularly the data for melilite. Based on the lack of any clear evidence for the alteration of melilite in ALHA 77307, Russell et al. (1998) suggested that alteration and disturbance of the isotopic systematics of these inclusions occurred prior to accretion. Indeed, for CO chondrites ranging from petrologic type 3.0 to 3.4, there is no clear relationship between the degree of isotopic disturbance and petrologic type. However, for higher petrologic type chondrites, a stronger relationship exists between melilite-bearing CAIs with disturbed Mg-isotope systematics and petrologic type. Although most melilite-bearing CAIs in CO

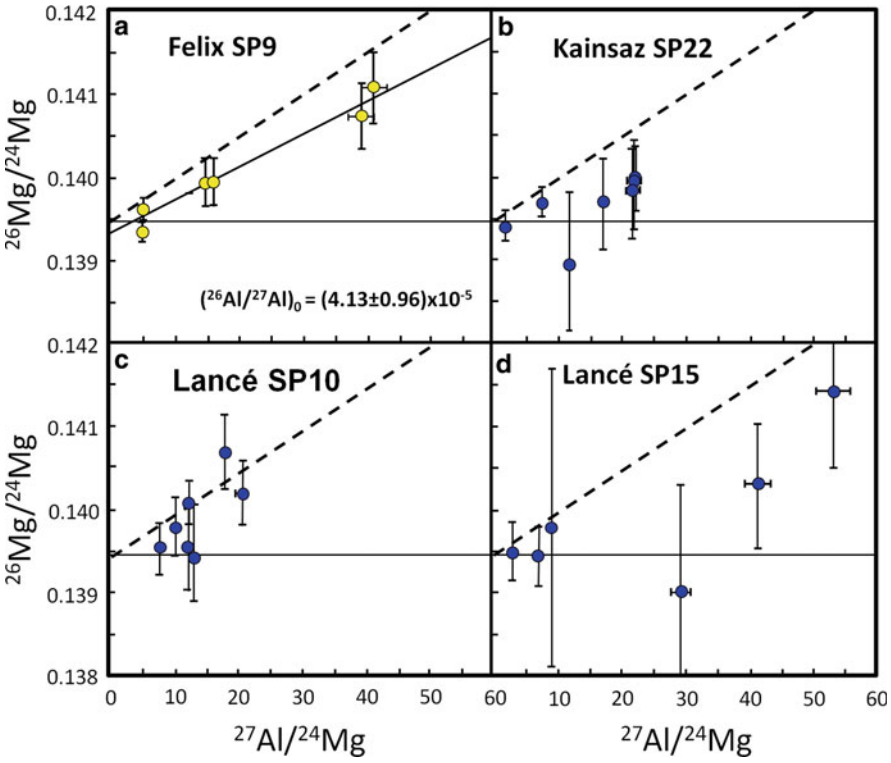

Fig. 15.57 Al-Mg isotope systematics for four different melilite-rich CAIs from Kainsaz (3.2), Felix (CO3.2), and Lancé (CO3.4) (After Russell et al. 1998). With the exception of (**b**) all the inclusions show evidence of ^{26} Mg* indicative of in situ decay of ^{26}Al, but all show evidence of varying degrees of isotopic disturbance that may be attributable to thermal metamorphism/metasomatism. The *dashed line* represents $(^{26}Al/^{27}Al)_0 = 5.0 \times 10^{-5}$. (**a**) Melilite-rich inclusion with a well-defined isochron that yields a low $(^{26}Al/^{27}Al)_0$ ratio. (**b**) Kainsaz CAI which shows no ^{26} Mg*. (**c**) CAI from Lancé that shows a distinct ^{26} Mg*, with some of the data points lying on the $(^{26}Al/^{27}Al)_0 = 5.0 \times 10^{-5}$ line. However, some data points show no ^{26} Mg* suggesting variable disturbance of some mineral phases. (**d**) CAI from Lancé that shows evidence of ^{26} Mg*, but the data show a poor correlation with Al/Mg indicating disturbance of the CAI as a result of metamorphism or metasomatism

chondrites, above petrologic type 3.4, do show ^{26} Mg*, only a few of these inclusions have well-behaved Al-Mg isochrons. Most inclusions show clear evidence of isotopic disturbance that correlates with the petrologic evidence of replacement of melilite by secondary phases (Fig. 15.57).

Oxygen-Isotope Systematics

Ion microprobe studies of CAIs in type 3.0 CO chondrites (Colony, Y-81020) show that the primary phases (anorthite, melilite, hibonite, spinel, diopside, Al-diopside,

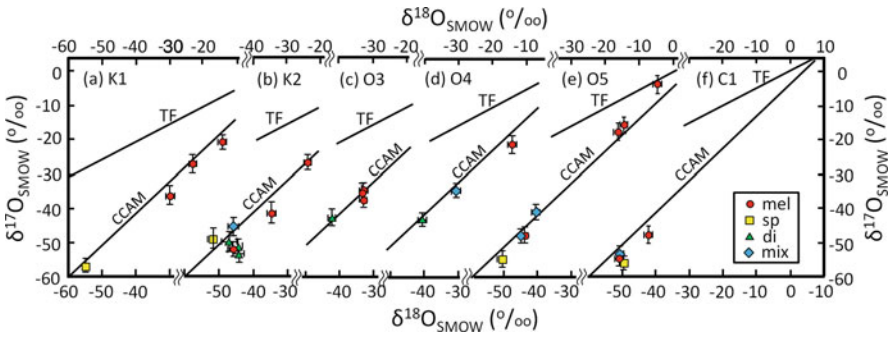

Fig. 15.58 Oxygen isotopic composition of phases in CAIs from three CO chondrites plotted on individual oxygen three-isotope diagrams (After Wasson et al. 2001). Inclusions K1 and K2 are inclusions from Kainsaz (CO3.2), O3, O4, and O5 are from Ornans (CO3.4) and C1 is from Colony (CO3.0). Melilite from C1 is isotopically light and plots with other phases such as melilite and spinel. However in both the Kainsaz and Ornans inclusions, the melilite has a distinct composition from spinel and diopside and is isotopically heavy. This behavior was interpreted by Wasson et al. (2001) as indicating that melilite in the Kainsaz inclusions had undergone recrystallization and isotopic exchange with a fluid on the CO3 parent body during metamorphism/aqueous alteration

and forsterite) have ^{16}O-rich ($\Delta^{17}O \sim -25‰$) oxygen isotopic compositions typical for pristine CAIs in carbonaceous chondrites (Wasson et al. 2001; Itoh et al. 2004). However, in higher petrologic type chondrites, such as Kainsaz (type 3.2) and Ornans (3.4), Wasson et al. (2001) found that the oxygen isotopic composition of melilite tends to be isotopically heavier, plotting further up the CCAM line closer to the terrestrial fractionation line (Fig. 15.58). This change in composition, as a function of petrologic type, is apparent in the $\Delta^{17}O$ values of the melilite, which decrease significantly as the petrologic type of the meteorite increases. These observations have been confirmed by Itoh et al. (2004), based on a detailed study of several fine-grained inclusions from Kainsaz (3.2). The alteration products of melilite and anorthite (mainly nepheline) have similar isotopically-heavy compositions to unaltered melilite and anorthite in this meteorite (Fig. 15.59). Itoh et al. (2004) also found that diopside in some inclusions has compositions that plot close to the terrestrial fractionation line.

Wasson et al. (2001) interpreted the oxygen isotopic data for melilite as indicating that melilite has undergone significant changes in oxygen isotopic composition as a result of aqueous alteration on the CO parent body. They suggested that the primary melilite has undergone dissolution, but recrystallized without any significant apparent change in texture, although there is certainly an increase in the Fe content of the melilite in this process. The complete dissolution of melilite appears to be required, because oxygen isotopic diffusion, at the likely temperatures of alteration, is too low to cause such extensive exchange in reasonable time periods. In practice, it seems probable that, given the lack of hydrous phases in the meteorites studied, metasomatism, rather than aqueous alteration, may be a more appropriate term to describe the process that has affected the melilite, as

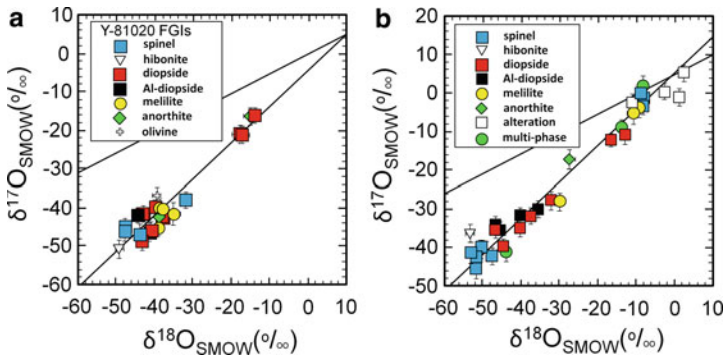

Fig. 15.59 Oxygen three-isotope diagrams showing the compositions of minerals in several CAIs from Y-81020 (CO3.0) and Kainsaz (CO3.2) determined by ion microprobe (After Itoh et al. 2004). (**a**) Data for CAIs from Y-81020. The data for all the primary phases, except rare analyses of diopside and anorthite in heavily altered inclusions, have ^{16}O-enriched isotopic compositions that plot on CCAM line in the range of compositions typical for primary nebular phases ($\delta^{17}O \sim -40‰$ to $-50‰$, $\delta^{18}O = -30‰$ to $-50‰$). (**b**) Data for CAI's from Kainsaz. The data for the primary phases show a much wider range of $\delta^{17}O$ and $\delta^{18}O$ values. In addition, secondary alteration products and some primary phases have compositions which plot close to the terrestrial fractionation line indicative of interaction with an aqueous fluid. In particular, melilite, anorthite, diopside, and spinel from some inclusions all show evidence of isotopic exchange with a heavy isotope enriched source

discussed in the Introduction. Wasson et al. (2001) suggested that the recrystallization of melilite was driven by the fact that the primary melilite may have been in a high energy state, possibly due to its fine grain size and/or the presence of defects and this excess energy drove recrystallization of the melilite in the presence of an aqueous fluid.

Itoh et al. (2004) have argued that the anorthite and melilite in Kainsaz CAIs first underwent oxygen isotopic exchange with a ^{16}O-depleted fluid that drove their compositions along the CCAM line towards the terrestrial fractionation line. However, the alteration occurred heterogeneously both within individual inclusions and from one inclusion to another. Following isotopic exchange, both phases underwent alteration to form ^{16}O-depleted secondary phases such as nepheline. Although spinel in these inclusions shows evidence of Fe-enrichment, these grains still preserve their ^{16}O-enriched primary nebular compositions. This observation can be reconciled with the fact that oxygen self-diffusion in spinel is 10 times slower than Mg-Fe interdiffusion (Itoh et al. 2004). In one heavily altered CAI from Kainsaz, Itoh et al. (2004) found that one part of the inclusion exhibits a higher degree of alteration and appears more porous that the rest of the inclusion. Spinel and diopside in the porous region of the inclusion have isotopic compositions that show heavy oxygen-isotope enrichments indicative of exchange with a fluid (Fig. 15.59b), that are not evident in spinel and diopside in the non-porous area of the inclusion. They argued that this change in oxygen isotopic composition was

the result of dissolution of the diopside, resulting in the formation of porosity, which reduced the effective grain size of the diopside grains and allowed oxygen self-diffusion to occur. Coupled with recrystallization of the diopside, oxygen isotopic exchange with the fluid occurred, resulting in the porous diopside having ^{16}O-depleted isotopic compositions comparable to other alteration products in the same heavily altered inclusion.

15.3.3.3 Timing of Metasomatic/Metamorphic Alteration in CO3 Chondrite Components

The Al-Mg isotopic systematics of Al-rich phases in CAIs and chondrules in CO3 chondrites show a progressive disturbance in their isochrons with increasing petrologic type as discussed above. Most CAIs in CO3.0 chondrites have $(^{26}Al/^{27}Al)_0$ of ~5×10^{-5} (Figs. 15.56, 15.57), although there are some CAIs which have disturbed isochrons with $(^{26}Al/^{27}Al)_0$ as low as 1.5×10^{-5} (Russell et al. 1998). On the other hand, plagioclase-bearing chondrules in Y-81020 (CO3.0) have lower $(^{26}Al/^{27}Al)_0$ ratios of ~ 3.8×10^{-6} (Kunihiro et al. 2004; Kurahashi et al. 2008). Assuming that the Al-Mg system has chronologic significance, these data indicate that plagioclase-bearing chondrules formed ~2.8 Ma after CAI formation. The timing of the primary formation events of these two different components are therefore reasonably well constrained.

Unfortunately, the effects of metamorphism/metasomatism on the Al-Mg isotopic systematics of CAIs in CO3 chondrites are complex and provide few constraints on the timing of alteration. In general, it appears that $(^{26}Al/^{27}Al)_0$ ratios of CAIs, based on the in situ *S*IMS measurements of primary CAI minerals, show more evidence of disturbance in higher petrologic type CO3 chondrites. However, the degree of disturbance is variable from one inclusion to another within any given chondrite (Russell et al. 1998). No $(^{26}Al/^{27}Al)_0$ ratios of alteration products from CAIs in CO3 chondrites have been determined, because of their fine-grained characteristics.

The data for plagioclase-rich chondrules provide somewhat better constraints. Hutcheon et al. (2009) reported data for four plagioclase-rich chondrules from Kainsaz (3.2); unlike data for plagioclase from chondrules in Y-81020, none of the Kainsaz chondrules have resolvable ^{26} Mg excesses. The inferred $(^{26}Al/^{27}Al)_0$ ratios of these Kainsaz chondrules are all $<2.2 \times 10^{-6}$, indicating that they could have been reset by thermal processing. Chronologically, however, these data only constrain the timing of metamorphism/metasomatism to have occurred more than 3 Ma after CAI formation. Given that Jones (1997) suggested that these chondrules may have experienced metasomatic alteration in the solar nebula, prior to accretion, this resetting may be indicative of a nebular thermal event.

The timing of thermal metamorphism and metasomatism of the CO3 chondrites is therefore currently essentially unconstrained.

15.3.4 Thermal Metamorphism of the CO3 Chondrites

There is an extensive body of evidence documenting thermal metamorphic effects in the CO3 chondrites. This evidence has been reviewed recently by Huss et al. (2006); only a brief summary will be provided here, updated with additional information as necessary.

McSween (1977b) first described clear petrographic evidence of metamorphism in the CO3 chondrites and argued that it represents a metamorphic sequence comparable to that observed in the unequilibrated ordinary chondrites. It has been demonstrated by several studies that there are significant correlations between the textural and mineralogical changes that occur in chondrules, CAIs, AOAs, matrix, and metal as a function of increasing petrologic type. As a consequence, there is widespread agreement that the well-defined metamorphic sequence observed in the CO3 chondrites occurred on an asteroidal parent body.

Detailed assignments of petrologic types to individual CO3 chondrites have come from several workers (Rubin et al. 1985; Scott and Jones 1990; Sears et al. 1991; Chizmadia et al. 2002; Grossman and Brearley 2005; Greenwood and Franchi 2004; Bonal et al. 2007; Kimura et al. 2008). These studies used a variety of different parameters, as discussed below, to assign petrologic types to the CO3 chondrites. As a result, there are some differences to the assignment of individual chondrites to a specific petrologic type and some disagreement as to which petrologic sequence is the optimal. The range of petrologic types, obtained from essentially the same suite of CO3 chondrites in these studies, is as follows (see also Huss et al. 2006); 3.0–3.7, Scott and Jones (1990); Bonal et al. (2007); 3.0–3.8, Chizmadia et al. (2002); 3.0–3.9, Sears et al. (1991). The least metamorphosed chondritic meteorites are characterized by a variety of different components (chondrules, matrix, refractory inclusions, metal, etc.) with highly variable compositions and textures. The process of thermal metamorphism involves a progressive equilibration of these diverse mineral compositions and recrystallization to approach textural equilibrium. The most widely used criterion for measuring the degree of thermal metamorphism of a given chondrite, originally established by Van Schmus and Wood (1967), is the heterogeneity of the Mg/Fe ratios of olivine and low-Ca pyroxene, i.e. the Fo and En contents, respectively. These two minerals are by far the most common phases in chondrules and hence are ideally suited as a sensitive indicator of thermal metamorphism. In chondrites, chondrules are generally more Mg-rich than the fine-grained matrix in which they are embedded. Therefore the compositional equilibration of olivine and pyroxene in chondrites

is a complex process involving Mg-Fe diffusive exchange between chondrules with different olivine and pyroxene compositions and the surrounding matrix. The spread in Fo and En contents, from randomly selected chondrule olivine and low-Ca pyroxene compositions, is then used as an indicator of the degree of thermal metamorphism. The least metamorphosed chondrites are defined as those showing the broadest range in Fo and En contents, i.e. the most heterogeneous compositions, with petrologic types being assigned by the decrease in heterogeneity of the olivine and pyroxene. For the ordinary chondrites, this parameter is described in quantitative terms, by the percentage mean deviation (PMD) as defined by Dodd et al. (1967). The PMD is high for low petrologic type chondrites (<type 3.4), but decreases above type 3.4. However, this parameter has not been adopted for the CO3 chondrites.

For the CO3 chondrites, Scott and Jones (1990), Grossman and Brearley (2005) and Bonal et al. (2007) have all used the compositions of chondrule silicates as a measure of the degree of thermal metamorphism. Scott and Jones (1990) and Bonal et al. (2007) focused on the complete range of metamorphism observed in the CO3 chondrites, and examined both major (Mg, Fe) (Fig. 15.60) and minor element equilibration (Cr, Ca, Al, Mn, etc.). This work shows that even in the most thermally metamorphosed CO3 chondrites, complete equilibration of olivine and low-Ca pyroxenes has not occurred and significant variability in Fo and En compositions is apparent. Due to the slower diffusion of Mg and Fe in pyroxene than olivine, the heterogeneity observed in pyroxene compositions is always much larger than that observed in olivine. This behavior can be observed qualitatively very distinctly by BSE imaging, with olivine showing the development of Mg-Fe zoning in low petrologic types, ultimately leading to almost complete compositional homogenization of the grains. Low-Ca pyroxene shows little evidence of zoning until petrologic types of around 3.5. Grossman and Brearley (2005) focused particularly on the behavior of Cr in type IIA chondrules that contain ferroan olivine (<Fa_{15}) as a sensitive indicator of very low degrees of thermal metamorphism (<3.2). This approach provides a basis for evaluating the very earliest stages of metamorphism and hence allows the most pristine CO3 chondrites with the least effects of thermal metamorphism to be identified.

Amoeboid olivine aggregates have been shown by Chizmadia et al. (2002) to be useful indicators of the extent of diffusional equilibration of CO3 chondrites during metamorphism. As discussed above, the primary mineralogy of these objects is dominated by forsteritic olivine with variable amounts of Al,Ti-diopside, anorthite, spinel, and, occasionally, melilite. These objects are extremely fine-grained and, as a consequence, are extremely sensitive indicators of thermal metamorphism. They are also quite abundant in CO3 chondrites (5–8 vol.% in CO3.0 chondrites – Rubin 1998). Chizmadia et al. (2002) demonstrated that both olivine and spinel in AOAs show trends of increasing Fe-enrichment that, in the case of olivine, are similar to those observed in olivine in chondrules. The Fe-enrichment in the olivine occurs along grain boundaries, but generally advances from the periphery of the AOA inwards. With increasing petrologic type, the distribution of olivine compositions in

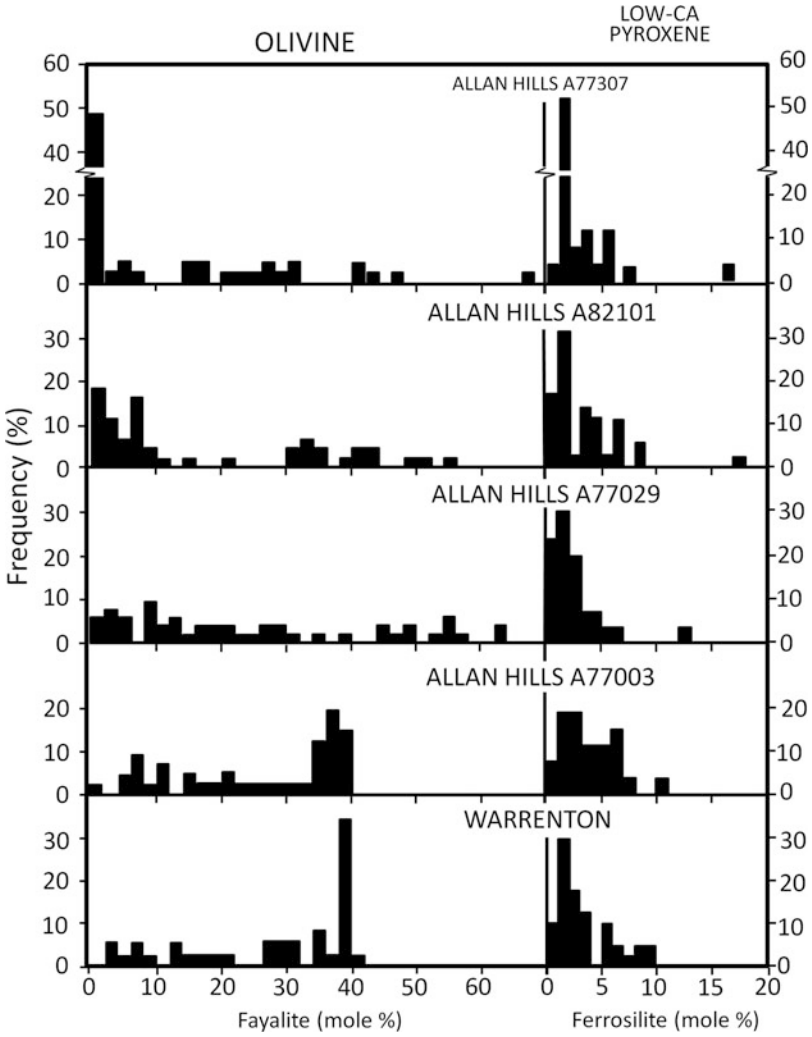

Fig. 15.60 Set of histograms plotting the distributions of the compositions of olivine (fayalite) and low-Ca pyroxene (ferrosilite) in several CO3 chondrites, which show the progressive changes that occur during thermal metamorphism (After Scott and Jones 1990). Individual analyses represent randomly selected olivine and pyroxene grains. In the least metamorphosed CO3 chondrite, ALHA 77307, there is a significant peak at very low fayalite contents, characteristic of olivines in Mg-rich type IA chondrules. With increasing metamorphism this peak diminishes and a peak at much more Fe-rich compositions begins to develop and dominate the olivine compositional distribution. Low-Ca pyroxene compositions also change but, due to lower Mg-Fe interdiffusion rates than olivine, lag behind the change in olivine

AOAs first begins to broaden as forsteritic olivine grains become enriched in FeO along grain boundaries. By petrologic type 3.4, a distinct bimodality in the olivine compositions develops, with the formation of high fayalite content olivine

overgrowths on the AOAs. The bimodal distribution progressively diminishes from type 3.5 to 3.7 as forsteritic olivine compositions equilibrate to a final FeO-rich olivine composition. The Fe-enrichment in spinel in AOAs is comparable to that observed for spinel in CAIs as reported by Kojima et al. (1995) and Russell et al. (1998).

Most recently, Bonal et al. (2007) used Raman spectroscopy to examine the degree of ordering of organic material in eight CO chondrites as an indicator of thermal metamorphism. Although the relative sequence of metamorphism determined for the Raman data is similar to that established in previous studies, the assignment of petrologic types is significantly different from previous studies based on the behavior of silicates (i.e. Mg-Fe equilibration in olivines). Based on organic material alone, the estimated petrologic type, based on the maturation of the organic material, yields significantly higher degrees of metamorphism for several chondrites, except for the highest petrologic type chondrites, where there is good agreement between the silicate-based petrologic types and those based on the ordering of organic material. The petrologic types based on Raman spectroscopy, compared with those of Scott and Jones (1990), are as follows (Scott and Jones 1990 in brackets) ALHA 77307 3.03 (3.0) < Colony 3.1 (3.0) < Kainsaz 3.6 (3.2) < Felix 3.6 (3.2) < Ornans 3.6 (3.3) < Lancé 3.6 (3.4) < Warrenton 3.7 (3.6) < Isna 3.7 (3.7). Bonal et al. (2007) suggested that the difference between the petrologic type assignments is the result of the fact that the behavior of organic material is independent of the presence of a fluid phase, whereas silicate equilibration can be affected by the presence of a fluid. This explanation is certainly possible, but an alternative explanation is that the organic material is more sensitive to thermal metamorphism and rapidly attains its maximum degree of maturity or ordering at a specific metamorphic temperature. In contrast, Mg-Fe interdiffusion between silicate minerals is sluggish, particularly so at the relatively low temperatures of thermal metamorphism in the CO chondrites. Therefore, the petrologic assignment based on silicate equilibration effectively measures the integrated effects of both time and temperature of the metamorphic event, but organic material measures the true metamorphic temperature that was reached. There are advantages and disadvantages to both approaches, but comparisons between the petrologic sequences, based on components that behave very differently during thermal metamorphism, should be exercised with caution.

Temperatures for thermal metamorphism for the CO3 chondrites have been estimated by a variety of different techniques (see review by Huss et al. 2006), including Mg-Fe interdiffusion in silicate minerals (Jones and Rubie 1991), interstellar grain abundances (Huss and Lewis 1994a), and the behavior of organic material (Bonal et al. 2007; Busemann et al. 2007; Cody et al. 2008). For CO3.0 chondrites, such as Colony and ALHA 77307, there is general agreement that the maximum metamorphic temperatures experienced by these meteorites was probably not significantly higher than 200°C. The range of temperatures experienced by petrologic type 3.0−3.7 CO3 chondrites was probably on the order of 400°C,

although there is certainly disagreement in the temperature range resulting from those different techniques. Maximum temperatures experienced by CO3 chondrites, based on different techniques, are in reasonable agreement. For example, for Isna (type 3.7), Jones and Rubie (1991) calculated a range of 510−570°C for the maximum temperature of metamorphism and Busemann et al. (2007) reported a value of 597°C based on Raman spectroscopic studies of ordering in organic material. Cody et al. (2008) derived two different values of 681 ± 118°C and 582 ± 120°C, based on analysis of two different ordering parameters in the spectra from organic material in Isna. In comparison, a temperature of 330°C determined by Bonal et al. (2007) for Isna, also based on the ordering of organic material, appears to be anomalously low.

15.3.5 Environment of Metasomatic Alteration of CO3 Chondrites

Although the effects of metasomatism on the CO3 chondrites are of lower degree and less studied than those in the CV3 chondrites, the environment where metasomatism occurred is still the subject of debate. Some workers have argued that in low petrologic type chondrites, there is clear evidence of metasomatic effects that occurred after accretion of the parent CO3 asteroid. On the other hand, there is a body of evidence that several workers have used to indicate that metasomatic events may have affected some components of CO3 chondrites prior to accretion. We evaluate the evidence for these different scenarios below.

Brearley (2003) discussed possible mineralogical, compositional, and isotopic criteria that might be used to differentiate between alteration processes (aqueous alteration and metasomatism) that occurred either prior to or post accretion of asteroidal parent bodies. The complexity and diversity of chondritic components essential precludes any single criterion as being uniquely indicative of one environment versus another. However, one potentially useful criterion is whether the effects of alteration are developed heterogeneously or homogeneously within similar components in an individual chondrite. This criterion is based on the assumptions that, given similar mineral compositions and grain sizes in a specific component (i.e. a CAI or a chondrule) and a homogeneous distribution of fluid on a local scale (10s to 100s of microns), components should alter to a similar degree if alteration occurred on a parent body after accretion. The same need not necessarily be true for alteration in the nebula prior to accretion, because mixing of different components with variable degrees of alteration may have occurred. Hence, the corollary of the argument for parent body alteration is that components in the same chondrite, with highly variable degrees of alteration, may be indicative of pre-accretionary alteration, provided that mixing of these components by processes, such as parent body brecciation, can be ruled out.

One problem with this approach is the fact that our understanding of the response of different mineralogical components in chondrites to metasomatizing fluids is still limited. All the available empirical observations of alteration in chondritic

meteorites suggest that the silicate phases, most susceptible to metasomatizing fluids, are Ca-bearing phases. Evidence from the CV3 chondrites (Sect. 15.2.2) and experimental studies (e.g., Nomura and Miyamoto 1998) show that melilite and anorthite in CAIs are sensitive indicators of mineral–fluid interactions (e.g., McGuire and Hashimoto 1989). On the other hand, Ca-rich pyroxenes are much more resistant to alteration processes. In the case of the CO3 chondrites, at least qualitatively, melilite in CAIs is also a sensitive indicator of alteration for limited to moderate degrees of alteration. Anorthitic plagioclase in both CAIs and plagioclase-bearing chondrules is useful for monitoring more advanced stages of alteration persisting in the CO3 chondrites to the most advanced levels. Mesostasis glass also has considerable potential as an indicator of metasomatism over a wide range of degrees of alteration. However, its utility as a measure of metasomatism is limited until the effects of composition on the susceptibility of glass alteration are understood more fully. Mesostasis glass in chondrites has remarkably variable compositions in terms of all major elements (Brearley and Jones 1998). Some compositions appear to be more susceptible to alteration than others, but the details of which compositions react most readily with aqueous fluids is poorly constrained. This situation causes considerable problems when attempting to evaluate the evidence for and against metasomatism in low petrologic type chondrites. When evidence of very limited minor metasomatic effects is observed in a few rare components in an apparently otherwise unaltered chondrite, what does this mean? It could be interpreted as evidence that these components were metasomatized prior to accretion, either in the nebular or some other protoplanetary body, as suggested by Brearley (2003). On the other hand, it may simply be the fact that the glass in this object had a composition that made it much more susceptible to alteration by a metasomatizing fluid of a particular composition.

The interaction of chondritic components with aqueous fluids is therefore complex and selectively affects some components preferentially to others. This is particularly true for metasomatic fluids that are alkali and halogen-rich, whose effects are most evident in Ca-Al-silicates and glasses. In addition to the sensitivity of phases such as melilite, anorthite and glass, to aqueous alteration, a second important fact is that these phases amy also contain Na and Cl. Because of their large ionic radii, Na and Cl are commonly incorporated into framework silicates such as feldspars (Na) and feldspathoids (Na and Cl). So the presence of Al in melilite and anorthite in CAIs effectively provides a local compositional control on the location secondary where Na and Cl-rich phases are likely to form. Unlike Si, Al appears to be relatively immobile during fluid–mineral interactions in chondrites. Therefore formation of Na and Cl-rich phases, such as nepheline and sodalite, which are the most important indicators of metasomatism in CO3 chondrites, is constrained to those chondritic components whose primary mineralogy is Al-rich.

In addition to compositional factors that control where and how secondary alteration phases develop in chondrites, the textural characteristics of these phases are also of considerable importance. Studies of CAIs in CV3 chondrites (section 15.2.2.1) show that the grain size of the primary phases has a major influence on the degree of alteration experienced by these objects. For example, fine-grained CAIs

in Allende are all highly altered (McGuire and Hashimoto 1989), whereas coarser-grained CAIs show much more limited evidence of alteration. The variation in grain size of primary phases, such as melilite and anorthite in CAIs in CO3 chondrites, is currently very poorly constrained, because the CAIs are smaller, rarer, and have been studied in much less detail than those in CV3 chondrites. Russell et al. (1998) showed that there is variability in the degree of alteration of CAIs within individual CO3 chondrites, but without the details of the grain size from primary phases in these CAIs, it is not possible to assess whether this heterogeneity in the degree of alteration is simply the result of differences in grain size between different CAIs.

Another factor which may contribute to the apparent heterogeneity in the degree of secondary alteration, is the distribution of fluid within any chondrite. The infiltration of fluids into a chondrite within a parent body, is dependent principally on the porosity and permeability of the fine-grained matrix of a chondrite or the presence of fine-scale fractures (Bland et al. 2009). There is no *a priori* reason why the porosity and permeability of the matrix should be uniform throughout the chondrite. Local variations in the degree of compaction of matrix materials could, for example, limit fluid infiltration on the scale of 10s of microns, or, in the case of fine-scale fractures, cause increased fluid infiltration on a highly localized scale. Such localized differences are likely to be of particular importance in fluid-limited systems that seem to be characteristic of the CO3 chondrites. A heterogeneous distribution of fluid would obviously cause differential development of metasomatic effects, which could be mistakenly attributed to alteration prior to accretion. Such effects are likely to be most evident in situations where only limited fluid is available, but might be expected to become less important as the water/rock ratio increases

With these caveats in mind, we evaluate evidence for metasomatic alteration of CO3 chondrites in both parent body and nebular environments below.

15.3.5.1 Evidence for Parent Body Metasomatic Alteration of CO Chondrites

There is widespread agreement that the well-defined metamorphic sequence observed in the CO3 chondrites occurred on an asteroidal parent body. This conclusion comes from numerous studies that have examined multiple different characteristics of a large number of CO chondrites (e.g., Scott and Jones 1990; Sears et al. 1991; Grossman and Brearley 2005; Bonal et al. 2007). It has been demonstrated that there are significant correlations between the textural and mineralogical changes that occur in chondrules, matrix, and metal as a function of increasing petrologic type. No other possible environment, other than progressive heating within a parent body, is currently able to explain the observed phenomena.

The concept of parent body thermal metamorphism has therefore become an important framework for considering where and when metasomatic alteration occurred. The relationships between thermal metamorphism and metasomatism are discussed in more detail below. This discussion focuses solely on the arguments

that indicate a general relationship between thermal metamorphism and metasomatism, i.e., supports a parent body environment for metasomatism.

The studies discussed above show that the style of metasomatic effects in the different components of CO3 chondrites, i.e. chondrules, AOAs, and CAIs, are all basically similar. All these studies show that the principle type of metasomatism involved is the introduction of Na into these objects, which has promoted the alteration of Ca-bearing phases (melilite, anorthite, and chondrule mesostasis) to form nepheline. There is minimal evidence of the halogen metasomatism that is widespread in the CV3 chondrites as indicated by the rarity of sodalite as a metasomatic alteration product in the CO3 chondrites. In addition, chondrules and AOAs show evidence of Fe metasomatism as indicated by the formation of fayalitic veins and overgrowths of fayalite on clinoenstatite grains. These lines of evidence indicate that all the components, within an individual chondrite, were affected by the same metasomatic fluid, i.e., all chondritic components had been assembled into a single parent body, prior to interaction with aqueous fluids.

The second line of evidence to support a parent body environment for alteration is the general correlation of increasing metasomatic effects in different components with petrologic type. As documented above, these include replacement of melilite and anorthite in CAIs, as described by Kojima et al. (1995) and Russell et al. (1998), the formation of rims of fayalite on AOAs (Rubin 1998; Chizmadia et al. 2002), the replacement of plagioclase in chondrules by nepheline (Tomeoka and Itoh 2004), and alteration of mesostasis glass to nepheline (Tomeoka and Itoh 2004). This correlation demonstrates that all the components must have been altered under the same conditions, which were unique for each meteorite. The fact that the extent of development of these different phenomena also shows a progressive increase, as a function of petrologic type, indicates that temperature and/or time were important controls on the reaction processes. This can most reasonably be attributed to a metamorphic process within an asteroidal parent body in which individual CO3 chondrites were heated to different temperatures and/or for different times.

15.3.5.2 Evidence of Nebular Metasomatic Alteration of CO Chondrites

As discussed by Brearley (2003), potential indicators of nebular alteration of chondritic components are variability in the style and extent of alteration effects between components with similar compositional and mineralogical characteristics. Heterogeneity in the extent of alteration has to be interpreted with caution, as discussed above. However, significant variability in the degree of alteration can, in some low petrologic type meteorites, be reasonably attributed to pre-accretionary processes, provided the effects of brecciation can be definitively ruled out.

With our current state of knowledge, the heterogeneity criterion is the one that is used most commonly to argue for pre-accretionary alteration. This perspective has been presented by Jones (1997) for the metasomatism of plagioclase-rich chondrules in CO3 chondrites, using two different lines of evidence. In Kainsaz (3.2) and Lancé (3.4), plagioclase-rich chondrules generally show similar degrees of nephelinitization

(minor in Kainsaz and intermediate in Lancé) and replacement of silica by salitic pyroxene in their mesostasis. However, in ALHA 77003 and ALH 83108 (3.6), three plagioclase-rich chondrules show quite different degrees of alteration, ranging from almost no development of nepheline in one chondrule to very extensive nephelinitization in two chondrules. Such an extensive difference in the degree of metasomatic alteration in comparatively highly metamorphosed chondrites cannot be easily reconciled with alteration on a parent body, leading to the conclusion that metasomatic alteration occurred in the nebula prior to accretion (Jones 1997).

Further support for this conclusion also comes from the compositions of olivine in the same chondrules. Based on the presence of Fe,Ni metal in plagioclase-rich chondrules, Jones (1997) argued that primary olivine in these chondrules should be highly forsteritic in composition ($<Fa_2$) and compositionally similar to olivine in type I chondrules. If Fe enrichment in these chondrules was driven solely by Mg-Fe exchange between chondrules and matrix during parent body metamorphism, any increase in Fe in chondrule olivines should be the same in both types of chondrules. However, this is not the case: olivine grains in plagioclase-rich chondrules are always more enriched in Fe than olivines in type I chondrules (e.g., Fig. 15.51). The difference in olivine compositions between the two types of chondrules is variable, but can range from as little as 7 mol% Fa in Kainsaz (3.1), to as high as 20 mol% in ALH 77003 (3.5). This decoupling of olivine compositions in the two types of chondrules was interpreted by Jones (1997) to indicate that Fe metasomatism must have occurred prior to parent body accretion in a nebular environment.

A similar conclusion was reached by Russell et al. (1998) based on their observations of CAIs in low petrologic type 3 CO chondrites. As discussed above, metasomatic alteration of CAIs in CO3 chondrites shows a general correlation with increasing petrologic type. However, rare inclusions in low petrologic type CO chondrites, such as Colony (3.0), show evidence of alteration and enrichment in alkalis that contrasts with the pristine, unaltered characteristics of other similar inclusions in the same chondrite. The anomalous degree of alteration of these inclusions cannot be related to metamorphism and suggests that the CAIs were altered prior to accretion and not within the parent body. This view is supported by the Al-Mg systematics of inclusions from these chondrites, some of which show disturbed isochrons. The occurrence of CAIs, with both pristine and disturbed isochrons within type 3.0 CO3 chondrites, shows that some inclusions were evidently processed prior to accretion and not within the parent body. However, it is not clear if resetting of the isotopic systematics of the CAIs is related to metasomatic effects. The environment under which objects were metasomatized prior to accretion is not well constrained, but may have been some kind of protoplanetary body, which was disrupted by impacts and the altered CAIs were re-accreted into the final CO3 chondrite parent body. Alternatively, metasomatism might have occurred in a nebular environment with very enhanced dust to gas ratios, where localized high temperature events may have caused evaporation of dust and transient increases in the vapor pressure of volatile elements.

15.3.6 Relationship Between Aqueous Alteration, Metasomatism, and Thermal Metamorphism in CO3 Chondrites

As summarized above, there is a considerable body of evidence demonstrating that aqueous fluids played an important role in the evolution of the CO3 chondrites. However, as discussed in the introduction, there is also considerable confusion regarding the use of the terms aqueous alteration, metasomatism and fluid-assisted metamorphism to describe the mineral–fluid processes that have affected chondrites. For the CO3 chondrites, some authors have used the term aqueous alteration to describe any kind of mineral–fluid interaction (e.g., Bonal et al. 2007), whereas Rubin (1998), Wasson et al. (2001), and Chizmadia et al. (2002) have used the term aqueous alteration to describe fluid–mineral interactions in low petrologic type CO chondrites, but fluid-assisted metamorphism for processes in higher petrologic types. Using the criterion discussed in the introduction, we attempt to clarify the processes that affected CO3 chondrites and the relative timing of these alteration processes.

As discussed in Sect. 15.3.3, there does appear to be a general correlation between the petrologic type of individual CO3 chondrites and the degree of metasomatism that has affected CAIs, AOAs, and chondrules etc., which is supportive of a parent body environment for metasomatism. This correlation has been used to indicate that metamorphism and metasomatism were coupled (e.g., Rubin 1998), and that these chondrites have therefore undergone fluid-assisted metamorphism, as defined in Sect. 15.1.4. However, the nature of the coupling between thermal metamorphism and metasomatism is not necessarily straightforward and it is useful to consider other possible scenarios. These scenarios relate to the timing and duration of the availability of fluids during metamorphism of the CO3 chondrites. In the first case, aqueous fluids could have been present for the entire duration of thermal metamorphism. Alternatively, the metasomatic effects observed in the CO3 chondrites could be the result of interactions caused by a pulse of aqueous fluid close to the maximum temperature of thermal metamorphism. Finally, the fluids could have been introduced following the metamorphic maximum, when temperatures were beginning to wane. These different models have rather different implications for the behavior of aqueous fluids on asteroidal parent bodies.

Models for thermal metamorphism of chondritic parent bodies (e.g., ordinary chondrites and CO3s) consider asteroidal heating to have occurred as a result of heat released by decay of ^{26}Al (e.g., McSween et al. 2002). The asteroidal parent body undergoes heating from the interior outwards and hence results in a radially structured sequence of thermal metamorphosed chondrites, with the most highly metamorphosed in the interior of the asteroid. In this model, chondritic materials are progressively heated, i.e. undergo prograde metamorphism and hence will evolve through different degrees of thermally-driven chemical and textural equilibration as temperature increases. Following the peak of metamorphism,

temperatures will begin to wane, with the most deeply buried undergoing the slowest cooling.

It is commonly assumed that the source of water that drives mineral–fluid interactions is water ice that was accreted with all the other components of chondrites to form asteroidal parent bodies (e.g., Grimm and McSween 1989; McSween et al. 2002). Therefore, as heating takes place, melting of this water ice will occur and will begin to drive mineral–fluid reactions. It will also result in a progressive movement of liquid water from the interior of the asteroid to the exterior in response to pressure gradients within the asteroid (McSween et al. 2002). In the initial stages of asteroidal heating, when temperatures are low, conditions will be in the regime of aqueous alteration and will result in the formation dominantly of hydrous phases, such as phyllosilicates (Zolotov et al. 2006). The extent to which aqueous alteration occurs will depend on the kinetics of the hydration reactions, the amount of water and the time available to drive the reactions. Experimental studies indicate that if the available fluid is significant (i.e. elevated water/rock ratios), then evidence of aqueous alteration will develop at temperatures of 100–200°C on timescales of weeks to months (Jones and Brearley 2006; Brearley and Burger 2007). This rate of reaction is much faster than the rate at which asteroidal bodies were heated during the prograde thermal path (e.g., McSween et al. 2002). At lower water/rock ratios, the extent of reaction will be much lower. Nevertheless, these data do indicate that if water is available, aqueous alteration of chondritic materials will take place during the prograde heating path.

If aqueous alteration does occur at low temperatures during the prograde heating path and results in the formation of phyllosilicate phases, these phases will become a potential source of water to drive fluid-assisted metamorphism as temperatures increase. If alteration at low temperatures is significant, then all the available fluid may be consumed during hydration reactions of the precursor materials and hence be unavailable to facilitate further aqueous alteration. Irrespective of whether complete consumption of any fluid phases does occur at low temperatures, the presence of phyllosilicate phases provides a potential reservoir of water that is available for reaction as temperature increases. The effective trapping of water in phyllosilicates during the prograde metamorphic path is important, because it prevents at least some fluid from being lost from the asteroid due to outgassing at the surface. As temperatures reach 300–400°C, dehydration of these phyllosilicates (Grimm and McSween 1989) will start and release aqueous fluid that can drive fluid-assisted metamorphism. The dominant reaction products of fluid-assisted metamorphism are anhydrous phases (Zolotov et al. 2006), therefore the aqueous fluids are not consumed in the reactions and hence may be continually available to act as a reactant, catalyst and mass transport agent to drive further metasomatic reactions.

An alternative model is that little fluid was present during the prograde thermal path and that aqueous alteration did not affect low petrologic type chondrites, hence development of phyllosilicates did not occur. In this case, then there was no potential mineralogical reservoir of aqueous fluid that could be released as

temperatures rose during the prograde heating path. In this scenario, an alternative external source of fluid is required that was introduced into the chondrite at some later stage in its thermal history. The timing and duration of the availability of this fluid phase is open to debate. The fluid could have been available transiently, rather than being present for an extended period of time. However, the apparent correlation between petrologic type and degree of metasomatic alteration suggests that fluid was certainly available at or close to the thermal peak of the metamorphic event.

The following observations from CO3 chondrites provide some constraints on which one of these models is most likely. In the first case, it is apparent that the availability of water in the CO3 chondrites was far more limited than in several other chondrite groups. The CI1, CM1/2, and CR2/3 chondrites all show significant evidence of aqueous alteration, as indicated by the development of phyllosilicate phases to varying degrees in the primary components of these meteorites (e.g., Zolensky and McSween 1988; Brearley 2006; Zolensky et al. 2006). Even petrologic type 3 unequilibrated ordinary chondrites, such as Semarkona (LL3.0) and Bishunpur (LL3.1), show significant evidence of aqueous alteration (Hutchison et al. 1987; Alexander et al. 1989) that has dominantly affected the matrix as well as the chondrules (Grossman et al. 2000, 2002). In contrast, there are no known CO3 chondrites that show significant evidence of aqueous alteration. Based on transmission electron microscope (TEM) studies of several CO3 chondrite matrices, which are the most sensitive component of chondrites to aqueous alteration, it is apparent that evidence of aqueous alteration, i.e. the presence of significant abundances of phyllosilicates, is minimal. There is evidence of aqueous alteration in the lowest petrologic type CO3 chondrite, ALHA 77307 (CO3.0), in the form of rare phyllosilicates in the matrix (Brearley 1993) and more commonly in the chondrules (Ikeda 1983). However, TEM studies of several CO3 chondrites, (Kainsaz, Ornans, Warrenton) (Keller and Buseck 1990b; Brearley 1994; Brearley and Jones 1998), show no evidence of the presence of phyllosilicates or other alteration products in their matrices. The only CO3 chondrite that shows clear evidence of aqueous alteration is Lancé, where the matrix olivines show evidence of incipient aqueous alteration, with the development of very minor Mg-rich serpentine and a poorly crystalline Fe^{3+} oxide dispersed between matrix olivine grains and along fractures within the olivine (Keller and Buseck 1990b).

With the exception of ALHA 77307, it is therefore clear that the term aqueous alteration as defined earlier, i.e. a process that has resulted in the formation of phyllosilicate phases, should not be applied to any of the key mineral-fluid interactions that may have affected these meteorites. The absence or rarity of hydrated phases in low petrologic type chondrites also indicates that fluid availability on the CO3 chondrite parent body was extremely limited and that the development of hydrous phases during the low temperature stage (<~100°C) of prograde thermal metamorphism did not occur. Furthermore, CO3 chondrite matrices do not contain olivines with textural characteristics that are indicative of formation by dehydration of pre-existing phyllosilicates. Such textures have been well-documented in the matrices of the unusual carbonaceous chondrites Y-

793321, Y-87620, and Y-82162 that have experienced aqueous alteration followed by thermal metamorphism (Akai 1988, 1992; Tomeoka et al. 1989). Therefore, the dehydration of pre-existing hydrous phases to provide an aqueous fluid phase, which drives fluid-assisted metamorphism as the temperature increased, seems highly improbable for the CO3 chondrites.

These constraints lead to the conclusion that metasomatizing fluids may not have been present throughout the period of metamorphic heating, but were introduced at some later stage in the thermal history of the chondrite. The constraints on when this happened are extremely limited and the source of the fluids is currently unknown. However, we can say, with considerable certainty, that either the amount of fluid that was available was extremely limited, compared with, for example, the $CV3_{OxA}$ subgroup, or that the duration of its interaction with the CO3 chondrite protolith material was short. If this is correct, then the processes of thermal metamorphism and metasomatism were not necessarily coupled in the sense that is often suggested in the literature. For example, thermal metamorphism of the CO3 chondrites could have proceeded, to a significant degree under relatively dry conditions, in the absence of a fluid phase, but a fluid was introduced close to the peak of thermal metamorphism. This could have occurred under either pre- or post-peak metamorphic conditions. In this scenario, the observed correlation of increased metasomatic effects with petrologic type would reflect the fact that reactions occurred at higher temperature and/or for longer periods of time depending on the maximum temperature of thermal metamorphism. The development of Mg-Fe compositional zoning in olivines and spinels would have occurred during dry thermal metamorphism, but the replacement of primary mineral phases, such as melilite, anorthite, and plagioclase, and the growth of fayalitic veins, in AOAs and fayalitic overgrowths on olivine and pyroxene, occurred during the period when a metasomatic fluid was present. In this model, although thermal metamorphism and metasomatism are interdependent, they are not necessarily coupled. In other words, the presence of a fluid did not necessarily drive metamorphic processes, throughout the metamorphic evolution of the CO3 chondrites.

These different models for the interaction of metamorphism and metasomatism clearly depend on the mobility of aqueous fluids on asteroidal parent bodies. For example, were fluids only mobile on a local scale (centimeters to meters) or did they move over long distances (kilometers), such that fluids could move from the interior of asteroidal parent bodies to the exterior and perhaps set up convection cells within the parent body? There has been discussion in the literature of the movement of fluids within asteroidal parent bodies and quite different perspectives have been presented. Bland et al. (2009) have provided a detailed summary of the current status of this debate; only a brief summary of the key elements of this subject will be presented here. Theoretical models of aqueous alteration on asteroidal parent bodies, pertinent to highly hydrated chondrites such as the CI and CM chondrites, invariably invoke large scale fluid flow over 10s of kilometers. Bland et al. (2009) have noted that these models fall into three different categories, as follows: (1) Exhalative models, which involve a single pass of water through the body, driven by increasing temperatures and resultant excess fluid pressures in the asteroid core

as a result of heating, usually considered to be caused by decay of ^{26}Al (Young et al. 1999; McSween et al. 2002); (2) episodic flow (Cohen and Coker 2000; Coker and Cohen 2001); and (3) convection cells in which fluid circulates within the parent body driven by thermal buoyancy (Grimm and McSween 1989; McSween et al. 2002; Young et al. 1999, 2003; Travis and Schubert 2005). These different models use a variety of assumptions about the structure, size, porosity, permeability, initial ^{26}Al content, etc. of the parent body. In the case of the models proposed by Young et al. (1999) and Young et al. (2003), the oxygen isotopic compositions of different carbonaceous chondrites is explained by a progressive isotopic evolution of the fluid as it passes through the parent body.

In contrast to, the usual model assumption of extensive fluid flow in asteroidal parent bodies, most observations of chondrites indicate that fluid flow was extremely limited and that mass transport generally occurred on scales of a few 100 μm at most. A variety of lines of evidence have been summarized by Bland et al. (2009) to support this conclusion, including the fact that even very extensively aqueously-altered chondrites show no evidence of depletions or enrichments in water-soluble, highly mobile elements such as the alkalis and alkali earths, i.e. alteration appears to have been completely isochemical. In addition, Bland et al. (2009) emphasized the fact that numerical models typically assume carbonaceous chondrite porosities of 10^{-13} to 10^{-11} m^2, whereas the true values are several orders of magnitude lower (10^{-19} to 10^{-17} m^2). Such low values would appear to preclude any extensive movement of fluids within asteroids and hence are very problematic for models of metasomatism such as those discussed above that require introduction of fluids into distinct regions of the chondrite parent body at different times during their thermal evolution.

However, an alternative perspective that can reconcile these two different extreme positions is possible. Brearley (2006) provided several lines of evidence that demonstrate that the geochemical conditions within carbonaceous chondrites are highly variable on a very localized scale and proposed the concept of microchemical environments with carbonaceous chondrites. In particular, Brearley (2006) drew attention to the fact that local variations in pH on length scales of 10s of microns are evidently present within carbonaceous chondrites. These variations in pH are attributable to the different reaction behaviors of highly unequilibrated mineral assemblages with different grain sizes that constitute carbonaceous chondrites. The local pH of the fluid is then controlled by these localized mineral reactions. As a consequence, highly fluid mobile elements, such as Ca, can be leached and transported in solutions that have a relatively low pH. However, whenever these fluids encounter geochemical reaction fronts where pH is slightly higher, precipitation of Ca-rich phases occurs. Brearley (2006) and Burger and Brearley (2005) have presented data that demonstrate this behavior for Ca-carbonates and Ca-phosphates in CM and CR chondrites. Ford and Brearley (2008) have also described the alteration and transport of Ca during the replacement of melilite in CAIs from Allende. In this latter case, although extensive removal of Ca from the CAI occurred during alteration of melilite, a simple numerical mass balance model shows that the entire mass loss can be accounted for by the formation

of Ca-rich phases, such as diopside-hedenbergite and andradite, which occur in a halo within the surrounding matrix around the CAI. These lines of evidence show that isochemical alteration of carbonaceous chondrites could have occurred, even if fluid flow was taking place. Extensive transport of soluble elements over considerable distances did not occur, because these elements were precipitated from solution as solid phases when they encountered geochemical reaction fronts that are present on the scale of 10s to 100s of microns in chondrites. The sequestering of soluble elements into solid phases, when they precipitate from solution under favorable pH conditions, could be an effective way of reducing or eliminating large-scale elemental transport in a flowing fluid. Hence, isochemical alteration behavior observed in chondrites does not necessarily preclude extensive fluid flow.

On the other hand, the very low permeabilities measured by Bland et al. (2009) would appear to severely limit the possibility of extensive fluid flow. However, these measurements are obviously made on the samples as they exist today. This does not necessarily mean that the present permeability is the permeability of the rock at the time that aqueous fluids were present. For example, the permeability of a chondrite could change significantly in the very last stages of alteration as the last dregs of an aqueous fluid react with silicate material, particularly the extremely fine-grained material in the matrix of carbonaceous chondrites. It is well recognized that the formation of hydrous alteration products from an hydrous phases causes an increase in volume (Jones and Brearley 2006). Hence the final absorption of the remaining fluid into solid hydrous phases could effectively fill any remaining porosity and dramatically reduce the permeability of the rock, compared with the permeability when active alteration was taking place. Further work is clearly needed to more fully understand the changes in permeability that may occur during fluid-mineral interactions within chondrites.

15.4 Metasomatic Alteration of the Ordinary Chondrites

15.4.1 Background

The ordinary chondrites represent the most comprehensive extraterrestrial sample suite covering the range from unmetamorphosed chondritic material to the highest temperatures of thermal metamorphism known. The so-called unequilibrated ordinary chondrites (UOCs), classified as petrologic type 3 meteorites, provide very important insights into the changes that occur during the very earliest stages of asteroidal metamorphism. Types 4–6 ordinary chondrites, the so-called equilibrated ordinary chondrites (EOCs), display numerous features indicative of extensive thermal metamorphism, including solid-state recrystallization and equilibration of heterogeneous mineral compositions. The highest grade, type 6 chondrites are highly recrystallized rocks with microstructures that approach textural equilibrium. Although ordinary chondrites represent the largest group of chondritic meteorites,

by far, the effects of metasomatism in this group of meteorites is still poorly understood, as is the relationship between metamorphism and metasomatism. The traditional view of metamorphism in the ordinary chondrites has been that it occurred under fluid-absent conditions. However, there is an increasing body of evidence that fluids played an important role in the evolution of at least some members of this group of meteorites. This group of meteorites represents fertile ground for exploring the effects of metasomatic processes and the interplay of metamorphism and metasomatism in chondritic meteorites.

15.4.2 Metasomatic Effects in Unequilibrated Ordinary Chondrites

Type 3 meteorites of all three of the groups of the ordinary chondrites (H, L and LL) occur as unequilibrated assemblages of chondrules, matrix, Fe,Ni metal, and Fe,Ni sulfides (mostly troilite), and rare refractory inclusions, and show considerable diversity in terms of texture and metamorphic variability (Scott and Krot 2005a). The lowest petrologic type 3 ordinary chondrites (type 3.0−3.2) commonly show evidence of interaction with aqueous fluids at low temperatures, indicated by the development of phyllosilicates, ferroan olivine, and magnetite in their matrices and sometimes chondrules (e.g., Hutchison et al. 1987; Alexander et al. 1989; Krot et al. 1997b, 2011; Choi et al. 1998). Metasomatic effects, on the other hand, tend to occur in type 3 chondrites that show higher degrees of metamorphism (above type 3.4). Although the two processes may be linked, there is, however, no evidence of any apparent correlation between the degree of metasomatism and petrologic type of UOCs. Metasomatism appears to have affected these meteorites in a highly heterogeneous fashion.

Mineralogically, the effects of metasomatism in UOCs are generally subtle and not widely developed. These effects have been well documented in Chainpur (LL3.4), Parnallee (LL3.6), and Tieschitz (H3.6). Although there is some variability between these meteorites, the key indicators of metasomatism are the presence of feldspathoids (nepheline and sodalite) and, to a lesser extent, scapolite ($Na_4A1_3Si_9O_{24}Cl$) (see Table 15.1 for a summary of secondary metasomatic minerals in ordinary chondrites). The heterogeneous development of metasomatic effects in UOCs has been clearly demonstrated by a detailed study of separated chondrules and clasts from Chainpur and Parnallee (Bridges et al. 1997). In Chainpur, just 3 out of 46 (7%) chondrules and clasts show evidence of metasomatism with Parnallee showing a similar proportion of metasomatized objects (3 out of 39 − 8%). In both meteorites, the effects of metasomatism are only apparent in Na, Cl-rich mesostasis of chondrules, which contain rare to minor microcrystalline nepheline, sodalite, and scapolite. Only one chondrule (in Parnallee) was observed where a feldspathoid phase (nepheline) is present within plagioclase. An occurrence

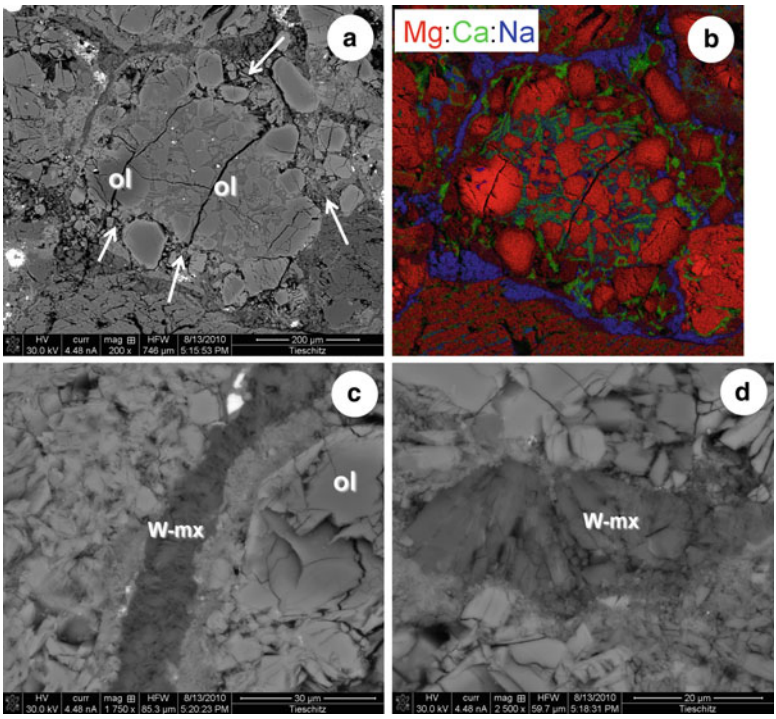

Fig. 15.61 BSE images and combined x-ray elemental maps of the so-called "White Matrix" (W-mx) and metasomatic alteration of a type IIA chondrule in Tieschitz (H3.6). (**a**) BSE image of a typical type IIA chondrule containing abundant phenocrysts of ferroan olivine embedded within a glassy mesostasis. The peripheral region of the chondrule shows an extensive porous zone due to leaching and alteration of the mesostasis glass (*arrowed*). Combined x-ray elemental map in Mg (*red*), Ca (*green*), and Na (*blue*) of the type IIA chondrule shown in (**a**). The map shows that the chondrule is surrounded by an almost continuous vein or layer of a Na-rich phase, most likely nepheline or albite. The interior of the chondrule consists of zoned olivine phenocrysts (*red*) with a mesostasis of Ca-rich pyroxene crystals embedded in an Na-bearing glass. The porous regions of the chondrule, (*arrowed* in (**a**)), are regions of mesostasis that have had the Na-rich glass leached from them. (**c**) Close-up image of the peripheral region of the chondrule showing a vein of "White Matrix" (W-mx) that occurs at the interface between two chondrules. (**d**) Region of white matrix at the edge of the chondrule. The area consists of blocky to elongate crystals of nepheline, which have parallel to subparallel orientations. An unknown phase with a higher BSE contrast is intergrown locally with the nepheline, suggesting that the white matrix consists of more than one phase

of scapolite, which may also have a metasomatic origin, has also been reported by Alexander et al. (1987) in Bishunpur (LL3.1).

The chondrules that contain the feldspathoids and scapolite show no other evidence of corrosion or alteration of primary chondrule phases or evidence for the Fe-alkali-halogen metasomatism that is widespread in CV3 chondrules. For example, Ca,Fe-rich phases, like hedenbergite and andradite, are absent. Further, the bulk compositions of these chondrules fall within the normal range for

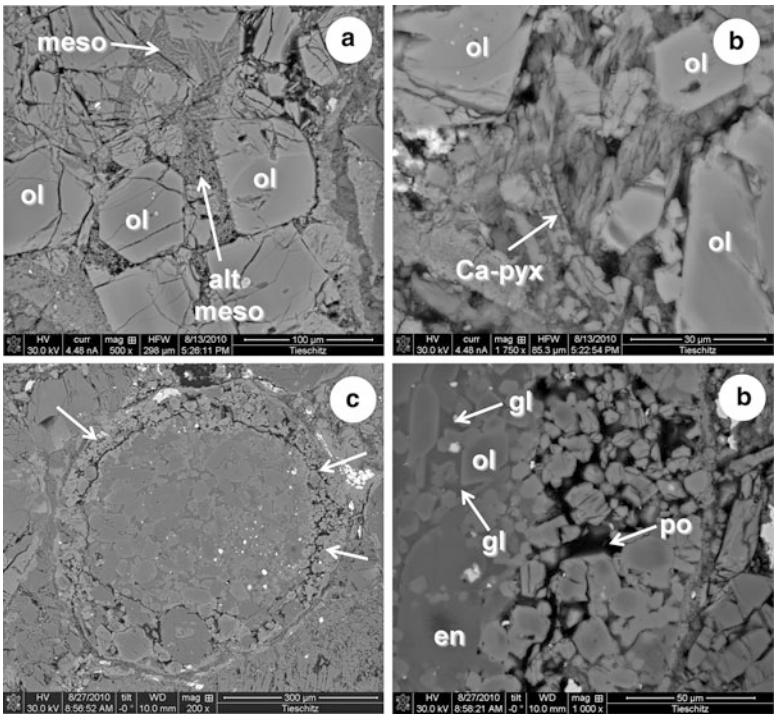

Fig. 15.62 BSE images showing evidence of metasomatic alteration of type IIA chondrules in Tieschitz (H3.6). (**a**) A region of a type IIA chondrule containing numerous euhedral and anhedral ferroan olivine (ol) crystals with interstitial mesostasis (*meso*). In the *upper part* of the image, the mesostasis consists of dendritic, Ca-rich pyroxene quench crystals with interstitial glass, but in the central and lower part of the image, the glass has been completely leached (*alt meso*) and now consists of a porous network of Ca-rich pyroxene quench crystals. (**b**) Close-up of a region in the chondrule showing olivine phenocrysts with interstitial mesostasis that has undergone extensive leaching. The mesostasis now consists of a framework of elongate and dendritic high-Ca pyroxene (Ca-pyx). No glass is present between the individual crystallites. (**c**) Type IAB chondrule consisting of olivine and enstatite phenocrysts with glassy mesostasis. The outer zone of the chondrule is highly porous where leaching of the glass has occurred. In this zone, the olivine grains have undergone more extensive metamorphic equilibration than those in the interior and consequently have a higher BSE contrast. (**d**) High magnification image of the outer porous region of the chondrule, where glass has been completely leached leaving abundant pores (po). On the *left*, the glass (gl), interstitial to phenocrysts of olivine and enstatite (en), is completely unaltered. There is no evidence of a transitional zone between porous and unaltered glass

chondrules and, with one exception, show no evidence of elevated Na or K contents, although one chondrule has 10xOC abundances of Cl. Ion microprobe analyses show that both plagioclase and nepheline are significantly enriched in Cl in these chondrules, in addition to significant concentrations of Cl in sodalite and scapolite as measured by electron microprobe.

Metasomatic effects in Tieschitz (H3.6) are significantly more prevalent than in either Chainpur or Parnallee. Historically, Tieschitz was the first unequilibrated

chondrite in which evidence of metasomatism was recognized in the form of an unusual "White Matrix", which was first described by Christophe Michel-Lévy (1976). This "White Matrix" occurs as veins or channels 10−50 μm wide between chondrules (Fig. 15.61) and is quite distinct from the typical, opaque, fine-grained matrix, which occurs in the least metamorphosed OCs. Several mineralogical studies have shown that the "White Matrix" consists of a blocky nepheline, albite and an unidentified Na-rich aluminosilicate phase (Christophe Michel-Lévy 1976; Ashworth 1981; Hutchison et al. 1979; Alexander et al. 1989).

Hutchison et al. (1998) studied several chondrules from Tieschitz, which contain two texturally distinct types of mesostasis (Fig. 15.62a, b). The dominant mesostasis has a smooth appearance and is unaltered primary chondrule glass. The second type of mesostasis has pervasive cracking, giving it a blocky appearance on the scale of ~ 10 μm and occurs only on the peripheral regions of the chondrules, suggesting that has formed as a result of alteration. An intermediate zone that is enriched in CaO and FeO occurs at the contact between the two texturally distinct regions of mesostasis. Although the mineralogical characteristics of the blocky mesostasis are poorly constrained, energy dispersive spectrometer (EDS) x-ray analysis shows that compositionally it is enriched in Al_2O_3, K_2O, Na_2O, and Cl and depleted in SiO_2, FeO, and CaO, compared with smooth mesostasis. Analytical totals for the blocky mesostasis are also significantly lower (81−89 wt.%) than smooth mesostasis (97−98 wt.%), due to the presence of voids, and possibly the presence of unanalyzed water within the blocky mesostasis. Trace element analyses by SIMS show that in the altered mesostasis, Li, K, Rb, and Ba are enriched 4−88× the concentrations present in the unaltered mesostasis with the halogens Cl and F showing variable enrichments of 5−47× and 2−56×, respectively. However, the incompatible elements, Y, Zr and REE are unfractionated between altered and unaltered mesostasis. Significantly, Hutchison et al. (1998) found that the elemental abundance patterns for Li, K, Rb, Ba, and the halogens in the Tieschitz "White Matrix" are very similar to altered, blocky mesostasis, but the REE are much more heterogeneous in the "White Matrix".

Chondrules in Tieschitz also exhibit effects which have been widely attributed to the presence of an aqueous metasomatic fluid. Kurat (1969) first noted the widespread occurrence of voids, ranging in size from a few 10s of microns to several hundred's of microns in size in chondrules from Tieschitz (Fig. 15.62c, d). This observation was confirmed by Christophe Michel-Lévy (1976) and Hutchison et al. (1998). Although some of these voids may have formed during primary crystallization of the chondrules, Hutchison et al. (1998) argued that many voids certainly have a secondary origin and were produced by leaching of the primary chondrule phases, particularly mesostasis glass.

Although Tieschitz appears to represent the most extreme example of metasomatic alteration of any known UOCs, evidence of metasomatism in type 3 OCs of higher petrologic type (> 3.4) is also known. The Bo Xian (LL3.9) chondrite is the most studied example of a UOC fall that shows both the mineralogic and stable isotopic effects of metasomatism. Li et al. (2000) carried out a petrologic and oxygen isotopic study of a large suite of separated chondrules from Bo Xian.

They found that 4% of the chondrules (exclusively Al-rich chondrules) in this meteorite contain alkali and Cl-rich phases, a proportion similar to that observed in Parnallee and Chainpur by Bridges et al. (1997). These phases are principally mesostasis with a mixed nepheline-anorthite composition with $\leq$4 wt.% Cl and localized Cl-bearing glass. It is notable that these alkali-rich phases occur exclusively in all the Al-rich chondrules in the chondrule suite studied. Such Al-rich chondrules have been described in detail by Bischoff and Keil (1984) and are much rarer than the more common ferromagnesian chondrules with mineralogies dominated by olivine and pyroxene. Aluminum-rich chondrules contain mineral assemblages that bear close affinities to those observed in CAIs in chondritic meteorites, such as spinel, anorthite, hibonite, and Ti-Al-rich diopside (commonly called fassaite in the older meteoritics literature, a mineral name which has been discredited; Morimoto et al. 1988).

Jones and Brearley (2010a, b) have documented additional multiple lines of mineralogic and textural evidence for the involvement of water in the evolutionary history of Bo Xian (LL3.9). These effects are widespread and indicate that the processes that affected Bo Xian were pervasive and not restricted to specific chondrule types. Primary anorthitic plagioclase in chondrules shows the development of submicron lamellae of a phase composed of an amorphous Si, Al-rich material, that is locally highly enriched in Cl. Calcium has been leached completely from these lamellae; however, no evidence of hydrous phases is present. Textural observations of rare chlorapatite grains in Bo Xian are also indicative of the presence of fluids. These grains contain numerous pore-like features that resemble those in terrestrial apatites that have undergone dissolution and reprecipitation (e.g., Harlov et al. 2002). Finally, enstatite grains in chondrules commonly show evidence of dissolution and overgrowth by ferroan olivine, in a textural relationship that is remarkably similar to that observed in Allende and other members of the Allende subgroup of the oxidized CV3 chondrites (Jones and Brearley 2010b). These observations indicate that the range of mineralogical effects caused by metasomatism in ordinary chondrites may extend significantly beyond the typical alkali-halogen metasomatism that has been more commonly documented.

Based on oxygen isotopic data from mineral separates from Bo Xian, Li et al. (2000) have suggested that a low temperature ($<$400°C) hydrous gas–solid event affected this meteorite, prior to thermal metamorphism. Framework silicates (feldspar and cristobalite) in Bo Xian have heavier oxygen isotopic compositions than olivine and pyroxene mixtures, evidence that was interpreted as the result of differential oxygen isotopic exchange rates between these different minerals at low temperatures. The isotopic differences between these two types of phases were not obliterated by thermal metamorphism.

Li et al. (2000) argued that the interaction of Bo Xian with aqueous fluids occurred prior to thermal metamorphism. However, this appears to be inconsistent with the mineralogical data of Jones and Brearley (2010a, b), which indicate that mineral–fluid interactions were late-stage and occurred during the waning stages of thermal metamorphism. The reasons for this dichotomy are not clear, but it is possible the Bo Xian experienced two episodes of mineral–fluid interaction.

However, the first stage, at least mineralogically, has probably been obliterated by thermal metamorphism and the late-stage mineral fluid interactions are of insufficient extent to produce significant isotopic exchange. Further studies are clearly necessary to evaluate these different possibilities.

15.4.3 Metasomatic Effects in Equilibrated Ordinary Chondrites

It has been commonly assumed that the equilibrated ordinary chondrites underwent metamorphism under essentially dry conditions. The possibility of the involvement of fluids in the process of metamorphism has not generally been considered, in detail, although evidence of oxidation during the thermal metamorphism of the ordinary chondrites has been attributed to the presence of a fluid phase (e.g., McSween and Labotka 1993). In view of the fact that there is evidence of mineral–fluid interactions in high petrologic type 3 chondrites, it is appropriate to consider the possibility that the equilibrated ordinary chondrites (types 4–6) may have been affected by aqueous fluids.

The timing of the presence of fluids relative to metamorphism is of key importance in type 4−6 chondrites. Mineralogical evidence, indicative of the presence of fluids during prograde metamorphism may have simply been obliterated by recrystallization and compositional reequilibration. However, post peak metamorphic interaction with fluids may be preserved. Limited evidence to suggest that this is the case has come from recent studies of feldspars in petrologic type 4 chondrites. Kovach and Jones (2010) found that feldspars in types 4 through 6 ordinary chondrites show heterogeneous compositions, which they suggested might be the result of formation by recrystallization of mesostasis glass in the presence of aqueous fluids. More recently, detailed studies of feldspar in the LL4 chondrite Bjurböle provide direct evidence that feldspars in this chondrite have interacted with fluids. However, this interaction has clearly not taken place during prograde metamorphism, but appears to represent a late stage event, probably during the waning stages of thermal metamorphism (Jones and Brearley 2010a).

Plagioclase feldspar grains in several Bjurböle chondrules have anorthitic cores with much more albitic rims, several microns in width. Transmission electron microscope studies show that the anorthitic cores contain myriad pores and submicron inclusions of crystallographically-aligned chromite grains, whereas the albitic rims contain much larger pores that have internal facets that are also crystallographically aligned. Other chondrules contain linear features (<0.2 μm in width) in the feldspar that are reminiscent of the lamellae of nepheline observed in plagioclase feldspar in CO3 chondrite chondrules, but also consist of aligned pores. On the TEM scale, the linear features consist of aligned, faceted pores along which larger chromites are present, but the silicate phase within the lamellae is actually albitic feldspar, not nepheline.

Collectively these features indicate that anorthitic feldspar, which likely crystallized from mesostasis glass during prograde metamorphism, has interacted

with an aqueous fluid that caused partial albitization of the feldspar. The fluid appears to have partially dissolved the feldspar, resulting in the development of abundant voids and has also driven the exsolution of chromite from the feldspar during this process. The voids may represent the remains of fluid inclusions.

The style of alteration is completely different from that observed in the CO3 and CV3 chondrites. Wholesale albitization of the feldspar has occurred in Bjurböle, demonstrating that Si and Na were exchanged with Al and Ca during the reaction, rather than leaching of Si and Ca as occurs during the replacement of plagioclase in CO3 chondrites. In addition, a further major difference between metasomatism in the ordinary chondrites, compared with the CO3 and CV3 chondrites, is the behavior of Al. In the carbonaceous chondrites, Al appears to behave as a quite immobile element, whereas in the ordinary chondrites, there is significant evidence that Al was more mobile. The extreme case of the mobility of Al is apparent in Tieschitz (H3.6), where transport of Al to form the "White Matrix", consisting largely of nepheline and albite, was clearly extensive and appears to have been largely derived from leaching of mesostasis glass in the chondrules. Clearly the conditions of alteration in the ordinary chondrites differed in important respects, as did the chemistry of the metasomatizing fluids, from those in the carbonaceous chondrites. However, there have, as yet, been no investigations to address these differences in behavior.

15.4.4 Origin of the Metasomatic Effects Observed in Unequilibrated and Equilibrated Ordinary Chondrites

The development of a full understanding of the role of metasomatism in the evolution of the ordinary chondrites is still in its infancy. This situation comes largely from the fact that much of the evidence of metasomatism is cryptic, developed on variable scale from one ordinary chondrite to another, and, where present, is developed on a very limited scale. Additional factors may be that such meteorites have not been studied in as much detail as carbonaceous chondrites or because metamorphic effects begin to dominate over metasomatic effects as petrologic type increases and hence become obscured as metamorphism increases. Research in this area has also suffered from the fact that metamorphism in the ordinary chondrites has generally been regarded as a process that occurred under water-absent conditions. This assumption is typically not stated explicitly, but the absence of any discussion of the role of fluids in reviews of metamorphism in the ordinary chondrites (e.g., Huss et al. 2006) underscores this assumption. Only a few pioneering studies, such as those by Christophe Michel-Lévy (1976), Bridges et al. (1997), Hutchison et al. (1998), and Li et al. (2000) have really pointed to the idea that hydrous fluids were present during metamorphism in the ordinary chondrites and were an agent that could promote metasomatic processes.

As a consequence, there is some discussion in the literature over the origin and processes responsible for the observed metasomatic effects in ordinary chondrites. As is the case for the CV3 and CO3 chondrites, the debate focuses on whether the metasomatic effects occurred prior to or post accretion of the ordinary chondrite parent bodies. As noted earlier Brearley (2003) has discussed in detail, mineralogic, textural, compositional, and isotopic criteria that may be used to differentiate between these two different scenarios. In general, these criteria focus on whether metasomatic indicators are developed heterogeneously or homogeneously within a chondrite, provided the initial compositional heterogeneities of the precursor materials (e.g., chondrules) are taken into consideration. In addition, they also consider whether evidence of elemental/isotopic exchange between different heterogeneous components (e.g., chondrules and matrix) is apparent. This latter criterion assumes that the components of chondrites could not undergo significant elemental exchange until they were physically assembled together into asteroidal parent bodies. In evaluating element exchange, it is also important to consider the geochemical versus cosmochemical behavior of different elements, notably the solubility versus volatility of individual elements. For example, geochemically, Ca is a highly soluble element in aqueous solutions, but cosmochemically, behaves as a highly refractory element. Therefore, extensive elemental exchange of Ca between different components in chondrites is indicative of the role of aqueous fluids, not extensive transport in a vapor phase. On the other hand, redistribution of Na, which is volatile in terms of its cosmochemical behavior, but also highly mobile in aqueous fluids, could have occurred by both vapor phase and liquid phase transport.

In the case of high petrologic type 3 chondrites (3.5–3.9) and types 4 through 6, there is general agreement that the metasomatic processes occurred after accretion on an asteroidal parent body (Hutchison et al. 1998). For example, the effects of metasomatism in Tieschitz which manifest themselves pervasively in both chondrules and matrix, provide strong evidence that all chondritic components were affected by the same process. The similar trace element compositions of altered chondrule mesostasis and "White Matrix" in this meteorite in particular indicate a common source for the fluids the formed both types of material. Similarly, in the higher petrologic types Bo Xian (LL3.9) and Bjurböle (LL4.0), alteration of anorthite in the chondrules and the overgrowth of olivine on enstatite appear to be widespread, indicating that all components were affected by the same type of processes.

In the case of Chainpur (LL3.4) and Parnallee (LL3.6), the origin of the alkali and halogen enrichment during chondrule mesostasis is not fully resolved. Unlike in Tieschitz, the effects of metasomatism are not pervasively developed throughout all chondrules. Only a few percent of the chondrules in these two meteorites show evidence of metasomatic effects. There is no evidence of leaching of chondrule glass or other kinds of evidence that might indicate that a hydrous fluid phase was involved in enriching some chondrules in these elements. These observations led Bridges et al. (1997) to favor a pre-accretionary environment for the metasomatism of Chainpur and Parnallee chondrules. They argued that enrichment of alkalis and

halogens during chondrule mesostasis must have occurred while the chondrules were partially molten, with the introduction of these elements into the melt. This could have occurred if the chondrules were melted in a local environment with elevated partial pressures of these elements. Although Bridges et al. (1997) suggested that this could have occurred during chondrule formation in the solar nebula, they favored a planetary setting for chondrule formation, where impacts between small planetesimals produced droplets of melt in a vapor that was enriched in alkalis and Cl.

One issue, however, that was not addressed by Bridges et al. (1997) is the fact that both of these meteorites have undergone metamorphism and therefore the primary characteristics of the chondrules may have been modified to some extent. In addition, the fact that such alkali and halogen enrichments have not been observed in more pristine type 3 chondrites, such as Semarkona (LL3.0) or Bishunpur (LL3.1), is an indication that this process may not be nebular, unless it affected only selected batches of chondrules that accreted to form the ordinary chondrites. An additional piece of information that argues against a pre-accretionary enrichment of mesostasis glass for these chondrules is the fact that Ba is also commonly enriched in the same chondrules that show Na and Cl enrichments. Cosmochemically, Ba, like Ca, is a highly refractory element and would not be expected to be enriched in a vapor phase, unlike the volatile elements Na and Cl. It is therefore extremely difficult to explain these Ba enrichments as a result of the interaction with a vapor phase. On the other hand, Ba, like Ca is also highly soluble and hence mobile in hydrous fluids. Barium is clearly not an element that would have been enriched in a vapor and therefore would have been extremely difficult to introduce into the melt from a vapor phase.

As discussed earlier for the CO3 chondrites, one possible explanation for the occurrence of Na and Cl enrichments only in a small subset of chondrules is because it is these chondrules that have primary minerals, which are (1) most susceptible to alteration by aqueous fluids and (2) have compositions that are favorable to the formation of Na and Cl-bearing minerals. As discussed by Li et al. (2000), all the chondrules in Bo Xian that contained evidence of enrichment in Na and Cl are Al-rich chondrules, consistent with this hypothesis. A similar explanation can be proposed to explain the selective development of Na and Cl-enrichments in Chainpur and Parnallee, rather than appealing to pre-accretionary processes.

One puzzling aspect of the ordinary chondrites is the fact that only a small subset of meteorites show evidence of metasomatic effects. This contrasts with the CO3 chondrites, which essentially all show evidence of metasomatic effects to different degrees, with the exception of the type 3.0 chondrites. In addition, the fact that low petrologic type UOCs frequently show evidence of low temperature aqueous alteration, indicated by the formation of phyllosilicates and partial alteration of chondrule glass, etc. (Hutchison et al. 1987; Alexander et al. 1989; Grossman et al. 2000, 2002), shows that fluids were available on the ordinary chondrite parent body. Aqueous alteration of ordinary chondrites happened pervasively and occurred prior to thermal metamorphism as indicated by the fact that so-called bleached

chondrules (Grossman et al. 2000) are present in many type 3 chondrites, and, to a lesser extent, in type 4−6 chondrites. These chondrules are radial pyroxene and cryptocrystalline chondrules that experienced low temperature aqueous alteration and leaching of glass from their outer peripheral regions, leaving a distinct outer porous zone that is texturally distinct from the unleached interior of the chondrule. Therefore, unlike the CO3 chondrites, the progressive dehydration of phyllosilicate phases during thermal metamorphism of ordinary chondrites would release fluids that were available to react at higher temperatures and promote fluid-assisted metamorphism. It is therefore paradoxical that metasomatic effects, that might be expected to accompany thermal metamorphism, are extremely limited in the ordinary chondrites.

On the other hand, the limited available mineralogical evidence from the equilibrated ordinary chondrites (e.g., Jones and Brearley 2010a) suggests that fluids did become available following the peak of metamorphism. Modification of metamorphic plagioclase by aqueous fluids clearly occurred at temperatures that were elevated enough to stabilized anhydrous phases, and not phyllosilicates. Such late stage modification might be attributable to convective transport of fluids from the cool exterior of an asteroid into the interior as cooling of the parent body proceeded. How widespread such late stage mineral–fluid interactions are in the equilibrated ordinary chondrites is currently unknown, but clearly represents further evidence that fluids played a significant role in the early and late stages of parent body evolution.

15.5 Summary and Conclusions

Metasomatic processes have evidently played a variable and complex role in the mineralogical, chemical, and isotopic evolution of carbonaceous and ordinary chondrites. Understanding these processes and their implications for early solar system processes is complicated by the lack of any geologic context for the origin of this sample suite and, in many cases, incomplete representation of samples that have undergone metasomatism. In the case of the CV3 chondrites, evidence of metasomatism has been recognized for almost 40 years, based largely on studies of CAIs, but it is only in the last 15–20 years that the possibility that these effects were caused by aqueous fluids has been suggested. The earlier view, that such alteration was the result of solid–gas interactions within the protoplanetary disk, at some lower temperature phase of nebular evolution, is widely established in the literature. This new perspective, on the origin of secondary mineralization in CV3 chondrites, has therefore produced a vigorous debate, which has resulted in a plethora of new observations in an effort to understand how the diverse primary components of chondritic meteorites have been altered. Unlike terrestrial samples, where the role of fluids in the metasomatic process is completely accepted and samples of the fluid phase may be present as fluid inclusions within minerals, evidence of metasomatism in CV chondrites is often cryptic and in many cases fine-grained and difficult to

characterize. Nevertheless, significant progress has been made in recognizing and understanding the fundamental processes involved in metasomatic processes. These advances have been made possible by major improvements in the spatial resolution of analytical techniques such as FEGSEM, SIMS, and NanoSIMS. In particular, mineralogical studies, combined with micro and nanoisotopic studies using SIMS techniques, have allowed isotopic characterization of secondary phases. These data have constrained both the timing of formation of secondary phases using ^{26}Al-^{26} Mg, ^{53}Mn-^{53}Cr, and ^{36}Cl-^{36} S short-lived radioisotope dating techniques as well as the oxygen isotopic compositions of the phases. These studies have demonstrated that secondary phases are relatively young compared with the primary nebular minerals. Further, the observation that alteration phases in CV3 chondrites have oxygen isotopic compositions that lie on a mass dependent fractionation line, consistent with the growth of these phases in the presence of an aqueous fluid, is especially important in this regard. These data provide strong evidence that the environment of alteration for the CV3 chondrites was within a parent body after accretion. In the future, further studies using combined analytical techniques, such as FIB/TEM/SIMS/NanoSIMS, are likely to continue to provide new insights into the role of fluids, especially the identification of small amounts of hydrous phases, which represent an additional "smoking gun" for the involvement of aqueous fluids.

It is these new insights from CV3 chondrites that have provided the impetus for a reappraisal of the processes that have affected the CO3 and ordinary chondrites. These two groups of meteorites present significant new opportunities to understand the interaction between thermal metamorphism and metasomatism, but at the same time present considerable challenges that has resulted in limited progress. The degree of metasomatism exhibited by these two groups of chondrites is much more limited than the CV3 chondrites and therefore our current understanding of even the basic mineralogical changes that have been caused by metasomatism are poorly constrained. In the CO3 chondrites, it does appear that most members of the group have experienced metasomatic effects and that there is a general correlation between metasomatism and thermal metamorphism. However, variability in the extent of metasomatism in individual chondrites of the same petrologic subtype is indicated, suggesting that the distribution of metasomatizing fluids was heterogeneous. Only more detail studies of these meteorites, focusing on characterizing the nature of the alteration products and the relationship between metamorphic and metasomatic effects, will help constrain important issues such as whether the two processes were truly coupled or whether aqueous fluids were only present for limited periods of time during metamorphism. In the least metamorphosed CO3 chondrites, which contain evidence for the alteration of CAIs and other components prior to accretion, in depth studies of individual objects are necessary to establish if the styles and degree of alteration in each component are distinct from each other. Further, oxygen isotopic data for the alteration products of CAIs that may have experienced alteration prior to accretion, is needed to establish if they have compositions distinct from phases formed during parent body metasomatism.

In the case of the ordinary chondrites, evidence of metasomatism has been recognized longer than in any other chondrite group, but our understanding of secondary alteration in this group of chondrites is still in its infancy. One significant issue is the fact that few members of the UOCs exhibit evidence of metasomatic effects. Therefore, fluids have had quite differential effects on individual chondrites, indicating that fluids were distributed heterogeneously within the ordinary chondrite parent bodies. The effects of water on higher petrologic types are only just beginning to be recognized and so there is even greater uncertainty as to the extent in which water has played a role in their geologic evolution. However, as the cryptic effects of mineral–fluid interactions in these meteorites become recognized, the possibility of constraining the role of water during metamorphism becomes a real possibility. This is of great potential significance because phases, such as phosphates, that are commonly used to date metamorphism in ordinary chondrites (e.g., Göpel et al. 1994), may have been recrystallized during late stage mineral–fluid interactions.

References

Abreu NM, Brearley AJ (2010) Early solar system processes recorded in the matrices of two highly pristine CR3 carbonaceous chondrites, MET00426 and QUE99177. Geochim Cosmochim Acta 74:1146–1171

Akai J (1988) Incompletely transformed serpentine-type phyllosilicates in the matrix of Antarctic CM chondrites. Geochim Cosmochim Acta 52:1593–1599

Akai J (1992) T-T-T diagram of serpentine and saponite, and estimation of metamorphic heating degree of Antarctic carbonaceous chondrites. Proc NIPR Symp Antarct Meteor 5:120–135

Aléon J, Krot AN, McKeegan KD, MacPherson GJ, Ulyanov AA (2005) Fine-grained, spinel-rich inclusions from the reduced CV chondrite Efremovka: II. Oxygen isotopic compositions. Meteor Planet Sci 40:1043–1058

Alexander CMO'D, Hutchison RH, Graham AL, Yabuki H (1987) Discovery of scapolite in the Bishunpur (LL3) chondritic meteorite. Mineral Mag 51:733–735

Alexander CMO'D, Barber DJ, Hutchison R (1989) The microstructure of Semarkona and Bishunpur. Geochim Cosmochim Acta 53:3045–3057

Amelin Y, Irving AJ (2007) Seven million years of evolution of the angrite parent body from Pb-isotopic data (abstract). Workshop on chronology of meteorites and the early solar system, Kauai, p 4053

Amelin Y, Krot AN, Hutcheon ID, Ulyanov AA (2002) Lead isotopic ages of chondrules and calcium-aluminum-rich inclusions. Science 297:1678–1683

Amelin Y, Kaltenbach A, Iizuka T, Stirling CH, Ireland TR, Petaev MI, Jacobsen SB (2010) Importance of uranium isotope variations for chronology of the solar system's first solids (abstract). Lunar Planet Sci 41:1648

Ash RD, Young ED, Rumble D III, Alexander CMO'D, MacPherson GJ (1999) Oxygen isotope systematics in Allende chondrules (abstract). Lunar Planet Sci 30:1836

Ashworth JR (1981) Fine structure in H-group chondrites. Proc R Soc Lond A374:179–194

Beckett JR, Stolper E (2000) The partitioning of Na between melilite and liquid: part I. The role of crystal chemistry and liquid composition. Geochim Cosmochim Acta 64:2509–2517

Beckett JR, Simon SB, Stolper E (2000) The partitioning of Na between melilite and liquid: part II. Applications to Type B inclusions from carbonaceous chondrites. Geochim Cosmochim Acta 64:2519–2534

Birck J-L, Allègre CJ (1988) Manganese-chromium isotope systematics and the development of the early solar system. Nature 331:579–584

Bischoff A (1998) Aqueous alteration of carbonaceous chondrites: evidence for preaccretionary alteration – A review. Meteor Planet Sci 33:1113–1122

Bischoff A, Keil K (1984) Al-rich objects in ordinary chondrites: related origin of carbonaceous and ordinary chondrites and their constituents. Geochim Cosmochim Acta 48:693–709

Bland PA, Jackson MD, Coker RF, Cohen BA, Webber JBW, Lee MR, Duffy CM, Chater RJ, Ardakani MG, McPhail DS, McComb DW, Benedix GK (2009) Why aqueous alteration in asteroids was isochemical: high porosity [≠] high permeability. Earth Planet Sci Lett 287:559–568

Bonal L, Quirico E, Bourot-Denise M, Montagnac G (2006) Determination of the petrologic type of CV3 chondrites by Raman spectroscopy of included organic matter. Geochim Cosmochim Acta 70:1849–1863

Bonal L, Bourot-Denise M, Quirico E, Montagnac G, Lewin E (2007) Organic matter and metamorphic history of CO chondrites. Geochim Cosmochim Acta 71:1605–1623

Brazzle RH, Pravdivtseva OV, Meshik AM, Hohenberg CM (1999) Verification and interpretation of the I-Xe chronometer. Geochim Cosmochim Acta 63:739–760

Brearley AJ (1993) Matrix and fine-grained rims in the unequilibrated CO3 chondrite, ALH A77307: origins and evidence for diverse, primitive nebular dust components. Geochim Cosmochim Acta 57:1521–1550

Brearley AJ (1994) Metamorphic effects in the matrices of CO3 chondrites: compositional and mineralogical variations (abstract). Lunar Planet Sci 25:165–166

Brearley AJ (1996) The nature of matrix in unequilibrated chondritic meteorites and its possible relationship to chondrules. In: Hewins RH, Jones RH, Scott ERD (eds) Chondrules and the protoplanetary disk. Cambridge University Press, Cambridge, pp 137–152

Brearley AJ (1997a) Contrasting microstructures of fayalitic olivine in matrix and chondrules in the Allende CV3 chondrite (abstract). Lunar Planet Sci 28:151–152

Brearley AJ (1997b) Disordered biopyriboles, amphibole, and talc in the Allende meteorite; products of nebular or parent body aqueous alteration? Science 276:1103–1105

Brearley AJ (1999) Origin of graphitic carbon and pentlandite in matrix olivines in the Allende meteorite. Science 285:1380–1382

Brearley AJ (2003) Nebular and parent body processing. In: Davis AM (ed) Treatise on geochemistry, vol 1, Meteorites, comets and planets. Elsevier, Oxford, pp 247–268

Brearley AJ (2006) The action of water. In: Dante L, McSween HY Jr (eds) Meteorites and the early solar system II. Arizona University Press, Tucson, pp 587–624

Brearley AJ, Burger PV (2007) Hydrothermal alteration behavior of Kainsaz (CO3) at low temperatures under reducing conditions: insights into incipient aqueous alteration of carbonaceous chondrites (abstract). Lunar Planet Sci 38:1687

Brearley AJ, Jones RH (1998) Chondritic meteorites. In: Paprika JJ (ed) Planetary materials. Mineralogical Society of America, Washington, DC, pp 1–398

Brearley AJ, Prinz M (1996) Dark inclusions in the Allende meteorite: new insights from transmission electron microscopy (abstract). Lunar Planet Sci 18:161–162

Brearley AJ, Shearer CK (2000) Origin of calcium-Fe-rich pyroxenes in Allende matrix: clues from rare-earth-element abundances (abstract). Meteor Planet Sci 35(Suppl):A33

Bridges JC, Alexander CMO'D, Hutchison R, Franchi IA, Pillinger CT (1997) Sodium, chlorine-rich mesostases in Chainpur (LL3) and Parnallee (LL3) chondrules. Meteor Planet Sci 32:555–565

Brigham CA, Hutcheon ID, Papanastassiou DA, Wasserburg GJ (1986) Evidence for ^{26}Al and Mg isotopic heterogeneity in a fine-grained CAI (abstract). Lunar Planet Sci 17:85–86

Buchanan PC, Zolensky ME, Reid AM (1997) Petrology of Allende dark inclusions. Geochim Cosmochim Acta 61:1733–1743

Burbine TH, McCoy TJ, Meibom A, Gladman B, Keil K (2002) Meteoritic parent bodies: their number and identification. In: Bottke WF Jr et al (eds) Asteroids III. Arizona University Press, Tucson, pp 653–667

Burger PV, Brearley AJ (2005) Localized chemical redistribution during aqueous alteration in CR2 carbonaceous chondrites EET87770 and EET92105. Lunar and Planetary Science XXXVI CDROM abstract, p 2288

Buseck PR, Huang B-J (1985) Conversion of carbonaceous material to graphite during metamorphism. Geochim Cosmochim Acta 49:2003–2016

Busemann H, Alexander CMO'D, Nittler LR (2007) Characterization of insoluble organic matter in primitive meteorites by microRaman spectroscopy. Meteor Planet Sci 42:1387–1416

Chizmadia LJ, Rubin AE, Wasson JT (2002) Mineralogy and petrology of amoeboid olivine inclusions in CO3 chondrites: relationship to parent body aqueous alteration. Meteor Planet Sci 37:1781–1796

Choi B-G, McKeegan KD, Krot AN, Wasson JT (1998) Oxygen with high $\Delta^{17}O$ in magnetite from unequilibrated ordinary chondrites. Nature 392:577–579

Choi B-G, Krot AN, Wasson JT (2000) Oxygen-isotopes in magnetite and fayalite in CV chondrites Kaba and Mokoia. Meteor Planet Sci 35:1239–1249

Christophe Michel-Lévy M (1976) La matrice noire et blanche de la chondrite de Tieschitz. Earth Planet Sci Lett 30:143–150

Ciesla F (2005) Chondrule-forming processes–an overview. In: Krot AN, Scott ERD, Reipurth B (eds) Chondrites and the protoplanetary disk, vol 341, Astronomical Society of the Pacific conference series. Astronomical Society of the Pacific, San Francisco, pp 811–820

Clayton RN, Mayeda TK (1999) Oxygen isotope studies of carbonaceous chondrites. Geochim Cosmochim Acta 63:2089–2104

Clayton RN, Onuma N, Grossman L, Mayeda TK (1977) Distribution of the pre-solar component in allende and other carbonaceous chondrites. Earth Planet Sci Lett 34:209–224

Clayton RN, Onuma N, Ikeda Y, Mayeda TK, Hutcheon I, Olsen EJ, Molini-Velsko C (1983) Oxygen isotopic compositions of chondrules in Allende and ordinary chondrites. In: King EA (ed) Chondrules and their origins. Lunar and Planetary Institute, Houston

Cody GD, Alexander CMO'D, Yabuta H, Kilcoyne ALD, Araki T, Ade H, Dera R, Fogel M, Militzer B, Mysen BO (2008) Organic thermometry for chondritic parent bodies. Earth Planet Sci Lett 272:446–455

Cohen BA, Coker RF (2000) Modeling of liquid water on CM meteorite parent bodies and implications for amino acid racemization. Icarus 145:369–381

Coker RF, Cohen BA (2001) The effect of liquid transport on the modelling of CM parent bodies. Meteor Planet Sci 36:A43–A44

Cosarinsky M, Leshin LA, MacPherson GJ, Guan Y, Krot AN (2008) Chemical and oxygen isotopic compositions of accretionary rim and matrix olivine in CV chondrites: constraints on the evolution of nebular dust. Geochim Cosmochim Acta 72:1887–1913

Desch SJ, Connolly HC Jr (2002) A thermal model of the processing of particles in solar nebula shocks: applications to the cooling rates of chondrules. Meteor Planet Sci 37:183–207

Desch SJ, Ciesla FJ, Hood LL, Nakamoto T (2005) Heating of chondritic materials in solar nebula shocks. In: Krot AN, Scott ERD, Reipurth B (eds) Chondrites and the protoplanetary disk, vol 341, Astronomical Society of the Pacific Conference Series. Astronomical Society of the Pacific, San Francisco, pp 849–873

Dodd RT, Van Schmus WR, Koffman DM (1967) A survey of the unequilibrated ordinary chondrites. Geochim Cosmochim Acta 31:921–951

Dohmen R, Chakraborty S, Palme H, Rammensee W (1998) Solid-solid reactions mediated by a gas phase; an experimental study of reaction progress and the role of surfaces in the system olivine + Fe metal. Am Miner 83:970–984

Fagan TJ, Krot AN, Keil K, Yurimoto H (2004) Oxygen isotopic compositions of amoeboid olivine aggregates in the reduced CV3 chondrites Efremovka, Vigarano and Leoville. Geochim Cosmochim Acta 68:2591–2611

Fagan TJ, Guan Y, MacPherson GJ (2007) Al-Mg isotopic evidence for episodic alteration of Ca-Al-rich inclusions from Allende. Meteor Planet Sci 42:1221–1240

Fahey AJ, Zinner E, Kurat K, Kracher A (1994) Hibonite-hercynite inclusion HH-1 from the Lance (CO3) meteorite: the history of an ultrarefractory CAI. Geochim Cosmochim Acta 58:4779–4793

Fedkin AV, Grossman L (2010) Condensation of the high-FeO silicates in primitive chondrites: still a problem (abstract). Lunar Planet Sci 41:1448

Ford RL, Brearley AJ (2008) Element exchange between matrix and CAIs in the Allende meteorite (abstract). Lunar Planet Sci 39:2399

Ford RL, Brearley AJ (2010) Discovery of vesuvianite and kaolinite formed during the alteration of melilite in an Allende Type A CAI: characterization by FIB/TEM (abstract). Lunar Planet Sci 41:1402

Fruland RM, King AE, McKay DS (1978) Allende dark inclusions. In: Proceedings of the 9th Lunar and Planetary Science Conference, Houston, pp 1305−1329

Göpel C, Manhes G, Allegre CJ (1994) U-Pb systematics of phosphates from equilibrated ordinary chondrites. Earth Planet Sci Lett 121:153–171

Greenwood RC, Franchi IA (2004) Alteration and metamorphism of CO3 chondrites: evidence from oxygen and carbon isotopes. Meteor Planet Sci 39:1823–1838

Greenwood RC, Hutchison R, Huss GR, Hutcheon ID (1992) CAIs in CO3 meteorites: parent body or nebular alteration? (abstract). Meteoritics 27:229

Grimm RE, McSween HY Jr (1989) Water and the thermal evolution of carbonaceous chondrite parent bodies. Icarus 82:244–280

Grossman JN, Brearley AJ (2005) On the onset of metamorphism in ordinary and carbonaceous chondrites. Meteor Planet Sci 40:87–122

Grossman J, Alexander CMO'D, Wang JH, Brearley AJ (2000) Bleached chondrules: evidence for widespread aqueous processes on the parent asteroids of ordinary chondrites. Meteor Planet Sci 35:467–486

Grossman JN, Alexander CMO'D, Wang JH, Brearley AJ (2002) Zoned chondrules in Semarkona: evidence for high- and low-temperature processing. Meteor Planet Sci 37:49–73

Guimon RK, Symes SJK, Sears DWG, Benoit PH (1995) Chemical and physical study of type 3 chondrites XII: the metamorphic history of CV chondrites and their components. Meteoritics 30:704–714

Harlov DE, Förster H-J, Nijland TG (2002) Fluid-induced nucleation of REE-phosphate minerals in apatite: nature and experiment. Part I. Chlorapatite. Am Mineral 87:245–261

Hashimoto A, Grossman L (1987) Alteration of Al-rich inclusions inside amoeboid olivine aggregates in the Allende meteorite. Geochim Cosmochim Acta 51:1685–1704

Hashimoto A, Wood JA (1986) Enhanced volatility of CaO in H2O-rich gas environments as a factor in the alteration of Ca, Al-rich inclusions (abstract). Meteoritics 21:391–392

Hayatsu R, Scott RG, Studier MH, Lewis RS, Anders E (1980) Carbynes in meteorites: detection, low-temperature origin, and implications for interstellar molecules. Science 209:1515–1518

Holmberg AA, Hashimoto A (1992) A unique, (almost) unaltered spinel-rich fine-grained inclusion in Kainsaz. Meteoritics 27:149–153

Housley RM, Cirlin EH (1983) On the alteration of Allende chondrules and formation of the matrix. In: King ED (ed) Chondrules and their origins. Lunar and Planetary Institute, Houston, pp 145–161

Hsu W, Guan Y, Leshin LA, Ushikubo T, Wasserburg GJ (2006) A late episode of irradiation in the early solar system: evidence from extinct ^{36}Cl and ^{26}Al in meteorites. Astrophys J 640:525–529

Hua X, Adam J, Palme H, El Goresy A (1988) Fayalite-rich rims, veins, and halos around and in forsteritic olivines in CAIs and chondrules in carbonaceous chondrites: types, compositional profiles and constraints on their formation. Geochim Cosmochim Acta 52:1389–1408

Hua X, Huss GR, Tachibana S, Sharp TG (2005) Oxygen, silicon, and Mn–Cr isotopes of fayalite in the Kaba oxidized CV3 chondrite: constraints for its formation history. Geochim Cosmochim Acta 69:1333–1348

Huckenholz HG, Lindhuber W, Springer J (1974) The join $CaSiO_3$-Al_2O_3-Fe_2O_3 of the CaO-Al_2O_3-Fe_2O_3-SiO_2 quaternary system and its bearing on the formation of granditic garnets and fassaitic pyroxenes. N Jb Miner Abh 121:160–207

Huss GR, Lewis RS (1994a) Noble gases in presolar diamonds I: three distinct components and their implications for diamonds origins. Meteoritics 29:791–811

Huss GR, Lewis RS (1994b) Noble gases in presolar diamonds II: component abundances reflect thermal processing. Meteoritics 29:811–829

Huss GR, Lewis RS (1995) Presolar diamond, SiC and graphite in primitive chondrites: abundance as a function of meteorite class and petrologic type. Geochim Cosmochim Acta 59:115–160

Huss GR, Lewis RS, Hemkin S (1996) The "normal planetary" noble gas component in primitive chondrites: compositions, carrier, and metamorphic history. Geochim Cosmochim Acta 60:3311–3340

Huss GR, Alexander CMO'D, Palme H, Bland PA, Wasson JT (2005) Genetic relationships between chondrules, fine grained rims, and interchondrule matrix. In: Reiperth B, Krot AN, Scott ERD (eds) Chondrites and the protoplanetary disk, vol 341, AIP Conference Series. AIP, San Francisco, pp 701–731

Huss GR, Rubin AE, Grossman JN (2006) Thermal metamorphism in chondrites. In: Lauretta D, McSween HY Jr (eds) Meteorites and the early solar system II. Arizona University Press, Tucson, pp 567–586

Hutcheon ID, Newton RC (1981) Mg isotopes, mineralogy and mode of formation of secondary phases in C3 refractory inclusions (abstract). Lunar Planet Sci 12:491–493

Hutcheon ID, Krot AN, Keil K, Phinney DL, Scott ERD (1998) ^{53}Mn-^{53}Cr dating of fayalite formation in the CV3 chondrite Mokoia: evidence for asteroidal alteration. Science 282: 1865–1867

Hutcheon ID, Marhas KK, Krot AN, Goswami JN, Jones RH (2009) ^{26}Al in plagioclase-rich chondrules in carbonaceous chondrites: evidence of an extended duration of chondrule formation. Geochim Cosmochim Acta 73:5080–5099

Hutchison R, Bevan AWR, Agrell SO, Ashworth JR (1979) Accretion temperature of Tieschitz H3, chondritic meteorite. Nature 280:116–119

Hutchison R, Alexander CMO'D, Barber DJ (1987) The Semarkona meteorite: first recorded occurrence of smectite in an ordinary chondrite, and its implications. Geochim Cosmochim Acta 51:1875–1882

Hutchison R, Alexander CMO'D, Bridges JC (1998) Elemental redistribution in Tieschitz and the origin of white matrix. Meteor Planet Sci 33:1169–1180

Ikeda Y (1982) Petrology of the ALH-77003 chondrite (C3). In: Proceedings of the 7th symposium on Antarctic meteorites. Memoirs National Institute of Polar Research special issue, vol 25. Tokyo, pp 34−65

Ikeda Y (1983) Alteration of chondrules and matrices in the four Antarctic carbonaceous chondrites ALH 77307 (C3), Y-790123 (C2), Y-75293(C2) and Y-74662(C2). In: Proceedings of the eighth symposium on Antarctic meteorites, Memoirs of the National Institute of Polar Research, vol 30. Tokyo, pp 93−108

Ikeda Y, Kimura M (1995) Anhydrous alteration of Allende chondrules in the solar nebula I: Description and alteration of chondrules with known oxygen-isotopic compositions. In: Proceedings of the NIPR Symposium on Antarctic Meteorites, vol 8. Tokyo, pp 97−122

Ishii HA, Krot AN, Bradley JP, Keil K, Nagashima K, Teslich N, Jacobsen B, Yin Q-Z (2010) Discovery, mineral paragenesis, and origin of wadalite in a meteorite. Am Mineral 95:440–448

Ito M, Nagasawa H, Yurimoto H (2004) Oxygen isotopic SIMS analysis in Allende CAI: details of the very early thermal history of the solar system. Geochim Cosmochim Acta 68:2905–2923

Itoh D, Tomeoka K (1998) Na-bearing Ca-Al-rich inclusions in four CO3 chondrites, Kainsaz, Ornans, Lancé, and Warrenton (abstract). Symp Antarct Meteorites 23:42–44

Itoh D, Tomeoka K (2003) Dark inclusions in CO3 chondrites: new indicators of parent-body processes. Geochim Cosmochim Acta 67:153–169

Itoh S, Kojima H, Yurimoto H (2004) Petrography and oxygen isotopic compositions in refractory inclusions from CO chondrites. Geochim Cosmochim Acta 68:183–194

Jabeen I, Kusakabe M, Nakamura T, and Nagao K (1998a) Oxygen isotopic signature in Allende chondrules (abstract). Meteor Planet Sci 33 (Suppl):A76−A77

Jabeen I, Kusakabe M, Nakamura T, Nagao K (1998b) Oxygen isotope study of Tsukuba chondrite, some HED meteorites and Allende chondrules. Antarct Meteor Res 11:122–135

Jabeen I, Kusakabe M, Nakamura T, Nagao K (1999) Parent body processes in Allende: evidence from oxygen isotope study of the Allende chondrules (abstract). Symp Antarct Meteorites 24:59–61

Jacobsen B, Yin Q-Z, Moynier F, Amelin Y, Krot AN, Nagashima K, Hutcheon ID, Palme H (2008) ^{26}Al-^{26} Mg and ^{207}Pb-^{206}Pb systematics of Allende CAIs: Canonical solar initial ^{26}Al/^{27}Al ratio reinstated. Earth Planet Sci Lett 272:353–364

Jogo K, Nakamura T, Noguchi T, Zolotov MYu (2009) Fayalite in the Vigarano CV3 carbonaceous chondrite: occurrences, formation age and conditions. Earth Planet Sci Lett 287:320–328

Jogo K, Nakamura T, Ito M, Messenger S (2010) Mn-Cr systematics of secondary fayalites in the CV3 carbonaceous chondrites A 881317, MET 00430 and MET 01074 (abstract). Lunar Planet Sci 41:1573

Johnson CA, Prinz M, Weisberg MK, Clayton RN, Mayeda TK (1990) Dark inclusions in Allende, Leoville, and Vigarano: evidence for nebular oxidation of CV3 constituents. Geochim Cosmochim Acta 54:819–831

Jones RH (1997) Alteration of plagioclase-rich chondrules in CO3 chondrites: evidence for late-stage sodium and Fe metasomatism in a nebular environment. In: Zolensky ME, Krot AN, Scott ERD (eds) Workshop on parent-body and Nebular modification of chondritic materials (abstract). Lunar and Planetary Institute, Houston, pp 30−31

Jones RH, Brearley AJ (2010a) Late-stage fluids on the LL chondrite parent body: evidence from feldspar in the LL4 chondrites Bo Xian and Bjurböle. LPI Contribution No. 1533:2133

Jones RH, Brearley AJ (1994) Reduced plagioclase-rich chondrules in the Lance and Kainsaz CO3 chondrites (abstract). Lunar Planet Sci 25:641–642

Jones CL, Brearley AJ (2006) Experimental aqueous alteration of the Allende meteorite under oxidizing conditions: constraints on asteroidal alteration. Geochim Cosmochim Acta 70: 1040–1058

Jones RH, Brearley AJ (2010b) Fluids on the LL chondrite parent body: evidence from the Bo Xian chondrites (abstract). Meteor Planet Sci 45(Suppl):A96

Jones RH, Rubie DC (1991) Thermal histories of CO3 chondrites — application of olivine diffusion modelling to parent body metamorphism. Earth Planet Sci Lett 106:73–86

Jones RH, Grossman JN, Rubin AE (2005) Chemical, mineralogical and isotopic properties of chondrules: clues to their origin. In: Reiperth B, Krot AN, Scott ERD (eds) Chondrites and the protoplanetary disk, vol 341. AIP Conference Series, San Francisco, pp 251–285

Kallemeyn GW, Wasson JT (1981) The compositional classification of chondrites-I. The carbonaceous chondrite groups. Geochim Cosmochim Acta 45:1217–1230

Keller LP, Buseck PR (1990a) Aqueous alteration in the Kaba CV3 carbonaceous chondrite. Geochim Cosmochim Acta 54:2113–2120

Keller LP, Buseck PR (1990b) Matrix mineralogy of the Lancé CO3 carbonaceous chondrite: a transmission electron microscope study. Geochim Cosmochim Acta 54:1155–1163

Keller LP, McKay DS (1993) Aqueous alteration of the Grosnaja CV3 carbonaceous chondrite (abstract). Meteoritics 28:378

Keller LP, Thomas KL, Clayton RN, Mayeda TK, DeHart JM, McKay DS (1994) Aqueous alteration of the Bali CV3 chondrite: evidence from mineralogy, mineral chemistry, and oxygen isotopic compositions. Geochim Cosmochim Acta 58:5589–5598

Kerridge JF (1972) Fe transport in chondrites: evidence from the Warrenton chondrite. Geochim Cosmochim Acta 36:913–916

Kim GL, Yurimoto H, Sueno S (2002) Oxygen isotopic composition of a compound Ca-Al-rich inclusion from Allende meteorite: implications for origin of palisade bodies and O-isotopic environment in the CAI-forming region. J Mineral Petrol Sci 97:161–167

Kimura M, Ikeda Y (1995) Anhydrous alteration of Allende chondrules in the solar nebula; II, Alkali-Ca exchange reactions and formation of nepheline, sodalite and Ca-rich phases in chondrules. Proc NIPR Symp Antarct Meteor 8:123–138

Kimura M, Ikeda Y (1998) Hydrous and anhydrous alterations of chondrules in Kaba and Mokoia CV chondrites. Meteor Planet Sci 33:1139–1146

Kimura M, Grossman JN, Weisberg MK (2008) Fe-Ni metal in primitive chondrites: indicators of classification and metamorphic conditions for ordinary and CO chondrites. Meteor Planet Sci 43:1161–1177

Kirschbaum C (1988) Carrier phases for iodine in the Allende meteorite and their associated $^{129}Xe_r/^{129}I$ ratios; a laser microprobe study. Geochim Cosmochim Acta 52:679–699

Kojima T, Tomeoka K (1996) Indicators of aqueous alteration and thermal metamorphism on the CV parent body: microtextures of a dark inclusion from Allende. Geochim Cosmochim Acta 60:2651–2666

Kojima T, Yada S, Tomeoka K (1995) Ca-Al-rich inclusions in three Antarctic CO3 chondrites, Yamato-81020, Yamato-820050 and Yamato-790992: record of low-temperature alteration. Proc NIPR Symp Antarct Meteor 8:79–96

Kovach HA, Jones RH (2010) Feldspar in type 4–6 ordinary chondrites: metamorphic processing on the H and LL chondrite parent bodies. Meteor Planet Sci 45:246–264

Krot AN, Scott ERD, Zolensky ME (1995) Mineralogic and chemical variations among CV3 chondrites and their components: nebular and asteroidal processing. Meteoritics 30:748–775

Krot AN, Scott ERD, Zolensky ME (1997a) Origin of fayalitic olivine rims and plate-like matrix olivine in the CV3 chondrite Allende and its dark inclusions. Meteoritics 32:31–49

Krot AN, Zolensky ME, Wasson JT, Scott ERD, Keil K, Ohsumi K (1997b) Carbide-magnetite-bearing type 3 ordinary chondrites. Geochim Cosmochim Acta 61:219–237

Krot AN, Petaev MI, Scott ERD, Choi B-G, Zolensky ME, Keil K (1998a) Progressive alteration in CV3 chondrites: more evidence for asteroidal alteration. Meteor Planet Sci 33:1065–1085

Krot AN, Zolensky ME, Keil K, Scott ERD, Nakamura K (1998b) Secondary Ca-Fe-rich minerals in the Bali-like and Allende-like oxidized CV3 chondrites and Allende dark inclusions. Meteor Planet Sci 33:623–645

Krot AN, Brearley AJ, Ulyanov AA, Biryukov VV, Swindle TD, Keil K, Mittlefehldt DW, Scott ERD, Clayton RN, Mayeda TK (1999) Mineralogy, petrography and bulk chemical, I-Xe, and oxygen isotopic compositions of dark inclusions in the reduced CV3 chondrite Efremovka. Meteor Planet Sci 34:67–89

Krot AN, Meibom A, Keil K (2000a) A clast of Bali-like oxidized CV3 material in the reduced CV3 chondrite breccia Vigarano. Meteor Planet Sci 35:817–827

Krot AN, Hiyagon H, Petaev MI, Meibom A (2000b) Oxygen isotopic compositions of secondary Ca-Fe-rich silicates from the Allende dark inclusions: Evidence against high-temperature formation (abstract). In: Lunar Planetary Science XXXI, Lunar Planetary Institute, Houston, CD ROM, No 1463

Krot AN, Petaev MI, Meibom A, Keil K (2001) In situ growth of Ca-rich rims around Allende dark inclusions. Geochem Int 36:351–368

Krot AN, Keil K, Goodrich CA, Scott ERD, Weisberg MK (2003) Classification of meteorites. In: Davis M (ed) Treatise on geochemistry, vol 1, Meteorites, comets and planets. Elsevier, Oxford, pp 143–200

Krot AN, MacPherson GJ, Ulyanov AA, Petaev MI (2004a) Fine-grained, spinel-rich inclusions from the reduced CV chondrites Efremovka and Leoville: I. Mineralogy, petrology, and bulk chemistry. Meteor Planet Sci 39:1517–1553

Krot AN, Petaev MI, Bland PA (2004b) Multiple formation mechanisms of ferrous olivine in CV3 carbonaceous chondrites during fluid-assisted metamorphism. Antarct Meteor Res 17:154–172

Krot AN, Petaev MI, Russell SS, Itoh S, Fagan TJ, Yurimoto H, Chizmadia LJ, Weisberg MK, Komatsu M, Ulyanov AA, Keil K (2004c) Amoeboid olivine aggregates and related objects in carbonaceous chondrites: records of nebular and asteroid processes. Chem Erde 64:185–239

Krot AN, Hutcheon ID, Brearley AJ, Pravdivtseva OV, Petaev MI, Hohenberg CM (2006) Timescales for secondary alteration of chondritic meteorites. In: Lauretta D, McSween HY Jr (eds) Meteorites and the early solar system II. Arizona University Press, Tucson, pp 525–555

Krot AN, Yurimoto H, Hutcheon ID, Libourel G, Chaussidon M, Petaev MI, MacPherson GJ, Paque-Heather J, Wark D (2007) Anorthite-rich, igneous (Type C) Ca, Al-rich inclusions from the CV carbonaceous chondrite Allende: evidence for multistage formation history. Geochim Cosmochim Acta 71:4342–4364

Krot AN, Chaussidon M, Yurimoto H, Sakamoto N, Nagashima K, Hutcheon ID, MacPherson GJ (2008) Oxygen isotopic compositions of Allende Type C CAIs: Evidence for isotopic exchange during nebular melting and asteroidal metamorphism. Geochim Cosmochim Acta 72:2534–2555

Krot AN, Amelin Y, Bland PA, Ciesla FJ, Connelly J, Davis AM, Huss GR, Hutcheon ID, Makide K, Nagashima K, Nyquist LE, Russell SS, Scott ERD, Thrane K, Yurimoto H, Yin QZ (2009) Origin and chronology of chondritic components: a review. Geochim Cosmochim Acta 73:4963–4997

Krot AN, Nagashima K, Hutcheon ID, Ishii HA, Jacobsen B, Yin Q-Z, Davis AM, Simon SB (2010) Mineralogy, petrography, oxygen and magnesium isotopic compositions and formation age of grossular-bearing assemblages in the Allende CAIs (abstract). Lunar Planet Sci 41:1441

Krot A, Hutcheon I, Nagashima K, Crites S, Gasda P, Hallis L, Jilly C, Petaev M, Robertson K, Taylor G, Telus M (2011) Origin of ferroan olivine in matrices of unequilibrated chondrites (abstract). Meteor Planet Sci 45 (Suppl):2443–2464

Kunihiro T, Rubin AE, McKeegan KD, Wasson JT (2004) Initial $^{26}Al/^{27}Al$ in carbonaceous-chondrite chondrules: too little ^{26}Al to melt asteroids. Geochim Cosmochim Acta 68: 2947–2957

Kurahashi E, Kita NT, Nagahara H, Morishita Y (2008) ^{26}Al–^{26}Mg systematics of chondrules in a primitive CO chondrite. Geochim Cosmochim Acta 72:3865–3883

Kurat G (1969) The formation of chondrules and chondrites and some observations on chondrules from the Tieschitz meteorite. In: Millman PM (ed) Meteorite research. Reidel, Dordrecht, pp 185–190

Kurat G (1975) De kohlige Chondrit Lance: Eine petrologische analyse der komplexen genese eines gchondriten. Tschermaks Min Petr Mitt 22:38–78

Kurat G, Kracher A (1980) Basalts in the Lancé carbonaceous chondrite. Zeitschr Naturforsch 35a:180–190

Kurat G, Palme H, Brandstätter F, Huth J (1989) Allende xenolith AF: undisturbed record of condensation and aggregation of matter in the solar nebula. Zeitschr Naturforsch 44a: 988–1004

Lavielle B, Marti K (1992) Trapped xenon in ordinary chondrites. J Cheochem Res 97:875–881

Li CL, Bridges JC, Hutchison R, Franchi IA, Sexton AS, Ouyang ZY, Pillinger CT (2000) Bo Xian (LL3.9): oxygen-isotopic and mineralogical characterisation of separated chondrules. Meteor Planet Sci 35:561–568

Lin Y, Guan Y, Leshin LA, Ouyang Z, Wang D (2005) Short-lived chlorine-36 in a Ca- and Al-rich inclusion from the Ningqiang carbonaceous chondrite. Proc Natl Acad Sci 102:1306–1311

Lugmair GW, Shukolyukov A (1998) Early solar system timescales according to ^{53}Mn-^{53}Cr systematics. Geochim Cosmochim Acta 62:2863–2886

MacPherson GJ (2003) Calcium–aluminum-rich inclusions in chondritic meteorites. In: Davis AM (ed) Meteorites, comets, and planets meteorites, comets, and planets, vol 1. Elsevier-Pergamon, Oxford, pp 201–241

MacPherson GJ, Wark DA, Armstrong JT (1988) Primitive material surviving in chondrites: refractory inclusions. In: Kerridge JF, Matthews MS (eds) Meteorites and the early solar system. Arizona University Press, Tucson, pp 746–807

MacPherson GJ, Davis AM, Zinner EK (1995) The distribution of aluminum-26 in the early solar system – a reappraisal. Meteoritics 30:365–386

MacPherson GJ, Simon SB, Davis AM, Grossman L, Krot AN (2005) Calcium-Aluminum-rich inclusions: major unanswered questions. In: Reiperth B, Krot AN, Scott ERD (eds) Chondrules and the protoplanetary disk, vol 341. AIP Conference Series, San Francisco, pp 225–250

Makide K, Nagashima K, Krot AN, Huss GR, Hutcheon ID, Bischoff A (2009) Oxygen− and magnesium-isotope compositions of calcium−aluminum-rich inclusions from CR2 carbonaceous chondrites. Geochim Cosmochim Acta 73:5018–5051

McGuire AV, Hashimoto A (1989) Origin of zoned fine-grained inclusions in the Allende meteorite. Geochim Cosmochim Acta 53:1123–1133

McSween HY Jr (1977a) Petrographic variations among carbonaceous chondrites of the Vigarano type. Geochim Cosmochim Acta 41:1777–1790

McSween HY Jr (1977b) Carbonaceous chondrites of the Ornans type: a metamorphic sequence. Geochim Cosmochim Acta 44:477–491

McSween HY Jr, Labotka TC (1993) Oxidation during metamorphism of the ordinary chondrites. Geochim Cosmochim Acta 57:1105–1114

McSween HY Jr, Ghosh A, Grimm RE, Wilson L, Young ED (2002) Thermal evolution models of asteroids. In: Bottke WF Jr et al (eds) Asteroids III. University of Arizona, Tucson, pp 559–571

Morimoto N, Fabries J, Ferguson AK, Ginzburg IV, Ross M, Seifert FA, Zussman J, Aoki K, Gottardi G (1988) Nomenclature of pyroxenes. Am Mineral 73:1123–1133

Nagashima K, Krot AN, Hua X (2007) Common presence of ^{16}O-rich melilite in calcium-aluminum-rich inclusions from the least metamorphosed CV carbonaceous chondrite Kaba (abstract). Lunar Planet Sci 38:2059

Nagashima K, Krot AN, Huss GR, Yurimoto H (2010) Micron scale oxygen isotope heterogeneity in anorthite of A forsterite-bearing Type B CAI E60 from Efremovka (abstract). Lunar Planet Sci 41:2255

Naumov GB, Ryzhenko BN, Khodakovki YL (1971) Handbook of thermodynamic quantities for geology. Atomic Press, Moscow, 240 p

Nichols RH Jr, Hohenberg CM, Olinger CT (1990) Allende chondrules and rims: I-Xe systematics (abstract). Lunar Planet Sci 21:879–880

Nomura K, Miyamoto M (1998) Hydrothermal experiments on alteration of Ca-Al-rich inclusions (CAIs) in carbonaceous chondrites: implication for aqueous alteration in parent asteroids. Geochem Cosmochim Acta 62:3575–3588

Palme H, Wlotzka F (1981) Iridium-rich phases in Ornans (abstract). Meteoritics 16:373–374

Paque JM, Cuzzi JN (1997) Physical characteristics of chondrules and rims, and aerodynamic sorting in the solar nebula (abstract). Lunar Planet Sci 28:1189

Peck JA (1988) Primitive material surviving in chondrites: matrix. In: Kerridge JF, Matthews MS (eds) Meteorites and the early solar system. Arizona University Press, Tucson, pp 718–745

Petaev MI, MFeenko MV (1997) Thermodynamic modeling of aqueous alteration in CV chondrites. In: Zolensky ME, Krot AN, Scott ERD (eds) Workshop on parent-body and nebular modification of chondritic materials, Maui, July 17−19, 1997, Hawai'i. LPI Technical Report, LPITR 97-02. Lunar and Planetary Institute, Houston TX, p 49

Pravdivtseva OV, Krot AN, Hohenberg CM, Meshik AP, Weisberg MK, Keil K (2003a) The I-Xe record of alteration in the Allende CV chondrite. Geochim Cosmochim Acta 67:5011–5026

Pravdivtseva OV, Hohenberg CM, Meshik AP, Krot AN, Brearley AJ (2003b) I-Xe ages of the dark inclusions from the reduced CV3 chondrites Leoville, Efremovka and Vigarano (abstract). Meteor Planet Sci 38(Suppl):A140

Putnis A, Austrheim H (2010) Fluid-induced processes: metasomatism and metamorphism. Geofluids 10:254–269

Rietmeijer FJM, MacKinnon IDR (1985) Poorly graphitized carbon as a new cosmothermometer for primitive extraterrestrial materials. Nature 315:733–736

Rubin AE (1989) Size frequency distributions of chondrules in CO3 chondrites. Meteoritics 24:179–189

Rubin AE (1998) Correlated petrologic and geochemical characteristics of CO3 chondrites. Meteor Planet Sci 33:383–391

Rubin AE (2010) Petrologic, geochemical and experimental constraints on models of chondrule formation. Earth Planet Sci Lett 50:3–27

Rubin AE, James JA, Keck BD, Weeks KS, Sears DWG, Jarosewich E (1985) The colony meteorite and variations in CO3 chondrite properties. Meteoritics 20:175–196

Rubin AE, Wasson JT, Clayton RN, Mayeda TK (1990) Oxygen isotopes in chondrules and coarse-grained chondrule rims from the Allende meteorite. Earth Planet Sci Lett 96:247–255

Russell SS, Huss GR, Fahey AJ, Greenwood RC, Hutchison R, Wasserburg GJ (1998) An isotopic and petrologic study of calcium-aluminum-rich inclusions from CO3 meteorites. Geochim Cosmochim Acta 62:689–714

Ryerson FJ, McKeegan KD (1994) Determination of oxygen self-diffusion in akermanite, anorthite, diopside, and spinel: implications for oxygen isotopic anomalies and the thermal histories of Ca-Al-rich inclusions. Geochim Cosmochim Acta 58:3713–3734

Ryerson FJ, Durham WB, Cherniak DJ, Lanford WA (1989) Oxygen diffusion in olivine: effect of oxygen fugacity and implication for creep. J Geophys Res 94:4105–4118

Scott ERD, Jones RH (1990) Disentangling nebular and asteroidal features of CO3 carbonaceous chondrites. Geochim Cosmochim Acta 54:2485–2502

Scott ERD, Krot AN (2005a) Chondritic meteorites and their components. In: Krot AN, Scott ERD, Reipurth B (eds) Chondrules and the protoplanetary disk, vol 341. ASP Conference Series, San Francisco, pp 15–54

Scott ERD, Krot AN (2005b) Thermal processing of silicate dust in the solar nebula: clues from primitive chondrite matrices. Astrophys J 623:571–578

Sears DWG, Batchelor DJ, Lu J, Keck BD (1991) Metamorphism of CO and CO-like chondrites and comparisons with type 3 ordinary chondrites. Proc NIPR Symp Antarct Meteor 4:319–343

Shu FH, Shang H, Gounelle M, Glassgold AE (2001) The origin of chondrules and refractory inclusions in chondritic meteorites. Astrophys J 548:1029–1050

Shukolyukov A, Lugmair GW, Irving AJ (2009) Mn–Cr isotope systematics of angrite North West Africa 4801 (abstract). Lunar PlanetSci 30:1381

Simon SB, Grossman L, Casanova I, Symes S, Benoit P, Sears DWG, Wacker JF (1995) Axtell, a new CV3 chondrite find from Texas. Meteoritics 30:42–46

Stolper E (1982) Crystallization sequences of Ca-Al-rich inclusions from Allende: an experimental study. Geochim Cosmochim Acta 46:2159–2180

Stolper E, Paque JM (1986) Crystallization sequences of Ca-Al-rich inclusions from Allende: the effects of cooling rate and maximum temperature. Geochim Cosmochim Acta 50:1785–1806

Swindle TD (1998) Implications of iodine-xenon studies for the dating and location of secondary alteration. Meteor Planet Sci 33:1147–1157

Swindle TD, Podosek FA (1988) Iodine-xenon dating. In: Kerridge JF, Matthews MS (eds) Meteorites and the early solar system. Arizona University Press, Tucson, pp 1127–1146

Swindle TD, Caffee MW, Hohenberg CM, Lindstrom MM (1983) I-Xe studies of individual Allende chondrules. Geochim Cosmochim Acta 47:2157–2177

Swindle TD, Caffee MW, Hohenberg CM (1988) Iodine-xenon studies of Allende inclusions: EGGs and the Pink Angel. Geochim Cosmochim Acta 52:2215–2229

Swindle TD, Cohen B, Li B, Olson E, Krot AN, Birjukov VV, Ulyanov AA (1998) Iodine – xenon studies of separated components of the Efremovka (CV3) meteorite (abstract). Lunar Planet Sci 29:1005

Tomeoka K, Buseck PR (1990) Phyllosilicates in the Mokoia CV carbonaceous chondrite: evidence for aqueous alteration in an oxidizing environment. Geochim Cosmochim Acta 54: 1745–1754

Tomeoka K, Itoh D (2004) Sodium-metasomatism in chondrules in CO3 chondrites: relationship to parent body thermal metamorphism. Meteor Planet Sci 39:1359–1373

Tomeoka K, Kojima H, Yanai K (1989) Yamato-86720: a CM carbonaceous chondrite having experienced extensive aqueous alteration and thermal metamorphism. Proc NIPR Symp Antarct Meteor 2:55–74

Tomeoka K, Nomura K, Takeda H (1992) Na-bearing Ca-Al-rich inclusions in the Yamato-791717 CO carbonaceous chondrite. Meteoritics 27:136–143

Travis BJ, Schubert G (2005) Hydrothermal convection in carbonaceous chondrite parent bodies. Earth Planet Sci Lett 240:234–250

Ushikubo T, Guan Y, Hiyagon H, Sugiura N, Leshin LA (2007) ^{36}Cl, ^{26}Al, and O isotopes in an Allende type B2 CAI: implications for multiple secondary alteration events in the early solar system. Meteor Planet Sci 42:1267–1279

Van Schmus WR, Wood JA (1967) A chemical-petrological classification for the chondritic meteorites. Geochim Cosmochim Acta 31:747–765

Wark D (1987) Plagioclase-rich inclusions in carbonaceous chondrite meteorites – Liquid condensates? Geochim Cosmochim Acta 51:221–242

Wasson JT, Yurimoto H, Russell SS (2001) ^{16}O-rich melilite in CO3.0 chondrites. Possible formation of common, ^{16}O-poor melilite by aqueous alteration. Geochim Cosmochim Acta 65:4539–4549

Weinbruch S, Palme H, Muller WF, El Goresy A (1990) FeO-rich rims and veins in Allende forsterite: evidence for high temperature condensation at oxidizing conditions. Meteoritics 25:115–125

Weisberg MK, Prinz M (1998) Fayalitic olivine in CV3 chondrite matrix and dark inclusions: a nebular origin. Meteor Planet Sci 33:1087–1111

Weisberg MK, Prinz M, Clayton RN, Mayeda TK (1997) CV3 chondrites: three subgroups, not two (abstract). Meteor Planet Sci 32(Suppl):A138–A139

Weisberg MK, McCoy TJ, Krot AN (2006) Systematics and evaluation of meteorite classification. In: Lauretta DS, McSween HY Jr (eds) Meteorites and the early solar system II. Arizona University Press, Tucson, pp 19–52

Wick M (2010) Formation conditions of plagioclase-bearing type I chondrules in CO chondrites: a study of natural samples and experimental analogs. M.S. thesis, University of New Mexico

Young ED, Ash RD, England P, Rumble D (1999) Fluid flow in chondritic parent bodies: deciphering the compositions of planetesimals. Science 286:1331–1335

Young ED, Zhang KK, Schubert G (2003) Conditions for pore water convection within carbonaceous chondrite parent bodies — implications for planetesimal size and heat production. Earth Planet Sci Lett 213:249–259

Yurimoto H, Morioka M, Nagasawa H (1989) Diffusion in single-crystals of melilite: I. Oxygen. Geochim Cosmochim Acta 53:2387–2394

Yurimoto H, Ito M, Nagasawa H (1998) Oxygen isotope exchange between refractory inclusion in Allende and solar nebula gas. Science 282:1874–1877

Yurimoto H, Krot AN, Choi B-G, Aléon J, Kunihiro T, Brearley AJ (2008) Oxygen isotopes of chondritic components. In: MacPherson GJ (ed) Oxygen in the solar system, vol 68, Reviews in mineralogy and geochemistry. Mineralogical Society of America, Chantilly, pp 141–187

Zolensky M, McSween HY Jr (1988) Aqueous alteration. In: Matthews M, Kerridge JF (eds) Meteorites and the early solar system. Arizona University Press, Tucson, pp 114–143

Zolensky ME, Krot AN, and Benedix G. (2008) Record of low-temperature alteration in asteroids. In *Reviews in Mineralogy & Geochemistry*, Vol. 68 (ed. G. MacPherson), pp. 429–462. Mineralogical Society of America.

Zolotov MYu, MFeenko MV, Shock EL (2006) Thermodynamic constraints on fayalite formation on parent bodies of chondrites. Meteor Planet Sci 41:1775–1796

Index

D.E. Harlov and H. Austrheim, *Metasomatism and the Chemical Transformation of Rock*, Lecture Notes in Earth System Sciences,
DOI 10.1007/978-3-642-28394-9,

B